DEEP FOUNDATIONS INSTITUTE

43rd Annual Conference

Hilton Anaheim | California | October 24-27, 2018

2018

PROCEEDINGS



Advancements in Instrumentation and Monitoring

Advances in Stress-Wave Nondestructive Testing Methods for Evaluation of Deep Foundations

Alireza Kordjazi, Joseph T. Coe and Siavash Mahvelati

1

FDOT Method of Independent Separation of Tip and Skin Capacities of Driven Concrete Pile with Embedded Sensors

Sastry Putcha, Ph. D., P.E., Aneesh Goly, Ph.D., P.E., Kumar Allady, P.E., Vamshi Vemula and E.I.

4

New Technology of Force Monitoring of Post-Tensioning Ground Anchors

Lucian Bogdan and Shahid Islam

14

Optimal Subsurface Investigation Approach for Overhead Transmission Structures

Haijian Shi, Ph.D., P.E., P.M.P., Drew Pizzo and P.E.

22

Reducing Construction Interference When Implementing Geotechnical Instrumentation and Monitoring in Urban Excavation Projects

Zhangwei Ning, Martin B. Hudson and Daniel Brescia

33

Analysis, Design and Construction for Extreme Events

A Study in Extreme Event Large Displacement Analysis of Large Diameter Piles

Bret N. Lingwall, Ph.D., P.E. and Byron Foster

43

Design and Construction of the Summit Senior Care Facility into the Side of an Unstable California Hillside

Harry W. Schnabel, P.E., Patrick O. Shires and G.E.

53

Constructability Issues and Design Aspects

An Investigation of Grouted Pile Capacity Using Instrumented Pile Load Tests

Hayel M. El-Naggar, Research Assistant, Sherif A. Akl and Associate Professor

61

Deep Foundation Shoring in South Florida

Douglas C. Brunot

76

Drilled Pile Design and Installation Challenges in an Urban Environment

Luis Berroteran, P.E., Satyajit Vaidya, P.E., Rudolph Frizzi, P.E., G.E. and D.GE

84

Drilled Shaft Difficulties and a Micropile Solution

Paul Axtell, P.E., D.GE, David Graham, P.E., Jeff Jackson and P.E.

93

Foundation Design and Construction Challenges with Marsh Deposits in a High Seismic Risk Zone

T. Ted Miyake, P.E., M. Reza Saberi, P.E. and G.E.

104

Micropiles below Groundwater at the South Auditorium Block Site, Buffalo, NY

Mary C. Nodine, P.E., M. ASCE, Paul Eggers, P.E., M. ASCE, Michael P. Walker, P.E. and Donald E. Aubrecht

106

Pore Water Pressure Response and Effect on Installation Torque of Large Diameter Helical Piles in Soft Soils

M. Mae Benvenga, P.E., Howard A. Perko, Ph.D., P.E., Heather H. Trantham, Ph.D., P.E., P.Eng., D.GE. and P.M.P.

108

Rock Socketed Drilled Shafts in Electrical Substations

Steve Davidow, P.E., S.E., Senior Vice President, Brock Wallis and Vice President

118

Ground Improvement

Application of Mammoth Vibro-Tamper (MVT) for the Shallow Compaction at Airport Runway Expansion Project on Florida Limestone Ground

Mitsuo Nozu, President/CEO, Frank Vespi, Senior Project Manager, Kazunori Matsushita, Project Manager, Emi Walder and Administration Manager

126

Ground Improvement Design and Construction for Seattle's Elliott Bay Seawall Replacement and Retrofit

William Perkins, P.E., LEG, Andrew Malinak and Project Manager

136

Railroad Bridge Approach Embankment Settlement Mitigation

Moi Arzamendi, Jose Ramirez, Kenneth Kniss, James Gingery and Sunil Arora

138

Soil Improvement Technique to Mitigate Extreme Settlements on Deep Compressible Deposits in the Bogota Valley

Roger A. Archabal, P.E., Gustavo Langoni, P.E., Omar A. Conte and E.I.T.

148

The Deep Soil Mixing for the Galataport Project in Istanbul, Turkey

Marco Chiarabelli, Federico Pagliacci and Salvatore Miranda

159

Toward Understanding the Seismic Performance of Rigid Inclusions

James R. Gingery, Ph.D., P.E., G.E., Lisheng Shao, Ph.D., P.E., G.E., J. Tanner Blackburn, Ph.D. and P.E.

161

Innovation Techniques for Earth Retention and Stabilization

2D and 3D Finite Element Analyses for Cantilever Slurry Walls in Cohesionless Soil

Ali Helwa, Ph.D., Manal Salem, Associate Professor, Mostafa Mossaad and Former Professor

175

Development of a New, Advanced Form of Sodium Silicate for Chemical Grouting

Michael McDonald, Tim Evans, Julie Shang, Bingfeng Xue and Yu Guo

186

Innovative Riverbank Erosion Control Retaining Wall System for the Brazos River

Will Bohlen, P.E., Tracy Brettmann, P.E. and D.GE

200

Non-Conventional Practice: Recent Case Histories of the Use of Vertical Buttress Piles in Deep Excavation Support

Abid O. Adekunte, David Greentree, Tony Brunger and George Munteanu

210

Retrofitting Drainage Systems with Pressed-In Sheet Piles in Very Hard Soil of Southern California

Takefumi Takuma, Christopher DellAringa and Masashi Nagano

222

Lessons Learned (Case Histories/Innovations/Forensic Work)

Deep Soil Mixing for Contaminated Soil Remediation at a Superfund Site

Larry Stearns, P.E. and Lori Tiefenthaler

232

Design-Build of Watertight Underground Structures for Tunneling in Miami, Florida - The Norris Cut Utility Relocation Project

Terrence Carroll, P.E., G.E., May ElKhattab, P.E., Eugene Mirsky, P.E., Eloy Ramos, P.E., Jose Torres, John Wise and P.E.

240

Development of New Shaft Resistance Models for Piles Driven in the Puget Sound Lowlands

Youssef Bougataya, Geotechnical Engineer, Armin W. Stuedlein, Ph.D., P.E. and Associate Professor

250

Different Drilling Techniques in Challenging Geology at Seminole Hard Rock Hotel and Casino

Jonathan Delgado, Michael Arnold and Ph.D.

260

Foundation Base Material Strength Assessment for Drilled Pipe Piles Using Force and Displacement Data

Rozbeh B. Moghaddam, Patrick J. Hannigan, Frank Rausche and Geir Veslegard

270

Large-Scale Earthquake-Induced Landslide Repair Following New Zealand's Kaikoura Earthquakes

Mathew Avery, Project Development Engineer, Colby Barrett and CEO

280

Lateral Forces on Pile Due to Soil Slope Creep

David E. Albus, G.E., Bidjan Ghahreman, G.E. and Ph.D.

290

Supported Excavation Movement Causing Lateral Displacement and Cracks in Drilled Shafts - Lessons Learned from a Case Study in Chicago

Amaneh E. Kenarsari, Ph.D., Project Engineer, M. ASCE, Eric R. Borys, P.E., Senior Project Engineer, M. ASCE, Brett Gitskin, P.E., Senior Principal Engineer and M. ASCE

292

Tunnel Headwall Softeyes: Fiberglass Design Applications and Constructability Challenges

Shawna Munn, P.Eng., Jakub Huder and P.Eng.

302

Mega Projects (Projected Work/Risk Mitigation/Contractual Aspects)

Deep and Extra Deep Diaphragm Walls in Shanghai - Increasing Demand for Infrastructure in Megacities Drives the Requirement of Increasing Depth for Diaphragm Walls

Franz-Werner Gerressen, Arthur Bi, Wu Jie Mei and Li Yao Liang

312

Wanapum Dam Repaired Using Post-Tensioning Anchors

Abigail Stein, Assistant Project Manager, Aled Hughes, P.E., Principal, Civil Engineer, Rick Deschamps, P.E., Ph.D., Vice President of Engineering, Brian Barkauskas, P.E. and Business Development Director

322

Other Deep Foundations-Related Topics

Centrifuge Modeling of Temperature Effects on the Pullout Capacity of Energy Piles in Clay

Ismaail Ghaaowd, M.S., Ph.D. Candidate, John McCartney, Ph.D., P.E. and Associate Professor

324

Design Approaches for Externally Supported Earth Retaining Systems - Details and Limitations

Matteo Montesi and P.E.

331

Ensuring Performance of Tip Post-Grouted Bored Piles (Drilled Shafts) through a Comprehensive Quality Assurance Program

Antonio Marinucci, Ph.D., MBA, P.E., Silas C. Nichols, P.E., Mary Ellen Bruce Large, P.E. and D.GE

342

Extrapolation of Unit Side Resistance in Drilled Shaft Foundations Based on Bi-Directional Load Test Data

Joseph A. W. Toth and Ramin Motamed

351

New Focus: Environmental Impact Reduction of Proper Slurry Waste Management

Zachary Q. Maassen and E.I.T

361

Value Engineering of Reinforcement Used in Large Diameter Drilled Shafts

Shahid Islam and Lucian Bogdan

369

Performance Based Deep Foundation Design

Analyzing the Load-Transfer Behavior (T-Z Curve) for Instrumented Test Piles Driven in Clayey Soil

Murad Y. Abu-Farsakh, Ph.D., P.E., Research Professor, Md. Nafiul Haque, Ph.D. and Geotechnical Engineer

377

Deep Jet Grouting Grids for Support of a 42-Story Tower Designed Using Performance-Based Seismic Design

Lori A. Simpson, P.E., G.E., Scott A. Walker, P.E., G.E., David A. Shook, P.E., Roberto A. Lopez and P.E.

387

Reinforcement of Existing Deep Foundations with Micropiles

Freddy Lopez, Mauricio Terceros and Martin Achmus

398

Three-Dimensional Numerical Modelling of Load Distribution and Settlement of Pile Groups

Onur Kacar

408

Value Engineering - Design Risk and Reward at Major Sport Arena Projects

Diane Fiorelli, P.E., G.E., Jeremy Zorne, Timothy Siegel, P.E., Peter Faust and Dipl.-Ing.

418

Risk Assessment and Mitigation

Evaluating Geotechnical Resiliency Solutions in New York City

Karen C. Armfield, Gisele R. Passalacqua and Joanna Smith

421

Seismic Design/Soil Structure Interaction/Lateral Loading

Axial Cyclic Degradation of Marine Piles: A Strain-Based Fatigue Limit

Aaron S. Bradshaw, Ph.D., P.E., Ryan M. Coulson and E.I.T.

434

Behavior of Battered Piles under Lateral Loads in Sandy Soils

Mohamed Ashour, Associate Professor of Civil Engineering, Jogeshwar P. Singh, Ahmed AlaaEldin and Teaching Assistant

444

Comparison of Pile Foundations and Ground Improvement for Reduction of Seismic Displacements for a Wastewater Treatment Plant

Ali Ghandeharioon and Andrew Port

454

Development of Site-Specific Acceleration Response Spectra for a Liquefiable Bridge Site

S. Ali Bastani, Ph.D., P.E., G.E., F. ASCE, Ashley Varni, M.Sc. and E.I.T.

464

Kinematic Response Characteristics of a Piled Raft Foundation

Ramon Varghese, A. Boominathan and Subhadeep Banerjee

473

Load Transfer Curve of Piles in Sands under Uplift Forces

Mohamed Ashour, Associate Professor of Civil Engineering, Jogeshwar P. Singh, Aser I. Abbas and Project Engineer

484

Nonlinear Response of Piles with Rigid Embedment: Lessons Learned from a Reduced-Scale Experiment

Camilla Favaretti, Ph.D., Anne Lemnitzer, Ph.D., Benjamin Turner, Ph.D. and P.E.

495

Performance Based Seismic Retrofit Design of Brooklyn Basin Wharf

Sam Yao, Ph.D., P.E., Ali Naeem, P.E., Sara Barrett and P.E.

497

Seismic Hazards Evaluation and Lateral Pile Design in Diatomaceous Earth

Matt Steffan and Arash Khosravifar

508

Spring Constants of Belled Caissons for Seismic Retrofit of an Existing Critical Structure in a Seismically Active Area

Bidjan Ghahreman, David E. Albus and Ahmadreza Mortezaie

520

The Use of Seismic Trace Characterization to Guide the Analysis of DST Results to Obtain More Accurate Soil Parameters

Erick Baziw and Gerald Verbeek

533

PREFACE

On behalf of Deep Foundations Institute (DFI) and the 2018 Annual Conference Organizing Committee, we would like to extend our gratitude and appreciation to all attendees, exhibitors, underwriters, speakers, and session moderators who invested their time and energy to make the 43rd Annual Conference on Deep Foundations a successful event. The event took place near the magical grounds of Southern California's Disneyland resort in Anaheim, Calif. A conference filled with presentations, keynotes and panels featured engineering ingenuity across a wide range of deep foundation design and construction. Presentations covered topics including ever more challenging projects and project sites involving deep foundation systems, ground improvement and earth retention systems.

Under the conference theme, *Mastering The Challenge: Engineering for Complex Loading Conditions*, the organizing committee was motivated to highlight benefits of reaching beyond the code when executing 21st century performance-based geotechnical engineering. Project presentations of various styles and lengths featured design and construction accomplishments, from small to mega scale. One particular theme targeted California's key infrastructure: The California High-Speed Rail, and the Los Angeles Metro Extension. Both talks featured design and construction that push boundaries, whether via statnamic testing of extra-large diameter shafts or excavating to threatening 110 ft depth into ground filled with tar. For all of the sports fans, the presentations on three mega stadiums highlighted how value engineering changed the course of the construction and saved thousands of thousands of dollars in foundation production. Our keynote panel on performance based design consisted of carefully selected experts from structural and geotechnical engineering, industry and academia, and discussed the state of the art and vision for future performance based geotechnical design.

This year's Hal Hunt Lecture on Communications, DFI's premiere presentation on the topic, was given by Carl Lewis, 10-time Olympic Medal winner. His presentation, "Taking Command: You Can Do That," highlighted his story of discipline and success, the fight and win over life's challenges, leaving the audience encouraged and stunned – ready to set their own world records.

In addition to the technical tracks, keynote sessions and Hal Hunt lecture, the conference offered plenty of professional opportunities for networking, business relationship building and educating each other on the professions most recent products and inventions. As always, a special thanks to the many sponsors and exhibitors. These events would not be possible without their continuing faithful support.

Within this proceeding publication, technical papers presented during the 43rd Conference on a variety of sub-topics selected by the Organizing Committee are summarized: Performance Based Deep Foundation Design; Constructability Issues and Design Aspects; Seismic Design, Soil-Structure Interaction, and Lateral Loading; Ground Improvement; Advancements in Instrumentation and Monitoring; Risk Assessment and Mitigation, Lessons Learned (Case Histories, Innovations and Forensic Work), Innovative Techniques for Earth Retention and Stabilization; Analysis, Design and Construction for Extreme Events; Mega Projects; and Other Deep Foundations-Related Topics.

In closing we would like to acknowledge the help of all contributors at the DFI headquarters, who performed a master job of organizing, coordinating and advertising this wonderful event. Specifically, we would like to acknowledge Mary Ellen Large, P.E., D.GE, DFI's director of technical activities, who continuously supported the local organizing committee, as well as Lauren Nance and Angie Gibble, DFI's event specialists, who fabulously arranged the conference logistics. Our special gratitude goes to Theresa Engler, DFI's executive director, whose contribution and leadership continues to make DFI the most versatile and attractive organization in the foundation engineering community.

The local organizing committee is grateful for the support received throughout this planning process and expresses their gratitude to have been selected to serve the professional community with yet another outstanding DFI Annual Conference.

Conference Chair: Anne Lemnitzer, Ph.D., *University of California, Irvine*

Program Chairs: Rick Walsh, P.E., G.E., *Hayward Baker Inc.*

Reza Mortezaie, Ph.D, P.E., *Caltrans*

ADVANCES IN STRESS-WAVE NONDESTRUCTIVE TESTING METHODS FOR EVALUATION OF DEEP FOUNDATIONS

Alireza Kordjazi, Temple University, Philadelphia, PA, USA, 267-774-0428, a.k@temple.edu
Joseph T. Coe, Temple University, Philadelphia, PA, USA, 215-204-6100, joseph.coe@temple.edu
Siavash Mahvelati, Temple University, Philadelphia, PA, USA, 215-992-4180, smahvelati@temple.edu

ABSTRACT

This paper introduces recent advances in stress-wave NDT systems for use in assessments of in-service foundation integrity and drilled shaft construction. The primary results of the laboratory experiments are very promising, as the acquired image was capable of differentiating changes in pile cross section as low as 0.3 cm. The preliminary results with the same hardware components on a relatively large scale cemented sand model were also promising. A brief overview is provided of both systems including hardware, survey methods, and data processing techniques, followed by a discussion on application of the results to QA/QC of deep foundations.

Keywords: Nondestructive testing, Stress waves, Foundation integrity, Inspection, Defects, Quality control, Quality Assurance, Scaled laboratory models, Numerical modeling.

INTRODUCTION

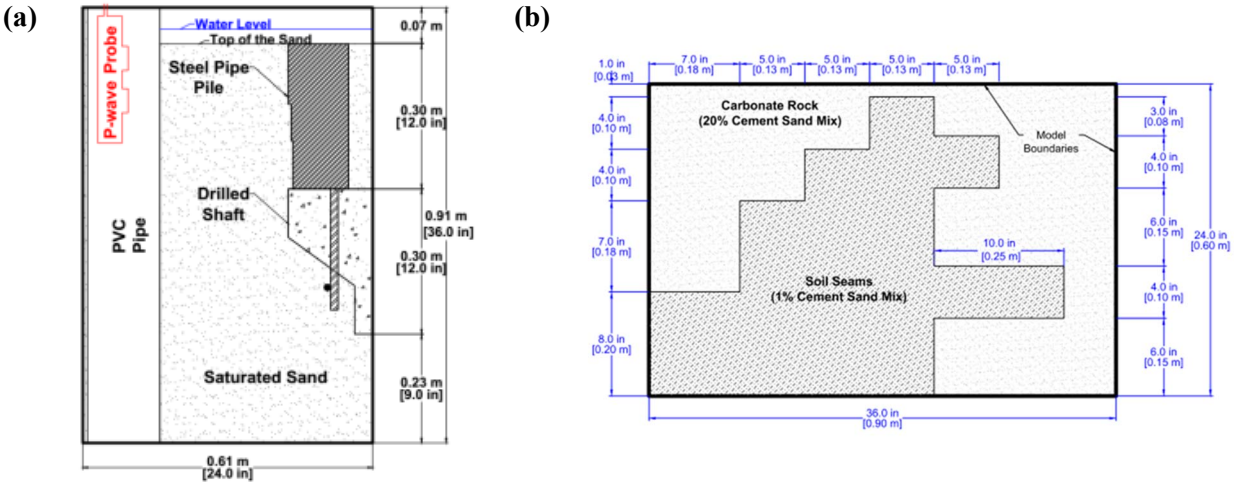


Fig. 1. Laboratory models: (a) in-service foundation defects; and (b) karst beneath drilled shaft.

There are two main applications in which current QA/QC NDT technology fails to provide sufficient information regarding deep foundation conditions: (1) detection of flaws in outside cover concrete of drilled shafts and corrosion in steel piling; and (2) evaluation of anomalies beneath the bottom of drilled shaft excavations. Previous studies have demonstrated the capabilities of high frequency stress waves for geotechnical and foundation evaluation purposes (Lee and Santamarina 2005; Coe and Brandenberg 2010; Coe and Brandenberg 2012; Coe and Kermani 2016). Higher frequency waves can visualize smaller anomalous features at the expense of higher attenuation and smaller propagation distance. Therefore, the goal of this study was to advance the state of NDT practice by development of a prototype high resolution stress-wave imaging system as proof-of-concept. The equipment and hardware were modular, which allowed simultaneous development of two system configurations for application to in-service foundations as well as drilled shaft excavations during construction. Results are presented based on two large scale soil models. The first laboratory model simulated section loss in an in-service steel

© 2018 Deep Foundations Institute

pipe pile and drilled shaft foundation (Fig. 1a). The second model simulated anomalous conditions beneath drilled shafts excavations as might be encountered in areas with significant karst (Fig. 1b). For both models, evaluation of foundation conditions relied on the propagation of small amplitude seismic stress waves using hardware similar to those described in Coe and Brandenberg (2010) and Coe and Brandenberg (2012).

DATA ANALYSIS AND RESULTS

Figure 2a presents the P-wave reflection signals acquired for the foundation defect model. Clearly visible are reflections from the steel pipe pile and from the drilled shaft, including the exposed steel rebar and anomalous void. The resulting reflection image sufficiently tracks the foundation elements so that conclusions can be made regarding geometry. However, the system in its current configuration can only evaluate exposed lengths of rebar and not rebar inside cover concrete. Based on first arrivals, Fig. 2a was used to estimate the thin section loss (8 mm) and total section loss (3 mm). These results agree reasonably well with the known differences in wall thickness between the sections (6 mm for the thin section, and 3 mm for the total loss section).

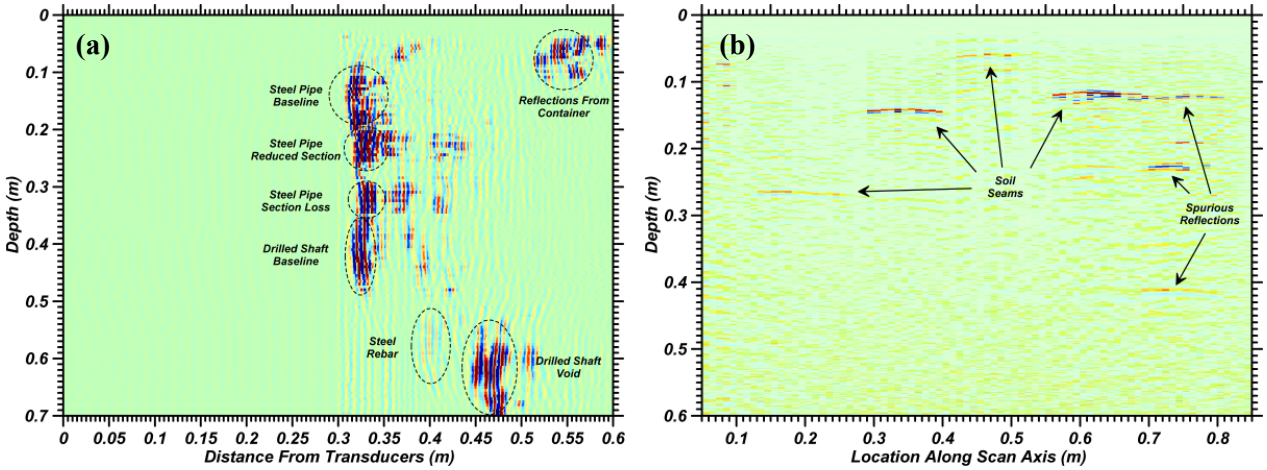


Fig. 2. Reflection images: (a) in-service foundation model; and (b) karst drilled shaft model.

Figure 2b presents the S-wave reflection signals acquired for the karst model. Generally, the estimated geometry of the soil seams agreed well with actual model dimensions. Strong reflections are clear from 0.13 m to 0.40 m along the horizontal scan axis that represent the vertical seams located at depths of 0.27 m and 0.15 m. Additionally, from 0.56 m to 0.70 along the position axis the horizontal seam can be identified at a depth of 0.12 m. These observations match well the expected location of the anomalies in the model. No meaningful evidence is present of the deepest vertical seam in Fig. 2b. This is also the case with the deepest horizontal seam located towards the far right side of Fig. 1. This suggests a lack of signal penetration owing to the very high operating frequency of the transducers (250 kHz). For practical field application, the depth of investigation would certainly need to be increased so that anomalous features affecting drilled shaft tip capacity could be explored (e.g., several meters below the shaft tip).

CONCLUSION

This paper presented ongoing efforts related to stress-wave NDT advancements and applications to QA/QC of deep foundations. Two ultrasonic transducer NDT systems were used on reduced scale laboratory soil models to evaluate the geometry of anomalous conditions in deep foundation elements. The results with the proposed NDT system in this study exhibited strong reflections from segments of a steel pipe pile that was machined to mimic section loss due to corrosion. The estimates of section loss

compared favorably with true foundation geometry. Additionally, the proposed NDT system was capable of locating a large void and the presence of rebar in an in-service drilled shaft element. A similar system was developed to be placed at the bottom of drilled shaft excavations for locating anomalous karst conditions prior to placement of concrete/rebar. Results from laboratory testing demonstrated some promise, but the system suffered from inadequate depth of investigation and limited applicability for resolving the true geometry of anomalous low velocity zones in rock. Future efforts in stress wave NDT should continue to address the advancements highlighted in this study for QA/QC of deep foundations. In particular, the proposed NDT methodologies require significant resources for scaling to field production. Nevertheless, it is clear that advancements in NDT technologies as highlighted in this paper will be necessary to ensure that QA/QC of foundation systems continues to address limitations in the current standard of practice.

REFERENCE

Coe, J. T. and Brandenberg, S. J. (2010). "P-wave Reflection Imaging of Submerged Soil Models Using Ultrasound." J. Geotech. Geoenviron. Eng., 136(10), pp. 1358-1367.

Coe, J. T. and Brandenberg, S. J. (2012). "Cone Penetration Test-Based Ultrasonic Probe for P-wave Reflection Imaging of Embedded Objects." J. Bridge Eng., 17(6), pp. 940 – 950.

Coe, J.T., and Kermani, B. (2016). "Comparison of Borehole Ultrasound and Borehole Radar in Evaluating the Length of Two Unknown Bridge Foundations." DFI Journal, 10(1), pp. 8-24.

Lee, J.S. and Santamarina, C.J. (2005). "P-Wave Reflection Imaging." Geotech. Test. J., 28(2), pp. 197 – 206.

FDOT METHOD OF INDEPENDENT SEPARATION OF TIP AND SKIN CAPACITIES OF DRIVEN CONCRETE PILE WITH EMBEDDED SENSORS

Sastry Putcha, Ph. D., P.E., Smart Structures, 4152 W Blue Heron Blvd, Suite 1114, Riviera Beach, FL, USA, 561-988-0070, sputcha@smart-structures.com
Aneesh Goly, Ph. D., P.E., Smart Structures, 4152 W Blue Heron Blvd, Suite 1114, Riviera Beach, FL, USA, 561-988-0070, agoly@smart-structures.com
Kumar Allady, P.E., RADISE International, 4152 W Blue Heron Blvd, Suite 1114, Riviera Beach, FL, USA, 561-841-0103, kumar.allady@radise.net
Vamshi Vemula, E.I., RADISE International, 4152 W Blue Heron Blvd, Suite 1114, Riviera Beach, FL, USA, vamshi.vemula@radise.net

ABSTRACT

Current dynamic testing practice to obtain pile total capacity will not yield optimum capacity due to the strain incompatibility between the side and tip resistances during driving. Superposition of end of initial drive- static tip capacity and the peak static skin capacity during beginning of restrike and adding them is the preferred method. The FDOT method determines independent pile static tip and skin capacities in real time analyzing appropriate blows from the embedded tip and top data of the Embedded Data Collectors (EDC). This data is collected through a wireless radio transmitter, receiver, and laptop software. The approach utilizes EDC tip and top data and nonlinear single degree of freedom system to satisfy force and energy equilibrium with a global genetic inversion analysis. Top impacted energy equals at pile tip as sum of Static, Damping and Inertial energy providing independent tip resistance. With EDC sensors as boundary conditions, pile is divided into desired segments and using global inversion techniques one dimensional equation is solved for independent skin friction for every blow. EDC data compared close static load test results. The EDC - FDOT method has enabled cost effective 100% testing of driven piles cost effective.

Keywords: Embedded, Sensors, Tip, Skin, Independent, Capacity, Settlement, FDOT, UF, Dynamic Testing

INTRODUCTION

Historical documentation has shown that not only driven piles have a long history of usage but also continues to advance unceasingly till today. Historians placed the first pile driving using timber piles in the 4th century BC. While modern pile driving systematically started around nineteenth century, the credit for conceiving the idea of the applicability of wave equation to driven piles goes to David Victor Isaccs of Australia. His 1931publication “Concrete Pile Driving Formulae” provides the basis for modern pile driving using stress wave theory. He felt that the dynamic formulae then in use lacked the capability of detecting integrity and hence developed stress wave theory. This work was further developed starting in 1938 by W.H. Glanville and colleagues of British Building Research Board as they developed the first solution to the wave equation. But these early efforts have really taken off only with the advent of computers. E.A.L. Smith (1960) published ‘Pile Driving Analysis with the Wave Equation’ and provided first numerical solution to the wave equation. Within few years, the FHWA funded research and in due course this effort ushered the era of externally instrumented pile driving.

CURRENT PILE DRIVING PRACTICES

Present practice of dynamic testing is to evaluate static pile capacity from a single hammer blow. But this practice will not yield optimum capacity due to the strain incompatibility between the side and tip resistances during pile driving. With increasing usage of High Strain Dynamic Testing (HSDT) the engineering community started paying more attention to the dichotomy between skin and tip mobilization. With this

© 2018 Deep Foundations Institute

background the advancements in dynamic testing continued and the joint efforts of Florida DOT (FDOT) and University of Florida (UF) resulted in embedded sensor technology.

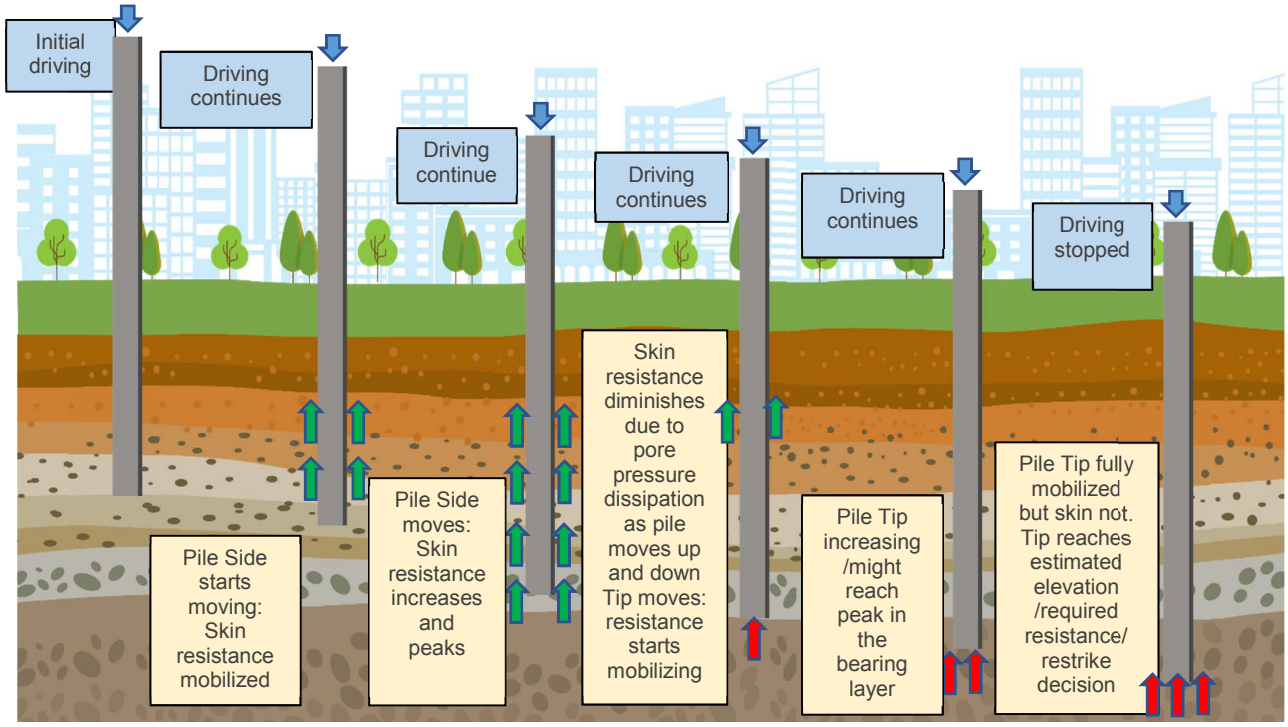


Fig. 1. Illustrates the strain incompatibility between tip and side mobilizations during pile initial driving (Putcha, Kumar, Goly, 2017, presentation ASCE conference-Orlando 2017)

NCHRP 418 Synthesis (2011) elaborated that the effect of strain incompatibility between side and base resistance during HSDT, results in the side resistance mobilizing and increasing and after some more blows diminishes after several blows before base resistance is fully mobilized. NCHRP therefore recommends that the "use of superposition to combine the back-calculated base resistance from a pile on initial drive or from a blow on redriving the pile with the back-calculated side resistance from the early blows at the beginning of restrike. This practice is perceived to overcome the limitations of HSDT related to the reduction in side resistance observed during driving that may occur before full mobilization of the base resistance".

FDOT-UF EFFORTS

After three to four decades of dynamic testing of driven piles using external gauges attached at the top of the pile along with user dependent signal match analysis, Florida Department of Transportation (FDOT) construction engineers started asking several questions. These can be summarized as follows:

- What if concrete piles could be instrumented without climbing the leads
- What if the labyrinth of wires obstructing the movement of personnel could be eliminated?
- What if pile testing did not impact construction operations?
- What if all foundations could be monitored and obtain real-time pile capacity instead of separate signal match analysis and avoid the blow count criteria.
- What if the driving stresses at the pile tip could be measured instead of estimations?

- What if such a technology could be developed at affordable cost while offering economical and safe construction environment?

The efforts to achieve resulted in the joint efforts of FDOT and UF (2002) resulting in embedded sensor technology.

EMBEDDED SENSOR TECHNOLOGY

The EDC system involves the use of internal embedded sensors located at both top and tip of a pile, a wireless radio transmitter a receiver, and laptop software to analyze the data. The EDC system does not require external wires and records information at both the top and the tip of the pile. Tip data along with top data is analyzed to measure the driving stresses and to provide independent tip and skin resistances in real-time for every hammer blow. Sensor packs consisting of accelerometers, strain gauges and temperature sensors that are embedded at the pile top and tip during casting provide valuable measurements.

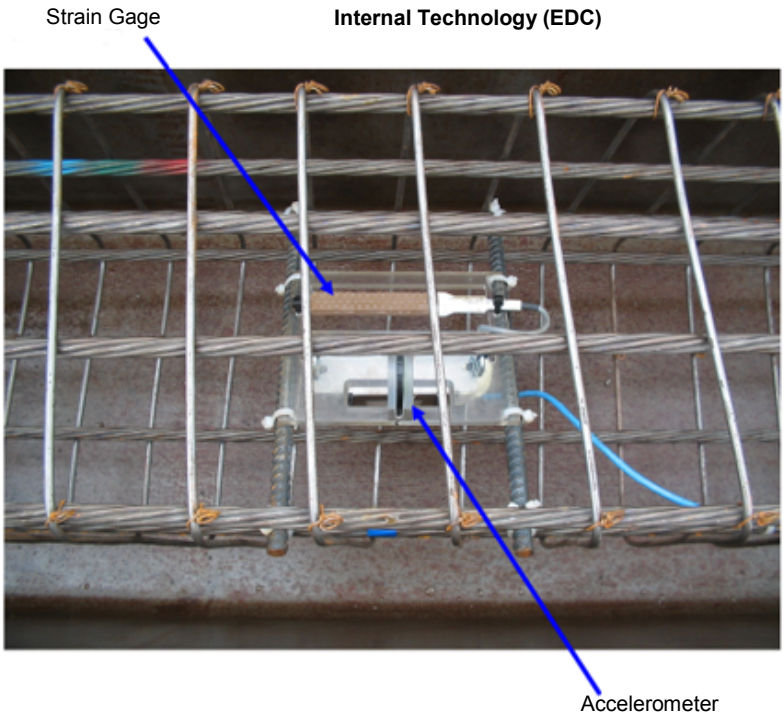


Fig. 2. Sensor pack consisting of accelerometer, strain guage and temperature sensor embedded before concrete placement (FDOT-UF 2002)

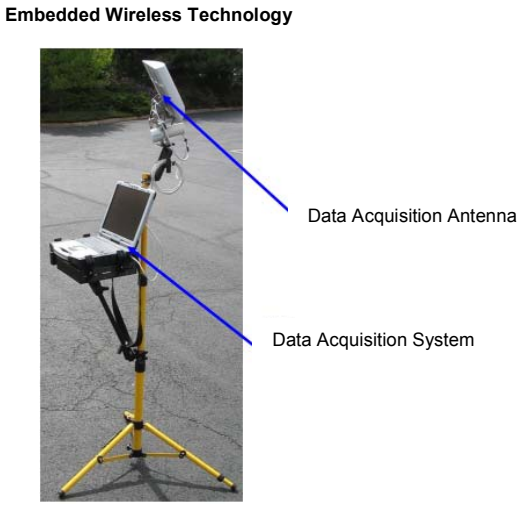


Fig. 3. Embedded Sensor System Details of Data Acquisition and Transmission

Software program developed by UF and named UF Method is used to analyze pile tip and top data. This data analysis calculates damping factor for every hammer blow. Thus, the UF Method is an advancement in the dynamic testing process. The previous technology of external gauge dynamic testing method uses Case Method to calculate the Static Tip Capacity by subtracting damping from the Total Dynamic Capacity. The damping factor used is constant and was input in the Case Equation. But in the UF Method, the damping factor is calculated for every blow from the tip and top data analysis and is the input in Case Equation to extract total static resistance.

UF method uses unloading point method to obtain static tip capacity. Unloading point approach formulates that unloading point of zero velocity occurs after the peak dynamic force is attained (Middendorp et al. 1992). Static resistance equals applied force when damping is zero.

$$F_{static} = F_{statnamic} - (ma)_{foundation} \quad [1]$$

where $F_{statnamic}$ is the applied force, F_{static} is the static tip resistance; m = mass and a = acceleration of the foundation which is considered negligible.

With known total resistance and tip resistance, UF Method allows for the separation of static and dynamic resistances in real time.

FDOT METHOD

Embedded tip and top data analysis further advanced into what is called FDOT Method of Analysis

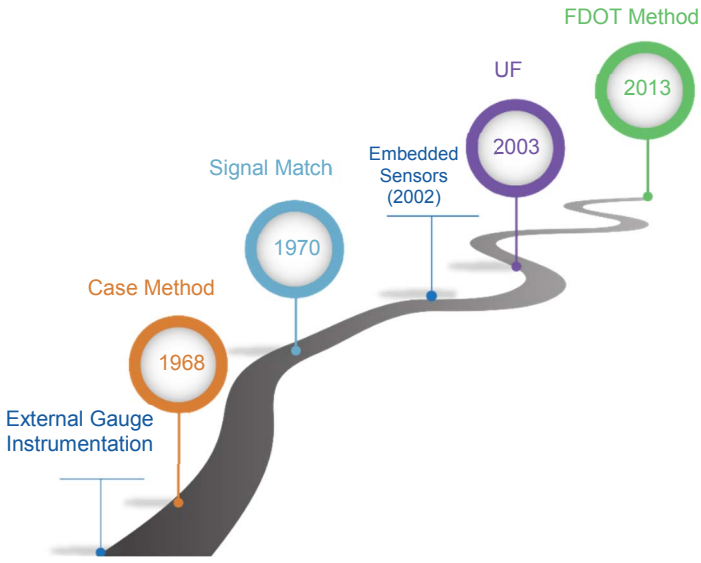


Fig. 4. Chronological advancement of instrumented dynamic testing (Putcha, Kumar, Goly, 2017)

This method measures driving stresses and determines independent static tip and skin resistances in real time analyzing the data collected for om tip and top embedded instrumentation.

TIP RESISTANCE ESTIMATION

In simple terms, applied energy as recorded in the tip gauge is the sum of static, damping and inertial energies. By balancing force and energy from inertia, damping, and stiffness against the measured tip data, the unknown parameters (mass, damping, and nonlinear stiffness) and the nonlinear static tip resistance are estimated. Since the applied force is measured directly, the tip analysis is independent of the skin analysis.

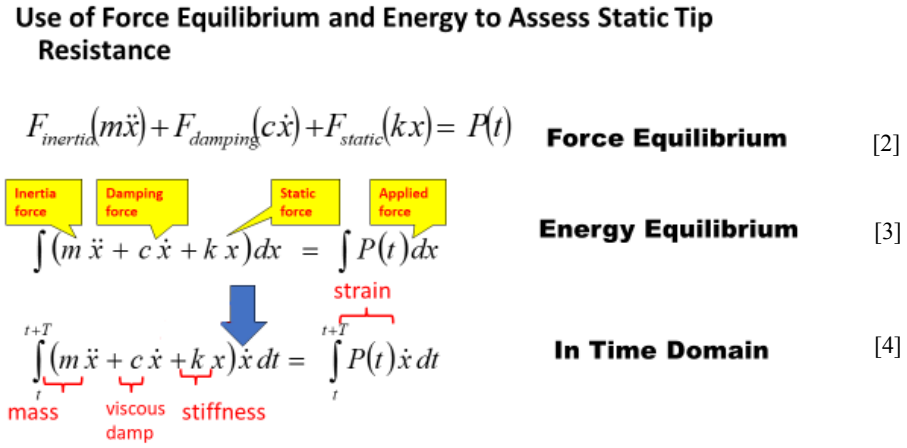


Fig. 5. Estimating static tip resistance of driven piles with bottom pile instrumentation (Tran, McVay, Herrera, and Lei, Canadian Geotechnical Journal, Vol. 49, April 2012)

Where $F_{inertia}$ = pile inertial force; m = pile mass; $\ddot{x}$ = acceleration); $F_{damping}$= damping force from soil; c = damping factor; $\dot{x}$ = velocity; F_{static}= static soil resistance; k = spring stiffness; x = measured displacement; P = applied force; t = time domain.

SKIN RESISTANCE ESTIMATION

The soil–pile system is modeled as a combination of pile segments with nonlinear skin friction and damping acting on each segment. Wave propagation in the pile segments is modeled with a 1-D partial differential equation. Monitored strains and accelerations at the top and bottom of a pile during a hammer blow are used to solve for the unknowns, like damping and loading and unloading stiffness in each segment in solving wave equation. Nonlinear skin friction is thus obtained.

Independent tip resistance and skin resistances contribute to Accurate Total Pile Resistance (Capacity) and the Total Pile Resistance(Capacity) = EOID tip resistance + BOR Peak Skin resistance. The FDOT Method enables selection of most suitable blow to analyse independent tip resistance and skin resistance. This provides an advantage to both the contractor and the engineer during construction contributing to optimization of foundation installation. For instance, independent skin resistance quantifies resistance loss due to pile jetting and preforming without depending on estimation.

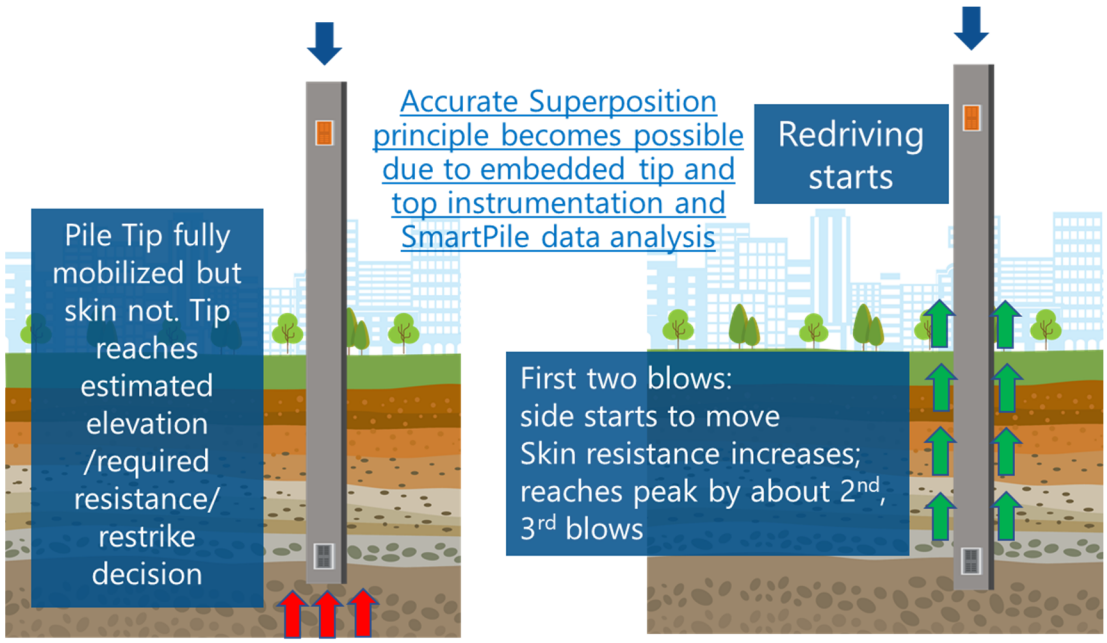


Fig. 6. FDOT Method – Independent Skin and Tip Capacities (Putcha, Allady, Goly 2017)

Since optimum tip and skin settlements do not occur at the same hammer blow, appropriate blows are analyzed to obtain optimum tip and skin settlements and resistances during both the EOID and BOR. Total capacity is the sum of these skin and tip capacities. This method demonstrates the Pile-Soil interaction during pile driving. Quantitative independent skin resistance and tip resistance provides several options to the stakeholders resulting in economical and accelerated construction in a safe environment.

100% DYNAMIC TESTING A REALITY—MINIMIZED UNCERTAINTIES

The nature of Embedded Data Collector technology has made 100% testing of driven pile foundations in a project cost effective. Due to100% testing of the foundations in a project with EDC instrumentation in the pile top and tip of each pile, uncertainties associated with probabilities of failure inherent in the nonhomogeneous materials in horizontal and vertical directions are minimized.

EDC technology with embedded top and tip gauges enabled practical, simplified measurement based 100% testing of driven piles more practical. With signal match being done automatically for every blow due to the data available from embedded top and tip instrumentation, 100% pile driving is achieved seamlessly. Once pile is brought to site, it is ready to be driven and contractor can keep driving pile after pile, with no waiting, thereby increasing the productivity and economy for the contractor. Due to measured driving stresses, pile cushions don't have to be changed arbitrarily but changed only when stresses exceeding the allowable limits thus resulting in savings.

Before the advent of EDC technology, it was not practical to do dynamic testing on 100% of the piles with top mounted technologies. While 100% monitoring was done, 100% signal match was not done on every pile since signal matching on each blow is simply impractical. Instead only 10% or less of signal match is done. Top mounted gauge system is a 2-step process of field measurements, followed by signal match analysis in the office. Even with 2 step process skin and tip capacities are only estimates and vary from individual to individual preforming the analysis.

SUPERPOSITION

Only EDC with top and tip instrumentation data analyzed by FDOT method of analysis could determine independent tip and independent skin resistances. By superposition of these, total pile bearing resistance can be obtained. But what is the basis for this superposition? There does exist data on measured vs. predicted resistances for independent side and tip, as well LRFD phi values for side, tip and total resistance (FDOT-UF (2013 and 2015). Consequently, the use of superposition i.e. adding skin friction from BOR and tip resistance from EOID is possible. But all studies on LRFD phi assessment for top mounted gauges with signal match report Phi values for one blow which uses both the side and tip resistance for that blow (i.e. no superposition). That is why top mounted gauges report different phi values for BOR and EOID blows (NCHRP 507 and FDOT-UF--2013 and 2015). Unfortunately, many consultants use superposition with top mounted gauges equipment, but there doesn't exist any data on LRFD phi for this important case.

The rationale of separation of tip and skin resistance is based on the dichotomy of optimum tip and skin mobilizations occurring at different times of different drive blows during pile driving operations. The optimum tip mobilization is achieved during End of Initial Driving (EOID); optimum skin mobilization occurs during beginning of redrive (BOR). Superposition is sum of these two independent resistances.
In summary, dynamic testing with only top mounted gauges system cannot obtain independent tip and independent skin resistances. The top mounted gauge system technology has been adding only estimated tip and skin resistances obtained from a single blow and this is not true superposition.

FIELD EXAMPLE- FDOT METHOD RESULTS

Subsurface Soils at Caminada Bay (Bent 7 location)

The project site is at Caminada Bay, Louisiana, 0.62 mile south of New Orleans. The subsurface soils consist of two uppers layers: 33 ft. of silty fine sand with clay (SPT N ~ 14) followed by zone of 33ft. of fine sand with silt (SPT N ~ 24); underlain by a high plasticity ($40 < PI < 70$) clay. The piles at the site are 30 sq. in. precast prestressed concrete pile installed about 70 ft. below the ground surface. Restrikes were conducted one month after installation, and the static compression load test was conducted 2 days after the restrikes.

Caminada Bent 7: FDOT Method of Analysis results compared with Static Load Test Results

Project EDC drive data is analyzed by UF Method for every blow resulting in Static Total and Static Tip capacities. Also obtained are the related information driving stresses, energy transferred to the pile, blow count per foot, hammer stroke length and integrity verification data. Due to measured driving stresses, pile cushions don't Next, the final ten blows before driving stopped are examined to select proper blows for analysis by the FDOT Method. Criteria for blow selection is based on load settlement considerations and consistency of energy and drive blows.

Selected EOID (01/27/2010, 1:49 pm) Blow 311 for analysis of Tip resistance = 25 kips (see Fig.7)
Selected BOR (02/24/2010, 3:26 pm) Blow 321 for analysis of Skin resistance = 531 kips (see Fig.8)
Total Capacity is sum of Tip Resistance and Skin Resistance = 556 (531+25) kips (seeFig.9)
Static Load Test capacity: 625 kips (Reference Fig 2-5 and section 5.3.2 from UF 2013 Report)

Table 1. (Embedded data collector (EDC) evaluation phase II – comparison with instrumented static load tests- McVay M.C., and Wassman, S.J., UF-FDOT final report (BDK75 977-24, 2013); (Reference Table 4.1 from UF-FDOT final report (BDV31-977-13, 2015)

Pile Number	Site and Location	Pile Dimensions		Measured Pile Capacity (Davisson)		
		Width (ft)	Length (ft)	Tip (kips)	Skin (kips)	Total (kips)
2	Caminada Bay Bent 7, Louisiana	2.5	69	80	545	62 5

Static Modulus = $57\sqrt{f'c}$ ski $=57*(6000)^{0.5}=4415$ ksi (using 28-day concrete strength of 6000 psi)

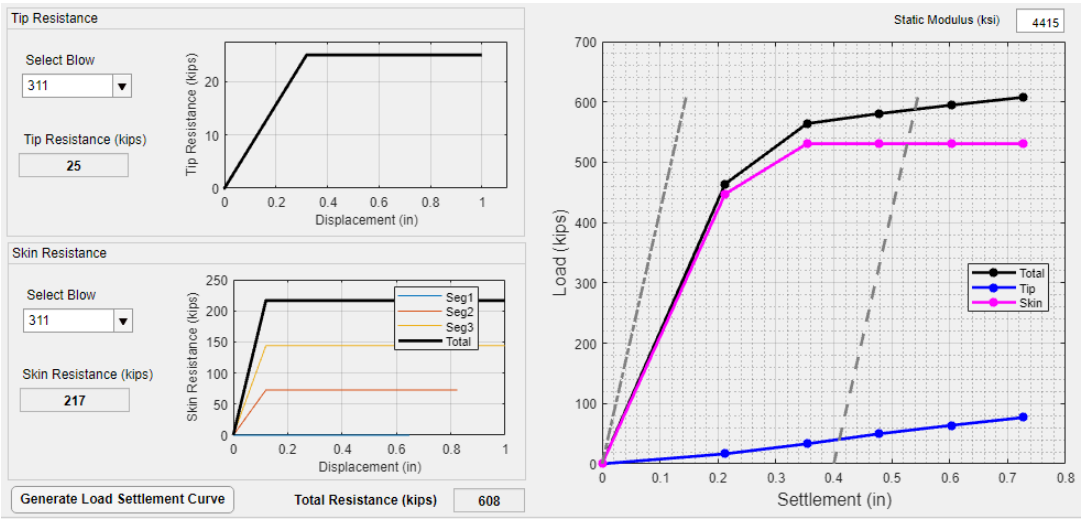


Fig. 7. Tip Resistance vs. Displacement; Skin Resistance vs. Displacement for selected EOID blow 311

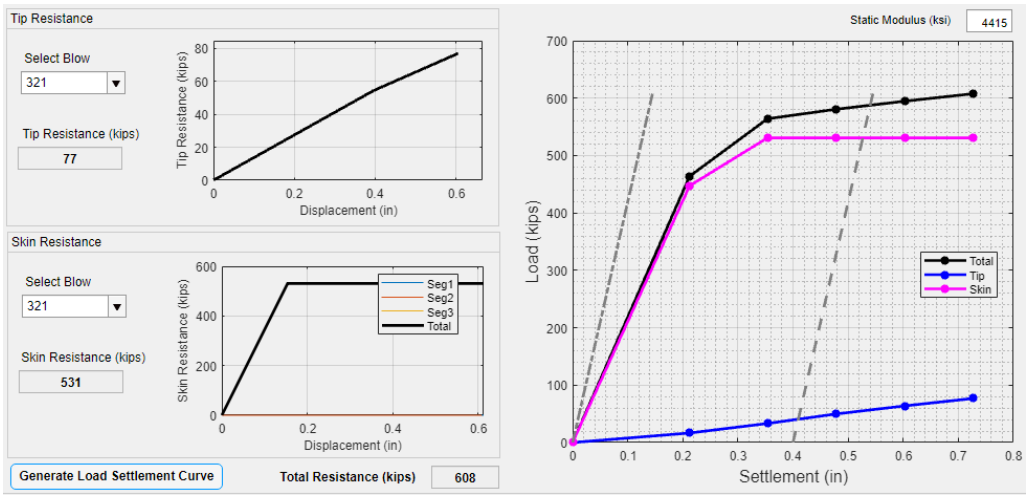


Figure. 8. Tip Resistance vs. Displacement; Skin Resistance vs. Displacement for selected restrike blow 3

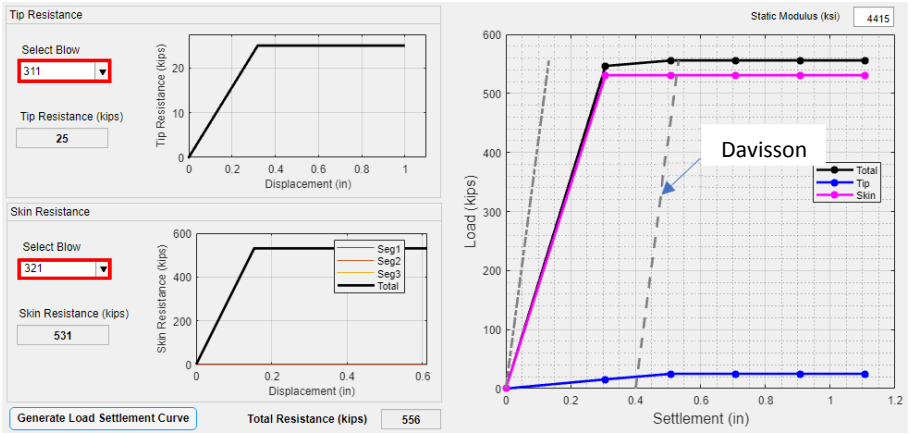


Figure. 9. Superposition of Tip Resistance Obtained from EOID blow 311 and Skin Resistance Obtained from blow restrike 321 to obtain Total Pile Resistance

SUMMARY AND CONCLUSIONS

Embedment of sensor pack instrumentation in concrete pile tip and top led the way to advance dynamic testing. Two types of analysis of the pile tip and top data area advanced. 1.UF Method and 2. FDOT Method. From UF Method, pile total Capacity and tip capacity can be obtained. With FDOT method of analysis, tip and skin resistances can be obtained independently. Since optimum tip and skin settlements do not occur at the same hammer blow, appropriate blows are analyzed to obtain optimum tip and skin settlements and resistances during both the End of Initial Drive and Beginning of Restrike. Total pile capacity is the sum of the optimum tip and skin and capacities. Also, pile freeze condition can be assessed by this process. This process of superposition remedies the strain incompatibility of skin and tip mobilizations which has been problem associated with High Strain Dynamic testing (HSDT). FDOT method made significant strides in choosing the proper blows to analyze for static tip and skin resistance. Independent skin resistance quantifies pile jetting and preforming skin resistance losses.

With the advent of EDC technology, 100% pile installation in a project became reality resulting in

construction savings. The EDC system requires no external wires. Since instrumentation is embedded, climbing leads are not required creating safer work zones. EDC instrumentation costs will be mostly offset by efficiencies from using an increased resistance factor. Construction savings occur due to measured driving stresses. Therefore, measurement based decision for pile cushion could be applied. Other construction savings include Speed of Construction, Reduction in Pile Driving Claims, Reduced Need for Verification Testing on Design Build Projects: Pile Capacity is verifiable without the normal verification testing associated with Design-Build Projects.

Finally, the EDC technology savings can be categorized as Time Savings, Material Savings, Labor Savings and Safety related savings.

ACKNOWLEDGEMENT

We acknowledge our appreciation of technical help by Dr. Michael McVay, Professor, University of Florida and Alekhya Kondalamahanthy, RADISE International, Florida. We thank Florida Department of Transportation for its continued support of EDC technology.

REFERENCES

Brown, Dan A. and Thompson III, W. Robert, 2011. NCHRP Synthesis 418: Developing Production Pile Driving Criteria from Test Pile Data, Dan Brown Associates, Sequatchie, Tennessee.

Gerald E.H. Verbeek, 2017. 30 years of experience with the wave equation solution based on the method of characteristics mpeter Middendorp, Profound BV, Waddinxveen, the Netherlands, VMS-profound,Tyler, TX, USA https://vulcanhammerinfo.files.wordpress.com/2017/08/middendorp.pdf.

Isaacs and Glanville, 2017. The beginnings of the wave equation for piles, (https://vulcanhammer.info/2017/09/18/isaacs-and-glanville-the-beginnings-of-the-wave-equation-for-piles/), https://www.aeyates.co.uk/tritech-ground-engineering/about/history.

Khiem T. Tran, Michael McVay, Rodrigo Herrera, Peter Lai, 2012. Estimation of nonlinear static skin friction on multiple pile segments using the measured hammer impact response at the top and bottom of the pile; Computers and Geotechnics.

McVay M.C., and Wassman, S.J., 2013. Embedded data collector (EDC) evaluation phase II – comparison with instrumented static load tests-final report submitted to FDOT, December.

McVay M.C. and Wassman, S.J., 2015. Embedded data collector (EDC) phase II load and resistance factor design (LRFD)- final report submitted to FDOT, September.

Smith, E.A.L., 1960. Pile Driving Analysis with the wave equation. Journal of Soil Mechanics and Foundation Engineering, ASCE, no. 86, August.

Tran K.T., McVay M., Herrera R., and Lai P., 2012. Estimating Static Tip Resistance of Driven Piles with Bottom Pile Instrumentation, Canadian Geotechnical Journal.

NEW TECHNOLOGY OF FORCE MONITORING OF POST-TENSIONING GROUND ANCHORS

Lucian Bogdan, DYWIDAG-Systems International, Long Beach, CA, USA, 1-562-295-3907, lucian.bogdan@dsiamerica.com

Shahid Islam, DYWIDAG-Systems International, Bolingbrook, IL, USA, 1-630-972-4028, shahid.islam@dsiamerica.com

ABSTRACT

There is a rapid expansion of world's infrastructure and simultaneously existing infrastructure is aging. The maintenance of infrastructures has been of particular concern to the engineering community. Monitoring and evaluating the structures have become more significant than ever. Ground anchor is an important part of the structure where it is installed. Unfortunately there are limited testing methods available to assess the force in the pre-stressing steel. High cost, complicated equipment and limitation of space often prevent these methods from being implemented. DYNA Force sensors have been developed to measure the force in the pre-stressing steel during construction and at any time during the lifetime of the structure. These sensors make use of the magneto-elastic properties of ferrous materials. A readout unit is designed to magnetically energize the steel through the sensor and measure the response of the steel to the process. The readout unit then converts the response into a direct force reading. They can be used for bare, epoxy-coated, galvanized and greased-sheathed steel in the bonded, un-bonded, grouted or un-grouted length of the tendon. It measures the force of the steel element at the location where it is installed and can be recorded manually, automatically, or remotely. The sensor is robust, requires no maintenance and it is expected to have a similar service life to that of the surrounding structure. Sensors have received attention in terms of accuracy, performance, ease in installation, durability, and cost effectiveness. Sensor readings provide a second measurement, in conjunction with the jack pressure gauge, of the post tensioning force during initial testing procedure for ground anchors. This paper describes its application in tie-back and tie-down anchors and force monitoring of retaining walls, bridge abutment and dams where the data were collected manually, automated and remotely.

Keywords: post-tensioning, force monitor, sensor, tie-back, retaining wall, dam

INTRODUCTION

Our infrastructure is expanding and the existing infrastructure is aging. Some structures are expensive to maintain and some occasionally fail. There is a large demand for implementing health monitoring of structures. Many tie-backs, retaining walls, dams and other geotechnical structures are post-tensioned and many of them need repair using a post-tensioned system. On many occasions during construction and service life of the structure, it is useful to know the force in the post-tensioning and anchor system. Many piles and drilled shafts are designed using reinforcing steel and the compressive forces in reinforcement are unknown. Although there are many methods to measure the tendon force, most of them are cumbersome, expensive, and the accuracy varies depending on the method used.

The elasto-magnetic (EM) technology is a novel approach to monitor forces in steel elements. The DYNA Force sensor is built based on EM technology (See Fig. 1). It is composed of a primary coil and a secondary coil (sensing coil). By passing current through the primary coil, ferromagnetic material is magnetized. The sensing coil picks up induced electromotive force that is proportional to change rate of applied magnetic flux (Faraday's law) and relative permeability. As permeability of core changes, output voltage changes.

© 2018 Deep Foundations Institute

The output voltage is calibrated to measure the force. A readout unit is designed to magnetically energize the steel through the sensor and measure the response of the steel to the process. The readout unit then converts the response into a direct force reading. The sensor has an embedded thermistor which allows for temperature compensation. Due to the diversity of the magnetic property of steel, calibration is done for each type of steel allowing the sensors to perform at their highest accuracy.

$$\varepsilon = -\frac{d}{dt}(\phi_B)$$

Where, $\varepsilon =$ electromotive force

$\phi_B =$ Magnetic flux

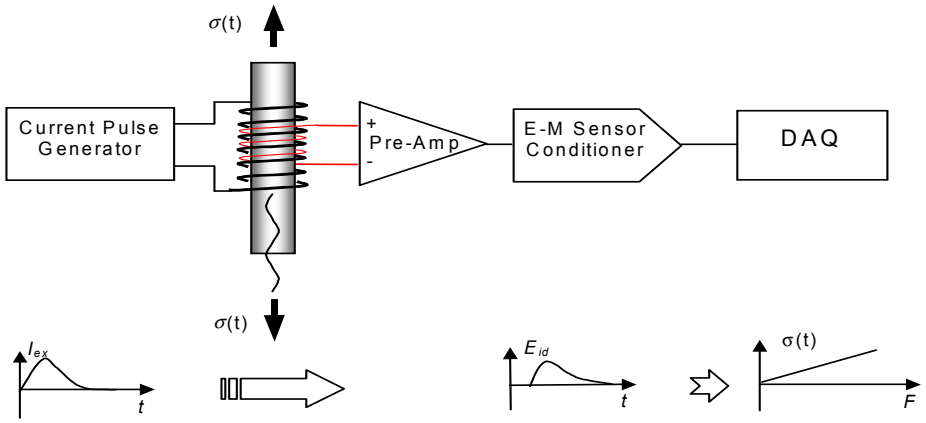


Fig. 1. Indicative working chart of elasto-magnetic sensor

Sensors are cylindrical in shape and are installed over steel elements prior to stressing. The sensor is robust, requires no maintenance, has no moving parts and is not subject to any load. It is expected to have a similar service life to that of the surrounding structure. They can be used for bare, epoxy-coated, galvanized and greased-sheathed steel in bonded, un-bonded, grouted or un-grouted length of the tendon. The accuracy of the force measurement for the sensor is equal or better than the conventional load cells.

TYPICAL SENSOR ARRANGEMENT

The Sensor Arrangement consists of mainly sensor and readout unit (See Fig. 2). Sensor dimensions are shown in Table 1. Additional cable connections, multiplexers, modem & controller are required for continuous and remote reading. In the Manual option, each sensor is individually connected to the readout unit and the force in the strand or bar can be obtained in a few seconds.

In the Automated option, all sensors are connected to the readout unit using extension cables, multiplexers and main cables. The readout unit is programmed to record the temperature and force readings of all sensors at a specified time interval. It can record up to a maximum of 2,400 sets of data. The recorded data may be downloaded to a laptop computer using a RS232 port attached to the Unit. The data is in Txt or ASCII format and can be imported to other programs and analyzed.

In the Remote option, all sensors are connected to the readout unit using extension cables, multiplexers and main cables. A modem and a controller are also attached to the readout unit. A cellular SIM card with a data plan or ethernet terminal server is installed to communicate from a remote computer with a static IP address. Software is provided to collect data from the readout unit through a RS232 port. It can either take readings from a remote computer as needed or can get data stored at specified intervals in the readout unit positioned

at the point of use. The output from the readout unit may be incorporated into other data acquisition systems as well. Data is in Txt or ASCII format and can be imported to other programs and analyzed.



Fig. 2(a). Sensor



Fig. 2(b). Readout unit



Fig. 2(c). Multiplexer

Table 1. Sensor dimensions

Strand Size	Strand Grade	Sensor Dimensions (in)		
[in]	[ksi]	I.D.	O.D.	Length
0.5-0.62	270	0.79	1.42	5.2
Bar Size	Bar Grade	Sensor Dimensions (in)		
[in]	[ksi]	I.D.	O.D.	Length
#7-#11	75-97	1.69	3.15	7.09
#14	75-97	2.09	3.90	7.87
#18/#20	75-97	2.87	5.71	12.20
#24	75-97	3.35	6.10	12.99
1”-1-3/8”	150	1.69	3.15	7.09
1-3/4”	150	2.09	3.90	7.87
2-1/2”	150	2.87	5.71	12.20
3”	150	3.35	6.10	12.99

Sensor over the tendon x-section will be provided upon request.

CASE HISTORIES OF EM SENSOR

Sensors have been successfully used in over eight projects in cable stay, post-tensioning tendons in bridge and building structures, ground & tie-back anchors, retaining walls, dams, air traffic control tower, wind energy tower and repair of various post-tensioned structures. Some of the sensor applications in geotechnical structures are presented below. Sensors readings were in line with jack pressure gauge readings during proof or performance testing and provided long term monitoring of lock-off load. Sensors are placed inside the anchors hole so will not increase top structural support as required by load cell system. Load cells work only placing them in compression between two bearing plates, requiring deep blockout for tiedown anchors and increase concrete cover wall for retaining walls.

DSI supplied three hundred forty five permanent tieback anchors with 9-0.6 inch diameter strands to retrofit the 1700-ft long crib wall of up to 50-ft tall of the Patton Creek shopping center in Birmingham, AL which

showed sign of slow moving. Tieback was fabricated with a double corrosion protection system. Anchors were proof or performance tested to 80% of strand ultimate strength and locked at a lower load. Partial view of wall with precast units and stressing of anchors are shown in Fig. 3. One sensor was installed in each of 4 anchors and the forces in these anchors were measured after lock-off, after 28 days and after 6 years in service and the results are shown in Fig. 4. The latest data shows the forces in three anchors have increased as compared to 28 days readings. The increase in load in the anchors may be a result of newly opened road adjacent to the anchor wall.



Fig. 3. View of wall with precast units and anchor stressing for Patton Creek complex, Alabama

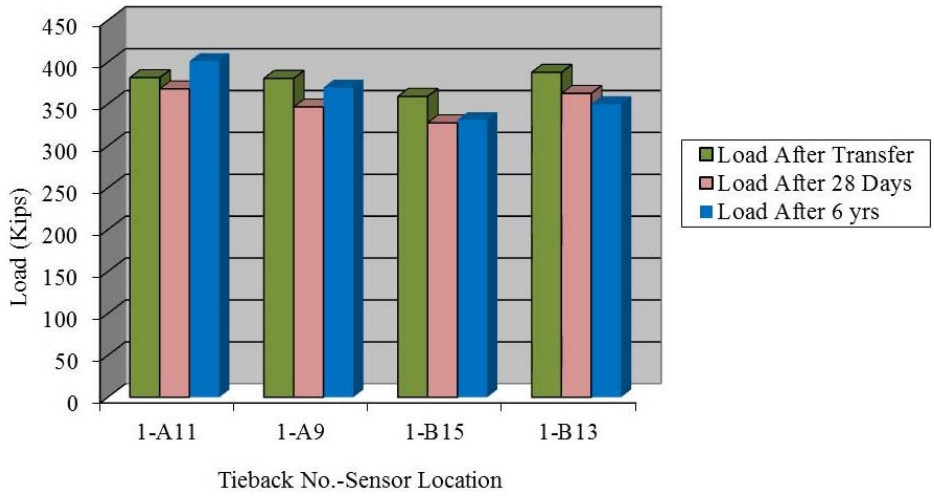


Fig. 4. Anchor force monitoring for slope stability of Patton Creek shopping complex, Alabama

Twenty-eight 59-0.6" strand anchors were used for the stability and safety of the dam at the Willow Island Hydroelectric project in West Virginia, USA. Rock mass was excavated to allow for installation of a power generator. In order to monitor the forces in the anchors during excavation of rocks, three sensors were installed in each anchor. A total of 84 sensors were installed in these permanent rock anchors. All sensors were connected to a multiplexer using extension cables and all multiplexers were connected to the readout

unit via main cable. Modem, controller and Cell SIM card were installed so the data could be accessed from a remote location. Battery and solar panels were used to power the readout unit. Figure 5 shows the anchor force at various loading stages. It is apparent that sensor readings were close to the jack readings as compared to the load cell readings. The data from all of the sensors are being taken remotely every 3 hours, analyzed and reported to the owner. The data provided valuable ifnormation to the owner.

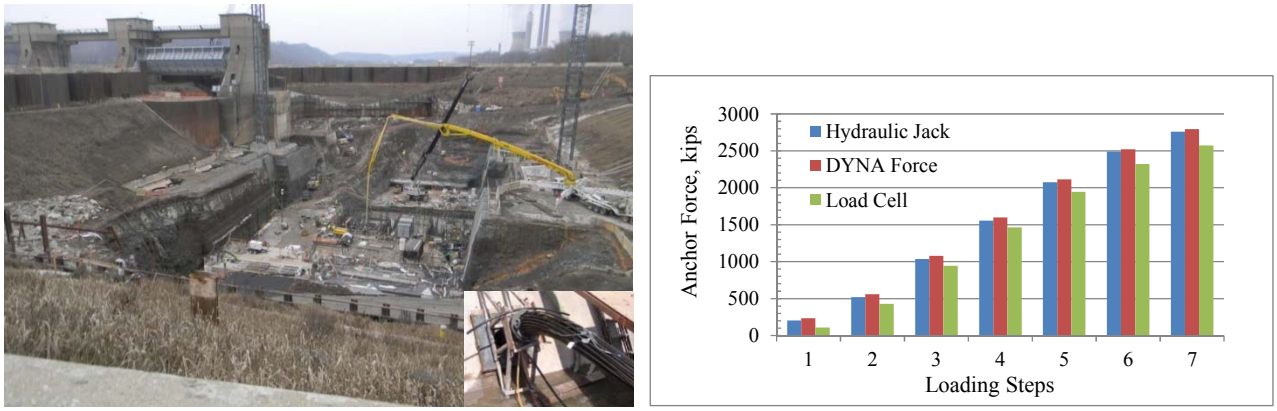


Fig. 5. Sensors for Willow Island Hydroelectric Project, West Virginia

DSI supplied 56 strand sensors for both permanent and test ground anchors for Sellwood Bridge in Oregon, USA (See Fig. 6). The main purpose was to monitor the slope stability in front of the bridge abutment. For the test anchors six sensors were installed in the bond length and one in the free length. For the permanent anchors two sensors were installed in each of the anchors with number of strand varying from 8 to 24. Fifteen automated readout units were installed to record the force readings of the sensors at every 4 hours. Software was provided so that the engineer could transfer the recorded data to a laptop. Sernsors provided valuable information for both test and permanent anchors.



Fig. 6. Sensor for bridge abutment for Sellwood bridge, Portland, Oregon

Four-hundred-seventy 4 thru 8-06” strand anchors were used as tie backs for two permanent retaining walls for a busy road widening in Rt. 405 in Los Angeles, CA, USA as shown in Fig. 7. Forty-eight sensors were installed on tie back anchors to monitor the performance of the retaining wall. Automated readout units were installed to record the force at every 4 hrs. Sensors are providing very consistent and valuable information to the owner.



Fig. 7. Sensor for retaining walls of Rt 405, Los Angeles, California

In order to prevent landslide of a major highway in North Dakota, tie-back anchors were installed. Sensors were installed in the bonded zone to monitor the forces along the length of the anchor. Sensor DF13 was at 40 ft into the bond length, Sensor DF14 was at 20 ft into bond length and sensor DF15 was at 5 ft into the bond length. The sensor readings were recorded at various stages of loadings. The force readings are plotted on a graph as shown in Fig. 8. Sensor located at 40 ft and 20 ft into bond length showed little or no force, i.e., full bond between the strand and soil through grout. Sensor located at 5 ft into bond length showed almost half of the jacking force indicating debonding at this location. The engineer reported the force transfer was as expected. The sensor readings provided valuable information to the engineer so that they can move with design and avoid any risk of anchor failure.

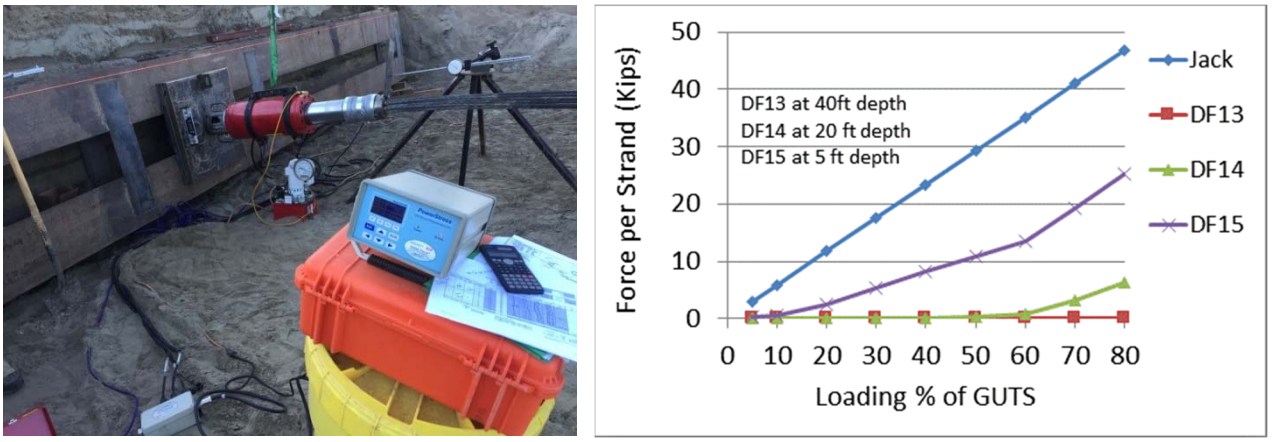


Fig. 8. Monitoring of Anchor force transfer in bonded zone for tie-back in North Dakota

CONCLUSIONS

DYNA Force system has been used in over eighty projects and proven to be the preferred technique to monitor forces in steel elements in terms of accuracy, its performance, ease in installation, durability, and cost effectiveness. The sensors can be used for bare, epoxy-coated, galvanized and greased-sheathed steel in bonded, un-bonded, grouted or un-grouted length of the tendon.

Sensors readings provide second measurement together with jack pressure gauge during proof or performance test of groud anchors. Sensors are placed inside the anchors hole so will not increase top structural support as required by load cell system. Load cells work only placing them in compression between two bearing plates, requiring deep blockout for tiedown anchors and increase concrete cover wall for retaining walls.

The owner can regularly monitor forces in pre-stressing steel manually, continuously and even from a remote access. The accuracy of the force measurement is equal or better than load cells. The sensor is robust, requires no maintenance, has no moving parts and is not subject to any load. It is expected to have a similar service life to that of the surrounding structure.

ACKNOWLEDGMENTS

The authors wish to acknowledge the support of Dr. Yang Zhao. Special thanks to Mr. Kerry Allen and Mr. Mike Kelley for their continuous support. The authors would like to thank all members of the DFI Annual Conference Technical Committee for their support and contribution.

REFERENCES

Islam, S., and Purinton, K. 2015. Long-term force monitoring of prestressed anchors used on dam rehabilitation projects. Dam Safety 2015 Conference, New Orleans, LA, USA.

Islam, S., 2014. Force monitoring of post-tensioned steel elements in bridge and building structures. Proc.

the fourth international fib Congress (pp. 733-737), Mumbai, India.

Bogdan, L., 2011. DYNA Force-An Elasto-Magnetic Sensor for Force Measuring of Post Tensioning Ground Anchors, Southwest Geotechnical Conference, Reno, NV, USA.

Islam, S., 2008. Long term force monitoring of post-tensioning tendons and cable stays in concrete segmental bridges, ASBI international symposium on future technology for concrete segmental bridges, San Francisco, California, USA.

Wang, M. L., Koontz, S., and Jarosevic, A., 1998. Monitoring of cable forces using magneto-elastic sensors, 2nd U.S.-China symposium workshop on recent developments and future trends of computational mechanics in structural engineering (pp. 337-349), Dalian, PRC.

OPTIMAL SUBSURFACE INVESTIGATION APPROACH FOR OVERHEAD TRANSMISSION STRUCTURES

Haijian Shi, Ph.D., P.E., P.M.P., Pepco Holdings, Washington D.C., hshi@pepcoholdings.com
Drew Pizzo, P.E., Pepco Holdings, dpizzo@pepco.com

ABSTRACT

This article focuses on the appropriate application of subsurface investigation methods for transmission structures, which are typically designed to resist lateral rather than vertical loads. Currently, the three methods used most often for the subsurface investigation of transmission structures in the field are the Standard Penetration Test (SPT), the Cone Penetration Test (CPT), and the Flat Dilatometer Test (DMT). Each of these methods has advantages and disadvantages, and each is more applicable to some scenarios than to others. To gain a better understanding of these test methods and the implications of using them for various kinds of applications, a comparison study was conducted in the field in Maryland, for three boring locations. Each boring location was explored using each of the three tests as stated. The results of the tests and lessons learned are presented and compared, and these comparisons show that the three test methods agree on the majority of the findings. The results from each test method were also used to derive key parameters such as the soil friction angle for given foundation designs considered in order to establish a clear basis for comparison. Recommendations for performing transmission structure subsurface investigations are made in order to optimize the use of each method and thereby optimizing subsequent foundation designs.

Keywords: transmission structure, subsurface investigation, SPT, CPT, DMT, lateral load.

INTRODUCTION

For overhead transmission structures, the most important structural requirement for determining the foundation design differs from the requirement for other structures such as buildings and bridges in accord with the conditions the transmission structures will need to withstand. In addition to the ability to bear a given vertical load consistent with its use, the foundation must bear lateral loads arising from wind and other weather conditions. The foundation types used most often for overhead transmission monopole structures include concrete drilled pier, vibratory caisson, and direct embedment. In order to determine an appropriate and even an optimum foundation design for any given set of conditions, an appropriate subsurface investigation method or approach is needed. Currently, the standard penetration test (SPT), the cone penetration test (CPT), and the flat dilatometer test (DMT) are the three most commonly used subsurface investigation methods.

For SPT, a hammer of 140 lbs is dropped in order to achieve a 6 in advancement of the shelby tube into the boring. The number of times the hammer must be dropped for this advancement to accrue is counted as blow counts. This process is then repeated for the second and third time. The standard penetration value (N) is determined by adding the second and the third blow counts to obtain the overall counts.

For CPT, a truck- or rig-mounted probe is inserted into the soil to explore it at a constant speed such as 0.79 in/second. The probe has sensors to collect data pertaining to such measures as tip resistance, sleeve friction, and pore water pressure. In this method, information used to derive the properties of the soil is collected continuously. A detailed account of the methods used to interpret CPT data can be found in Robertson and Cabal (2015).

Like CPT, DMT also relies on a probe, in this case a wedge-shaped probe with a membrane, inserted into the soil to collect information. However, in DMT the information is collected at intervals rather than

© 2018 Deep Foundations Institute

continuously. Once the probe reaches the desired depth, the membranes are inflated by the supplied gas and expands in the soil. The pressure readings from this membrane are recorded and used to establish the parameters for soil properties such as the material index, the horizontal stress index, and the dilatometer modulus. The probe is then placed at a greater depth in the soil, where more data is collected. A detailed account of how DMT readings are collected, calculated, and interpreted can be found in Braja (2011).

It is clear that each testing approach has different features to measure the soil properties. To compare their performance, all three of the test approaches under discussion here were employed at the same location for three boring locations B-6, B-19, and B-54 (Fig. 1).

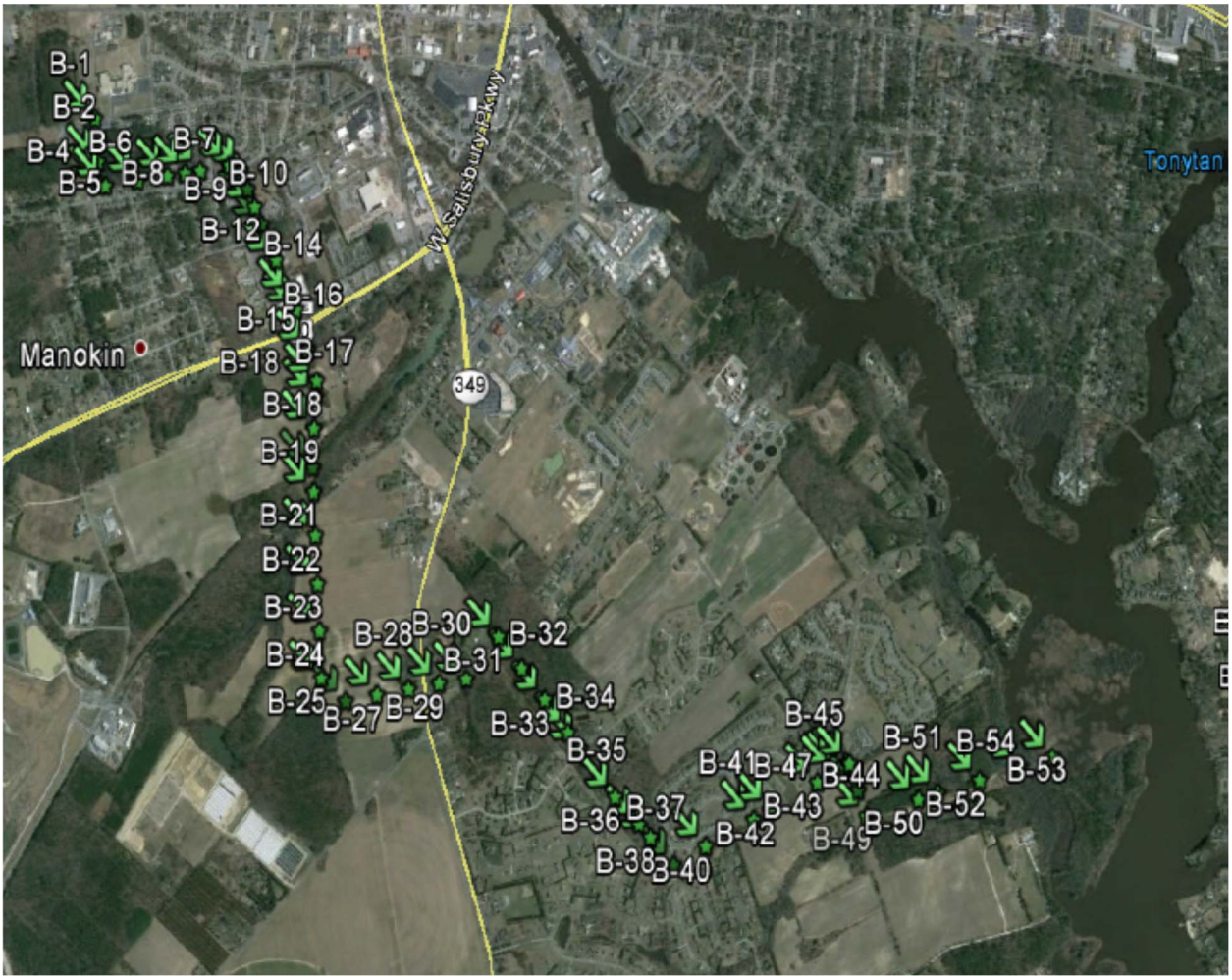


Fig. 1. Soil boring locations

TEST PARAMETERS

Located in Wilcomico County, Maryland, the three boring locations had foundations that were expected to resist the lateral force exerted by the top pole structures and conductors. Each boring hole was 5 ft away from the next closest boring hole. In each test method, all the soundings were performed to a minimum depth of 50 ft below the existing grade.

The SPT borings, made using hollow-stem augers, were sampled at intervals. The samples were taken using a split-spoon sampler with an inside diameter measuring 1 3/8 in and an outside diameter of 2 in. The CPT

cone tip, which had a cross-sectional area of 1.55 in^2 and a corresponding diameter of 1.42 in, penetrated the ground at a controlled rate of 0.79 in/seconds. The electronic CPT cones also employed a pressure transducer with a filter to collect pore water pressure data. For DMT the membrane on the side of the blade-shaped tool was expanded into the sidewall of the soil to a depth of 0.04 in. The pressure readings were recorded as A, B, and C readings.

TEST RESULTS

For the sake of brevity, the test results for the top 20 ft of soil are reported here for only one soil boring (B-54). This boring was very close to a marsh, which was, in turn, next to a river, and represented a relatively complex soil condition for the study. The soil boring log from SPT for the top 20 ft is shown in Fig. 2. Hollow stem augers were used to advance the boring and collect the soil samples. It should be noted that to a depth of 24 inches the soil constituted fine to medium sand that was brown in color. The standard penetration resistance value N was 16, and underground water was found at 1.5 ft below the ground surface. With the increase in depth to 15 ft below grade, the N value dropped in the range of 4 to 6. At a depth of approximately 20 ft, however, the N value rose from the 4 to 6 range to a value of 10. Through an examination of the soil sample collected from a shelby tube used in the testing at various depth, the soil was found to be fine to medium sand with trace clay and silt.

The CPT results are shown in Fig. 3. The tip resistance (q_c), sleeve friction (f_s), and pore water pressure (u_2) were recorded continuously. Through an interpretation of these three basic parameters, an energy ratio value of N_{60} was obtained, indicating 60% of the N value if an SPT test were to be performed at the same location. It can be seen that the N_{60} value reached its peak of 32 at around 2 ft below the ground surface and then gradually decreased back to a value of between 4 and 6 at a depth of 4 ft. Next, the N_{60} value remained below 15 until a depth of approximately 19 ft. At a depth of 20 ft, the N value returned to 16. The curve for the constrained modulus in fine-grained soils for the boring location is also shown. Based on the soil classification and SPT energy ratio as established by Lunne et al. (1997), the soil is classified as Zone 7 (silt sand to sandy silt) in the range of between 0 and 11 ft and in the range of between 14 and 16.5 ft below the ground surface. The rest of the soil layers were interpreted as Zone 8, which is defined as sand to silty sand.

The DMT test results for the same location were slightly different from the SPT and CPT results (Fig. 4). The material index I_D shows some clay layers and silt layers at a depth of between 2 and 10 ft below the ground surface. A silty sand layer was identified at 11 ft below grade. The distribution curve for the vertical drained constrained modulus (M), the dilatometer modulus (E_D), the undrained shear strength (S_u), and the overconsolidation ratio (OCR) are plotted in Fig. 4.

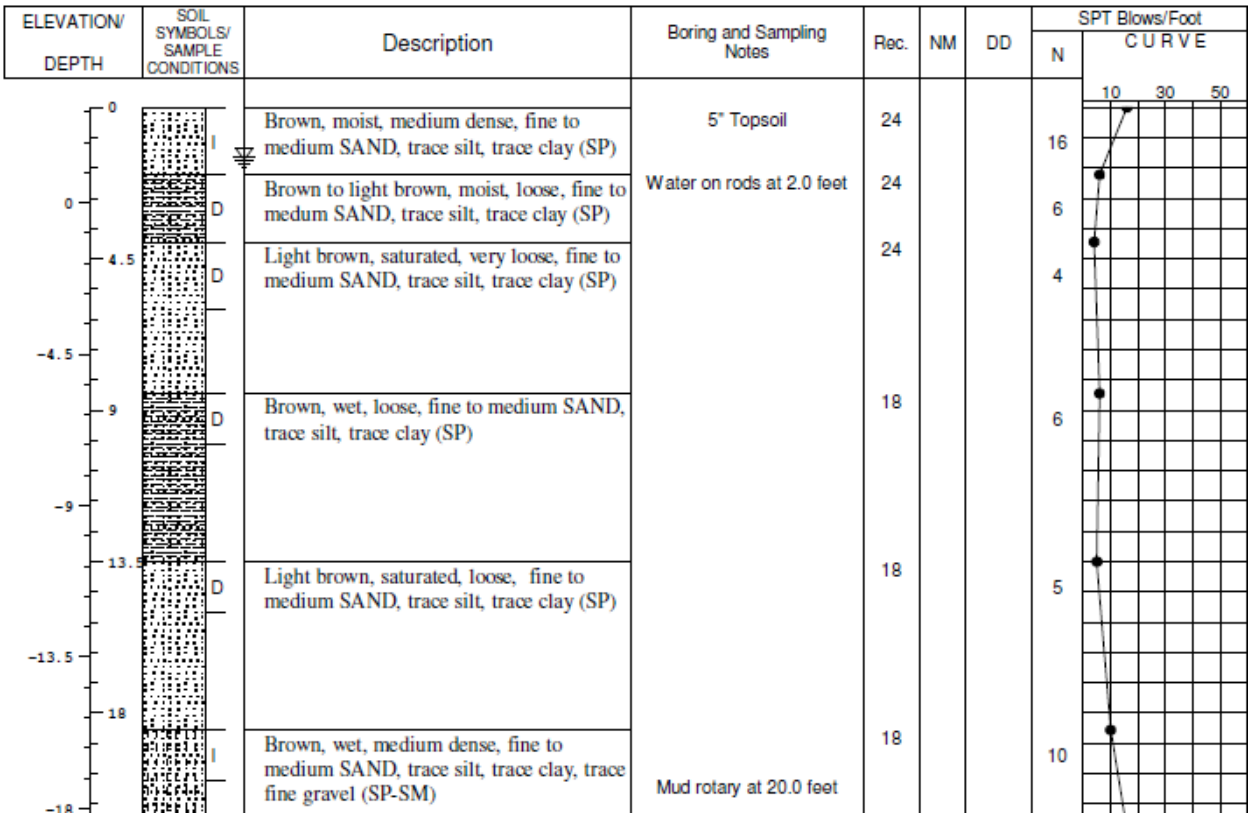


Fig. 2. SPT results for the top 20 ft of soil at B-54

COMPARISON OF RESULTS ACROSS THE THREE TEST METHODS

It is clear that each test method leads to a different set of parameters for the design of a foundation. Therefore, it is not a simple matter to effect a direct comparison between the methods. However, several aspects can be examined closely.

Soil description

First, the three methods returned similar results in terms of determining the depth and nature of the various kinds of soil layers identified. The visual examination of the soil samples from SPT, which relies on collecting data at intervals, produced a description of the soil as brown medium to fine sand at the top 2 ft, fine to medium sand with traces of silt and clay for the rest 18 ft below grade. For CPT, the correlation between the soil behavior and the ratio of $\frac{(q_c/p_a)}{N_{60}}$ was used to determine the nature of the soil layers: q_c is the tip resistance measured directly by the cone and read by computer via an electronic transducer; p_a is the atmosphere pressure; N_{60} is the average energy ratio of 60%. The correlation table can be found in Lunne et al. (1997). The CPT results are interpreted as showing the soil to be a mix of silty sand and sandy silt. This interpretation is consistent with the interpretation of the corresponding result derived from the SPT sampling.

For DMT, the material index I_D is used to identify soil type. I_D is defined as

$$I_D = \frac{p_1 - p_0}{p_0 - u_0} \qquad [1]$$

where p_1 is the corrected second reading, p_0 is the corrected first reading, and u_0 is the pre-insertion pore pressure.

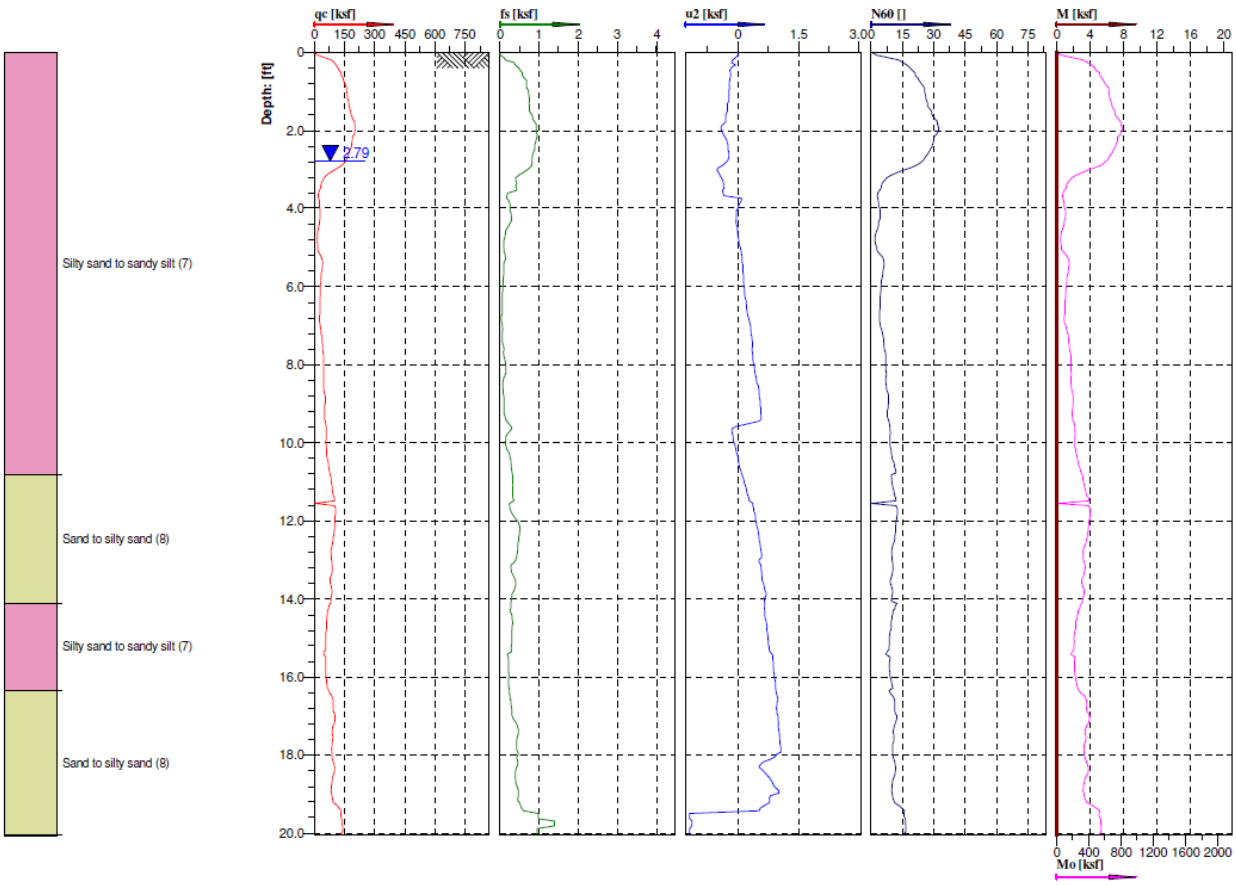


Fig. 3. CPT results for the top 20 ft of B-54

The chart (Figure 3) from DMT shows that some layers of clay and silt are present at a depth of between 2 and 10 ft below grade. This result differs from the observations for SPT and the interpretation of CPT because both of them have not identified any clay or silt layers. The rest was identified as silty sand, which is consistent with the observations from SPT and CPT.

Standard penetration resistance N

Many engineers have considerable experience with design approaches based on SPT correlations, and for this reason prefer to see CPT results in the form of an equivalent SPT N value (Robertson and Cabal, 2015). Engineers, therefore, generally accept an N_{60} value, which is a standard penetrating number corrected for field condition at an average energy ratio of 60%.

Jefferies and Davies (1993) proposed the following relationship between N_{60} and the soil behavior type index I_c:

$$\frac{(q_c/p_a)}{N_{60}} = 8.5\left(1 - \frac{I_c}{4.6}\right) \qquad [2]$$

where the soil behavior index is

$I_c = ((3.47 - logQ_t)^2 + (logF_r + 1.22)^2)^{0.5}$; Q_t is the normalized cone penetration resistance; and F_r is the normalized friction ratio.

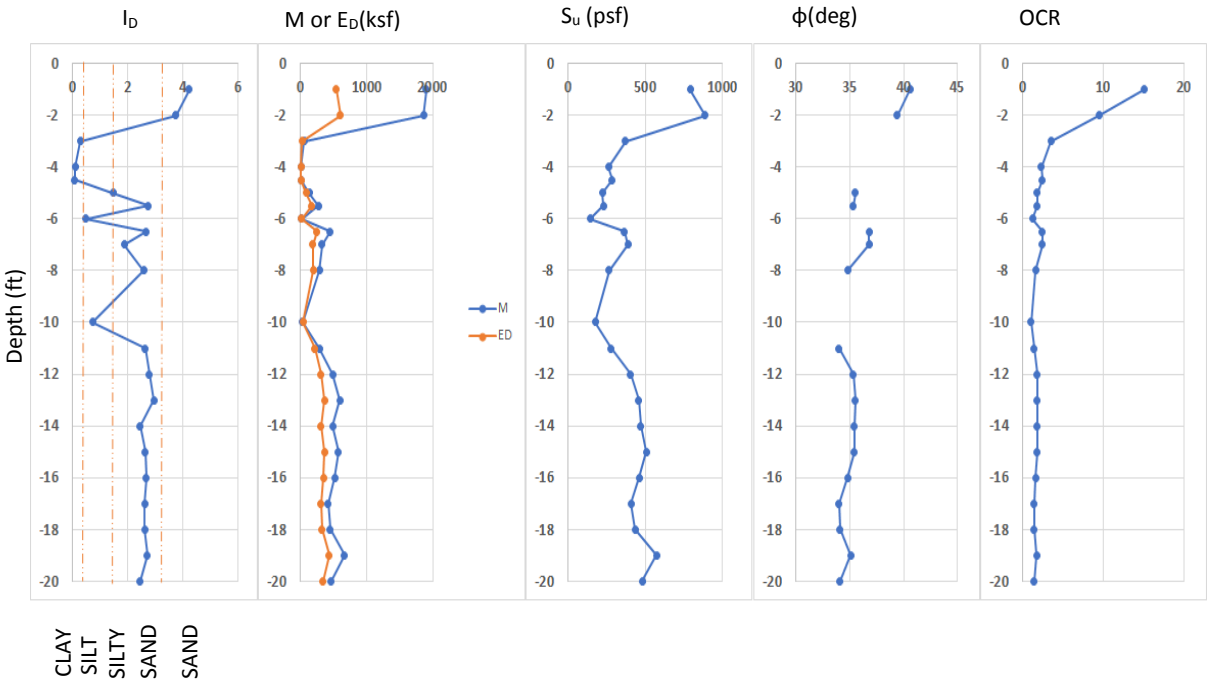


Fig. 4. DMT results for the top 20 ft of B-54

The N_{60} value typically mimics the curve of q_c. The comparison shows that at 4 ft below grade, the N value from SPT generally agrees with the N value from CPT. However, there is a discrepancy between SPT and CPT for the range between the ground surface and a depth of 4 ft. That is, for this range, the CPT value is higher than the SPT value.

Friction angle ϕ

The friction angle ϕ can be interpreted using the correlation of the friction angle with the standard penetration number (Transmission Structure Foundation Design Guide, 2012). The correlation chart shows that for an N value of between 5 and 15, the friction angle for granular-type soil is between 30 and 34 deg. This result is close to the DMT interpretation, which is between 32 and 36 deg, for the soil at a depth of between 10 and 20 ft below grade. However, the SPT interpretation is lower than the DMT interpretation for the top 8 feet, the latter of which is between 35 and 40 deg.

Soil elastic modulus

The soil elastic modulus values for all three of the tests for B-6 and B-19 were also compared, as shown in Figs. 5 and 6. For SPT, the elastic modulus was obtained using the correlation

$$E = 10 \times (N + 10) \qquad [3]$$

The constrained modulus M_0(ksf) was used in the comparison with the elastic modulus from SPT for the CPT results:

$$M_0 = \begin{cases} 4q_c & for\ q_c < 208.8\ ksf \\ 2q_c + 517.6 & for\ 208.8 < q_c < 1044\ ksf \\ 2509 & for\ 1044\ ksf < q_c \end{cases} \quad [4]$$

The vertical drained constrained modulus M_{DMT} was used to generate the DMT results:

$$M_{DMT} = R_M \cdot E_D \quad [5]$$

where R_M is the defined ratio and E_D is the dilatometer modulus. A detailed description of the above mentioned parameters can be found in Totani et al. (2001).

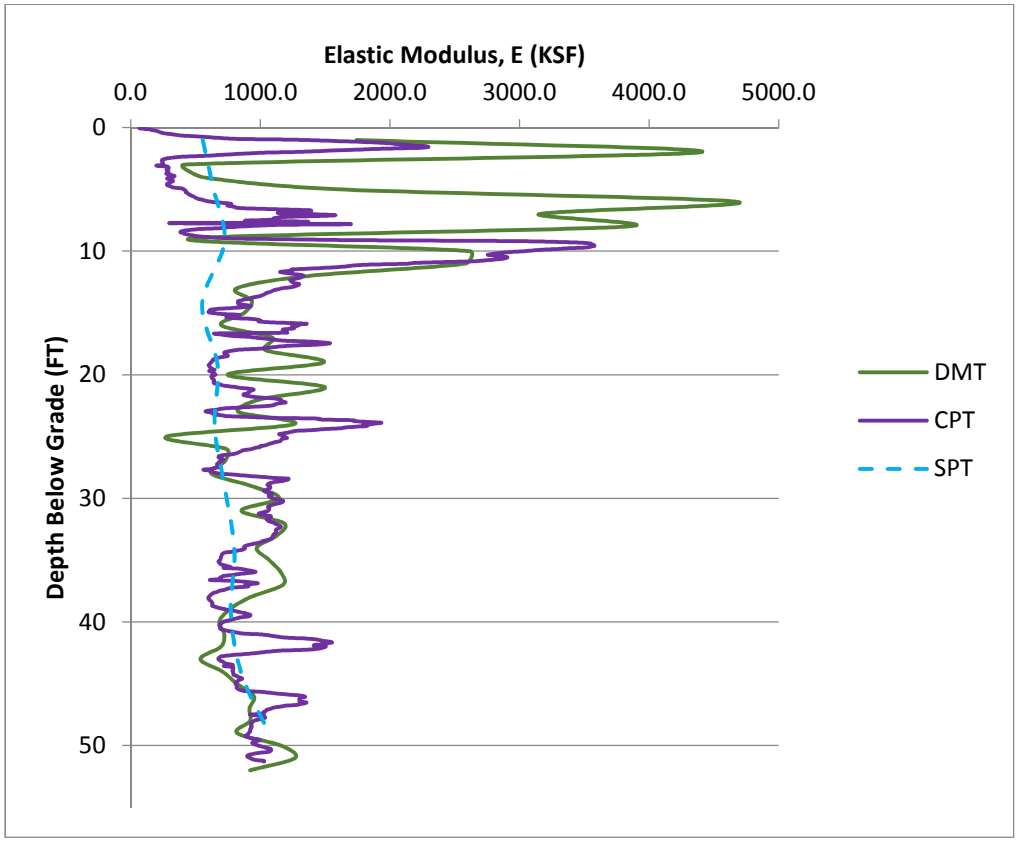


Fig. 5. Comparison of soil elastic modulus values across the three tests for B-6

From the comparison (Figs. 4. and 5), it can be seen that the curves from the three tests overlaps at a various depth. However, the peaks and valleys are clearly filtered out in the SPT and DMT curves because the results were taken at intervals, whereas CPT collected the testing data continuously. The results from DMT generally show higher peaks and greater variation of the elastic modulus value than is the case in the other two approaches. The results for CPT are between those for SPT and those for DMT.

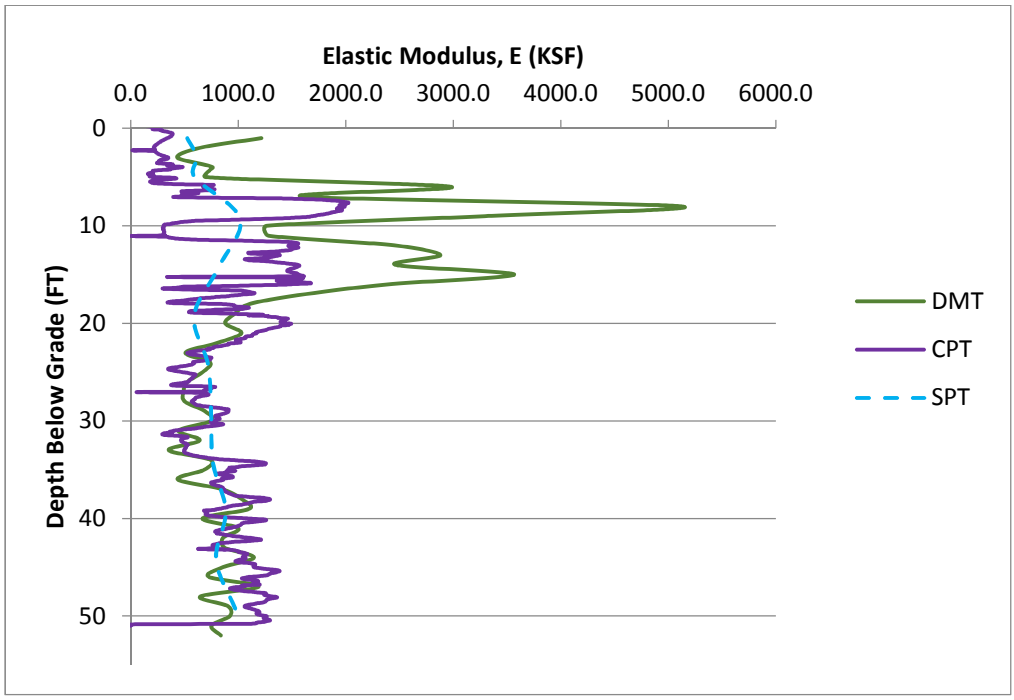


Fig. 6. Comparison of the soil elastic modulus values across the three tests for B-19

Project design used parameters for the three boring locations

The parameters used the project design phase for the three aforementioned soil borings are in Table 1.

Table 1 Design Parameters for Three Soil Borings

Boring Locations	Groundwater Depth (ft)	Depth ft)	USCS	Average N_{60}	Wet Density (pcf)	Cohesion (psf)	Φ (deg)
B-6	10	0-4	SM/SC	8	105.6	0	30
		4-8.5	CL	11	126.0	1,375	0
		8.5-28.5	SM	10	108.8	0	30
		28.5-50	SP-SM	16	115.3	0	33
B-19	17	0-2	SM	4	96.0	0	28
		2-8.5	CL	8	123.1	1,000	0
		8.5-50	SP-SM	14	113.4	0	32
B-54	1.5	0-23.5	SP	8	105.6	0	30
		23.5-50	SP-SM	27	122.6	0	37

OVERALL COMPARISON OF SPT, CPT, AND DMT

Through a detailed comparison of the results from the three boring locations, ratings for the test approaches were established, as shown in Table 2. SPT has the advantage of being the only approach through which a soil sample can be retrieved. However, although this is, indeed, an advantage of SPT as compared to the other two approaches, it should be noted that the split spoon may have the negative effect of disturbing the sample such that it may not constitute a precise reflection of the original soil property after all. In comparison, however, neither CPT nor DMT can be used to obtain samples with the inserted probe that

each of these methods rely on unless the probe is replaced by a sampler during the probing process, which is vary rare in the field testing. Of the three methods, CPT is the only one that continuously collects the soil response during the inserting phase. SPT typically has a 1.5 or 2 ft interval for collecting samples and for determining the N value. DMT also has certain intervals such as 6 in or 1 ft. CPT, therefore, is the most sensitive of the three methods for detecting variations in the soil strata. On the other hand, of the three methods, SPT is most likely to miss thin soil strata because of its large sampling interval.

In regard to identifying the underground-water level, DMT is the least satisfactory of the three methods. The reason: the probe used in DMT lacks a pore water pressure sensor whereas the probe used in CPT has a pore water pressure sensor capable of sensing the presence of underground water and in SPT underground water can be observed through the bore hole. However, in CPT, it is possible for the soil to be disturbed during the boring process such that the immediately observed underground-water level may not reflect the true underground-water level. CPT, therefore, is the most best precise of the three methods for detecting the level of underground water.

Table 2 SPT, CPT, and DMT Ratings

Test Method	SPT	CPT	DMT
Soil sampling	★★★★★	★	★
Continuous boring	★★	★★★★★	★★★★
Soil strata identification	★★★	★★★★★	★★★★
Underground water–level identification	★★★	★★★★★	★
Soil lateral strength	★★★	★★★★	★★★★★
Reading accuracy	★★★	★★★★★	★★★★★
Crew size	★★★	★★★★★	★★★★★
Operation simplicity	★★★★★	★★★	★★★
Efficiency	★★★	★★★★★	★★★★★
Marine environment	★	★★★★★	★★★★★
Settlement-related	★★★	★★★★	★★★★★

The lateral strength of the soil is a very important parameter for determining the foundation design of a transmission structure because most structures of this kind must be capable of resisting a significant lateral load from such factors as extreme wind conditions. The ideal approach to measuring soil lateral resistance is DMT because it relies on the direct inflation of the membrane on the testing probe against the surrounding soil. By comparison, both SPT and CPT are effective at measuring the vertical resistance of soil but are considerably less effective at measuring lateral soil resistance than DMT is.

These methods also differ in terms of their respective field applications. SPT typically requires sizeable field crew, each of whom oversees a specific task such as operating the hammer or recording the blow counts. Compared with the crew needed for SPT, a much smaller crew is needed for CPT and DMT because each of these methods rely on probes, which are mounted on rigs and inserted into the ground by machinery at a constant speed. The smaller crew size means that CPT and DMT are both more cost effective than SPT is. For both CPT and DMT, unlike SPT, the reading or collection of the data is processed automatically by a computer. Therefore, SPT clearly has disadvantages in comparison with the other two methods in terms of data reading ease and accuracy and crew size. However, SPT has the advantage of being relatively simple to implement. For CPT and DMT, the crew must know how to operate the machinery in order to obtain an accurate reading.

For some special settings, such as marine environments, it is not possible to use SPT simply because the hammer is not effective under water. However, CPT and DMT can each be used in marine environments.

Further, SPT is not an effective method for soil that is very weak as such soil is not capable of sustaining the weight of the hammer. Yet, SPT is the best method for use with dense sand or boulders whereas CPT and DMT are both limited in regard to the drilling depth they can achieve in such conditions. In regard to settlement-related work, DMT is the best choice from among the three methods because its overconsolidation ratio (OCR) specifically addresses the settlement history of the soil.

CONCLUSIONS

Each test method has distinct advantages and disadvantages in comparison with the other two explored herein. The test results from these three methods all show differences. There is no one-size-fits-all approach for every situation.

To summarize, for granular soil strata identification, CPT and SPT produce similar results whereas DMT sometimes produces results that differ from those of the other two methods. For the N_{60} value of CPT, though it is intended by researchers to replace the N value from SPT, the two test methods show some differences in terms of the values generated. There is also a discrepancy in N value between SPT results and CPT results in regard to the soil strata above underground-water level. For the friction angle for granular soil, a difference between SPT results and CPT results exists for some top soil strata. In terms of the soil elastic modulus, the curves across the three approaches are broadly similar, although differences in the details of the curves are also evident.

For overhead transmission structures, the lateral resistance of the soil is an important parameter for determining the foundation design. Therefore, DMT is recommended for dead-end poles that must have the capacity to bear large lateral loads. DMT would also be an excellent candidate for situations in which long-term settlement is anticipated. For a light angle pole with a medium lateral load, CPT is recommended. CPT would also be an ideal candidate for soft granular soil with relatively shallow ground water, such as in the southern New Jersey area. SPT remains one of the major approaches to subsurface investigation because of its simplicity and its ability to retrieve soil samples for further testing. However, SPT is not a sufficient approach when used alone for this purpose. Instead, SPT used with CPT is recommended as the primary approach given that this combination would produce the most accurate results in interpreting soil properties.

ACKNOWLEDGEMENTS

The authors would like to acknowledge the valuable contribution to this study of Hillis-Carnes Engineering Associates, whose representatives conducted the subsurface investigation and provided technical support.

REFERENCES

Braja D., 2011, Principles of foundation engineering, Global Engineering, 7th edition, Global Engineering, Stamford, CT.

Lunne, T., Robertson, P.K. and Powell, J.J.M., 1997, Cone Penetration Testing in Geotechnical Practice, Blackie Academic/Routledge Publishing, New York, NY.

Jefferies, G. and Davies, P., 1993, Use of CPTU to estimate equivalent SPT N_{60}. Geotechnical Testing Journal, ASTM, 16(4): 458 –468.

Robertson, P.K. and Cabal, K.L., 2015, Guide to Cone Penetration Testing for Geotechnical Engineering, 6th edition, Gregg Drilling & Testing, Inc., CA.

Totani, G., Marchetti, S., Monaco, P. and Calabrese, M. 2001, Use of the flat dilatometer test (DMT) in geotechnical design, International Conference on In Situ Measurement of Soil Properties, Bali, Indonesia.

Transmission Structure Foundation Design Guide, 2012. Electric Power Research Institute, Palo Alto, CA.

REDUCING CONSTRUCTION INTERFERENCE WHEN IMPLEMENTING GEOTECHNICAL INSTRUMENTATION AND MONITORING IN URBAN EXCAVATION PROJECTS

Zhangwei Ning, Sixense Inc., Seattle, WA, USA, 206-276-4485, zhangwei.ning@sixense-group.com
Martin B. Hudson, Wood Environment & Infrastructure Solutions, Inc., Los Angeles, CA, USA, 323-889-5344, marty.hudson@woodplc.com
Daniel Brescia, Sixense Inc., Torrance, CA, USA, 213-700-049, daniel.brescia@sixense-group.com

ABSTRACT

Due to the complexity and sensitivity of surrounding environments, instrumentation and monitoring (I&M) is critical for many urban deep excavations. The objects to be monitored include shoring bulkheads, retained embankments, adjacent buildings and roads as well as underground utilities. However, there are also plenty of constraints on the implementation of I&M such as: congested site space, difficult access to instruments, coordination among multiple contractors, and installation permits for private or public properties. Because of these constraints, sometimes the implementation of the initially planned I&M is delayed, its scope is reduced, and/or the continuity of monitoring is interrupted. For these reasons, it is important to implement the I&M with robust and redundant capabilities while providing minimal interference to the project construction and schedule. This paper describes state-of-the-art I&M technologies including automatic motorized total station (AMTS) with camera and automatic leveling device, reflectorless AMTS and IoT-based wireless sensors based on a case study of an on-going deep excavation project.

Keywords: instrumentation, monitoring, excavation, IoT, wireless sensor, AMTS, reflectorless, shoring

INTRODUCTION

In urban environments, deep excavations requiring the construction of temporary shoring bulkheads are becoming increasingly common, with the associated need to provide protection of the surrounding built environment during construction. Protection of the surrounding environment requires planning, engineering, construction, monitoring, and excessive shoring movement mitigation. The I&M is a vital component of the deep shoring implementation.

In public projects, geotechnical I&M is often placed within the general contractor's scope, whereas the majority of deep excavations are privately undertaken. For those private developments, sometimes the developer contracts the geotechnical I&M directly with the project geotechnical engineer or by a geotechnical I&M specialist hired by the project geotechnical engineer. In either the public project or private development case, the effective deployment of the I&M system relies heavily on coordination and collaboration with the project contractor.

Today's state-of-the-art I&M technologies include automatic motorized total station (AMTS) with camera and automatic leveling device, reflectorless AMTS and IoT-based wireless sensors. These technologies are performed in conjunction with more traditional surveying techniques for validation and redundancy of monitoring. The I&M program can be implemented in ways to reduce interference with construction activities as described herein.

© 2018 Deep Foundations Institute

INTERFERENCE TO CONSTRUCTION DUE TO INSTRUMENTATION

The installation of a geotechnical instrumentation system and baseline monitoring before starting construction activities are often part of the critical path to an urban excavation project. Some of the instruments of an I&M program can only be installed at a specific stage of construction (e.g. installing load cells on shoring bulkhead tieback anchors). Most of the instruments require varying degrees of maintenance and protection during the entire project. Therefore, considering the site and schedule constraints as described above, the execution of the I&M program can interfere with the construction to certain extents. For example, a lengthy installation procedure could delay the commence of construction; intrusive installation can require permits from a 3rd party; (re)access to instrument locations may require special access equipment; or maintenance and repair of instruments can sometimes require a temporary pause of certain construction activities. Table 1 shows some potential interferences to project construction when using two types of instruments in urban excavation monitoring: Automatic Motorized Total Station (AMTS) and geotechnical/structural sensors. In the following sections, the techniques used to minimize such interference are described.

Table 1. Potential interference of instrumentation to construction

Instrument	Tasks	Interference to construction
AMTS	prism installation	difficulty access to prism locations obtaining permits for prism installation
	prism commissioning	difficulty providing access to AMTS locations
	line-of-sight verification	difficulty access and clear line-of-sight
	AMTS (re)leveling	difficulty providing access to AMTS locations
Geotechnical/Structural Sensors	establishing node communication via cable	lengthy installation install protective conduit repair due to damage
	establishing node communication via radio	radio troubleshooting installing of additional radio repeaters
	supplying power	frequent battery replacement

AMTS WITH IMAGE CAPTURE AND AUTO-LEVELING

Using AMTS for automatic 3D deformation monitoring at construction sites started in the 1990s. After nearly 30-years of experience and hard/software development, today AMTS has become a standardized tool when near-real time, high precision deformation measurement is required. It has been used in a wide range of project scenarios, such as surface ground settlement monitoring in tunneling, and shoring structure lateral movement monitoring in deep excavations. The advantage of AMTS over conventional manual surveying includes: 24-hour/7-day continuous operations, automatic data processing, minimal maintenance, and lower continuing labor costs. A schematic of an AMTS system is shown in Figure 1. One among the very few disadvantages of AMTS compared to manual optical survey is its lack of mobility. Also, the need for accessing the AMTS locations for periodic maintenance could be difficult for the project contractor; difficulty accessing the AMTS locations can, in-turn, affect the effectiveness of the monitoring system. Fortunately, there are devices that can provide effective solutions but are neither commonly seen in practice

nor reported in literatures, such as the AMTS in-body camera and the automatic leveling device (ALD), described in this section.

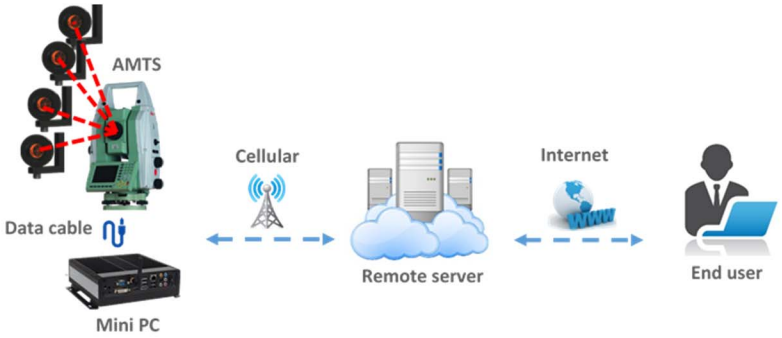


Fig. 1. Schematic of AMTS system

Needs for (re)accessing the AMTS

In order to reduce the quantity of AMTS therefore the cost, ATMS are usually placed at locations with maximum line-of-sight to monitored targets. These locations are usually high and/or near the edge of excavation, requiring ladders, temporary scaffolding or a man lift to access. All these means of access can result in a safety hazard to the operator, interruption to normal construction activities, and/or additional maintenance costs. Due to the fast and constantly changing site conditions inherent to active construction sites, re-accessing the instrument locations are often much more challenging or can even be practically impossible. However, for a regular AMTS setup, the need to re-access the instruments is almost inevitable during an averaged 1.5 to 2.0 years period of monitoring of an excavation project, which is typically needed for commissioning (learn) prisms, releveling the AMTS, as well as verify lines-of-sight.

Usually the entire set of AMTS prisms (targets) can not be installed at one time because some monitored points are not exposed to the line-of-sight during the initial stage of construction, or because some installed prisms need to be relocated during the project. Under most circumstances, prism learning could not be effectively done without having an operator aim the prism through the telescope of the AMTS. Remotely controlling AMTS to 'blind-search' prisms (relying on automatic target recognition (ATR)) could easily lead to acquisition of the wrong prism (e.g. an array of prisms at different shoring piles yet in a narrow viewing window along the same line-of-sight).

The AMTS needs to be operating with precise horizontal leveling in order to achieve the level of accuracy desired. Although all modern AMTS come with integrated compensators, its adjustment range is very limited (about 4 minutes), which is not sufficient to correct excessive tilting of the AMTS caused by temperature effects or construction induced vibration, which is very common for urban excavation projects involving pile driving, existing structure demolition etc. When excessive tilt occurs, the standard way to re-level the AMTS requires an operator to be able to manually reach and adjust the tribrach on which the AMTS is sitting.

Due to the fact that the AMTS is usually fixed to a location during a project, it could lose its line-of-sight to certain prisms during certain periods, which is more likely to happen in a congested urban site filled with a variety of equipment. When the line-of-sight to the monitored prism is blocked, it results in interrupted measurement. If the line-of-sight to the monitored prism is only partially interfered, it could result in erroneous readings because the ATR is affected when determining the center of the prism. Or if the line-of-sight to a large portion of reference prisms are lost, it could affect or cease the least square adjustment of the measurements so as to impact the determination of the positions of all the monitored points.

Unfortunately, line-of-sight validation is not always convenient and could be debatable without accessing the AMTS to see through its telescope.

Image capture

Some recent models of the AMTS are equipped with an in-body camera which allows the operator to remotely see what the total station can see. It helps the operator to precisely position the AMTS so as to learn the prism promptly without the need to access to it. It also helps to effectively verify the line-of-sight from the AMTS to specific prism, especially when the line-of-sight is not easy to be validated via visual inspection (e.g. when a tree branch is in the way). The design of the AMTS camera is more complicated compared to the general purpose camera because the image or stream video has to be transferred from the telescope through slip rings onto the main part of the instrument with minimal latency. It also serves as a good tool for construction site visual documentation.

Automatic Leveling Device

Automatic leveling device (ALD) integrates components including servomotors, adjustment units, inclinometers and measuring and control electronics into a dust- and water-proof housing. Compared to AMTS's internal compensator, the ALD has a much wider adjusting range usually up to +/- 12 gon (400 gon equals 360 degree) and is usually capable of supporting devices with weight up to 10 kg. Due to the low power consumption of the servomotors, the ALD could be left running continuously or only turned on temporarily when the AMTS is out of level though a remote relay controller. With the AMTS's ability to continuously monitor its tilting, using ALD could completely eliminate the effort to manually relevel the AMTS once the system is put in place.

AMTS IN REFLECTORLESS MODE

Technically speaking, AMTS-based deformation monitoring could be considered as a non-contact measurement technique. However, the fact that the prisms need to be attached to the monitored object make this method still an intrusive method. This brings about the non-technical challenges which could be more difficult to deal with in practice compared to those technical challenges discussed earlier. If the prisms need to be installed at private or public properties and areas outside the construction limit, it would usually require the permit of installation, which often becomes the first obstacle for the implementation of the AMTS, leading to the delay of delivery. There are also scenarios that the desired locations of the prism are not accessible or could be dangerous for the operator, e.g. in the middle of a highway.

It is due to these demands, the capability of carrying out AMTS reflectorless measurement has been developed and reportedly applied in tunnel project since 2005 (ITAtech, 2015). The reflectorless technique also uses electro-magnetic waves (as the standard AMTS does) but measures directly an object's surface having appropriate reflectivity. Unlike the standard AMTS, for which the ATR is guiding the AMTS to shoot the same target, reflectorless measurement can only approximate such repetition by fixing the horizontal and vertical angle of the AMTS. An immediate and obvious issue is that if the measurement surface deforms (e.g. settlement), the AMTS is not shooting the same point (as shown in Figure 2). This effect therefore restricts the reflectorless method to only deliver 1D deformation although being a 3D measuring technique.

Although the restriction described above is inherent to the technique, mm-level precision is achievable by reflectorless AMTS when limiting the measuring distance to within 80 meters and having an incidence angle (the angle between the line-of-sight and the measured surface) greater than 1:10, as well as having a physically consistent surface condition. When the point density is high enough, a deformation surface can be generated though interpolation. Having most of the benefits of AMTS while avoiding the installation of

monitoring targets (prisms), reflectorless AMTS has gained increasing attention and practical experience in recent years and is beginning to become the specified method for automatic deformation monitoring of roads with active traffic. For urban excavation projects, it is suitable for monitoring of settlement of adjacent paved roads, or monitoring of the lateral movement of the facade of adjacent buildings, eliminating the need to obtain prism installation permits and therefore creating minimal interference.

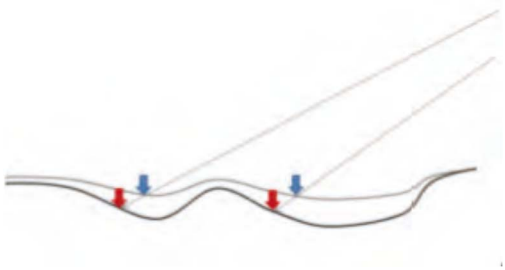


Fig. 2. Different points measured due to surface deformation. (after ITAtech 2015)

IoT AND WIRELESS SENSOR

Geotechnical I&M technology has evolved slowly over the past few decades with a few exceptions (Bayrd, 2018; Dunnicliff, 1993). By reviewing the milestones of its developments from the 1950s (Mazzanti, 2017), it can be seen that it generally takes 10 to 15 years for a new technique to be well accepted and popularized in practice. This trend started to change in the past few years as the much faster adoption of newly emerging technologies such as IoT (the Internet of Things) and wireless sensors have been witnessed.

There are well recognized challenges with deploying conventional geotechnical and structural sensors which require cable connections for communication and/or power purposes. Cables between the sensors to the data acquisition box are prone to damage by construction activities, which also poses constraints in locating the data acquisition device due to the effort of shorting the cable. At locations where a permanent power supply is not available or the use of solar panel is restrained, replacing a battery on a regular basis is necessary.

Wireless sensors built upon Low-Power, Wide-Area Network (LPWAN), one of the fastest growing IoT technology, provides an alternative solution to reduce site interference when installing cable-dependent sensor and data acquisition equipment. Take Lora, one of the prevailing LPWAN technologies for example (Lora Alliance, 2015; Semtech, 2017): Lora enables up to 15 kilometers of wireless communication distance while also being battery-operated with over 10 years of battery life (with a moderate sampling frequency), which significantly outperforms most of the existing standard RF radio communication technologies being popular for geotechnical I&M in the last two decades. Lora's long distance capability results from its unique wireless modulation, called chirp spread spectrum modulation, and its communication protocol. Although such long communication distance might not seem necessary since it greatly exceeds the scale of a typical urban excavation site, it demonstrates Lora's high radio link-budget which brings the capability of deep penetration in dense urban/indoor environment, expected in most urban excavation sites. The core strategy for reaching long distance adapted by Rora is repeating the message or in other words increasing the message traveling time in air. This is described by a parameter named spreading factor (SF). Low SF indicates faster data transmission is used for short distance communication while high SF indicates slower data transmission, better immunity against interference but also more power need for long distance communication. A mechanism called ADR (Adaptive Data Rate) allows the node to automatically negotiate the lowest SF possible with the gateway based on the signal strength so as to balance the signal resolution, transmission rate, and power consumption. Figure 3 is a conceptual diagram showing the relationship between communication distance and SF. Note that, due to its superior point-to-point communication distance, the Lora network utilizes star topology, which does not require a node in the

network to receive and forward information from other nodes as in a mesh topology network, therefore reduce network's complexity and increase its robustness. Also the nodes in a LoRa network are asynchronous and communicate only when they have data ready to send, which is different from a synchronous network, such as cellular, in which the nodes have to frequently 'wake up' to consume more power. Although the sensors for I&M applications usually have a much higher sampling rate than other IoT devices, thus shorten the battery life, they can still function without battery replacement for the averaged 1 to 2-year duration of most urban excavation projects.

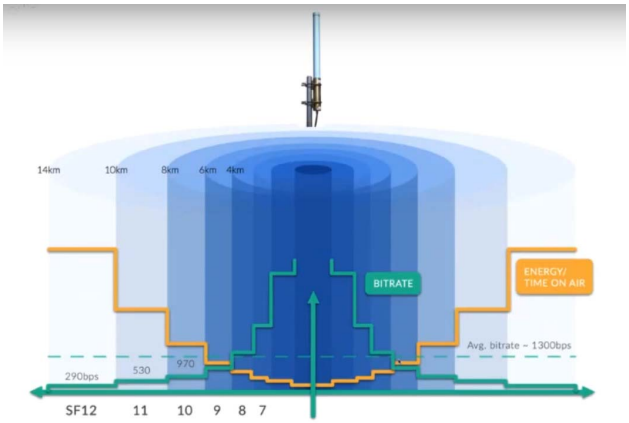


Fig. 3. Spreading Factor (SF) and communication distance in LoRa network (from LoRa crash course by Thomas Telkamp)

CASE STUDY

In one recent on-going deep excavation project, the New Century Plaza in Los Angeles, all of these technologies and devices mentioned herein have been deployed by a close collaboration between the geotechnical engineer and the geotechnical I&M specialist. The fast and effective deployment of the instrumentation system has resulted in minimal interference to construction activities.

This $2.5-billion project includes adding twin 46-story towers to, and rehabilitation of the existing 50-year-old hotel, designed by the famed architect Minoru Yamasaki, requiring a significant demolition component, and also excavation next to the historical hotel, adjacent streets and properties. The instrumentation system consists of three AMTS with over 150 prims, 9 wireless tiltmeters, several load cells and strain gauges to monitor the temporary shoring, adjacent roads as well as the surrounding structures. Figure 4 shows a panoramic view of the site after a portion of demolition has occurred, but before major excavation has occurred.



Fig. 4. New Century Plaza excavation site (a panoramic view looking towards the northeastern direction)

AMTS for structural deformation monitoring

Three AMTS systems were installed for near real-time monitoring of displacement at the shoring bulkheads, the existing hotel, selected adjacent structures and an adjacent private roadway. The locations of the three AMTS were initially proposed with one on the top of a parking lot building to the West of the excavation, and the other two on the balconies of the south and the north corner of the existing hotel respectively, in order to obtain a good line-of-sight to the monitored points as well as allow for easy access for maintenance. However, during the pre-installation site visit, it was found that the entire facade of the exiting hotel would be covered by screening and scaffolding for the rehabilitation work during the majority of the time of excavation, which ruled out the possibility of installing the two AMTS on the balconies. The AMTS on the south side was able to be installed on a pole right next to the periphery of the excavation after gaining the permission from the adjacent private property owner. However, locating an AMTS north of the project site outside the construction limit would be difficult to be approved since it would be on public right-of-way. Therefore, after further site investigation, the final location of the AMTS near the northwestern corner of the site was selected to be at an exposed steel column of the existing hotel structure (Figure 5 shows the layout of three AMTSs and monitoring prism.). This location provided clear line-of-sight but the access to the AMTS was difficult, requiring significant collaborative work and extra safety measures to be put in place by the contractor. To avoid re-accessing the AMTS, a total station with in-body camera and an ALD was installed at this location as shown in Figure 6. The AMTS on the south side installed on top of a high pole is also equipped with a camera. With the aid of instant image capturing by the camera, prisms were learned (commissioned) with ease remotely. At times when certain prisms stopped reporting data, the camera images provided clear evidence that either the prisms' line-of-sight was blocked or the prisms were removed due to construction activities. Figure 7 shows a close-up photo of a prism covered by grout, which was taken by the AMTS camera when the engineer wanted to investigate the cause of missing readings. With the ALD, the AMTSs have been operating nearly a year at the time when this paper was written without any need for re-leveling any of them. As shown in Figure 8, the ALD also helps effectively reduce the instability caused by temperature effects which have an obvious impact on a standard AMTS setup.

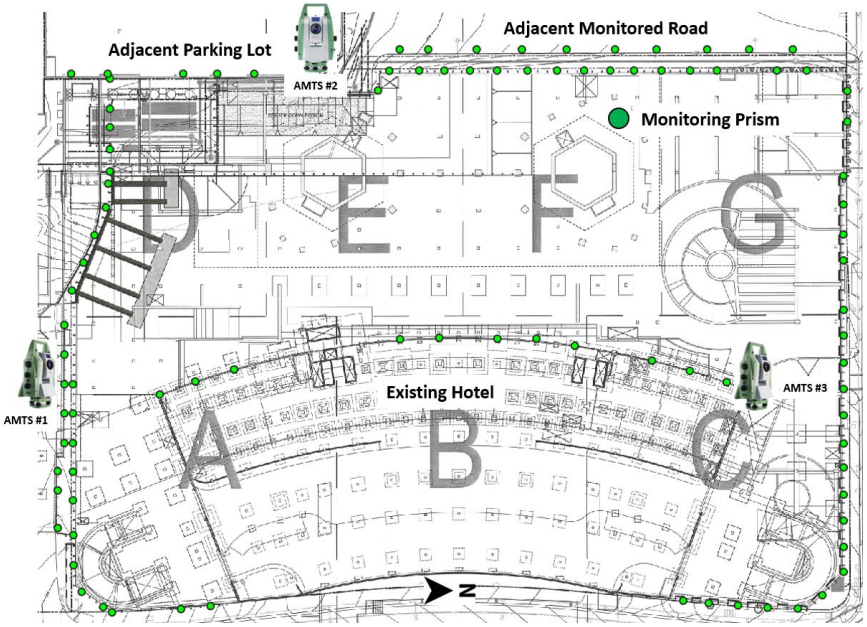


Fig. 5 An AMTS equipped with ALD and in-body camera at an 'inaccessible' location

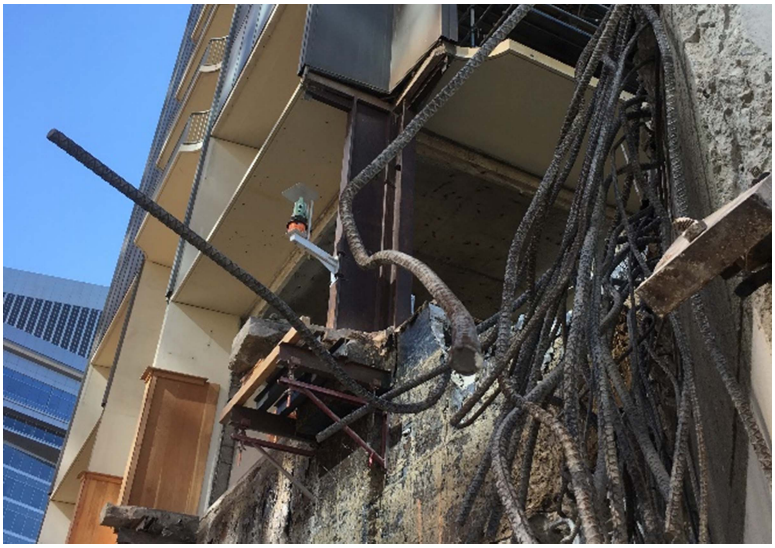


Fig. 6 An AMTS equipped with ALD and in-body camera at an 'inaccessible' location



Fig. 7 A close-up image taken by AMTS camera showing an 'un-seen' prism covered by grout

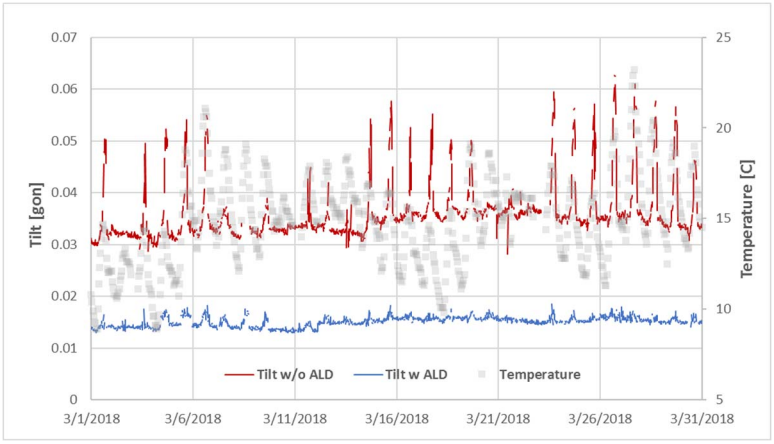


Fig. 8 Comparison of tilting between AMTS with ALD and AMTS without ALD

Regarding the monitoring of the adjacent private street to the west of the excavation, traffic rated road prisms were initially proposed and installed. However, the routinely running street sweeper to clean the road after the commencement of construction deteriorated the prisms at a much faster rate than anticipated, which adversely affects the quality of the monitoring data. Therefore, the I&M specialist also commissioned reflectorless monitoring points next to each road prism, which though only monitored ground deformation in vertical direction (settlement or heaving), provides the geotechnical and shoring engineers with valuable information complementing the lateral deformation measured at the shoring bulkhead.

Wireless tiltmeter

In order to monitor the potential impact of the excavation to the adjacent structures, nine tiltmeters were proposed in 4 separate zones as shown in Figure 9: three tiltmeters under a vehicular bridge to the southwest of the excavation, two tiltmeters in a pedestrian tunnel to the south of the excavation, three tiltmeters on the wall of a subterranean parking, which is also the southern boundary of the excavation, and one tiltmeter on a basement's wall close to the east boundary of the excavation. The vehicular bridge installation locations are above grade, requiring a manlift to access. Other tiltmeter locations are in closed, below grade environments with very weak or zero cellular signal coverage. If the standard tiltmeter and data acquisition system were to be used, the challenges would be: at least one data acquisition box is needed at each zone; long cables is required to connect individual tiltmeter to the data acquisition box; the underground locations have no internet access neither can they be linked to a gateway above ground through standard RF radio, whose signal could not penetrate the concrete structure.

To overcome these challenges, therefore a Lora based wireless tiltmeters system was deployed which provided a single solution resolving all the concerns: elimination of installing and routing the sensor cables significantly saved material, time and labor cost, and more importantly received immediate approval from the property owner for the installation. With one gateway install on the roof of the parking lot to the west of the excavation, it is able to remotely connect to all the wireless tiltmeters without using any signal repeater or booster in-between. This demonstrated Lora wireless technology's exceptional penetration to signal blockage and its immunity to interference. Note that the tiltmeters at the subterranean parking are three levels below grade and the only connection to the ground is a ventilation shaft, completely covered by metallic conduit and other facilities. Different SF (indicating the easiness to be communicated from the gateway) assigned by ADR for each tiltmeter are also shown in Figure 9.

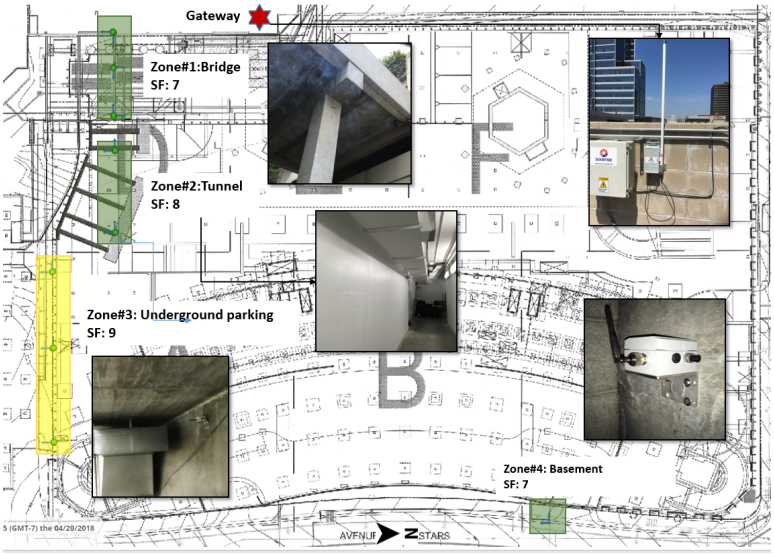


Fig.9. Wireless tiltmeter locations and their spreading factor

Monitoring data reporting and alert system

All the monitoring data from the automatic instruments are transmitted wirelessly at varying intervals of 1 to 4 hour to a remote server hosting the data management system. These data are then processed and presented in forms of GIS view, time series graph, profile graph (e.g. inclinometer data) etc. via a user-friendly web portal allowing convenient and fast data access and evaluation. A near real-time alert system is established so that when measured values exceed their thresholds pre-defined by the engineer, alert message will be transmitted to concerning parties including engineer, I&M specialist, contractors, and the project owner via email or text message. An action plan will be promptly followed up under the direction of the geotechnical engineer.

For the New Century Plaza project, when a monitoring alert is triggered, the geotechnical engineer evaluates the alert collaboratively with the I&M specialist. The contractor is then informed either to pause the excavation in the alerted area, perform a mitigation measure, or continue work with additional monitoring. Since the system has been operating from September 2017, it has helped the geotechnical engineer several times to timely capture excessive movements occurred at the shoring structure and have the contractor take corrective action to stabilize the further development of movements at an early stage.

SUMMARY

New geotechnical instrumentation and monitoring technologies that improve the current state of the practice have been described, with an emphasis in techniques to minimize the interference of I&M system to construction activities. The capabilities of new AMTS features, and Lora Based wireless sensor in reducing the interference to the construction site and improving the effectiveness of the I&M program have been demonstrated through the New Century Plaza deep excavation project.

From a practical perspective, without intensive technical discussion, the authors hope to have encouraged the geotechnical community to accelerate embracing of new technologies into the traditionally slow-evolving I&M practices.

ACKNOWLEDGEMENT

The authors wish to thank the project ownership, Next Century Associates, the project shoring designer, Cefali & Associates, the project contractor, Webcor, and the project shoring contractor, Calex, for their support and work in planning, designing, and executing the monitoring system for the New Century Project.

REFERENCES

Dunnicliff J, 1993. Geotechnical instrumentation for monitoring field performance, John Wiley & Sons.

Bayrd G, 2018. Extract/Transform/Load (ETL) processes for instrumentation data transfer. Geotechnical Instrumentation News, March 2018, pp: 38-40.

ITAtech, 2015. ITAtech Report n°3-V2 - Guidelines for Remote Measurements Monitoring Systems.

LoRa Alliance Technical Marketing Workgroup, 2015. A technical overview of LoRa and LoRaWAN.

Mazzanti, P. J, 2017. Toward transportation asset management: what is the role of geotechnical monitoring. Journal of Civil Structural Health Monitoring, 7: 645. pp 645–656.

Semtech, 2017. LoRa Technology: Ecosystem, Applications and Benefits.

A STUDY IN EXTREME EVENT LARGE DISPLACEMENT ANALYSIS OF LARGE DIAMETER PILES

Bret N. Lingwall, Ph.D., P.E, CEE Department, South Dakota School of Mines and Technology, 501 East St. Joseph Street, Rapid City, SD; e-mail: bret.lingwall@sdsmt.edu
Byron Foster, Department of Civil and Environmental Engineering, University of Utah, 110 Campus Drive Center, Salt Lake City, UT; e-mail: byron.foster@utah.edu

ABSTRACT

The problem of reliable extreme event modeling of large diameter piles under enormous structural or kinematic loads has gained more attention in recent years. In particular, the soil response around the foundation and impacts to buried adjacent infrastructure has gained interest. One of the principal shortcomings with analysis of large diameter pile foundations under extreme event lateral loading is the reliance on conventional beam on elastic foundation methods, which do not model the soil field response around the pile. These methods are limited for large displacement problems, and for large diameter piles. However, the fundamental interactions between steel and concrete, and structure to soil are difficult to constrain, especially in large strain problems where the structural elements become inelastic. The non-linear interaction of the structural materials and soil is desirable so that assessment of stress changes in the field and effects on adjacent facilities can be modeled. A numerical modeling methodology that addresses these shortcomings has been developed. This method utilizes the interaction of brittle concrete with discrete steel reinforcing and casing in a robust manner capturing inelastic non-linearity in both soil and structure. This paper presents a comparison study of the method, wherein three different validation studies were made to data from full scale laterally loaded pile testing.

KEYWORDS: Shafts, Extreme Events, Lateral Loading, Landslides, Modeling, Inelastic Behavior

INTRODUCTION

Extreme event lateral loading of deep foundations comes in many forms including earthquakes, landsliding, tsunamis, hurricanes, surface fault rupture, liquefaction induced lateral spreads and many more. These extreme events induce loads on foundations far greater than service or strength loads. Perhaps the most dangerous extreme event loads are those of large soil displacements such as landslides, lateral spreads, and surface fault rupture, wherein the soil surrounding the foundations can move laterally 100 mm to 3 m! In these extreme event loading scenarios, small diameter foundations are pushed past their limits and many engineers prefer large diameter deep foundations for these situations. These deep foundations of diameter 900 mm or greater may be auger cast in place piles, cast in drilled hole piles, cast in steel shell piles, cased or uncased drilled shafts, bored precast piles, etc. For convenience in this paper, large diameter deep foundations will be referred to as Large Diameter Shafts (LDS). In LDS, steel may or may not used as a shell around the perimeter of the concrete and/or as internal tensile reinforcement. The interaction between brittle concrete and ductile steel within and/or along the perimeter of the LDS is critical to understanding the non-linear inelastic behavior of LDS for problems of large lateral displacements from extreme events.

© 2018 Deep Foundations Institute

The conventional approach to modeling LDS under extreme lateral displacement loading is via a Winkler beam on elastic foundation (BEF) approach such as P-Y methods (Ensoft 2013). The soil-structure interaction (SSI) is modeled in BEF approaches as a local phenomenon, whereas extreme event large displacement problems such as lateral spreading have soil-structure interaction over large areas. The use of an empirically derived P-Y curve with a non-linear inelastic structural model has been demonstrated to be appropriate for small displacement problems (Reese and Wang 1994). Similarly, strain wedge methods utilizing passive earth pressure wedges have been demonstrated to be appropriate for those problems with LDS (Ashour et al. 2001). However, for large displacement problems of LDS, the pile influences soil behavior as much as the soil influences the pile behavior, such that an interactive relationship between soil and structure is needed for analysis and design. For these types of problems, the pile structural model must have realistic non-linear inelastic behavior with the ability to rotate, bend, shear, compress (or "oval") and otherwise undergo complex movements from complex lateral loading. Use of Finite Element Analysis has been employed on many occasions to solve this problem (Lombardi et al. 2010), with varied success.

Typical full scale lateral load tests on slender piles and LDS are often limited to 50 mm of pile head displacement, however large displacements from landsliding or fault rupture are much greater than 150 mm. Landsliding is the prime example of large displacement loading on a LDS, where displacements may be on the order of meters with damage and non-linear inelastic behavior of the LDS (Ong et al. 2015). Lateral spreading, with displacements of one half to several meters is another large displacement problem. In conventional SSI modeling of landslides and lateral spreads, a displacement profile is imposed upon the BEF pile and resultant moments within the pile are determined. This method assumes that free-field landslide or spreading displacements are identical to those imposed on the LDS, with no influence of the LDS on the soil displacements. Another example of a large displacement problem is surface fault rupture, where normal, reverse, or strike-slip faulting can displace several meters. It is well known that Mat foundations influence surface fault rupture (Oettle and Bray 2013), it is likewise known that LDS also influence these soil movements. The amount of soil displacement in landslides, lateral spreads, and surface fault rupture depend on the fixity, size and rigidity of any present LDS (i.e. the pinning effect of the pile). The amount of non-linear inelastic behavior of the LDS will depend on the amount and distribution of the soil displacements and the grip of the soil on the LDS. The coupled process of these large displacement problems requires analytical techniques which can simulate this effect of soil on LDS. Limitations remain for this problem in P-Y and Strain Wedge methods; Dodds and Martin (2007) summarize these limits.

The method of this paper was developed to overcome these limitations. Dodds and Martin note diameter effects and resulting rotational moment stiffness as a principal limitation of the conventional methods. Research indicates that the assumption of soil response independent of LDS diameter appears incorrect. LDS are more likely to undergo rigid body rotation due to rotational moment stiffness than slender piles (Adams and Radhakrishna 1973). Dodds and Martin and Ashour et al. stress the importance of a reliable non-linear inelastic structural model for extreme event LDS modeling. Abridging the findings: in zones of maximum moment along a LDS where non-linear inelastic structural behavior is mobilized, appreciable reductions in P-Y resistance to pile movement have been observed. One additional limitation noted by Dodds and Martin is perfect-versus-imperfect soil contact. Conventional approaches assume perfect soil contact remains around the entire circumference of the LDS even at high displacements, with no gapping. This assumption also presumes that the LDS cannot undergo torsional rotations or torsional stresses from unbalanced superstructure or soil displacement loads. These limitations aside, the non-linear structural

models developed and used by engineers such as those from Ensoft (2013) are robust. Limitations enter when applying these non-linear structural models to problems of LDS at large displacements. To circumvent these limitations, use of advanced numerical techniques has been proposed.

There are several methods of modeling a laterally loaded LDS using finite elements or finite differences, with usefulness varying from small to large lateral displacement problems. The simplest approach, (used for small displacement problems) is to treat the soil as a continuum and to model the foundation using beam elements (or "pile" elements if soil interfaces are included with the beam elements). It has been shown that pile elements can reasonably capture the behavior of laterally loaded piles; however, it is not known whether representation of the interaction between a rupturing fault plane or other large displacement problem and a highly non-linear LDS using one-dimensional pile elements is reasonable given the volume of the LDS is not represented by a non-dimensional pile or beam element. Additionally, the use of pile elements may preclude modeling the highly non-linear behavior of the pile if the terms in the pile element stiffness matrix are constant in software packages. A simple way to implement the continuum model approach is to model the foundation using an elastic constitutive model and material properties as demonstrated by Kim and Jeong (2011). This method was shown to yield satisfactory results under certain small displacement conditions; however, this method requires the analyst to use a composite elastic modulus for the foundation since the material is composed of reinforcing steel, concrete, with or without a permanent steel casing. This linear-elastic approach is not realistic for all analysis cases because significant nonlinearity in LDS is expected at extreme event large soil displacements. An alternative approach is to model the foundation using a non-linear constitutive model such as the Mohr-Coulomb model. The disadvantage of the Mohr-Coulomb model is that it is an elastic-perfectly plastic model, so the "cracked" zones in the concrete will still exhibit constant strength and after the concrete has yielded, unless the model is heavily modified to incorporate brittle behavior.

To compensate for the lack of physical volume of beam elements in finite element modeling of large displacement LDS problems, Wu (2006) uses 4 2-node beam elements spaced at the equivalent boundaries of the shaft. The purpose for using the 4 pile elements is to take into account the effect of pile diameter on pile response via "outlining" the volume of the shaft. The use of one or multiple 8-node pile elements to represent a large-diameter structure (such as a caisson, a vertical tunnel, or a shaft) section makes it possible to account for the diameter effect on response. When a structure section is represented by multiple pile elements, the geometric properties (bending moment of inertia and section area) are evenly distributed to the number of elements on the section. This approach is useful for conventional analysis of laterally loaded single piles or pile groups where displacements are small, and effect of the pile movement is inconsequential to the surrounding soil mass. Two alternative approaches that have been proposed in recent years that compensate for all the limitations are Khosravifar et al. (2014) and McGann et al. (2012). McGann et al. (2012) and Khosravifar et al. (2014) both use a very complex approach to 3D modeling of LDS for large displacement lateral spreading using a combination of structural beam-column elements at the center of the LDS linked to soil contact elements lining the annulus of a void in the location of the LDS. The formulation of the linkages and soil contact elements differ between these two methods. Both methods rely on a void in the location of the LDS lined and linked to a single beam element at the center of the LDS and require use of the OPENSEES Finite Element Package (Mazzoni et al. 2009). These methods have a drawback that the physical mass of the LDS is not imparted into the soil mass beneath and around the LDS, which alters the stress state of the surrounding media from a true field condition. This stress in-turn affects the soil stiffness

and strength locally around the LDS. We propose a method for capturing the non-linear SSI of large displacement loading of LDS using finite difference techniques.

MEANS AND METHODS

The proposed method is described in Lingwall et al. (2017). The method utilizes continuum elements for soil, rock and concrete. Soil and rock are modeled with a stress-dependent non-linear strain softening constitutive model in FLAC3D (Itasca 2013). Although not shown in this paper, the method works well for cases of pile groups. A similar approach is proposed by Bruneau et al. (2018) using ABAQUS. The Bruneau method uses a similar concrete-steel friction algorithm with material strain softening. Figure 1a shows the soil/rock conceptual model based on FLAC's strain-softening model modified to make moduli stress-dependent and non-linear (zone 1) after Duncan et al. 1980. The model uses standard modulus reduction curves to soften relative to the 50% secant strain. The material reaches initial yield and enters dilation (zone 2) until peak after which the material softens (zone 3) to constant volume conditions (zone 4). At very large strains the material softens again to the residual state (zone 5) (if applicable for the material ex: plastic clay). Transitions are defined by plastic shear strains via calibration to triaxial, simple shear, and/or torsional shear tests. Examples of similar calibrations for direct shear tests are given by Anastasopoulos et al. (2007). Portland cement concrete is modeled similarly as shown in Figure 1b. Concrete zones use a stress dependent non-linear modulus with minor dilation upon cracking (zones 1 and 2) using the method and parameters outlined by Chen (2007) based on Mander (1988), with failure in uniaxial, bi-axial and tri-axial compressive, shear, and tensile conditions defined by stress normalized compressive strength as shown by Kupfer et al. (1969). Softening post-failure is defined by concrete plasticity theory Chen (2007) and Mander (1988) defined in FLAC3D by plastic shear strains (zone 4) and the friction angle which largely depends on the mineralogy of the aggregate, until ultimate failure (zone 5) found by calibration to concrete compressive/tensile tests from the design or construction of the LDS. Thus, the concrete is modeled through initial cracking to ultimate failure conditions. Steel reinforcing is modeled as individual linear elasto-plastic ductile tensile cable elements with frictional and adhesive bond with concrete. Steel shells are modeled with linear elasto-plastic shell elements utilizing frictional and adhesive interfaces between steel:concrete and steel:soil that allow slip and sliding before and after peak strength conditions. The composite action of continuum elements, cable elements, and shell elements is a fiber analysis, which behaves in a non-linear inelastic manner. Lingwall et al. (2017) show calibrations to load tests, verification and validation.

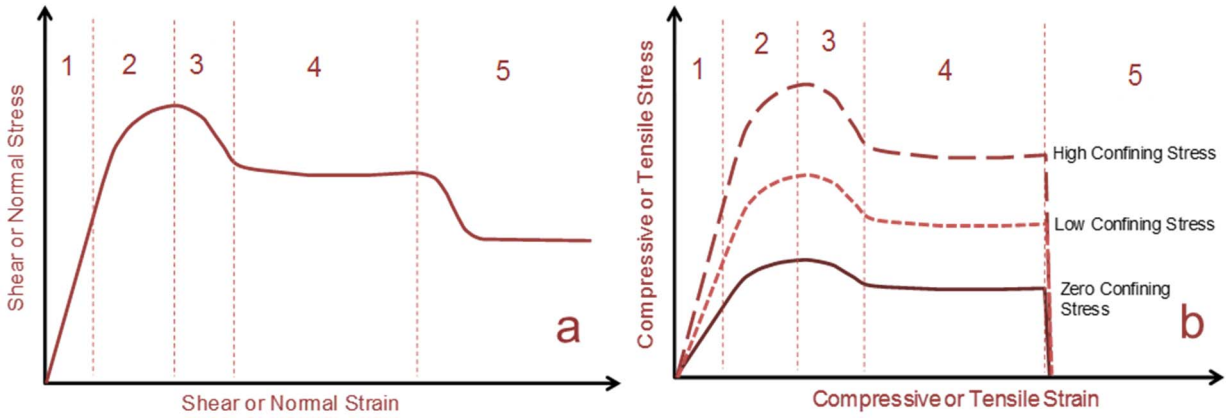


Figure 1. Conceptual model for continuum elements. a) Soil/Rock. b) Concrete.

A pile is constructed in finite difference space surrounded by soil and rock (Figure 2). Interfaces are placed between pile and soil with or without a steel shell using the same basic formulation built into FLAC that allows slip and sliding. Soil and rock are placed with appropriate Ko and baseline stress conditions are solved. The LDS is then installed, and any axial load is applied. If large axial loads are to be applied to the LDS, the model extents are lengthened below the pile to allow for numerical stability. Once the initial conditions are established, a lateral load can be applied to the pile head with appropriate fixity, or at any location on the pile. Alternatively, if a landslide or lateral spread is being simulated, the displacing soil mass applies the load. Complex interactions develop as the system responds to the given load condition. As the formulation is finite difference, the model can handle very large displacements and very large strains. In problems such as surface fault rupture and landsliding, the strain softening model in soil allows for distinct slip planes to develop with strains exceeding 30% if necessary. As the method is 3D in nature, the ability of eccentric loading to cause torsional rotations and torsional shear on the LDS are captured. Rotations about the pile head can occur in all three dimensions. Rigid body rotation is captured. Gapping behind the LDS occurs as does shoving of the soil material in front of the pile. The formation of active earth pressure and passive earth pressure wedges can be observed in the soil continuum around the LDS.

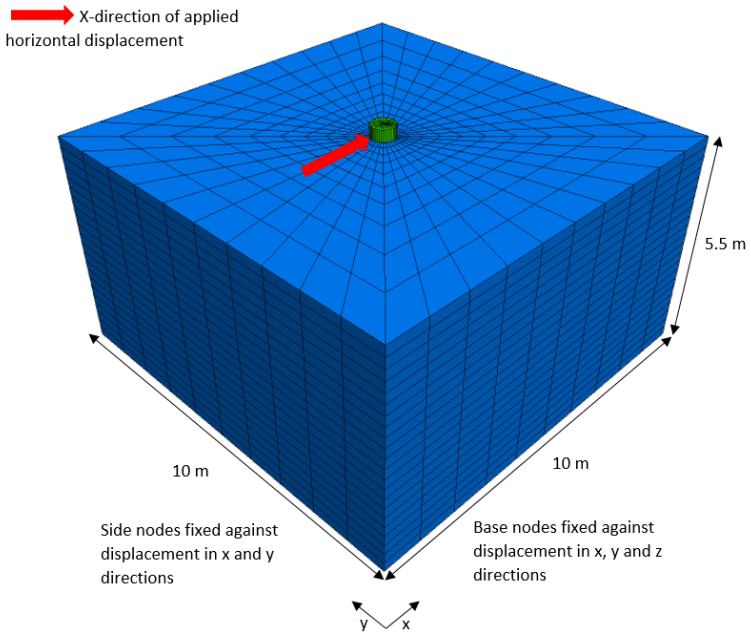


Figure 2. Finite Difference Model Example Mesh. This model is from the comparison simulations for Ismael (1990) pile load tests.

For comparison with structural analysis of the LDS, FLAC3D does not produce an overall structural moment or shear at any location on the length of the LDS. For this, the method of this paper measures the displacement, rotation and curvature of the LDS along the length of the LDS, and then uses moment-curvature relationships and differentiation to obtain moments and shears at any location along the LDS length. Moment-curvature relationships can be obtained from non-linear structural analysis of the LDS based on the concrete and steel quantities and locations. The moment-curvature relationship can also be obtained in FLAC3D via a parallel push-over analysis of the LDS with no soil present. Theoretical moment-curvature relationships should be used with caution, as some relationships are specific to certain conditions

and may not apply to LDS. The results are most sensitive to 1) presence of transverse reinforcement, 2) Young's Modulus of concrete, and 3) tensile strength of the concrete. Prior to using the method for rigorous analysis of piles in extreme event large displacement problems of lateral spreading, landsliding, and surface fault rupture, the method is validated against full scale pile load tests in which the capabilities of lateral loading in pile load tests are pushed to the limits. The lateral displacements in these tests remain small compared to extreme event loading. However, the largest available displacement tests are used until lateral load testing capabilities improve to the point where a meter of lateral loading can be both applied an measured. Three of these case histories are presented and modeled in this paper.

ISMAEL (1990) PILE LOAD TESTS

Ismael (1990) performed full scale load tests of reinforced concrete piles in weakly cemented dry sand. For this validation, the 0.3m diameter, 5m long free-headed pile was chosen. Weakly cemented dry sand is a strain softening material, and Ismael provides detailed triaxial tests across a range of confining stress levels so that both peak and fully softened strengths can be established along with the plastic shear strains at which peak and softening occur. The cemented sand was 3m thick at the site of the load tests, with dense un-cemented sand below. Table 1 shows the material properties provided by Ismael or derived from the data for the soil materials at the load test site, including stress-dependent modulus. Ismael also provide concrete test results and details of reinforcing steel. The study is ideal for this current paper as all of the critical inputs are readily available for both the soil and structure. In numerical simulations the same properties are used directly with an assumption that the frictional interface between concrete and soil is 2/3 of the internal frictional coefficient of the surrounding soil.

Table 1. Material properties for Ismael (1990) pile load tests

Material	ρ (Mg/m^3)	C/m	ν	ϕ'_{pk} (deg)	ϕ'_{cv} (deg)	c'_{pk} (kPa)	c'_{vc} (kPa)	f'_c (MPa)	E (MPa)	γ_{ps} *
Upper Sand	1.83	35 / 0.39	0.33	35	28	20	0	N/A	N/A	0.08
Lower Sand	1.94	35 / 0.39	0.3	43	32	0	0	N/A	N/A	0.06
Concrete	2.4	N/A	0.2	N/A	N/A	N/A	N/A	27.57	22,000	0.01

* *γ_{ps} is the plastic shear strain at which strain softening is complete.*

FLAC3D simulations were performed with the same geometry, parameters, and configurations as in the comparative study. Several parametric analyses were also performed. Figure 3 shows a comparison between simulations and the measured force (P) deflection (Y) at the pile head including the parametric study results. The primary analysis is with a stress-dependent strain softening soil material, which shows a good comparison to the experimental data. Three other simulations were performed with constant modulus but with strain softening materials, using the minimum, average and maximum moduli (35, 47.5, and 60 MPa) in triaxial tests. These simulations had similar ultimate resistances as the primary analysis but had softer initial PY behavior. A fourth parametric analysis was performed with no strain softening, i.e. a conventional Mohr-Coulomb type analysis. This simulation resulted in much higher ultimate resistance than the other simulations. This showed the importance of the strain softening approach for large displacement problems, and the importance of a non-linear stress dependent approach for small displacements. Several other

parametric analyses were performed, varying concrete modulus, strength, and reinforcement details. These other parametric analyses confirmed that an accurate concrete modulus is essential for realistic results, and that the analysis is insensitive to the strength of steel and the exact amount/configuration of transverse reinforcement as long as confining steel is present and that the amount of confining steel is within 25% of the actual conditions. The work by Ismael had already demonstrated that conventional PY methods require significant modification to PY curves for reliable calculation for pile head deflection. This validation study shows that the proposed numerical modeling approach can reliably and accurately determine the pile response if sufficient soil and structural data are available.

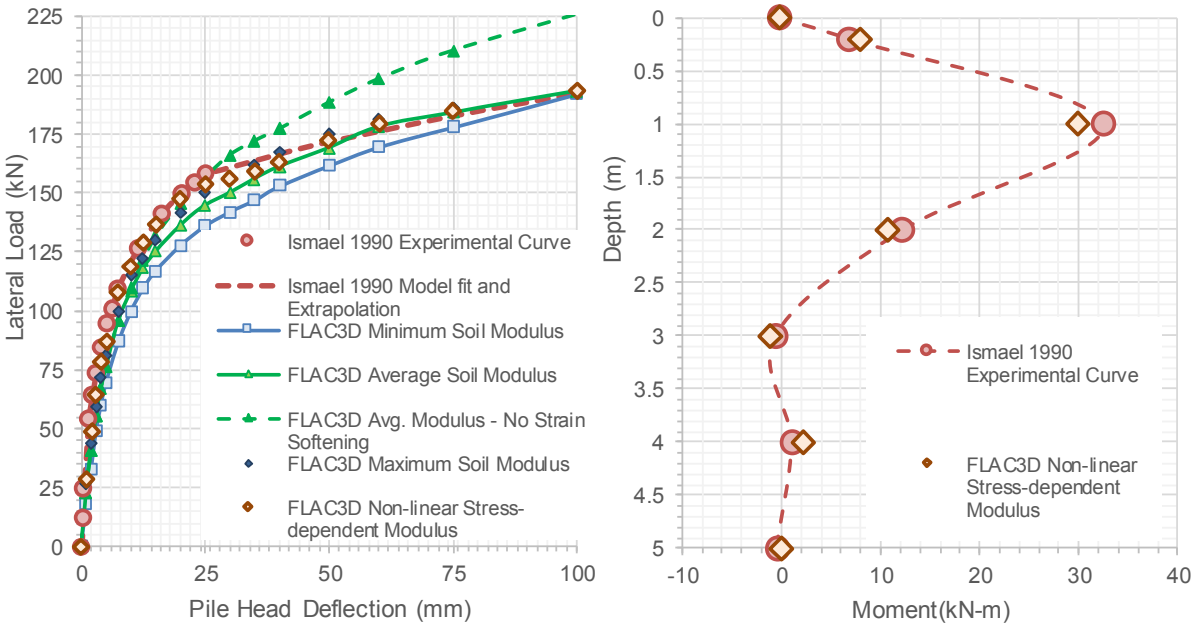


Figure 3. Comparison of 3D non-linear inelastic numerical simulations with Ismael (1990) 5m laterally loaded free headed pile load test in weakly cemented sand in Kuwait.

BHUSHAN ET AL. (1981) PILE LOAD TESTS

Bhushan et al. (1981) performed a series of pile load tests in dense dry sand on piles 5.2 to 5.6 m in length. The pile load tests were performed in southern California in coarse silty sand with appreciable gravel content. For this validation exercise, Test #5 is used, a 1.0 m diameter reinforced concrete drilled shaft with 14 US Standard #11 longitudinal reinforcing bars (transverse #4 hoops spaced at 50 mm assumed). Concrete compressive strength and Young's Modulus were provided (39.3 and 29,850 MPa), as were triaxial test results across a range of pressures (ϕ'=36° in the upper 1 m, and 43° below). However, the traixial tests did not indicate substantial strain-softening in the sand, so in these simulations, a Mohr-Coulomb material model was used with dilation of 3° below 1m. SPT blowcounts at the site increase linearly with depth from 12 at the surface to 50 at the bottom of the test piles. CPT tip resistance increased similarly from 50 tsf to 300 tsf. Multiple correlations to penetration resistance were used and averaged to determine soil E. The same framework was used in these simulations as in the Ismael 1990 simulations. Results comparison between simulation and the data provided by Bhushan et al. are shown in Figure 4 (only pile head deflections available from the authors). Figure 5 shows the deformed pile (exaggerated for demonstration) at 40 mm of pile head displacement.

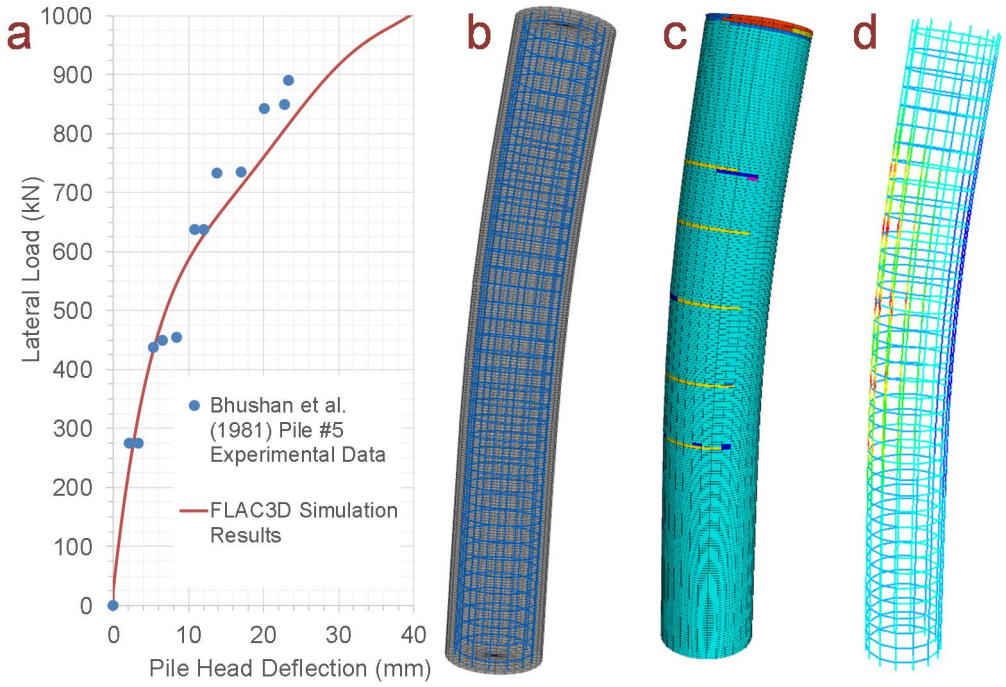


Figure 4. a) Comparison of 3D non-linear inelastic numerical simulations with Bhushan et al. (1981). b) 15x Exaggerated pile deformation at 40 mm of displacement with reinforcing cable zones shown. c) Concrete zone state (yellow is tensile failure). d) rebar yield (red)

ADAMS AND RADHAKRISHNA (1973)

This study was performed in loose (upper 2 meters) to medium dense sand, with 1.0 m diameter 6.1 m long drilled shafts. Pressuremeter tests provide the soil modulus at depth (650 increasing to 1600 kPa), with SPT blowcounts increasing with depth from 10 to 30 providing friction angles (32° to 39°). For brevity, complete details of soil properties are not shown. Reinforcement was only reported as "heavy" in the study, so the numerical analysis was performed multiple times with the best estimate of steel at 3.5%. Results from different simulations with varying amounts of steel were only moderately sensitive to the reinforcing. These experiments used a fixed head condition with an applied moment rather than shear at the top of the pile. Results comparisons are shown in Figure 5 for FLAC3D and other conventional laterally loaded pile analyses, wherein 3.5% steel of identical size is used in all analyses.

SUMMARY AND CONCLUSIONS

For analysis of extreme event large displacement lateral loading of LDS, conventional methods and many finite element method approaches have several key deficiencies when transitioning from lateral pile head loading to large soil displacement problems like landsliding and lateral spreading. For these complex large displacement problems, a new method has been proposed with non-linear inelastic stress-dependent strain-softening relationships for soil and concrete with discrete tensile and shell elements for steel. The method is validated in this paper against three full scale laterally loaded pile case histories of moderate to large displacements demonstrating that method is reliable and accurate. With this validation (and additional

validations to landslide and lateral spreading case histories forthcoming), the method is proving to be very promising for use in solving complex large displacement problems where soil and structure interact at large scales of greater than 50 mm displacement. The method appears to be robust up to several meters of soil displacement. Key parameters for analysis are 1) Young's Modulus of concrete, 2) tensile strength of concrete, 3) use of a strain softening soil model that incorporates both dilation and contraction volume change, with 4) a model for concrete capable of capturing brittle behavior. Results are sensitive to these four factors. Results are moderately sensitive to the amount and strength of the steel.

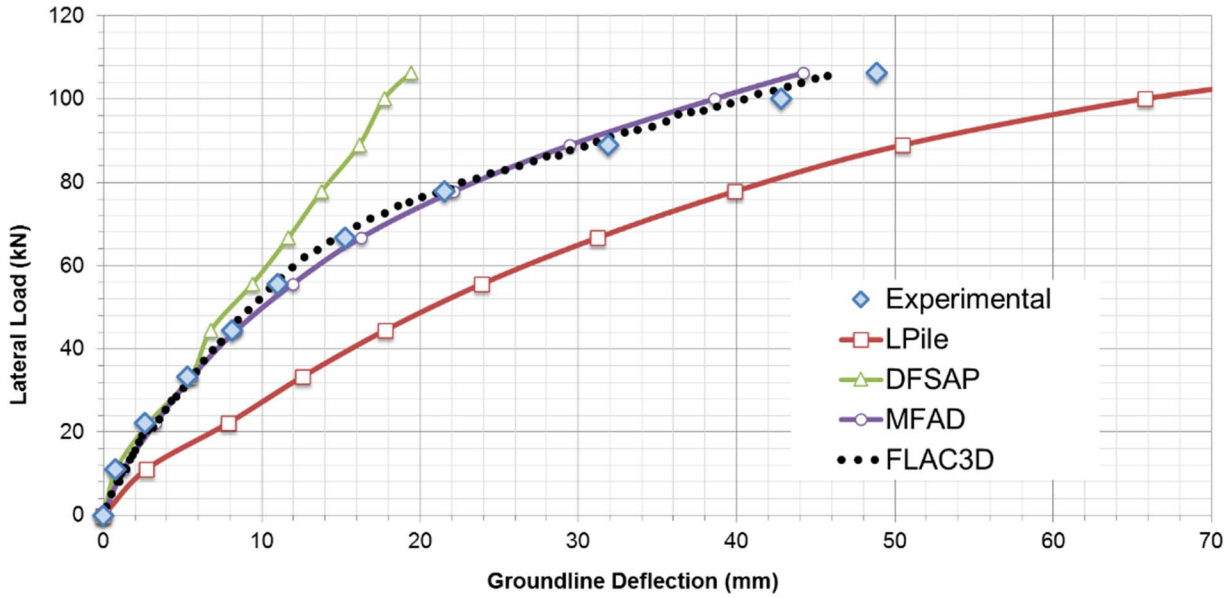


Figure 4. a) Comparison of 3D various simulations with Adames & Radhakrishna (1973).

ACKNOWLEDGEMENTS

The authors would like to thank Professor Evert Lawton of the University of Utah, Dr. James Gingery of Hayward-Baker Keller Inc. and Professor Jonathan Bray of the University of California at Berkeley for their helpful insights and reviews during conceptual and numerical modeling approach development.

REFERENCES

Adams, J.I. and Radhakrishna 1973. "The Lateral Capacity of Deep Augured Footings," *Proc. 8th ICSMFE*, Vol. 2.1, pp. 1-8.

Anastasopoulos, I., Gazetas, G., Bransby, M. F., Davies, M. C. R., and El Nahas, A. 2007. "Fault rupture propagation through sand: Finite element analysis and validation through centrifuge experiments." *Journal of Geotech. and Geoenviron. Engineering*, 133(8), 943-958.

Ashour, M., Norris, G., and Shamsabadi, A. 2001. "Effect of the Non-Linear Behavior of Pile Material on the Response of Laterally Loaded Piles." *4th International Conferences on Recent Advances in Geotechnical Earthquake Engineering and Soil Dynamics*. San Diego, CA.

Bhushan, K., Lee, L. J. and Grimp, D. B. 1981 "Lateral load tests on drilled piers in sand. Drilled piers and caissons," *Proceedings, Geo-technical Engineering Division at ASCE National Convention*, St. Louis, MO.

Bruneau, M., Kenarangi, H., and Murphy, T.P. 2018. Contribution of Steel Casing to Single Shaft Foundation Structural Resistance. *NCHRP Report 872, NCHRP Project 12-93.*

Chen, W.F. 2007. *Plasticity in Reinforced Concrete,* McGraw-Hill, New York, NY.

Dodds, A.M., and Martin, G.R. 2007. "Modeling Pile Behavior in Large Pile Groups under Lateral Loading." *Technical Report MCEER-07-0004*, Buffalo, NY.

Ensoft 2013, LPILE v. 2013.7.03, Ensoft Inc., Austin, TX.

Ismael, N.F. 1990. "Behavior of Laterally Loaded Bored Piles in Cemented Sand." *J. Geotech. and Geoenviron. Eng.*, 116(11), 1678-1699.

Itasca 2013. Fast Lagrangian Analysis of Continua in 3 Dimensions, Itasca Consulting Group, Inc.

Kim, Y. and Jeong, S. 2011. "Analysis of Soil Resistance on Laterally Loaded Piles based on 3D Soil-Pile Interaction," *Computers and Geotechnics*, 38, 248-257.

Khosravifar, A., Boulanger, R.W., and Kunnath, S.K. 2014. "Effects of Liquefaction on Inelastic Demands on Extended Pile Shafts." *Earthquake Spectra*, 30(4), 1479-1773.

Kupfer, H.B., and Gerstle, K.H. 1973. "Behavior of concrete under biaxial stresses." *Journal of the Engineering Mechanics Division*, ASCE, 99(4), 852-866.

Lingwall, B.N., Foster, B., Ogunseye, O., Gingery, J.R. 2017. "A robust method for lateral loading analysis of large diameter piles." *Geotechnical Frontiers 2017*, Orlando, Florida.

Lombardi, D., Durante, M.G., Dash, S.R., and Bhattacharya, S. 2010. "Fixity of Piles in Liquefiable Soils." *5th International Conferences on Recent Advances in Geotechnical Earthquake Engineering and Soil Dynamics.* San Diego, CA. Paper 5.39a.

Mander, J.B., Briestley, M.J.N., and Park, R. 1988. "Theoretical Stress-Strain Model for Confined Concrete." *Journal of Structural Engineering*, 114(8), 1804-1826.

Mazzoni, S., McKenna, F., Scott, M.H., and Fenves, G.L. 2009. *Open System for Earthquake Engineering Simulation*. University of California at Berkeley.

McCann, C.R., Arduino, P., and Mackenzie-Helnwien, P. 2012. "Development of Simplified Analysis Procedure for Piles in Laterally Spreading Layered Soils." *Pacific Earthquake Engineering Research Center*, December 2012.

Ong, D.E.L., Leung, Y.K., Chow, Y.K., and Ng, T.G. 2015. "Severe Damage of a Pile Group Due to Slope Failure." *J. Geotech. and Geoenviron. Eng.,* 141(5).

Oettle, N.K., and Bray, J.D. 2013. "Geotechnical Mitigation Strategies for Earthquake Surface Fault Rupture." *Journal of Geot. and Geoenviron. Engineering*, 139(11), 1864-1874.

Reese, L.C., and Wang S.T. 1994. "Analysis of piles under lateral loading with nonlinear flexural rigidity." *U.S. FHWA Int. Conf. On Design and Construction of Deep Foundation, FHWA,* Washington, D.C.

Wu, G. 2006. VERSAT-P3D Dynamic 3D Finite Element Analysis of Single Piles and Pile Groups. Wutech Geotechnical International, B.C., Canada.

DESIGN AND CONSTRUCTION OF THE SUMMIT SENIOR CARE FACILITY INTO THE SIDE OF AN UNSTABLE CALIFORNIA HILLSIDE

Harry W. Schnabel, P.E., Schnabel Foundation Co., Sterling, VA, USA (703) 742-0020, hank@schnabel.com
Patrick O. Shires, G.E., Cotton, Shires and Associates, Inc., CA, USA (408) 354-5542

With stable building sites becoming scarce in the greater San Francisco Bay Area, the new Summit Senior Care Facility is being built into the side of an unstable hillside adjacent to the San Ramon Regional Medical Center in San Ramon, California. This hillside has had a long history of instability and the site of the new Senior Care Facility required excavation into both a historic old landslide and a more recent active landslide. After a thorough geotechnical study, it was concluded that the best way to build the new facility would be to construct a tied-back retaining wall in the area of the old landslide, since it extended off-site onto two adjacent properties, and remove the active landslide and replace it with compacted fill before cutting into its toe area with an additional tied-back retaining wall. The design was further complicated by the proximity of the site to several active faults. In the area of the old landslide, the combination of an ascending slope behind the wall, landslide forces and seismic forces resulted in total design pressures between 365 to 4,575 PSF for a wall with a maximum height of 30 feet. The wall for the old landslide was constructed by first drilling and placing steel soldier piles in concrete. The tip of the soldier piles extended a minimum of 12 feet below the landslide plane that was up to 36 feet below the bottom of the wall. Permanent double corrosion protected tiebacks were then installed through the soldier beams and anchored below the slide plane. A shotcrete facing was then installed on the face of the wall.

Keywords: tiebacks, landslide, soldier beams, shotcrete

BACKGROUND

The site of the Summit Senior Care Facility is located on the southwest flank of Mount Diablo adjacent to San Ramon Valley which is characterized by gently rolling hills. The San Ramon Valley Regional Medical Center, which opened in 1990, is located to the north and an existing church is located to the southwest. There are also private residences located to the southeast. The site is shown in Figure 1.

Numerous faults run close to the site, the most significant of which are the Calaveras and Pleasanton faults. The site has also had a long history of slope instability and has been the subject of numerous investigations. Studies conducted in 1979 and 1984 concluded that there was a landslide in the area and recommended that a buttress shear key be constructed between the subject site and the existing church for a sewer main as well as removal and replacement of the head area of the old landslide to stabilize the hospital site. While two previous geotechnical studies in 2008 and 2016 identified slope instability, they did not recognize the genesis and limits of the old landslide on the western portion of the site or the limits of the active landslide on the eastern portion of the site.



Figure 1 - Location of Summit Senior Care Facility

© 2018 Deep Foundations Institute

Cotton Shires and Associates (CSA) was engaged to review the previous studies and perform additional investigations to provide recommendations for development of the Summit Senior Care Facility. CSA's investigation included review of geotechnical documents pertaining to adjacent properties, evaluation of historical pairs of aerial photographs, engineering geologic mapping, downhole logging of five (5) large-diameter bucket auger exploratory borings, laboratory testing of representative samples and slope stability analyses. The conclusion of this investigation was that there were two landslides on the site (Fig 2).

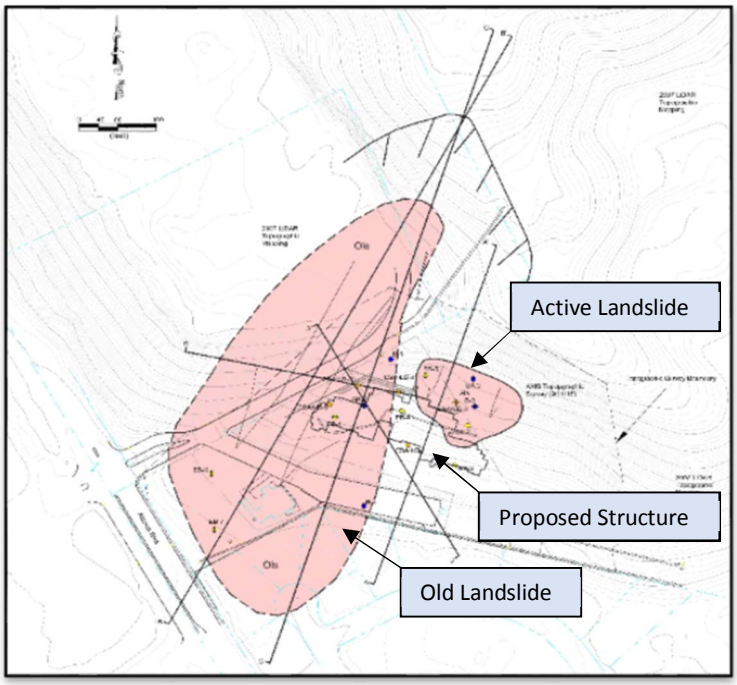


Figure 2 – Location of landslides

On the northwest side of the site there is a larger "old landslide" that has been static for a significant period of time. This landslide was around 900 feet long by 150 to 450 feet wide and extended beyond the property line to the southwest. The slide plane is estimated to be up to 45 feet below the ground surface within the confines of the site. The upslope portion of the old landslide was removed and replaced with fill during the construction of the adjacent hospital project and a buttress fill was placed across the central portion of the landslide for a sewer line, but the portions of the landslide on the subject site and to the southwest were left in place, creating a seismic ground movement problem.

In addition, an active landslide was identified on the east side of the site. This landslide appears to have failed after the 1980's, based on a review of historical photographs. The active landslide was estimated to be around 170 feet long, 235 feet wide and over 21 feet deep.

To mitigate the landslides and allow for development of the site, CSA recommended that the smaller active landslide be removed and replaced with engineered fill with subdrains prior to any other work on the site. The remaining portion of the old slide would be stabilized using a tieback retaining wall with shear pins (soldier piles) that intersect the slide plane and tiebacks anchored in the ground below the slide plane.

Subsurface conditions at the tieback wall consist of fill over sandy silty clay colluvium and landslide deposits. The large-diameter borings indicated a slide plane that was up to 45 feet below the surface. The old landslide was underlain by Green Valley and Tassajara formations of sedimentary claystone and sandstone bedrock. Groundwater was encountered at depths of 43 to 45 feet, but previous investigations indicated shallower groundwater depths (as shallow as 10 to 16 feet below ground surface in areas).

DESIGN

A tieback wall located to the north and west of the new facility was designed to retain the existing slope, including landslides, from existing grade to the pad grade for the new structure. The tieback wall had a height of up to 30 feet. The western half of the tieback wall restrains the remaining portion of the old landslide, and the eastern half restrains soils in the toe area of the remediated active landslide. City of San

Ramon restrictions required that the highest portion of the western section of wall be stepped. This was accomplished by constructing two stepped soil nail walls at the top of a 75-foot long portion of the wall and fill walls at the top of the remainder of the wall. A typical section through the wall is included as Figure 3.

The wall in the area of the old landslide was designed to increase the factor of safety in the slope to at least 1.5 under static conditions and 1.1 under seismic conditions with a cumulative displacement of less than 6 inches during the design earthquake.

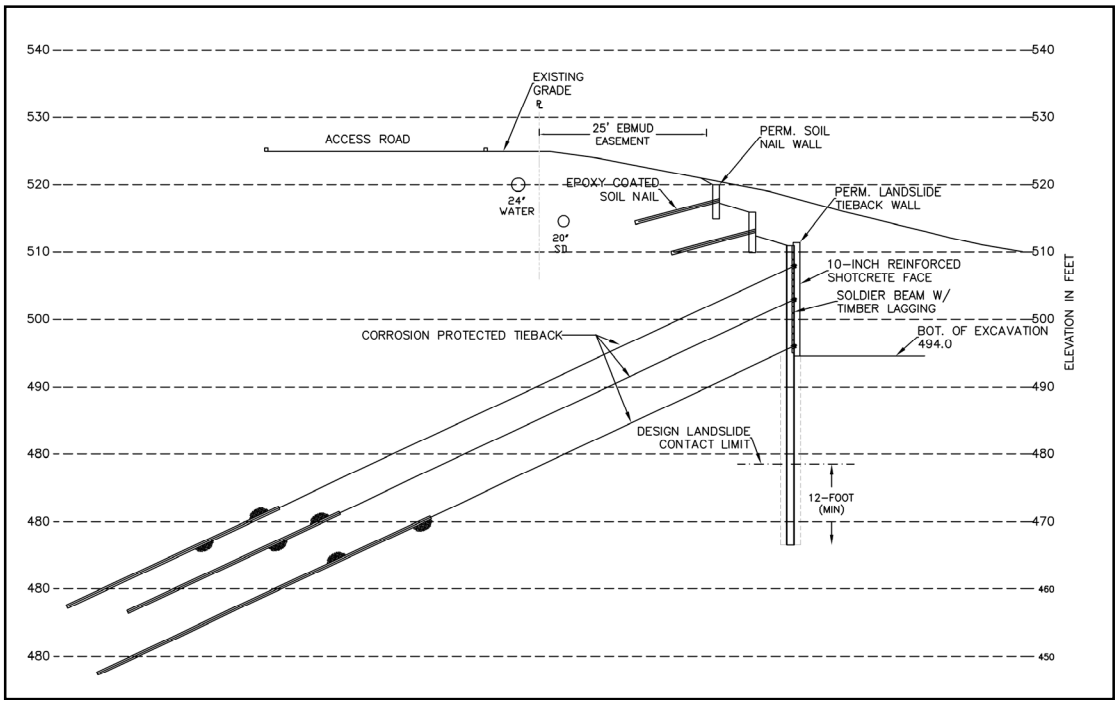


Figure 3 – Typical Section Through Landslide Wall

The assumed soil properties used for the analysis were:

Table 1 – Summary of Soil Parameters Used in Design

Material	Unit Weight (pcf)	Cohesion (psf)	Friction Angle (^{o})
Old Landslide Deposits	123	0	24
Artificial Fill (Drained)	122	500	24
Artificial Fill (Undrained)	122	600	14
Green Valley and Tassajara Formation	125	1,000	25

The basic design procedure followed was to analyze the existing slope for various design sections (Figure 4) and back-calculate a friction angle for various groundwater depths using a limit equilibrium slope stability analysis. The shear zone geometry was based on data obtained from the subsurface explorations and a review of previous reports. The analysis was performed with SLOPE/W (By Geo-Slope International) using the Morgenstern-Price method of slices. The analysis indicated that a friction angle of 12.2 degrees and no cohesion be used for the failure surface of the old landslide. This value was very close to or lower than the residual shear strength determined by previous investigations.

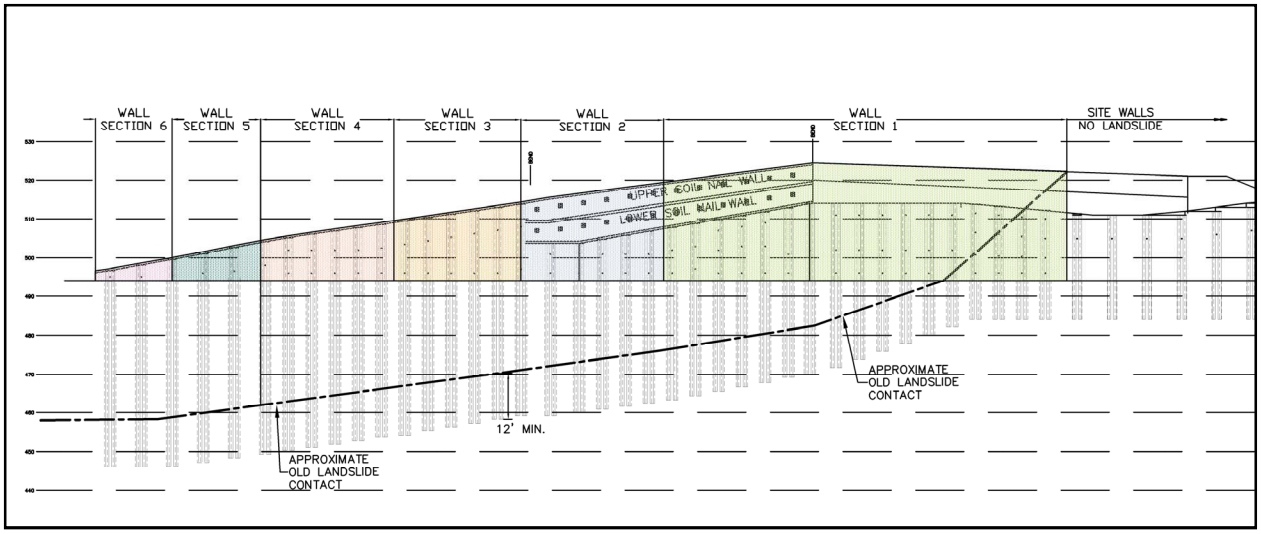


Figure 4 – Elevation View Showing Design Sections

Seismic deformation analyses were conducted by varying the horizontal seismic coefficient (k_y) value for different slope geometries and allowable displacements. The reinforcement loads were then increased until a F.S. of 1.0 was achieved for 6 inches of displacement. The peak ground acceleration assumed for analysis was 0.85g due to the numerous faults in the area. Liquefaction potential is considered low due to the presence of fine grained soils at the site.

The resulting required slope reinforcement are as follows:

Table 2 – Results of Slope Analysis

Wall Section	Wall Height (ft)	Depth of Shear Plane (ft)	Static Loading (kips/lf)	Seismic Loading (kips/lf)
1	25-30	0 - 45	60	105
2	20-25	42 - 45	48.4	88
3	15-20	42 - 44	36.8	71
4	10-15	42 – 44	25.2	54
5	5-10	42 – 44	13.6	37
6	<5	42 - 44	2	20

CSA provided the resulting loads from the stability analysis to Schnabel Foundation Company who used these loads to complete the wall design. The loads were applied to the back of the wall as a uniform pressure extending from the slide plane to existing grade. The contribution to the passive pressure from the soil above the slide plane was conservatively neglected, however the weight of the soil was used in calculating the passive pressures below the slide plane. An intermediate groundwater level was used despite subdrains installed by previous construction in the upper portion of the old landslide and the mid-landslide buttress.

The soil nail walls were designed using SNAILZ for both the static and seismic conditions, but offered no contribution to the stabilization of the landslide. The weight of the soil nail walls and fill walls were applied as a surcharge load on top of the tieback walls.

Each design case was then analyzed for three critical design combinations in the California Building Code:

Table 3 – Load Combinations used in Design

Load Combination	Description	
16-9	D+H+F+L	D = Dead Load
16-12	D+H+F+(0.6W or 0.7E)	H = Earth Load
16-14	D+H+F+0.75(0.7E)+0.75L+.75S	F = Fluid Load (F=0 because wall is free draining)
		W = Wind Load (W=0)
		S = Snow Load (S=0)

Using the prescribed loads in Table 2 for the various load combinations in Table 3 the required section modulus for the soldier piles varied from 153 in^3 for design section 1 to 384 in^3 for design section 5. In general, the section modulus decreased as the distance from pad grade to the slide plane decreased as would be expected given the design assumption that there was no passive resistance above the slide plane and no tiebacks would be installed below pad grade.

A double wide flange beam was selected for the soldier piles to accommodate the multiple tiers of tiebacks without altering the properties of the beams themselves. Double wide flange beams are constructed by laying two wide flange beams side by side and welding steel plates between the piles to strap them together. A gap is left between the piles that is wide enough to accommodate the drill bit for the tieback installation. To account for corrosion, the properties of the portion of the soldier pile above pad grade was reduced to account for 1/16-inch steel loss as recommended in the FHWA 1998 "Design Manual for Permanent Ground Anchor Walls" (pg. 153). The portion of the soldier pile below subgrade was encased in structural concrete and thus no loss of steel was required.

The design analysis also indicated that up to four (4) tiers of tiebacks would be required. Tieback loads varied between 69 and 205 kips. Double corrosion protected (DCP) strands were used for the tiebacks. The unbonded lengths were designed so that the bond length would be completely below the slide failure plane. This resulted in unbonded lengths that varied from 30 to 85 feet.

CONSTRUCTION

Schnabel was originally supposed to begin construction of the tieback wall in the summer of 2017 but was delayed until October because the active slide took longer to repair than anticipated due to difficult moisture conditioning of the highly plastic earth materials and the slide being deeper than originally expected. This pushed the construction of the tieback walls into the rainy winter months, but luckily it was a relatively dry winter. There were, however, a few days where the rain made the benches too slick to get concrete trucks to the holes. After the active slide was remediated (Figure 5), a bench and access roads were cut into the sides of the hill to allow access for drilling equipment and concrete trucks.



Figure 5 – Removal of Active Landslide

The soldier beams were installed using a rotary rig drilling a 36-inch hole. The sides of the holes were relatively stable and all the holes could be drilled without casing. Some of the holes were drilled on a slope, and since the drill could only drill facing downslope, it was necessary to drill

alternate holes and then return to drill the intermediate holes. The steel piles had to be placed in the hole using a separate 75-ton crane due to their heavy weight and the bench restrictions imposed by working on the side of a hill. After the piles were placed in the holes, they were backfilled with structural concrete to within two feet of pad grade and topped off with lean concrete to the top of the hole. Water was encountered in a few of the holes and was pumped out prior to placing concrete. A CSA field engineer was on site whenever drilling took place to ensure that the soldier piles extended at least 12 feet below the slide plane. The soldier piles along the west side of the wall were skewed 15-degrees out of the plane of the wall to allow a larger component of the force from the tiebacks to oppose the slide (Figure 6).

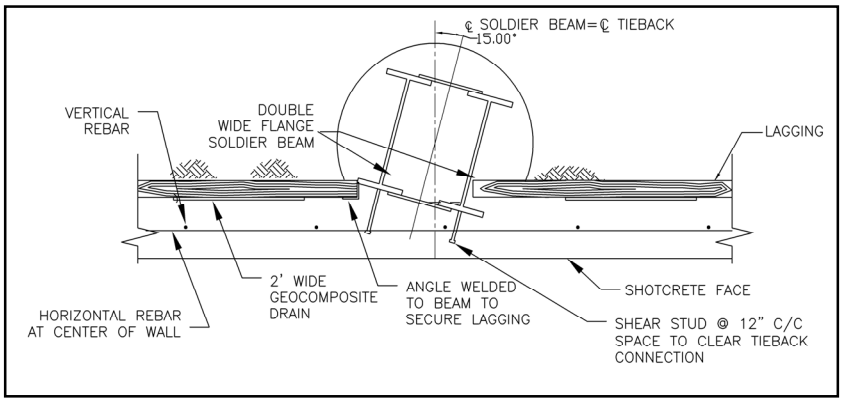


Figure 6 – Soldier Pile Detail

Timber lagging was placed between the soldier beams to temporarily hold the soil until the permanent shotcrete facing could be constructed. Angle iron was welded to the face of the skewed piles to allow the lagging to be placed in the plane of the wall.

The tiebacks were installed using double rotary drill rigs and 6-inch casing. Initially the ties were drilled open hole but this method was abandoned as being too unreliable. In addition, open hole drilling created communication between the tiebacks where air used to flush the holes blew the grout out from previously installed tiebacks. A casing handler mounted to a mini-excavator was used to load and unload the sectional casing. A horizontal uncoiler was used to load the tendons in the holes. Tieback installation is shown in Figure 7.



Figure 7 – Tieback Installation

The tiebacks were grouted using a neat cement grout. After the initial grouting, the tiebacks were re-grouted 1 or 2 times to increase their capacity. Initially, a water reducing admixture was used to increase the strength of the grout and reduce the cure time. After grouting a number of the tendons this way, it was discovered that the grout would set up too quickly to allow regrouting. The grouting procedure was revised and the Intrusion Aid was used to grout inside the corrugated sheath and for the re-grouts but not the initial grouting outside the corrugation.

Every tieback on the job was either proof tested to 120% of design load or performance tested to 133% of design load. Creep rates for the tiebacks varied between 0.000 and 0.037 inches with an average of .008 inches for the 1 to 10-minute load hold. Total movement varied from 88.5% to 143.0% of the elastic deformation of the unbonded length and 60.5% to 96.8% of the elastic deformation of the unbonded length plus half the bond length.

Once the wall was excavated to subgrade, drain board was applied to the face of the lagging and studs were welded to the soldier beams to secure the shotcrete facing. A single mat of reinforcing steel was then placed against the lagging at the center of the wall. The shotcrete, was then applied to the surface of the lagging. The shotcrete was 10 inches thick in the landslide area and was reduced to 8 inches thick outside the landslide. The finished wall is shown in Figure 8.



Figure 8 – Finished Wall

CONCLUSIONS

The use of a tied-back retaining wall allowed for the development of land that was previously not thought to be useful. This required a thorough study of the property history, a detailed geotechnical study, an owner willing to invest sufficient resources to make the site safe, a contractor with experience in challenging hillside development and careful observations and testing during construction. The Summit Senior Care Facility will be protected by the tieback wall during static and seismic conditions and the foundation of the building will be founded on a deep reinforced concrete pier foundation to accommodate foundation loads and highly expansive earth materials. While there were significant geologic and geotechnical hazards at this site, safe development was achieved.

REFERENCES

Design Manual for Permanent Ground Anchor Walls (1998), Publication No. FHWA-RD-97-130 Federal Highway Administration (FHWA)

Schnabel, Harry Jr., Schnabel, Harry W. 2002 Tiebacks in Foundation Engineering and Construction – Second Edition, A.A. Balkema Publishers

Geotechnical Design Investigation Report, Summit Senior Living Facilities, 12700 Alcosta Boulevard, San Ramon, CA December 2016, Cotton, Shires and Associates, Los Gatos, CA

Geotechnical Evaluation, New Senior Living Center, 12700 Alcosta Boulevard, San Ramon, CA March 9, 2016, EEI Geotechnical & Environmental Solutions, Carlsbad, CA

Geotechnical and Geologic Investigation, Medical Office Building and Church Expansion, 12700 Alcosta Boulevard, San Ramon, CA April 15, 2008, Cornerstone Earth Group, Walnut Creek, CA

AN INVESTIGATION OF GROUTED PILE CAPACITY USING INSTRUMENTED PILE LOAD TESTS

Hayel M. El-Naggar, Research Assistant, Geotechnical Engineering Department, Housing and building Research Center, Cairo, Egypt, hayel@hbrc.edu.eg
Sherif A. Akl, Associate Professor, Faculty of Engineering, Cairo University, Cairo, Egypt, sherif.akl@cu.edu.eg

ABSTRACT

Although grouted piles have been used for several decades since the idea was proposed in the 1970s, their design is mostly based on experience and unpublished proprietary methods. There is little research on grouting drilled shaft tips and even less on grouting shaft sides. This paper presents the analysis of 4 instrumented pile loads tests on base and shaft grouted piles from different sites in Egypt; with emphasis on one of the tests, to demonstrate the analysis process. The data from the tests are analyzed to model the development of unit side friction (USF) with relative displacement. A numerical model using the finite element software PLAXIS is used to investigate the effect of grouting on the surrounding soil stress state. The paper combines the observations from full scale pile load tests and results from the numerical model to suggest an idealized behavior of side friction development with relative displacement of the grouted part of the shaft. The suggested model considers an envelope of Unit Side Friction (USF) with relative displacement, initially dominated by the grout resistance then at higher relative displacements, the friction with radially pressured soil takes over. The grout provides very high USF values up to a relative displacement of 2mm. Then, the USF drops to a typical pile soil side friction behavior; however, this friction is affected by the contact stress between pile and soil, which significantly increases due to compaction grouting.

KEYWORDS: Grouted Piles, Shaft grouting, Base grouting, Instrumented grouted Pile Load Tests, soil-cement-pile interaction.

INTRODUCTION

Base and shaft pile grouting has been significantly developing in recent years to accommodate the unfavorable conditions in major projects such as the high loads in high rise building and founding on problematic soil formations. Grouting aims to decrease settlements and increase the capacity of the pile under axial load. The technique is first introduced by Kraft (1974) but gained popularity in the 1980s. Typically there are two types of grouting; compaction, and permeation. Compaction grouting is more common in pile foundations practice, and many researchers have provided case histories of pile load tests on base grouted piles and base and shaft grouted piles (Gouvenot and Gabaix,1975; Stocker, 1983; Ghazali et al., 1988; Fleming, 1993; Kusakabe et al., 1994; Robson and Wahby,1994; Joer and Randolph, 1998; Hamza and Leoni, 1998; Mullins et al. 2000; Littlechild et al., 2000; Suckling and Eager, 2001; Dapp and Mullins, 2002; Ho, 2003; Fu and Zhou, 2003; Brettmann and NeSmith, 2005; Ruiz, 2005; Mullins, 2006; Dapp and Brown, 2010; Beadman et al., 2012; Nguyen et al., 2013; Miller et al., 2013; Sinnreich and Simpson, 2015; Hui and Lin, 2015). Compaction grouting is meant to densify the soil around the pile and below the base rather than permeate this soil and increase its cohesion. Research showed that grouting increases the capacity of the piles by a factor of 2~5. The variation in capacity increase depends on pile type, grouting process, and especially grouting pressure. Although there are many case histories of pile load tests on grouted piles but there is no well-defined agreed-upon method to predict grouted pile capacity as typically done in ungrouted piles. Few lab experiments discussed the shaft grouting effects on the soil especially the compaction grouting. The experiments concluded that the

© 2018 Deep Foundations Institute

compaction grouting forms a homogeneous layer between the pile and the soil, and a residual effective stress is achieved simultaneously with a significant densification of the soil around the pile with noticeable decreasing in void ratio. (Fattahpour et al., 2015; Wang et al., 2015). Recently, studies used numerical analysis to investigate the behavior of the grouted piles and the changes in the surrounding soil (Chiang et al., 2013). That study presents a simulation of the base pressure grouting with a simple FE model and predicts the reduction of the pile settlement by 10 to 20%. Another numerical study using a complex model conducted by Zhou et al. (2017), presents a clear understanding of the friction capacities of the grout-pile interface and the grout-soil interface.

This paper presents data from instrumented load tests on base and shaft grouted piles. The analysis of the pile load test results and a numerical simulation of the grouting process provide insight into the resistance mechanisms of axially loaded post grouted bored piles. This study is part of a continuous effort to compile an electronic database of field scale pile load tests. The paper concludes by proposing a side friction development model with displacement based on the field tests and the numerical simulation.

EGYPT FOUNDATIONS DATABASE (EFD)

An electronic database namely Egypt Foundations Database (EFD) is under development for the purpose of improving the design practices of geotechnical foundation systems. This database is being developed at Cairo University by the Geotechnical Analysis and Reliability Assessment Studies team (GARAS). EFD houses data from axial load tests on drilled shafts, driven piles, shaft and base grouted piles, and micro piles. The database also includes data on laterally loaded drilled shafts, tests for ground anchors, tension tests on piles, and axial load tests on footings. Furthermore, EFD includes comprehensive records related to the soil profile, in-situ tests, and pile characteristics.

In this study, the authors focus on the Grouted Pile Load Tests (GPLT) included in the EFD which contain data from 11 reliable GPLT conducted in Egypt. Only Seven tests are instrumented, and the summary of all the tests are shown in Table 1. For the piles in project (ID=1), piles ends are in limestone and the bottom 5.5 meters as well. For each of the remaining tested piles, the bottom part of the shaft is grouted in sand as well as the pile tip.

Table 1. Geometric and design information of GPLT

Project ID	Test No.	Shape	Instrumented test	Dimension, mm	Pile length, m	Test Load, kN	Base Grouted	Shaft grouted length, m
1	TP1	C	√	1200	33.55	15560	√	10.0
	TP2	C	√	1500	33.55	21260	√	10.0
	TP3	R	√	1000 x 2800	33.55	32220	√	10.0
2	TP4	C	√	1200	26.30	11600	√	9.0
3	TP5	C	√	1000	17.70	8910	√	8.0
4	TP6	C	√	1000	37.50	11300	√	10.0
	TP7	R	√	800 x 2800	37.50	28000	√	10.0
5	TP8	C	×	1000	18.00	12000	√	6.0
	TP9	C	×	1200	18.00	17000	√	6.0
6	TP10	R	×	800 x 2800	37.00	25000	√	3.0
	TP11	R	×	640 x 2800	37.00	20000	√	3.0

Shaft and base grouting practice in Egypt

For the purpose of shaft grouting, bundles of poly-ethylene pipes are fixed to the reinforcement cage. Each bundle consists of a number of grout pipes (22mm diam.) and each pipe covers 2m of grout length. The number and arrangement of pipes depends on the size of pile. Approximately two days after concreting, cement grout (consisting of cement and water with w/c = 0.5) is pumped under pressure through the grouting pipes. The green concrete cover is easily fractured thus allowing the grout to flow freely around the shaft along the grouted length. Past experience shows that the grout initially travels along and completely fills the interface between the shaft and soil, and then radially compresses surrounding soil. The design of the grouting procedure and distribution of grouting pipes takes into consideration that 25 % of the installed pipes may be lost. The criterion for shaft grouting is to reach a pressure of 50 bars. Normally, this is reached in one phase of grouting. If, however; this pressure is not reached after pumping 100 liters of grout per pipe, grouting shall be temporarily stopped, and a second phase of grouting shall take place after a minimum of 12 hours to reach the required value.

The base grouting is performed using the flat jack method. The flat jack at the bottom acts as a one-way valve and is connected with two grout pipes (one is spare). Not earlier than 2 days after shaft grouting completion, the flat jack is charged with grout (with the same mix used for shaft grouting) at pressure ranging from 30 to 50 bars. The circumferential seal between the steel top plate and the thin steel membrane is broken and grout initially compacts and then flows into the soils beneath and around the toe. The criteria for base grouting is either reaching a grouting pressure of 50 bars or a maximum uplift of 2 mm, whichever occurs first. If however the required pressure is not reached after pumping of 100 liters, grouting will be temporarily stopped and repeated later.

Description of a demonstrative Pile load test

The demonstration test case (TP4 in Table 1) is performed on a trial ordinary bored pile, 1.20 m in diameter, and a depth of 26.3 m with the bottom 9 meters of the shaft is grouted two days after the construction. The base grouting is carried out two days after the shaft grouting. The pile is reinforced along its entire length with a high-strength steel reinforcing case. The used concrete is of strength, f_{cu}= 25 MPa and stiffness, E = 21,000 MPa. As the pile, should extend to platform level, a double wall casing extending from platform level to cut-off level was installed to eliminate the skin friction along this part during the loading test. The soil strata and their properties are obtained from a comprehensive site investigation program comprised of four boreholes that are drilled to a depth of 50 m from the ground surface. The ground water table (G.W.T.) is observed in piezometers at 4.5 m below ground surface as presented in Fig.1 [A].

The maximum applied load is 11,600 kN, administered in two cycles of loading and unloading in accordance with ASTM D 1143. The test arrangement, shown in Fig.1 [B], includes a reaction system comprised a crown restrained by twelve ground anchors distributed around the pile as shown in Fig.1 [C]. The axial load is applied using three 6,000 kN hydraulic jacks that are placed between the pile head and the loading crown. The pile is instrumented with distributed vibrating wire sister bar strain gauges (VWSG) to be used to measure the strain at five different levels of the pile. The levels are selected based on soil strata; cut off level, top of sand level, and grouted length. Strain gauges are located at the top, middle and 1 m above the end of the grouted length. Each level is equipped with four VWSG which are located opposite to each other. The axial pile head movement is measured by four dial gauges with a precision of 0.01mm. A precise level equipped with plane plate micrometer with 0.1 mm resolution is

used to measure and backup check the axial movement at three points fixed to the pile head. In addition, to measure the relative displacement along the shaft, three tell-tales extensometer are fixed to the pile at three levels; top of sand, top of shaft grouting and toe of pile as shown in Fig.1 [A&D].

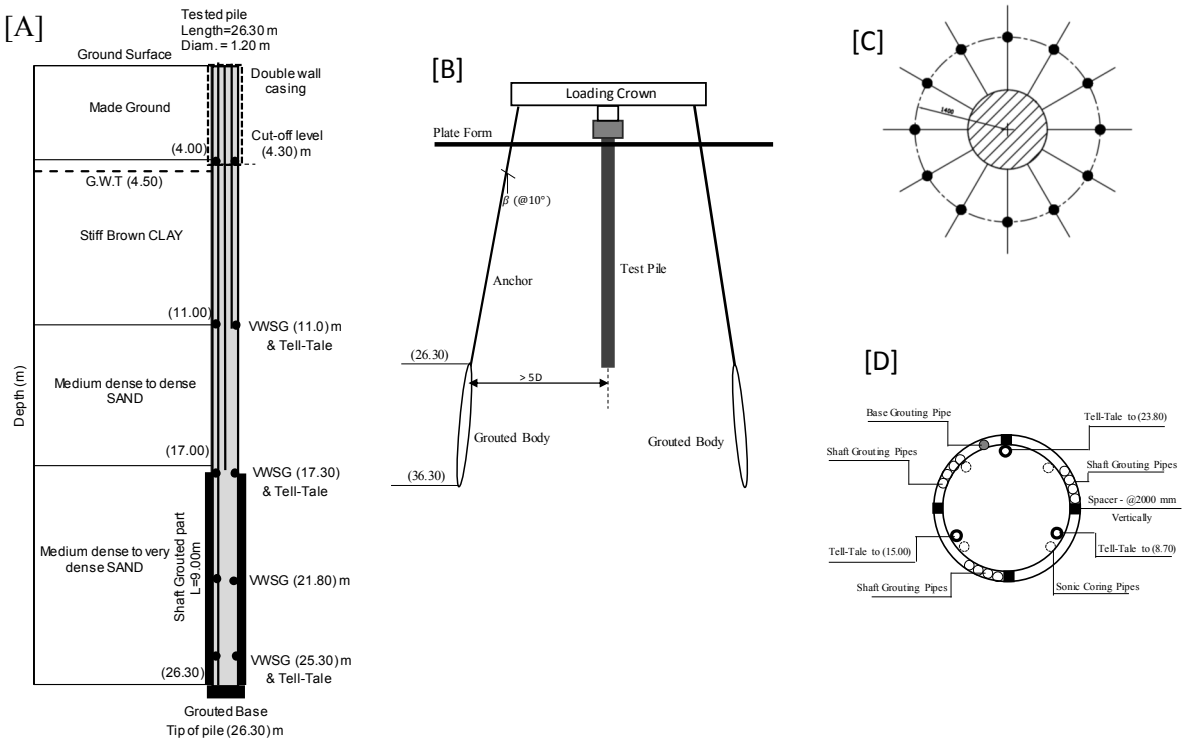


Fig. 1. [A] schematic of the test pile and soil profile; [B] Filed test apparatus; [C] anchors arrangement; [D] test pile cross-section

Test results

The axial strain profiles (ε_{axial}) measured from VWSG are shown in Fig. 2 [a] at each load increment, and hence the axial force can be calculated using Equ. 1.

$$F_{axial} = EA \cdot \varepsilon_{axial} \quad [1]$$

Where F_{axial} = the axial force at certain depth from the pile top, EA= axial rigidity of pile (E is the Young's modulus = 21000 MPa, A is the cross-sectional area $= \pi(0.6)^2\ m^2$). The axial force is shown in Fig. 2 [b]. The values of load obtained at the lowest level of VWSG (1.0 m above the pile tip) are taken as the pile tip load. Fig. 2 [c] shows the displacements at each load increment, obtained from tell-tales. The data show that the base pressure is mobilized during the loading process by significantly low rates. The rate of mobilizing base resistance in this grouted pile is much lower than that typically observed in non-grouted piles. The load settlement curve presented in Fig. 3, shows that the pile carries the maximum load (11,600 kN) safely at the small settlement of (9.13 mm). Although the pile load test reached a high value of load, the ultimate shaft friction has not been fully mobilized. The shaft friction resists most of the load compared to the base resistance which bears only 22 % of the load. The total, shaft, and end-bearing load curves do not exhibit any non-linearity as shown in Fig. 4. The measured displacements at each level are presented in Fig. 5, and it can be observed that although the displacements are very small in sand and clay layers, ultimate values of loads are reached. It can be concluded that the clay and sand layers resist the load initially during the test, and when they reach their ultimate capacity, the grouted layers begin to resist

the load as shown in Fig. 6. The lower half of the grouted layer is subjected to less loads than the upper. The part of the double wall casing did not exhibit any significant friction values compared to the total value of load.

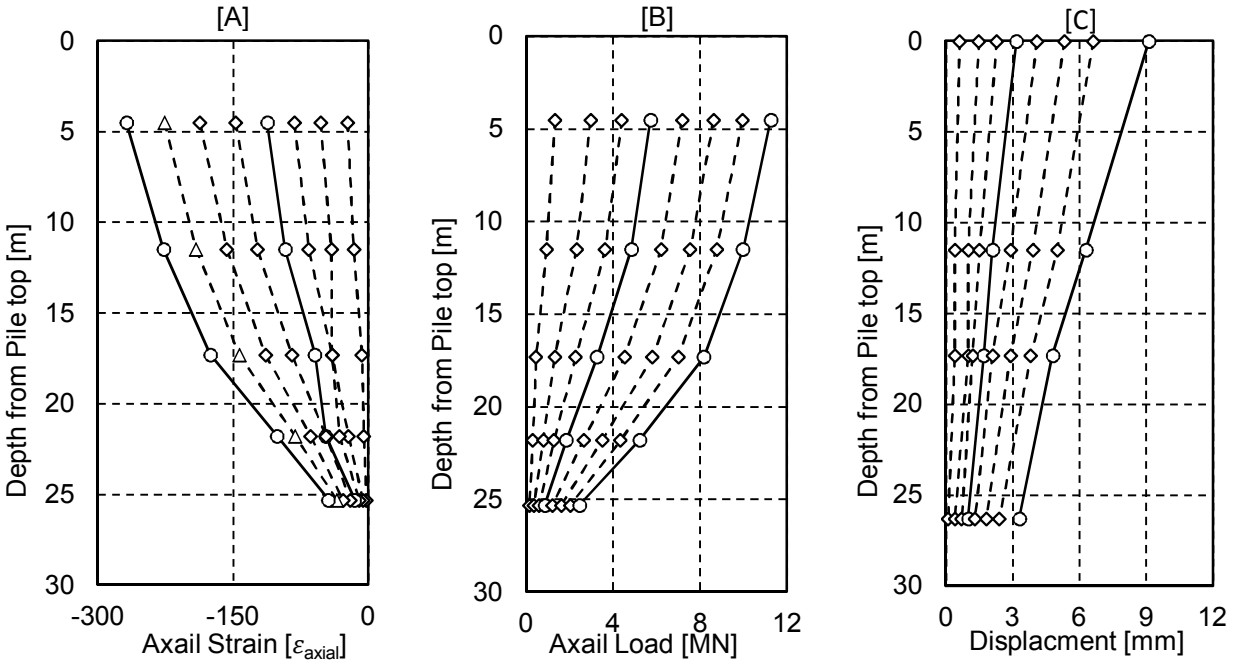


Fig.2: (a) Axial Strain; (b) Axial Load; (c) Vertical Displacement along the pile shaft

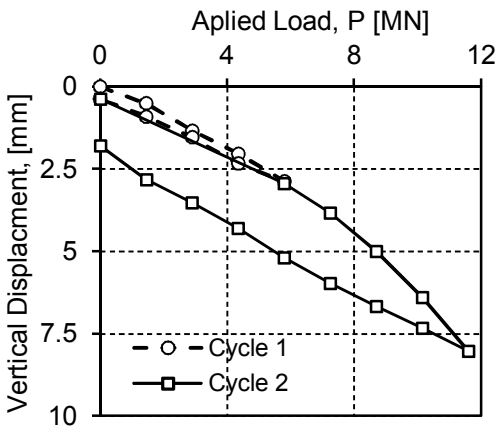


Fig. 3: applied load-head displacement

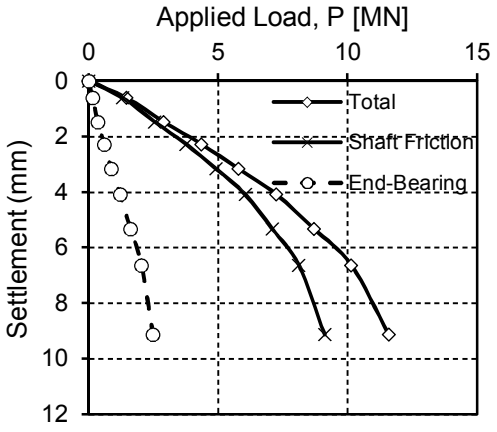


Fig. 4: Components of pile resistance

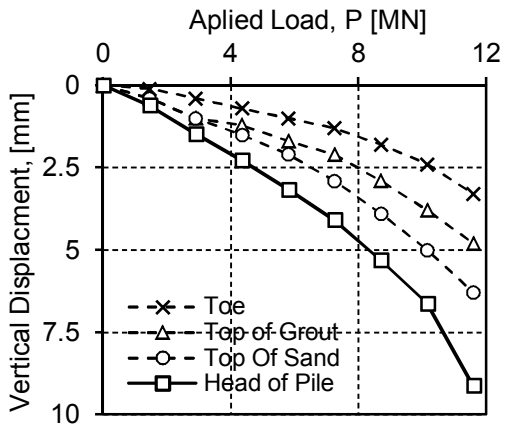


Fig. 5: applied load-displacement at different depths

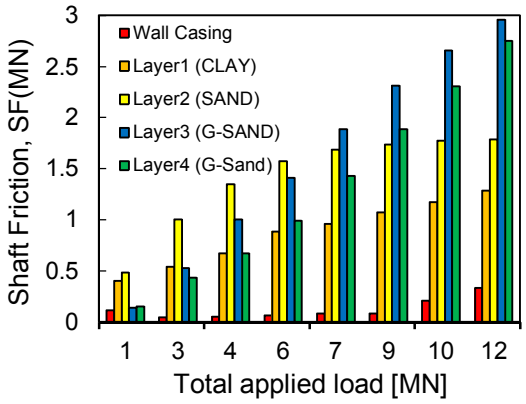


Fig. 6: Friction Component at different levels.

Behavior of Clay, Sand, and Grouted layers

The behavior of the un-grouted soil layers, clay and sand layers, is investigated by many studies, and is almost fully theorized (Fleming et al., 1985, 1992, 2014; Tomlinson and Woodward, 2008, 2014). Figs. 7 and 8 show the variation of the unit side friction with the applied load (P) and the displacement at pile head (U_Z), respectively. The unit side friction (USF) of each layer *i* is calculated according to Pelecanos et al. (2017).

$$USF_i = \frac{F_{axial_i} - F_{axial_{i+1}}}{A_i} \quad [2]$$

Where F_{axial_i} = The axial force at the top of layer i, A_i = surface area of side friction with layer *i*. The shaft friction of the clay and sand layers are fully mobilized, and a yielding point is clearly developed. The maximum unit side friction (USF_u) for the clay layer is 50 kPa, and for the sand layer is 75 kPa. These results are in good agreement with many values existed in the standards such as FHWA (2010) and AASHTO (2007). However, grouted layers behave very differently as shown in Figs. 7-8. The behavior is almost linear and do not present a yielding point. The grouted sand layers have reached USF close to 200 kPa which is greater that the un-grouted ones by 140% to 170 % and the ultimate values have not been observed. On the other hand, base resistance like grouted shaft layer resistance reaches 2.20 MPa (right hand scale), where the curve behaves linearly, and the maximum value may not be determined.

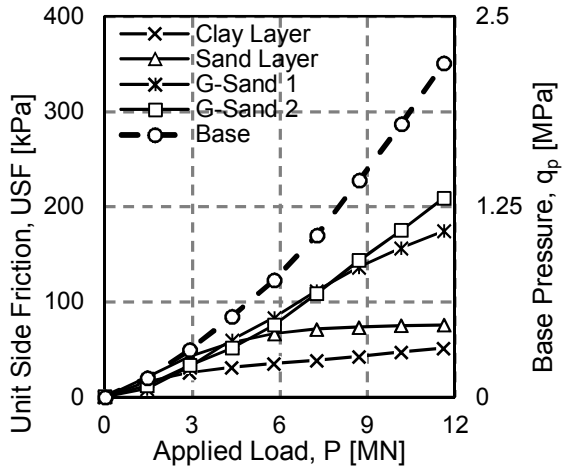


Fig. 7: Applied load-displacement at different levels

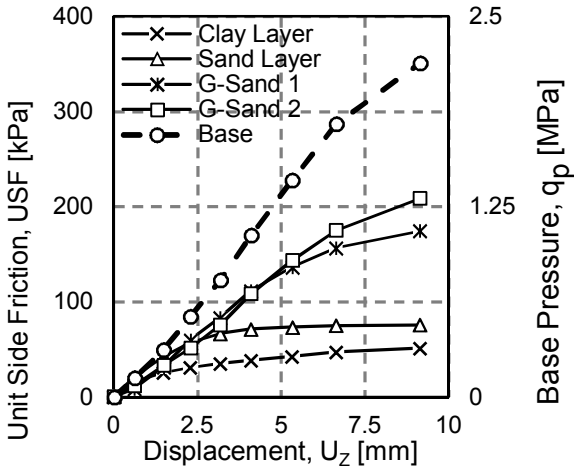


Fig. 8: Applied load-displacement at different levels

Ultimate Axial Capacity Evaluation

The ultimate capacity (UC) is obtained using Chin-Kondner extrapolation method (1972) and the Decourt extrapolation method (2008) as shown in Figs. 9-10. The UCs for the two methods are very close to each other and the difference between them is around 7%.

This measured capacity (P_M) is compared to the calculated capacities (P_C) obtained from static methods considering the pile is conventional pile using the AASHTO (2007) FHWA (2010). The calculated nominal capacities are 8822 and 9141 kN respectively. The ratio of (P_M / P_C) equals 3, approximately.

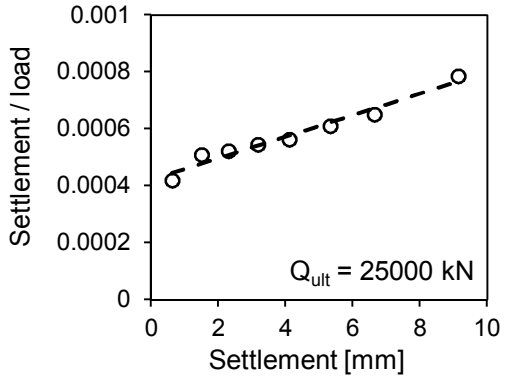


Fig. 9: Ultimate resistance using Chin-Kondner method

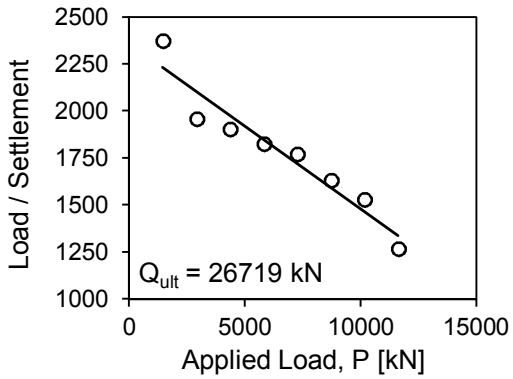


Fig.10: Ultimate resistance using Decourt method

ANALYSIS OF GROUTED SHAFT AND BASE RESISTANCE MECHANISMS

The first 4 tests in Table 1 (TP1, TP2, TP3, TP4) are considered usable for interpreting grouted shaft and base behavior in resisting loads. In this section, the data from the 4 pile tests are compiled to shed light on the rates of gaining resistance with relative displacement. Then, a numerical simulation of the grouting process describes the stress state of the soil around the grouted pile. The load-displacement curves of the test piles are shown in Fig. 11. The Shaft Friction (SF) and the End-Bearing (EB) values at every

displacement are separated in Fig. 12 and Fig. 13. In general, SF values are much higher than EB. The range of SF is from 9 MN to 14 MN at the maximum applied load, however in TP3 which is on a rectangular section, SF is 29 MN at the maximum load. The range of EB is between 1.5 MN and 3.5 MN at the maximum load, except for TP2, EB is 7.30 MN. It can be seen, that grouting the tested pile results in very low settlements; hence an observed failure is impossible to achieve (Zhou et al. 2017). Fig. 14 shows how the relationship between base pressure and tip displacement does not follow any conceivable trend. This might be attributed to the possible drilling problems of large diameter bored piles which typically leads to soft and full of debris hole bottoms. Hence, it is more prudent to focus on the trends possibly observed from the side friction behavior.

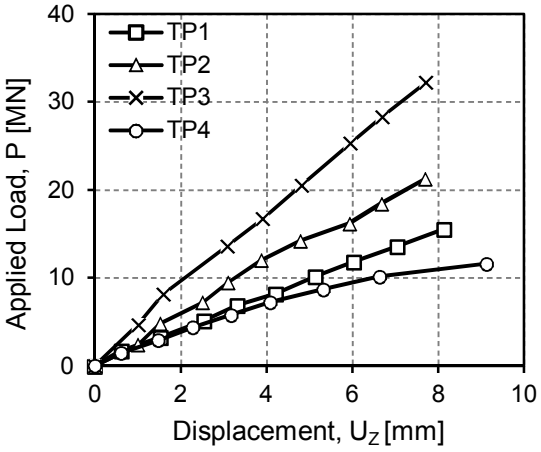


Fig.11: Applied load verses head displacement

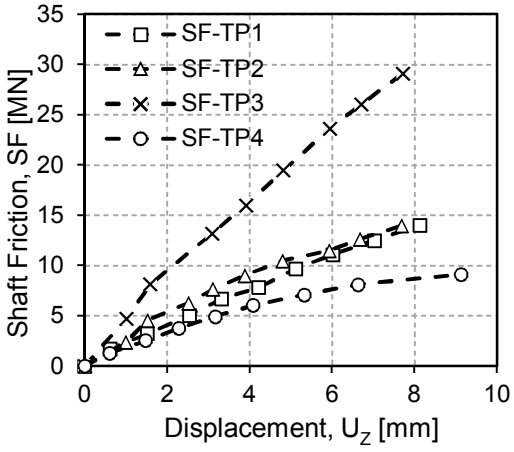


Fig.12: Shaft Friction versus head displacement

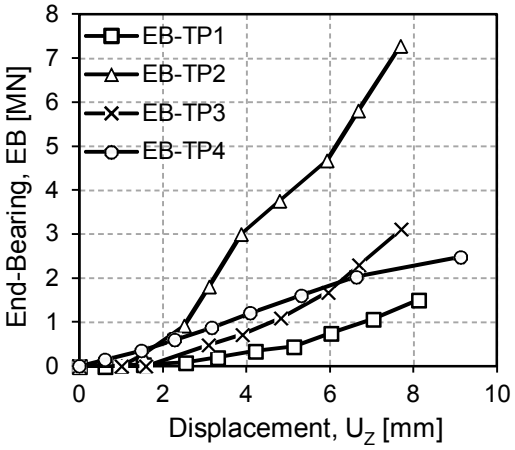


Fig.13: End Bearing verses head displacement

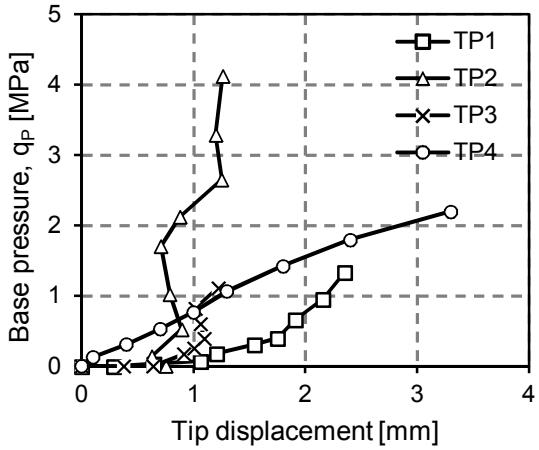


Fig.14: Base pressure verses tip displacement

Analysis of Unit Side Friction Measurements

The data are interpreted for grouted sand and rock layers from VWSG data as shown in Fig.15 and Fig.16 respectively. The USF in these figures are plotted against relative displacements after Pelecanos et al. (2017)

$$u = u_{i+1} - u_i \quad [3]$$

where u_i is the vertical displacement at the top of layer i.

The side shear failure mechanism for grouted pile is different from the ordinary bored pile as shown in Fig. 17 and Fig. 18. The cement layer around the grouted pile enables high unit side frition but exhibits brittle failure when relative displacement of 2mm is reached (Lehane et al., 2005; and Zhou et al., 2017); then no meaningful friction is mobilized. However, the compaction grouting will lead to significant change in the stress state around the grouted pile which would alter the USF_u typically calculated for a non-grouted pile in Equ. (4).

$$USF_u = \beta P_0 = (Ktan\delta)P_0 \quad [4]$$

Where P_0 = the normal effective overburden pressure K = lateral at rest earth pressure coefficient, δ = interface effective angle of friction. The rate of increase of the USF with relative displacement due to grouting and due to soil compaction are dubbed k_{grout} and k_{comp} respectively.

Fig. 19 and Fig. 20 present the best estimate for the slope shown in Fig. 17 from the instrumentation data for rock and sand layers respectively. It can be concluded that k_{grout} in rock is 457 kPa/mm and in sand is 112 kPa/mm.

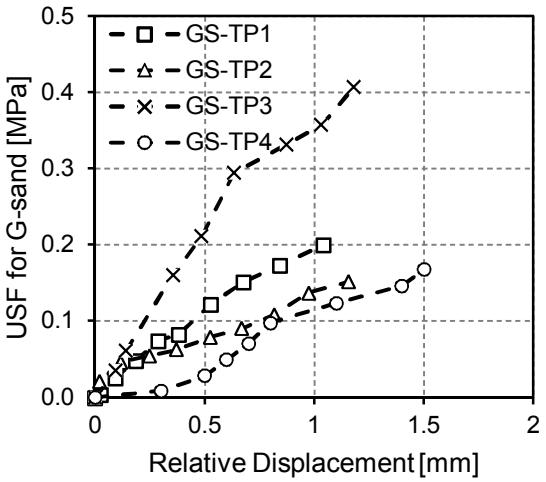


Fig.15: USF for G-sand layers verses relative displacement

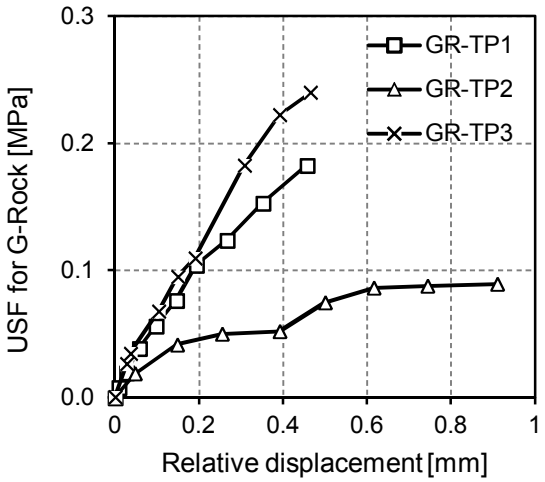


Fig.16: USF for G-rock layers verses relative displacement

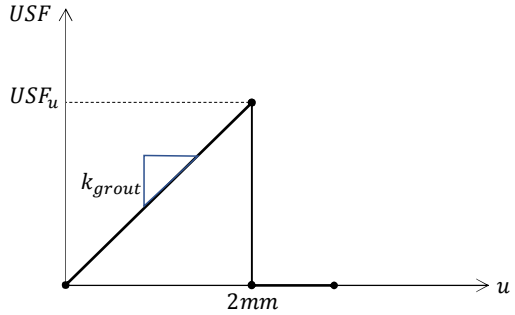


Fig.17: Elastic model for failure mechanism in Grout (after Lehane et al., 2005).

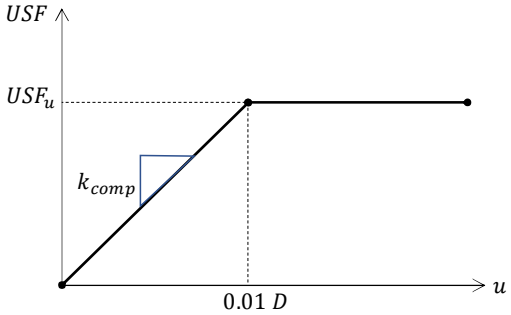


Fig. 18: Elastic model for friction failure between pile and non-grouted soil.

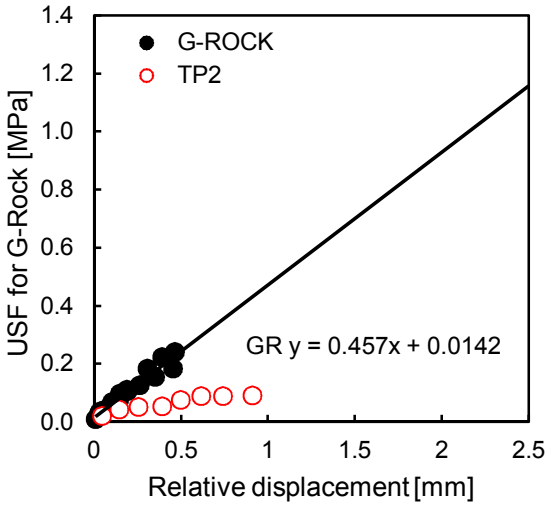


Fig.19. k_{grout} for Rock Layers

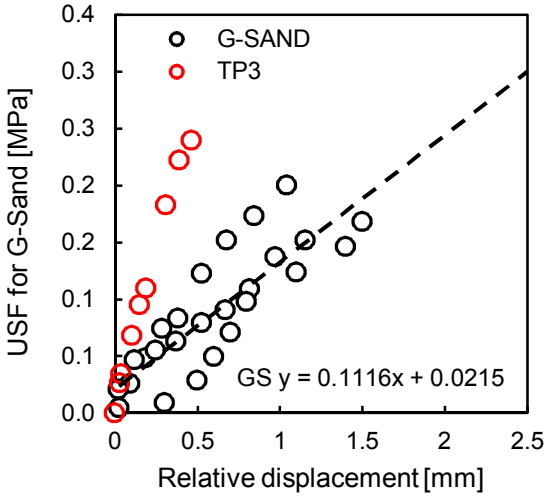


Fig.20. k_{grout} for Sand Layers

Numerical Simulation of Radial Grouting in TP4

A simple axisymmetric model of the pile from the demonstrative case (TP4) is created in the 2D finite element program PLAXIS as shown in Fig. 21. The model focuses only on the behavior of the soil around the lower part of the shaft during grouting. The grouting process in this case and typically in Egypt is compaction grouting rather than permeation grouting. The simulation of the grouting process focuses on the response of the soil, with its inherent properties, to the radial pressure emanating from the pile (the embedded tubes in the pile); rather than improving the properties of such soil. The model considers the compacting grout effect which displaces the soil laterally and changes its stress state. If the grout is to permeate the soil, its properties (cohesion) would improve which is not the case (Warner, 2004).

The lower cluster of elements simulating the grouted part of the shaft is radially engorged by applying volume strain to this body only in the radial directions and not in the vertical direction, as the shaft grouting is the focus of this model (Fig. 21). The applied volume strain is a numerical artifact and does not have much of a physical meaning. The volume of the lower part of the pile is increased until the radial pressure around the pile reached the 5000 kPa typically used in grouting.

The stress state of a soil element at the mid-depth of the layer is monitored throughout the simulated grouting process. The ratio of horizontal to vertical effective stresses (K) is shown in Fig. 22. Two soil models are used in this analysis, the typical Mohr Coulomb (MC) model and the Hardening Soil (HS) model. The input parameters of the MC model are shown in Fig. 22 and derived from SPT data using typical correlations. The HS stiffness parameters are suggested with less certainty using rules of thumb listed below, while the shear failure parameters are not changed ($\phi = 40^0$).

$$E_{50} = E_{oed} = E_{Mohr-Coulomb} \quad [5]$$

$$E_{ur} = 3E_{Mohr-Coulomb} \quad [6]$$

Where E_{50} and E_{oed} are the 50% secant modulus and the 1-D (oedometer) modulus of the soil. E_{ur} is the unload/reload modulus of the soil.

The value of K increases significantly from the K_0 state typically found in soils before any disturbance. It is assumed that $K_0 = 1 - sin\phi$ in the initial conditions of the model. The two models show significant increase in K, however only the HS model predicts that K_p is reached ($K_p = \frac{1+sin\phi}{1-sin\phi}$). The MC model predicts that K exceeds unity as well, but at the 5000kPa grouting pressure, K asymptotes to a value of 3.2. Fig. 22 shows that failure is predicted by the HS model early on during the grouting process; however, the analysis is not terminated indicating that failure is local and does not cause well developed sliding surfaces.

Derivation of a model for USF_{grout} relationship with displacement

The results from the previous two sub-sections can be combined and a proposal for the friction mechanism between a grouted pile and surrounding soil is proposed. Fig. 23 shows the proposal for Unit Side Friction change with relative displacement along the pile shaft. The values in Fig. 23 are calculated using the data introduced earlier from TP4. Initially the bond between the soil and the pile is dominated by the strength of the cement layer and side friction can be calculated using k_{grout} only until the 2mm threshold is reached. Typically, relative displacements in this area does not exceed 2mm even at high loads; and head displacements compress the pile rather than induce displacements along the grouted part of the shaft. However, in the unlikely event that threshold is reached, it may be assumed the typical pile soil friction behavior takes over. However, this pile soil behavior is now affected with the significant lateral pressures applied to the soil during grouting and the ratio to horizontal to vertical effective stresses may be taken as 0.75 K_p rather than the value of 1.0 as proposed by Chen and Kulhawy (1994). The value of K_p itself is not recommended as this would indicate local failure in the soil which is unlikely. Only, the HS models predicted this local failure where the input parameters are chosen using rules of thumb and not accurately calibrated.

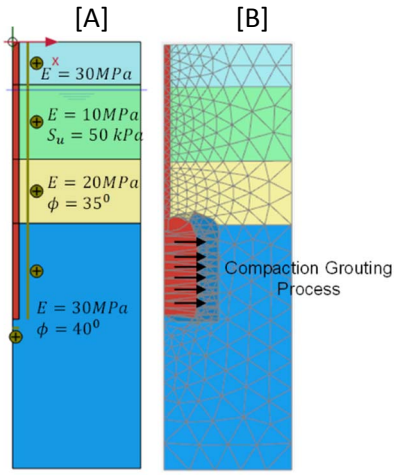


Fig. 21: [A] The 2D numerical model of a pile being grouted, and [B] The simulation of the shaft grouting process

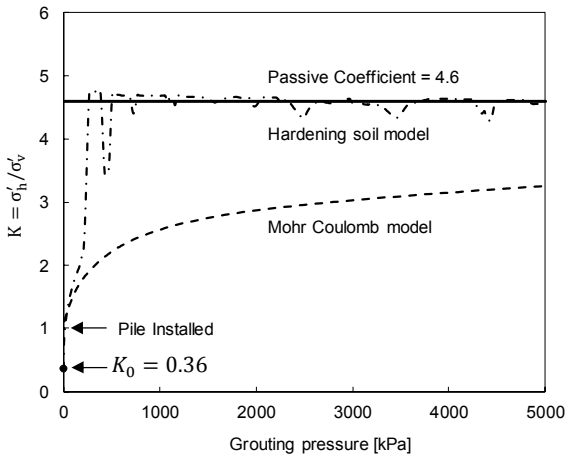


Fig. 22: The state of stress at a soil element adjacent to the grouted part of the shaft.

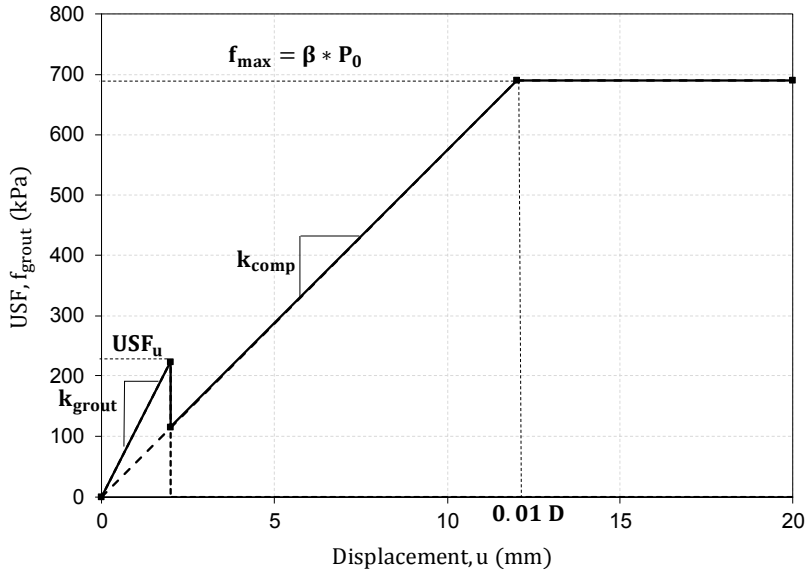


Fig. 23: A proposed USF -displacement model applied to the TP4 demonstrative case.

CONCLUSIONS

The paper presents data from the Egyptian Foundation Database (EFD) regarding instrumented load tests on base and shaft grouted piles. The analysis of one of the pile load tests is presented to demonstrate the data acquired from the instrumentation and the separation between side friction and base resistance developing with head and tip displacement. The paper focused on the side friction resistance around the grouted part of the shaft and fitted the available data to a model for Unit Side Friction (USF) developing with relative displacement. This is combined with results from a numerical simulation of the grouting process to delineate the change in stress state of the soil around the grouted shaft. The following points can be concluded.

- The capacity of the pile due to grouting is much higher than any prediction from static formulae. The ultimate capacity of the pile is not easily predicted because recorded displacements in tests are typically very low, and the lack of standard methods to predict the ultimate capacity.
- The recorded behavior of the base pressure with tip displacements did not show any usable trends, but the data from the grouted part of the shaft shows a clear mechanism when interpreted in the form of USF and relative displacement.
- The rate of friction increase with relative displacement (k_{grout}) is different for each soil type around the pile. k_{grout} between pile and rock is found to be 457 kPa/mm and between pile and sand is found to be 112 kPa/mm. More data is needed to prove the consistency of these values and if similar values may be found with other types of soils.
- Compaction grouting leads to significant changes in the soil stress state. It is proposed to consider the value of horizontal to vertical effective stress ratio (K) as 0.75 the passive earth pressure coefficient (K_p).
- A model is proposed for the USF development with displacement. The model assumes the dominance of grout resistance until a relative displacement of 2mm is reached (k_{grout}). Then USF

drops to the typical pile soil side friction development. However, the soil resistance to the displacement of the pile is affected by the increased values of K due to grouting radial pressures.

REFERENCES

AASHTO (2007) LRFD Bridge Design Specifications. Customary U.S. Units, 6th edition (2013 Interim), Washington, D.C.

ASTM D 1143 Standard Test Methods for Deep Foundations under Static Axial Compressive Load.

Beadman, D., Pennington, M. and Sharratt M. (2012). "Pile test at the Shard London Bridge." Ground Engineering, 45 (1), 24–29.

Brettmann, T., and NeSmith, W. (2005). "Advances in auger pressure grouted piles: design, construction and testing." In Advances in Deep Foundations (pp. 1-13).

Brown, D.A., Turner, J.P., and Castelli, R.J. (2010). Drilled Shafts: Construction Procedures and LRFD Design Methods. Publication FHWA-NHI-10-016, FHWA, Washington, D.C.

Chen, Y. J., and Kulhawy, F. H. (1994). Case history evaluation of drilled shaft behavior. Report TR-104601, Electric Power Research Institute, Palo Alto.

Chiang, C. C., et al. (2013) "Effects of Drilled-Shaft Tip Grouting in Numerical Simulations." Danjiang Institute of Science and Technology 16.1: 41-44.

Chin, FV, and Kondner, A. (1972) "Estimation of the ultimate load of piles not carried to failure." Proceedings of the 2nd Southeast AsianConference on Soil Engineering, Singapore, pp. 81–90.

Dapp, S., and Brown, D. (2010). "Evaluation of base grouted drilled shafts at the Audubon Bridge." In GeoFlorida 2010: Advances in Analysis, Modeling & Design (pp. 1553-1562).

Dapp, S. D., and Mullins, G. (2002). "Pressure grouting drilled shaft tips: Full-scale research investigation for silty and shelly sands." In Deep Foundations 2002: An International Perspective on Theory, Design, Construction, and Performance (pp. 335-350).

Decourt, L. (2008). "Loading tests: interpretation and prediction of their results." ASCE GeoInstitute Geocongress New Oreleans, March 9-12, "Housing John from Reaserch to Practice in Geotechnical Engineering", Geotechnical Special Publication, GSP180, Edited by J.E. Laier, D.K. Crapps, and M.H. Hussien, PP. 452-488.

Fattahpour, V., Baudet, B. A., and Sze, J. W. C. (2015). "Laboratory investigation of shaft grouting." Proceedings of the Institution of Civil Engineers-Geotechnical Engineering, 168(1), 65-74.

FHWA (2010). Federal Highway Administration, FHWA-NHI-10-016, Drilled Shafts Manual, chapter 13, pp. 13-17, and pp. 19-23.

Fleming, K., Weltman, A., Randolph, M., and Elson, K. (2014). Piling engineering. CRC press.

Fleming, W. G. K. (1993) "The improvement of pile performance by base grouting." Proceedings of the Institution of Civil Engineers: Civil Engineering. Vol. 97. No. 2.

Fleming, W. G. K., Weltman, A. J., Randolph, M. F., & Elson, W. K. (1992). Piling Engineering, 2nd. Edition. Blackie, Glasgow & London.

Fleming, W. G. K, Weltman, AJ, Randolph, MF and Elson, WK (1985). Piling engineering.

Fu, X., and Zhou, Z. (2003). "Study on bearing capacity of bored cast-in-situ piles by post pressure grouting." In Grouting and Ground Treatment (pp. 707-715).

Ghazali, F. M., Sotiropoulos, E., and Mansour, O. A. (1988). "Large-diameter bored and grouted piles in marine sediments of the Red Sea." Canadian Geotechnical Journal, 25(4), 826-831.

Gouvenot, D. and Gabaix, J. (1975). "A new foundation technique using piles sealed by cement grout under high pressure." Proceedings Offshore Technology Conference, Texas, Paper Number OTC 2310.

Hamza, M.M. and Ibrahim, M.H.Z. (2002). "Performance of base and shaft grouted barrettes." Proceeding of III regional conference on civil engineering technology, American society of civil engineers (ASCE), Egypt section, Cairo, Egypt.

Hamza, M.M. and Leoni, F. (1998). "High capacity, long-life bored piles in Bibliotheca Alexandrina Project," Proceedings of 7th International Conference on Piling and Deep Foundations, DFI98, Vienna, Austria, pp. 1.12.1-1.12.25.

Ho, C. E. (2003). "Base grouted bored pile on weak granite." In Grouting and Ground Treatment (pp. 716-727).

Chun Hui, S., Jian Lin, M., and Cong, S. (2015). "Post-Grouting to Reduce Bridge Settlement in Beijing-Shanghai High-Speed Railway." Electronic Journal of Geotechnical Engineering, 20, 971-979.

Joer, H.A. and Randolph M.F. (1998). "Capacity and model grouted piles in calcareous sediments." 7 th International Conference and Exhibition on Piling and Deep Foundations, DFI98, Vienna, 1.4.1-1.4.11.

Kraft, L. M., and Lyons, C. G. (1974) "State-of-the-Art: Ultimate Axial Capacity of Grouted Piles." Offshore Technology Conference. Offshore Technology Conference.

Kusakabe, O., Kakurai, M., Ueno, K., and Kurachi, Y. (1994). "Structural capacity of precast piles with grouted base." Journal of geotechnical engineering, 120(8), 1289-1306.

Lehane, B. M., C. Gaudin, and Schneider, J. A. (2005). "Scale effects on tension capacity for rough piles buried in dense sand." Géotechnique 55.10: 709-719.

Littlechild, B. D., Plumbridge, G. D., Hill, S. J., and Lee, S. C. (2000). "Shaft Grouting of Deep Foundations in Hong Kong." In N. D. Dennis Jr., R. Castelli and M. W. O'Neill (Eds.), New Technological and Design Developments in Deep Foundations Geotechnical Special Publication No. 100 (pp. 33-45). Reston, VA: ASCE.

Miller, M., et al. (2013). "Improving the capacity of bored piles by shaft grouting." Proceedings of the 18th International Conference on Soil Mechanics and Geotechnical Engineering, Paper. No. 2525.

Mullins, G., Winters, D., and Dapp, S. (2006). " Predicting end bearing capacity of post-grouted drilled shaft in cohesionless soils." Journal of Geotechnical and Geoenvironmental Engineering, 132(4), 478-487.

Mullins, G., Dapp, S. D., and Lai, P. (2000). "Pressure-grouting drilled shaft tips in sand." In New technological and design developments in deep foundations (pp. 1-17).

Nguyen, V. L., L. Nie, and M. Zhang (2013). "Method cement post-grouting to increase the load capacity for bored pile." Research Journal of Applied Sciences, Engineering and Technology: 5.19 4727-32.

Pelecanos, L., et al., (2017). "Distributed Fiber Optic Sensing of Axially Loaded Bored Piles." Journal of Geotechnical and Geoenvironmental Engineering, 144(3), 04017122.

Robson, R.J. and Wahby, A. (1994). "Base and shaft grouted bored pile foundations for the first residential complex, Giza, Egypt." Proceedings International Conference on Piling and Deep Foundations, Balkema, Rotterdam.

Ruiz, M. E. (2005). Study of axially loaded post grouted drilled shafts using CPT based load transfer curves. M.Sc. Thesis, University of Porto Rico

Sinnreich, J., and Simpson, R. C., (2015). "Case Histories of Full-Scale Comparative Load Testing of Base Grouted and Ungrouted Test Shaft Pairs." In IFCEE 2015 (pp. 486-499).

Stocker, M., (1983). "The influence of post-grouting on the load-bearing capacity of bored piles." 8th European Conference on Soil Mechanics and Foundation Engineering, Helsinki.

Suckling, T.P. and Eager, D.C. (2001). "Non-base grouted piled foundations in Thanet sands for a project in East India Dock, London." Underground Construction Symposium, Brintex, London, UK, 2001, pp. 413–424.

Tomlinson, M., and Woodward, J., (2014). Pile design and construction practice. CRC Press.

Wang, D., Wang, L., and Zhang, L. (2015). “Experimental study on post grouting bearing capacity of large diameter bored piles.” In MATEC Web of Conferences (Vol. 22, p. 04029). EDP Sciences.

Warner, J. (2004). Practical handbook of grouting: soil, rock, and structures. John Wiley & Sons.

Zhou, J. J., Gong, X. N., Wang, K. H., Zhang, R. H., and Yan, J. J. (2017). “Testing and modeling the behavior of pre-bored grouting planted piles under compression and tension.” Acta Geotechnica, 12(5), 1061-1075.

DEEP FOUNDATION SHORING IN SOUTH FLORIDA

Douglas C. Brunot, Mabey Inc., Elkridge, Maryland, United States of America, (410) 567-1959, d.brunot@mabey.com

ABSTRACT

Mabey Inc. is providing for the shoring design for the Naples bay Center project, located in Naples, FL. The excavation is approximately 374' long by 164' wide and is 27'-8" deep at the shoring line with a groundwater level six feet below present grade. The project Excavation is for a multi-use facility for residential and retail with underground parking. The shoring design will be incorporated into the foundation walls for the building. Mabey is using its pre-engineered Super Powerbrace Plus (SPP) wales and Mega Struts to support the excavation in two phases. The system design and the design of all the pre-engineered components are by Mabey. The foundation is supported on drilled shafts arranged with the building column grid.

The excavation will be completed in two phases to allow for equipment mobilization and operation on a site with limited access. The construction sequence will begin with placement of the drilled shafts. The drilled shafts will also serve as the building columns. After the drilled shafts have cured, 630 AZ24-700 x 45 ft. long sheet piles will be installed. The sheets will be arranged in two phases, divided by a center row of piles. Since de-watering in south Florida is very expensive and often downright impossible prior to placing the seal slab, all the initial foundation and excavation bracing work will be completed with groundwater in situ. The entire excavation will be excavated to 5 ft. below ground surface to allow for the installation of the wale support brackets at 12 ft. on center, welded to the sheet piles. After the support brackets are installed, the SPP hydraulic wales and the Mega Strut hydraulic braces may be installed for both phases. Once the frames and struts are in place, Phase 1 excavation is completed, followed by Phase 2 excavation. The 4-ft. thick seal slab is then placed and cured in the wet. De-watering is now possible with the seal slab in place. Once the excavation is de-watered the leveling slab is placed and cured. The center row of sheet piles is then cut off at the top of leveling slab. With the leveling slab cured, the sheet piles have enough strength to support the excavation without the frames and struts near the ground surface. The permanent sheet piles are then seal welded for water proofing and the foundation walls are cast with the sheet piles.

The design is modelled in 3D using REVIT to ensure accuracy of the design. The earth pressures are developed using Coulomb theory as there is a top frame and the frame and sheet pile are flexible and move to develop an active pressure wedge. Earth pressure uniform loads and loads from predicted surcharge are modeled in STAAD to determine load effects on the SPP frames and Mega Struts. Coulomb theory and Mabey's structural model will be tested through monitoring with Mabey's LIVEPin system. LIVEPin will be placed in struts for each phase of construction. The LIVEPin results will be calibrated with the structural model to determine actual frames forces and will also determine the actual earth pressures applied to the system from surrounding soil. Mabey has used the LIVEPin system in similar applications and this has helped us determine modelling accuracy.

KEYWORDS

BIM; COULOMB; DEWATERING; LIVEPIN; TERZAGHI

DESIGN PROCESS

The generalized subsurface profile presented in the site geotechnical report is shown in the following table:

© 2018 Deep Foundations Institute

Table 1. Site generalized subsurface profile

GENERALIZED SUBSURFACE PROFILE			
DEPTH (FT)		SOIL DESCRIPTION	USC
FROM	TO		
0	5.0	Very Loose to Medium Dense Sand	SP
5.0	13.0	Variable Stratum, Very Loose to Medium Dense Sand	SP
13.0	17.0	Hard Limestone (Caprock)	N/A
17.0	22.5	Soft Limestone	N/A
22.5	50.0	Very Soft to Soft Limestone	N/A
		USC = Unified Soil Classification	

The soil borings provided for the project included information about the soil type and the Standard Penetration Resistance (N). With the information provided soil properties were assumed in order to calculate parameters for the excavation design.

Table 2. Assumed soil properties for Excavation design

ASSUMED SOIL PROPERTIES									
DEPTH (FT)		SOIL DESCRIPTION	φ	δ	BULK DENSITY (PCF)	SATURATED DENSITY (PCF)	SUBMERGED DENSITY (PCF)	Ka	Kp
FROM	TO								
0	4.0	Loose Medium Sand	33	17.8	97	122	59	0.27	6.62
4.0	6.0	Medium Dense Medium Sand	35	18.9	107	128	66	0.25	7.88
6.0	12.5	Very Loose Medium Sand	30	16.2	93	119	57	0.30	5.22
12.5	17.5	Dense Medium Sand	38	20.5	116	134	72	0.22	10.50
17.5	22.5	Medium Dense Medium Sand	35	18.9	107	128	66	0.25	7.88
22.5	35.0	Very Looses Medium Sand	30	16.2	93	119	57	0.30	5.22
35.0	50.0	Loose Medium Sand	33	17.8	97	122	59	0.27	6.62

The task necessary after these steps was to select the appropriate lateral earth pressure model. The excavation is 27'-8" deep and will be braced by a top frame. The frame is rigid and deflects up to 2.3 inches under maximum lateral earth pressure load. The AZ24-700 sheet piles deflect 0.60 inches during stage 1 maximum load. AASHTO LRFD 7th Ed. C3.11.1 defines mobilization of the active pressure as the ratio of deflection at the top of the wall to the wall height. For the considered application, this ratio is 0.006 which exceeds the 0.002 ratio limit defined in AASHTO. This is an important distinction when considering the use of a lateral earth pressure theory. The deflection of the sheet is also an important consideration as this tends to mobilize the soil's shear strength and thus reduces the applied lateral earth pressure. The choices at hand for the analysis are Rankine, Coulomb and Terzaghi.

Rankine Theory neglects the soil-structure interaction accounted for in the friction between the sheet pile and the soil. Rankine is often preferred for quick hand calculation estimates, but is not preferred for refined analyses. Shear stresses between the wall and the soil have a significant effect on the analysis results for braced excavations. This leads us to Coulomb's theory for lateral earth pressure. In Coulomb's Theory, the shear stresses develop down the wall with deflection of the wall face. The lateral earth pressure resulting from this condition is an inclined angle with the back of the wall, or the angle of wall friction δ. This theory seems to be a good choice as we have the deflections in our design and the deflection to height ratio indicates an active pressure envelope. We can also be certain that this friction does exist as the wall material is steel and will have considerable friction and adhesion with the contacting soil. However, this is a relatively deep excavation and it is a braced excavation.

Terzaghi and Peck studied and tested braced cofferdams starting c. 1967. The results of their study have developed another lateral earth pressure theory that is more appropriate for deep braced excavations. The application for this theory is a system where deflection is tightly controlled by the installation of multiple levels of bracing as the excavation progresses. Under this type of construction scenario, classical earth pressure models mentioned above cannot be used because of the different behavior of the soil-structure interaction during construction. The lateral earth pressure envelope for the Terzaghi method starts out as an inclined angle from the wall face like Coulomb and Rankine theory. The pressure envelope for Terzaghi theory remains constant or parallel to the back of the wall as each brace prevents the development of soil shear stresses and the pressure model remains at rest condition.

After carefully considering the soil properties and soil-structure interaction characteristics, the Coulomb method of lateral earth pressure is the appropriate application for the project. The deflections developed throughout the system and in the sheet pile show that the active wedge will develop and behave more like Coulomb than any other theory. Consideration to the possibility of the lateral earth pressure coefficient ranging between active and at rest resulted in the conclusion that the active earth pressure coefficient was sufficient due to the amount of movement.

The soil structure interaction model is completed with proprietary software that estimates earth pressures and considers soil properties listed in Table 2 as well as live load surcharges. The model predicts the sheet length required to achieve fixed earth support and the loads imparted to the supporting frame at the top of the excavation. The frame loads from the soil-structure model are then transferred to a structural model developed in Finite Element Analysis software (FEM). The frame wales and struts are modelled in FEM and linear loads are applied to the wales. The challenge in developing the FEM is considering the model boundary conditions. Boundary conditions or supports must be included for the model to be stable. The sheet and frame system derives its stability from the fact that it is continuously supported on the perimeter by soil. This is the same soil that is applying an active load to the frame. It certainly does not make sense to expect the soil to apply active pressure and at the same time offer passive resistance. But we do know that the soil provides support. The answer to this question is resolved by developing an elastoplastic spring to model the soils interaction behavior with the structural system.

The elastoplastic spring can be modeled to allow for deformation of the system with respect to the surrounding soil. The springs must consider elastic stiffness, tangent stiffness and yield force. For this project we considered the soil properties and one of them is the soil's modulus of subgrade reaction. The subgrade modulus is a measure of the soil's ability to behave as an elastic material. A medium dense sand has a modulus of subgrade reaction ranging between 91 and 460 lbs./in^3. The wale is near the ground surface, therefore a subgrade modulus at the lower bound was selected, 91 lbs./in^3. The wale flange is 20 inches deep and one pair of sheets is 55 inches wide. This assumed contact area multiplied by the assumed soil subgrade modulus is approximately 100 kip/in. The spring constant will be applied for the global X and Global Z directions in the FEM. This is to account for the fact that the sheets develop considerable shear strength with the soil in both directions. All the elastoplastic springs are defined as compression only

and linearly varying in resistance based on deflection with a maximum resistance of 100 kip/in. The springs are applied at the corners and at intersections between the wales and the struts. This is a realistic depiction of the soil-structure interaction as these locations are where the system will create a demand on the soil for stability. The springs also help the FEM more accurately predict system deformation, strut axial forces and frame moments and shears as well as axial forces in the frame.

Evaluating the FEM output for equipment limit states is the next step in the design process. Limit states to be considered are flexure, shear and web buckling of the wales. Consideration must be given to the positive and negative moment limit states at the pinned wale joints. Axial force and combined stress limit states must also be considered for the wale system and the hydraulic rams. The strut axial forces must be considered as well. The controlling elements in the frame design are the wales. The FEM allows us to predict loads resulting from the soil-structure interaction. This approach will be calibrated by the use of monitoring with the LIVEPin system. The LIVEPin system can accurately predict our strut loads and will be discussed further in this article. Knowing the actual strut loads will allow for adjusting model parameters and boundary conditions to more accurately predict the soil-structure interaction behavior. Allowable Stress Design (ASD) is used to evaluate system stresses and compare to tabulated values for the pre-engineered equipment. The AZ24-700 sheets are also evaluated for stress and deflection in the soil-structure interaction model.

ENGINEERING GRAPHICS

A project of this size and complexity is best designed using Building Information Modelling (BIM) software. The image below shows part of our BIM that depicts the LIVEPin end connection.

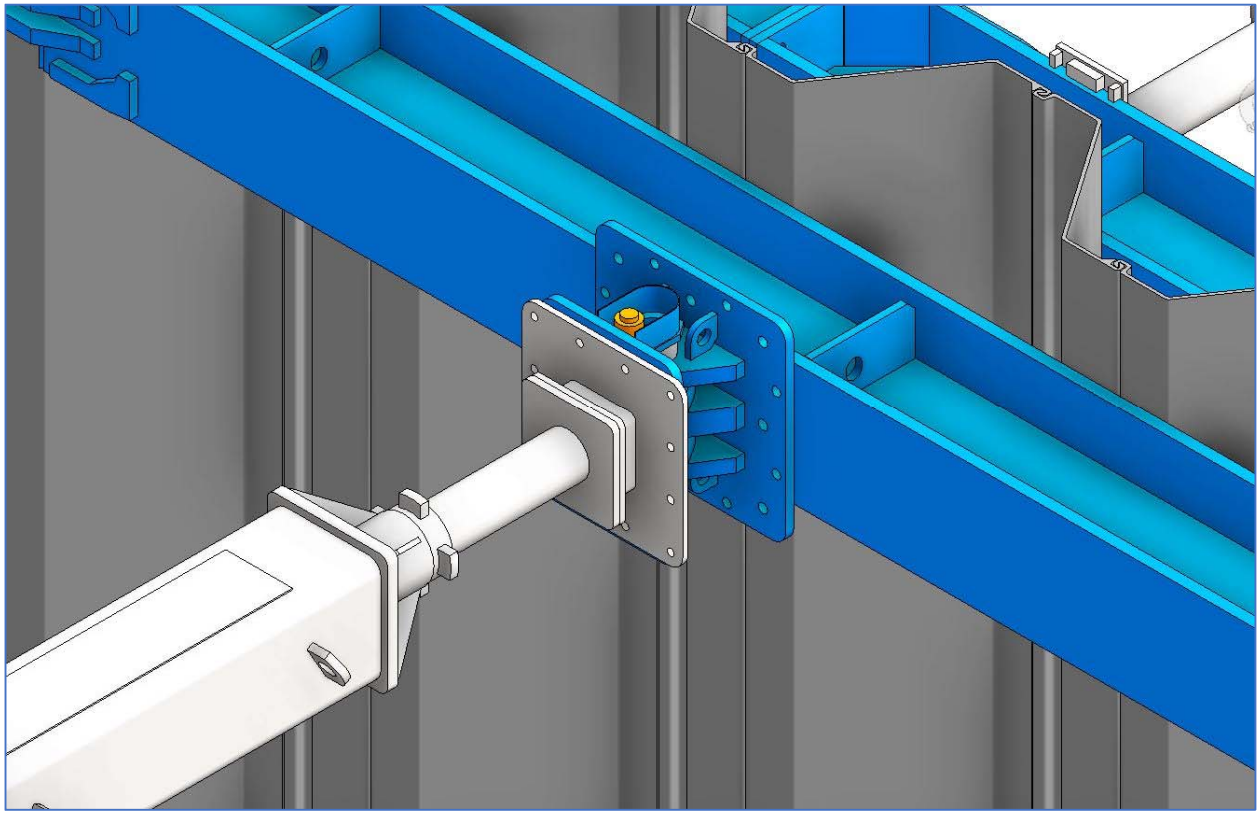


Fig. 1, BIM image showing LIVEPin connection

The development of the BIM is advantageous for the project as it can be integrated with other discipline models. The models can predict clashes and allow for multiple views extracted from one model. Model changes are automatically updated in all views. The model can project 2D representations with dimensions and text in a similar way to traditional CAD and add the benefit of 3D visualization. The BIM can also generate automated equipment lists showing the parts required, materials, weights and source for the component. Equipment lists are automatically updated when the model changes. With the use of BIM, we could create custom corner closure sheet piles in the model and translate these into fabrication drawings for the sheet manufacturer. BIM was developed using the proposed building design drawings as a template.

DIGITAL ENGINEERING

Digital engineering includes BIM, but also incorporates animation and virtual reality. The product animations are used to clearly show how the support of excavation (SOE) design will be sequenced during construction. This was used effectively to show the owner how this will work. The construction sequence will be discussed later in the article. Our animation is also incorporated into a virtual reality (VR) environment. This puts the viewer into a realistic visual environment with the support of excavation design. In this environment, the viewer will "touch off" the cue to run the animation while in the VR environment. The virtual reality environment and the animation will be demonstrated as part of the presentation at DFI in October 2018.

PROPOSED CONSTRUCTION SEQUENCE

The first step in the construction for the SOE is to layout the locations for all the sheeting. The civil engineer will provide survey information for the northing easting and elevations on the site and the SOE designer can use this information to accurately locate the sheets. Construction staking will be used to position the sheets. The 45ft long AZ24-700s will have to be driven with a large crane-mounted vibratory hammer. Positioning of the cranes will be challenging. The picture below shows a representation of the site.



Fig. 2, Naples Bay Center project site

The concern for site construction is limited access due to the adjacent bulkhead walls and channel to the south and to the east for boat traffic. Set up and site access to the west will also be challenging, both for installation and removal of SOE. Our recommended approach is to set up two cranes of reasonable size to the east and a barge mounted crane to the west. This will permit driving operations for the circumference of the SOE as well as the center row of piles. Once the sheet piles have been installed, the auger-cast piles will be installed for the building foundation. No dewatering is intended outside the excavation as this would be very difficult and expensive to accomplish. Once the piles have been installed, the excavation will proceed to about 5ft below ground surface. This will be above the expected water level at 6ft below ground surface. Steel angle brackets will be welded to the face of the sheet piles to support the hydraulic wales that weigh approximately 250 lbs./ft. All wales and struts will be installed at this point. Installation will go quickly because the components are all pinned together and are also hydraulically adjustable at the ends. Once the system is in place, and all hydraulics are engaged, further excavation can commence. This will be done with water at 6ft below ground surface inside and outside the excavated area. The picture below shows an example of what this looks like on another project.



Fig. 3, Excavation in SOE with water inside the excavation

Excavation can commence one cell at a time or both at once. The reason for the split excavation is mainly to limit the length of the struts required to brace the wales. Once the excavation has progressed to 27'-8" below ground surface, the installation of a 4ft thick tremie slab will be accomplished to cut-off water from entering the excavation from below the sheet pile tip elevation. The plug slab will cure, and allow for de-watering inside the excavation to 24'-8" below ground surface (bgs). This will accomplish the dewatering as well as acting as a wale to relieve the top frame from some loading. After de-watering is accomplished, an 8-inch leveling slab will be placed in dry conditions. This will provide enough support for the sheets to act as a cantilever without frame support at the top. With the top frame removed, the center row of piles can be cut, and the insides of the sheet piles are seal welded to the top and shear studs are installed at the

slab levels. Once the leveling slab is cured, the 12-inch structural slab is installed and the building walls are then formed into the sheet piles. The building slabs are then constructed using the auger-cast piles as the building columns.

LIVEPIN MONITORING AND SPECIFICATION

This project will involve monitoring using LIVEPin and Live Site. The LIVEPin is an 80mm stainless steel pin that includes 8 shear planes with embedded strain gages that are accurate within a 2% tolerance. The LIVEPin is housed in a steel connector and the assembly has a load capacity of 786,000 pounds. The LIVEPin connector includes a wireless transmitter that relays load information to a local transmitter/receiver data hub. The hub transmits data every sixty seconds to the Live Site designed and serviced by Mabey. The Live Site records strut loads for up to 8 channels as well as ambient temperature at the site. The data is then trackable as the excavation progresses and in its final design state.

We developed the monitoring to help construction projects with better data for more efficient and safer designs. The use of this technique has allowed us to calibrate observed strut loads with the soil structure interaction models from FEM and other software. Our approach in the future is to continue use of this technology for excavation bracing design, bridging and vertical shoring (falsework). The monitoring technology can help produce smarter designs that allow for adjustment during construction and create an opportunity to test our theoretical models with actual data.

The monitoring specification is written to aid the use and interpretation of LIVEPin results. The specification will list strut loads at each location. The strut loads will be cross referenced to maximum frame loads which control the design of the bracing system. The alarm load may be established as 120% (F.O.S. = 1.25) of the maximum allowable frame load for each phase of construction. The specification will establish a protocol for load events recorded on Live Site such as the threshold loads and the alarm load. If the observed loads are lower than the predicted loads for the load case, then it would be permissible to change from the more conservative design based on the load condition to the design based on the observed results. If the alarm load is triggered, this would alert engineers and installers by email from Live Site and mitigating measures could be taken if necessary.

SUMMARY AND CONCLUSIONS

SOE construction techniques are as important as the design parameters for a successful project. The unique application of working in phases and in the wet in challenging site geometry makes deep foundation shoring in south Florida a challenging application. The use of LIVEPin and hydraulic adjustable equipment makes the application easier and faster as well as working in the wet to avoid expensive dewatering that must be disposed of in container trucks. The project developed in BIM with the use of VR and monitoring improve quality and safety. Monitoring will also help understand the assumptions of the lateral earth pressure theory selected and can expand the body of knowledge on braced excavations with tolerable movements. Specific load information and summary results will be presented with this topic as construction for the project is scheduled for the summer of 2018.

ACKNOWLEDGEMENTS

Andy Wilkin, P.E. and Jeff Dippel were instrumental in helping me with the design and formulation of the concept for the project. Andrew Gascoine was also instrumental in assisting me with Animation and VR. I would also like to acknowledge Paul McLaughlin for help and assistance with BIM on the project.

REFERENCES

Braja M. Das, Principles of foundation engineering, 1990. 2nd Ed., PWS-KENT Publishing, Boston, 731 p.

Holtz, R.D. and Kovacs, W., D., 1981. An introduction to geotechnical engineering. Prentice-Hall Inc., New York, 780 p.

AASHTO LRFD, 7th Edition, 2014

US Steel Sheet Piling Manual, 1984

DRILLED PILE DESIGN AND INSTALLATION CHALLENGES IN AN URBAN ENVIRONMENT

Luis Berroteran, P.E., Langan Engineering, Denver, Colorado, USA, 303-486-6990, lberroteran@langan.com
Satyajit Vaidya, P.E., Langan Engineering, Parsippany, New Jersey, USA, 973-560-4573, svaidya@langan.com
Rudolph Frizzi, P.E., G.E., D.GE., Langan Engineering, Parsippany, New Jersey, USA, 973-560-4703, rfrizzi@langan.com

ABSTRACT

This paper presents design and construction challenges associated with a high-capacity rock-socketed drilled pile foundation system for a 60-story building recently constructed in an urban environment. The site is in very close proximity to surrounding 1-to-6-story buildings and a commuter rail subway tunnel structure. High compression, uplift, and lateral loads imposed by the tall, slender tower constructed over a relatively small site footprint posed a significant design challenge due to the close proximity of the subway tunnel and other structures. Construction challenges included those associated with advancing the drilled pile casings through overburden materials using internal flush method mandated by the Transit Agency, advancing the casings through very dense glacial till materials encountered above top of rock, and drilling rock sockets in variable rock conditions. This paper provides a brief overview of the site and subsurface conditions, and discusses the resulting design and construction challenges for the drilled pile foundation system and how they were addressed.

Keywords: drilled pile, glacial till, rock socket, internal flush, duplex drilling.

SITE AND SUBSURFACE CONDITIONS

The 8,350-square-foot site is located in a busy neighborhood in downtown New York City (NYC). Buildings neighboring the site are supported on shallow foundations, and their basements extend about 15 feet below the sidewalk level. A NYC-Landmarked building is located within a NYC Department of Buildings (DOB)-designated 90-foot influence limit from the Project site. NYC Transit Authority (NYCTA) subway tunnel and station structures are located in close proximity to the Project site. The subway tunnel structure extends about 50 to 55 feet below the sidewalk level. Although the upper portion of the tunnel structure is about 13.5 feet away from the site property line, the lower portion is only about 1 foot away from the property line. A site location plan is presented as Fig. 1.

Geotechnical borings revealed subsurface conditions generally consisting of successive strata of surficial fill, sandy and silty soils, and glacial till (predominantly consisting of cobbles and boulders) overlying mica schist bedrock. A generalized subsurface profile is presented in Fig. 2. The surficial fill stratum was about 10 to 23 feet thick, and generally consisted of loose to medium dense sandy soils with varying proportions of silt, gravel, and miscellaneous debris such as brick. The underlying sandy and silty soil stratum was about 60 to 79 feet thick and generally consisted of loose to medium dense inter-bedded layers of fine to coarse sand, silty fine sand, and silt. The underlying glacial till stratum was about 26 to 70 feet thick and generally consisted of cobbles and boulders embedded in a very dense soil matrix. Top of bedrock was encountered in the borings about 110 to 150 feet below sidewalk level. Groundwater level was measured at about 30 feet below sidewalk level.

© 2018 Deep Foundations Institute

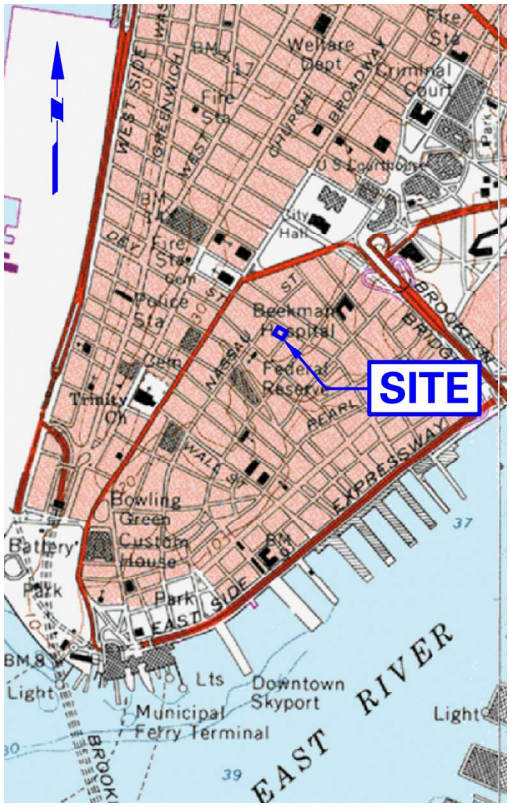


Fig. 1: Site Location Plan

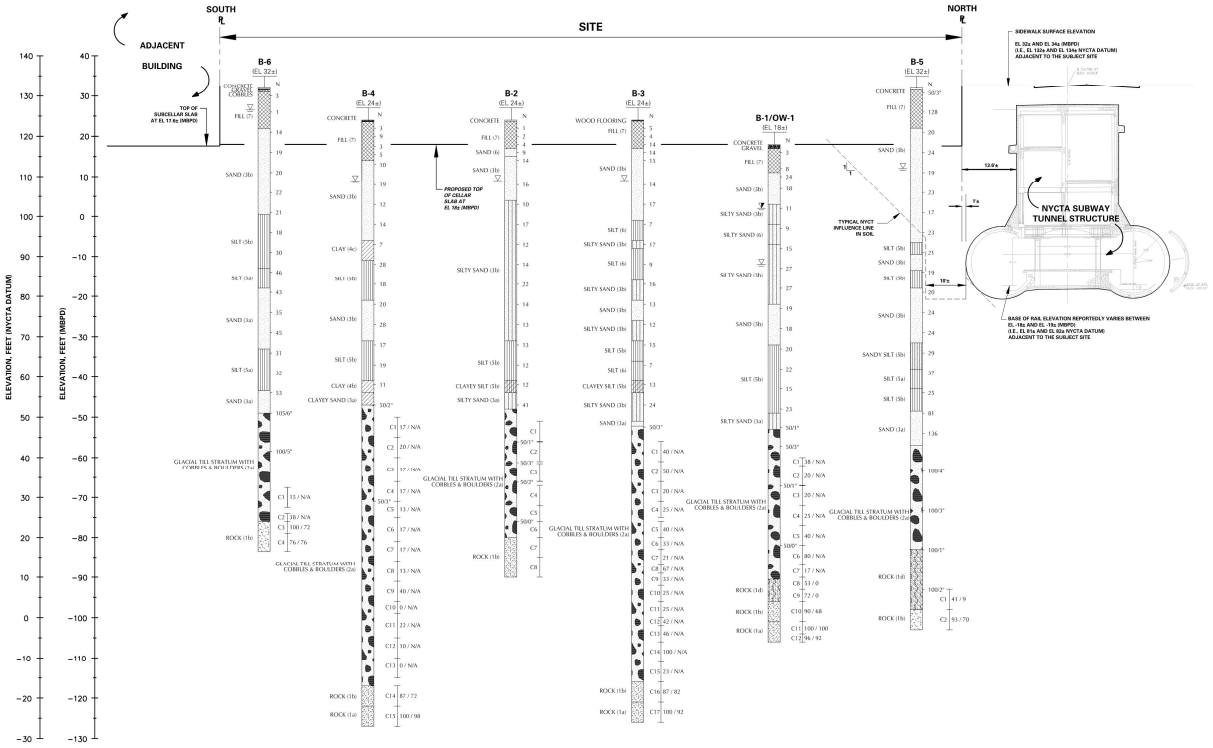


Fig. 2: Generalized subsurface profile

DEVELOPMENT SCHEME AND STRUCTURAL LOADING

The development consisted of constructing a 60-story residential building with one basement level occupying the entire site footprint; the basement floor slab was about 15 feet below the sidewalk level. The column service compression loads ranged from about 290 to 3,650 kips. The shear wall compression and tension loads were as much as about 440 kips/foot and about 110 kips/foot, respectively, with base shear loads on the order of about 1,300 to 2,400 kips.

FOUNDATION DESIGN

Because the surficial fill and underlying loose to medium dense sandy and silty soils were not suitable to adequately support the very high concentrated column and shear wall loads, a deep foundation system capable of transferring the building loads into the glacial till stratum or bedrock was required. The use of driven piles was not permitted due the close proximity of the neighboring NYCTA tunnel structure, relatively old vibration-sensitive buildings surrounding the site, and the adjacent NYC-Landmarked building. Because of the site constraints and anticipated construction challenges, design and construction reviews were performed during the project design phase to evaluate various foundation alternatives, including:

- A structural mat supported on a grid of hollow-bar ground-inclusion elements having an individual compression capacity of 420 tons. Although this foundation system would have avoided drilling foundation elements through the very dense glacial till stratum and into the underlying bedrock, a large number of closely spaced ground inclusion elements would have been required. In addition, supplemental tie-down anchors would have been required. In addition, lateral load resistance of the foundation system would have required special consideration. Although technically viable, an extensive NYCTA and NYCDOB review and approval process was anticipated, and therefore this foundation alternative was considered to be challenging to permit.

- 30-inch-diameter and 36-inch-diameter rock-socketed drilled piles with individual compression capacities of 2,500 tons and 4,000 tons, respectively, and individual uplift capacities of 835 tons and 1,333 tons, respectively. This alternative offered the advantage that field load testing would not be required by the NYCBC provided the rock socket was visually verified.

- 16-inch-diameter drilled piles bearing in the glacial till and designed to provide compression and tension capacities of 650 tons and 300 tons, respectively. Although technically viable, this alternative was not considered further, because a large number of elements would have been necessary to satisfy the serviceability requirements.

- 16-inch-diameter rock-socketed drilled piles designed to provide compression and uplift capacities of 850 tons and 285 tons, respectively. This alternative offered the advantage that field load testing would not be required by NYCBC provided the rock socket was visually verified.

The 16-inch-diameter rock-socketed drilled pile alternative was finally selected, and consisted of a 16-inch-O.D. X 0.6-inch-thick, 75 ksi steel casing advanced at least 6 inches into NYC Building Code (NYCBC) Class 1c or better rock, with a minimum 14-inch-diameter rock socket extending at least 17 feet below the casing into NYCBC Class 1c or better rock. Per the requirements of the NYCBC, mica schist rock is generally considered of Class 1c or better quality when the Rock Quality Designation of the rock cores is at least 35%. The casing and rock socket were filled with cement grout having a minimum 28-day compressive strength of 7,000 psi. The drilled piles were reinforced with three (3) full-length #28 Grade 75 bars and one additional #28 Grade 75 bar in the rock socket; the additional bar was to extend at

least 7 feet into the casing. Refer to Figure 3 for a pile schematic detail. The 2013 version of ENSOFT, Inc.'s L-Pile software was used to evaluate lateral capacity of the drilled piles under full head-fixity conditions per the requirements of the 2008 NYCBC. The calculated drilled pile lateral capacities under fixed head conditions were 18 tons, 12 tons, and 10 tons for the leading, 2nd, and trailing rows, respectively, under group conditions. The final foundation design consisted of a total of 148 drilled piles. Refer to Figure 4 for a foundation layout and to Figure 5 for a pile-to-cap connection detail.

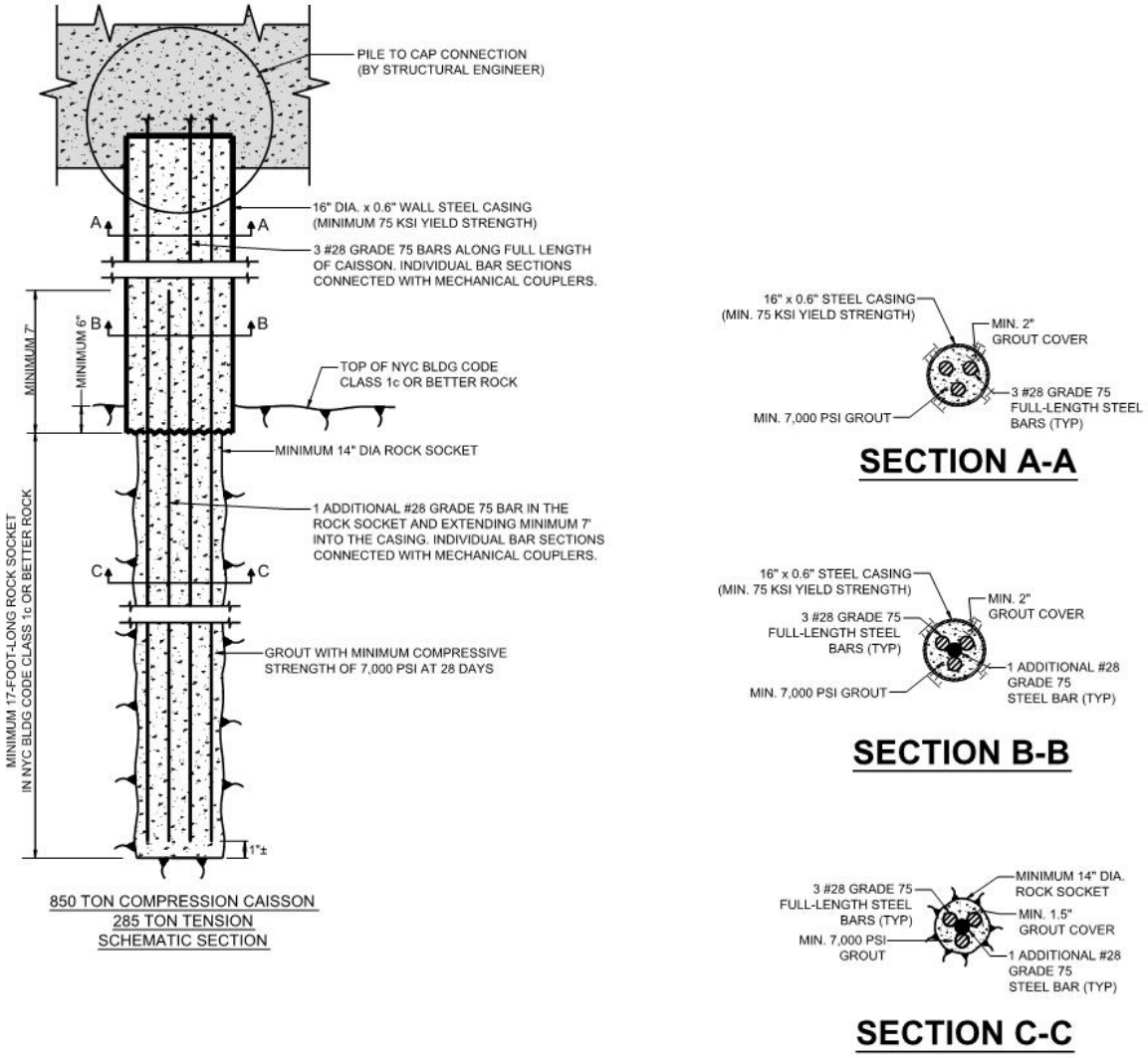


Fig. 3: Pile Schematic Detail

Because the NYCTA subway tunnel structure is located in close proximity to the site property line, NYCTA performed an extensive review of the building's foundation and structural designs. NYCTA considered an influence zone from the tunnel corresponding to a 1H:1V theoretical influence line extending upward from the bottom of the tunnel structure, and required that the foundation system be designed such that only the drilled piles located beyond this influence zone would be capable of resisting the entire base shear loading from the building; no contribution from drilled piles within the influence zone was permitted; refer to Figure 6 for a cross section showing the NYCTA theoretical influence line. In addition, NYCTA required that the drilled piles located within the NYCTA influence zone would be

capable of resisting all imposed axial loads while acting as free-standing columns above the NYCTA influence line. The purpose of these requirements was to ensure the building foundation would continue to perform as intended in case of an unlikely breach of the tunnel wall resulting in loss of ground above the NYCTA theoretical influence line. NYCTA also required calculations to be submitted demonstrating that the lateral pressure transmitted to the tunnel wall from drilled piles subject to lateral loading was of magnitude acceptable to NYCTA.

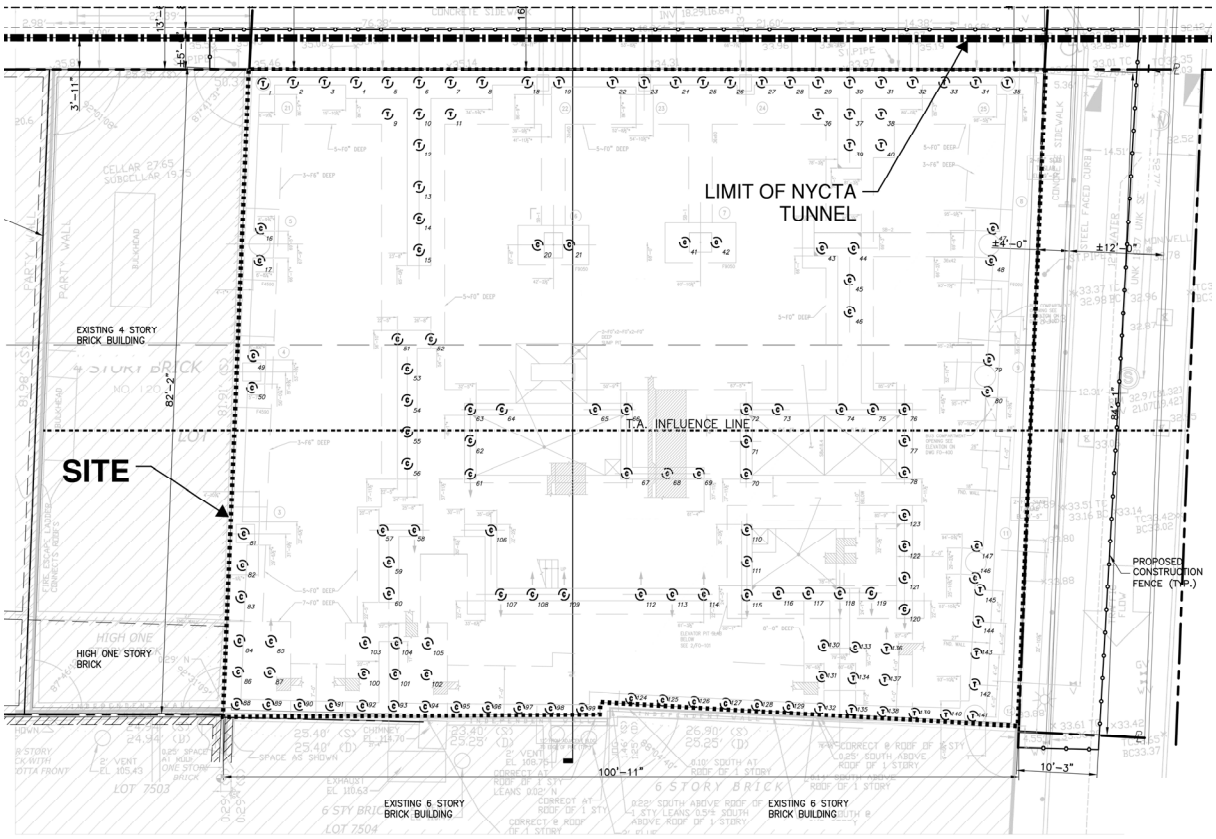


Fig. 4: Foundation Layout

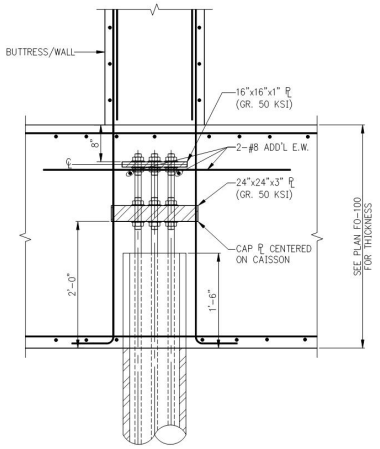


Fig 5: Pile-to-Cap Connection Detail

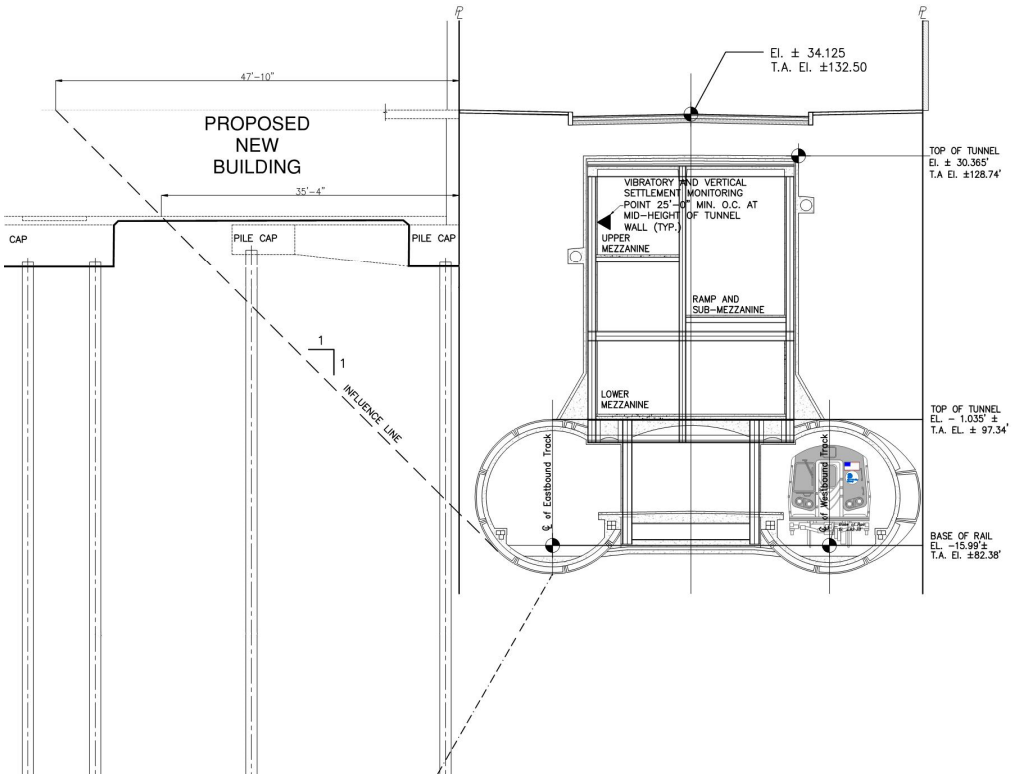


Fig. 6: Cross Section

DRILLED PILE CONSTRUCTION

Specification Requirements

Project specifications were developed requiring the drilled pile casings to have a carbon steel shoe that would allow the casings to be seated at least 6 inches into NYBC Class 1c or better rock and prevent the flow of water and soil into the drilled pile shafts. Drilled pile casings were required to be advanced to top of rock using duplex rotary drilling with internal liquid flush. Within the NYCTA influence zone, the drilled pile drilling procedure mandated by NYCTA was specified, which required the drill bit to be maintained at least 2 feet above the bottom of the casing during duplex drilling. Beyond the NYCTA influence zone, the drill bit was allowed to extend up to 6 inches below the bottom of the casing. The specifications required that the drilled pile Contractor perform casing installation without causing any loss of ground or adverse impacts to the surrounding structures. Rock socket drilling was permitted using rotary drilling or a down-the-hole percussion hammer. It was required that once the minimum design rock socket length was drilled, the Contractor should clean the drilled pile shaft of all debris and flush the shaft with clean water until the entire socket was clearly visible, such that a down-the-hole underwater camera could be used to visually observe the rock socket per the requirements of the NYCBC (and allow for design, construction, and approval without the need for full scale field load testing). Reinforcement installation and grouting of drilled piles was required to be completed on the same day of socket observation. Per the NYCBC requirements, drilled pile construction was subject to full-time observation by a Professional Engineer licensed in the State of New York.

Drilled pile Construction Challenges

The following paragraphs discuss challenges encountered during drilled pile installation, and approaches utilized to address these challenges.

- Casing advancement through the Sand and Silt Stratum

  When working within the NYCTA influence zone, challenges were initially encountered while advancing the casings through the upper silt and sand stratum while maintaining the drill bit 24 inches above the casing bottom. The Contractor reported that the casings behaved as if plugged, and the equipment was unable to advance the casing even when full downward pressure (crowd) was being applied. This resulted in significantly increased drilling time and equipment malfunctions. The Contactor repeatedly discussed these site-specific issues with NYCTA, and eventually obtained permission to reduce the drill bit clearance above the casing tip to 6 inches. However, even with this modified requirement, the Contractor continued to face challenges with casing advancement, and the drilling work was occasionally stopped by the Special Inspector and/or NYCTA due to observation of external flush evidenced by reduction in internal return and drilling fluid finding a pathway around the casing. Based on field observations, the external flush was attributed to the high drilling fluid pressure used by the Contractor.

  For drilled piles outside the NYCTA influence zone, the Contractor was able to advance casings through the sand and silt stratum using internal liquid flush duplex rotary drilling with the drill bit extending no more than 6 inches beyond the bottom of the casing. No external flush was observed in this case. These observations were subsequently discussed with the NYCTA, and a project-specific approval was obtained to allow casing drilling within the NYCTA influence zone with the drill bit flush with the bottom of the casing. The Contractor was able to install casings using this procedure through the silt and sand stratum with relatively better success.

- Casing Advancement through the Glacial Till Stratum

  The Contractor also faced challenges advancing the casings through the glacial till stratum. To overcome these challenges, the Contractor proposed to use an alternative proprietary casing ring bit system that appeared to be similar in concept to other ring bit systems previously approved by NYCTA and used successfully on other project sites adjacent to the NYCTA subway tunnel structures. NYCTA and the Design Team provided conditional approval for use of the alternative system on the project site, provided it did not result in ground loss and adverse impacts to the adjacent buildings and the NYCTA tunnel structure. Although increased casing advancement production rate was realized with the use of the ring bit system, external flush was observed at some of the drilled pile locations. Surface depressions, evidencing ground loss, were observed at these drilled pile locations within a day of casing installation. Due to this condition, the use of the alternate ring bit system was discontinued. The Contractor then attempted to advance casings through the glacial till using a conventional down-the-hole percussion hammer (DTHH) extended ahead of the casing; however, the DTHH procedure also resulted in external flush followed by evidence of ground loss. As such, the use of the DTHH technique was discontinued. The casings were ultimately successfully advanced through the glacial till stratum using conventional duplex rotary drilling with internal liquid flush from a tri-cone roller bit extending less than 6 inches beyond the bottom of the casings. The casings were installed much more efficiently and without any evidence of external flush or ground loss. Considering the successful site-specific experience with this drilling technique beyond the NYCTA influence zone, NYCTA permitted the use of this technique even within their influence zone.

- Rock Socket Drilling

Top of rock was variable across the site, and varying amounts of fractured/weathered rock was present at the top of rock. These conditions required careful operator observation during casing installation to assure accurate top of rock determination as well as sufficient casing penetration below the top of rock (as opposed to embedment in boulders in the glacial till above the top of rock). In some instances, video observation of the drilled holes revealed that some casing tips were in fact still within the glacial till stratum. To avoid potential ground loss in such instances, the casings were partially filled with grout and the rock sockets re-drilled after the grout had sufficiently cured; additional reinforcement was extended above the casing tips in such instances.

Rock sockets were visually observed using a video camera to verify design bearing materials; in instances where rock socket observation using a conventional video camera was not possible, observation was performed using an acoustic televiewer logging system. A representative acoustic televiewer log is presented in Fig. 7. The final pile depths typically ranged between about 135 feet to about 195 feet below the sidewalk level.

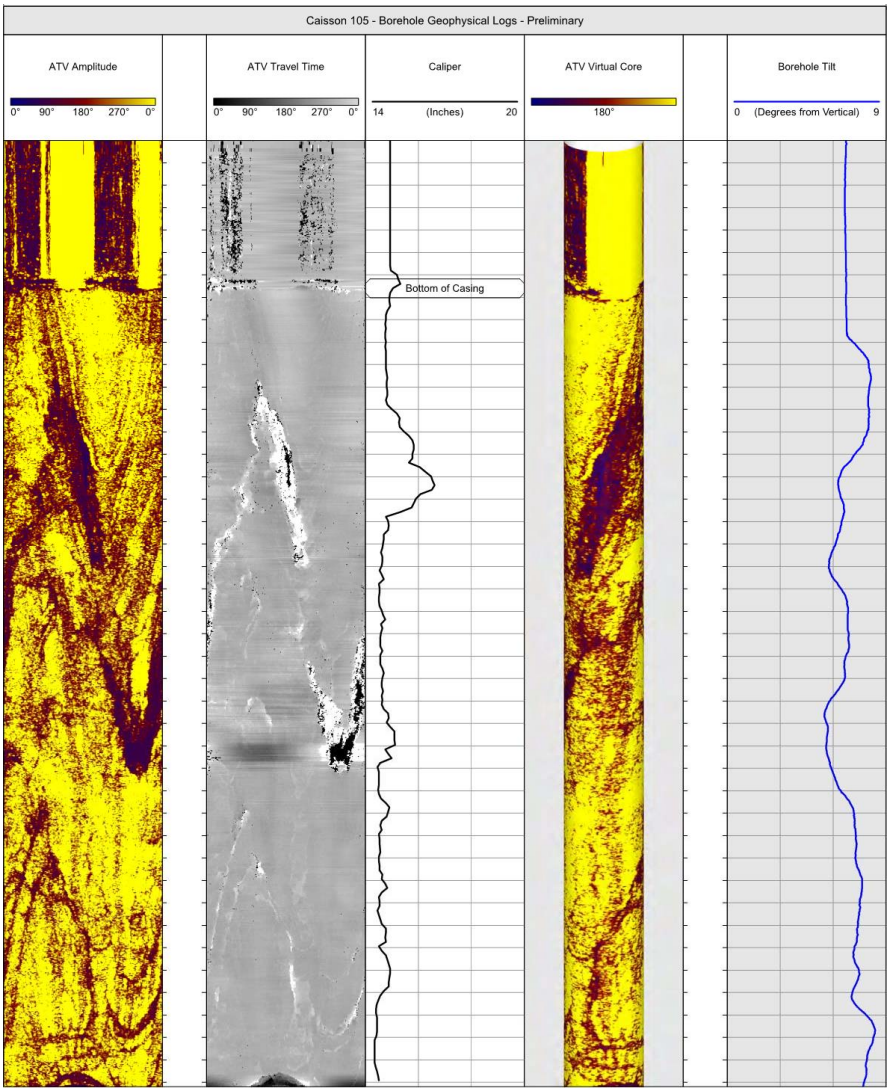


Fig. 7: Typical Accoustic Televiewer Log

CONCLUSIONS

The following conclusions are drawn from the design and construction experience on this project:

1. Drilled pile construction activities have the potential to cause ground loss and settlement to adjacent areas and structures unless properly planned and performed.
2. Duplex drilling performed with the drill bit recessed above the casing tip in sand and silt soils can cause external flush if high drilling fluid pressure is used and the casing is not advanced at a sufficient rate.
3. Ring bit systems used for advancing casing can potentially result in significant external flush and ground loss when drilling in glacial till materials. With appropriate drilling equipment and techniques, duplex rotary drilling with a tri-cone roller bit can be successfully used to advance casings through very dense glacial till soils consisting of cobbles and boulders while maintaining an internal flush.
4. An acoustic televiewer can be used as a suitable alternative to video observation of drilled pile rock sockets.

DRILLED SHAFT DIFFICULTIES AND A MICROPILE SOLUTION

Paul Axtell, P.E., D.GE, Dan Brown and Associates, Overland Park, KS, paxtell@dba.world
David Graham, P.E., Dan Brown and Associates, Chattanooga, TN, dgraham@dba.world
Jeff Jackson, P.E., Montana Department of Transportation, Helena, MT, jejackson@mt.gov

ABSTRACT

The Montana Department of Transportation recently awarded a contract to construct a replacement bridge across the Clark Fork River in Heron, MT. Both abutments and both intermediate bridge bents were to be founded on 6-ft and 8-ft diameter, permanently cased drilled shafts with rock sockets, respectively. Two drilled shafts per substructure location were designed for a total of eight drilled shafts. The original design included 6-ft diameter drilled shafts at the abutments but the Contractor elected to submit a Value Engineering proposal that increased them to 8-ft diameter. On the basis of the subsurface exploration program, extremely challenging subsurface conditions were known to exist, including the potential presence of large boulders within the predominantly sand and gravel soil matrix.

The successful bidder elected to use an oscillator to install the permanent casing to the top of bedrock, while simultaneously removing the spoils from inside the casing with a clam-grab. On seven of the eight shafts, this approach worked well. Unfortunately, on one of the shafts, the casing met refusal on one or more boulders encountered in the predominantly sand and gravel soil overburden. Following several attempts, and despite several variations of approaches, it was determined that the casing could not be advanced beyond the obstruction without unacceptable risks to the pile-supported temporary work trestle (i.e., loss of soil and reduction in pile capacity for the foundations supporting the work trestle).

To mitigate the problematic drilled shaft, a unique solution was designed and successfully constructed. The solution involved the construction of seven 16-in diameter micropiles constructed within the confines of the obstructed casing. The micropiles were drilled to bedrock through the sand, gravel, and boulders and include rock sockets to satisfy axial design requirements. The micropile casing thickness, grade and grout strength were designed to provide adequate flexural strength as well as to satisfy other design requirements. Upon completion of the micropile installation, the upper portion of the drilled shaft above the boulders and within the permanent casing was constructed as usual.

This paper discusses the difficult subsurface conditions at the site, the drilled shaft construction difficulties, and the design and construction of the micropile solution.

INTRODUCTION

The replacement bridge over Cabinet Gorge Reservoir at Heron, Montana, was recently completed and opened to traffic. The project is in Sanders County, which is located in northwestern Montana near the Idaho border as shown in Figure 1. The Cabinet Gorge Reservoir is the result of a dam built on the Clark Fork River a few miles downstream of the bridge project.

The new three-span steel plate girder structure is founded on eight drilled shafts. Both end bents and the two intermediate bridge piers are founded 1x2 groups of drilled shafts oriented transverse to the bridge alignment. Both intermediate piers include a waterline strut at the top of the 8.2-ft inside diameter drilled shafts and individual pier columns on top of both shafts. The drilled shafts include ¾-in wall permanent steel casing to the top of bedrock and 8.0-ft diameter rock sockets beneath the casing.

© 2018 Deep Foundations Institute

The bridge was designed by Morrison-Maierle under contract to the Owner, the Montana Department of Transportation. Dick Anderson Construction is the General Contractor that was awarded the bridge construction contract.

Following the successful construction of the first six drilled shafts at the three other substructure locations, the first of the two Pier 2 shafts constructed encountered a large boulder or possibly multiple closely spaced large boulders in the primarily sand and gravel soil overburden during casing installation. The casing met refusal on the boulder(s) and despite substantial efforts to continue advancing the casing, a remediation plan became the only practical and feasible solution. Note that the work was being performed from a temporary trestle bridge supported on driven piles bearing in the sand and gravel overburden. Safety of the work trestle was paramount and became a concern during the efforts to advance the casing through the boulder(s).

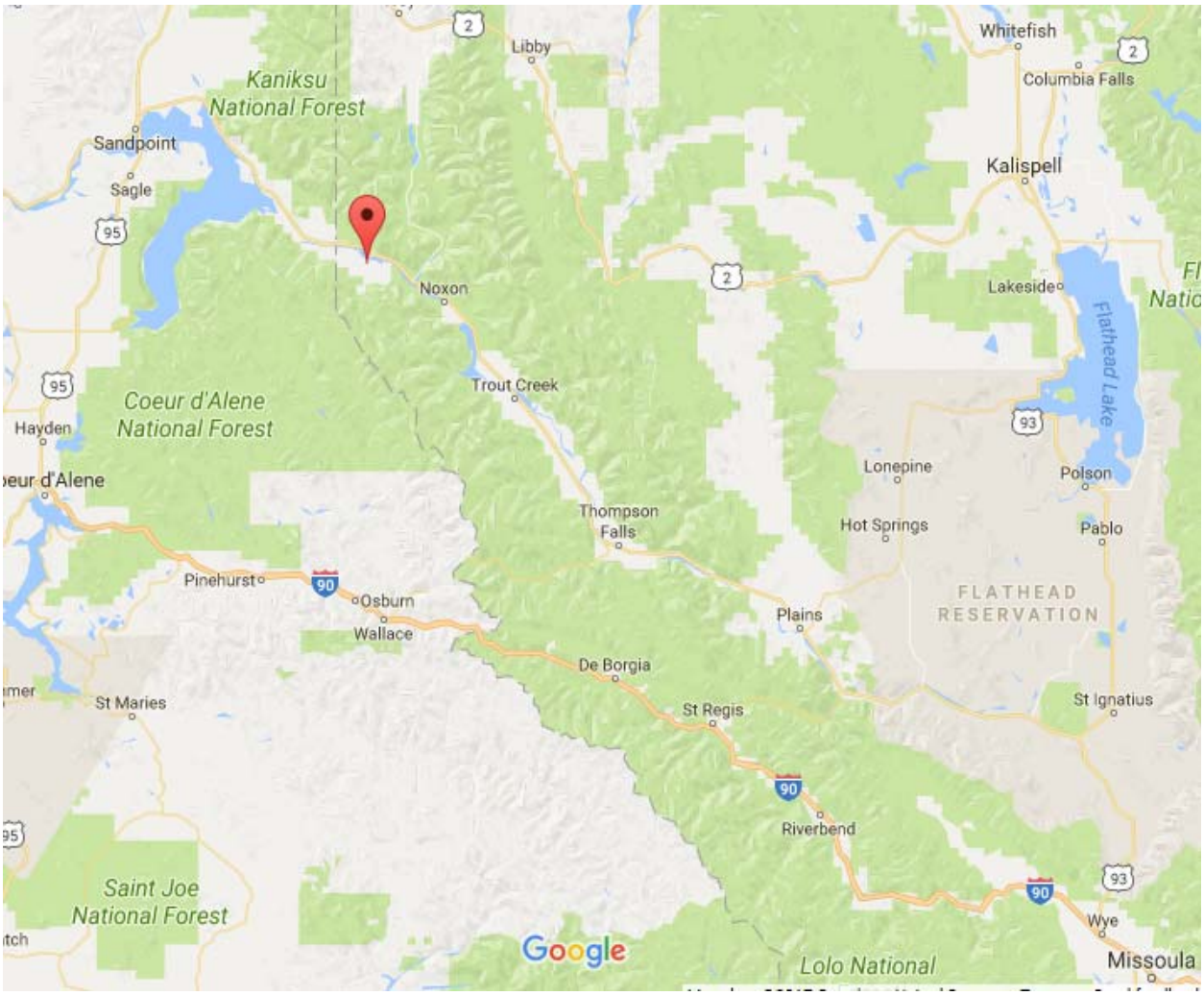


Figure 1: Project location in northwest Montana near the Idaho border.

Dan Brown and Associates was retained by the Owner to develop foundation design alternatives to remediate the problematic drilled shaft. Accordingly, several potential remedies were developed and evaluated until the preferred solution was identified. The selected remediation plan included leaving the partial length permanent casing in place as-installed, installing seven 16-in diameter micropiles cased to

bedrock, and constructing the upper portion of the drilled shaft as designed, with the top of the micropiles encased in the drilled shaft. Condon-Johnson and Associates was awarded a contract to install the foundation remediation described in this paper. The remediation was successfully constructed and the bridge is now open for traffic.

Discussion of the site conditions, design, and construction of the foundation remediation are included in the following sections.

SUBSURFACE CONDITIONS

A generalized site plan is shown in Figure 2 and a generalized soil profile is shown in Figure 3. Where the problematic drilled shaft is located, the water depth is approximately 40 ft; the normal pool elevation is around Elevation 2,178 ft and the mudline is around Elevation 2,138 ft. Beneath the mudline is a 25-ft thick stratum of loose to medium dense silty gravel. Beneath the silty gravel is at least one but possibly multiple boulders with a vertical dimension of approximately 20 ft. A similar argillite rock boulder encountered in an exploratory boring near the drilled shaft indicated an average measured uniaxial compressive strength of 17,761 psi. The measured values for the nine uniaxial strength tests on HQ3 core samples recovered from the boulder ranged from 12,415 psi to 25,555 psi with a standard deviation of 4,163 psi. Recovery and Rock Quality Designation (RQD) were generally 100 percent.

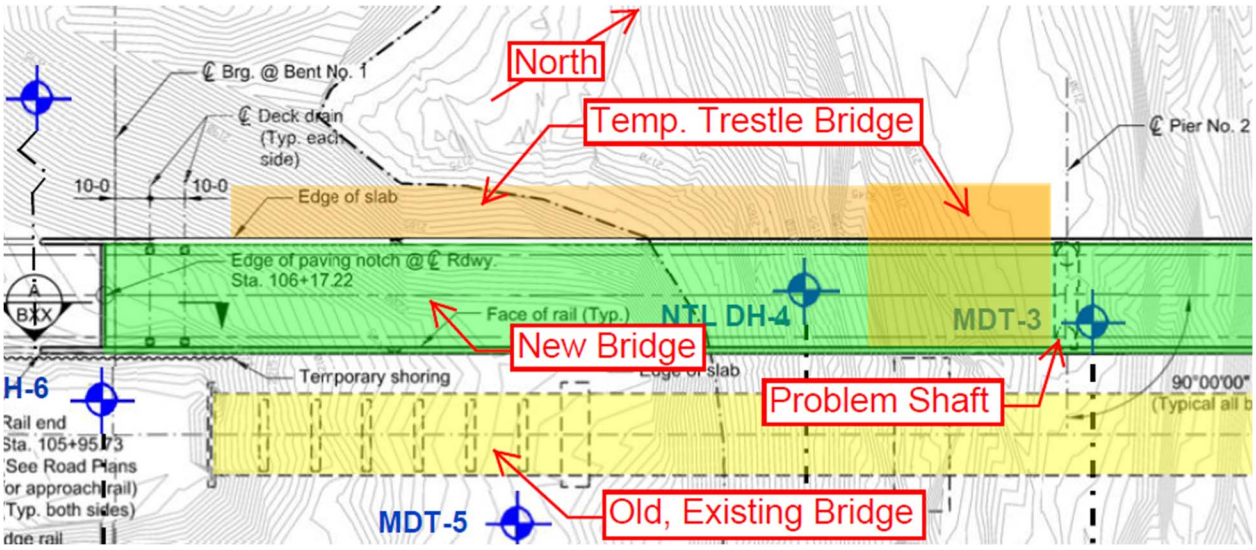


Figure 2: Generalized site plan.

Beneath the boulder is 80 ft of predominantly dense to very dense, poorly graded gravel with isolated layers of hard clay and dense sand. Argillite bedrock exists beneath the soil overburden; the top of the bedrock is at approximately Elevation 2,013 ft.

FOUNDATION REMEDIATION DESIGN

Preliminary analyses were developed for multiple remediation options. The team evaluated all the potential paths forward and ultimately selected the preferred alternative considering relative risk, schedule, and cost. Upon selection of the preferred remediation option, a two-phase analysis was performed. The computer software GROUP was utilized to first evaluate the three dimensional factored force effects acting on each drilled shaft at Pier 2. In this first phase of analysis, beneath the partial length permanent casing, the problematic drilled shaft was assigned an equivalent bending stiffness

representative of the proposed micropile group. Therefore, the foundation response under lateral load was slightly different between the two foundations supporting Pier 2. This initial effort using GROUP was necessary to ascertain the demand acting on the problematic drilled shaft, which was different than the original design due to the change in stiffness beneath the permanent casing.

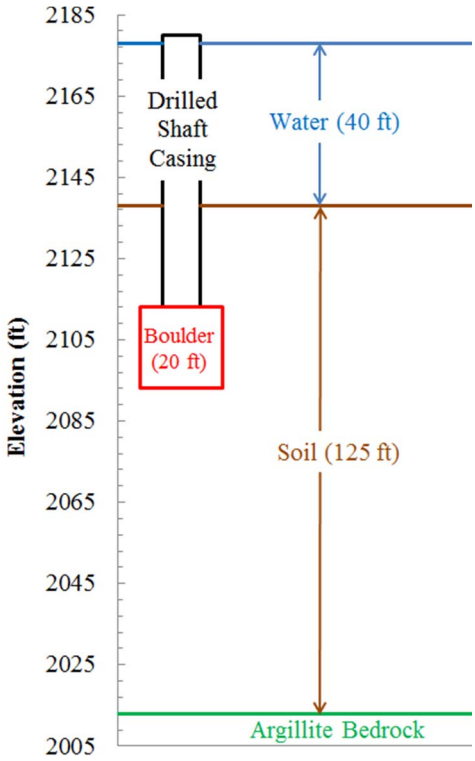


Figure 3: Generalized soil profile.

Once the three dimensional factored force effects acting on the problematic drilled shaft were determined, a second GROUP model was developed to evaluate the three dimensional factored force effects acting on each individual micropile. This allowed the specific structural and geotechnical design aspects of the micropiles to be completed.

The resulting configuration of the micropiles is shown in Figures 4 and 5. As can be seen, the permanent casing of the problematic drilled shaft terminated at the top of the boulder. Through this casing, a group of seven micropiles were installed prior to placement of the reinforcing cage and concrete inside the permanent casing; i.e., the micopiles were installed in advance of the shaft concrete. The tops of the micropiles were ultimately cast into the upper portion of the drilled shaft above the boulder. The working platform elevation was effectively the top of the temporary trestle bridge deck around Elevation 2,190 ft. This resulted in a total micropile depth of just over 200 ft at the time of installation, but the tops were later cut to final length. It is noted that prior to placement of the concrete in the drilled shaft, the upper 75 feet of the micropiles were temporarily unsupported.

The micropiles included 16-in diameter, 5/8-in wall, minimum 50 ksi yield strength permanent pipe installed to bedrock. A 20 ft uncased socket was constructed in the bedrock for each micropile. A sanded grout with a minimum uniaxial compressive strength of 7,000 psi was also used. The reinforcement included a single, full-length, 3-in diameter Grade 75 all-thread center bar. The center bar was necessary to transfer the uplift resistance developed in the socket. A cross-sectional view of an individual micropile through the cased section is provided in Figure 6.

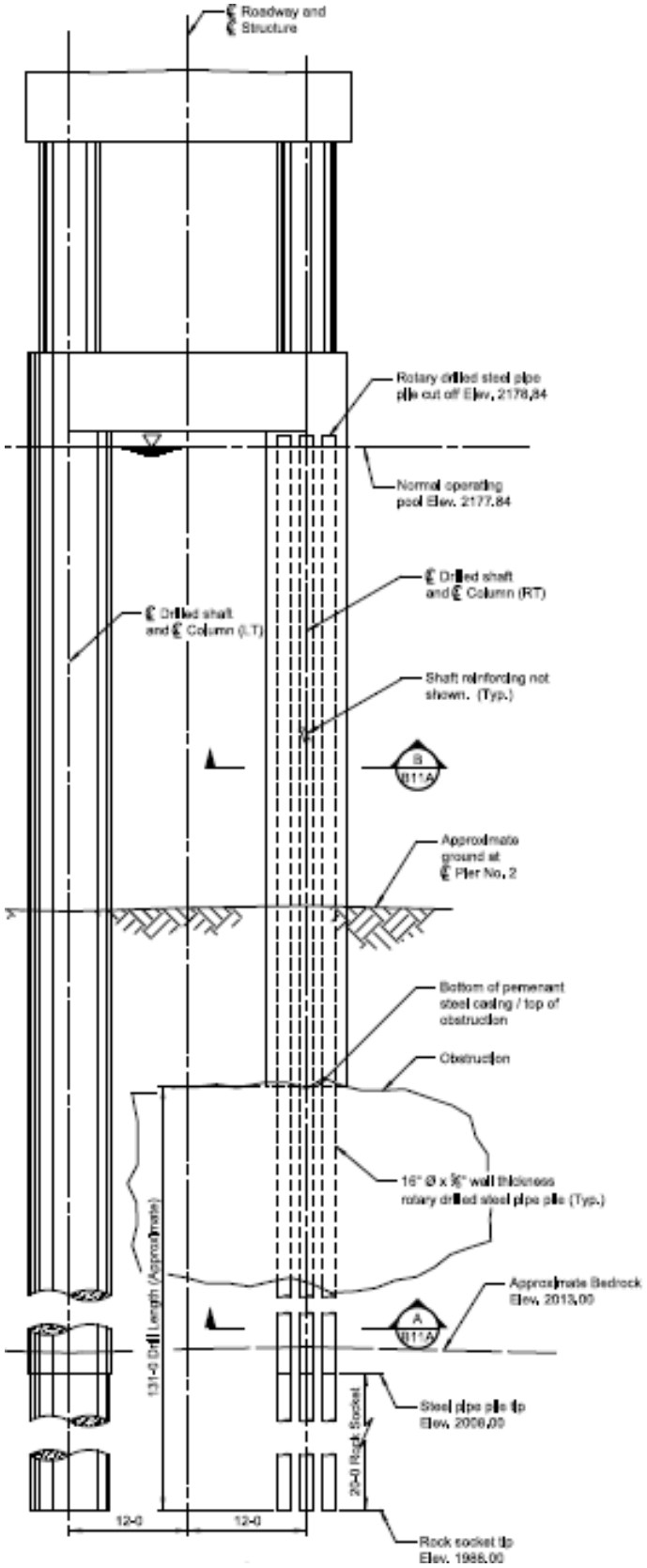


Figure 4: Drilled shaft repair design; elevation view.

It is noted that determining the micropile layout was an iterative process in which slight variations in location, diameter, pipe wall thickness, grout strength, and verticality all produced noticeable influences on the results. In addition, the final group configuration is non-symmetrical and was optimized considering the three-dimensional loading. Also, given the relatively tall configuration of Pier 2 and the large unsupported foundation length above the mudline, tight tolerances on verticality were necessary.

Prior to submitting the final released for construction remediation documents, multiple meetings involving the Designer, Owner, General Contractor, and Specialty Sub-Contractor were held to optimize the design. During these meetings, the preliminary micropile design was presented and detailed discussions ensued to ensure the remediation plan was optimal with respect to the available construction equipment and materials. The availability of the pipe was perhaps the biggest factor in these discussions as approximately 1,200 ft of permanent pipe was required in relatively remote northwestern Montana. Accordingly, upon checking the lead time on a few various pipe diameters, wall thicknesses, and grades of steel, it was concluded that the 16-in by 5/8-in Grade 50 pipe was the preferred material. Using this information, the final design was performed using the iterative process described above and the final released for construction documents were submitted.

During design development, a sacrificial demonstration pile and a load testing program were considered but not performed. It was agreed that the critical and controlling issues regarding the micropile constructability and performance was the presence of the boulder just beneath the permanent casing and the need to work from an elevated work platform over the river (temporary trestle bridge). These conditions could not be replicated in a test program. Furthermore, with respect to an axial load test, the lateral considerations, namely flexure and shear, effectively controlled the design of the micorpiles.

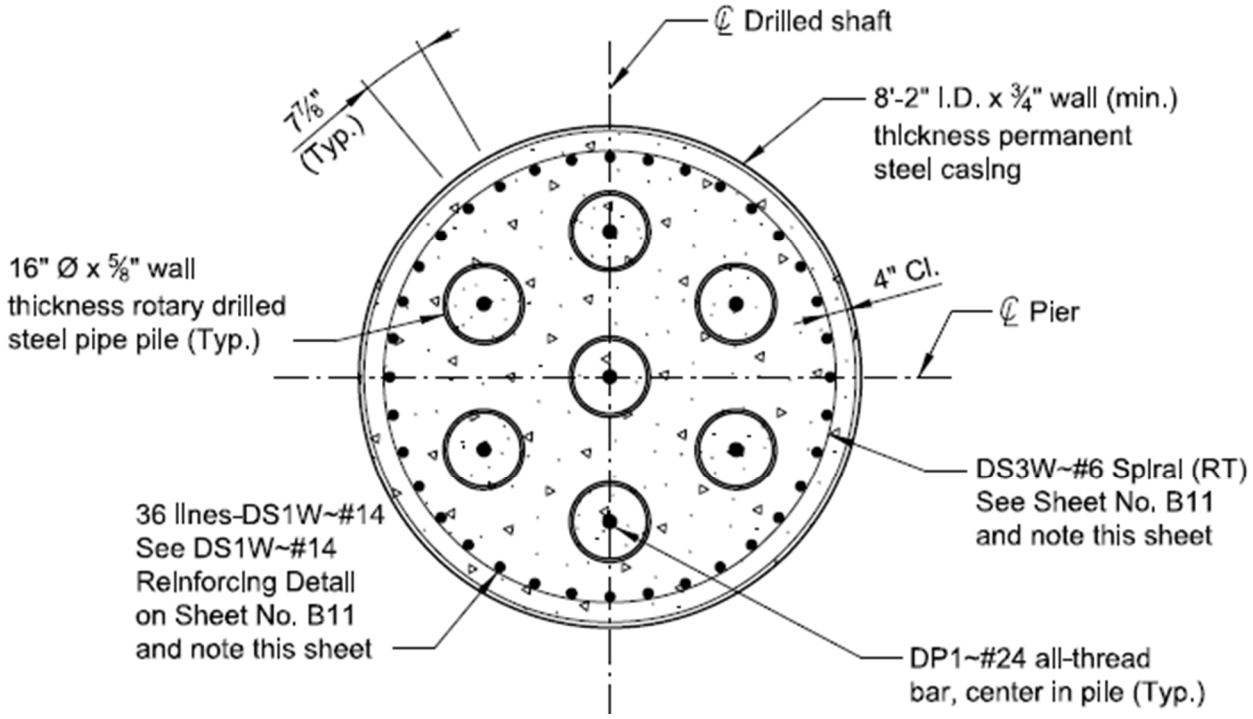


Figure 5: Cross-section B (through permanent cased drilled shaft section).

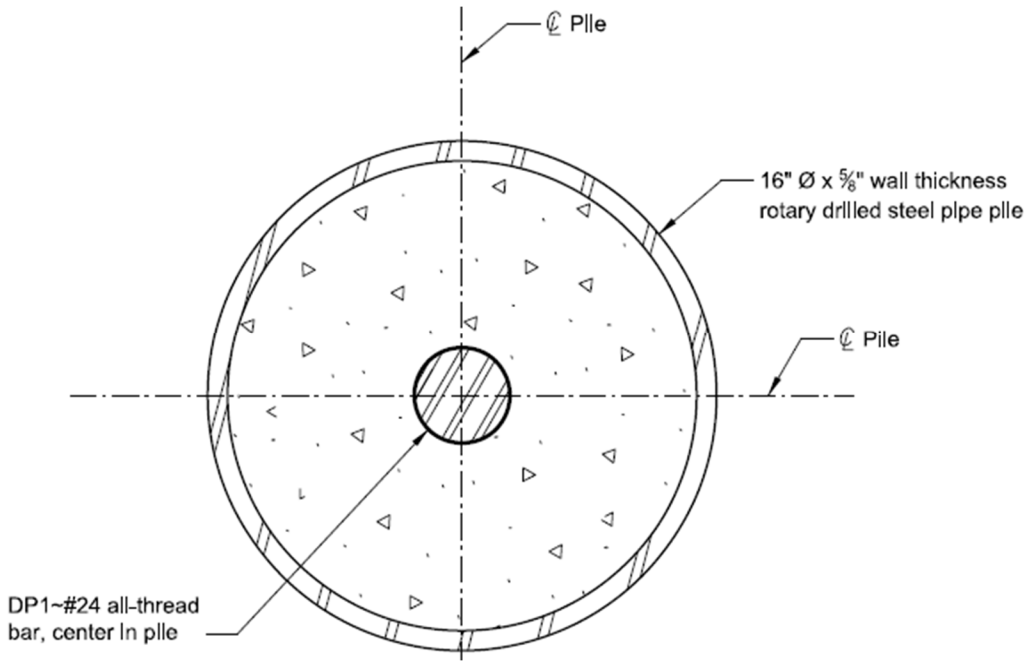


Figure 6: Cross-section of 16-in diameter micropile in the permanently cased zone.

FOUNDATION REMEDIATION CONSTRUCTION

Construction of the group of micropiles within the confines of the permanent casing was performed from the temporary work trestle, as shown in Figure 7. A Foremost DR-24 dual rotary drill rig owned and operated by Layne was utilized for the installation, as shown in Figure 8. A dual rotary drill was the preferred rig due to the strict requirements related to verticality. It was postulated that the ability to turn the micropile casing independently of the drill stem would allow more control of the verticality.



Figure 7: Overview of project site, micropile rig and service crane.



Figure 8: Foremost DR-24 dual rotary drill rig used for micropile installation.

The micropile pipe included a cutting ring welded to the base, as shown in Figure 9. Down-the-hole pneumatic hammer drill heads rotating independently of the casing were utilized and both were advanced at the same rate. Reverse circulation methods were used to extract the cuttings.



Figure 9: 16-in diameter, 5/8-in wall permanent micropile casing with cutting shoe.

Aside from the substructure geometry, the relatively slender dimensions of the micropiles relative to the drilled shaft accentuated the need for maintaining verticality during installation. Accordingly, a very robust template was constructed and temporarily attached to the inside of the permanent drilled shaft casing along its entire length. In addition, the installation method included a partial length, oversized temporary casing through the boulder. The combination of the template and temporary casing provided sufficient annular space to accommodate minor adjustments to the permanent micropile casings. This allowed precise control of the verticality and was very effective.

Upon completion of each micropile, the temporary casing was removed. Prior to retrieval of the temporary casing, a cement-bentonite mix was tremie placed in the annular space between the OD of the permanent pipe and the ID of the temporary casing. The cement-bentonite mix was designed to replicate the stiffness of the surrounding soil, thereby preventing the potential for hard spots that may attract elevated shear forces.

An unforeseen difficulty that arose during construction involved the permanent micropile pipe seam. The pipe included a straight seam along the longitudinal axis of the pipe sections. The weld bead of the seam protruded approximately ¼ to ½ inch into the ID of the pipe. This resulted in difficulties installing and removing the down-the-hole tools. Ultimately, this weld bead had to be removed by mechanical means prior to installation. A photograph of the seam protrusion is included in Figure 10.

Upon the successful installation of the seven micropiles, the temporary template inside the permanent drilled shaft casing was removed. Following that, a typical drilled shaft reinforcing cage was placed around the micropiles to the bottom of the permanent casing and concrete was tremie-placed as usual. The finished foundation is shown in Figures 11 and 12 prior to construction of the water line strut.



Figure 10: Weld bead protrusion into the ID of the pipe.



Figure 11: Plan view of completed drilled shaft repair prior to construction of the pier cap.

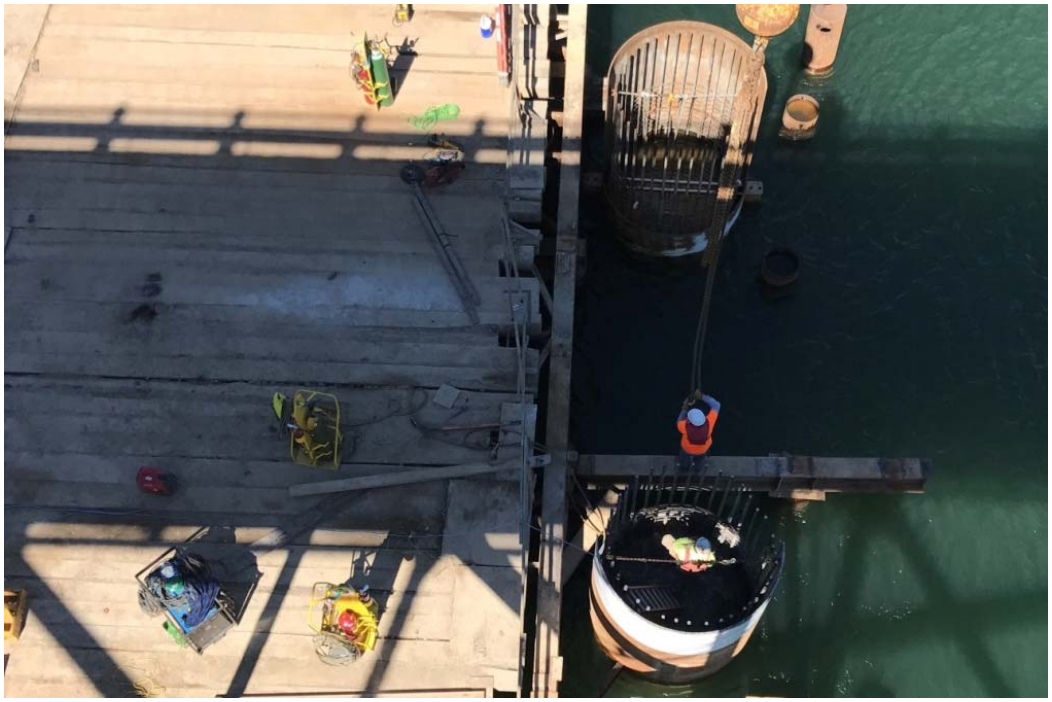


Figure 12: Completed foundations prior to construction of the pier cap.

SUMMARY

A group of micropiles constructed inside the confines of a drilled shaft permanent casing that met early refusal was successfully designed and constructed to remediate the difficulties associated with the drilled shaft construction. The associated design was complex and required an iterative approach involving multiple degrees of freedom. Early involvement by the Contractor was essential to not only the constructability but also the optimization of the solution.

ACKNOWLEDGEMENTS

The following individuals had prominent roles in the development and implementation of the successful foundation remediation described herein and their contributions are greatly appreciated: Jim Scoles, P.E., S.E., Bridge Design Engineer for Morrison-Maierle; Tami Hembree, Construction Project Manager for the Montana Department of Transportation; and Ty Jahn, Project Manager for Condon-Johnson and Associates. The authors also wish to express gratitude to Dick Anderson Construction for their support.

FOUNDATION DESIGN AND CONSTRUCTION CHALLENGES WITH MARSH DEPOSITS IN A HIGH SEISMIC RISK ZONE

T. Ted Miyake, PE[1], and M. Reza Saberi, PE, GE[2]

Driven piles are a common tool in any engineer's toolbox for supporting large structures over very soft ground, especially in high seismic risk zones. Challenges include achieving sufficient vertical and lateral load capacities within the constraints of pile spacing and geologic conditions. This was the case for a project in Orange County, California with a state-of-the-art, $180 million plant for biosolids processing, biogas management and energy recovery located in marshland next to an existing waste water treatment plant. The new construction for the Irvine Ranch Water District included a 70-foot (21 m) tall building and three closely spaced, 90-foot (27 m) high, 65-foot (20 m) diameter, egg-shaped steel digester tanks. The lower 35-feet (11 m) of the tanks were constructed below ground level.

The site was underlain by up to 45 feet (14 m) of highly compressible peat and organic clays with standard penetration test (SPT) blows as low as 2 blows/ft (30 cm). Some of the peat layers had measured in-situ dry densities of less than 30 pcf (480 kg/m^3) with moisture contents of over 250 percent. The soft clays and peat were underlain by a dense layer of sand and gravel at depth. Groundwater was very shallow.

While nearby sites were designated by others as seismic site class "D", this site was clearly class "F" (S_F) which required site specific seismic hazard and time history analyses. Six recorded time histories were selected from the 1994 Northridge, 1989 Loma Prieta (California) and 1999 Chi Chi (Taiwan) earthquakes for the ground motion analysis considering the magnitude of the earthquake, distance to the source, characteristics of the earthquake source (i.e. type of fault displacement), peak ground acceleration, local site geology, station type (i.e. free-field or small structure stations), and spectral content that was similar to the period range of interest. Following ASCE's Guideline Document 7-05, a site-specific horizontal acceleration response spectra (ARS) was developed for the maximum credible earthquake (MCE) associated with the site.

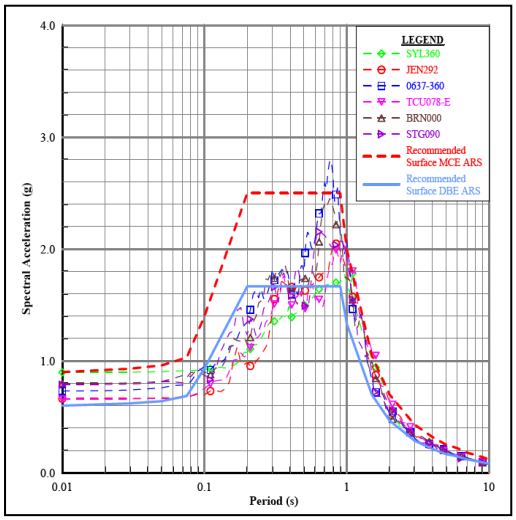


Figure 1: Acceleration Response Spectra

Ground improvements and drilled pier options to support the structures were ruled out because of the shallow groundwater and peat which provided insufficient lateral support. Driven piles proved to be the best foundation alternative. A 14-inch (.36 m), square, pre-cast, pre-stressed concrete pile with a 200-ton (890 kN) axial capacity was selected for the baseline pile type (locally, referred to as a "Caltrans" Class 200-type pile). In close collaboration with the structural engineer, both pile caps and uniform thickness mat slabs alternatives were evaluated for the structures. The mat slab solution proved to be the most cost effective. The resulting total number of piles was just over 3,000 for all the major plant structures, with over 1,200 for the digester

[1] Principal Engineer, NMG Geotechnical, Inc., Irvine, California. Email: tmiyake@nmggeo.com
[2] Principal Engineer, NMG Geotechnical, Inc., Irvine, California. Email: rsaberi@nmggeo.com

© 2018 Deep Foundations Institute

tank complex which included the three 90-foot (27 m) tall tanks and associated buildings. For the small 4.5-acre (1.8 hectare) site that equated to an average of one pile per 65 square feet (6 m^2).

An indicator (test) pile program including a pile driving analyser (PDA) was executed to verify pile integrity, to evaluate the preliminary pile designs, and allow for adjustment for the production pile lengths as needed. The PDA results were also used to develop acceptance criteria based on pile hammer blow counts for use by pile driving inspectors during production pile installation. The test pile data was used to reduce the total design pile lengths by over 52,000 linear feet (16,000 m). Besides the material cost savings, this also greatly reduced the work required to cut off excess pile lengths for piles that could not be driven to design elevations.

The approximately 3,000 production piles were driven for the structures over the course of seven months with two pile driving rigs. Even with the reduced pile lengths from the indicator pile program, many of the production piles in certain areas of the site could not be driven to the full design depth. For some of the larger structures, though these piles achieved the design axial capacity, the total design penetration into the denser granular soil layer was needed in order to provide the designed lateral load capacity. For these piles, the contractor had to pre-drill the entire design pile lengths with a 14-inch (.36 m) diameter, solid flight auger in order to drive the piles to the design tip elevations.





Figures 2 and 3: Aerial view of pile driving for digester tank complex and the complex under construction.

The piles which encountered driving refusal that did not require the full design penetration had to be cut off following installation in order to be tied into the mat slabs of the foundation system. Over 330 piles (about 10 percent of the production piles) fell into this category, with cut off lengths ranging from several inches to over 12 feet (3.7 meters). The total combined length of pile that was cut down was approximately 750 feet (229 m).

The project was instructive of the importance of adequate characterization of geologic conditions even in small sites; the necessary iterative collaboration process between geotechnical and structural engineers; and the value of a well designed test pile program. The test pile program for the case provided valuable data which allowed for refining (shortening) the design pile lengths for considerable cost savings and reduced installation time.

MICROPILES BELOW GROUNDWATER AT THE SOUTH AUDITORIUM BLOCK SITE, BUFFALO, NY

Mary C. Nodine, P.E., M. ASCE[1]; Paul Eggers, P.E., M. ASCE[2]

[1] Mary C. Nodine, P.E.; GEI Consultants, Inc.; 400 Unicorn Park Drive, Woburn, MA 01801; mnodine@geiconsultants.com; 781-721-4111.

[2] Paul Eggers, P.E., GEI Consultants, Inc.; 4601 DTC Boulevard, Suite 900, Denver, CO 80237; peggers@geiconsultants.com; 303-264-1032.

[3] Michael P. Walker, P.E.; GEI Consultants, Inc.; 400 Unicorn Park Drive, Woburn, MA 01801; mwalker@geiconsultants.com; 781-721-4057.

[4] Donald E. Aubrecht,; Fontanese Folts Aubrecht Ernst Architects, P.C.; 6395 West Quaker Street, Orchard Park, NY, 14127; daubrecht@ffae.biz; 716-662-2200.

ABSTRACT

The CANALSIDE commercial development in Buffalo, New York serves to revitalize the former site of the Buffalo Memorial Auditorium, adjacent to Lake Erie. The Auditorium was constructed in 1940 and founded on steel H-piles driven to limestone bedrock. After decades of professional sport and entertainment events, the "Aud," as it was locally known, was closed in 1996. It sat vacant until it was demolished in 2009, at which time plans were made to revitalize the area with shops, restaurants, and a historic replica canal.

The only portion of the Aud that was left intact was a subbasement boiler room. The subbasement was renovated in 2014 and has since been used to house water and ice making equipment for the historic replica canals, which boast recreational ice skating in the winter. The subbasement floor was about 10 feet below groundwater and the Lake Erie water level. The floor consisted of an approximately 4-foot-thick layered inverted waffle slab system, with reinforced concrete grade beams and concrete infill between the grade beams. A waterproofing membrane was located near the base of the slab. There were no major seepage issues in the subbasement, so the existing waterproofing membrane was assumed to be intact and performing adequately.

A four-story building housing a children's museum was proposed to be constructed directly above the subbasement. The loads imparted by the new building would exceed the capacity of the existing piles, so it was determined that drilling micropiles through the subbasement floor would be the most practical means of supporting the new building. Drilling through the existing slab and waterproofing system was a concern due to the challenges of controlling water during construction and the importance of maintaining the integrity of the permanent waterproofing system.

The concept for the micropiles included drilling from the subbasement roof through a standpipe that extended up from the basement floor. The standpipe was bolted to the existing slab using a flange, and a neoprene gasket was installed between the flange

© 2018 Deep Foundations Institute

and the existing slab for waterproofing. The standpipe was used to control water during drilling, and the groundwater pressure below the floor was balanced by the fluid head inside the standpipe. After micropile installation, both the permanent micropile casing and the annulus between the micropile casing and the standpipe were tremie grouted to displace water within the micropile, the annulus, and any cracks in the slab system. The standpipe was then cut off at the same elevation as the micropile casing.

A mock-up micropile installation was completed in advance of production to test drilling and waterproofing procedures. A leak occurred during the test installation prior to grouting, resulting in several lessons learned and modifications to the waterproofing and standpipe configuration for production piles.

The micropiles used for the foundation system were 9-5/8-inch diameter with steel casing seated in bedrock, and rock sockets ranging from 3 to 10 feet. All micropiles had #11, #18 or #28 full length center bars. The micropiles were designed for compression loads up to 334 kips and tension loads up to 261 kips. Column loads were transferred to the micropiles through pile caps up to 82 inches thick.

The number of columns within the subbasement were limited due to the need to avoid existing structures, which resulted in high vertical and lateral loads on the columns. This meant that up to seven micropiles were needed beneath the large pile caps in the subbasement. The micropiles themselves had to avoid grade beams within the waffle slab system, which resulted in unusual configurations and highly eccentric loading conditions. One of the pile caps was required to span the basement wall and support a permanent basement roof beam in addition to the column for the new building.

Several significant challenges were encountered during drilling of the production piles, despite lessons learned during the test installation. The first major challenge was that the condition of the 75-year-old waffle slab was inconsistent. The project specifications called for the micropile standpipes to be bolted to the top of the original slab, located beneath a concrete overlay and gravel drainage layer installed during the 2014 subbasement renovation. However, in some areas the surface of the waffle slab was not suitable for the standpipe connection due to the presence of subfloor utility trenches, soil fill instead of concrete infill, and/or water infiltration. The project team developed solutions for standpipe installation in each of these conditions.

The second major construction challenge was leakage during installation of production piles. During installation of an early production pile, significant grout loss occurred when grouting the annulus between the standpipe and the micropile casing. When the standpipe was cut off, the grout did not hold and a substantial leak occurred. After some trial and error, the project team found that use of a mix of cement and bentonite grout in the annulus was more effective than cement grout alone in preventing water infiltration. In addition, a fast-set polyurethane pressure grout was used when needed to stop leaks quickly. With these changes in installation procedures, the remaining production piles were completed successfully.

PORE WATER PRESSURE RESPONSE AND EFFECT ON INSTALLATION TORQUE OF LARGE DIAMETER HELICAL PILES IN SOFT SOILS

M. Mae Benvenga, P.E., Magnum Geo-Solutions, LLC, Loveland, CO, USA, 970-635-1851, mbenvenga@magnumgeo.com
Howard A. Perko, Ph.D., P.E., Magnum Geo-Solutions, LLC, Loveland, CO, USA, 970-635-1851, hperko@magnumgeo.com
Heather H. Trantham, Ph.D., P.E., P.Eng., D.Ge., P.M.P., Tellus Geotechnical, LLC, Fort Collins, CO, USA, 970-232-8766, hhtphd98@gmail.com

ABSTRACT

Displacement of soil and groundwater during helical pile installation can produce excess pore water pressures (PWP) in fine-grained soils. Pore water pressure reduces effective stress in the soil immediately adjacent to the helical pile shaft and near the helical piles. Previous studies have shown generation of PWP may affect the capacity to torque ratios of the helical bearing elements. Large diameter helical piles that generate much of their torque and capacity from shaft adhesion are affected by PWP and therefore exhibit significant pile "freeze" after installation.

Computer modeling is used herein to evaluate PWP immediately adjacent to helical pile shafts during installation in various soil types. The models show the degree and distance from the shaft that is influenced by PWP during installation and the amount of time required for the PWP to dissipate.

Pile freeze has been measured on several project sites by re-torque measurements. These re-torque data are compared with computer modeling and correlations between saturated hydraulic conductivity and dissipation time are presented and discussed.

Keywords: helical piles, pore water pressure, installation torque, pile freeze

INTRODUCTION

Helical piles are full-displacement piles, meaning installation does not produce drill spoil. Soil is displaced laterally as the pile progresses into the ground. This displacement of soil causes an increase in PWP, which reduces adhesion between the pile and the soil. For helical piles with small-diameter shafts, adhesion contributes little to the overall capacity and torque of the pile, so PWP changes are not typically considered in determining pile capacity. In modern construction, the use of larger diameter helical piles has become very common. For large-diameter helical piles, changes in PWP immediately adjacent the shaft can be quite large during installation. Increased pore water pressure and reduced adhesion can have a temporary effect on pile capacity and installation torque.

As excess PWP dissipates, adhesion between the soil and pile increases, which results in an increase in the pile capacity and torque. The process of increasing capacity with dissipation of PWP is known as pile "freeze" or “setup”. In some cases, the final adhesion between the pile and soil may be greater than the predicted adhesion for in-situ conditions due to consolidation. When helical piles are installed in sandy soils excess PWP dissipates almost instantaneously, effects of increased confinement are immediate, and time-dependence of pile freeze is not a concern. In fine-grained soils, time to dissipate excess PWP can be significant.

© 2018 Deep Foundations Institute

The phenomenon of pile freeze or pile setup has been studied since the 1970's. Most studies have been performed to determine excess PWP and dissipation resulting from driven pile installation. Some studies have investigated driven pile setup. Research indicates that pile setup can be significant and that pile setup may affect pile end bearing capacity as well.

Methods for quantitatively predicting the time to observe pile setup and strength increase are not widely adopted. Most pile designers do not quantitatively take into account time related effects due to pile setup. To date, there is little published regarding a quantitative correlation between pile setup and pile type, installation method, or soil type. Most engineers who do consider pile setup in their design, use empirical correlations and/or personal experience. There is even less information regarding setup of helical piles.

This paper utilizes Seep/W and Sigma/W, Finite Element Modeling (FEM) computer software programs and an MS Excel based finite difference model to predict the induced excess PWP build-up around a helical pile during installation and the time to dissipate said PWP. The models were compared to each other and with field re-torque measurements to verify the validity of the modeling. Recommendations are made for continued research.

BACKGROUND

Titi and Wathugala (1999) used the strain path method to develop a general numerical procedure for predicting the variation of driven friction pile capacity in saturated clay. The study focused on predicting the pile capacity at different degrees of consolidation post installation. The numerical model was confirmed by instrumenting and load testing a 1.72-inch diameter pile and a 3-inch diameter pile. The study concluded that numerical modeling could be used to predict pile setup, but that full-scale pile load tests would be required to validate the procedure.

Whittle and Sutabutr (1999) conducted similar research to Titi and Wathugala (1999) except they looked at how the over-consolidation ratio affected pile setup. They concluded that reliable predictions of pile setup depend on accurate estimates of the over consolidation ratio.

Some studies have been specific to helical piles. "Weech (1996) measured pore water pressure generated by helical piles installed in sensitive saturated fine-grain marine soil in southwestern British Columbia and found that an average of 7 days was required for dissipation of pore water pressures and reconsolidation of soil around helical piles. Helical piles tested after 7 days had approximately 17 percent greater strength compared to those tested only 19 hours after installation. Based on this, Perko (2009) suggested load tests should be delayed by a minimum of 1 week after helical pile installation in sensitive fine-grain soils to allow for dissipation of PWP." (Perko, 2009).

Vyazmensky (2005) used a numerical model to predict PWP induced by installation of helical piles in fine-grained soil. This study utilized NorSand coupled with Biot formulation to represent the behavior of the soil. The study found an increase in PWP occurred after the pile tip penetrated the soil. The study found that the contribution from the helices to the magnitude of the generated PWP during installation appeared to be quite significant. Dissipation of PWP occurred more quickly below the lead helix than the trailing helix and was found to be independent of the number of helices. Complete dissipation occurred approximately 7 days after installation in most locations tested. The study concluded that prediction of PWP dissipation could be modeled with reasonable results and noted the results were sensitive to the hydraulic conductivity, as well as over-consolidation ratio, shear modulus, k_o, and Poisson's ratio input parameters.

In order to better understand the effects of PWP on helical piles, it is important to take a moment and discuss the empirical/theoretical capacity to torque ratio. It has been known practically since the invention of the helical pile that the torque required to install a helical pile is related to shear strength of soil and helical pile

shaft diameter. In modern construction, installation torque should always be measured at project specified increments and at final depth. These measurements often can be related to soil consistency and strength and can be used to detect changing subsurface conditions. See Perko (2009) for a discussion on the development of capacity to torque ratios for helical piles.

When working in fine-grained soils with large shaft diameter helical piles, torque measured immediately upon pile installation does not match predictions. In these cases, PWP may be temporarily lowering the torque and capacity of the helical pile. Therefore, it is important to better understand PWP generation, its modeling, and develop methods for prediction of setup times.

NUMERICAL MODELING

The objective for this numerical modeling is twofold: to estimate the time required to dissipate the excess water pressure along the pile shaft and to compare numerical modeling to observed field results. Numerical modeling of helical piles was performed utilizing a ground water seepage finite element program, Seep/W and an MS Excel spreadsheet using an average finite difference method (FDM). To supplement the study, numerical modeling of field installed helical piles was performed utilizing a stress-deformation finite element program, Sigma/W, coupled with a ground water seepage finite element program, Seep/W (FEM).

Seep/W modeling

A cross section of a 12-inch diameter by 20-foot long pile was modeled in Seep/W for five soil types. The ground water table (GWT) was set to 8 feet below finished grade, an elevation of 32 ft above the model datum. Representative values for saturated hydraulic conductivity, porosity, and volumetric water content (VWC) were chosen for each soil type. Soil types modeled were: sand and gravel (SP/GP), clayey/silty sand (SC/SM), low plasticity silt (ML), organic clays/silts and high plasticity silt (OH/MH), and clay (CL/CH). Table 1 provides a summary of the soil properties used for modeling.

Table 1. Soil Properties Used in Numerical Model

Soil	Sat. Hydraulic Conductivity, ft/hr	Porosity	Volumetric Water Content
Sand & Gravel (SP/GP)	6.00E-02	0.5	0.5
Clayey/Silty Sand (SC/SM)	3.00E-02	0.5	0.5
Low Plasticity Silt (ML)	6.00E-03	0.5	0.5
Organic Clays/Silts & High Plastic Silts (OH/MH)	6.00E-04	0.5	0.5
Clay (CL/CH)	3.00E-04	0.5	0.5

A constant head boundary condition equal to 32 feet was placed at each side of the model (far field). An intermittent total flux was assigned to a node centered in the saturated zone of the displaced material. Total flux was used to simulate the water displaced by pile installation. The displaced volume of water was divided by pi to account for 2-dimensional nature of the profile modeled. The model was performed in three stages: steady state, pile installation, and near complete dissipation. Near complete dissipation was established as, when the total head around the pile was within 1 foot of steady state (33 ft).

A set of example figures, Figure 1(a)-1(d), illustrate total head developed and dissipated around the pile shaft, in ML material. Figure 1(a) illustrates a constant steady state total head of 32 feet across the site. Figure 1(b) illustrates a total head of 60 feet at the tip of the pile, immediately after pile installation. Figure 1(c) illustrates a total head of 33.8 feet at the tip of the pile at 15 minutes after the end of pile installation.

Figure 1(d) illustrates a total head of 33 feet at the tip of the pile after near complete dissipation (0.45 hr in the case of ML soil). Table 2 summarizes the numerically calculated time for PWP dissipation for each soil type.

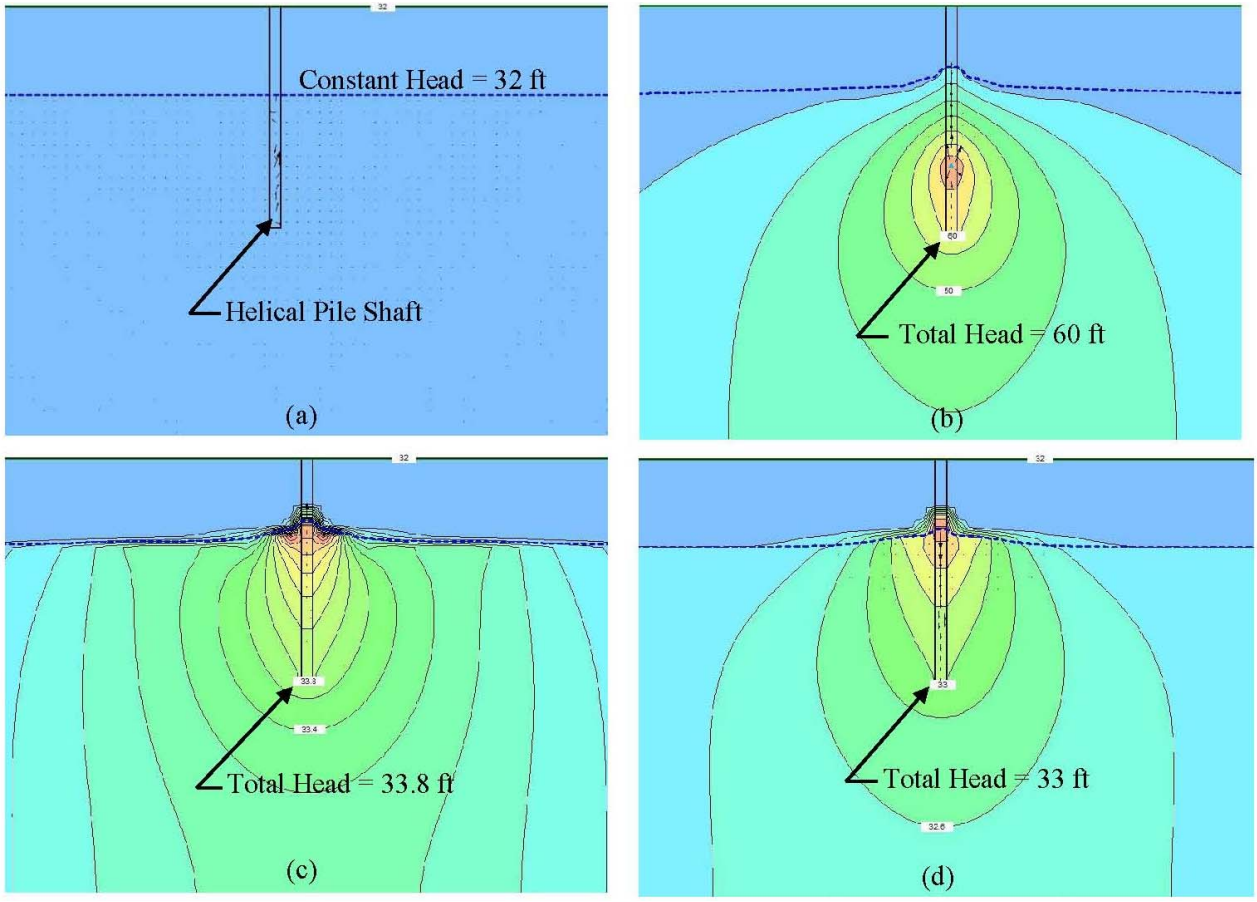


Figure 1. (a) Seep/W Model at Steady State; (b) Seep/W Model at End of Installation; (c) Seep/W Model 15 min. After Installation; (d) Seep/W Model Near Complete Dissipation.

Finite difference method

A 12-inch diameter by 20-foot long pile was modeled in pseudo-3D plan using an MS Excel spreadsheet for five soil types. To simulate the increase in PWP resulting from pile installation, the cells representing piles were increased to the total head plus the saturated head. Equation 1 was developed to estimate PWP dissipation.

$$H'_F = H_F + \frac{k_{sat}(B+C+D+E-4B)H_{GWT}\delta t}{d^2} \qquad [1]$$

Where H'_F = head in cell B after change in time, H_F = head in cell F at beginning of time step, k_{sat} = saturated hydraulic conductivity, B, C, D, and E = head in the cells surrounding cell F, as illustrated in Figure 2, H_{GWT} = head from ground water table, δt = change in time, and d = width and depth of the cells.

To be consistent with the Seep/W modeling, the ground water table (GWT) was set to 32 feet, 8 feet below finished grade. The saturated hydraulic conductivity and porosity used for each soil type are the same as those used for the Seep/W modeling.

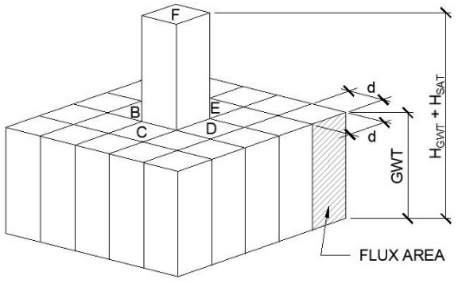
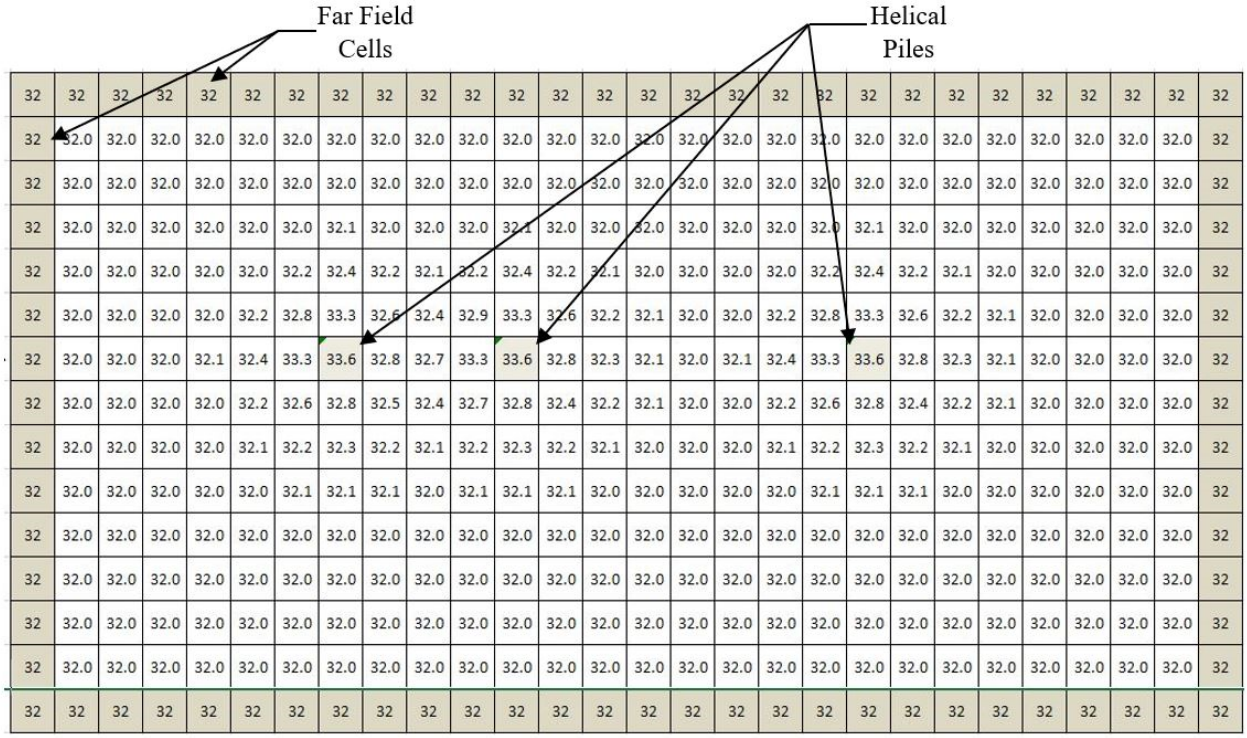


Figure 2. Sketch of FDM Method Used to Develop Equation 1.

A constant head boundary condition equal to 32 feet was placed in the far field cells of the model. The model was performed in three stages: steady state, pile installation, and dissipation. Total head dissipation was recorded at various time steps. Steady state was assumed for time step zero; pile installation occurred instantaneously after time step zero. The final time step was considered to be when the total head around the pile was reduced to near steady state (33 feet). Figure 3 is an example of the FDM model output for a single time step. The cells around the perimeter are far field and the three highlighted cells in the field area, represent helical piles. Cell dimensions shown are 1 foot by 1 foot.



32	32	32	32	32	32	32	32	32	32	32	32	32	32	32	32	32	32	32	32	32	32	32	32	32	32	32
32	32.0	32.0	32.0	32.0	32.0	32.0	32.0	32.0	32.0	32.0	32.0	32.0	32.0	32.0	32.0	32.0	32.0	32.0	32.0	32.0	32.0	32.0	32.0	32.0	32.0	32
32	32.0	32.0	32.0	32.0	32.0	32.0	32.0	32.0	32.0	32.0	32.0	32.0	32.0	32.0	32.0	32.0	32.0	32.0	32.0	32.0	32.0	32.0	32.0	32.0	32.0	32
32	32.0	32.0	32.0	32.0	32.0	32.0	32.1	32.0	32.0	32.0	32.1	32.0	32.0	32.0	32.0	32.0	32.0	32.0	32.1	32.0	32.0	32.0	32.0	32.0	32.0	32
32	32.0	32.0	32.0	32.0	32.0	32.2	32.4	32.2	32.1	32.2	32.4	32.2	32.1	32.0	32.0	32.0	32.0	32.2	32.4	32.2	32.1	32.0	32.0	32.0	32.0	32
32	32.0	32.0	32.0	32.0	32.2	32.8	33.3	32.6	32.4	32.9	33.3	32.6	32.2	32.1	32.0	32.0	32.2	32.8	33.3	32.6	32.2	32.1	32.0	32.0	32.0	32
32	32.0	32.0	32.0	32.1	32.4	33.3	33.6	32.8	32.7	33.3	33.6	32.8	32.3	32.1	32.0	32.1	32.4	33.3	33.6	32.8	32.3	32.1	32.0	32.0	32.0	32
32	32.0	32.0	32.0	32.0	32.2	32.6	32.8	32.5	32.4	32.7	32.8	32.4	32.2	32.1	32.0	32.0	32.2	32.6	32.8	32.4	32.2	32.1	32.0	32.0	32.0	32
32	32.0	32.0	32.0	32.0	32.1	32.2	32.3	32.2	32.1	32.2	32.3	32.2	32.1	32.0	32.0	32.0	32.1	32.2	32.3	32.2	32.1	32.0	32.0	32.0	32.0	32
32	32.0	32.0	32.0	32.0	32.0	32.1	32.1	32.1	32.0	32.1	32.1	32.1	32.0	32.0	32.0	32.0	32.0	32.1	32.1	32.1	32.0	32.0	32.0	32.0	32.0	32
32	32.0	32.0	32.0	32.0	32.0	32.0	32.0	32.0	32.0	32.0	32.0	32.0	32.0	32.0	32.0	32.0	32.0	32.0	32.0	32.0	32.0	32.0	32.0	32.0	32.0	32
32	32.0	32.0	32.0	32.0	32.0	32.0	32.0	32.0	32.0	32.0	32.0	32.0	32.0	32.0	32.0	32.0	32.0	32.0	32.0	32.0	32.0	32.0	32.0	32.0	32.0	32
32	32.0	32.0	32.0	32.0	32.0	32.0	32.0	32.0	32.0	32.0	32.0	32.0	32.0	32.0	32.0	32.0	32.0	32.0	32.0	32.0	32.0	32.0	32.0	32.0	32.0	32
32	32.0	32.0	32.0	32.0	32.0	32.0	32.0	32.0	32.0	32.0	32.0	32.0	32.0	32.0	32.0	32.0	32.0	32.0	32.0	32.0	32.0	32.0	32.0	32.0	32.0	32
32	32	32	32	32	32	32	32	32	32	32	32	32	32	32	32	32	32	32	32	32	32	32	32	32	32	32

Figure 3. Example Output from FDM Model for a Single Time Step.

Figure 4 illustrates total head dissipation with time for time steps 0 hr, 0.15 hr, 0.25 hr, and 1.13 hours. The peaks shown in Figure 4 correspond to the total head immediately after helical pile installation, at the center of each pile.

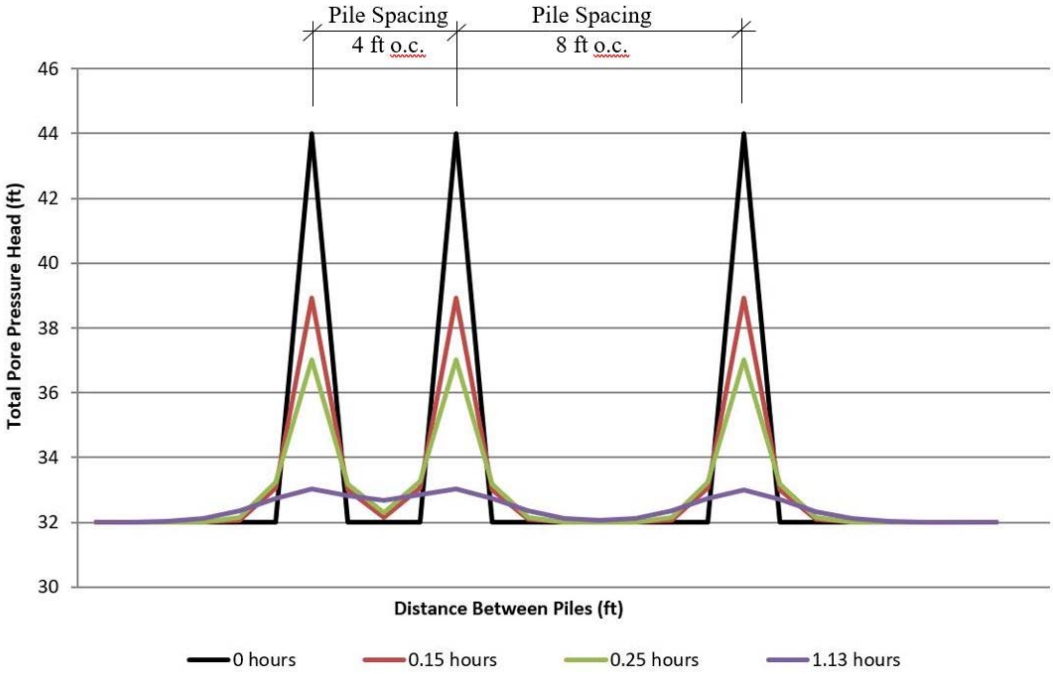


Figure 4. Example Plot of Total Head Dissipation vs Time Based on Pile Spacing.

Sigma/W and Seep/W Coupled Analysis

A cross section of the soil stratum as well as the soil properties for each stratum were modeled in Sigma/W based on estimated soil properties from two field test sites. The sites were located in South Louisiana and East Texas. The piles were modeled in 5-foot stages. Stage 0 represents the in-situ soil conditions. The boundary conditions for stage 0 consisted of a steady-state ground water table at a below grade elevation based on geotechnical reports. The left and right sides of the model were restrained from movement in the horizontal direction, and the bottom of the model was restrained from movement in both horizontal and vertical directions. Boundaries were placed far enough from the pile location so as not to affect impending results. The boundary conditions for all installation stages included a potential seepage face at the ground surface and a unit gradient at the bottom boundary.

The helical piles were comprised of composite sections consisting of a larger diameter shaft near the ground surface and a smaller diameter shaft extending to the bearing stratum. The larger diameter shaft is primarily used to improve the lateral capacity of the piles but can have a significant effect on PWP increases. The pile for the Louisiana site had a 13.4-inch outside diameter upper shaft and 5.5-inch outside diameter lower shaft section. The pile for the Texas site had an 18.6-inch outside diameter upper shaft and a 9.6-inch outside diameter lower shaft. Helical piles were installed to approximate depths of 52 and 70 feet in Louisiana and Texas, respectively. The piles in Louisiana has 4 helices while the piles in Texas had 6 helices. Maximum helix diameter was 24 inches due to site constraints.

Figure 5(a) and 5(b) illustrate total head generation at the end of pile installation and at the end of head dissipation for the Louisiana. Figure 5(c) and 5(d) illustrate total head generation at the end of pile installation and at the end of head dissipation for the Texas site. The volume of pore water injection in the model roughly corresponded to the volume of the pile in question. Maximum head predicted by the model was on the order of 60 feet, which when converted to stress, exceeds the anticipated shaft to soil adhesion value, indicating that a near complete reduction in shaft adhesion would occur as the helical pile is installed. This suggests the required torque during installation could be reduced to that required for the helical pile

based on helix size alone. Shaft adhesion would be expected to increase with time as PWP dissipates adding capacity and increasing torque required to remobilize the helical pile.

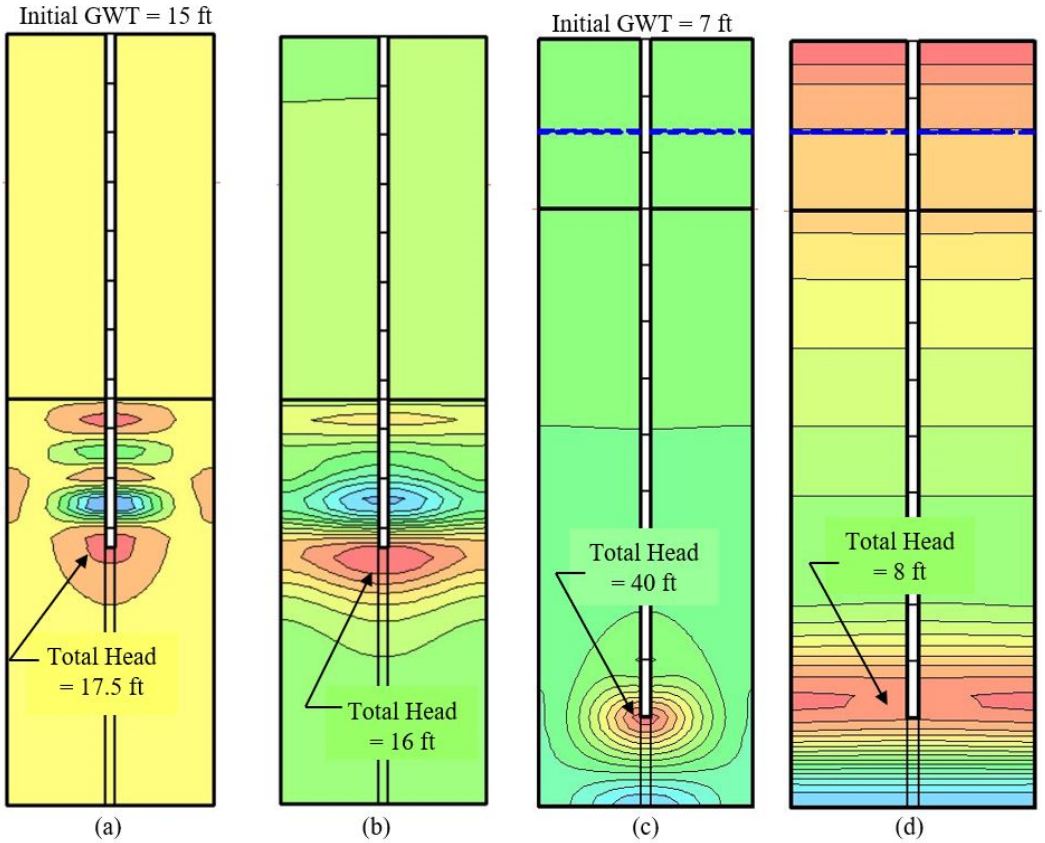


Figure 5. Coupled Models at (a) End of Installation for Louisiana Site; (b) End of Dissipation for Louisiana Site; (c) End of Installation for Texas Site; (d) End of Dissipation for Texas Site

COMPARISON

Results from the Seep/W and FDM modeling were compared to determine if PWP dissipation could be estimated using a simple finite difference method spreadsheet. Table 2 summarizes the dissipation times for various hydraulic conductivity based on the two modeling methods.

Table 2. Dissipation Time for Seep/W and FDM Model

Hydraulic Conductivity (ft/hr)	Dissipation Time per Seep/W (hr)	Dissipation Time per FDM (hr)
6.00E-02	0.12	0.7
3.00E-02	0.21	1.02
6.00E-03	3.37	5.7
3.00E-03	3.37	10.75
6.00E-04	120	67
3.00E-04	260	115
1.20E-04	404	300
8.00E-05	476	467
4.80E-05	543	756
1.20E-05	3500	3016
1.20E-06	154750	31500

The FDM overestimated dissipation time for soils with hydraulic conductivity greater than 1e-3 ft/hr and underestimate dissipation time for soils with hydraulic conductivity less than 1e-5 ft/hr. For soils with hydraulic conductivity between 1e-3 and 1e-5, the FDM model dissipation times were in general agreement with the dissipation times estimated by the FEM. Figure 6 illustrates the estimated time for PWP dissipation using the FDM and Seep/W for soils with hydraulic conductivity between 1e-1 ft/hr and 1e-6 ft/hr.

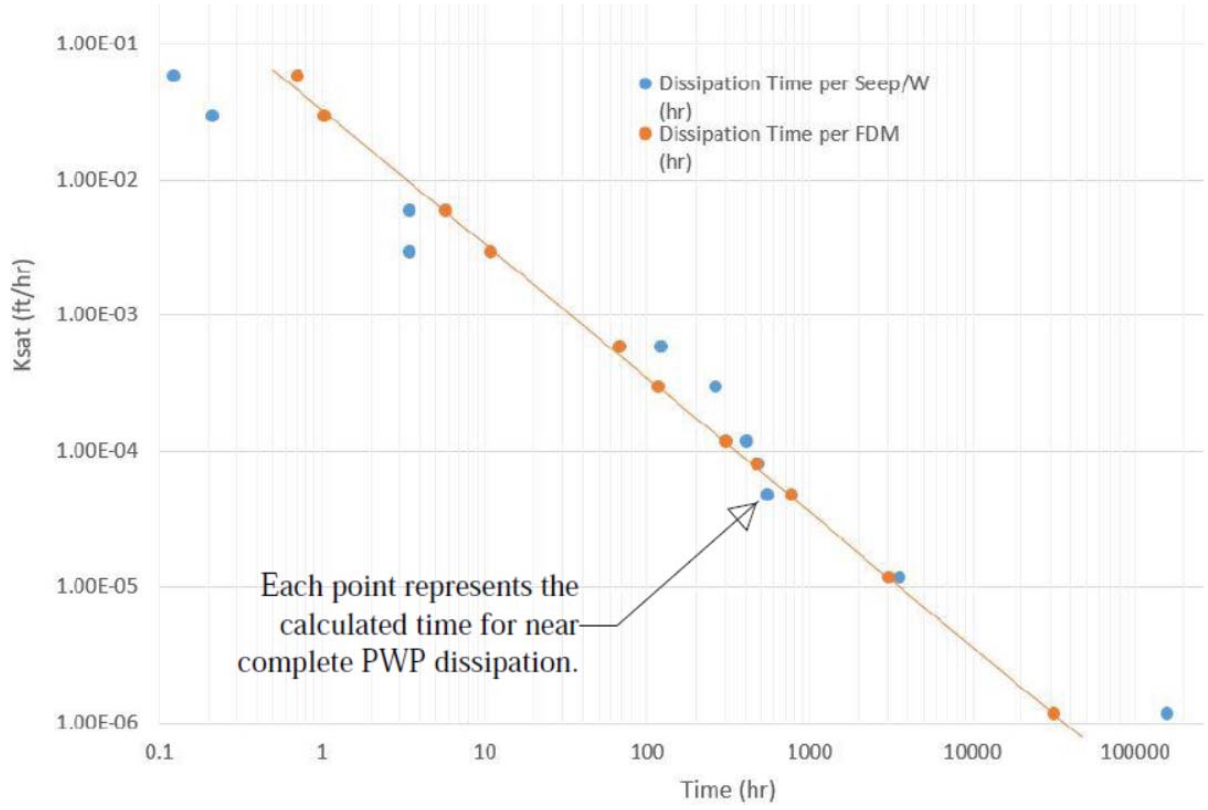


Figure 6. PWP Dissipation Time vs Hydraulic Conductivity

Field results from the two projects were compared to the results of the numerical models. Several piles installed at these two sites did not reach the specified torque/capacity. The installation of the piles was terminated prior to achieving torque, knowing that pile setup should occur at some point. After several days, the piles were re-torqued and achieved or exceeded the design torque/capacity.

It appears, from the field data, that piles achieved the specified design torque after a setup time of 2-14 day for the Louisiana site. The helical piles at the Texas site, in general, appeared continue gaining strength even after 15 days of set time. As seen by the scatter in Figures 7 and 8, the increase in torque varied based on time and the location on the site. The FEM and the FDM investigated the time for dissipation for one location at each site. Soil is not homogeneous nor isotropic. Soil properties and stratum can change significantly from one location to another on the same site.

It also should be noted that a different torque motor and different torque monitoring device was used at the Texas site for re-torque measurements. It is important to keep equipment and methods similar when conducting re-torque measurements as shown by the increased scatter in Figure 8. Re-torque measurements were made by attaching the torque motor to the previously installed helical pile and advancing the pile approximately 1/2 to 1 revolution.

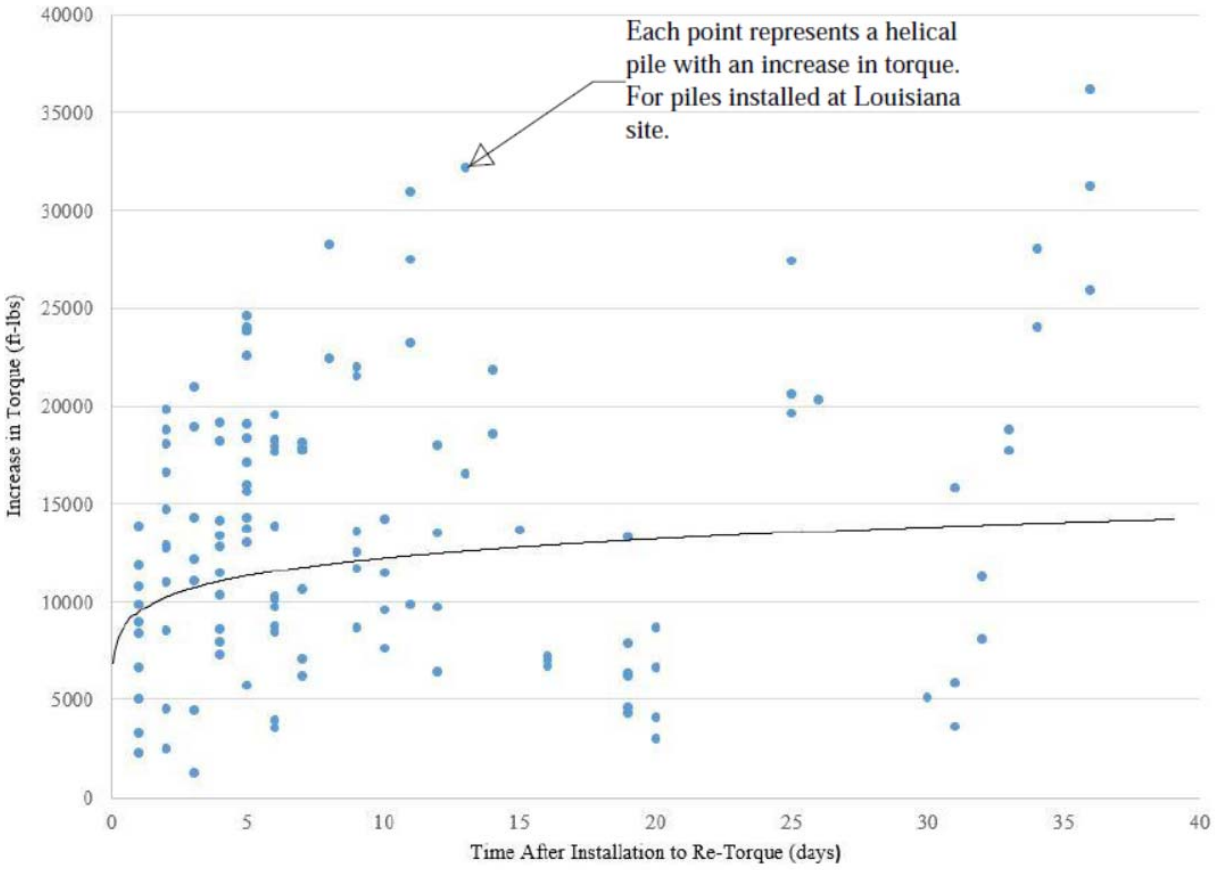


Figure 7. Change in Torque with Time After Installation for Louisiana Piles

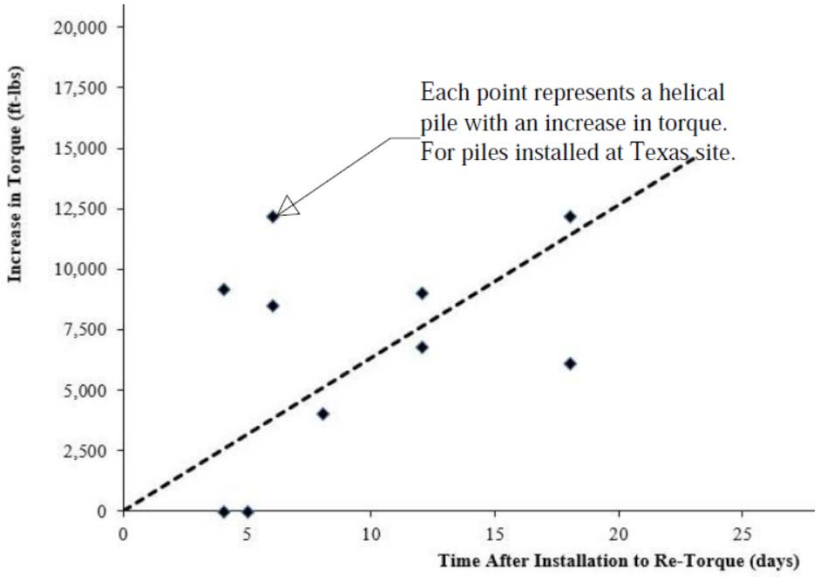


Figure 8. Change in Torque with Time After Installation for Texas Piles.

DISCUSSION

If the pile designer knows that the soils on site have properties prone to generate PWP resulting from installation, then required installation torque may be reduced to account for the anticipated decrease in shaft adhesion during installation. If the construction schedule allows for setup time, a re-torque test may be performed and compared with the un-reduced required installation torque.

Previous modeling by Vyazmensky (2005) suggested helices can have a large effect on PWP change. Our modeling did not indicate such effect. The generation of PWP mainly depended on total volume of soil/water displacement which was most dependent on shaft diameter.

The development of PWP and helical pile setup is a broad topic that requires additional research. Soil heave as a result of displacement pile insertion and affects on surrounding buildings is related topic that this work may benefit but should be studied further. Soil characteristics such as PI, gradation, and classification should affect hydraulic conductivity and therefore the time rate of PWP dissipation. Pile diameter should increase PWP. Effect of pile diameter and soil type should be further studied using the models here developed.

CONCLUSIONS

It appears from the field data that PWP dissipation can be estimated using a simple FDM by use of hydraulic conductivity and porosity. The FDM conservatively overestimated the time required to dissipate the excess PWP but resulted in reasonable times.

The FDM must be used for each soil stratum and for the corresponding depth. The initial total head was calculated by adding the length of pile in the saturated zone to the ground water table head.

Piles at both sites illustrate PWP dissipation after a setup time of 2 to 14 days. The increase in torque varied based on time and the location on the site. Some of the differences in final torque or the change in torque may be explained by the fact that the FEM and the FDM investigated the time for dissipation for one location at each site. Soil is not homogeneous nor isotropic and soil properties and stratum can change significantly from one location to another on the same site.

It is clear from these data and this analysis that subtle differences in installation and soil conditions at pile locations can result in a degree of scatter. Until more research is done, modeling may be used as an approximation of the order of magnitude of time required for pile setup only.

REFERENCES

Perko, H.A. (2009) *Helical Piles: A Practical Guide to Design and Installation*, Wiley, NY

Titi, H., Wathigala, G. (1999). "Numerical Procedure for Predicting Pile Capacity – Setup/Freeze." *Transportation Research Record: Journal of the Transportation Research Board.* Vol. 1663, pp. 25-32.

Vyazmensky, A. (2005). "Numerical modeling of time dependent pore pressure response induced by helical pile installation" *The University of British Colombia*: Thesis submitted in partial fulfilment of the requirements for the degree of master of applied science.

Whittle, A.J. and Sutabutr, T., (1999). "Prediction of Pile Setup in Clay." *Transportation Research Record: Journal of the Transportation Research Board.* Vol. 1663, pp. 33-40.

ROCK SOCKETED DRILLED SHAFTS IN ELECTRICAL SUBSTATIONS

Steve Davidow, P.E., S.E., Senior Vice President, Quanta Subsurface
Spokane, WA, United States, 509.789.7787, SDavidow@quantasubsurface.com

Brock Wallis, Vice President, MJE Drilling
Iron Mountain, MI, United States, 906.776.4450 – Bwallis@MJElectric.com

ABSTRACT

The following text will present the concept of rock socketed drilled shafts used to support electrical substation structures, and discuss the cost and schedule risks that traditional design responses to unforeseen shallow rock can pose to a project. Design considerations will be detailed, including rock characterization, shear strength of drilled shafts, and modeling lateral resistance of the shaft and surrounding rock. The specific case of drilled shafts installed for heavily loaded structures at the Moxie Freedom Substation will provide an example of how close collaboration between the engineer and contractor to refine designs based on site-specific feedback can provide tangible benefits to the project. In this example, value engineered designs resulted in an approximate 40% reduction in shaft/concrete volume and a 60% reduction in total rock socket depth.

Keywords: Drilled Shaft, Shallow Rock, Value Engineering, Concrete Shear

PROJECT OVERVIEW

The Moxie Freedom Project included the construction of a new 500 kV switchyard in Berwick, Pennsylvania. The foundation contractor was selected to install both small and large diameter drilled shaft foundations to support the structures within the switchyard. The small diameter shafts were utilized to support transformers, switches, bus supports and a static mast, while the large diameter shafts were used to support one 180-foot monopole and six H-Frame structures.

CHALLENGES: ROCK SOCKETED DRILLED SHAFTS

Available geotechnical data at the time of bid included limited borings and seismic refraction. The borings were not located at every structure, and the contractor and design engineer were left to interpret desktop studies and geophysics to determine the probable site-specific conditions at each foundation. The data suggested substantial variability in the quality and depth to bedrock across the project area, indicating significant risk of deep embedment into bedrock at all seven large diameter shaft locations.

Rock socketed drilled shafts pose unique challenges for both designers and contractors, and the topic has become a focus of national foundation organizations. Traditional design models result in deeper and/or larger diameter shafts where rock is encountered. In the case where site-specific geotechnical conditions are not clearly understood and rock is encountered at shallow depths, this can lead to significant additional rock drilling, impacting overall project cost and schedule. Rock drilling can result in more than ten times the cost of soil drilling and can easily take in excess of ten times longer to excavate.

In many situations, rock exists under a stratum of overburden of sufficient thickness compared to the pile length. In such cases, the computed deflection of the pile at the rock interface is so small that the resistance

© 2018 Deep Foundations Institute

of the rock is insignificant, and the response of the pile minimal, regardless of the stiffness of the rock. In contrast, drilled shafts are used in situations where the rock contact is near or at the ground surface, imparting a significant amount of lateral demand and deflection into the rock mass. In these cases, particularly where axial loads are low and lateral loads are high, as in electrical structures, lateral loading will dictate the design rock penetration length. It has been customary in the industry to apply the same techniques developed for laterally-loaded piles in soil to laterally-loaded rock socketed drilled shafts, which can yield conservative results and often leads to excessive socket length.

Key variables in defining the demand on the drilled shaft, and proportioning the shaft reinforcing and length, include assumed depth to rock, rock mass stiffness, and concrete shear strength. In many cases, electrical structures are specified in locations with no site-specific borings and therefore no actual measurement of rock contact elevation or rock strength. Minimum shaft lengths and minimum socket lengths into rock are typically defined by the designer based on assumptions regarding site-specific geotechnical conditions. Drilled shafts socketed into rock see a significant amount of peak shear at the rock interface as a result of common methods of foundation evaluation. The minimum depth of embedment into rock is an iterative evaluation of internal stress due to lateral bearing on the rock and the assumed concrete shear capacity.

In cases where the rock contact surface is encountered shallower than anticipated, the designer and contractor must consider the value of shortening the shaft length, modifying the reinforcing cage, and eliminating some of the rock excavation. The designer must also evaluate the capacity of the rock mass to develop the assumed lateral resistance illustrated by the design method used. The rock mass may be assumed to be homogeneous in nature, when in fact has highly weathered and fractured rock over a more intact rock mass. These conditions can often be identified through the drill action during construction. Small changes in assumed rock quality can yield significant differences in peak shear forces in the shaft design models.

With a spike in peak shear demand for shallow rock socketed drilled shafts, the designer is typically left with three options to mitigate the excessive shear force; increase shaft diameter, increase shaft length, or add shear reinforcing. Typically, a combination of these results in the optimal solution. The designer can also review the assumed concrete shear strength using either American Concrete Institute (ACI) simplified or detailed design methods; based upon the final shaft geometry, reinforcing ratio, and internal forces.

ORIGINAL DESIGN REVIEW

MJE Drilling (MJD), the foundation contractor, engaged Quanta Subsurface (QS), the design engineer, to review available geotechnical data and structure loading, and to determine if an alternate shaft design could be employed if shallow rock was encountered. Of key importance was the determination of rock risk to the installations, and the development of mitigation options to deal with unforeseen subsurface conditions.

Substation buildouts consist primarily of an assembly of smaller components and switch gear, which are supported by relatively small foundations. Larger structures, such as H- or A-frames and self-supporting dead-end poles or towers, are required where the transmission line enters and exits the substation. These structures develop much larger foundation reactions. The focus of the geotechnical and foundation review for this project was on three H-Frame structures and one self-supporting dead-end pole.

A desktop study revealed that regional topography in the project area ranges from broad low relief alluvial terraces and rolling hills with incut streams and river valleys, to high relief elongated ridges separated by narrow valleys. The overburden soils generally consist of Olean Till. The bedrock underlying the project site is mapped as alternating beds of olive- gray siltstone, mudstone, and sandstone, with red siltstone, mudstone, and shale. Initially, seven borings were provided within the substation footprint, with seismic refraction provided between the borings as shown in Fig. 1. None of the borings were located directly at the four structures under consideration, leaving the designer and contractor to make interpretations on the actual depth to rock and quality of rock at each location. The use of geophysics, such as seismic refraction, can be a very useful tool for designers and contractors in situations where precise geological data cannot be obtained at a foundation site. The borings shown in Fig. 1 were used to calibrate the seismic refraction data obtained from the field, and estimate the probable depth to rock. Like any estimate, the interpretation of this data is subjective and poses a risk of changing conditions to the contractor. It is important to note that in electrical transmission and substation design, as opposed to transportation or commercial structure projects, the foundation designer is often left to design with representative geotechnical information and not site-specific borings. Interpretation of representative borings, geophysics, and desktop geotechnical studies create subjective approaches to modeling that should be revisited throughout construction as actual site conditions may differ.

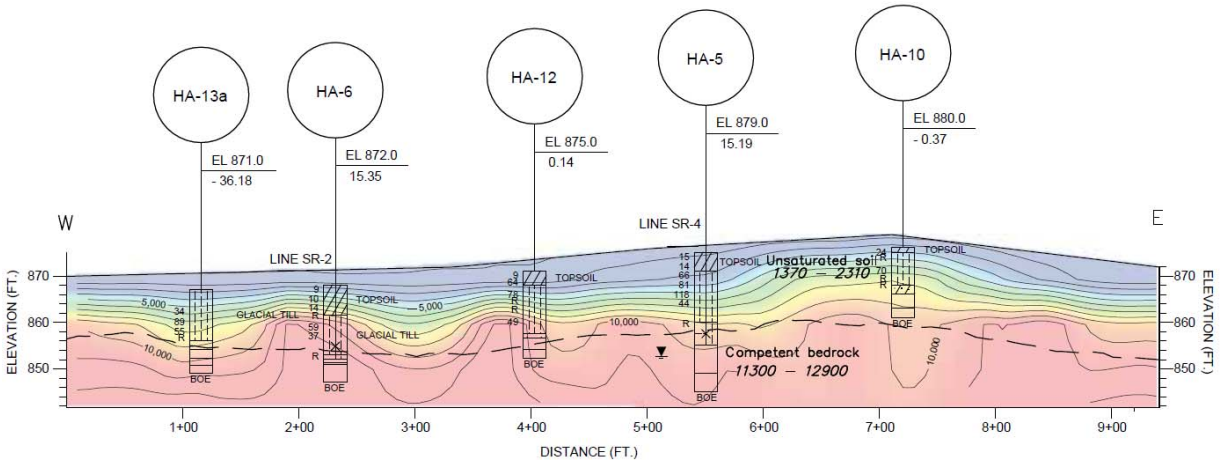


Figure 1. Seismic Refraction Results

As shown in Table 1, the H-frame structures had relatively moderate to low loading but a high risk of shallow bedrock, based upon the borings and geophysics provided by the owner. Drilling at adjacent foundations identified that the bedrock strata mapped by geophysics was variable. The dead-end pole reaction was fairly high and required a significant minimum embedment into rock to minimize the shear demand on the shaft.

Table 1. Structure Loading

Structure Type	Moment (K-Ft)	Shear (K)	Axial (K)
M-7 H-Frame DE	6,606	72	111
M-8 H-Frame DE	5,144	67	82
M-9 H-Frame DE	4,879	62	53
180-foot Monopole	30,847	219	150

Original shaft designs specified diameters ranging from 9 to 12 feet, with rock embedments ranging from 11 to 28 feet. Designs for the largest structure, the 180-foot monopole, consisted of a 12-foot-diameter, 34-foot-deep shaft with a minimum shaft embedment into rock of 28 feet.

The construction approach for these designs would have entailed a large production drill rig with 192,000 foot pounds of torque, along with various sized rock augers and core barrels to drill each hole to the designed diameter and depth. A series of pilot holes would need to be drilled for relief utilizing a small diameter core barrel, and the shafts would need to be sized to the design diameter utilizing rock augers and large diameter core barrels. Based on the amount of rock drilling these designs called for, project costs would have increased significantly due to extended work hours and additional crew support required to maintain the project schedule.

DESIGN OPTIMIZATION

QS coordinated closely with MJD to compare the available tooling on or near the project location to the tooling required for proposed shaft designs, and to quantify the impact on the drilled shaft designs should rock be encountered shallower than expected. From this set of criteria, alternate drilled shaft designs were developed and potential impacts to project cost and schedule were analyzed. These designs incorporated detailed geotechnical assessments and constructability reviews derived from continuous interaction between project team members. As previously described, a review of site-specific rock modeling results and code provisions for shear design of concrete shafts was conducted to better characterize the issues and solutions surrounding rock socketed drilled shafts.

During initial drilling operations for the dead-end pole, weathered sandstone was encountered at a depth of 17 feet. The rock mass was fairly weak to a depth of 27 feet, and particularly weathered in the upper 3 to 5 feet of the rock contact. This was based on initial boring data and observations made by QS field geotechnical and geology groups. Close interaction between the contractor and the field engineering staff is critical to determining if and when technical adjustments in modeling and approach are necessary. Initial shaft modeling using both LPile and MFAD had assumed fairly strong, uniform rock, which developed a tremendous peak shear demand on the shaft at the rock contact surface. By reviewing the lateral earth pressure generated by the peak shear at this upper rock contact surface in combination with the observed drill resistance during the excavation of the rock, it was determined that the physical demand of the shaft lateral bearing against the observed rock mass was not correct in the initial models. By accounting for the site-specific rock quality observed during construction and modeling the p-y rock response of the upper rock surface as a weaker, more weathered material, the peak shear demand was reduced, and a smoother shear distribution was developed.

The initial approach looked at concrete shear using the ACI simplified shear equations (shown in Table 2), which is standard and conservative for most concrete shear analyses. In this case, where shear is critical and the combinations of applied loads are somewhat unique, a more detailed assessment of shear strength can be helpful. By considering the amount of reinforcing utilized in the preliminary design, and acknowledging the amount of shear and moment that occur simultaneously in the critical section of the shaft, a 75% increase in shear strength can be recognized.

Table 2. Summary of ACI Shear Provisions

ACI 318-14	Simplified Method	Detailed Method
V_n	$V_n = V_c + V_s$ $V_u \le \phi(V_c + 8\sqrt{f'_c}\, b_w d)$	
RC, V_c	$V_c = 2\lambda\sqrt{f'_c}\, b_w d$	Lesser of: $V_c = \left[1.9\lambda\sqrt{f'_c} + 2500\rho_w \frac{V_u d}{M_u}\right] b_w d$ $V_c = \left[1.9\lambda\sqrt{f'_c} + 2500\rho_w\right] b_w d$ $V_c = 3.5\lambda\sqrt{f'_c}\, b_w d$
V_c with axial load N_u	Axial compression: $V_c = 2\left[1 + \frac{N_u}{2000 A_g}\right]\lambda\sqrt{f'_c}\, b_w d$ Axial tension: $V_c = 2\left[1 + \frac{N_u}{500 A_g}\right]\lambda\sqrt{f'_c}\, b_w d$	Axial compression (lesser of): $V_c = \left[1.9\lambda\sqrt{f'_c} + 2500\rho_w \frac{V_u d}{M_u - N_u \frac{(4h-d)}{8}}\right] b_w d$ $V_c = 3.5\lambda\sqrt{f'_c} b_w d \sqrt{1 + \frac{N_u}{500 A_g}}$
PC, V_c	Lesser of (a), (b), and (c), but > (d): $V_c = \left[0.6\lambda\sqrt{f'_c} + 700\frac{V_u d_p}{M_u}\right] b_w d$ (a) $V_c = \left[0.6\lambda\sqrt{f'_c} + 700\right] b_w d$ (b) $V_c = 5\lambda\sqrt{f'_c} b_w d$ (c) $V_c = 2\lambda\sqrt{f'_c} b_w d$ (d)	Lesser of V_{ci} and V_{cw}: $V_{ci} = 0.6\lambda\sqrt{f'_c} b_w d_p + V_d + \frac{V_i M_{cre}}{M_{max}}$ or $1.7\lambda\sqrt{f'_c} b_w d$ (use largest) $V_{cw} = (3.5\lambda\sqrt{f'_c} + 0.3 f_{pc}) b_w d_p + V_p$
V_s	$V_s = \frac{A_v f_{yt} d}{s}$	

By employing a combination of revised rock modulus and strength parameters in combination with more detailed shear strength provisions within ACI, the rock socket lengths, and in some cases the shaft diameters, were reduced.

VALUE ENGINEERING RESULTS

Final designs, and those ultimately approved by the facility owner, resulted in an approximate 40% reduction in shaft/concrete volume and a 60% reduction in total rock socket depth. The drilled shaft supporting the 180-foot monopole was redesigned as an 11-foot-diameter, 25-foot-long shaft with a minimum shaft embedment into rock of 7 feet. The results of the analysis are shown in Table 3.

Table 3. Comparison of Design Results

	Original Design				QS Design Results				
			Longitudinal Reinforcement				Longitudinal Reinforcement		
Structure[1]	Diameter (ft)	Length (ft)	No. of Bars	Bar Size	Diameter (ft)	Length (ft)	No. of Bars	Bar Size	Bar Spacing (Unbundled) (in)
180-foot Monopole	12	37	64	#14	11	25	58	#14	5.0
M-7 H-Frame DE (Utility Take-off H-frame Structure)	9	25	34	#11	8.5	15	30	#11	8.4
M-8 H-Frame DE (Unit 11 Tie-in H-frame)	9	25	34	#11	8.5	14	27	#11	9.5
M-9 H-Frame DE[6] (Transformer Take-off H-frame)	8	24	28	#11	8	23	25	#11	9.6

The assumptions made in rock quality and strength play a critical role in the development of peak shear demand in rock socketed drilled shafts. The designer must decide if the rock mass should be modeled as a homogeneous unit or broken out into layers to better represent the weathering and strength properties at the site. Once the initial analysis is complete, the designer must determine if the rock mass can support the lateral loading defined by the modeling. In this case, feedback from field operations determined that the upper five feet of the rock mass was not capable of supporting the peak shear loads developed in the original model, and a revised lateral resistance model was created. Unique rock resistance models were created for each foundation site during drilling operations by generating modified p-y curves representing the variable rock quality at each site. These new models recognized the more significant weathering and reduced rock quality identified during site activities. The structural engineers also utilized the detailed shear modeling to determine if an increased concrete shear capacity would benefit the shaft construction. Both of these design refinements were instituted in an iterative process to converge on an optimal solution.

Utilizing the same construction approach described previously, the reduction in concrete volume and rock socket depth reduced construction schedules by two weeks, and eliminated the need for extended work hours and additional crew support. A combination of better rock mass characterization during drilling operations and recognition of higher concrete strength values provided the opportunity to significantly reduce the rock excavation volumes and total concrete required on the project. Table 4 provides a more detailed comparison of foundation construction between the preliminary and final designs.

Table 4. Comparison of Construction Results

Structure I.D.	Foundation Quantity	Neat Diameter (inches)	Length (feet)	Concrete Neat Yardage	Assumed Depth to Rock	Rock Drilling Feet	Rock Drilling Neat Yardage
ORIGINAL DESIGNS							
Utility H-Frame	2	108	25	117.81	8.00	17.00	80.11
Tie-In H-Frame	2	108	25	117.81	7.00	18.00	84.82
Transformer H-Frame	2	96	24	89.36	1.00	23.00	85.64
180' Monopole	1	144	37	154.99	7.00	30.00	125.66
Original Design Total Neat Yardage				**479.97**			**376.23**
VALUE ENGINEERED DESIGNS							
Utility H-Frame	2	102	14	58.85	8.00	6.00	25.22
Tie-In H-Frame	2	102	13	54.64	7.00	6.00	25.22
Transformer H-Frame	2	96	22	81.91	1.00	21.00	78.19
180' Monopole	1	132	24	84.47	7.00	17.00	59.84
QS Design Total Neat Yardage				**279.88**			**188.47**
Total Volume Savings				**200.09**			**187.77**

SUMMARY & CONCLUSIONS

Rock socketed drilled shafts continue to challenge designers and contractors alike, particularly where high lateral loads and flexure are applied. Current modeling techniques conservatively predict very high peak shear demand in shallow rock conditions, requiring the designer to generate large shaft designs with significant rock excavation. To achieve optimal design and construction results, the contractor and designer should work in tandem to define the actual site conditions during construction, and be prepared to adapt the modeling and approach to site-specific feedback.

As the Moxie Freedom Substation heavy load structure foundations were initially excavated, constant interaction between the design engineer's field geotechnical staff, the foundation designers, and the subsurface contractor, created a more accurate view of the subsurface resistance. This created the opportunity to refine conservative initial modeling based upon limited data, generate foundation solutions that matched the site conditions, and create significant value for the customer.

REFERENCE LIST

ACI Committee 318. *318-14: Building Code Requirements for Structural Concrete and Commentary*. American Concrete Institute, 2014, *318-14: Building Code Requirements for Structural Concrete and Commentary*.

ACI Committee 336. *336.3R-14 Report on Design and Construction of Drilled Piers*. American Concrete Institute, 2014, *336.3R-14 Report on Design and Construction of Drilled Piers*.

Benz, Evan C., and Michael P. Collins. “Updating the ACI Shear Design Provisions.” *Concrete International*, vol. 39, no. 9, 9 Jan. 2017, pp. 33–38.

APPLICATION OF MAMMOTH VIBRO-TAMPER (MVT) FOR THE SHALLOW COMPACTION AT AIRPORT RUNWAY EXPANSION PROJECT ON FLORIDA LIMESTONE GROUND

Mitsuo Nozu, President/CEO, Fudo Construction, Inc., San Mateo, CA, USA (www.fudo-const.com), 650-477-6505, mitsuo.nozu@fudo-const.com
Frank Vespi, Senior Project Manager, ditto, 239-398-8629, frank@fudo-const.com
Kazunori Matsushita, Project Manager, ditto, 650-477-6501, kaz@fudo-const.com
Emi Walder, Administration Manager, ditto, 650-678-1341, emi.walder@fudo-const.com

ABSTRACT

During the runway expansion project at the Fort Lauderdale-Hollywood International Airport in Florida (FLL project), therewere complicated geotechnical issues with a number of cavities in the limestone-loose sand mixed ground thatexisted in many areas below the existing ground. Collapsing the cavities and compacting the runway foundation to secure the take-off and landing of aircrafts was a necessary requirement for the project. The Mammoth Vibro-Tamper (MVT) which produces less vibration and noise level, was proposed and accepted as the alternative to the originally specified Deep Dynamic Compaction (DDC) for the runway with its length of 1.5 miles and area of 570,000 square yards. In this report, the shallow compaction effect and reduced ground vibration with the MVT are presented in comparison with the DDC which was utilized on the same project in a different area of the airport.

Keywords: airport, densification, shallow compaction, ground improvement

INTRODUCTION

MVT was developed by Fudo Tetra Corporation in the 1960's and has been widely used in Japan (more than 14,400,000 square yards). For example, at the Kansai International airport, a large area including aprons was compacted with the MVT. It is capable of compacting up to approximately 5m in depth by using a heavy steel plate (3m x 3m) and a strong vibrator motor (V-180, 10Hz) on top of the steel thick plate with specified time duration.

We were involved in densification work with the MVT at the Fort Lauderdale Airport Project (Figure 1) from June, 2012 to February, 2014. Deep Dynamic Compaction (DDC) was originally specified as the compaction method to secure the relative density over 70% in every 2,000 square yards grids, however, we proposed the application of MVT to reduce the vibration risk and it was accepted as the alternative (Figure 2). The compaction work was completed in February 2014, without causing any delay in regard to the residual settlement due to the high embankment (H=60ft=18m).

Throughout the precise test trials, the improvement methods and their quantities were changed as shown in Table 1 and Table 2. At first, MVT with 10'x10' plate type with 120 sec continuous tamping was employed where the area improvement depth was 10 feet and the Vibro-Rod (VR) method was proposed for the area with 20 feet. Figure 3 shows the time settlement curve measured at the test area. However, through the in-situ testing, it was changed to use a combined method of MVT and Stone

© 2018 Deep Foundations Institute

Columns that were allocated beneath the MVT densification areas. With the revised application, the Stone Columns had the function of supporting all the upper loads while the MVT densified area functioned as the load transfer platform. The production rate of one rig operation with the MVT was approximately 2,000 square yards per 10-hour shift.

Table 1 Initial work volume

Depth	Spec.	Proposed method	Improved area (sy)
-10ft(-3m)	Dr>70%	MVT (90sec)	450,700
-20ft(-6m)	Dr>75,80%	Vibro-Rod	197,500

Table 2 Final work volume

Depth	Spec.	Proposed method	Improved area (sy)
-10ft(-3m)	Dr>70%	MVT (120s x2)	372,593
-20ft(-6m)	Ave. Dr>70%	MVT (90s x2)	195,174
	12ft spacing	Stone Column	

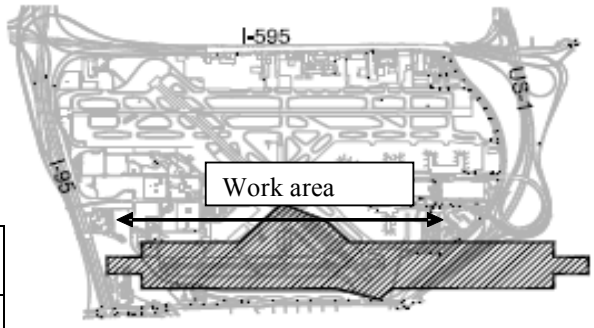
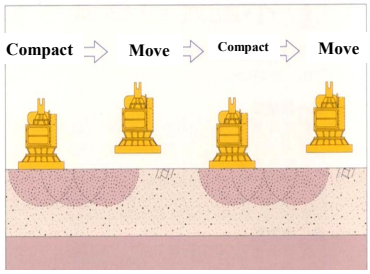


Fig.1 Location of the runway





Type	Vibration force(ton)	Plate size
V-180	88.0	10’ x 10’
V-120	60.0	7’ x 7’

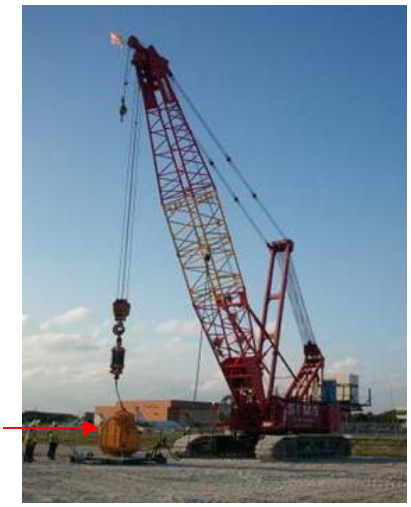


Fig. 2 MVT method

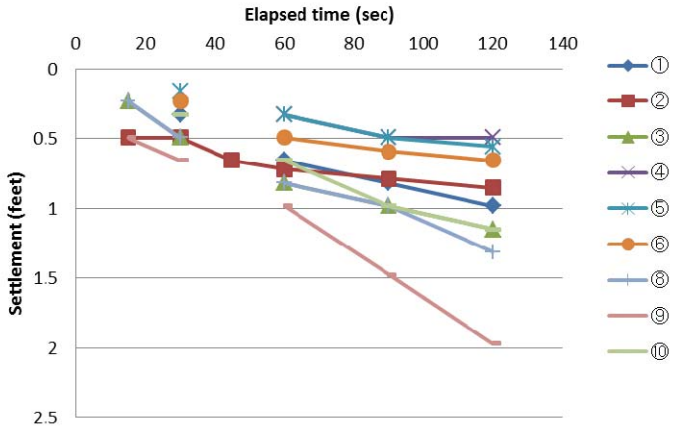


Fig.3 Time settlement curve of MVT tamping in ten locations

Boring data along the runway shown in Figure 4. In some of the areas in the west section of the runway, small cavities (approximately 10 inches in diameter) existed among the subsurface soils and were covered by a shell type of hard limestone (Figure 5), whereas grains of porous oolitic limestone 2 to 3 inches in diameter were deposited at the depth of 20ft in some of the east sections, just like the layer of Figure 5[1)]. Finally, we had to abandon to compact such layer at east section due to its single size lime-stone gravel.

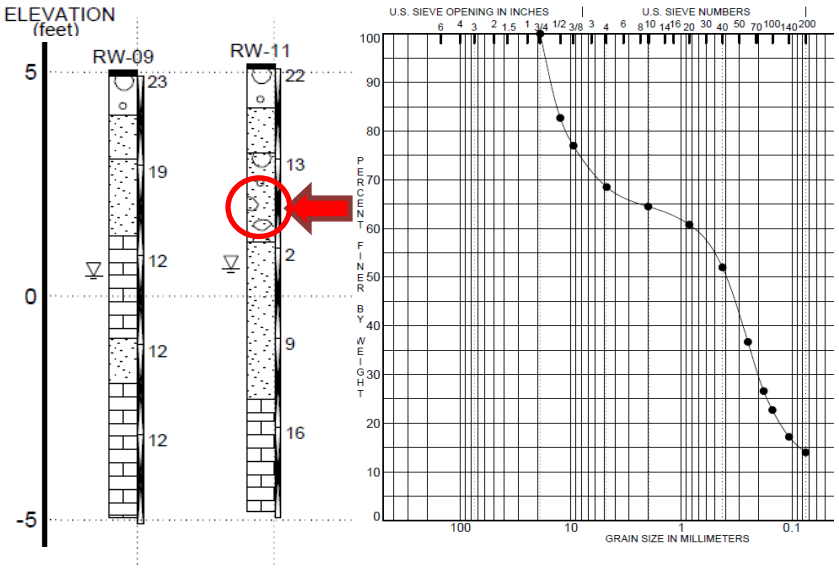


Fig.4 Typical soil profile (SPT-N) along the runway

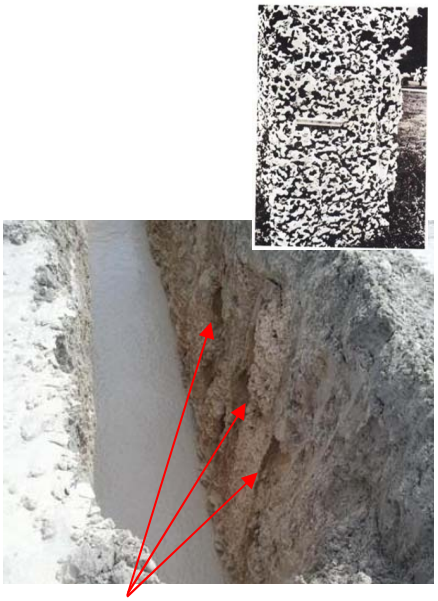


Fig. 5 Small cavities and Porous Oolitic Limestone [1)]

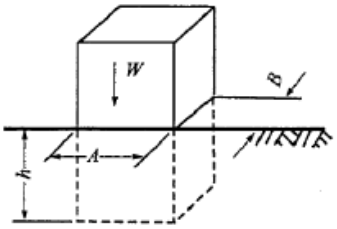
EFFECT OF MVT IN COMPARISON WITH DDC

Required Performance Criteria (Relative density (Dr): equal to or greater than 70%)

To convert from SPT N-value to a relative density, the following formula (Meyerhof's formula[2)]) has been applied. To decide the effective overburden pressure, the Bowles's correction between SPT N-value and Unit weight[3)] has been used.

$$\mathrm{Dr} = \sqrt{\frac{N}{17 + 11.8\sigma_v'}} \times 100(\%) \ldots\ldots Eq(1)$$

Where, σ_v' is the effective overburden pressure (ksf).



a : Amplitude (cm)	1.1	B : Effective width (cm)	310
W : Weight (tf)	21.5	n : Number of applications (No.)	2~4
F : Oscillatory force (tf)	87.7	t : Time of application (min)	
f: Frequency (cpm)	560	h : Thickness of improvement (cm)	400
A: Effective width (cm)	310		

Fig. 6 Energy calculation for MVT [4), 5)]

Comparison between MVT and DDC in surface energy calculation

Table 4 shows the comparison of vibration surface energy level by MVT and DDC. For the estimation of MVT energy level at the ground surface, Tanimoto's formula[4), 5)] was revised to apply for energy level for a unit area (Figure 6).

Table 4 Comparison of energy level between MVT and DDC

Mammoth Vibro Tamper (MVT)				Dynamic Compaction			
E = E0 x n x t x 60 / (A x B x h)				E = W x H x N / (A x B)			tf ft/SF
E0 = 2 x a x (W + F / 2) x (f / 60)							
E0	Compaction Energy to ground per unit time			W	weight	15	tons
n	Number of Compaction	3		H	height	60	ft
t	Duration (min)	1		N	Time of drop	5	drops
A,B	Effective width (cm)	300		A,B	Effective width	8.48	ft
h	Thickness of layer (cm)	500					
a	Vibration amplotude (cm)	2.63					
W	Weight (tf)	25					
F	Vibration force (tf)	80	*)				
f	Frequency(rpm)	560					
	*) Thewe data are coming from the Fudo's Vibrator.						
	E0=	3,191.1	tf cm/sec	E=	62.6	tf ft/SF	(per unit area)
	E=	0.0128	tf cm/cm3				
		127.6	tf m/m3				
	E=	638.2	tf m/m2 (per unit area)				
		194.4	tf ft/SF (per unit area)				

Energy Calculation:
DDC: E=Weight x Drop height x Number/Area
MVT: E= (Weight+Vibration Force) x Frequency x N/Area

Murayama and Tanimoto[6] have indicated that the following 'Compaction factor' α is the key factor for plate compaction and higher densification will be achieved in the case of α<1 (see Figure 7). Thus, it is easy to suppose that the vibration plate will be jumped in the case of α<1. In the case of MVT, the α value is approximately 0.31, so this causes high energy and performance for MVT consequently.

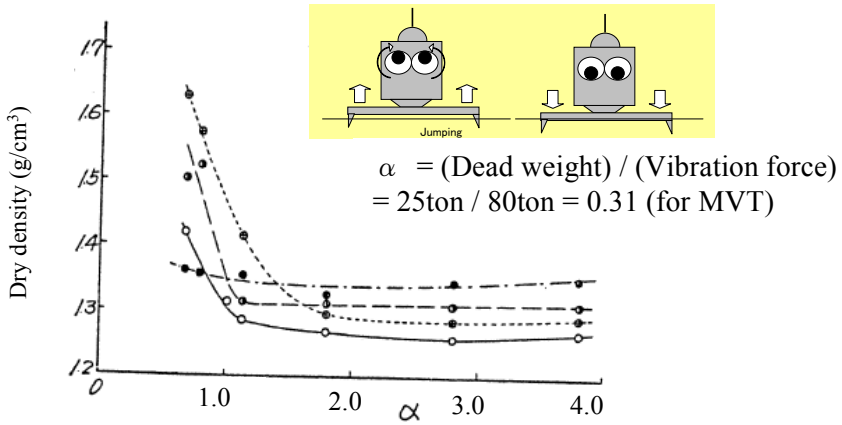


Fig. 7 Effect of α (Murayama & Tanimoto[6])

According to the Table 4, the energy level of MVT (1-minute x 3-times) is approximately 3.1 times larger than that of DDC (15-ton weight is dropped five times from 60ft (18.3m) height. This is regarded as the largest DDC specification in the U.S. due to its limit of equipment capacity.

During this same airport project, another ground compaction contract was issued for an adjacent area. Then DDC was applied to the area and the results (increase of SPT-N value) were investigated and compared with the MVT results. The comparison results have indicated that the MVT is much more effective than DDC under the condition of the same energy level.

Figure 8 is the frequency distribution of SPT-N value of the original ground before densification up to 15ft (=4.6m) in depth. Table 5 shows the test trial specification of DDC. At Grid#1, due to the unsuccessful results of the initial DDC performance to meet the projects specifications, additional dropping were performed in-between the initial targeted compaction locations.

Table 6 and Figure 9 through Figure 13 present the results of DDC and MVT (Area 1A, without trenching). Because of the higher average SPT-N value and lower failure rate of the MVT in comparison to the DDC, MVT is regarded as more effective than DDC. The failure rate is defined as the number representing Dr (relative density) that is lower than 70% divided by the total number representing Dr.

Furthermore, the relationship between the energy level calculated by using Table 4 and the average SPT-N value is shown in Figure 14. The MVT method shows that the large increases of the SPT values is induced through the MVT's higher compaction energy. The advantages of MVT versus DDC are listed as follows.

(1) Higher densification effect with higher surface energy
(2) Higher work productivity
(3) Lower impact of vibration and noise on adjacent existing structures (Safety work)
(4) 100% improvement area coverage is achievable.

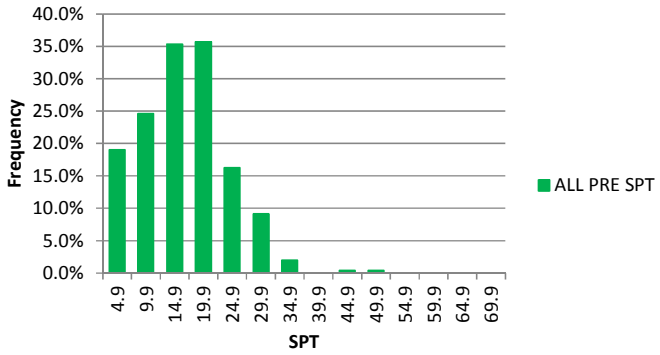


Fig. 8 Frequency of SPT data in the original ground (depth up to 15ft) Average N=13.5

Table 5 Specification of test trial for DDC (WP304/305)

			First Round (Aug-2 to Aug-21)				2nd Round (Aug-22 to Aug-25)		
	Weight (ton)	Height (ft)	Spacing (FT)	Effective area (SF)	Number of Drop (N)	Energy (tf ft/SF)	Spacing (FT)	Effective area (SF)	Energy (tf ft/SF)
Grid#1	15	60	15.0	225.0	5	20.0	7.5	56.25	80.0
Grid#2	15	60	10.6	112.4	5	40.0			
Grid#3	15	60	8.5	71.9	5	62.6			
Grid#4	15	60	10.6	112.4	10	80.1			
Grid#5	15	60	10.6	112.4	5	40.0			
Grid#6	15	60	10.6	112.4	5	40.0			
Grid#7	15	60	10.6	112.4	5	40.0			

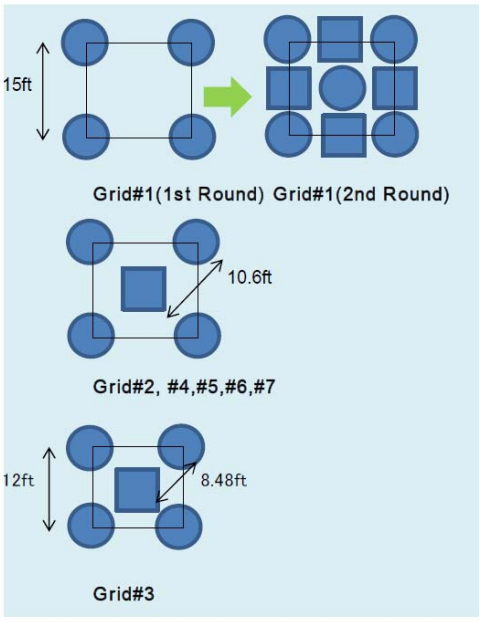


Table 6 Comparison between DDC and MVT

	Spacing (FT)	Effective area(SF)	Number of Drop	Energy (tf ft/SF)	Average SPT-N	Fail Rate (%)
DDC Grid#1-1	15.0	225.0	5	20.0	12.9	42.1%
DDC Grid#1-2	7.5	56.3	5	80.0	18.0	30.4%
DDC Grid#2	10.6	112.4	5	40.1	17.9	18.3%
DDC Grid#3	8.5	71.9	5	62.6	19.3	11.6%
DDC Grid#4	10.6	112.4	10	80.0	22.9	6.9%
DDC Grid#5,6,7	10.6	112.4	5	40.1	16.3	20.5%
DDC Grid#8	8.5	71.9	5	62.6	15.4	20.0%
DDC Grid#22,23,24,27,29	8.5	71.9	5	62.6	15.2	32.7%
MVT tamp No Trench				194.0	25.6	9.7%

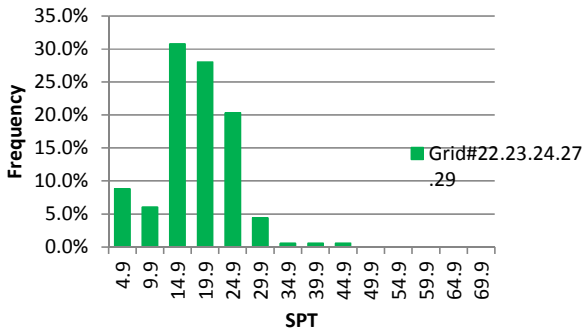


Fig. 9 SPT after DDC (Ave, N=15.2)

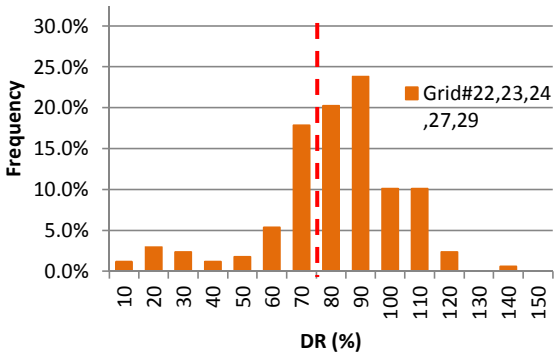


Fig. 10 Dr (Relative density) after DDC (Fail rate: 32.7%)

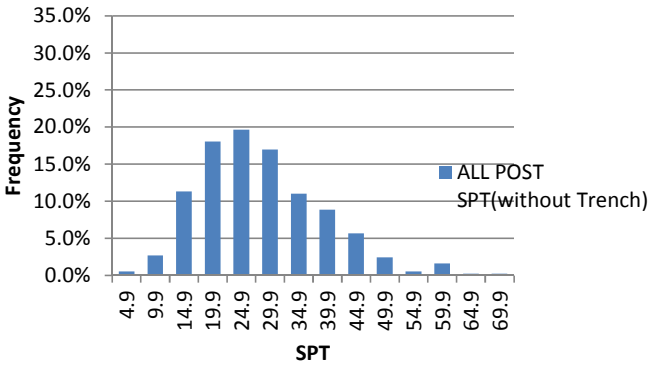


Fig. 11 SPT after MVT (Ave. N=25.6)

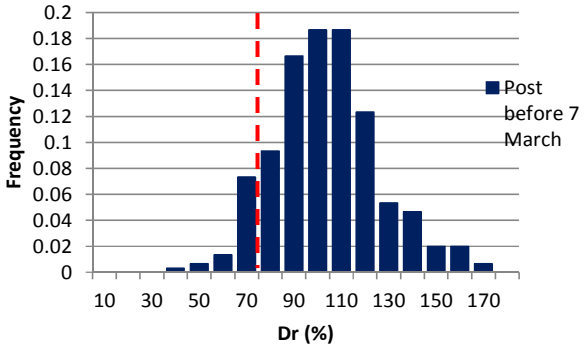


Fig. 12 Dr (Relative density) after MVT (Fail rate: 9.7%)

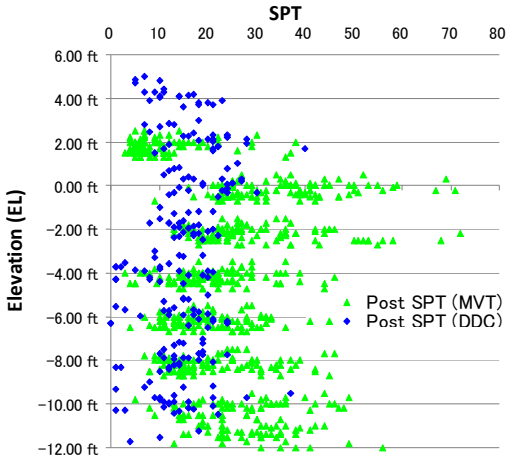


Fig. 13 Comparison between MVT and DDC (SPT-N)

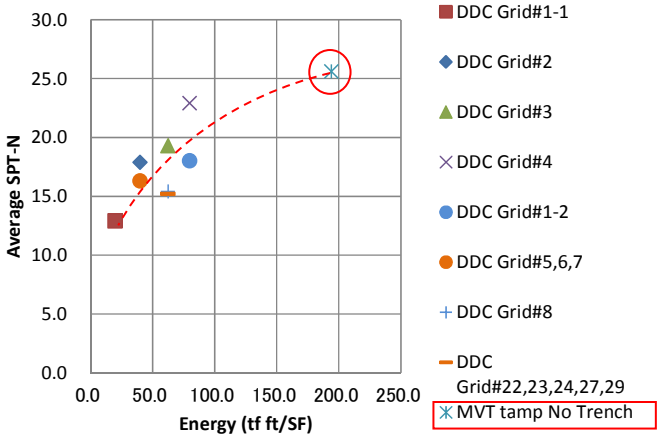


Fig. 14 Relationship between the surface energy level and average SPT-N values after improvements

As shown in the Figure 15 and Figure 16 which were obtained at this project, there was some appreciable compaction effect even at 5.2m (17ft) depth which is 1.73 times that of the plate size of 3m. The average N value was increased from 27.8 to 37.5 after the MVT tamping.

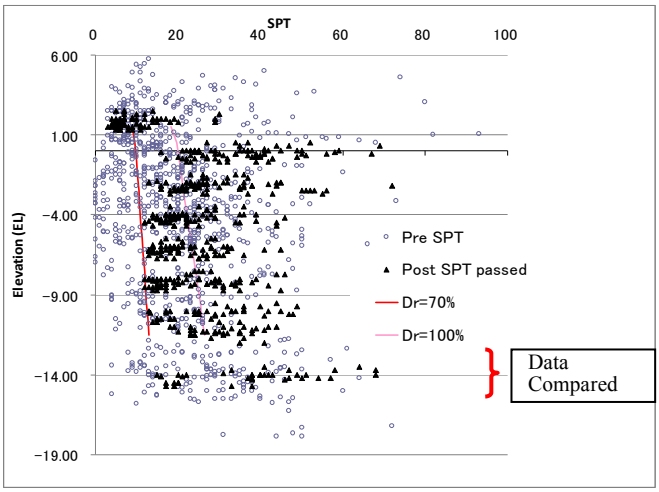


Fig. 15 Pre and post-SCP data

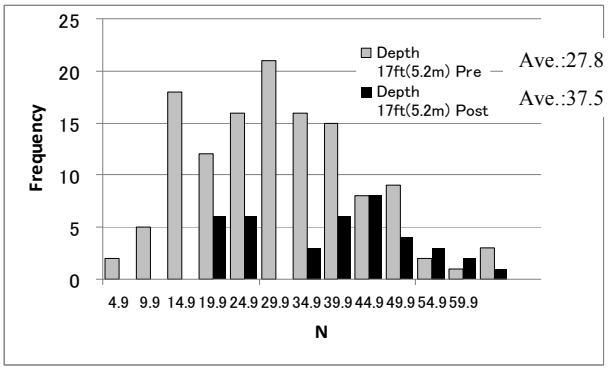


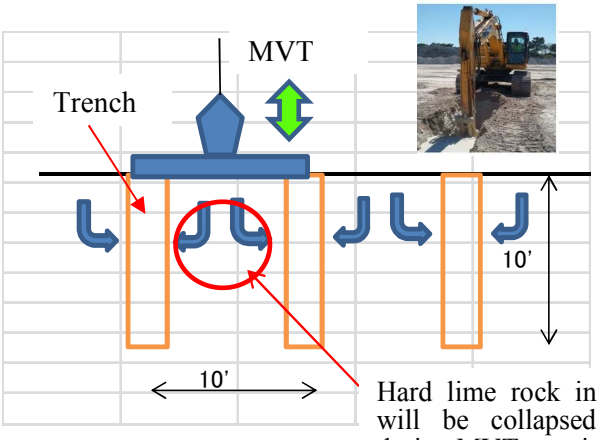
Figure 16 Comparison between Pre- and Post-data at deeper zone

TECHNICAL INNOVATIONS FOR MVT

Trenching and subsequent backfilling

The main reason for the above failure (9.7% at Figure 12) after verification testing was the difficulty to collapse the small cavities below the existing hard shell type of limestone. To address this issue, we applied a fracturing method (trenching and subsequent backfilling) to 10ft in depth and 3ft in width prior to the MVT tamping in order to collapse the limestone structures (Figure 17).

As shown in Figure 17, 18 and 19, the fracturing was very effective in assisting the compaction by MVT which produced a consequential increase in SPT values and a significant settlement caused by the compaction effect.



Hard lime rock in between trenches will be collapsed by lateral flow during MVT tamping.

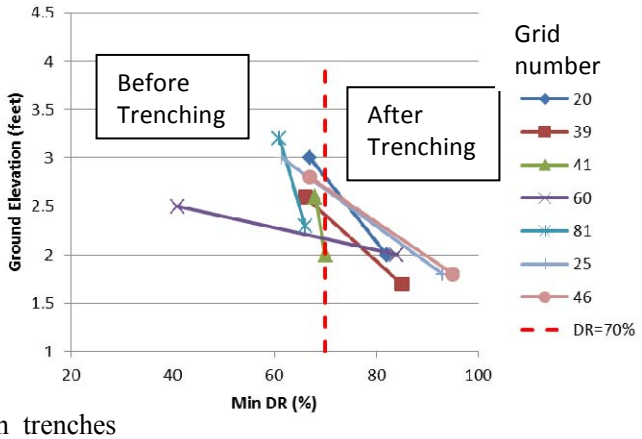


Fig. 17 Trench and the tamping effect (ground settlement after fracturing/MVT)

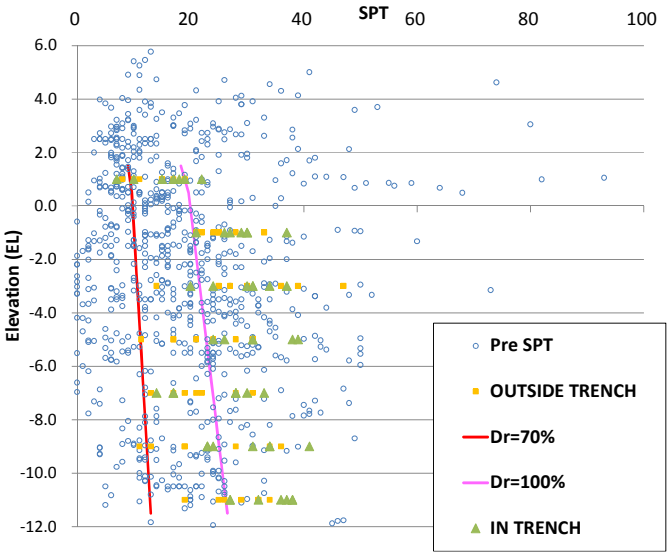


Fig. 18 Increase of SPT-N value after MVT with trenching

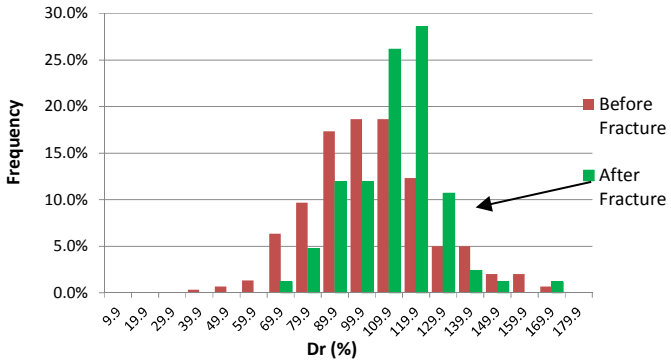


Fig. 19 Effect of trenching

Double MVT tamping sequence

At this project, the double tamping sequence was very effective in areas where considerable ground water surfaced during the 1st tamping (Figure 20) due to the generation of excess pore water pressure with a 'Negative dilatancy effect'. However, no water came up during the 2nd tamping (Figure 21) at few hours later of the 1st tamping. In addition, large increases of SPT-N value were obtained after the 2nd tamping as shown in Figure 22. The mechanism of double tamping effect is supposed as follows (Figure 23).

(1) During the 1st tamping, the compaction energy is absorbed by the surfaced ground water, and the ground surface area becomes very well compacted.

(2) During the 2nd tamping, since the surface area has been already compacted, a deeper zone is now densified by the vibration force.



Fig. 20 1st tamping (A Lot of water comes up)



Fig. 21 2nd tamping (No water comes up)

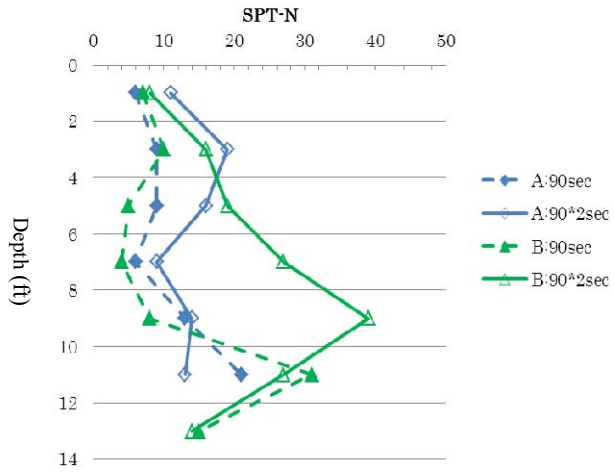


Fig. 22 Effect of double tamping

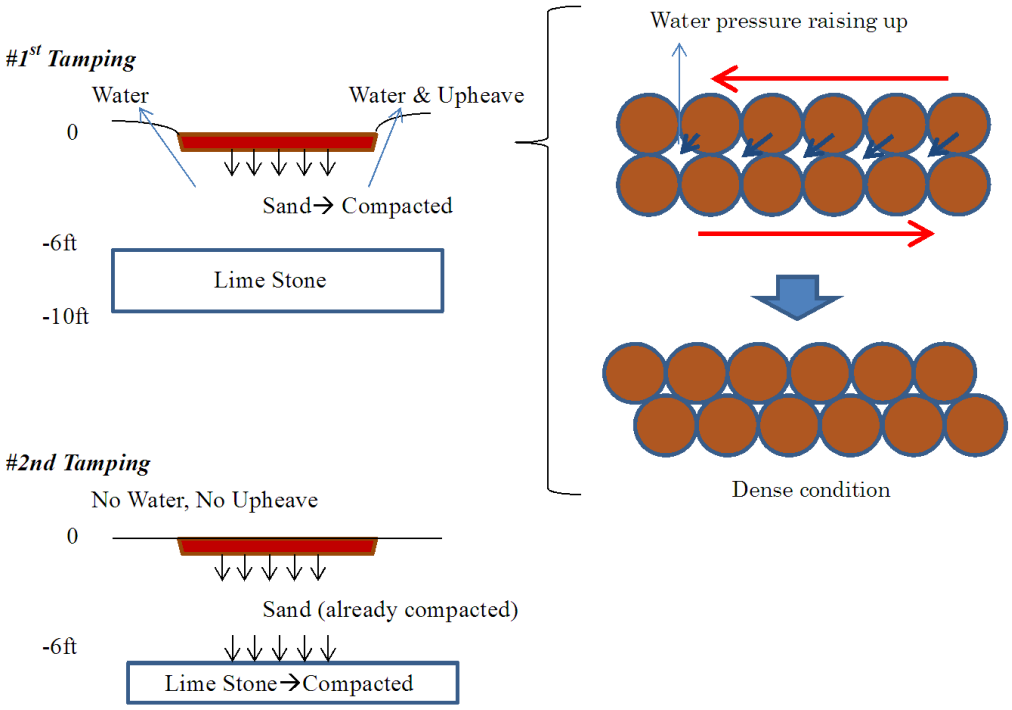


Fig. 23 Mechanism of double tamping

THE VIBRATION REDUCTION EFFECT

Figure 24 through 26 shows the vibration level with the distance from vibration source. Approximately a 40ft (=12.2m) distance from the MVT equipment makes it possible to secure the criterion (velocity, ppv: less than 0.5inch/sec).

Moreover, during the trial performance of the MVT, a vibration isolation trench was installed at a depth of 4ft and 70 feet to the south side of the MVT. The vibration reduction effect was approximately 0.15 inch/sec.

Figure 26 shows the comparison of vibration levels between DDC and MVT, and it is obvious that the vibration impact of DDC is much larger than that of the MVT in an area of less than 150 feet from the equipment.

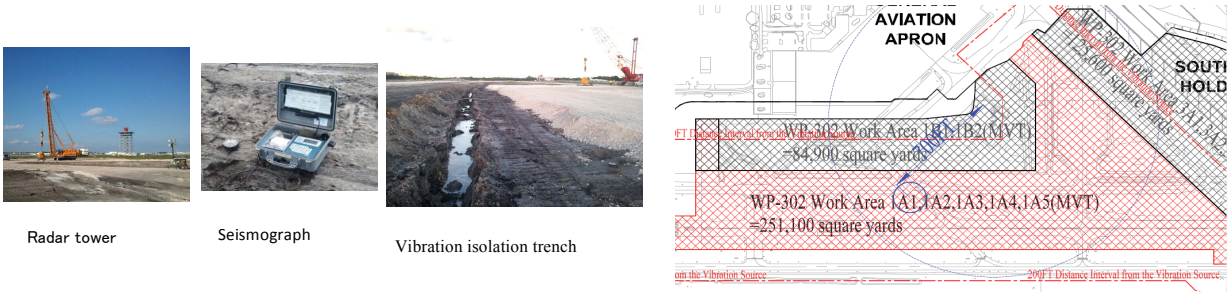


Fig.24 Vibration monitoring

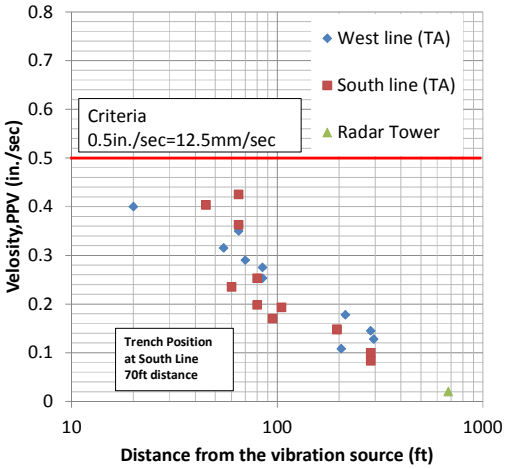


Fig. 25 Vibration of MVT and trench effect

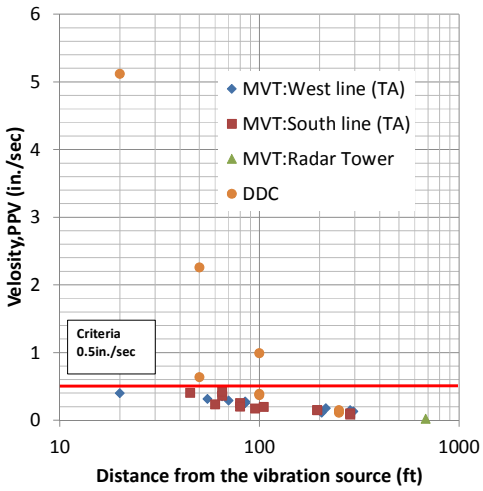


Fig. 26 Comparison of vibration level

CONCLUSIONS

At this project, several advantages of the MVT have been discovered again and some technical innovations have been introduced.

- In regard to the shallow compaction, the 'Compaction factor: α' is the key index. It should be less than 1.0 which means the vibration force is beyond the dead load so that the plate will jump up during the vibration. This causes the greater compaction effect consequently.
- The relationship between the calculated energy level and the average SPT-N value indicate that MVT method has both large increases of the SPT values and higher compaction energy.
- A fracturing method (trenching and subsequent backfilling) to 10ft in depth and 3ft in width prior to the MVT tamping in order to collapse the limestone structures was very effective in assisting the compaction by MVT which produced a consequential increase in SPT values
- The double tamping sequence was so effective in this kind of limestone ground.
- The comparison of vibration levels between DDC and MVT shows that the vibration impact of MVT is much smaller than that of the DDC in an area of less than 150 feet from the equipment.

REFERENCES

1) L.A. Prieto-Portar, 1983. Elastic and Strength Properties of Calcareous Rocks of Dade County, Florida, *ASTM special technical publication*
2) Mayerhof, G.G. 1957. Discussion on Research on determining the density of sands by penetration testing, *Proc. 4th Int. Conf. on Soil Mech. And Found. Engrg.*, Vol.1: 110
3) J.E.Bowles, 1977. Foundation Analysis and Design, Fourth Edition, McGraw-Hill Book Company.
4) Tanimoto, K, 1958. Basic study regarding the soil compaction by surface vibration, Doctoral thesis in Kyoto University
5) The Japanese Geotechnical Society. 1998. Remedial Measures against Soil Liquefaction, From investigation and design to implementation
6) Murayama, S., Tanimoto, K. and Matsuno, S., 1957. Experimental study regarding compaction induced vibration for confined soil, *Journal of Japan Society of Civil Engineers*, No.43, pp.55-59. (in Japanese)

GROUND IMPROVEMENT DESIGN AND CONSTRUCTION FOR SEATTLE'S ELLIOTT BAY SEAWALL REPLACEMENT AND RETROFIT

William Perkins, PE, LEG, Shannon & Wilson, Inc., Seattle, WA, USA, 206-632-8020, wjp@shanwil.com

Andrew Malinak, Project Manager, Hayward Baker, Inc., Seattle, WA, USA, 206-223-1732 andrew.malinak@HaywardBaker.com

Seattle's Elliott Bay Seawall protects the 1½ miles of downtown waterfront between South Washington and Broad streets. The seawall supports the urban waterfront and infrastructure, including the Alaskan Way Viaduct and Alaskan Way, access to historic waterfront piers, and numerous essential buried utilities.

Most of the original seawall was constructed between 1916 and 1936 over soft/loose non-engineered fill, estuary, and beach deposits. The majority of the original seawall was a pile-supported timber relieving platform that extended up to 60 feet behind the face of the wall (Figure 1). With maximum spacing between the timber piles of 3 to 5 feet, a virtual forest of timber piles were driven for the original wall.

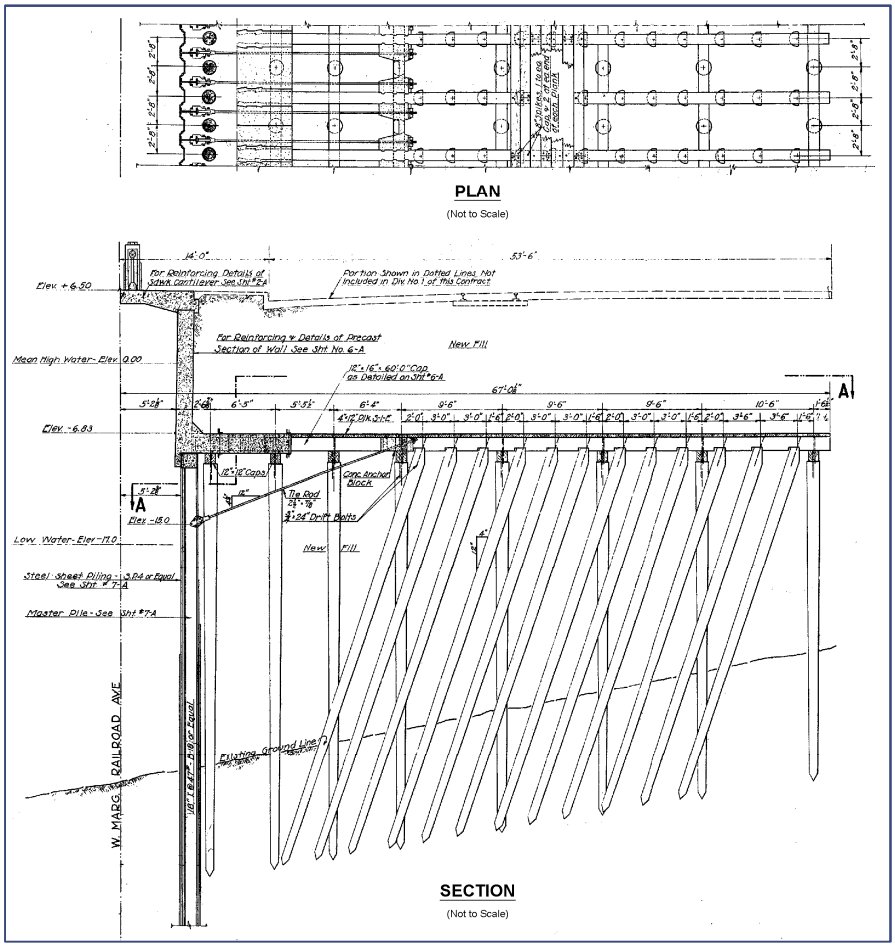


Figure 1. 1934 Type B Seawall

Much of the fill behind the seawall is a sand and gravel backfill placed hydraulically during seawall construction in the 1930s. Fill placed prior to the 1930s includes debris from historic waterfront sawmills (sawdust, wood chips, mill ends), debris from the 1889 Great Seattle Fire, and other non-engineered fill and debris. The fill thickness ranges between 25 and 50 feet. Located up to 500 feet seaward of the original shoreline, the seawall retains these predominantly loose, liquefaction-susceptible, non-engineered fills.

Because of the effects of the 2001 Nisqually earthquake on the waterfront, the City embarked on an evaluation of the existing seawall, including a condition and seismic vulnerability assessment. This evaluation determined that the seawall and the infrastructure it supports were at significant risk from even a moderate ~100-year seismic event. This conclusion led to design and construction of nearly 3,200 feet of replacement seawall and retrofit of an additional 500 feet.

© 2018 Deep Foundations Institute

Several seawall replacement/retrofit designs were considered. The final design utilizes an improved soil mass (ISM) constructed of a cellular arrangement of jet-grouted soil-cement columns that extend vertically from about 10 to 15 below the street level (the bottom of the original seawall relieving platform) down to the top of the glacially overridden Pleistocene soils. The cellular structure consists of a seaward ISM front panel, landward back panel, and a connecting center panel constructed of overlapping jet-grout columns. The panels and overlapping jet-grout columns are shown schematically in cross section and plan in Figure 2; the top of the completed ISM is shown in Figure 3.

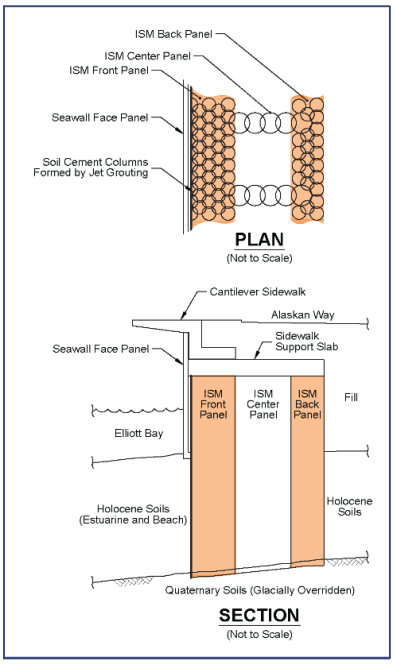


Figure 2. ISM Schematic (looking north)

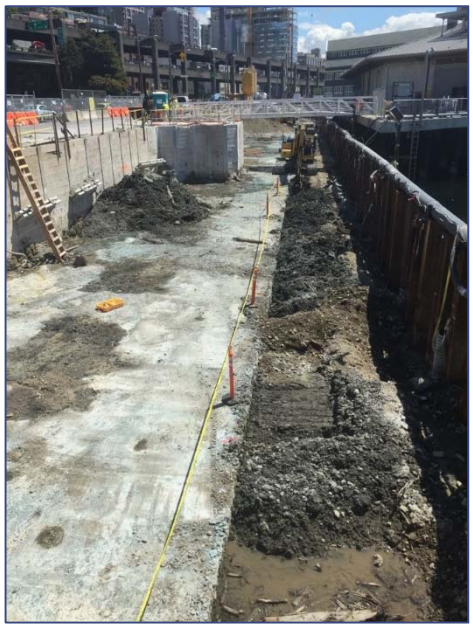


Figure 3. Top of Constructed ISM (looking south). Light-colored material is improved ground; dark-colored material is unimproved soil.

The ISM supports a seawall superstructure and provides all seismic lateral restraint. ISM seismic performance criteria are based on allowable seawall displacement for three earthquake ground motion levels. Consequently, final ISM design utilized non-linear dynamic soil-structure interaction time history analyses. To meet performance criteria, ISM widths range between 26 and 60 feet, ground improvement area replacement ranges between 50 and 64 percent, and jet-grout soil-cement unconfined compressive strength ranges between 125 and 400 pounds per square inch (psi), depending on the soil type.

Jet grouting was selected for ISM construction because of the variable soil conditions, debris, thousands of potential obstructions posed by the 8,300 original seawall piles and other undocumented piles, and physical constraints imposed by the dense urban waterfront environs. The City's geotechnical engineering consultant developed jet-grout plans and specifications to construct the ISM. The City provided the plans and specifications to ground improvement subcontractors and ultimately awarded the subcontract to Hayward Baker, Inc. who installed ~6,000 jet-grout columns in three construction seasons. With jet-grout columns up to 93 feet deep with a total volume of approximately 175,000 cubic yards, the Elliott Bay Seawall Project is one of the largest jet-grout projects ever constructed.

ISM construction issues included equipment selection, limited space, spoils handling, wood debris, and obstructions (e.g., buried utilities, piles, and temporary shoring). Lessons learned included jet grouting was the best construction method given the utilities and thousands of piles beneath the site, early obstructions identification and contingency plans are critical to maintain production, and an understanding of space requirements for all construction activities is required for safe and productive working conditions.

RAILROAD BRIDGE APPROACH EMBANKMENT SETTLEMENT MITIGATION

Moi Arzamendi, WSP, San Diego, CA, U.S.A, Moi.Arzamendi@WSP.com
Jose Ramirez, Kleinfelder, Inc., San Diego, CA, U.S.A, jramirez@kleinfelder.com
Kenneth Kniss, Hayward Baker, Odenton, MD, U.S.A, KTKniss@HaywardBaker.com
James Gingery, Hayward Baker, San Diego, CA, U.S.A, james.gingery@haywardbaker.com
Sunil Arora, Hayward Baker, San Diego, CA, U.S.A, Sarora@HaywardBaker.com

ABSTRACT

Construction of a new approach embankment for a railroad bridge over a river in Southern California required placing up to 12 ft of fill over soft to medium stiff silts and clays along an approximate 1,500-ft long stretch. The embankment, situated within a narrow railroad right-of-way between an existing live track and existing buildings, would have been susceptible to excessive settlement that could damage existing buildings and numerous underground utilities if regular weight soil fill had been placed over the unimproved ground. To limit total and differential static settlements to tolerable levels, a design was developed using a combination of mechanically stabilized earth wall with lightweight cellular concrete fill and rigid inclusions ground improvement. This paper describes the design of the ground improvement system, construction methods used, and challenges of working next to live railroad traffic. Ground improvement quality control and assurance measures, and verification of performance by settlement monitoring are also addressed.

Keywords: ground improvement, settlement monitoring, rigid inclusions, cellular concrete

INTRODUCTION AND BACKGROUND

The 0.9-mile San Diego River Double Track (SDRDT) project is located on the Los Angeles-San Diego-San Luis Obispo (LOSSAN) Corridor in San Diego, California. The project includes the replacement of the existing 900-ft long single track railroad bridge over the San Diego River with twin double track structures. Construction of the project is phased and closely coordinated with the associated Mid-Coast light rail project (San Diego Trolley Blue Line Extension).

The new bridge is a 7-span, twin steel, through girder structure supported by six cast-in-place reinforced concrete pier caps and two abutments. The large diameter cast-in-drilled-hole (CIDH) foundations are up to 9 ft in diameter, with upper portions encased in a 1.5-in.-thick permanent steel casing. The north abutment approach embankment includes a mechanically stabilized earth (MSE) retaining wall up to approximately 10 ft high and 1,520 ft long. This paper focuses on the design and construction of the north approach embankment.

The project site is characterized by challenging geotechnical and seismic conditions. The site contains liquefiable soils interbedded with soft cohesive soils, underlain by competent layers of sand/gravel/cobble and other sedimentary formations. Static settlement of the new railroad, crossing utilities and adjacent buildings was a primary design concern for the north approach embankment.

The MSE wall used lightweight cellular concrete fill (LCCF) to reduce imposed loads and settlements. Ground improvement below the wall consisted of rigid inclusions (RIs) to mitigate the static settlements to existing nearby site improvements including single track railway embankment, light industrial buildings, roadway and numerous buried underground/overhead utilities.

© 2018 Deep Foundations Institute

GEOLOGIC CONDITIONS AND SITE CHARACTERIZATION

The site is located within the historic San Diego River floodplain. The river was channelized in the early 20th century by placing fill at what are now the north and south abutments of the bridge. Ground surface elevations within the river channel are about +5 to +9 ft above mean sea level (MSL). The pre-construction elevation in the north approach MSE wall area was +20 to +26 ft above MSL. A groundwater elevation of +5 ft above MSL was used for design. Field explorations consisted of rotary-wash borings (up to 140 ft deep), resonant sonic borings (up to 150 ft deep), CPTs (up to 100 ft deep), and refraction microtremor geophysical surveys (up to 250ft in depth).

The west-flowing San Diego River basin incises the coastal plain and terraces, forming steep-sided canyons and broad estuary systems in-filled with late Pleistocene to Holocene age deposits (Kennedy, 1975). The site is underlain by a sequence of artificial fill, estuarine, alluvium and terrace deposits that are greater than 150 ft in depth. The embankments and levees along the San Diego River have up to 15 ft of undocumented artificial fill which mainly consists of loose to medium dense silty sand and poorly graded sand. Other near surface sediments include recent alluvial deposits (Qa) and young estuarine deposits (Qyes) which collectively consist of loose to medium dense sandy soils and soft to medium stiff compressible silty and clayey soils. The Qyes is underlain by young alluvial deposits (Qya) which generally consists of medium dense to dense sandy soils. In turn, these materials are underlain by very competent Late Pleistocene age old alluvial (Qoa) and marine terrace (Qt) deposits that consist of mostly dense to very dense granular and hard fine-grain sediments. A geologic profile of the project alignment is presented in Fig. 1.

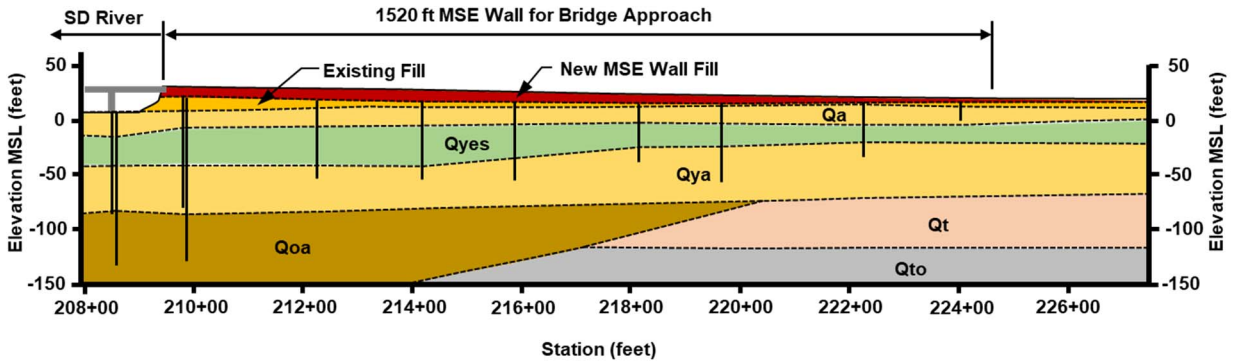


Fig. 1. Geologic Profile of Project Alignment (northern segment).

Site-specific design ground motions were developed for the project in accordance with AREMA (2014), which include three seismic design Ground Motion Levels (Levels 1, 2 and 3) which correspond to Serviceability, Ultimate and Survivability limit states, respectively. The Rose Canyon fault is less than 1,500 ft from the site and an earthquake magnitude of 6.8 was used for design. The design AREMA Survivability Earthquake peak ground acceleration (PGA) is 0.53g.

The project area was considered moderately to highly compressible under static loading and prone to liquefaction. Preliminary design calculations showed conventional site grading and earthwork to achieve the required track elevation would cause significant ground settlement. Potential static settlements for adjacent building foundations, existing railroad tracks and existing buried utilities were deemed unacceptable. In this respect, the design team decided that approach embankment and retaining walls would be constructed using lightweight cellular concrete and ground improvement. The lightweight cellular concrete reduced driving shear stresses sufficiently such that liquefaction lateral spreading displacements became negligible even without reinforcement by ground improvement.

Geotechnical strength parameters were selected based on the results of field/laboratory investigations, review of existing published information, previous experience in the site vicinity, and professional judgment. Under seismic conditions, liquefiable layers were modeled using liquefied undrained residual shear strength ratios developed by Idriss and Boulanger (2008). Selected strength parameters are presented in Table 1. An equivalent Cooper E80 train surcharge load of 1,800 psf over the railroad tie length was included in static analyses.

Table 1. Summary of Geotechnical Parameters Used in Various Analyses

Material	Approx. Elev. (ft)	γ_t (pcf)	φ' (deg)	Su or c' (psf)	$S_{u,r}$ (psf)	OCR / Void Ratio	Drained Poisson Ratio (ν)	Elastic Modulus (ksf)
Qaf	15 to 7	120	33	c'=100	-	-	0.33	200
Qa	7 to -9	119	32	c'=0	440	-	0.33	100
Qyes (sandy)	-9 to -41	118	32	c'=50	170	-	0.33	100
Qyes (silt/clay)	-9 to -20 -20 to -30 -30 to -41	114 115 116	-	Su=800 Su=1,000 Su=1,200	-	1.2 / 1.1 1.3 / 1.0 1.4 / 0.9	-	Note (1)
Qya_1 (upper)	-41 to -63	129	35	0	1,040	-	0.33	400
Qya_2 (lower)	-63 to -81	132	37	0	1,040	-	0.33	800
Qoa (gravelly)	<-81	141	42	0	-	-	0.33	3,000
Qoa (sandy)	<-81	135	38	0	-	-	0.33	2,000
Qoes	<-81	141	42	0	-	-	0.33	3,000
Ballast	Embank.	120	40	0	-	-	0.33	1,000
Sub-Ballast	Embank.	120	40	0	-	-	0.33	1,000
Class II LCCF	Embank.	30	38	0	-	-	0.22	68,000
Class IV LCCF	Embank.	42	38	0	-	-	0.22	120,000
Stone Column	Grd. Imp.	110	40	0	-	-	0.33	1,300
Compac. Grout	Grd. Imp.	120	-	36,000	-	-	0.25	180,000
Rigid Inclusion	Grd. Imp.	130	-	100,000	-	-	0.20	300,000
Concrete	Grd. Imp.	150	-	300,000	-	-	0.15	500,000

Note: (1) Modified Cam-Clay parameters $\lambda = 0.13$ and $\kappa = 0.033$

GEOTECHNICAL ANALYSES AND DESIGN CONSIDERATIONS

Geotechnical analyses and design for the project consisted of a wide spectrum of strength, deformation and stability evaluations. Analysis methods included conventional hand calculations and numerical simulations for all critical bridge foundations, abutment slopes, retaining walls and approach embankments. Stability analyses showed that the embankments easily met the minimum design requirements with factors of safety of at least 1.5 and seismic stability analyses showed that seismic displacements would be negligible. Conversely, the static settlement design requirements were found to govern the design of the embankment and ground improvement. The following section presents the results of selected settlement analyses that include ground improvement and approach embankment design alternatives.

Mechanically Stabilized Earth Walls with Lightweight Cellular Concrete Fill

Approach embankment retaining walls have been designed as MSE walls with LCCF in accordance with AASHTO LRFD Bridge Design Specifications (AASHTO, 2012) as adopted by the California Department of Transportation (Caltrans) with the 2014 California Amendments. Cellular concrete is a lightweight cement-based material containing many gas bubbles evenly distributed in the volume. It is produced by blending and maturing a mixture of cement, filler, water, and foaming agent. It has relatively low density and high strength/stiffness. It has been used previously in heavy rail applications to reduce settlements (Anderson, 2012). Due to its cemented but brittle nature, it was assumed that random long-term micro-cracking propagation could develop throughout the embankment mass. Thus, the stability analyses conservatively modeled the cellular concrete with an internal angle of friction of 38°.

The MSE wall foundation zone included a minimum over excavation and replacement with LCCF of at least 1.5 ft below and 3 ft in front of the wall. This zone bears directly on top of ground improvement, as described later. The wall was constructed allowing the facing panels to be used as formwork during placement of the fluidized LCCF. A cross section of the MSE wall with LCCF at Station 214+00 is presented in Fig. 2.

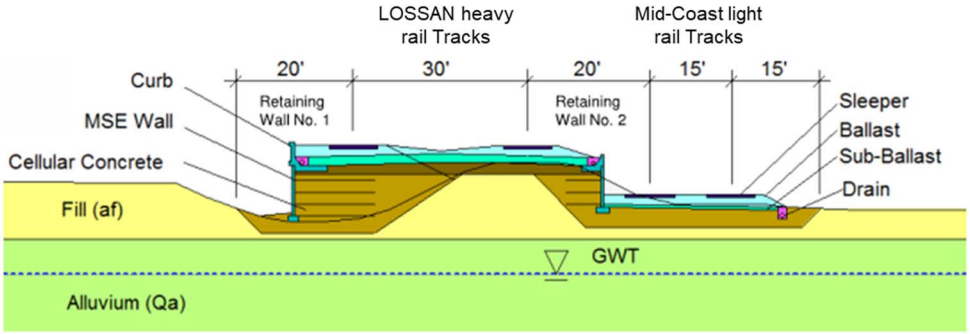


Fig. 2 - Typical Cross Section of the MSE Wall with LCCF

Ground Improvement and Settlement Analyses

Analyses showed that the use of LCCF alone was not sufficient to reduce settlement at adjacent buildings to permissible values (e.g., 0.25 in. inch or less). A ground improvement program to further reduce static settlement of the embankment and adjacent structures was therefore deemed appropriate. Numerous ground improvement methods were initially considered for the project, with stone columns (low stiffness) and rigid inclusions (high stiffness) selected for further consideration.

Settlement analyses for the approach embankment and retaining walls were performed for various scenarios of staged construction, loading conditions, embankment material composition, and type of ground improvement. These analyses were performed to evaluate the potential ground deformation due to anticipated dead and live load configurations with respect to existing buried utilities, existing buildings adjacent to the west right-of-way, and the existing railroad track. Settlement analyses were performed based on two progressive scenarios of construction which included staged Phase 1 (build the MT-2 heavy rail line while MT-1 remains in service) and Phase 2 (remove and rebuild MT-1). These scenarios were evaluated using both normal weight fill and LCCF and with and without ground improvement.

Stone columns and rigid inclusions were initially evaluated using the computer program StoneC (GeoLogismiki, 2006) which uses the method of Priebe (1995) to account for settlement reduction through ground reinforcement. The geometric layout within the treatment zone was based on column

locations with an equilateral triangle or square spacing (*S*) pattern and effective diameter (*D*). The area ratio (*Ar*) is defined by the effective area of the columns (*Ac*) divided by the gross treatment area (*A*). Analyses were performed for stone columns 24 and 30 in. in diameter with square spacing of 5, 6 and 8 ft that extend down into the medium dense to dense upper young alluvium (Qya). The analyses indicated that stone columns could effectively reduce ground settlement 50 to 80 percent with *Ar* values of 5 to 15 percent, respectively (Fig. 3).

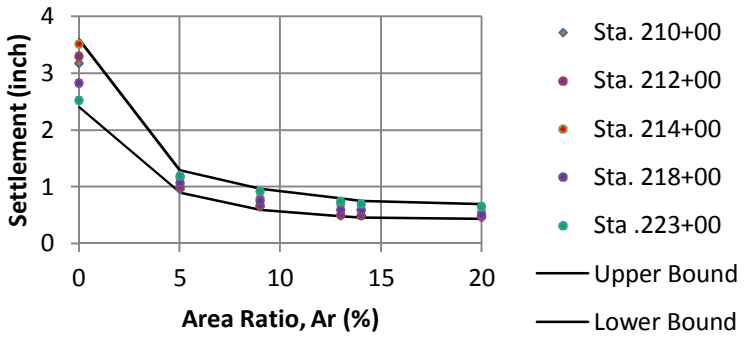


Fig. 3. Stone Column Analyses Results

The Priebe method cannot estimate settlement outside of the treatment area nor is it suitable for evaluation of rigid inclusions. To overcome these limitations, additional analyses were performed using the 2D finite element computer program SIGMA/W (Geo-Slope International, 2013). Approximate 2D equivalencies for strength and geometry were used assuming linear proportionality with assumed 3D material properties and loadings. Densification of the in situ soil between rigid inclusions was ignored because of relatively high fines contents and low area replacement ratios. The 2D results were compared with equivalent Priebe method calculations and found to produce similar results. Settlement analyses results for four design alternatives at Station 214+00 for the fully built approach embankment are presented in Table 2. Contour plots of Y(vertical)-displacement for these cases are presented in Figures 4a to 4d.

The results of the study indicated a combined system of LCCF and RIs was a superior alternative because of its ability to minimize numerous pertinent deformation control points. The RIs changed the subsurface stress distribution such that stress increases and soil compressions below the buildings were negligible. The analyses showed that stone column alternative would reduce settlements of the embankment sufficiently, but settlement of the buildings could reach unacceptable values.

Table 2. Settlement Analyses Results for Station 214+00

MSE Wall Backfill	Ground Improvement	Maximum Settlement (inch)	Settlement along West R.O.W. (inch)	Differential Settlement between MT-1 Rails (inch)	Settlement by parked Locomotive (inch)	Yield Acceleration (g)
Structure Backfill	None	4.8	1.3	0.5	1.6	0.40
LCCF	None	1.9	0.7	0.2	1.2	0.45
LCCF	Stone Columns	1.2	0.5	0.1	0.2	0.47
LCCF	Rigid Inclusions	0.5	0.2	< 0.1	0.1	0.87

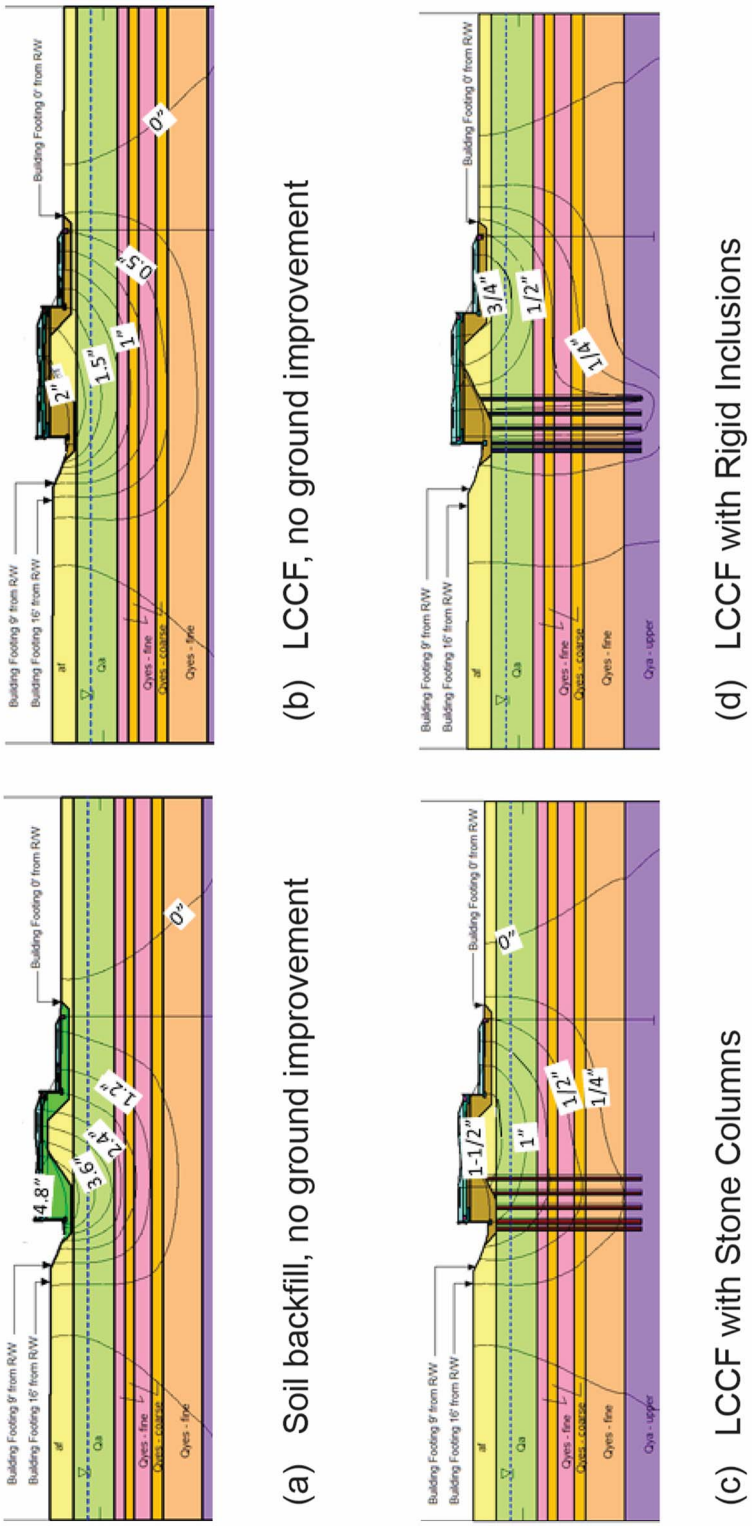


Fig. 4. Settlement Contour Plots (inches) for Station 214+

MSE WALL ANALYSIS AND DESIGN

For cost efficiency, the contractor was given the flexibility of subcontracting to an MSE wall manufacturer of choice to provide the proprietary MSE wall components. As such, the MSE wall manufacturer was responsible for the internal stability design of the MSE wall, while the Engineer of Record was responsible for providing the wall geometric parameters and ensuring external stability could be met within the project constraints.

The ability to achieve external wall stability was explored by checking sliding, overturning and bearing failure modes. The analysis and design process was as outlined in FHWA (2009) GEC 011 for designing conventional MSE walls. The following assumptions were made:

- backslope is horizontal and wall face is vertical
- influence of ballast and sub-ballast loads as earth surcharge
- foundation, retained, and reinforced zones are all backfilled with LCCF with zero cohesion

When checking sliding, overturning, and bearing failure modes for MSE wall design, the driving and resisting forces caused by earth loads depend on the soil reinforcement length. In addition, the vertical earth loads act as both driving and resisting forces. Consequently, the analysis was performed by applying the minimum load factors prescribed by AASHTO to resisting forces and the maximum load factors to driving forces.

The design was achieved by iterating the soil reinforcement length until all the external stability failure modes were satisfied. The required soil reinforcement length was calculated based on the governing failure mode and was verified to fit within the retained mass of lightweight cellular concrete backfill. The process was done for design heights varying between 4 to 10 ft. A typical cross section of the project's north embankment can be seen in Fig. 5.

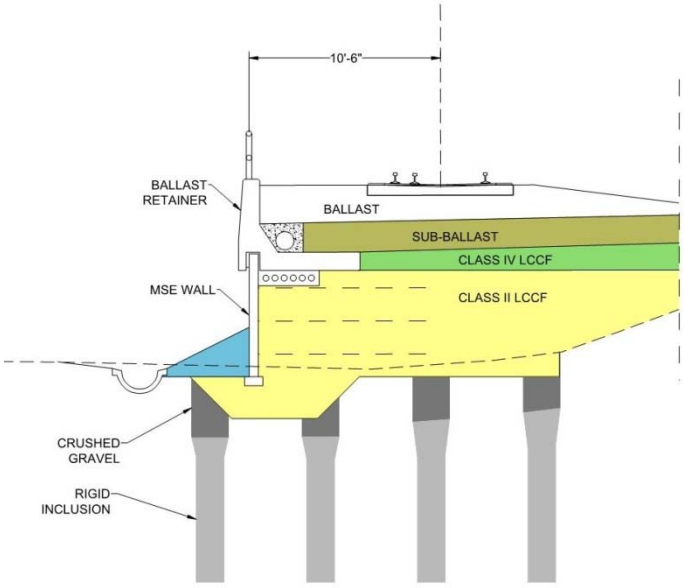


Fig. 5. Typical Project Cross-section

GROUND IMPROVEMENT FINAL DESIGN AND CONTRUCTION

A specialty geotechnical contractor performed final design and construction of ground improvement for the north approach embankment. Compaction grouting and RIs were considered, with RIs ultimately selected as the primary ground improvement method because of concerns that adequate grout take in shallow soil could not be accomplished with compaction grouting. The RI solution, however, ensures a full diameter element over the full depth of installation and was chosen as the optimal ground improvement solution.

RIs are a ground improvement system in which high modulus columns are constructed through compressible soils to reduce settlement and increase bearing capacity. An ideal ground improvement system for the support of large foundations on soft soils, RIs are typically used to reinforce buried soft compressible soils by transferring stresses from a near surface granular soil to a deeper competent stratum. The composition, diameter, depth and number of inclusions are designed based on the planned loading and settlement requirements. RIs have been constructed beneath buildings, roadways, and large loaded areas (such as tanks).

Due to the high modulus differential between the RIs and the surrounding soft soils, stress is attracted to the RI elements and passed through the soft compressible layer. Load is transferred to the RIs in part through a load transfer platform (LTP). The LTP is designed to distribute the stress concentration and prevent cracking or damage to the supported structure.

In addition to avoiding the heaving concerns faced with compaction grouting, the RI program was selected as the primary method of ground improvement because it treated the entire subsurface profile and offered a reduced schedule when compared to compaction grouting. Some limited compaction grouting was also used in portions of the site where confined spaces and overhead restrictions precluded the installation of RIs.

The final RI design determined the spacing and diameter of the elements to reduce static settlements of the MSE wall and prevent contact pressures between the RIs and cellular concrete from exceeding the allowable unconfined compressive strength of the concrete. This work complemented the preliminary design performed using 2D finite element method as described earlier.

For this project, minimum 18-in diameter RIs were installed into the upper young alluvial deposit and young estuarine deposits (Qya and Qyes). The design unconfined compressive strength of the RIs was 2,500 psi. The LTP was designed for compatibility with the LCCF. Specifically, the Unconfined Compressive Strength of the LCCF specified for this project was 40 psi and an allowable stress of 27 psi (1.5 factor of safety) was required for the LTP design under Cooper E80 train surcharge loading.

A finite element (FE) software program, Plaxis 2D 2015, was used to evaluate the soil-structure interaction and calculate the maximum vertical stress at the base of the LCCF. An axisymmetric unit cell model was used to evaluate this condition. The axisymmetric model is most applicable to large area treatment with a constant applied load. However, this model can be used to obtain conservative results with other loading conditions.

A triangular grid pattern with a nominal center-to-center spacing of 7 ft was selected. RIs were installed by advancing the RI tooling through the compressible soil to the upper young alluvial soil layer or until practical refusal of tooling was encountered. The stress at the bottom of the LCCF was reduced to allowable levels through use of a 2-ft diameter by 3-ft deep crushed gravel “cushion” LTP between the top of RI and bottom of LCCF. A representative geometry for the FE analysis is shown in Fig. 6 (a)

while Fig. 6 (b) shows model results for vertical stress contours. The calculated average vertical stress above the RI was 23 psi, which was less than the allowable stress level of 27 psi.

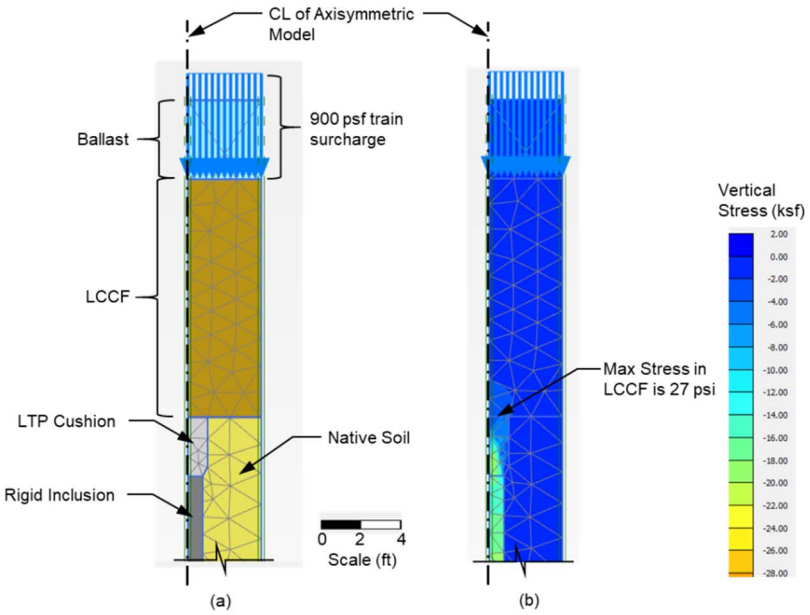


Fig. 6. (a) Axisymmetric finite element model (upper 23 ft of model) and (b) model results for vertical stress distribution contours.

During construction, the main challenge was working in limited space between the live train traffic and existing structures (Fig. 7). Over 800 RIs were installed to depths of up to 65 ft, meeting the tight construction schedule. A data acquisition (DAQ) system was used to monitor time, drill rig torque and crowd pressure, grout pumping rate and pressure, and to confirm that the grout volumes were achieved. DAQ read-outs were provided on-screen in the drill rig cab so that the operator could control quality in real time during construction. Daily reports for work done were provided to the design engineer for quality assurance monitoring. Grout was sampled, cast in cylinders and compression tested to confirm the that minimum specified compressive strength of 2,500 psi was met.



Fig. 7. The ground improvement contractor completed RI work alongside live train traffic

SETTLEMENT MONITORING DURING CONSTRUCTION

Settlement was monitored at over three dozen locations including building and ground points adjacent to the embankment. Survey measurements were taken at least twice a day using remote and automated total stations equipment. At the time this paper was written, the embankment had been in place and in operation for several months and measured settlements were 0.125 in. or less.

SUMMARY AND CONCLUSIONS

A combination of RI ground improvement and LCCF embankment were used to limit the potential for settlements which could impact adjacent structures and utilities. The RI's were designed to transfer imposed loads to deeper bearing layers, avoiding stress increases and settlements under adjacent buildings and other existing surface/buried improvements. RI construction was performed in a limited work area between existing buildings and live railroad traffic. DAQ monitoring during construction provided data to show that the required diameters and depths of treatment were achieved. The estimated maximum induced settlement without any mitigation was nearly 5 in. at the railroad and 1.3 in. at the property line. The estimated maximum settlement using RIs and LCCF was about 0.5 in. at the railroad and less than 0.125 in. at the property line. Actual measured maximum settlement was 0.125 in. or less. Ground strengthening using RIs and load reductions using LCCF was shown to be a reliable method of controlling total and differential settlements.

REFERENCES

AASHTO 2012. LRFD Bridge Design Specifications, (Sixth Edition) with 2014 California Amendments.

American Railway Engineering and Maintenance-of-Way Association (AREMA), 2014. Manual for Railway Engineering.

Anderson, J. et al., 2012. Development of Seismic Design Approach for Freestanding Freight Railroad Embankment Comprised of Lightweight Cellular Concrete. GeoCongress 2012, State of the Art and Practice in Geotechnical Engineering, pp. 1720-1729.

Federal Highway Administration (FHWA) 2009. Design and Construction of Mechanically Stabilized Earth Walls and Reinforced Soil Slopes, Volume 1, Geotechnical Engineering Circular No. 11.

GeoLogismiki, 2006. StoneC Version 3, Vibro-replacement design software.

Geo□Slope International, 2013. SLOPE/W and SIGMA/W, GeoStudio Version 8.

Idriss, I. M., and Boulanger, R. W., 2008. Soil Liquefaction During Earthquakes. Monograph MNO□ 12. Earthquake Engineering Research Institute, Oakland, CA, 261 p.

Kennedy, Michael P., 1975. Geology of the San Diego Metropolitan Area, California, Bulletin 200, California Division of Mines and Geology, 56 p.

Priebe, H.J. 1995. The design of vibro-replacement. Ground Engineering Technical Paper 12-61E, December.

SOIL IMPROVEMENT TECHNIQUE TO MITIGATE EXTREME SETTLEMENTS ON DEEP COMPRESSIBLE DEPOSITS IN THE BOGOTA VALLEY

Roger A. Archabal, P.E., Langan, Miami, Florida, USA, rarchabal@langan.com
Gustavo Langoni, P.E., Langan, Panama City, Panama, glangoni@langan.com
Omar A. Conte, E.I.T., Langan, Panama City, Panama, oconte@langan.com

ABSTRACT

This international case study focuses on the rigorous geotechnical interaction and results of a soil improvement program utilized to mitigate consolidation settlements of over 1.5 m [5.0 ft]. The extreme settlement results from very deep, nearly normally consolidated clay and the required high floor loading of a new Logistics Park near Bogota, Colombia. The general subsurface conditions consist of very soft clay extending to depths beyond the 50 m [164.0 ft] explored. A required 1.2 m [3.9 ft] thick fill combined with high floor loads resulted in an applied areal load of approximately 7 ton/m^2 [1300 psf] (equivalent to about 4.5m [15.0 ft] of fill). Langan recommended performing a test section to validate the initial consolidation settlement calculations and evaluate possible optimization of the prefabricated vertical drain (PVD) spacing and length. The test section sizing was designed to accurately represent the stresses at depth of the future structures. Extreme settlements of over 1.5 m [5.0 ft] in the center and large differential settlements of over 0.6 m [2.0 ft] were measured between the center and corners of the test section over a relatively short test time. Discussion on the methodology, instrumentation, measured results and future optimization are presented. The recommended soil improvement varied from the standard approaches typically utilized in the area.

Keywords: consolidation, wick drain, soft clay, Bogota clay, deep settlement, vertical drain, soil improvement

PROJECT LOCATION AND DESCRIPTION

The project site is immediately north-northwest of the city of Bogota in the Bogota Valley. The site is bordered with, and has historically been, farming land bordered to the south by the El Rosal-Bogotá highway. The overall site encompasses about 570,000 m^2 [141.0 acres] of gross area and about 484,000 m^2 [119.6 acres] of net buildable area. The warehouse complex will consist of 10 very large warehouses with footprints ranging from about 15,000 m^2 [3.7 acres] to 30,000 m^2 [7.4 acres]. The total building area is about 210,000 m^2 [51.9 acres] with most of the remaining areas being paved principal drives, truck parking or administrative parking.

The topography of the site is relatively flat and close to final grade in roadway areas. However, the warehouse floors will be raised about 1.2 m [3.9 ft] (equivalent to about 2 t/m^2 [370 psf] considering engineered fill) to allow for truck docking. In addition, the design floor loads are heavy and estimated to be up to 5 t/m^2 [930 psf] and equivalent to about 2.5m [8.2 ft] of fill. Geotechnical conditions at the site are very weak at depths of 50 meters [165 ft] or more, with soft compressible clays comprising the majority of the soil profile. The Bogota Valley is composed in some areas of very deep alluvial deposits. These deposits have been classified as an important challenge and limitation to the development of high/heavy structures such as the project in question for many years (Orozco, 2006). Soft clay deposits have been encountered even beyond depths of 100 meters [328 ft] in some regions of the Bogota Valley (Sanz, 1994). Extreme settlements can be expected if extensive and high permanent loads (above preconsolidation stress levels) are supported in these thick alluvial deposits.

A preliminary evaluation showed that the ground improvement design performed by other geotechnical consultants had not considered deep consolidation settlements appropriately and, therefore, the development was at risk of severe total and differential consolidation settlements and likely serviceability issues over the life of the structure. The local geotechnical consultants proposed that a ground

© 2018 Deep Foundations Institute

improvement system using short rigid inclusions was viable for the project. Due to the large areal extent of the applied surface loads, the structure would be subjected to extreme consolidation settlement of the clays below the depth of the rigid inclusions. For these reasons, a full-scale field test section was approved, constructed, instrumented, and monitored.

SITE SPECIFIC SUBSURFACE CONDITIONS

A former geotechnical investigation consisting of 24 borings and Cone Penetration Tests (CPT's) was conducted at the site, but only the upper 25 meters were investigated. Based on this previous geotechnical investigation, the general subsurface conditions consist of a "thin crust" of relatively stiffer silt underlain by very soft to soft highly plastic clay to at least 25 meters [82.0 ft]. Langan recommended and observed a confirmatory boring (L1) to a depth of 50 meters [164.0 ft.] in the area of the first phase development in order to document the presence of the soft clay at depths deeper than 25 meters [82.0ft]. In this boring, the very soft to soft clay layer was confirmed to extend down to at least 50 meters [164.0 ft]. The generalized stratigraphy of the site is presented in Figure 1 for reference. Geologic references for the area indicate the soft compressible clays may extend as deep as 85 meters [279.0 ft] and general alluvial deposits may extend to about 260 meters [853.0 ft] before rock is encountered (Sanz, 1994). In the borings performed, groundwater was observed at depths ranging between 1m [3.3 ft] and 6 meters [19.7 ft] below the existing ground surface at the time of drilling or within 24 hours thereafter. It is likely that stabilized water levels are generally around 4 to 4.5 meters [14.7 ft] below existing grade. These stabilized values may rise during periods of heavy precipitation. The following paragraphs summarize the subsurface strata:

Soft to Stiff Brown Clay (Stratum 1)

The uppermost stratum of clay is a thin "crust" and generally consists of soft to stiff brown clay with silt. The thickness of this stratum varies from about 3 to 5 meters [9.8 to 16.4 ft]. Standard Penetration Test (SPT) resistance N-values typically range from 2 to 17 blows per 0.3 meters [1.0 ft] and averaged about 5 to 9 blows per 0.3 meters [1.0 ft]. CPT tip resistance values (q_u) typically range from 1 to 4 kg/cm^2 [14.2 to 56.9 psi]. Natural moisture contents range from 40 to 70%, Liquid Limits range from 80 to 140% and Plasticity Indices (PI) range from 25 to 100%. Based on the coloration, N values, q_u values and penetrometer tests, this thin surficial stratum is generally over-consolidated and is assumed to behave in a relatively elastic manner under the loads to be imposed.

Very Soft to Soft Gray to Brown Clay (Stratum 2)

Below the thin pre-compressed Stratum 1, very soft to soft gray to brownish gray clay with traces of sand was encountered. The thickness of this stratum was determined to be at least 50 meters [164.0 ft] based on the supplemental boring, L1, performed by Langan. The stratum N-values ranged from 1 to 2 blows per 30 cm [1.0 ft] to a depth of 16 m [53.0 ft] and 1 to 4 blows per 0.3 m to a depth of 50 m [164.0 ft] CPT tip resistance values (Qu) typically range from 0.1 to 0.5 kg/cm^2 [7.1psi]. Natural moisture contents range from 90 to 180%, Liquid Limits range from 100 to 175% and Plasticity Indices (PI) range from 40 to 120%. By observations this clay appears to be normally consolidated. However, based on the consolidation tests performed for Langan in boring L1, this stratum is considered to be slightly over-consolidated with an average OCR of about 1.1 to 1.3, at least in the upper 30 m. The compression index, Cc, varies between 1.05 and 2.89 with an average of about 1.5. The recompression index, Cr, varies between about 0.09 and 0.44 with an average of about 0.3. The time-rate coefficient, Cv, derived from boring L-1, generally varies between about 0.025 cm^2/min [14.1 ft^2/yr] and 0.040 cm^2/min [22.6 ft^2/yr]. in the anticipated load ranges. This soft gray clay is considered very compressible and will exhibit significant consolidation settlement under the new load.

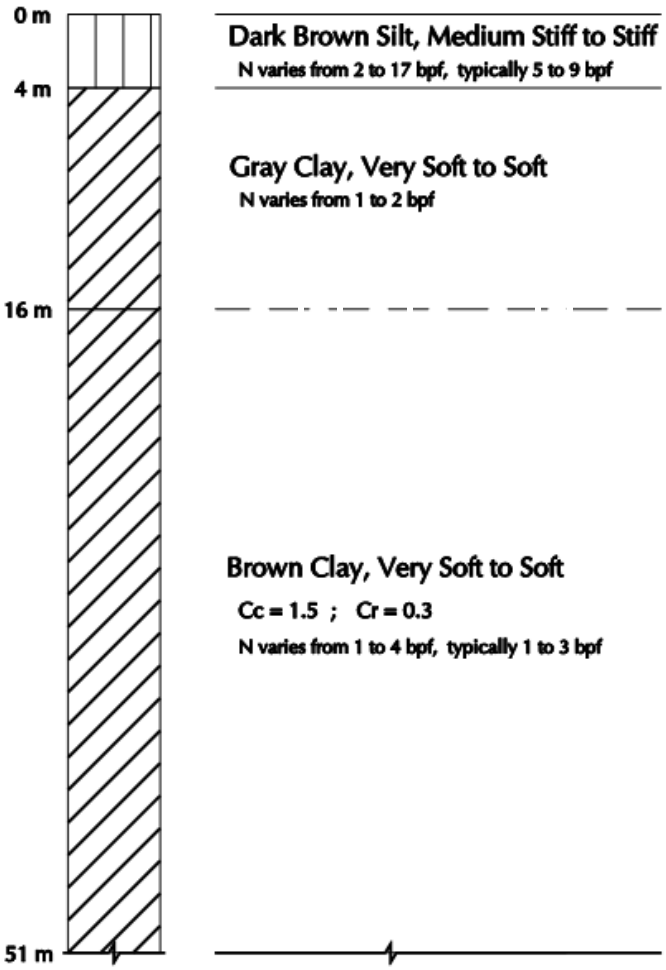


Figure 1. Summarized soil profile for boring L-1.

FULL SCALE PILOT TEST PROGRAM

A properly engineered, instrumented, and analyzed full scale field test section was recommended to better determine the performance (settlement behavior) of the proposed structures and to determine the most efficient ground improvement system for the project. Considering that the test section must simulate the imposed subsurface stresses of the proposed structures in a much smaller area, the surcharge height and geometry of the test section were designed to create relative stress compatibility at depth.

Test Section Layout

To determine the most effective geometry and surcharge height, stress distribution and consolidation analyses were performed using SETTLE 3D for several geometries and surcharge configurations. Because of the weak soil conditions extending to depths of greater than 50 meters [164 ft], extreme consolidation settlements at the site were originally estimated with significant contributions occurring at depth. These settlements without appropriate ground improvement would occur over a period of many years, potentially decades, due to the consolidation characteristics of the clayey soils underlying the site.

A summary of the stress distribution with depth for the warehouse floor stress, recommended test section area stresses and the design preload stress are presented in the following graph (Figure 2). The continuous black lines show the stress distribution versus depth for the estimated warehouse loading (line with filled squares) as well as the estimated preload stress (line with cross-hatches) under the design surcharge for

the final warehouse area. The dashed-line curve is the theoretical stress distribution versus depth for the recommended test section area discussed above.

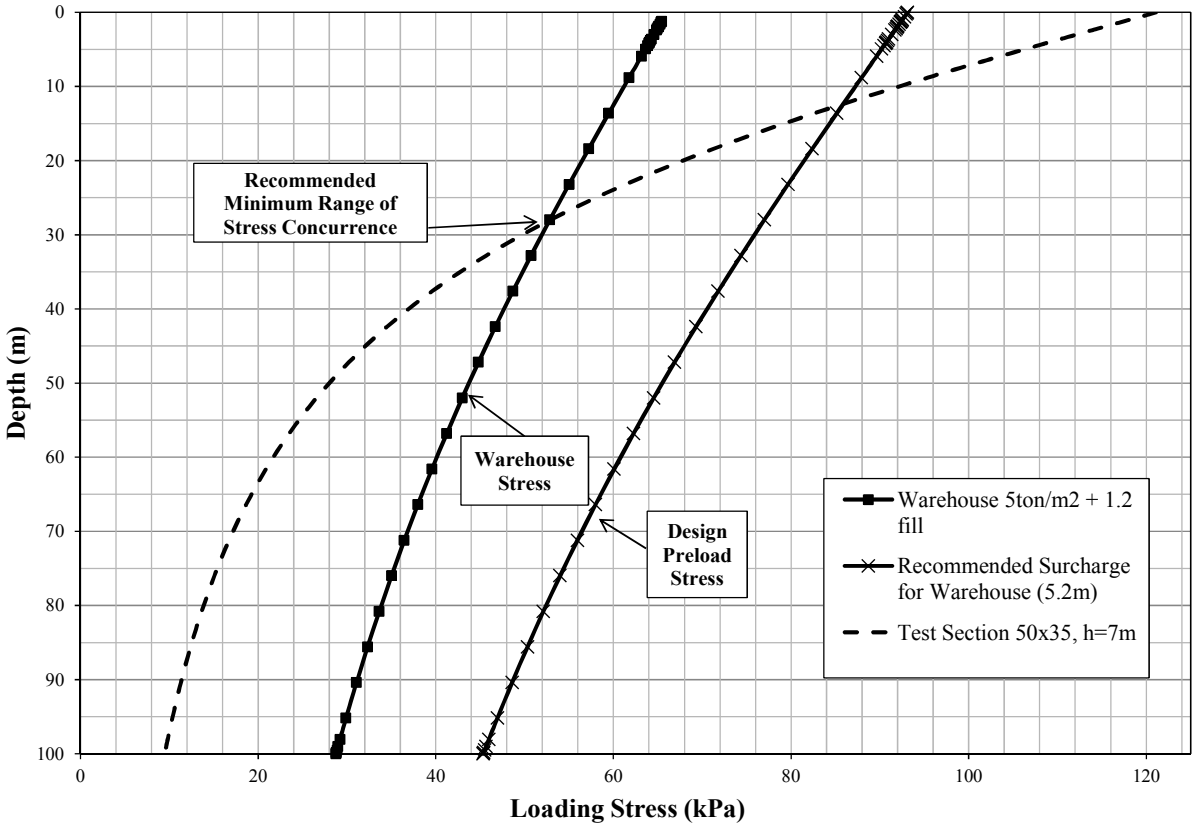


Figure 2. Loading Stress vs. Depth Varied Test Section Dimensions and Preloads LatAm Logistics.

The test section was designed to induce similar stresses than the future structures, particularly at depth (approximately 20 m [65.6 ft] to 30 m [98.4 ft]). Figure 3 on the next page shows the warehouse loading stress and estimated pre-consolidation pressures with depth. As shown in Figure 3, it was important to match the stresses at a depth of approximately 30 m because at this depth the pre-consolidation pressure was estimated to become greater than the stresses in the soil column. Measuring the subsurface behavior at greater depth was also a critical parameter for the test section because a greater range of ground improvement alternatives would be feasible if settlements were limited to the upper 15 to 20 m [49.2 to 65.6 ft]. Theoretical estimates of consolidation based on laboratory consolidation testing predicted significant settlement at depths beyond 20 m. The recommended minimum range of stress concurrence, shown in Figure 2, highlights the zone of the graph between 20 m [65.6 ft] to 30 m [98.4 ft] in which stress concurrence between the recommended test section and the proposed warehouse was obtained. Based on this analysis and due to budget and scheduling constraints, Langan concluded that a rectangular test area equivalent to 50 m [164.0 ft] by 35 m [114.8 ft], along with a surcharge of 7 m [22.9 ft], was necessary to induce similar design loading stresses at our target depth of about 30 m [98.4 ft].

Construction and Instrumentation Details

The test section was constructed between 9 October and 27 November 2017, in a future parking lot area of the project between two proposed warehouses. Wick drains were installed on a 1.5 m [4.9 ft] diagonal spacing pattern to a depth of 30 m [98.4 ft], over and penetrating through a working platform consisting of granular engineered fill and surficial drainage course. The surficial 40cm [1.3 ft] layer of crushed stone fill was placed to provide horizontal drainage for the wick drains. A non-woven geotextile was installed as a separator over the horizontal drainage layer and the fill material. The surcharge process consisted of

placing 30 cm [1.0 ft] layers until a height of 7 m [22.9 ft] (above original grade) was achieved. Figure 4 shows a plan view and cross sectional view of the test section for reference.

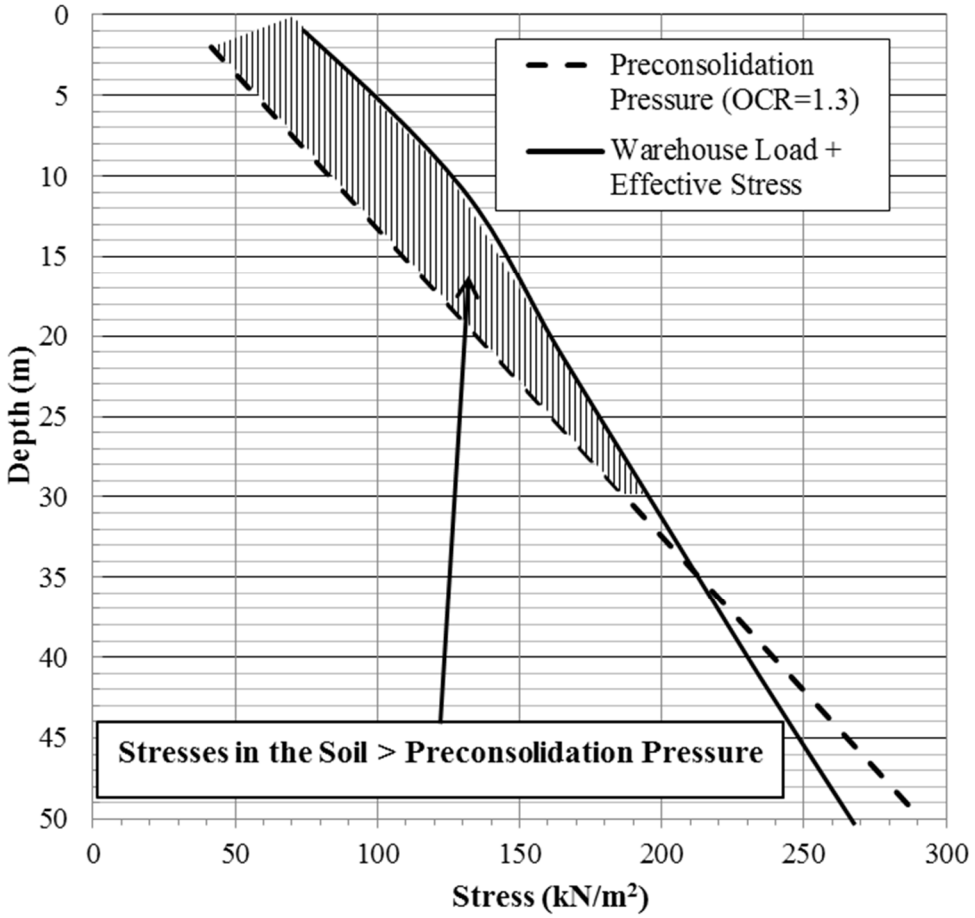


Figure 3. Warehouse Loading Stress and Pre-consolidation Pressure vs. Depth

The test section was instrumented with ten settlement plates (identified as SP-1 through SP-10), three installed near the center and the rest spaced throughout the mid-span and corners. Also, two multi-level extensometers ("spider magnets") were installed near the center of the test section on approximately 5 m [16.4 dt] depth intervals to a maximum depth of 40 meters [131.2ft]. These are identified as "DSE-A" and "DSE-B". The approximate locations of the instrumentation installed in the test section are presented in Figure 4. The instrumentation of the test section was monitored daily during the earthwork and surcharge placement and post surcharge top-out for a period of 8 weeks. Monitoring was performed by elevation survey using an optical level. The benchmark used was a bronze elliptical monument on a reinforced concrete stormwater culvert located approximately 20 m [65.6ft] away from the project entrance. The surveying procedure required the subcontractor to cross check the benchmark with another elevation reference located across the street on a bi-weekly basis. Extensometer measurements were performed using a magnetic probe by the specialty subcontractor. Extensometer readings were referenced to the top of the extensometer tube, which was in turn was surveyed using an optical level every time an extensometer reading was taken.

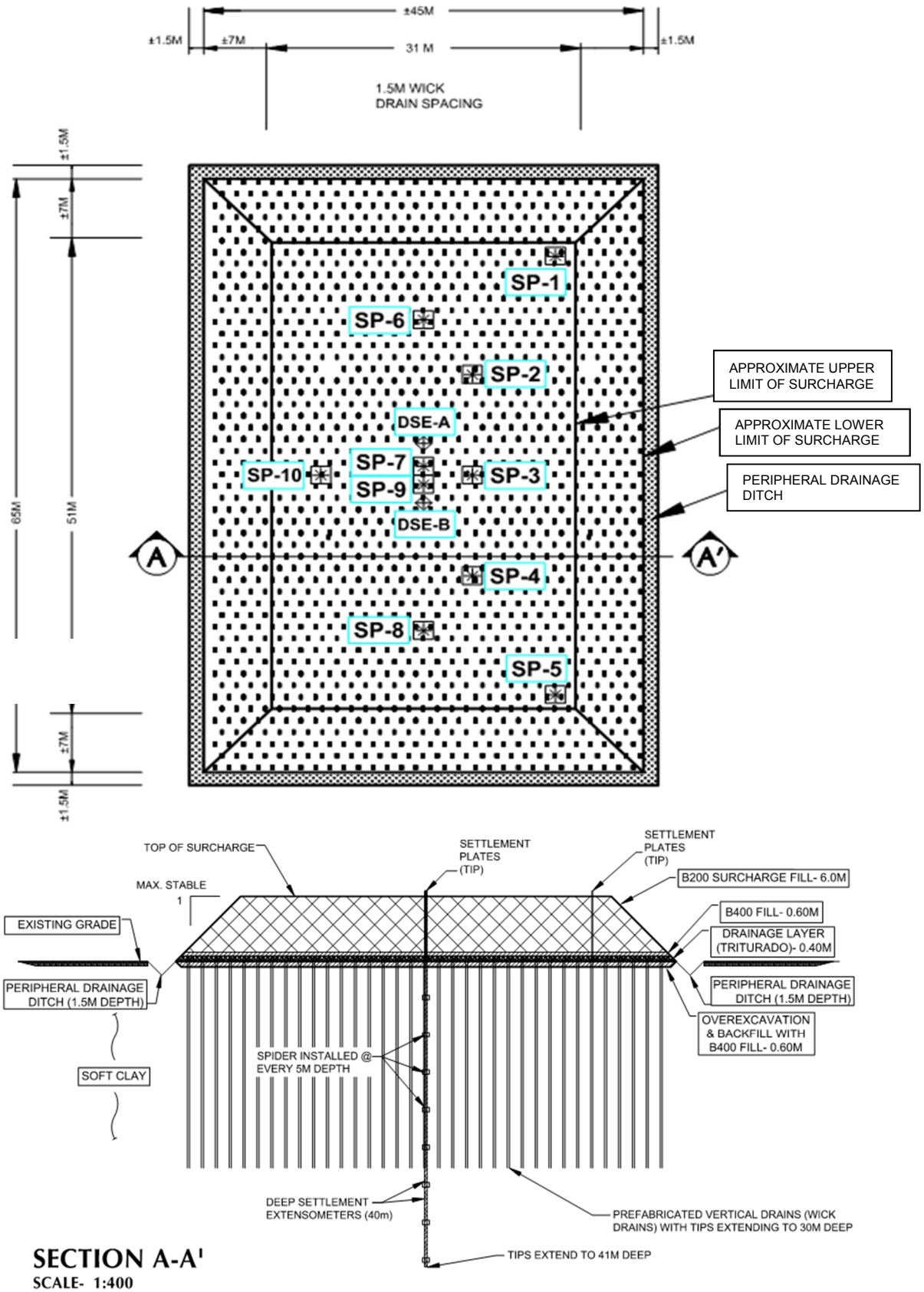


Figure 4. Plan and cross-section view of the test section

EVALUATION OF MEASUREMENTS

The test section was surcharged for a period of a little over two months after preload topout. Filling of the test section began on 1 November 2017 and preload top-out occurred on 28 November 2017. During this time, elevation readings were taken daily. Details and results of the monitoring program are summarized in the following sections.

Settlement Plates

Total consolidation settlement was measured using settlement plates. Settlement plates were installed near the original ground surface elevation prior to surcharging the test section, at the locations shown in Figure 4. Averaged settlement readings for the center, corner, and mid-span locations are shown in graphical format in Figure 5.

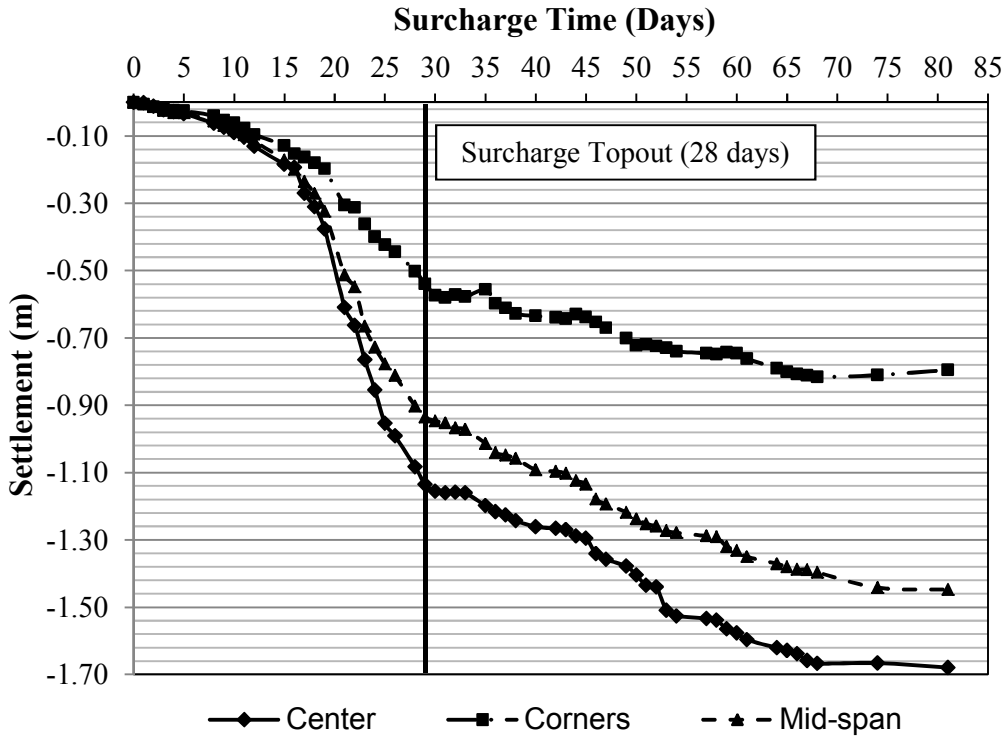


Figure 5. Averaged Settlement Plate Measurements

The averaged total settlement in the center of the test section was measured to be approximately 1.70 m [5.6 ft]. The averaged total settlement in the corner of the test section was measured to be approximately 0.80 m [2.6 ft]. The averaged total settlement between the center and the corner of the test section was measured to be approximately 1.45 m [4.8 ft]. The difference between the settlement observed in the corner of the test section and the center of the test section is approximately 1.10 m [3.6 ft] over an approximately length of 30m [98.4 ft]. These measured settlement values correlate very well to estimated total settlement values calculated using theoretical estimations based on laboratory consolidation testing.

Settlement readings show approximately 90% of the total consolidation occurring approximately 30 days after surcharge topoff. Considering the actual filling time, approximately 90% of the consolidation occurred within 45 to 60 days after the commencement of filling. This benchmark of consolidation (90%) is discussed because of its importance in soil mechanics theory and its use in determining the time-rate of consolidation parameter, which is used to evaluate the optimal spacing of wick drains.

Multi-level Extensometers

In order to measure settlement versus depth, multi-level extensometers (also identified as "spider magnets") were installed in the test section in the locations shown in Figure 4 labeled as DSE-A and DSE-B. Settlement versus depth is an important parameter when selecting targeted depths of improvement. Two multi-level extensometers were installed at the center of the test section. Both multi-level extensometers were installed in a 10 cm [3.9 in] borehole approximately 40 m [131.2 ft] deep, using mud rotary techniques. Spider magnets were attached to the outside of a 2.5 cm [1.0 in] diameter polyvinyl chloride (PVC) guide tube at 5 m [16.4ft] depth intervals. Thus, with this configuration, settlement measurements were taken in each extensometer at varied depths of 5 m [16.4 ft] (EXTA-1), 10m [32.8 ft] (EXTA-2), 15 m [49.2 ft] (EXTA-3), 20 m [65.6 ft] (EXTA-4), 25 m [82.0 ft] (EXTA-5), 30m [98.4 ft] (EXTA-6), 35 m [114.8 ft] (EXTA-7) and 40 m [131.2 ft] (EXTA-8). The elevation of the spider magnet was measured by lowering a magnetic probe sensor through the PVC guide tube that indicated the depth (below top of tube reference) at which each spider was located at any given time. By establishing the elevation of the top of the guide tube, using optical elevation surveying, the elevation for each spider magnet can be determined. Hence, the incremental settlement at any of the spider magnets would be the elevation difference of the respective magnet between any given time interval. Averaged measurements for both extensometers installed (DSE-A and DSE-B) are presented in Figure 6.

Measurements were acquired every day during construction of the test section and until approximately 80% of the total settlements occurred. After 27 days of monitoring and after the top out surcharge height was reached; the extensometers could not be measured due to obstructions to lowering the measuring probe. Two new extensometers were installed as a replacement about 3 meters [9.8 ft] away from the abandoned/obstructed extensometers. During installation of the new extensometers a data gap of approximately 12 days occurred (between 16 and 27 November 2017). Correlation using the settlement plates was made to estimate the consolidation of the different spider magnets while the extensometers were replaced.

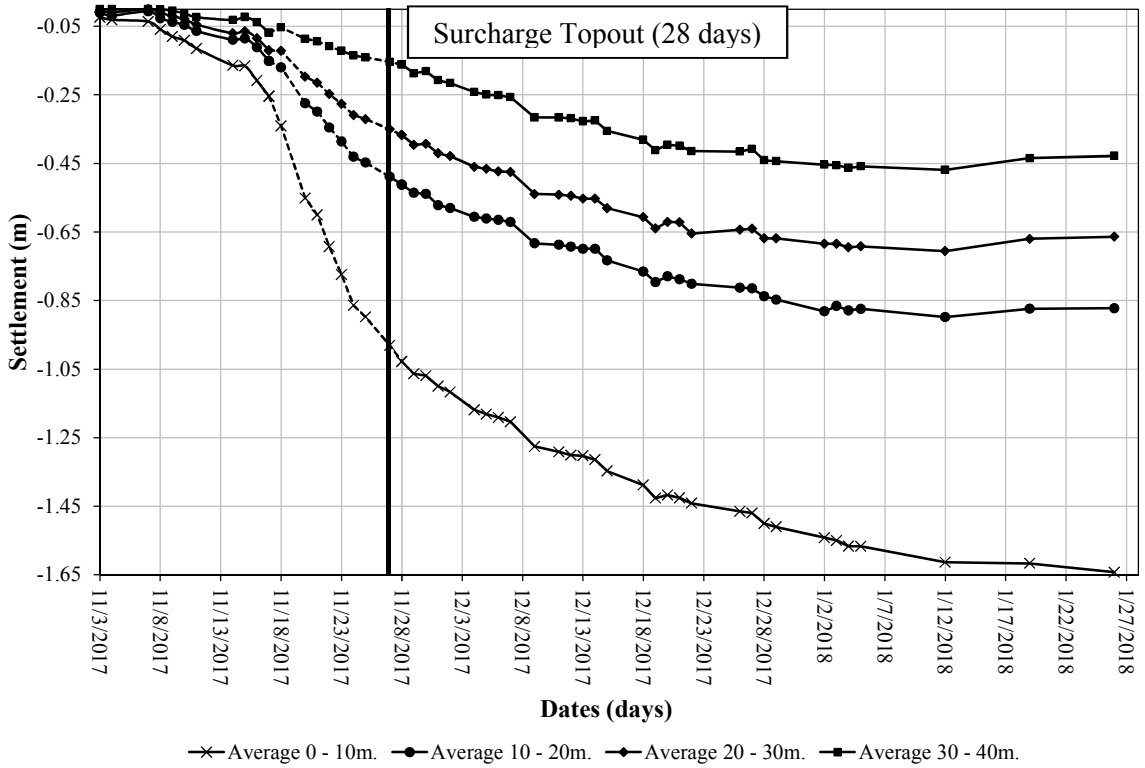


Figure 6. Settlement Values vs. Depth- Average Measurements for Extensometers.

In addition, a 0.15 m [0.5 ft] drop was measured on 7 December 2007. Interpolation and engineering judgment was used to fill both the data gap between replacement extensometer installations and to correct the anomalous readings on 7 December 2017. While caution should be exercised in analyzing the extensometer information, the trends in magnitude of settlement versus depth of each spider magnet appear to be suitably consistent and viable.

Measured settlements in the extensometers documented anticipated trends of lower magnitudes of settlement with depth. The following summary of approximate settlement versus depth is as follows:

- Below the 10 m [32.8 ft] depth, about 1.65m [5.4 ft] of settlement was observed
- Below the 20 m [65.6 ft] depth, between about 0.60 [2.0 ft] and 0.85 m [2.8 ft] of settlement
- Below the 30 m [98.4 ft] depth, between about 0.40 [1.3 ft] and 0.65 m [2.1 ft] of settlement
- Below the 40 m [131.2 ft] depth, between about 0.15 [0.5 ft] and 0.45 m [1.5 ft] of settlement

Deep settlement (below 30 m [98.4ft] to 40 m [131.2ft] depth) appears to stabilize or significantly reduce in rate approximately 30 to 45 days after surcharge top out.

EVALUATION OF TEST SECTION RESULTS AND CONSOLIDATION PARAMETERS

The data collected during the construction and monitoring of the test section was analyzed theoretically to better understand the full scale compressibility properties and behavior of the soft clays at the site. The data collected during the test section was used to optimize the SETTLE 3D (3-dimensional program) model in order to better represent full scale behavior. After analyzing the collected data from the test section, the geotechnical model was modified to correlate with the measured results. The adjusted geotechnical model settlement curve in comparison with the test section results are presented in Figure 7.

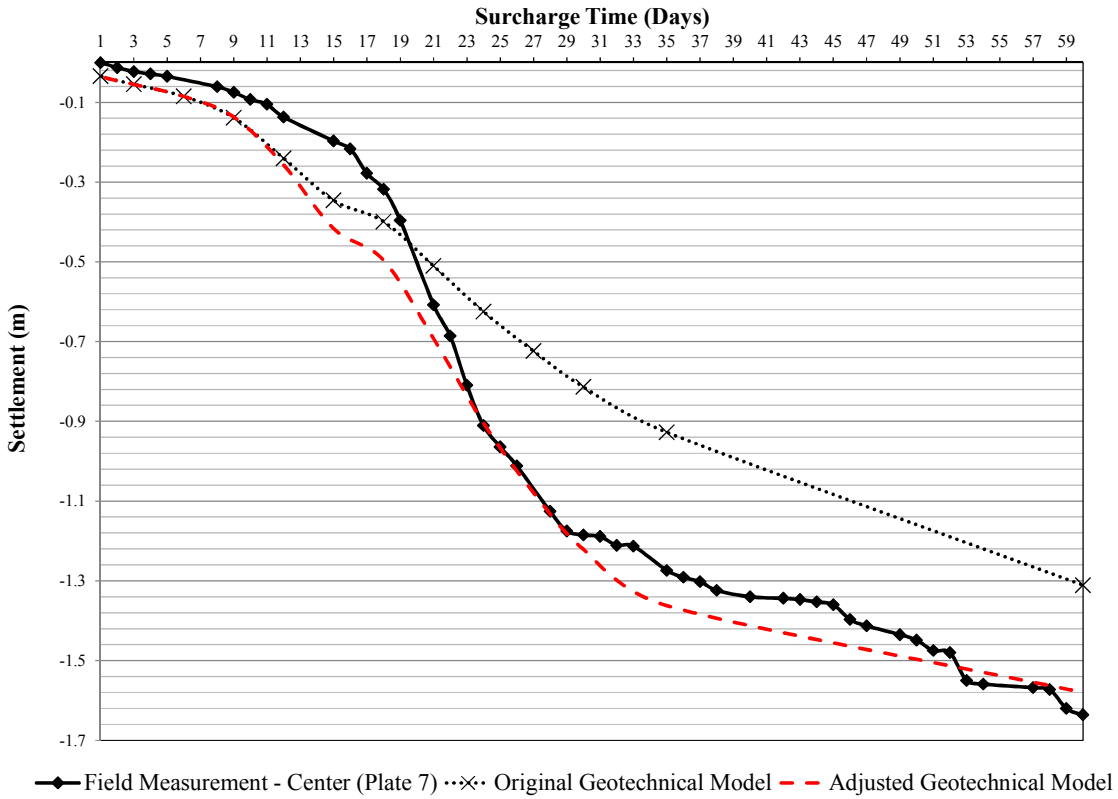


Figure 7. Comparison between Settle 3D models and field measurements.

Several variations of the model were attempted and compared to the test section results to evaluate the initial input values. The geotechnical model was adjusted to capture the time rate behavior of the test section as well as the settlement measurements obtained at different depths using the extensometers. The key parameters analyzed for consolidation estimation where the horizontal coefficient of consolidation (C_h), which was initially correlated from the laboratory testing results from the vertical coefficient of consolidation (C_v), and the pre-consolidation ratio of the soft clay strata. All geotechnical models and settlement curve estimates were estimated at the center. The soil properties used in the original and adjusted Settle 3D models are presented in Table 1.

Table 1. Key Soil Properties Used in the Settle 3D Models.

Input Property	Original Geotechnical Model	Adjusted Geotechnical Model
C_c	1.5	1.5
C_r	0.225	0.225
e_0	2.79	2.79
OCR	1.3	1.4
c_v	1.85 m^2/yr [20.0 ft^2/yr]	9.28 m^2/yr [100.0 ft^2/yr]
c_h	4.62 m^2/yr [49.7 ft^2/yr]	23.51 m^2/yr [253 ft^2/yr]

Based on the laboratory consolidation tests performed at the site prior to Langan involvement, all of the pre-consolidation ratios were close to 1 indicating a low degree of pre-consolidation or essentially "normally consolidated" clay. This contradicted published information about the Bogotá Valley that indicated slight pre-consolidation of the clay with depth. Laboratory testing performed after Langan's involvement showed slight pre-consolidation pressure in the clay which was in line with ranges shown in literature. Based on these findings, a pre-consolidation ratio of 1.2 to 1.3 was used for our initial evaluation of the site. The test section results confirmed the initial assumption of pre-consolidation ratio were reasonable as evidenced by the very close correlation of estimated total settlements and measured total settlements. The horizontal coefficient of consolidation (C_h) plays a significant role in the wick drain spacing design. Ground improvement design was preliminarily performed using a C_h value of 4.62 m^2/yr [49.7 ft^2/yr]. Based on the test section performance the adjusted model resulted in a C_h value of 23.51 m^2/yr [253.0 ft^2/yr], an approximate 5 fold increase. It is not uncommon for C_h to be a few folds higher than C_v as has been documented in literature (Lee et. al.). In addition to this, full-scale field testing has the capability of capturing the full extent of drainage characteristics and paths, which for a large area will result in more realistic and less conservative C_h values. Because of this, the test section settled at a faster pace than was initially estimated. This could be observed in Figure 7 by the difference in slope of the settlement curve and the better fit of the adjusted geotechnical model versus the original geotechnical model. This ultimately allows for an increased spacing in the wick drains.

Lastly, the depth of soil subject to consolidation was re-evaluated based on the measured deep settlements in the extensometers. The thickness of the consolidation strata, which is determined by the depth at which settlement was measured, affects the depth of improvement required. Although stresses caused by the large warehouse structures are capable of reaching depths in excess of 30 m [98.4 ft], the anticipated slight pre-consolidation at depth combined with the stress distribution of the surface loading was anticipated to result in relatively lower consolidation settlements below 30 meters [98.4 ft]. The test section showed more settlement associated with the deeper strata than preliminarily estimated. This could be caused by slightly less favorable compressibility properties below 30 meters [98.4 ft]. Although deep settlement measurements were greater than preliminarily estimated, the settlement readings stabilized or showed significantly reduced settlement rates in the relatively short time frame of 30 to 45 days post surcharge topout.

CONCLUSIONS

The deep compressibility potential of alluvial soils in the Bogotá Valley was confirmed through full-scale load testing program, including direct measurements on a representative test section. The extreme magnitudes of settlement observed, close to 2 m [6.5ft.] of measured settlement at the center of the full-scale field section, corresponded very well with our original estimates based on laboratory testing and theoretical analysis. The observed settlement magnitude was 10 to 20 times greater than the estimates presented by two local geotechnical consultants and the standing geotechnical recommendations for the site prior to our involvement. Essentially, the consolidation behavior below shallow ground improvement using rigid inclusions was disregarded. In this regard, another key finding that was established based on the extensometer measurements was that improved consolidation properties with depth were not observed and in actuality the measured deep consolidation settlements exceeded theoretical estimates based on laboratory tests. This could present significant challenges not only for large heavy structures as previously documented in literature, but for structures with large areal loadings that transmit stresses to greater depths, such as the subject Logistics complex. The results of the full-scale field test also suggests that deep ground improvement would provide significantly better performance than shallow ground improvement, particularly for projects with large heavy areal loading. Given the depth of weak compressible clays, and the estimated time required for consolidation settlements to occur at these depths due to the long drainage paths, wick drains combined with surcharge is an effective approach compared to other ground improvement techniques.

REFERENCES

Geotechnical Studies, Full-Scale Testing Data and Long Term Performance Data developed by Langan International for the Santa Maria Golf and Country Club Project, Panama City, Panama, 2006-2012.

Lobo-Guerrero Sanz, Alberto, “Geología del Subsuelo del Nororiente de la Ciudad de Santafé de Bogotá”, Lobo-Guerrero Geología Ltda., Bogotá, Colombia, November 1994.

Orozco R., Luis Fernando, “Asentamientos de Fundaciones en la Arcilla Bogota”, IV Encuentro Nacional de Ingenieros de Suelos y Estructuras, LFO Ingeniero de Suelos, Mayo de 2006.

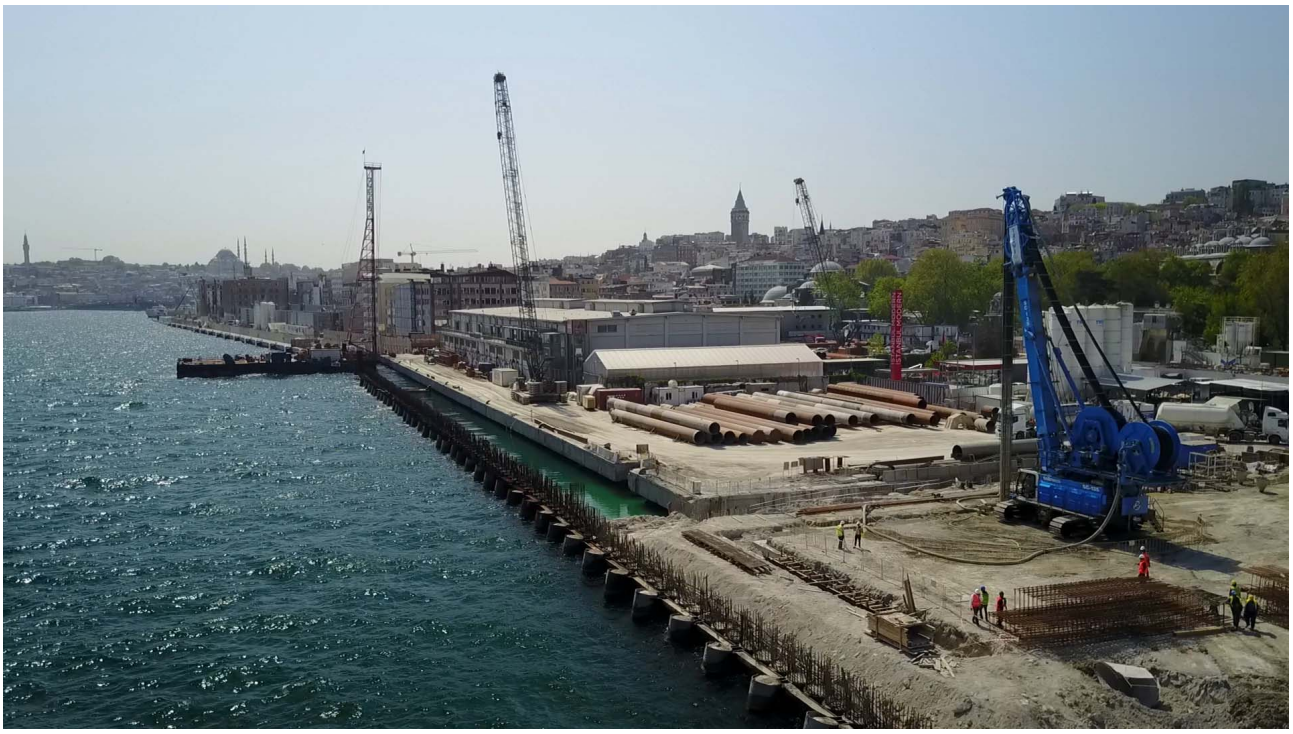
C.F. Lee et. al., “Soft Soil Engineering”, Proceedings of the Third International Conference on Soft Soil Engineering, 6-8 December 2001.

THE DEEP SOIL MIXING FOR THE GALATAPORT PROJECT IN ISTANBUL, TURKEY.

Marco Chiarabelli, SOILMEC North America, Inc.
Federico Pagliacci, SOILMEC SpA
Salvatore Miranda, Trevi SpA

The paper describes the adopted technologies and performance controls related to a special geotechnical engineering solution provided within the scope of the Galataport Project, in Istanbul, Turkey. The scheme is the one applied to the new quay of Salipazari, which is a combination of retaining structure and ground improvement, formed by a combi-wall, a reinforced concrete diaphragm wall and a soil improvement by deep soil mixing (Turbojet). The paper highlights the importance of employing cutting-edge technologies within the foundation engineering field and state-of-the-art electronic control devices, in parallel with the essential human expertise, in order to obtain the desired results in this high profile Project. The results of the in-situ and laboratory tests carried out on the improved soil are also presented.
Main discussed points are:

- History of Galataport and main Project details.
- Design principle and soil condition for the new quay of Salipazari.
- Difficulties encountered during execution of DSM.
- Preliminary field trial tests conducted to establish the operational parameters, with relevant in-situ and laboratory tests executed.
- Preliminary tests on material used for DSM (seawater and CEM IV SR).
- Electronic equipment mounted on the rig, which allows the automatic execution of DSM columns.
- Final QA/QC tests conducted to verify the performance of DSM, mainly consisting in: coring with relevant laboratory tests on samples (UCS + E_s), seismic refraction tomography and seismic cross hole tomography. Correlations between UCS and E_s, and between E_s and E_{dyn} are also presented.
- A cross section of the executed treatment could be inspected on site during excavation. Photos and considerations are also presented.



© 2018 Deep Foundations Institute

THE NEW QUAY OF SALIPAZARI

An interesting design solution was adopted for the seaside section of the new quay wall and terminal building. The new quay is composed of a combi-wall, formed by bored-cast-in-situ piles, excavated through a driven permanent steel casing, which was installed from a barge, while demolition of the existing deck-on piles was started (Figure 1.a). The main alignment of contiguous piles is supported by inclined piles installed at the center/center distance of 5m. Subsequently, the area was backfilled with a gravel/cobble size controlled fill (Figure 1.b), which was lately improved by a massive deep soil mixing treatment, consisting of 1500mm diameter tangent columns (Figure 1.c). The soil improvement had three main goals:

- to stabilize the loose man-made fill prior to the execution of the diaphragm wall,
- to reduce the risk of liquefaction of the in-situ loose sand below natural seabed level,
- to create a stiff block between the new quay wall and the diaphragm wall/terminal building, in order to properly dissipate the ship load.

Deep soil mixing columns were executed on a triangular pattern and an empty row was left in correspondence of the future diaphragm wall alignment. At this stage, the 1200mm thick diaphragm wall was constructed (Figure 1.d). The diaphragm wall has a reduced cut-off level and the area between new quay and diaphragm wall is designed to be a gangway platform for passengers. Once the diaphragm wall was completed, the bulk excavation and construction of gangway started, so that the new quay and the diaphragm wall were permanently connected (Figure 1.e). Activities were finalized by completing the whole excavation down to 13m below sea level, constructing the terminal building and removing the inclined support piles at seaside (Figure 1.f).

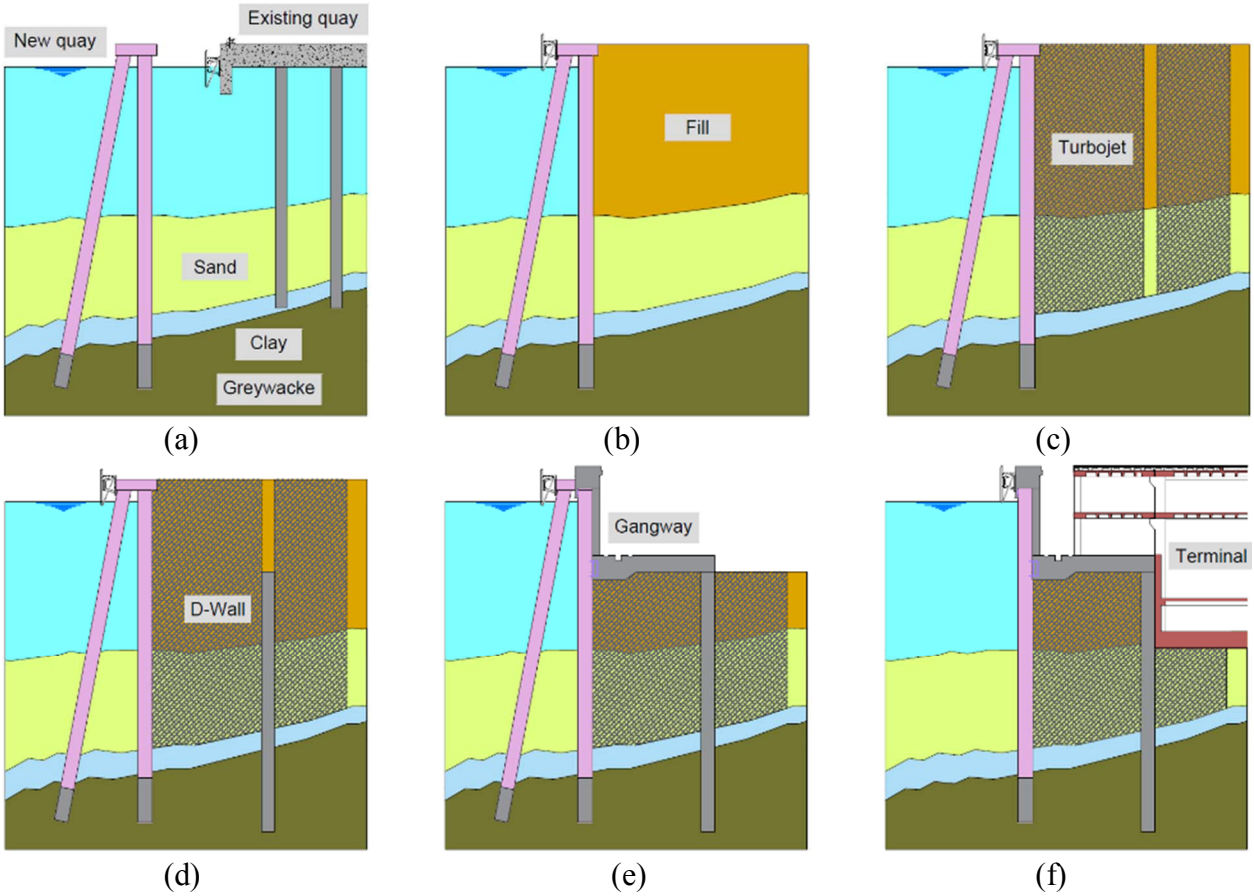


Figure 1. Construction phases of quay and terminal building at sea-side

TOWARD UNDERSTANDING THE SEISMIC PERFORMANCE OF RIGID INCLUSIONS

James R. Gingery, Ph.D., P.E., G.E., Hayward Baker, San Diego, CA, U.S.A,
james.gingery@haywardbaker.com
Lisheng Shao, Ph.D., P.E., G.E., Hayward Baker Inc., Santa Paula, CA, U.S.A.,
LShao@HaywardBaker.com
J. Tanner Blackburn, Ph.D., P.E., Hayward Baker Inc., Hanover, MD, U.S.A,
JTBlackburn@HaywardBaker.com

ABSTRACT

Rigid inclusions consist of grout columns installed using displacement auger or vibrated tooling. The columns are typically installed in an array to provide support for footings, mats, or embankments. Due to the relative small column diameter and low replacement ratio, the surrounding soils typically have minimal densification or improvement. A gravel load transfer platform is commonly used above the rigid inclusion head to distribute stresses more broadly to the supported structure. The axial stiffness and geotechnical engineering mechanics of rigid inclusion design are similar to those of deep foundation systems, but they are typically only lightly- or un-reinforced and are not structurally connected to the above-grade structure. The popularity of rigid inclusions is increasing in the Western U.S., where many urban areas are subject to moderate to high seismic hazard levels. However, the performance of rigid inclusions under seismic loading is poorly understood, and seldom addressed in current designs. The elements are brittle, with limited or no ductility and relatively low moment capacity, and therefore may be prone to damage under seismic loading. Three modes of seismic loading should be considered: inertial loading from the structure, kinematic loading from vertically propagating shear waves, and kinematic loading from ground failure-related permanent ground deformation. This paper focuses on the first two modes. A simplified procedure for evaluating kinematic and inertial loading of rigid inclusions is described, and its use is illustrated through application to a site in Southern California. The results show that moderate to severe kinematic loading can generate plastic hinges in the rigid inclusions. Engineering consequences of this hinging could include settlement or bearing failure.

Keywords: Rigid inclusions, seismic, kinematic bending, ground improvement

INTRODUCTION

In this paper the term 'rigid inclusion' (RI) refers to grout or grouted aggregate columns that are installed using either drilled or vibration displacement techniques. They are commonly installed in arrays to support vertical loads from footings, mats, or embankments. RIs are not structurally connected to footings they support. Rather, it is typical for a dense gravel load transfer platform (LTP) to be installed as a cushion between the RI head and supported footing or new fill. In cases of RI support of fill embankments, the LTP may be reinforced with horizontal layers of geogrid.

The vertical load carrying mechanism of RIs in one in which footing or embankment loads are transferred through the LTP and shared between the RI head and the soil around the RI. The stiff RI attracts more stress than the softer soils around it. Stresses imparted to the soil cause settlement of the soil which applies negative skin friction to the RI until a neutral plane[1] is reached, at which point load is shed back from the RI to the soil. Fig. **1** presents an illustration of this concept.

[1] The neutral plane is the depth at which the ground and the RI settlement are the same.

© 2018 Deep Foundations Institute

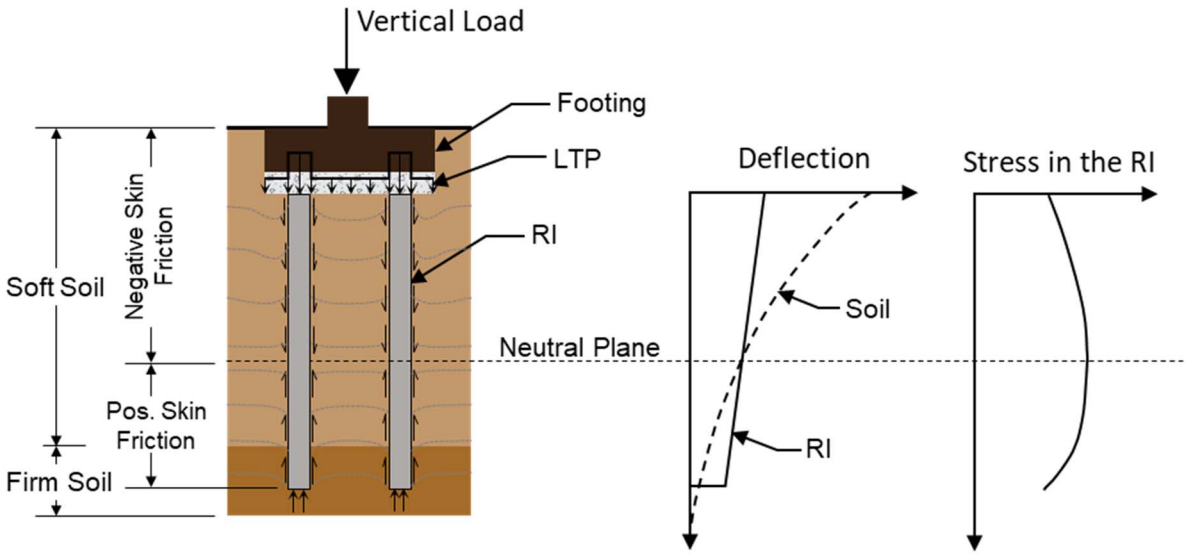


Fig. 1. Schematic vertical load transfer mechanism of RI-reinforcement

RIs differ from other stiff columnar forms of ground improvement, such as deep soil mixing and jet grouting, since these techniques generally have higher replacement ratios and lower strengths and stiffnesses compared to RIs[2]. While many of the same seismic loading principles apply to the design of mechanically mixed and jet grouted soilcrete columns, the stiffness, strength, and area replacement ratio differences compared to RIs mean that significant differences in response can be expected.

In the U.S., RI diameters typically range from 12 to 18 inches and spacing ranges from 3 to 7 diameters. This yields typical area replacement ratios (A_r, area in plan of the rigid inclusions divided by the gross treatment area) of 1.5 to 10 percent. In comparison, typical A_r values for vibro-replacement stone columns, which are frequently designed to densify *in situ* soil, are 8 to 20 percent. *In situ* soil densification is possible in the upper range of RI A_r, but little to no densification is expected of RIs in the lower range typical A_r. If densification is expected, and used in the project design, soil densification should be verified by post-construction exploration. RIs are identified by various industry trade names including: Controlled Modulus Columns, Grouted Impact® Piers, GeoConcrete® Columns, Cast-in-Place Ground-Improvement Elements, Controlled Stiffness Columns and Drilled Displacement Columns™.

Modern RIs were developed in the 1970's in Europe IREX (2012). Their popularity in the U.S. has been increasing in the past approximately 20 years, and in recent years they have seen increasing use in areas of the U.S. with moderate to high seismicity, such as California and the Pacific Northwest. Publicly available information regarding the performance of RIs in actual seismic events is limited. Moreover, very little research has been performed on the seismic performance of RIs, and there is very little guidance available on seismic analysis and design methods for RIs.

This paper contains a brief review of the limited literature available on RI seismic analysis and design; followed by a discussion of the fundamental mechanisms of seismic loading on RIs and potential damage modes that could affect the seismic performance of structures supported by RIs. Finally, a simple method for evaluating RI seismic loading is proposed, with demonstration of the method on a sample site in Southern California.

[2] Typical soil cement unconfined compressive strengths range from 100 to 500 psi and typical rigid inclusion UCS range are 2,500 to 4,000 psi. Grout is typically about 20 to 120 times that of soil-cement.

SEISMIC LOADING MECHANISMS AND DAMAGE POTENTIAL OF RIGID INCLUSIONS

Although RIs are distinctly different from deep foundations in that they are not structurally connected to the superstructure, the seismic loading mechanisms are very similar. While RI's primary function is for support of vertical loads, like piles they are not immune from seismically-generated lateral loads. This has been recognized by IREX (2012), which identified two seismic loading mechanisms that are well known for piles (e.g., Mylonakis and Nicolaou 2002): 1) kinematic loading from ground deformation; and 2) inertial loading from the dynamic response of the superstructure. These mechanisms are illustrated schematically in Fig. 2, where ground deformation produce the kinematic bending moments and the seismic superstructure response produces inertial loading (shear load V and Moment M), which top load the RI and induce moments.

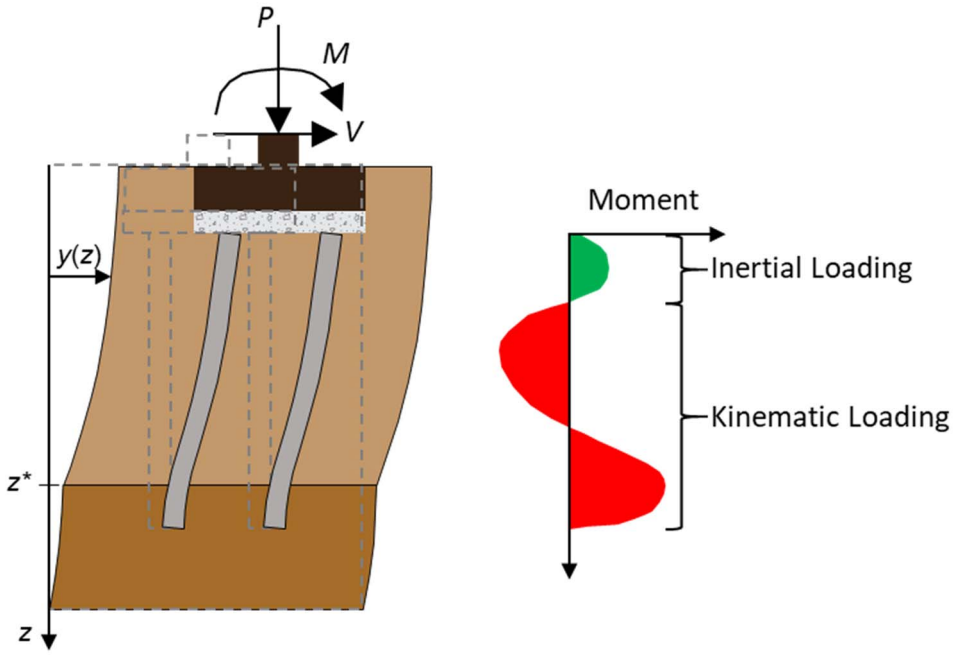


Fig. 2. Inertial and kinematic loading mechanisms of rigid inclusions.

Kinematic Loading from Wave Passage or Lateral Spreading

Kinematic bending has long been recognized as a source seismic loading on piles (e.g., Margason and Halloway 1977). The kinematic loading can either be from vertically propagating shear waves that cause (mostly) transient deformations, or from permanent ground deformation that results from ground failure such as slope instability, ground lurching or liquefaction lateral spreading. Damage in piles tends to be concentrated at interfaces between stiffer and softer soil where inflection points in the displacement profile occur (e.g., see z^* in Fig. 2) (Mizuno 1987).

A classic example of kinematic pile bending damage that occurred to the NHK building in the 1964 Niigata, Japan earthquake is shown in Fig. 3 (Hamada 1992). The photo shows an excavation that was made to expose pile foundations below a building at a site where about 3 to 6 feet of liquefaction-induced lateral spreading occurred. The piles hinged, formed pins, and, in some cases, sheared off near the top and bottom of a liquefiable layer through which they penetrated. These were 14 inch diameter cylindrical piles with relatively low levels of longitudinal reinforcement and minimal confining steel, resulting in relatively low flexural ductility.

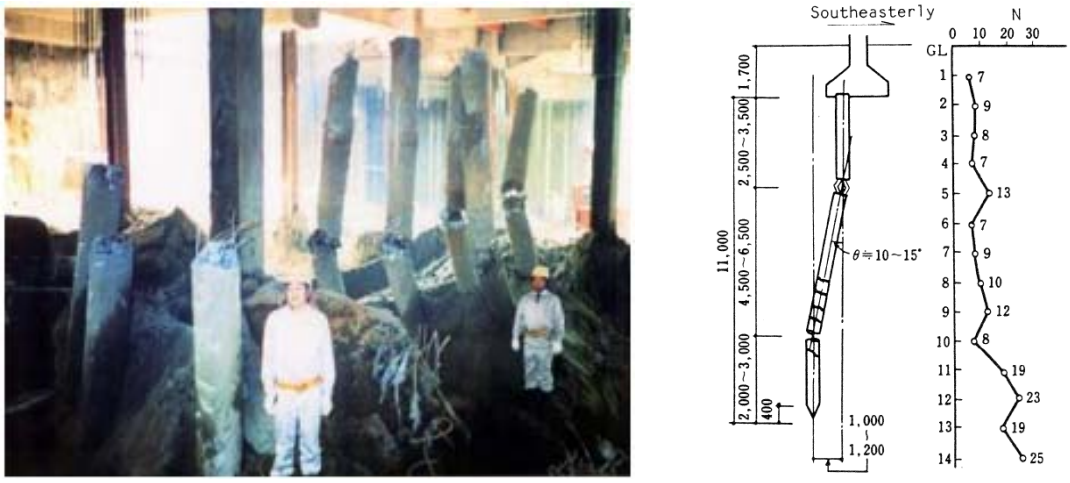


Fig. 3. Piles damaged to the NHK building in the 1963 Niigata, Japan earthquake as a result of kinematic loading from lateral spreading.

Many design codes recognize the kinematic pile bending mode, and include requirements for analysis and detailing. Caltrans (2017) requires analysis and design of bridge pile foundations for kinematic loading by lateral spreading. Section 1810.2.4.1 of the 2016 International Building Code (ICC 2016) requires that piles be specifically designed for curvatures resulting from kinematic loading, or else detailed in accordance with certain IBC and ACI 318 (ACI 2014) requirements that provide enhanced flexural capacity and ductility.

Loading from Inertial Response of the Superstructure

Inertial loads imparted to the footing from the superstructure (P, V and M in Fig.'s 2 and 4) are resisted by a combination of passive pressure (σ_p) and shear resistance between the base of the footing and top of the LTP. The LTP shear is then transferred partially to the RI head (V_{RI}) and partially to the soil (V_{soil}). Figure 4 shows a free body diagram of the footing and LTP, with the lateral forces shown in diagram (a) and the moments and vertical forces shown in diagram (b). Lateral loads transferred to the ground as passive resistance (σ_p) and LTP-soil shear (V_{soil}) generate shear deformation of the ground below the footing that can result in kinematic loading (additional to the wave passage kinematic effects) to the RI. Shear forces imparted on the RI head are analogous to a pile with pinned head condition and an applied shear load.

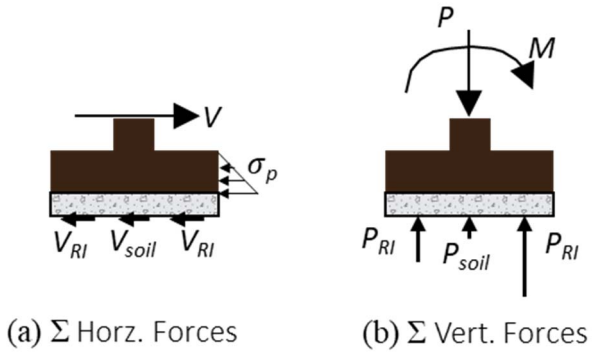


Fig. 4. Free body diagram of Footing and LTP under seismic loading conditions

RI Seismic Vulnerability and Performance

Whereas RIs are either unreinforced or contain minimal steel reinforcement, they are structurally brittle and non-ductile, and vulnerable to damage under bending. To the authors' knowledge, there are no case histories of RI ground improvement that has been subjected to a Western U.S.-type design-level seismic event. Nor have large scale, shake table or centrifuge experiments been performed. Therefore, RI technology is unproven in terms of its seismic performance. This is in contrast to other ground improvement methods that have been used in seismically active areas for many decades such as stone columns, jet grouting, and deep soil mixing. These methods have been the subject of extensive experimental research (e.g., Adalier et al. 2003, Rayamajhi et al. 2015) and have been generally performed well in significant earthquakes (Hausler and Sitar 2001, Martin et al. 2004). Indeed, there is an acute need for academic research into the seismic performance of RIs.

Considering the lack of performance data and the potential fragility and damage susceptibility of RIs under seismic loading, it is critical that they be analyzed and designed appropriately for earthquake effects when used in seismically active areas. The following sections present potential methods of analysis and a sample application of these methods.

RIs that undergo significant bending due to seismic loading may develop plastic hinges, which, depending on the ductility of the RI and level of loading, could degrade to pins, dislocate in shear, crush, etc. Fig. 5 shows potential failure modes that could occur when hinges develop in an RI. Cyclic loading of an RI hinge could result in crushing, softening and bulging of the hinge zone, which would lead to compression of the hinge zone and additional vertical deformation of the RIs and footing, as shown in Fig. 5(a). Fig. 5(b) shows a mode in which permanent shearing displacement of a soft soil zone results in permanent footing offset and potential settlement (as in the case of the NHK building in Fig. 3). Where RIs are relied upon to prevent footing bearing capacity failure, development of hinges may lead to foundation bearing failure, as shown in Fig. 5(c). Fig. 5(d) shows concentrated shearing of a weak soil layer which could lead to RI dislocation and loss of bearing capacity. Plain grout RIs are considered more susceptible to these failure modes, since a plastic hinge without reinforcing steel loses all structural continuity and has no ductility.

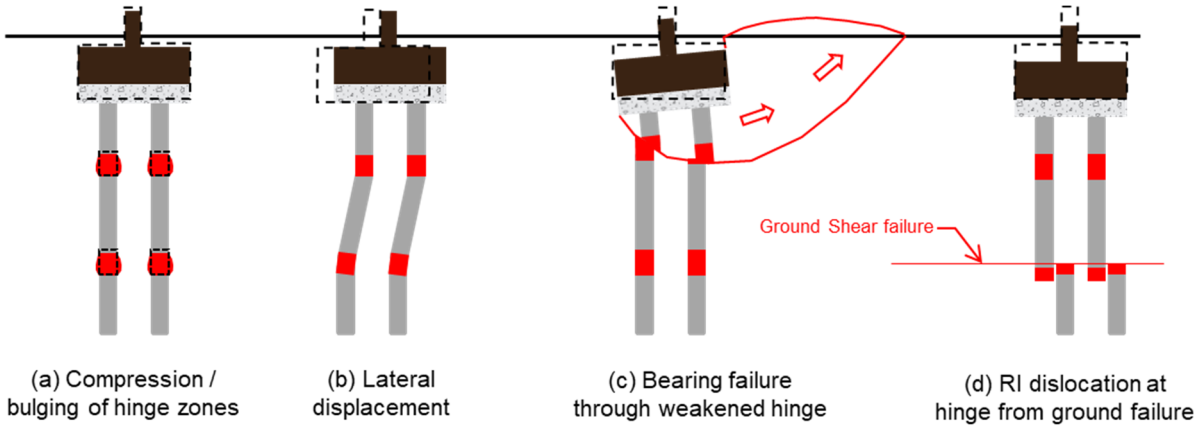


Fig. 5. Examples of damage modes resulting from RI hinge development

METHODS OF ANALYSIS

Because of the complex soil-structure interaction between the RIs, LTP, structure, and surrounding soils, three-dimensional dynamic time history numerical analyses would likely provide the most representative

evaluation of the RI ground improvement system performance. However, the effort and expense involved in such analyses is seldom justified, except for large scale and critical projects. For routine projects, a simplified approach with a level of rigor similar to that of a typical pile design analysis is warranted. Inertial and kinematic loads can be evaluated by applying a pseudostatic analysis of a beam on a nonlinear Winkler foundation ("p-y"); this analysis can be readily performed with commercial software such as LPILE. As described earlier, the loading is decomposed into kinematic and inertial components. The loads are then applied to the RI to determine the potential for plastic hinge formation. If hinges form, consequential failure mechanisms and structure performance should be evaluated. More details on the components of this analysis are provided herein. Because of space limitations, the analysis methods in this paper focus on kinematic loading from wave passage effects. However, ground failure displacements should not be ignored since they are generally greater in magnitude than wave passage displacements, produce more severe loading and have more potential to generate damage. The pseudostatic p-y method of the analysis used herein for wave passage loading can also be used for ground failure loading (e.g., Caltrans 2017).

Kinematic Loading Evaluation

The pseudostatic beam on nonlinear Winkler foundation approach has been shown by Tabesh and Poulos (2001) to provide reasonable estimates of pile bending moment and shear resulting from kinematic wave passage loading. This evaluation is made using a decoupled method, where free field soil displacements ($y(z)$ in Fig. 6) are determined by a ground response analysis, then the peak ground displacements are applied as on the free field end of the p-y springs. The ground response analysis can be performed using one dimensional equivalent linear or nonlinear methods (e.g., Hashash et al. 2016), or simplified shear strain estimation methods can be used (Gingery 2007, Gingery et al. 2009, FHWA 2009). The former is more rigorous and preferred for critical and important projects. The free field displacements are applied to the free-field end of the p-y springs as shown in Fig. 6.

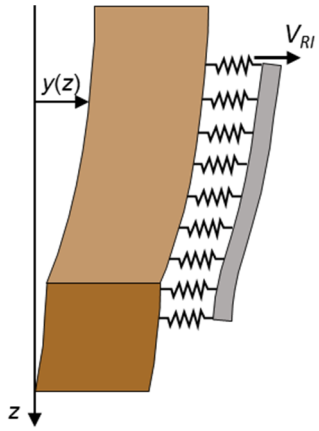


Fig. 6. p-y analysis or RI loading due to seismic wave passage

Inertial Loading Evaluation

As shown in Fig. 4, inertial loads imparted on the footing are resisted by soil passive pressure on the side of the footing and LTP (σ_p), shear between the LTP base and soil (V_{soil}), and shear between the LTP and RI (V_{RI}). The load V_{RI} can be easily represented in the p-y method with a top shear load (head free to rotate – free head condition) (see V in Fig. 6).

The loads σ_p and V_{soil} impart shear stresses to the ground that generate shear strain and ground displacements in addition to those from vertically propagating shear waves. IREX (2012) suggests calculating the profile of ground displacement that results from footing shear loading as:

$$y_V(z) = \int_{z_0}^{0} \frac{\tau_{Iner}(z)}{G(z)} dz \quad [1]$$

where $\tau(z)$ is the shear stress imparted to the ground by the inertial load, $G(z)$ is the shear modulus of the soil (reduced in accordance with expected shear strain levels) and z is the depth below the RI head. For simplicity the shear stress at the foundation level for (S_{col}) can be calculated as:

$$\tau_{Iner}(z = 0) = \frac{V_{soil} + P_p}{{S_{col}}^2} \quad [2]$$

where P_p is the total passive force. The $\tau(z)$ profile should spread and dissipate with depth in a manner similar that of vertical stresses (e.g., Boussinesq or using the 2V:1H spreading rule). Partitioning of V to V_{soil}, V_{RI} and σ_p will depend on the relative shear stiffness and strength of each of the resisting forces. A rigorous determination of this partitioning would require three-dimensional soil structure interaction numerical analyses. For routine project where this is not practical, this partitioning can be performed using some judgment. This analysis proposes that half of V can be assigned to V_{soil} and P_p and the other half can be assigned to V_{RI}. Sensitivity analyses can be conducted to assess the influence of this partitioning. Other partitioning methods are described in IREX (2012). The peak inertial response may occur in or out of phase with wave passage loading, so the analysis should include positive and negative polarities when evaluating load combinations.

EXAMPLE ANALSYIS

Site, Foundation and RI Parameters

The application of the simple analytical techniques discussed above is illustrated through a hypothetical site located in the Los Angeles Basin area of California. The project consists of a multi-story building with a typical column design load of 450 kips, a seismic shear load of 108 kips per column and structural column spacing of 30 feet in each way. Footings are 8 by 8 feet with 4 feet of embedment. The design earthquake considers a peak ground acceleration (PGA) of 0.65g based on a magnitude 7.5 event. There are four RIs per footing, each extending from 5 feet to 35 feet below ground surface and bearing into a dense sand layer. A one-foot thick dense gravel LTP separates the footings from the RI head. The soils consist of 4 feet of new dense sand fill over sand and clay alluvium. Groundwater is below a depth of 50 feet. Soil engineering properties are summarized in Fig. 7. The alternating sand/clay layering leads to stiffness variations within the profile, which are shown to affect seismic response and RI loading.

The RIs are 16 inches in diameter with two RI configurations are considered: (1) plain unreinforced concrete and (2) inclusion of a single No. 10 (1-1/4 inch diameter) bar with 60 ksi yield strength. The unconfined compressive strength (f_c') of the RI concrete is 2,500 psi and the Young's modulus is $57{,}000\sqrt{2{,}500psi} = 2{,}850\ ksi$. The RI's were modeled as nonlinear beams using moment curvature relationships as described herein. For the unreinforced RI the nominal moment capacity is calculated as $M_n = S \cdot (p_{RI} + f_r)$, where S is the section modulus, $p_{RI} = P_{RI}/A_{RI}$ is the pressure from the axial thrust force (P_{RI}) and cross section area (A_{RI}). This assumes brittle failure will occur when tensile cracks develop at the RI, which is reasonable considering the cyclic and bi-directional nature of the kinematic loading will crack the RI in multiple radial directions. The average thrust force in the RI was as 80 percent of ¼ (four RIs per column footing) of the column load, which is 90 kips. The modulus of rupture was calculated according to ACI (2014): $f_r = 7.5\sqrt{f_c'} = 375\ psi$. This results in a nominal moment capacity of 27.6 kip-feet for the unreinforced RI. As

shown by the moment-curvature relationship in Fig. 8, the unreinforced RI is elastic in bending until it reaches the nominal moment, at which point it is assumed that brittle failure occurs and all moment capacity is lost. For the reinforced RI, a fiber element analysis was performed in LPILE to develop the moment curvature, which accounts for concrete cracking, crushing, and steel yielding. The resulting moment curvature is shown in Fig. 8. The nominal moment of the reinforced RI is 55.3 kip-feet, about double that of the unreinforced RI.

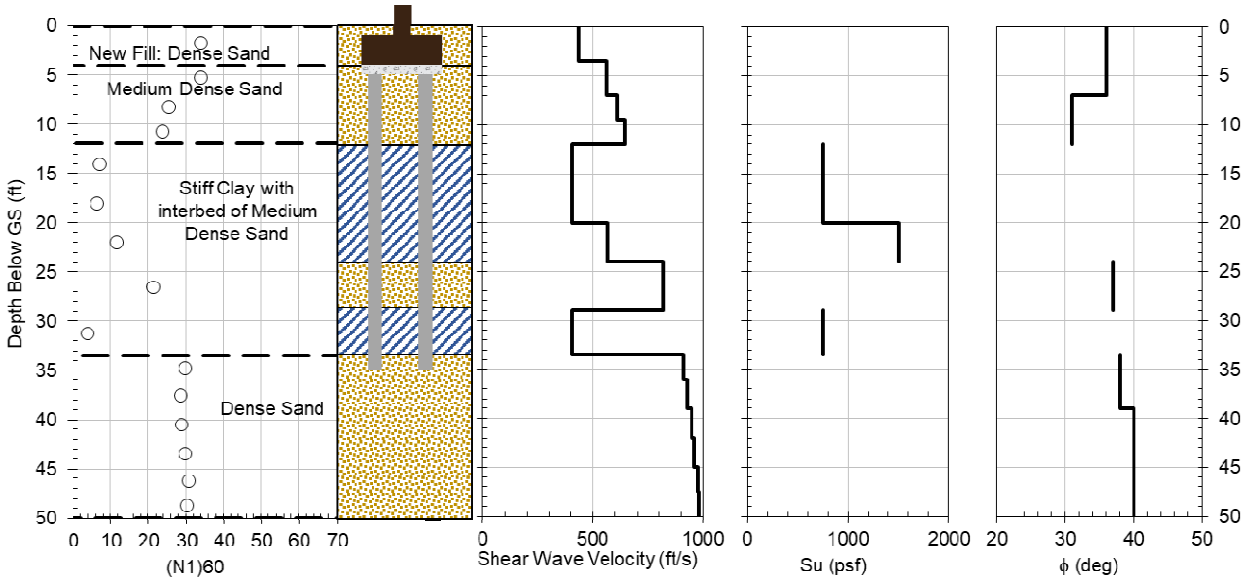


Fig. 7. Example site stratigraphy and soil engineering parameters

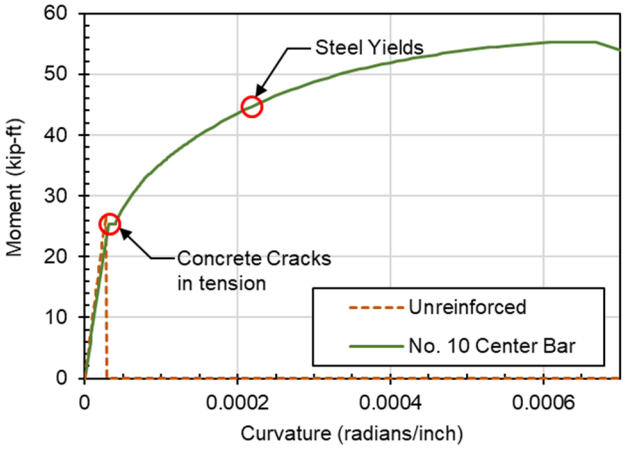


Fig. 8. Moment-curvature behavior of unreinforced and center bar-reinforced RIs

Kinematic Loading Evaluation

Ground displacements from vertically propagating shear waves were calculated using a simplified method adapted from Gingery (2007), where the peak strain (γ_{peak}) is estimated for each depth as:

$$\gamma_{peak} = \frac{3}{2} \cdot \gamma_{eff} = \frac{3}{2} \cdot \frac{\tau_{eff}}{G} \quad [3]$$

where γ_{eff} is the effective shear strain and the effective shear stress calculated by:

$$\tau_{eff} = \frac{2}{3} \cdot \frac{PGA}{g} \cdot \sigma_{v0} \cdot r_d \quad [4]$$

where σ_{v0} is the initial total vertical stress, and r_d is the stress reduction factor. Cetin et al. (2004) was used to calculate r_d since it includes an average shear wave velocity term that accounts for site-specific ground stiffness whereas other methods do not. This calculated shear strain assumes a free field condition, which is reasonable since the shear stress reduction for the overall area replacement ratio of 2 percent would be negligible (Rayamajhi et al. 2014). The small strain shear modulus was calculated from the shear wave velocity and density (ρ), $G_0 = \left(V_s{}^2 \cdot \rho\right)/g$. The strain compatible shear modulus, G, was then determined using modulus reduction curves by Darendeli (2001), modified for strength compatibility using Gingery and Elgamal (2013), and iterating until a strain compatible value was reached. The resulting ground displacement profile is shown in Fig. 9.

Inertial Loading Evaluation

Ground shear displacements from transfer of inertial loads back to the ground were calculated using Equations 1 and 2, taking $V_{soil} + V_p$ as half of the 108 kip seismic shear load. The shear stress was reduced with depth according to the 2:1 (V:H) spreading rule. The resulting soil shear displacement at the ground surface was only 0.3 inches, compared to the wave passage displacement of 7.6 inches. Fig. 9 shows the ground displacement profile with addition (inertial loads in-phase with kinematic loads; 'positive') and subtraction ('negative polarity') of the inertial displacements. Since half of the seismic shear load was taken by passive resistance and LTP-soil friction, the remaining force is resisted by shear loading of the RI head. The load per RI head is 50%·108 kips / 4 RIs = 13.5 kips

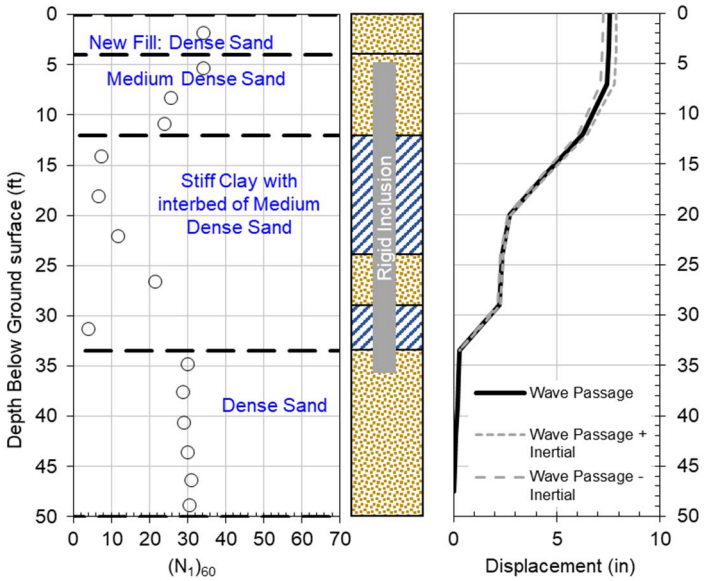


Fig. 9. Seismic ground displacements due to wave passage, and with positive and negative polarity inertial load ground shearing.

Analysis of Kinematic and Inertial Loads

LPILE v2016, a commercially available software package, was used to perform the RI seismic demand calculations. Preliminary analyses showed that the case of negative inertial load polarity (inertial loading direction is opposite of the kinematic loading) resulted in the maximum loading conditions, so only the results of the negative inertial load polarity analysis are presented herein. The pile is loaded with the ground displacement profile in Fig. 9 and the top shear load of 13.5 kips.

The brittle behavior of the unreinforced RI requires that special care be taken when applying loading for this case. The kinematic load was applied incrementally until the first hinge location was identified. The hinge zone was then manually assigned a flexural stiffness of near zero (nonzero for numerical stability purposes) and subsequent increments of the total kinematic loading were applied. The incremental load stepping and manual assignment of hinge zone stiffness was repeated until the full kinematic loading was reached. This incremental loading procedure is essential to achieving a realistic response for the case of unreinforced RI where the moment curvature behavior is very brittle.

Fig. 10 presents the resulting pile shear and bending moment for the unreinforced case. Three plastic hinges develop at depths (from the pile head) of 5, 16 and 24 feet when only 10% of the kinematic load plus all of the negative polarity inertial load is applied. These depths correspond to locations of inflection points in the soil profile. For the 100% loading plus 100% of the negative polarity inertial load, the four hinge locations are assigned near-zero flexural stiffness at depths of 5, 16 and 24 feet to simulate non-ductile hinges. With the 100% loading, additional hinges develop 19.5 and 28.5 feet, making a total of five nonductile hinge locations. A loading case with inertial loading and no kinematic loading is shown for reference in Fig. 10. In this case the RI remains elastic. **Clearly, omitting the kinematic loading grossly underestimates the seismic demands on the RI.**

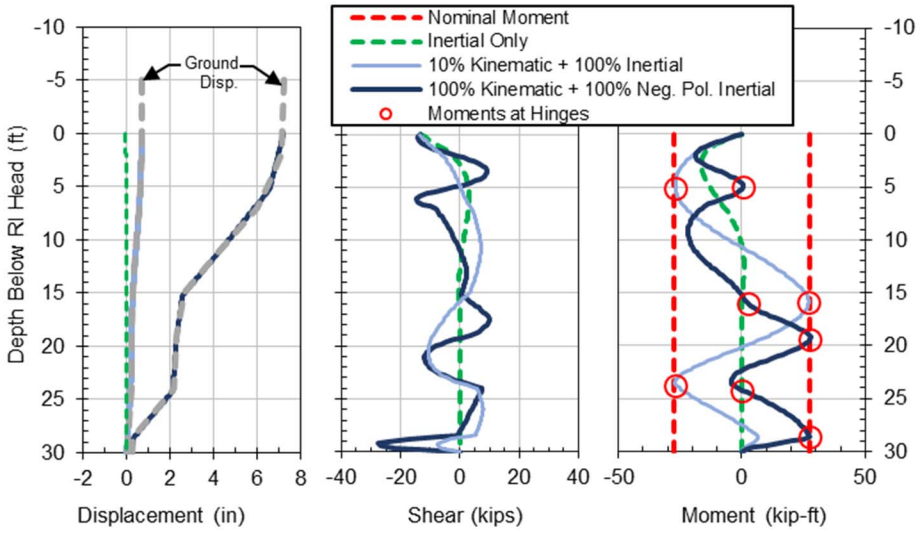


Fig. 10. Results of seismic loading on unreinforced RI

The results for the reinforced RI case are shown in Fig. 11. In this case, the RI reaches its nominal moment capacity at depths of 6, 16, 24 and 28.5 feet when the full kinematic and negative polarity loading is applied.

Since the reinforced RI behaves in a more ductile way, it is worth examining the ductility demand[3] at the plastic moment locations. From Fig. 3, we define the yield curvature at 0.00022 rad/in where steel yielding first occurs. The curvature ductility demands are 2, 8.6, 35, and 14 for the hinges at 6, 16, 24 and 28.5 feet, respectively. With the exception of the hinge at 6 feet, the ductility demands are high and suggest that pins could form at the hinge locations.

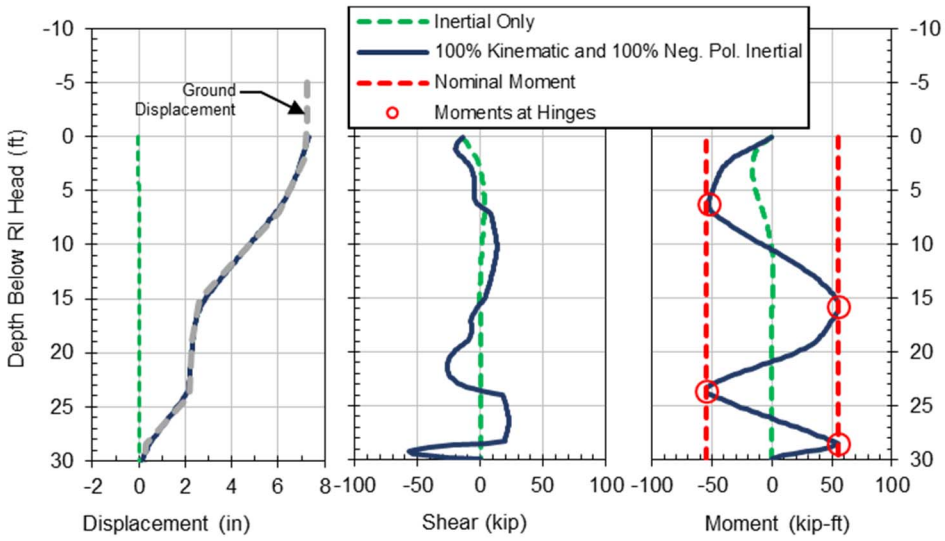


Fig. 11. Results of seismic loading on RI reinforced with No. 10 bar

Evaluation of Damage Modes

The influence of seismically-induced hinges on the anticipated performance of the RI ground improvement system must be evaluated as part of a thorough RI system design. For this case the potential damage modes are: 1) loss of system bearing capacity and 2) settlement due to compression or bulging of the hinge zones. For this project, conventional bearing capacity analyses show that the footing achieves a bearing capacity factor of safety of 3.8 without any contribution from the RIs, so hinging of the RIs should not result in bearing capacity failure. It is noteworthy that had the medium stiff clay with cohesion of 750 psf been present below the footing, the bearing capacity factor of safety without the RI would be 0.9, and more detailed study of the bearing capacity with post-hinge shear resistance of the RI would need to be performed to show that an adequate post-seismic bearing failure could be achieved.

An axisymmetric finite difference numerical model of a single RI unit cell was performed using the program FLAC (Itasca Consulting Group 2016) to assess potential settlement due to bulging and compression of the hinges. Space limitations of the paper preclude a detailed presentation of this analysis, so only a brief summary is provided herein. After establishing equilibrium with the pre-construction condition, the footing and RI ground improvement system was modeled under static conditions. To model the RI condition during and after a seismic event, at each anticipated hinge location the concrete RI material was replaced with a dense gravel material model (to simulate crushed concrete) and the numerical model was cycled to equilibrium. The material substitution made for the post-seismic model condition generated an additional ½ inch of seismically generated footing settlement. With an adequate bearing capacity factor of safety and anticipated seismic settlement of ½ inch, the RI ground improvement system is acceptable in this case.

[3] Caltrans (2013) defines ductility demand as the ratio of induced displacement (in this case, RI curvature) to the yield displacement.

COMMENTS ON LIQUEFIABLE SITES

The focus of this paper has been on non-liquefiable sites where strain levels under strong seismic shaking are typically a few tenths of a percent to a few percent and peak ground displacements are typically up to a few inches. For liquefaction sites, peak shear strain is an order of magnitude greater than this and shear displacement of a few feet may occur. For sites where lateral spreading occurs, even larger shear displacements could result. These larger displacements generate much more severe kinematic RI loading. Considering this and the potentially poor seismic performance of slender minimally reinforced piles in liquefiable ground, as shown in Fig. 3 and previously discussed, use of RIs for sites with moderate to severe liquefaction hazards are not recommended unless rigorous kinematic analysis shows that acceptable performance can be achieved.

SUMMARY AND CONCLUSIONS

When appropriately designed, rigid inclusions (RIs) are can provide a cost-effective ground improvement solution for many structures, facilities, and infrastructure projects in seismic areas. However, designers must recognize that RIs are subject to seismic loading from kinematic and inertial sources. Kinematic loading may result from wave passage or ground failure, with the latter a typically more severe loading case. As lightly to unreinforced elements with relatively high stiffness, RIs have little to no ductility and are vulnerable to damage as a result of bending under kinematic and inertial loading. Seismic loading evaluations of RIs can be accomplished using relatively simple methods with a level of effort similar to that of a conventional deep foundation lateral loading analysis and design. If the design seismic loading generates hinges in the RI, the damage potential and performance should be evaluated in terms of loss of bearing capacity, settlement, and lateral displacement. These evaluations should confirm that the RIs continue to meet the expected performance requirements after the design seismic event.

A case study for a hypothetical site in the seismically active Los Angeles Basin of was presented that illustrates the use of the simple analytical methods. In this case, both unreinforced and reinforced RIs develop plastic hinges due to kinematic loading. For the sample case provided, the foundations would be expected to maintain adequate bearing capacity, but could be subjected to ½ inch of seismic settlement from compression and bulging of the hinge zones.

The results of the analysis described herein indicate that the kinematic soil demand on the RI is significantly greater than the superstructure inertial demands. Therefore, neglecting kinematic soil loading conditions will grossly underestimate the potential damage to the RIs, possibly resulting in unconservative performance calculations.

There is a need for additional research through physical testing and advanced analysis to better understand the seismic response and performance or RIs. In particular, the characteristics of hinges in unreinforced RIs in terms of their composition, compressibility and shear strength would lead to a better understanding of damage potential. Research could also help in developing guidance on how to partition inertial load resistance between the RIs and the soil.

REFERENCES

Adelier, K. Elgamal, A., Meneses, J., Baez, J.I. 2003. Stone columns as liquefaction countermeasures in non-plastic silty soils, Soil Dynamics and Earthquake Engineering, Vol. 23 pp 571-584.

American Concrete Institute (ACI) 2014. Building Code Requirements for Structural Concrete (ACI 318-14).

Caltrans 2013. Seismic Design Criteria, Version 1.7.

Caltrans 2017. Lateral Spreading Analysis for New and Existing Bridges. Memo to Designers 20-16.

Cetin, K. O., Seed, R. B., Der Kiureghian, A., Tokimatsu, K., Harder, L. F., Kayen, R. E., and Moss, R. E. S. 2004. Standard penetration test-based probabilistic and deterministic assessment of seismic soil liquefaction potential, J. Geotech. and Geoenvr. Engrg., ASCE 130(12), 1314–340.

Darendeli, M. 2001. A new family of normalized modulus reduction and material damping curves for equivalent linear analysis, PhD Dissertation, University of Texas, Austin.
Federal Highway Administration (FHWA) 2009. Technical Manual for Design and Construction of Road Tunnels – Civil Elements.

Gingery, J.R. 2007. A simplified method for estimating shear strains for ovaling and racking analysis of tunnels, Proceedings of the 4th International Conference on Earthquake Geotechnical Engineering, June 25-28, 2007, Thessaloniki, Greece.

Gingery, J.R., J. Meneses and Z. Zafir, (2009). Addressing kinematic pile bending design requirements in the International Building Code, International Foundation Congress & Equipment Expo, March 15-19, Orlando, Florida.

Gingery, J.R. and Elgamal, A., 2013. Shear stress-strain curves based on the G/Gmax logic: a procedure for strength compatibility, 2nd International Conference on Geotechnical Earthquake Engineering, October 25-27, Chengdu, China, ASCE.

Hamada, H. 1992. Large ground deformations and their effects on lifelines: 1964 Niigata earthquake, in Case Studies of Liquefaction and Lifeline Performance During Past Earthquakes, Vol. 1 Japanese Case Studies, edited by H. Hamada and T.D. O'Rourke, Technical Report NCEER-92-0001.

Hashash, Y.M.A., Musgrove, M.I., Harmon, J.A., Groholski, D.R., Phillips, C.A., and Park, D. 2016. DEEPSOIL 6.1, User Manual, Urbana, IL, Board of Trustees of University of Illinois at Urbana-Champaign

Hausler, E.A. and Sitar, N. 2001. Performance of soil improvement techniques in earthquakes, International Conferences on Recent Advances in Geotechnical Earthquake Engineering and Soil Dynamics 6.

International Code Council (ICC) 2015. 2015 International Building Code.

IREX (2012). Recommendations for the design, construction and control of rigid inclusion ground improvements, ASIRI National Project, Intitut pour la recherche appliquee et l'experimentation engenie civil.

Itasca Consulting Group, Inc. 2016. Fast Lagrange Analysis of Continua (FLAC) Version 8.00.

Margason, E. and Halloway, D.M. 1977. Pile bending during earthquakes, Proc., Sixth World Conf. on Eq. Engr., Sarita, Prakashan, Meerut, India, pp 1690-1696.

Martin, J.R., Olgun, C.G., Mitchell, J.K., Durgunoglu, H.T. 2004. High-modulus columns for liquefaction mitigation, J. or Geotech. and Geoenviro. Engr., 130(6).

Mizuno, H. 1987. Pile damage during earthquakes in Japan (1923-1983), Dynamic response of pile foundations: experiment, observation and analysis, T. Nogami, ed.,, ASCE, New York, 53-78.

Mylonakis, G. and Nikolaou, S. 2002. Design methods for earthquake-induced pile bending, Proceedings of the 27th Annual Conference on Deep Foundations, 2002, San Diego, CA, Deep Foundation Institute.

Rayamajhi, D., Nguyen, T.V., Ashford, S.A., Boulanger, R.W., Lu, J., Elgamal, A. and Shao, L.2014. Numerical study of shear stress distribution for discrete columns in liquefiable soils, J. Geotech. and Geoenvr. Engr., 140(3), ASCE.

Rayamajhi, D., Tamura, S., Khosravi, M., Boulanger, R.W., Wilson, D.W., Ashford, S.A. and Olgun, C.G. 2016. Dynamic centrifuge tests to evaluate reinforcing mechanisms of soil-cement columns in liquefiable sand, J. Geotech. and Geoenvr. Engr., 141(6), ASCE.

Tabesh, A. and Poulos, H.G. 2001. Pseudostatic approach for seismic analysis of single piles, J. Geotech. and Geoenvr. Engr., 127(9), pp 757-765, ASCE.

2D AND 3D FINITE ELEMENT ANALYSIS FOR CANTILEVER SLURRY WALLS IN COHESIONLESS SOIL

Ali Helwa[1], Manal Salem[2], and Mostafa Mossaad[3]
[1]PhD, Senior Engineer, Thornton Tomasetti, Boston, USA, AHelwa@thorntontomasetti.com
[2]Associate Professor, Faculty of Engineering, Cairo University, Giza, Egypt, manalasalem@eng.cu.edu.eg
[3]Former Professor, Faculty of Engineering, Cairo University, Giza, Egypt, mmossad51@yahoo.com

ABSTRACT
Support of excavation (SOE) design practice tends to model SOE elements using two-dimensional (2D) analyses to avoid the complexity associated with three-dimensional (3D) analyses. Such practice overlooks soil arching in the horizontal plane and prevents designers from accounting for elements such as capping beams as part of the statical system. This study simulates square excavations supported by cantilever slurry walls in dry cohesionless soil using 2D and 3D finite element (FE) models. First, side support wall behavior is compared from 2D and 3D FE models for variable excavation length to depth (L/H) ratios. Second, the effect of slurry wall lateral bending stiffness on wall behavior is studied by modeling the wall using plate element with isotropic and anisotropic wall stiffness. Finally, the sensitivity of cantilever wall behavior to the presence of capping beam is illustrated. The study concludes that unbraced excavations with L/H ratios greater than 5 almost resemble plane-strain conditions. Slurry walls are better simulated in 3D FE models by dividing the plate element into discrete panels or by assigning anisotropic bending stiffness to the plate element. Finally, the presence of capping beam affects the behavior of cantilever walls resulting in reduction of deflections and redistribution of bending moments.

Keywords: 3D finite element, slurry wall, cohesionless soil, capping beam, bending stiffness

INTRODCUTION

Support of excavation (SOE) design practice ranges in complexity from conducting simple hand calculations to performing three dimensional numerical modeling depending on several factors among which is the geometry of the design problem. This paper addresses walls that are designed using numerical modeling, and discusses the factors governing the choice of the most suitable modeling approach. It has been believed for a while that modeling excavations using 2D numerical models would lead to a more conservative solution, which turned out to be incorrect in specific cases. This paper attempts to describe cases where 2D finite element modeling could be on the conservative side and other cases where it could be less conservative than the more complex 3D modeling.

Terzaghi (1936) experimented filling a box with a sluice gate at the bottom. Once the sluice gate is open, the soil falls and gradually arches around the opening; this experiment was called the "trap door" experiment. Terzaghi (1936)'s experiment demonstrated "arching" of soil in the lateral direction within a vertical plane. Another form of soil arching happens in the vertical direction adjacent to braced excavations and results in the "apparent earth pressure". This paper addresses the arching of soil in the lateral direction. Several studies compared 2D and 3D modeling approaches illustrating the necessity of using 3D modeling. Ou et al. (1996) compared 2D and 3D finite element modeling of the Hai-Hua Building in Taipei city with field measurements obtained from central and corner sections. The study normalized the three dimensional ground movements to the plane strain deformations defining the "Plane strain ratio" (PSR) for a section of slurry wall. The study indicated that 2D modeling could be realistic to model the behavior at the center of relatively long walls. At corners, 2D finite element analyses over predicted the wall deflection by about 100-300%; while the 3D finite element analysis resulted in wall deflection with an error of ± 20%. Lee et al. (1998) conducted 2D and 3D finite element analyses for an excavation of 4-level basement supported by slurry wall diagonally braced by struts in Singapore in soft marine clay. Three-dimensional analyses

© 2018 Deep Foundations Institute

well predicted maximum deflection at each stage, whereas the plane strain 2D analysis consistently over predicted the maximum wall deflection by about 30%. Lee et al. (1998) suggested that some corner effects extended to the wall center and plane strain conditions did not completely prevail even at the central section of the wall. For the corner section, both 2D and 3D analyses over predicted the maximum wall deflection by about 200% and 30%, respectively.

Zdravkovic et al. (2005) noted that a slurry wall, a contiguous pile wall, a secant pile wall, or a sheet pile wall should not be modeled as isotropic solid element as it consist of continuous vertical elements (e.g. slurry panels, piles) with discontinuities in the horizontal direction. Zdravkovic et al. (2005) compared the deflections calculated for square excavation using plane strain and axisymmetric analyses for central and corner sections, to those evaluated using 3D modeling with anisotropic (lateral to vertical stiffness ratio of 10^{-5}) and isotropic walls. For central section, anisotropic 3D modeling resulted in about 13% less deflections than those evaluated using plane strain analysis, and about 20% more deflections than axisymmetric analysis. For corner section, anisotropic 3D modeling resulted in 33% less deflections compared to those calculated using axisymmetric analysis, and about 40% less deflections compared to those calculated using plane strain analysis. Finno et al. (2007) investigated the differences between 2D plane strain and 3D finite element analyses. Analyses were conducted for 20m and 80m square excavations. The movements computed by the 3D finite element analysis were less than those computed by 2D plane strain simulations for the smaller excavation, but were almost the same for the larger excavation.

Lin and Woo (2007) conducted 2D and 3D modeling of an excavation in Taipei 101 project supported by strutted slurry wall, and compared the results of the two modeling approaches to the actual (measured) deformations of the excavation at the center of the retaining walls. Good agreement was observed between the actual deflections and those evaluated using 3D modeling. However, the 2D modeling consistently overestimated the deflections by about 100%. Accordingly, the numerical results revealed that the lateral wall movements of evaluated central sections along the slurry wall were restrained by the wall corner during the excavation even though a heavily supporting system was installed. The authors concluded that the corner effects were not suppressed by the strutting system and that it was very crucial to apply 3D modeling approach in Taipei 101 construction project to reflect realistic deformation behavior of multi-strutted deep excavation.

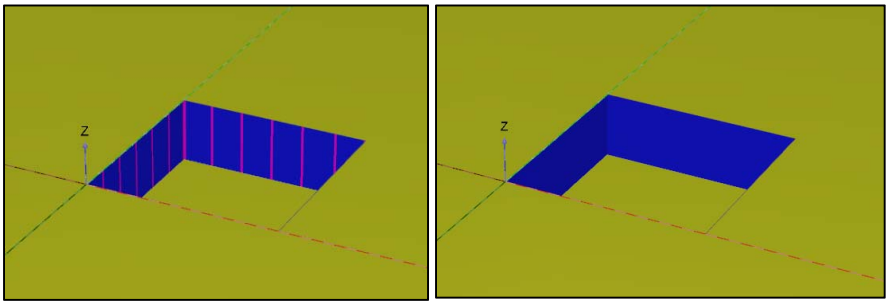
The scope of this study is to investigate the differences in estimated deflection and bending moment profiles from 3D modeling of slurry walls and how it compares to the 2D plane strain conditions for a 6m deep square excavation in dry cohesionless soil. The slurry wall is of cantilever type with 6.5m embedded length. First, the wall is modeled using a 2D plane strain model with no capping beam as a reference. Second, side support wall behavior is compared from 2D and 3D FE models for variable excavation length to depth (L/H) ratios to investigate how the geometry of excavation could cause deviation from plane strain conditions. Third, the effect of slurry wall lateral bending stiffness on wall behavior is studied by modeling the wall using plate element with isotropic and anisotropic wall stiffness. This section investigates how the separation between discrete panels of slurry walls could be modeled. Forth, the sensitivity of cantilever wall behavior to the presence of capping beam is investigated by comparing the generated deflection and bending moment profiles with and without capping beam. Finally, side support wall behavior is compared from 2D and 3D FE models for a theoretical case where the soil surrounding a square shaped area is excavated. This case resembles irregularly shaped excavations such as an L-shaped area, specifically the one corner of the excavation that has 270^{o} within the excavated area surrounded by 90^{o} within the soil.

FINITE ELEMENT MODEL

This study focused on square shaped excavations (Figure 1), with dimensions varying from 6 to 42m. The excavation depth (H) was maintained at a constant value of 6m. The behavior of the cantilever retaining wall was investigated for (L/H) ratios of 1, 2, 3, 4, 5, and 7. The parametric analyses were conducted for

medium dense sand soil profile. Groundwater was assumed throughout the analysis to be at 1m below final excavation level. Wall penetration was determined based on limit equilibrium analysis for a factor of safety of 1.2, which equaled 6.5m. The wall had a thickness of 0.7m. PLAXIS 2D was used for the plane strain FE analyses, while PLAXIS 3D was used for the 3D FE analyses. The effect of wall lateral bending stiffness on modeled wall behavior was investigated by modeling the wall as:

1- Continuous plate with isotropic wall properties.
2- Continuous plate with anisotropic wall properties: E_2/E_1=0.001, 0.01, 0.1, where E_1 and E_2 are the wall section Young's moduli in vertical and lateral directions, respectively.
3- Discrete panels with separating elements in between that have reduced stiffness properties.



(a) (b)

Fig. 1. Different 3D wall modeling approaches: (a) Paneled wall (b) Continuous wall

Hardening soil model was used in the current study. Typical soil parameters for medium dense sand provided in Kulhawy and Mayne (1990) were used in the conducted parametric study. The input hardening soil properties for the medium dense sand are summarized in Table 1, where γ is the bulk unit weight, E'_{50} is secant modulus of elasticity at 50% peak stress, E'_{oed} is secant modulus of elasticity from primary Oedometer loading, E'_{ur} is unloading/reloading modulus of elasticity, ϕ' is the effective angle of shearing resistance, c' is effective soil cohesion, m is power for stress level dependency of stiffness, k_o is at-rest lateral earth pressure coefficient, R_{inter} is interface parameter, and P_{ref} is the reference pressure.

Slurry walls were modeled using linear elastic model. Input wall properties for 2D and 3D modeling are summarized in Tables 2 and 3, respectively, where E is Young's modulus, A is cross sectional area, I is area moment of inertia, G_{12} is in-plane shear modulus, G_{13} and G_{23} are out-of-plane shear modulus in vertical and lateral directions, respectively, and ν is Poisson's ratio. The discrete paneled wall consisted of two plate elements, namely main panels and separating panels. The separating panels had a reduced lateral Young's modulus (E_2) to model the lack of wall flexural resistance in the lateral direction between panels of slurry walls. Main panels and separating panels shared nodal points and were not permitted to slide relative to one another; however, rotation between panels were allowed around the vertical axis. The model was simulated in three stages: 1. Initial stresses were generated using k_o condition; 2. Wall was wished-in-place; and 3. Six meters of soil were excavated.

PLANE STRAIN FINITE ELEMENT MODEL RESULTS

The results of the 2D plane strain modeling of the wall retaining the 6m excavation depth are presented in this section. Variation of deflection with depth is presented in Figure 2a, and variation of bending moment in the vertical direction (M_{11}) with depth is shown in Figure 2b. The wall exhibited maximum deflection at the wall top of 21mm, and maximum bending moment of 188 kN.m/m at 7.2m below the wall top.

Table 1. Hardening soil properties for medium dense sand

Property	Value
γ (kN/m^3)	18
E'_{50} (kN/m^2)	50,000
E'_{oed} (kN/m^2)	40,000
E'_{ur} (kN/m^2)	150,000
φ' (degree)	34
c' (kN/m^2)	1
m	0.5
k_o	0.44
R_{inter}	0.67
P_{ref} (kN/m^2)	100

Table 2. Wall properties assigned in 2D models

Property	Value
EA (kN.m^2/m)	14E+6
EI (kN/m)	5.71E+5

Table 3. Wall properties assigned in 3D models

Property	Discrete paneled wall		Continuous wall
	Main panel	Separating element	
Length (m)	2.6 - 2.8	0.2	-
E_1 (kN/m^2)	20E+6	20E+6	20E+6
E_2 (kN/m^2)	20E+6	1000	Variable
G_{12}, G_{13}, G_{23} (kN/m^2)	8.7E+6	8.7E+6	8.7E+6
ν	0.15	0.15	0.15

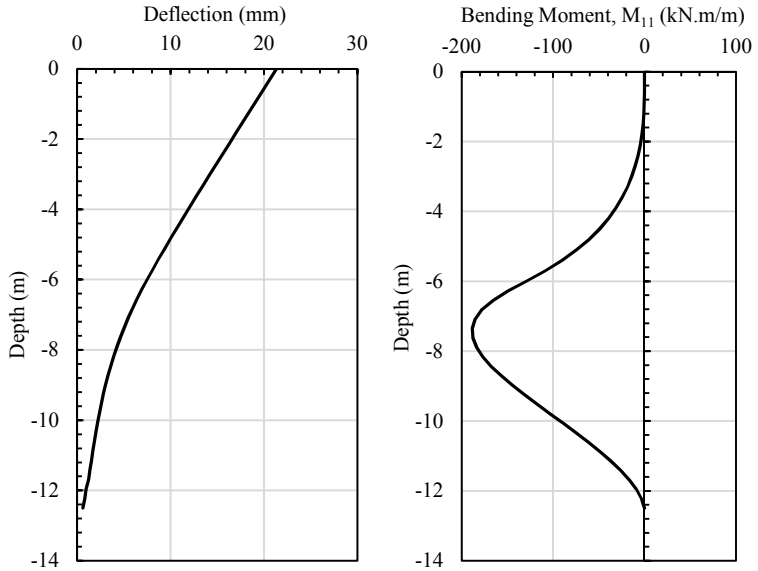


Fig. 2. Plane strain FE model results (a) Deflection profile (b) Bending moment profile

THREE DIMENSIONAL FINITE ELEMENT MODEL RESULTS

Vertical variation of the wall deflections and bending moments were studied at the mid span of excavation length (i.e. at L/2) where maximum wall deflections and bending moments were observed. Wall deflections were investigated at the wall top (ground level), where maximum deflections of a cantilever wall took place. Lateral variation of wall bending moment (M_{11}) is studied at depths with maximum M_{11} values. All the deflections and bending moments obtained from the 3D models were normalized to the deflection and bending moment obtained from the plane strain condition. The normalized deflection is referred to as Deflection Plane Strain Ratio (PSR), and the normalized bending moment is referred to as Bending Moment PSR.

Evaluated deflection PSR values at the center of the wall at ground level (maximum deflection) for L/H values ranging from 1 to 7 for paneled walls, anisotropic walls (E_2/E_1 = 0.001, 0.01, and 0.1) and isotropic walls are presented in Figure 3. Results reported in the literature are presented on the same figure as well. As the excavation length increased, the deflection PSR increased approaching plane strain conditions. For 3D FE models adopting discrete wall panels, the deflection PSR increased as the excavation length increased to reach an asymptotic value of 0.9 at L/H = 5. These results show reasonable agreement with case histories measurements reported in the literature at various L/H ratios. For 3D FE models adopting continuous plate with anisotropic wall properties, the deflection PSR showed lower values compared to that calculated for the paneled wall, i.e., more deviation from plane strain conditions. The lower lateral to vertical wall stiffness (E_2/E_1) ratio, the higher the deflection PSR. Deflection PSR values at L/H = 5 are 0.76, 0.72, and 0.67 for E_2/E_1 ratios of 0.001, 0.01, and 0.1, respectively. Modeling the wall as continuous plate with isotropic wall properties showed results that are of the least match to the results obtained from paneled wall model, with a plane strain ratio of 0.53 at L/H = 5. Assuming that the paneled wall modeling approach presented herein resembles the configuration of slurry walls, 3D FE models could substantially underestimate wall deflection if isotropic walls are adopted or even if anisotropic walls are adopted with E_2/E_1 ratio higher than 0.001.

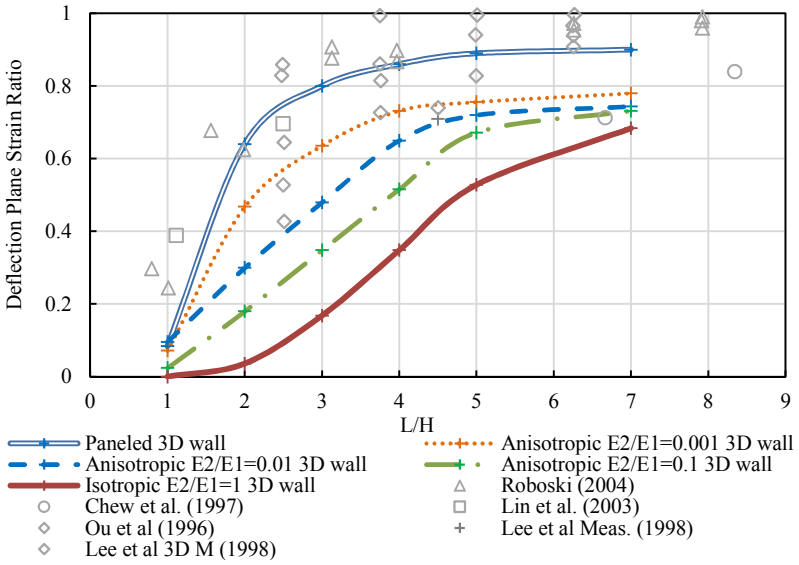


Fig. 3. Maximum deflection PSR for variable excavation length to depth ratios adopting isotropic wall stiffness, anisotropic wall stiffness, and paneled walls

The variation of deflection PSR in the lateral direction at elevation of maximum deflection values (ground surface) is presented for paneled walls in Figure 4 for L/H ratios of 2 and 5. In Figure 4, the distance from the center of the wall (x) is normalized to the wall length (L). The deflection PSR at corner panels are less than the mid-point panel; PSR for corner and mid-point panels at L/H=5 are 0.6 and 0.9, respectively. Variation between corner and center panels is less pronounced for L/H ratio of 2. The variation of bending moment PSR in the lateral direction at elevation of maximum bending moment values is presented for paneled walls in Figure 5 for L/H ratios of 2 and 5. Bending moment PSR at corner panels are slightly less than the mid-point panel. Variation between corner and center panels is similar for L/H ratios of 2 and 5.

Bending moment PSR evaluated at the center of the wall at elevation of maximum bending moments for L/H ratios ranging from 1 to 7 for paneled, anisotropic, and isotropic walls are presented in Figure 6. As the excavation length increased, the bending moment PSR increased approaching plane strain conditions. For 3D models adopting discrete wall panels, the bending moment PSR increased as the excavation length increased to reach an asymptotic value of 0.95 at L/H = 5. For 3D FE models adopting continuous plate

with anisotropic wall properties, the bending moment PSR showed lower values compared to that calculated for the paneled wall, i.e., more deviation from plane strain conditions. The lower lateral to vertical wall stiffness (E_2/E_1) ratio, the higher the bending moment PSR. Bending moment PSR values at L/H = 5 are 0.85, 0.75, and 0.70 for E_2/E_1 ratios of 0.001, 0.01, and 0.1, respectively. Modeling the wall as continuous plate with isotropic wall properties showed results that are of the least match to the results obtained from paneled wall model, with a bending moment plane strain ratio of 0.61 at L/H = 5. Similar to the deflection PSR, 3D FE models could underestimate wall bending moments if isotropic walls are adopted or even if anisotropic walls are adopted with E_2/E_1 ratio higher than 0.001.

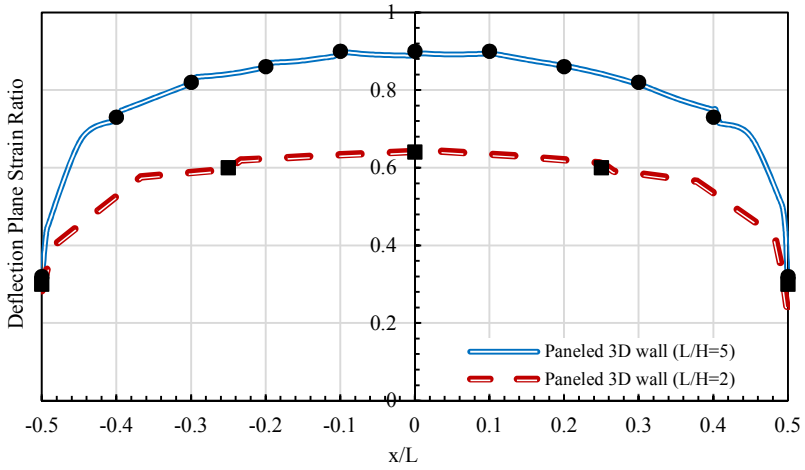


Fig. 4. Deflection PSR lateral profile at wall top for paneled walls at L/H = 2 and L/H = 5

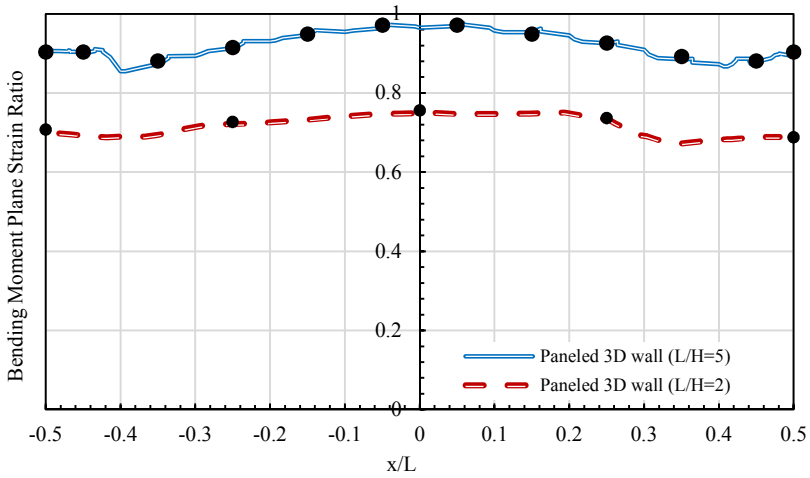


Fig. 5. Variation of maximum bending moment PSR across excavation width for paneled walls at L/H = 2 and L/H = 5

It is noted that the above parametric study was conducted for loose and dense sands (Helwa, 2012), which showed that walls approached plane strain conditions at excavation length to depth ratios greater than 5 similar to the medium dense sand reported herein. Simic and French (1998) quantified the savings that could be maintained if 3D analyses is applied to the design of slurry walls supporting underground station box. When comparing results with plane strain analyses, Simic and French (1998) concluded that steel quantities could be reduced by about 25% for the studied project.

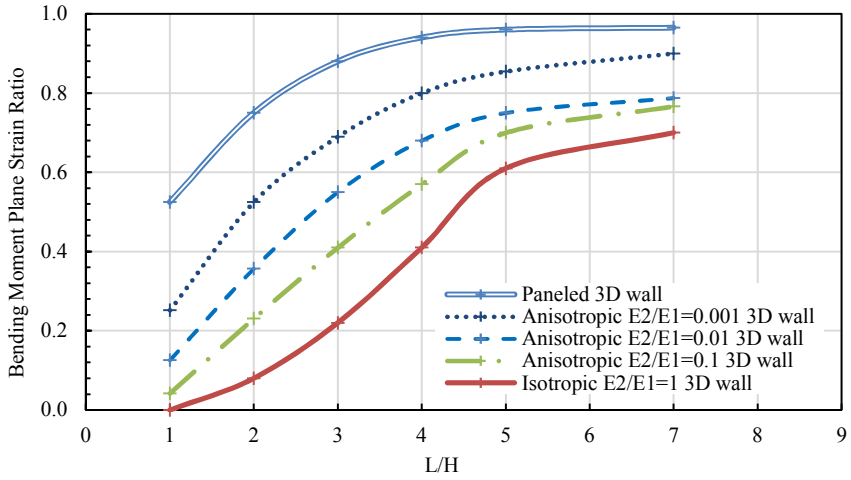


Fig. 6. Maximum bending moment PSR for variable excavation length to depth ratios adopting isotropic wall stiffness, anisotropic wall stiffness, and paneled walls

CAPPING BEAM EFFECT

This section presents the influence of the capping beam on the three dimensional behavior of slurry walls. The capping beam acts as a support on top of the wall. The stiffness of this support varies across the excavation length, depending on its deflection. At the excavation corner, the capping beam deflection is minimal, and thus the wall element is supported with a high stiffness support. The presence of capping beam is usually ignored during the structural design of walls using plane strain design approach because the variation of support stiffness along the excavation length is not accounted for in the 2D analysis. In addition, the presence of capping beam is generally conceived as conservative because it reduces wall deflections. However, supporting the wall top with capping beam induces negative bending moments in the wall sections where 3D effects are pronounced. This negative bending moment cannot be captured under plane strain conditions unless a spring/support is simulated in the 2D analysis. This section presents two 3D FE modeling approaches: paneled wall with and without capping beam for different L/H ratios ranging from 1 to 7. The capping beam is 0.7m wide and 1m high, and has a bending stiffness (EI) of 5.71E+5 kN.m/m.

Variation of deflection with depth and variation of bending moment in the vertical direction (M_{11}) with depth for L/H ratios of 2 and 5 are shown in Figures 7a and 7b, respectively, for paneled walls with and without capping beam. As shown in Figure 7, the depth of influence of capping beam on estimated wall deflections and bending moments was not limited to the upper portion of the wall only; in fact, the influence extended to the whole depth of the wall. The bending moment trends computed in cases adopting capping beam are different from that of walls without capping beam. At L/H ratio of 2, the capping beam resulted in redistribution of bending moments along the wall depth, which accordingly reduced the maximum bending moment acting on the wall. The effect of the capping beam on the redistribution of bending moments faded as L/H ratio increased to 5. Considering the redistribution of bending moment along the wall depth would result in more efficiently designed wall.

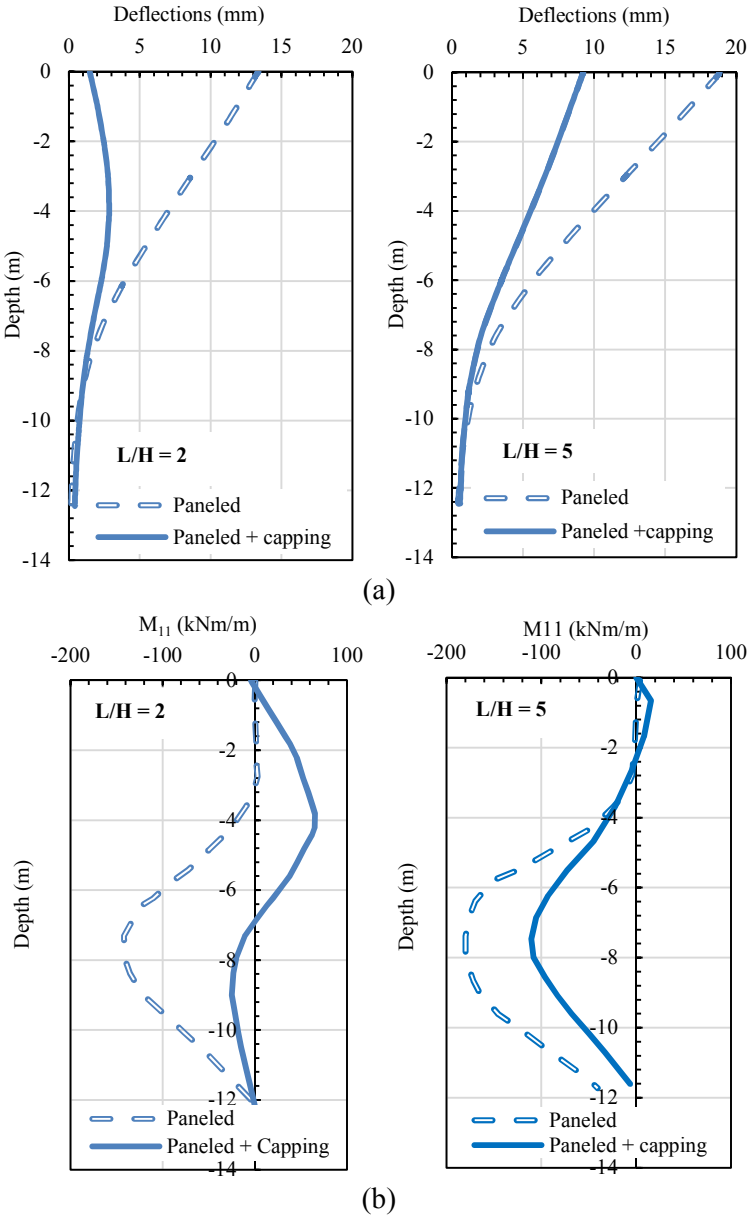


Fig. 7. 3D FE model results for paneled walls with and without capping beam: (a) Deflection profile (b) Bending moment profile

Evaluated deflection PSR values at the center of the wall at ground level (maximum deflection) for L/H ratios ranging from 1 to 7 are presented in Figure 8 for paneled walls with and without capping beams. As L/H ratio increased, the deflection PSR increased. For the same L/H ratio, the presence of capping beam resulted in significant reduction in the estimated deflection PSR. The deflection of the capping beam is proportional to the excavation length cubed. As the excavation length increased, the support stiffness decreased at the center of the wall resulting in increase of deflection PSR. Bending moment PSR evaluated at the center of the wall at elevations of maximum positive and negative bending moments for L/H ratios ranging from 1 to 7 are presented in Figure 9 for paneled walls with and without capping beams. As the L/H ratio increased, the positive bending moment PSR increased, while the negative bending moment PSR decreased. For the same L/H ratio, the presence of capping beam resulted in redistribution of the estimated bending moment PSR.

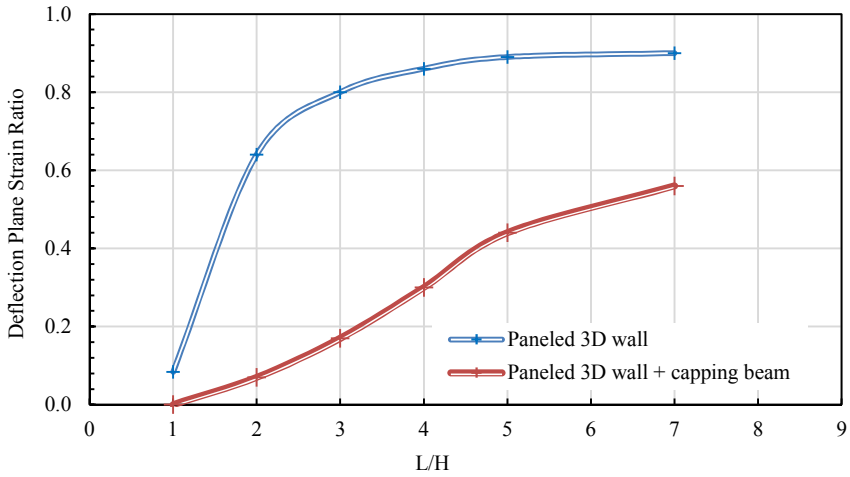


Fig. 8. Maximum deflection PSR at variable excavation length to depth ratios, using paneled wall 3D models with and without capping beam

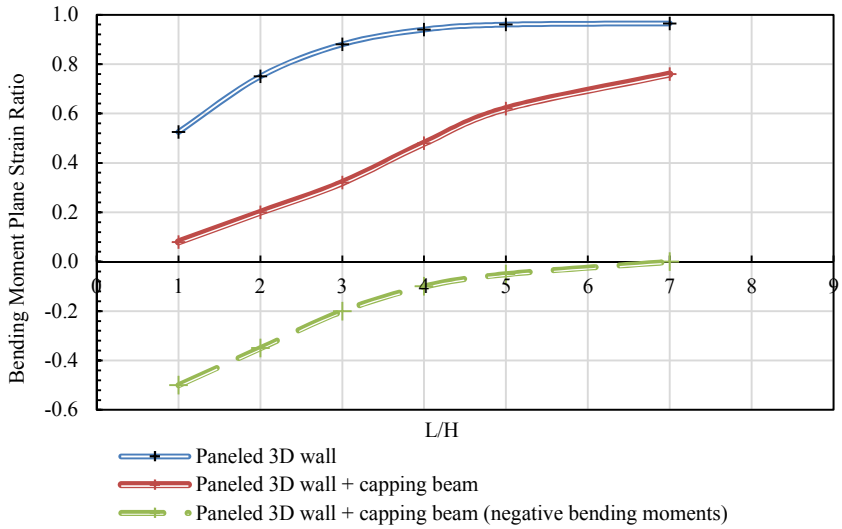


Fig. 9. Maximum bending moment PSR at variable excavation length to depth ratios, using paneled wall 3D models with and without capping beam

COMPARISON BETWEEN 270º AND 90º EXCAVATIONS

Two cases of excavations are compared in this section: (1) a theoretical case where the soil surrounding a square shaped area is excavated, referred to herein as 270º excavation; (2) the conventional case where the soil within a square shaped area is excavated, referred to herein as 90º excavation. Excavating around a square shaped area may not be practical; however, it attempts to resemble irregularly shaped excavations such as an L-shaped area (Figure 10), specifically the one corner of the excavation that has 270º within the excavated area surrounded by 90º within the soil.

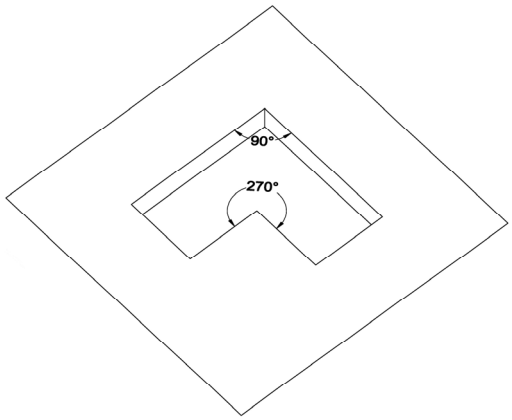


Fig. 10. Sketch illustrating the difference between 90º and 270º excavations

Evaluated deflection PSR values at the center of the wall at ground level (maximum deflection) for L/H values ranging from 1 to 7 are presented in Figure 11 for paneled walls with 270º and 90º excavations. For L/H ratios greater than 3.5, the deflection PSR for 270º excavations exceeded 1, which means that the wall exhibited higher deflections than those obtained under plane strain conditions. In case of 90º excavations, the soil arches around the excavation in a state similar to hoop stresses; while, in the case of 270º excavations, the soil tends to radially expand. Therefore, designing the 270º case of excavation using 2D plane strain conditions would result in underestimated deflections and bending moments, leading to unsafe design.

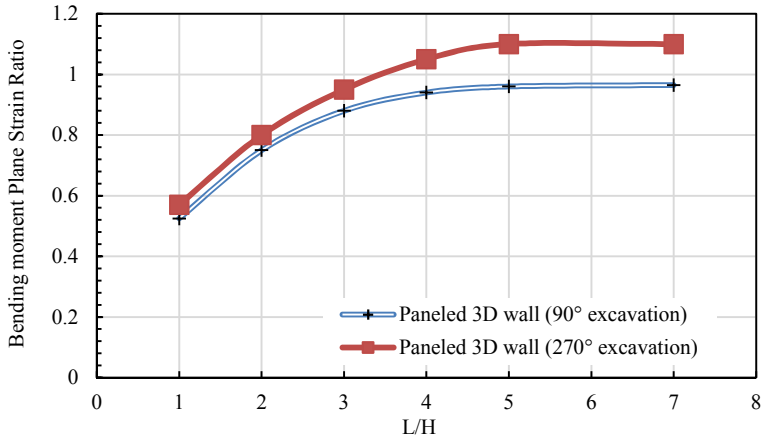


Fig. 11. Maximum deflection PSR for variable excavation length to depth ratios, for 90º and 270º excavations

CONCLUSIONS

This study attempts to aid the engineer in selecting the optimum modeling approach for the design of SOE projects. Based on the conducted study on square excavations supported by slurry walls in dry cohesionless soils, it was concluded that walls approach plane strain conditions at excavation length to depth ratios greater than 5. Slurry walls are better simulated using discrete panels rather than continuous wall with anisotropic stiffness. However, discrete paneling could be cumbersome; thus, modeling the wall using continuous plate may be used with anisotropic stiffness ratio less than or equal to 0.001. Modeling the capping beam in the 3D model is important as it leads to reduction in the estimated deflections and redistribution of bending moments inducing negative bending moments on the walls, especially in cases of low L/H ratios. Designing excavation corners that have three quarters of excavated soil (270º excavation)

to one quarter of retained soil using 2D plane strain conditions would result in underestimated deflections and bending moments, leading to unsafe design; therefore, 3D effects should be considered for this case.

REFERENCES

Chew, S.H., Yong, K.Y., and Lim, A.Y.K., 1997. Three-dimensional finite-element analysis of a strutted excavation. Computer methods and advances in geomechanics, Yuan, ed., Balkema, Rotterdam, The Netherlands, Vol. 3, pp. 1915-1920.

Finno, R.J., Blackburn, J.T., and Roboski, J.F., 2007. Three-dimensional effects for supported excavations in clay. Journal of Geotechnical and Geoenvironmental Engineering, 133(1) 30- 36.

Helwa, A.F. (2012). "Three dimensional analysis of excavations supported by cantilever diaphragm walls in cohesionless soil" Master's Thesis, Cairo University, Egypt.

Kulhawy, F.H. and Mayne, P.W. (1990). "Manual on estimating soil properties for foundation design." Cornell University, Ithaca, New York.

Lee, F.H., Yong, K.Y., Quan, K., and Chee, K.T., 1998. Effects of corner in strutted excavations: field monitoring and case histories. Journal of Geotechnical and Geoenvironmental Engineering, 124(4) 339-349.

Lin, D.G. and Woo, S.M., 2007. Three dimensional analyses of deep excavation in Taipei 101 construction project. Journal of GeoEngineering, 2(1) 29-41.

Lin, D.G., Chung, T.C., and Phien-wej, N., 2003. Quantitative evaluation of corner effect on deformation behavior of multi-strutted deep excavation in Bangkok subsoil. Geotechnical Engineering Journal, South East Asian Geotechnical Society, 34(1) 41−57.

Ou, C.Y., Chiou, D.C., and Wu, T.S., 1996. Three-dimensional finite element analysis of deep excavation. Journal of Geotechnical Engineering, 122(5) 337-345.

Roboski, J.F., 2004. Three-dimensional performance and analyses of deep excavations. PhD. Dissertation, Northwestern University, Evanston, IL, USA.

Simic, M., and French, D., 1998. Three dimensional analysis of deep underground stations. Proceedings on the Conference of Value of Geotechnics, Institution of Civil Engineers, London.

Terzaghi, K., 1936. Stress distribution in dry and in saturated sand above a yielding trap-door. Proceedings of the First International Conference on Soil Mechanics and Foundation Engineering, Cambridge, MA, pp. 307-311.

Zdravkovic, L., Potts, D.M., and St. John, H.D., 2005. Modelling of a 3D excavation in finite element analysis. Geotechnique, 55(7) 497-513.

DEVELOPMENT OF A NEW, ADVANCED FORM OF SODIUM SILICATE FOR CHEMICAL GROUTING

Michael McDonald, PQ Corporation, Toronto, Ontario, Canada, mike.mcdonald@silicates.com
Tim Evans, PQ Corporation, Toronto, Ontario, Canada
Julie Shang, University of Western Ontario, London, Ontario, Canada
Bingfeng Xue, University of Western Ontario, London, Ontario, Canada
Yu Guo, University of Western Ontario, London, Ontario, Canada

Abstract

Effective chemical grouting represents a technical and economic solution to many challenges related to soil stabilization and blocking the flow of water. Chemical grouts are facing increasing demands in durability, environmental impact and value. To better meet these challenges, a novel and cost effective process was developed to produce a sodium silicate that increases the ratio (i.e. silica to alkali) beyond what has been used in traditional silicate-based grouts.

The move to a lower sodium form of silicate was anticipated to have two desirable performance enhancements; a reduction in leachable sodium and improvement in the durability of the silicate grout. An in-depth study was performed at the University of Western Ontario Geotechnical Research Centre to quantify improvement in durability as well as other performance properties such as compressive strength. The study began by first modelling the gelation time and reaction kinetics of the high ratio sodium silicate over a range of silicate concentrations using two different setting agents as well as with/without a hardener. As expected, reducing the level of sodium produced a much more water resistant grout. These same formulations also showed a four order magnitude reduction in permeability. Somewhat surprising, test results showed the higher ratio silicate having much higher compressive strength.

At the time of this abstract, the high ratio silicate was moving to the trial stage for geotechnical applications while the petroleum industry was further along with several successful field trials for water blocking as well as cement remediation. This paper will review the chemistry, testing and features of this next generation form of sodium silicate.

Keywords; sodium silicate, high ratio, colloidal silica, water blockage

Introduction

Sodium silicate based grouts have been used for decades for soil stabilization and water control. Over the years, several silicate-based systems have been tailored for specific application conditions to maximize performance and reduce cost. Past research has also focused on the selection of setting agents and hardeners for silicate grouts.

A constant in the development effort has been the grade of sodium silicate. The vast majority of chemical grouts have been formulated using a ~3.2 ratio sodium silicate. As a very brief overview on the meaning of "ratio" and why it is so important to performance properties. The ratio describes the proportion of sand to alkali or SiO2:Na2O used to make different grades of sodium silicate. Comparing a 2.2 ratio to a 3.2 ratio, it is easier to polymerize and set the 3.2 ratio. Upon setting and forming a silica gel, the system has higher compressive strength values and improved durability with a reduced level of syneresis (i.e. shrinkage). This leads to the question if 3.2 is better than 2.2 why not go to 4.2 or higher?

© 2018 Deep Foundations Institute

The short answer is conventional manufacturing procedures limits the upper end of ratio to approximately 3.2 for sodium silicate.

Recently, a novel and cost-effective procedure has been developed to produce high ratio silicates for subterranean applications (McDonald, 2012). These high ratio silicates can be thought of as a product that is between conventional sodium silicate and colloidal silica. Within the range of high ratio silicates, the ratio of "4.5" was found to be the sweet spot as a function of molecular speciation, reactivity, cost and performance. Table 1 provides a comparison of the physical and chemical properties of a 4.5 ratio vs. 3.2 ratio vs. a typical colloidal silica.

Colloidal silica is referenced in this paper as it is derived from sodium silicate and is also used in chemical grouting for water blockage applications. In comparison to sodium silicate, the colloidal silica based-grouts tend to be less prone to syneresis (i.e. shrinkage), provide more controllable set times and tend to have better durability characteristics. The trade-offs with using colloidal silica gel is they provide much less strength enhancement and require a higher starting concentration. Further, colloidal silica is a considerably more expensive product.

The chemistry of high ratio silicate and gelation kinetics has been well documented in other papers. Nordstrom (2012) provides details on the size, internal structure, degree of condensation, shape and distribution of silicate molecules within the SiO_2:Na_2O range of 3.3 to 8.9. Hatzignatiou (2018) provides details of gelation kinetics as a function of salt and hardness. The focus of this paper will be on the comparison of performance properties of 3.2 vs. 4.5

	Colloidal Silica	3.2 ratio	4.5 Ratio
SiO_2:Na_2O	52	3.22	4.5
% SiO_2	30	28.7	21.1
% Na_2O		8.9	4.7
% Solids	30	37.6	25.8
pH	10.2	11.3	11.0
Density (g/cm^3)	1.22	1.38	1.22
Viscosity (centipoise)	5	180	100
Average size (nm)	7	1	3

Table 1. Physical properties of colloidal silica vs. 3.2 ratio vs. 4.5 ratio

HS&E Considerations & Selection of Setting Agents

Sodium silicate is considered one of the oldest and safest of the chemical-based grouts. The benign nature of sodium silicate is reflected in various regulatory approvals as well as end-uses such as potable water treatment. (Schleyer, 1982, FDA). In looking at potential setting agents for evaluation in a 4.5 ratio system the following questions were asked,

-is the setting agent safe?

-what are the reaction products with sodium silicate?

-will there be a negative impact on soil and water?

These questions precluded some of the historic and well proven silicate-based grout formulations. A wide range of environmentally - acceptable setting agents still remain and some of the chemicals making the short list were; triacetin, citric acid, sodium acid pyrophosphate, sodium chloride, acetic acid and lactose. These setting agents were then ranked on;

-prior use & performance properties

-ease of use

-handling characteristics

-cost

From this screening, triacetin and citric acid were selected as the settings agents for investigation. Citric acid was particularly appealing in that it had very favorable ecological profile with very low aquatic toxicity and readily biodegradable (HERA). Additionally, citric acid was relatively inexpensive and it was available as an easy – to - dissolve powder.

Alkalinity of 3.2 ratio vs. 4.5 ratio

A mass balance calculation can show a significant amount of sodium being present in a sodium silicate grout. This has led to concerns and questions about the potential to impact surrounding groundwater and soil. The study by Esiwirth (1999) observes there was no significant impact on groundwater chemistry in the study of 3.3 ratio sodium silicate grouts. This is related to the relative permanent nature of the silicate grout. However in certain jurisdictions, sodium silicate-based grouts are being scrutinized for the potential impact of sodium. Per table 1, the 4.5 ratio sodium silicate has significantly less sodium compared to conventional sodium silicate. As will be illustrated later, once polymerized the 4.5 ratio gel extends the durability of the silica gel which reduces the rate of sodium dissolution.

Experimental

As a new technology, it was important the 4.5 ratio sodium silicate be vetted and further developed by a reputable third party. The University of Western Ontario Geotechnical Research Centre (GRC) was selected to run a comparative study based on expertise as well as in-house testing capabilities.

A review of prior research (Ata, 1999, Gonzalez, 2007, Porcino, 2012, Schiffman, 1956, Vipulanandan, 1986) and field application (Brachman, 2004, Chi, 1985, Hamderi, 2015) helped to establish the performance metrics of chemical grouts for stabilizing soils. These served as a starting point to evaluate the suitability of the new silicate for chemical grouting on sand and provide a comparison with traditional silicates in terms of static mechanical properties of grouted samples. Industry experts from several grouting companies were consulted to ensure the research was current to market conditions. Summarizing the feedback;

-water blockage is more prevalent vs. strength enhancement

-sodium silicate-based grouts are typically used in sand

-concentration of sodium silicate ranges from 30% to 60%

-set time of ~3 to 5 hours would be considered reasonable or typical

Sands used in this study were medium to fine Barco silica sand. The indexed properties of the sand are summarized in Table 2. The specimens for grouting were prepared at a controlled moisture content of 5% and dry density of about 16.5 kN/m^3. The grouted samples were cured in a plastic mold that had an inner diameter of 50 mm and a length of 100mm. A detailed experimental design is shown in Tables 3a, b.

Specific gravity, Gs		2.65
Hydraulic conductivity (m/s)		10^{-4}
Target water content		5%
Color		White
Particle size	D_{10}	0.163 mm
	D_{30}	0.230 mm
	D_{60}	0.330 mm
The coefficient of uniformity, C_u		2.02
USCS classification		SP

Table 2. A summary of properties of silica sand

Silicate Type	Vol. Conc.	Setting agent	Hardener	Gel time (hours)	Curing time (days)
3.2	30%	Citric Acid	1% $CaCl_2$ solution[1]	4~5	1,7,14,28
	40%		N/A		
4.5	40%		N/A		
	50%		N/A		
	60%		N/A		

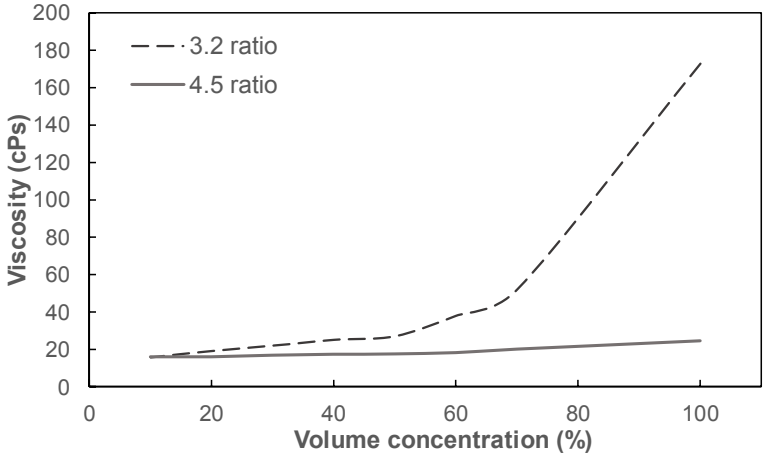
[1]$CaCl_2$ solution has a concentration of 1g/L

Silicate Name	Setting agent	Part A		Part B			Gel time (hours)
		Silicate (mL)	Tap water (mL)	Triacetin (mL)	Tap water (mL)	100g/L $CaCl_2$ (mL)	
S45	Triacetin	50	30	1	19	N/A	4~5 hrs
		50	30	1	18	1	2hrs10mins

Tables 3a,b: summary of experimental design

Viscosity

Depth of penetration for a given pressure and soil permeability is fixed by the viscosity of the grout and molecular size. Prior to the gelation process, the viscosity of a silicate solution is primarily controlled by the ratio of silicate to water. As shown in graph 1, the viscosity of 3.2 vs. 4.5 is close at the higher dilution rates with water (i.e. 10 cps) as the dilution factor decreases the 4.5 ratio maintains a lower viscosity and would allow for injection at lower pressure and/or to a greater depth.



Graph 1: Viscosity of 3.2 vs. 4.5 at 20C

Silica Gel Durability

Durability to water and high temperature cycling was measured as a function of water and volume changes (swell and shrinkage) using a modified version of ASTM D559/D559M, "standard test methods for wetting and drying compacted soil-cement mixtures". This test method calls for consolidated sand to be oven-dried for 42 hours and then submerged in water for 5 hours. Measurements are taken over 12 cycles.

Medium to fine Barco silica sand was consolidated with a 4.5 ratio sodium silicate diluted 1:1 with water and then polymerized using citric acid or triacetin. Table 4 summarizes the loss of weight after each cycle. The 4.5 ratio set with triacetin showed only a slightly loss of weight over the 12 cycles, while the sample set with citric acid had good durability until the 6th cycle: after that a crack developed in the consolidated sand (figure 1). It will be appreciated that a crack is less likely to develop under downhole conditions as there is a confining pressure. Testing also excluded other silicate reactions, such as with calcium, which would enhance durability to temperature cycling.

4.5 ratio-50%	Setting agent			
	Citric acid		Triacetin	
Test cycle	Remaining weight, g	Cumulative weight loss	Remaining weight, g	Cumulative weight loss
Original oven dry mass	325.6	N/A	321.8	N/A
1	324.5	0.3%	320.0	0.6%
2	323.8	0.6%	319.1	0.8%
3	323.7	0.6%	318.9	0.9%
4	322.7	0.9%	318.7	1.0%
5	316.8	2.7%	318.9	0.9%
6	238.6 (Cracked)	26.7%	318.5	1.0%
7	218.7	32.8%	318.0	1.2%
8	215.3	33.9%	317.7	1.3%
9	210.7	35.3%	317.6	1.3%
10	200.9	38.3%	317.3	1.4%
11	200.6	38.4%	317.6	1.3%
12	194.3	40.3%	314.4	2.3%

Table 4. Durability of consolidated sand after curing 14 days with 4.5 ratio silicate using citric acid and triacetin



Figure 1: Sand consolidated with 4.5 ratio-citric acid, cracked at the 6th cycle (dry vs. wet)

Permeability Reduction

To assess reduction in permeability, a similar formulation of 4.5 ratio silicate/citric acid/Barco sand was tested using ASTM D5084−16a, "Standard Test Methods for Measurement of Hydraulic Conductivity of Saturated Porous Materials Using a Flexible Wall Permeameter. Applying Darcy's law, the permeability of the sand is reduced by 4 orders of magnitude to the permeability of wet silt.

Sample	Curing time	Permeability
Control Pure sand	N/A	$2.14x10^{-4}$ m/s
50% S45-Citric	7 days	$9.72x10^{-8}$m/s
50% S45-Citric	28 days	$3.64x10^{-7}$m/s

Table 5. Permeability of pure sand vs. consolidated sand with 4.5 ratio and citric acid

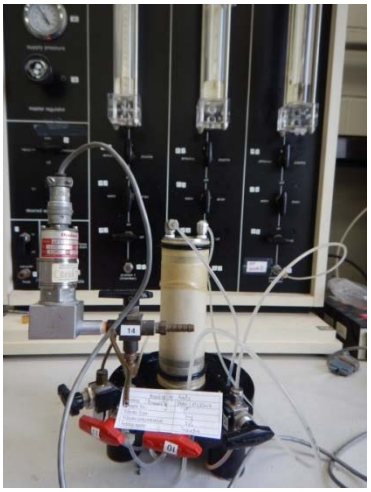


Figure 2: Permeability test set up

Environment Scanning Electron Microscope (ESEM)

ESEM analysis was performed to further study the cementation of grouted sand. Figure 3a,b,c provide ESEM images of three silicate grouted sand samples. As seen, the samples treated by three silicate grout solutions (S45-50%-Citric Acid, S45-50%-Triacetin, and NS-40%-Citric Acid) exhibited similar microstructures: A large number of soil voids were filled with chemical grout patches, the grout acted as chemical bonding, connecting the sand particles, and the surface morphology of silica sand was coated by silicate gel. These observations were consistent with the working mechanism of chemical grouting proposed by Vipulanandan and Krizek (1986). Compared with sample 3.2 ratio-40%-CA (Figure 3a), a relatively denser matrix is seen in samples 4.5-50%-CA and 4.5-50%-Tri, as illustrated in Figure 3b,c . This may be attributed to a lower level of syneresis (i.e. gel shrinkage) observed in 4.5 ratio compared to 3.2 ratio.

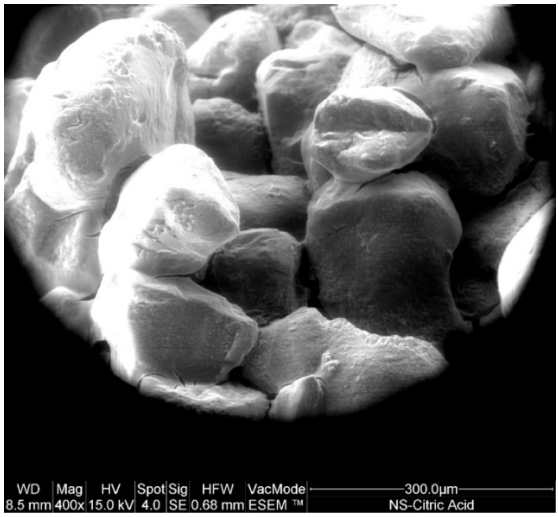


Figure 3a ESEM imaging on sample NS-Citric Acid-40%-7Days (Mag=400X)

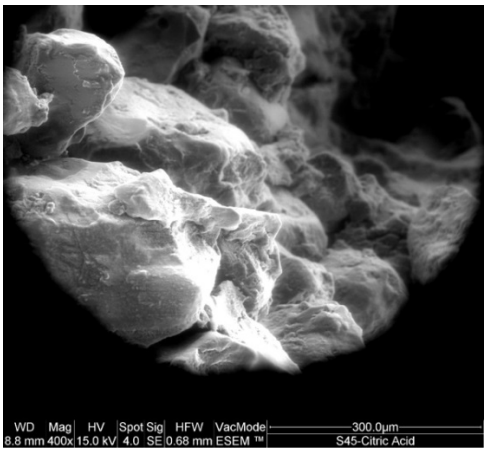


Figure 3b: 50% 4.5-Citric Acid, 7 Days

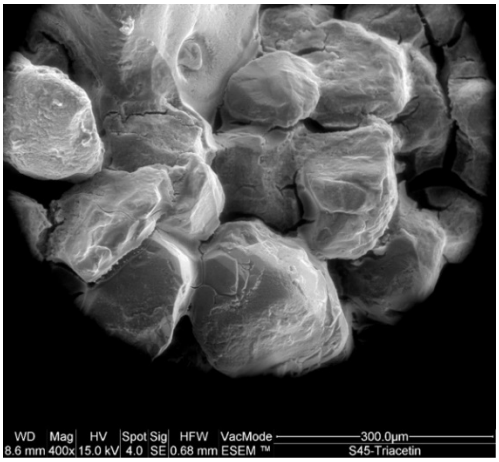


Figure 3c: 50% 4.5-Triacetin, 7 days

Syneresis

Syneresis is the chemical phenomenon whereby a polymer continues to crosslink after it appears to have set. As the polymer structure increases in the number of chemical bonds, there is a tightening/contraction within the polymer that results in the loss of volume. The loss of volume is undesirable as it decreases the efficacy of the polymer to block water. Most polymers including silica gels experience some degree of syneresis. For silica gels, syneresis is specific to the silanol groups crosslinking to form siloxane linkages (figure 4).

The impact of syneresis was not observed in sand injected with 3.2 and 4.5 ratio sodium silicate. Samples of sand consolidated with sodium silicate showed no measurable change in volume (figures 5a, b). A similar situation has been reported for medium to fine sands by other researchers (Karol, 1990, Porcino, 2012). Moving from a high permeably matrix such as sand to a fracture, the impact of syneresis can be observed on silica gels. A glass bottle test provides a visual observation on silica gel shrinkage and extrusion of water. A 4.5 ratio sodium silicate shows dramatically less syneresis (graph 2, figure 6). The reason for the reduction in syneresis is partially explained in Krumrine (1985). Setting of sodium silicate occurs as three simultaneous processes;

1. Small silicate species form higher order oligomers.
2. The intramolecular condensation of silanol groups within the silicate leading to ring closure and eventual particle formation.
3. The aggregation of silica particles to form chains and microgels.

Based on the molecular structure of a 4.5 ratio silicate, steps 1 and 2 for polymerization have largely taken place during the manufacturing of the 4.5 ratio. The reduction of silanol groups (Si-OH) silicate equates to less syneresis (and better control over the gelation process).

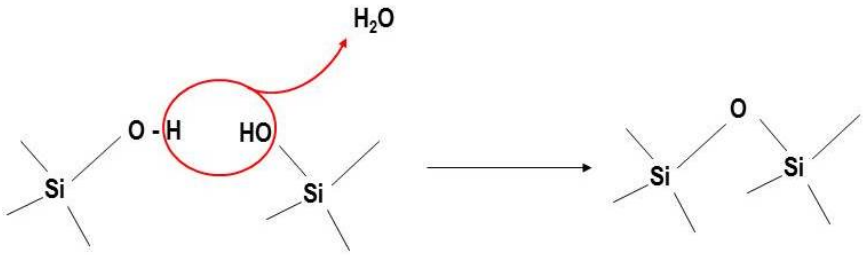


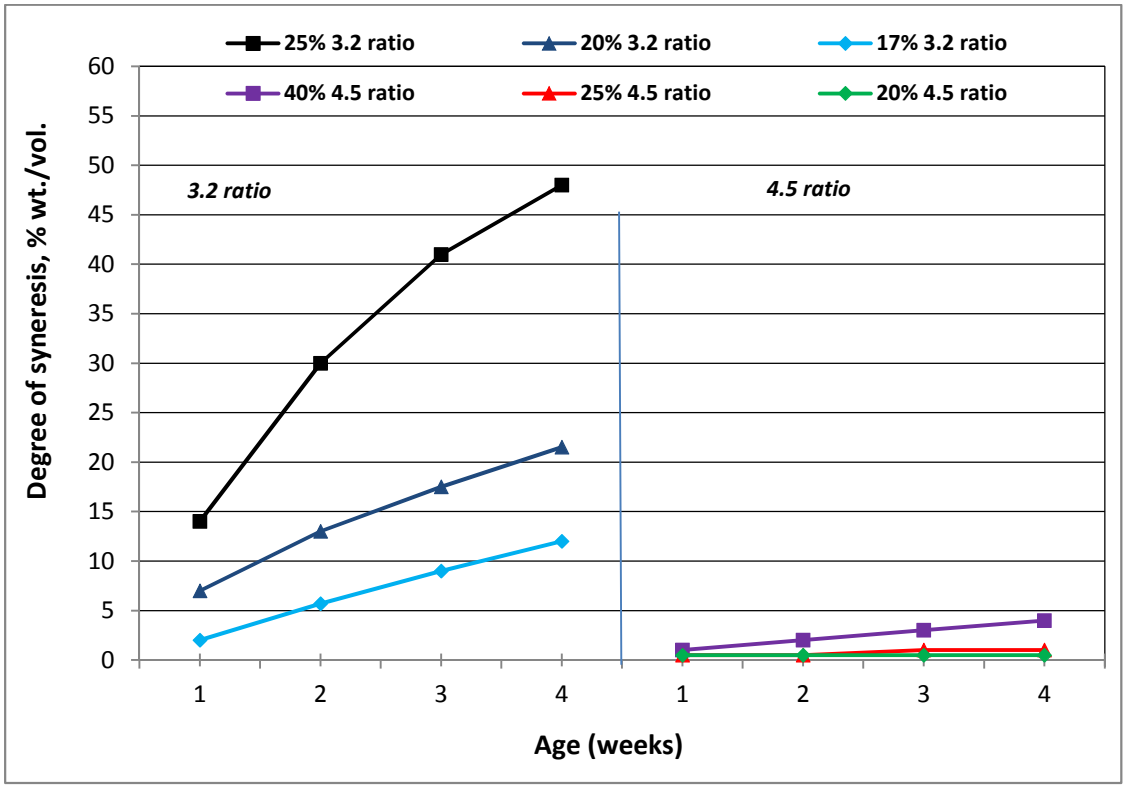
Figure 4: post reaction of silanol groups to form siloxane bonds leading to a tighter gel structure



Figure 5a: Mold for sand consolidation



Figure 5b: silicate treated sand showing no loss of volume



Graph 2: Synersis vs. Ratio vs. Time



Figure 6: visual observation of syneresis after four weeks aging

Field Trials - Oilfield

It was noted by Krumrine (1985) that technology and techniques developed for the grouting industry could be applied to water shut-off applications in oilfield. This time around, oilfield shares some of their learnings with using the 4.5 ratio material for water shutoff, gas blockage and cement remediation. The use of 4.5 ratio silicate can be split between applications where it is used as a standalone product and as a solids free material that was pumped ahead of microfine or ordinary Portland cement.

Similar to many grouting applications, a challenge with using Portland cement or microfine cement is bridging when squeezing into fine fissures, microcracks or high permeable matrices. A best practice to emerge in Western Canada for blocking gas or water is to pump a small volume of 4.5 ratio (or 3.2 ratio sodium silicate) before a remedial cement squeeze. Typically, these squeezes involve a preflush of water with a softener followed by 500 litres to 1 m3 of diluted sodium silicate. Once the silicate is squeezed then it is followed by a water spacer and then the cement. (figure 7). This approach allows sodium silicate to deeply fill and block microchannels that would otherwise quickly bridge with cement. This technique has increased the success rate of cement remediation for blocking gas. Over a dozen trials were run with the 4.5 ratio sodium silicate. Initial results show a similar level of performance as conventional sodium silicate but treated wells will be monitored for potential differences in long term performance. Trial work continues with placement techniques being modified to allow for deeper placement and the development of a hard set material.

The 4.5 ratio sodium silicate has also been used as a standalone product to block low volume leakage of methane. In one application, the 4.5 ratio was diluted 1:1 vol/vol with water. Prior to pumping the sodium silicate solution, the well was treated with a small volume of hydrochloric acid to better open perforations and pathways. A fresh water preflush was then pumped to remove residual hydrochloric acid and dissolved metals such as calcium. Upon placing a third of the 4.5 ratio treatment volume, the pump pressure rapidly increased to the fracture gradient indicating the high ratio silicate had set hard. The gas

flow rate was reduced by a factor of 10 and was trending towards 0. The trial was deemed successful, but future work would involve a larger preflush of water to allow for a larger volume/deeper placement of the silicate.

Several trials took place where the 4.5 ratio sodium silicate was squeezed into a high permeable zone to block the flow of gas and/or water. A chemical injection pump (figure 8) is used to pump the 4.5 ratio silicate and setting agent. In most cases the 4.5 ratio was able to completely block the flow of water and/or gas. Cases where there was only limited or marginal blockage were attributed to under sizing the treatment volume and poor placement of material.



Figure 7: sodium silicate being squeezed ahead of cement



Figure 8: sodium silicate being squeezed with a setting agent

Conclusion

The development of a high ratio sodium silicate captures the performance features associated with colloidal silica while retaining and/or significantly improving the advantages associated with conventional sodium silicate. Specific enhancements of 4.5 ratio sodium silicate over conventional sodium silicate include;

-less leachable sodium

-better control over gelation times

-less syneresis

-a more durable, longer lasting gel

To date, there have been several field trials of the 4.5 ratio sodium silicate but they been have been restricted to oil field applications. Most of these trials were rated as technical and economic successes by the end-user and this is reflected with the continued use of the product.

The geotechnical industry has begun their own evaluation of 4.5 ratio sodium silicate and it is anticipated that it will soon move to commercial applications.

Acknowledgements

The authors would like to acknowledge Dr. Hatzignatiou for his early research into the application of polysilicate material for conformance applications. Recognition also goes to Darrell Lindstrand of Charger Pumping Solutions as well as Colin Logan of Earth Fluids for running the first field trials in oilfield.

A very special thanks to Xinglian Li of PQ Corp. who was critical to development of this technology and we wish her all the best in retirement.

References

1. Ata A., C. Vipulanandan. "Factors affecting mechanical and creep properties of silicate-grouted sands." Journal of geotechnical and geoenvironmental engineering 125.10 (1999): 868-876.

2. Brachman R., Martin C. D., Gilliss S. A.. "Grout field trials in outwash sands." Canadian geotechnical journal 41.1 (2004): 1-11.

3. Chi B.P.C., Yang J. “Chemical grouting in Taipei Basin.” (1985) Proc. 11th international Conf. on soil Mechanics and Foundation Engineering, San Francisco, Vol. 3, 1693-1696.

4. Eiswirth M et al., “Impact of chemical grout injection on urban groundwater”, Impacts of Urban Growth on Surface Water and Groundwater Quality (Proceedings of IUGG 99 Symposium HS5, Birmingham, July 1999). IAHS Publ. no. 259, 1999. 187

5. FDA, SCOGS-61 “Evaluation of the Health Aspects of Certain Silicates as Food Ingredients.”

6. Gonzalez H. A., Vipulanandan C.. "Behavior of a sodium silicate grouted sand." Grouting for Ground Improvement: Innovative Concepts and Applications. 2007. 1-10.

7. Hamderi M., Gallagher P. M.. "Pilot-scale modeling of colloidal silica delivery to liquefiable sands." Soils and Foundations 55.1 (2015): 143-153.

8. Hatzignatiou D.G, Giske N., "Sodium silicate gelants for water management in naturally fractured hydrocarbon formations", Chemical Engineering Research and Design 132 92018) 40-56

9. HERA - Human and Environmental Risk Assessment on ingredients of Household Cleaning Products Substance: Citric Acid and Salts (CAS# 77-92-9; 5949-29-1; 6132-04-3) - Edition 1.0 - April 2005

10. Karol R. H, Chemical Grouting, 2d edition, Marcel Dekker, Inc., New York, 1990, p. 143.

11. Krumrine P. H. and S.D. Boyce, Profile Modification and Water Control with Silica Gel-Based Systems, SPE 13578 presented at the 1985 SPE International Symposium on Oilfield and Geothermal Chemistry, Phoenix, AZ, April 9-11, 1985

12. McDonald M. Canadian Patent, 2771577 A1 "USE OF HIGH RATIO AQUEOUS ALKALI SILICATES FOR PROFILE MODIFICATION, WATER CONTROL AND STABILIZATION"

13. Nordstrom J. et al., "Silica/alkali ratio dependence of the microscopic structure of sodium silicate solutions", Journal of Colloid and Interface Science 397 (2013) 9-17

14. Porcino D., Marcianò V., Granata R.. "Static and dynamic properties of a lightly cemented silicate-grouted sand." Canadian Geotechnical Journal 49.10 (2012): 1117-1133.

15. Schleyer W. L., Blumberg J.G., "Health, Safety, and Environmental Aspects of Soluble Silicates." The 1982 American Chemical Society

16. Schiffman L., Wilson C. R.. "Mechanical behavior of chemically treated soils, Oct. 1956." (1956) Lehigh University.

17. Vipulanandan C., Krizek R.J.. "Mechanical behavior of chemically grouted sand." (1986) Journal of geotechnical engineering, 112(9), 869-887

INNOVATIVE RIVERBANK EROSION CONTROL RETAINING WALL SYSTEM FOR THE BRAZOS RIVER

Will Bohlen, P.E., BGE, Inc., Houston, TX, Tracy Brettmann, P.E., D.GE, A. H. Beck Foundation Company, Houston, TX

Abstract: An innovative retaining wall design consisting of tangent drilled shafts with supplementary seal piles was used to limit continuing bank erosion along the Brazos River in Southeast Texas. The riverbank erosion had progressed to where it was threatening the stability of both the bridge abutment and corresponding approach embankment of the heavily travelled Highway 99 bridge at this location. A tangent pile design was selected because it was both much faster to install and more cost effective than a secant pile system. The design included both 5.5-ft and 10-ft diameter shafts with depths up to 130-ft and comprised both anchored and cantilevered sections. Supplementary seal shafts were also installed between the structural tangent drilled shafts to help plug any gaps between the tangent shafts. The plumbness and diameter of the shafts were tested using a sonic caliper to make sure the shafts were installed within the specified tolerance. The initial design had to be revised when a record flood from Hurricane Harvey impacted the site during construction.

Introduction

The Fort Bend Grand Parkway Toll Road Authority (Owner) needed to protect the north bridge abutment with a retaining wall system due to rapidly eroding conditions of the Brazos River banks within the 300-feet-right-of-way of the State Highway 99 Jodie Stavinoha Bridge. The extent of the local scour and erosion along the north bank of the Brazos River has caused concern for the structural integrity of the bridge. The magnitude of the erosion along the north bank at the location of the bridge has been measured at about 120 feet over three recent hydrologic flood events locally referred to as Memorial Day 2015, Memorial Day 2016, and Tax Day 2016. During construction, a new record flood level occurred due to Hurricane Harvey in August of 2017 that resulted in a portion of the retaining wall needing to be redesigned due to even more erosion occurring.

The Brazos River is an actively eroding and meandering alluvial river plain that naturally meanders and migrates over time. The processes of bank erosion and meander migration were ongoing before the bridge was constructed and will continue in the future. These recurring major flood events, however, rapidly increased the rate of erosion in just a few years.

Background. Due to the need to protect the bridge as soon as possible, the Owner selected a project team consisting of the designer, general contractor and specialty deep foundation contractor prior to final design to work together in developing a cost-effective design that could be implemented rapidly. The project team initially considered both a secant pile and tangent pile retaining wall system using drilled shafts. After reviewing various alternative designs, a tangent pile wall with seal piles was selected based on both cost effectiveness and speed of installation. The tangent pile with seal pile option was approximately 20 percent lower in cost and 50 percent faster to install.

Secant Pile Walls. Secant pile walls are formed by constructing intersecting reinforced concrete drilled shafts. The secant piles are reinforced with either steel rebar or with steel beams. Primary piles are installed first with secondary piles constructed in between primary piles once the latter gain sufficient strength. Pile spacing is typically between 0.7 to 0.9 times the pile diameter to provide the overlap.

The main advantages of secant pile wall construction are alignment flexibility; higher wall stiffness compared to sheet piles; they can be installed in difficult ground (cemented soils, rock, cobbles, boulders)

© 2018 Deep Foundations Institute

and in limited headroom conditions; and can be constructed with low noise and little vibration compared to sheetpiles. The main disadvantages of secant pile walls are verticality tolerances may be hard to achieve for deep piles and total waterproofing is very difficult to obtain in joints.

Tangent Pile Walls. In a tangent pile wall there is no pile overlap as the piles are constructed adjacent to each other with a design clear spacing ranging from a few inches to one foot depending on the diameter of the shaft. Factoring in shaft overpour (the volume actually placed relative to the theoretical volume) one pile can come into contact with the other. Compared to secant pile walls, tangent pile walls offer the advantages of better construction alignment flexibility; the ability to install larger diameter shafts with protective steel casings, easier and quicker construction; and lower cost. The main disadvantage of tangent pile walls is there is a small gap between the piles. Thus, they cannot be made watertight which could allow for groundwater flow and erosion to occur between the piles.

Tangent Pile Wall with Seal Piles. A third variant of the secant pile/tangent pile retaining wall options is a tangent pile wall with "seal" piles placed behind and between the structural tangent piles. The seal piles do not provide any structural support but are installed simply to plug the gap between the tangent piles. This is effectively a second row of unreinforced tangent piles typically of a smaller diameter. These seal piles can be installed as drilled shafts, but usually are installed faster and more economically as Augered Cast-in-Place (ACIP) piles. Pumping fluid grout under pressure with ACIP piles is considered to provide a better seal than tremied concrete used in drilled shafts.

Highway 99 Bridge. The bridge is situated where Texas State Highway 99 crosses the Brazos River just upstream of Sugar Land, Texas. State Highway 99 is known locally as the Grand Parkway, and is an important regional transportation corridor linking the Sugar Land area with southwest Houston and Katy. The 8-span, 1,200 foot long bridge structure was originally designed in the late 1980's and constructed in the early 1990's. Spans 1, 2, 3, 4, and 8 are 115-foot long approach spans comprised by AASHTO Type IV Girders supporting a cast-in-place (CIP) concrete deck with simple span configuration. Spans 5, 6, and 7 provided the original Brazos River crossing, and are comprised with 195-235-195 foot long continuous span steel plate girders supporting a CIP concrete deck. The substructures included concrete columns supported by a battered pile group foundation for the concrete spans, and concrete column pier walls supported by a battered pile group foundation for the steel spans. Change orders were executed during construction which modified the foundations at Bents 8 and 9 (abutment) to include four 5.5-ft-diameter concrete drilled shafts directly integral with the bent caps, in lieu of the pile-supported columns. The pile tip elevations for Bent 8 were located at -45.0 feet at Bent 8 and at elevation -35.0 feet at Bent 9. This change recognized that the river was moving to the north and was an important aspect for the design of the bridge.

Brazos River Erosion. The Brazos River is the 11th longest river in the United States, with a length of 1,280 miles and a combined rivershed of about 45,000 square miles. The geography and river morphology indicated that the Brazos River was meandering to the north at the river crossing. Since the completion of the bridge in the early 1990's, the centerline of the approximately 200-ft wide river channel has moved nearly 250 feet from the midspan of Span 6 to a location just south of Bent 8. The north bank of the river has reportedly eroded about 120 ft in the past 3 years due to the multiple flood events. The river bottom grading has changed, and the former riverbank which was offset by 50 feet from interior Bent 8 is now encroaching directly on the riverbank immediately adjacent to Bent 9 and the approach roadway.

During flood events, the clays comprising the upper strata are in a saturated condition. Direct erosion and scour occurs from the flow of the river during the floods. In addition, rapid drawdown occurs as the floodwaters subside resulting in slope failures along the steep riverbank. This is a continual process with each flood event and as a result the river channel is migrating northward towards the bridge abutment. The continued erosion of the north riverbank threatened the abutment and roadway approach for the bridge structure, as well as the adjacent New Territory protection levee located just north of Bent 9.

Geology and Soil Conditions

Regional Geology. The site is located in the Northwestern (Texas) Gulf Coastal Plain geologic province of the continental United States. These Quarternary deposits form an outcrop belt about 100 miles wide generally parallel to the coastline. The stratigraphy to a few thousand feet consists of one Recent and five Pleistocene units. This site is located on an outcrop of the Beaumont formation that has a maximum thickness of 700 ft. The Beaumont formation was deposited at the beginning of the early Wisconsin glacial stage, approximately 75,000 to 100,000 thousand years ago. Beaumont sediments are deltaic and fluvial deposits laid down in distributaries and flood plains of rivers and in shallow lagoons. The soil at this site is non-marine and deposited by the Brazos River. The major streams changed courses frequently during the period of deposition, generating within the Beaumont formation a complex stratification of sand, silt and clay.

With the glacial advance of the Second Wisconsin Ice Age, the sea level lowered more than 400 feet, permitting the soil formation to desiccate for thousands of years. The desiccation process compressed the clays such that they became overconsolidated to a great depth. Subsequently, the sea level rose during the last 25,000 years and reached its present level approximately 5,000 years ago.

Soil Conditions. The soil conditions at the site generally consist of an upper stratum of stiff to very stiff clay extending to a depth of 53 ft below grade (top of wall). Below that a 22-ft-thick dense to very dense sand stratum with an average SPT blow count of 40 is present to a depth of 75 feet. A stiff clay layer is present below this sand to a depth of 83 ft and is underlain by another dense to very dense sand stratum extending to a depth of 103 ft. Very stiff clay was then encountered to a depth of 130 ft which was the maximum depth of the two closest borings. The groundwater level is typically about 30 ft below grade or slightly above river water level, but this can vary dramatically depending of the river level and rainfall.

Retaining Wall Design

The layout for the wall included enough length to protect the soil regions that supported the north abutment and roadway approach. The original design selected 5.5-ft-diameter concrete primary drilled shafts spaced at 6.5 ft center-to-center. Secondary seal shafts were 2-ft-diameter unreinforced Augered Cast-in-Place (ACIP) piles. Reinforced concrete tie beams and deadmen were included to anchor the main wall. The top of the drilled shafts was elevation +73.0, with the shaft tips located at elevation -51.0 ft. The embankment stabilization extended 100 feet on either side of the roadway as shown on Figure 1. The walls were extended approximately 75 additional feet to both the east and west flanks because of a local partnering agreement with the adjacent levee improvement district. The concrete anchor systems were not included in these extensions. However, the wall is constructed to the same specifications to facilitate installation of future anchors by the levee district. The retaining wall typical section is shown in Figure 2.

Since the Owner preferred a design that allowed at least one lane of traffic to remain open in each direction during the construction, the original design included a section of wall located to the river side of existing Bent 9. The same primary drilled shafts and secondary seal piles formed the substructure of this wall section, with top of drilled shaft at elevation +45.0 ft. A reinforced concrete retaining wall with soil nail anchors was selected to protect the soil around the abutment and roadway approach.

The project design criteria established that the wall would be designed for typical design requirements and safety factors for scour to elevation +25.0, and to a safety factor of 1.0 to 1.1 for the extreme scour condition to elevation +0.0. The top of the wall was at elevation +75.0, which lead to design wall heights of 50 feet and 75 feet.

The factored design loads of approximately 50 kips per foot for the in-service condition and 80 kips per foot for the extreme condition were driven by active earth pressure, hydrostatic water pressure, and nominal 250 psf surcharge load.

The drilled shaft reinforcement included bundled No. 11 reinforcement steel, with shaft spiral spaced between 6 and 12 inches. The longitudinal shaft reinforcement was placed eccentrically in the section, and cut off in several locations based on the unidirectional nature of the applied loads. SP Column was used to determine the structure capacity of the shafts based on the soil-structure interaction analysis performed using LPILE+. The maximum design loads in the shaft were approximately 600 kips shear and 12,500 kip-feet for bending moment. The point of maximum bending moment was located at about 5 times the shaft diameter below the ground elevation.

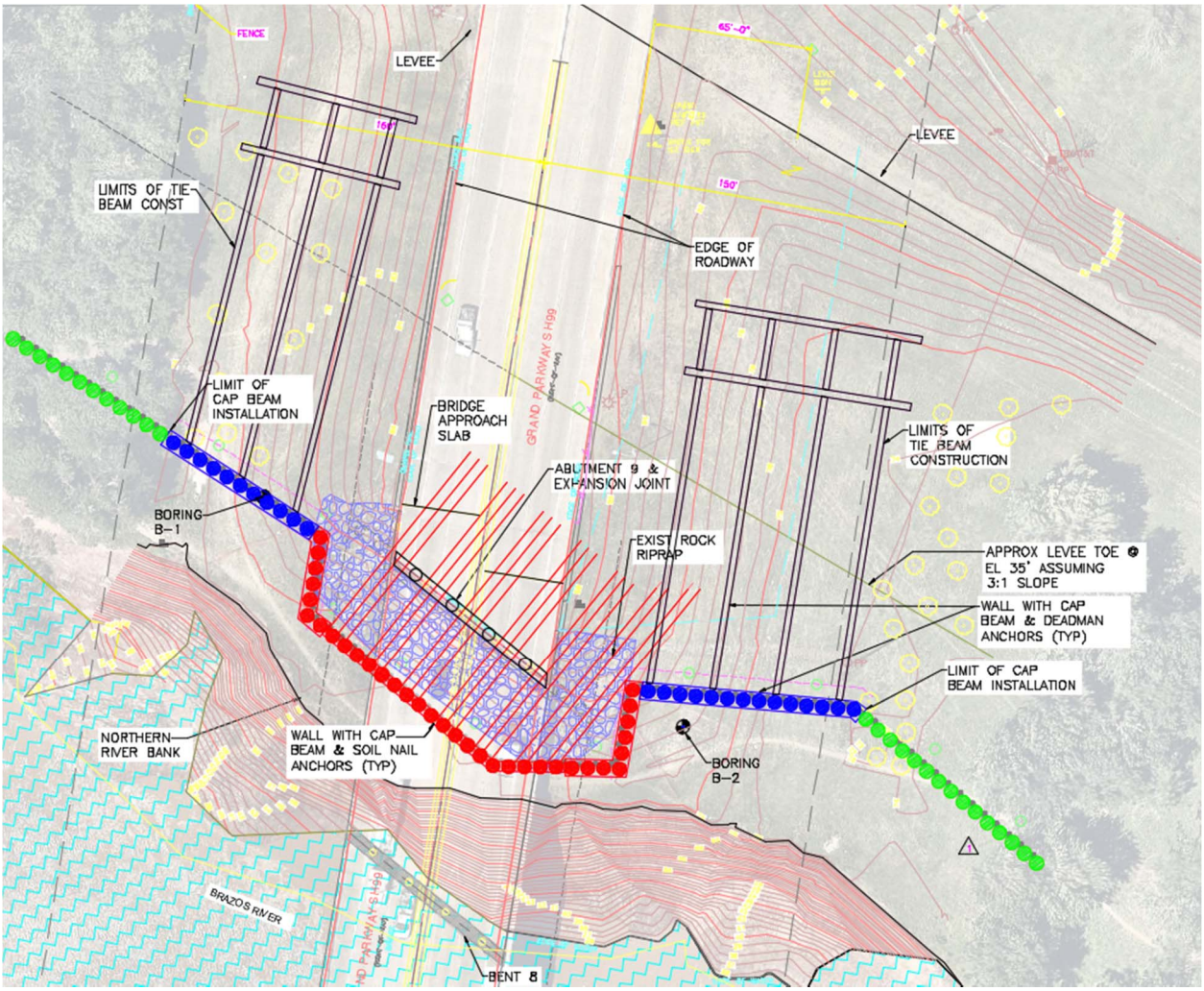


Figure 1 - Site Layout per the Original Design pre-Hurricane Harvey

Construction began in July 2017 on a 24-hours per day, 7-day a week schedule with one drilled shaft installation crew positioned on each side of the roadway. Anticipated completion for the entire project was scheduled for early 2018. With the arrival of Hurricane Harvey at the end of August 2017, the site topography was radically changed from that which existed during the final stages of project planning and the first phase of construction. Early in September, the project stakeholders determined that the elements of the retaining wall located under the end of the bridge were no longer constructible due to erosion and poor soil conditions.

Two primary elements were redesigned post-Harvey. The first item was the design of the wall anchors changed to high-strength steel tie rods with a steel sheet pile deadman system in lieu of the concrete grade beam anchor system. The typical anchor details are shown in Figure 3. Note that while the vibrations

associated with the driving of the steel sheet piles were a primary concern due to the erosion and soil conditions, the steel sheets were not installed until the drilled shaft tangent wall installation was complete, thereby the harmful effects of vibration on precarious soil slopes were already mitigated.

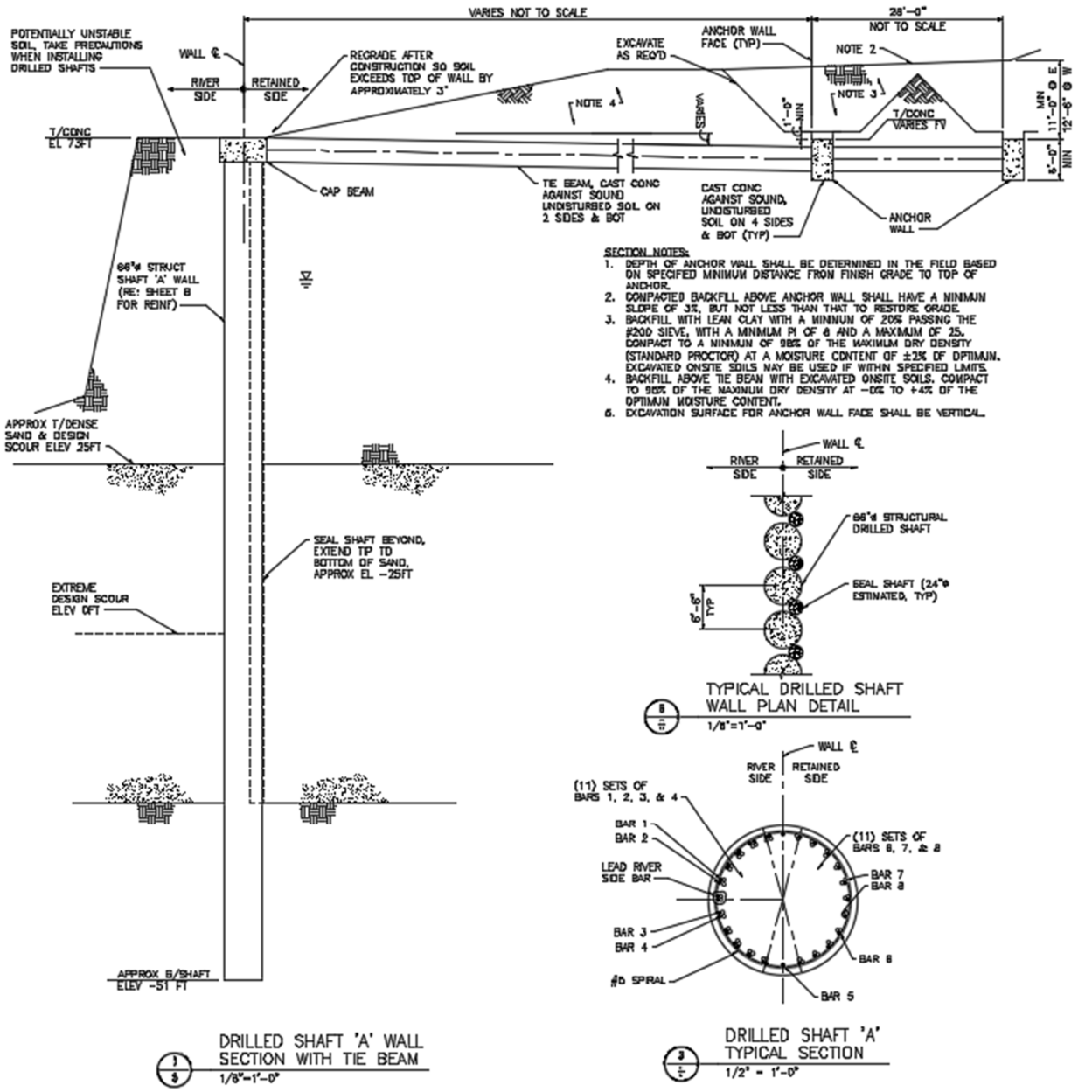


Figure 2 - Typical Section for Retaining Wall per the Original Design pre-Hurricane Harvey

The rapid erosion also required redesign of the wall within the footprint of the existing roadway corridor. It was determined that 10'-0" diameter shafts could be installed using the equipment already on site. Subsequent engineering studies showed that the 10'-0" shafts could resist the lateral earth pressures as a cantilever wall system and did not require installation of an anchor system. This modified layout is shown in Figure 4.

Further studies showed that anticipated erosion of the soils surrounding existing Bent 9 required analysis to confirm it was adequate for a transition from a closed abutment to an interior bridge bent. Original

ground elevations near Bent 9 were approximately elevation +70, while the anticipated scour elevation was considered to at least elevation +25.0 and ultimately to the final river flowline elevation. Bent 9 was determined to be adequate to support the bridge as an interior bent.

After consideration and study, it was concluded that the new cantilever wall system crossing to the north (land) side of Bent 9 would provide the required erosion protection without affecting shaft stability at Bent 9. While this required the removal and replacement of the bridge approach slab, it eliminated the requirement to build the complex retaining wall and soil nail system under the bridge profile.

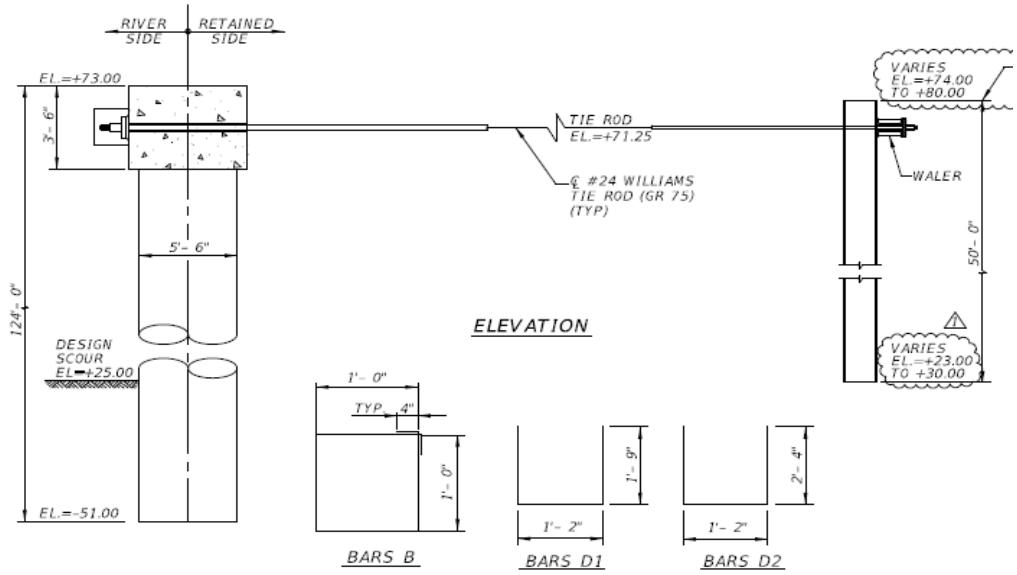


Figure 3- Typical Anchor Wall Details

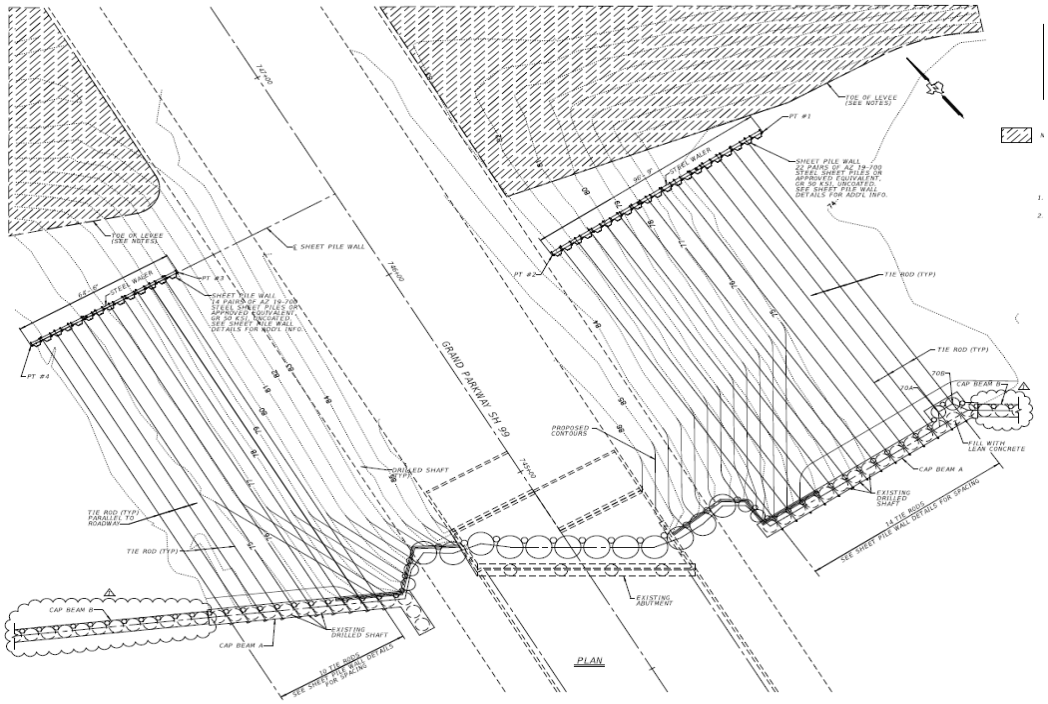


Figure 4 - Modified Site Layout - post-Hurricane Harvey

Hurricane Harvey

Hurricane Harvey made landfall along the middle Texas coast near Rockport Aug 25. Harvey generally spared the site and the Brazos watershed during its first few days, as Sugar Land fell between hurricane bands rotating through the Houston area. The Brazos River had been running at minimal levels prior to the storm. Based on the projected storm path the nearest NOAA river height projections in nearby Richmond were raised to a record 59.0 ft (gauge level) Sunday, August 27 with an extended flood level duration. Mandatory evacuations were ordered that evening for the adjacent New Territory subdivision. Between August 26 and August 29 (4 days) Hurricane Harvey dumped 35 inches of rain at this location and similar amounts were recorded over the entire region, although some areas received up to 52 inches of rain during this time.

The Brazos River actually peaked at 55.2 ft gauge level (also a record) on August 31 and the evacuation order was changed to voluntary on September 2. The drilling equipment was moved to the top of the roadway embankment and edge of levee prior to stopping work due to the hurricane and fortunately none of the equipment was damaged by the floodwaters. A picture of the flooded jobsite is shown in Figure 6.

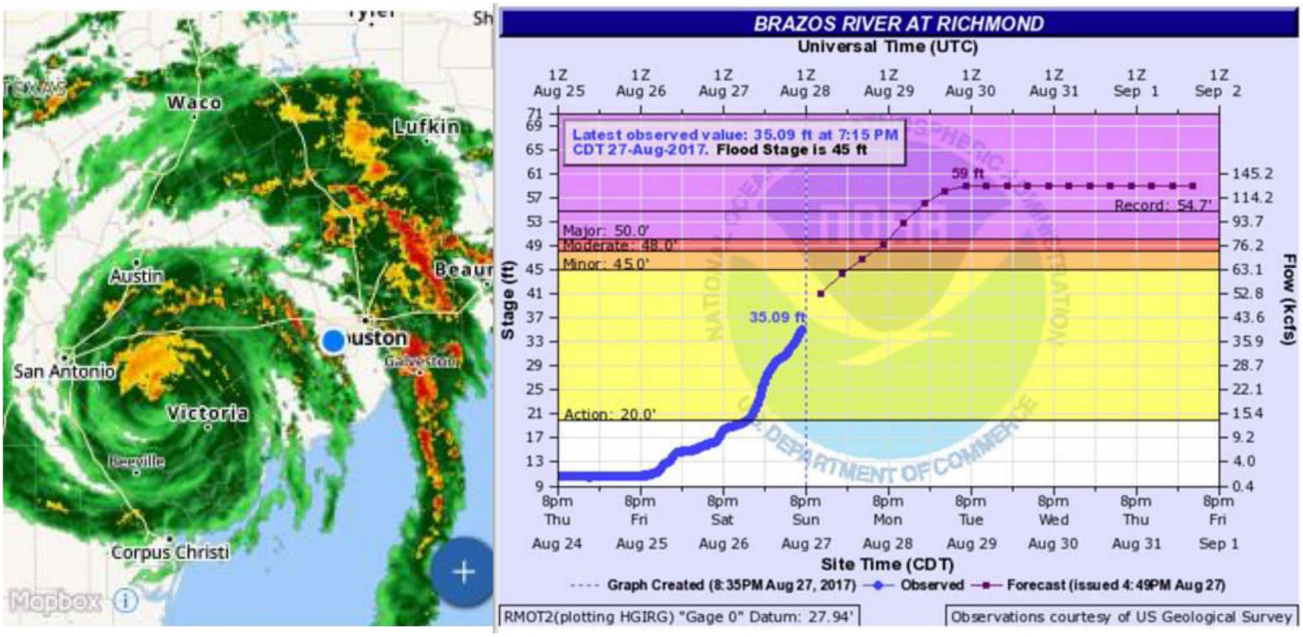


Figure 5. Hurricane Harvey Radar Image and Projected River Flooding



Figure 6. Flooded Jobsite on August 30

Installation of Drilled Shafts and ACIP Piles

The structural drilled shafts used to form the wall were typically 5.5-ft-diameter and 120-ft-long spaced at a 6.5-ft center-to-center spacing except where the wall alignment went through the highway embankment. Since those shafts could not be tied back they were designed as a cantilevered wall. Those 12 shafts were 10-ft-diameter and typically 130-ft-long, and were spaced at an 11.0-ft center-to-center spacing. Both shaft diameters thus had a plan 1 foot clear spacing between them (see Figure 4). All of the shafts included a 40-ft-long permanent steel casing in the upper portion of the shaft which penetrated below the bottom of bank level. This protected the shafts from blowing out laterally through the bank during drilling and concreting. In some areas the bank erosion had already encroached to the shaft alignment.

Drilled Shaft Installation. The drilled shafts were advanced using a bentonite slurry to keep the holes open during drilling. Once the final depth was reached, the slurry was de-sanded and the bottom of the hole was cleaned out with a clean out bucket. The full length rebar cage was then installed and the shafts were then concreted using a tremie pipe. The slurry was returned to the slurry tanks and re-used on the next shaft.

ACIP Seal Pile Installation. The seal piles were 24-inch-diameter and 95-ft-long and were placed immediately adjacent to the gap between the 5.5-ft-diameter structural drilled shafts. These seal piles were installed using ACIP pile installation techniques. A 24-inch-diameter hollow stem auger was used to drill down to 95 ft where fluid grout was then pumped under pressure through the hollow stem of the auger and out the drill bit. Prior to withdrawing the auger a 5 ft grout head was pumped in the bottom. Once the grout head was established the auger was continuously withdrawn while pumping at least 115 percent of the theoretical volume in each increment until grout was observed flowing from the ground surface, which is defined as the grout return depth. The grout return depth should be at least the same at the initial grout head but was typically 10 ft or more.

When initially spotting up on each drilling location the bit and auger were placed directly against the two adjacent steel casings for the structural drilled shafts. The leads were then plumbed and adjusted to maintain verticality. The auger then drilled down beside both casings with the casings acting as a guide below grade.

The total volume pumped in the seal piles averaged 132 percent of the theoretical volume with an average grout return depth of 12 ft. The average in-situ pile diameter based on the actual volume pumped in the piles was 27.5 inches. All piles were installed using a Pile Installation Recorder (PIR) to automatically monitor and record key aspects of the pile installation process. The PIR monitors depth, time, incremental and total grout volume, grout pressure and hydraulic pressure (torque) at the gearbox. The operator is able to monitor these values in real time as the pile is being installed and make any required adjustments. The PIR also provides a digital record of this information for each pile.

Drilled Shaft Seal Pile Installation. The nine seal piles between the 10-ft-diameter structural drilled shafts that went through the embankment were 30-inch-diameter and 100-ft-long and were installed using slurry displaced drilled shaft techniques. This was done primarily for schedule issues as the drilled shaft rig was already in place on the roadway since it had just installed the structural drilled shafts. One direction of the highway had to be shut down to install these shafts and all traffic was being detoured so speed of installation was a primary concern to meet the schedule. A high slump and flowable concrete was used for these seal shafts. The concrete was placed with a full length enclosed system tremie. During concrete placement we first established a concrete head outside of the tremie prior to lifting the tremie pipe. The concrete depth in the seal shaft was monitored to make sure the tremie pipe was always in the concrete a minimum of 5 ft. In this sense, the drilled shaft seal piles were installed similarly to the ACIP pile seal piles. A larger diameter seal pile was used for drilled shaft application than the ACIP seal piles for both constructability and conservatism.

SoniCaliper Testing. The project specifications listed a vertical tolerance for the shafts at 1 inch off center per 10 ft vertical (0.83%) out of plumb consistent with TxDOT specifications for drilled shafts. Because

these are part of a wall that utilizes seal piles it was important to measure both the shape (diameter) and verticality of the shafts to determine what the clear spacing was between the shafts. Per the specifications, if the clear spacing between shafts was greater than 18 inches at the maximum depth where a seal is still required of 95 ft then a larger 30-inch-diameter seal shaft would be required.

The verticality and shaft diameter was measured using the SoniCaliper tool. The SoniCaliper™ is a quality assurance tool for drilled shafts that has the ability to virtually "see" foundation excavation shapes prior to placing concrete in dry or slurry conditions. This sonar calipering technique provides results in real-time display and it creates "as-constructed" images and calculations immediately after the excavation has been profiled. This information gives the engineer and contractor confidence that the end product is manufactured according to specification. Utilizing sonar technology, the SoniCaliper provides a full 360-degree profile and can determine diameter, assess verticality and calculate volume.

The initial phase of the testing plan was to run a SoniCaliper test on the first 10 shafts to check the verticality and diameter. The project team would then evaluate the data to determine if continued shaft testing would be necessary. We actually tested the first 13 shafts to provide a little extra data to evaluate. The center offset measured at 100 ft ranged from 0.25 inches to 5 inches with an average of 2.6 inches on the first 13 shafts. The offset standard deviation was 1.6 inches. The tolerance at 100 ft was 10 inches so all the shafts were well within tolerance. The direction the shafts were off center were primarily perpendicular to the wall alignment so the clear spacing between shafts had not increased to the point where a larger seal shaft would be needed. Based on these excellent results the project team determined that further SoniCaliper testing was not required.

Figure 7 shows the erosion of the riverbank post hurricane flooding along the retaining wall.



Figure 7. Post Hurricane Erosion Along Retaining Wall Under Construction

Summary and Conclusions

Even with a record hurricane impacting the site resulting in major design changes the project was quite successful. The work was done on budget and completed ahead of schedule. Even the lane closures that required traffic detours were completed ahead of schedule in both instances. Everyone on the project team should be commended for working together to achieve this level of success under such challenging circumstances. Our conclusions are as follows:

- An innovative retaining wall design consisting of tangent drilled shafts with supplementary seal piles was used to limit continuing bank erosion along the Brazos River in Southeast Texas. The riverbank erosion had progressed to where it was threatening the stability of both the bridge abutment and corresponding approach embankment of the heavily travelled Highway 99 bridge at this location.
- The tangent pile with seal pile retaining wall system selected for this project was not only more cost effective and faster to install than secant shafts, it also allowed for better flexibility in design, which ended up being needed due to design changes resulting from Hurricane Harvey.
- The Owner's selection of the entire project team prior to final design proved to be very prudent in this case. It allowed both the designers and contractors to develop a more effective design by putting together the best ideas from all parties.
- This excellent working environment between the project team created from the very beginning of the project continued throughout the entire project and was equally useful in quickly coming up with the required re-design.

Acknowledgments

The following main project team members were involved with the project.

- Fort Bend Grand Parkway Toll Road Authority (Owner)
- BGE, Inc. (General Engineering Consultant, Project Designer Post Harvey)
- NBG Constructors (General Contractor)
- A.H. Beck Foundation Company (Specialty Deep Foundation Contractor)

NON-CONVENTIONAL PRACTICE: RECENT CASE HISTORIES OF THE USE OF VERTICAL BUTTRESS PILES IN DEEP EXCAVATION SUPPORT

Abid O. Adekunte, Geobond (UK) Limited, Farnborough, Hampshire, U.K, +44 1252 515 168, abida@geobond.co.uk
David Greentree, Geobond (UK) Limited, Farnborough, Hampshire, U.K, +44 1252 515 168, engineers@geobond.co.uk
Tony Brunger, RC Structures & Basements Limited, Surrey, U.K, +44 2086 697, tony.brunger@rcstructures.co.uk
George Munteanu, OpticRealm Limited, London, U.K, +44 2077 135 994, george@opticrealm.co.uk

ABSTRACT

A number of novel solutions have been proposed in recent years as alternatives to props and tie-backs in deep excavation support e.g. Adekunte (2008), Deschamps et. al. (2008), Adekunte et al. (2010) and Adekunte (2014). A number of these non-standard restraining solutions involve the construction of permanent or temporary vertical or raking buttress piles that are rigidly connected to the excavation support wall at regular intervals along the wall run.

This paper chiefly focuses on the design and construction of twin-vertical buttress piles as restraining systems behind or in front of embedded retaining walls. The system essentially relies on the push-pull mechanism that develops between the twin piles, to maintain the overall stability of the excavation support. The paper's main areas of concentration include; finite element modelling, geostructural design, construction procedure, instrumentation and monitoring that are associated with the application of twin-buttress pile systems. These are supported with project details of three recently completed high-end luxurious residential developments in Greater London, England, on which the twin-buttress pile system was used to restrain the excavation support walls for the basements on the sites.

The mode of application of the system varies across the three sites. While the system was adopted as a long term solution behind the retaining wall on one of the sites, it was designed and constructed for temporary use in front of the retaining walls on the other two sites. Instrumentation and monitoring results from all the sites show the non-traditional system to be safe and effective, whilst having significant beneficial effects on construction programme, sequence of works and project cost.

Keywords: excavation support, retaining wall, buttress piles, push-pull mechanism, finite element modelling, geostructural design, instrumentation, monitoring.

INTRODUCTION

It is becoming increasingly difficult to restrain bored pile retaining walls in urban areas with the well-established traditional systems; props and tie-backs. Due to inadequate space in built-up areas, many urban construction sites are tight and as contractors are compelled to maximise working space, they often prefer to avoid the use of temporary props and braces. In addition, the existence of neighbouring buildings and sensitive underground services in built-up areas often makes the application of ground anchors difficult.

For the above reasons, the use of twin buttress pile systems (TBPs) is increasingly becoming popular on urban sites, as suitable alternatives to conventional props and ground anchors. This alternative solution essentially involves the construction of twin vertical bored piles at right angle to the main retaining wall line, at regular intervals along the wall. The TBPs are connected to the main pile retaining wall by reinforced concrete capping beams. If the TBPs are only required for temporary use, they may be installed in front of

© 2018 Deep Foundations Institute

the pile wall (i.e. within proposed excavation area), such that they may be trimmed off once the permanent reinforced concrete slabs in front of the pile wall achieve sufficient structural strength. For TBPs to be adopted as permanent solutions, they need to be installed behind the retaining wall (i.e. outside the excavation/basement area), where they would be out-of-sight and non-obstructive in both temporary and permanent conditions.

The choice of suitable buttress pile size and spacing is typically an iterative process, with the underlying aim of striking a reasonably good balance between efficiency and economy. However, it is advisable to adopt a buttress pile size that is equivalent to the diameter of the piles that make up the main pile retaining wall, so as to limit differential behaviour between the pile wall and the TBP systems. In addition, the gap between the two piles in a TBP system must be at least 3D (where D is pile diameter), so as to limit the interaction between the twin piles, especially below excavation level.

This paper chiefly focuses on the design and construction aspects of three separate sites on which TBPs have been adopted as temporary and/or permanent restraining systems. The paper accounts for the associated numerical modelling procedures, geotechnical/geostructural design approaches, construction procedures and performance monitoring.

GROUND CONDITIONS & MODELLING

This study focuses on three separate sites; site 1, which is located in Chiswick, West London, site 2, which is located in Hadley Wood, Hertfordshire and site 3, which is located in Virginia Water, Surrey. Stratigraphy on site 1 comprises of 2m thick made ground underlain by a 7m thick layer of medium dense to dense river terrace deposit, which in turn overlies a stiff to very stiff London clay stratum that extends down to the limit of ground investigation at 20m depth.

The river terrace deposit is chiefly made up of pebble-gravel and sand. These were deposited 500,000 years ago when the River Thames was diverted from its original course to its current channel. The London clay stratum is essentially an overconsolidated material of low permeability and high plasticity, with measured plasticity indices ranging between 40%-50%. Monitored highest static groundwater level over the winter months was 4m below ground level (bgl).

Stratigraphy on site 2 mainly comprises of stiff to very stiff London clay. Ground conditions on site 3 comprise of 2m of made ground overlying alternating layers of very soft to soft to firm sandy clay and loose to medium dense sand, which are underlain by stiff to very stiff sandy clay at 8m depth. Measured overconsolidation ratio (OCR) of samples of the stiff to very stiff clay reduces from 60 at 8m depth to 20 at 20m depth. Measured coefficient of earth pressure K_o varies between 1.5-2.5. Generalised stratigraphy and associated geotechnical design parameters for sites 1, 2 & 3 are presented in tables 1, 2 & 3 respectively. In tables 1, 2 & 3, N_{spt} = standard penetration test N value, z = depth below top of stratum.

In order to allow for the influence of stress relief and remoulding during excavation and basement construction, coefficients of earth pressure K_o for the overconsolidated materials were limited to 1.0, in accordance with the recommendations of the CIRIA report No. C580 (2003). The clay layers were modelled with total stress parameters in the temporary condition. In the permanent condition, the clay layers were assumed to exhibit drained behaviour and thus modelled with effective stress parameters. All other soil layers were conservatively assumed to exhibit drained behaviour in both temporary and permanent conditions and thus modelled with effective stress parameters only.

Coefficients of active and passive pressure K_a and K_p were deduced from Caquot & Kensel's (1984) chart. Effective wall friction angles δ on the passive and active sides were generally taken to be $0.5\phi'$ and $0.67\phi'$ respectively (where ϕ' is the effective angle of shearing resistance).

SITE 1 (CHISWICK, WEST LONDON)

Proposed Development: the project on site 1 was centred on the redevelopment of the pre-existing surface car park on the site into 6 units of town houses, with an underground car park spanning across the entire site area. It was proposed to support the 4m deep excavation for the basement car park with a contiguous bored pile retaining wall. The pile retaining wall was also required to function as a permanent component of the finished basement structure. Typical section of the earth retention system on site 1 is shown in figure 1. The TBPs were only required for temporary use and therefore, they were designed and installed in front of the pile wall (within proposed excavation/basement area), while they were subsequently trimmed down to depths below basement level once the basement slab and ground floor slab were constructed.

Geotechnical/Geostructural Design: the design for the deep excavation support system involved 4 main stages, which are described below.

- Ultimate Limit State (ULS) Analysis: this essentially involved the use of factored soil parameters to estimate the required embedment of the pile retaining wall, for overall stability to be maintained, whilst considering the pile wall to be restrained at capping beam level. The analysis was carried out with CADS PWS 5.6 modelling programme for pile retaining walls. The analysis also provides information on ultimate bending moments and shear forces on the pile wall.

- Serviceability Limit State (SLS) Analysis: this involved the use of unfactored soil parameters to estimate the potential lateral displacement of the pile wall, as well as service bending moments and shear forces on the pile retaining wall. This analysis has also been carried out with CADS PWS 5.6 modelling programme for pile retaining walls.

- Geostructural Finite Element Analysis of Pile Wall-Twin Buttress Pile System: the potential behaviour of the pile wall-buttress system was analysed by finite element (FE) modelling. This involved the use of unfactored soil parameters. The behaviour of the pile wall–buttress pile system is a complex soil-structure interaction problem that cannot be adequately catered for with simple empirical structural or geotechnical calculation methods. The geostructural assessment of such an earth retention system needs to consider not only the separate capacities of the individual components of the system, but their combined capacities and interaction under service loading e.g. the push-pull mechanism between twin buttress piles, load transfer between the pile wall, capping beam and buttress piles, etc.

  Based on the above, the finite element method was considered to be a more appropriate solution. The potential behaviour of the pile wall–buttress system on site 1 was analysed with PLAXIS 2D finite element modelling programme, which links the pile wall, buttress system, existing neighbouring structures, ground and ground water into a single soil-structure model. The FE model was based on very fine 16-node meshes, while soil parameters used have already been presented in table 1. The piles and capping beams were modelled as beam elements, while the permanent reinforced concrete (RC) slabs were modelled as fixed-ended anchors. Analysis was based on unfactored loads and soil parameters and it did provide information on potential ground movement, pile vertical & lateral deflections, pile & beam bending moments, shear forces and axial forces. A sample exaggerated deformed mesh is shown in figure 2, while a copy of the output file illustrating the predicted ground movement within the vicinity of the site is shown in figure 3. In addition, the main results of the FE analysis are summarised in table 4. Service forces and moments shown in table 4 were subsequently factored up to arrive at ultimate (design) values for the structural design of the twin buttress pile system.

Table 1 – Generalised stratigraphy & geotechnical design parameters for site 1 (Chiswick, West London)

Depth (m) bgl	Description	N_{spt}	Angle of Shearing Resistance ϕ' (°)	Cohesion C_u or [C'] (kPa)	Young's Modulus E_u or [E'] (kPa)
0.0 – 2.0	Made Ground/Firm Slightly Sandy Clay	13-32	30.0	[0.0]	[30000]
2.0 – 9.0	Medium Dense to Dense Sand & Gravel	18-42	37.0	[0.0]	[75000]
Below 9.0	Stiff to Very Stiff London Clay	28-40	25.0	90 + 8z [5.0]	72000 + 6400z [57600 + 5120z]

Table 2 – Geotechnical design parameters for site 2 (Hadley Wood, Hertfordshire)

Stratum	Bulk Density γ (kN/m^3)	E_{50}^{ref} (kPa)	E_{oed}^{ref} (kPa)	E_{ur}^{ref} (kPa)	Cohesion C_u (kPa)	Angle of Shearing Resistance ϕ' (°)	Coefficient of Earth Pressure K_o
Stiff to Very Stiff London Clay	19.0	76000 + 6400z	76000 + 6400z	228000 + 19200z	95 + 8z	-	1.0

E_{50}^{ref} = secant stiffness in standard triaxial test, E_{oed}^{ref} = tangent stiffness for primary oedometer loading,
E_{ur}^{ref} = unloading/reloading stiffness.

Table 3 – Geotechnical design parameters for site 3 (Virginia Water, Surrey)

Depth (m) bgl	Stratum	Bulk density γ (kN/m^3)	Young's modulus E_u or [E'] (kPa)	Cohesion C_u or [C'] (kPa)	Angle of shearing resistance ϕ' (°)	Coefficient of earth pressure K_o
0.0 – 2.0	Made Ground	18.0	[30000]	[0.0]	25.0	0.5
2.0 – 8.0	Very Soft to Soft to Firm Sandy Clay/ Loose to Medium Dense Sand	19.0	[40000]	[0.0]	28.0	1.0
Below 8.0	Stiff to Very Stiff Sandy Clay	19.0	120000 [96000]	150.0 [5.0]	25.0	1.0

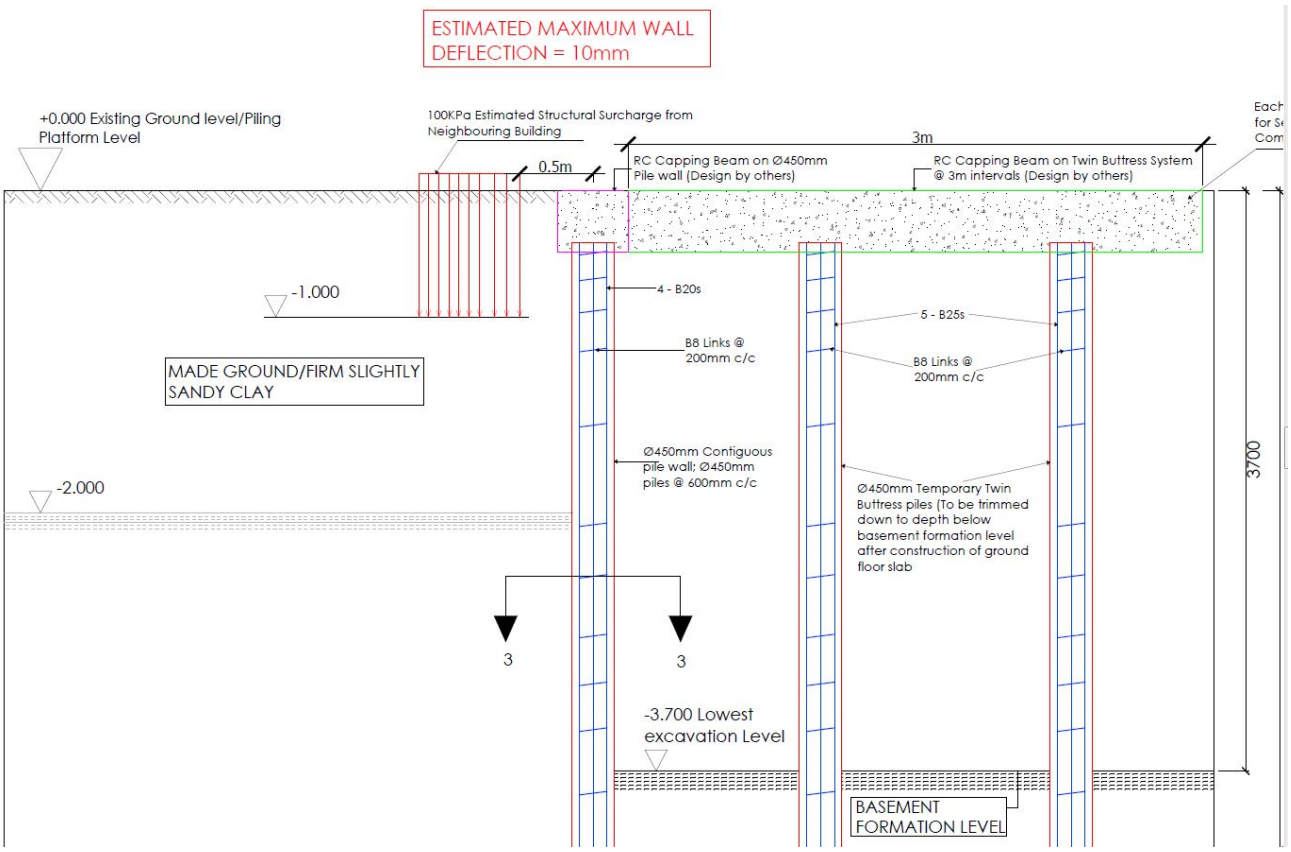


Figure 1 – Typical section of the earth retention system on site 1 (Virginia Water, Surrey).

Essentially, the FE model had predicted the maximum ground movement within the vicinity of the site and the worst case lateral deflection of the pile wall to be 7.5mm and 4mm respectively. Also, the maximum displacement of the buttress piles was estimated to be 3.5mm.

- Capacities of Twin Buttress Pile System and Pile Wall under Vertical Loading: the FE output files show the buttress piles to be subject to axial tension and compression during and after bulk excavation (see table 4). Also, the FE analysis results show the pile retaining wall to be subject to axial compression and tension. The designs for the pile wall and the twin buttress pile systems to support vertical axial loading were based on the traditional bearing capacity approach for axially loaded piles. However, the pile wall was assumed to act as a continuous deep strip footing below basement formation level, surrounded by a block of soil, with the assumption of a block type failure mechanism in the ultimate state. In addition, the bearing capacity factors N_c & N_q in the cohesive and cohesionless strata respectively were reduced with a factor f, to account for the existence of gaps between piles in the contiguous pile wall.

  The reduction factor f is expressed as;

$$f = \frac{\pi D}{4S} \qquad \text{---------- [1]}$$

where D = pile diameter and S = pile centre to centre spacing. The above approach produces an estimate of the axial capacities of the pile wall per metre run; see Adekunte (2014) for more detailed information on this methodology.

- Structural Designs for Pile Wall, Twin Buttress Pile System and RC Capping Beam: based on the worst case results of the different sets of analysis described above, structural designs for the pile wall, TBPs and RC capping beams were carried out in accordance with the recommendations of the BS 8110 (1997).

Construction Sequence Adopted on Site: the sequence of construction followed on site 1 is presented below:

1. Install ∅450 piles @ 600mm c/c from piling platform level to specified depths, to form contiguous pile wall.
2. Install ∅450 twin buttress piles at 90° angle to pile wall run, at 3m intervals in front of pile wall (proposed bulk excavation/basement area).
3. Break down contiguous piles and buttress piles to 75mm above proposed soffit levels of RC capping beams.
4. Construct RC capping beams on contiguous pile wall and buttress piles. The capping beams on buttress piles must be rigidly connected to capping beam on pile wall.
5. Carry out bulk excavation to basement formation level (approx. 4m dig).
6. Construct basement slab and dowel into pile retaining wall.
7. Construct RC liner wall in front of pile retaining wall.
8. Construct ground floor slab.
9. Cut down buttress piles to depths below basement formation level.
10. Construct superstructure.

Performance Monitoring of Pile Wall-Buttress System: upon completion of the installation of the pile wall, the twin buttress pile systems and the RC capping beams, the pile wall was instrumented with survey targets, while the movements of the targets were monitored by optical survey during and after bulk excavation. The instrumentation and monitoring procedure followed is concisely outlined below:

- after pile installation and capping beam construction, shot fix nails were installed as targets at selected positions on capping beams;
- initial coordinates of targets were recorded using survey instrument;
- after recording initial coordinates, readings of coordinates were taken at 1 working day-interval during excavation and every two weeks after completion of excavation;
- monitoring continued over a period of 6 weeks after completion of bulk excavation until the basement and ground floor slabs achieved sufficient structural strength.

Monitoring results show maximum pile wall lateral deflection to be 2 mm, which was approximately 50% of the theoretically estimated potential wall lateral deflection, as described earlier in this section. As overall wall movement was relatively negligible, no serviceability issues were recorded on the adjacent buildings, which were located at relatively close proximity to the excavation area.

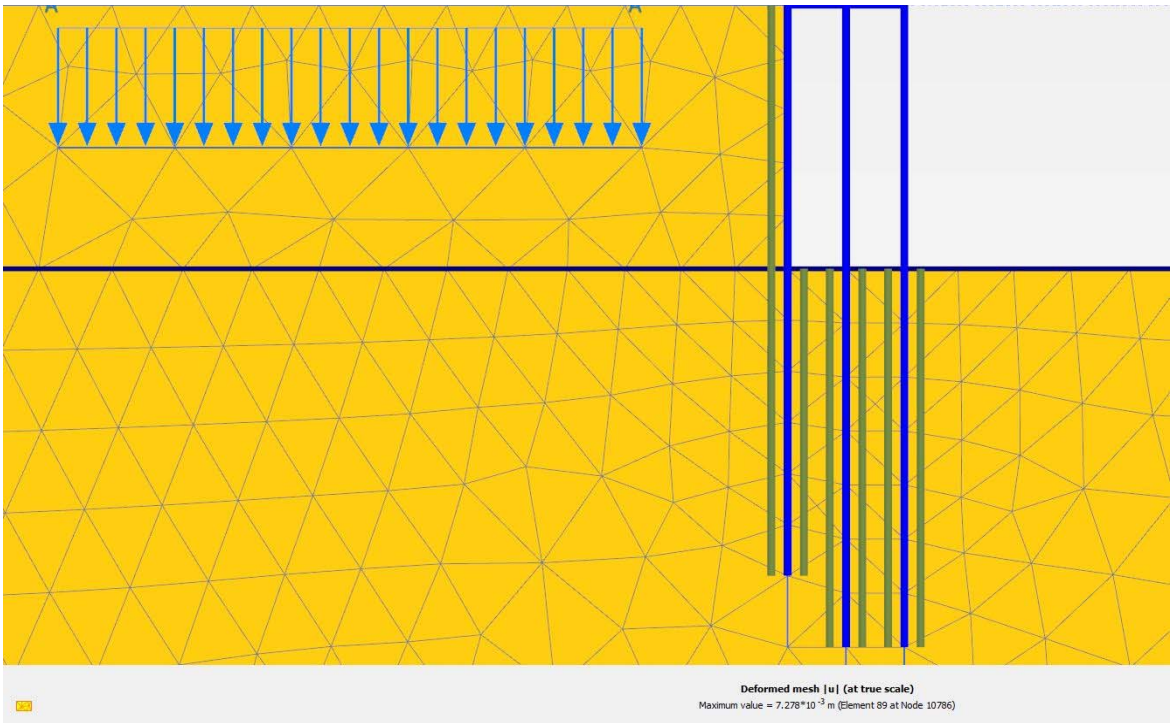


Figure 2 – Typical deformed FE mesh for site 1 (Virginia Water, Surrey).

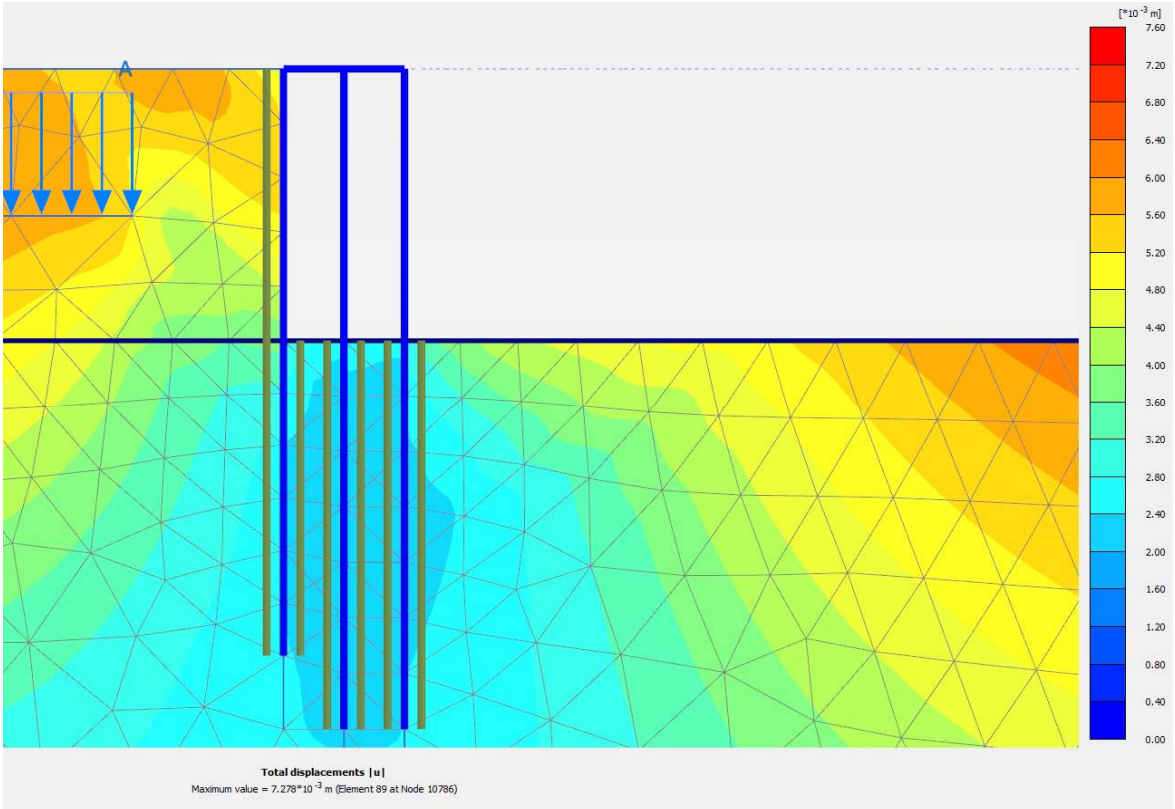


Figure 3 – FE prediction of ground movement within the vicinity of site 1 (Virginia Water, Surrey).

Table 4 – Summary of FE analysis results for site 1 (Virginia Water, Surrey).

Description	Estimated Value
Maximum Ground Movement (mm)	7.5
Maximum Pile Wall Lateral Deflection (mm)	4.0
Maximum Displacement of Buttress Piles (mm)	3.5
Maximum Settlement of Neighbouring Foundations (mm)	6.5
Maximum Compressive Loading on Buttress Piles (KN/m)	40.0
Maximum Tension Loading on Buttress Piles (KN/m)	-10.0
Maximum Bending Moment on Buttress Piles (kNm/m)	40.0
Maximum Shear Force on Buttress Piles (KN/m)	50.0
Maximum Axial Loading on Buttress Capping Beam (KN/m run of wall)	15.0 (compression)
Maximum Bending Moment on Buttress Capping Beam (kNm/m run of wall)	10.0
Maximum Shear Force on Buttress Capping Beam (KN/m run of wall)	20.0

SITE 2 (HADLEY WOOD, HERTFORDSHIRE)

Proposed Development: the development on site 2 comprised of two separate 4 storey-residential blocks of luxury apartments; Blocks A and B, with separate single level basements for both blocks, which were required for underground parking, communal gyms and cinemas. It was proposed to support the 5.5m deep excavation for the basements with contiguous bored pile retaining walls. Typical section of the earth retention system on site 2 is shown in figure 4. In contracts to the solution adopted on site 1, the TBPs on site 2 were installed behind the pile retaining wall (i.e. outside the proposed excavation/basement area); this approach offered the additional benefits completely maximising the available working space in the basement area, while there was no requirement for the trimming down of buttress piles after basement construction and ultimately, the solution was advantageous to the main contractor's construction programme.

Design, Construction Sequence & Performance Monitoring: the design approaches, construction sequence, instrumentation and monitoring procedures adopted on site 2 were similar to those adopted on site 1 as already described in the penultimate section of this paper. Piles for the main pile wall were 8m long, while the buttress piles were 9m long, as illustrated in figure 4 overleaf.

Instrumentation and monitoring results show maximum pile wall lateral deflection to be 4 mm, which was less than 60% of the theoretical prediction made with the FE model for the earth retention system on the site. Overall, the TBPs were found to be quite efficient, as no serviceability issues were recorded within and outside the site, while they did allow the main contractor to make a total savings of 4.5 weeks in construction time, when compared with the Supervising Project Engineer's original proposal for the use of temporary flying struts and corner braces for the basement scheme.

SITE 3 (VIRGINIA WATER, SURREY)

Proposed Development: the development on site 3 was centred on the construction of a new underground car park next to the west wing of an existing 3 storey-mansion. A contiguous pile retaining wall was required to provide lateral support for the 2.3m-6.0m deep excavation for the new subterranean structure. The pile retaining wall comprised of ∅350 piles @ 500mm c/c. The twin buttress pile system for the pile wall was installed in front of the pile wall and the system comprised of ∅450 twin buttress piles installed at right angles to the pile wall run, at 3m intervals in front of the wall. Figure 5 shows the layout of an installed buttress pile system in relation to the pile wall run, while figure 6 shows the pile wall and buttress pile system after completion of bulk excavation.

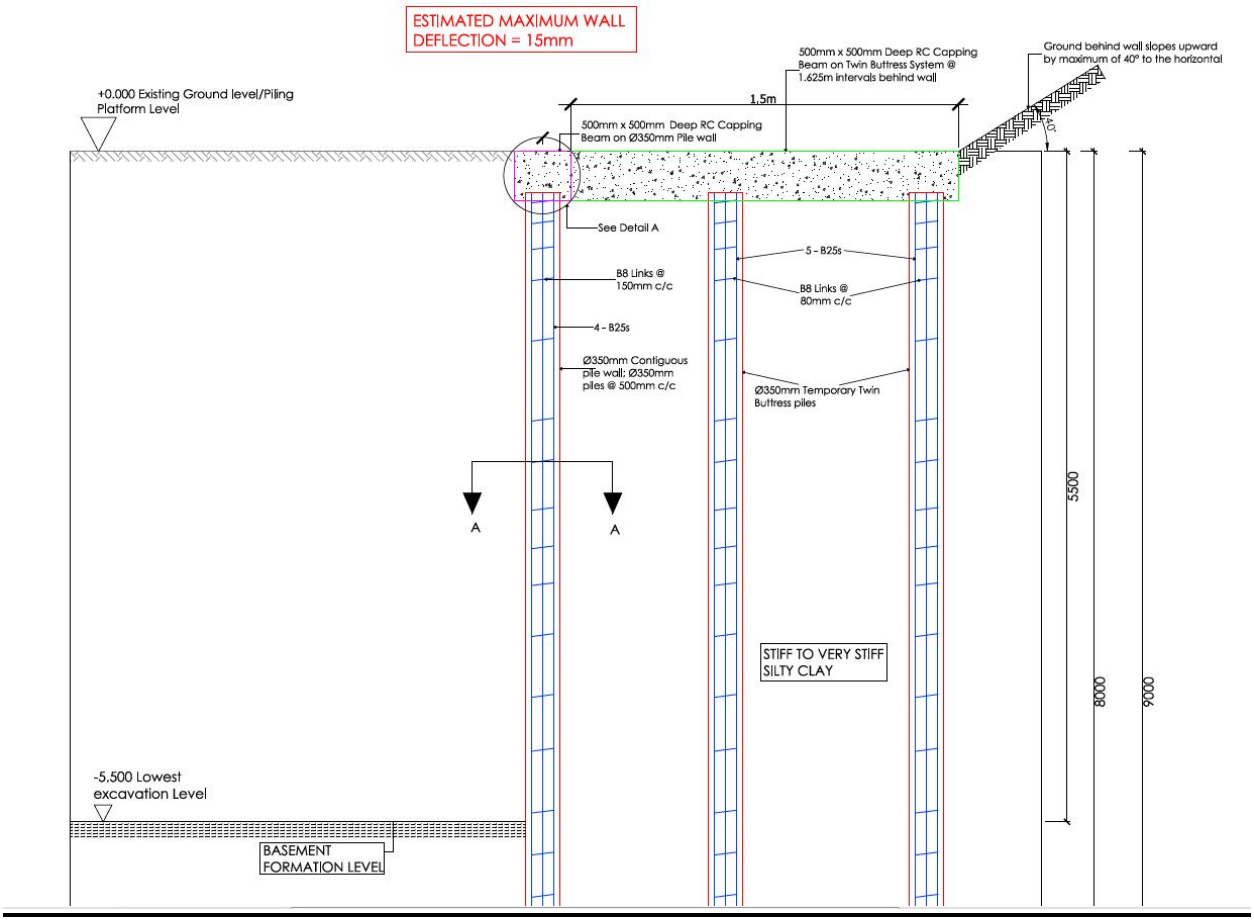


Figure 4 – Typical section of the earth retention system on site 2 (Hadley Wood, Hertfordshire).



Figure 5 – Layout of pile wall, as well as twin buttress piles installed at 90° angle to wall run on site 3 (Virginia Water, Surrey).



Figure 6 – Installed twin buttress pile systems, after completion of bulk excavation for basement on site 3 (Virginia Water, Surrey).

In similarity with sites 1 & 2, on site 3, the TBPs were efficient at limiting the overall movement of the pile retaining wall. Maximum pile wall lateral movement of 9mm was recorded in the deepest area of the basement (6.2m excavation zone). No serviceability issues were recorded on the immediately adjacent substantial building during and after bulk excavation.

SUMMARY & CONCLUSIONS

Detailed information on the numerical modelling, design, construction, instrumentation and monitoring of pile retaining walls restrained with twin buttress pile systems (TBPs) on three separate basement schemes have been provided. The paper clearly lays out the typical construction sequencing and performance monitoring procedures involved with the application of the non-traditional system and these are supported with excerpts of project drawings and site photographs.

Essentially, the TBPs have been found to be quite efficient at limiting wall movements and maintaining overall stability on all the three sites covered in the study. Monitored pile wall deflections were generally

much lower than theoretical design estimates, while no serviceability issues were recorded on neighbouring properties or within the sites.

The main benefits of the TBPs over traditional propping and ground anchorage include; maximisation of working space within excavation areas (an advantage over props) and the significantly reduced potential of intrusion into neighbouring properties (an advantage over tie-back anchorage). In addition, as the TBPs are installed concurrently with the pile retaining wall, with the same equipment, they offer significant benefits towards the contractor's construction programme/work schedule.

REFERENCES

ADEKUNTE, A., 2014. Dealing with complexities associated with the application of bored pile retaining walls in urban developments. Proceedings of the Deep Foundation Institute's 39th Annual Conference on Deep Foundations, Atlanta Georgia, October 2014.

ADEKUNTE, A., O'HARA, P., and DENNANY, A., 2010. Novel methods of restraining embedded retaining walls. Proceedings of the Deep Foundation Institute's 35th Annual Conference on Deep Foundations, Hollywood Ca., October 2010.

ADEKUNTE, A., 2008. An innovative use of bored tension piles in embedded retaining wall design and construction. Proceedings of the Deep Foundation Institute's 33rd Annual Conference on Deep Foundations & 11th International Conference on Piling & Deep Foundations, pp. 167-176, New York, October 2008.

BRITISH STANDARDS INSTITUTION., 1997. BS 8110-1: 1997 – Structural use of concrete. Part 1: code of practice for design and construction. BSI, London, 1997.

CAQUOT, A. and KERISEL, J., 1948. Tables for the calculation of passive pressure, active pressure and bearing capacity of foundations. Gauthier-Villars, Paris, 1948.

CONSTRUCTION INDUSTRY RESEARCH AND INFORMATION ASSOCIATION., 2017. Report No. C760 – Guidance on Embedded Retaining Wall Design, CIRIA, London, 2017.

DESCHAMPS, R., BONITA, G., and KARTOFILIS, D., 2008. Introducing VCE's – Support of Excavation without Tie-backs. Proceedings of the Deep Foundation Institute's 33rd Annual Conference on Deep Foundations & 11th International Conference on Piling & Deep Foundations, pp. 39-46, New York, October 2008.

ACKNOWLEDGEMENTS

The first author would like to dedicate this paper to my daughter; Omojadesola Adebimpe Aduke, her mum Adedoyin, every child in Yewaland Southwest Nigeria and every member of the Young Yewa Professionals Foundation. The first author is also grateful to the entire management of GEOBOND (UK) Limited and ABTECH Basements (UK) Limited for their unrelenting support before, during and after the preparation of this paper.

Also, the first author would like to express his special gratitude to his Dad, Mum, siblings (Adeoniye, Oluyemi, Adefunke & Adeola) and the following individuals, whose support and words of encouragement have kept his career going over the years; Dr. Francis Lucas, Akin Fasipe, Segun Olukoya, Bayo Badmos, Dr. Akin Babatunde, Abiodun Ogunnaike, Yinka Ogun, Tunji Alade, Mr. Bankole, Dr. F.A Olutoge, Dr. G.A Alade, Dr. Kenneth Gavin, Bernard Casey, Richard Holmes, Andy Sneddon, Bishop & Pro. Lucas and Pastor Beckley. You would all forever be loved and appreciated!

RETROFITTING DRAINAGE SYSTEMS WITH PRESSED-IN SHEET PILES IN VERY HARD SOIL IN SOUTHERN CALIFORNIA

Takefumi Takuma, Giken America Corp., Orlando, FL, 407-380-3232, takefumi_takuma-email@yahoo.co.jp
Christopher DellAringa, Blue Iron Inc., Sacramento, CA, 916-340-5600, chris@blueironinc.com
Masashi Nagano, Giken America Corp., Orlando, FL, U.S.A., 407-380-3232, nagano@giken.com

Keywords: press-in, sheet pile, crush auger, simultaneous augering, low noise, low vibration

ABSTRACT

Multiple agencies in Southern California are retrofitting and upgrading their levees to catch up with ever-advancing urbanization affecting the requirements for existing channels and levees in this seismically active zone. Pressed-in sheet piles have been specified on some of these projects to minimize noise and vibration problems associated with sheet pile installation. This paper will study three Southern California levee and sewer pipeline retrofit projects that utilized pressed-in sheet piles in hard soil conditions with N-values higher than 50.

BACKGROUND

Southern California is home to numerous drainage channels fortified with earthen levees. In spite of the region's semi-arid climate with varying annual precipitation from year to year, winter storms can bring in heavy and continuous rainfall to the area which overwhelms the levees' capacities at times. Some levees are running through densely populated areas with homes and other sensitive structures such as underground utilities and bridge piers. Conventional sheet pile driving utilizes either percussive or vibratory pile driving methods, both of which generate high levels of noise and vibration, causing nuisance and potential damage to nearby structures. On the other hand, the press-in piling method utilizes a hydraulic force to push piles into the ground, thus practically eliminating the noise and vibration issue. Although there are types of press-in piling systems mounted on tall leaders on large crawler-base machines, they are less frequently used due to its much larger size and more limited drivability than the type discussed hereunder. The other type of press-in machine sits on top of already installed piles and is anchored with its own weight and additional counter weight when starting off as shown in Figure 1. Once the first few piles are pressed in, the equipment grips on top of the installed piles and moves forward on its own as the pile installation progresses. See Figure 2. This method does not use a vibratory or percussive force to install piles.

Its advantages are:

1. Low noise and practically vibration free (White et al., 2002). It enables piling projects close to houses, schools, hospitals, and other sensitive structures as well as in the areas where sensitive fish and/or animals are around. This feature was the primary reason that the method was specified for the case study projects being discussed.

2. The equipment size is relatively small while its clamping points are much lower than those of other pile driving methods. This feature enables the equipment to work in physically tight working conditions, both horizontally and vertically, such as an area under railway girders (Takuma et al., 2015) or right next to existing structures.

3. With attachments, it can press in piles into hard soil effectively. A high pressure water jet attachment or a continuous flight auger attachement allows the piles to be driven simultaneously as the attachment loosens the hard soil (details to be discussed later in the next section) without having to bring in a large predrilling machine.

© 2018 Deep Foundations Institute

4. It can achieve much more accurate and safer pile installation due to a combination of better control of the piles and lower clamping points compared with other pile driving methods.

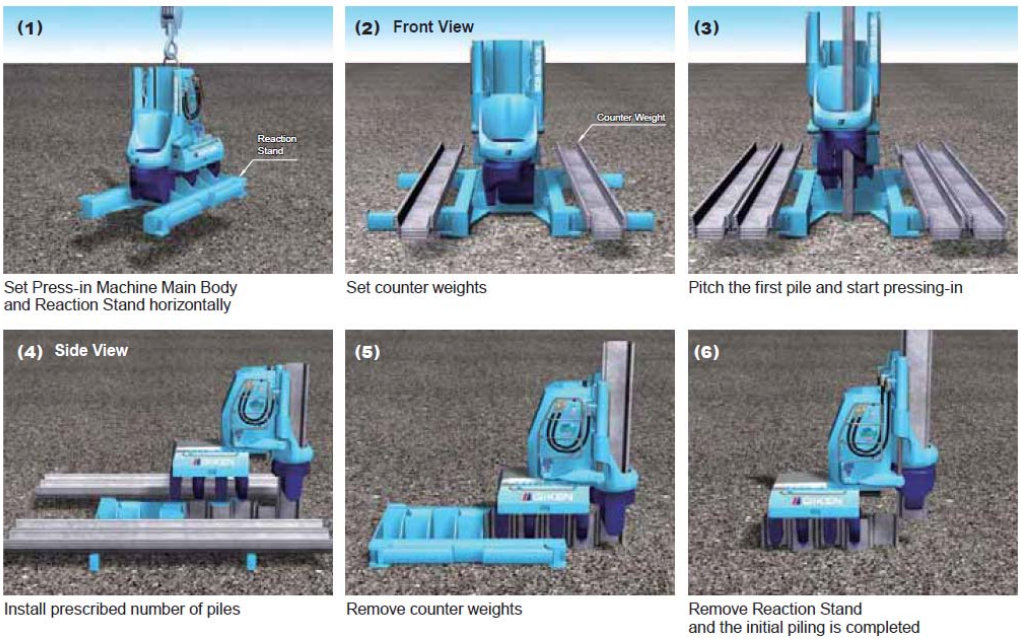


Figure 1 Starting of Press-in Piling

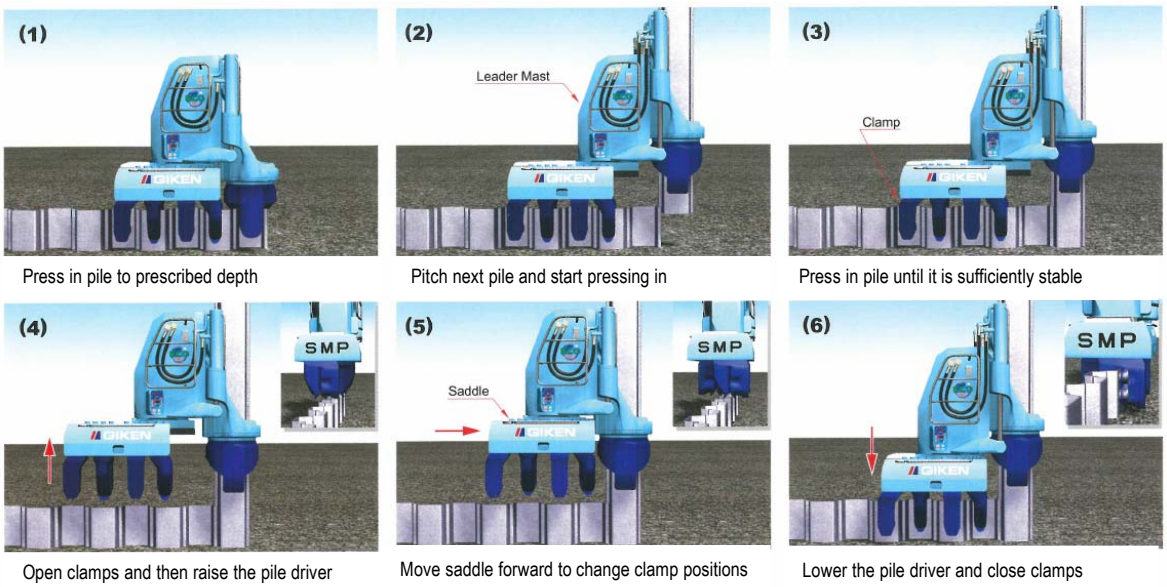


Figure 2 "Self-walk" Sequence With Press-in Piling Equipment

SHEET PILE INSTALLATION IN HARD GROUND

Depending on the types of soil and how hard it might be, either water jetting or predrilling becomes necessary for sheet pile installation in hard soil with N-values of higher than 25 to 30. Water jetting is effective for dense sand, silt, and some clay, while predrilling is suited for denser sand and silt, stiff clay, gravel, boulders, and soft rock. Although water jetting utilizes smaller size equipment than predrilling and can achieve high production, it works well only in the above-mentioned soil types and poses potential risk of loosening too much of surrounding soil. In addition, treatment of effluent is usually required before discharge.

As to predrilling for the use of a vibratory or percussive hammer, it is normally done with a crawler-mounted tall drilling machine prior to sheet pile installation. Its operation requires large working space horizontally and vertically due to its machine size and weight in addition to the solid working ground necessary for its stability. Although some types of earth drills can press in sheet piles while drilling with limited press-in force, most of the drills are used for predrilling purposes only. That means that the typical sheet pile installation into hard soil requires two sets of equipment, one for predrilling and the other for subsequent sheet pile driving.

In the case of the smaller type press-in piling system, an auger attachment (a continuous flight auger with a drill head and a drill casing) is recommended for stiff clay, gravel, cobbles, boulders and soft rock with N-values over 50 and a uniaxial compressive strength of 5,000 to 10,000 psi (34.5 to 69.0 MPa). Figure 3 shows how this type of auger attachment works. It is integrated with the press-in piling machine. This attachment drills simultaneously while the press-in base machine presses in piles. The maximum depth that the auger can bore is approximately 75 feet (23m) and sheet piles of mid to high rigidity are normally used for the stability of the press-in machine and the auger attachment during its operation. Its vertical stroke (range of one pass of press-in movement) is up to 40 inches (1.0m).

Figure 4 shows the plan view of a pair of sheet piles on the right (in black) being pressed in by using the simultaneous drilling operation with the auger attachment (the circumference of the drilled area shown in alternate long and short dashed lines). As can be seen, most of the footprint of the sheet piles is inside the drilled areas with the exception of the flanges and interlocks on the lower side.

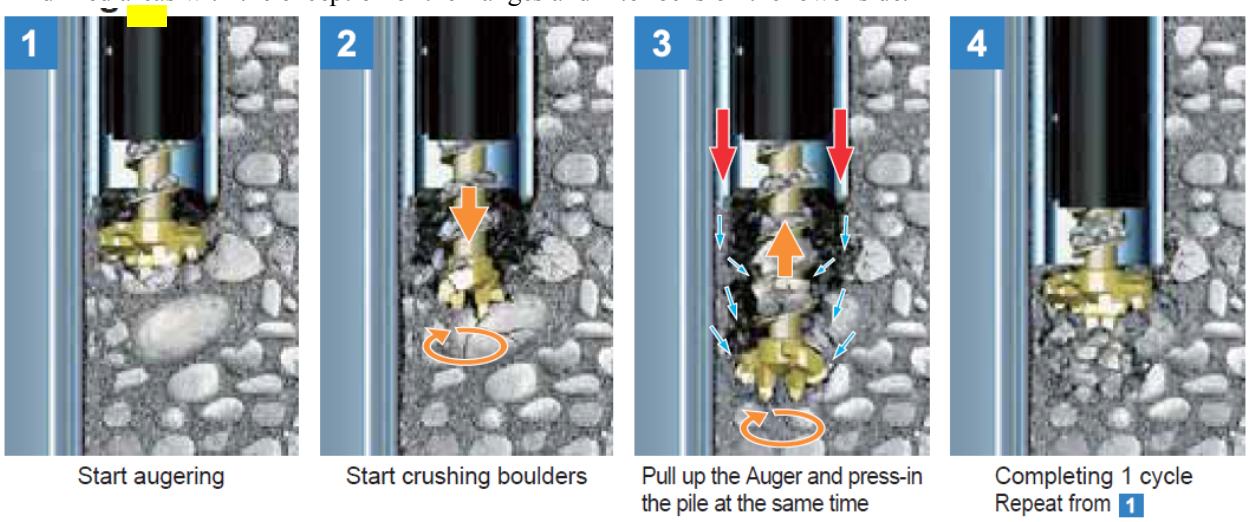


Figure 3 Crush Auger Attachment

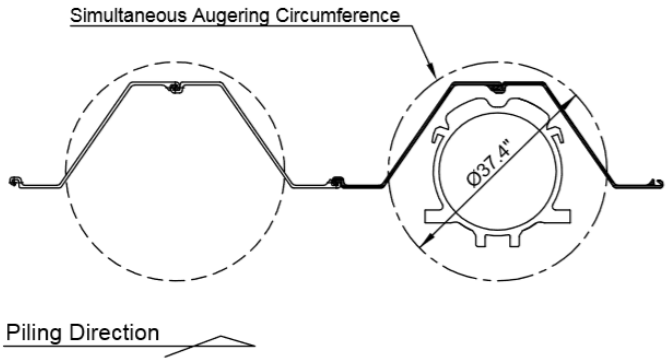


Figure 4 Plan View of Sheet Piles and Simultaneous Augering

If this press-in plus a "simultaneous augering" operation encounters difficulties, "predrilling" with this attachment can be done to cover the entire footprint of the sheets in the following manner.

- After a pair of sheet piles is installed, the auger attachment is moved further ahead to "predrill" without the next sheet pile pair as shown on the left side of Figure 5. The sheet pile pair shown in broken lines is not placed yet at this point (shown as reference only).
- Once "predrilling" is complete, the auger attachment is brought back to the next piling position (shown on the right side of Figure 5). Then, the same pair of sheet piles is provided as shown in thick black lines and pressed in simultaneously with the auger's drilling operation.
- The auger attachment is always integrated with the press-in base machine during the "predrilling" as well as the "simultaneous augering" operations.
- The area "predrilled" with the auger attachment receives the sheet pile almost immediately after "predrilling", so it can minimize the ground settlement or movement which might be otherwise caused by continuous predrilling with a separate drill machine for other types of installation.

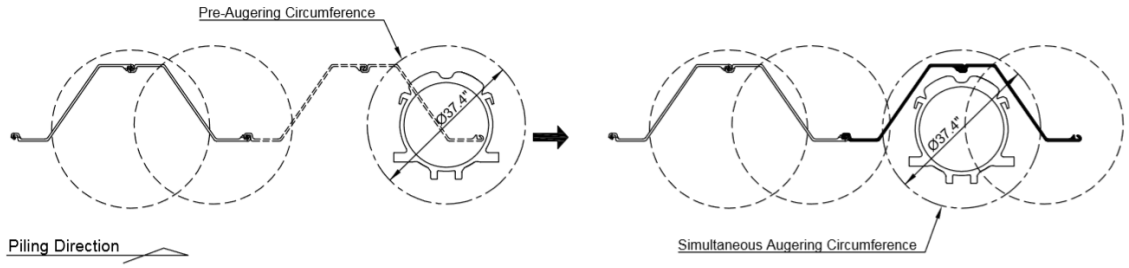


Figure 5 "Predrilling" with Auger Attachment

SOUTHERN CALIFORNIA DRAINAGE CHANNEL AND PIPELINE RETROFIT PROJECTS WITH PRESSED-IN SHEET PILES

Since the Public Works Department of Orange County, California successfully utilized the press-in piling method for its emergency levee repair project in Huntington Beach in early 2008 (Fayad et al., 2015), many of the repair and retrofitting projects of drainage channels and river levees in the area have been specifying press-in piling to take advantage of the method's non-vibratory/low noise features and the small footprint requirement. Southern California's drainage channel locations are often situated on hard soil including dense sand, gravel, and boulders brought over from the upstream mountains. Recent projects in Ventura, Orange, and Riverside Counties that utilized pressed-in sheet piles installed in hard soil will be studied below. No vibration monitoring was conducted on these projects probably because previous press-in specified projects in the area received no complaints about vibration by sheet pile installation.

"J" STREET DRAIN IMPROVEMENT, ORMOND BEACH LAGOON TO DOWNSTREAM OF HUENEME ROAD IN VENTURA COUNTY

The Watershed Protection District of the County of Ventura Public Works Agency specified the pressed-in sheet piles for temporary earth retaining to build vertical concrete walls and a concrete invert in the City of Oxnard due to the following reasons:

- Proximity to an apartment complex and a large sewer treatment plant.
- Proximity to an existing 33-inch (84cm) diameter VCP sewer pipe.

Figure 6 shows its typical cross section with pressed-in sheet pile walls. The single hatched earth and existing concrete lining were to be removed for a larger drainage capacity. Note that the existing VCP was running parallel to the sheet pile wall on the right at a very close distance (12 inches, i.e., 30 cm away). Figure 7 shows typical soil conditions at the site. The N-value of the dense sand layer at 18 to 20 feet below the ground is above 50. However, the piling subcontractor did without the auger attachment on this project (see Figure 8) because the hardest part of the sand was relatively thin and the rest of the soil was generally much softer. The press-in piling machine employed for the project was able to exert the maximum press-in force of 170 tons (1,500kN). Although approximately 60% of installed 35-foot-

long PZC19 sheet piles were extracted after the new channel structure was built, the rest of them were left in the ground for enhanced safety of the nearby structures. Almost all of the extracted sheet piles were found to be free of damage or deformation. The project was successfully completed in the fall of 2014 with much of positive local media coverage thanks to the press-in piling's advantages. See Figure 9 for the completed sheet pile installation right next to a building wall.

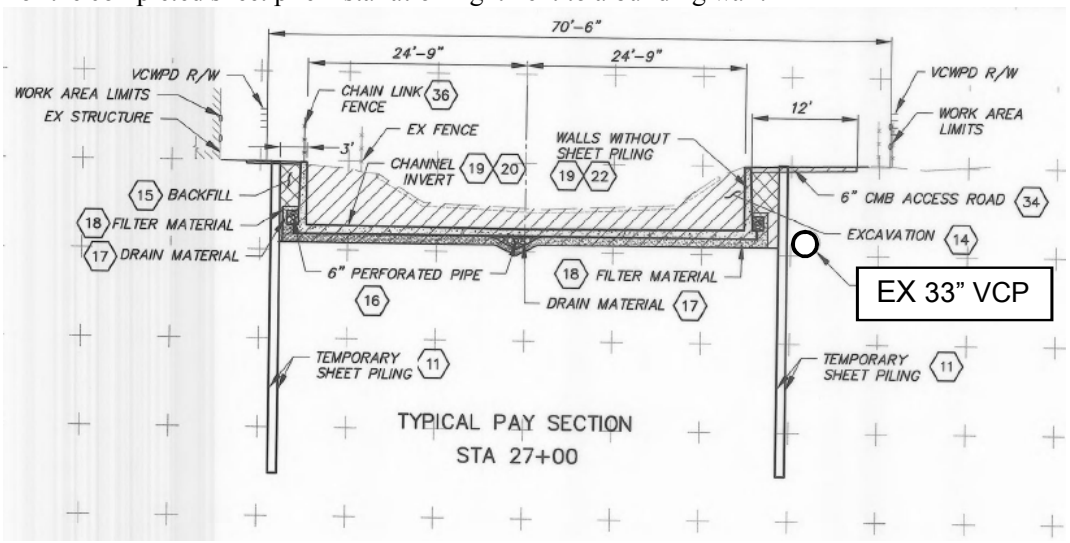


Figure 6 Typical Cross Section of "J" Street Drain Improvement

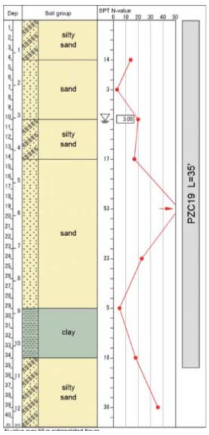


Figure 7 Typical Soil Conditions on "J" Street Drain Project



Figure 8 Press-in Operation on East Wall Near Ormond Lagoon



Figure 9 Pressed-in Sheet Piles Next to Industrial Building Wall

TRABUCO CREEK CHANNEL LEVEE PROTECTION PHASE VII IN ORANGE COUNTY

The Public Works Department of the County of Orange is responsible for levees of the Orange County Flood Control District. "The Trabuco Creek Channel was built in 1962 as a soft-bottom trapezoidal channel with 4-inch thick unreinforced concrete lined walls (2:1 side slopes)" (Orange County Website "Trabuco Creek Channel (L02) Levee Protection, Phase VII"). The levees are located in the City of San Juan Capistrano just north of the confluence with the wider San Juan Creek. Although the Trabuco Creek levees have been repaired each time after the repeated damage was caused by past storms, they remained vulnerable to future storms and earthquakes. This project was Phase 7 out of 8 phases and was designed to reinforce the existing levees against channel bottom scour in anticipation of future floods by installing steel sheet piles at the inside hinges of the maintenance roads as shown in Figure 10.

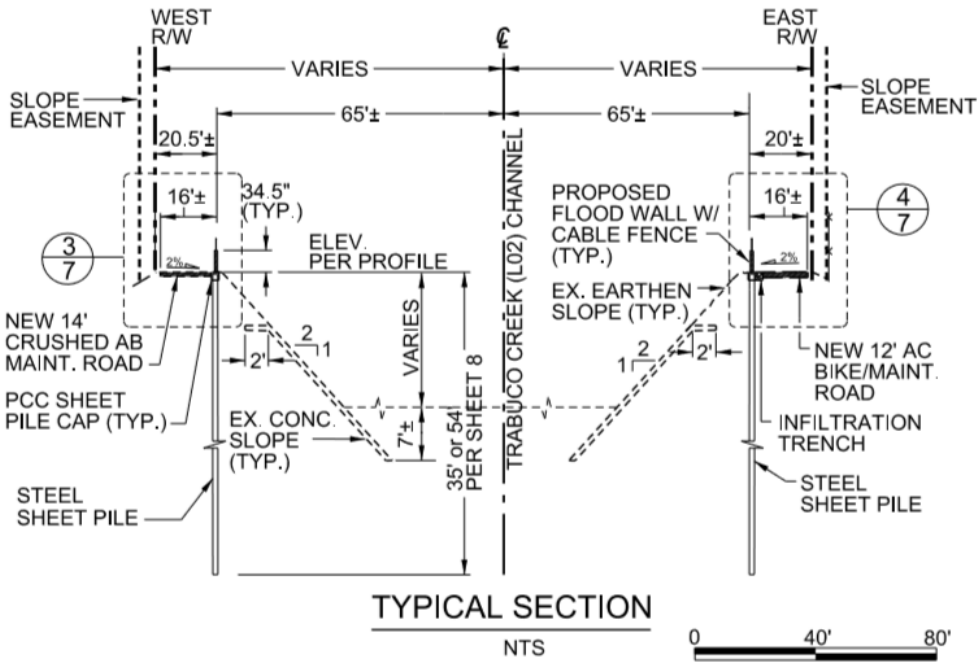


Figure 10 Typical Cross Section of Trabuco Creek Levee Improvement

The typical soil conditions are shown in Figure 11. The fill materials consisted of silty and gravelly sand with cobbles larger than 3 inches in diameter. See Figure 12 for the sheet pile press-in operation with the auger attachment. Figure 13 shows a cobble and gravel encountered during sheet pile installation. The press-in piling with pre-augering was specified on the west bank of the levee to minimize the noise and vibration impact to the rows of residences that run parallel to the levee at a close distance (see Figure 14) while a successful contractor was let to choose between a low noise vibratory installation method or press-in for the east bank, which was adjacent to businesses with just a bit wider open space. As it turned out, the foundation subcontractor used the press-in system with the auger attachment for all of 1,316 pairs of coated AZ19 and AZ25 sheets.

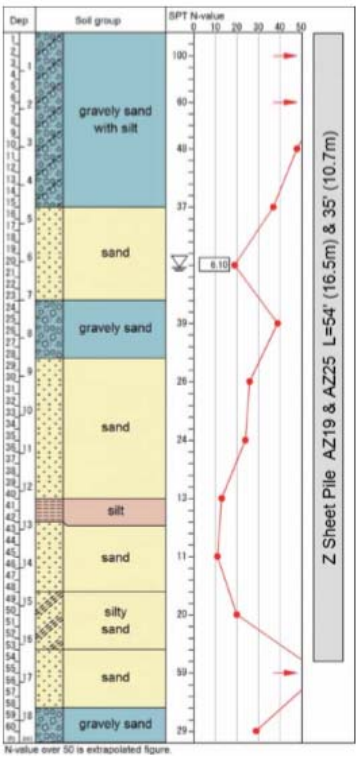


Figure 11 Soil Conditions



Figure 12 Press-in with Auger Attachment



Figure 13 Cobble and Gravel Encountered

A sequence of three 54-foot-long (16.5m-long) sheets and one 35-foot-long (10.7m-long) sheet was repeated to facilitate ground water migration through the "windows" below the toes of the shorter sheets. The auger attachment with "predrilling" was used to deal with hard soil. Large boulders slowed down the rate of progress by as much as 50% at locations. Although this project did not monitor vibration, the maximum peak velocity of 0.0738 inches (1.9mm) per second was recorded at 7.5 feet (2.3m) from the press-in piling with "simultaneous augering" in a limestone layer on a different project that utilized a similar machine set-up. The Trabuco Creek Levee sheet pile installation was successfully completed in October 2014.



Figure 14 Sheet Pile Being Installed Next to Mobile Home Park

SANTA ANA CANYON – BELOW PRADO INLAND EMPIRE BRINE LINE PROTECTION PROJECT

The Riverside County Flood Control and Water Conservation District was responsible for this project to protect the existing 48-inch (122cm) RCP Brine Line against a maximum controlled flood released from Prado Dam (Uhley, J., 2017). See Figure 15 for a typical cross section with the Brine Line approximately 20 feet (6.1m) or less away from the sheet pile alignment (brine line = high-saline waste water pipeline).

The general contractor, Blue Iron, Inc., furnished and installed approximately 2,220 wall feet (677m) of sheet piles. Sheet piles ranged from 39 feet (11.9m) to 53 feet (16.2m) long and were pressed through silty sand, sand, sandy gravel, and sandstone at varying depths. At some locations the N-values were above 50 for the entire depth of sheet pile penetration as indicated in Figure 16. The Owner elected to use the Press-in installation technique with "simultaneous augering", as opposed to the traditional pile driving techniques which cause excessive vibrations and noise. The press-in piling method was specified here for the following reasons: increased likelihood of driving all sheet piles to the correct tip elevations given the tough ground conditions, decreased risk of damaging the existing 48-inch Brine Line, and reduced the environmental impact of affecting nesting birds.

All of the 483 pairs of sheet piles were installed to the specified tip elevation in a span of approximately five months. Two press-in machines were utilized simultaneously to press all the piles to meet the schedule. An additional scope of work included approximately 13,300 CY (10,200 cubic meters) of excavation and backfill, concrete cap for the sheet piles, 120 CY (92 cubic meters) of 1 ton rip-rap rock slope protection, rock slope protection fabric and filter blanket, and tiebacks with 243 ground anchors. See Figure 17 for an aerial view of the sheet pile installation work and Figure 18 for the augering operations with cuttings on the side of the auger attachment. The "pre-drilling' by the auger attachment

was also utilized here to install sheets in the hard soil. Void created by augering is backfilled normally with cuttings and compacted unless they are not suited for backfilling. The project was successfully completed in 2016.

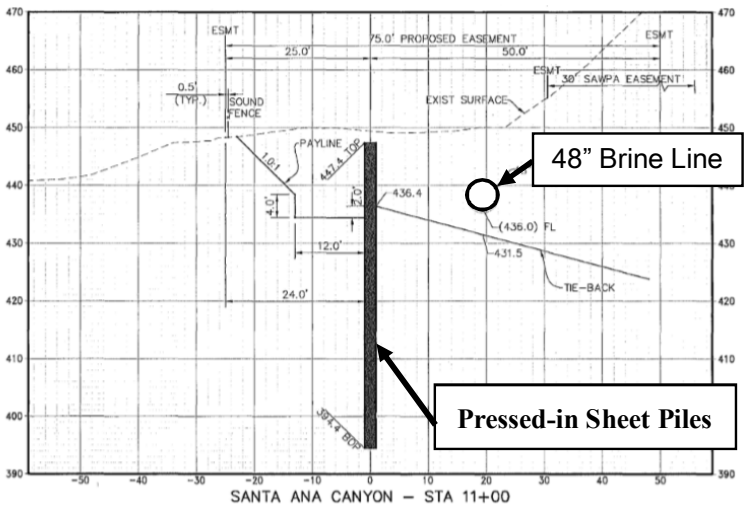


Figure 15 Typical Cross Section

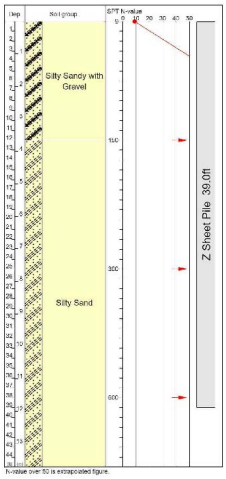


Figure 16 Hard Soil



Figure 17 Press-in with Simultaneous Augering (Source: https://vimeo.com/157547078)



Figure 18 Cuttings from Simultaneous Augering (Source: https://vimeo.com/157547078)

CONCLUSIONS

Press-in sheet pile projects in Southern California, such as those highlighted herein, are good examples that the factors once considered as prohibitive for usage of sheet piles are no longer applicable. Pressed-in sheet piles with "simultaneous augering" can provide a solution to many projects with difficult site conditions including proximity to densely clustered residences, sensitive existing structures, environmentally protected species, low headroom, and hard soil. Further monitoring and studying of vibration during "simultaneous augering" and "predrilling" on future projects in various soil conditions are likely to enhance the confidence in the method.

ACKNOWLEDGEMENT

The authors appreciate the support and assistance provided by the following individuals.

Shigeru Kambe and Brett Bennett, Blue Iron Foundations and Shoring LLC
Ian Vaz, Giken America Corp.

REFERENCE

Fayad, A., Takuma, T., and Kambe, S., (2015), Levee Repair and Upgrade by Dual Sheet Pile Walls and Accordion Sheet Pile Wall, Proceedings of Deep Foundations Institute 2015 Annual Conference

Takuma, T., Nishimura, H., and Kambe, S. (2015), Development of Very Low Head Room Sheet Piler Press in Driver, Proceedings of 2015 International Foundations Congress and Equipment Expo

Uhley, J., (2017), Zone 2 Report to the Zone Commissioners "Current/Recent Construction Project", Website of Riverside County Flood Control and Water Conservation District

White, D., Finlay, T., Bolton, M., and Bearss, G. (2002), Press-in piling: ground vibration and noise during piling installation, ASCE Special Publication 116.

DEEP SOIL MIXING FOR CONTAMINATED SOIL REMEDIATION AT A SUPERFUND SITE

Larry Stearns, P.E., NorthStar Contracting Group, Inc., East Hanover, NJ, USA (609) 361-4739; lstearns@northstar.com

Lori Tiefenthaler, Lehigh Hanson, Inc., Irving, TX, USA (972) 653-6130; Lori.tiefenthaler@lehighhanson.com

ABSTRACT

Remediation of contaminated soil represents a significant market for application of Deep Soil Mixing (DSM). Eighty-one percent of U.S. Environmental Protection Agency (EPA) Superfund Program's site remedies have involved contaminated soil. Contaminated soil is frequently treated by In-situ Solidification/Stabilization (ISS). ISS treatment of contaminated soil involves mixing binding agents into soil using DSM techniques. DSM is a core business for many DFI members. Members may improve and broaden their services to clients by learning about the recent ISS treatment of contaminated soil at a Superfund site. ISS treatment is part of the EPA-selected remedy for a Superfund Site in the metro New York City area. The property has seen heavy industrial use for more than a century. Soil at the site is contaminated with a variety of volatile organic compounds (VOCs), polycyclic aromatic hydrocarbons (PAHs) including coal tars and heavy metals, principally arsenic and lead. Beginning in 2017 and continuing through 2018, approximately 150,000 cubic yards (115,000 cubic meters) of soil will be treated by ISS at the case study site. Portland cement and slag cement are mixed into the soil by DSM techniques using GPS guided excavators to immobilize the hazardous constituents within the treated soil. ISS treatment by DSM will contribute to redevelopment of this valuable property. This paper will describe ISS constructability and performance, case study grout mix design with geotechnical results for strength and permeability, and deep soil mixing techniques.

Keywords: in-situ solidification/stabilization, deep soil mixing, VOC and PAHs contaminated soil remediation, GPS excavator guidance, ground granulated blast furnace slag (GGBFS), slag cement lowers hydraulic conductivity and improves sustainability

INTRODUCTION

In-situ solidification and stabilization (ISS) is a deep soil mixing (DSM) technique applied in the environmental remediation field to physically encapsulate, or chemically bind, contaminates of concern such that the impacts to human health and the environment are mitigated. Common remediation applications of ISS include mixing cementitious reagents into contaminated soils to form a monolithic mass with desired performance characteristics, and the installation of vertical subsurface walls designed to control groundwater movement. A key characteristic of ISS is that the contaminated soils are treated in their existing location at the project site and then are left in place after treatment. Typical performance characteristics of the ISS treated soils include improved unconfined compressive strength (UCS), reduced hydraulic conductivity (HC), and reduced leaching potential of soil contaminants. Increased shear resistance of the treated soil may also be a performance requirement where seismic loading is a concern.

Excavating and transporting contaminated soils to an authorized off-site treatment/disposal facility is expensive and time consuming. It increases the risk of public and worker exposure to the contaminants via direct contact, odors, dust, sediment transport, and spills. Community impacts include noise and truck traffic. Significant sample collection and analytical costs are needed post excavation to demonstrate the excavated site has achieved required regulatory remediation goals. For deeper excavations, substantial costs may be necessary to address shoring, dewatering, and safety issues. Where desired, backfilling the excavation further increases material consumption requirements, work duration, and site restoration costs.

© 2018 Deep Foundations Institute

Depending upon the circumstances, the cost of off-site transportation and land-based disposal of contaminated soils can often exceed the cost of ISS by two or three times.

All construction methods for ISS fundamentally involve mixing a liquid cementitious grout containing binders with wet soil. Wet soil and liquid cementations grout aids in lubricating the mixing device and provides moisture for cement hydration. Dry grout (powder) mixing with wet soil is less frequently used for remediation work because it is more difficult to assure a homogeneous mix. Four common techniques for performing ISS remediation include: mixing the grout into the soil with an excavator bucket ("bucket mixing"), injecting the grout into the soil while mixing with one or more hollow stem augers ("auger mixing"), injecting the grout into the soil while mixing with a large vertical "chain-saw" like device ("single pass mixing"), or injecting grout into the soil while mixing with a rotating cutter head mounted on a horizontal axis ("cutter head mixing"). Other methods are also used such as direct injection, and the selected method is dependent on project conditions and requirements. Figures 1 through 4 show representative equipment.

The practical depths of ISS mixing are limited by the equipment used. Bucket mixing is generally limited to about 35 to 40-feet deep (10 to 12 meters). Auger and single pass mixing can achieve 100-foot depths (30 meters) but 80-foot depths (24 meters) and less are more common. Cutter head mixing is generally used for shallower mixing depths up to 26 feet (8 meters). These are only general comments on mixing depths; specialized equipment or project specific needs may lead to other equipment setups.



Figure 1: Bucket Mixing



Figure 2: Cutter head Mixer



Figure 3: Auger Mixer



Figure 4: Single Pass Mixer

ISS GROUT MIX

The composition of the grout mix depends upon the ISS performance objectives of the project. Such objectives typically include increased UCS, decreased HC, and decreased leachability of chemicals of concern. Common ISS grout reagents include mixtures of portland cement, ground granulated blast furnace slag (GGBFS or slag cement), Class F fly ash, bentonite, and as needed, a variety of other reagents can be added in smaller amounts such as elemental sulfur (for mercury binding) and ferrous sulfate (for heavy metals binding). When using slag cement, an "activator" reagent such as portland cement, lime, or other alkalis is included in the grout mix to initiate the cementitious chemistry of the slag (Morganville-Regourd; p. 642).

Since project site conditions and grout reagent costs vary considerably, most projects perform a bench scale treatability study to determine the best grout mix, and often a pilot demonstration is subsequently performed to assure that the selected grout mix performs as expected under field conditions. For example, in preparation for field work in the case study discussed below, two treatability studies and one pilot demonstration were conducted. The treatability studies screened a wide range of grout mixes that ultimately determined a 2-percent portland cement plus 6-percent slag cement grout mix would provide the required performance for this project. These percentages are the weight of reagent relative to the wet weight of soil being treated.

A key observation during these studies included that for test grout mixes with 8-percent portland cement or more, the increased pH led to increased leachability of metals. For HC, the testing indicated that increasing the proportion of slag cement relative to portland cement in the grout mix consistently led to decreased hydraulic conductivity (into the 10^{-7} to 10^{-9} cm/sec range) while still maintaining an acceptable 28-day UCS of 100 psi (690 kPa) or greater. A relative weight ratio of 1:3 parts portland cement to slag cement was found to provide the most effective overall performance for the case study project, which was then verified during the field pilot demonstration. As is further discussed below, the partial replacement of portland cement with slag cement in the ISS grout mix not only improved the ISS performance but generated significant reductions in environmental impacts related to the manufacturing of these reagents.

SUSTAINABILITY BENEFITS FROM USING SLAG CEMENT

Environmental life cycle impact of producing slag cement is much lower than producing portland cement. An iron and steel manufacturing byproduct called granulated blast furnace slag (GBFS) is the raw material in the production of slag cement. This recovery of an industrial byproduct, grinding and reuse, generates fewer environmental impacts and consumes considerably less energy and non-renewable materials as compared to production of portland cement. For example, the production of slag cement generates only 14-percent of the amount of global warming potential compounds compared to a like amount of portland cement. Figure 5 below compares life cycle assessment results of portland cement and slag cement.

Category Indicator	Unit	Per Metric Ton of Portland Cement	Per Metric Ton of Slag Cement
Global warming potential	kg CO_2 eq.	1040	147
Acidification potential	kg SO_2 eq.	2.54	2.1
Eutrophication potential	kg N eq.	1.22	0.27
Smog creation potential	kg O_3 eq.	48.8	26.5
Ozone depletion potential	kg CFC 11 eq.	2.61E-05	1.69E-05
Total primary energy			
Non-renewable (incl. fossil and nuclear)	MJ	5595	2434
Renewable (incl. solar, wind, biomass, hydroelectric & geothermal)	MJ	292	76
Material resources consumption			
Non-renewable materials	kg	1420	11
Renewable materials (incl. recovered materials)	kg	7.64	1105
Net fresh water	L	9700	32
Total waste generated			
Non-hazardous	kg	8.99	0.3
Hazardous	kg	0.0518	0.02

Figure 5: Comparison of Life Cycle Assessment Results of Portland Cement and Slag Cement (Source Wilk and Tiefenthaler 2017)

CASE STUDY: Bucket ISS Mixing at a Northern New Jersey CERCLA Site

Located in northern New Jersey near New York City, the 16-acre (6.5 hectare) project site was used for coal tar distillation operations that produced a variety of paving and roofing materials from the 1870s through the 1970s. Various oils were produced at the site from 1909 through the 1950s. These businesses eventually declined, and from the late-1970s to early 1980s the site was used for the storage and recycling of waste oils. During the next 20 years, several cleanup actions were conducted that removed approximately 1.35-million gallons (5.1-million L) of waste oil for offsite treatment, over 1.5-million gallons (5.6-million L) of stored coal tar for recycling, and the removal of dozens of aboveground and underground storage tanks having over 9-million gallons (34-million L) cumulative capacity. In the early-2000s the EPA placed the site on the CERCLA National Priorities List and a Record of Decision (ROD) was issued in 2011. ISS was part of the selected remedy in the ROD. Remediation field work began in 2017 and is currently ongoing.

The site near-surface geology is highly heterogeneous. All the site soils are constructed land built up during the last century with non-engineered fills of rock, soils, and debris from many sources. Buried layers of dense meadow mat (peat) 6-feet (2 meters) thick have been found in several areas. Competent rock is roughly 40 to 60-feet (12 to 18 meters) below grade depending upon location. Soils are generally unconsolidated silty sands (SM) containing boulders, extensive timber piles, concrete pier caps, concrete ring tank foundations, buried building foundations, and a variety of other materials discarded over many decades of heavy industrial use at the site. Groundwater is typically within 6-feet (2-meters) of the surface and is tidally influenced by a large river. The site is within the 100-year flood plain.

Site soils are contaminated with polycyclic aromatic hydrocarbons (PAHs), volatile organic compounds (VOCs), and metals. The groundwater table is tidal and normally within 5-feet (2-meters) of the surface depending upon tide and weather conditions. Several non-aqueous phase liquid (NAPL) plumes exist beneath the site and have been found pooled on top of dense meadow mat layers. Considerable portions of the site contain waste tar deposits that are very hard and difficult to excavate.

The source remediation includes an estimated 150,000 cubic yards (115,000 m^3) of soils for ISS treatment with an average depth of 12-feet (3.6 meters) but up to 30-feet (9.1 meters) deep in several areas. Bucket mixing was selected instead of other mixing platforms due to the favorable depth, the presence of substantial obstructions that would need less clearing for bucket mixing than for other mixing methods, and cost considerations.

During remediation, quality control included collecting real-time and as-built data for the ISS bucket mixing using a 3-dimentional Global Navigation Satellite System (GNSS) machine guidance system available from the excavator manufacturer coupled to an aftermarket real-time cab display with cloud-based data collection system. A 50 metric ton- and 70 metric ton-class hydraulic excavators with the machine guidance systems and in-cab displays were used. After the machine was measured for the specific boom, stick, and bucket configuration being used, and the configuration data entered into the machine guidance system, multiple sensors on the excavator recorded the 3D spatial coordinates of the bucket teeth via the GNSS to +/- 0.1 foot (0.03 meter).

A professional surveyor prepared a digital model of the ISS depths at any given location from the CAD design drawings for the remediation (Figure 6). This model was uploaded into the machine guidance system (Figure 7) providing the excavator operator with a real-time display of where the bucket teeth were located relative to the design contours for ISS depth. As the ISS mixing was completed in each cell, the as-built spatial coordinates of the cell floor elevations and perimeter were collected by the excavator operator (Figure 8). This data automatically uploaded to a cloud-based platform where the surveyor could track and document the as-built progress of the ISS work. Figure 9 shows a typical daily sample collection of the ISS grout/soil mix for quality control performance testing.

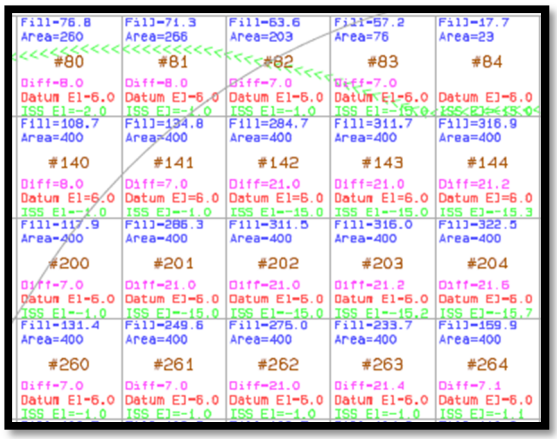


Figure 6: Example of ISS grid model

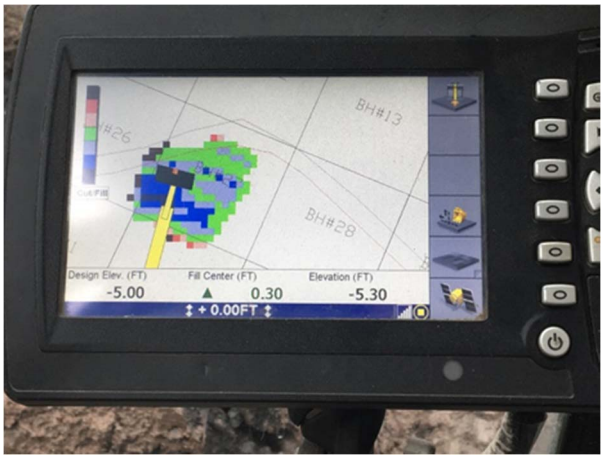


Figure 7: Cab display of GNSS on grid model



Figure 8: ISS bucket mixing in a cell



Figure 9: Collecting ISS samples

Project specifications for ISS required a grout with 2-percent Type I portland cement and 6-percent slag cement with reagent weight calculated from the weight of the soil being treated. In some locations, a 4-percent portland cement plus 6-percent slag cement mix was used to provide more rapid strength gain. Water was added to the grout at a typical 0.70 water to cement-pozzolan ratio [w/(c+p)] to keep the grout pumpable. To simplify plant operations and quality control, "standard" grout batches were mixed with consistent weights of reagents and water. The soil weight of a given cell was calculated from the cell area, average depth, and unit weight of soil. Then the number of standard grout batches needed to provide the required weights of reagent for the given cell was calculated. The unit weight of soil was measured frequently prior to mixing to confirm the required quantity of reagents were added to the cells.

The project provided ISS performance criteria of 40-psi (276 kPa) or greater unconfined compressive strength (UCS) and less than 1.0 x 10^{-6} cm/sec hydraulic conductivity (HC) tested at a 28-day cure time. Samples were collected daily from the ISS and tested by ASTM D2166 and ASTM D5084. Figure 10 shows the ISS performance data currently available.

ISS Grout Mix (% of Soil Weight)	**5-DAY UCS**	**14-DAY UCS**	**28-DAY UCS**	**28-DAY HC**
2.0 % Portland Cement + 6.0 % Slag Cement	AVE = 98 psi (676 kPa) n = 96 SD = 67 psi (462 kPa)	AVE = 266 psi (1834 kPa) n = 96 SD = 124 psi (855 kPa)	AVE = 369 psi (2544 kPa) n = 96 SD = 143 psi (986 kPa)	AVE = 3.54 x 10^{-7} cm/sec n = 96 SD = 2.54 x 10^{-7} cm/sec

AVE = average, psi = pounds per square inch, kPa = kilopascals, n = number of tests ran, SD = standard deviation

Figure 10: ISS Performance Data for Northern New Jersey CERCLA Remediation Site

REDUCED LIFE CYCLE IMPACTS BY USE OF SLAG CEMENT AT CASE STUDY PROJECT

Using slag cement in lieu of some of the portland cement at the Northern New Jersey CERCLA Remediation Site reduced life cycle impacts of the project since the production of slag cement has a lower life cycle impact than the production of a like amount of portland cement. The case study remediation project involves treatment of approximately 150,000 cu. yd. (115,000 m^3) of soil. Note that life cycle impacts are calculated in the metric system (SI) units. Using an average soil unit weight of 1900 kg/m^3 (120 pcf), approximately 220,000 metric tons (243,000 tons) of soil is to be treated.

The approximate life cycle impact savings of the use of a slag cement and portland cement grout compared to straight portland cement grout can be calculated using methodology described in Wilk and Tiefenthaler 2017 as shown in Figure 11. A grout mix design of 2-percent Type I portland cement and 6-percent slag cement to weight of the soil being treated is used at most of the site locations. This means that approximately 13,200 metric tons of slag cement, 4,400 metric tons of portland cement for a total of 17,600 metric tons cementitious material (SC/PC) is being used at the site. In comparison a straight portland cement grout would have used a minimum 17,600 metric tons of portland cement, or potentially even more, for a similar performance on this project.

Category Indicator	Life Cycle Savings/Benefits
Global warming potential	Emitted 12,800,000 fewer kg of CO_2 equivalents (12,800 metric tons/14,100 tons US)
Total primary energy	Consumed 45 million fewer MJ of energy (12.5 million kWh)
Non-renewal materials	Consumed 18,600,000 fewer kg of non-renewable materials (18,600 metric tons/20,500 tons US)
Renewable material uses	Reused/recovered 14,490,000 kg more material (14,490 metric tons/15,970 tons US)
Fresh water use	Consumed 127.6 million fewer L of fresh water (33.7 million gallons)

Figure 11: Estimated Life Cycle Savings Using SC/PC Grout at Northern New Jersey Project

SUMMARY AND CONCLUSIONS

Environmental remediation projects are increasingly using the deep soil mixing technique of In-situ Stabilization and Solidification (ISS) where feasible due to the performance efficacy, the reduction in nuisance issues during construction, and the substantial cost savings offered in relation to excavation with off-site land-based disposal of impacted materials. While several techniques and equipment platforms are available to perform ISS, the use of excavator mounted bucket mixing can be an economical choice for treatment depths up to 40-feet (12 meters). The application of global navigation satellite system technology to monitor machine position, and the use of modern display technologies for equipment operators in the cab, provides real-time quality control and precision of mixing operations under field conditions. Using real-time capture of as-built surveying data and cloud-based data storage simplifies the monitoring of ISS treatment progress, increases confidence in the installed work, and eliminates the need for a full-time on-site surveyor.

The use of ground granulated blast furnace slag (GGBFS), or slag cement, as the major reagent component of ISS grout has well demonstrated performance in increasing the 28-day unconfined compressive strength and decreasing the hydraulic conductivity of treated soils. In addition, the use of slag cement to replace some portland cement provides reductions in the consumption of energy, non-renewable resources and water, while minimizing the production of global warming emissions.

ACKNOWLEDGMENTS
The authors wish to acknowledge the assistance of Lehigh Hanson, Inc. in providing information on slag cement; the Antraquip Corporation for the photograph of Figure 2; the First Energy Corporation for the photograph of Figure 4; and the NorthStar Contracting Group, Inc. for the photographs of Figures 1, 3, and 6 through 9.

REFERENCES

1. Morganville-Regourd, M., 1998. Cements Made from Blast Furnace Slag; published in Hewlett, P. C. "Lea's Chemistry of Cement and Concrete," 4th ed., Elsevier Ltd.; Chapter 11.
2. American Society for Testing and Materials; ASTM D 2166 Standard Test Method for Unconfined Compressive Strength of Cohesive Soil.
3. American Society for Testing and Materials; ASTM D 5084-00 Standard Test Methods for Measurement of Hydraulic Conductivity of Saturated Porous Materials Using a Flexible Wall Permeameter.
4. Wilk C.M., and Tiefenthaler L., 2017. Sustainability: A Role For Blended Cements and Industrial Byproducts in Soil Mixing, Grouting, and Slurry Walls, Proceedings of Deep Foundations Institute 42nd Annual Conference on Deep Foundations, October 23-28, New Orleans, Louisiana, USA.
5. Kosmatka, S.H. and Wilson M.L., 2016. Design and Control of Concrete Mixtures. EB01, 16th Edition, Portland Cement Association, Skokie, Illinois, USA.
6. Deep Foundations Institute Soil Mixing Committee, 2016. Guidelines For Soil Mixing, Deep Foundations Institute, Hawthorne, New Jersey, USA.

DESIGN-BUILD OF WATERTIGHT UNDERGROUND STRUCTURES FOR TUNNELING IN MIAMI, FLORIDA - THE NORRIS CUT UTILITY RELOCATION PROJECT

Terrence Carroll, P.E., G.E., HOCHTIEF Engineering GmbH, Frankfurt am Main, Germany, terrence.carroll@hochtief.de
May ElKhattab, P.E., Arup, New York, NY, USA, may.elkhattab@arup.com
Eugene Mirsky, P.E., Nicholson Construction Company, Canonsburg, PA, USA, eugene.mirsky@nicholsonconstruction.com
Eloy Ramos, P.E., Nicholson Construction Company, Canonsburg, PA, USA, eloy.ramos@nicholsonconstruction.com
Jose Torres, Nicholson Construction Company, Canonsburg, PA, USA, jose.torres@nicholsonconstruction.com
John Wise, P.E., Nicholson Construction Company, Canonsburg, PA, USA, john.wise@nicholsonconstruction.com

ABSTRACT
In 2017, Nicholson Construction Company completed a $72.1 million design-build contract for Miami Dade Water and Sewer Department to replace an existing 54-inch diameter pre-stressed concrete force main that runs from the Virginia Key Central District Wastewater Treatment Plant, under the Biscayne Bay at Norris Cut, to Fisher Island. In order to install the new sewer pipe below the bottom of Biscayne Bay, a tunnel boring machine (TBM) was launched from a 42ft diameter and 89ft deep shaft on Virginia Key and a precast segmentally lined tunnel was constructed towards a 28ft diameter and 72ft deep retrieval shaft on Fisher Island.

Both shafts were constructed through sand and highly permeable limestone, primarily the Fort Thompson Formation which is part of one of the most permeable aquifers in the United States and two different techniques were used to ensure a water-tight shaft at each end of the tunnel drive. The launch shaft structure was built using the secant pile technique, wet excavation and a tremie plug. For the tunnel break-in a soil freeze block was installed after the ground was treated with low mobility grout. The retrieval shaft was built using the Deep Soil Mixing (DSM) technique and excavated in the dry. Precedence of any other structure built this deep through hard layers (UCS over 3,000 psi) using this technique was not found.

This case study addresses the challenges of constructing watertight underground structures in highly porous ground for launching and retrieving a TBM. Design challenges from complex asymmetric loading, selection and comparison of the construction techniques, the installation and excavation of both shafts, and their performance are also discussed herein.

Keywords: secant pile shaft, deep soil mixing, water-tight construction, design-build, ground freezing, Fort Thompson Formation.

INTRODUCTION
The Norris Cut Utility Relocation Project consisted of the replacement of an existing force main from the Virginia Key Central District Wastewater Treatment Plant (CDWWTP) under Biscayne Bay Norris Cut to Fisher Island. The project involved replacing an existing 54in diameter pre-stressed concrete sewer force main with a 60in diameter force main. The primary scope included the construction of two shafts and the installation of a precast concrete segmentally-lined tunnel with a Tunnel Boring Machine (TBM), which will stretch more than a mile from the treatment plant on Virginia Key to Fisher Island. The shafts and tunnel were constructed through highly permeable limestone, primarily the Fort Thompson Formation, with frequent solution cavities filled with sand or silt. Construction of the shafts was particularly challenging in the high permeability limestone, requiring significant changes during the project. The nature of the design-build project allowed for the changes to occur seamlessly and without delay.

© 2018 Deep Foundations Institute

GEOLOGY

The soil profile at the site consists mainly of sands and limestone up to an explored depth of 120ft from ground surface. Primary components of the soil stratigraphy are detailed below and a geological profile across the site is presented in Figure 1.

1) The Artificial Fill generally consists of loose sands and silts extending from the ground surface to 23ft. The average N-value was 4 blows per foot.
2) The Miami Limestone formation is a soft to medium hard limestone with small solution cavities extending from 23ft to 28ft. One Standard Penetration Test was performed within the formation and the N-value was 17 blows per foot. The layer was not cored.
3) The Fort Thompson formation typically consists of hard vuggy limestone with frequent solution cavities. All solution cavities encountered during the geotechnical site investigation were found to be filled with sand or silt. For the purposes of design, the Fort Thompson formation was divided into four sub-layers of alternating sand and limestone.
    a. Fort Thompson Sand, FT-1, with an average N-value of 3 blows per foot extending from 28ft to 38ft.
    b. Fort Thompson Limestone, FT (A), extending from 38ft to 83ft with an average N-value of over 50 blows per foot. Cored samples obtained were influenced by low recovery and an average RQD of 10 was obtained.
    c. Fort Thompson Sand, FT-5, extending from 83ft to 93ft consisting of poorly graded sand with an average N-value of 6 blows per foot.
    d. Fort Thompson Limestone, FT (B), extending from 93ft to 103ft with an average N-value of 18 blows per foot. The layer was not cored.
4) The Taimiami limestone underlies the FT (B) layer but was not a significant geologic unit for this project.

The ground water table is located 6ft below the existing ground surface.

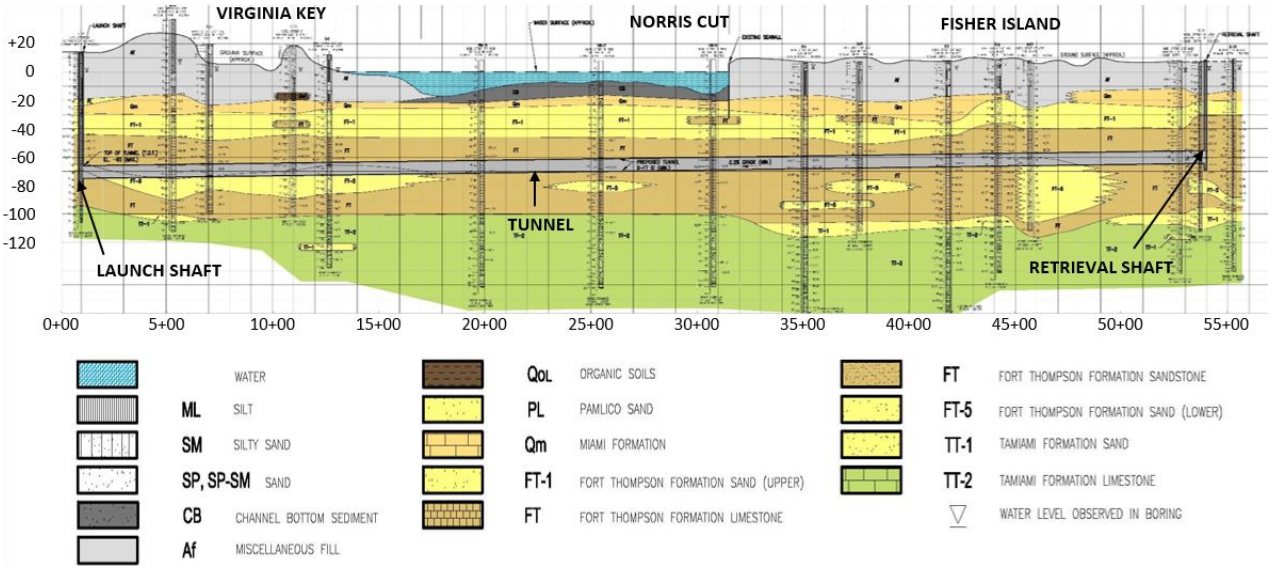


Fig. 1. Geological Profile

LAUNCH SHAFT

Selection of the Technique

Based on the geology and permeability of the ground, secant piles were chosen as the technique for launch shaft construction. Temporary casing was installed to the full required depth of the secant piles. The casing served two primary purposes which were key to creating a watertight shaft: maintain borehole stability and limit deviation due to the stiff drill string.

Design

The design of the secant pile shaft included shafts walls, tremie slab, and additional provisions to support the launch of the TBM. The shaft was designed as a generally unreinforced secant pile shaft in hoop compression. For an unreinforced shaft to work in hoop compression, the loads on the shaft must be balanced. However, the TBM launch process required ground freezing to support the TBM break-out, thrusting of the TBM off the back wall of the shaft during break-out, and adjacent cranes to lower the TBM and its components. All these activities generated asymmetric loads on the launch shaft. A fully integrated, three-dimensional structural model was developed using the software program GSA (Oasys, General Structural Analysis) to model the asymmetric loads from all these activities and develop the most economical solution to resist them. The solution constituted reinforcing only selected piles and installation of an internal steel ring to maintain the shape of the shaft. Figure 2 shows the ground freezing load applied to the shaft and the internal ring beam designed to keep the shaft from ovalizing.

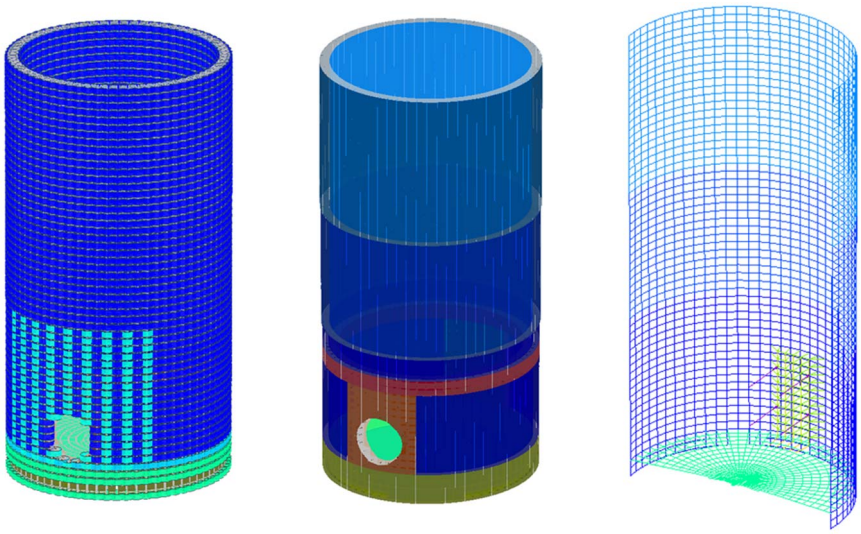


Fig. 2. GSA Model – Left: Ground Freezing, Middle: Ring Beam, Right: TBM Thrust

Ground freezing at the shaft's exterior allowed the TBM to break-out into dry conditions, lowering the risk of shaft flooding and allowing for inspection of the TBM cutter head after break-out. However, the frozen block imposed lateral loads on the launch shaft as the water/ice block expanded. This could lead to the ovalization of the shaft, disrupting the hoop action and leading to cracking and leakage. Therefore, a W14x233 steel ring beam was installed just above the TBM break-out level to resist the ice pressure and keep the secant shaft circular and nine piles were required to be reinforced to further resist cracking. Three Glass Fiber Reinforced Polymer (GFRP) reinforcement cages were substituted in the piles at the break-out zone to allow excavation at the face without damaging the TBM machine, while providing similar tension capacity as the steel reinforcement. Figure 3 shows the design of the ring beam, and Figure 4 shows the pile reinforcement distribution.

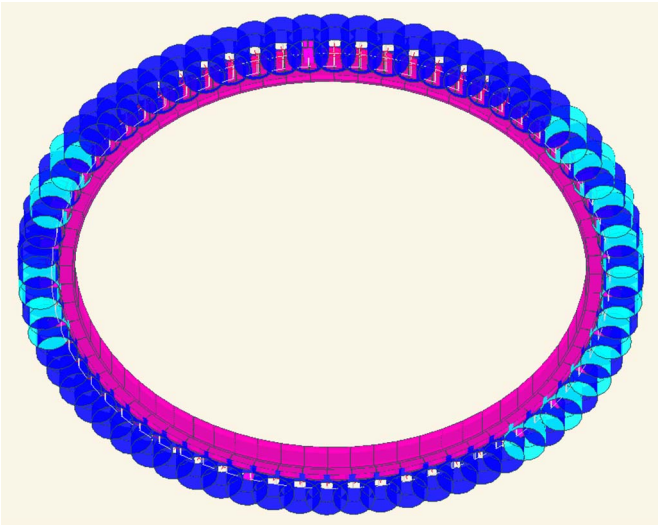


Fig. 3. Ring Beam model in GSA

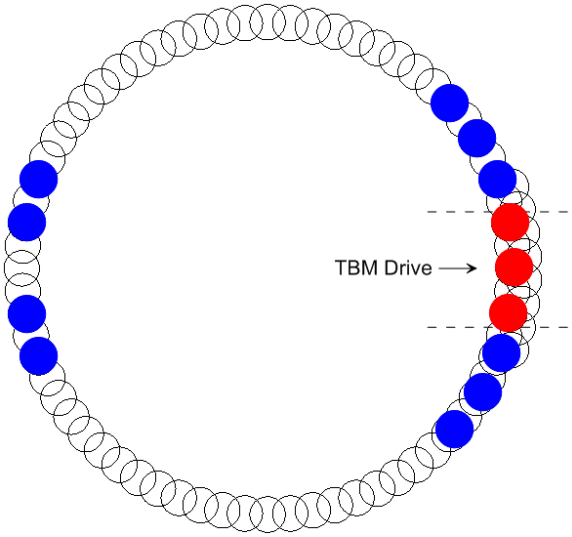


Fig. 4. Blue piles – steel reinforcement; red piles – Fiberglass reinforcement

One innovative aspect of the launch shaft and tunnel design was the use of a combination of typical TBM installation means and methods with a tunnel jacking process for initial segments of the tunnel. The approach involved tunnel pipe jacking the first 170ft from inside the launch shaft. A wall was constructed on the back wall of the secant pile shaft to provide a flat surface for the TBM tunnel jacking process. The thrust wall was constructed of reinforced concrete and four of the secant piles behind the thrust wall were reinforced with steel cages. The main benefit of this process was allowing for a smaller diameter launch shaft to be constructed.

A concrete guide wall was constructed at the ground surface to facilitate accurate and plumb installation of the secant piles. While typically only a single-purpose feature, the guide wall was incorporated into the shaft design to serve as a capping beam to help resist the crane loading. The design required only minimal amount of reinforcement and higher strength concrete as compared to a typical temporary guide wall, serving as an economical solution.

The tremie slab was designed as a pinned "2-way" spanning slab to resist the large hydrostatic uplift forces. Divers were utilized to install the reinforce, drill and grout-in dowels around the inside perimeter of the shaft, and to clean the slab/shaft interface. To minimize the extent of work required to be done by divers, the slab was designed with top reinforcement only. In addition, the design of the slab-to-wall interface was optimized to limit the number of dowels. This was achieved by taking full account of the available axial, friction and bond capacities at this location.

Installation

The secant piles were constructed using conventional bored cast in-situ techniques with a Bauer BG39 fixed-mast drill rig. A total of 68 piles were installed, ten were reinforced with steel cages and three were reinforced with GFRP cages. The remainder of the shaft was unreinforced. The piles were excavated inside the temporary casing using a combination of augers, coring barrels, and digging buckets as was required based upon the ground conditions to the design tip elevations, approximately 100ft below ground surface. The secant piles were fully cased using sectional heavy wall casing.

The water tightness of the system was critical as the bottom of the shaft was 85-ft below the water table in

very porous ground conditions. The water tightness relied completely on the quality of the interlock between the piles. The verticality of the piles was the most important aspect of the construction. Pile verticality was monitored using two independent quality control devices which ensured the targeted 1:200 or 0.5% tolerance was achieved for all 68 piles.

Sequencing the secant pile installation was also a key challenge on the project as several factors were involved in making sure the piles were installed within tolerance. First, the pile sequence was developed to keep the heavy drilling equipment away from concreting equipment to allow for continuous operations. Second, rigorous trial programs were conducted to create a proper concrete mix design to maintain slump, flow, and workability during concrete placement meanwhile also achieving low-early compressive strengths to allow adjacent piles to be drilled. When piles were undisturbed for longer than expected and the concrete allowed to gain near to its full design strength, maintaining a drill string within tolerance was cumbersome and created a domino effect with subsequent piles. Determination of an appropriate concrete mix was further complicated by the high permeability of the limestone bedrock and the challenges of reaching the site with ready-mix concrete in high ambient temperatures. As such, the mix design also had to prioritize minimizing bleeding to eliminate the potential of mix dehydration in the porous limestone.

Excavation

Prior to mass shaft excavation, the overburden and limestone layers located within the footprint of the shaft were pre-drilled using the continuous flight auger (CFA) method. The purpose of the pre-drilling was to aid with in-the-wet excavation efficiency. The predrilling loosened the ground through the advancement of the auger to shaft bottom. The auger was then withdrawn by reversing direction so as not to remove material and maintain the stability of the work platform.

Due to the highly porous ground, significant concrete losses during concrete placement (overbreak up to 60%) were encountered. Therefore, in addition to the predrilling, line drilling around the interior of the shaft was performed using a Casagrande C-12 drill rig tooled with a down the hole hammer (DTH) in order to remove any potential concrete bulges that had permeated into the shaft diameter.

The shaft was excavated “in the wet” with a friction crane equipped with a mechanical clamshell until reaching the bottom of the shaft. However, in the limestone formation where concrete losses were prevalent, a combination of vibro-chiseling and excavation with a clamshell were used to penetrate the layer. Excavating “in the wet” provided many challenges including removing the concrete bulges about 50ft below ground surface and excavating in lifts to confirm all material was removed.

Tremie-Slab

At the completion of excavation, a reinforced tremie-slab was poured. Prior to concreting, steel dowels were drilled and epoxied into the wall by divers to transfer the uplift force from the slab to the piles. A re-injectable flexible grout tube with ports was secured to the secant piles near the top of the slab, to act as a secondary measure of water tightness. The pre-fabricated steel reinforced cage was secured in place by divers and concrete pumped via tremie to construct the 5ft thick base slab. After the concrete had reached design strength, the shaft was dewatered.

RETRIEVAL SHAFT

Selection of the Technique

A watertight TBM retrieval shaft was also necessary for the project. During bid, the retrieval shaft was proposed to be a secant pile shaft, similar to the launch shaft. However, as the project advanced, the team realized that there would be additional difficulties to construct a secant pile shaft on Fisher Island. Fisher Island is accessible only by ferry and with that came concerns about reliable concrete delivery and a construction method that was not reliant on ready-mix concrete was preferred. For that reason, soil-cement mixing was determined to be the preferred method of construction for the TBM retrieval shaft.

Design

The design of the DSM retrieval shaft consisted of a two-stage process. The initial phase was a series of analytical calculations to assess the hoop stress levels in the shaft walls and the stress concentrations around the wall opening at the TBM break-in. The second phase of analysis consisted of a three-dimensional finite element numerical model (Plaxis 3D, Brinkgreve 2013) to appropriately model construction staging, asymmetry, crane loadings, and expected deformations.

Closed-form solutions exist for the determination of hoop stresses in a thick-walled cylinder (Young and Budynas, 2002). Similarly, a combination of closed-form solutions can be used to estimate the stress-concentrations around the opening caused by the TBM break-through. In one case the σ_2 stress is set to zero and in the second, σ_2 is set equal to σ_1. Superimposing the results allows for the calculation of the stresses at the opening. The analyses are discussed in more detail in Carroll et al., 2017 and Figures 5 and 6 show the conditions assumed in the closed-form solutions.

The hoop stresses and stress concentrations determined by these formulas were used as minimum required values on top of what was calculated by the finite element modeling.

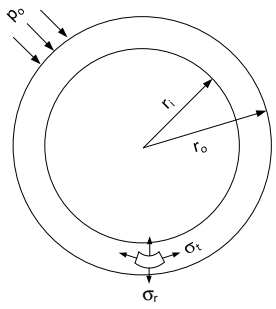
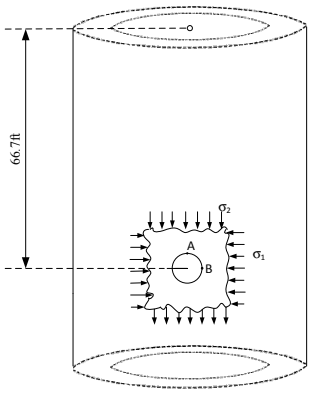


Fig. 5. Hoop Stress on a Cylinder



Case 1

$If\ \sigma_2 = 0$

$\sigma_A = 3\sigma_1$ and

$\sigma_B = -\sigma_1$

Case 2

$If\ \sigma_2 = \sigma_1$

$\sigma_A = \sigma_B = 2\sigma_1$

Fig. 6. Stress Concentrations Around Opening

The nature of a tunnel intersection with the shaft and the presence of the crane used to remove the TBM required the problem to also be analyzed using PLAXIS 3D as an axisymmetric model cannot capture the asymmetric loading and geometry. The finite element model is also able to calculate deformations, which is a significant advantage over the closed-form solutions. Figures 7 and 8 show outputs from the finite element model indicating that stresses and heave in the base plug were the dominant design concerns.

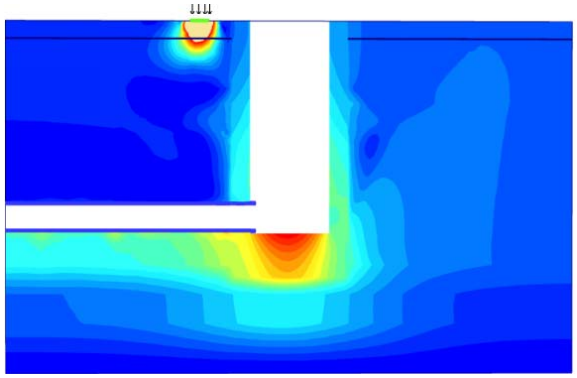


Fig. 7. Total Deformation from 3D Plaxis Model

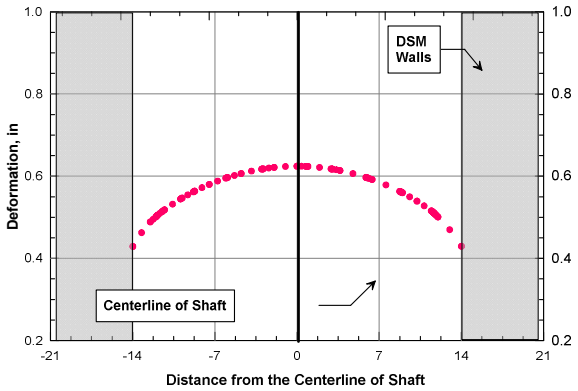


Fig. 8. Heave in Base Plug

One of the primary design challenges was the determination of the strength and stiffness of the DSM. Initial values based on an adjacent site and literature studies indicated that an unconfined compression strength (UCS) of 400psi could be attained in the limestone. However, a full-scale field trial indicated that a UCS

of only 200psi was reliably attainable. Determination of acceptable tension capacities for the DSM was challenging as there is little codified precedent. The Federal Highway Administration (FHWA, 2013) guidelines indicate that tension between 5% and 20% of the UCS values can be present, but ultimately the guidelines recommend using zero. An assumption of zero tensile strength was too conservative for the design and a conservative value of 2.5% was assumed. Design values for the elastic modulus at 50% of deviatoric stress (E_{50}), were also evaluated during the field trial and related as a factor of the UCS.

The design-build project approach allowed the flexibility to compensate for the lower UCS values with changes to the construction sequencing that allowed the DSM longer curing times before excavation. Areas requiring higher strength grout mixtures were also identified, such as at the TBM break-through location.

Installation

A grout plant was set up on Fisher Island to facilitate the mixing of the grout to be combined with the soils. Cement pigs (large horizontal silos with blowers) were installed and set on the barge used to transport materials to Fisher Island. The silos were used for storage of the slag cement, which was a major component of the grout mix. HDPE Lines were buried from the barge dock to the vertical silos at the grout plant for blowing and filling of the cement from the barge. The horizontal storage silos removed the logistics of using a ferry to transport ready-mix concrete between the mainland and Fisher Island.

The field trial was performed using a Bauer BG-39 to install 5 DSM columns to depths of 60ft and 87ft. Core samples and wet grab samples of the DSM were obtained to verify the UCS for various grout mixtures, with a camera inspection completed to verify the integrity and continuity of the cored hole. In additional, rising head permeability tests were completed in the core holes drilled to assess water tightness.

A pattern of 75 overlapping DSM columns were constructed for the shaft. As shown in Figure 9, the shaft was constructed with forty-eight "wall" columns where the DSM was mixed along the full depth to 87ft and twenty-seven "base plug" columns where the DSM was only mixed between 72ft and 87ft. See the cross-section of the shaft in Figure 10. Tolerances for the drilling were measured using a PRAD TLK sensor manufactured by Jean Lutz. The verticality measurements ranged between 0.1%-1.5% to a depth of 72ft, and 0.2% to 2.5% at a depth of 87ft. Some small gaps were identified at the bottom of the base plug which necessitated additional remediation columns to be installed to ensure water tightness prior to excavation.

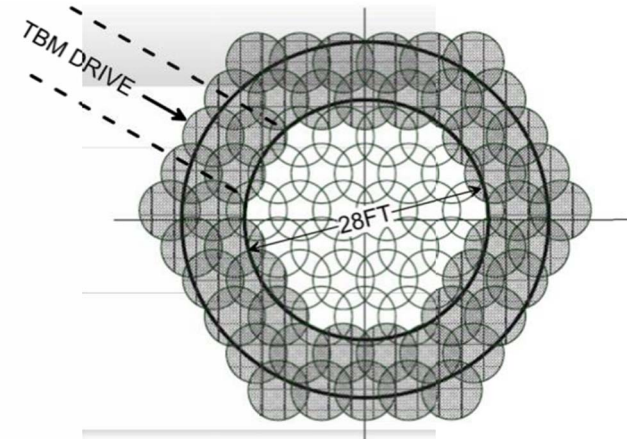


Fig. 9. DSM Shaft Plan View

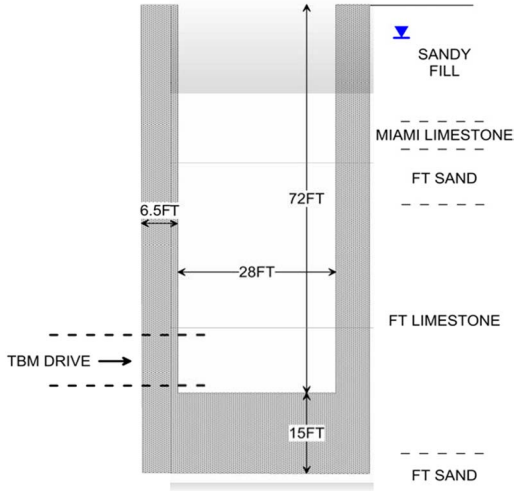


Fig. 10. DSM Shaft Cross Section

Excavation of the shaft was performed in the dry, with a small excavator lowered into the shaft. A guide wall was built at the top of the shaft to dictate the limits of excavation with the excavator. This method was significantly shorter than the dewatering and excavation of the launch shaft. Groundwater inflow was

limited during excavation, and inflow after TBM break-out measured at approximately 0.31 gal/s (~5gpm). The shaft was excavated and fully dewatered to check for leaks, then backfilled with a lean-mix to a depth of 50ft (i.e. above the top of the TBM break-through) and flooded with water prior to the TBM arrival.

SHAFT COMPARISON

Design

The two shafts, being of completely different construction methods, necessitated entirely different design approaches. The designs were led by teams with different specialties and the focus of the design was similarly different. For both cases, water-tightness, and therefore potential cracking, was a primary focus but the location of the potential water ingress varied as a result of the construction methods.

The launch shaft was designed with a primarily structural model (GSA) with the soil and rock represented by springs. Aside from the influence of ground freezing on the shaft, the largest risk of leakage was the cold-joint interface between the secant pile shaft and the tremie concrete slab. Significant design effort was required to calculate a robust yet economical connection between the tremie slab and the secant wall.

Conversely, the retrieval shaft was modeled using a geo-mechanical finite-element model (Plaxis 3D). For the DSM shaft, the largest risk of leakage came from cracking occurring in the base plug under hydrostatic uplift. For the launch shaft the uplift in the base slab was resisted with a single level of reinforcement in the tremie slab, but reinforcing the DSM base plug was not possible. However, as the base plug was constructed integrally to the walls of the shaft, the interface was not a major source of water ingress. Much of the design then, was focused on how thick the base slab must be to resist the uplift forces with limited cracking and water ingress.

Deep Foundation Methodologies

The retrieval shaft was intentionally designed to be constructed using the same drill rig used for the secant pile launch shaft. Both systems were composed of secant elements drilled on a primary/secondary sequencing. For both systems the water tightness relied on the quality of the interlock between the deep foundation elements making verticality of the drilled elements the most important aspect of the construction. The secant pile drilling, using the combination of segmental casing and rock auger, cut through the hard limestone easier and with higher vertical accuracy (<0.5%). The DSM drilling involved the insertion of a continuous hollow stem rod with mixing paddles and a rock auger tip which could not easily drill through the hard limestone and as a result verticality was difficult to obtain (<2.5%). Another notable difference is the diameter of the deep foundation elements, the secant piles used 3-ft diameter elements while the DSM used 6-ft diameter elements, which also contributed to slower advancement.

The most significant difference between the two methodologies is the process of concreting/grouting. With the secant pile methodology, each pile is fully drilled as a shaft and later tremie concreted with a 4,000 psi aggregate based mix. With the DSM methodology, the soil mixing between injected grout and the in-situ soil occurs during the penetration of the drilling tool to depth and its retrieval. The strength of the soil mix was only 200 psi.

Shaft Excavation

The wet excavation of the launch shaft was more challenging than the excavation of the retrieval shaft which was performed in the dry. Wet excavation is a much slower process performed with limited visibility. The excavation of the hard limestone at the launch shaft using vibro-chiseling was cumbersome whereas because the DSM columns had advanced to the base plug elevation prior to excavation and broken apart the limestone at depth, the excavation of the DSM was relatively simple and performed with small backhoe. The inspection of wet excavation using divers also contributed to the slower progress. Figures 11 and 12 illustrate the difference in the two excavation methods.

An advantage of the dry excavation is that deficiencies or water leaks can be identified and remediated as the excavation progress, on the wet excavation, as opposed to wet excavation where deficiencies cannot be discovered after the shaft is fully excavated and dewatered.

The wet excavation method is also more intrusive, as the excavated material is initially deposited in the working platform and a larger working area and dewatering control measures are necessary to maintain a clean site.



Fig. 11. Launch Shaft being Excavated in the Wet



Fig. 12. Retrieval Shaft being Excavated in the Dry

Base Slab

The DSM methodology had the benefit of allowing construction of the support of excavation and the bottom plug in one operation, eliminating the need for a tremie slab and facilitating excavation in the dry. The tremie slab construction at the launch shaft was a difficult process requiring installation of the reinforcing steel and dowels by divers. Because of the deep water depths, the divers could only work for a limited amount of time before decompression stops and diver rotation were needed.

Schedule

The entire process to complete the retrieval shaft structure using DSM, guide wall and dry excavation took 50% of the time per square foot of wall compared to the time used to construct the launch shaft structure using secant piles, wet excavation, tremie slab and dewatering.

Cost

When comparing cost, the launch shaft structure including the secant piles, wet excavation, tremie slab and dewatering was 10% less expensive per square foot of wall than the cost of the retrieval shaft using the DSM technique and dry excavation. This comparison is based on the direct cost spent at each structure and does not factor in the cost associated with overhead and general conditions from the difference in time. The comparison also does not consider the inefficiencies associated with the retrieval shaft being located on an island accessible only by ferry.

Conclusions and Lessons Learned

Having completed two large diameter and deep shafts in similar geology, but with significantly different techniques affords the opportunity to compare not only the design and construction efforts, but also the cost schedule implications. The 89ft deep, 42ft diameter, secant pile launch shaft performed well with only minimal, localized reinforcement and without the need for pre-grouting. Despite being the more complicated construction technique, requiring wet excavation and a reinforced tremie slab, the secant piles remain an economical solution, especially for deeper shafts. The 72ft deep, 28ft diameter, DSM retrieval shaft performed quite well even though field trials indicated weaker UCS values than anticipated. Full-scale field trials remain a necessary part of any significant DSM construction. The DSM shaft demonstrated that single axle DSM can be performed effectively to depths of up to 75ft deep and through hard limestone with UCS of over 3,000 psi. While ultimately more expensive than the secant pile approach (despite also being to a shallower depth) the DSM shaft was faster to construct and excavate. Working in the dry provided a safer working environment where leaks could be detected earlier and divers were not required. The DSM shaft was also an excellent solution for the site constraints.

This project was a success in large part because of the design-build approach. The advantages of the design-build for this project were 1) completion under budget, 2) schedule efficiency as construction was able to begin and progress prior to completion of the design, and 3) allowing for a change in the means and methods of construction from secant piles to DSM at the retrieval shaft without affecting the overall project schedule.

REFERENCES

Brinkgreve, 2013. PLAXIS 3D 2013, User Manual.

Federal Highway Administration (FHWA), 2013, Design Manual: Deep Mixing for Embankment and Foundation Support, U.S. Department of Transportation, October.

Young and Budynas, 2002. Roark's Formulas for Stress and Strain, McGraw-Hill.

DEVELOPMENT OF NEW SHAFT RESISTANCE MODELS FOR PILES DRIVEN IN THE PUGET SOUND LOWLANDS

Youssef Bougataya, Geotechnical Engineer, Jacobs, Seattle, Washington, USA, (541) 908 5472, youssef.bougataya@ch2m.com

Armin W. Stuedlein, PhD, P.E.(WA), Associate Professor, Oregon State University, Corvallis, Oregon, USA, (541) 737 3111, armin.stuedlein@oregonstate.edu

ABSTRACT

Early stage design of driven piles primarily relies on static analysis based on one or a combination of total and effective stress approaches, the latter known as the β–method to estimate axial capacity. A database of 85 piles driven in the Puget Sound Lowland region and monitored at End of Driving (EOD) and Beginning of Restrike (BOR) was compiled along with capacities estimated using the CAPWAP procedure. Established soil profiles based on borings with standard penetration tests (SPT), cone penetration tests, and geologic maps were matched with their corresponding unit shaft resistance profiles from the CAPWAP procedure and resulted in more than 1,200 observations. In this study, eight new models were developed to predict the β–coefficients at EOD and BOR, based on the corresponding USCS categorization. Each β–coefficient model is formulated using a three-parameter exponential function, calibrated to capture the profile of β–coefficients with depth. These models could benefit the designer by providing them with a simple, empirical model that accounts for soil type and setup in a smooth, continuous function with depth. A parallel analysis was performed to assess the accuracy and variability of the formulated prediction models to facilitate implementation in load and resistance factor design (LRFD).

Keywords: axial bearing capacity, driven piles, end of driving, beginning of restrike, reliability, LRFD

INTRODUCTION

The design of the axial capacity of driven piles during the planning stages of a project is typically based on a static analysis approach. The goals of this approach are to predict the components of capacity, consisting of the shaft and toe bearing resistances, and to assess project concept feasibility and preliminary lengths. In most cases, this analysis is based on empirically-developed methods, such as the total stress method, also known as the α–method (Tomlinson 1987) or the effective stress method known as the β–method (Esrig and Kirby 1979; Fellenius 1991). Many other methods, such as those based on in-situ test results exist and rely on correlations of blow counts from the standard penetration test (SPT), and cone tip and sleeve friction resistance from the cone penetration test (CPT), to shaft and toe pile resistances (Schmertmann 1978; Meyerhof 1976; Nottingham and Schmertmann 1975; Nordlund 1963; Eslami and Fellenius, 1997; De Ruiter and Beringen 1979). Although these methods were generally developed using data from specific geological regions, they are often recommended in national design manuals (e.g., FHWA, Hannigan et al. 2006).

The study described in this paper aims to develop new effective stress-based models for piles driven in the Puget Sound Lowlands in the State of Washington, USA. Although the models themselves are calibrated for use in a specific region of the USA, the functional form of the model should serve well for general use and applicability to other regions. The models are developed for End-of-Driving (EOD) and Beginning-of-Restrike (BOR) driving conditions. Instead of using β-coefficients based on total capacity back-calculated from non-instrumented static pile testing, the specific soil types and pile segments are considered in the development of the new models. Finally, considerations of the sample size, accuracy, and uncertainty of

© 2018 Deep Foundations Institute

the new developed models are evaluated as required for reliability theory-based LRFD implementation (Allen et al. 2005; Bathurst et al. 2011).

SELECTION OF THE REFERENCE CAPACITY: CASE PILE WAVE ANALYSIS PROGRAM (CAPWAP) TECHNIQUE

Any consideration of the accuracy and uncertainty of a given design methodology requires the selection of the interpreted failure capacity (Stuedlein et al. 2014). In this study, the results of dynamic loading tests (DLTs) assessed with the stress wave analyses are used to develop the static failure capacity that will serve as the reference capacity for the development of accuracy statistics. The CAPWAP technique is a post-processing signal matching method based on results gathered through the Pile Driving Analyzer (PDA; Rausche et al. 1972). The instrumentation consists of two accelerometers and two strain gages mounted in diametrically opposed pairs near the pile head. The signal matching procedure, described in detail by Rausche et al. (2010), uses the force time history computed from the measured dynamic strain as a reference, from which iterative trials of computed force time history with varying assumed static and dynamic soil resistance parameters are evaluated against. This iterative approach uses the product of the velocity time history (deduced from the acceleration measurements) and the pile impedance as an independent forcing function from which the error in signal matching iteration may be minimized. The computed force time history curve requires the selection of appropriate shaft and toe quake (i.e., the displacement corresponding to the transition from the assumed elastic and plastic displacement response), the shaft and toe damping (correlated to the dynamic component of resistance); and the static load transfer distribution along the pile.

Using measurements of the strain (and computed force) and acceleration time history at the pile head from a single blow during dynamic testing, the CAPWAP user iteratively changes the quake and damping parameters used in the soil model to obtain the best match of a complimentary stress wave. Since this procedure requires user input; they are affected by engineering judgment and experience. Of the parameters the user may alter (i.e., soil quake, damping, shaft resistance distribution) the most critical factor affecting the interpreted failure capacity is the shaft resistance distribution (Hannigan et al. 2006). CAPWAP models a driven pile as a series of masses connected by springs which in turn are connected to the surrounding soil by springs (static resistance) and dashpots (dynamic resistance) based on the modified Smith soil model (Smith 1960). Individual spring-mass pairs are then used to predict soil resistance distribution. CAPWAP discretizes the pile into n equal segments and the user may assign a fraction of the total shaft resistance, R_s, to each segment to produce a signal (i.e., stress wave) that matches the measured signal. The β-coefficient may then be determined by comparing the unit shaft resistance, r_s, to the estimated effective stress, σ'_v, at the center of each pile segment:

$$\beta = \frac{r_s}{\sigma'_v} \qquad [1]$$

Most of the soil segments used in this study are 2 m (6.5ft) long and the corresponding shaft resistance percentage is estimated by a specialist based on the soil profile, the observed driving resistance (bpf / blows per 0.3 m) during pile driving.

DATABASE OF CAPWAP DYNAMIC ANALYSIS RECORDS

CAPWAP signal matching was performed by independent, specialized professional engineers with significant experience in dynamic testing in the Puget Sound Lowlands. For this study, all dynamic tests were performed by either GRL, Inc. (42 %) or RMDT, Inc. (58 %). Because the CAPWAP technique necessitates assumptions as to the shaft resistance distribution and other soil model parameters, sound

experience and judgment are of critical importance; data generated by these specialists allow for a reduced, but unquantifiable magnitude of interpretational error.

Reddy and Stuedlein (2013) collected a database of more than 237 dynamic pile tests. Of these piles, CAPWAP was performed on a subset of over 180 piles. Bougataya and Stuedlein (2016) analyzed the accuracy and uncertainty of the capacity of the piles in the database associated with wave equation analysis. For the purpose of study, the same case histories were screened to filter piles that meet the following conditions:

- Both EOD and BOR CAPWAP records are available for each pile of interest;
- Depth of penetration remains approximately the same at both conditions to avoid overlap between the assumed soil segments at EOD and BOR and to maintain consistency for purposes of shaft resistance model development; and,
- Enough soil information was available to establish the soil profile for the pile of interest.

Representative soil profiles were obtained using borings with split-spoon sampling, cone penetration test data, and/or generalized subsurface cross-sections established by the original design team. Whenever a test pile was located within 9 m (30 ft) of an exploration, the soil profile from the exploration was assumed to represent the conditions at that pile. If a generalized soil profile for the project of interest was made, the pile of interest was located and the corresponding soil layering at that location on the cross-section assumed. Filtering of the larger database resulted in 85 driven piles with all necessary information including CAPWAP records at EOD and BOR, pile geometry and soil profile information. Following an initial review of the data, it was concluded that differentiating the dataset by pile type (e.g., concrete vs. steel, open-ended vs. closed-ended) did not appear warranted, despite anticipated differences.

This study was limited to the Puget Sound Lowland area in the State of Washington in the USA. This region has been subjected to several consecutive glaciations, with at least six documented glaciations occurring during the Pleistocene (Easterbrook 1994). Typical Puget Sound Lowland geology consists of near-surface fill soils underlain by alluvial and estuarine deposits, which in turn are underlain by very dense, glacially over-ridden soils (Borden and Troost 2001). The majority of driven piles considered in this study were founded in glacial soils and therefore exhibited high driving resistance (> 80 bpf) at the end of driving and during restrike (Reddy and Stuedlein 2013).

METHODOLOGY FOR THE DEVELOPMENT OF THE NEW β-MODELS

The methodology implemented to achieve the aim of this paper by development of new β-coefficient models includes the following components:

1) Filtering of data for piles where both End of Driving (EOD) and Beginning of Restrike (BOR) records are available. The data is filtered again to only admit those piles where the depth of penetration remains approximately the same at both EOD and BOR driving conditions.
2) Establish representative soil profile for each pile by (a) gathering all available in situ data from geotechnical reports, (b) develop representative generalized soil profile, (c) consider specific geology for uncertain strata and finally infer soil profile coinciding with desired pile location; and (d) correlate soil profile, including soil type based on Unified Soil Classification System (USCS; ASTM 1985) and soil density or consistency to the unit shaft resistance determined for the EOD and BOR conditions;
3) Compute the effective stress at the mid-point of each CAPWAP soil-pile segment;
4) Compute the normalized unit shaft resistances using the effective stress at the corresponding depth (i.e., the β-coefficient);

5) Separate or "bin" the computed β-coefficient values by USCS depending on the magnitude of fines content and/or plasticity; and,
6) Develop a suite of continuous β-coefficient models by ordinary least squares fitting.

The soil segmentation in the CAPWAP records did not always coincide with the corresponding soil stratigraphy. Often a CAPWAP segment will overlap two consecutive soil layers. One solution is to assign the CAPWAP segment to the thicker of the two corresponding soil layers. Another solution is to average the parameter of interest (e.g., unit weight) with respect to depth. The former solution is conservative but simplistic, whereas the latter is more realistic but time consuming. The loosest soil will likely return the highest setup ratio, so the most likely attribution for "setup" would be for the loosest and softest soil. However, the potential for error is the largest with the "simplistic" approach. Therefore, a weighted average of relevant soil parameters weighted by the thickness of the layer portion corresponding to the "setup" observation was used. For example, if setup quantity observed spans 0.6 m (2 ft) of soft soil, and 1.4 m (4.5 ft) of dense soil, the unit weight is computed as follows:

$$\gamma_{avg} = [(0.6\text{ m})\gamma_{ss} + (1.4\text{ m})\gamma_{ds}]/(2.0\text{ m}) \quad [2]$$

where γ_{avg} = averaged unit weight, γ_{ss} = unit weight of soft soil, and γ_{ds} = unit weight of dense soil in kN/m^3. The soil unit weights were estimated using recommendations from Peck et al. (1974).

NEW DEVELOPED MODELS FOR β-COEFFICIENT SPECIFIC TO THE PUGET SOUND LOWLANDS

Typically-accepted β-coefficient models vary as a function of depth for deep foundations, such as driven piles (Meyerhof 1976) and drilled shafts (O'Neill and Reese 1999). However, the statistical treatment of the proposed models is rarely presented along with appropriate soil descriptions, such as the USCS classification, or the density/consistency of the soils considered. Owing to the transition of design from a deterministic framework to a reliability based design approach, quantification of accuracy and uncertainty are required to develop appropriate resistance factors. In this study, a general mathematical form based on visual quality of fit was adopted to capture the variation of β-coefficient as a function of depth based on the USCS classification. Each specific model is described independently (see Table 1) in the following sub-sections. All the proposed models follow the same general functional form used by Miyata and Bathurst (2012):

$$\beta(z) = \frac{\beta_0 - \beta_1}{\exp(\beta_2 \cdot z)} + \beta_1 \quad [3]$$

where z is the depth below the ground surface, and β_0, β_1 and β_2 are fitting parameters. This expression seems to capture the variation of β-coefficient as a function of depth. Because the continuous exponential function is differentiable and strictly positive, the proposed expression for β-coefficient can be easily used in further mathematical treatments. Some of the characteristics and advantages are the following:

- The function is smoothly continuous with depth z;
- β_0: captures the initial value of β-coefficient. It corresponds to β-coefficient at the ground surface or mudline. Although it is expected that β_0 should be largest near the ground surface due to the effects of stress-dilatancy, it can often take very low or high values owing to the data available;
- β_1: captures the asymptotic value of β-coefficient. At large depths where z tends infinity, β-coefficient tend toward β_1 as expected from stress-dilatancy effects (i.e., the acquisition of the critical state of the soil); and,
- β_2: captures the slope of curvature from the initial value of β-coefficient (equal to β_0) to the asymptotic value of β-coefficient (equal to β_1). The larger the value of β_2, the steeper the curvature.

To determine the most appropriate β-coefficient model parameters, a fitting procedure is necessary. In this study, the model is fitted to the data for all of the USCS classes considered. To determine the three parameters β_0, β_1 and β_2 several options are possible. It is possible to minimize the coefficient of determination (also known as R^2) by varying those coefficients (β_0, β_1 and β_2) without any constraints. This method assures a minimum R^2, but the model might under- or over-estimate the measured β-coefficient values to produce a consistent bias. In this investigation, the parameters were determined by optimizing the mean bias, defined as the back-calculated β-coefficient over the predicted β-coefficient, using ordinary least squares regression. Instead of varying the model fitting coefficients by minimizing squared errors between the observed and predicted β-coefficient, the fitting coefficients were optimized to produce a mean bias of near-unity (i.e., to produce and unbiased model). This condition ensures that the model can be used in reliability theory or the framework of load and resistance factor design (LRFD). It is always desirable to have a low value of coefficient of variation (*COV*) as this ensures that the model has a small variation and thus the predicted value can be used with more confidence. The assessment of low variation is subjective and depends on the phenomena studied (Miyata and Bathurst 2012).

β-COEFFICIENT MODELS BASED ON USCS CLASSIFICATION

The compilation of unit shaft resistances from the CAPWAP segments produced 1,216 data pairs. Significant effort was made to partition the data into groups according to USCS classification while respecting two requirements:

- Each group must have a significant number of data points so any subsequent treatment does not suffer from sampling size issues. Some studies have shown that an appropriate sample size for reliability-based, foundation engineering design models are those that are larger than about 40 (Stuedlein and Reddy 2014);
- A given group must have some corresponding physical compatibility (i.e., sandy soils should not be combined with clayey soils).

Eight groups were selected to meet the requirements discussed above as summarized in Table 1. The USCS classifications can be divided into four major groups: gravel, sand, and inorganic and organic, fine-grained soils including plastic silts and clays. It should be noted that one of the groups considered, SM/ML, does not correspond to any specific group with USCS categorization, but was adopted in local practice by some firms in the Pacific Northwest. In this study, the β-coefficient data points within the upper 4 m were not used when fitting the model due to errors associated with near-surface effective stress calculations (e.g., due to matric suction effects).

Table 1. Fitting parameters for proposed β-coefficient models per USCS class

Model No.	USCS group(s)	EOD					BOR				
		β_0	β_1	β_2	$\bar{\lambda}$	*COV* (%)	β_0	β_1	β_2	$\bar{\lambda}$	*COV* (%)
1	CH; CL; CL-ML	0.448	0.037	0.078	1.00	100	0.832	0.099	0.073	1.00	83
2	GP; GW; GM; GW-GM; GP-GM	1.152	0.109	0.146	1.00	180	1.522	0.220	0.107	1.00	124
3	ML	1.072	0.068	0.222	1.00	109	1.664	0.191	0.140	1.00	101
4	OH; OL; PT	0.108	0.108	1.045	1.00	81	0.292	0.292	2.172	1.08	72
5	SM; SC	0.424	0.039	0.073	1.00	161	0.825	0.000	0.038	1.00	113
6	SM / ML	0.234	0.077	0.175	1.00	75	0.341	0.000	0.017	1.00	62
7	SW-SM; SP-SM	0.456	0.108	0.117	1.00	111	1.064	0.059	0.051	1.00	82
8	SW; SP	0.699	0.157	0.334	1.00	97	3.110	0.391	0.431	1.00	96

Model No 1: CH, CL, and CL-ML

This family of models applies to clayey soils including CH, CL and CL-ML groups based on USCS method of classification. Figure 1 (a) shows the 168 data corresponding to clayey soils at EOD as well as the suggested model based on (1) best fit using the least squares procedure and (2) forcing the mean bias to be independent of the predicted or nominal β-coefficient, and (3) ignoring the back-calculated β-coefficients within the upper 4 m when fitting the proposed equation. Figure 1 (b) shows the computed sample biases. The variability in the model is quantified by coefficient of variation (*COV*), defined as the standard deviation of the sample biases normalized by the mean bias. At EOD, the fitted model has a *COV* of 100% and a mean bias of one as shown by the trend line in Figure 1 (b).

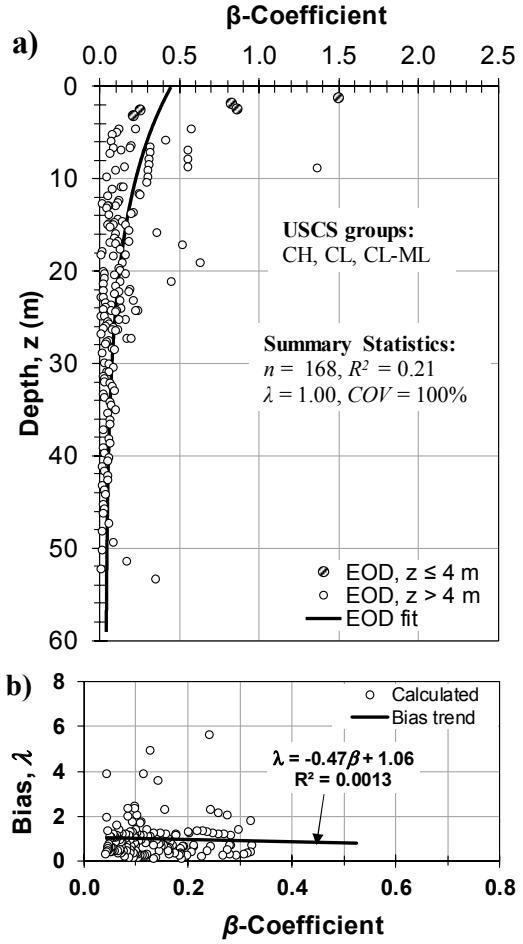


Fig. 1. Determined β-coefficient values from CAPWAP records and effective normal stress filtered for clayey USCS soils CH; CL; and CL-ML, and fitting exponential function at End of Driving (EOD). (a) Determined β-coefficient values versus depth and model curve. (b) Model bias

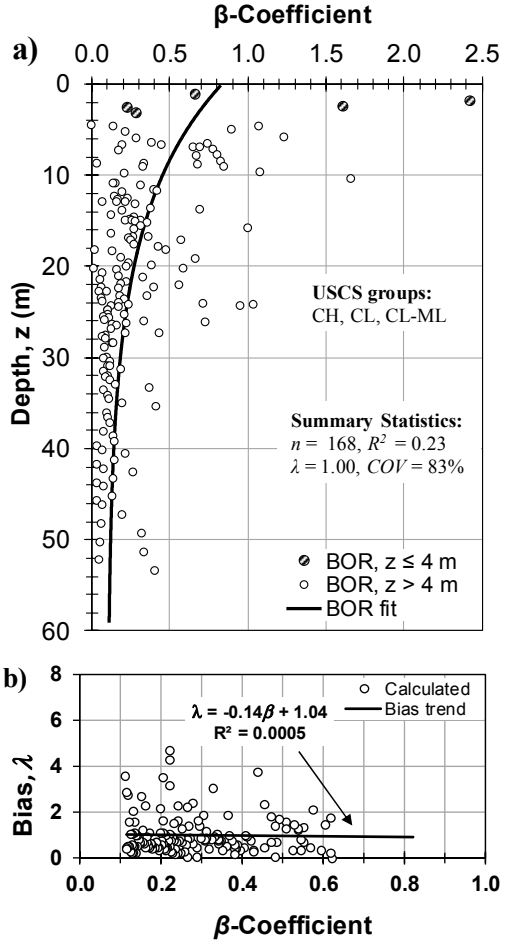


Fig. 2. Determined β-coefficient values from CAPWAP records and effective normal stress filtered for clayey USCS soils CH; CL; and CL-ML, and fitting exponential function at Beginning of Restrike (BOR). (a) Determined β-coefficient values versus depth. (b) Model bias

For both conditions, EOD and BOR, the trend in bias has a small slope and very low R^2, meaning that the proposed model does not depend significantly on the magnitude of the nominal β-coefficients. This requirement ensures compatibility with LRFD framework where non-dependency between nominal

resistance and sample bias must be verified. Figure 2 (a) shows the back-calculated values of β-coefficient versus depth below the ground surface at BOR for clayey soils. The *COV* in back-calculated data at BOR for the clayey group is 83%, smaller than the COV at EOD by 17%. Figure 2 (b) shows the variation in sample bias with β-coefficient at BOR, where similar conclusions with respect to the lack of bias in the model may be made.

Model No 2: GP, GW, GM, GW-GM, and GP-GM

In this subset, the database was filtered for all gravelly soils, including those falling under the USCS groups of GP; GW; GM; GW-GM; GP-GM. A major reason for using this family of soils under one group is to ensure the requirement of sample size representability by having a relatively high number of segments. This group included 82 segments of unit shaft resistance to a depth over 80 meters, making it the deepest sample size of those considered in this study. As expected, the β-coefficient values are larger at EOD and BOR on average when compared to other USCS groups because of their greater frictional resistance, general higher permeability, and the ability to densify these materials during pile driving (e.g., Stuedlein et al. 2016). It should be noted that only few CAPWAP segments were available for the depths of 20 and 50 meters. Also, at larger depths, some measured β-coefficients are very small (close to zero).

Model No 3: ML

For this group, the best fit resulted in a β-coefficient at the ground surface $\beta_0 = 1.07$ at EOD, whereas at BOR, $\beta_0 = 1.66$. Although it might be expected to have a larger value of β-coefficient at EOD compared to BOR at shallow depths because of heave due to dilation, the observed values can be justified by the fact that data in the upper 4 m were ignored when fitting Equation (3). The asymptotic value of β-coefficient at EOD occurring at approximately 15 m at EOD is equal to 0.07, whereas the asymptotic value for β-coefficient at BOR is 0.19 starting around 20 m. A practical implication of this observation is that shaft resistance at least doubled in silty soils following setup. Similar to Models No. 1 and No. 2, the mean bias is equal to one suggesting that the proposed models are accurate on average.

Model No 4: OH, OL, and PT

This model is specific to organic soils including USCS groups OH, OL and PT. This group of soils consisted of 26 data points making it the smallest sample in this USCS based categorization used in this study. The back-calculated values of β-coefficient are derived from relatively shallow depths as compared to other soils. This is expected as most of the organic soils are typically found near the ground surface. Similar to the ML group at EOD, β-coefficient models for organic soils group has $\beta_0 = 0.11$ and $\beta_0 = 0.29$ at EOD and BOR, respectively. Again, those values can be attributed to the range of values of back-calculated β-coefficient and/or the fitting process. Of note, β-coefficient values at BOR for the organic soils group is larger than that for clays and silts.

Model No 5: SM and SC

This subset of soils includes silty sand (SM) and clayey sand (SC). It is based on 213 data points back-calculated from CAPWAP records normalized by estimated effective stress at the same depth. It extends to approximately 50 meters (164 ft) below ground surface. This fitted β-coefficient model for EOD resulted in a mean bias of one and a *COV* of 161%. The high value of *COV* can be attributed mainly to the large scatter in the CAPWAP-based unit shaft resistances for depths less than 20 m. It should be noted that this model presents the most gradual transition from the initial value $\beta_0 = 0.42$ to the asymptotic value $\beta_1 = 0.04$. This is quantified by the small $\beta_2 = 0.07$, which captures the lack curvature of the

proposed model. Sample biases are compared to the predicted β-coefficient for SM and SC at EOD. The mean bias is equal to one ensuring that the model is accurate on average. At BOR, the fitted model also exhibits low curvature with $\beta_2 = 0.04$, which is the smallest for all models at BOR. The best fit resulted in a *COV* of 113% and an R^2 value of 0.06, suggesting relatively large uncertainty in the back-calculated data of β-coefficient for SM and SC soils.

Model No 6: SM/ML

This group is unique as it does not correspond directly to any of the existing USCS groups. During review of the database, it was noted that many sublayers contain silty sand (ML) intermixed with sandy silt (SM) without a clear or definitive indication that the soil layer should be attributed to one group or the other. Note that USCS suffers from a considerable limitation as it does not explicitly differentiate between plastic silt and non-plastic silt, but rather includes both of them under the group name ML. In general, these observations were derived from deltaic soil deposits near the mouths of the Puyallup and Duwamish rivers, though other locations are also present in the database.

The filtration of back-calculated values of β-coefficient points corresponding to SM/ML soils resulted in 113 data pairs. All data values of β-coefficient at EOD are less than 0.4, even at shallow depths. This is in contrast to other soil groups where at shallow depths the β-coefficient are relatively large. For this reason, the best fit using the proposed exponential function resulted in an approximately constant function. The model at BOR naturally returns larger β-coefficients than at EOD, but the increase in resistance is low to moderate.

Model No 7: SW and SP

Sand is by far the most common major soil type in the database collected in this study from Puget Sound Lowlands. The filtered group herein corresponds to relatively clean sand with less than 5% fines as observed in the samples obtained from in-situ investigations. The family of soils filtered in this group includes USCS groups SW and SP. The group contains 242 data points distributed from the ground surface to a depth of 46 m. Although, as with all soil groups in this study, significant scatter is observed, it can be inferred that the proposed model suitably captures the trend in β-coefficient with depth at EOD and BOR. Equation (3) is fitted to the data at both driving conditions. A *COV* of 97% and 96% was obtained with a mean bias of one at EOD and BOR, respectively. The asymptotic β-coefficient is the largest of all soil groups for EOD and BOR, with values of 0.16 and 0.39, respectively.

Model No 8: SW-SM and SP-SM

This group is the last in the USCS categorization used in this study to capture the variation of β-coefficient as function of depth. This group includes both SW-SM and SP-SM soils. The model at BOR is less variable compared to EOD with a *COV* = 82% at BOR and a *COV* = 111% at EOD.

DISCUSSION

Eight soil groups based on the USGS were created and 16 β-coefficient models proposed, with two models per soil group: one corresponding to the EOD driving condition and one corresponding to the BOR driving condition. All of the proposed models correspond to a general three parameter exponential function. This function seemed to capture the general trend of the back-calculated β-coefficient data in addition to providing advantages. Table 1 summarizes the model parameters β_0, β_1 and β_2 corresponding to each USCS group, and the associated mean bias, λ, and coefficient of variation (COV). An advantage of this study is

the use of a considerable number of β-coefficient data therefore providing realistic bounds on observed shaft resistance and a representative statistical sample. Except for the organic soils group Model No. 4 (OH, OL, PT) with 26 data points, all other soil groups has over 80 data points each. An overall conclusion is that considerable scatter exists in back-calculated β-coefficient values determined using CAPWAP records from experienced practitioners and soil profile determined using state of the practice procedures. This scatter is a good indicator of the magnitude of the quality of correlation between (1) subsurface investigation (2) CAPWAP shaft distribution (3) physical representability of shaft resistance magnitude by USCS classification without direct consideration of relative density, gradation, or the spatial variability of soils, and (4) inclusion of both steel and concrete piles in the data without separate consideration of the frictional interface characteristics. For all of USCS subgroups, the *COV* at BOR is lower than that at EOD. It should be noted that although the value of β-coefficient at the ground surface, β_0, is expected to be higher at EOD due to the heave that occurs after the pile toe passes the near surface, unconfined soil, the models exhibit a larger β_0 at BOR. This is a result not only of the available data but also the fitting procedure and therefore the limitation of the model in capturing all expected soil mechanics should be acknowledged and addressed when the proposed models are used. Nonetheless, these models can help inform pile design and drivability studies conducted using wave equation analyses.

SUMMARY AND CONCLUSIONS

This paper discusses the development of a new framework for axial static capacity analysis of driven piles. A new suite of effective stress (β-coefficient) models specific to the Puget Sound Lowlands was developed based on USCS classification of soils. The method uses the shaft distribution back-calculated from CAPWAP analysis at both driving conditions, EOD and BOR, and matches unit shaft resistance for each soil layer to the corresponding soil type with consideration of its depth. Based on USCS rules, eight groups of soil were defined with two models for β-coefficient, one for EOD and the other for BOR. All models followed a general mathematical form corresponding to a three-parameter exponential function. The fitting parameters were fitted to the back-calculated data using the least squares approach with a constraint as to ensure a mean bias of unity for all models to ensure LRFD based design implementation. These models are specific to the Puget Sound Lowland, such that its applicability to other geologic regions is limited. The implementation of these methods within an LRFD approach is readily feasible should it be desired.

REFERENCES

Allen, T.M., Nowak, A.S., Bathurst R.J. 2005. Calibration to Determine Load and Resistance Factors for Geotechnical and Structural Design, Transportation Research Board Circular E-C079, Washington, DC.

Bathurst, R.J., Miyata, Y., Konami, T. 2011. Limit states design calibration for internal stability of multi-anchor walls. Soils and Foundations, 51 (6) (2011(a)), pp. 1051-1064.

Borden, R.K., Troost, K.G. 2001. Late Pleistocene Stratigraphy in the South-Central Puget Lowland, Pierce County, Washington. Washington Division of Geology and Earth Resources: Report of Investigations 33.

Bougataya, Y., and Stuedlein, A.W. 2016. Region-Specific Calibration of Resistance Factors for use with Static and Wave Equation Analyses of Driven Piles. J. Deep Found. Ins., 10(3), 143-152.

De Ruiter, J., Beringen, L.F. 1979. Pile foundations for large North Sea structures. Marine Georesources & Geotechnology, 3. 267-314.

Easterbrook, D. J. 1994. Chronology of pre-late Wisconsin Pleistocene sediments in the Puget Lowland, Washington. Regional geology of Washington State: Wash. Div. Geol. Earth Res. Bulletin 80, 191-206.

Eslami, A.E. and Fellenius, B.H. 1997. Pile capacity by direct CPT and CPTu methods applied to 102 case histories. *Canadian Geotechnical Journal* 34(6): 886-904.

Esrig, M.I., and Kirby, R.C. 1979. Soil Capacity for Supporting Deep Foundation Members in Clay. ASTM STP. No. 670, pp. 27–63.

Fellenius, B.H., Riker, R.E., O'Brien, A.J. and Tracy, G.R. 1989. Dynamic and Static Testing in a Soil Exhibiting Set-up. ASCE, J. Geotech. Engrg. Div., 115(7), 984-1001.

Hannigan, P.J., Goble, G.G., Likins, G.E.,and Rausche, F., 2006. Design and Construction of Driven Pile Foundations. Report No. FHWA-NHI-05-042, Nat. Highway Institute, FHWA, USDOT, Washington, D.C. 968 p (Vol 1), 486 p (Vol 2).

Meyerhof, G.G. 1976. Bearing Capacity and Settlement of Pile Foundations. J. Geotech. Engrg. Div., ASCE, New York, NY, Vol. 102, No. GT3, pp. 196–228

Miyata, Y., Bathurst, R.J. 2012. Reliability Analysis of Soil-Geogrid Pullout Models in Japan. Soils and Foundations; 52(4):620–633.

Nordlund, R.L. 1963. Bearing capacity of piles in cohesionless soils. ASCE Soil Mech. Found. Div, 89(SM3).

Nottingham, L. and Schmertmann, J. 1975. An investigation of pile capacity design procedures, Final

Report D629, FLDOT, 159 pp.

Peck, R.B., Hansen, W.E., and Thornburn, T. H. 1974. Foundation Engineering.

Rausche, F., Moses, F., and Goble, G., 1972. Soil resistance predictions from pile dynamics. ASCE Soil Mech. Found. Div., 98(SM9) 917-937.

Rausche, F., Likins, G., Liang, L., Hussein, M. 2010. Static and dynamic models for CAPWAP signal matching. Art of Foundation Engineering Practice Congress 2010. West Palm Beach, Florida, Vol. 198, 534-553

Reddy, S.C., and Stuedlein, A.W. 2013. Accuracy and reliability-based region-specific recalibration of dynamic pile formulas. Georisk: Assessment and Management of Risk for Engineered Systems and Geohazards, 7(3) 163-183.

Reddy, S.C. and Stuedlein, A.W. 2014. Time-Dependent Capacity Increase of Piles Driven in the Puget Sound Lowlands. Soil Behavior Fundamentals to Innovations in Geotechnical Engineering, Honoring Roy Olson, GSP No. 233, pp. 464-474.

Schmertmann, J. 1978. Guidelines for cone penetration test, performance and design, U.S. Department of Transportation, FHWA-TS-78-209: 145 pp.

Smith, E.A.L., 1960. Pile driving analysis by the wave equation. American Society of Civil Engineers, ASCE Soil Mech. Found. Div., 86(SM4) 35-61.

Stuedlein, A.W., Neely, W.J., and Gurtowski, T.G. 2012. Reliability-based Design of Augered Cast-In-Place Piles in Granular Soils. J. of Geotech. Geoenv. Engrg., 138(6) 709-717.

Stuedlein, A.W. and Reddy, S.C. 2014. Factors Affecting the Reliability of Augered Cast-In-Place Piles in Granular Soils at the Serviceability Limit State. Journal of the Deep Foundations Institute, 7(2) 46-57.

Stuedlein, A.W., Reddy, S.C., and Evans, T.M. 2014. Interpretation of Augered Cast-In-Place Pile Capacity Using Static Loading Tests. Journal of the Deep Foundations Institute, 8(1) pp. 39-47.

Stuedlein, A.W., Gianella, T.N., and Canivan, G.J. 2016. Densification of Granular Soils using Conventional and Drained Timber Displacement Piles. J. of Geotech. Geoenv. Engrg., 142(12) 04016075.

Tomlinson, M.J. (1987). Pile Design and Construction Practice. Viewpoint Publication.

DIFFERENT DRILLING TECHNIQUES IN CHALLENGING GEOLOGY AT SEMINOLE HARD ROCK HOTEL AND CASINO

Jonathan Delgado, Bauer Foundation Corp., Odessa, Florida, (727) 531-2577
jonathan.delgado@bauerfoundations.com
Michael Arnold – Ph.D, Bauer Foundation Corp., Odessa, Florida, (727) 531-2577
Michael.Arnold@bauerfoundations.com

ABSTRACT

In 2017, Bauer Foundation Corp. (BFC) was awarded the contract to install the deep foundations for the new 17-story Hotel Tower and the Low Rise Casino Expansion at the Seminole Hard Rock Hotel and Casino in Tampa, Florida. The site was underlain by extremely challenging Florida Limestone geology and surrounded by occupied existing buildings and infrastructure. To overcome the challenges of the difficult subsurface conditions, and to successfully complete the foundation installation without impact to the surrounding buildings and casino operation, Langan Engineering (EOR) and BFC were required to modify both the design and installation techniques during construction.

The scope of work included 147 temporarily cased drilled shafts to depths up to 230 ft (70 m) below ground surface (BGS), 76 permanently cased micropiles up to 200 ft (61 m) BGS, and more than 300 augered-cast-in-place (ACIP) piles up to 125 ft (38 m) BGS. Voids and zones of high permeability in the limestone created many challenges for execution of the foundation scope including ACIP piles overbreaks of more than 400% above neatline volume, and construction induced ground subsidence/collapses adjacent to structures supported on shallow foundations. This paper will discuss site limitations, design and construction challenges, difficult geology, varied soil conditions, and lessons learned.

Keywords: drilled shafts, augered-cast-in-place (ACIP) piles, micropiles

PROJECT

The project is located at Seminole Hard Rock Hotel and Casino Tampa, Florida, as shown in Fig. 1. Seminole Tribe, the owner, started the construction of a new 17-story Hotel Tower and the Low-Rise Casino Expansion at the beginning of 2017.



Fig. 1. Project rendering (Seminole Tribe) and location (Source: Google Maps)

From February to December 2017, BFC provided the client with the deep foundation package that included the installation of drilled shafts, ACIP piles, micropiles and low mobility grouting.

© 2018 Deep Foundations Institute

The new Hotel Tower is supported primarily on 86 36-inch (910 mm) and 55 48-inch (1,220 mm) diameter drilled shafts. The drilled shaft depths varied from 100 ft (30 m) up to 230 ft (70 m) BGS. The Low-Rise Expansion is supported primarily on 302 18-inch (460 mm) diameter ACIP piles up to 125 ft (38 m) BGS.

BFC designed and installed 71 9 5/8-inch (245 mm) diameter micropiles from 90 ft (27 m) up to 200 ft (61 m) BGS as part of the deep foundation package for both buildings. Based on the geotechnical engineer's recommendation, the client requested ground improvement in some areas at the Hotel Tower footprint using a low mobility grouting program. BFC performed a detailed load testing program designed for each foundation technique used during the project. Both building perimeters are marked in Fig. 2.

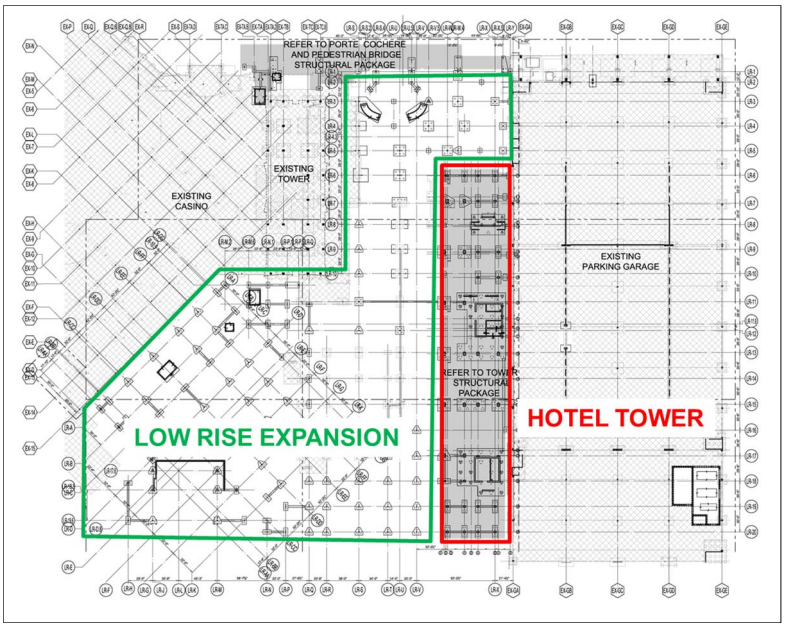


Fig. 2. Hotel Tower and Low-Rise Expansion Areas (Source: Seminole Tribe)

SUBSURFACE CONDITIONS

According to Allen et al. (2005) about 530 million years ago, the Florida plateau was formed by volcanic activity and marine sedimentation. During periods when the sea levels were high, topographic features and surficial sediments were created or deposited. The waves and currents of the ancient seas helped to erode the rock formations, remodeling and redistributing sediments over the area. As the sea levels constantly varied, the calcium carbonate remains of sea creatures and algae formed sedimentary limestone bedrock. This rock layer was considered the competent bearing stratum for the foundations of these two new buildings.

Tihansky (2014) explained how the soluble limestones (carbonate rocks) are sculpted by dissolution and weathering processes into a distinct geomorphology known as karst. Karst topography is directly related to limestone dissolution and ground-water flow. As a result, karst terrains are characterized by sinkholes, springs, caves, disappearing streams, internally drained basins, and subsurface drainage networks. While constructing the deep foundations for this project, voids and zones of high permeability in the limestone were expected due to the Tampa regional geology features.

Tihansky (2014) also presented that typical west-central Florida limestone has irregular surfaces within the same area. Highly variable limestone surfaces become a critical design element when measuring the structural integrity of the bedrock. Cavities, sudden tooling drops, and lost circulation are frequently reported during drilling in this location. According to this project's geotechnical reports, the site has the soil profile divided by two zones due to the extreme variation in depth to bearing stratum. Figure 3 shows a generalized soil profile of the site.

Zone I soil profile consists of five strata: asphalt / fill from grade to a depth of 2 ft (1 m), underlain by sand with some clays to a depth of 26 ft (8 m), followed by clay and clay with some sands to a depth of 49 ft (15 m), then silty clay with highly weathered limestone to a depth of 60 ft (18 m), and atop the weathered limestone layer.

Zone II soil profile consists of six strata: asphalt / fill from grade to a depth of 7 ft (2 m), underlain by sand with some clays to a depth of 45 ft (14 m), followed by clay and clay with some sands to a depth of 60 ft (18 m), then silty clay with highly weathered limestone to a depth of 80 ft (24 m), underlain by sand, mud and clay with sand to a depth of 150 ft (46 m), and atop the weathered limestone layer.

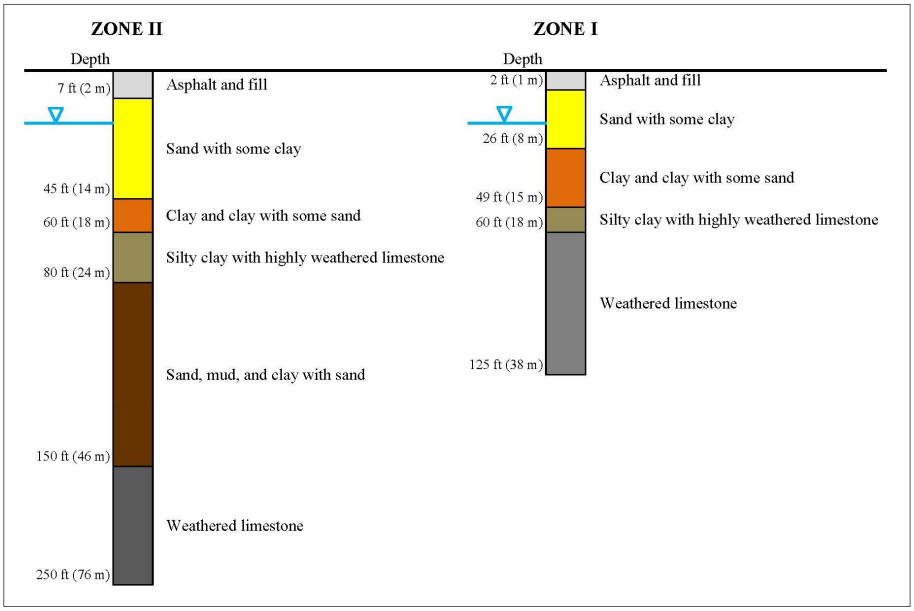


Fig. 3. Generalized soil profiles

The working grade elevation of the site was generally + 35 ft NGVD. On average, the groundwater table was encountered at 18 ft (5.5 m) BGS.

DRILLED SHAFTS

Drilled shafts were selected by the design engineer as the primary foundation system for the new hotel tower. All shafts were drilled with a BG40 (Bauer drill rig) machine. A 110 T crawler crane was used to install onsite tied rebar cages, which were spliced directly over the holes. To work in an efficient and safe manner, BFC used auxiliary equipment such as loader, telescopic handler, man lift, and skid steer. Pours were completed by means of a concrete pump truck, using the tremie method, and concrete ready-mix trucks.

Additionally, BFC setup a polymer slurry batching plant onsite. Shafts were installed using polymer slurry as support fluid. The plant was designed as a slurry recycling and storage system (as presented in

Fig. 4). Furthermore, BFC implemented an automatic gravity system to supply the open shafts with polymer slurry overnight without extra manpower.



Fig. 4. BG40 drilling and polymer slurry batching plant setup

Voids and high permeability zones in the limestone caused rapid loss of support fluid. In several occasions, this problem produced ground subsidence around the casing as shown in Fig. 5. Some shafts caved in or collapsed for this reason. For safety reasons, these shafts were immediately backfilled with lean concrete. In addition, BFC implemented a safety protocol when collapses and ground subsidence occurred including, a requirement that all personnel are tied off when going near open shafts. In an attempt to limited additional collapses, BFC worked with the polymer supplier to improve the polymer supply system, batching plant and construction techniques, as well as installing an overnight gravity system in order to maintain slurry head at all times. Modifications to the slurry properties were prepared with support of the manufacturer including further additives and improvement in the mixing plant. The polymer supply system was also enhanced in order to provide enough volume and head pressure in open shafts at all times, including tool withdrawal. The use of additional segmental casing, a slower drilling rate, and ground improvement were also utlilized.



Fig. 5. Ground subsidence at two different drilled shaft locations

In February, BFC started with the test shaft program on Zone I. Also at that time, the client was performing demolition of existing buildings and utilities to release Zone II area at the end of June.

Zone I shafts were designed with 1,000 T (8,900 kN) compression and 500 T (4,450 kN) tension capacity. They were defined with a tip elevation of -80 ft NGVD / 115 ft (35 m) BGS. The capacity would be derived from the limestone stratum with a minimum rock socket length of 45ft. An Osterberg load cell (O-cell method, a bi-directional embedded jack system) method was performed on a 48-inch (1,220 mm) diameter test shaft as shown in Fig. 6, with a tip elevation of -65 ft NGVD / 100ft (30 m)

BGS. Additionally, a lateral load test was performed on another Zone I shaft with a 200 kips (890 kN) lateral capacity.

After load tests, the drilled shaft capacities were revised. Both side shear and end bearing contributed to a higher ultimate bearing capacity and a reduction in rock socket lengths. The new average design tip elevation was -72ft NGVD with values varying from -65ft NGVD to -90ft NGVD, deepening as they were getting close to zone II (deeper top of rock elevation).



Fig. 6. Rebar cage with O-cell to be installed on test shaft and Mini-Sid photo inspection

Most of zone I shafts were installed using 30 ft (9 m) temporary casing. Shafts located adjacent to existing structures supported on stone columns and shallow foundations were installed using 50 ft (15 m) temporary segmental casing to reduce risk of ground subsidence induce by construction activities.

In July, after the demolition works were completed, the Zone II area geotechnical engineering study was executed. While finishing all zone I drilled shafts, BFC performed the test shaft program on the Zone II.

Zone II shafts were designed with 750 T (6,670 kN) compression and 350 T (3,110 kN) tension capacity. There were defined with a tip elevation of -175ft NGVD / 210 ft (64 m) BGS and with a minimum rock socket length of 45ft. The same O-cell load method was used on a 36-inch (910 mm) diameter test shaft with a tip elevation of -170 ft NGVD / 205 ft (63 m) BGS. After geotechnical and structural engineering analysis of the load test results, zone II shafts had lower ultimate bearing capacity contributed only from side shear. These shafts capacities were downgraded to 630 T (5,600 kN) and their rock socket lengths were extended in some locations. The new average design tip elevation was -168ft NGVD with values varying from -110ft NGVD to -190ft NGVD. Additionally, some shafts units were added to increase shaft cap capacities.

In consideration of the encountered soil conditions, the Zone II test shaft results, the deeper tip elevations, and experience in Zone I, the drilling method was modified. Most of Zone II shafts were installed using deep temporary segmental casing (up to 150 ft (46 m) deep), an oscillator or casing clamp, longer Kelly bar, and BG mast extension. All Zone II shafts located near existing structures were cased to top of rock.

Due to the test shaft dimensions, BFC experienced difficulties using a 36” diameter production shaft for the O-cell test. With the O-cell located at 23ft (7 m) from the bottom of the cage, there was not enough space for the tremie pipe. Changes in O-cell plates, reduction of the tremie pipe diameter, the concrete mix aggregate magnitude, the tie size, and the rebar cover were some of the modifications required to successfully install the shaft.

The quality and integrity of the test shafts were evaluated with Cross Hole Sonic Logging (CSL), Soni-Caliper, Mini-Sid, concrete tests (UCS, slump, etc.), slurry properties test (viscosity, density, pH and sand content), and Non-Destructive Pile Integrity Testing (PIT). For shafts that encountered any problems during installation, additional testing was requested by the geotechnical engineer. The supplementary

testing included dynamic tests (Rapid Axial Load Tests), Cross Hole Tomography Tests, and Non-destructive Pile Integrity Tests. All additional tests confirmed the integrity of installed shafts.

In the transition from Zone I to Zone II, BFC experienced some issues when pouring concrete. Rapid concrete slump loss was experienced when deeper tremie pipes were used and longer pouring times were taking place. An investigation at the concrete batch plant was carried out to ascertain the causes for these problems. It was determined that the cause was the use of dry aggregate due to limited bin space at the plant. A dry aggregate would retain a significant amount of the batched water/admixture therefore causing the mix to underperform. The batch plant management developed a daily material monitoring system and provided shipment from a different plant when the new aggregate had not had enough time to reach proper moisture levels. Changes to the concrete mix design and a stricter quality control program were also implemented to improve concrete properties.

One of the biggest challenges throughout the project was the working platform conditions. Many delays were experienced due to lighting and heavy, frequent rain. A lack of proper platform maintenance by the general contractor often lead to a flooded job site that prohibited Bauer from working safely and efficiently. Look-ahead planning plus proper coordination with the client, trades and subcontractors helped reduce the impact of these natural events (see Fig. 7).



Fig. 7. Working platform condition after heavy rain (Florida summer)

Conflicts with existing underground utilities were an ongoing problem for the project. Buried dead and live electrical lines, footings, deep foundations, water and gas pipes, among others, limited the work sequence and delayed production. The client did not have accurate as-built drawings of the existing structures. These conflicts were not only a safety risk for the drilling operation, but were also a major cause of delays. On several occasions there were no available piles to drill due to conflicts with utilities or existing structures.

BFC implemented a plan to soft dig in areas where utilities may be encountered to avoid impacting the utilities and creating an unsafe condition. These issues became an opportunity as well to use other drilling techniques such as micropiles, low mobility grouting, ACIP piles, etc., when limited space, access and overhead conditions were present.

As the project advanced, space and access limitations increased as exposed in Fig. 8. There was only one access point for all trades and very little traffic control. Once the shaft cap excavation started, the space restrictions worsened. The jobsite was exceedingly crowded with diverse trades working in the same area. Coordination, planning, and scheduling with all parties was needed to successfully execute the project.



Fig. 8. Space and access limitations due to crowded jobsite

Hurricane Irma winds passed over the Seminole Hard Rock Hotel and Casino at the beginning of September. One week before the hurricane landed, the jobsite was prepared and secured. All cranes, auxiliary equipment, and drill rigs were laid down so they could safely weather a potential hurricane strike. The jobsite was closed during the event, but all activities were promptly reestablished once the hurricane passed without any major damages and delays.

ACIP PILES

ACIP piles were selected by the design engineer as the primary foundation system for the Low-Rise Casino Expansion. ACIP piles were designed with 250 T (2,220 kN) compression and 80 T (710 kN) uplift capacity. The piles were defined with a tip elevation of -50 ft NGVD /85 ft (26 m) BGS. The ACIP piles were considered to have a 25 ft (8 m) minimum rock socket.

Test pile program included an O-cell simulation pile, an O-cell load test pile, and a Rapid Axial Load Test (see Fig. 9). The quality and integrity of the test piles were verified thru concrete tests (UCS, flow cone test, etc.), field inspection, and through the use of automated monitoring equipment (AME).



Fig. 9. ACIP piles installation. Rebar cages with O-cell to be installed on test piles

In June 2017, BFC started ACIP pile production with a subcontractor. During ACIP pile operation, BFC faced extreme grout loss as expected from the preliminary subsurface studies. 70 out of 313 piles were redrilled due to no grout return or grout related issues. In addition, this grout loss triggered ground subsidence induced by ACIP pile installation similar to what happened in the drilled shaft area. Fig. 10 shows some examples of this subsidence.



Fig. 10. Ground subsidence in ACIP pile operation. Extreme grout loss.

When this happened, the area was first secured (red tape). Immediately concrete was ordered to backfill the void with a pump truck. After concrete was set, the ground was compacted with excavators and vibro-compactors. A secondary pump was also brought to site to be able to top off piles rapidly when extreme grout loss occurred (see Fig. 11).

Another grout related issue was grout overconsumption. The average grout factor was 3.2 times the neat volume. There were piles overbreaks of more than 400% above neatline volume.

According to geotechnical specification, piles were not to be drilled within 12 hours at a distance 6 times the pile diameter. However, communication was observed between piles located at a distance 10 times the pile diameter. The working sequence was adapted to the new circumstances to avoid connections and quality issues. Piles with apparent connections were tested with PIT to confirm quality. Some others were replaced with supplemental ACIP piles or micropiles.

Other issues encountered were similar as the ones faced with the drilled shaft operation. Some of them were crowded jobsite, limited access and space, severe weather, and lack of piles available to drill due to conflicts with existing utilities and buildings. Many of this issues were solved throughout proper planning, scheduling and alternate working shifts.



Fig. 11. Top off piles after grout loss. Grout overconsumption in ACIP piles.

MICROPILES

Micropiles design was provided by BFC thru Terracon Consultants Inc., according to the geotechnical engineer's specifications. Micropiles were designed with 150 T (1,330 kN) compression and 75 T (670 kN) tension capacity. 9 5/8 inch (245 mm) diameter permanent casing was installed up to the top of rock. The piles were defined to have a 35 ft (11 m) minimum rock socket and a minimum tip elevation of -50 ft

NGVD / 85 ft (26 m) BGS. Compression micropiles had a 50 ft (15 m) #24 threaded bar at the rock socket and tension micropiles had full length coupled threaded bar.

There were micropiles located at the Low-Rise Expansion area with depths of 85 ft (26 m) BGS. There were likewise micropiles located at the Hotel Tower area with depths of 120 ft (37 m). Micropiles were used as supplemental support as well. Some micropiles were installed as replacements for ACIP piles and as adjacent remedial foundations for downgraded drilled shafts.

In August 2017, BFC started micropile production. The drill rig was the Bauer Klemm KR806-2. To increase production, BFC used a mini-excavator with a manipulator device to handle the casing sections (as shown in Fig. 12). BFC setup an onsite grout batching plant to provide the micropile operation. The plant included silo, desander, concrete pumps, and tanks.



Fig. 12. Mini-excavator with manipulator. Klemm drilling close to existing structure.

The geotechnical reports showed a high risk on extreme grout loss for micropiling as well. Many piles were redrilled to due to no grout return and/or drilling fluid loss. The average grout factor was 2.18. However, 20% of the piles took more than 300% neat-volume of grout. Changes in drilling operation, polymer slurry usage, and modified grout mix design reduced the grout overconsumption (see Fig. 13).



Fig. 13. Pumping polymer slurry while drilling pile. Micropiling field inspection

Other issues and challenges with micropiling were the same as with the drilled shaft and ACIP pile operations mentioned above.

SUMMARY AND CONCLUSIONS

Four different techniques were used by BFC as part of the deep foundations package for the new Hotel Tower and Low Rise Expansion of the Seminole Hard Rock Hotel and Casino Tampa. The project was variable in all aspects, having elements of different diameters, depths, varied construction methods,

machinery, tooling, types of soils, etc. BFC showed its technical and engineering expertise in foundations facing various challenges and solving them with the most efficient, safe and productive approach. Despite the difficult soil conditions, idle periods due to lack of available pile locations and a severely congested site, the project team succeeded to complete this job in a safe way, providing high standards of quality, without major delays and great client satisfaction.

REFERENCES

Allen, G. M., and Main, M. B., 2005. Florida's Geological History. IFAS Extension, University of Florida, Gainesville, Florida. Fact Sheet WEC 189.

Desimone, 2016. Seminole Hard Rock Hotel & Casino – East Tower Combined Structural Permit Set and LowRise Core and Shell Combined Structural Permit Set

Langan Engineering & Environmental Services, 2016. Performance Specifications for Micropile, Installations and Load Test Program, and Technical Specifications for ACIP Test Pile, Installations, Production Installations and Load Test Program. Seminole Hard Rock Hotel & Casino Expansion – Low-Rise and Back-of-House Structure

Langan Engineering & Environmental Services, 2017. Subsurface Investigations at Proposed Hotel Tower and Low Rise Expansion, and Technical Specifications for Drilled Shafts, Method, Test, and Production Installations and Load Test Program. Seminole Hard Rock Hotel & Casino Expansion – Proposed Tower

Tihansky, A. B., 2014. Sinkholes, West-Central Florida – A link between surface water and ground water. U.S. Geological Survey, Tampa, Florida.

FOUNDATION BASE MATERIAL STRENGTH ASSESSMENT FOR DRILLED PIPE PILES USING FORCE AND DISPLACEMENT DATA

Rozbeh B. Moghaddam, GRL Engineers, Inc., Cleveland, OH, USA, 216-831-6131,
rmoghaddam@grlengineers.com

Patrick J. Hannigan, GRL Engineers, Inc., Cleveland, OH, USA, 216-831-6131,
phannigan@grlengineers.com

Frank Rausche, GRL Engineers, Inc., Cleveland, OH, USA, 216-831-6131,
frausche@grlengineers.com

Geir Veslegard, Hallingdal Bergboring, Gullhagen, Norway
geir@bergboring.no

ABSTRACT

A common type of deep foundation used in Norway to support bridge structures is the drilled pipe piles (piles) filled with concrete reinforcement after installation. The standard installation practice is the use of down-hole hammers. Complex geology and difficult subsoil conditions in Norway causes a high variability of soil and rock layers which in turn make for differences between actual subsurface conditions and those expected from geotechnical exploratory borings. This situation is strongly noted when the foundations are not fully socketed, and the rock layer is sloped. In this particular case, special testing procedures are required to assess the drilled pile base material and evaluate the rock-socket to ensure full contact between the foundation base and the rock surface. The local standard practice to verify the latter condition, consists of coring and visually evaluating the material recovered at the bottom of the drilled pile. This paper presents a case where the coring and visual inspection were not possible and alternatively the geological material encountered at the base of the deep foundations was evaluated using force-displacement measurements. Two 1016-mm (40in) diameter open-end drilled piles identified as P02-04 and P02-05 were tested and evaluated using *in-situ* force-displacement data prior to filling the piles with concrete. Test results showed an average displacement of 7mm (0.28in) corresponding to 35MPa (5.1ksi) stress level for P02-04, and 7.2mm (0.28in) corresponding to a stress level of 38MPa (5.5ksi). Based on testing results, both drilled piles were within the established material assessment criterion presented by the local authorities.

Key Words: Drilled Pipe Piles, Down-Hole Hammers, Rock Socket, Open-End pipe piles, Force-Displacement, Stress levels

© 2018 Deep Foundations Institute

INTRODUCTION

This paper presents a case study in Norway where the material encountered at the base of an open-end drilled pipe pile (pile) was evaluated using force-displacement data. In the deep foundation industry in Norway, it is a common practice to install piles to support transportation structures. Once the piles reach the embedment elevation, and the pile base is assessed, these are filled with concrete. In projects where sloping rock is the supporting layer, and all nominal loads are supported by the pile base resistance, assessing the material encountered at the pile base to ensure full contact with the rock becomes critical. The local practice to make this assessment consists of the use of weighted tape, coring, or inspection cameras. However, similar to any other testing and evaluation methods, these come with their own limitations. The variability associated with the use of the weighted tape, accessibility for the coring equipment to complete a coring process, or the conditions at the foundation base such as murky water or thick drilling fluids could significantly impact the photo or video quality taken at the pile base. In such conditions, it is important to consider alternate testing methods to evaluate the material at the foundation base.

Throughout this manuscript, the project and its associated deep foundations properties are introduced followed by a brief description of the site subsurface conditions. Foundation installation methods and local practice for pile base assessment are presented. Finally, the alternate testing device and method is introduced and the testing results are discussed from a qualitative and quantitative approach using the shape and behavior of the force-displacement plots.

It is important to note that in many occasions in the United States, the foundation base assessment has been carried out using *in-situ* testing such as the Standard Penetration Test (SPT) or the Cone Penetration Test (CPT) to evaluate the competency of the foundation base material. Results from such tests are evaluated qualitatively (visual inspection) and quantitatively (by analyzing N-values or Tip resistances) to assess the material encountered at the foundation base. For example, the North Carolina Department of Transportation (NCDOT, 2012) specifies “SPT are generally required for drilled piers with the tip just into rock or not in rock…”. Or in the case of Florida Department of Transportation (FLDOT, 2016) the SPT is allowed to be used instead of coring to assess the competency of the foundation base material. The testing method used in the project presented in this paper, could be considered as an alternate or supplement method since force-displacement data can also be evaluated qualitatively and quantitatively.

PROJECT DESCRIPTION

The project described in this paper is related to the foundation system of a vehicular bridge crossing the Seutelva River, located in Fredrikstad, Norway. According to the project information, the proposed bridge will be supported by 15 − 1016-mm (40-inches) and 10 − 813 mm (32-inches) diameter open-end piles which were advanced to the competent rock layer. Each bridge bent consists of five open-end piles which were filled with concrete after reaching the final base elevation, Figure 1. These piles were installed using a down the hole (DTH) hammer system which uses the rotary-percussion drilling method with a button bit with the inner diameter being the same as the pipe pile. The drilling process is completed by using a first pile section with the button driving ring and a button-bit hammer fitted through the pile using drill strings, Figure 2a and 2b.

SUBSURFACE CONDITIONS

According to the available geotechnical information, the subsurface condition for the project site was described as very soft plastic clay extending from the mudline to a depth of 30m (98.4ft) followed by a 6m (20ft) of moraine silt located above the bedrock. The rock formation was encountered to be steeply sloped which made the moraine silt layer thickness varying between 6m (20ft) and 11m (36ft). The rock increasing slope was reported to run from southeast to northwest with several sudden drops and abrupt change in slope.

DRILLED PIPE-PILES BASE ELEVATION

The foundation system for the project presented in this manuscript was designed as end-bearing only where all nominal loads are supported by the foundation's base. However, due to difficult subsurface conditions and the sloping rock, each drilled pile had to be installed at a different base elevation, Figure 3. The criteria that was followed to decide the final base elevation consisted of several parameters with primary focus on (1) drilling advance rate: 40min/m minimum which corresponded to approximately a limit base resistance of 150MPa (22ksi), and (2) visual inspection with a down-hole camera. Considering uncertainties associated with the rock elevation, the contractor had to continue drilling until encountering a material that took approximately 40 minutes or more to advance 1m (3.28ft). Once the elevation was defined using the drilling rate data, the base of the drilled pile was cleaned using an airlift system, and a down-hole camera was lowered to inspect the bottom of the pipe to ensure full contact with the rock layer.

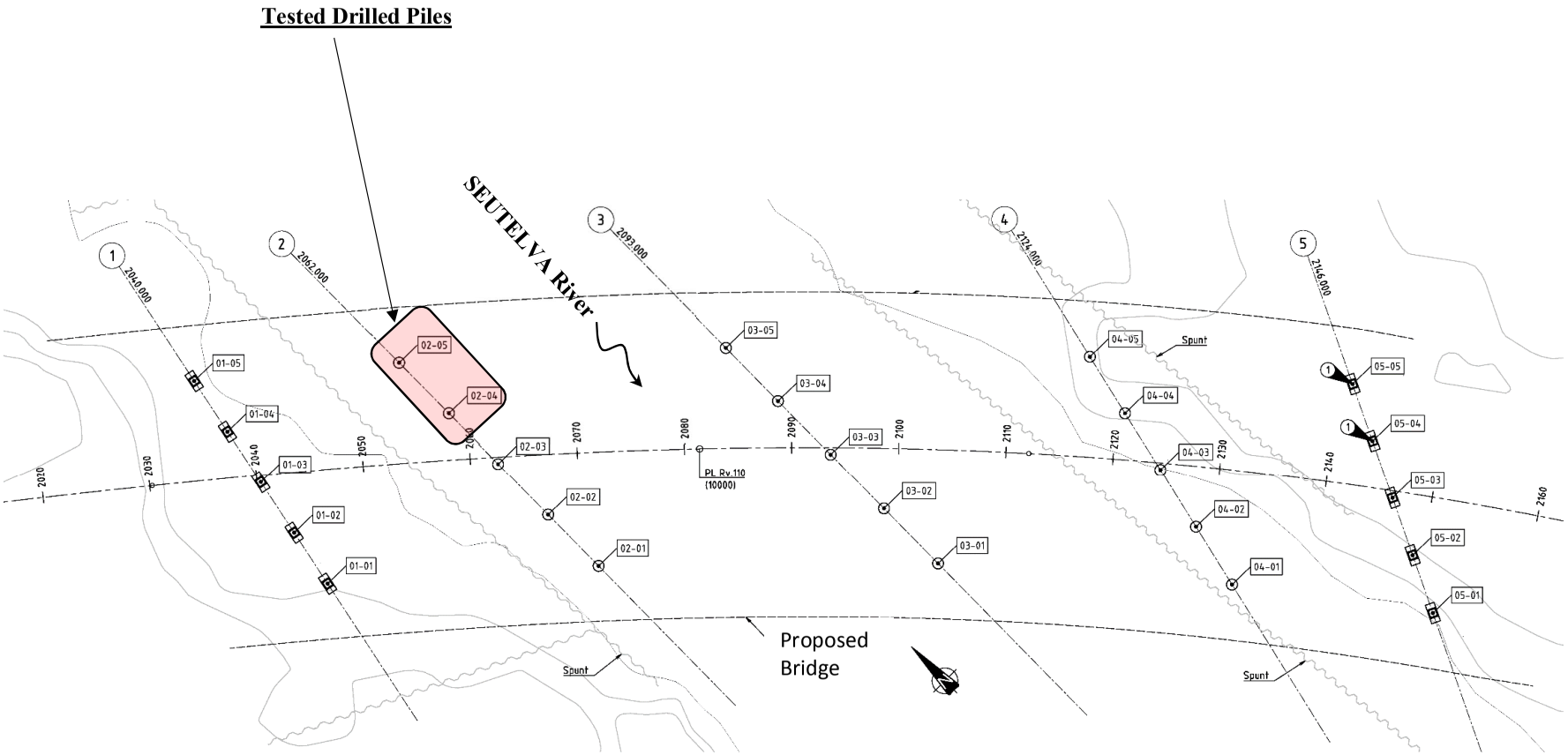


Figure 1. Proposed Bridge and corresponding Bents



(a) (b)

Figure 2. Down the Hole Hammer System **(a)** First section with Driving ring and **(b)** Hammer

For two piles located on Bent 2, the camera range and the conditions at the bottom of the pile didn't allow to capture a clear photo or video to confirm the contact between the foundations base and the rock surface. In those locations, a third criterion was established based on rock strength properties where a material with a resistance to penetration of 30 MPa (4.35ksi) with a deformation less than 8 mm (0.32in) was considered as a competent rock to receive the foundation and support the loads. To meet this criterion, it was required to obtain force and displacement data at the base of the foundation to empirically evaluate the material located at the base of the pile. If the force and displacements corresponded to established values (minimum of 30MPa for a maximum displacement of 8mm) then the material was considered competent and the final base elevation was confirmed. Force and displacement plots were determined at the pile base using a testing device known as the shaft quantitative inspection device or the SQUID.

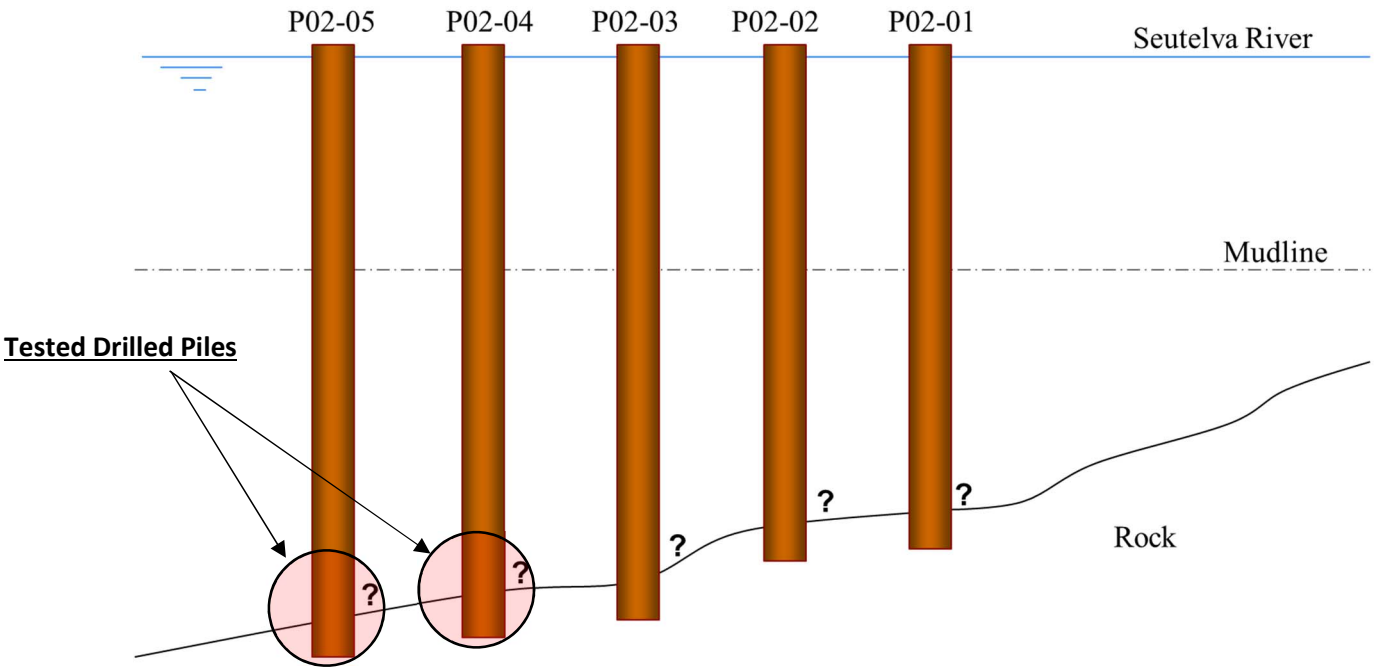


Figure 3. Schematics of base elevations for Bent 2, P02-01 to P02-05

TESTING DEVICE

The SQUID device has an octagonal shape with a maximum diagonal length of 647-mm (25.5-inches) and height of 635-mm (25.0-inches). Three penetrometers and three retractable displacement plates are attached to the device which are used to measure strain and displacements simultaneously. The penetrometers are designed to have conical or flat tips with an average cross-sectional area of 10-cm^2 (1.55-in2) which for purposes of this particular project, conical tips were used.

TESTING PROCEDURE AND RESULTS

The SQUID device was attached to the drilling strings using an American Petroleum Institute (API) adapter located between the swivel plate and the drill string and lowered into the drilled pipe to initiate test runs at the foundation base, Figure 4. Once at the base, axial force was applied using the drill rig crowd and the resistance to penetration was measured by the penetrometers, whereas measured displacements were determined by retractable plates.



Figure 4. Testing procedure for Bent 2, Drilled Pile P02-05

Drilled Pile P02-04

A total of 10 runs were completed at the base of the drilled pile P02-04 obtaining force-displacement data. All applied forces were then divided by the penetrometer cross-section area to obtain applied stresses. Stress-displacements plots for the Pile02-04 were plotted individually to observe the criterion established for the material at the foundation base. Results obtained for Pile02-04 showed that all three penetrometers follow a similar trend. However, the nonuniform (i.e., not overlapping) plots behavior indicated that the foundation base was not completely flat. Furthermore, according to the plots, the average stress and displacement for the material at the foundation base were registered to be 35MPa (5.1ksi) and 7mm (0.28in). These values were within the establishes resistance and displacement for the competent material at the foundation base. Figure 5 illustrates the average stress-displacement plot for the runs at the base of pile P02-04. Note that FD1 plot is slightly passing the threshold limit of 8mm (0.32in) with a stress value of 24MPa (3.5ksi) and a maximum stress if 34MPa (5ksi). However, the other two plots are within the established threshold. Another important observation is the shape of the plots from the start or the test up to approximately 10MPa (1.45ksi) where a steady increasing slope is observed. Beyond this point, the plots start to have a more constant and gentler slope with increasing stress which

could be indicating an abrupt change of material property going from softer rock to more competent rock. However, a visual inspection using a down-hole camera showed no softer material accumulated nearby the penetrometers. Therefore, the existence of a softer rock versus a more competent rock is more likely to be the case.

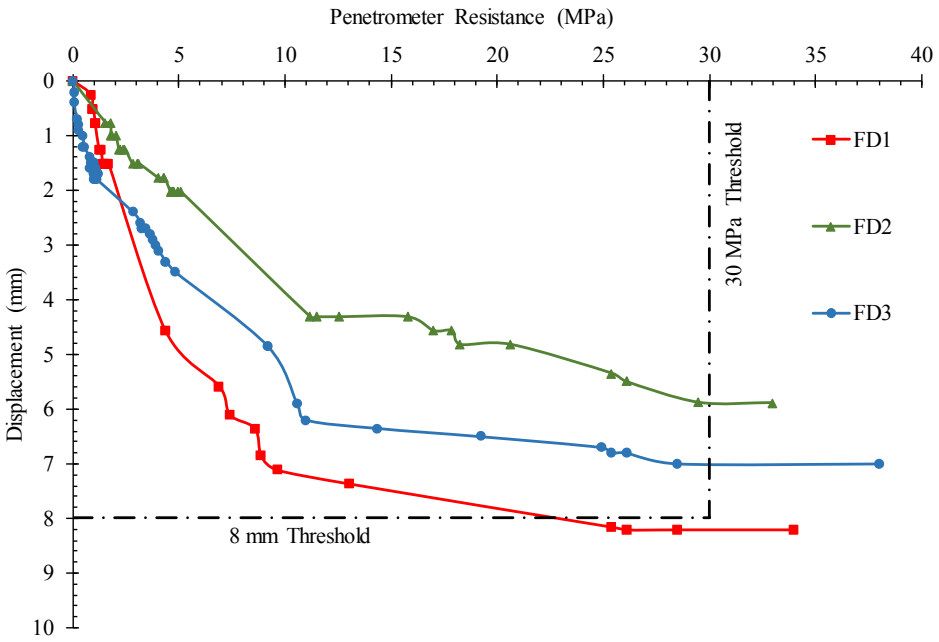


Figure 5. Average stress-displacement at the bottom of the Drilled Pile 02-04

Drilled Pile P02-05

A total of 13 runs were completed at the base of the drilled pile P02-05 and similar to the previous pile, stresses at the foundation base were determined by dividing measured forces by the penetrometers cross-section area. Stress-displacements plots were individually analyzed to observe the criterion established for the foundation base material. Results showed that all three penetrometers follow a similar trend, specially toward the end of the test. Similar to the previous test, a nonuniform foundation base material was detected since the plots are not overlapping. Considering each maximum stress registered by each penetrometer and their corresponding displacements, the average stress and displacement for the material encountered at the foundation base were registered to be 38MPa (5.5ksi) and 7.2mm (0.28in), respectively. These values were within the established resistance and displacement for the competent material at the foundation base. Figure 6 illustrates the average stress-displacement plot for the runs at the base of the pile P02-05. Note that FD2 trend is different compared to the other two plots (i.e., FD1, and FD3). The FD2 plot shows a linear behavior with a constant slope up to approximately 20MPa (2.9ksi) when the abrupt change of slope occurs. From this point forward, the plot turns to an almost zero slope

line with increasing stresses and very small change in the displacement. The other two plots on the other hand, follow the same shape and can be divided into three segments: (1) a steep slope from 0 to 1.7MPa (0.25ksi), (2) small slope between 1.7MPa(0.25ksi) and 29MPa (4.20ksi), and (3) zero slope line after 29MPa (4.20ksi). The first portion of these plots could correspond to a very soft material accumulated at the foundation base followed by a material with higher strength (e.g., weak or weathered rock). The third segment is where the abrupt change occurs similar to FD2 and plots corresponding to P02-04 indicating the existence of competent material or rock that meets the established criteria.

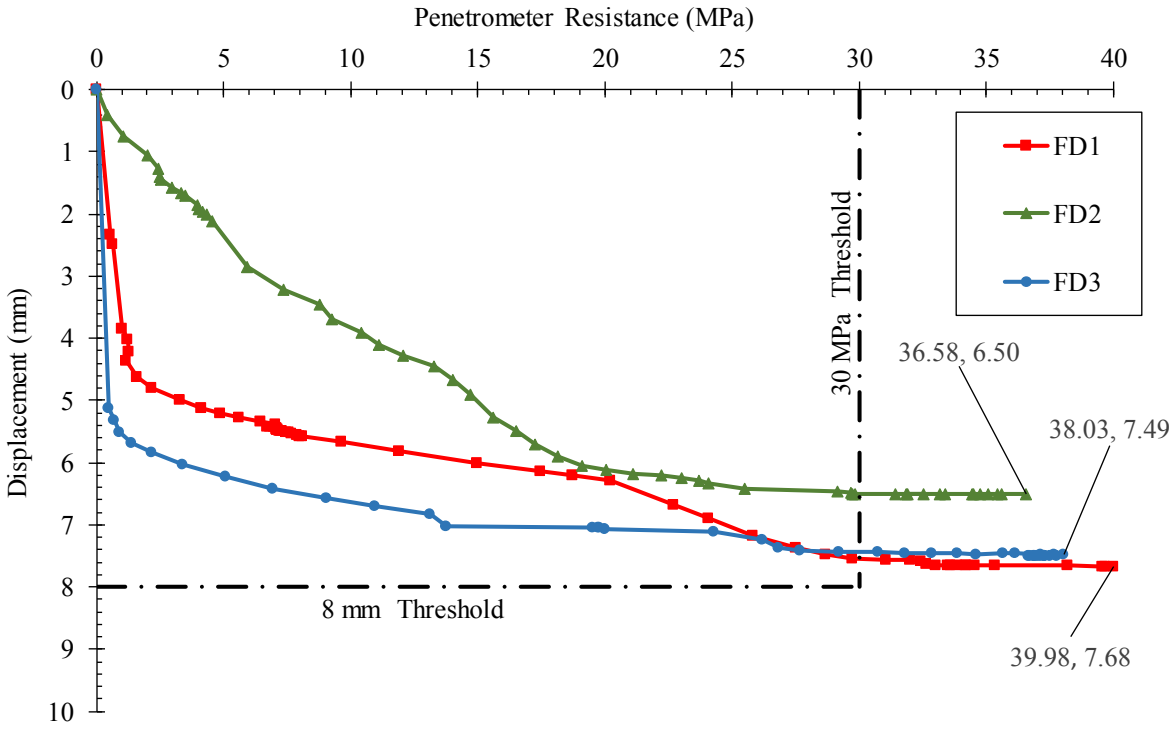


Figure 6. Average stress-displacement at the bottom of the Drilled Pile 02-05

SUMMARY AND CONCLUSIONS

This paper presented results from SQUID testing two 1016-mm (40-in) diameter open-end drilled piles installed for a vehicular bridge crossing the Seutelva River in Fredrikstad, Norway. These pipes were installed using a down the hole (DTH) hammer system which uses the rotary-percussion drilling method with a button bit and filled with concrete.

The foundation system for the project presented in this paper was designed as end-bearing only where all nominal loads are supported by the foundation's base. However, due to difficult subsurface conditions and the sloping rock, each drilled pile had to be installed at a different base

elevation. One of the foundation base material assessment criteria proposed by local authorities was to obtain the material strength and perform the assessment based on the applied stress and measured deformations. In order to obtain such data, the SQUID device and test was selected and completed for two piles identified as P02-04 and P02-05. Results from the SQUID testing showed an average displacement of 7mm (0.28in) corresponding to a 35MPa (5.1ksi) of stress level for P02-04, and 7.2mm (0.28in) corresponding to a stress level of 38MPa (5.5ksi).

The resistance to penetration determined from the SQUID testing is not a correlation to other strength properties defined for soil, intermediate geomaterials, or rock. Therefore, one of the limitations of the SQUID at this time is the lack of correlations with strength parameters determined from laboratory testing such as unconfined compression test. However, in circumstances where access to the pile base is limited and a sampling process is significantly impacting the construction schedule, results such as those obtained from the SQUID could be evaluated qualitatively and quantitatively assessed by qualified geotechnical engineer to further determine the suitability of the tested material.

REFERENCES

FLDOT (2016) *Standard Specifications for Road and Bridge Construction*. Florida Department of Transportation

NCDOT (2012) *Standard Specifications for Road and Structures,* North Carolina Department of Transportation

LARGE-SCALE EARTHQUAKE-INDUCED LANDSLIDE REPAIR FOLLOWING NEW ZEALAND'S KAIKOURA EARTHQUAKES

Mathew Avery, Project Development Engineer, Hiway Geostabilization Ltd., 10 Ingot Place, Silverdale, Auckland NZ, +64-27-552-8306, mat@hgs.nz
Colby Barrett, CEO, GeoStabilization International, 4475 E. 74th Ave., Suite 100, Commerce City, CO USA, +1-303-909-6083, colby@gsi.us

ABSTRACT

In November 2016, a 7.8-magnitude earthquake caused more than 100,000 cubic meters of rock and debris to tumble down and bury the transportation infrastructure below Ohau Point in New Zealand. All routes between the northern and southern portions of South Island were severed. To undertake the rebuilding efforts, the New Zealand government established North Canterbury Transport Infrastructure Recovery (NCTIR) – an alliance to repair the road and rail networks between Picton and Christchurch. NCTIR's aim was to have the road open by Christmas 2017, but work also continued into 2018 to complete a number of safety improvements along the highway. The presentation will review the initial remediation attempts, the necessity to re-evaluate the original efforts, the need to incorporate techniques that were "outside-the-box" and different from traditional methods, and the logistics and planning that were required to complete the work safely.

Keywords: Earthquakes, Landslide Repair, New Zealand, Logistics

INTRODUCTION

Shortly after midnight on Monday 14th November, a magnitude 7.8 earthquake struck the small South Island settlement of Waiau in North Canterbury, 100km north of Christchurch. The quake was the largest in New Zealand since the magnitude 7.8 Dusky Sound earthquake in 2009 (GNS 2016). While shaking was widespread with over 15,000 recorded 'felt reports,' the worst shaking occurred about 50 seconds after the quake rupturing started. The energy of the tremor progressed north over several minutes with surface rupture recorded on a total of 21 faults. The length of all the fault ruptures combined was close to 100km (GNS 2016).

The degree of ground shaking was high, recorded as Modified Mercalli Intensity Scale (MMI) Level 8 – Severe. This level of shaking causes considerable damage in ordinary buildings with partial collapse including fall of chimneys, factory stacks, columns, monuments, walls, etc. At a human level, people experience difficulty standing; while furniture and appliances shift. Geologically, the damage depends on the geological setting. In Kaikoura and the surrounding area, especially the coastal highway State Highway 1, north and south of the town, many of the slopes consist of over steepened weathered, fractured greywacke. During the quake, the shaking caused significant and widespread damage with a total of 26 major slips (and many smaller slips); closing both State Highway 1 and the Main North Rail Line between Picton and Christchurch.

The earthquake most severely impacted the coastal road and rail which hugs the coastline along a stretch of some 20 km north and south of the coastal tourist town of Kaikoura. These links serve as the South Island's primary rail and state highway routes. The transport corridor follows the coastal alignment and is situated on a very narrow bench at sea level. The coastal mountain range rises from sea level up to some 500 meters of elevation. The earthquake triggered a significant series of rock slides in the region with some 40 major slides reportedly dislodging some 750,000

© 2018 Deep Foundations Institute

m^3 of rock and soil debris, some of which buried many sections of the transport corridor. The town of Kaikoura was completely isolated for over a month until access south was re-established via an alternative inland route. During November and December, the initial recovery effort involved helicopter support to service Kaikoura and this effort was primarily supported by the coincidental presence of an international Navy operation which provided airlift and marine support from USA, Canada, Australia, and New Zealand.

The highway and rail north arteries were closed for 12 months and a reconstruction team, North Canterbury Transport Infrastructure Recovery (NCTIR), was quickly established as a government led alliance, tasked with the rebuild. A deadline of 12 months was established to have the full length of the alignment (southern and northern road and rail corridor) opened by Christmas 2017. The monumental task of the design-build recovery at an initial value of $1.5 billion and a workforce of up to 3000 personnel began in earnest in January 2017.

INITIAL REMEDIATION ATTEMPTS

Immediately following the earthquake, it was imperative to get an understanding of the situation; what damage had occurred to what infrastructure. Representatives from the two main transport networks, New Zealand Transport Agency (NZTA) (road) and KiwiRail (rail), and their respective engineers inspected the main routes by helicopter. At the same time, geologists and earthquake specialists from the Institute of Geological and Nuclear Sciences (GNS) and around the world were undertaking more specific scientific inspections. It soon became very apparent that the severity of this quake was far worse than initially thought, and the damage to infrastructure was significant.

Geotechnical engineers identified over 85 slope failures affecting the road alone, while GNS scientists reported 21 faults (later expanded to nearly 30 separate fault surface ruptures). The slope failures affecting the road were categorized into primary, secondary and tertiary failures depending on the level of effect to the road. Primary failures, over 40 in total, were those directly affecting the highway, i.e., presenting an immediate hazard such as debris on the highway, or debris subject to imminent failure. Secondary and tertiary failures would likely affect the highway at some point (following future trigger events) but weren't immediately of concern.

Engineers quickly determined that treatment of the failed primary slopes was going to be non-conventional. The slopes were surrounded by inaccessible terrain and too steep to allow treatment using excavators and bulldozers, as would normally be used in such circumstances. The slopes were also too active, and the area was at high risk of further ground shaking events through the expected typical aftershock sequences.

Heli-sluicing was quickly identified as the most appropriate primary means of treating the slopes while the ground shaking activity subsided; this would also allow time to consider more direct, permanent treatment options. Heli-sluicing involves the use of helicopters fitted with firefighting 'monsoon' buckets dropping around 1000 liters of water at a time directly onto the slope. In the case of Kaikoura, the buckets were filled from the ocean and water washed onto the slopes in a targeted manner. Geotechnical engineers monitored the sluicing operations directing the helicopter pilots to target areas.

At the peak of operations, thirteen helicopters were in use, and in some cases, up to seven machines focused on single areas. This repeated washing of the slopes released significant volumes of material. While not as effective as manual/mechanical scaling, sluice cannon, or blasting activities, in the area near Kaikoura heli-sluicing was deemed the only suitable (safe) option in the short term. Adding to reduced effectiveness was the fact that the slopes were dry with very little



Figure 1: Kaikoura heli-sluicing operations - www.matthayes.co.nz

rainfall in the weeks preceding the earthquake (heli-sluicing is most effective on already saturated slopes where even small volumes of additional water can mobilize, or keep mobilized, saturated soils). The total volume of water used in the heli-sluicing operations exceeded 152 Million litres (the equivalent of over 60 Olympic-sized swimming pools) which had a profound effect on the slopes.

Sluice cannons were proposed initially but considered by NCTIR to be too ineffective and the decision was made to use helicopters. The benefit of using cannons is the delivery of high pressure and high volume. Heli-sluicing provides high volume, but only low-pressure water delivery. To improve the effectiveness of the helicopter operations, some operators, especially those from the Central Otago region of the South Island where heli-sluicing is quite common, used modified buckets with a funnel at the outlet to concentrate the flow of water and increase the delivery pressure.

After some weeks of heli-sluicing, several of the sites were able to be treated through more traditional manual scaling operations using geotechnical rope access techniques. The slopes were treated from the top down with scaling work focused on the head scarp area of the failures. This was to reduce the risk to the geotechnical rope access technicians by limiting their exposure to rockfall further down the slopes, while still managing to create safer work areas at the base of the slopes for protected machinery to operate.

Extensive manual scaling and blasting began in earnest initially in the southern zone (the area of State Highway 1 south of Kaikoura) where NCTIR saw an opportunity to reopen this section of

the road before Christmas 2016. Rope access technicians were flown to the top of the slips and began clearing all large debris from the top down. Blasting was common on hard-to-move blocks, but high-capacity airbags were more commonly used as a fast and highly effective way to dislodge blocks weighing more than 20 tonnes.

Shortly prior to Christmas 2016 the first heavy machinery was used to clear slip material from the road. The initial efforts used remote-controlled excavators, which were originally developed following the 2011 Christchurch earthquakes. This technique provided heavy machinery access into areas where ongoing rockfall presented too high a risk for human-operated machines, even with the most heavily armoured equipment. These efforts, clearing hundreds of thousands of cubic meters of slip material from the road, led to the southern zone reopening for the busy Christmas holiday traffic. Traffic resumption allowed a degree of normality to return to Kaikoura and boosted the local economy which is heavily dependent upon tourism.

Heli-sluicing continued at various locations around Kaikoura through May 2017 with an estimated cost of USD 1.2M per week. Manual scaling activity reduced during September and October 2017 with no further large-scale work undertaken by Christmas of that year. Earthworks were all but complete by Christmas 2017.

REEVALUATING THE ORIGINAL EFFORTS

Following Christmas of 2016, the focus moved onto designing and constructing more permanent stabilization solutions, as well as focusing on reopening the road in the northern zone (SH1 north of Kaikoura). The first durable design, for Slip 6 North Ohau Point, was released to invited tenderers in February 2017. This site was identified as the largest, most hazardous site on the network, and a potential choke point for rebuilding the road north of Kaikoura; due to its sheer size, the significant area requiring treatment, and the high degree of exposure from out-sized rockfall.



Figure 3: Ohau Point, December 2016 (photo courtesy Opus)

Hiway Geostabilization (HGS), a joint venture between Geostabilization International and the Hiway Group from New Zealand, were the successful tender winners with work starting mid-March of 2017. The solution for this slope was typical for almost all the remainder of slope treatments throughout the Kaikoura region and included pattern bolting and meshing of affected areas. Due to durability requirements, most of the slopes, including Ohau Point, were treated with a high-tensile, diamond shaped, steel wire mesh of woven construction incorporating a protective coating well-suited for coastal environments.

Completion of the installation at Ohau Point would allow safe access to the lower reaches of the slope that required additional remedial work, as well as significant debris clearance on the highway platform below. Before the meshes' and anchors' installation, significant manual scaling was needed to prepare the slopes and make them safe for access. Again, this was typical of all sites in the rebuild. The total area of treatment on the upper slope at Ohau Point was in the order of 5,600 m^2. The lower face, requiring manual scaling and localized rock bolting, had an area of around 12,500 m^2. The total area of slopes on the NCTIR network treated with this same or similar solution exceeded 50,000 m^2.

For Ohau Point, HGS proposed the use of low carbon, low phosphorous steel hollow bar product as an alternative to the proposed standard galvanized steel hollow bar. The reduced carbon content bar improves both the durability and ductility of the steel, which is critical in a coastal, high seismic environment.

Other sites throughout the rebuild involved very similar designs with local variations in dowel/nail depth and spacing. High angle, high risk, unstable slopes were predominantly treated with dowels/nails and high-tensile steel wire mesh while low angle, lower risk sites used dowels/nails and mild steel wire double twist mesh. Only a few sites were treated with dowels alone and several sites were treated with various draped mesh solutions.

In addition to the slope treatments, extensive rockfall and debris flow barrier installations were completed in the south with several long, moderate capacity (2000 to 3000 kJ) systems planned for construction in the north zone during 2018. The majority of the systems have been installed at or slightly above road level which reduced installation time and costs. In areas where space was available, rockfall and debris flow bunds were constructed. All these systems have already been proven effective with several requiring emptying and repair following recent (early 2018) rainfall-triggered slope failures. At these specific sites, no material reached the highway.



Figure 4: Rockfall barrier adjacent Raramai Tunnels



Figure 5: Rockfall/debris flow bund

THINKING OUTSIDE THE BOX

Several sites were remediated with unique solutions considered outside-the-box compared to more traditional slope remediation techniques. One of these is Site 14 South where treatment of the source area was deemed not to be cost-effective. A bespoke rockfall attenuator was designed for the site in combination with the early massive scaling and heli-sluicing operations. A sluice cannon was also used at this site, with great effect, to remove more unstable surficial material.

The installed rockfall attenuator is a modification of a traditional rockfall barrier that incorporates top and bottom support ropes connected to wire rope anchors installed in line with the barrier's posts. The attentuator is the same in regards to posts, base plates, and upslope anchors, but varies with a reduced number of lateral wire ropes (no bottom rope is used). The ring net and secondary mesh of the main system are not attached at the bottom and are left to hang down the slope beyond the base of the normal rockfall barrier structure. This provides similar energy absorbing capacity of the original barrier, but allows the captured material to continue downslope to an area where it can be easily removed. These systems are ideal for sites where a high volume of material is expected to impact the system, or where access for future cleaning and maintenance is difficult.

This is the second installation of these high energy attenuators in New Zealand with similar versions (two (2) 3000 kJ and one (1) 5000 kJ) installed on SH6 at Diana Falls (Haast Pass) following a significant landslide event in 2013. While these systems have required ongoing maintenance due to a very high energy environment, the road has not yet been affected by rockfall since the installation was completed.

Ohau Point was another site where non-traditional solutions were employed. During the early stages of the rebuilding process, the New Zealand Government pledged that up to NZ $2B would be spent to open this vital road and rail link. In addition to this funding pledge, the government pledged that the road would be open by December 15, 2017. The original programme for Ohau Point allowed for approximately three months of construction time including manual scaling, pattern bolting, and mesh installation. Understandably, the client required access to the road and beach platform below in the shortest timeframe possible to enable construction of a new seawall and highway.



Figure 6: Installing the drape on Ohau Point

Along with this increased pressure from the government and the people of New Zealand, significant weather delays, unfavourable winter conditions, and challenging & dangerous ground conditions were causing delays in completing the original design work. To accelerate access below Ohau Point, NCTIR requested HGS provide an alternative methodology/solution.

Some options to accelerate the programme for the original solution were proposed; however, after lengthy consideration, all were deemed to be unsuitable for various (mainly safety-related) reasons. HGS then started to think outside-the-box and suggested some alternative solutions including a polypropylene fiber-reinforced Gunite treatment of the entire slope.

After careful consideration including material availability and project schedule, the client accepted a ring net drape option to be installed as an addition to the existing permanent pinned mesh solution. Sequencing involved installing the drape system immediately and, in its entirety, with tensioned wire ropes across the bottom of the drape creating a closed system allowing access to the beach platform below, with the pinned mesh solution constructed later. The drape design included perimeter anchors connected with wire rope, a primary ring net drape over the full 5,600

m^2, followed by a secondary high-tensile mesh drape over the top of the ring net. Lastly, wire ropes were installed across the base of the system and tensioned.

Differences between a pinned mesh and drape system include:

- A drape's mesh is attached to a top support rope secured to anchors along the top of the slope. Any rockfall energy is contained by the fabric and individual rocks are allowed to travel down the length of the drape; the rocks come to rest along the bottom of the slope.
- A pinned mesh system incorporates rock bolts drilled into the slope in a regular pattern with the mesh bolted securely to rockface to capture any rock material and keeping it from falling off the slope.

While in many situations the original high-tensile mesh could be installed to act as a drape and no further work would be required, the large size of potential rock failures behind the mesh at Ohau would have risked compromising a high-tensile system. The ring net was chosen to protect against more significant potential failures, with the high-tensile secondary mesh installed to contain the smaller material. A 6-on-1 ring net was chosen as it maintains its width when lifted (i.e., doesn't choke in the middle) – which is critical when installation is conducted via helicopter. The ring net was installed first as it conforms to the slope better than the high-tensile mesh. At the completion of the drape, the pattern bolts of the original design were installed directly through the drape with all components (ring net and high-tensile mesh) which completed the permanent system.

LOGISTICS & PLANNING

Undertaking construction work of this nature is challenging at the best of times, even when resources, services, and transport options are abundant. Add to the mix the remoteness of the Kaikoura area, combined with severely restricted services following a major earthquake (including limited transport routes and essential emergency services), and it is easy to imagine the significant logistical exercise these projects became.

Planning for replenishment of materials and consumables required careful consideration of numerous factors, none the least the weather. With construction continuing through the winter, an average week saw the loss of 2-3 work days. The steepness of the terrain in the region means that the majority of the slip sites have only helicopter access to and from the work site. This predestined air delivery of all staff, materials, tools, plant & equipment, and regular replenishing of consumables (such as water and fuel for grouting operations) - a very laborious effort.

While helicopters are great tools in the geotechnical construction industry, they have considerable downsides. They are highly dependent on weather, and the Kaikoura region is subject to regular low sea fog which inundates the coastal cliffs; as well as strong coastal winds. For safety reasons, work around Kaikoura was cancelled for the day if either of those conditions set in since the only emergency rescue option available is via helicopter and being left stranded on the top of the site overnight is not very appealing, nor safe, for geotechnical rope access workers.

With such irregular and uncontrollable delays inflicted on the construction programme, daily and weekly planning takes considerable time and effort. Coordination with local and national providers is essential. Even with the significant improvements to the slip sites, the road south of Kaikoura was regularly closed due to fresh activation of slips. This led to considerable delivery delays and local providers had only limited stock that needed to be continuously replenished.

For the redesign of Ohau Point, considerable challenges needed to be overcome. The design (by HGS) and review process were completed within one week, and perimeter anchor installation began immediately following. Sourcing of the 6-on-1 ring net resulted in a worldwide search, and eventually, the global supply was exhausted. Suppliers were found in North America and Western Europe, and due to the significant pressure from the government, the ring net was flown into New Zealand on specially chartered aircraft. The ring net installation began three weeks after the start of the perimeter anchor installation.

Further logistical issues arose with New Zealand's supply of shackles, required to connect the ring nets, being exhausted before even the first order was completed. The remainder of the product came from as far away as Europe as Australian suppliers scrambled to maintain stock. This replenishment in itself became a daily struggle, balancing daily quantities of ring net installation with urgent courier deliveries of bags of shackles.

While Ohau Point had significant challenges, these were combined with logistical problems from 40 other rockfall construction projects, over 60 km of road reconstruction, over 1 million cubic meters of earthworks, and rebuilding of 100 km of rail including collapsed bridges and damaged tunnels.

SUMMARY

The rebuild of the road and rail networks damaged after the Kaikoura earthquakes has been the largest such undertaking ever in the history of New Zealand. With four of the largest contracting firms in the country combining their resources to form the NCTIR alliance, and a plethora of sub-contractors ranging from bridge experts to rockfall specialists, at times up to 3000 workers have been involved in the rebuild.

Remedial measures have at times been somewhat rudimentary and at others entirely left field from more traditional solutions. During the initial response, many decisions were made on the fly in order to simply make the area safe for restricted access, and while longer term, permanent solutions were being designed. Add to this the political pressures requiring significant design changes only further complicated the already incredibly challenging task of working in this environment.

While work will be ongoing through 2018 and beyond, the target to get the road open on December 15th, 2017 was achieved to the relief of the nation.

Major project milestones:

- 19th November 2016 - Inland Road into Kaikoura open, 5 days after quake
- 12th December 2016 - SH1 south into Kaikoura open (restricted)
- 9th June 2017 - First rail into Kaikoura (from south)
- 8th September 2017 - SH1 north into Kaikoura, safe route under Ohau Point established

- 15th September 2017 - Rail open north and south of Kaikoura. The first train to pass through Kaikoura since the November earthquake.
- 15th December 2017 - SH1 Road Open. One year, one month, one day following the earthquake.

ACKNOWLEDGEMENTS

Matt Hayes Photography - www.matthayes.co.nz, for the use of photos.
NCTIR for access to work sites throughout the rebuild zones.
South Pacific Helicopters for ongoing helicopter support.

REFERENCES

GNS Science, 2016. M7.8 Kaikoura quake the biggest since the Dusky Sound jolt in 2009 - 15/11/2016, *GNS media release*, 14/11/2016 7:49am

WSDOT, 2009. Use of Ring Nets for Slope Protection for Rockfall: End-of-Construction Report. Experimental Feature Study, Geotechnical Report C-7540, SR 28, Rock Island – Rock Slope Nettings.

NCTIR, 2017. SH1- Ohau Point, the last slip in the red zone. September-November 2017 - milestones achieved. *NCTIR Newsletter, online release.*

LATERAL FORCES ON PILE DUE TO SOIL SLOPE CREEP

David E. Albus, GE[1], Bidjan Ghahreman, GE, Ph.D[2]

A single-family home constructed on the side of a slope in Los Angeles, CA, was subjected to lateral forces due to soil slope creep on the pile foundation supporting the home. Impacts to the property included cracking and separations in the street, retaining walls, exterior concrete flatwork, and decorative concrete features in the rear yard area. The home was supported by concrete piles that penetrated the surficial soil mantle and were embedded in underlying bedrock. However, the home exhibited minor distress that suggested even the home was being affected by soil creep.

Selected points on the home were monitored with an optical survey method and manometer over a period of two years to assess if the home was undergoing vertical or lateral movement. Monitoring data indicated the home was in fact moving down slope in a manner consistent with slope creep. As a result, the authors were concerned that continued movement due to slope creep could result in over-stressing of the piles that support the home and ultimately lead to failure of the foundation system. An evaluation was then undertaken to evaluate the behavior of the foundation system due to forces from slope creep.

Research was performed during the course of evaluating the conditions to consider various approaches to modeling pile behavior of the piles supporting the home. Some research has been performed to field measure creep displacement of soils and rock in slopes. These previous works have found a diverse behavior of the soil displacement with depth (velocity profile) indicating the process is very complex. An example of various velocity profiles measured in field experiments is depicted in Figure 1. Other research focused on theoretical models of velocity profiles and exhibited similarities to some of the field measured cases.

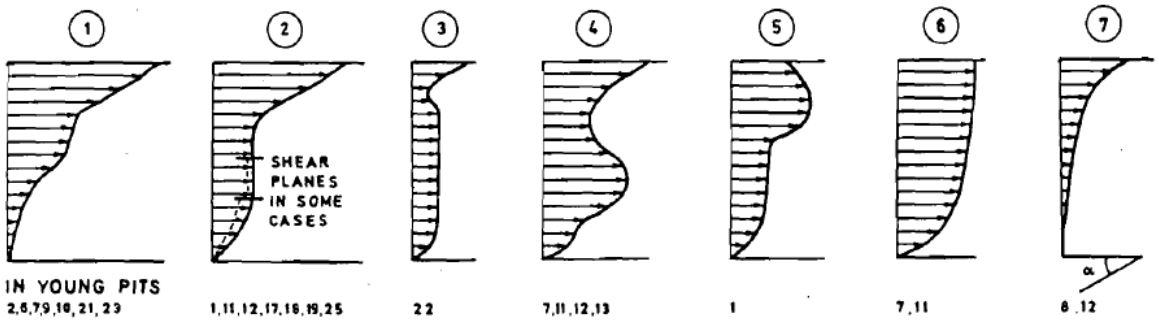


Figure 1- Groups of Velocity Profiles- From Moeyerson (1988)

There is also significant research on the forces imparted upon a pile due to lateral movement of soil surrounding a pile primarily due to lateral spreading, mass sliding upon a discrete plane, and lateral forces from a nearby embankment. However, there appears to be limited research into the evaluation of forces imparted on a pile due specifically to soil slope creep. Previous work has not provided a clear

[1] Geotechnical Engineer, Albus-Keefe & Associates, Inc,. Anaheim, CA, US, dalbus@albus-keefe.net
[2] Geotechnical Engineer, Albus-Keefe & Associates, Inc., Anaheim, CA, US, bghahreman@albus-keefe.net,

© 2018 Deep Foundations Institute

methodology for establishing an appropriate velocity profile for a particular site condition and thus, a model for evaluating the distribution of lateral forces upon a pile subjected to lateral soil slope creep.

To access the potential forces on a pile subjected to lateral soil slope creep, the authors performed three-dimensional analyses using the computer program "Group." Soil parameters where established from site investigation and laboratory testing of soil samples. Various velocity profiles indicated by previous field studies were considered in the model. The authors found that a simple linear distribution of velocity that had a maximum at the surface then decreased with depth provided a good match to the actual behavior of the piles based on field measurements of movement in the home.

Monitoring indicated the creeping soils were advancing laterally at a rate of about ½ in/yr. at the ground surface in a north-northeast direction with the easterly component representing 0.16 in/yr. Over the time frame prior to monitoring, soils are estimated to have moved horizontally about 1.6 inches at the ground surface in an easterly direction. Over the next 2 years of monitoring, the soils moved an additional 0.32 inches for a total of 1.9 inches. From our analyses, we obtain a pile head rotation of 0.10 degrees from a change in displacement of 1.6 inches to 1.9 inches. Optical monitoring of the home indicated a horizontal movement in the easterly direction of 0.04 feet (0.48 inches) at a vertical distance of about 23 feet above the pile grade beam. This movement translates to an angular rotation of 0.10 degrees in the pile head. Manometer data indicated the floor along the northerly wall of the home experienced an additional vertical differential movement of 1/8 inch within a span of 6 feet during a similar span of time. This movement translates to an angular rotation in the east to west direction of 0.10 degrees. As can be seen, the estimated rotation of the pile foundation from the GROUP analysis matched very well with two different types of measurements of movement in the structure.

Assuming the rate of creep was constant over the period of 12 years and a total soil displacement of 1.9 inches did occur, the estimated maximum moment induced into the pile located at the northeast corner of the structure is estimated to be approximately 210 ft-kips. Assuming the concrete has only a compressive strength of 2,500 psi, we estimated the ultimate moment capacity of the pile would only be approximately 185 ft-kips, a value less than the estimated induced moment. However, the concrete is likely significantly stronger due to age effects and the concrete also likely had a higher 28-day strength than the assumed value. The authors concluded the pile foundation is likely loaded to very near the ultimate capacity.

While studies have demonstrated the wide variety of velocity (soil displacement) profiles in creeping slopes, our work indicates that a reasonable estimate of lateral forces on piles due to soil slope creep can be made assuming a linearly-varying displacement profile with a maximum occurring at the ground surface and diminishing to zero at the assumed depth of creep. The response of a pile subjected to slope creep can be modeled using commercially available computer programs such as Lpile or GROUP. From our own analyses using GROUP and P-y curves typically used for the types of materials present, we found that moment in the pile was reaching a maximum when soil displacement reached about 10% of the pile diameter. This result is consistent with work by Chen & Poulos (1997) and we therefore suggest that maximum moments and shears in the piles should not exceed the values obtained at a soil displacement of about 10% of the pile diameter.

SUPPORTED EXCAVATION MOVEMENT CAUSING LATERAL DISPLACEMENT AND CRACKS IN DRILLED SHAFTS - LESSONS LEARNED FROM A CASE STUDY IN CHICAGO

Amaneh E. Kenarsari, Ph.D., Project Engineer, M. ASCE, ECS Midwest, LLC, Chicago, IL, 847.777.0371, AKenarsari@ecslimited.com

Eric R. Borys, P.E., Senior Project Engineer, M. ASCE, ECS Midwest, LLC, Chicago, IL, 847.777.0340, EBorys@ecslimited.com

Brett Gitskin, P.E., Senior Principal Engineer, M. ASCE, ECS Midwest, LLC, Chicago, IL, 847.777.0342, BGitskin@ecslimited.com

ABSTRACT

This case study discusses impacts of excessive Earth Retention System (ERS) lateral movement at a project in city of Chicago. The ERS (cantilevered sheeting) moved inward towards the excavation and caused lateral displacement and cracks in six drilled shafts located about 1 to 2 lateral feet (0.3 to 0.6 m) from the face of the sheet pile wall. Up to 9 inches (23 cm) of horizontal movement was observed on top of the supporting sheet-pile. Similarly, survey measurements showed the top of the drilled shafts moved laterally up to 8 inches (20.3 cm). To evaluate the cause of failure and determine a remediation solution, the soil, shaft and site conditions were investigated. Pile Integrity Tests (PIT) were conducted at the affected drilled shafts. The shafts with identified anomalies were cored and video-recorded. The cause of the failure was determined to be related to variable soil conditions across the site, deeper excavation (i.e., increased effective ERS wall height), and other differences between design and as-built conditions. Internal bracing, in the form of walers and rakers, was installed to limit further movement of the sheet pile as a short-term solution, with additional grade beams framed into the basement slab-on-grade as a long-term solution. Five of the six cracked shafts were spliced with reinforcing bars and high strength grout and one shaft was replaced.

KEYWORDS: Case Study, Lateral Movement, Supported Earth Retention System, Drilled Shaft Cracks, Remediation

INTRODUCTION

The subsoil in the Chicago Area mostly consists of glacial till clays underlain by water-bearing granular soil over bedrock. The glacial clays have very soft to medium consistencies for a typical thickness of 30 to 50 feet (9.1 to 15.2 m) below which hard clays (Hardpan, i.e., heavily over-consolidated clay soils) are encountered. The soft clays are often referred to as the "Chicago Blue Clay". Beach Sands are also found above upper soft clays in several areas, especially within a three-mile strip near Lake Michigan (Peck and Reed 1954). Due to the existence of soft clay in Chicago area, supporting the mid to high rise buildings on drilled shafts extended to Hardpan is a common practice in modern building design.

In the early 19th century it used to take about 3 weeks to excavate 1 shaft hole and about 1½ days to fill the shaft with concrete in Chicago (Manierre 1916). The early 19th century methodology of excavating a shaft consisted of hand digging the shaft, installing wood lagging as temporary shoring with spoils removed with a rope and pulley system from the surface. Today, the excavation of a typical drilled shaft in Chicago uses heavy drilling equipment and requires much less time for excavation and concrete placement. It is not uncommon for contractors to excavate shafts and place concrete at a rate of about 2 to 5 drilled shafts per day (with one drill rig).

This paper examines a case study near downtown Chicago where lateral movement of an Earth Retention System (ERS) caused cracks in recently placed drilled shafts. Our case first studies the as-built

© 2018 Deep Foundations Institute

construction condition to identify the nature and extent of the affected drilled shafts due to the ERS movement. Next, the soil properties, design parameters and as-built conditions are revisited to identify the possible causes of the ERS movement. Finally, the lessons learned from this case study are discussed.

PROJECT DESCRIPTION

The project site is located in the City of Chicago. The neighborhood was historically an industrial community with limited commercial or residential development. Today, the neighborhood is redefining itself with an abundance of new commercial and residential structures. The proposed project was a 7-story hotel building, with roof amenity level and a basement level for parking. The typical maximum column loads were anticipated to be around 1,000 kips (4,448 kN) with some perimeter columns loads in the range of 200 kips (890 kN). The design team planned to support the columns on straight or belled drilled shafts extending to about 85 feet (26 m) below grade, bearing on Chicago Hardpan, with a design bearing pressure of 35 ksf (1,676 kPa).

The drilled shaft diameters ranged from 3 to 3½ feet (about 1 m) in diameter with bell diameters ranging from 4 to 8 feet (1.2 to 2.4 m) in diameter. The drilled shafts were typically 70 to 72 feet (21.3 to 22 m) long, concrete was placed in the dry. The shaft reinforcement was extended to a depth of about 10 feet (3 m) below the top of shafts as most shafts transmitted only axial loads. A total of 73 drilled shafts with general spacing of about 20 to 25 feet (6 to 7.6 m) grid pattern were placed across the building pad. The drilled shafts were installed from the original site grades. The top of each drilled shaft location was surveyed the day of construction. An excavation to a depth of about 16 feet (4.8 m) below existing site grade was required for the basement level.

To accommodate the below grade excavation, continuous, cantilevered CSZ 14 sheet piles were utilized as the ERS. The ERS system was designed to retain a total of up to about 16 feet (5 m) of soil. The upper 6½ feet +/- (2 m) was back sloped and the remaining 9½ feet +/- (3 m) was supported as a cantilevered sheet pile section. In the southeast corner of the ERS system, walers and corner braces were also incorporated to help support the adjacent, existing building surcharge loading (east of the southeast corner). The sheeting was driven after the drilled shafts were installed. The typical design penetration of the ERS sheet pile walls was to a depth of 30 feet (9 m), or about 15 to 16 feet (4.6 to 5 m) below the bottom of the basement excavation. Figure 1 shows the project site temporary excavation (after the movement). The boundary of the project site is shown with a red line.

ERS MOVEMENT OBSERVATIONS

Upon installation of the continuous sheet pile ERS system and initial basement excavations, no unusual movement of the ERS system was initially realized. However, about one month after the ERS system was constructed, lateral movement was realized along the southern portion of the east wall of the sheet pile ERS. The ERS (cantilevered sheeting) moved inward towards the excavation and caused lateral displacement and cracks in six drilled shafts, these 6 shafts were originally placed 1 to 2 lateral feet (0.3 to 0.6 m) from the face of the sheet pile wall. The yellow outline in Figure 1 shows the approximate extent of the affected drilled shafts.

The movement was confirmed when subsequent surveys were performed at the top of each drilled shaft location. Survey readings compared with the initial survey indicated lateral movement at the top of the drilled shafts up to 8 inches (20.3 cm). The drilled shaft movement was in the western direction. The top of the sheet pile also moved west toward the basement excavation.

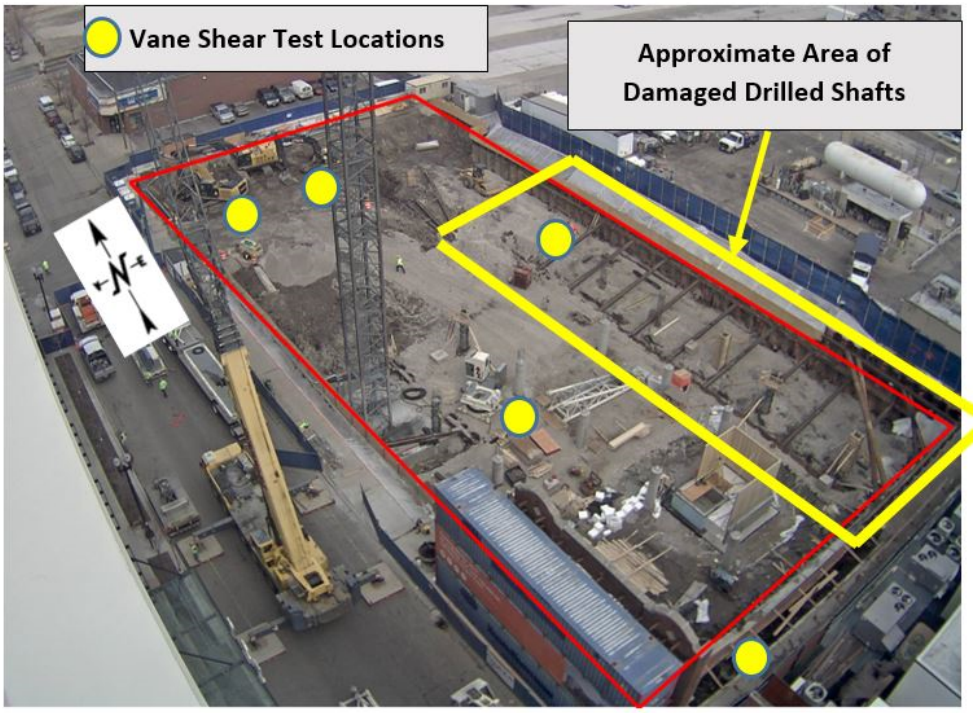


Figure 1: The project site temporary excavation battered rakers along east face of sheet pile wall added after movement was observed

Table 1 shows the survey of the top of the center-line of effected drilled shafts before and after movement. This table details relative displacement of the top of the drilled shafts compared to design 0N – 0E in cardinal directions.

Table 1: Survey of top centerline of the drilled shaft, the movements from the original placement on January 28 to March 14th, 2016

Drilled Shaft No.	Drilled Shaft as-built, as of		Movement, inch	Movement, cm
	1/28/2016	03/14/2016	01/28/2016-03/14/2016	01/28/2016-03/14/2016
	Top Centerline, inch	Top Centerline, inch		
1	0N-0 E	2⅜S-1 W	2⅜S-1W	7.3 S-2.54 W
2	0N-0 E	2⅜S-1⅜ W	2⅜S-1⅜W	6.0 S-3.5 W
3	0N-0 E	1⅜S-⅝W	1⅜S-⅝W	4.8 S-1.6 W
4	0N-1 E	⅞S-¼E	⅞S-¾W	2.2 S-1.9 W
5	1S-0 E	1⅜S-1½W	⅜S-1½W	1 S- 3.8 W
6	0N-0 E	⅜S-5⅞W	⅜S-5⅞W	1 S-14.9 W
7	0N-0 E	1S-5⅜"W	1S-5⅜W	2.54 S- 13.7 W
8	0N-0 E	1½S-7⅜W	1½S-7⅜W	3.8 S-18.7 W
9	0N-2W	1⅛S-6⅝W	1⅛S-4⅝W	2.9 S- 11.7 W
10	0N-0 E	1½N-3⅝W	1½N-3⅝W	3.8 N- 9.2 W

IDENTIFYING DAMAGED DRILLED SHAFTS

Pile Integrity Tests

To evaluate the shafts, low strain Pile Integrity Testing (PIT) was performed on 9 drilled shafts along the eastern column line in general conformance with ASTM D5882 (2016). The low-strain dynamic test involves inducing a stress wave in the foundation by tapping the accessible top of the foundation with a small hammer and recording the ensuing top motion. Records of several hammer impacts are averaged, filtered and exponentially amplified to enhance recorded features. One accelerometer was attached to the prepared drilled shaft top and the top of the drilled shaft was struck with a hand held hammer. The stress waves created from the hammer strikes were recorded. A stress wave generated by a hammer impact in a uniform rod is reflected if the wave encounters a change in shaft impedance, i.e., EA/c. A structurally intact drilled shaft is indicated by a) reflections from the toe of the drilled shaft, b) only relatively minor variations of the record amplitudes between impact (labeled top in the velocity records) and toe reflection. A region of impedance reduction exhibits a positive reflection and high soil resistance along the shaft or under the toe would cause negative reflections.

Figure 2 shows some of the PIT results recorded at testing drilled shafts along the eastern column line. As this figure shows, strong toe reflections were indicated in the velocity records at or near the installed drilled shaft length for unaffected, intact drilled shafts (e.g., drilled shafts 3, 4). However, the velocity records for drilled shafts 5, 6, 7, 8 and 9 indicated premature reflections well above the bottom of the drilled shaft. The reflections recorded for the drilled shafts are pronounced, with no or only minor amplification of the rests records.

From the PIT, strong premature reflections were noticed at about 19 to 21 feet (5.8 to 6.4 m) below the top of the drilled shaft which indicated installation condition or post-construction performance concerns. The questionable drilled shafts were cored and video recording was also conducted.

Coring and Photograph/Video Recording of Drilled Shafts

Drilled shaft cores and down-hole video observations were performed to evaluate the depth and nature of the premature reflection identified by the PIT. Coring was performed through the affected drilled shafts, with an offset of approximately 8 inches (20.3 cm) from the center of the drilled shafts and was advanced to an approximate depth of 32 feet (9.8 m). Figure 3 shows the cracked core sample from drilled shaft #7.

The holes were dewatered to an approximate depth of 25 feet (7.6 m) and prepared for video observations. Utilizing a video camera attached to a PVC pipe with demarcated lengths, down-hole video observations were performed. Figure 4 shows the camera set up and crack observed at about 19 feet (5.8 m) in drilled shaft #7. A measuring tape was attached to the PVC pipe to aid in estimating the crack thickness. As Figure 4 shows, the crack appeared to be approximately ¼ inch (0.6 cm) in thickness for drilled shaft #7. Similar cracks were observed in 5 other shafts.

The video-recorded crack depths concurred with the estimated crack depths utilizing the PIT. No additional anomalies were identified within drilled shaft cores to a depth of 25 feet (7.6 m) below grade (due to limitation of the dewatering depth). The concrete above the cracks appeared sound and continuous. The top and bottom core pieces (directly above and below the crack) were extracted and

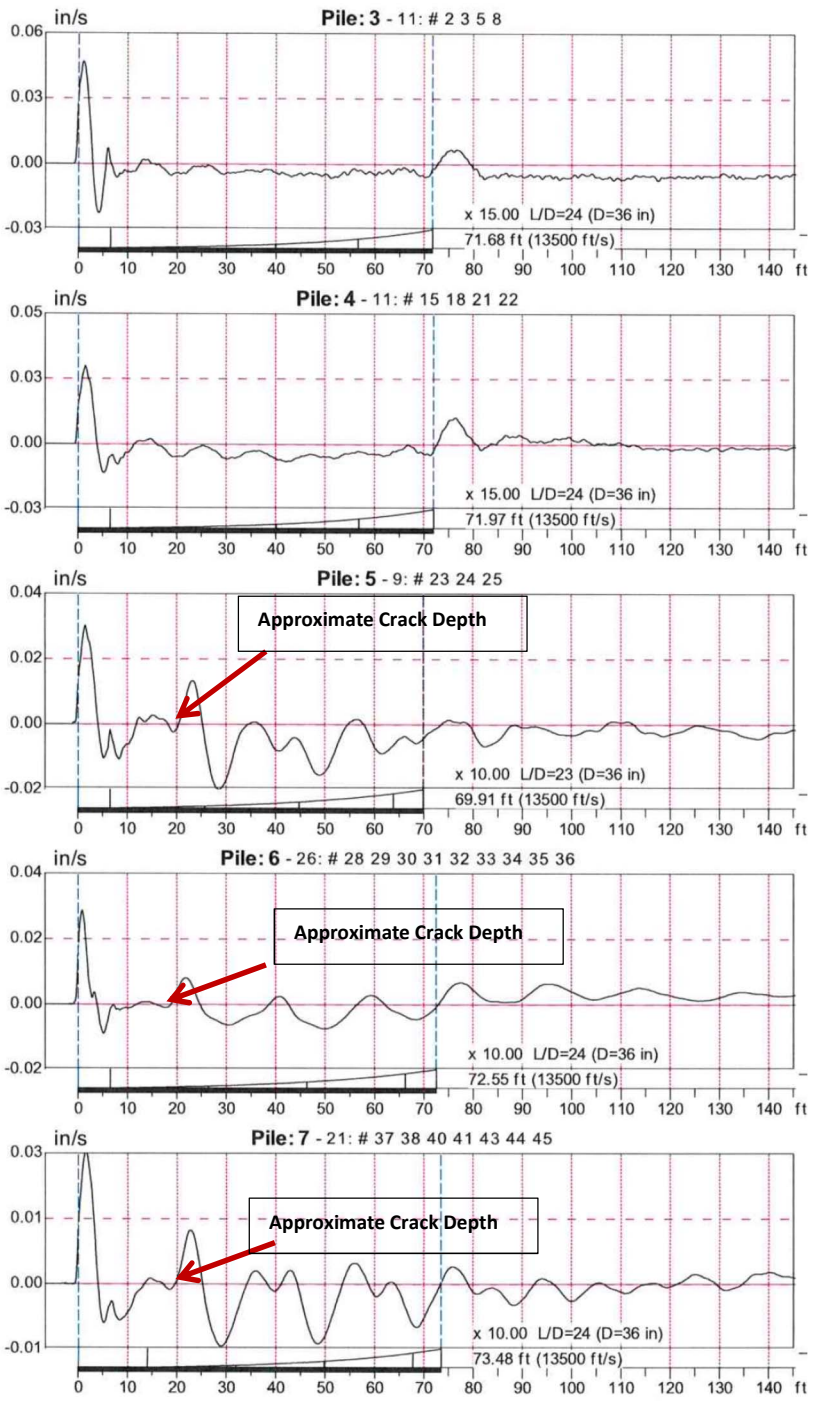


Figure 2: Pile Integrity test results conducted on affected drilled shafts #3 through #7

appeared to be recovered intact. The core pieces were aligned and no indications of lateral shift or offset were observed in the core at the crack location. A test pit was excavated alongside drilled shaft #5 and the crack was observed to extend to the perimeter of the shaft, with no lateral displacement of the shaft observed indicating a rotation about the crack.



Figure 3: Interlocked core pieces from drilled shaft #7



Figure 4: Camera set up (left) and crack observed in video recording at about 19 ft (5.8 m) in drilled shaft #7 (right)

CAUSES OF ERS MOVEMENT

To investigate the cause of the ERS movement observed along the eastern sheet pile wall, the design and construction of the ERS system was re-evaluated. The re-evaluation consisted of both global stability and internal ERS stability analyses. Soil properties and ground water conditions utilized in the initial designs were re-examined as well as comparing original ERS designs with as-built conditions.

Subsurface Soil Properties

Five borings were drilled within the approximate footprint of the proposed construction to depths in the range of 101½ to 125 feet (31 to 38 m) below existing site grades. The long term water level was estimated at about 13 feet (4 m). This is about 3 feet (0.9 m) higher than the basement excavation. The upper 6 to 7 feet (1.8 to 2.1 m) of material consisted of predominantly granular Urban Fill soils. Below the urban Fill soils, a desiccated layer of stiff silty clay typically extended to about 15 feet (4.6 m) below the existing grade. Firm to soft clay soil was encountered below the desiccated layer to about 50 feet (15.2 m) below grade. A series of in-situ vane shear tests were performed during the initial site investigation within the soft clay soils to estimate undrained shear strengths. The yellow circles in Figure 1 above show the approximate locations of in situ vane shear testing. The soils from a depth of 50 feet (15.2) below grade were further scrutinized to better investigate the ERS wall movement condition. Specifically, the soil properties near the eastern wall where the movement was observed.

As Table 2 shows, the in-situ vane shear data indicated soft soils, with shear strengths in the range of approximately 500 psf to 900 psf (24 to 43 kPa), across the project site between depths of 15 to 45 feet (4.6 to 13.7 m). The south side of the site, however, indicated lower in-situ shear strengths than those in the central and northern portion of the site, typically between 500 and 600 psf (24 to 29 kPa).

*Table 2: In situ vane shear test results, *Closest to movement of the ERS system*

Depth, ft (m)	Undrained Shear Strength, Su, psf (kPa)			
	Southwest Corner	Northwest Corner	South-Central	East-Central*
15 (4.6)		597 (28.6)		1476 (70.7)
20 (6.1)	531 (25.5)	536 (25.7)		591 (28.3)
25(7.6)	497 (23.8)	929 (44.5)		
30 (9.1)	579 (28.6)	893 (42.8)	651 (31.2)	995 (43.3)
35 (10.7)	533 (25.5)		597 (28.6)	1105 (53.0)
40 (12.2)			669 (32.0)	
45 (13.7)			804 (38.5)	

As-Built Construction Details

Two as-built conditions were considered as likely factors contributing to the ERS system movement. The ERS wall was originally designed to be a 9½ foot (2.9 m) cantilevered sheet pile wall.

1. The upper 6 to 7 feet (1.8 to 2.1 m) of the excavation was to be performed as an open cut above the sheet pile wall system with a design slope above the top of the sheet pile wall at 1.5:1 (H:V). The as-built condition was observed to be closer to about 0.5:1 to 1:1 (H:V) along the eastern site boundary.
2. To stabilize the soft clay soils, it is common practice in Chicago to temporarily over excavate and replace 1 to 2 feet (0.3 to 0.6 m) of soft clay soil at basement excavations. Contractors prefer to replace the soft clay soil with either a granular working mat 1 to 2 feet (0.3 to 0.6 m) in thickness or place a 3 to 4 inch (7 to 10 cm) lean concrete mud slab to stabilize the working grade. A 2 foot (0.6 m) undercut was performed at this basement excavation and replaced with open graded granular materials. The ERS designer was told of the planned undercut and recommended the undercuts be performed in maximum 10 foot (3 m) lateral segments and backfilled with gravel (or mud slab) immediately. The as-built condition was not performed in conformance with the conditions anticipated during the design. Instead, the undercuts were performed at much greater lateral lengths and were also not immediately backfilled.

ERS Stability Analyses

Further analyses performed considering the above details, ruled out a Global Stability concern. The soil properties that were used for the initial design of the ERS system and the revisited deign parameters are given in Table 3. Revisited parameters focused on the lower typical values for the affected, southern portion of the site.

Shoring Suite program (CivilTech 2017), also known as CT Shoring, was utilized to assess the internal stability of both the originally designed and as-built wall condition. The active and passive lateral earth pressures acting on the sheet pile were manually calculated using the parameters provided in Table 3 and input in CT Shoring software for the internal stability of the wall. Figure 5 and Figure 6 show the lateral earth pressures acting on the sheet pile. (The laid back slopes above the sheet pile wall were considered in our calculations and input into CT Shoring but the output diagrams do not depict the laid back slopes above the sheet pile wall (Figures 5 and 6 below). The building surcharges (located southeast of the excavation) were not considered to contribute to lateral earth pressure along the ERS system as the building was located beyond the critical influence zone of consideration.

Likely contributions to the ERS system movement include:

- Excavating in front of the sheeting in large widths reduces the passive forces acting on the sheeting. Because the sheeting is cantilevered, even a small amount of over excavation has a severe effect the ERS system stability. Not excavating in small widths also negated the

contributions of soil arching, considered when the designer recommended maximum 10 foot (2.9 m) widths.

Table 3: Soil properties for designing the ERS system

Initial Design Parameters			Revisited Design Parameters		
Depth below top of sheet pile, ft	Undrained Shear Strength, psf	Friction Angle	Depth below top of sheet pile, ft	Undrained Shear Strength, psf	Friction Angle
0-1.5	NA	28	0-1.5	NA	28
1.5-5.5	1500	NA	1.5-5.5	1500	NA
5.5-7.5	750	NA	5.5-19.5	550	NA
7.5-19.5	600	NA	19.5-25	675	NA
19.5-25	980	NA			

Initial Design Parameters			Revisited Design Parameters		
Depth below top of sheet pile, m	Undrained Shear Strength, kPa	Friction Angle	Depth below top of sheet pile, m	Undrained Shear Strength, kPa	Friction Angle
0-0.5	NA	28	0-0.5	NA	28
0.5-1.7	71.8	NA	0.5-1.7	71.8	NA
1.7-2.3	36	NA	1.7-7	26.3	NA
2.3-6	28.7	NA	7-7.6	32.3	NA
6-7.6	47	NA			

- Averaging the soil undrained shear strengths along the entire eastern length of the Sheet pile wall resulted in an under-designed ERS for the southern portion of the wall, where the soil was noticeably softer. Lower-strength soils at the southern end of the site result in additional active forces pushing on the sheeting and reduced passive forces available in front of the sheeting to resist the active forces behind the sheeting.
- Due to pumping out the basement excavation, unbalanced ground water elevations added hydrostatic forces on the retained side of the wall (active side) which would not be negated on the passive side, again due to pumping.
- This excavation was performed during the rainy season in Chicago. Perched water in the top Urban Fill layer also added to the active forces, in turn reducing the stability of the ERS system.
- The sloped cut above the sheet pile wall was not laid back at the design slope of 1½:1 (H:V). Instead the cut was much steeper (½:1 to 1:1 (H:V) which added to the lateral pressure on the active (driving) side of the wall.

Based on the discussed construction conditions and computer modeling detailed in Figure 6, a factor of safety below 1 could be possible. A factor of safety below 1 does not necessarily equate to a catastrophic failure in ERS, especially in a soft clay soil profile. As the wall deflects away from the retained soil, the lateral pressures redistribute and the ERS system reaches a new equilibrium. The movement at this ERS system, was problematic due to proximity to the drilled shafts. Movement of the ERS system caused cracks in the drilled shafts, which ultimately was the subject of delayed construction and increased costs.

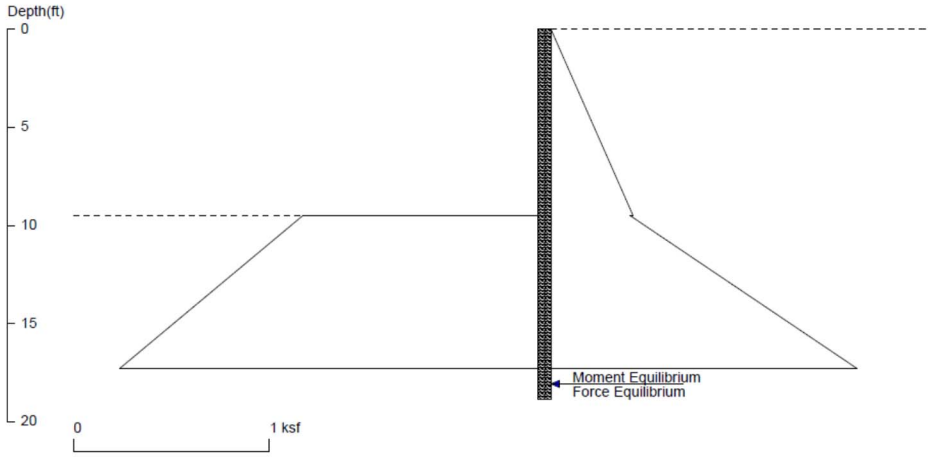


Figure 5: Initial sheet pile lateral earth pressure diagram, 9½ feet (2.9 m) of excavation resulting in a FS=1.66 for overturning.

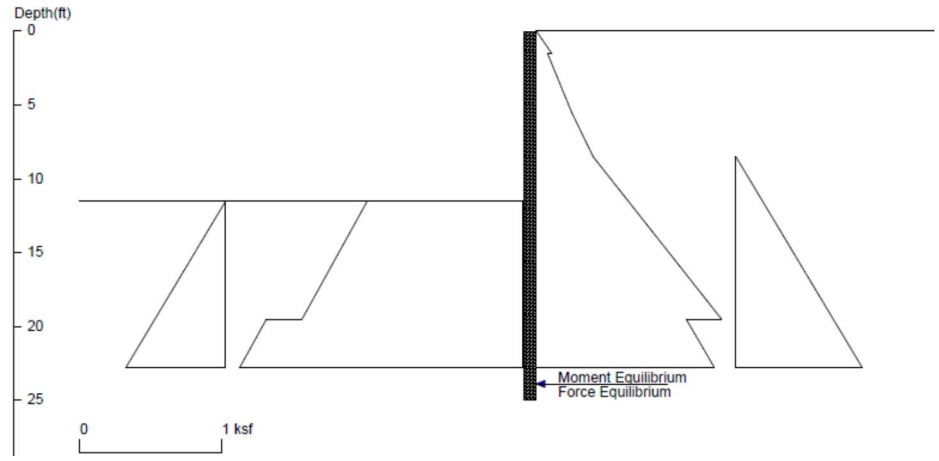


Figure 6: Revisited sheet pile lateral earth pressure diagram, 11½ feet (3.5 m) of excavation with revisited soil properties resulting in a FS=0.71 for overturning. Unbalanced groundwater conditions modeled reflecting the excavation was pumped dry.

REMEDIAL ACTION

The contractor reinforced the southern portion of the eastern ERS sheet pile system after the excessive movements were first observed. The reinforcement of the sheet pile wall consisted of driving additional sheet piles inboard (westward) of the eastern perimeter wall about 34 feet (10.4 m). A series or reinforcing walers and rakers were connected to the new sheet pile wall. The walers and rakers increased resistance to the passive side of the wall, helping to stabilize further movements.

Fortunately, the affected shafts were supporting axial loads only. The majority of the damaged shafts on the eastern sheet pile wall were spliced together. The splices were accomplished by coring the existing shaft from the top to a sufficient depth below the observed cracks. New, high strength vertical reinforcement bars were installed in the cored holes, set in high strength grout. The length and diameter of the new vertical reinforcement splices were designed to transfer axial loads. One of the damaged shafts was abandoned in place and a new caisson was drilled. The structure has been completed and no further movement or distress has been observed, the repairs were successful.

CONCLUSION- LESSONS LEARNED

The design and construction of an ERS system is a complex process and requires that all parties, designer and contractors work together. The use of average soil properties should always be reviewed carefully, especially when small differences in soil properties can have a large impact on ERS performance. Further, conditions understood at the time of design, must be met in the field, for the design to function as intended. Changes in soil conditions or construction, need to be brought to everyone's attention promptly. In this case changes included steeper slopes above the top of the sheet pile wall, pumping of water and excavation in front of the sheet piles increasing the effective retained height by 2 feet (0.6 m). The designer must be provided an opportunity to review and revise the design or provide other guidance base upon changed conditions or deviations from the design documents. The contractors should follow revised guidance when provided by the designer of record.

As demonstrated on this project, delays and costs due to ERS failures could have been avoided if the project team would have communicated better between design and construction. Fortunately, once the issues arose, everyone communicated and cooperated extensively to mitigate and remediate the situation, substantially reducing the impact to the project.

In this case:

- the soil conditions varied significantly south to north, and an average shear strength value was not appropriate for design of the ERS
- field as-built conditions deviated from the design, including both
    - additional loads behind the wall, increasing the active forces
        - change in slope
        - additional 2 feet of water pumped from the excavation
    - a reduction in the passive forces resisting loads
        - excavation in front of the ERS
- due to forces in excess of those considered in the design pushing on the wall and resisting forces less than available in the design, the wall moved into the excavation. This sheeting movement applied lateral force onto the tops of the drilled shafts, causing 6 shafts to shift laterally at the top and crack at a depth of about 20 feet (6.1 m).

Fortunately, the design and construction team worked quickly and cooperatively to reinforce the ERS wall to prevent further movement, determine the causes for the movement, determine the extent of the damage to the shafts and finally design and implement a remedial program. As a result, the project was completed with minimal delay and continues to perform as intended.

REFERENCES

CivilTech, 2017. Shoring Suite version 8, http://www.civiltech.com

ASTM D5882, 2016. Standard Test Method for Low Strain Impact Integrity Testing of Deep Foundation. ASTM International, West Conshohocken, PA

Manierre G., 1916. A Description of Caisson Work to Bed Rock in Chicago for Modern High Buildings. Journal of the Illinois State Historical Society (1908-1984) 9(3), 296-300

Peck R., Reed W., 1954. Engineering Properties of Chicago Soils, Engineering Experiment Station, University of Illinois Press on behalf of the Illinois State Historical Society Stable URL: http://www.jstor.org/stable/40194182. Accessed: 12-12-2017 14:59 UTC

TUNNEL HEADWALL SOFTEYES: FIBERGLASS DESIGN APPLICATIONS AND CONSTRUCTABILITY CHALLENGES

Shawna Munn, P.Eng.,
Isherwood Geostructural Engineers, Mississauga, Ontario, Canada; 905-820-3480;
Shawna@isherwood.to

Jakub Hudler, P.Eng.,
Isherwood Geostructural Engineers, Mississauga, Ontario, Canada; Jakub@isherwood.to

ABSTRACT

This paper outlines the use of tunneling headwall softeyes for transit construction projects in the Greater Toronto Area (GTA) over the past decade. Due to spatial constraints, tunnel boring machines were used to construct the underground tunnels requiring the design of launch and exit shafts with headwall softeyes to facilitate tunneling operations. Variable ground conditions and shaft geometries lead to the development of innovative headwall and tunnel softeye design applications using fiber reinforced polymer (FRP) elements (beams, reinforcing bars, and tiebacks). This paper outlines the challenges and benefits associated with designing and constructing shafts using various systems. Lessons learned throughout design and construction of more than 20 structures over the past 10 years are outlined. The constructability challenges with using FRP and design performance are also discussed.

Keywords: fiberglass, fiber reinforced polymer, headwall, tunneling, constructability, softeye, innovation, performance, FRP, GFRP

For over a decade, the City of Toronto has been expanding its metropolitan transit network with a variety of new transit construction projects. Two recent projects in the Greater Toronto Area (GTA) for underground infrastructure include the Toronto York Spadina Subway Extension and the Eglinton Crosstown Light Rail Transit project. These add a total of 31 new stations and 18.6 km (11.5 miles) of underground transit (TTC 2017) (EllisDon 2016).

Due to ground conditions and spatial constraints of existing surface infrastructure, these projects utilized tunnel boring machines (TBMs) to construct the underground tunnels requiring the design of various types of shafts and headwalls to facilitate underground tunneling operations. To allow for tunneling through the headwalls, these shafts were designed with “softeyes” - a section of the wall without metal reinforcement that allows the TBMs to tunnel through.

PURPOSE OF SOFTEYES IN TUNNELING

A softeye is a wall type which can be drilled through and penetrated by a TBM cutterhead. This can be accomplished in a variety of ways including: mass concrete non-reinforced drilled wall, Fiberglass Reinforced Polymer (FRP) secant pile or slurry wall, jet grout block, or ground freezing (Hunt 2008). In the GTA, we have used FRP secant pile headwalls in the following applications: Launch Shafts, Exit Shafts, Advance Headwalls, Mining Excavation Shafts, and other Access Shafts.

As their names suggest, a Launch Shaft accommodates hoisting, assembly/launch of TBMs, and mucking operations whereas an Exit Shaft is meant to receive, disassemble, and hoist a TBM. Advance Headwalls are typically installed at boundaries of future excavations, such as underground subway stations, to allow the TBM to pass through the headwall prior to excavation of the future shaft. Mining Excavation shafts are access shafts to accommodate mining operations utilizing a Sequential Excavation Method (SEM) or New Austrian Tunneling Method (NATM). Access Shafts are used to proactively provide access to the

© 2018 Deep Foundations Institute

TBM for maintenance of cutter heads at some part through the tunnel drive between the Launch and Exit Shafts. Each of these provides unique design challenges and requires design capacities, geometries, and other considerations for the uses of FRP reinforced secant pile headwalls. In Toronto, FRP reinforced softeyes have been designed and used in a wide range of variable ground conditions and adjacent structure geometries, resulting design pressures with K values from 0.25 to 1.0, FRP excavated heights of up to 20 m (65 ft), and unsupported spans of up to 5 m (16 ft).

FRP DESIGN CONSIDERATIONS

Fiber reinforced polymer materials are considered suitable for use in softeyes mainly due to their 'cuttability' by the TBM's cutterhead during tunneling operations. FRP exhibits brittle failure which is different from steel's ductility. Brittle failure allows the FRP to break into pieces without obstructing the TBM during operation. Brittle failure is also a main consideration in the design of FRP systems, and one of the reasons why current design codes such as the CAN/CSA-S806-02 apply significantly more conservative factors of safety than other design materials. Figure 1 illustrates the significantly different behavior of FRP and Steel anchor bolts.

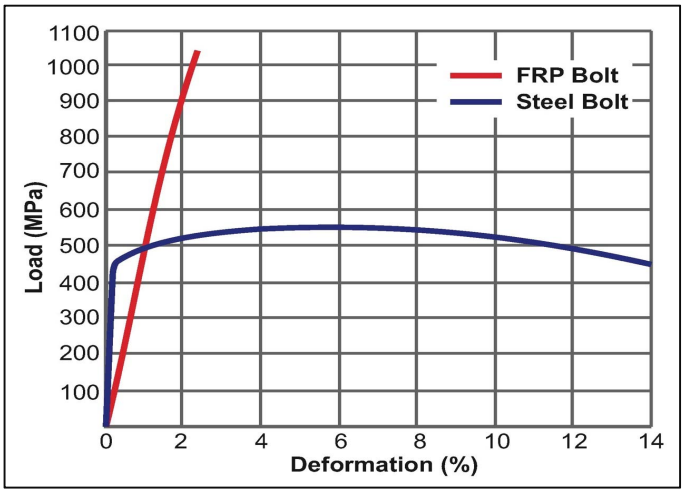


Fig. 1. Comparison of Material Behavior of FRP and Steel Bolts (Mohanty 2014)

The manufacturing process used to produce most fiberglass products, called pultrusion, results in an anisotropic material with directional material properties. Therefore, stresses in the transverse and longitudinal directions must be considered in design. Most notably, this results in a significantly smaller allowable shear capacity compared to conventional steel beams. FRP also has a significantly lower modulus of elasticity than steel. This leads to specific design considerations when using a composite steel/FRP system like a Steel/FRP headwall. Table 1 outlines a comparison in material property values between a typical FRP pultruded shape (I-beam) versus the typical steel pile secant wall reinforcing used in the GTA. The contrast in the modulus of elasticity of the two materials needs to be accommodated in the design and can lead to different deformation behavior of the two materials resulting in load redistributions in the system (Schürch 2006). For this reason, the steel/FRP connection is modelled as a hinge since moment transfer is hard to achieve due to strain compatibility issues. This poses a design challenge as the fiberglass beam has low shear capacity. Therefore, the concrete in the secant pile wall acts as additional reinforcing, and the strength should be increased to accommodate shear stresses that exceed the FRP reinforcing capacities. The authors have used concrete strengths ranging from 15 MPa (2200 psi) to 25 MPa (3600 psi) to act as additional shear reinforcing for FRP reinforced secant pile headwalls.

Table 1 – Mechanical Property Comparison of GFRP Beams vs. Steel Beams

Parameter	**Glass Fiber Reinforced Polymer Shapes Lengthwise/Crosswise**	**G40.21 Structural Steel F_y = 350 MPa (50 ksi)**
Ultimate Tensile Strength **MPa** (ksi)	**207 / 48.3** (30/7)	**450** (65)
Ultimate Compressive Strength **MPa** (ksi)	**207 / 110** (30/16)	**450** (65)
Ultimate Flexural Strength **MPa** (ksi)	**207 / 68.9** (30/10)	**450** (65)
Modulus of Elasticity – Full Section **MPa** (ksi)	**19300** (2800)	**200000** (29000)
Shear Modulus – Full Section **MPa** (ksi)	**2930** (425)	**77000** (11165)
Ultimate Shear Strength **MPa** (ksi)	**31** (4.5)	**231** (34)
Unit Weight **kN/m^3** (pcf)	**18** (114)	**77** (490)

(Strongwell 2012) (CISC 2010)

It is important to note the properties of FRP materials depend on the material used to reinforce the polymer (glass, aramid, carbon, etc.) and the manufacturing process used. As illustrated by the variability in the preceding examples, design strengths, design recommendations, and material property values from the specific manufacturers should be consulted when designing FRP systems.

FRP IN HEADWALL DESIGNS

A fiber reinforced softeye can be accomplished in several ways. In all cases, the steel pile reinforcing typically used for the excavation support system is replaced in the softeye zone with FRP reinforcing. This reinforcing can consist of FRP beams bolted to similar depth steel beams or reinforced cages with fiberglass reinforcing bars through the softeye zone.

Fiberglass Beams

In the GTA, FRP beams have been more commonly used for softeye reinforcing. Figures 2 and 3 illustrate a few iterations of FRP/steel softeye splices using either FRP splice plates and bolts or typical steel plates and bolts. Since FRP shapes come in a smaller variety of sizes and thicknesses, special consideration for shim plate sizing and preferred pile layout in the headwall needs to be considered.

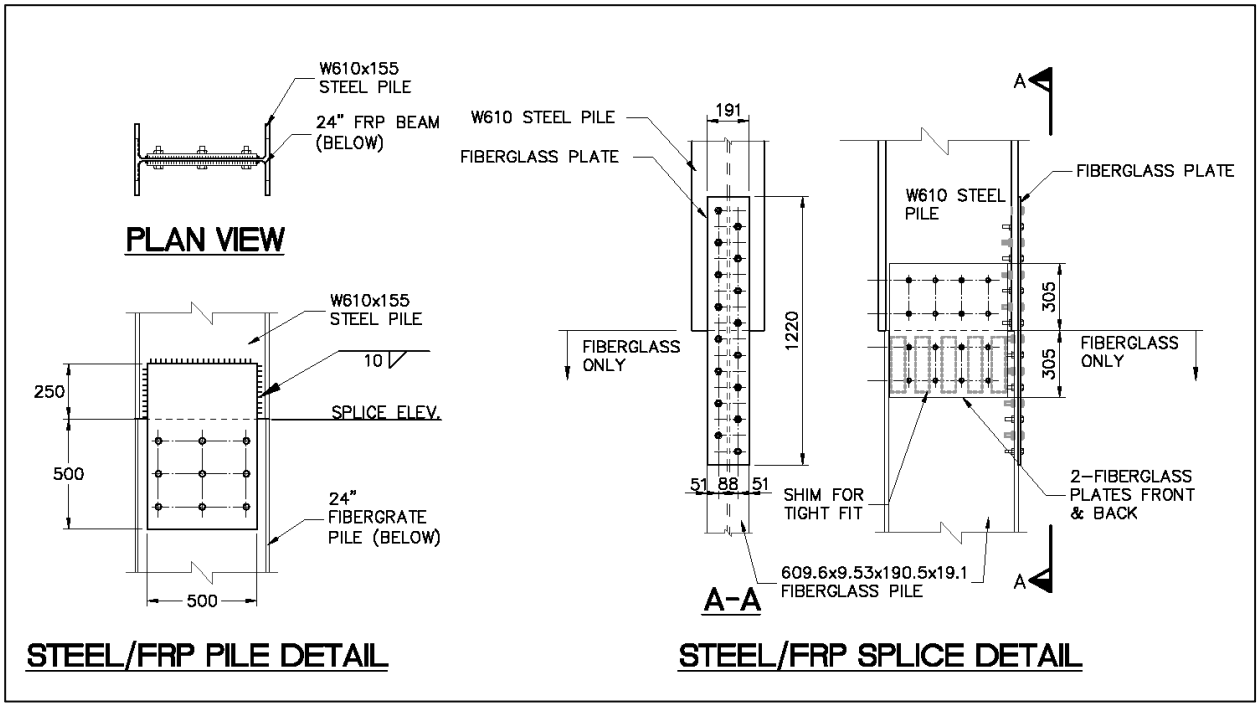


Fig. 2. Steel/FRP Splice Details – Steel Plate and Bolts (Left) and FRP Plates and bolts (Right) (Units in mm)



Fig. 3. Fabrication and Installation of FRP/Steel Beam at an Advance Headwall

FRP beams can also be built up using other FRP shapes to create composite design sections for loading cases where single FRP beams lack capacity. Figure 4 shows an example of a built up pile layout used for a FRP reinforced headwall for a TBM exit shaft. Special attention to bracing connection detailing (I.e. walers and corner bracing, etc.) and excavation activities needs to be considered prior to construction when using built up FRP connections. In the project example shown in Figures 4 and 5, the secant pile wall was not trimmed back to the front of the steel pile flanges above the softeye to avoid damage to the built up FRP shape through the softeye.

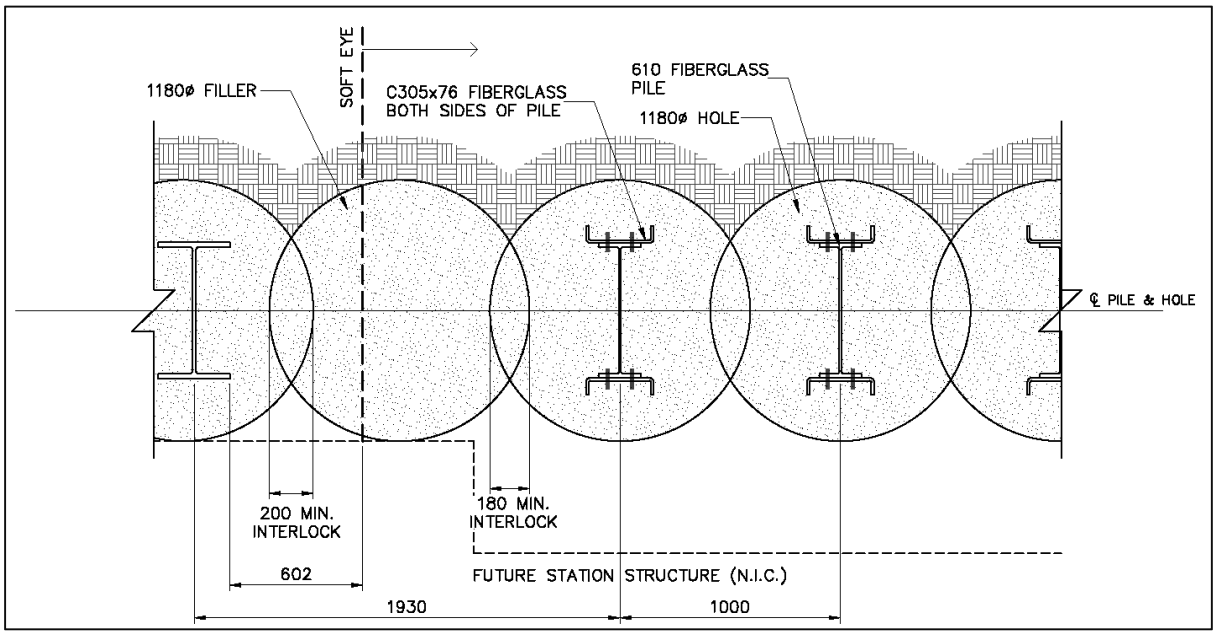


Fig. 4. Example Pile Layout of Built Up FRP Section (Units in mm)



Fig. 5. Breakthrough of TBM through FRP Beam Reinforced Softeye

Fiberglass Reinforced Cages

Using reinforced cages with steel/fiberglass for headwall softeyes provides its own unique set of design challenges. Current fiberglass design codes specify conservative allowable stresses for fiberglass design (allowable = 30% ultimate) due to a number of factors (CSA 2009). These include the failure mode of the material, lack of differentiation between temporary and permanent uses, as well as the lack of historical data for use of FRP as a design material compared to other materials. This results in an increased number of bars in the FRP section of the cage to achieve the same required design capacity as the steel section (illustrated the design example shown in Figure 6). Figure 7 shows the FRP/steel cage assembly on the spine support prior to lifting and installation.

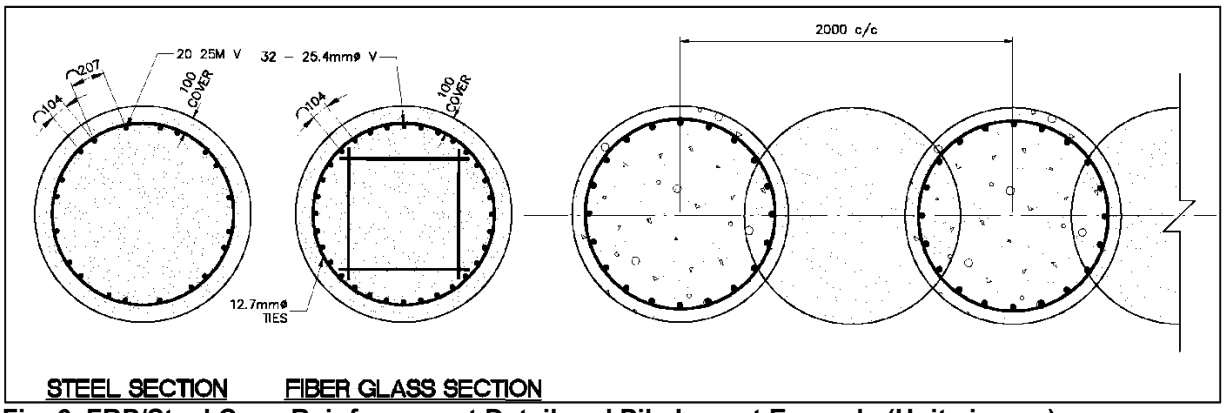


Fig. 6. FRP/Steel Cage Reinforcement Detail and Pile Layout Example (Units in mm)

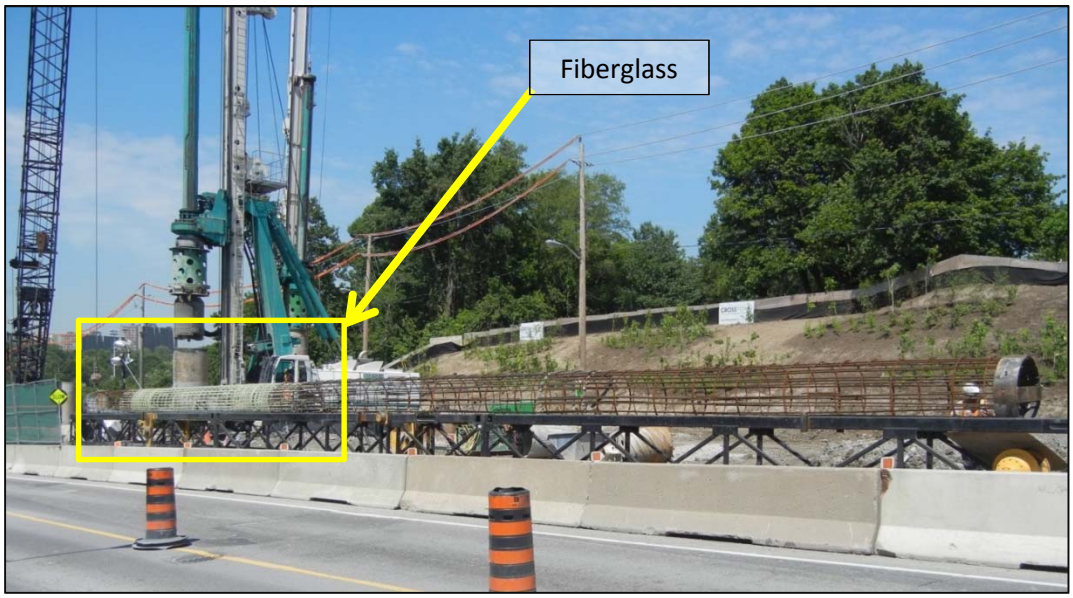


Fig. 7. Steel/FRP Cage Assembly on Spine Support Beam prior to Lifting

Fiberglass Anchors

The other strategy used for design of Launch or SEM shaft headwalls is the addition of fiberglass anchors to decrease bending in the FRP pile section, and decrease the shear at the steel/fiberglass splice connections. Use of these anchors has resulted in simplified pile layouts due to the decrease in required fiberglass material, as well as a decrease in the required concrete strength to resist the shear at the connections. Figure 8 shows the design detail developed for use of the fiberglass anchors. Due to the limited availability of high tensile capacity fiberglass anchors, three 25 mm (1 inch) GFRP bars were used

per location to achieve the required design capacities. In addition, due to limited availability of FRP anchor plates and other bolt accessories, the secant pile wall had to be further broken around to allow enough room to separate the FRP bars for three separate anchor connections at the face of the wall. These FRP anchor connections were recessed into the secant pile wall to allow the bars to be trimmed back. The recess was filled with concrete prior to launching the TBM to allow for a continuous mining face.

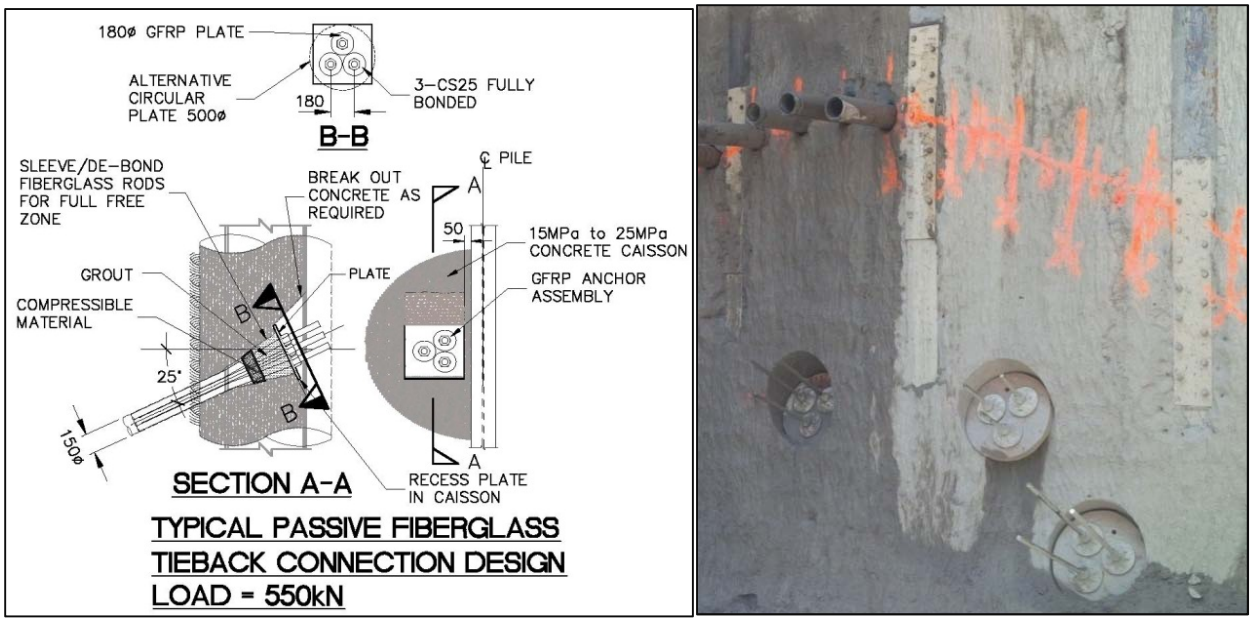


Fig. 8. FRP Anchor Connection Detail and Example of use at a Launch Shaft (Units in mm)

Use of the FRP anchors has also allowed for larger design heights and different shaft geometries since internal bracing of the FRP beams is not required. This has allowed for more open excavations, and sequential mining of SEM headwalls as anchor elevations can be customized to the required geometry. Figure 9 shows a progress photo of the excavation for the SEM access shaft to allow mining for future light rail station using the Sequential Excavation Method.



Fig. 9. Mining Access Shaft Headwall with FRP Anchors – Sequential Mining in Progress

CONSTRUCTABILITY CHALLENGES

Throughout the design and construction of these FRP reinforced systems, several constructability challenges have been experienced.

General Challenges

Hoisting/Assembly: Due to the low modulus of elasticity of the FRP reinforcement, the designer and contractor should work closely to understand the forces which may be encountered during hoisting and placement of the FRP reinforcement to ensure the cage or pile integrity. To minimize these forces, two different systems have been used in the GTA:

- "Dummy holes" – Vertical splicing over a sacrificial hole followed by vertical hoisting and placement of the reinforcement into the drilled secant pile wall.
- Support frames to act as a rigid spine to support the FRP reinforcement during the lifting process. Once the cage is vertical, the spine is disconnected prior to lowering the cage in the drilled hole.

Other means of lifting, such as the use of multiple pick points with the use of strong backs and rolling blocks, have been used in other jurisdictions.

Excavation/Shaving: Secant Pile walls in the GTA are typically reinforced with steel I-Beams in low strength concrete (4 MPa/ 580 psi) whereas FRP reinforced headwalls can have concrete strengths of up to 25 MPa (3600 psi). Excavators are used to trim the rounds of the secant pile walls to accommodate bracing/support connections and the proposed permanent wall locations, where applicable. Due to the different geometries of the FRP sections and weaker material strength, damage to the FRP materials from the excavator was experienced, such as over-excavation through FRP pile sections and bolted splice connections being sheared off during excavation to the pile face as seen in Figure 10.

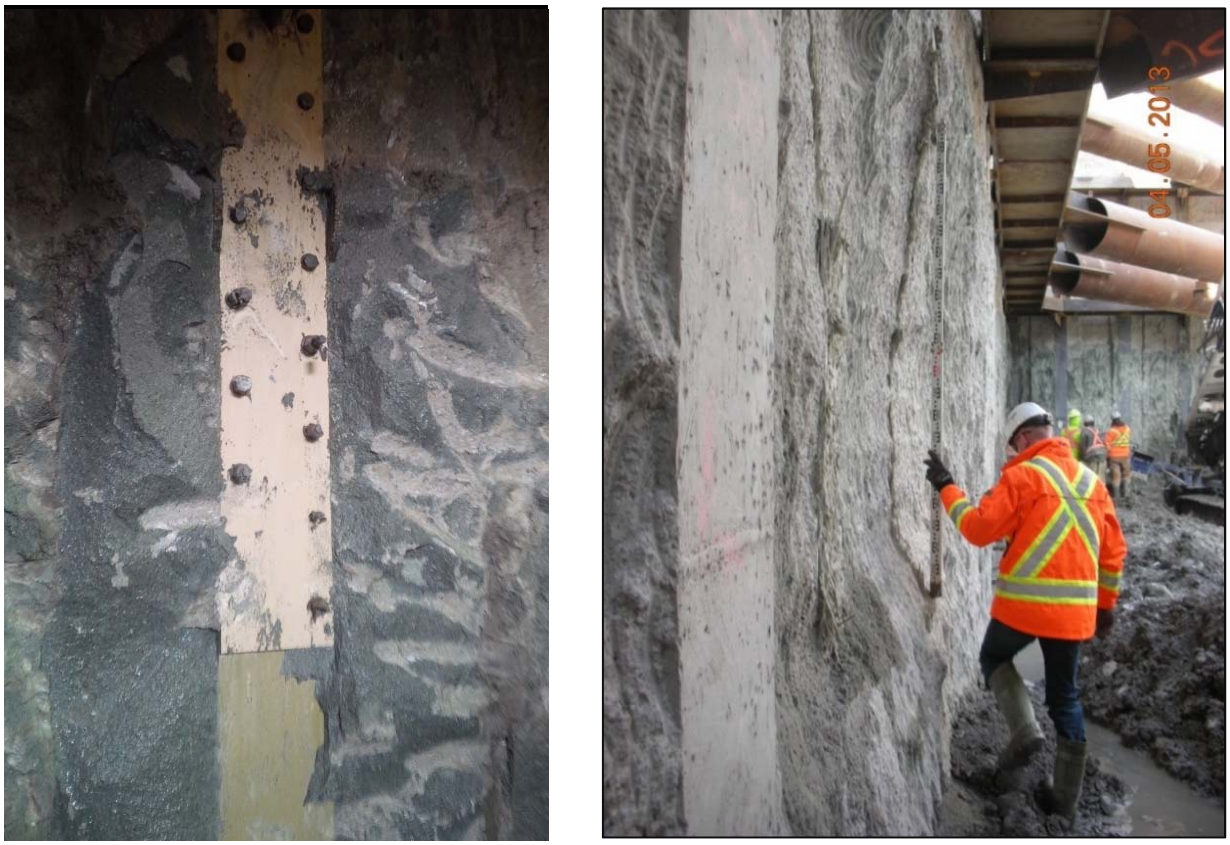


Fig. 10. Broken FRP bolts (Left) and Over-excavation through FRP Piles (Right)

TBM Forces: The Shoring wall designer must understand the temporary supernormal loading pressures, which may occur when the TBM is approaching the back of the shoring headwall prior to breakthrough. Earth Pressure Balance Machine's used in the GTA can impose a pressure of up to 200 kPa (30 psi) on the back of the shoring headwall. To ensure adequate FRP Exit Shaft Headwall performance, removable internal bracing can remain in place until TBM makes contact with the back of the headwall and earth pressure forces are negated.

Softeye Placement Accuracy: Placement of the FRP/steel reinforcing requires coordinating installation of the FRP within tolerances necessary for tunneling by the headwall Shoring Contractor. This can be particularly challenging when trying to mimic the circular tunnel liner shape with the FRP softeye.

Monitoring Programme: Based on the design challenges mentioned above, a quality monitoring programme for the temporary FRP walls in softeye applications is prudent. On these projects, a combination of 3D Precision Survey Monitoring, Inclinometers, and Load Cells on the anchors between the tunnels were successfully used.

FRP Reinforced Cages

Although our experience in the use of FRP reinforced cages is limited, several important lessons were learned through the construction process. During installation of the 33 m (108 ft) long reinforced cages, several of the cages broke in the FRP section resulting in the top section of the steel cage falling into the required softeye clearance zone. Upon review of each of these occurrences, two main modes of failure were determined after cage recovery.

Initially, the bars were fixed together with binding wire and scattered U-bolts at the FRP/steel splice location. After the initial splice failure, additional U-bolt reinforcing was added to the splice connections shown in Figure 11, a recommendation also reinforced by Schürch and Jost in their 2006 paper.

After the initial failure mechanism was resolved, some of the cages began to break within the FRP only section during drill casing extraction. This was determined to be a result of the small 50 mm (2 inch) cover between the inside of the drill casing and the outside of the cage. To resolve this issue, additional FRP ties were added to the cage, and an oscillator was used for liner extraction of the remaining piles to limit the torque applied to the cages from continuous rotation in one direction.



Fig. 11. Reinforced FRP/Steel Splice Connection

Future recommendations for design of FRP cages include:

- Increased cover between drill casing and cage reinforcing;
- Additional U-bolt reinforcing at splice connections where large forces are transferred;
- Use of reverse spiral shear reinforcing on the inside and outside of the cage in lieu of single tie shear reinforcing to limit shear forces applied to the cage during liner extraction; and
- Special attention to concrete mix design and forces on cages during construction.

CONCLUSIONS

Underground transit infrastructure projects in metropolitan areas provide an excellent opportunity for use of Tunnel Boring Machines (TBMs) to minimize impacts to existing surface and shallow infrastructure and surrounding communities. Use of TBMs requires construction of various Launch, Exit, and Auxiliary Shafts to facilitate tunneling operations requiring the design of shaft headwall softeyes. The use of FRP reinforcement and bracing has proven to be an effective and efficient means of providing structural support of the shaft and suitability for accommodating tunneling operations. The design of FRP systems provides unique construction challenges compared to more common construction materials; therefore, special attention needs to be given to material properties and constructability challenges. Overall, use of FRP has been found to be the most effective solution for softeyes in large diameter tunneling applications in various soil conditions in the Greater Toronto Area.

ACKNOWLEDGEMENTS

Acknowledgement is given to Todd Barlow of Bermingham Foundation Solutions for his assistance and support.

We thank Alan Macnab and Nadir Ansari for comments that improved this paper.

REFERENCES

1. Canadian Standards Association (CSA), 2009. CAN/CSA-S806-02. Design and Construction of Building Components with Fibre-Reinforced Polymers. Rev. 5. 177p.
2. Canadian Institute of Steel Construction (CISC), 2010. Handbook of Steel Construction, Tenth Edition.
3. EllisDon, 2016. Toronto Eglinton Crosstown LRT. http://www.ellisdon.com/project/eglinton-crosstown-lrt/. Accessed 18.04.16
4. Hunt, S. W., Finney, A.J. (2008). Mitigating Tunnel Launch and Reception Challenges. Society for Mining, Metallurgy & Exploration, 812-823.
5. Mohanty, S., Vandergrift, T., Ross, T., Hwi, G., Lee, M. (2014). Fiber Reinforced Polymer Rockbolts for Ground Control in a Strong Jointed Rock Mass. 33rd International Conference on Ground Control in Mining, 193-198
6. Schürch, M., Jost, P. (2006). GFRP Soft-Eye for TBM Breakthrough: Possibilities with a Modern Construction Material. International Symposium on Underground Excavation and Tunnelling. 397 - 404.
7. Strongwell FRP Specifications, 2012. Section 06600 Fiberglass Reinforced Polymer (FRP) Products and Fabrications. 218p.
8. TTC, 2017. Toronto-York Spadina Subway Extension - Overview. https://www.ttc.ca/Spadina/About_the_Project/Overview.jsp. Accessed 18.04.16.

DEEP AND EXTRA DEEP DIAPHRAGM WALLS IN SHANGHAI – INCREASING DEMAND FOR INFRASTRUCTURE IN MEGACITIES DRIVES THE REQUIREMENT OF INCREASING DEPTH FOR DIAPHRAGM WALLS

Franz-Werner Gerressen, BAUER Maschinen GmbH, Germany
Arthur Bi, BAUER Technologies Taiwan Ltd., Taiwan
Wu Jie Mei, Shanghai Foundation Engineering Group CP., LTD, China
Li Yao Liang, Shanghai Foundation Engineering Group CP., LTD, China

ABSTRACT

Diaphragm walls (D-walls) are known as underground structural elements commonly used for retention systems and permanent foundation elements. In addition, they are also quite often used as deep groundwater barriers, called Cut-Off-Walls (COW).
Shanghai ranks third among the most densely populated metropolises in the world. In 1990, only eight million people lived there. Today, Shanghai has about25 million inhabitants.
The increasing demand to accommodate the infrastructure of growing megacities like Shanghai pushes the required depth for subway, sewage and foundation projects to the limit.
Future projects will demand excavation depths of more than 100 m (328 ft) on a regular basis.
Already carried out reference projects will be described and a general outlook for upcoming projects will be given.
The paper also explains the installation process in general focusing on the use of trench cutter technology.

Keywords: Diaphragm Wall, Trench Cutter

INTRODUCTION

D-walls are known as underground structural elements, commonly used as retention systems for excavation pits and shafts as well as permanent foundation walls or elements.
It is anticipated that, with the increasing trend of utilizing more and more underground space to accommodate environmental considerations and urban/suburban development, there will be an increasing requirement for diaphragm wall usage in even more difficult conditions and with increasing depth.
The trench cutter is the most important tool for performing this work. The hydraulic grab, a well-known and valuable excavation tool for d-walls reaches its limits in terms of depth and when cutting rock. Therefore the trench cutter technology will be in the focus of this paper.

The trench cutter itself is a reverse circulation excavation tool. It consists of a heavy steel frame with two drive gears attached to its bottom end, which rotates in opposite direction around the horizontal axis. Cutter wheels are mounted onto the drive gears. As they rotate, the soil beneath the cutter wheels is continuously broken up, removed, mixed with the bentonite slurry in the trench and moved towards the opening of the suction box of the pump? A centrifugal pump located right above the cutter wheels conveys the slurry via a hose system up to a desanding plant. There the slurry loaded with soil and rock particles is cleaned and returned into the trench.

The torque of the cutter wheels combined with the weight of the cutter is strong enough to cut into hard soils, crush stones up to a certain grade and overcut into the concrete of adjacent panels.
Depending on the soil, different types of cutter wheel configurations and teeth can be deployed, ranging from aggressive teeth for cutting fine-grained soil to percussive teeth for crushing boulders. Cutter wheels may conveniently be changed to suit different types of rock. Experiences were made with cutting strengths of up to 250 MPa (36,250 psi).

© 2018 Deep Foundations Institute

EQUIPMENT AND TOOLS

Working sequence

The typical working sequence for the construction of a diaphragm wall using a trench cutter as shown in figure 1 comprises the following key steps:

- Site preparation,
- Guide wall construction
- Trench pre-excavation
- Panel excavation
- Panel cleaning (desanding)
- Reinforcement installation (for retaining walls)
- Concreting

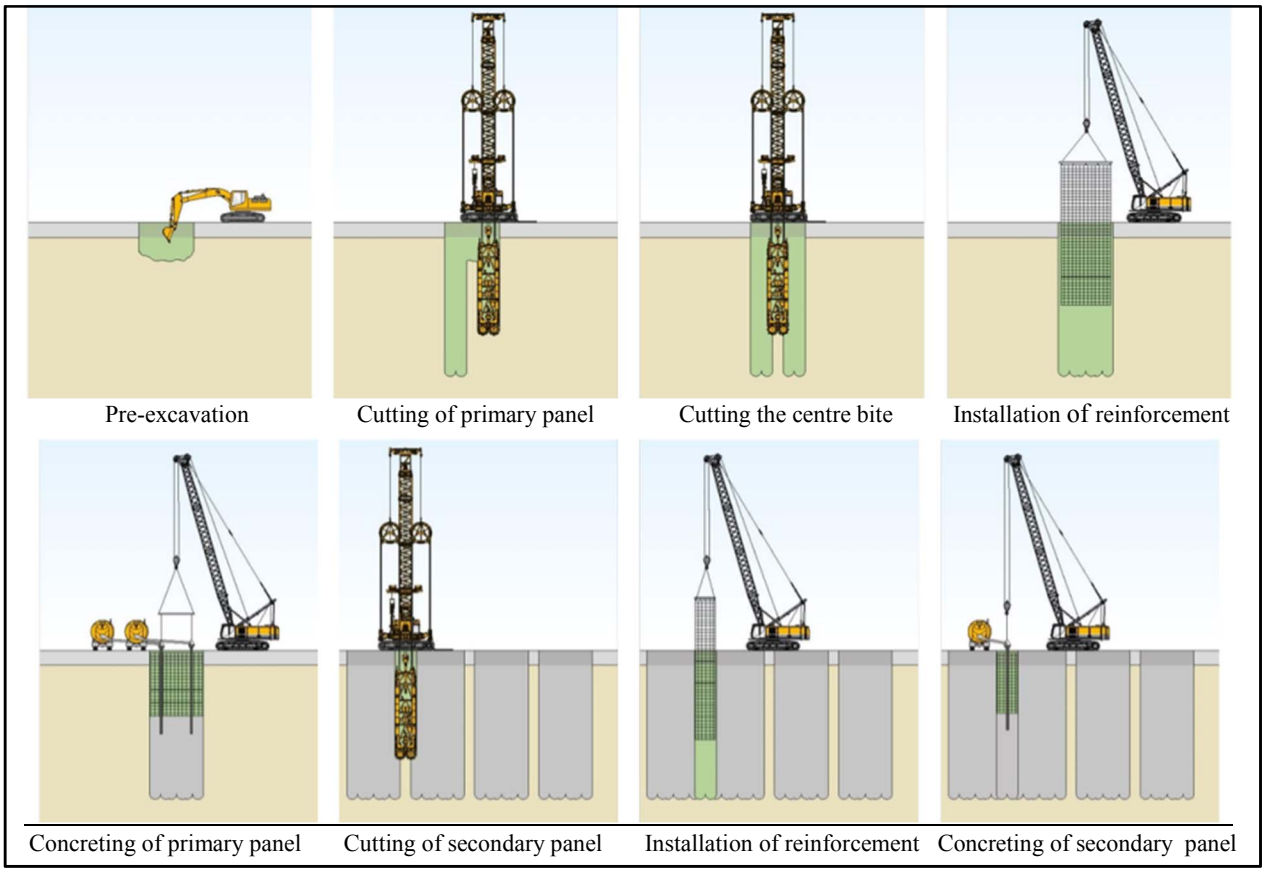


Figure 1: Construction process, exemplary for the diaphragm wall process

Wheels and teeth

The use of the most appropriate cutting wheels and teeth is one of the main key factors to reach optimal productivity. Trench cutters are typically equipped with one of three types of wheels and teeth. Their different features are depending on the range of rock strengths they are being used.. Figure 2 shows the three types of wheels.



Figure 2: Standard Cutter Wheel (left), Round shank chisel cutter wheel (centre), Roller bit cutter wheel (right)

The "Standard Cutter Wheels" are usually used in all types of soils with various types of teeth, but are also able to cut into weak to moderately strong rock conditions. Starting from rock strengths in the range of approx. 50 MPa (7,250 psi), which means cutting strong and hard rock, using a more aggressive wheel like the "Full Face Cutter Wheel (or Round shank chisel Cutter Wheel (RSC))" equipped with special chisels, will result in a better cutting process. At the upper end of the scale, when dealing with rock strengths exceeding 120 MPa (17,400 psi), using the "Roller bit cutter wheel" has to be considered. Usually, when using the Roller bit cutter wheels, a high weight of the cutter is required, as each roller bit requires a load of at least 4-8 metric tons for a reasonable functionality.

JOB SITE REFERENCES

More than 10 years back, Shanghai started the application of deep and ultra-deep diaphragm walls. The following references will describe projects of the more recent past., starting with a depth of 58.5 m (191ft) ending with the latest trials reaching a depth of 150 m (492ft).

Shanghai 2010 World Expo 500 kV Transformer Substation (2006)

Shanghai 2010 World Expo 500 kV Transformer Substation was the first cutter project in Shanghai. Located in the centre of Shanghai city, the 500 kV substation is the first 130 m diameter underground station built in China. It did not only provide electric power to 2010's Expo, but also ensures the energy supply to sustain the urbanization development of Shanghai ever since.

Geology

After approx. 2 m (6ft) of backfill, the geology could be described as mainly soft to firm silty clay to clay down to a depth of 27 m (88ft), followed by stiff clay to a depth of 30 m (98ft). Underneath the sandy silt was very stiff to a depth of 36 m (118ft). Thereafter very dense, silty sand was encountered with SPT values in a range of 50 - 80 blow counts to a depth of 47 m (155ft). To the final depth of 58.5 m (191ft) and underneath it changed back to a stiff to very stiff silty clay.

Execution

The installation of the diaphragm wall with a thickness of 1,200 mm (4ft) was carried out using a combination of hydraulic grab and trench cutter. For the soft to stiff clays down to a depth of 30 m (98ft) the hydraulic grab was used. The system was then changed to the cutter mode to reach the final depth of 58.5 m (191ft). A specific requirement of trench verticality was defined by 1/600. The layout of the shaft and the used H-Beam joint system is shown in figure 3.

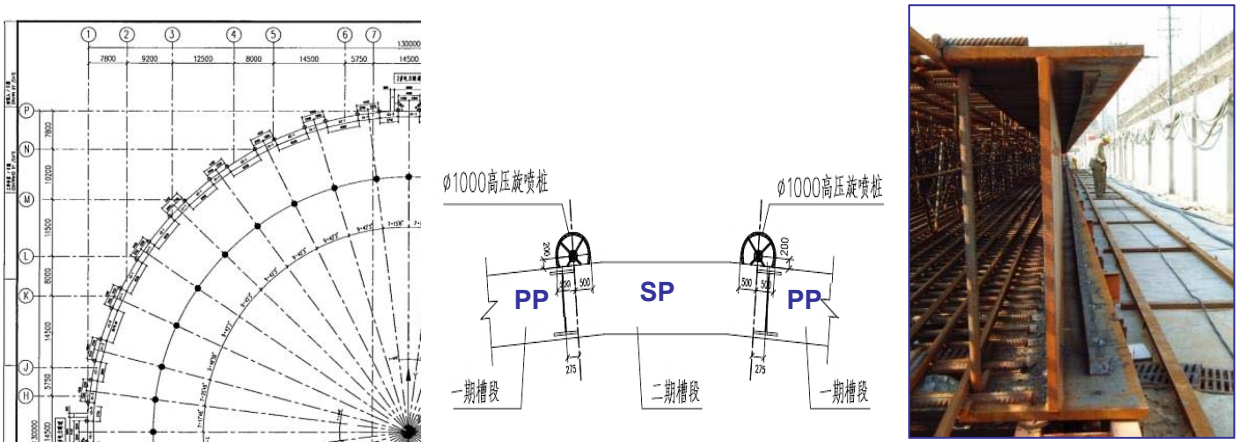


Figure 3: General layout of the shaft (left), detail (centre) and the used H-Beam joint system (right)

Shanghai Tower (2009)

The Shanghai Tower is a 632-meter (2,073ft), 128-story tall skyscraper in Lujiazui, Pudong Shanghai. With Shanghai World Financial Center (height 492 m (1,614ft)) to the east and Jin Mao Tower (height 420 m (1,378ft)) to the north, Shanghai Tower is China's tallest building. Beside the installation of 2,758 piles of various diameters and depths, the project required two diaphragm walls, one for the tower area with a depth of 50 m and one for the podium area with a depth of 48 m. (see figure 4). Both walls had a width of 1,200 mm (4ft) with a total volume of 66,400 m³ (86,848 cubic yards).

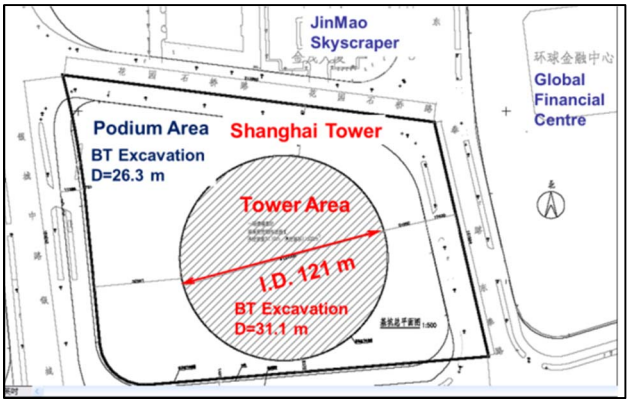


Figure 4: Site layout

Geology

The geology can be described as mainly soft to firm silt and clay down to a depth of approx. 30 m (98ft), followed by hard, sandy silt to a depth of approx. 38 m (125ft). To the final depth of 50 m (164ft) very hard, silty sand was encountered.

Execution

The installation of the diaphragm wall was carried out using a combination of hydraulic grab for the soft to stiff clays down to a depth of 30 m (98ft). The system was then changed to the cutter mode to reach the final depth of 50 m (164ft). A specific requirement of trench verticality was defined by 1/400. As a joint system for the general installation in the tower area a v-steel joint system was used (see figure 5).

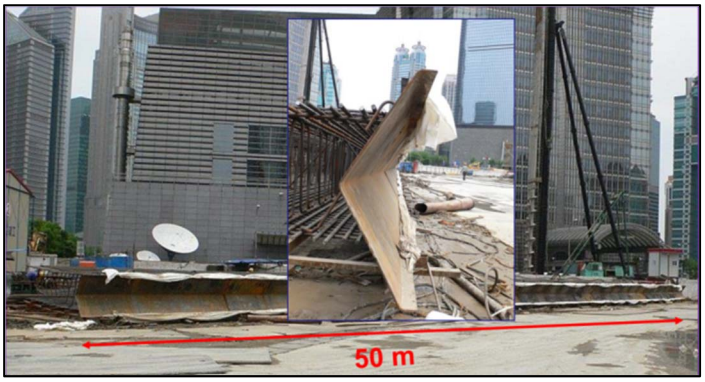


Figure 5: V Steel Plate Joint (Tower area)

In addition, a trial using the Overlap Cutter Joint (OCJ) system was carried out for the first time. Three primary and two secondary test panels were installed to prove the alignment during overcutting was kept as well as to check the influence on performance cutting into a C55 concrete with an overcut of 200 to 295 mm. The layout for the test is shown in figure 6.

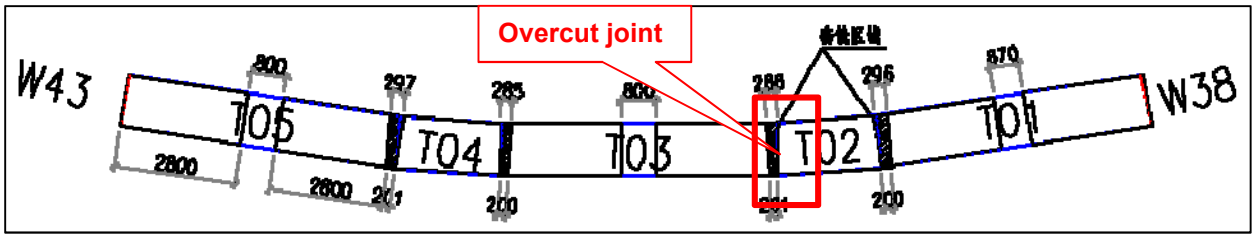


Figure 6: 5 trial panels in Tower Shaft for verifying the Overlap Cutter Joint system

The results of this test showed that the requirements for the trench alignment were fully satisfied in both directions and the performance being 10 -13 m³/h was within a reasonable range.
Figure 7 shows the exposed wall face at excavation depths of 26 m. Dry and watertight.


Figure 7: Dry and watertight excavated joint

The successful test of the OCJ system and the fact that the joint system is in principle without depth limitation opened the door to reach bigger depths.

Shanghai MRT Line 13 Huaihaichonglu Station (2011~2012)

The Huaihaiconglu station is a station on Line 13 of Shanghai Metro. It is the first SMRT diaphragm wall project using Overlap Cutter Joint (OCJ) and a maximum wall depth of 72 m (236ft) was reached.

Geology

The geology could be described as soft to stiff silt and clay down to a depth of 27 m (88ft), followed by very stiff to hard sandy silt to a depth of approx. 37 m (121ft). Underneath it changed to dense to very dense silty sand with SPT values of up to 75 blow count down to 57 m (187ft). After a layer of approx. 10 m (33ft) of stiff silty clay, a very dense to extremely dense silty sand was encountered again to the final depth of 72 m (236ft).

Execution

The installation of the diaphragm wall with a thickness of 1,200 mm (4ft) was carried out using a combination of hydraulic grab and trench cutter. For the primary panels, down to a depth of 30 m (98ft) the hydraulic grab was used. The system was then changed to the cutter mode to reach the final depth. As the Overlap Cutter Joint (OCJ) system was used, the secondary panels were installed by the trench cutter only. A specific trench verticality of 1/400 was required.

Shanghai Zongshan Park Shaft (2016)

The Zongshan Park shaft with a total length of 19.1 km (1..8 miles) (inclusive 8 km (5 miles) underground section located in northern part of Shanghai city centre is part of North Cross Passage Project. It was built for arriving and re-launching of a mega tunnel boring machine with a diameter 15.56 m (51ft). Besides the diaphragm wall to the final depth of 65 m (213ft), 3 test panels with a minimum depth of 110 m (361ft) were constructed: The aim was not only to prove the cutter capacity in cutting deep trenches, but also to provide a detailed study on ultra-deep diaphragm walls for future deep excavation projects in Shanghai. These test panels were included in the general layout of the project (see figure 8).

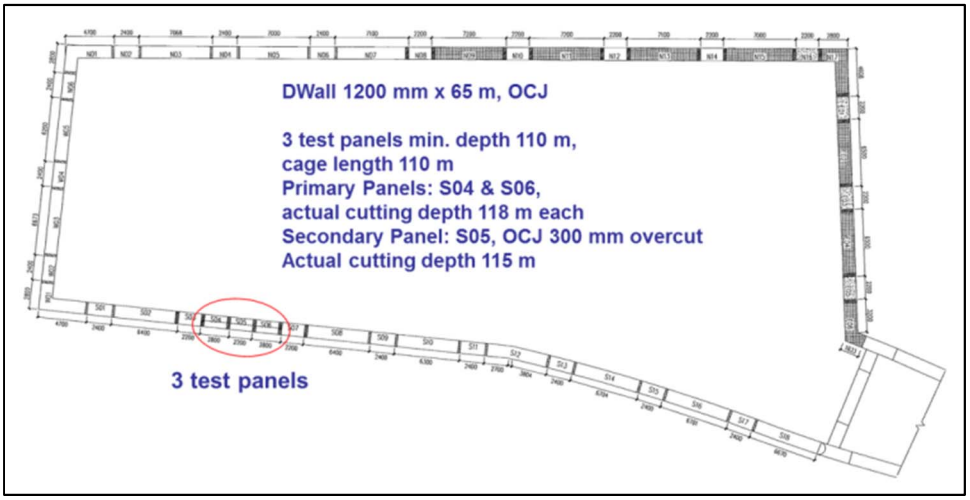


Figure 8: Site layout

Geology

The geology could be described generally as soft to stiff cohesive soils down to a depth of 30 m (98ft). Followed be varying layers of hard, silty clay and dense, silty sands to a depth of 65 m (213ft).
The soil conditions down to the final depth of the test panels can be described as follows: Very dense, fine sand and extremely dense, medium to coarse sands existed for the next 20 m (66ft) followed by varying layers of extremely dense, silty sands and very hard, silty clays.

Execution

The installation of the diaphragm wall was carried out using a combination of hydraulic grab and trench cutter. For the primary panels, down to a depth of 30 m (98ft) the hydraulic grab was used. The system was then changed to the cutter mode to reach the final depth. As the Overlap Cutter Joint (OCJ) system was used, the secondary panels were installed by the trench cutter only.
For the test panels the procedure was slightly changed. Only the upper 5 m (16ft) were excavated using the grab. From there onwards to the final depth the cutter was used to assure trench verticality. A typical Koden record proved the success of the required alignment showing deviations less than 10 cm in both directions (figure 9).

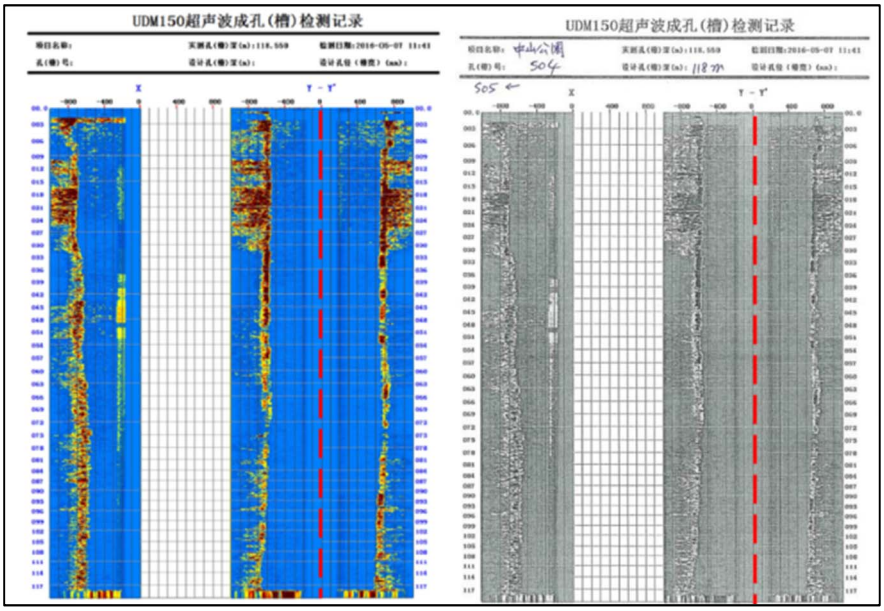


Figure 9: Typial Koden record

Xuhui Center (2017.03-2018.01)

Currently, two new skyscrapers with 43 and 69 floors are under construction in the Xuhui district, the commercial centre of Shanghai. Due to a demanding project programme, Shanghai Foundation deployed 3 units of trench cutters, mounted on duty-cycle cranes equipped with either a BC 40 cutter or a CBC 30 compact cutter for the diaphragm wall work. 393 panels with a total volume of 115,240 m³ (150,728 cubic yards) were installed in a 10-month period.

Geology

The geology was described as soft to stiff, silty clay down to a depth of 47.5m (156ft) followed by a 3 m (10ft) hard layer of sandy silt. To the final depth 75.5 m (248ft) very dense silty sand was encountered.

Execution

The diaphragm wall was split in two different widths and depths using different joint systems. One section was a 1,000 mm (3.3ft) and 1.200 mm (4ft) wide wall to a depth of 58 m (190ft) using a cross steel plate joint (see figure 10). This covered about 20,400 m³ (26,682 cubic yards). The main section with a width of 1,200 mm (4ft) and a depth of 75.5 m (248ft) was carried out using the Overlap Cutter Joint (OCJ) system. This section covered a volume of 94,840 m³ (124,046 cubic yards).

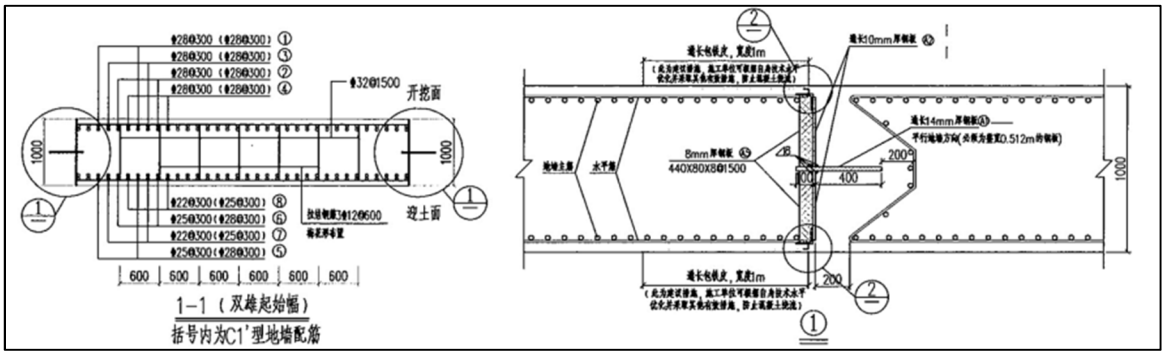


Figure 10: Cross Steel Plate Joint for wall thickness 1,000 mm (3.3ft)/ 1.200 mm (4ft)

Yunlingxi Deep Shaft (2017~2018, under construction)

The Yunlingxi Deep Shaft is part of the Suzhou River "Deep Tunnel" Project in Shanghai. The deep drainage, regulation and storage pipeline is the advanced section of this with a total length of 15.3 km (9.5 miles). Considering lower water surface ratios, higher construction density, complexity of underground pipelines, dense population, high pressure of flood prevention security and other characteristics of the central urban area in Shanghai, the use of large-scale deep regulation and storage tunnels supplemented by run-off control systems are the construction requirements of Shanghai Municipal Government.
This particular shaft requires diaphragm walls with various widths of 1,000 mm (3.3ft), 1,200 mm (4ft) and 1,500 mm (5ft) to a maximum depth of 105 m (344ft) and is presently under construction.
In order to gain not only valuable experience, but to prove the technological feasibility of the construction of diaphragm walls to depths of more than 120 m for future underground projects in the Shanghai area, a test program was defined and carried out. For the first time 3 test panels were cut down to 150 m (492ft) by using the trench cutter only (see figure 11).

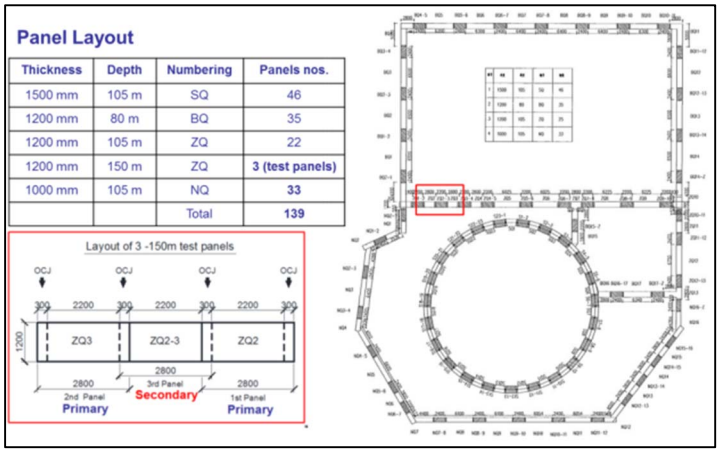


Figure 11: Site layout

Geology

The geology was described as soft to firm, silty clay and clay down to a depth of 35 m (115ft), followed by various layers of stiff to very stiff, silty clay and medium dense, sandy silt to a depth of 65 m (213ft). To approx. 90 m (295ft) dense to very dense sand was encountered. For the following 20 m (65ft) hard clay was found. Very dense sands and very hard clays alternate several times down to a depth of 145 m (476ft). Finally a hard clay layer was found to the final depth of 150 m (492ft).

Execution

The installation of test panels was done with the cutter only after a 3m (10ft) pre-excavation using a backhoe. During their excavation, the three diaphragm wall panels penetrated multiple soil layers – more specifically ten to eleven layers of alluvial and marine sediments, comprising six clayey layers which were sandwiched by five layers of sand deposits (aquifers). As a result, both the stability of the trench and the verticality control of the cutter became key issues during trench construction. Nevertheless, Shanghai Foundation Engineering Group Co. Ltd. successfully completed the construction of these three ultra-deep diaphragm wall panels in January 2018. For the construction of the three panels of 1,200 mm (4ft) x 2,800 mm (9.2ft) and depths of 150 m (492ft), a BC 40 trench cutter on a duty-cycle crane (see figure 12) was deployed. The specific requirement for the alignment of 1/1000 was proven by an ultrasonic probe which showed a maximum vertical trench deviation of less than 15 cm.



Figure 12: Cutter Configuration at final depth

CHALLENGES, LESSONS LEARNED AND OUTLOOK

Shanghai has very soft to soft cohesive soils with SPT values of N < 4 in the upper 20~30 m (65 – 98 ft) below surface. This requires continuous soil improvement like soil mixing to ensure the trench stability during panel excavation, cage installation and concreting. In fact the soil improvement before commencement of trench excavation became a standard procedure adopted for thick and deep d-wall projects, as one panel may take several days for installation.

There are also extremely strict requirements for trench verticality being 1/400 or less. This definitely requires experienced operators and time for trimming has to be considered. To get a clear Koden record when checking the trench alignment, slurry density shall be low. In most cases, hours of desanding is needed before the Koden measurement can be conducted.

It is common practice lifting 40~50 m (131 – 164 ft) long steel cage in one piece. That requires not only two big cranes for handling, but also R.C. working platform with a thickness of min. 300 mm (12 in)

In order to shorten the concreting time contractors nowadays deploy concrete mixers with a capacity of 18 m^3 (23.5 cubic yard) per truck. The diameter of tremie pipes used on site is 305 mm (12 in) and minimum two numbers of sets are used for a big three-bite primary panel.

Besides, logistic issues especially during peak hours are crucial and have to be considered.

In figure 13, a few typical d-wall projects were selected using cutters in Shanghai, The purpose is to show the depths have gone deeper and deeper in the last few years, especially after OCJ has successfully been introduced to Shanghai market. For instance, two ultra-deep projects, Miaopu shaft widths 1,200 mm (4ft) and 1,500 mm (5ft) to a depth of 103 m (338 ft) and Zhangjiang shafts (4 numbers in total) with width 1,200 mm (4ft) to a depth of 90 m (295 ft), just recently started in Shanghai in June and July this year. It can be noticed and anticipated, that the request for deep and ultra-deep d-walls will increase in the future.

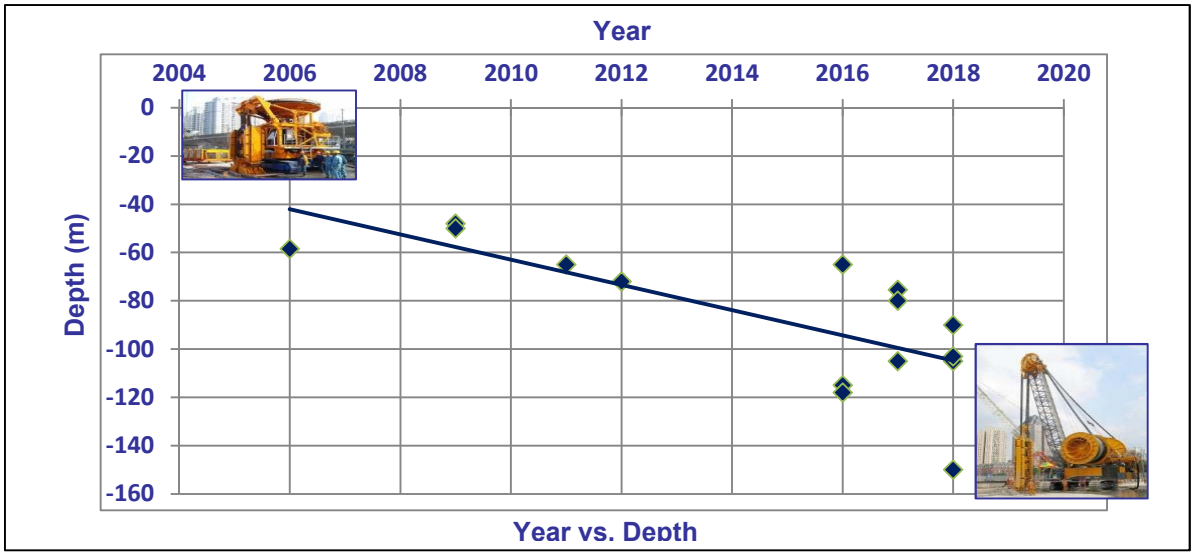


Figure 13: Selected cutter projects in Shanghai – Year vs. Depth

SUMMARY

As there is no rock in Shanghai, one may ask why a cutter is required for diaphragm wall construction. There are some reasons which can be summarized as follows:

- Extremely fast growing infrastructure, like subway flood control and sewage systems. The foundation for skyscraper projects demand deep and ultra-deep diaphragm walls where an excavation depth of more than 100 m (328ft) will be required more frequently.
- Very hard and dense soil layers are encountered, where the SPT values exceed 50 blow counts and rising even up to 200. The use of the grab system is no more practical, especially due to demanding project programmes as well as very tight construction schedules.
- High standard of trench verticality, e.g., 1/400, and long rebar cages with maximum lengths of 50 m (164ft) per section require very straight panels.
- The Overlap Cutter Joint (OCJ) is a simple and easy to handle joint system with almost no depth limitation.
- Trench cutter use becomes preferable as limited working space in city area requires high output, low noise and less vibration of excavation equipment.

Finally it can be said that the cutter technology provides good opportunities to handle the increasing demands of the future.

REFERENCES

Gerressen, F.-W., Neumann, A. 2016: EXECUTION OF DIAPHRAGM AND CUT-OFF-WALLS IN ROCK – APPLICATIONS, PERFORMANCE AND LIMITS, DFI Annual Conference, New York, US, October 2016

WANAPUM DAM REPAIRED USING POST-TENSIONING ANCHORS

Abigail Stein[1], Aled Hughes, P.E.[2], Rick Deschamps, P.E., PhD[3], Brian Barkauskas, P.E.[4]

In central Washington, six miles south of the small town of Vantage, the flow of the Columbia River is harnessed by the Wanapum Dam which is part of the Priest Rapids Hydroelectric Project owned and operated by Grant County Public Utility District (GCPUD). Extending more than 8,300-feet from bank to bank, the dam includes left and right earth embankments, left and right concrete gravity sections and a 10-unit powerhouse. Adjacent to the right embankment is a concrete gravity spillway featuring radial gates measuring 50-feet-wide and nearly 70-feet-high. In the early 1960's when Wanapum Dam was built, these seven-story spillway gates were the highest in the world.

In late February 2014, 50-years into its service life, during a routine maintenance inspection, observant workers noticed a slight misalignment in the roadway deck curbs and handrails located on top of the spillway. Further survey and inspection efforts uncovered a 65-foot-long by two-inch-wide crack that spanned the full length of Monolith 4.

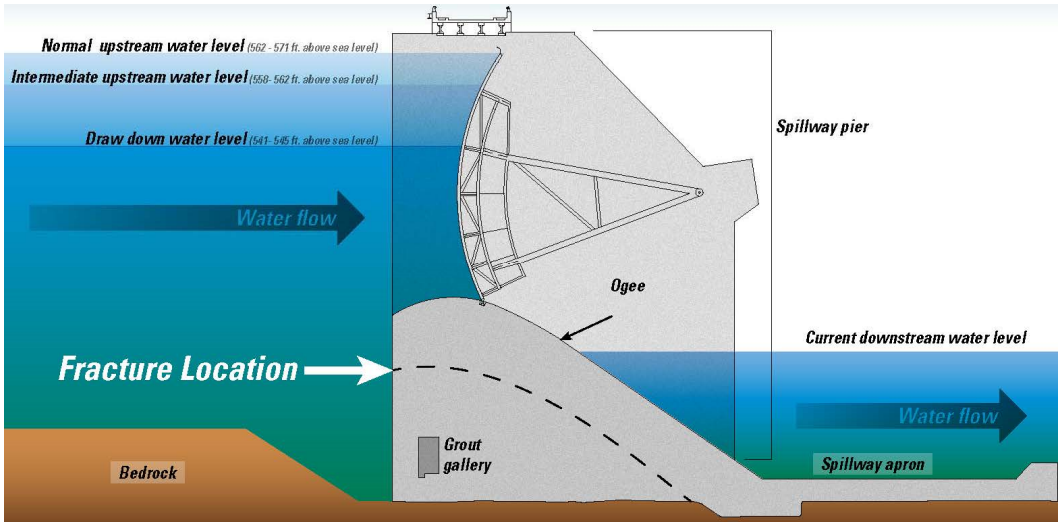


Figure 1: Section through Wanapum Dam highlighting fracture location

On discovering the extent of the damage, GCPUD initiated immediate drawdown of the reservoir to relieve pressure on the spillway monoliths. Wanapum Reservoir and the areas directly downstream of the dam were immediately closed, boat ramps and inlets were left completely dry, campsites were closed and boating activity was banned on the lake until further investigations and remedial procedures were in place and completed. An extensive root cause analysis ultimately led to the conclusion that errors in the initial design calculations and late changes to the final spillway design led to a condition that generated tensile stresses in the concrete at the upstream face, which

[1]Assistant Project Manager, Nicholson Construction, Canonsburg, PA, Email: Abby.Stein@nicholsonconstruction.com
[2]Principal, Civil Engineer - Waterpower and Dams, Stantec, Denver, CO, Email: Aled.Hughes@stantec.com
[3]Vice President of Engineering, Nicholson Construction, Canonsburg, PA, Email: Rick.Deschamps@nicholsonconstruction.com
[4]Business Development Director, Nicholson Construction, Canonsburg, PA, Email: Brian.Barkauskas@nicholsonconstruction.com

© 2018 Deep Foundations Institute

over a period of 50-years resulted in the formation of a crack along a horizontal lift joint located about 85-feet below normal pool elevation. Further analysis showed that, although visible distress was found at Monolith 4, there was nothing preventing this issue from happening at other locations along the dam spillway. Although no visible cracking was found in the other monoliths, repair procedures for Monolith 4 would have to be replicated at the remaining monoliths.

Two-weeks after being awarded the repair project, Nicholson Construction Company (NCC) joined the project team on-site to begin around-the-clock emergency remedial procedures to repair the crack in the dam. The work consisted of a preliminary coring program within the dam to map out the location and propagation of the crack and to assist with establishing the bond length criteria based on bedrock quality, the installation of thirty-five each 61-strand tendon anchors (2,500-kip lock off loads) with lengths up to 260-feet installed through the dam structure, sixty-nine each solid bar anchors installed under water through the ogee spillway and a grouting program to seal the initial cracks in the spillway.

In addition, specific mention will be made to the installation and testing process of the post-tensioned underwater anchors required for remedial repairs on Monolith 4. Two anchor systems were evaluated in part with the accelerated design process due to the emergency nature of the project. Pre-encapsulated solid bar anchors were selected due to complications envisioned with grouting and post-tensioning multiple strand anchors in an underwater environment. Sixty-nine bar anchors were installed through the ogee spillway of which most were installed below water and on the upstream side of the radial gates. Extensive coordination and planning were required to adequately prepare, perform and to install the anchors. Of the techniques employed in performing the emergency repair work on the spillway, drilling and installation of the underwater anchors proved to be the most challenging. The process required innovative construction techniques and extensive pre-planning by the drillers, divers, engineers and project management team. Rehearsals were conducted, in the dry, on a full-scale mock-up of an underwater anchor installation along with the grouting, load testing, anchor lock-off and completion.

Drilling and installing anchors were performed from work platforms, suspended 80-feet above the surface of the ogee spillway using specialized tooling for drilling the boreholes and recessed sockets 50-feet below water. Significant consideration was given to environmental concerns. To prevent grout fluid loss into the water specialized packers designed to seal around the bar anchor were used. Throughout the process a collaborative approach with the various project teams fostered creative solutions to overcome unique challenges in design and construction to successfully complete the underwater anchors.

This case history paper and presentation will highlight in more detail the intricacies of the overall repair procedures and the collaborative efforts of the project team that ultimately resulted in a successful project.

CENTRIFUGE MODELING OF TEMPERATURE EFFECTS ON THE PULLOUT CAPACITY OF ENERGY PILES IN CLAY

Ismaail Ghaaowd, M.S., Ph.D. Candidate, University of California San Diego
John S. McCartney, Ph.D., P.E., Associate Professor, University of California San Diego

ABSTRACT

This study presents the results from centrifuge modeling experiments performed to understand the effects of temperature changes on the pullout capacity of scale-model energy piles embedded in normally-consolidated clay layers. The energy pile under investigation is an aluminum cylinder instrumented with internal strain gages and thermocouples, and its temperature is controlled using an internal electrical resistance heater. The energy pile was first heated until the temperature, pore water pressure, and volume change of the surrounding clay layer stabilized, after which the energy pile was cooled. Pullout tests were then performed on the energy piles heated to different temperatures to understand the effects of the preceding heating-cooling cycle on the pullout capacity. In addition, the clay undrained shear strength profiles were measured using push-pull T-bar penetration tests before and after heating.

Keywords: soft clay, energy pile, pullout capacity, undrained shear strength

INTRODUCTION

When a heat source such as an energy pile is embedded in a saturated clay layer, temperature changes will result in changes in pore water pressure as the rate of heating is typically faster than the rate of pore water drainage (Campanella & Mitchell 1968, Abuel-Naga et al. 2007, and Ghaaowd et al. 2016). Although all soils will initially expand during undrained heating, normally consolidated soils typically exhibit permanent contraction while overconsolidated soils exhibit expansion after sustained heating when drainage is allowed (Vega & McCartney 2015). Subsequent drained cooling typically leads to elastic contraction. Thermally-induced changes in pore water pressure and volume during transient heating and cooling may affect the soil-structure interaction of energy piles, as well as the ultimate capacity of the energy pile. This study is relevant as relatively few studies have been performed on the behavior of energy piles in soft clay (e.g., Ng et al. 2014), with most focused on the behavior of drilled shaft energy piles in stiff rock or overconsolidated clays (e.g., Laloui et al. 2006; Murphy et al. 2015; Wang et al. 2015; McCartney and Murphy 2017).

This study uses a centrifuge modeling approach developed by Ghaaowd et al. (2018) to evaluate the effects of drained heating-cooling cycles on energy piles embedded in soft clay layers. Centrifuge modeling was used in this study because the pore water pressure generation during undrained heating is sensitive to the initial mean effective stress in the clay layer, and the effective stresses in a centrifuge model clay layer are similar to those in a prototype clay layer. The Actidyne C61-3 centrifuge at the University of California San Diego was used to perform three tests on energy piles in separate soil layers. The first and second tests involved installation of energy piles into clay layers using jacked-in procedures (i.e., insertion at a constant displacement rate), heating to a target temperature (the first energy pile was heated to 63 °C and the second energy pile was heated to 44 °C), cooling back to ambient temperature, and finally pullout of the energy piles at a constant rate. The third test involved installation of a baseline energy pile using similar procedures to the other tests without heating followed by pullout at a constant rate after reaching equilibrium. In addition to presentation of the pullout versus displacement curves for the three tests, T-bar penetration results permit evaluation of the impact of heating and cooling on the undrained shear strength profiles in the three clay layers. Representative time series from the different tests were presented by Ghaaowd et al. (2018).

© 2018 Deep Foundations Institute

Materials

Kaolinite Clay

The soil used in the experiments was commercially-available Kaolinite clay from M&M Clays Inc. of McIntyre, Georgia whose geotechnical properties of the clay are summarized in Table 1. The clay classifies as CL according to the Unified Soil Classification Scheme. An isotropic compression test indicates that the slopes of the normal compression line (λ) and the recompression line (κ) for the clay are 0.100 and 0.016, respectively. The clay specimens were formed from a slurry to reach initially normally consolidated conditions as will be described below.

Table 1. Properties of the Kaolinite clay and initial conditions of the specimen used in this study.

Liquid limit	47%
Plastic limit	28%
Plasticity index	19
Specific gravity	2.6

Experimental Setup

Scale-Model Energy Pile

The scale-model energy pile is a 25 mm-diameter, 255 mm-long, split-shell aluminum cylinder having a wall thickness of 3.3 mm, as shown in the schematics in Figure 1. At 50 g, the model pile corresponds to a prototype pile having a diameter of 1.25 m and a length of 12.75 m. Although the length:diameter ratio of the model pile is 10, which is smaller than the ratio of 25 typical of most reinforced concrete energy piles (Bourne-Webb 2013), the model energy pile still represents short piles jacked or driven into place through soft soils. The insides of the cylinder halves were instrumented with five temperature-compensated strain gages and thermocouples at the locations shown in Figure 1(b). The halves are held together by screw-on top and bottom caps. An internal electrical resistance heater running the length of the energy pile is connected to the top cap, and heat is conducted from the heater to the outside of the pile through a sand fill. The top cap of the pile was fabricated from Delrin to minimize heating of the water ponded on the soil surface, and all wiring passes through the top cap. Pictures of the energy pile are shown in Figure 2.

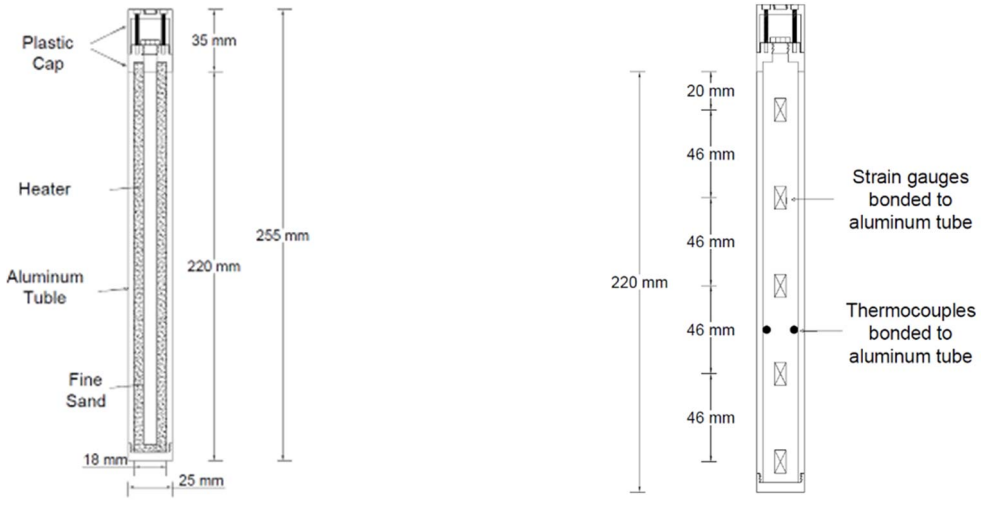


Figure 1. Schematics of the centrifuge-scale energy pile: (a) Cross-section showing central heating element; (b) Cross-section showing internal instrumentation locations.

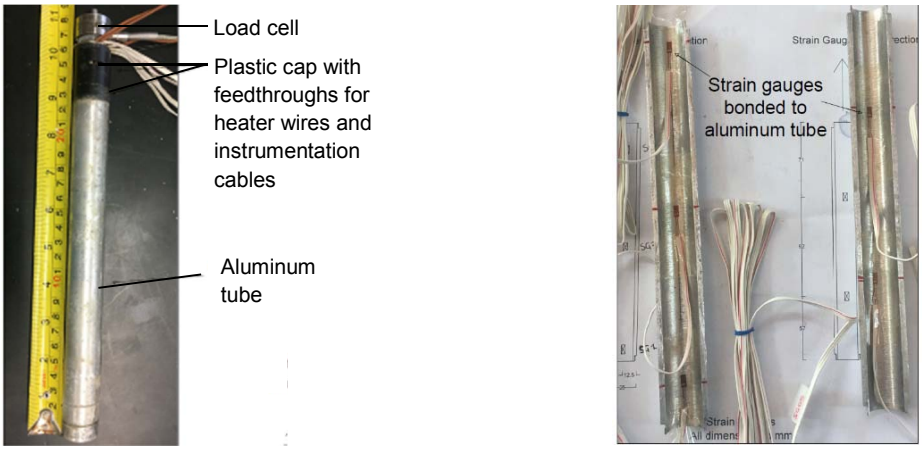


Figure 2. Pictures of the centrifuge-scale energy pile: (a) Assembled energy pile; (b) Picture of the inside of the energy pile with strain gages bonded to the aluminum tube.

Centrifuge Container

A schematic of the container used in this study to evaluate temperature effects on the pullout capacity of energy piles in clay is shown in Figure 3. The aluminum container consists of a base plate, a cylindrical tank, and an upper reaction plate. The base and reaction plates of the container have dimensions of 0.62 m × 0.62 m × 0.05 m. The cylindrical tank has an inside diameter of 0.55 m, a wall thickness of 16 mm, and a height of 0.47 m, and was connected to the base plate via four threaded rods atop an "O"-ring seal. The top reaction plate was connected to the top ends of the same threaded rods. The reaction plate supports stepper motors for loading the energy pile and T-bar, as well as linearly variable differential transformers (LVDTs) to monitor soil surface settlement and energy pile head movement.

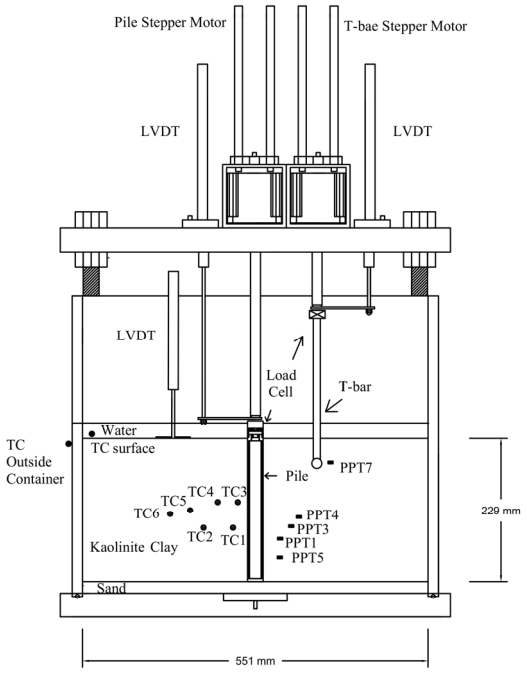


Figure 3. Cross-section of the setup using the three experiments showing the energy pile, T-bar, thermocouples (TC), and pore water pressure transducers (PPT).

Experimental Procedures

Dry kaolinite clay was mixed with water under vacuum to form a slurry having a gravimetric water content of 130%. The slurry was carefully poured into the container to avoid air inclusions. The clay layer was drained from the bottom via a sand layer having a thickness of 20 mm thickness and from the top via a filter paper and a 50 mm-thick porous stone placed on the top of the slurry. After 24 hours of self-weight consolidation, dead-weights applying vertical stresses of 2.4, 6.3, 10.2 kPa were added atop the porous stone in 24-hour increments. The surcharge was then increased to 23.6 kPa using a hydraulic piston reacting against the top reaction plate of the container and was maintained for another 24 hours. The container was placed inside the centrifuge basket for in-flight self-weight consolidation at 50 g. This procedure was found to produce a normally-consolidated clay layer with an overconsolidated portion near the surface. After the 1g consolidation of the clay layers was completed, six thermocouples and five miniature pore water pressure sensors were inserted through the container side wall into the clay layer at the locations shown in Figure 3. During in-flight self-weight consolidation at 50 g, the excess pore-water pressures were monitored using the pore pressure transducers and the surface settlement was monitored. A typical time series of the pore water pressure during centrifugation was presented by Ghaaowd et al. (2018) that confirms that the clay layer reached more than 90% of the primary consolidation before moving to the next testing stage. The gravimetric water content of the clay layer with the unheated pile measured at the end of testing ranged from 38.5 to 52%, while the void ratio ranged from 1.0 to 1.35. These values can be assumed to correspond to the initial conditions for the energy piles before application of the heating and cooling cycles. Because the positions of the sensors may change after consolidation in the centrifuge, the final positions of the sensors were verified at the end of the experiment by excavating the clay layer.

After the additional consolidation of the clay layer during centrifuge at 50 g, the energy piles were installed in flight using a stepper motor into the sedimented clay layers having a thickness of 228 mm at a model-scale velocity of 0.1 mm/s until the pile tip reached the dense sand layer. The energy pile was inserted so that the aluminum portion was embedded in the clay and the plastic top cap was above the clay surface, with a prototype-scale embedment below the clay surface of approximately 11 m. The piles were loaded to a prototype-scale compressive load of 1445 kN, which is expected to mobilize most of the side shear resistance and a fraction of the end bearing. The stepper motor movement was controlled using a LabVIEW program capable of applying both constant-displacement conditions as well as constant axial head loads (i.e., to simulate the dead weight of an overlying structure), and the applied axial head load was measured using a load cell. When the excess pore water pressure generated due to the pile insertion dissipated, the temperature of the heated energy pile was increased using the Watlow heat controller until reaching the target temperature at the pile wall. Heating continued during centrifugation until the soil temperature and pore water pressure stabilized. After reaching equilibrium during heating, which required approximately 30 hours for the heat tests, the pile was cooled and was then pulled out at the same speed used for installation.

A T-bar with a diameter of 14 mm and length of 57 mm was used to measure the undrained shear strength profiles of the clay layers containing heated and unheated energy piles. Insertion of the T-bar into the clay layer can be used to infer the undrained shear strength of the intact clay layer as a function of depth, while extraction of the T-bar can be used to infer the undrained shear strength of disturbed clay as a function of depth (Stewart & Randolph 1994). The T-bar was designed to permit model-scale penetrations up to 230 mm and was driven by a second stepper motor at a model-scale velocity of 0.2 mm/s to ensure undrained conditions during insertion and extraction. T-bar penetration tests were executed in each clay layer at a radius of 100 mm from the heated and unheated energy piles, which is far enough away to be undisturbed from the pile insertion and extraction but close enough to be influenced by temperature.

T-BAR MEASUREMENTS AND INTERPRETATION

The T-bar penetration results for the clay layers with unheated and heated energy piles permit evaluation of the effects of cyclic heating-cooling to different temperatures on the behavior of normally consolidated clay layers. The undrained shear strength profiles for the clay layer at a model-scale distance of 100 mm from the three energy piles are shown in Figure 4. The correlations of Stewart & Randolph (1991) were used to interpret the undrained shear strength profiles from the T-bar penetration results. The pile temperatures are shown in Figure 4, but these do not correspond to the temperatures at the location of the T-bar penetration tests. When heating the energy pile to 63 °C, the soil temperature at the location of the T-bar increased by 10.5 C, and when heating the energy pile to 44 C, the soil temperature increased by 4 °C. The initial T-bar position is slightly below the clay surface to maximize the stroke of the T-bar test, so the undrained shear strength near the surface of the clay layer was not characterized. The undrained shear strength profiles indicate that a drained heating-cooling cycle leads to an increase in undrained shear strength of the clay layer, and that heating the energy pile to higher temperatures leads to a greater improvement. Greater differences in undrained shear strength were observed deeper in the clay layer, which may be because the thermally induced excess pore water pressures were greater at these depths (Ghaaowd et al. 2018). The void ratios inferred from gravimetric water content samples at the end of the tests are shown in Figure 5. Lower void ratios are observed in the clay layers that experienced higher temperatures, which correspond well with the increases in the undrained shear strength with temperature inferred from the T-bar penetration tests.

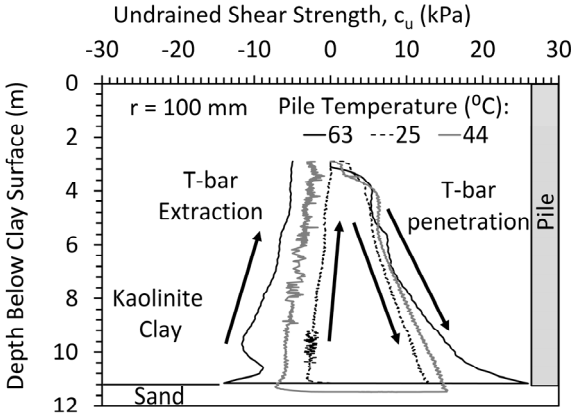


Figure 4. Undrained shear strength profiles measured by the T-bar in the three tests (positive values for insertion and negative values for extraction)

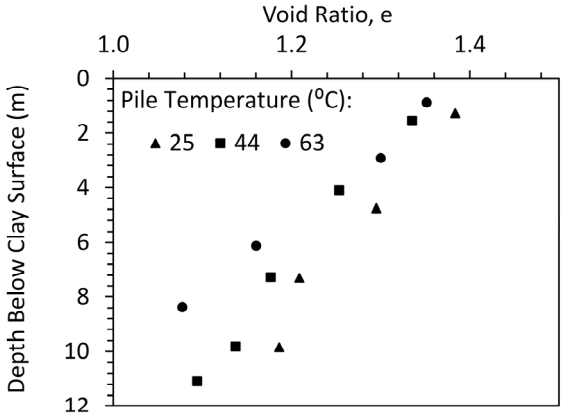


Figure 5. Void ratio profiles at the end of testing at a model-scale distance of 100 mm from the energy piles

PULLOUT CAPACITY MEASUREMENTS AND INTERPRETATION

The pullout load versus displacement curves for the heated and unheated energy piles in clay layers having similar initial conditions are shown in Figure 6(a). All three pullout curves start from an initial compressive seating load of 1445 kN. A clear increase in pullout capacity is observed with an increase in the temperature that the energy piles experienced during the heating stage. The net percent increase in pullout capacity versus the change in pile temperature is shown in Figure 6(b), indicating that the increase in pullout capacity may be approximately linear. The heated energy pile at 63 °C had a net pullout capacity of -723 kN that is approximately 95% greater than that of the unheated energy pile that had a net pullout capacity of -370 kN. The net pullout capacity for the energy pile heated at 45 °C was -520 kN which is approximately 40% greater than that of the unheated energy pile. These increases in net pullout capacity confirms that the drained heating-cooling cycle in the clay layer leads to substantial improvements in the undrained shear strength of the clay surrounding the heated energy pile, resulting in an improvement in soil-pile interaction. An unexpected observation in Figure 6(a) is that the slopes of the pullout curves are similar. It was expected that the increase in undrained shear strength of the clay layer with temperature would also correspond to an increase in stiffness. The similar slopes in Figure 6(a) may have occurred because the heated aluminum energy piles experienced thermal axial strains in the direction opposite to the downward seating load during heating that may have counteracted the positive effect of the thermal improvement of the soil layer. During pullout, the piles were likely following an elastic loading-unloading curve until shortly before failure.

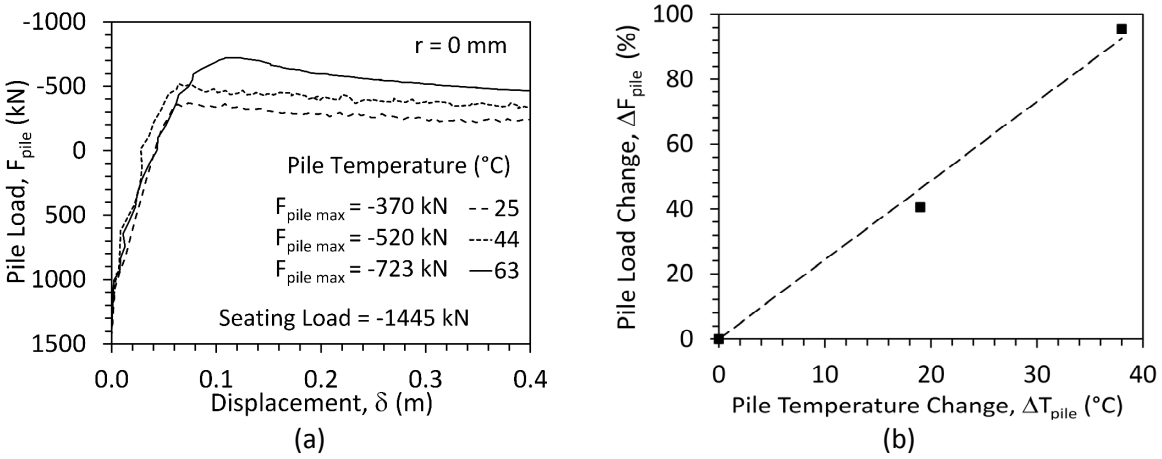


Figure 6: (a) Pullout-displacement curves for energy piles in prototype scale at different temperatures, (b) Pile load change versus pile temperature change

CONCLUSION

Heated and unheated scale-model aluminum energy piles were tested to evaluate the impacts of temperature on the normally consolidated clay layer and on the corresponding pullout capacity of the energy pile. The following specific conclusions can be drawn:

- The undrained shear strength of the clay surrounding the heated-cooled energy piles was greater than that of the clay surrounding the unheated energy pile, with greater increases in undrained shear strength deeper in the soil layer.
- The pullout capacities of the energy piles that had experienced greater changes in temperature were greater than that of the unheated energy pile. The slope of the pullout load versus displacement curves were similar, which may be due to the impact of upward displacements due to thermal expansion of the energy pile prior to pullout, leading to an initially elastic pullout response for all of the energy piles.

REFERENCES

Abuel-Naga, H.M., Bergado, D.T., & Bouazza, A. 2007. "Thermally induced volume change and excess pore water pressure of soft Bangkok clay." Engineering Geology. 89, 144-154.

Bourne-Webb, P.J. 2013. "An overview of observed thermal and thermo-mechanical response of piled energy foundations." European Geothermal Congress. 1-8.

Campanella, R.G. & Mitchell, J.K. 1968. "Influence of temperature variations on soil behavior." Journal of the Soil Mechanics and Foundation Division, 94(SM3), 709-734.

Ghaaowd, I., Takai, A., Katsumi, T., & McCartney, J.S. 2016. "Pore water pressure prediction for undrained heating of soils." Environmental Geotechnics. 4(2): 70-78.

Ghaaowd, I., McCartney, J.S., Huang, X., Saboya, F., & Tibana, S. 2018. "Issues with centrifuge modeling of energy piles in soft clays." 9th International Conference on Physical Modelling in Geotechnics. London. Jul. 17-20. 1-6.

Laloui, L., Nuth, M., & Vulliet, L. 2006. "Experimental and numerical investigations of the behaviour of a heat exchanger pile." Int. J. Numer. Anal. Methods Geomech., 30(8), 763–781.

McCartney, J.S. & Murphy, K.D. 2017. "Investigation of potential dragdown/uplift effects on energy piles." Geomechanics for Energy and the Environment. 10(June): 21-28.

Murphy, K.D., McCartney, J.S., & Henry, K.S. 2015. "Evaluation of thermo-mechanical and thermal behaviorbehaviour of full-scale energy foundations." Acta Geotechnica, 10(2): 179–195.

Ng, C.W.W., Shi, C., Gunawan, A., & Laloui, L. 2014. "Centrifuge modelling of energy piles subjected to heating and cooling cycles in clay." Géotechnique Letters 4: 310–316.

Stewart, D. & Randolph, M. 1994. T-Bar penetration testing in soft clay. Journal of the Geotechnical Engineering Division. ASCE. 120(12): 2230-2235.

Vega, A. & McCartney, J.S. 2015. "Cyclic heating effects on thermal volume change of silt." Environmental Geotechnics. 2(5): 257-268.

Wang, B., Bouazza, A., Singh, R., Haberfield, C., Barry-Macaulay, D., & Baycan, S. 2014. "Post-temperature effects on shaft capacity of a full-scale geothermal energy pile." Journal of Geotechnical and Geoenvironmental Engineering. 04014125.

DESIGN APPROACHES FOR EXTERNALLY SUPPORTED EARTH RETAINING SYSTEMS – DETAILS AND LIMITATIONS

Matteo Montesi, PE, WSP, 401 B Street, Suite 1650, San Diego, CA, +1 619-849-5429,
Matteo.Montesi@wsp.com

ABSTRACT

Deep foundation elements are often used as discrete elements in externally supported earth retaining structures such as soldier piles and lagging walls, secant/tangent pile walls, anchored walls, etc. These structures can be designed using different approaches such as conventional limit equilibrium methods, finite element/difference analyses, and soil spring (p-y) analyses which are contained in various commercially available computer programs used by engineers worldwide. Although these programs usually undergo various degree of verification and validation, users must be aware of each program's limitations and conditions in which each design approach should or should not be used. These programs may incur difficulties when non-continuous deep foundation elements are used as part of the retaining system and in cases of non-uniform geometry where closed-form solutions are not available. Design input parameters such as passive arching width, wall-to-soil friction, and p-multipliers (pm) are not always given enough attention which may result in potential design deficiencies. This paper presents the main features of various earth retaining structure design approaches and discusses their advantages/disadvantages. The paper addresses some of the limitations and difficulties that may be faced with when utilizing non-continuous discrete deep foundation elements and identifies key elements that are sources of potential deficiencies and errors. An example comparing the design outcomes using different design approaches is presented.

Keywords: earth retaining systems, p-y analyses, deep foundations, limit equilibrium, finite elements, finite differences.

INTRODUCTION

Earth retaining structures are used to retain soil and create or maintain a difference in ground elevation between grades in front and behind the retaining structure. Deep foundation elements have been used for decades to support earth retaining structures. Earth retaining structures that are supported by deep foundation elements are typically referred to as externally stabilized system (O'Rourke and Jones, 1990). An externally stabilized system uses an external structural element, in contrast to internally stabilized systems which rely on reinforcements installed within and extending beyond the potential failure mass.

The design of externally supported retaining structures can be accomplished using different approaches, which can be challenging under certain conditions. Each approach has been discussed extensively in available literature, and is well summarized in the and Federal Highway Administration (FHWA) guidelines. The objective of this paper is to present the most widely used design approaches and discuss their limitations and difficulties in one concise and brief document, giving the reader a good source for comprehensive understanding of the various design approaches, supported by a technical example. This paper is not intended to be a comprehensive review of all available design methods and formulations available in the literature.

DETERMINATION OF EARTH PRESSURES

A critical component of every externally supported retaining wall design is the determination of lateral earth pressures. Nowadays, there are several computer programs available to design engineers which can compute lateral earth pressures quickly and for almost any given geometry. The importance and support

© 2018 Deep Foundations Institute

that these programs brought to the engineering community must be acknowledged. However, in the author's experience, none of these programs is so robust to be applicable to every scenario that the design engineer might face without a proper and careful evaluation of the conditions in which the program is to be used. As such, a necessary step required when designing earth retaining structures is the determination of lateral earth pressures. This is a necessary step regardless of what design approach is chosen and what computer program is used.

As discussed in the following sections, the limit equilibrium methods make direct use of the active and passive pressures by utilizing them to compute force and/or moment equilibrium and determine the required design outputs. As such, the determination of lateral earth pressures is obviously a critical and necessary step which must be performed prior to performing the design calculations. Soil Spring (p-y) analyses involve a larger computational effort, and computer programs (such as LPILE, PYWALL, RSPILE, etc.) are typically used. In such programs, determining the lateral earth pressures is still a necessary step to validate the program inputs and calculations. Similarly, when using finite element or finite difference methods, it is also important to determine the lateral earth pressure to identify potential issues in the models.

The determination of lateral earth pressures is discussed in numerous geotechnical textbooks and applicable industry codes. In the transportation industry, the American Association of State Highway and Transportation Officials (AASHTO) and Federal Highway Administration (FHWA) guidelines are most commonly used as design guidelines and references. The latest FHWA publication specifically on Earth Retaining Structures is dated December 2007, and titled NHI-07-071 "Earth Retaining Structures". The latest "AASHTO LRFD Bridge Design Specification", 8th editions (September 2017) includes a detailed discussion of determination of lateral earth pressures. Active pressures are typically computed by using either the Rankine or Coulomb earth pressure theories. The equivalent fluid method can also be used for free drainage materials where Rankine earth pressure theory is applicable. For complex geometries, the generalized trial wedge method is recommended for computing the active pressures. Passive pressures can generally be computed with the same methods. However, a logarithmic spiral failure surface is often considered when computing the passive pressure, as wedge solutions (such as Coulomb) are inaccurate and unconservative for larger values of wall friction angles.

Rankine Earth Pressures

The Rankine state considers the condition of limit equilibrium under the geostatic state of stress, which occurs with a horizontal surface and no shear stresses on horizontal and vertical surfaces. Under these conditions, the horizontal stress is decreased or increased until reaching failure. The horizontal stresses for these conditions are called the active and passive stresses, and the ratios of horizontal to vertical stresses are called coefficient of active and passive pressures, respectively (k_a and k_p). The states of stress at these two extreme conditions are called Rankine states, after the British Engineer Rankine who discovered this relationship in 1857. Through Mohr circles, it can be shown that the failure planes are inclined by an angle of 45 degrees plus or minus half of the soil friction angle. The equations for calculating the Rankine Active and Passive coefficient are well known, and the resulting K_a and K_p values are tabulated or presented through graphs in many sources.

Coulomb Earth Pressures

In reality, the backface of retaining walls is always rough to some extent, and therefore The Rankine earth pressure theory is no longer applicable. Coulomb (1776) introduced two additional factors in the computation of lateral earth pressures, which are the wall to soil friction angle and the back-face wall inclination. When these two factors are zero, Rankine's conditions are verified, and the two approaches yield the same results. A key assumption in the Coulomb earth pressure theory is that the failure surface is planar. However, the surface of sliding is curved to some extent. To simplify the computations, Coulomb assumed it to be planar. This carries some error, which is in most cases small and negligible. Unless a

wall is settling, friction on its back acts upward on the active wedge, reducing the active earth pressures, while it generally acts downward on the passive wedge, increasing the passive earth pressures. For active earth pressure coefficients, a wall friction value of 2/3 of the soil friction angle has often been used in practice, while other references (such as Das, 2014) suggest a range of 1/2 to 2/3. For passive earth pressure coefficients, it is important to recognize that the passive earth pressures increase very quickly with increasing wall to soil friction angle. However, if the wall to soil friction angle is greater than 1/3 of the soil friction angle the failure surface becomes strongly curved. As such, the error carried with the Coulomb simplification of planar wedge becomes significant and on the unconservative side, and a method accounting for the curvature of the sliding surface (Caquot and Kerisel,1948, or generalized trial wedge method) should be used. The designer should assess the sensitivity of the design to different values of the wall to soil friction angle.

Los-spiral Earth Pressures

Based on the above discussion the wall to soil friction angle affects the magnitude of the earth pressures. The wall friction also affects the shape of the failure surface. When the friction value is realtively low the failure wedge is nearly linear, and Coulomb theory is applicable. For larger wall friction values, and especially when calculating passive pressures, the curvature of the failure surface becomes strongly non-linear. In these cases, it is recommended that the log-spiral theory be used for determination of the earth pressure coefficients. Caquot and Kerisel (1948) charts are based on the log-spiral theory, and are included in the latest AASHTO LRFD Bridge Design Specifications (2017), and provide values of active and passive earth pressure coefficient under ranges of values of soil friction angle, wall to soil friction angle, and considering a logarithmic spiral sliding surface.

General Trial Wedge Method

The generalized trial wedge method involves solving force equilibrium equations for several trial wedges at discrete intervals along the wall. By analyzing several wedges, the critical ones resulting in the largest force (active condition) or the smallest force (passive condition) can be identified, and used to compute the lateral earth pressures. This procedure is repeated at discrete intervals along the wall, so that incremental lateral forces can be computed. The lateral earth pressure distribution can then be obtained through derivatives of the incremental forces. This method is well suited for irregular ground or surcharge geometries, or in rare cases where the layer contacts are not horizontal. It is also used when it is desired to include the adhesion between wall and soil. The generalized trial wedge method requires significantly more calculation efforts than all the other methods presented, and it is available in various computer programs (Shoring, DeepEx, CWALSHT).

DESIGN APPROACHES

Earth retaining structures can be design with different approaches, which can be grouped into three different categories:

1) Limit equilibrium methods
2) Soil spring (p-y) methods
3) Finite element or finite different methods

Design of externally supported retaining walls typically follows one or more of the approaches listed above. The next sections describe the details, limitations, advantages and disadvantages of each approach.

Limit equilibrium methods

Limit equilibrium methods (LE) are, historically speaking, the most widely used methods to design externally supported earth retaining structures (and earth retaining structures in general). In fact, earth retaining structures have been designed for decades using these methods, especially before the development of sophisticated computer programs that can simplify and perform calculations which would otherwise require a significant amount of time. The large number of retaining structures built over time

and designed with these methods have proven them to be very reliable if applied correctly.

The fundamental principle on which limit equilibrium methods are based is that the soil masses in front and behind the wall have reached a "limit equilibrium" state, in which the determination of the earth pressures is well known from the available earth pressure theories. The limit equilibrium methods calculate the embedment necessary to achieve force and moment equilibrium, and then apply a factor of safety depending on the nature of the analysis (permanent, temporary, seismic). The limit equilibrium methods are the simplest methods from a computational perspective.

Details and Limitations

When dealing with cantilever structures, it is important to note that there are mainly two limit equilibrium methods commonly used. The first one, referred to as the "Simplified Method", assumes a simplified earth pressure distribution, consisting of full active pressures on retained side and full passive pressures on the opposite side. The idea behind this approach is to simplify the calculations and determine the required embedment to achieve moment equilibrium. The actual force and moment equilibrium is then achieved by adding a 20% embedment to the calculated embedment required to obtain moment equilibrium. However, the FS of the system remains 1.0 when adding this 20% factor. The more comprehensive method, known as "Conventional Method", includes the rotation point where active and passive pressures reverse sides, and computes the required embedment to achieve moment and force equilibrium. Therefore, this calculated embedment has already a FS of 1.0. This is often source of confusion, especially since computer programs can use any of the two different methods, and some already add the 20% increase by default while others do not. It is imperative that the user knows the details of the two methods and how they are implemented in the program used.

Another key element is the arching width for the passive resistance offered by soldier piles. Active pressures are applied to the soldier pile width (pile diameter) but passive pressures are computed over a larger width due to arching of the soil. There are guidelines available to estimate the arching width, which typically varies from 2 to 3 times the pile diameter depending on the soil type and construction methods. The arching width is often computed automatically by computer programs. However, two conditions must be given special attention. In cases where the piles spacing is lower than 3D, the arching width must always be limited to the pile spacing. This might seem an obvious statement, but it has been found to be a source of errors often. The second condition is when the structural elements spanning the piles (for example sheeting) are driven deeper than the excavation subgrade. This situation needs to be handled with caution, as ignoring the additional length of sheeting driven below the excavation is not always conservative. In fact, the additional length will provide some additional active and passive pressure, both applied to a width equal to the pile spacing. Active and passive pressures are a function of the lateral earth pressure coefficients but also of the vertical effective stresses. While passive earth pressure coefficients are much larger than active coefficients, the overburden on the retained side is far greater than the one on the passive side. The balance between the two needs to be determined each time.

The wall to soil friction angle value is also often a source of debate. The applicability of it has been discussed in previous sections, and will not be repeated herein. However, it is an item to be listed as a difficulty and source of errors in the design with limit equilibrium methods. The wall to soil adhesion is rarely used in design, and most computer programs cannot include that in the design. Should the designer wish to account for wall adhesion, a generalized trial wedge method can be used to account for wall adhesion. The program CWALSHT has the capability to handle adhesion, but it must be noted that CWALSHT was developed by the US Army Corps of Engineers in the 1990s, and it has not been updated in recent years. This implies a lack of updates as well as potential compatibility issues with today's computers.

One of the main limitations of the limit equilibrium methods is that they do not account for soil-structure

interaction. As such, their results are typically conservative, and the displacements calculated are not very reliable (purely based on structural calculations and dependent on boundary conditions). The other limitation is that these methods assume full development of active and passive pressures. However, the development of these pressures is a function of the wall displacement, which is not captured in limit equilibrium analyses. Furthermore, since lateral earth pressures must be calculated prior to performing the analyses, these are often computed with simple methods, such as with Rankine or Coulomb equations. The applicability of these methods should be carefully verified, and in cases such as irregular geometries, or irregular contacts between layers, other methods (such as trial wedge analyses) for calculating lateral earth pressures should be considered, or other design approaches (such as finite elements, finite differences) should be used.

Vertical surcharges are often accounted for with the theory of elasticity. Different methods are available in computer programs, which can also yield different results. The flexibility of the wall is often accounted for by multiplying the surcharge by a factor varying between 1.0 and 2.0. Alternatively, trial wedge analyses can be performed with and without the vertical surcharge to study the impact of the surcharge.

Soil spring (p-y) methods

Soil pring (p-y) methods solve the equations governing the mechanics of beams resting on elastic springs assuming that the soil mass is replaced by a finite number of springs. Each spring is characterized by a force vs. displacement relationship, typically nonlinear and a function of the soil type, soil parameters, effective stress and pile diameter. The computational efforts for this method are such that computer programs (such as LPILE, PYWALL, RSPILE) are often if not always used to solve these equations. In general, active pressures above the excavation depth are input in the programs as loads. Since active pressures are mobilized with relatively small wall displacements, using full active pressures above the excavation subgrade is typically a reasonable assumption. Programs then solve equations governing the behavior of beams on elastic springs to compute bending moment diagrams and lateral wall displacements.

Details and Limitations

The biggest challenge using these methods is related to the estimate of the soil resistance. Most programs have force vs. displacement (p-y) curves already built into the program. The designer needs to select soil type, certain soil parameters, and the program will generate the curve defining the soil spring as a function of the pile diameter and depth. However, it must be recognized that these p-y curves were formulated based on experimental tests performed on single piles. p-y curves generated following Matlock (1970) for soft clays, and Reese (1974) for sands, fall into this category. As such, the designer must reduce the p-y curves to account for the interaction with adjacent piles and other factors which might reduce the soil resistance. This is routinely done for pile group analyses. However, there are various challenges that arise when dealing with earth retaining structures. Firstly, piles can be so close to each other to practically form a continuous wall. This is an occurrence that is not typical in foundation group analyses. Secondly, the ground can be irregular, and affect significantly the maximum available passive resistance. These two factors need to be combined, and ultimately provide a soil resistance curve that is used in the analyses. When both factors are present (closely spaced piles wall and irregular ground geometry) it can be challenging to accurately estimate the reduction in soil resistance, as shown in the technical examples presented in the next section. Ultimately, the reduction in soil resistance is also a function of the loading conditions. This might not be obvious, as foundation engineers typically estimate the soil resistance reduction of pile groups based on just the pile arrangement and geometry. However, this is not the case for earth retaining structures, and when the loading conditions change (application of surcharge, additional backfill, change in groundwater levels, etc.) the value of the p-multipliers can change as well.

Another limitation applicable to continuous structures (tangent piles, secant piles, etc.) is the choice of

pile diameter. This is not a determining parameter in limit equilibrium analyses. If the pressures and the structural properties are computed appropriately for the given wall width, the required embedment, maximum moment and wall deflections remain the same. This is not the case for p-y springs, since the p-y curves depends on the pile diameter. Ultimately, the combination of pile diameter and soil resistance reduction (p-multiplier) should provide a soil resistance that is always within the maximum available passive resistance.

The main advantage of the soil spring (p-y) methods is that they try to capture a more realistic stress state of the soil, i.e. they do not assume full mobilization of active and passive pressures. In fact, the resistance offered by each spring is a function of the spring displacement. This is a better and more realistic representation of the actual stress and displacement states, especially at depths where the wall might not displace significantly. It must be recognized though that the springs generated by most programs account for pressures on both sides of the pile and include the shear resistance on the pile faces that are parallel to the direction of loading, as they were developed based on single pile tests. As such, full active pressures must only be input above the excavation line, while only the overburden contribution is input below the excavation line. Ignoring this second part can have significant consequences, especially for closely spaced piles and continuous structures.

Another advantage of the soil spring (p-y) methods is their ability to model multiple pile sections and to consider the non-linearity of the bending stiffness. This, combined with the ability to mobilized soil resistance as a function of displacement, makes these methods more reliable in estimating deflections (if the soil resistance is modeled accurately). Modeling the non-linearity of the bending stiffness allows full modeling of the cracking of the section when concrete is utilized, and full modeling of steel reinforcement and construction of the interaction diagrams. As such, p-y analyses provide a better estimate of wall displacement than limit equilibrium methods.

The required embedment is on the other hand a source of debate when using these methods. Contrary to the limit equilibrium methods, the soil spring (p-y) methods do not compute a unique required embedment to obtain a FS equal to 1.0. The reason is inherent in their formulation, since they solve for non-linear equations in which the pile embedment is an input. The most common way to obtain a check on the required embedment is to perform several analyses with varying embedment, and generate a top of pile displacement vs. pile length plot. This plot provides a general indication of the stability of the system in relation to the pile embedment. This is discussed in more details in the example section.

Other key limitations of the soil spring (p-y) analyses are the difficulties in handling non-uniform geometries, surcharge distributions and soil layer boundaries. These are all consequences of the dependence on available computer programs and of their limitations.

Finite element and finite different methods

The finite element (FEM) and finite difference (FDM) methods are both numerical methods that discretize the soil into small elements and solve the equations governing the behavior of soils, structural elements, fluid flow etc. at discrete points. These methods are coded in several commercially available computer programs (such as PLAXIS, FLAC, MIDAS, etc.) and can be three dimensional. Both methods can be effectively used to model practical problems involving externally supported earth retaining structures. These methods are especially well suited for staged construction problems, complex non-uniform geometries, and for problems for the three-dimensional effect is important.

Details and Limitations

The greatest strength of these methods is the flexibility. An experienced and skilled user can virtually model almost any problem. However, compared to the other methods discussed in this section, finite element and finite difference methods require the largest computational efforts. The computer programs

available are quite complex, and specific skillset and experience are required to master such programs.

These methods cannot directly compute a required embedment. A workaround is to perform a "factor of safety" analysis. In this analysis, the soil strength parameters are proportionally reduced until "failure" is reached. The failure criterion is handled differently in each program, but it is an indication of a state where the movements become drastically large due to a small variation of soil strength parameters. This type of analyses can be performed modeling the earth retaining structure, and therefore obtaining a system factor of safety which is representative of the safety margin of the wall embedment (if the failure is indeed due to inadequate embedment). This analysis can be cumbersome, as the wall embedment needs to be iteratively changed until finding the one corresponding to a FS of 1. It is however a great tool, especially for cases where the designer desires to check the factor of safety for an existing design. Note however that this factor of safety is not the same as a factor of safety applied to the embedment such as the one discussed in the limit equilibrium methods.

TECHNICAL EXAMPLE

A technical example was chosen to illustrate the differences between the design approaches presented in this paper. Example geometry and parameters were selected to generate a simple case that can easily be reconstructed by the reader while preserving the main intent of illustrating the concepts discussed in this paper. For this example, the required embedment was first calculated with limit equilibrium analyses and then soil spring (p-y) and finite element analyses were performed using the calculated embedment. Factor of safety, bending moment diagrams, and lateral deflection are compared and discussed.

Technical Example No. 1

The first example is a 2 feet diameter tangent pile wall, with a 15 feet exposed height. The soil is one layer only, and it is a sand with friction angle of 30 degrees and unit weight of 120 pcf. The soils are dry (no groundwater) and the wall to soil friction angle is ignored. Under these simplified assumptions, a limit equilibrium analysis was performed by using the simplified and the conventional method. Results are summarized in the Table 1.

Table 1. Technical Example No.1 – Limit Equilibrium Analysis Results

Method	Calculated Embedment, ft	Required Embedment* (FS=1), ft	Max Moment per Pile (kip-ft)
Simplified	13.9	16.7	101.3
Conventional	15.1	15.1	101.3

* Required embedment (FS = 1) is calculated with an increase of 20% when using the Simplified Method.

The required embedment calculated with the simplified method is slightly conservative. This however must be assessed on a case by case basis. In this specific example, the ratio between the required embedment computed with the conventional method and the calculated embedment with the simplified method is about 1.1. The Simplified Method is detailed in the British Steel Corporation Piling Handbook (1984), which specifies this ratio to be 1.2. This implies that each case is unique, and the actual conservatism inherent in the simplified method should be assesses on a case by case basis. For this example, a "design" embedment of 15.1*1.3 = 20 ft (corresponding to a total length of 35 ft) is assumed.

The value of the maximum moment is independent of the method being used. This is expected, since the point of zero shear occurs above the inflection point. The maximum lateral deflections were checked with different programs, namely Shoring, CWALSHT, and DeepEx. Table 2 shows that the computed maximum deflections are quite variable (likely due to the numerical method and boundary conditions

used), highlighting the difficult reliability of the limit equilibrium methods in computing wall displacements.

A soil spring (p-y) analysis was then performed for the same example. Given the difficulties estimating the p-multiplier discussed in the previous section, a parametric analysis was performed. Results are summarized in Fig. 1 (a), together with results obtained from the limit equilibrium methods. Note that the required embedment based on limit equilibrium shown in this figure is the one corresponding to a factor of safety equal to 1.0. It is interesting to note that in this specific example even a p-multiplier equal to 1.0 would provide "embedment" results in good agreement with the limit equilibrium method. The top lateral deflection becomes flat at around 30 feet pile length, indicative of a near failure state. Using a p-multiplier less than 1.0 would yield more conservative solutions. Note that this is not a generic conclusion.

Table 2. Technical Example No.1 – Top Lateral Deflection

Method	Top Lateral Deflection (in)	Max Moment per Pile (kip-ft)
LE – Conventional (CWALSHT)	0.76	101.3
LE – Simplified (Shoring)	0.27	101.3
LE – Simplified and Conventional (DeepEx)	0.24	101.3
p-y (pm = 0.5) - LPILE	1.26	94.6
FEM - PLAXIS	0.72	63.3

In this specific example, without vertical surcharge or any other additional loads other than the active earth pressure due to horizontal backfill, and with horizontal ground in front of the wall, the additional mobilized soil resistance due to the high p-multiplier value of 1.0 is not enough to cause tangible variations in the solution. This is not always the case. The appropriate p-multiplier should always be assessed on a case by case basis. The large variability of the solutions with varying p-multiplier exemplifies the importance of this parameter. Fig. 1 (b) is generated to compare the mobilized soil reaction and the maximum available passive pressure. Soil reaction is an output of the soil spring (p-y) analysis, while the maximum available passive pressure was calculated based on Rankine's theory.

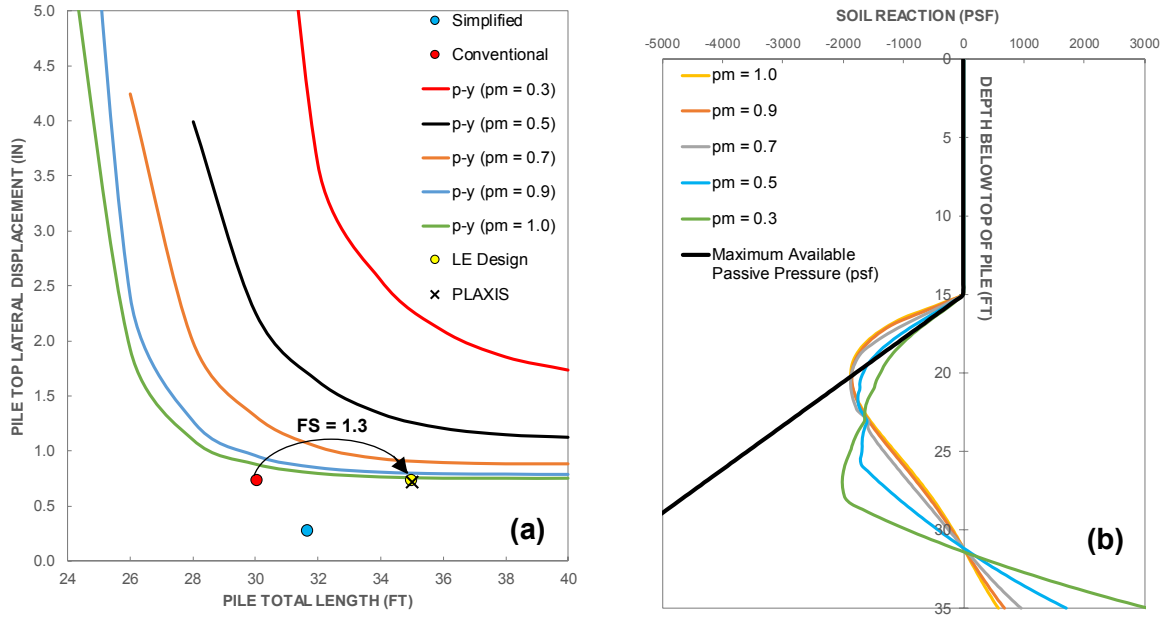


Fig. 1 – Relationship between pile length and top of pile displacement, compared with solutions from Limit Equilibrium Methods and Finite Element analyses (a), Mobilized soil reaction for different values of p-multipliers (b)

It is evident that p-multiplier values higher than 0.5 tend to generate a zone between 15 and 20 feet depth where the mobilized soil reaction is greater than the passive resistance. In this example, the excess soil reaction becomes negligible when the p-multiplier value approaches 0.5. This also is not a generic conclusion. In addition, the influence of the p-multipliers to the bending moment must be assessed as well. As shown in Fig. 2(a), the peak of the maximum moment increases and shift downwards when reducing the p-multiplier. In this specific case, the difference between the maximum moment under full soil resistance and 50% of the soil resistance (p-multiplier equal to 0.5) is "only" about 12 kip-ft, or about 13% of the value calculated with a p-multiplier equal to 0.5. However, the shift of the maximum moment downward can have severe repercussions if there is a weaker soil layer at depth which does not provide enough passive resistance, and which therefore causes the peak of the maximum moment to shift downwards even more and to increase drastically.

Lastly, a finite element analysis using the software PLAXIS was performed for this example. As discussed in the previous section, the finite element method can be used to obtain a required embedment by means of a generalized factor of safety analysis. It is noted that other parameters such as the soil Elastic Modulus and Poisson Ratio, as well as the construction sequence, also play a role in this analysis. For this example, an elastic modulus of 320 ksf was used, together with a Poisson Ratio value of 0.25. These are typical values for medium dense sands based on AASHTO LRFD Bridge Design Specification guidelines. The PLAXIS analysis showed that a factor of safety of 1.0 is achieved with a wall embedment of about 10.5 ft. The factor of safety corresponding to the design embedment of 20 ft is equal to 1.73.

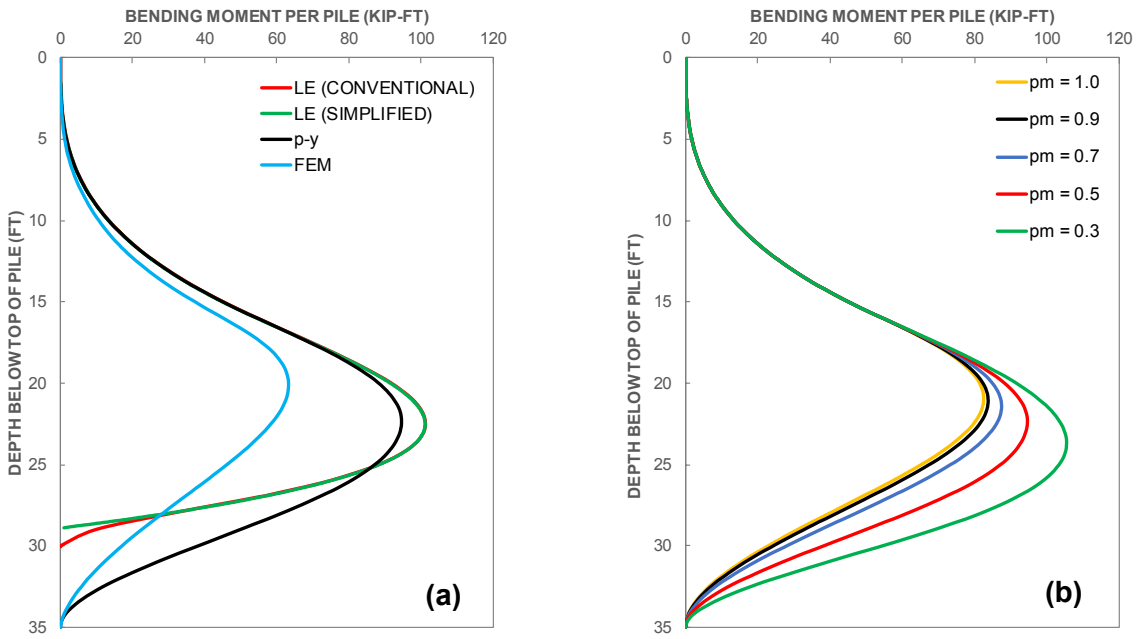


Fig. 2 - Bending moment diagrams for different values of p-multipliers (a); Bending moment diagrams for various design approaches (b)

The results in terms of bending moment diagrams were also compared in Fig. 2(b). As discussed, the conventional and simplified methods yield the same bending moment diagrams. The only difference is related to the portion of pile below the inflection point. For the example considered, this is located at about 27 feet depth below the top of pile. The soil spring (p-y) and finite element analyses returns a smaller bending moment compared to the limit equilibrium analyses. This comparison also shows that in cases where fine tuning is needed to optimize the design, more sophisticated analyses such as p-y analyses and/or finite element/difference analyses could be performed.

SUMMARY AND CONCLUSIONS

The main methods to calculate lateral earth pressures for externally supported earth retaining structures were presented. Determining lateral earth pressures is critical for the design of externally supported retaining structures regardless of the design approach which is chosen for design. The most common approaches for design of externally supported earth retaining structures are the limit equilibrium methods, the soil spring (p-y) analyses, and the finite element/finite difference methods. The details and limitations of each method were discussed, with focus on the main design parameters and on the computer programs available to support these methods. Finally, an example was presented, showing a comparison between the different methods and discussing various design challenges.

While all design approaches are viable alternatives if approached correctly, the design engineer should exercise caution in estimating the soil resistance when using soil spring (p-y) analyses, as the consequences of overestimating the soil resistance can be severe. When possible, a design approach should be supplemented with analyses performed with a different design approach, and lateral earth pressures compared to assess the validity of the solutions. Lastly, the design engineers should be aware of the different capabilities and limitations of each computer program, and validate the program outputs with independent calculations whenever possible.

REFERENCES

AASHTO (2017) "AASHTO LRFD Bridge Design Specifications", 8th Edition, American Association of State Highway and Transportation Officials, Publication Code: LRFD-8, Washington D.C.

Caquot, A., and Kerisel, F. (1948). "Tables for the calculation of passive pressures." Active Pressure and Bearing Capacity of Foundations, Gautheir-Villars, Paris, France.

Civiltech Software (2014). "Shoring Suite Version 8 User's Manual"

Das, B. (2014), "Principles of Foundation Engineering", Eight edition

DeepExcav (2011). "DeepExcav Theory Manual", a Software for Analysis and Design of Retaining Walls.

Ensoft, Inc. (2016). "Technical Manual for LPILE 2016", A Program for the Analysis of Deep Foundations Under Lateral Loading

Federal Highway Administration (FHWA) (2007). Publication No. FHWA NHI-07-071 – Earth Retaining Structures, NHI Course No. 132036, Reference Manual

Lambe T. W., Whitman R. V. (1969). "Soil Mechanics"

Matlock, H. (1970). "Correlations for design of laterally loaded in soft clay," Proc. 2nd Offshore Technology Conference, Offshore Technology Conference, Houston, Vol.1, p. 577-594

NAVFAC (1986b). "Foundations and Earth Structures," Design Manual 7.02, Re-validated by change 1 September 1986, Department of the Navy, Naval Facilities Engineering Command, Alexandria, Virginia.

O'Rourke, T.D., and Jones, C.J.F.P. (1990). "Overview of earth retention systems: 1970-1990." Proc. of Conf. on Design and Performance of Earth Retaining Structures, Geotechnical Special Publication No. 25, Cornell University, Ithaca, P.C. Lambe and L.A. Hansen, eds., ASCE, New York, NY, 22-51

Reese, L.C. (1958). Discussion of "Soil Modulus for Laterally Loaded Piles," by B. McClelland and J.A. Focht, Jr., Transactions, ASCE, Vol. 123, p. 1071-1074.

Terzaghi, K., Peck, R., and Mesri, G. (1996) Soil Mechanics in Engineering Practice, Third Edition, John Wiley and Sons, New York.

U.S. Army Corps of Engineers (1991). "User's Guide: Computer Program for Design and Analysis of Sheet-Pile Walls by Classical Methods (CWALSHT) Including Rowe's Moment Reduction.

USS Steel Sheet Piling Design Manual (1984), Updated and reprinted by U.S. Department of Transportation/FHWA with permission

ENSURING PERFORMANCE OF TIP POST-GROUTED BORED PILES (DRILLED SHAFTS) THROUGH A COMPREHENSIVE QUALITY ASSURANCE PROGRAM

Antonio Marinucci, PhD, MBA, PE, V2C Strategists LLC, Brooklyn, NY, USA. +1 (401) 261.9102, Email: antmarinucci@gmail.com
Silas C. Nichols, P.E., Federal Highway Administration, Office of Bridges and Structures, Washington, D.C. USA. +1 (202) 366.1554. Email: silas.nichols@dot.gov
Mary Ellen Bruce Large, P.E., D.GE, Deep Foundations Institute, Hawthorne, NJ USA. +1 (724) 942.4220. Email: melarge@dfi.org

Keywords: tip post-grouting, drilled shafts, bored piles, QA, performance

ABSTRACT: Tip post-grouting of bored pile (drilled shaft) foundations refers to a method where cementitious grout is injected beneath the tip of a shaft to improve the overall performance of the constructed foundation. This technique, when performed satisfactorily and in the appropriate ground conditions, enhances axial load-displacement performance by improving the mobilization of pile's resistance. Potential benefits associated with tip post-grouting include reduced settlement under loading, better alignment of load transfer curves, and improved ground beneath the base of the bored pile. However, to be able to realize the benefits attributed to this method, the design, construction, of both the bored pile and the post-grouting system must meet a minimum level for quality assurance. The various factors affecting the successful installation and performance of a bored pile (e.g., workmanship, base cleanliness, borehole integrity, and concrete placement) have been discussed by numerous practitioners and researchers in the available technical literature. For a conventional (i.e., ungrouted) bored pile, acceptance is based on a combination of visual inspection, material testing, and the results of integrity and/or performance testing of the constructed pile. A properly executed tip post-grouting program can be a relatively comprehensive and complex process, which is typically evaluated throughout the construction process based on the results of prior projects and/or on test pile(s) at the particular site. For tip post-grouting programs, verification procedures and acceptance criteria should be established during and incorporated into the design process to ensure design intent and objectives are achieved. Project specifications should be produced to ensure performance requirements are achieved. This paper will present and discuss factors affecting the successful execution of tip post-grouting, including grouting criteria, instrumentation, reliability and uncertainty with the method and outcome, and verification and acceptance.

INTRODUCTION

Constructing bored piles (drilled shafts) is increasingly more challenging given the lack of ideal site locations, tight project site confines, difficult or restricted access, greater demands on drilling equipment, and close proximity to adjacent structures. To evaluate the feasibility of bored piles as an appropriate foundation system, a myriad of factors is evaluated during design, including site conditions and constraints, budgeting and scheduling, reliability and risk exposure, presence of and depth to adequate load bearing soils/rock, and the magnitude of the imposed loading. Moreover, updated design codes increased load demand per element, and improved material strengths have led to more complex foundation designs, larger foundation elements, and significant increases in load magnitude. Monopile (monoshaft) foundations have been utilized where one large bored pile is used in lieu of a group of piles connected via a pile cap. In addition, to accommodate the design criteria, site conditions, and imposed loading, the geometry of the bored piles being designed and installed have been as large as 13 feet (4 m) or greater in diameter and to depths in excess of 260 feet (80 m).

Given the various concerns and uncertainty faced during design and construction, understanding load transfer in side and tip resistance and the factors that affect each component are essential to ensure the

© 2018 Deep Foundations Institute

design is optimized and constructible as much as practical (or permissible). Some of the various factors affecting the successful construction and performance of a bored pile include borehole integrity, workmanship, base cleanliness, and concrete placement.

Even if a bored pile were to be constructed perfectly, designers often neglect either side or tip resistance (or reduce their respective contributions to the overall resistance) due to strain incompatibility in the mobilization of side and end resistances when subjected to axial compressive loading. When an axial compression load is applied to the top of a conventional (i.e., ungrouted) bored pile, an idealized load - displacement relationship can be represented by the "combined" curve shown in Fig. 1a. It has been well documented and established that, as the axial compressive load increases, the pile is compressed and displaced downward into the ground, and that the pile's resistance is first mobilized in side friction and then in tip resistance. Irrespective of ground type, side resistance is fully mobilized at relatively small displacements equal to about 0.2% to 0.4% of the pile's diameter. However, the tip resistance available when side resistance becomes fully mobilized is minimal, and it becomes fully mobilized at relatively large displacements equal to about 4% to 5% of the pile's diameter in cohesive soils and about 10% of the pile's diameter in cohesionless soils.

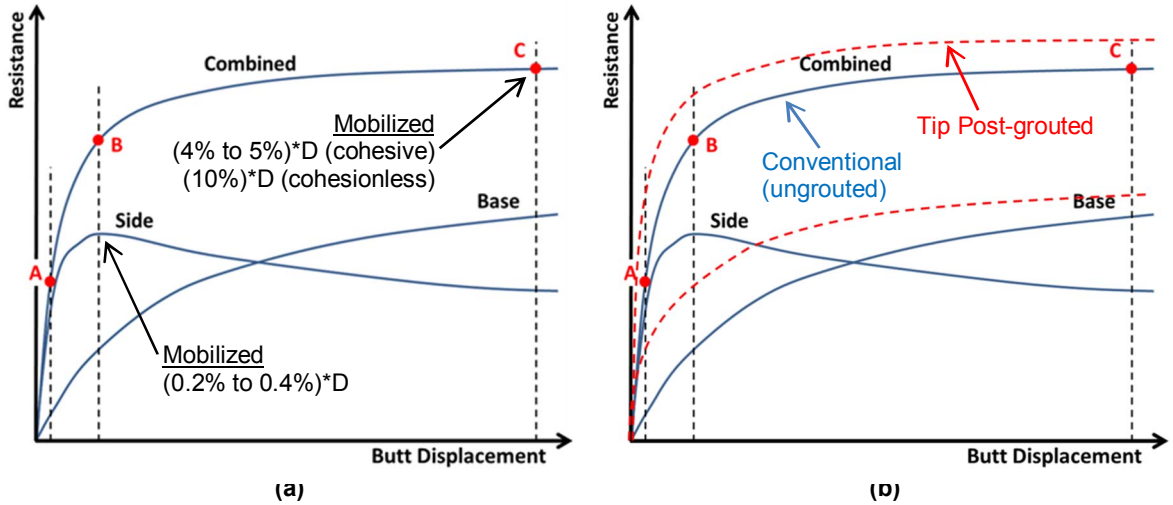


Fig. 1. Idealization of load transfer (mobilization of side and end resistances) of a conventional (ungrouted) bored pile and (b) tip post-grouted bored pile due to axial compressive loading

An optimized maximum resistance (incorporating the full contributions of both side and tip resistance) cannot be realized with a conventional bored pile because the full side resistance is mobilized at very small vertical displacements, while the full tip resistance is mobilized at relatively large vertical displacements. Therefore, tip post-grouting of bored piles has been used to optimize the design and construction of bored piles, which would better align the load transfer curves in side and tip resistance to maximize their resistance to applied loading (Fig. 1b).

Tip post-grouting is a technique used to inject, under pressure, a neat cement grout beneath the base of a bored pile (Fig. 2a) to enhance or improve the axial load-displacement performance of the pile by improving the mobilization of side and tip resistance and/or by increasing the axial resistance of the pile. During the grouting operation, the bi-directional force induced by the pressurized grout on the bored pile and to the soil below results in negative side resistance and positive tip resistance (Fig. 2b). After the pile has been grouted, the tip resistance has been mobilized and there is a reversal of side resistance to resist axial loading and self-weight, such that there is positive tip and side resistance. The improvement of the axial compressive load-deformation response of bored piles due to tip post-grouting has been realized in a range of ground conditions from cohesionless soils to cohesive soils, even in rock. In addition to optimizing the load transfer curves, other benefits of tip post-grouting include stiffening the load-deformation response under working loads, reducing settlement of the pile under loading, decreasing the

pile length, utilizing additional (or usable) tip resistance in design computations, verifying a lower bound of axial resistance, and improving the ground beneath the base of the pile.

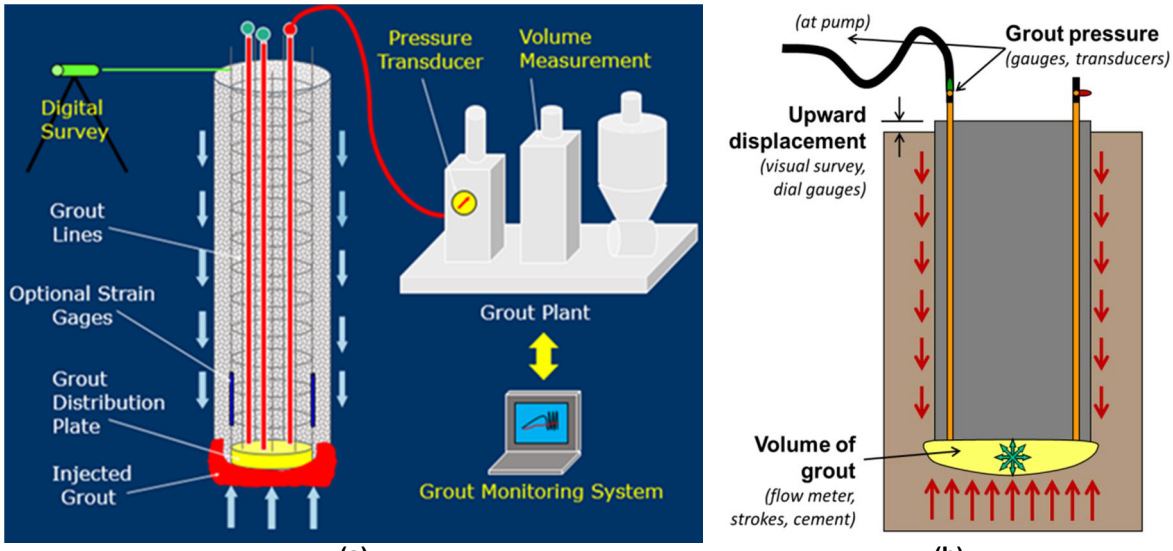


Fig. 2. Schematic depictions of (a) the setup used for tip post-grouting of bored piles; image courtesy of Applied Foundation Testing (Large, 2016), and (b) negative side resistance and positive tip resistance mobilized due to bi-directional force induced by the pressurized grout (grouting control criteria also shown).

Nonetheless, despite the numerous load test results and case histories published in the literature, many areas of concern regarding the execution and reliability of tip post-grouting remain unresolved. Different empirical and semi-empirical design methods have been proposed by different researchers (e.g., Mullins et al. (2006), China Academy of Building Research (2008), and Pando and Ruiz (2005)) based on select test data from local or regional geography. Furthermore, these predictive methods themselves are sources of uncertainty, as they require input of data that is difficult to define, and the methods may not explicitly consider the effect of different ground conditions, grout distribution systems, grout characteristics, grouting procedures, and other construction variables. The ideal manner to evaluate the efficacy and reliability of tip post-grouting is to perform, analyze, and compare results from full-scale load tests on conventional (ungrouted) piles and on tip post-grouted piles. However, developing and executing a comprehensive quality assurance (QA) program that addresses the known areas of possible concern and uncertainty will improve the reliability of tip post-grouted bored piles.

GROUTING EQUIPMENT

The equipment set up for typical tip post-grouting applications includes the grout plant (i.e., high speed / high shear mixers with two tanks), water pump, grout delivery system, and piston pump. To mix the neat cement grout thoroughly, the type of shear mixer used is extremely important to ensure proper consistency and quality, which is essential to minimize bleeding and segregation and to reduce the potential for plugging the grout lines. Two tanks are typically used with this type of operation: one is used to prepare a new batch of grout and the other serves as a storage tank from which the grout is pumped, and ensures that grout flow is uninterrupted during grouting. Single-/double-acting positive displacement piston pumps are ideal for these applications as they can achieve the desired high grout pressures (750 to 800 psi (50 to 55 bar)) as well as delivering the low flow rates (less than about 1 to 3 gpm (4 to 11 l/min)) during grouting. Grout flow volumes are measured using flow meters that are attached directly to the grout plant. If required as a backup system, the volume of grout can be recorded manually using a count of the calibrated strokes of the grout pump, but this requires calibration at the site prior to the commencement of grouting.

In essence, there are two types of grout delivery systems (open-type or closed-type) used for tip post-grouting applications. Irrespective of the system type, the device must be located at the base of the pile below the reinforcing cage and in contact with the in-situ soil to be able to perform as intended. The water pump is used to flush the grout lines and delivery system prior to grouting and, again, if staged grouting is required; therefore, the pump must be sufficient to deliver water down to the delivery system and back up a return line to ensure there are no blockages in the system. Moreover, concrete may flow around and encapsulate the grout delivery system during placement, especially if a bottom plate separating the two zones is not used. Therefore, the concrete around the delivery system, if present, must be cracked using pressurized water before the concrete fully hardens to allow the tip post-grouting to function as intended. The pressure and volume used to crack the concrete should be recorded and used as a basis for the subsequent tip post-grouting. However, tip post-grouting cannot be performed until the concrete in the bored pile has fully hardened or has achieved an unconfined compressive strength (f_c') of at least 3,000 psi (20.7 MPa).

In an open-type system (i.e., sleeve-port or tube-á-manchette), which is applicable for all diameters especially larger piles, the grout is injected into the ground through small ports along the horizontal portion of the U-tube below the base of the pile. The key to this system is ensuring the flow of grout out into the formation and across the entire base of the pile. This grout flow is facilitated by using multiple grouting circuits for redundancy and better coverage across the bottom of the pile. In a closed-type system, which is applicable for smaller diameter piles ($\leq$ 6 ft (1.8 m)), the grout is injected into an enclosed area that uses a steel plate on bottom of pile, and a flexible rubber membrane to protect the tubes during concrete placement and to provide separation between the grout and the formation. As grout fills and expands the space between the steel plate and rubber membrane, the membrane should rupture at relatively low pressure, which then allows the grout to flow out into the formation akin to the open-type system. The key to this system is ensuring the flow of grout across the entire base of the pile while the membrane is still intact.

Gravel bedding has been used with bored piles greater than about 6 ft (1.8 m) in diameter to facilitate the flow and distribution of grout across the base of the pile. In addition, the gravel bedding has been used to produce a level surface at the bottom of the borehole when construction tooling results in a contoured hole. The gravel bedding should be as thin as possible with a minimum thickness of about 4 to 12 in (100 to 305 mm), but no greater than about 24 in (600 mm). The bedding should consist of clean, coarse gravel (particle sizes between 0.625 and 1.25 in (16 to 32 mm)) that extends across the entire base of the pile, and the bedding should be tamped down prior to placement of the reinforcement cage with grout delivery system.

GROUT MIX CHARACTERISTICS

The grout mix used for tip post-grouting applications is neat grout mix, typically consisting of Type I/II Portland, water, and admixtures if required to control flowability, bleeding, and set time. The grout mix does not contain aggregates. The water-to-cement (w/c) ratio ranges from about 0.4 to as high as about 0.9. When the grouting operation first begins, higher w/c ratios (around 0.7 to 0.9) are typically used to ensure the grout delivery system, grout tubes, grout lines, and void space in the gravel bedding (if used) are full of grout (net volume). The net volume is defined as the amount in excess of the volume needed to ensure that the delivery system is filled, there is no blockage in the lines, and that the grout is reaching the base of the pile. As grouting continues, the w/c ratio is reduced gradually to a range between 0.4 and 0.6 to ensure control of the grout, and to facilitate delivery at the desired grout pressure. There should be flexibility in the specifications to modify the mix to adjust to conditions encountered in the field during grouting.

Some important characteristics of the grout mix should be monitored including flow (pumpability), specific gravity, viscosity, and compressive strength. Specific gravity and grout viscosity (indirect

measurement of flowability and fluidity) are measured using a mud balance and a Marsh funnel, respectively, where both measurements may be made during and throughout the grouting operation to provide real-time indications of the properties of the fluid grout. Fluidity (or flowability) of the fluid grout is measured with a flow cone. Typically, project specifications do not mandate the quantity or frequency of tests performed during the grouting operation, but the tests should be performed at a frequency that ensures proper behavior and required properties of the grout are maintained. Compressive strength testing of the grout is performed on cured samples of the grout. Typically, a minimum 28-day compressive strength may be specified between 2,000 and 4,000 psi (13.8 and 27.6 MPa)). The grout does not need to achieve similar strength as the concrete in the pile, but needs to be stiffer than the soil around the pile. That is, the post-grouting operation is intended to pre-mobilize end bearing. While it is a component of the development of load transfer along and at the base of the shaft, the grout is not a structural component of the shaft itself.

GROUTING PROCEDURES, VERIFICATION, AND ACCEPTANCE

The key consideration during any grouting operation is control of the grout, which, unfortunately, does not always occur for a variety of reasons. Mullins and Winters (2004) and Muchard and Farouz (2009) reported fluid grout flowing from the base, upward along the sides of the pile for distances of 60 ft (18 m) or more during tip grouting. As an unintended benefit, this upward flow of grout likely resulted in an increase in side resistance; however, control of the grout was lost and the system did not function as intended. In other instances, the grout has been found to have traveled some distance away from the edge of the pile. This outward flow of grout has generally been due to either hydrofracture or travel along a looser/weaker seam/void, and reflects a loss of control of the grout.

To ensure control of the grout and its effect on the load response behavior of the bored pile, various parameters are measured as a function of time, recorded, and analyzed throughout the grouting operation as part of termination criteria and the overall QA program. These main parameters include grout pressure, grout volume, and upward displacement of the bored pile during grouting (Fig. 3). The termination criteria for tip post-grouting includes a target grout pressure, net grout volume in excess of the amount to fill the delivery system and tubes yet below a maximum amount, and maximum upward displacement of the pile during grouting; however, the termination criteria typically vary from project to project based on the engineer's experience, site conditions, and the project requirements.

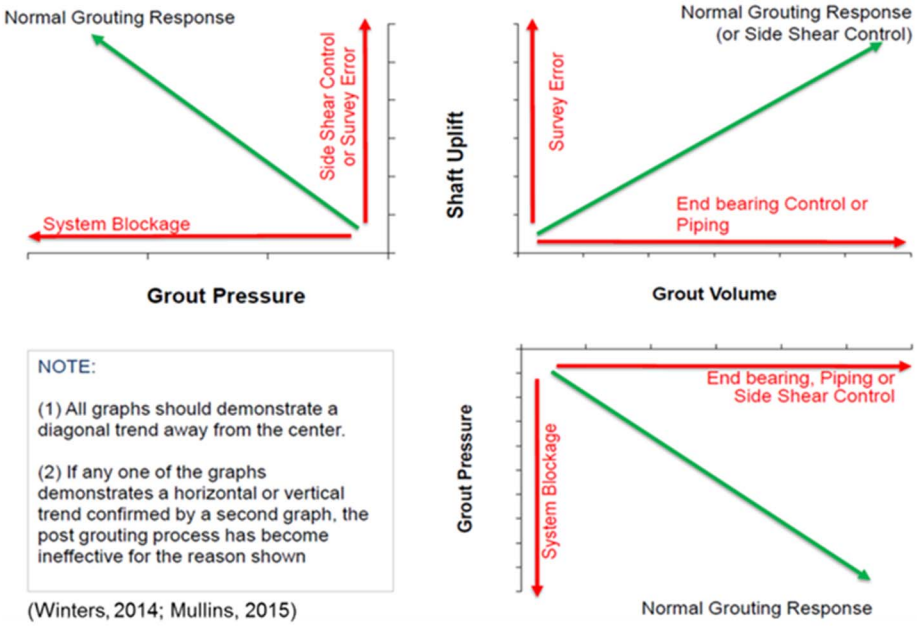


Fig. 3. Idealized graphs of grouting parameters measured during the tip post-grouting operation and analyzed in real-time (Winters, 2014; Mullins, 2015)

The target grout pressure is considered the most important parameter for tip post-grouting, and is a function of a variety of factors, including in-situ stress state, soil type, the presence of weak or soft layers, available reaction force (i.e., self-weight of the bored pile plus available side friction resistance), location of groundwater table, head losses in the system, and the hydrofracture potential of the in-situ soil. The greater the magnitude of the bi-directional load induced into the shaft during tip post-grouting results in an enhanced performance of the grouted shaft. Grout pressures used when tip post-grouting in sands and clays/silts have been reported as high as 2,180 psi (150 bar) and 1,160 psi (80 bar), respectively. As the grout pressure approaches / exceeds about 600 psi (45 bar), there is concern about the risk of clogging in the grout lines due to the squeezing out of water from and in front of the fluid grout mix. Commonly used upper limits of grout pressure are in the range of 750 to 800 psi (50 to 55 bar) and are measured using analog or digital pressure transducers or gauges attached directly to the grout plant at the discharge line and, at times, additional transducers or gauges are used near the connection at the top of the bored pile. In addition, once the target pressure has been achieved, it is sustained for a specified duration. The hold time is typically around 2 min in the U.S. but may vary considerably based on the contractor and geographical location to ensure that the grout below the base of the pile is pressurized and performing as intended. For open-type systems, the above process is repeated for each circuit in the grout delivery system in a continuous operation; however, the process is only performed once when used with closed-type systems.

In tip post-grouting applications, hydrofracture of the in-situ soil formation is highly undesirable, as this condition causes a loss of control of the grout. Hydrofracture can occur when the applied grout pressures become greater than the tensile strength or shear strength of the in-situ formation (and implicitly the overburden pressure) and is more likely to occur in low strength soils, fine-grained or granular soils with more than about 20 to 30% fines, in lower permeability soils were the grout remains more fluid for a longer period, and with higher mobility grouts. When hydrofracture initiates, observations include relatively large grout takes with little-to-no increase in the measured grout pressure along with small-to-no upward displacement of the pile. Different means to minimize the potential of hydrofracture include using a less mobile grout mix, using lower grout pressures, and performing staged grouting.

The target grout volume is dependent upon the diameter of the bored pile being grouted, the grout delivery system used, and the condition of the ground beneath the base of the pile (e.g., relative density, presence of a soft bottom, etc.). The target grout volume should be a net volume, which is typically in the range of 2 to 5 cu. ft (55 to 140 liter). The volume of grout being delivered and measured using flow meters attached directly to the grout plant at the discharge line location. Some specifications provide a maximum grout volume, which can vary greatly depending upon the diameter of the pile, engineer, and ground formation. Based on conversations with service firms and contractors performing this work, grout volumes have ranged from 5 to 30 cu. ft (140 to 850 liter). In practice, if the maximum specified grout volume is achieved at grout pressures considerably lower than anticipated, staged grouting may be required. However, when possible, it is advantageous to achieve the grout pressure in the initial grouting even if that means exceeding the maximum grout volume specified.

The upward displacement of the bored pile during the post-grouting is the third commonly monitored termination criterion. To minimize the potentially negative effects to side friction due to the reversal of side resistance, the upward displacement measured at the top of the pile during any one stage of grouting is limited to between 0.25 and 0.75 in (6 and 19 mm). If the upward displacement limit is reached prior to achieving the target grout pressure, staged grouting is performed. An excessive amount of upward displacement may be indicative of insufficient side resistance, which may negate the benefit of performing staged grouting below the base of the pile. To measure the upward movement at the top of the pile, displacement transducers or gauges are commonly used in conjunction with an independent reference beam. At times, an optical survey may be performed as a backup.

Staged grouting is an approach that is employed with open-type grout delivery systems when the grouting termination criteria are not achieved. Staged grouting entails performing a modified initial grouting

sequence multiple times, but usually, no more than four, until the grouting termination criteria are achieved. As described in Figure. 4, the initial grouting is performed, then the grout in the grout tubes and delivery system is flushed using pressurized water. Two to four additional phases of grouting are then performed through the grout delivery system. The key is to perform the additional grouting phases before the previously injected grout fully sets but has achieved enough strength to seal off potential escape paths. It is preferable to avoid performing staged grouting, as doing so introduces additional concerns and uncertainties, including being able to deliver the pressurized grout across the full area of the base of the pile, to deliver the grout beyond the delivery system itself, and to determine the area over which the grout is being injected.

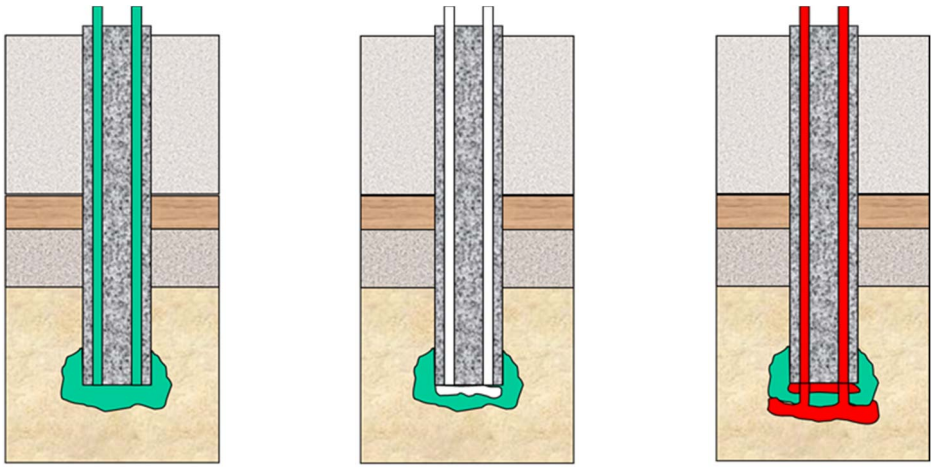


Fig. 4. Idealized depictions of the different phases of staged grouting: (a) initial grouting below base of bored pile, (b) flushing of grout in the tubes and in delivery system, and (c) additional grouting through delivery system (images courtesy of Applied Foundation Testing (mod. from Large, 2016))

Embedded within the bored pile, strain gages and/or telltale rods have been used to evaluate the effectiveness of grout distribution across the base of the pile, to evaluate load transfer along the length of the pile during the tip post-grouting or during load testing, and to provide an indication of a possible blocked circuit / line or hydrofracture during grouting. A multi-axis plot of grout pressure and strain measurements versus time during the grouting operation is presented in Figure 5. In the figure, the plot indicates eccentricity, but the average strain indicates excellent trending with the applied grout pressure. However, the use of strain gages and telltales is not common in current practice on production piles. Nonetheless, the use of strain gauges can provide an estimate of the relative displacement and axial load in the pile at their locations and can provide a measure of any relaxation as the grout cures.

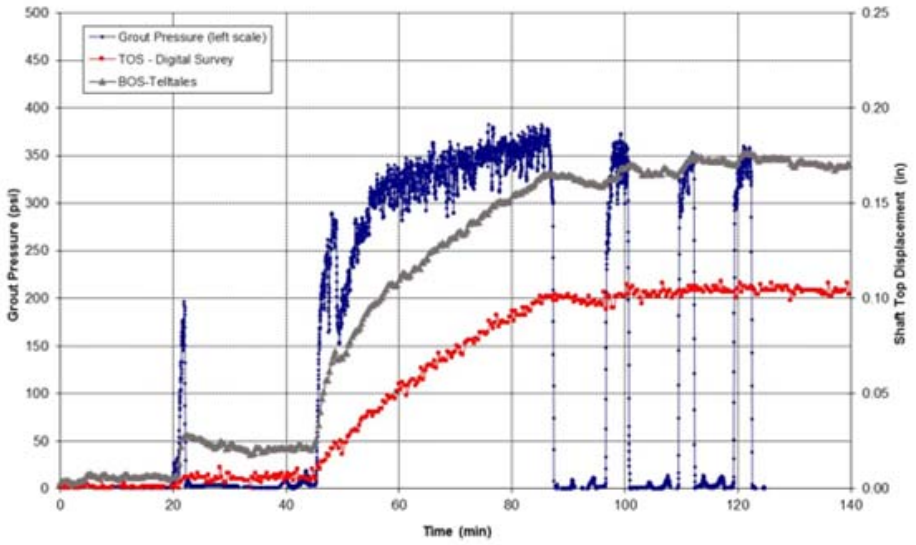


Fig. 5. Measurements of grout pressure (blue, left axis), top of shaft displacement from digital survey (red, right axis), and displacement near bottom of shaft from telltales (gray, right axis) versus time during grouting (Large, 2016)

RELIABILITY AND UNCERTAINTY – METHOD AND OUTCOME

A clear and rational process for assuring the quality of tip post-grouting is a clear obstacle to full implementation. The reliability of a tip post-grouted pile, as indicated through safety margins or resistance factors, should not be less than for an ungrouted pile, but is not as yet defined in practice. Understanding the elements of QA is necessary to ensure that the tip post-grouting process has occurred and is complete. However, an assessment of the reliability of the process is more complex. Typically, uncertainty in ungrouted bored pile construction is addressed by monitoring the means and methods for the construction of the pile. Demonstration or technique shafts are constructed to verify means and methods, and construction inspection and materials testing ensures repeatability. Some combination of performance and integrity testing allows the designer to assure reliability in bearing resistance.

Tip post-grouting provides a difficult problem for designers and owners since it is clear that the construction process clearly improves the performance of the foundation element. This leads one to conclude that any QA requirements for tip post-grouting would certainly be excessive. Acceptance of any foundation element must include assurance that the post-grouting process is performed consistently from element to element, and that bearing resistance can be reliably estimated. There are inherent difficulties in performing adequate QA to capture, quantify, and minimize the potential uncertainty resulting from a construction activity that is understood to absolutely improve the existing condition.

A QA program for tip post-grouting should try to achieve two goals. First, the means and methods must demonstrate that construction results in a pile that performs as expected in axial compression. Second, the means and methods must be repeatable for all elements. This means that the projects that use tip post-grouting should always have a test shaft that allows the contractor to demonstrate its construction means and methods along with some frequency of testing primary metrics (e.g., pressure, volume and displacement) to verify repeatability of the construction process.

CONCLUSIONS

Tip post-grouting has been demonstrated in different ground formations to provide various benefits and enhancement to the axial load-displacement response of a grouted bored pile compared to conventional (ungrouted) piles. It has been shown that this technique can increase the axial nominal resistance of the pile, improve the mobilization of pile's resistance, and better align the load transfer curves. The various

factors affecting the performance of a tip post-grouted pile include the size (diameter and length) of the pile, grout delivery method, grout injection pressure, grout volume, and upward displacement during grouting. To achieve the myriad benefits, the construction of the bored pile and the implementation of the tip post-grouting program must be performed to a high level of quality and control throughout the entire grouting operation. Successful and reliable implementation of tip post-grouting will allow designers to optimize the design of a tip post-grouted pile by stiffening its end-bearing response and by allowing the maximum tip resistance at a downward displacement that is consistent with the maximum side resistance (i.e., optimizing of load transfer curves). Using these optimized load transfer curves, cost efficient bored piles can be designed leading to a reduction in the overall cost of, and greater reliability with, bored pile construction. However, tip post-grouting or any other enhancement or remedial technique should never be used in lieu of proper execution and good workmanship in the construction of a bored pile.

REFERENCES

Castelli, R.J., (2012). "Guidelines for Application of Base Grouting for Drilled Shafts"; *Proceedings of GeoCongress 2012*, ASCE, Recent Advances in Foundation Engineering, pp. 225-234.

China Academy of Building Research (2008). *Technical Code for Building Pile Foundations,* JGJ 94-2008, Architecture and Building Press, Beijing.

Large, M.E.B. (2016). "Workshop on Quality Assurance for Post-grouted Drilled Shafts." Submitted to the Federal Highway Administration. Report No. FHWA-HIF-16-015. 187 pp.

Loehr, J.E., Marinucci, A., Hagerty Duffy, P., Gómez, J., Robinson, H., Day, T.J., Boeckmann, A.Z., and Cadden, A.W. (2017). *Evaluation and Guidance Development for Post-Grouted Drilled Shafts for Highways*, Report No. FHWA-HIF–17-024, Federal Highway Administration. March. 158 pp.

Marinucci, A. and Nichols, S.C. (2016). "Optimized Drilled Shaft Design through Post-Grouting," ASCE/Geo-Institute *GeoStrata* Magazine. May/June.

Muchard, M.K. and Farouz, E. (2009). "Broadway Viaduct Design Phase Load Test Program for Post-grouted Shafts," 34th Annual Conference on Deep Foundations, DFI, Kansas City, Missouri.

Mullins, G. (2015). "Grouting Effectiveness – Construction QA/QC of Post-grouted Shafts." Presentation delivered at FHWA/Caltrans Workshop on Quality Assurance for Post-grouted Drilled Shafts. April 15-16. Oakland, CA.

Mullins, G. and Winters, D. (2004). "Post Grouting Drilled Shaft Tips – Phase II." Final Report to the Florida Department of Transportation.

Mullins, A.G., Winters, D., and Dapp, S.D. (2006). "Predicting End Bearing Capacity of Post- Grouted Drilled Shaft in Cohesionless Soils," *Journal of Geotechnical and Geoenvironmental Engineering*, Vol. 132, No. 4, pp. 478-487.

Nichols, S.C., Marinucci, A., and Rivers, B. (2012). "Evaluating Post-Grouting to Improve Drilled Shaft Capacity." In *A Compendium of Research Reports and Invited Technical Papers*, Geo-Construction Conference Proceedings of the 2012 ADSC-IAFD Equipment Exposition and Technical Conference. A. Marinucci and W.T. Witherspoon, editors.

Pando, M.A. and Ruiz, M.E. (2005). *Study of axially loaded post grouted drilled shafts using CPT based load transfer curves*, Geotechnical Engineering Research Report No. CIRC/GT/05-02, Civil Infrastructure Research Center, University of Puerto Rico, Mayaguez, PR, June 2005, 287 p.

Ruiz, M.E. and Pando, M.A. (2009). "Load Transfer Mechanisms of Tip Post-Grouted Drilled Shafts in Sand", *Contemporary Topics in Deep Foundations*, Proceedings, 2009 International Foundation Congress and Equipment Expo, Orlando, Florida, ASCE, GSP 185, pp. 23-30.

Winters, D. (2014). "Selected Topics in Foundation Design, Quality Assurance, and Remediation." Ph.D. Dissertation, University of South Florida, Tampa, FL.

EXTRAPOLATION OF UNIT SIDE RESISTANCE IN DRILLED SHAFT FOUNDATIONS BASED ON BI-DIRECTIONAL LOAD TEST DATA

Joseph A.W. Toth, University of Nevada Reno, Nevada, USA, josepht@nevada.unr.edu
Ramin Motamed, University of Nevada Reno, Nevada, USA, motamed@unr.edu

ABSTRACT

Evaluation of the capacity of large-diameter drilled shafts using current load test methods present challenges when considering the magnitude of loads required to fully mobilize their capacities. Often, these full scale tests do not fully mobilize the capacity through side resistance. Therefore, the need for innovative solutions to extrapolate side resistance and interpret nominal capacity are of key interest. In this study, we evaluate three methodologies for extrapolating unit side resistance based on bi-directional load test data. Fellenius (2001) presented these methods for interpretation of pile capacity using static load tests. Our interpretations are based on the evaluation of 116 load tests. Unit side resistance was calculated and reviewed for each load test and categorized using three criteria of mobilization; (A) full, (B) partial and (C) linear. This study specifically focuses on load tests that showed fully mobilized unit side resistance behavior (Criteria A). The three methodologies were applied assuming Criteria (A) load tests were mobilized to 50% of their measured values. Subsequent comparisons of each extrapolation were then compared against the full measured values for each test and generally showed good agreement.

Keywords: drilled shaft, bi-directional load test, unit side resistance, extrapolation

INTRODUCTION

It is widely accepted that conducting load tests such as standard top-down tests or bi-directional (i.e. O-cell) tests can help designers understand load-settlement behavior and the nominal resistance of drilled shaft foundations. These load testing methods provide the advantage of confirming design assumptions as well as improving the reliability of the foundation design. The potential cost savings from the application of these methods for mid to large size projects is self-evident. For example, in a recent project in Northern Nevada, an O-cell test on a 6.9 ft diameter, 114.8 ft length drilled shaft imposed an initial cost of $125k to the project, resulting in a 15% reduction on the total foundation cost; equivalent to $1.3 million in overall savings (Pease, 2014). However, the costs of implementing such methods on smaller projects can be prohibitively expensive (Hagerty et al, 2016).

Despite the clear advantages of drilled shaft load testing, the current practice is not without limitations. Performing load tests on large-diameter drilled shafts with high capacities is a challenge considering the significant loads required to fully mobilize the capacity of such foundations. In some cases, the feasibility of these tests is impractical because the associated initial cost is not guaranteed to outweigh the final savings. As a result, large scale load tests are sometimes ruled out from the design phase of projects. Furthermore, in the majority of load tests the magnitude of loads applied are specifically selected to not approach failure, so the shafts can be used in the future foundation system (i.e. production shafts). This practice of field testing restricts our knowledge of the true capacity of the drilled shaft at failure; hence the nominal resistance remains unknown.

The design of large diameter drilled shafts could benefit from the development of cost-effective and innovative solutions through utilizing load tests on scaled smaller diameter shafts. One such solution is to use extrapolation methods with bi-directional load test data to predict the nominal capacity. Fellenius (2001) presented five different methodologies in interpreting capacity of pile foundations using static load test data. This study evaluates the efficacy of three of those methodologies for extrapolation of unit side resistance of drilled shafts based on bi-directional load test data. In developing our dataset, we reviewed

© 2018 Deep Foundations Institute

149 bi-directional load test records for drilled shaft foundations. Each load test comprising our final database of 116 load tests contained a complete record of strain gage force diagrams, bi-directional displacement diagrams and shaft construction summary information that included elevations, shaft dimensions and subsurface details. Load test records that did not include all relevant detailed information or could not be inferred were not included in the database. Comprehensive review was conducted for each load test record and included digitizing all relevant strain gage forces and bi-directional load and displacement information. Using the digitized data we calculated unit side resistance curves for each section of shaft between strain gages installed both above and below the bi-directional cell. A total of 590 curves were calculated using the load test records in our database. Each curve was evaluated and visually categorized using three levels of mobilization resistance; (A) full, (B) partial and (C) linear. The slopes of the final portion of each unit side resistance were further used to define these mobilization criteria. This study focused on the curves that displayed fully mobilized behavior (Criteria A) and were evaluated using the three methodologies presented by Fellenius (2001).

BACKGROUND

Limitations in predicting the ultimate capacity of drilled shaft foundations has always been understood. This is especially true regarding estimating the capacity through mobilization of side resistance along the shaft. Current design procedures for drilled shaft foundations consider maximum side resistance to be independent of shaft diameter (Brown et al., 2010). Contrary to this assumption, evidence of a diameter-dependent relationship suggesting that smaller diameter drilled shafts exhibit greater side shear resistance when compared with larger diameter shafts exist (Lizzi, 1983; Brown et al., 2010). Despite this evidence, very little research has been conducted exploring any diameter-dependency relationships for drilled shafts in soil. Lizzi (1983) proposed a methodology to predict the ultimate capacity of piles based on load test data from smaller diameter piles tested to failure.

Data utilized in this study evaluated 116 projects where bi-directional testing was performed on drilled shaft foundations. The dataset consisted of shafts ranging in lengths of 13.2 to 250.5 feet and diameters ranging from 2 to 9.8 feet. A distribution summary of shaft lengths and diameters of all load test records fitting Criteria A are presented below in Fig 1. Data utilized in our study was collected through the Arizona Department of Transportation (ADOT), Alabama Department of Transportation (ALDOT), California Department of Transportation (Caltrans), Nevada Department of Transportation Deep Foundation Load Test Database (NDFLTD) (Motamed et al., 2016), North Carolina Department of Transportation (NCDOT), Oregon Department of Transportation (ODOT) and the Washington Department of Transportation (WSDOT). Table 1, presented below, summarizes the location of each Criteria (A) load test record. It should be noted that Criteria A projects located in LA and MS and presented in Table 1 were part of a research study conducted through Caltrans.

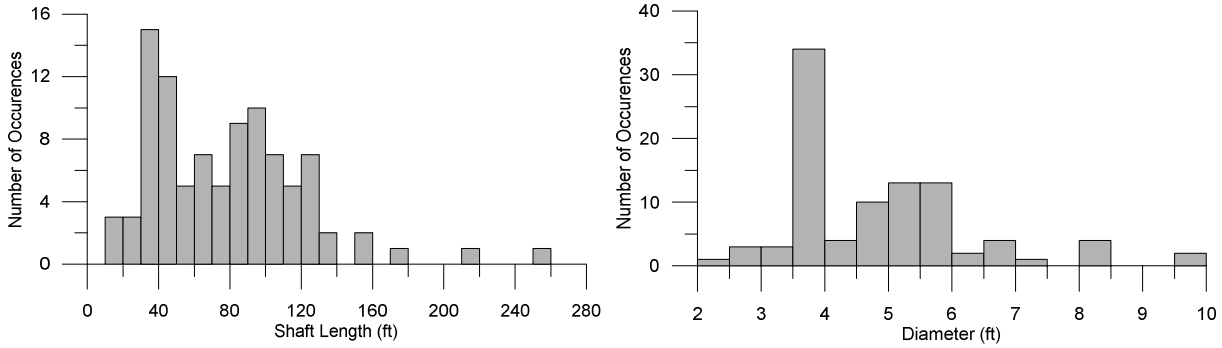


Fig. 1. Distribution of Overall Dataset Shaft Lengths of Criteria (A) Load Test Data

Table 1. Summary Table of Location for Criteria (A) Projects

State	No. of Load Tests	State	No. of Load Tests	State	No. of Load Tests
AL	1	MS*	44	WA	3
AZ	7	NC	1		
CA	2	NV	19		
LA*	16	OR	2		

*Included in Caltrans Study

EXTRAPOLATION OF UNIT SIDE RESISTANCE

Using the available bi-directional load test data, unit side resistance curves were generated for each of the projects comprising our database. In total, 590 unit side resistance curves were estimated from the 116 load test projects. Figure 2 presents the bi-directional cell plot as well as typical unit side resistance curves estimated using measured load test data (LT-1404) for a project located in Arizona for a drilled shaft meeting the dimensions of 115.3 feet in length and 72 inches in diameter. The data presented in Fig. 2 was plotted using measured strain gage data above the bi-directional cell; no extrapolation is presented in this figure. It is important to note that our evaluations did not account for elastic compression of the shaft in our calculation of unit side resistance thus assuming each drilled shaft was rigid. Although a change in shaft length due to elastic compression will result in a higher calculated unit side resistance, the increase is considered insignificant and does not affect the interpretation of our results. The typical calculations presented in Fig. 2 show the mobilization of unit side resistance for six intervals of strain gage sections developed over a maximum shaft displacement of approximately 2.25 inches. Subsurface conditions along the shaft sections presented below consisted of interbedded poorly graded gravels and sands with trace to moderate silt. Groundwater was noted between strain gage intervals 4 and 5, perched above an approximate 7 ft high plasticity clay layer.

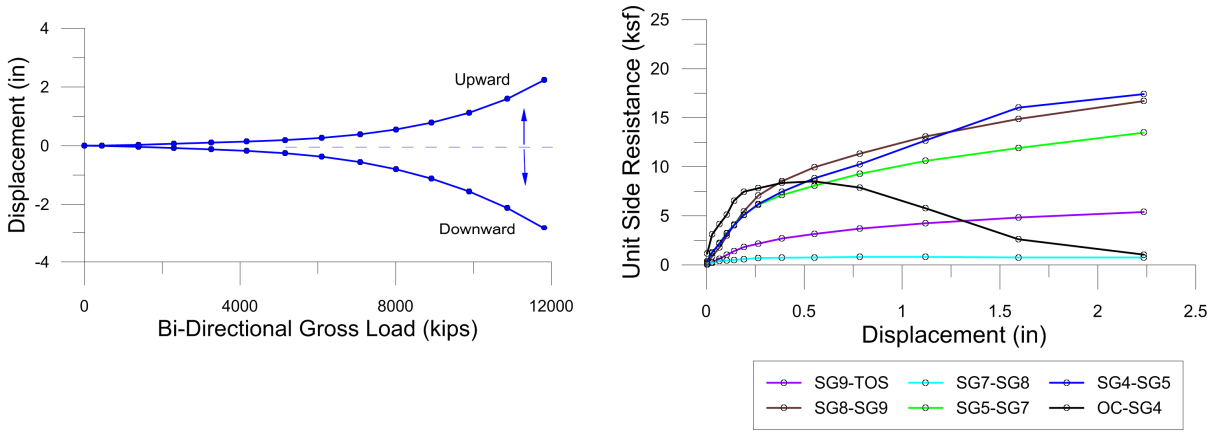


Fig. 2. Bi-Directional Plot and Typical Calculated Unit Side Resistance (LT-1404)

Observation of each calculated curve revealed three general trends in the mobilization of unit side resistance. Each curve was visually inspected and assigned one of three general criteria representing degree of mobilization of unit side resistance; (A) full, (B) partial and (C) initial. Criteria (A) are considered curves that clearly show an asymptotic behavior, Criteria (B) are considered to be approaching an asymptotic

behavior while all Criteria (C) were considered to display neither, appearing linear in mobilization (Fig. 3). The unit side resistance curves in Fig. 2 are considered to represent both Criteria (A) and (B). The strain gage intervals for OC-SG4, SG7-SG8 and SG9-TOS are each considered to Criteria (A) while the remaining intervals are considered Criteria (B). Further evaluation of the three criteria focused on the slope of the final portion of each curve. Values of the slope were estimated for each curve using the last two measured data points defining the curve. The estimated slope of each curve and visually assigned criteria was used to establish a distribution representing each criterion. A summary of the distributions and statistical summary are presented in the following Fig. 4 for Criteria (A) load test data.

Results of each criteria were fit using a normal distribution and define a reasonable range in values of slopes that could be used to establish mobilization criteria. The summary statistics based on the distribution of slopes comprising Criteria (A) as well as Criteria (B) and (C) are presented below in Table 2.

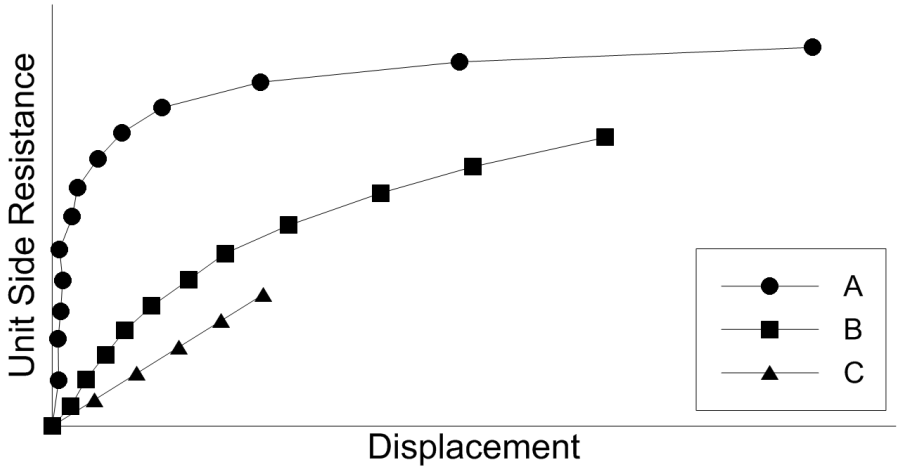


Fig. 3. Degree of Mobilization of Unit Side Resistance Criteria

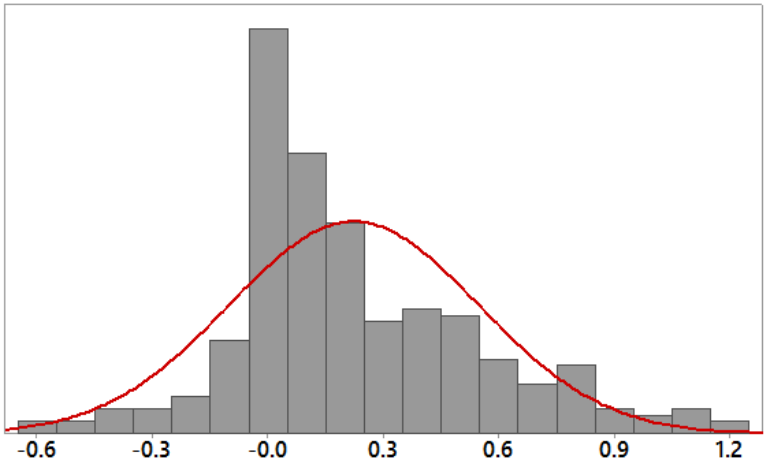


Fig. 4. Criteria A Load Test Data - Distribution of Slope of Unit Side Resistance

Table 2. Summary Statistics for Slopes of Criteria (A), (B) and (C)

Criteria	Mean	Standard Deviation	Median	95% Confidence Interval (Mean)	95% Confidence Interval (Median)
A	0.223	0.325	0.134	0.187 - 0.265	0.099 - 0.191
B	3.311	2.139	2.833	2.982 - 3.640	2.247 - 3.143
C	20.603	15.941	17.310	17.770 - 23.437	14.159 - 20.563

Limitations in predicting capacity of drilled shaft foundations has always presented a challenge when considering the magnitude of loads required to fully mobilize their capacity (Brown et al., 2010). Often static load tests do not fully mobilize the capacity and therefore the prediction of their ultimate capacity is determined though several interpretation techniques (Paikowsky and Tolosko, 1999). Fellenius (2001) evaluated some of these techniques in interpreting pile capacity. These techniques were derived to evaluate capacity using load-movement records from static load tests. Our study explored some of the techniques discussed by Fellenius and other researchers to explore the potential in extrapolation of unit side resistance of drilled shaft foundations. For the purposes of our study, we did not consider a load criteria in estimating the nominal capacity of drilled shaft foundations. Our focus was to estimate the maximum mobilized unit side resistance between strain gages along the length of a drilled shaft.

Fellenius (2001) presents a discussion on predicting ultimate pile capacity using five different techniques. Our study specifically focused on three of those methods presented as (1) Hansen 80%, (2) Chin-Kondner and (3) Decourt extrapolation techniques. In the following subsections we will briefly review each extrapolation technique and present sample results to further illustrate the technique. Although the extrapolation techniques presented by Fellenius (2001) are intended for predicting the ultimate capacity of pile foundations for static load tests, we utilized the general relationship of each technique to predict loads of individual sections measured by strain gages along the length of a subject shaft. In general, certain limitations should be expected in use of the following methods. Consideration should be given to the quality of load test data regarding magnitude of measured displacement and its corresponding load. Potential defects in the shaft could exaggerate the magnitude of displacement. These predicted loads are then used to estimate unit side resistance at specified shaft displacements. The unit side resistance eq. [1] is determined as the difference in net load between strain gage intervals divided by the product of the perimeter and length of shaft between the strain gages.

$$f_{(z)} = \frac{\Delta Q_{(z)}}{(p)(\Delta z)} \qquad [1]$$

Extrapolation was performed using each of the following three techniques presented in Fellenius (2001). In our study, extrapolation was performed for the final 50% of each measured displacement record. The following sample results, presented with each method, utilized data calculated from the previously presented project (LT-1404) and represent strain gage sections SG1-SG2.

Hansen 80% Extrapolation

The first technique, Hansen 80% extrapolation, is based on the assumption that the capacity is defined as four times the movement of the pile head as obtained for 80% of the load (Paikowsky and Tolosko, 1999; Fellenius, 2001). The load-settlement relationship for Hansen 80% is defined using the following eq. [2]. The ultimate capacity at failure assumes a hyperbolic relationship between load and pile displacement.

$$Q = \frac{\sqrt{\Delta}}{C_1\Delta + C_2} \quad [2]$$

Where Q = applied load, Δ = movement, C_1 = slope of the straight line in the $\sqrt{\Delta}$/q versus movement diagram, and C_2 = y-intercept of the straight line in the $\sqrt{\Delta}$/q versus movement diagram. Figure 5 presents a typical plot of the load-settlement relationship used for Hansen 80% extrapolation. Additionally, Figure 5 also presents the measured bi-directional plot with subsequent extrapolated loads. The straight-line portion of the plot is used to define the slope and y-intercept.

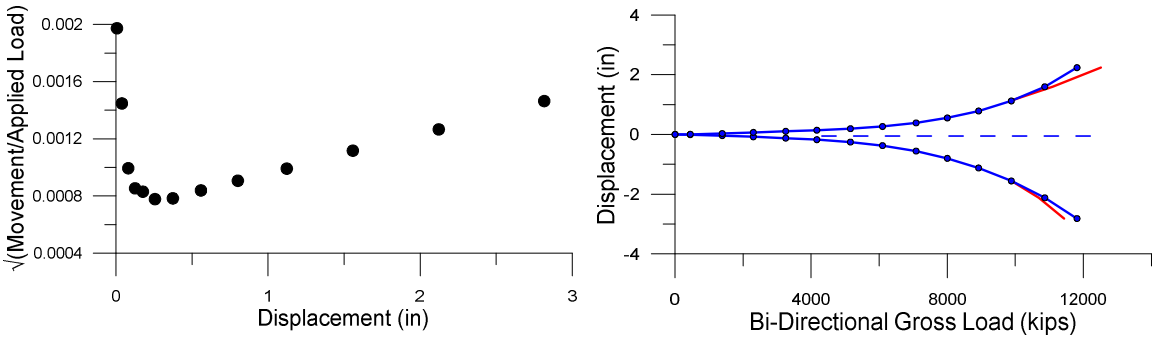


Fig. 5. Hansen 80% Extrapolation Method Example Result

Chin-Kondner Extrapolation

The second technique, the Chin-Kondner extrapolation, is based on a similar hyperbolic relationship to Hansen 80%. The load-settlement relationship for Chin-Kondner is defined using the following eq. [3].

$$Q = \frac{\Delta}{C_1\Delta + C_2} \quad [3]$$

Where Q = applied load, Δ = movement, C_1 = slope of the straight line in the Δ/q versus movement diagram, and C_2 = y-intercept of the straight line in the Δ/q versus movement diagram. Figure 6 presents a typical plot of the load-settlement relationship used for Chin-Kondner extrapolation as well as the extrapolated portions of the bi-directional plot.

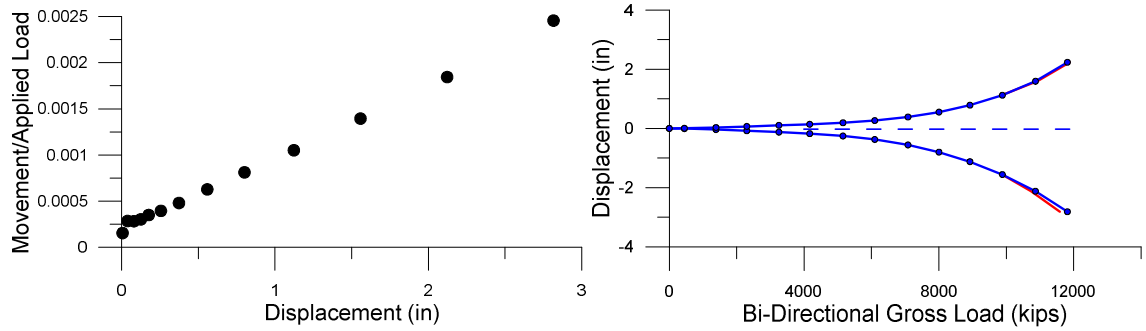


Fig. 6. Chin-Kondner Extrapolation Method Example Result

Decourt Extrapolation

The final technique, Decourt extrapolation, utilizes linear regression to establish a straight-line portion on the curve of the load/movement plotted against the load. The load relationship for Decourt is defined in the following eq. [4].

$$Q = \frac{C_2 \, x \, \Delta}{1 - C_1 \, x \, \Delta} \qquad [4]$$

Where Q = applied load, Δ = movement, C_1 = slope of the straight line in the Q/Δ versus movement diagram, and C_2 = y-intercept of the straight line in the Q/Δ versus movement diagram. Figure 7 presents a typical plot of the load-settlement relationship used for Decourt extrapolation as well as the extrapolated portions of the bi-directional plot.

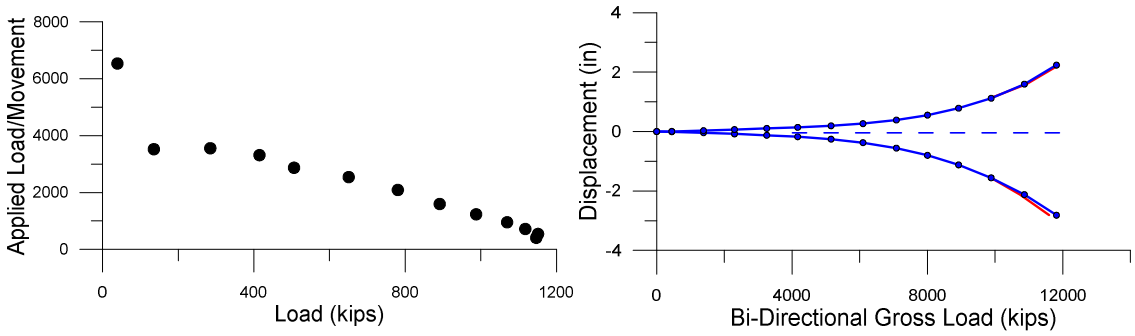


Fig. 7. Decourt Extrapolation Method Example Result

The slopes derived from each extrapolation were estimated by using the using two data points that bounded the displacement equal to 50% of the measured record.

RESULTS

Applying the extrapolation techniques (Hansen 80%, Chin-Kondner and Decourt) from the previous section, we extrapolated unit side resistance for the Criteria (A) dataset. The following Figs. 8, 9 and 10 present the results of each extrapolation technique applied to the measured data for LT-1404. Each figure presents the full measured record of displacement and calculated unit side resistance for each interval of strain gages above the bi-directional cell. All extrapolations are presented using a red dashed line and originate from 50% of the original measured displacement record and are estimated to the final displacement of the measured record.

Extrapolated unit side resistance was compared to the calculated curves by applying the Root Mean Square Error (RMSE) as a means of quantifying the accuracy of the three techniques. RMSE is the average vertical distance of the actual data points from the extrapolated line and is calculated using the following eq. [5] (Salkind, 2010). Where x_i = measured value, x = extrapolated (predicted) value, and n = number of residuals used in the extrapolation.

$$RMSE = \frac{\sqrt{\Sigma(xi - x)\text{^}2}}{n} \qquad [5]$$

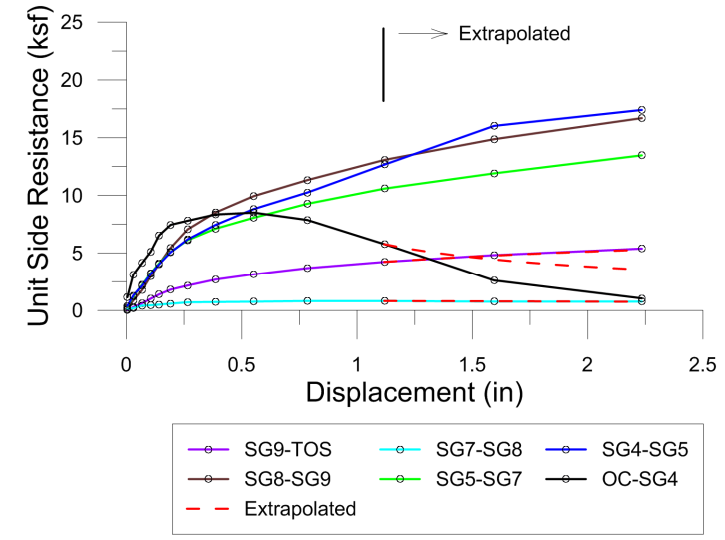


Fig. 8. Extrapolated Unit Side Resistance (Hansen 80% Method)

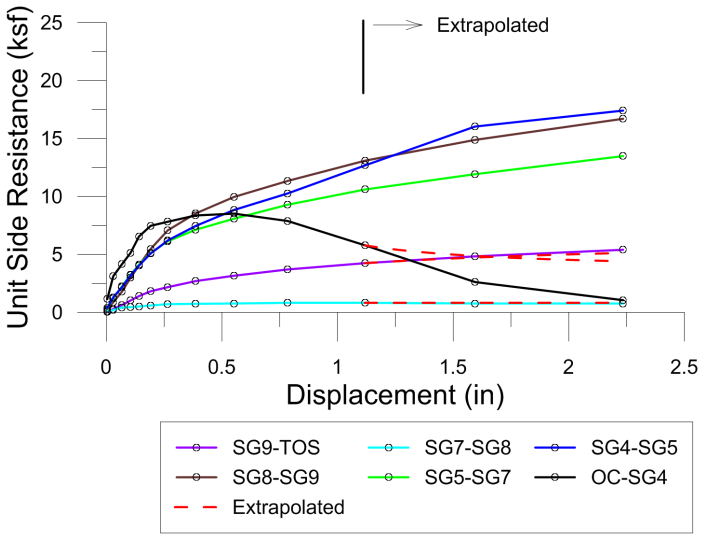


Fig. 9. Extrapolated Unit Side Resistance (Chin-Kondner Method)

Comparison of RMSE for all Criteria (A) curves show comparable results as presented in Table 3. First, we observed that the values of RMSE calculated using the Chin-Kondnder extrapolation method are identical to the values calculated using the Decourt extrapolation method. Subsequent statistical review of each calculated RMSE suggest that both the Hansen 80% and Chin-Kondner extrapolation methods produce similar results. Summary of the statistical results are presented below in Table 3.

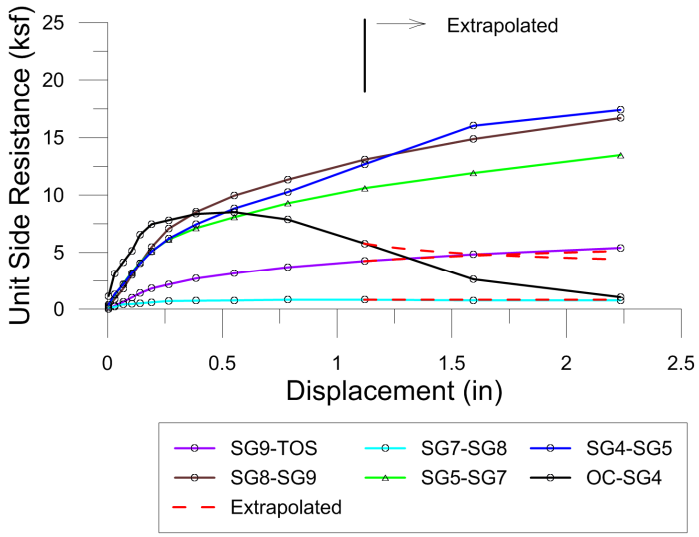


Fig. 10. Extrapolated Unit Side Resistance (Decourt Method)

Table 3. Summary Statistics for RMSE of Extrapolations Techniques

Technique	Mean	Standard Deviation	Median	95% Confidence Interval (Mean)	95% Confidence Interval (Median)
Hansen 80%	0.521	2.799	0.0864	0.135 - 0.906	0.071 - 0.108
Chin-Kondner	0.627	5.889	0.057	-0.1843 – 1.438	0.041 – 0.074
Decourt	0.627	5.889	0.057	-0.1843 – 1.438	0.041 – 0.074

SUMMARY AND CONCLUSIONS

Current load test methods present challenges when considering the magnitude of loads required to fully mobilize their capacities. Application of these full scale load tests, often times, do not fully mobilize the capacity through side resistance. The evaluation of three techniques (Hansen 80%, Chin-Kondner and Decourt) to extrapolate unit side resistance based on bi-directional load test data was presented. These evaluations utilized a database consisting of 116 bi-directional load test records. Each load test record within the database was digitized and used to calculate unit side resistance curves for each interval of strain gage instrumentation installed along the length of the shaft. Unit side resistance curves were assessed for degree of mobilization and assigned one of three Criteria (A), (B) and (C). Criteria classified by degree of mobilization were classified by the following behavior; Criteria (A) – Unit side resistance behavior is fully mobilized and asymptotic, Criteria (B) – Approaching asymptotic mobilization and Criteria (C) – mobilization appears linear in behavior and does not fit Criteria (A) or (B). Criteria of each curve was further evaluated by reviewing the slope of the final portion of each unit side resistance curve. These slopes were used to derive statistical summaries of each criteria. This study focused solely on unit side resistance curves classified as Criteria (A) or fully mobilized.

Extrapolation of all Criteria (A) curves were performed using three extrapolation techniques to predict nominal capacity of pile foundations using static load tests. Extrapolations of unit side resistance were performed using the final 50% of measured displacement records. Results of each extrapolation were compared to the measured values using the Root Mean Square Error (RMSE). Results of the evaluations show that two of the methods, Chin-Kondner and Decourt, produce identical results in predicting unit side resistance. Comparison of Hansen 80% and Chin-Kondner show reasonable agreement.

Future evaluation of these techniques will include extrapolation of measured records at different levels of displacement (i.e. 10%, 25% and 75%). A similar approach will be performed using all available Criteria (B) and (C) from our dataset, drawing any conclusions by comparison of the RMSE. Lastly, the intent of this exercise is to explore any diameter dependency of unit side resistance for drilled shaft foundations installed in similar soil types.

ACKNOWLEDGMENTS

We would like to thank the International Association of Foundation Drilling (ADSC) for providing funding to conduct this study. We would also like to personally thank Robert Simpson, Jon Sinnreich, Ray Fassett and Peggy Hagerty Duffy for their useful discussion, invaluable insights on drilled shaft foundations and coordination in obtaining load test data. In addition, we would also like to thank the Arizona Department of Transportation (ADOT), Alabama Department of Transportation (ALDOT), California Department of Transportation (Caltrans); namely Xinbao Yu (UT Arlington) and Murad Abu-Farsakh (LSU) who provided load test data from LA and MS for their research study, Nevada Department of Transportation (NDOT), North Carolina Department of Transportation (NCDOT), Oregon Department of Transportation (ODOT) and Washington Department of Transportation (WSDOT) for their generous contributions in load test data.

REFERENCES

Brown, D.A., Turner J.P., & Castelli, R.J., 2010. Drilled Shafts: Construction Procedures and LRFD Design Methods. US Department of Transportation, Federal Highway Administration.

Fellenius, B.H., 2001. What Capacity to Choose from the Results of a Static Loading Test. Deep Foundations Institute, Fulcrum, May 2001, 4 p.

Hagerty Duffy, P., Holman, T.P., and Sellountou, E.A. 2016. Small Scale, Large Benefit. Foundation Drilling, November/December 2016, 4 p.

Lizzi, F. 1983. Ultimate Bearing Capacity of Friction Piles Calculated from Load Tests on Pilot Piles. Ground Engineering, pg 41-45.

Motamed, R., Stanton, K., Elfass, S., and Kluzniak, B. 2016. Development of the Nevada Deep Foundation Load Test Database: Drilled Shaft Component. TRB 95th Annual Meeting, January 10-14, 2016, Washington D.C., Presentation No. 16-3925.

Pease, J. 2014. Southeast Connector Project Foundation Design. Personal Communication

Paikowsky, S.G., and Tolosko, T.D., 1999. Extrapolation of Pile Capacity from Non-Failed Load Tests. Federal Highway Administration (FHWA), FHWA-RD-99-170, 172 p.

Salkind, N.J. 2010. Encyclopedia of Research Design. SAGE Publications, 2 p.

NEW FOCUS: ENVIRONMENTAL IMPACT REDUCTION OF PROPER SLURRY WASTE MANAGEMENT

Zachary Q. Maassen, E.I.T, BOS Solutions, Houston, Texas, USA, #817-805-5858
Zachary.Maassen@bos-solutions.com

ABSTRACT

The purpose of this paper is to highlight the environmental benefits of properly managing slurry waste as it is generated on site. The following projects will be used to illustrate the importance of proper onsite waste management.

Project: Jet Grout Backflow Dewatering

The goal was to dewater the backflow directly onsite to produce a dry, solid waste and reusable water. The backflow spoil was pumped directly to the dewatering system as it was generated. Utilizing mechanical separation equipment and flocculation polymer the waste volume was reduced by 44%. Due to the site footprint and high volumes, slurry waste removal and onsite processing were the only two feasible options. Onsite dewatering proved to be the environmentally beneficial option as it eliminated the need for slurry waste hauling and disposal. The benefits of utilizing a dewatering system are listed below:

Project: Soil Mixing Spoil Recycling for Slurry Wall Construction

In this application the spoils generated contain bentonite mud, cement mixture and organic ground soils. The goal of this project was to process the backflow mixture to recover reusable bentonite mud and separate the soil as a dry, stackable waste product. The treatment system replaced the traditional method of vacuum truck extraction and facility disposal. The environmental benefits of properly handling the backflow is a decrease in fresh water usage, bentonite additive reduction, and the reduction of CO_2 emissions.

The paper will consist of a project scope, technical equipment and process description, environmental impact reduction calculations and lessons learned for each project.

© 2018 Deep Foundations Institute

PROJECT 1 – JET GROUT BACKFLOW DEWATERING

SCOPE OF WORK

Jet grouting is a method of ground improvement that relies on the erosive capacity of high-speed jets to cut and mix the ground in place with a cementitious grout. A continuous return flow of cuttings, called jet grout backflow or spoils, is expelled to the surface during the grouting process. The backflow, or spoils, is a mixture of grout, water and soils. Traditionally, the spoil would be collected in in-ground pits and allowed to solidify for a few days prior to hauling to a final disposal site. For this project, the jet grouting work was performed at street level, in high traffic congested areas, presenting the challenge of insufficient space for the contractors to process the jet grout spoils in the traditional way. At first, attempts were made of using vacuum trucks to collect and haul the wet spoils to an off-site location where the spoils would be allowed to solidify. However, this method proved cumbersome and expensive due to the high volumes of spoils generated daily and the high number of vacuum trucks required to support the jet grouting operations, respectively.

The equipment utilized was a tank system, centrifuges and flocculation additives to remove the ground soils and grout product from the slurry producing clean water for reuse. This is an environmentally friendly process and reduces several steps of the conventional handling and disposal methods.

OBJECTIVES

1. Process jet grouting waste to:
    - Reduce overall waste volume and cost
        - Eliminate vacuum truck hauling
        - Reduced environmental impact of waste hauling
2. Provide a clean fluid for reuse and/or economical disposal methods
    - Control pH in recovered water as needed to pass for reuse or disposal
3. Operate at full capacity of operations to eliminate downtime associated with disposal or waste treatment

EQUIPMENT & PERSONEL REQUIRED

- BOS PreMix Tank – 79.5 m^3 (500 bbl)
    - 2 Derrick Drying Shakers mounted on top
- BOS III Tank – 34 m^3 capacity (246 bbl)
    - 2 BOS 40 Centrifuges on hydraulically lifted stand
- Shale Bin
- Track Hoe
- Ancillary Equipment (Pumps, Hoses, Pipe Fittings, Tools)
- 1 BOS Field Technician

PROCEDURE

The following bullet points explain the typical flow pattern in treating the jet grout waste. Refer to Figure 1 for an onsite diagram of the equipment.

1. Jet grouting spoils slurry is pumped to the BOS System.
2. The slurry is pumped over the Drying Shakers to remove large solids and floating debris.
3. The Drying Shaker underflow is contained in the BOS PreMix tank and is pumped to the BOS III Tank system to remove the remaining ground soils, colloidal solids and grout.
4. The BOS III Tank is primed with fresh water such as lake, river or storm water. These are ideal fresh water sources as chlorines and other chemicals in typical city water can contribute to micro toxins in the clear treated fluid to be pumped off.
5. The fresh water is circulated through the BOS 40 centrifuge establishing the BOS Clear Water Loop.
6. Polymer is mixed to a specific and predetermined concentration.
7. Screened slurry from the BOS PreMix is injected into the BOS Clear Water Loop.
8. The polymer mixture is injected with the slurry before the centrifuge.
9. This process is continuous until the waste is treated. This results in an increased volume of clean water in the BOS III Tank. This additional water that was removed from the slurry is called recovered fluid.
10. The recovered fluid can be used to mix new polymer batches, flush equipment and reused on next project or pumped down a sanitary sewer.
11. Solids that are removed will be collected on ground or in supplied bin for removal.
12. Once processing is complete, equipment will be drained, serviced and prepared to be on standby for next batch to be processed.

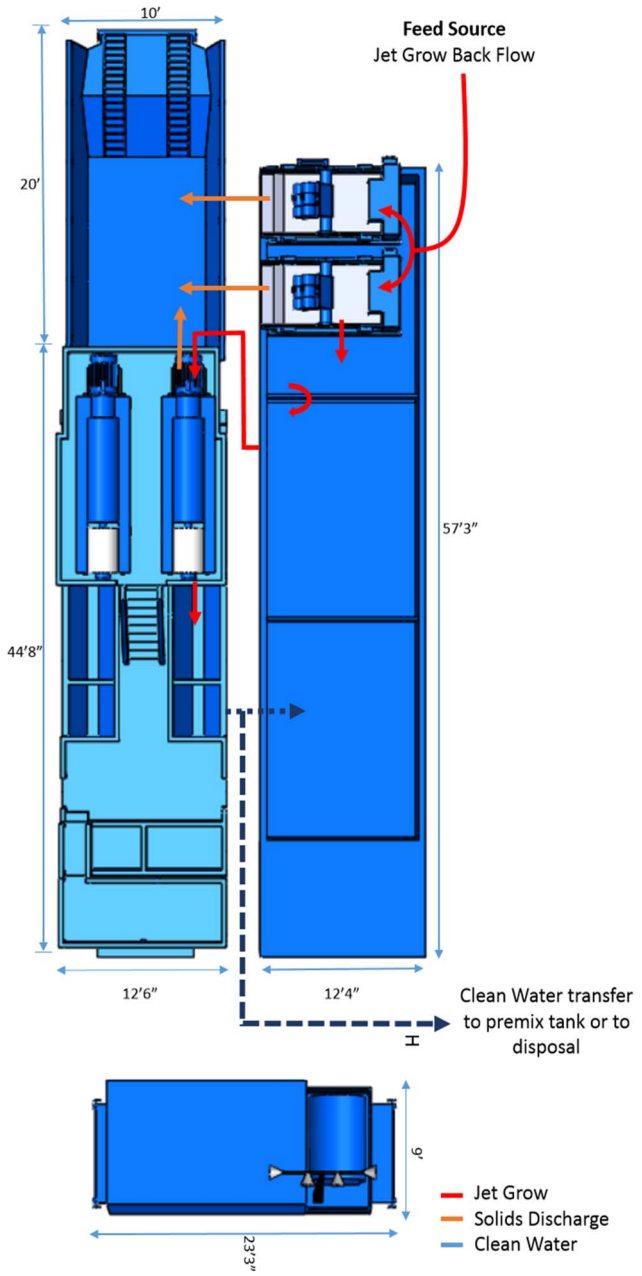


Figure 1: Jet Grout Flow Pattern & Design

PERFORMANCE

Job Details

- Location: Ottawa, Ontario, Canada
- Number of columns: 60
- Column Diameter (m): 1.8 (5.9 ft)
- Column Depth (m): 24 – 31 (78.74 – 101-71 ft)
- Volume of Jet Grout Spoils per Column (m^3): 29 (1,024 ft^3)
- Daily Volume of Jet Grout Spoils Generated (m^3): 58 (2,048 ft^3)
- Jet Column Length Range: 5 – 23m (16.4 – 75.46 ft)
    - Average: 11.1 m (36.42 ft)
- Specific Gravity of Jet Grout Spoils: 1.2 – 1.8

Results

This process successfully reduced the overall waste volume and created a dry, stackable waste product, resulting in fewer truck loads needed to haul off spoils to disposal. Additional water was added to the spoils. This water addition was required to reduce the density and viscosity of the spoils for them to be pumped over to the BOS System. The addition of water would have been used in either disposal method whether it was by traditional vacuum truck transportation or an onsite treatment option such as the BOS System. These water additions did increase the volume of recovered water. Due to the chemical properties of the grout and hole conditions, citric acid was added to the spoils to lower the pH within the City of Ottawa's disposal criteria. The addition of citric acid to reduce the pH would have been needed regardless of the method of onsite treatment. Technicians used 88 bags of citric acid for the entirety of the project. No downtime to the jet grout operation was ever caused by the implemented process. The cleaned fluid met the Ottawa City Sewer disposal criteria and the disposed solids complied with all the solid waste landfill requirements.

At the conclusion of this project, a total project savings analysis is provided in Table 1 and Figure 2.

Table 1. Total Project Savings

Total Project Savings					
Vacuum Trucks			***BOS System***		
Parameters	**Value**	**Units**	**Parameters**	**Value**	**Units**
Waste for Disposal (Grout, Soil, and Water Mix)	2,177 (2,399)	tonnes (tons)	Waste for Disposal (Dried Grout and Soil)	1,161 (1,279)	tonnes (tons)
Vacuum Truck Cost ($.30 cents/L) *projected	$525,000.00	Canadian Dollars	End Dump Truck Cost ($133.19 per tonne)	$154,637.00	Canadian Dollars
			BOS Equipment and Labor Costs	$247,947.00	Canadian Dollars
TOTAL COST	$525,000.00		$402,584.00		
TOTAL COST SAVINGS			**$122,416.00 (23% reduction)**		
TOTAL WASTE SAVINGS			**1,016 tonnes (1,119 tons) (47% reduction)**		

*NOTE: The traditional disposal method of utilizing vacuum trucks is an estimated cost. It was calculated using an industry stand of 30 cents per litre. This estimate covers both the trucking and disposal of the liquid waste.

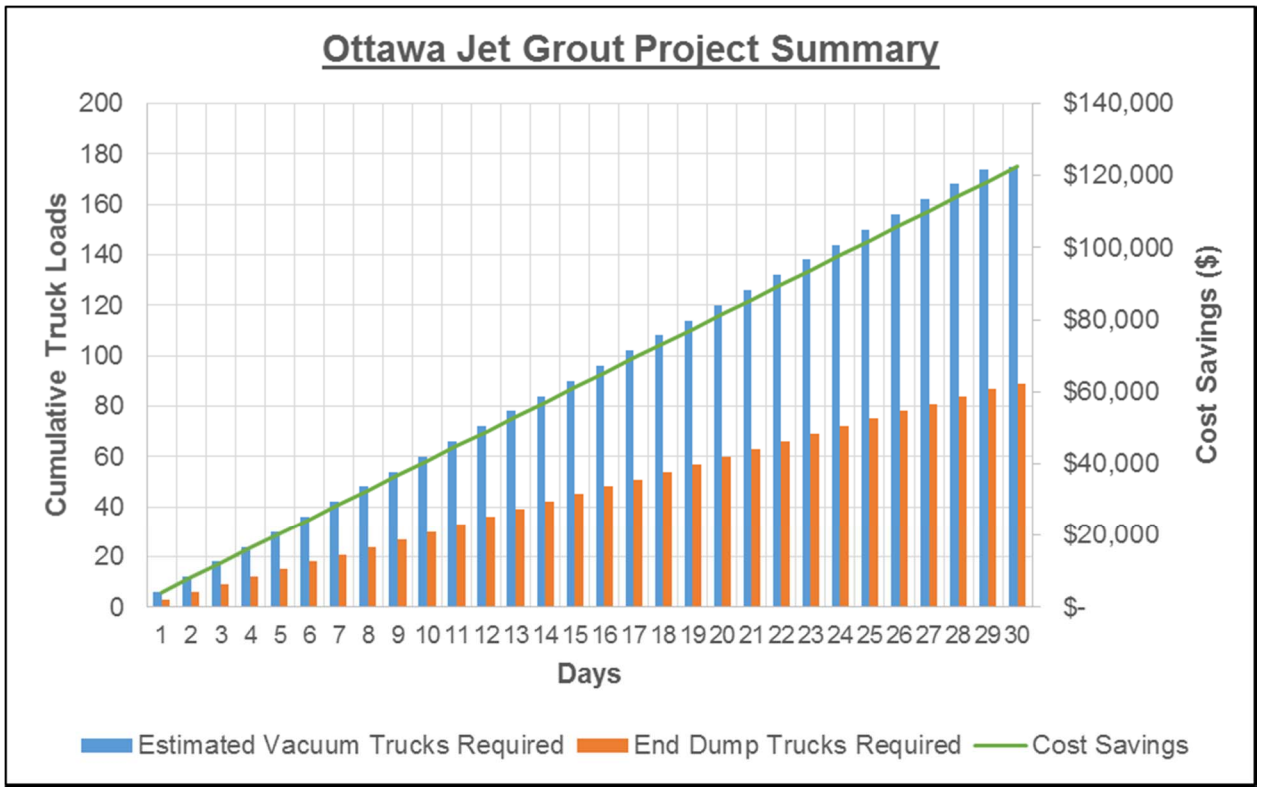


Figure 2: Ottawa Truck Load Reductions and Cost Savings

Additional Project Savings

In addition to the spoils treatment and disposal savings, numerous environmental savings can be contributed as a direct result from utilizing the onsite waste management described. Through creating a dry, stackable, solid material this process significantly reduced the amount of waste hauling trucks that would have been required using traditional methods. Thus, resulting in less traffic, decreased carbon footprint and increasing public safety by reducing potential vehicular accidents or spills that could have occurred.

A summary of estimated environmental savings can be seen in Table 2.

Table 2. Estimated Environmental Savings

Environmental Impact Reductions	
Waste Trucking Loads Saved	**240**
Fuel Cost Savings	**$15,396**
Fuel Saved, L (gal)	**14,453 (3,818)**
Mileage Saved, km (miles)	**18,867 (11,723)**
Greenhouse Gas Emissions Reduced, kg CO_2 (lbs)	**38,814 (85,570)**

PROJECT 2 – SOIL MIXING SPOIL RECYCLING FOR SLURRY WALL CONSTRUCTION

SCOPE OF WORK

Slurry walls are constructed using a bentonite or cement-bentonite slurry to stabilize the trench during excavation. The cement-bentonite mixture will mix with insitu soils to harden and form a wall. The excess backflow and bentonite mud is typically removed from the cutter head with a loader or vac truck and either hauled to drying pads or disposal facilities. New bentonite and grout mixture is constantly made up to accommodate the volume needed. Depending on the size of the project this results in a large volume of waste and product usage.

Equipment was deployed onsite that was self-powered to reprocess the backflow. By utilizing the combination of a shaker, centrifuge and tank system, this equipment was able to remove dry solids from the backflow and condition the bentonite mud to within spec for reuse.

OBJECTIVES

1. Process slurry wall backflow waste to:
    - Recover and reused bentonite mud
        - Reduces consumable usage onsite
    - Reduce overall waste volume and cost by producing a dry waste product
        - Eliminate vacuum truck hauling
        - Reduced environmental impact of waste hauling
2. Operate at full capacity of operations to eliminate downtime associated with disposal or waste treatment

EQUIPMENT REQUIRED

- BOS IV Tank – 32 m^3 capacity (200 bbl)
    - 2 BOS 40 Centrifuges on hydraulically lifted stand
    - Shale Shaker
- Track Hoe / Loader (to feed system)
- Ancillary Equipment (Pumps, Hoses, Pipe Fittings, Tools)

*Zero full time personnel required to operate system

PROCEDURE

The following letter points explain the typical flow pattern in treating the soil mixing backflow waste. Refer to Figure 3 for an onsite diagram of the equipment.

1. Spent bentonite slurry is pumped to the Shale Shaker
2. Large debris and solids are separated out of the fluid and discharged to the Shale Bin
3. Fluid will pass through the shaker screen and is discharged in to cell 3 of the BOS IV Tank
4. Fluid is pumped to the centrifuge
5. Solids are discharged to the Shale Bin
6. Centrifuge effluent is discharged in to Cell 1 of the BOS IV Tank
7. Conditioned mud is pumped out of the BOS IV Tank to the bentonite plant or a holding cell for reuse

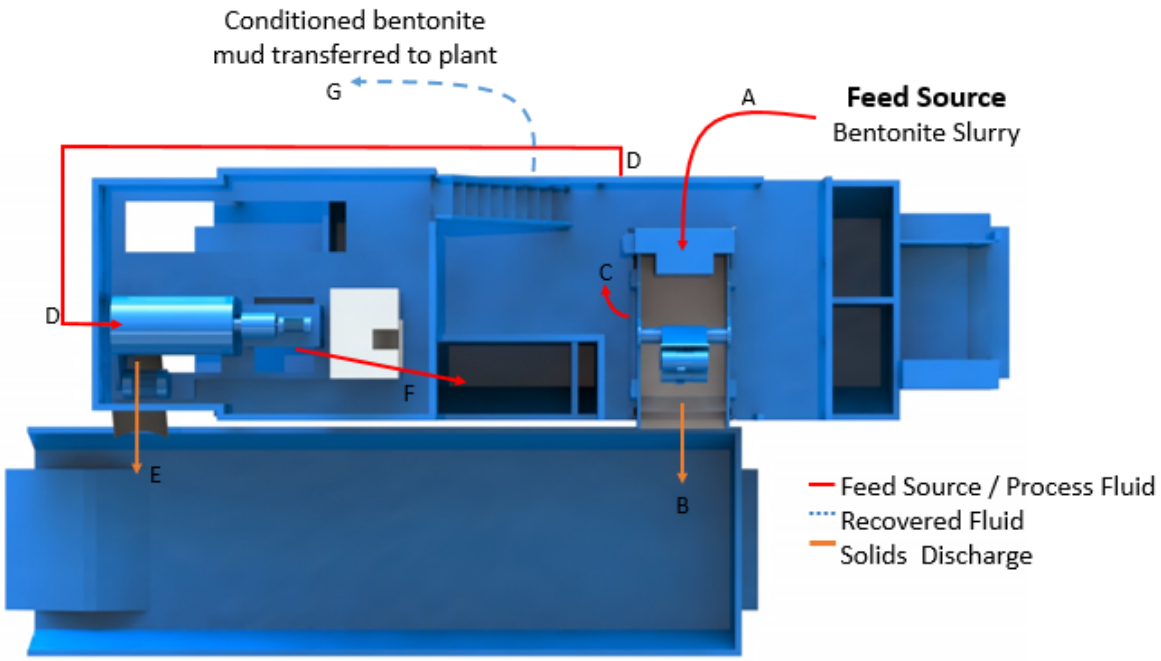


Figure 3: Soil Mixing Flow Pattern and Design

PERFORMANCE

Job Details

- Location: Vancouver, British Columbia, Canada
- Project Length: 3 Months
- Volume of Bentonite Plant (m^3): 30 (7925 gallons)
- Desired Bentonite Viscosity (sec/L): 30-35 (32-37 sec/qt)
- Desired Bentonite Mud Specific Gravity: 1.05 – 1.10
- Specific Gravity of Spoils Mixture: 1.15-1.30

Results

By processing the spoils, reusable bentonite is removed from the soil producing a dry waste product. This volume accounted for a 40% reduction. This also eliminated the need for vacuum trucks to haul a liquid waste slurry to disposal. Reconditioning the bentonite allows for the recycling of product reducing the overall need for fresh bentonite additives. The only transferred bentonite mud back to the plant for reuse, was the volume that met the specifications listed above.

The deployed equipment was able to reduce operational cost by eliminating the need for liquid waste disposal, reuse mud product and eliminate operational downtime due to traditional operation. Refer to Table 3 for key results; total values are based upon 75 operating days and daily averages.

Table 3. Estimated Environmental Savings

Operating Results		
	Metric	**Imperial**
Average Density of Recovered Bentonite Mud	1,073 kg/ m^3	8.955 ppg
Average Viscosity of Recovered Bentonite Mud	34 sec/L	36 sec/qt
Average Volume of Recovered Bentonite Mud per Day	8.9 m^3	2,340 gallons
Average Bentonite Usage Reduction per Day *(assuming 2.5 kg / m3 addition rate)*	22.1 kg	49 lbs.
Total Volume of Recovered Bentonite Mud *(fresh water saved)*	664 m^3	175,410 gallons
Total Bentonite Usage Reduction	1,657 kg	3,653 lbs.

CONCLUSION

In both case studies presented, the proper solids control equipment and expertise decreased the traditional fluid system and waste handling costs by an estimated 20-30%. Another key benefit was decreasing the environmental impact by replacing the traditional handling procedures. These clients were not only able to substantially reduce their spoils treatment costs, but were also able to vastly reduce their environmental footprint by utilizing less trucking services. Specifically, for the Jet Grout Backflow Recycling project, operating that particular system decreased the consumption of over 14,000 L (3,800 gal) of diesel fuel resulting in a decreased greenhouse gas, CO_2, Methane, and Nitrous Oxide, emissions by over 38,000 kg (85,000 lbs). The implementation of proper onsite waste and fluid management is more important now than it has been in years past with decreasing site footprints, increased environmental regulations and disposal costs.

VALUE ENGINEERING OF REINFORCEMENT USED IN LARGE DIAMETER DRILLED SHAFTS

Shahid Islam, DYWIDAG-Systems International, Bolingbrook, IL, USA, 1-630-972-4028, shahid.islam@dsiamerica.com

Lucian Bogdan, DYWIDAG-Systems International, Long Beach, CA, USA, 1-562-295-3907, lucian.bogdan@dsiamerica.com

ABSTRACT

Deep and large diameter drilled shafts use mostly bundles of Grade 60 (415 MPa) reinforcing bars as longitudinal reinforcement with rebar splices to make it longer. Lower Grade steel requires large number of bars which result in rebar congestion and difficulty in placing concrete. This leads to increased labor cost for fabrication and installation. By utilizing larger size and higher strength threadbar, the congestion of rebar can be reduced significantly and bundling of bars can be avoided. The lap splices are replaced with simple threaded couplers and end hooks are replaced with end terminators. Threadbar conforms to ASTM A615-15 and can be epoxy coated if required for corrosion protection. This paper describes an attractive value engineering of replacing Grade 60 (415 MPa) bundle of rebars with larger diameter Grade 75 (515 MPa), Grade 80 (550 MPa) and Grade 100 (690 MPa) threaded bars and threaded couplers in some specific drilled shaft projects in the USA.

Keywords: drilled shaft, rebar, high strength, threadbar, congestion

INTRODUCTION

A drilled shaft which may also be referred to as drilled piers, caissons, cast-in-drilled-hole piles and bored piles is the key element to the foundation of massive structure. They are used for tall buildings, bridges and foundations for other applications such as retaining walls, sound walls, signs, or high mast lighting. Drilled shaft foundations are typically 3 to 12 feet (0.9m to 3.7m) in diameter cast-in-place deep foundation elements constructed in a drilled hole that is stabilized to allow controlled placement of reinforcing steel and concrete. Drilled shafts for transportation structures are commonly used to depths of up to 200 ft (61m) in the USA. Drilled shafts can be installed in a variety of soil and rock profiles, and are most efficiently utilized where a strong bearing layer is present. The reinforcing cage is typically lowered into position within the hole and then concrete placed through the center of the shaft, flowing from bottom to top through the reinforcement to fill the hole.

The design of the reinforcing cage for a drilled shaft is a necessary step in the engineering process. Rebar cages are considered from two perspectives- geometry of the steel necessary to resist stresses that develop because of loads applied to the drilled shaft and the characteristics of the cage from the perspective of constructability. A rebar cage for a drilled shaft is made up of longitudinal bars that are normally distributed with equal spacing around the outside of a cylinder. Transverse reinforcing is placed around and attached to the longitudinal bars, with the longitudinal and transverse steel being held together with ties. The properties of steel that may be employed for building rebar cages is based on ASTM A615-15 of Grade 60 (415 MPa) thru Grade 100 (690 MPa) and available larger bar sizes (refer to Table 2 & Table 1 of ASTM A615). Per section 5.4.3.1 of AASHTO LRFD 7th Edition, steel with yield strength of 75 ksi can be used for design purposes. Furthermore per Section 5.4.3.3 of AASHTO LRFD, steel with a yield strength of 100 ksi (690 MPa) can be used for all elements in seismic zone 1. Although current ACI 318-14 allows yield

© 2018 Deep Foundations Institute

strength of 80 (550 MPa) ksi in design, it is expected that this will change to 100 ksi (690 MPa) in the next edition of ACI 318.
The minimum clear spacing between longitudinal bars (and between transverse bars or spiral loops, as well) must be sufficient to allow free passage of the concrete through the cage and into the space between the cage and the borehole wall. This spacing is particularly important because drilled shaft concrete is placed without resorting to vibrating the concrete to consolidate (See Fig. 1). It is suggested that a minimum spacing of 8 times the size of the largest coarse aggregate in the mix is needed to avoid blocking for tremie-placed concrete. The recommendations for minimum clear spacing should also apply to access tubes which may be included for non-destructive testing. In some instances, two or three bars can be clustered, or "bundled," together to increase the steel percentage while maintaining a cage with appropriate rebar spacing. Bundling of bars may require a greater development length beyond the zone of maximum moment.

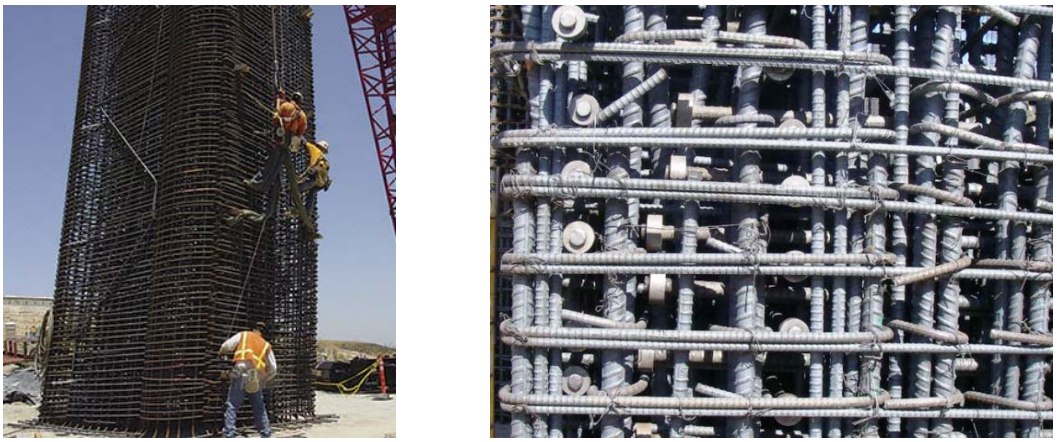


Fig. 1. Congestion of rebars makes difficult concrete flow

Two concentric rebar cages have occasionally been used to provide an increased amount of steel for drilled shafts with unusually large bending moments. However, the two cages result in increased resistance to lateral concrete flow during placement, and greatly increase the risk of defective concrete at the perimeter of the drilled shaft and in the space between the two cages. In such cases, consideration should be given to using high strength and larger diameter threadbars.

In order for the reinforced concrete to function as designed, the longitudinal bars must bond to the concrete, and therefore the surface of the bars must be free of excessive rust, soil, oils, or other contaminants. Deformed bars are used to ensure that adequate bond to the concrete is achieved. Galvanized or epoxy-coated steel is also available for longitudinal and transverse reinforcement for those cases where there is increased risk of corrosion.

Transverse reinforcing steel needs to be added to resist the shearing forces that act on a drilled shaft, hold the longitudinal steel in place during construction, provide the drilled shaft with sufficient resistance against compressive or flexural stresses, and confine the concrete in the core of the cage to give the drilled shaft post-yield ductility. The transverse reinforcing steel is provided in the form of ties, hoops or spirals. Particularly in seismic regions relatively large amount of transverse reinforcement may be required. If these longitudinal bars are bundled, the spacing of transverse ties/hopes are reduced to half. Tight spacing on spiral reinforcement can result in constructability problems with concrete flow through the cage. The failure of the concrete to flow through the cage results in inadequate cover and poor contact between the soil and shaft and even potential defect in drilled shaft concrete which is mostly found by the Crosshole Sonic Logging (CSL) method.

Splicing of the longitudinal reinforcement is required when the length of the cage exceeds the length of the available reinforcing bars, which is normally supplied in lengths of 60 ft or less. Splices in the longitudinal steel can be made by lapping the bars so that the bond in the rebar is sufficient to develop the full capacity of the bar in tension or compression in each bar at the point of the splice. Bundled bars require longer splice length. Larger size and higher strength threadbar can solve this congestion problem easily if threaded couplers are used.

There are cases where the cage is so long that it cannot be lifted conveniently in one piece, or where restricted vertical clearance precludes installation of a full length cage. In such a case, the cage can be spliced in the borehole. The lower portion of the cage is lifted, placed in the excavation, and held with its top at a convenient working level while the upper portion is lifted and positioned so that the two portions of the cage can be spliced together. If threadbar is used, connecting of the vertical bars using a coupler simplifies this operation.

THREADBAR APPLICATIONS

Threadbars have been used in many building and bridge foundations over the period of last twenty years. Some of the applications are described below.

Threadbars were used in the construction of St. Anthony Falls (I-35W Bridge- Fig. 2a) in Minneapolis, MN. The original design called for Grade 60 (415 MPa) reinforcement. The vale engineering proposal used Grade 80 (550 MPa) bar of larger size to reduce the number of vertical bars. Minnesota Department of Transportation approved the proposal. A total of over 187,000 ft of #20 (63mm) Grade 80 (550 MPa) threadbars and over 2000 couplers (full tension-compression coupling capacity) were used for vertical reinforcement of the drilled shaft foundation elements (See Fig. 2b). Due to this alternate proposal, there was a potential reduction of bar quantity and weight, elimination of rebar splices and finally reduced the congestion. There were significant savings in terms of labor and construction time resulting in a monetary savings realized by the owner.



Fig. 2a. I-35W Bridge after completion



Fig. 2b. #20 Grade 80 Threadbars used in drilled shaft of I-35W Bridge

For the St. Croix crossing bridge, 40 caissons in diameters of approx. 9 ft (2.7m) were installed. The drilled shafts were originally designed with an inner reinforcing cage consisting of 16 #14 (44 mm), Grade 60 (415 MPa) vertical reinforcing bars and an outer cage consisting of 32 #14, Grade 60 vertical reinforcing bars inside the steel casing. New proposal included a more economical alternative using only 22 high strength, #20 (63mm), Grade 75 (515 MPa) threadbars for the longitudinal reinforcing bars. Two sets of vertical rebars per contract drawing were substituted with just one set of vertical bar as shown in Fig. 3. The owner, Minnesota Department of Transportation, accepted the proposal and a total of 98,590ft (30,060m) of threadbars were supplied to the jobsite together with 1,470 EA Couplers. There was 16% weight reduction in rebars. Fig. 4 shows a complete caging and its installation.

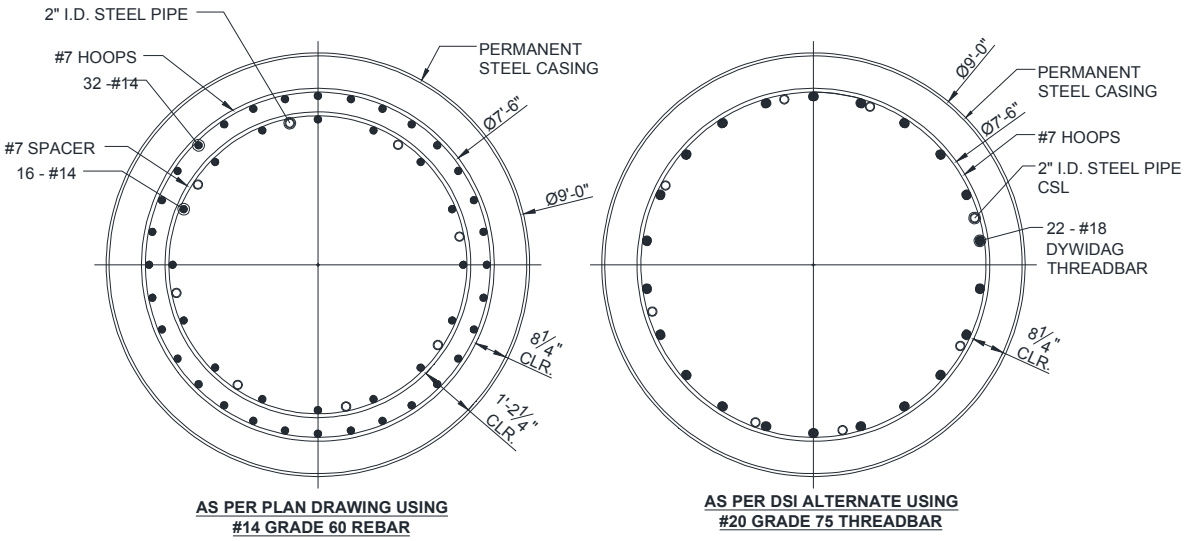


Fig. 3. Omision of inner longitudinal bars in drilled shafts on the St. Croix Bridge, MN



Fig. 4. #20 Grade 75 Threadbars used in drilled shaft of St. Croix Bridge, MN

Drilled shaft for I-29 over Mosquito Creek, Pottawattamie County, Iowa was originally designed with Grade 60 rebars. There were various sizes of drilled shafts ranging from 5 ft diameter to 6.5' diameter. Reinforcement in 5 ft (1.5m) diameter had 20#10 (32mm) Gr 60 (415 MPa) bars, which was substituted with 10#14 (44 mm) Gr 75 (515 MPa) bars. Reinforcement in 6.5 (2m) ft diameter had 48#9 (28mm) Gr 60 (415 MPa) bars, which was substituted with 18#14 (44 mm) Gr 75 (515 MPa) bars. Minimum steel ratio of 0.8% to the drilled shaft area was maintained. This resulted in a 7% rebar reduction in terms of weight. Iowa Department of Transportation approved the proposal. Full tension-compression couplers were supplied. Fig. 5a shows the cage and installation of it. Some shafts required hook bars at the top to resist the uplift. The hooks were substituted using end terminators as shown in Fig. 5b. This reduced the congestion of steel significantly. In addition, one drilled shaft was instrumented with four elasto- magnetic sensors on four longitudinal threadbars to monitor the compression forces taken by the bars as shown in Fig. 5c. Force readings were monitored at different stages of construction.



Fig. 5a. Threadbar cage and it's installation

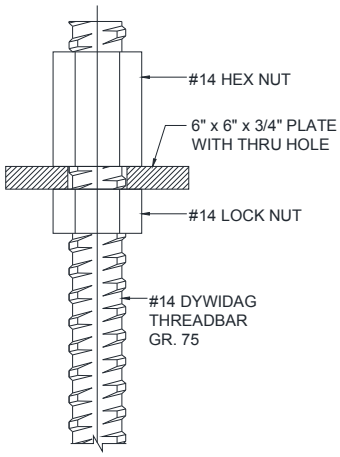


Fig. 5b. Threadbar terminator at top



Fig. 5c. Threadbar with sensors

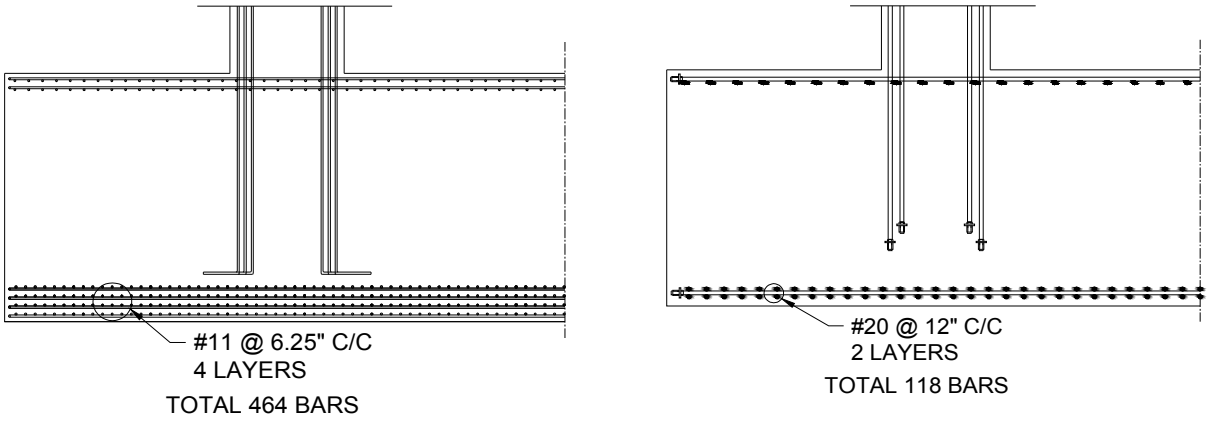
It is advantageous to use high strength reinforcement, such as Grade 75 (515 MPa), Grade 80 (550 MPa) or even Grade 100 (690 MPa) to reduce the congestion of rebars, eliminate the bar bundles and increase the spacing of transverse reinforcement, especially for seismic applications since no bundling will be allowed. Using threadbars, full load coupler can be used instead of lap splicing. This will reduce the congestion significantly. Usages of higher strength and larger size bar will reduce the number of longitudinal bars and weight of the steel caging. The labor to tie all bars to the transverse reinforcement will also reduce significantly. Table 1 provides a comparison of a drilled shaft originally designed with Grade 60 (415 MPa) rebar and replaced with Grade 100 (690 MPa) threadbar. For a 9 ft diameter shaft the plan drawing calls for 60 #14 (44 mm) Grade 60 longitudinal bars (Yield force = 60x2.25x60 = 8100 kips (36029 kN) and 100 ft (30.5m) deep drilled shaft. It can be substituted with 21 #18 Grade 100 longitudinal bars (yield force = 21x4x100=8400 kips (37363 kN)). As seen in Table 1, there will be over 37% rebar weight saved and there will be 65% less longitudinal bar handled. The required crane size will be smaller and the number of tying will be significantly reduced and will save labor.

Table 1. Comparison Grade 60 Rebar and Grade 100 THREADBAR

Shaft Type	Number of Vertical Rebars		Vertical Rebar, kg	
	Plan- #14 Gr 60	Alternate-Threadbar- #18 Gr. 100	Plan	Alternate
2.7m dia	44mm dia- 415 MPa	57mm dia- 690 MPa		
	60	21	20826	12958
Total Savings		39		7868
% Saved	# of Bar = 65.0%		Wt. = 37.8%	

John James Audubon Bridge is a cable-stayed bridge built across the Mississippi River to connect St. Francisville with new roads just north of Baton Rouge, Louisiana. The two towers were anchored by 42 drilled shafts. The massive footing called for four layers of #11 (35mm) Grade 60 (415 MPa) rebars at a c/c spacing of 6.25" (16 cm) as shown in Figure 6. DSI proposed using #20 (63mm) Grade 80 (550 MPa) threadbar in just two layers increasing the c/c spacing to 12" (30 cm) as shown in Fig. 6. Full tension-compression coupling meeting the slip requirement of ACI were used and the proposal was approved by Louisiana Department of Transportation. The congestion was significantly reduced and it saved the

contractor significant amount of labor in terms of installation and placement of threadbars as compared to conventional reinforcement.



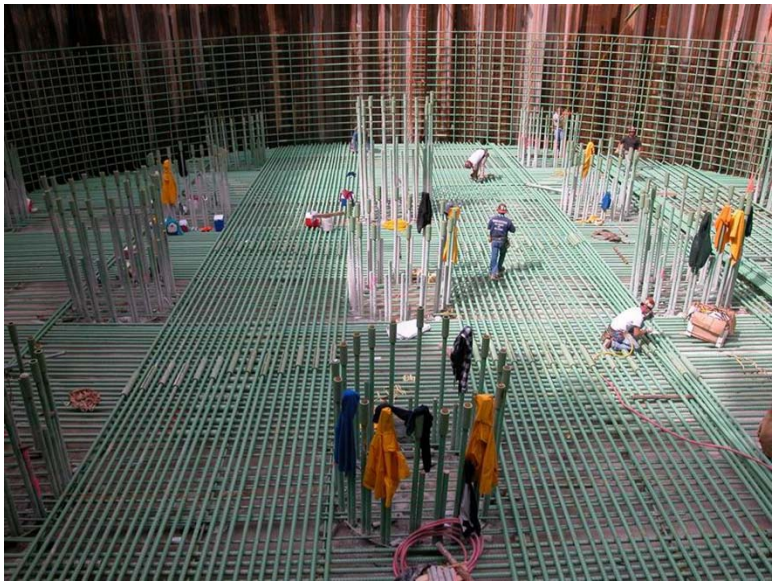


Fig. 6. Grade 80 Threadbars used in footing for St. Francisville Cable Stay Bridge over Mississippi River, Louisiana

LESSONS LEARNED

The use of higher strength and larger diameter threadbar over conventional reinforcement reduces the congestion in drilled shaft and footing significantly resulting in concrete without defects. The reduction of weight and fewer numbers of threadbars leads to labor savings. For deeper drilled shafts, caging can be installed in segments by splicing the threadbars using full load couplers, which will enhance field installation and require smaller size crane.

CONCLUSIONS

High Grade Threadbar is proven to be the best option to reduce the congestion of rebars in drilled shaft. It reduces the weight of steel and significantly reduces the number of bars to be handled which results in significantly less tying operation of spirals or hoops. The lap slice is substituted with mechanical coupling and the end hooks are easily substituted with end terminators. Due to reduced congestion of rebars, it makes the concrete flow smooth and produces drilled shafts with no defects in concrete. A full load tension-compression coupling meets ACI slip requirements. The use of high strength threadbar saves both crane time and labor to fabricate and install the reinforcement case.

REFERENCES

AASHTO LRFD Bridge Design Specifications, 7th Edition, 2014.
ASTM 615-15 Standard Specifications for Deformed and Plain Carbon Steel Bar for Concrete Reinforcement.
ACI 318-14 Building Code and Commentary.

ANALYZING THE LOAD-TRANSFER BEHAVIOR (T-Z CURVE) FOR INSTRUMENTED TEST PILES DRIVEN IN CLAYEY SOIL

Murad Y. Abu-Farsakh, Ph.D., P.E.[1] and Md Nafiul Haque. Ph.D.[2]

[1]Research Professor, Louisiana Transportation Research Center, Louisiana State University, Baton Rouge, LA 70808. (Corresponding Author; Email: cefars@lsu.edu and Phone: 225-767-9147)

[2]Geotechnical Engineer, Kleinfelder, Greensboro, North Carolina.

ABSTRACT

This paper presents the analyses of load-transfer (t-z) behavior of twelve prestressed concrete (PSC) instrumented test piles that were driven in different locations of Louisiana. The load transfer method is an efficient and practical tool for the analysis of single driven pile to predict the ultimate load. The test piles were instrumented with vibrating wire strain gauges in order to calculate the shear transfer for different soil layers during the static load test. The static load test was performed on all the test piles after 10 to 14 days of end of driving. Empirical load-transfer models were proposed previously by different researchers (Fleming 1992, Hirayama 1990, Krasinski 2012, Bohn et al. 2017) after analyzing the instrumented test pile results. For this study, load transfer of each soil layer was measured and compared with the previously developed existing model. The stiffness parameter (M) for the hyperbolic equation was calibrated in order to best match the measurements. The good agreement of the proposed curves was then confirmed by applying them to assess the overall load-settlement curve of other pile load test results available in the literature.

INTRODUCTION

The load transfer mechanism (stress-strain relationship) for an axially loaded pile usually comprises of three loading mechanisms: axial deformation in the pile (z), soil skin friction along the shaft (q_s), and soil end-bearing (q_b). The development of soil skin friction with axial deformation is referred as the t-z curve, and the development of soil end-bearing with axial deformation is referred as the q-z curve. Figure 1 presents the load transfer mechanisms in an axially loaded pile and the corresponding spring mass models for t-z and q-z curves (API, 2002). In order to construct the load transfer curve in clay under vertical load, the axial load transfer (t-z) curve and end-bearing load transfer (q-z) for that particular soil should be assessed separately. The axial load transfer (t-z) method is probably the most widely used technique to study the problem of single axially loaded piles. Therefore, the load transfer through the shaft of the pile and are getting more and more important compared to the only the pile capacity analyses. The load transferred from shaft to the surrounding clay soil is a function of the width of the pile and the surface roughness of the pile and clay properties. The development of a representative procedure allows the assessment of the t-z curve in soil (sand and/or clay) that leads to the prediction of a nonlinear vertical load-settlement response at the pile head.

The most common approach to establish the skin friction load transfer (t-z curves) is the method proposed by Seed and Reese (1957). In their method, the associated t-z curves were developed using experimental test data from the vane shear test to represent the relationship between the induced shear stress (due to load transfer) and the vertical movement (z) along the

© 2018 Deep Foundations Institute

side of the pile. Following Seed and Reese (1957), Coyle and Reese (1966), Grosch and Reese (1980) and Holmquist and Matlock (1976) developed t-z curve which are mostly empirical and based on field and experimental data. There are other available methods that are based on theoretical concepts such as the methods presented by Randolph and Worth (1978) and Kraft et al. (1981). There are methods proposed by Poulos and Davis (1968) and Butterfield and Banerjee (1971) based on finite element too. Different curve types (e.g., hyperbolic, cubic, root) with different degrees of complexity and number of soil parameters are developed in the literature. Vijayvergiya (1977), Hirayama (1990), Fleming (1992) (only for the pile shaft), API (1993), and Krasiński (2012a, b) consider fixed parameters, for example, a limit settlement defined as the settlement full resistance mobilization. Most of them are explicit, meaning that all curve parameters are completely defined by the authors for a direct use; other authors have proposed to derive the stiffness from a case-by-case calibration procedure (Fleming 1992; Randolph and Wroth 1978). The stiffness of the load transfer curves is either derived from a measured soil deformation parameter or a fixed parameter. Frank and Zhao (1982) use the pressuremeter modulus, Randolph and Wroth (1978), Verbrugge (1981), and Fleming (1992) (only for the pile tip) use an equivalent ground Young's modulus or oedometer modulus based, for example, on correlations with measured soil resistance parameters. The linear curves of Randolph and Verbrugge correspond to an elastic calculation with the use of usual correlations to determine the linear curve stiffness. Table 1 summarizes some of the available curves to estimate t-z curve.

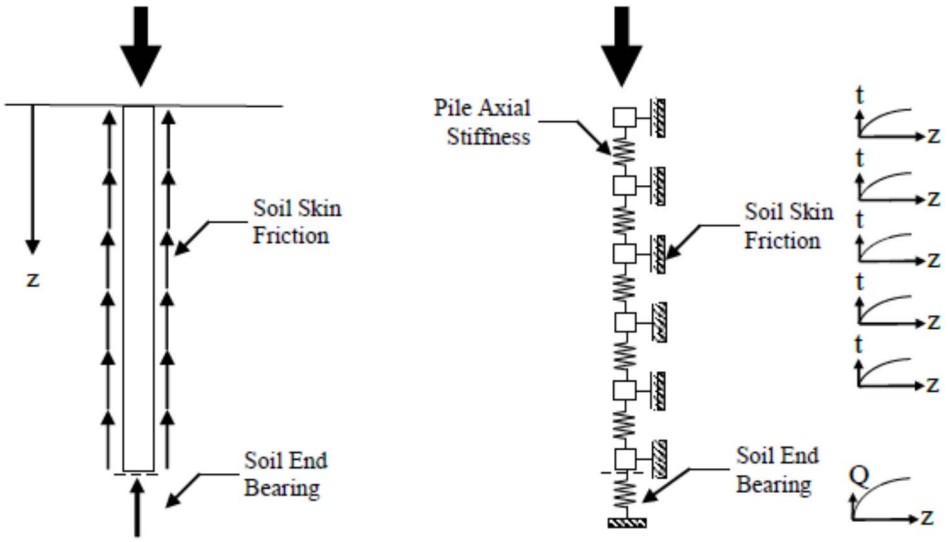


Figure 1: Load transfer mechanisms in an axially loaded pile, and (b) Spring mass models (API, 2002)

The estimation of the ultimate value of the skin friction and of the end-bearing resistance depends mostly on local soil properties and on local practice. Hence, the load transfer method is an intermediate tool between fundamental soil mechanics and empirical implementation. It provides a good engineering judgment in foundation design with meaningful output results in the form of profiles with depth of settlement, mobilized skin friction, load, and stress. However, finite-element analyses offer a wider range of applications and are very powerful if the soil parameters

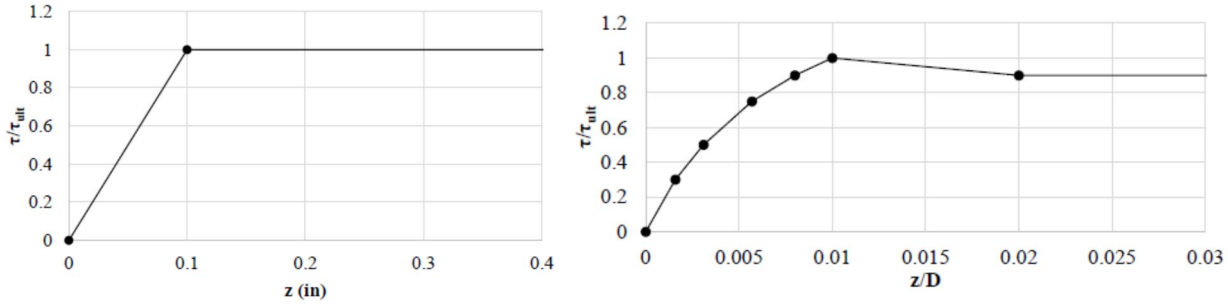
are well-calibrated. The practitioners prefer to use the empirical approach over finite element approach. This study focuses the development of an empirical approach to estimate the skin friction load transfer of the pile.

Table 1: Available t-z curves

Reference	Curve Type	Mathematical Expression	Parameters
Vijayvergiya (1977)	Trilinear	$q_s = \min\left(\left(2\sqrt{\frac{S_s}{S_{slim}}} - \frac{S_s}{S_{slim}}\right).q_{s',ult}; q_{s',ult}\right)$	S_s= Limit settlement q_{ult}= Ultimate capacity
Randolph and Wroth (1978)	Linear	$q_s = \min\left(\frac{G}{B/2.\ln\left(\frac{r_m}{B/2}\right)}.S_s; q_{s',ult}\right)$	B = width of pile S_s= Limit settlement q_{ult}= Ultimate capacity G = Shear modulus
Verbrugge (1981)	Linear	$q_s = \min\left(0.22.\frac{a.b.E}{B}S_s; q_{s',ult}\right)$ $E = 3600 + 2.2q_c$	S_s= Limit settlement E = Youngs modulus q_{ult}= Ultimate capacity Qc =Tip resistance
Hirayama (1990)	Hyperbolic	$q_s = \frac{q_{s\,ult}.z}{M.B+z}$	M = 0.0025 Z = Limit settlement q_{ult}= Ultimate capacity
Fleming (1992)	Hyperbolic	$q_s = \frac{q_{s\,ult}.z}{M.B+z}$	M = 0.004 Z = Limit settlement q_{ult}= Ultimate capacity
Krasinski (2012)	Root	$q_s = \min\langle q_{s',ult}\left(\frac{S_s}{S_{s',lim}}\right)^a; q_{s',ult}\rangle$	a = 0.38 S_s= Limit settlement q_{ult}= Ultimate capacity
Bohn et al. (2016)	Hyperbolic	$q_s = \frac{q_{s\,ult}.z}{M.B+z}$	M = 0.0038 Z = Limit settlement q_{ult}= Ultimate capacity

T-Z Curve

As mentioned earlier, the load transfer along the side of the pile with relative movement (z) is referred as t-z curve. Researchers proposed linear, hyperbolic and cubic root curve to calculate the mobilized skin friction. The American Petroleum Institute (API) recommends a linear elastic perfectly plastic t-z load transfer curve for sand as shown in Figure 2a; and recommends a non-linear t-z load transfer curve as presented in Figure 2b for clay (API, 2002). In this study, the calibration of the stiffness parameter of hyperbolic equation for clayey soil was focused.



(a) (b)

Figure 2: t-z load transfer curve for (a) sand (b) clay (API, 2002)

OBJECTIVE

The objective of this study is to develop simple shaft friction load transfer curves from the locally tested instrumented test piles. This is done by a detailed investigation of pile load tests. In order to achieve this goal, the following tasks haven been performed; (a) Instrument the test piles with vibrating wire strain gages, (b) Perform detailed soil investigation to classify the subsurface soil condition, (c) Perform the static load test to verify the design capacity, (d) Calculate the load distribution plot from the strain gage measurements, (e) Calculate the shaft friction load transfer for each segment and relative movement and (f) Determind the stiffness parameter (M) of the hyperbolic curve equation (i.e., $\frac{q_s}{q_{ult}} = \frac{S}{M.B+S_s}$) for all the segments of the shaft load transfer.

PILE LOAD TEST PROGRAM

Test Sites and Test Piles

A pile load test program was undertaken for the test piles in different bridge sites of Louisiana to generate data aiming to quantify the load transfer of each soil layer for instrumented driven piles. Pile load tests were usually performed during the construction of any bridge and the authors performed the load tests on the test piles with Louisiana Department of Transportation and Development (LADOTD) engineers. All the test piles were prestressed concrete test (PSC) piles. The details of the load test program and test piles can be found on Abu-Farsakh et al. (2016). Table 2 summarizes the information of the test piles.

Instrumentation

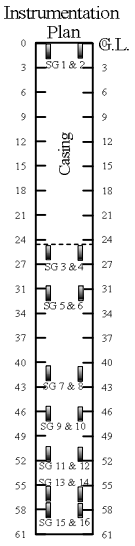
Test piles were instrumented with vibrating wire “sister bar” strain gages (VWSG) (Geokon-4911). The strain gages were installed in pairs on the opposite sides of the piles; the gages were attached to the side of a section on the rebar at selected depths as shown in Figure 3a. The locations of strain gages were targeted specific soil layers, based on the subsurface soil classification. An example of instrumentation plan for test pile is shown in Figure 3b.

Table 2: Information of the test piles

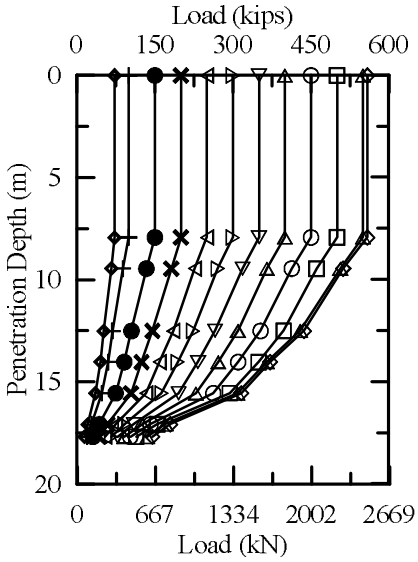
Project Name	Pile ID	Pile Type	Width inch (mm)	Length ft. (m)	Hammer Type
LA-1	LA-1-TP-2	PSC	18 (406)	130 (39.6)	Vulcan 010
	LA-1-TP-3		30 (762)	190 (57.9)	Vulcan 010
	LA-1-TP-4a		24 (610)	160 (48.8)	Vulcan 020
	LA-1-TP-4b		24 (610)	210 (64.0)	Vulcan 020
	LA-1-TP-5a		24 (610)	145 (44.2)	Vulcan
	LA-1-TP-5b		24 (610)	170 (51.8)	Vulcan
Bayou Lacassine (BL)	BL-TP-1		30 (762)	75 (22.9)	ICE I-46
	BL-TP-3		30 (762)	75 (22.9)	ICE I-46
KCS Bridge Site	KCS-TP-1		30 (762)	60 (18.3)	Delmag D
Bayou Zourie (BZ)	BZ-TP-1		24 (610)	55 (16.8)	ICE I-62
Caminada Bay (CM)	Cam-Bay-TP-1		36 (914)	69 (21.0)	Pileco D100-13
	Cam-Bay-TP-7		36 (914)	72 (22.0)	



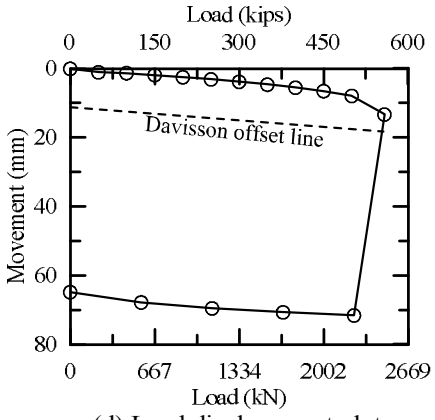
(a) Installation of strain gages



(b) Instrumentation plan



(c) Load distribution plot



(d) Load displacement plot

Figure 3: Example of instrumentation plan, installation of strain gages load distribution plot and load-displacement plot

RESULTS AND ANALYSES

Static Load Test

The static load tests were conducted on the test piles from 7 days to 14 days after pile installation. The reaction system for the static load tests was provided by sixteen pipe piles, which were installed a few days after the installation of the test piles. The tests generally followed the quick load test procedure (ASTM D1143) with holding periods of 5 minutes of each load increment. After holding the maximum load for 5 minutes, the applied load was removed in four equal decrements so that the shape of the rebound curve could be determined. Figure 3d presents an example of the load-movement plots for the test pile at Caminada bay site. The results of the other test piles can be found at Abu-Farsakh et al (2016).

Converting Strain to Load

The main objective of instrumenting the test piles with strain gages was the ability to calculate the shaft and end-bearing capacities separately for the static load tests, and to determine the skin friction along the side of the pile. A pair of strain gages installed near the ground surface, just above the zone of soil resistance, was used to calculate the section modulus of the pile. The load (P) was then calculated to that corresponding strain from the following equations:

$$P = E_t \varepsilon A \quad \ldots(1)$$

$$\text{And } E_t = \frac{d\sigma}{d\varepsilon}$$

where, E_t = Tangent modulus, ε = measured strain, $d\sigma$ = change of stress from one load increment to the next, $d\varepsilon$ = change of strain from one load increment to the next, and A = cross sectional area of the pile. A detailed procedure of calculating the load from the tangential modulus and varying strain was presented by Fellenius et al. (1989). Figure 3c presents an example of load distribution plot of Caminada bay site. The results of the other test piles can be found at Abu-Farsakh et al (2016).

Load Transfer Curves

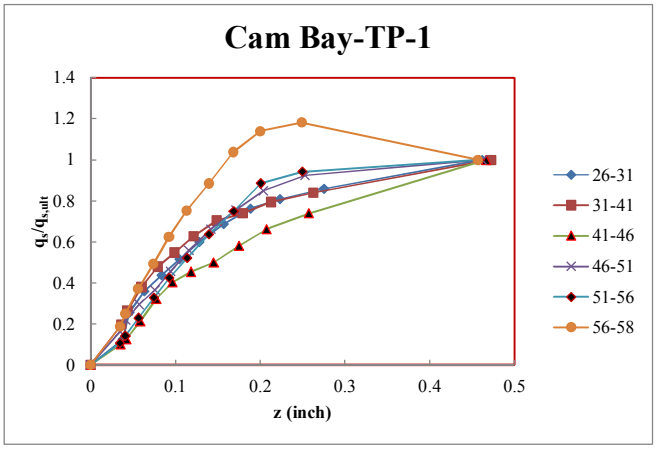
All the test piles were failed to the designed load during performing the static load test. Hence, the ultimate load were determined from the performed static load test. The piles were instrumented with eight to nine pairs of strain gages. As defined in the API (1993), the skin friction in between the vibrating wire strain gages were calculated under relative movement (z). The mobilized skin friction (q_s) in between two strain gages was divided by the maximum skin friction (q_{ult}) and was plotted against the relative movement (z) for all the segments of the test piles and are presented in Figure 4.

Calibration of the Stiffness parameter (M) and Comparison with Available Models

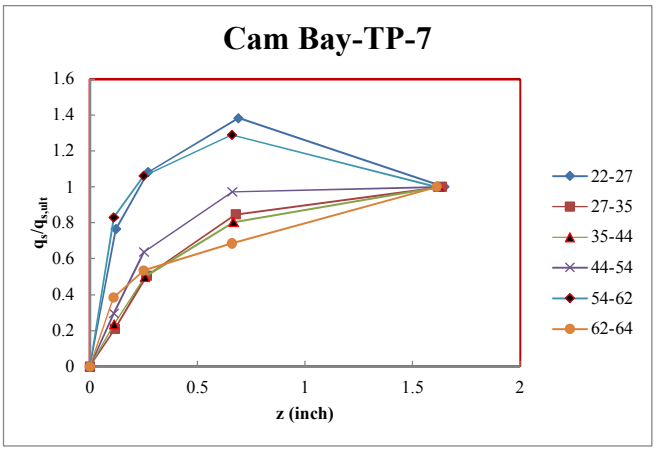
The shear load transfer curves can be estimated by hyperbolic, root or linear curves. The objective of this study was to calibrate the stiffness parameter (M) of hyperbolic equation. The hyperbolic equation can be defined as:

$$\frac{q_s}{q_{ult}} = \frac{z}{M.B+z} \quad \ldots (2)$$

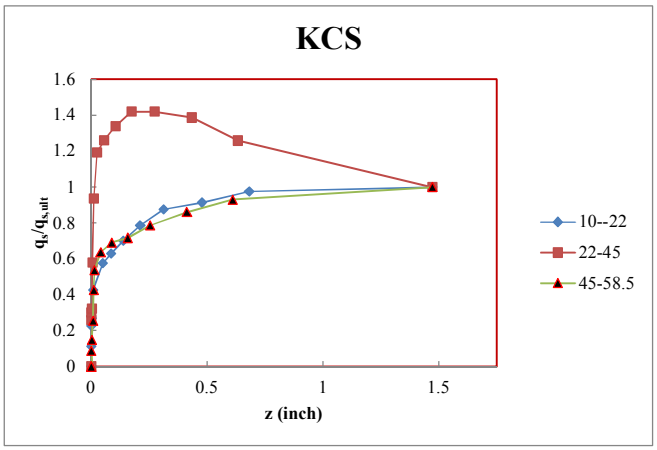
Where, q_s/q_{ult} is the normalized load transfer in between pile segments, B is the width of the pile, z is the relative movement at that pile segment and M is the stiffness parameter.



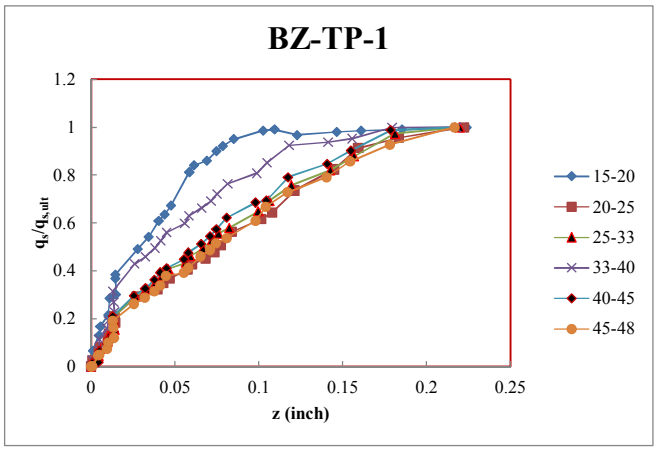
(a)



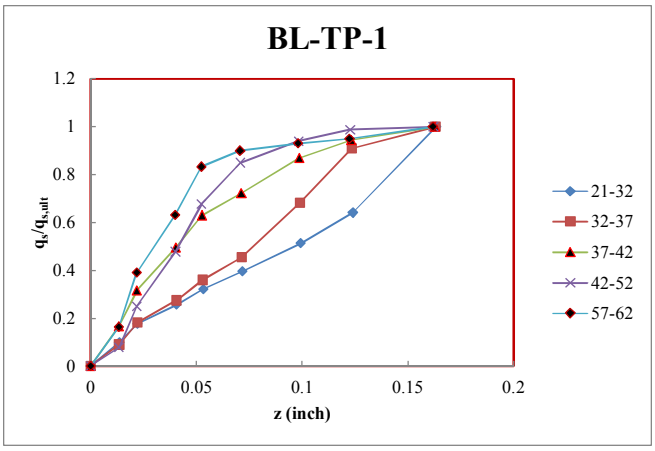
(b)



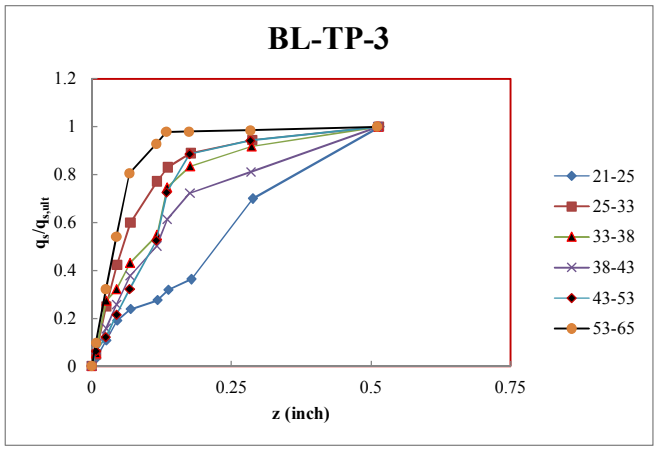
(c)



(d)



(e)



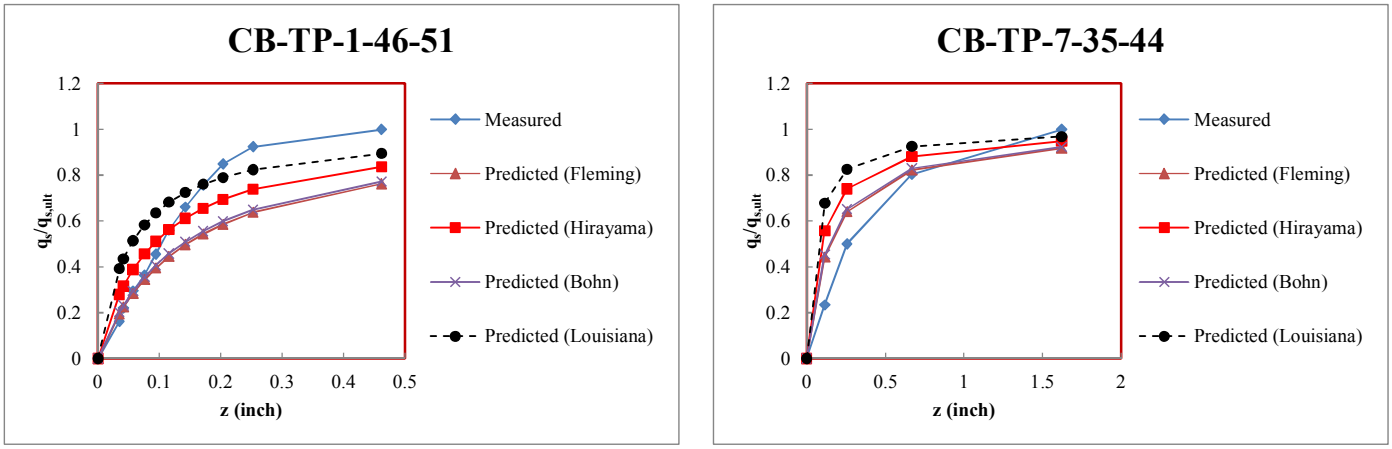
(f)

Figure 4: Shaft friction-displacement plot for the instrumented test piles

The objective of the study is to calibrate that stiffness parameter (M) for the hyperbolic curve so that the load transfer of each segment of pile can be estimated. The ultimate load (q_{ult}) can be calculated from the local practice. However, the ultimate load for the clayey soil usually calculate using the total stress method (α method) and for the sandy soil the capacity usually calculated through the effective stress method (β method). In this study, q_s/q_{sult} with the displacement (z) was plotted according to the equation (2) and the stiffness parameter (M) was back-calculated for all the twelve test pile segments. Moreover, the hyperbolic models proposed by other researchers (i.e., Hirayama 1990, Fleming 1992 and Bohn et al. 2016) was plotted and compared with the present cases and the results are depicted in Figure 5. Finally, the regression analyses were performed with the aid of SAS® software to determine the stiffness parameter (M) for the overall cases. The stiffness parameter (M) for the hyperbolic equation is 0.0012 from this study with compared to 0.0025 for Hirayama 1990, 0.004 for Fleming 1992 and 0.0038 for Bohn et al. 2016.

CONCLUSIONS

In this study, twelve prestressed concrete instrumented test piles were driven in different locations of Louisiana and static load tests were performed from 7 to 14 days after driving. A simple hyperbolic curve is developed for the prediction of the axial behavior of piles. The curve is based on deformation parameters that have been calibrated on load tests made on instrumented test piles. They have been validated on various cases with a good accuracy and compared with the other developed hyperbolic models available in the literature. Hyperbolic curves are proposed comparable to ones of Hirayama (1990), Fleming (1992) and Bohn et al. (2016) at the shaft, with stiffness parameters, M = 0.0012. The ultimate value contribute a significant role in the stiffness of the curve. As in all load transfer method modeling, an accurate determination of the ultimate capacity reflecting the specific behavior of the soil types is particularly complex and decisive. These values can be derived from the available local practice.



(a) (b)

Figure 5: Verification of the proposed model and comparison with the other available models for shaft friction-displacements plots of the instrumented test piles (cont.)

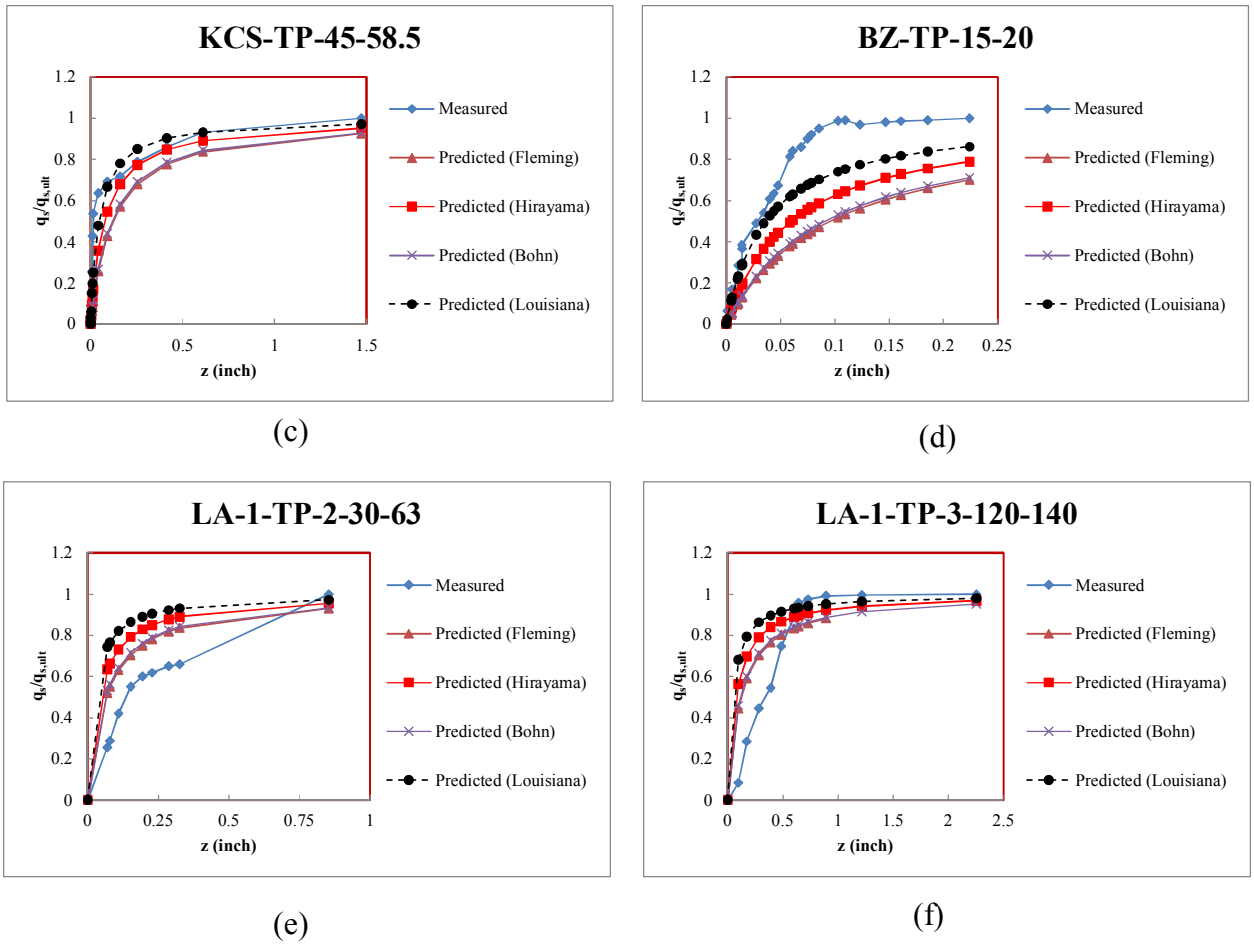


Figure 5: Verification of the proposed model and comparison with the other available models for shaft friction-displacements plots of the instrumented test piles

REFERENCES

Abu-Farsakh, M. Y., Haque, Md. N., and Chen, Q. (2016). "Field instrumentation and testing to study set-up phenomenon of piles driven into Louisiana clayey soils." *Report No. FHWA/LA.15/562*, Louisiana Transportation Research Center, Baton Rouge, Louisiana.

API (American Petroleum Institute). (1993). Recommended practice for planning, designing and constructing fixed offshore platforms–Working stress design, 20th Ed., Washington, DC.

Bohn, C., Santos, A. L. D. and Frank, R. (2016). "Development of axial pile load transfer curves based on instrumented load tests" *Journal of Geotechnical and Geoenvironmental Engineering,* Vol. 143(1), pp. 1–15.

Butterfiled, R. & Banerjee, P. K. (1971a). "The elastic analysis of compressible piles and pile groups." *Geotechnique,* Vol. 21(1), pp. 43-60.

Butterfiled, R. & Banerjee, P. K. (1971b). "A rigid disc embedded in an elastic half space." *J. S.E. Asian Sot. Soil .Engng,* Vol. 2(2).

Coyle, H. M., and Reese, L. C. (1966). "Load transfer for axially loaded piles in clay." *Journal of Soil Mech. Found. Div.,* Vol. 92(2), pp. 1–26.

Frank, R., and Zhao, S. R. (1982). "Estimation à partir des paramètres pressiométriques de l'enfoncement sous charge axiale de pieux forés dans des sols fins." *Bulletin de Liaison des Laboratoires des Ponts et Chaussées,* vol. 119, pp. 17–24.

Fleming, W. G. K. (1992). "A new method for single pile settlement prediction and analysis." *Geotechnique,* Vol. 42(3), pp. 411–425.

Grosch, J.J., and Reese, L.C. (1980). "Field tests of small scale pile segments in a soft clay deposits under repeated axial loading." *Proceedings of the offshore technology conference*, Paper 3869, Houston, Texas, USA.

Hirayama, H. (1990). "Load-settlement analysis for bored piles using hyperbolic transfer functions." *Soils Foundation,* Vol. 30(1), pp. 55–64.

Holmquist, D. V. and Matlock, H. (1976). "Resistance=displacement relationships for axially loaded piles in soft clay." *Proceedings 8th offshore technology conference,* Houston, Texas, Paper OTC 2474, pp. 554-569.

Poulos, H. G. & Davis, E. H. (1968). "The settlement of single axially-loaded incompressible piles and piers." *Gotechnique,* Vol. 18, No. 3, pp. 351-371.

Krasiński, A. (2012b). "Proposal for calculating the bearing capacity of screw displacement piles." *Studia Geotechnica et Mechanica,* Vol. 34(4), pp. 41–51.

Kraft, L. M., Ray, R. P., and Kagawa, T. (1981). "Theoretical t-z curves." *Journal of Geotechnical and Geoenvironmental Engineering*, 107(11), 1543–1561.

Randolph, M. F., and Wroth, C. P. (1978). "Analysis of deformation of vertically loaded piles." *Journal of Geotechnical and Geoenvironmental Engineering,* Vol. 104(12), pp. 1465–1488.

Seed, H. B., and Reese, L. C. (1957). "The action of soft clay along friction piles." *Trans. Am. Soc. Civ. Eng.,* Vol. 122, pp. 731–754.

Verbrugge, J.-C. (1981). "Evaluation du tassement des pieux à partir de l'essai de penetration statique." *Revue Française de Géotechnique,* Vol. 15, pp. 75–82.

Vijayvergiya, V. N. (1977). "Load-movement characteristics of piles." Ports '77: *4th Annual Symp. of the Waterway, Port, Coastal, and Ocean Division,* ASCE, Los Angeles, pp. 269–284.

DEEP JET GROUTING GRIDS FOR SUPPORT OF A 42-STORY TOWER DESIGNED USING PERFORMANCE-BASED SEISMIC DESIGN

Lori A. Simpson, PE, GE, Langan Engineering & Environmental Services, Inc., Oakland, California, USA (510) 874-7000, lsimpson@langan.com
Scott A. Walker, PE, GE, Langan Engineering & Environmental Services, Inc., Oakland, California, USA, (510) 847-7000, swalker@langan.com
David A. Shook, PE, Skidmore, Owings & Merrill LLP, San Francisco, California, USA , (415) 352-6887, david.shook@som.com
Roberto A. Lopez,, PE, Malcolm Drilling, San Francisco, California, USA, (510) 780-1167, rlopez@malcolmdrilling.com

ABSTRACT

500 Folsom Street is part of the new Transbay neighborhood in San Francisco, which is being redeveloped after the 1989 Loma Prieta Earthquake damaged a freeway viaduct; removal of the viaduct created parcels of land available for development. The development consists of a 42-story residential tower with a six-level basement. The slender, core-only structure was designed using performance-based seismic design.

Subsurface conditions include undocumented fill, Dune sand, marsh deposits, sand, and clay, all overlying sloping bedrock of the Franciscan Formation. The building is supported on a 10-foot-thick mat foundation approximately 62 to 72 feet below street grades; clay, sand, and bedrock are all present at mat subgrade. Under a portion of the mat, sand susceptible to liquefaction was present. The variable subgrade conditions and potential for ground failure, along with the depth of mat subgrade below street grade, created a challenge for the design and construction team to solve. The ground below mat subgrade needed to be improved to mitigate the liquefaction potential and provide more uniform support.

The areal extent and depth of ground improvement necessary to support the mat with an acceptable amount of deformation was determined. Settlement was analyzed and subgrade moduli were provided for design of the mat, with multiple iterations performed to converge between the geotechnical and structural models.

Based on the project schedule and logistics, it was beneficial to work from street grade to improve the ground. In order to target the depths below the mat and minimize wasted effort and materials within the depth of excavation, grids of jet grouting were determined to be the most economical ground improvement method; however, it was challenging to install the columns from 65 feet above the top of the target zone. During installation, QA/QC was performed to check that the jet-grouted columns were installed to the design depth and diameter and developed the design strength.

INTRODUCTION

A new high-rise building at 500 Folsom Street is under construction at Transbay Block 9 in the Transbay redevelopment area of San Francisco. The new tower will occupy a site formerly occupied by the Embarcadero Freeway, a double-decker elevated freeway that was damaged during the 1989 Loma Prieta San Francisco earthquake and subsequently razed. The site is roughly trapezoidal, with maximum plan dimensions of about 275 by 155 feet.

The tower is an important fixture of San Francisco's new Transbay District, especially situated on Folsom Street which is termed San Francisco's 'New Main Street'. The building will consist of a 42-story tower constructed in the central portion of the site with a nine-story podium surrounding the tower. A rendering

© 2018 Deep Foundations Institute

of the building is shown on Fig. 1. The building has 6 levels of below-grade parking; excavations for the basement extended to 76 feet below adjacent street grades. Structural loading includes static bearing pressures ranging from 2,500 psf to 13,000 psf under the tower core.



Fig. 1 – Proposed 42-Story Building

The site generally slopes down from west to east (assuming project north is parallel to First Street); with an elevation change of about 9 feet across the site. The site has been vacant since the removal of the overhead freeway structure, but foundations consisting of large groups of driven piles remained in the ground. Buried foundations and slabs from earlier developments were also present within the upper 15 feet of existing site grades. Existing buildings, streets, and an elevated viaduct surround the site, as shown on Fig. 2.

The project team included SOM, the lead architect, STRUCTUS and SOM as structural engineers, Langan, the project geotechnical engineer, Balfour Beatty, the general contractor, and Malcolm Drilling, the specialty support-of-excavation and ground improvement contractor.

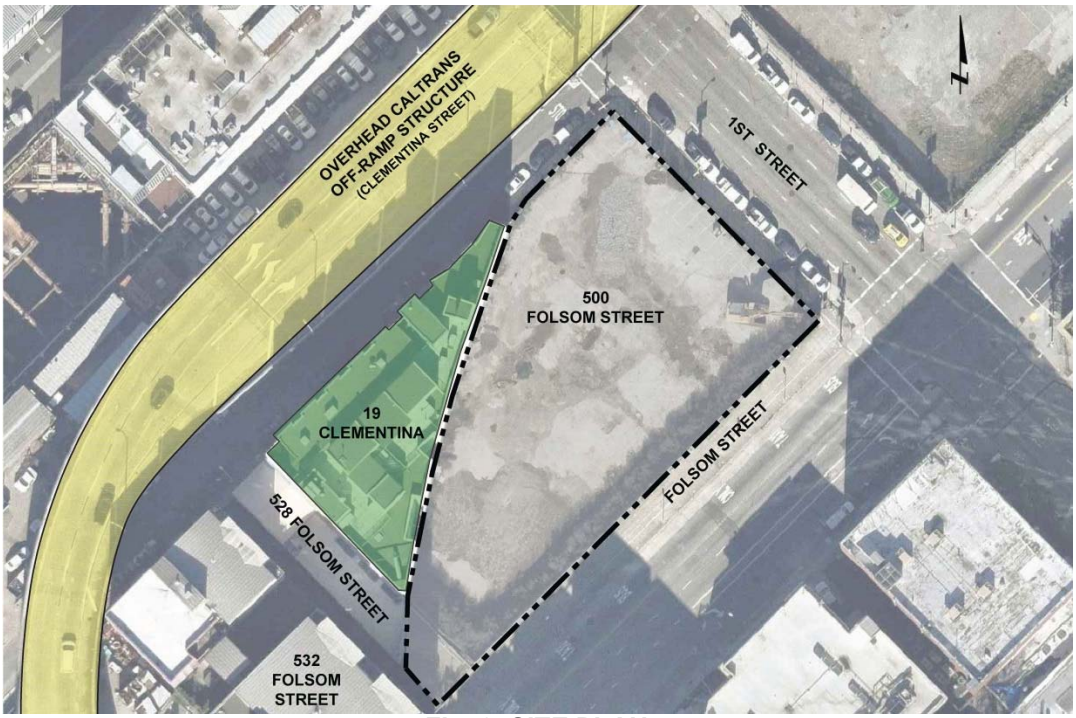


Fig. 2–SITE PLAN

SUBSURFACE CONDITIONS

Prior to development in the 1850s, the site and vicinity were covered by windblown sand dunes that blanketed an old marsh deposit layer. Beginning in the 1850s, the sand dunes were leveled and partially removed to accommodate roadways and buildings. By 1900, the neighborhood was developed; however, it was destroyed by the fire following the San Francisco Earthquake of 1906. During reconstruction, former basements were backfilled with dune sand, clay, gravel, and debris left by the earthquake and fire ("earthquake fill").

Present day subsurface conditions were explored by drilling rotary wash and hollow stem auger borings. Six to fourteen feet of earthquake fill was encountered throughout the site. The fill is underlain by a layer of clean, uniformly-graded, Dune sand and a 2- to 10-foot-thick marsh deposit. The marsh deposit is underlain by dense to very dense sand of the Colma formation to depths of about 45½ to 79 feet below ground surface. The Colma Formation sand is strong, has low compressibility, and is capable of accommodating large compression loads. Underlying the Colma sand is a layer of older alluvial layers of interbedded sand and clay. The sands are medium dense to very dense, and some layers are potentially liquefiable. The interbedded sand and clay are underlain by bedrock consisting of sandstone and sheared shale of the Franciscan Mélange Complex. The bedrock surface slopes steeply down from southwest to the northeast; bedrock was encountered at depths between about 60 and 140 feet across the site. A subsurface profile is shown on Fig. 3.

Groundwater was monitored using a vibrating wire piezometer over the course of 2½ years and was consistently measured at a depth of about 32 feet below ground surface (bgs), corresponding to Elevation 6 feet (elevations referenced herein correspond to North American Vertical Datum (NAVD 88).

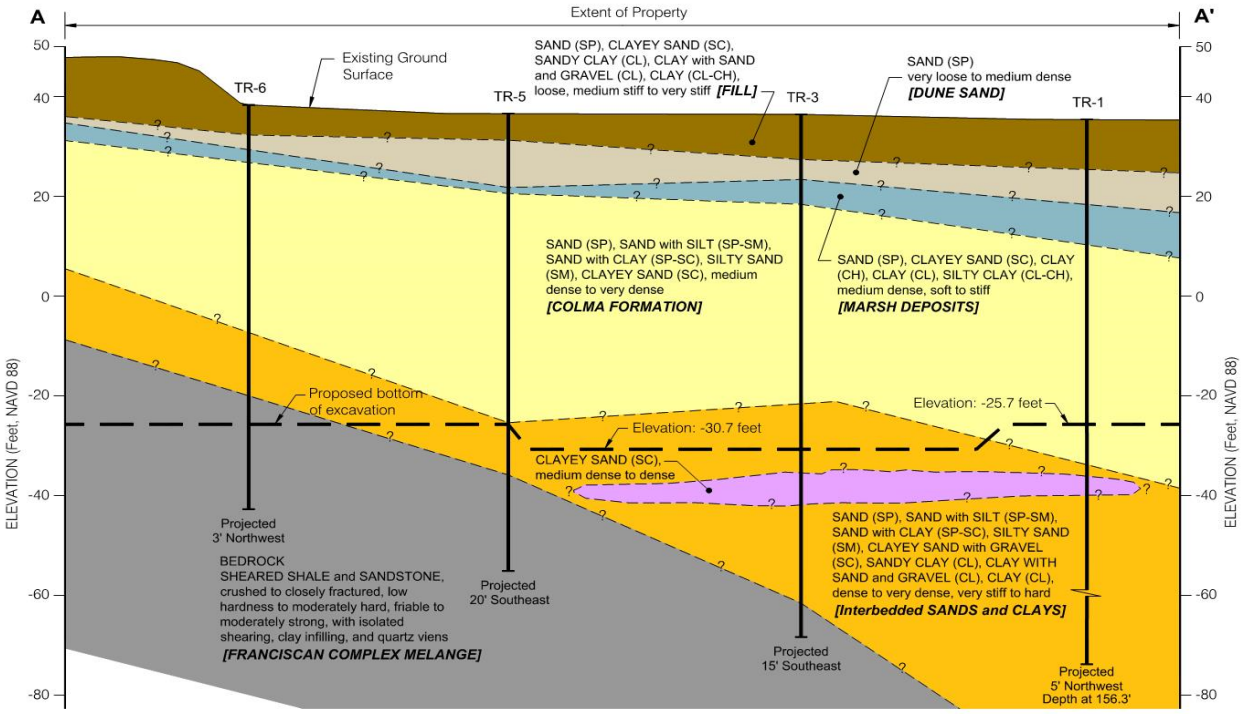


Fig. 3 – East-West Subsurface Profile

SEISMICITY, FAULTING, AND SEISMIC HAZARDS

The site is in a highly seismic region, with two major faults the San Andreas and Hayward faults, approximately 13 and 16 miles from the site, respectively. These faults are capable of producing earthquakes with mean characteristic moment magnitudes of 7.9 and 7.3, respectfully. These and other faults in the region, plus recent earthquakes, are shown on Fig. 4.

The project geotechnical engineer performed probabilistic and deterministic seismic hazard analysis for the project, developed site-specific and conditional mean spectra, and prepared scaled time histories for the seismic evaluation of the new structure. Peak ground accelerations are predicted to be about 0.49g and 0.55g for the design basis earthquake (DBE) and maximum considered earthquake (MCE) levels of shaking, respectively.

During a major earthquake on a segment of one of the nearby faults, strong to very strong ground shaking is expected to occur at the project site. Liquefaction is a phenomenon where loose or medium dense, saturated, soil with little to no cohesion experiences a temporary loss of shear strength caused by transient rise in excess pore pressure generated by strong cyclic loading, such as that caused by earthquakes. The site is located within a zone identified on local maps as having a high potential for liquefaction; however, there was no documented observation of ground disturbance from liquefaction at this site during the 1906 Earthquake or the 1989 Loma Prieta Earthquake.

The procedure outlined in the proceedings of the NCEER workshops (Youd 2001) and Idriss and Boulanger (EERI 2008) was used for the evaluation of liquefaction triggering for the soils at the site, using a modified peak geometric mean ground acceleration (PGA_M) of 0.55g corresponding to the MCE level of shaking. All of the borings drilled the southeastern portion of the site encountered a layer of medium dense fine clayey sand between the depths of 69 to 84 feet below the ground surface, which was within a few feet of the bottom of the proposed excavation and foundation. This layer, which has a plasticity index (PI) ranging from zero to 7, could be susceptible to excess pore pressure generation and,

potentially, liquefaction. Using the Tokimatsu and Seed (1987) method for evaluating earthquake-induced liquefaction settlement, this deep potentially-liquefiable soil was estimated to have the potential to settle up to 1½ inches during and immediately after a major earthquake. With the proximity of this soil to the proposed bottom of mat foundation, there was also a potential for loss of foundation bearing, and settlement of the new building could be erratic and significant if founded on or just above this soil.

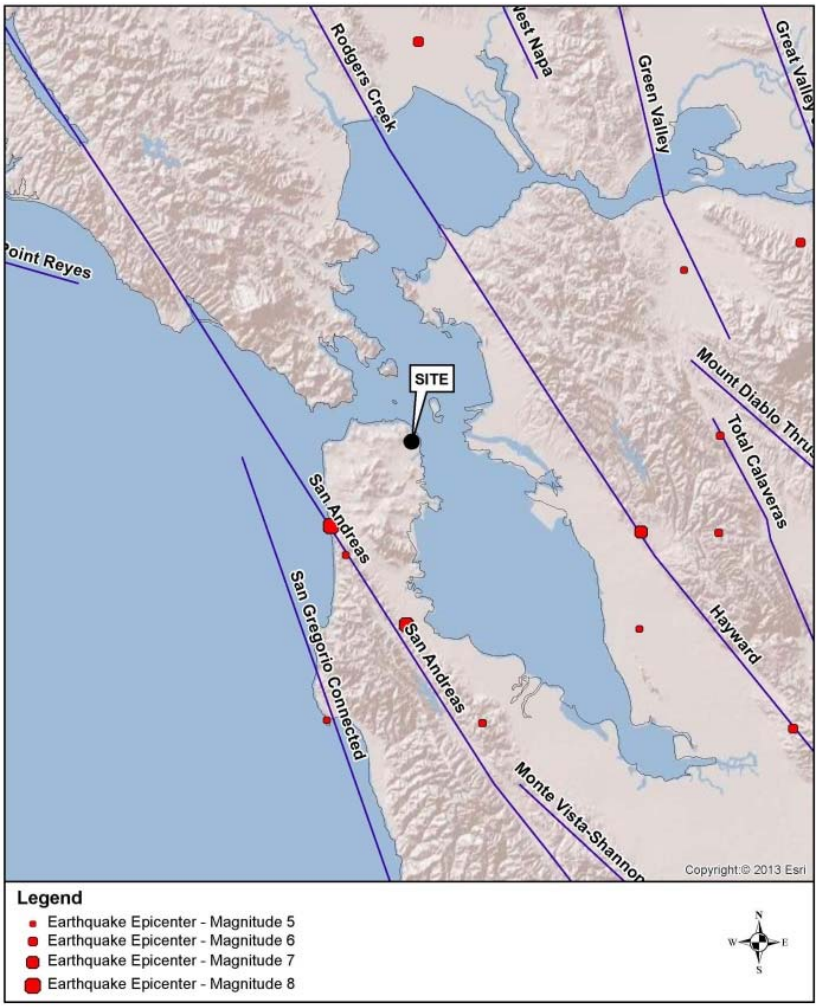


Fig. 4 – Faults

FOUNDATIONS

Because of the sloping bedrock, the excavation would expose a variety of materials: bedrock, dense to very dense sand, medium dense potentially liquefiable sand, and stiff to hard clay. The challenge was to design a foundation that performed well under earthquake loading and also would have relatively uniform bearing and performance under static conditions. Under static conditions, the soil at basement subgrade would be capable of supporting heavy foundation loads, but the bearing layers had varying properties. The potentially liquefiable soils are predicted to lose their strength under seismic conditions, causing loss of foundation bearing and significant differential settlement.

The team evaluated several foundation alternatives that would extend through the potentially liquefiable soils, but varying construction considerations limited the options. Ultimately, the team concluded that the most appropriate and cost-effective approach would be to mitigate the liquefaction using ground improvement techniques. The use of ground improvement would then allow for the design of a

conventional mat foundation which would bear on a combination of bedrock, stiff and dense undisturbed native soils, and improved ground. The ground improvement would: 1) mitigate liquefaction potential; and 2) transfer vertical building loads to the bedrock, dense sand, or very stiff clay.

GROUND IMPROVEMENT

Upon evaluating several ground-improvement techniques, the geotechnical engineer concluded that a closed grid of deep soil mixed (DSM) columns or jet-grout columns extending through the liquefiable soil layers into the underlying strata would improve the soil, and transfer the imposed structural gravity and seismic loads to competent bearing layers. DSM is installed by advancing augers or a cutter tool and injecting cement slurry through the tip of the tooling during withdrawal. The soil is mixed with the cement slurry in situ, forming a continuous vertical element of strengthened material. Jet-grouting is performed by advancing a small diameter, 6-inch hole to allow placement of a jet grout monitor and drill steel to depth, and jetting cement grout sheathed in air at high-pressures of 200 to 400 bar (3000 to 6000 psi) within the zone to be improved. The high pressure jet cuts and erodes the surrounding soil and mixes the cement grout with the soil in place, resulting in columns of soil cement. Construction was complicated by the team's decision to construct the ground improvement prior to basement excavation-- from the existing site grades through up to 63 feet of overburden.

The contractor elected to construct the soil-cement cells using overlapping large-diameter jet grout columns in lieu of more conventional single-axis or multi-axis soil mixing. Unlike soil mixing, where the mixing is done mechanically from working grade to the bottom of the treatment zone, jet grouting allows for more surgically constructing the soil cement columns with varying top and bottom elevations, without having to construct the columns all the way to pad grade. The jet grout columns were constructed from the anticipated bottom of basement mat to top of bedrock or to Elevation -50 feet, whichever was shorter. This resulted in jet grout columns varying in length from 10 feet on the west portion of the site to 26 feet on the east side. Had mechanical soil mixing been used from pad grade, the columns would have been up to 63 feet longer, with the corresponding significant increase in construction time, materials, and spoils handling. Furthermore, excavation of the basement would have had to proceed in hardened soil cement. Finally, installing the jet grout grids prior to basement excavation also presented significant scheduling advantages and allowed the use of increased passive resistance at the point of contact between the jet grout grids and the temporary shoring walls.

The jet grout columns were designed with 8 foot diameters, spaced at 7 feet on centers to obtain a 1 foot overlap between columns and form closed cells of soil cement, from bottom of mat to bedrock or hard clays, as shown in Fig. 5. By forming closed cells, the liquefiable soils are encapsulated during a seismic event, mitigating liquefaction. Effective liquefaction mitigation is a function of grid spacing and diameter (i.e., replacement ratio), as well as the relative density of the treated soils and the unconfined compressive strength of the soil cement material (Nguyen et al, 2013). Bearing capacity and static deformations of the jet grout columns were also computed under the anticipated structural loads. The final column layout and east-west ground improvement cross section are shown on Fig. 5.

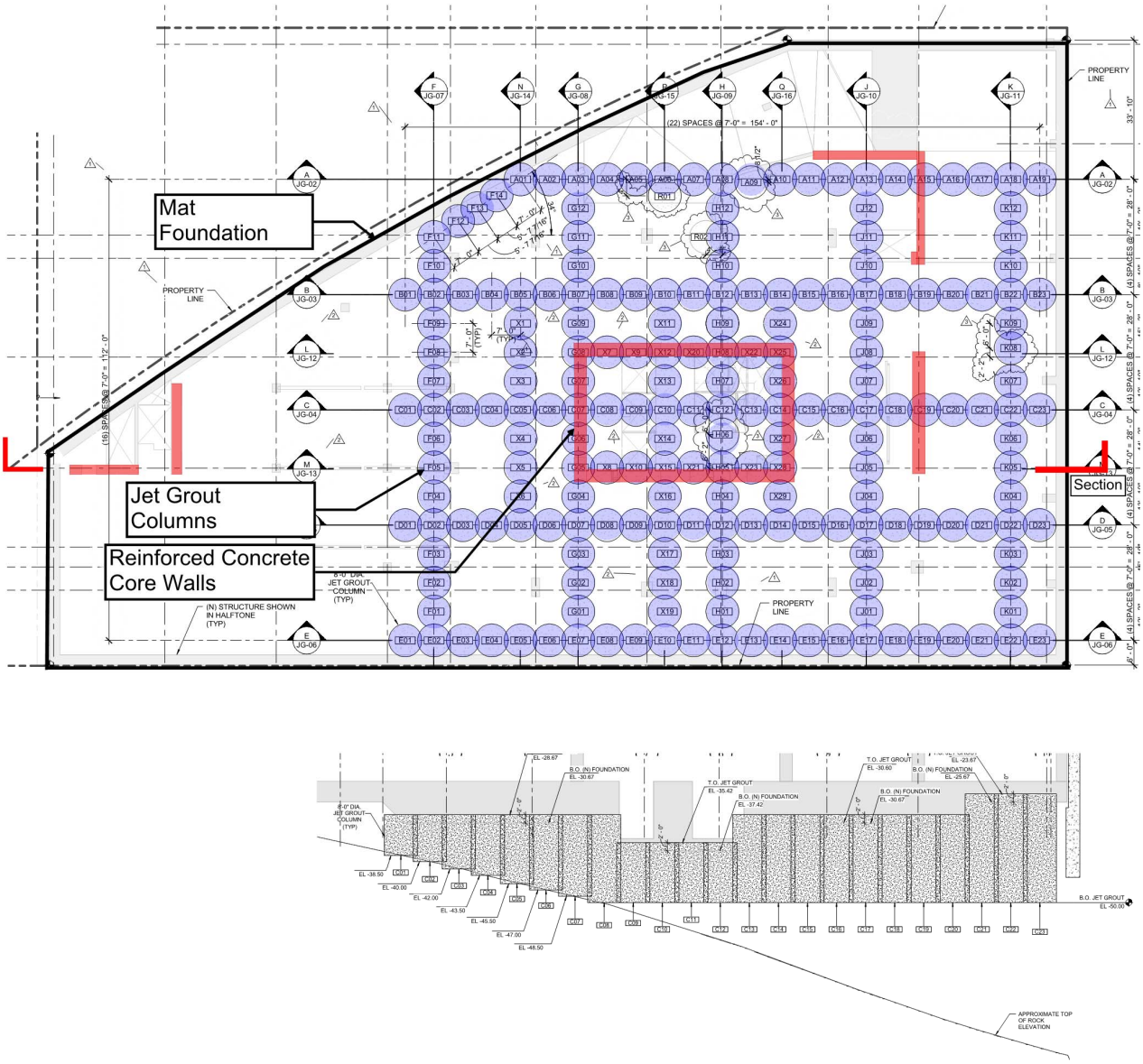


Fig. 5 – Jet grouting grid plan (above) and section (below)

MAT DESIGN AND PERFORMANCE ANALYSIS

The tower was designed using Performance Based Seismic Design (PBSD) with Nonlinear Response History Analysis (NLRHA) considering 22 spectrally scaled ground motions (Fig. 6). The nonlinear analysis model not only included extensive modeling of nonlinear coupling beams and shear walls at all floors, but also included detailed transfer diaphragms, foundation walls, and mat foundation components modeled with shell elements. Soil springs, coordinated with the geotechnical engineer, were used under the mat foundation shell elements. This highly detailed model revealed behaviors not captured by traditional response spectrum analysis.

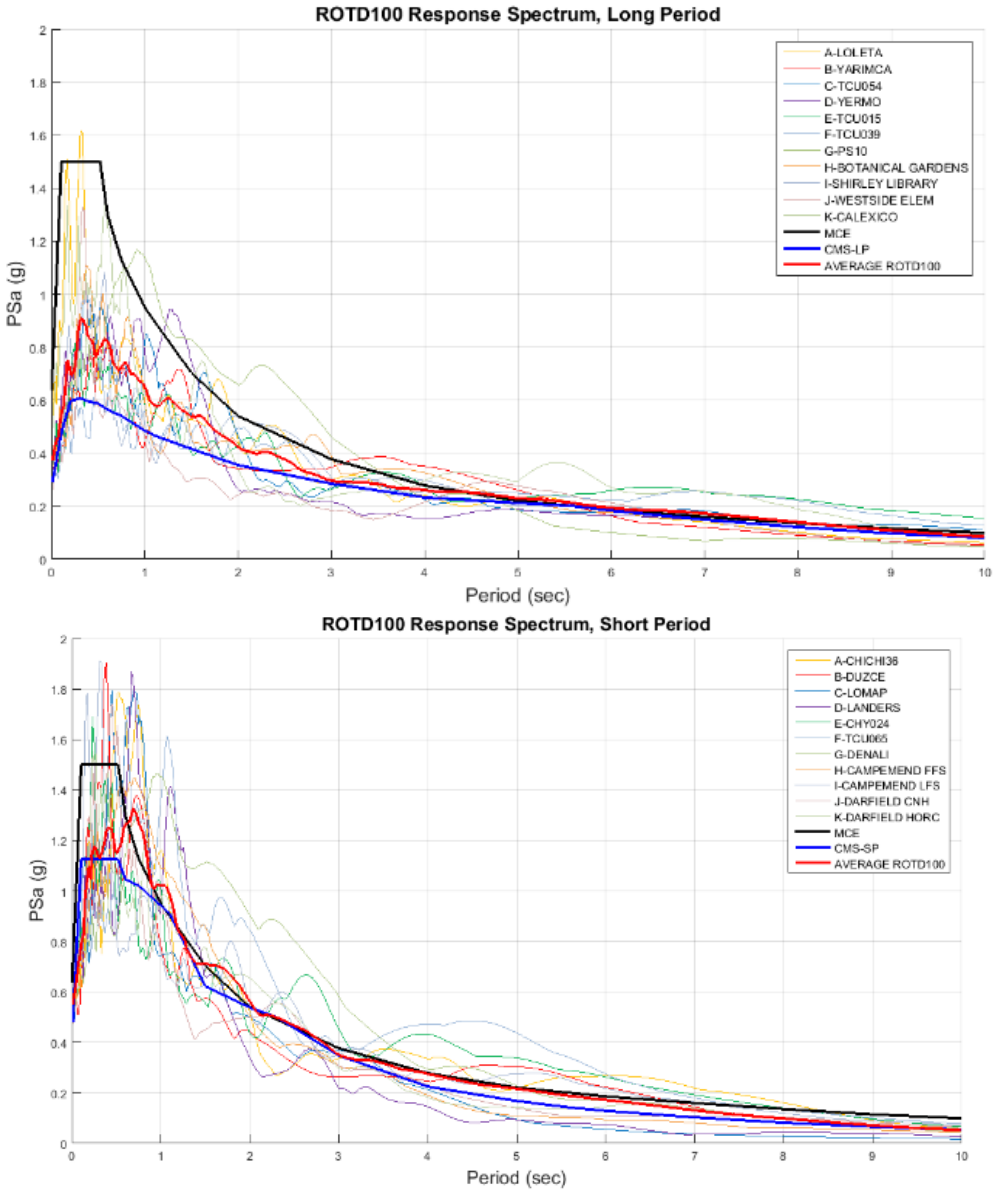
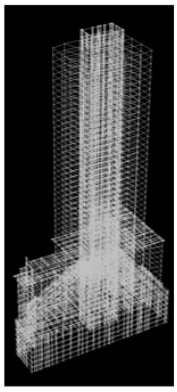


Fig. 6. Spectrally Scaled Ground Motion RotD100 Plots

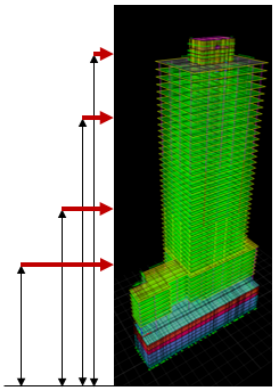
The magnitude and distribution of foundation and basement framing demands observed in NLRHA was substantially different than response spectrum analysis with significantly more demands being transferred always from the core and into the perimeter foundation walls through transfer diaphragms at Levels 1 and 9. For reinforcement design of the mat foundation, SAFE finite element analysis was conducted. Since NLRHA results from Perform3D are not directly exportable to SAFE software, a novel and highly accurate method of enveloping demands was obtained from Perform3D and applied to a linear static ETABS analysis model that could export demands to SAFE. By capturing global overturning and shear concurrently with core-only overturning and shear in ETABS, accurate force demands could be directly exported to SAFE for reinforcement design. To identify accurate and representative linear static force demands in ETABS, an optimization was conducted using basic statics in Rhino/Grasshopper/Octopus software. By obtaining a set of linear static forces which concurrently produced exactly global and core overturning moments and shears, a highly accurate understanding of foundation demands could be produced in ETABS and exported, node by node, to SAFE for detailed reinforcement design. (SAFE is a

RC analysis and design software, ETABS is a general building analysis software, and Perform3D is a nonlinear analysis software, all by Computer and Structures, Inc.)



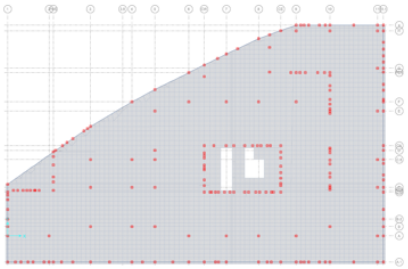
For long and short period suites obtain:

1. Global MX and MY
2. Core MX and MY
3. Shear X and Y



Four variable diaphragm loads at variable height:

1. Match global MX and MY
2. Observe core MX and MY
3. Match shear X and Y



Comparison of ETABS/PERFORM3D

Global Moment Mx	1.0
Global Moment My	1.0
Core Moment Mx	1.0
Core Moment My	1.0
Shear X	1.0
Shear Y	1.0

Fig. 7. Development of Accurate Global and Core Demands in ETABS for Export to SAFE using Optimization

The use of ground improvement allowed for the building to be supported on a shallow mat foundation. This system simplified concrete construction and reduced foundation costs by eliminating the need for deep foundations. The structural and geotechnical engineers worked collaboratively to evaluate the design of the foundation under static and seismic conditions. The structural engineer performed SAFE analyses and provided load bearing plots for the geotechnical engineer's settlement analysis. Several rounds of iterations were needed to converge on a solution, wherein the geotechnical engineer provided a plot of subgrade reaction moduli for mat design. The detailed soil information allowed for very important local changes in substrate stiffness to be identified and the mat to be reinforced appropriately. Ultimately, analyses of mat performance indicated that static settlement would be on the order of ½ to 1¾ inch, with differential of ½ inch. A plot of static settlement is presented on Fig. 8. Seismic settlement during a major earthquake is predicted to be less than 2½ inches.

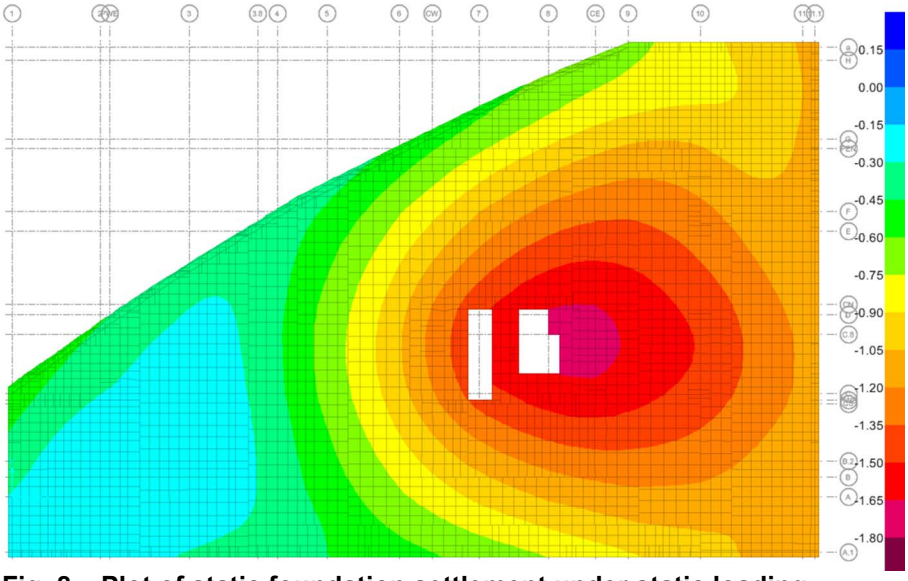


Fig. 8 – Plot of static foundation settlement under static loading.

JET GROUT TEST PROGRAM AND PRODUCTION INSTALLATION

Prior to production jet grouting, the contractor installed two sets of overlapping jet grout column (4 columns total) within the production zone. The test sections were intended to evaluate the soil-cement diameter (i.e. effectiveness of soil erosion) and strength of the jet-grout columns at two locations within the ground improvement zone. The jet grout equipment consisted of a 6-inch-diameter drill bit and monitor with high pressure nozzles, mounted on a Bauer BG-15 drill rig. the contractor employed a two-fluid jetting system, whereby the grout is sheathed in air for maximum cutting efficiency, achieving large diameter columns Test columns were installed at two different extraction rates and grout was injected at pressures of 400 bar (5800 psi). Real-time installation data was displayed on a touch screen on the drill rig.

An engineer was on site full time to observe the installation of the columns and to obtain the following data from the QC data-acquisition system for each panel: start and end times, column depths, grout injection pressures and rates, and extraction rates. Approximately 7 to 8 days after installation, two cores were taken at points immediately between overlapping jet-grout columns to evaluate the effective diameter and strength of the columns. The cores were obtained using PQ triple-barrel coring equipment from the same working pad elevation as the jet-grout was installed. After the cores were obtained, inclinometer equipment was used to check the borehole verticality through the overburden soil.

The results of the initial test section indicated that both of the test extraction rates resulted in adequate soil-cement diameters within Test Section A, where the soil within the ground improvement zone consisted almost exclusively of clayey sand. However, within Test Section B, the ground improvement zone also included hard clay layers that were interbedded with the clayey sand. In this section the cores showed that the slower extraction rates created more thorough mixing and sufficient diameter within the sandy materials, however zones of hard clay remained in the outer edges of the columns (i.e. column diameters necked somewhat within the hard clay). The geotechnical engineer performed supplemental analyses to evaluate the overall effects of column necking and confirmed that the column necking to a diameter of 4 feet would be acceptable in hard clay, but that the full 8-foot diameter would be required within the sandy layers. They recommended additional production columns be cored in the vicinity of the Test Section B. Ultimately, an additional 8 production columns were cored at locations within 6 inches of their theoretical perimeter; all of which showed adequate mixing and diameters within the sandy layers. Within the hard clay layers the cores indicated the jet grout columns range in diameter from 5 to 8 feet.

Representative samples from the cores, including many with visible soil inclusions/anomalies, were selected by the geotechnical engineer for testing. The target average unconfined compressive strength (UCS) for the columns was 350 pounds per square inch (psi), with an additional requirement that 90 percent of the test's results be above this value. The average UCS for the columns was 372 psi, well within the target requirements.

After completion of production jet-grout column installation, the excavation proceeded to the bottom of mat elevation (65 to 74 feet below grade**)**. At final subgrade, the geotechnical engineer inspected the exposed jet grouting, performing an inspection to confirm that all columns were present and overlapping as designed. Fig. 9 shows the subgrade as the jet-grouted columns were exposed. The final inspection indicated that the columns had all been successfully installed; no additional grouting at excavation subgrade was necessary.

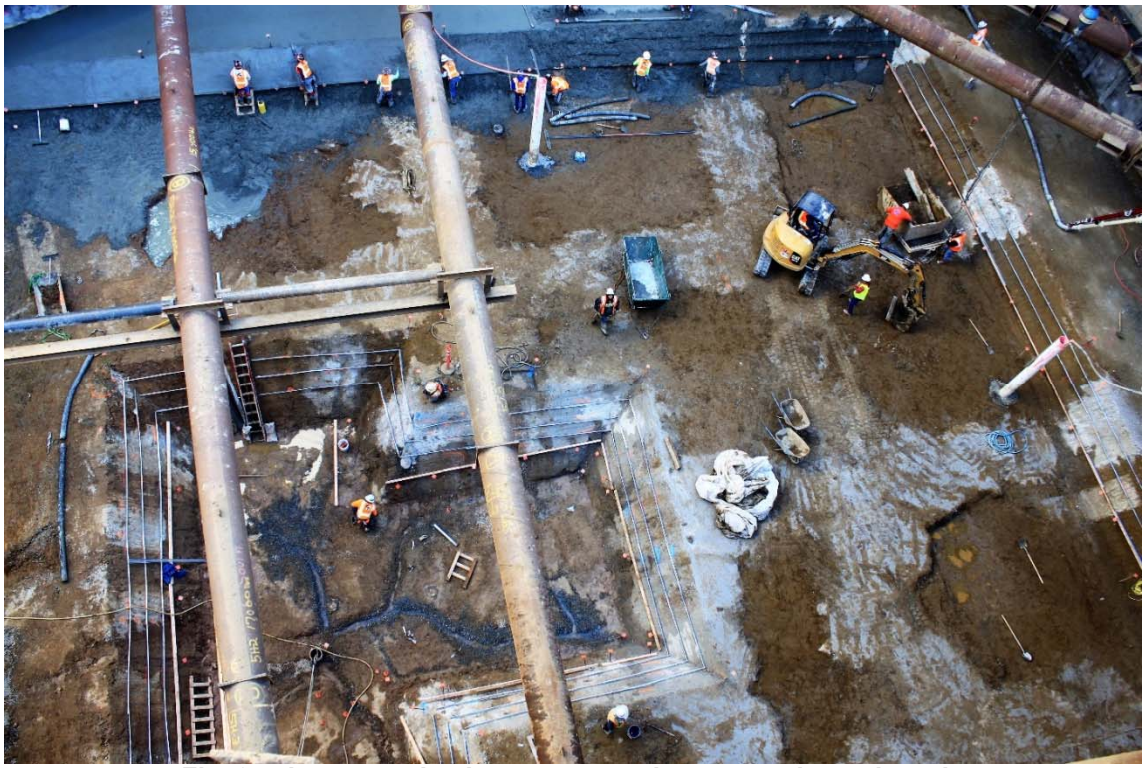


Fig. 9 – Jet-grouted columns exposed at excavation subgrade

CONCLUSIONS

Design and construction were complicated by the fact that the site is in a high seismicity region, is in a dense urban environment, and included a deep basement (one of the deepest in the San Francisco Bay Area to date). Subsurface conditions include the potential for liquefaction and a varying profile across the basement subgrade. Rigorous analysis was needed between the structural and geotechnical engineers to verify design assumptions.

The contractor had to provide liquefaction mitigation and foundation support and construct it from about 65 feet above the target zone. A test program was important to prove out the contractor's methods to show that the needed verticality, overlap, and strength could be attained. During production installation, continued monitoring and evaluation was needed to check possible anomalies and provide mitigation where needed. The test program and production inspection proved out that the jet-grout columns could be constructed at depth to the design diameter and overlap.

Through design and construction iterations between the structural engineer, geotechnical engineer, and specialty contractor were needed to achieve a successful design and product. Extensive communication and collaboration overcame difficult site conditions and founded this vital development of San Francisco's new Transbay District.

REFERENCES

Nguyen, T.V., Rayamajhi, D., Boulanger, R.W., Ashford, S.A., Lu, J., Elgamal, A., Shao, L., 2013. "Design of DSM Grids for Liquefaction Remediation". Journal of Geotechnical and Geoenvironmental Engineering, ASCE.

REINFORCEMENT OF EXISTING DEEP FOUNDATIONS WITH MICROPILES

Freddy Lopez, Friedr. Ischebeck GmbH, Ennepetal, GERMANY
Mauricio Terceros, Institute for Geotechnical Engineering/Leibniz University of Hannover, GERMANY
Martin Achmus, Institute for Geotechnical Engineering/Leibniz University of Hannover, GERMANY

ABSTRACT

The massive use of deep foundations had a remarkable influence in the building industry in the 20th century. Piles and micropiles made possible to erect thousands of civil structures around the world, changing quintessentially the urban and rural landscapes.

Especially in urban areas, the ongoing development requires not only new infrastructure, but also to increase the capacity and/or to extend the serviceability of existing structures (buildings, bridges, etc.).

Factors such as the change of use of existing facilities or the requirement to comply with updated building regulations confront Civil Engineers with the question, whether to tear down and build new structures, or to reinforce the existing structures from their foundations.

Micropiling has enabled designers to come up with technical feasible solutions to retrofit the existing deep foundations, making the structural reinforcement a real option, even under considerable changes in the loading conditions.

The following article presents an overview of an intervention project, where micropiles were designed to reinforce the original pile foundation of an existing building, enabling it to be reused with a different structural function.

This paper will focus mainly on the analysis of the interaction between the existing piles and the reinforcing micropiles, especially in terms of settlements' compatibility. Finally, the adopted solution, with its correspondent design considerations and execution process will be presented.

Keywords: Existing structures, deep foundations, retrofitting, micropiling, design and construction

SI CONVERSION FACTORS

Table 1. Approximate conversions from SI Units

Dimension	Symbol	When you know	Multiply by	To Find	Symbol
Length	cm	centimeters	0.394	inches	in
	m	meters	3.281	feet	ft
Force	kN	kilonewtons	224.81	poundforce	lbf
	MN	meganewtons	224.81	kilopoundforce	kip
Stresses	kPa (kN/m^2)	kilopascals	0.145	Poundforce / square inch	psi
	MPa (MN/m^2)	megapascals	145	Poundforce / square inch	psi

INTRODUCTION

Several structures (buildings, bridges, industrial facilities, etc.) are built on piled foundations. In many cases, the existing structures and their foundations need to be reinforced or retrofitted, because the original use of these structures has been subjected to changes that require increased load bearing capacities (i.e. former industrial facilities are reused for housing), or because the serviceability needs to be enhanced, even though the original use remains the same. The latter is a common case when national building codes are updated or when the structures behave differently than originally planned (i.e. unacceptable absolute or differential settlements, etc.).

© 2018 Deep Foundations Institute

For the reinforcement of foundations, it is certainly common to undertake the retrofitting works from the existing foundation levels, with the corresponding space restrictions (limited working heights). The most usual constructive measures consider ground improvement (i.e. with injections) and underpinning with additional load bearing elements (jet grout columns, micropiles, etc.).

The present article describes a proposed reinforcement of a deep foundation (cast-in-place bored piles) with self-drilling micropiles. The definition of the project and the interaction of the existing piles with the reinforcement (micropiles) will be presented on the following pages.

PROJECT DESCRIPTION

The scope of the intervention involves the reuse of a two-story parking deck (with one underground level) to house an extension of the attached five-story building. According to the information provided by the Structural Engineer, the existing parking decks are founded on 9.0m-long cast-in-place bored piles (D= 0.9m). An overview of the planned intervention is presented in Fig. 1.

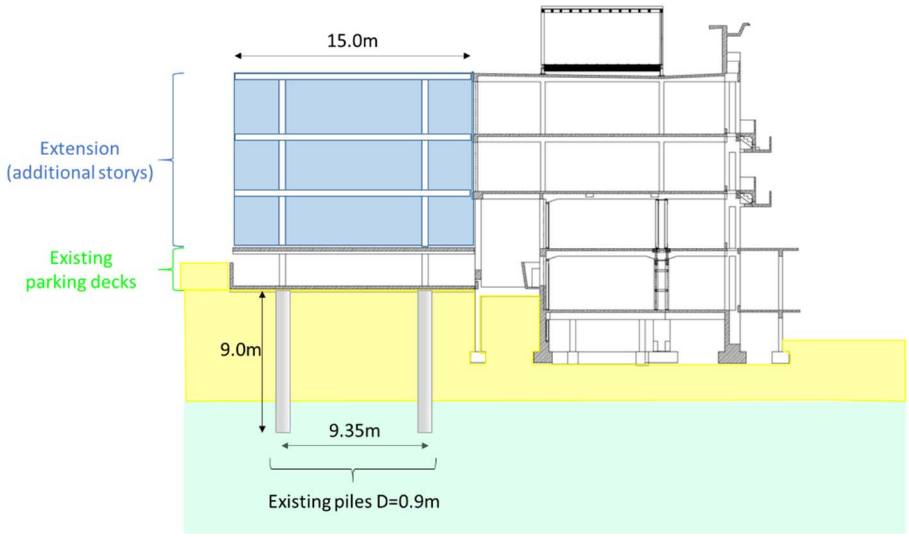


Fig. 1 Overview of the intervention

The bored piles were designed in 1999 for a compressive service load of $\mathbf{N_{serv,0} = 1500kN}$ according to the German Standards DIN 1054 and DIN 4014, valid at that time. Due to the extension of the facilities, the existing piles will be loaded with a new service (characteristic) load of $\mathbf{N_{serv,1} = 3000kN}$, meaning a load increment of $\mathbf{\Delta N_{serv} = 1500kN}$.

It is clear that the existing piles cannot fulfill the new load requirements without additional reinforcement, therefore the retrofitting with self-drilling micropiles was presented to the Structural Engineers for the feasibility study.

Self-drilling micropiles consist of continuously threaded hollow bars, made out of seamless steel pipes, installed via rotary percussive drilling. During the drilling process, the micropiles are continuously grouted (dynamic injection), building a rough interlocking at the interface grout-soil, increasing the skin friction (Lopez and Fernandez, 2017). The use of self-drilling micropiles has been proven to be a very versatile and cost-effective solution and is increasingly implemented in different intervention projects, both for the construction of new infrastructure and as reinforcement to retrofit existing structures, since they can be installed using very flexible drilling equipment, enabling the assembly of long micropiles even in confined spaces (Fig. 2), obtaining high drilling performances associated to very low vibrations (Lopez and Severi, 2017).

It is considered to install the micropiles from the underground level, in order to reduce as far as possible disturbances of the operative capacity of the existing facilities. The structural reinforcement of the existing superstructure lays outside the scope of this document and will not be further treated.

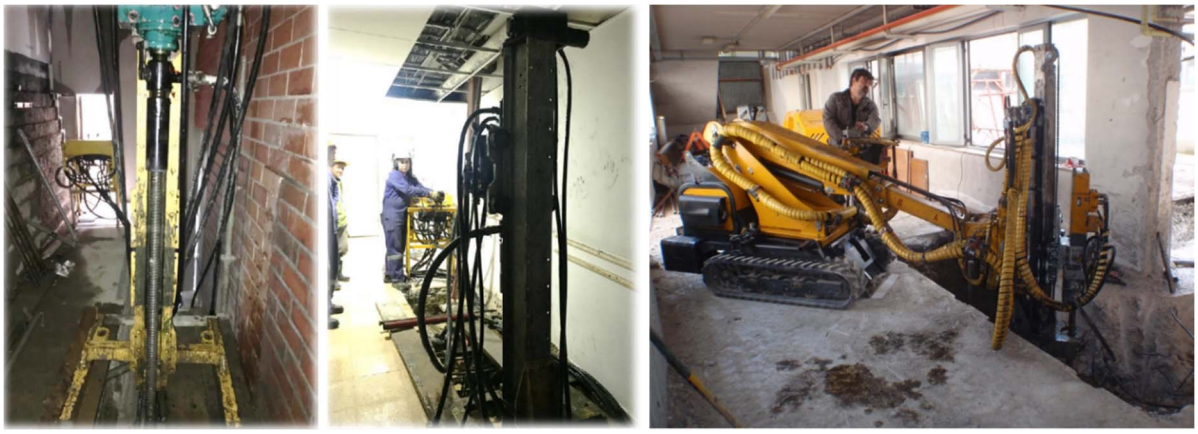


Fig. 2 Installation of reinforcement micropiles in confined spaces (Lopez and Severi, 2017)

ANALYSIS OF THE REINFORCED DEEP FOUNDATIONS

The proposed solution is presented conceptually in the following figures. The general idea is to install a group of four micropiles, symmetrically arranged around each cast-in-place bored pile, to resist the above mentioned load increment of $\mathbf{\Delta N_{serv} = 1500kN}$. The reinforced foundation was analyzed to resist a service (characteristic) load of $\mathbf{E_k = 3000kN}$ (Fig. 3).

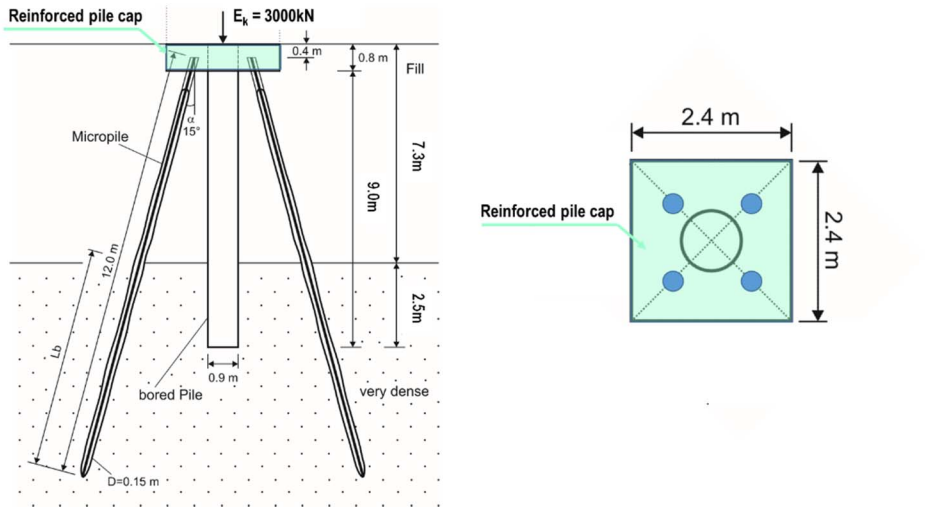


Fig. 3 Schematic presentation of the proposed reinforcement

For the analysis of the proposed solution, the following sequence was considered:

1) Evaluation of the existing bored piles: estimation of the load bearing behavior
2) Evaluation of the pile – micropiles interaction, considering different micropiles' inclinations
3) Selection of the optimal micropiles' layout

Existing piled foundation – Load bearing behavior

A detailed design report was not available at the time of the analysis, therefore the estimation of the load bearing behavior was performed using the existing information. The subsoil in the area consists mainly of granular soil deposits, with increasing compaction grades with increasing depths. The installation protocols

refer to the absolute elevations of the pile (head and toe), the pile length, as well as the upper level of the load bearing stratum and the pile embedment within it (2.5m). The assumed ground conditions and properties are summarized in Fig. 4.

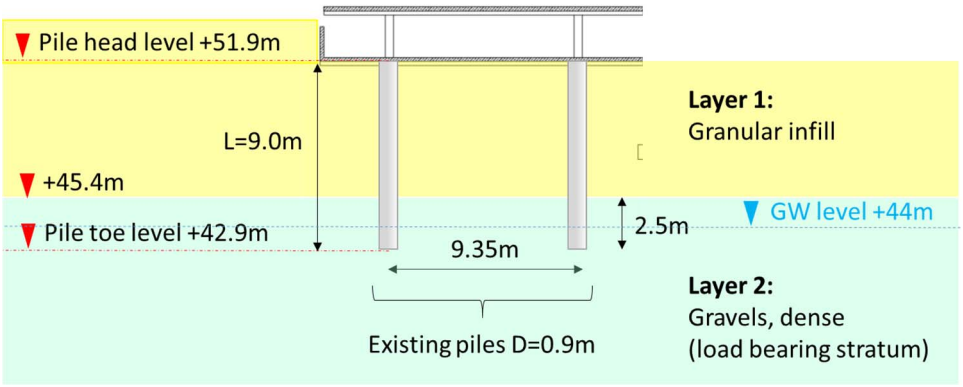


Fig. 4 Assumed ground conditions for the existing parking decks

Load bearing behavior with the analytical model of EAP 2012.

The existing piled foundation was verified, in compliance with the current European regulations for geotechnical design, the Eurocode 7 (EN 1997-1, 2010), and the Recommendations on Piling (EAP, 2012), published by the German Geotechnical Society (DGGT).

The characteristic pile resistance ($R_{c,k}$), can be obtained from the tip or base resistance ($R_{b,k}$) and the shaft resistance ($R_{s,k}$):

$$R_{c,k} = R_{b,k} + R_{s,k} \quad [1]$$

Both the base and the shaft resistance are dependent of the pile settlements (s), and in concordance with the current German practice, the estimation of the load bearing capacity for a single pile under compression can be obtained using an analytical model. According to (EAP, 2012), the base and shaft resistance can be obtained from the pile geometry, the characteristic base pressure ($q_{b,k}$) of the load bearing stratum for settlements corresponding to 2%, 3% and 10% of the pile diameter (D) and the characteristic skin friction ($q_{s,k}$) of the surrounding soils, which increases linearly with the settlements until a limit value (s_{sg}) is reached:

$$s_{s,g} = 500 * R_{s,k\,(s_{s,g})}\,[in\ kN] + 0.5\ cm \leq 3cm \quad [2]$$

Furthermore, an extensive, calibrated database of empirical values is provided for both the base pressure and skin friction, in dependence of the average penetrometer (CPT) tip resistance (q_c) for non-cohesive soils, and the undrained shear strength for cohesive soils (c_u).

Based on the information available, the parameters listed in Table 2 were adopted to evaluate the load bearing behavior of the existing piles for the analytical model.

Table 2. Adopted parameters for the existing piles according to (EAP, 2012)

Layer	Description	Tip resistance CPT q_c (MN/m²)	Base pressure $q_{b,k}$ (kN/m²)			Skin friction $q_{s,k}$ (kN/m²)
			s/D=0.02	s/D=0.03	s/D= .10	
1	Granular infill, loosen to medium dense	< 5	-	-	-	20
2	Sandy gravels, dense to very dense	20	1400	1800	3500	115

The results of the analytical model are presented in Fig. 5. Based on the resistance behavior simulated by the analytical model, a settlement of **s ≈ 1.0cm** would be expected for a service load of $\mathbf{N_{serv}}$ **= 1500kN**.

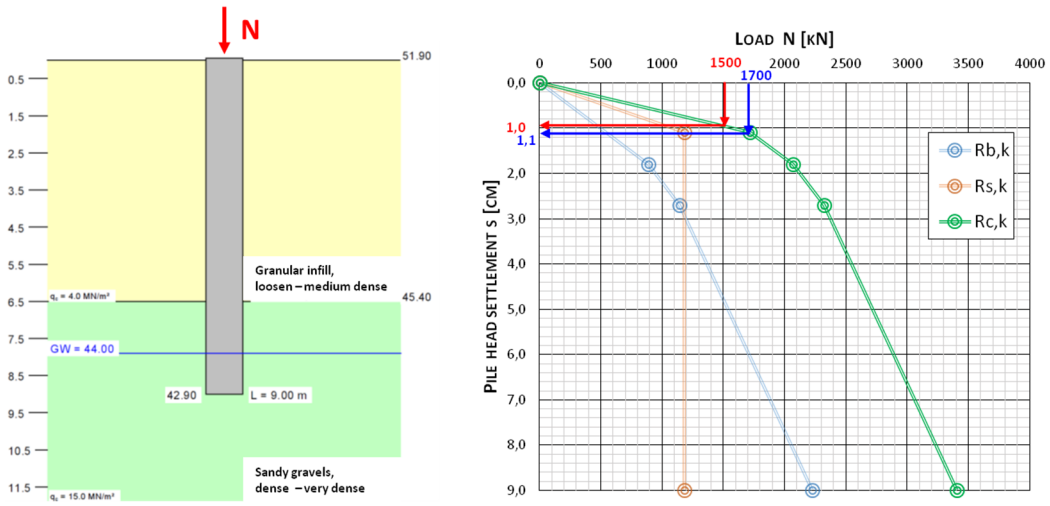


Fig. 5 Load - settlement curve from the analytical model according to EAP 2012

Considering an usual safety factor **FS=2.0**, applied to the ultimate resistance of piles under compression loads, an allowable loading $\mathbf{R_{allow} = 1700kN}$ results, with a correspondent settlement of **s ≈ 1.1cm.**

Load bearing behavior with a numerical model

There is no analytical model to evaluate the interaction between the existing piles and the reinforcement, therefore the evaluation was carried out with a three-dimensional numerical model of the reinforced pile foundation system, developed using the finite element program PLAXIS3D (Brinkgreve et al., 2013). With regard to the symmetry of both geometrical and loading conditions, only one quarter of the pile foundation was modeled in order to reduce computational effort.

Preliminary analyses focused on evaluating the behavior of the single pile, comparing the results with the analytical model previously described. The soil model width is chosen to 15-times the pile diameter (D) in both horizontal directions. The model depth is set two times the pile length (L). The mesh fineness and model dimensions were chosen to reach sufficiently accurate results and avoid an impact of the boundary conditions. The mesh of the finite element model and its geometry is presented in Fig. 6. A 3D simulation was applied in order to easily extend the system by the micropiles in the following step.

The pile is modeled as a concrete pile element with a diameter (D). An elasto-plastic contact was implemented between pile and the adjacent soil. The maximum shear stresses in the contact surface (τ_{max}) result from the product of the horizontal stresses (σ_H) and the contact friction angle (δ), equal to 80% of the friction angle (φ').

The calculation is done in several steps. In the first step the initial stress state is generated by consideration of soil elements only. The horizontal stresses σ_H are defined by a coefficient of horizontal earth pressure at rest (k_0). Subsequently, the predefined elements defining the pile geometry are replaced by concrete elements with a linear elastic material law (wished-in-place procedure). In the same step, the contact between the pile and the surrounding soil is activated. In a third step, an incremental vertical load ($\mathbf{N_{inc}}$) is applied to the center of the pile until a settlement, equal to 10% of the pile diameter, is reached.

To model the soil, the HSsmall model according to Benz (Benz, 2006) was used. This soil model is an upgrade of the sophisticated Hardening Soil Model according to Schanz (Schanz, 1998) which enables for instance the consideration of the stress-dependency of soil stiffness. The HSsmall model is additionally able to account for the strain dependency of soil stiffness, being crucial for small loads.

The numerical formulation of the required parameters for the constitutive models is explained in detail in the user´s manual of PLAXIS3D (Brinkgreve et al., 2013) and won´t be further treated in this article.

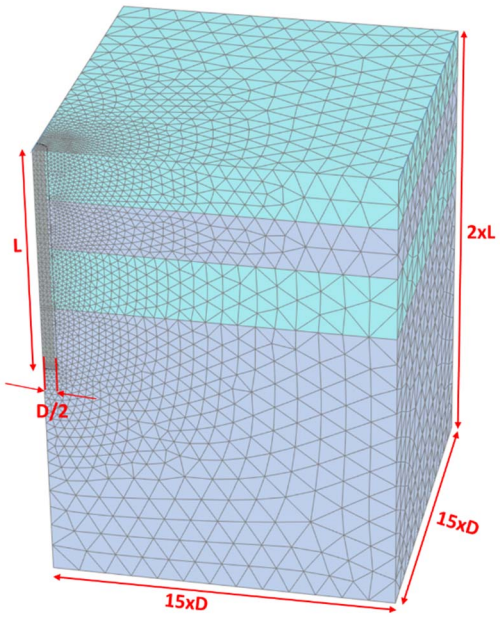


Fig. 6 Finite element mesh used in the simulations (D = 0.9m, L = 9m)

The following tables present the adopted parameters for the simulation:

Table 3. Bored pile, parameters used in the simulations – Material law: Linear elastic

Structural element	Bored pile
Upper level (m)	0.0
Length (m)	9.0
Diameter: D (m)	0.9
Unit weight: γ (kN/m^3)	25
Young modulus: E (kN/m^2)	30x10^6
Poisson's ratio: υ (-)	0.3

Table 4. Soil parameters used in the simulations – Material law: Hardening Soil Small (HSSmall)

Layer	1a	1b	1c	2
Upper level (m)	0.0	-2.0	-4.0	-6.5
Description	Granular infill, loosen to medium dense			Gravels, dense to very dense
Unit weight (effective): γ' (kN/m^3)	8.8	8.8	8.8	10.3
Void ratio: e (-)	0.85	0.85	0.85	0.60
Secant triaxial loading stiffness: E_{50}^{ref} (kN/m^2)	1452	3497	5471	65014
Tangent oedometer loading stiffness: : E_{oed}^{ref} (kN/m^2)	1177	2835	4436	43174
Triaxial unloading/reloading stiffness: : E_{ur}^{ref} (kN/m^2)	4356	10490	16414	195041
Exponent: m (-)	0.8	0.8	0.8	0.5
Cohesion: c' (kN/m^2)	0.0	0.0	0.0	0.0
Friction angle: φ' (°)	28	28	28	40
Dilatancy: ψ (°)	0	0	0	10
Reference shear strain: $\gamma_{0.7}$ (-)	1x10^{-4}	1x10^{-4}	1x10^{-4}	1x10^{-4}
Dynamic shear modulus: : G_0^{ref} (kN/m^2)	19650	34035	45023	109696
Poisson's ratio: υ (-)	0.3	0.3	0.3	0.2
Reference stress p^{ref} (kN/m^2)	6.05	18.14	31.74	66.57
At-rest earth pressure coefficient:k_0 (-)	0.531	0.531	0.531	0.357
Strength reduction factor for interfaces R_{inter} (-)	0.8	0.8	0.8	0.8

The results of the numerical and analytical models for the single bored pile are presented in Fig. 7, where the figure on the right corresponds to a close-up of the highlighted portion of the left diagram.

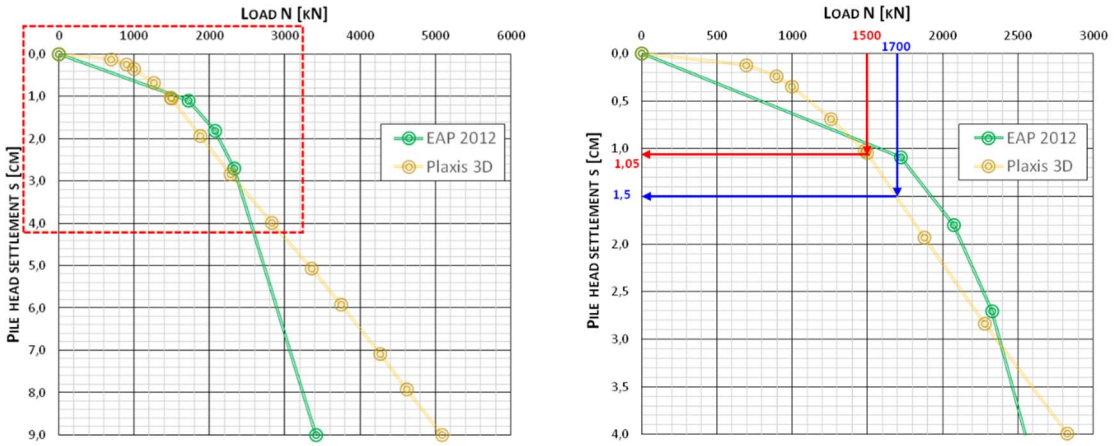


Fig. 7 Results of the analytical (EAP, 2012) and numerical (PLAXIS 3D) models for a single bored pile

There is a congruency in the mobilized pile resistances for settlements up to 4.0cm, corresponding to 4.4% of the pile diameter (D). As expected, the numerical model presents a stiffer response for small settlements (< 1.0cm), consistent with the hardening soil behavior for small strains. A very good agreement can be observed for a settlement range of 1.0cm – 3.0cm. Compared to the analytical model, larger pile resistances are obtained from the numerical model for increasing settlements. This behavior is plausible, since the numerical model takes into consideration the stress-dependency of the soil stiffness, expressed as the moduli E_{50} (triaxial) and E_{oed} (oedometer). The analytical model doesn´t take these considerations into account.

Since the admissible settlements for the serviceability of the foundations are commonly in the range of 2cm – 3cm, the resistance behavior of the piled foundation, simulated by the numerical model, can be considered as suitable for the subsequent analysis of the reinforcement, and its interaction with the existing pile. Based on the results of the numerical model, settlements of **s ≈ 1.05cm** and **s ≈ 1.5cm** would be expected for service loads of $\mathbf{N_{serv}}$ **= 1500kN** and $\mathbf{N_{serv}}$ **= 1700kN**, respectively.

Interaction pile - micropiles

As previously explained, the foundation reinforcement consists in a group of four self-drilling micropiles, symmetrically arranged around each cast-in-place bored pile. Different micropile inclinations (referred to the vertical) are considered in the analysis: 5°, 10°, 15°, 20° and 25°. A concrete pile cap (2.4mx2.4mx0.8m) was modelled to materialize a rigid connection between the bored pile and the micropiles.

In the numerical model for the reinforced foundation, the micropiles are defined as “embedded piles” and the input values for the skin friction ($q_{s,k}$) are adopted from the empirical values recommended in (EAP, 2012). The adopted parameters for the micropiles are listed in Table 5.

Table 5. Micropiles, parameters used in the simulations – Material law: Linear elastic

Structural element	Embedded piles, only skin resistance
Drill bit diameter: d_b (cm)	13.0
Shaft diameter: d (cm)	15.0, considering an expansion of 2.0cm, acc. to (EAP,2012)
Length (m)	12
Unit weight: γ (kN/m^3)	25
Young modulus: E (kN/m^2)	30x10^6
Skin resistance T_{max} (kN/m)	33 (layers 1a - 1c) (for a limit settlement $s_{s,g} \leq$ 3cm, Equation [2])
	143.7 (layer 2) (for a limit settlement $s_{s,g} \leq$ 3cm, Equation [2])

The calculation is done in five steps, as schematically presented in Fig. 8. In the first step the initial stress state is generated by consideration of soil elements only. Subsequently, the predefined elements defining the pile geometry are replaced by concrete elements with a linear elastic material law. In the same step, the contact between the pile and the surrounding soil is activated. In a third step, the vertical load of $\mathbf{N = N_{serv} = 1500kN}$ is applied to the center of the pile. In a fourth step, the predefined elements representing the micropile and the rigid pile cap are activated and rigidly connected to the pile. In the last step, an incremental vertical load ($\mathbf{N_{inc}}$) is applied to the center of the pile cap until a settlement, equal to 10% of the pile diameter (D), is reached.

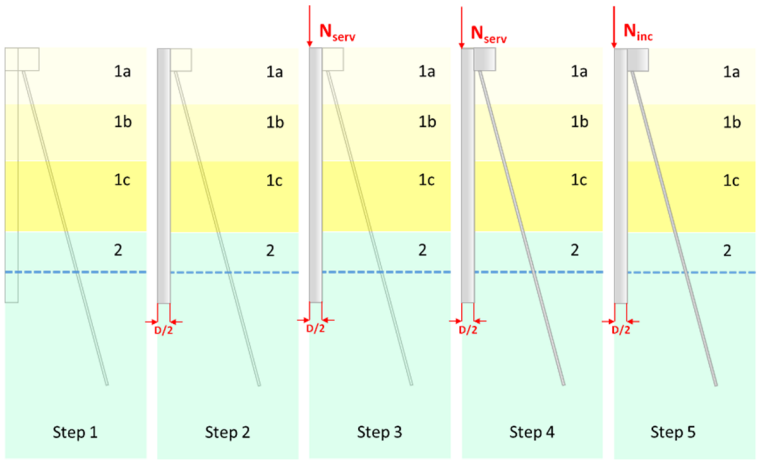


Fig. 8 Schematic presentation of the calculation steps (axial symmetrical model)

The results of the analysis are shown in Fig. 9. While the single pile would require a settlement of $\mathbf{s_{single\ _pile} \approx 4.0cm}$ to mobilize a resistance equal to the required service load of $\mathbf{N_{serv} = 3000kN}$, the reinforced foundation (bored pile and micropiles) requires a much lower settlement of $\mathbf{s_{reinf.-found} \approx 1.5cm}$, making the contribution of the micropiles evident. Due to the rigid connection between the different elements, the incremental settlements of the reinforced foundation are also induced to the bored pile. For the above mentioned settlement of $\mathbf{s_{reinf.-found} = 1.5cm}$, the bored pile would be receiving a service load of $\mathbf{N_{serv,pile} = 1800kN}$, and the micropiles $\mathbf{N_{serv,mp} = 1200kN.}$ The load bearing behavior of the reinforced foundation can be considered as completely satisfactory.

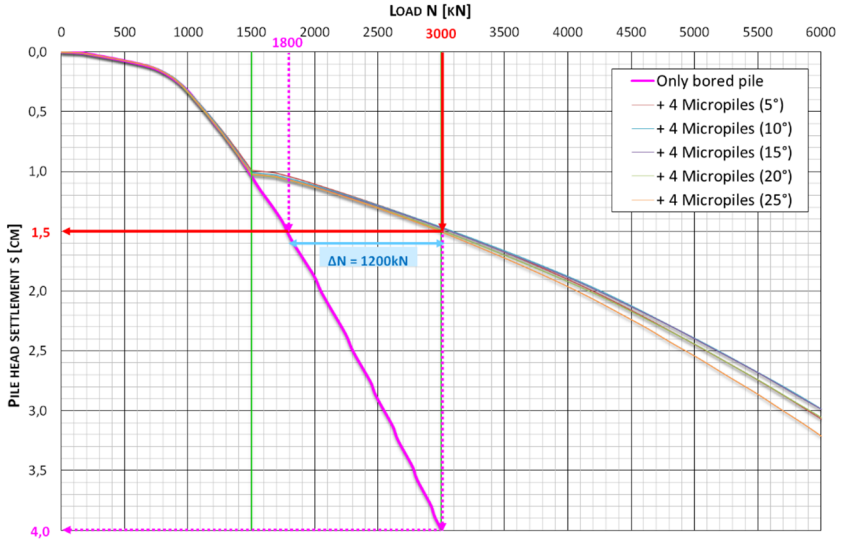


Fig. 9 Load bearing behavior of the reinforced foundation

The distribution of the load to the elements of the retrofitted foundation is presented in Fig. 10.

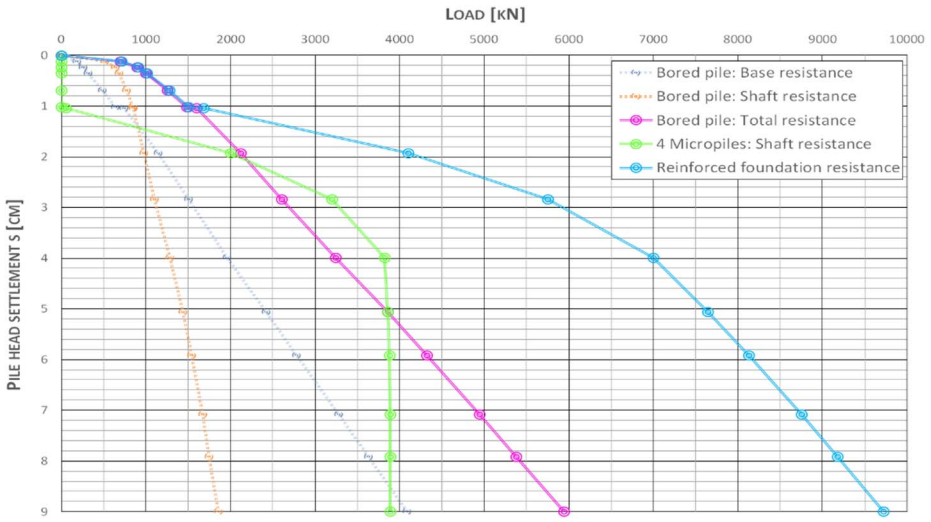


Fig. 10 Load distribution of the retrofitted foundation

Each of the four micropiles is designed according to the Eurocode 7 (EN 1997-1, 2010), considering a vertical service load of $\mathbf{N_{mpi,k}}$ **= 300kN** (25% of the total service load of the micropiles' group). For the design, an inclination of **15°** (from the vertical) was adopted so that the micropiles can be installed very close to the existing bored pile, reducing considerably the footprint of the reinforced pile cap, avoiding any interaction at the pile base level. The micropiles' design is summarized in Table 6.

$$R_{M,d} = \frac{R_{M,k}}{\gamma_M} \geq E_{i,d} = E_{i,k} * \gamma_{G,Q} \quad [3]$$

$$E_{i,k} = \frac{N_{mpi,k}}{\cos(\alpha_{vert})} \quad [4]$$

Table 6. Design summary for the self-drilling micropiles according to Eurocode 7 (EN 1997-1, 2010)

Micropiles	MP 1 to 4
Micropile inclination: α_{vert} (°)	15
Characteristic axial load: $E_{i,k}$ (kN)	310.6
Design axial load: $E_{i,d}$ (kN)	465.9 (with a partial safety factor $\gamma_{G,Q}$ = 1.5)
Type:	TITAN Ischebeck 52/26
Characteristic Load bearing capacity: $R_{M,k}$(kN)	650, according to Ischebeck approval Z-34.14-209 (DIBt, 2014)
Design Load bearing capacity: $R_{M,d}$ (kN)	565 (with a partial safety factor γ_M = 1.15)
Length (m)	12
Drill bit / diameter (cm)	Cross-cut / 13.0

The layout of the reinforced foundation is schematically presented in Fig. 11.

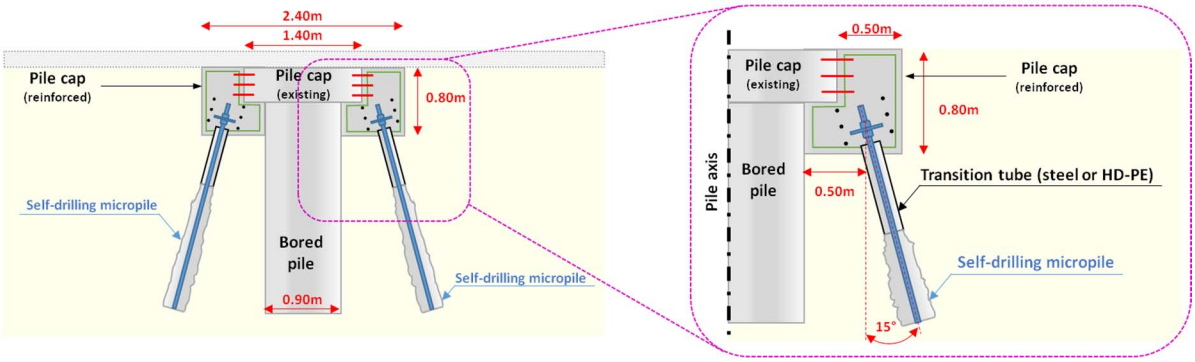


Fig. 11 Schematic layout of the reinforced foundation

According to the German Technical Approval (DIBt, 2014), the use of a tube (steel or HD-PE) is recommended to provide a constructive protection of the grouted body in the transition zone between the underground and the pile cap, i.e. against damages during the final excavation and placing of the reinforcement cages.

SUMMARY AND CONCLUSIONS

The present document described the analysis of the reinforcement of an existing deep foundation (cast-in place bored piles) with micropiles.

The existing piles, with a diameter of 90cm, were originally designed for a service load of 1500kN. Due to new structural conditions, the service load was increased up to 3000kN. A group of symmetrically arranged micropiles, rigidly connected to the existing foundation, was used to increase the load bearing capacity of the reinforced system to fulfill the new structural requirements.

A numerical model was developed using the finite element program PLAXIS3D, to evaluate the interaction of the existing pile foundation and the reinforcement. For the definition of the numerical model, a preliminary analysis of the load bearing capacity of the single piles was carried out, and the results were compared to the results of an analytical method, based on the load-settlement of a compression pile, as currently adopted in the German practice. Both methods have a good accordance in the settlement's range of 3% of the pile diameter (approx.3cm).

The results of numerical model show, that the load bearing capacity of the reinforced piled foundation is effectively increased, with very low additional settlements. The settlements associated to the new service load of 3000kN are smaller than 1.7% of the pile diameter (approx.1.5cm), laying within an acceptable range (<2cm), therefore the load bearing behavior can be considered as completely satisfactory.

For the reinforcement, the use of self-drilling micropiles was chosen, since their flexible installation enables to carry out interventions even in areas with restricted space, causing only small affection to the surrounding work environment.

REFERENCES

Benz, T., 2006. "Small Strain Stiffness of Soils and its Numerical Consequences", Ph.D. thesis, University of Stuttgart.

Brinkgreve, R.B.J., Engin, E., Swolfs, W.M., 2013. PLAXIS 3D 2013 Manual.

German Geotechnical Society (DGGT), 2012. Recommendations on Piling (EAP)

Deutsches Institut für Bautechnik (DIBt), 2014. Allgemeine bauabsichtliche Zulassung Z-34.14-209: Mikropfähle TITAN

European Norm EN 14199: 2015: Execution of special geotechnical works – Micropiles, 2015.

European Norm EN 1997-1: Eurocode 7, Geotechnical Design – Part 1: General Rules, 2010.

German Norm DIN 1054: Subsoil: Permissible loading of subsoil, 1976

German Norm DIN 4014:1990-03: Subsoil: Bored cast-in-place piles – Construction, design and bearing capacity, 1990

Lopez, F., Fernandez, J.M., 2017. Edificio Piedra Real – Concepcion, Chile. Case study of an uplift reinforcement project. Proceedings of the 13th International Workshop on Micropiles, Vancouver, March 29-April 1.

Lopez, F., Severi, G., 2017. Micropiling in Urban Infrastructure: Advantages, Experience and Challenges. Accepted for the Proceedings of the DFI-EFFC International Conference on Deep Foundations and Ground Improvement, Rome, June 5-8.

Schanz, T., 1998. "Zur Modellierung des Mechanischen Verhaltens von Reibungsmaterialien", Habilitation, University of Stuttgart (in German).

THREE-DIMENSIONAL NUMERICAL MODELLING OF LOAD DISTRIBUTION AND SETTLEMENT OF PILE GROUPS

Onur Kacar, Arup Inc., New York City, NY, USA. Phone: 212-896-3019 onur.kacar@arup.com

ABSTRACT

A numerical approach has been implemented to assess the settlements of pile groups bearing in clay. A three-dimensional finite element program has been utilized to model a vertically loaded spread footing, a single pile and a pile group. The soil-pile interaction was modeled with elastoplastic soil and interface elements. The model has been calibrated using a full scale load test results of the spread footing. The load transfer between the pile cap and the piles was assessed and compared with the measured load transfer. The predicted settlements for the pile group were compared with the settlements measured in the load test. Two analytical methods were adopted to predict the pile group settlements and they were compared with the measured values. The group effect determined from the analysis and load tests was compared with the interaction factor approach. It was shown that three-dimensional finite element approach can be successfully utilized to assess the soil-structure interaction and hence the load transfer between the piles and pile cap. Also, it was shown that the interaction factors method and equivalent footing method work well in the working stress range, however they underpredict the settlements at larger loads.

Keywords: pile group, settlement, numerical modelling

INTRODUCTION

The settlement and stress distribution of pile groups have been traditionally estimated based on load test results of single piles and accounting for the group effect using various approaches. The most widely used approaches are group interaction factor method, equivalent footing method and equivalent pier method.

These approximate solutions are used very commonly in practice as full-scale load tests on pile groups are very expensive and time consuming. These approximate solutions are also adopted in design guidelines such as AASHTO LRFD Bridge Design Guidelines (2014) and FHWA Design and Construction of Driven Pile Foundations (2016).

In this paper, a full-scale foundation load tests performed by Nagai et al. (1961) and reported by Koizumi and Ito (1967) is modelled using a three-dimensional numerical method. The settlements and the stress distribution on foundations were then compared with the traditional equivalent footing method and interaction factor methods.

© 2018 Deep Foundations Institute

LOAD TEST

Nagai et al. (1965) conducted a comprehensive load test program on pile foundations. The tested foundations consisted of a nearly full-size pile group foundation, a single pile and footings with the same size as the pile cap. The test program included vibration tests, lateral load tests and axial load tests. Only the axial load test program is covered in this paper. All the piles tested were 300 mm diameter, closed end pipe piles with a length of 5.5 m and a wall thickness of the piles were 3.2 mm. The pile group was arranged in a 3x3 square array with a center to center spacing of 900 mm. Three of these nine piles were instrumented with earth pressure cells, pore water pressure cells and wire strain gauges. Piezometers were installed adjacent to the piles prior to pile driving. A pile was driven 4.8 m away from the pile group to measure the load-settlement behavior of a single pile. The vertical load tests were performed 7 months after driving the piles, allowing the excess pore pressure developed during pile driving to dissipate. To investigate the load distribution between the pile cap and the piles, footings with the same sizes as the pile caps were also installed at the same elevation with the pile caps. The foundation layout is shown in Figure 1.

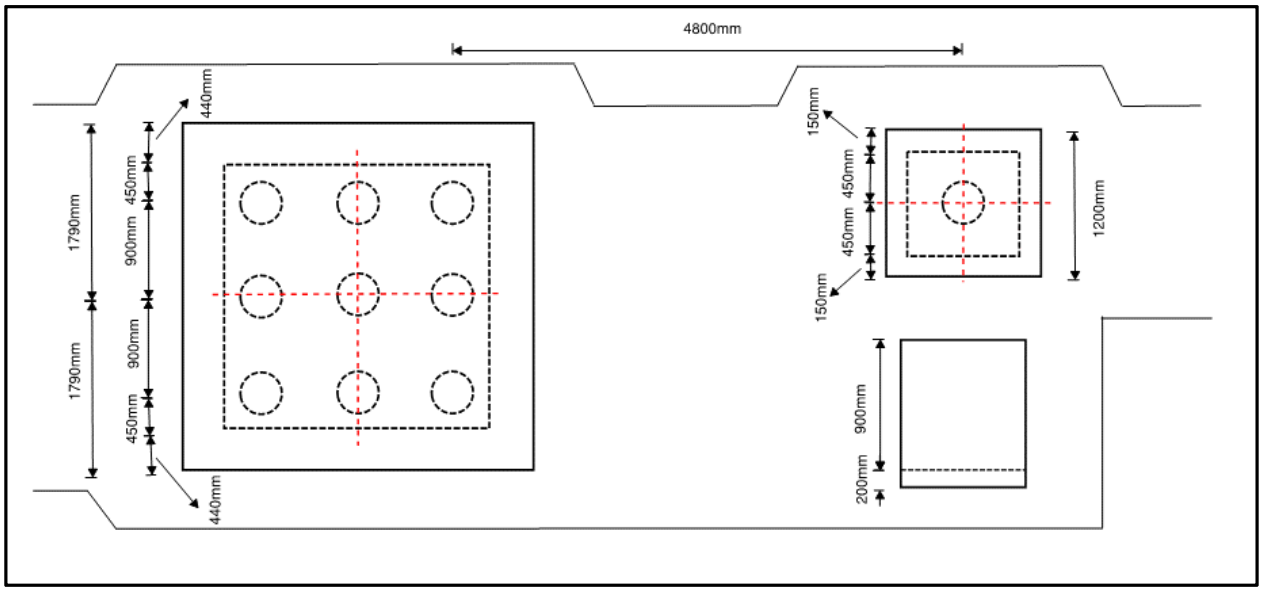


Fig. 1. Test Foundation Layout (After Koizumi and Ito, 1967)

The test site was chosen due to its relatively uniform soil stratigraphy. Three boreholes and six Cone Penetrometer tests (CPT) were performed to investigate the soil conditions at the site. Soil stratigraphy at the test site consists of about 1.5 m of sandy silt with gravel, and a layer of slightly organic silty clay extending to a depth of 13.5 m. Below this layer, a gravel and dense sand layer was observed. Prior to construction of the foundations, the top 1.5 m of soil was removed so that the foundations were supported by the relatively homogenous clay.

The clay is highly plastic with an increasing plasticity index with depth. The natural water content is between 80% to 130% and it is very close to the liquid limit in the upper half of the stratum. The undrained shear strength of the clay at the foundation level is about 25 kPa and it increases to 40 kPa at the pile tip elevation based on the field cone test results and unconfined compression test results. The unconfined

compression test results are generally lower than the field cone results, likely due to in-situ stresses present during cone testing. The clay is slightly overconsolidated and highly sensitive The sensitive nature of the clay may have led to sample disturbance and thus resulting in lower shear strength of the tested samples. The soil stratigraphy and soil strength profile is shown in Figure 2.

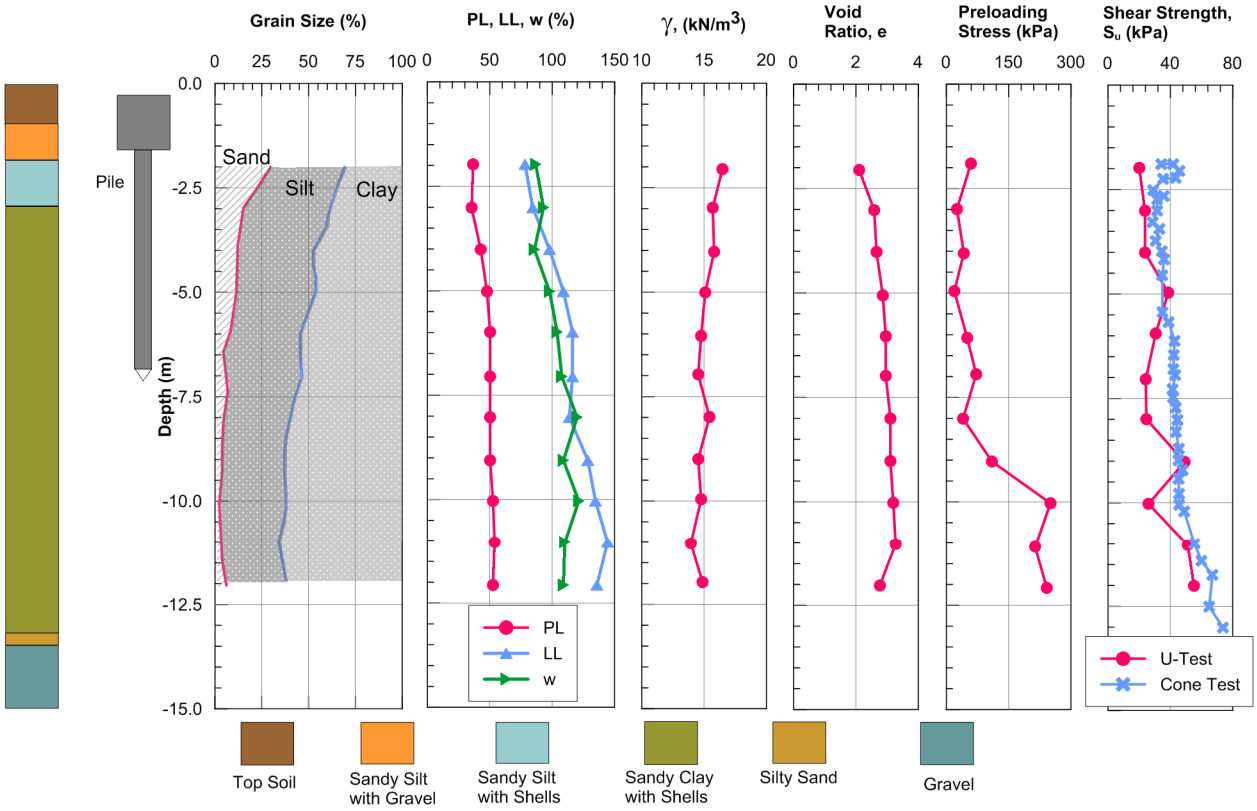


Fig. 2. Boring logs and soil properties (Koizumi and Ito, 1967)

As a best estimate of the undrained shear strength, an average undrained shear strength profile was developed. The undrained shear strength of the clay layer is increasing with depth and was expressed as a function of depth as follows:

$$S_u = 25\ kPa + 2.7z \qquad [1]$$

Where S_u is the undrained shear strength, and z is the depth below the foundation level in meters. The elastic modulus (E) of the clay layer was estimated based on empirical correlations since there were no tests conducted to determine the elastic modulus. The elastic modulus of clay can be estimated using the correlations reported in the literature. These correlations are generally based on the undrained shear strength of the clay and the OCR. Charts suggested by Duncan and Buchinagi (1976) where the E/S_u ratio is given as a function of OCR and PI, the estimated ratio for clays at the test site is:

$$E/S_u = 250 \text{ to } 300 \qquad [2]$$

Plate load tests conducted by Duncan and Buchinagi (1976) also showed that, E/S_u ratio for clays with OCR < 2 and PI=50% is 300. Therefore, an E/S_u ratio of 300 was adopted in this study. The average S_u value throughout the length of the piles is about 32.5 kPa. Using this average undrained shear strength and E/S_u ratio of 300, the elastic modulus is estimated as 9,750 kPa.

Since the top 1.5 m of the existing ground was removed prior to the pile driving, the sandy-gravelly silt layer was not modelled. The silty sand layer below the clay layer was encountered at a depth of 5 m below the tip of pile level (more than 16D), the effect of this layer on pile behavior is negligible. However, in order to verify this assumption, representative strength and stiffness values were assigned to the silty sand layer and included in the numerical model. A friction angle of $\varphi' = 32^0$ and an elastic modulus of $E = 80\ MPa$ was adopted in the numerical model. The negligible effect of this layer in the settlement estimation was verified by checking the vertical stress increments in this layer and it was confirmed that the stress increase was very small as discussed in the results section. This assumption is also verified by measurement of the vertical settlement of the reference point installed at 7.5 m depth during the load test where the settlements were less than 2 mm whereas the pile top settlement exceeded 200 mm.

NUMERICAL MODEL

The load tests conducted on the spread footing and piles have been modelled using a three-dimensional numerical model, PLAXIS 3D. The soil is modelled as elastic-perfectly plastic using Mohr-Coulomb failure criterion and the footings are modelled as linear elastic materials. The piles are modelled using the PLAXIS embedded pile elements feature. The material properties used in the model are shown in Table 1.

The soil behavior for all three foundations is assumed to be undrained as the load test were completed within few hours for each test. The load tests were performed about 7 months after the pile driving and therefore, the excess pore water pressures were dissipated by the time of the load tests (Koizumi and Ito, 1967).

Table 1. Soil Parameters used in the Numerical Model

Soil Layer		Undrained Shear Strength, S_u (kPa)	Friction Angle, φ' (deg.)	Modulus of Elasticity, E (MPa)
Clay				
	Initial	25.0+2.7z	---	9.75
	After calibration	22.5+2.7z	---	10
Sand		---	32	80

The first analysis that was carried out was for the 0.9m x 0.9m spreads footing. The soil was modeled using 10-node tetrahedral elements and the footings were modeled as 6-node plate elements. The model dimensions are set as 20 m in width, 30 m in length and 30 m in depth to avoid boundary effects. A total of 78,123 elements were used in the model.

The soil parameters reported in Table 1 was used initially to model the soil-structure interaction. Later, the soil strength and stiffness parameters of the clay were slightly modified to achieve a better match between the measured and predicted load-settlement curves. The modified soil parameters are also presented in Table 1.

The second analysis was performed for the single pile. The pile was modelled using the "embedded pile" feature in PLAXIS. A total 102,445 elements were used in this analysis. The calibrated soil properties were used in this analysis. The skin friction and end bearing values were also calibrated to match the single pile load-settlement curve more closely.

The third analysis was modelling the 3x3 pile group. The calibrated soil properties and the skin friction and end bearing values from the single pile analysis were used in all piles in the pile group. A total number of 109,089 elements were used in this analysis. The soil model and the mesh for the pile group model is shown in Figure 3.

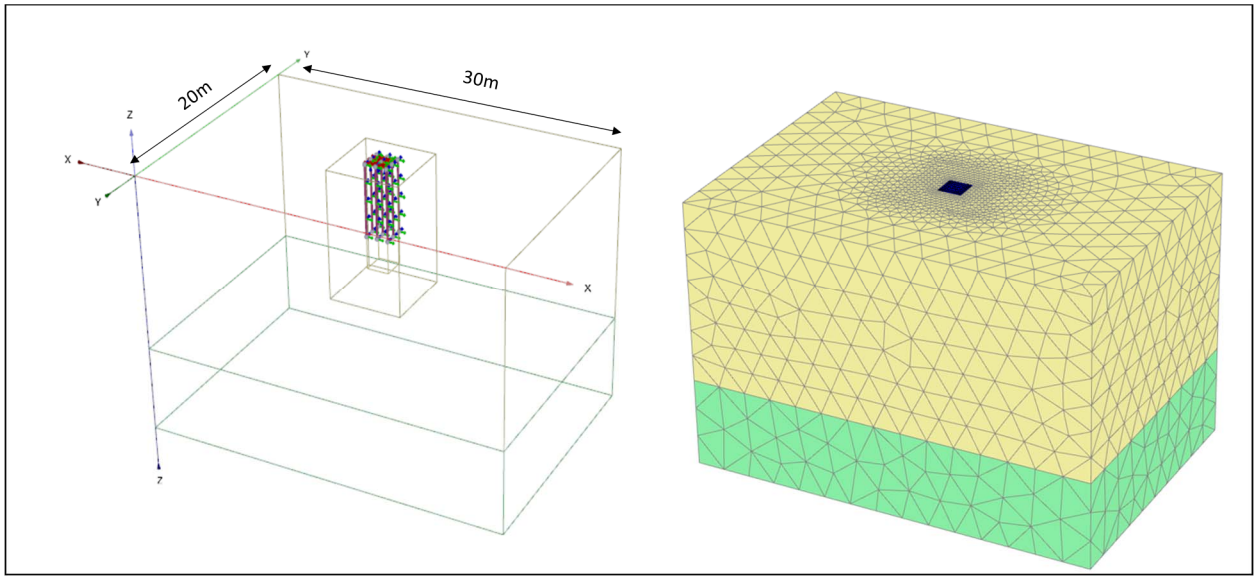


Fig. 3. 3D Model and Mesh for the Pile Group Analysis

COMPARISON OF MODEL RESULTS WITH MEASURED VALUES

The load-settlement curve obtained from the numerical model for the 0.9 m x 0.9 m footing is in agreement with the measured load-settlement from the load test for the majority of the applied loads.
As it can be seen in Figure 4, the predicted settlements become higher than the measured settlements as the load approaches the failure load. This behavior is most likely due to larger strains associated and numerical models not capturing the failure strains as accurately as the strains in the working stress range.

The 0.9 m x 0.9 m footing load settlement curve shows that the vertical displacement of the footing is nearly linear up to 100 kN and then the deformations get nonlinear, and the deformations increase rapidly beyond a 130 kN of applied load. The estimated theoretical bearing capacity of the footing is about 150 kN, therefore in reasonable agreement with the measured capacity.

As seen in Figure 4, the load-settlement curve of the single pile is fairly linear and the settlements are relatively small up to an applied load of 215 kN. Beyond this load, the deformations become excessive and the pile-pile cap system seems to fail. The failure is more ductile than usually expected. Therefore, the load-

settlement curve obtained from the numerical model matches the measured load-settlement curve up to the failure loads, but beyond the failure load, the estimated settlements are less than the measured.

During the load test, the pressure beneath the pile cap was measured. The 3D model takes into account the soil-structure interaction and therefore, the percentage of the load transfer to the pile cap and the piles can be determined separately. The load transferred to the pile cap base and to the pile/ piles is shown in Figure 5. As it can be seen in the figure, for the single pile, the majority of the applied load is transferred to the piles up to an applied load of approximately 180 kN. At applied loads greater than 180 kN, most of the additional load is transferred to base of the pile cap. This behavior is expected, as beyond 180 kN, the pile is getting closer to failure. The base reaction estimated from the numerical model is slightly higher than the measured values, but overall, they are in good agreement. The loads transferred to the piles also match reasonably with the measured values, especially up to an applied load of 180 kN.

For the pile group, the measured and the predicted pile cap base reactions match up to an applied load of 1050 kN. For applied loads greater than 1050 kN, the measured base reaction is higher than the predicted value. The loads transferred to the piles match up to an applied load of 1050 kN as well. Generally, the factor of safety against axial compression capacity of piles is 2 or 3, and therefore it can be concluded that, majority of the applied loads will be transferred to the piles in the working stress range, and the base reaction will be mobilized only when the applied loads get closer to the ultimate capacity of the piles.

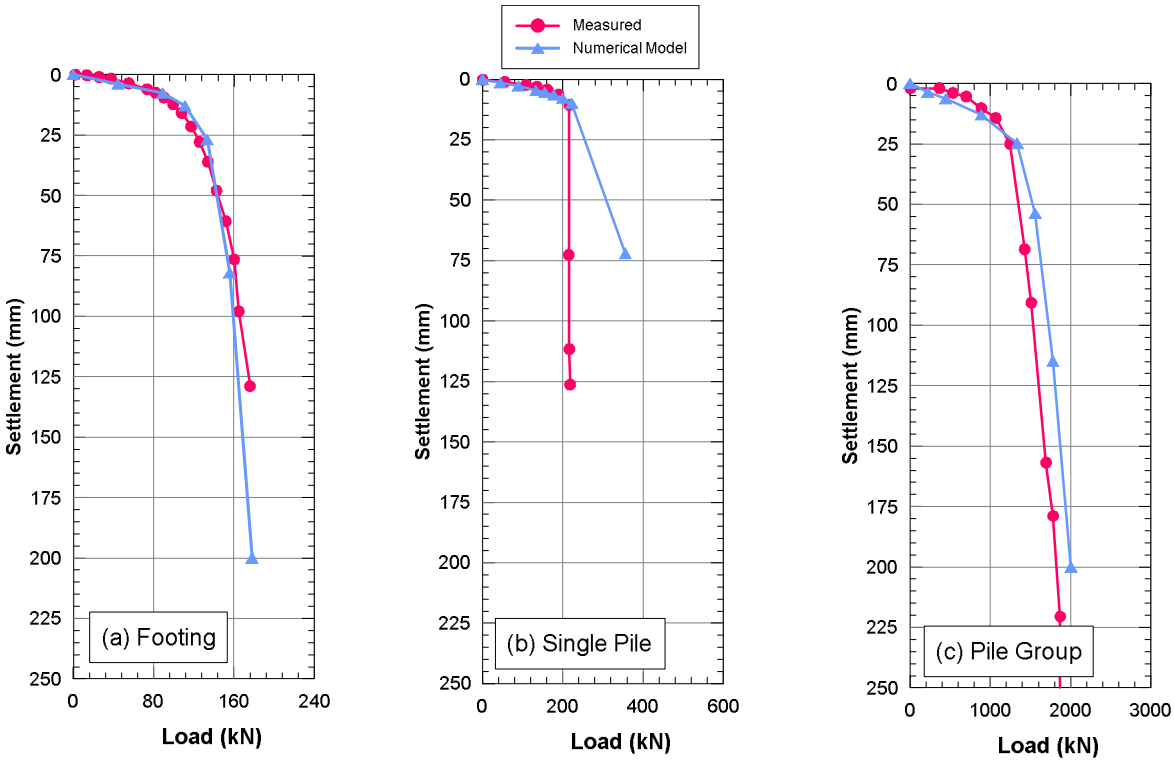


Fig. 4. Measured and Estimated Settlements of Foundation Load Tests

COMPARISON OF MODEL RESULTS WITH ANALYTICAL SOLUTIONS

In practice, the settlement of pile groups is usually estimated using analytical or empirical methods. As discussed earlier, interaction factors method and equivalent footing method are among the most widely used methods. The settlements obtained using these two methods are compared with the measured and estimated settlements values.

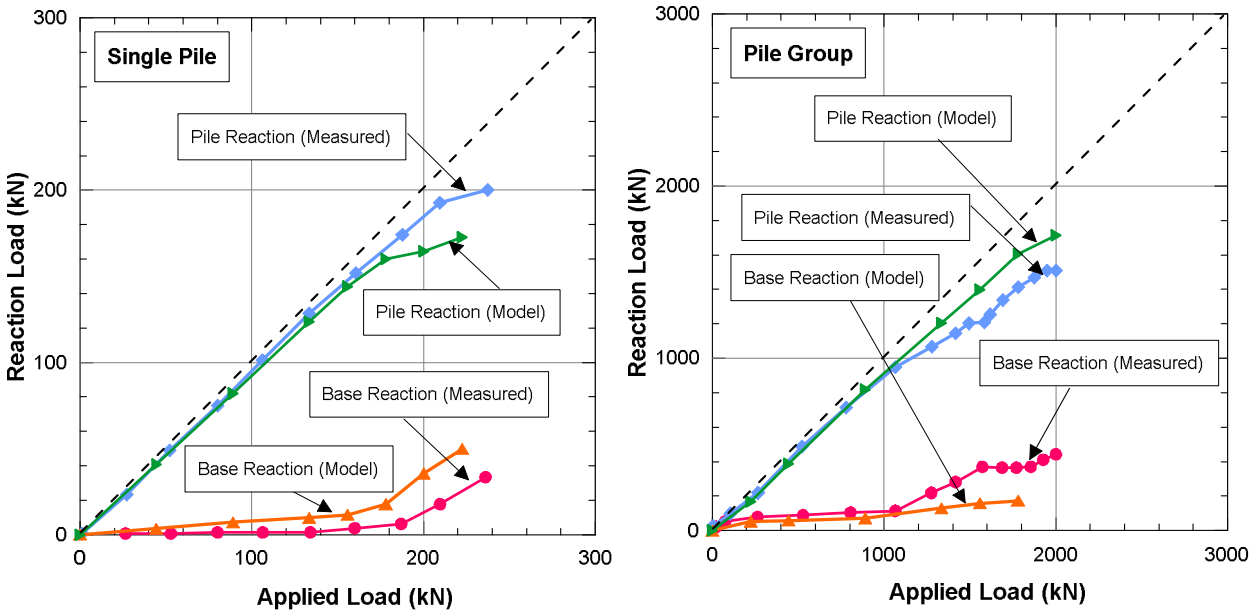


Fig. 5. Comparison of Measured and Predicted Base Reactions and Loads on Piles

The interaction method, originally proposed by Poulos (1968) states that the ratio of the additional settlement due to adjacent pile to the settlement of pile under its own load is referred as the interaction factor, α. Poulos (1968) provides interaction factors as a function of pile spacing, pile diameter and pile length in graphical form. The settlement of any pile in a pile group can be estimated using the interaction factors, as:

$$S_i = \sum_{j=1}^{n} P_{av} S_1 \alpha_{ij} \qquad [3]$$

Where P_{av} = average load on a pile within the group; S_1 = settlement of a single pile under unit load (i.e., the pile flexibility); α_{ij} = interaction factor for pile (i) due to any other pile (j) within the group, corresponding to the spacing d_{ij} between piles (i) and (j).

If the load on each pile within the group is assumed to be equal, the above equation can be written as:

$$S_i / S_1 = \sum_{j=1}^{n} \alpha_{ij} \qquad [4]$$

Using the chart suggested by Poulos (1968), the sum of interaction factors for 3 piles in the pile group is calculated as shown in Figure 6. These values are compared in Figure 6, with the sum of interaction factors derived from load-settlement curve for the pile group. To determine the sum of the interaction values from the load test, the total applied load is divided to total number of piles, assuming the load is distributed to all piles equally. The ratio of the pile group settlement to the single pile settlement under the same applied load is then equal to the sum of interaction factors. As seen in Figure 6, the sum of interaction factors for Piles 1, 2 and 3 are 4.19, 4.80 and 4.46, respectively. The derived sum of

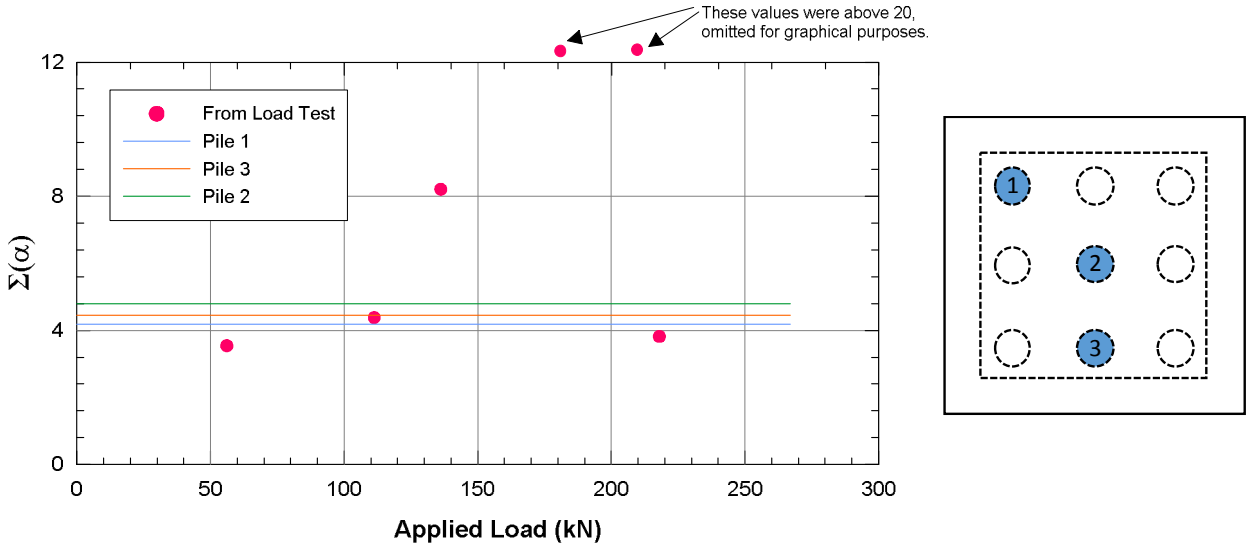


Fig. 6. Comparison of Measured and Estimated Sum of Interaction Factors

interaction factors from the load test is in agreement up to an applied load of about 105 kN, but for loads greater than that, the measured sum of interaction factors become significantly larger. This behavior is most likely due to larger and deformations beyond this load where the load settlement curve start becoming highly nonlinear.

The second method considered for estimating pile groups settlement was the equivalent footing method (AASHTO, 2014). In this method, the group settlement is estimated by creating an equivalent footing at a depth which is a function of the pile length and soil type. The stresses acting on this equivalent footing is estimated by dividing the total load to the equivalent footing area and the settlements are evaluated as for a spread footing. Once the size of the footing and the stress acting on the equivalent footing is determined, a linear elastic approach can be adopted. For a long term settlement analysis in clay, instead of the elastic solution, a consolidation settlement analysis is carried out. The settlement of a footing on a homogenous soil of infinite depth is given in AASHTO LRFD Guidelines (2014) as:

$$S_e = \frac{q_0(1-\upsilon^2)\sqrt{A}}{E\beta_z} \qquad [5]$$

Where S_e is the settlement of the footing, q_0 is applied vertical stress on the footing, A is the footing area, E is the elastic modulus of the soil and β_z is the shape factor.

Figure 7 shows the settlements estimated using the interactions factors method and equivalent footing method along with the measured settlement for the pile group. Since the equivalent footing approach utilizes an elastic settlement approach, the nonlinearity of the load-settlement curve is not captured, hence resulting in unconservative settlements predictions beyond an applied load of 150 tons. In the working stresses ranges, both methods predict the settlements reasonably well.

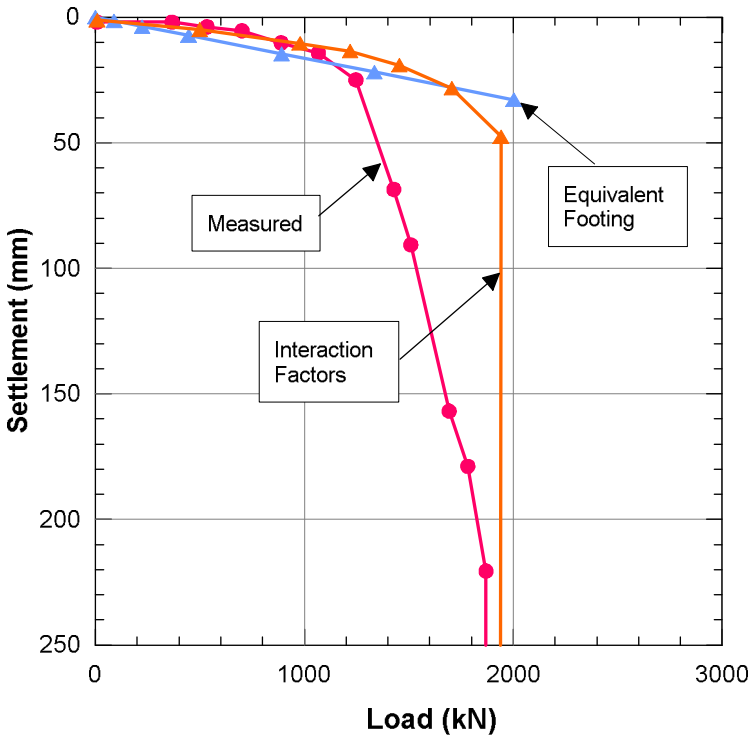


Fig. 7. Comparison of Estimated Settlements using Analytical Methods with Measured Settlements

CONCLUSIONS

A three-dimensional finite element software was used to predict the settlements of pile groups. Foundation load tests including a full-scale spread footing, a single pile and a pile group was modelled and the predicted results were compared with the measured results. Two analytical methods, (1) interaction factor and (2) equivalent footing, were also used to estimate the settlements of the pile group. Concerning the numerical model and analytical results, the following conclusions are:

(1) The three-dimensional numerical model captured the load settlement curves for all foundations reasonably, especially in the working stress range.
(2) The predicted load transfer between the piles and the pile cap in the numerical model was compared with the measured load transfer and it was found that the soil-structure interaction was captured. Moreover, it was shown that, almost all the applied load was transferred to the piles in the working stress range and the soil beneath the pile cap was mobilized only at stresses closer to pile failure.

(3) The interaction factors determined from analytical method and the back-calculated interaction factors from the load test matched relatively well up to 130 kN/pile, however the back-calculated interaction factors were significantly larger beyond of 130 kN/pile.
(4) The estimated settlements using the equivalent footing method was in fair agreement with the measured settlements up to a load of 1300 kN but, beyond this load, the estimated settlements were smaller than measured settlements.

Since this study considered only one set of load tests, the conclusions herein are limited to the soil conditions and pile type discussed. Further study is needed to confirm these conclusions for other soil conditions and pile types.

REFERENCES

American Association of State Highway and Transportation Officials, 2014. LRFD Bridge Design Specifications, 7th Edition, Washington DC, 1704 p.

Nagai, H. 1965. Committee of Research for Piled Foundations against Earthquake; Behaviors of Pile Foundations under Lateral Loading and Vibration. Bearing Capacity of Single and Group Pile Foundation.

Duncan J. M., Buchinagi A.L. 1976. An engineering Manual for Settlement Studies, Department of Civil Engineering, University of California, Berkeley, 94 p.

Federal Highway Administration, 2016. Design and Construction of Driven Pile Foundations Volume I., Washington DC, 517 p.

Federal Highway Administration, 2016. Design and Construction of Driven Pile Foundations Volume II., Washington DC, 541 p.

Koizumi Y., Ito K. 1967. Field Test with Regard to Pile Driving and Bearing Capacity of Piled Foundations. Soil and Foundations 7 (3) pp. 30-53.

PLAXIS 3D, 2017. Version 2017.01 Reference Manual 2017.

Poulos, H. G. 1968. Analysis of the Settlement of Pile Groups. Geotechnique (18) pp. 449-471

Poulos, H. G. 2006. Pile Group Settlement Estimation-Research to Practice. Proceedings of GeoShangai, Shangai, June 6-8, GSP153, pp. 1-22

VALUE ENGINEERING – DESIGN RISK AND REWARD AT MAJOR SPORT ARENA PROJECTS

Diane Fiorelli, P.E., G.E., QSD/QSP, Langan Engineering and Environmental Services, Irvine, CA, +1 (949) 255-8640, dfiorelli@langan.com
Jeremy Zorne, Geocon Consultants Inc., Rancho Cordova, CA, USA, zorne@geoconinc.com
Timothy Siegel, P.E., Dan Brown and Associates, LLC, Knoxville, TN, USA, tsiegel@dba.world
Peter Faust, Dipl.-Ing., Malcolm Drilling Company Inc., San Francisco, CA, USA, pfaust@malcolmdrilling.com

Professional sport venue construction follows a very simple rule. Once the decision has been made to move the team to a new place, construction shall begin immediately, so that not more than one or two seasons pass by stuck in the old home. Such tight construction schedules require a different approach than traditional design-bid-build contracts. Design is mostly done on the fly, the construction schedule becomes a main risk factor and an early contractor involvement is desired. As specialty contractors become more and more sophisticated, owners, their construction managers or the general contractor have realized the value of ideas and modern technology they can bring to the table for a successful and fast project completion. Local knowledge and experience in a variety of solutions play a key role in the specialty contractor's ability to provide added value to the project.

This is also true for the specialty foundation contractor, who needs to understand the complexity of such modern structures from its integrate foundation, over the delicate concrete structure to a potentially fancy movable stadium roof. Not to mention all the modern high tech equipment which shall make such a place a great customer experience.

His expertise shall enable him to propose the most suitable foundation element for the given ground condition and application. Rather to build what others have designed, his strength is to propose alternate concepts which will be faster and (hopefully) more cost effective. This paper highlights different value engineering (VE) input a specialty foundation contractor had on 3 major sports arena projects in California. Together with the entire team from owner to GC, including the Geotechnical (GEOR) and the Structural Engineer of Record (SEOR), the most efficient and best performing foundation solution can be found every time. But such an approach also requires the open mind of the owner to entertain last minute changes when the permit drawing set has already been submitted for approval.

LAS VEGAS STADIUM



The New Las Vegas Stadium will be the home of the Raiders upon the team's relocation in 2020. The Stadium is near the airport and has view of the Las Vegas Strip. The 65,000 seat facility is designed to have retractable turf field and large operable walls that open to views of the Las Vegas Strip. Subsurface conditions in Las Vegas typically call for Drilled Shafts as there are caliche layer of variable thickness found in the thick alluvial deposits. Caliche is a sedimentary rock predominantly made of cemented sand and gravel with strength of up to 15,000 psi. Foundation loads were spread out and not very high, so that only relatively short and small piles are required in such good ground conditions. Therefore, both – the GEOR and the specialty foundation contractor (independently from each other) proposed CFA piles as an alternate pile system to save cost and time. Due to limited history of CFA pile performance in

© 2018 Deep Foundations Institute

caliche in Las Vegas, the question suddenly became a constructability issue, while the design and submittal phase was progressing rapidly. Due to previous good relationship between the GC, the design team and the specialty subcontractor, a test program to check on drill-ability and load carrying capacity was initiated on a fast track schedule. The switch to CFA piles enabled the team to tighten up the short construction schedule even more, while adapting to ongoing design modifications and variable subsurface conditions. Communication and close coordination between the various team members was the key to this VE proposal.

GOLDEN 1 CENTER, SACRAMENTO



The Sacramento Entertainment and Sports Center (ESC) site presented challenging subsurface conditions including soft compressible soil, shallow groundwater, soil/groundwater contamination and high seismic-induced liquefaction potential. A deep foundation system was required to accommodate the high structural loading and the poor ground conditions. The elevation and consistency of the bearing layer was highly variable across the site. In addition, the site still contained piles from a previous foundation, which were to be avoided as much as possible by the new foundation piles. The City would not allow driven piles due to noise and vibration concerns in this highly-developed, and active downtown area. This left only a few pile type choices and in close cooperation with the owner, the GEOR and the specialist foundation contractor, drilled displacement piles were chosen as the most suitable option. In addition to flexibility in pile length (variable bearing layer elevation), the displacement piles would generate very little spoils which would significantly reduce the need for off-haul of contaminated soil. To reduce the potential conflicts between the abandoned piles and new piles, a larger pile diameter of 24in was introduced by the specialty contractor as his VE proposal. Uncertainties in required pile capacity due to insufficient penetration into the dense gravel bearing layer had to be verified in an extensive static load test program as the foundation design was prepared by the SEOR. Since there was little time for verification, the load test program occurred during site demolition and prior to mass excavation.

Only the rapid and effective collaboration and cooperation of the owner's design team with the specialty foundation contractor enabled the team to beat the aggressive project schedule using a foundation system specifically tailored to the very unique geotechnical and structural site conditions.

CHASE CENTER, SAN FRANCISCO



The Warriors new home will be situated right on the waterfront of San Francisco, just South of the Bay Bridge on the edge of Mission Bay - the newest and largest mixed development area in the city. The project includes two office and residential tower in addition the large enclosed arena and its training facilities. Ground condition are very variable with bedrock outcrops almost all the way to the surface right next to thick but weak and compressible marine clay layers. The deep foundation system was required to carry the loads all the way to bedrock in up to 140 feet depth. This included the high lateral loads due to the large roof structure as well as wind and seismic forces. Original foundation plans were proposing

CFA piles with 10-30 feet penetration into bedrock. Despite the typical soft nature of the local bedrock material (Franciscan Formation is a mélange of clay-, silt- and sandstone with occasional hard Greywacke inclusions), there is the risk of hidden hard rock layers with UCS values above 20,000 psi. Penetrating those with even the most modern CFA equipment becomes impossible. As these zone can be very localized, no additional subsurface investigation would have revealed the extend of them, thus exposing the team to possible design changes during construction. To minimize the risk, the specialty contractor proposed an VE alternate based on drilled shafts which could penetrate the bedrock as deep as it would be needed. In close cooperation with the entire team, a combination of CFA piles and Drilled Shafts was chosen to utilize the benefit of both systems. Multiple drilling units were squeezed onto a congested site with mass excavation and concrete works going on simultaneously during pile and shaft installation.

CLOSING REMARKS

The development of sports arenas (and other "large" private projects) exhibit similarities with one another and certain differences from public projects and smaller private projects. As a result, a foundation design-build/assist contractor must develop a specialized skill set to be successful with his VE proposal. Three broad specialized skills are required.

The first would be a solid understanding of local conditions (geological, environmental, historical and geographical) to establish credibility. Project location can also provide hints to the cultural background of the project team that can better facilitate communication and interaction. That is, people want to work with people they like and respect so it is wise to take care avoid social mistakes.

Competence, flexibility, and tenacity are qualities that may likely to be decisive to acceptance. Competence is the ability to satisfactorily accomplish the task. Flexibility is adjusting the design, construction technique, and/or schedule to best match the desires of the decisionmakers. Tenacity is maintaining focus as loads undergo multiple revisions and stumbling blocks arise. All three equally important to convey the benefit of your VE proposal.

The third skill is socially known as reading the room" or, if fishing, "reading the water". In design-build/assist pursuits it is crucial to develop a reasonably accurate understanding of the emotions and thoughts of the other interested parties (*e.g.,* the owner, the GC and the design team). The contractors and the owner's consultants may have developed informal or formal alliances, have reputations for good or bad, and have well-known tendencies. At the very least, getting a read on these will provide an indication that bias may exist among the project team.

As long as the contractor has establishing his technical competence and qualification, promoted the advantage of his VE proposal early enough, and conveyed a realistic schedule, he has made 3 important steps to turn his VE proposal into a successful project for all involved parties.

EVALUATING GEOTECHNICAL RESILIENCY SOLUTIONS IN NEW YORK CITY

Karen C. Armfield, AECOM, New York, NY, USA, 1-212-377-8652, karen.armfield@aecom.com
Gisele R. Passalacqua, AECOM, New York, NY, USA, 1-212-377-8648, gisele.passalacqua@aecom.com
Joanna Smith, AECOM, New York, NY, USA, 1-212-377-8646, joanna.smith@aecom.com

ABSTRACT

When selecting a solution for improving resiliency at facilities, such as airports, utility and transit sites, there are many options to protect structures and equipment against potential flooding. Each case involves an evaluation of the several key factors such as: design flood parameters, the geography and geological conditions below the site, the facility, and the layout of buildings and equipment to be protected. Upon reviewing these conditions and conducting a cost analysis of various options, the most suitable approach to protecting a facility can be determined. This paper will compare the conditions at various New York City sites, and give detail to the solutions utilized at these sites to improve resiliency and protect each facility. Flood wall types varied as did the strategies for raising critical equipment, to meet the Federal Emergency Management Agency (FEMA) and American Society of Civil Engineers (ASCE) 7 guidelines. Due to granular soil conditions, some sites may experience soil seepage below the flood wall resulting in the need for underground cut off systems. The authors will also present detail regarding the solutions used to control seepage. Various cut off systems will be discussed such as grouting and sheeting, explaining the factors that may impact the choice of systems. Another consideration in flood resiliency is the potential for a buoyancy condition on basement slabs when localized flood barriers are employed on first floor doors and windows. The authors will discuss the potential impacts of this condition on facilities and methods to mitigate this issue.

Keywords: resiliency, flooding, solution

1. INTRODUCTION

New York City is an urban coastal Metropolis with varied geology and low land areas. This includes but is not limited to sandy soils at Coney Island and the John F. Kennedy Airport. Soft marshes are found near Flushing Queens and LaGuardia Airport. Heavy rains and coastal storms caused disruption to daily life and heavily affected the economy of this vibrant City. For instance, in lower Manhattan business was interrupted in the Financial District. Power outage was widespread; commuter trains and subways were stopped and put out of service. Additionally, numerous residential homes were damaged in Coastal Neighborhoods such as the Far Rockaways and Staten Island.

1.1. Superstorm Sandy Flood Statistics

On October 29, 2012 Superstorm Sandy impacted numerous facilities in the New York City Metro area. The resulting damage cost New York City more than $42 billion in repair costs. $33 billion was allocated to repair housing and infrastructure, and $9 billion was allocated to protect transit systems[1]. One of the major issues that impacted the city in terms of its preparedness was the high flood surge. The surge surpassed the former base flood elevation and reached as high as 13.88 feet (above mean lower low water - MLLW) in Battery Park at 9:24pm that evening. Tottenville, Staten Island experienced more damage where the water was recorded at +16 (North America Vertical Datum of 1988 - NAVD88), which is equivalent to 18.7 feet above MLLW (see Fig. 1). Not only was the surge at record levels, the waves in New York Harbor were also at record level where some buoy stations recorded waves of up to 32.5 feet. The City released “A Stronger, More Resilient New York” in June 2013, a plan laid out to rebuild communities impacted by Sandy and improve the resiliency of the infrastructure and buildings in New

© 2018 Deep Foundations Institute

York City. Figures below help to illustrate the extent of the inundation relative to the projects being discussed.

Peak Storm Surge Elevations During Sandy		
Location	**Time Oct. 29, 2012**	**Water Level in Feet (NAVD88)**
1. Tottenville, Staten Island	8:38 p.m.	+16.0
2. Great Kills Harbor, Staten Island	8:52 p.m.	+13.2
3. South Beach, Staten Island	8:23 p.m.	+15.0
4. Sea Gate, Brooklyn	8:23 p.m.	+13.3
5. Gowanus Canal, Brooklyn	9:04 p.m.	+11.1
6. Broad Channel, Queens	9:18 p.m.	+10.4
7. Howard Beach, Queens	9:23 p.m.	+11.2
8. Whitestone, Queens	10:06 p.m.	+10.6
9. World's Fair Marina, Queens	10:06 p.m.	+10.4
10. Inwood, Manhattan	10:06 p.m.	+9.5
11. The Battery, Manhattan	9:24 p.m.	+11.3*

* Equivalent to 14 feet above Mean Lower Low Water (MLLW) Source: USGS, NOAA

Fig. 1. Peak storm surge elevaions during Sandy.

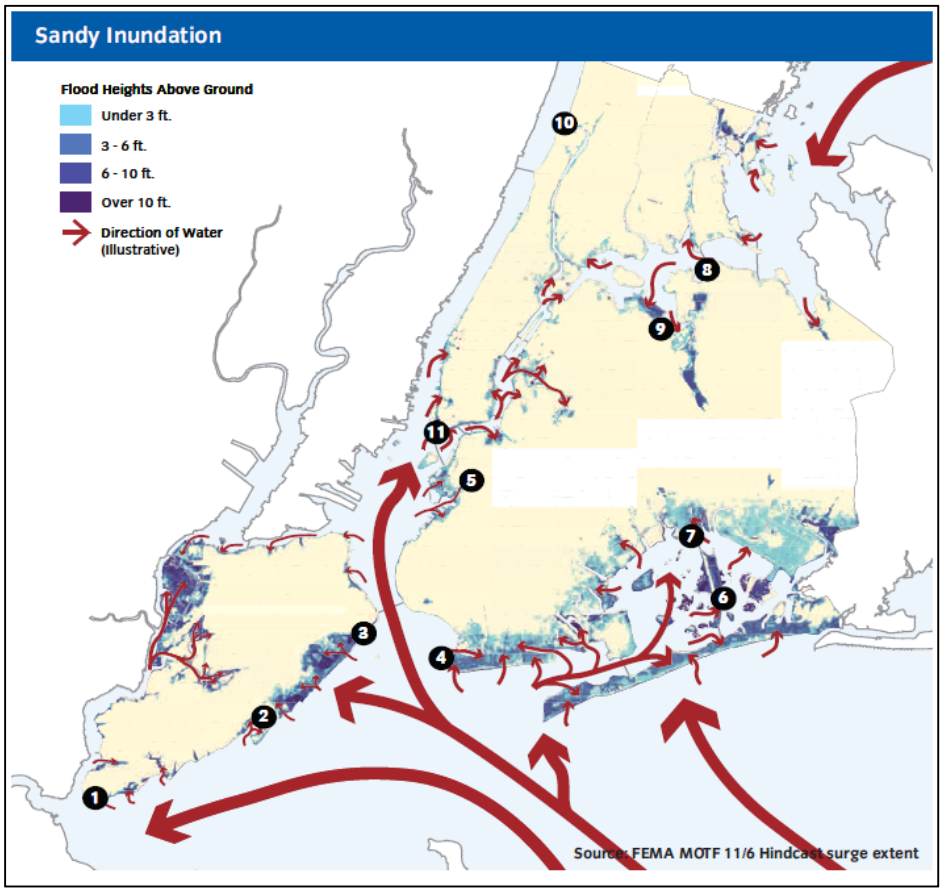


Fig. 2. Image: Plan NYC: A Stronger and More Resilient New York.

According to Plan NYC, "A Stronger and More Resilient New York", the Sandy's storm tide caused flooding that exceeded the 100-year floodplain boundaries by 53 percent citywide.

Due to lower design flood parameters prior to the storm, many of the city's electrical equipment and generators were set at a level that left them compromised. This created numerous power issues throughout the city, leaving more than 600,000 people without power. Many emergency generators were submerged and unable to work due to the extremely high surge level.

Transportation damage was also a major issue. This was especially true in southern Manhattan where numerous subway and rail tunnels flooded when the surging waters entered the subway entrances and filled the tunnels. This left the system crippled for several days while the water needed to be pumped out and electrical systems repaired. Figure 3 demonstrates past flood events relative to the level that triggers subway flooding.

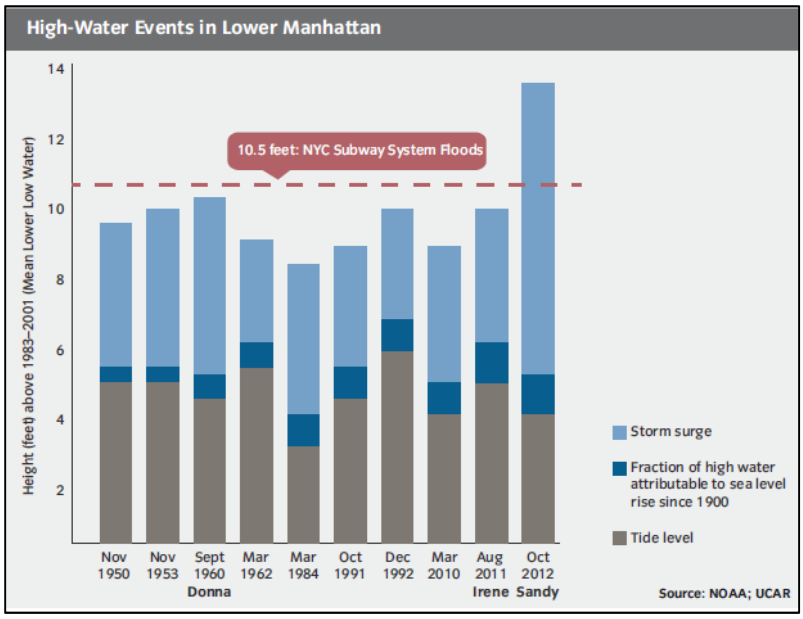


Fig. 3. Image from Plan NYC: A Stronger and More Resilient New York

2. RELEVANT FLOOD DESIGN CODES

2.1. ASCE 7 Requirements

ASCE 7 (Minimum Design Loads for Buildings and Other Structures) and ASCE 24 (Flood Resistant Design and Construction) discuss design requirements for structures to resist floatation and lateral movement, downfall, erosion and scour. Hydrostatic and hydrodynamic loads as well as loads on breakaway walls are to be designed to the largest load that would act perpendicular to the plane of the wall specified by Chapter 26 and 12 with the ASCE Manual. Breaking wave loads on vertical pilings and columns, non-vertical walls, and breaking waves from obliquely incident waves are variables taken into consideration upon design. FEMA flood design includes and discusses openings in flood walls and walls of Enclosures, Flood Damage resistant material requirements, Homeowners Guide to retro fillings, and Recommended Residential Construction for coastal Area Building on Strong and Safe foundations. These codes are relevant and necessary upon the resiliency process and varies based on the type of storm.

Impact loads are taken into account based upon objects transported by flood waters that would possibly impact a structure due to striking. Design Impact loads are analyzed based on concentrated loads which

act at the most critical location. This location is perpendicular to the structure or below the Design Foundation Elevation (DFE). Hydrostatic loads are also taken into account and are based upon the depth of water at the level of the DFE. Design depth should increase by 1ft. Hydrodynamic loads also are taken into account upon evaluating effects of moving water based on laws of fluid mechanics. Thus flood walls and structures are designed based upon the heights expected from wave loads.

2.2. FEMA Requirements

Flood Maps must be understood for clearer interpretation of risks. High flooding risk is recognized as the 100-year flood plain. The FEMA mapping breaks down risk into zones.

The proximity for water bodies with potential for waves and overtopping of barriers are determined by the updated FEMA BFE maps and Zone VE also known as the Coastal high hazard area where waves are likely to be three feet or higher. Areas within Zone AE are likely to have fewer waves above three feet. The Limit of Moderate Wave Action (LiMWA) recognizes areas where building heights should be elevated or standards for building height should be raised so to aid in the development of structures within the area. FEMA's flood maps and BFE's are used for building standards and determination of building costs.

Climate change and rising water levels in the waterways around New York City are also considered. Local data clearly indicates a trend of increasing water levels taking place each year. The National Oceanic and Atmospheric Administration (NOAA) has depicted the increase in water levels over the span of 100 years, data specific to New York, which shows the relative Sea Level trend, in Battery Park. The relative sea trend is 2.84mm (0.11in) per year +/- 0.09mm (0.0035in) per year. There is a linear relationship between the rise in water levels and the advance in years, as can be viewed in this NOAA tide station data from Battery Park Tide Station in Fig.4. The water level has consistently risen for over 100 years of data.

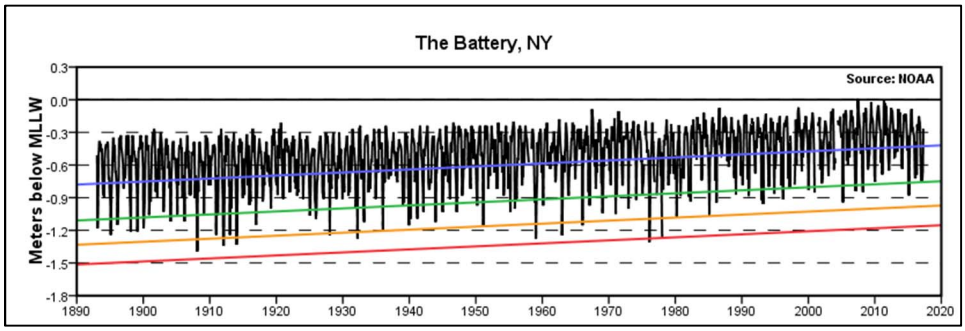


Fig. 4. Increase in water level over 100 years (reference: NOAA).

As a result of the anticipated sea level rise, FEMA has developed projected flood mapping for 2013, 2020 and 2050. The map in Fig.5, excerpted from Plan NYC, "A Stronger and More Resilient New York", shows the projected increase in impacted area over time. Projects design life should be considered in terms of future flood protection.

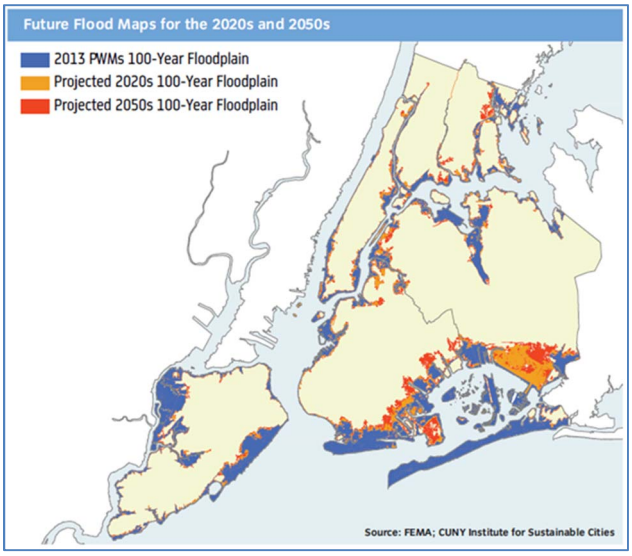


Fig. 5. Future Flood Prediction (Plan NYC: A Stronger and More Resilient New York).

3. DESIGN LOADING CONSIDERATIONS

When designing a flood protection system, the design team should review and perform a FEMA Benefit-Cost Analysis (BCA) for multiple alternatives before proceeding with a full design. BCA is the method by which the future benefits of a hazard mitigation project are determined and compared to its costs. The end result is a Benefit-Cost Ratio (BCR), which is calculated by a project's total benefits divided by its total costs. The following force parameters will be considered in design:

- Hydrostatic Pressure: This would be based on a water height corresponding to the still water flood level. The Base Flood Elevations (BFE) shown on FEMA's maps typically includes an allowance for wave activity. The still water flood elevation may be lower than the BFE, and would need to be determined based on knowledge of FEMA's modeling. In addition, the FEMA BFE does not include an allowance for sea level rise. This allowance is determined in conformance with the client's policy on sea level rise and would then be added to the base flood elevation.
- Hydrodynamic Pressures: These pressures arise from both wave and current effects, including AE zones.
- Wind Pressure: In addition to water pressures acting on the outside surface of the floodwall, the wall can also be subject to a simultaneous wind-induced suction on the inside leeward surface of the wall.
- Floating Debris: This is considered to be a transient impact load resulting from floating objects propelled by the water currents. Impact velocity would be based on the current parameters determined by the standard recommendations provided by the Authority and/or ASCE guidance. According to ASCE standards, the debris might consist of floating dislodged timbers. Considering the location and experience during Super Storm Sandy, the possibility that floating debris might also consist of heavier objects, such as vehicles propelled by the waters, would also be considered; these would be figured at a lower impact velocity than smaller debris objects.

4. RESILIENCY SOLUTIONS

4.1. Above Ground Flood Protection

There are many potential solutions to consider when determining how to achieve flood resiliency on a facility. Below are some typical solutions and issues to consider when employing each.

a) Raising Ground Level or Raising Structure
The most obvious way to prevent flooding is to raise the occupied space of the facility above the design flood elevation. For a new facility you can select the grade at a proper elevation, but many existing sites can also be raised. In some cases, the entire structure is raised in others only critical components. When raising an existing structure, the design team needs to verify the structural suitability of the facility.

b) Flood Proofing Structures or Other Localized Flood Devices
One of the most common and inexpensive ways to protect a facility is to add a commercial stop log system to the doors and windows. This is especially effective when the flood level is only a few feet above grade and the existing walls are strong enough to carry the water pressure. The pressure also needs to be evaluated on any basement that may be present.

One thing to consider when taking this approach is whether the systems will be manual or automated. A manual system often requires the system components to be stored on site and deployed by staff in advance of the storm.

c) Site Perimeter Protection
Often when it is not practical to raise, or to locally protect a facility with flood proofing structures, the area can be protected with a perimeter wall or berm. The wall can be constructed similar to a typical seawall from concrete or steel sheeting. The wall will be designed for the loading of the water pressure from the design flood water level as well as the impact load of floating debris as per ASCE guidelines. The design should also consider an allowance for overtopping and wave action depending on the proximity to open water. If selecting a berm, the material choice needs to be designed as a typical levee being sure to select materials with minimal seepage, an impermeable core and sufficient protection on the surface to protect against wave action and scour during flood events.

In some cases existing perimeter walls can be extended with temporary flood proofing to reduce the costs of reconstruction of existing perimeter walls. If this solution is chosen, the design team will have to determine if the existing wall can carry the flood design loads. Also, the facility will need to consider the practicality of having trained staff available to extend the walls in advance of an incoming storm and also creating a storage location on site where the flood proofing can be stored and easily deployed in a short time frame.

4.2. Seepage Prevention: Pumping or Physical Barrier

Another point to be considered during the wall design is whether or not a seepage cut off is required under the wall. The design team will look at the soil conditions and determine the amount of seepage that can be anticipated under the wall during a flood event. This can be performed with commercial seepage software such as SEEP/W from GeoStudio. Once the water flow is estimated, the design team can determine if the client's preference is to pump the water from the site or to create an impermeable barrier under the wall. One consideration with pumping systems is that, although the pumps will not be utilized in a regular basis, they still need regular maintenance to keep them functional during storm events.

Various strategies can be employed to control seepage infiltration below flood barriers. Some options are discussed below.

a) Pump system – no barrier

- Description of Solution: in some cases the amount of seepage expected is small and the determination is to install a pumping system rather than a seepage barrier.
- Benefits: the benefit of this solution is the fact that the expense of the barrier is eliminated.
- Issues: the cost of the pump system and the cost of its regular maintenance need to be included. The pump size will be determined by the volume of inflow calculated by seepage analysis.

b) Sheeting barrier

- Description of Solution: typical steel or plastic sheeting can be driven as a barrier to seepage flow.
- Benefits: can be driven to an impermeable layer or to a layer with low permeability to prevent or reduce inflow via seepage. Even if impermeable layer is not present, it will lengthen the path of water flow and slow the seepage especially in a short duration storm event.
- Issues: obstructions in the soil strata such as boulders or debris may hinder driving. Noise and vibration may occur during driving of sheeting. Often utilities cross a site and can create unprotected zones if sheet is not driven in these areas. This can be remedied by localized grouting if seepage is anticipated to be too large through the unprotected area. It is important to confirm if rainwater from normal rain events can still escape.

c) Jet Grout Barrier

- Description of Solution: a below grade impermeable barrier can be created by installation of a jet grout curtain under the location of the perimeter wall.
- Benefits: jet grout can be installed in a variety of different soil conditions. It can be installed around utilities with minimal impact.
- Issues: test section may be required. It needs to consider site specific soil conditions to determine most suitable jet grout pressure to create adequate overlap between columns for effective cut off. It cannot be installed up to ground surface. Embedment of surface wall needs to be deep enough to prevent heaving at the surface near existing structures. It can create spoils at the surface during installation. It needs room for grout production and equipment in the area of installation.

d) Chemical or Permeation Grout Barrier

- Description of Solution: injection of chemical or permeation grout to reduce the permeability of the soil strata.
- Benefits: smaller size equipment and less noise than sheeting or jet grouting installation. Less spoil created during chemical grout operation than a jet grouting operation. It can be installed around existing utilities without damaging them.
- Issues: successful use of chemical grout depends on the soil conditions and the suitability for adequate penetration of grout to create a proper seal. Test sections or laboratory testing may be needed to confirm adequate reduction in permeability.

4.3. Let Facility Flood

Sometimes non-critical structures can be allowed to flood and this is considered as “controlled flooding”. This may be suitable for facilities that are easily dried out and repaired after a flood. A good example of this is rail tracks. However, this method is also sometimes used on buildings, such as basements and first floors, if it is possible to protect key electrical elements such as mechanical equipment and elevator pits. Note that all finishes need to be made from materials that are non-absorbent and easily drained and cleaned after an extreme event. One situation where this might be employed is a basement where the walls and floors are not structurally stable under flood conditions and the basement needs to be flooded to balance the water pressure to prevent failure.

4.4. Facilities with Basement Space

Protecting facilities with basement space adds a new level of complexity to the flood protection. Some key items to consider are basement buoyancy, wall pressures and crack/penetration leaks. If a building with a basement cannot be protected with a perimeter wall and needs to be protected locally with flood proofing, or other similar commercial system, the basement may need reinforcement to handle the above mentioned issues.

Buoyancy of the basement slab under a flood condition can be significantly higher than under the normal design condition. This may lead to the need to add tie down anchors, slab stiffening or thickening to balance the added design force of the flood. Another consideration is the increased pressure on basement walls. Similarly, this may require reinforcement to carry the added loading. Lastly, cracks and penetration in the basement floors or walls may leak during flood events. These should be proactively water proofed as part of any flood protection scheme to prevent excessive water penetration and can be protected by injecting chemical or cementitious grout through the floors or walls as needed.

When the costs of such repairs are excessive, the facility may consider letting the basement flood fully, or partially, and be pumped after the storm event as mentioned above. This will require pumping systems and extensive cleaning after flood events and would restrict the practical use of the basement space. It would typically involve the relocation of mechanical equipment commonly found in basements and may render elevators temporarily inoperable if not locally protected.

5. EXAMPLE RESILIENCY PROJECTS IN NEW YORK CITY

5.1. Metro North Hudson Line – Elevating Structures – Spread Footing

The Metro North Hudson Line is a design build project involving reconstruction of 39 electrical transformer pads along 16 miles of track to raise equipment above required FEMA DFE. At this site the track and associated equipment lies directly adjacent to the Hudson River (see Figs. 6 and 7). Due to the length of the site, adding a wall is not a practical solution. Also since the tracks are continually in operation it is not practical to raise the grade of the tracks. Therefore it was determined that the best course of action was to let the tracks flood during a storm event, but to raise all of the transformer pads and other essential equipment onto platforms above the DFE.

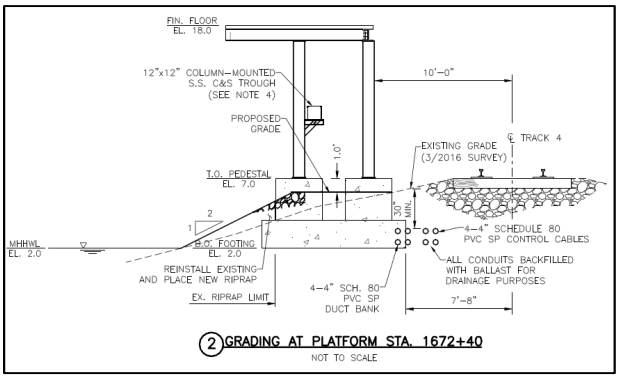


Fig. 6. Typical frame utilizing mass spread footing to carry equipment above flood level.



Fig. 7. View of rail tracks adjacent to the Hudson River.

5.2. ConEdison 28th Street Facility – Elevating Structures – Pile Foundation

Project involves improvements to the electrical substation that supplies power to wastewater treatment system. Due to Superstorm Sandy, the wastewater treatment plant and associated power system for treating pump water were damaged. The system was partially submerged so pumps, treatment components, and piping were damaged beyond repair. The scope of work includes a new design system including raise it 3 feet above FEMA required flood design criteria. This new system is built to be adaptable and to be put into a container, thus allowing for transport as necessary. The design criteria is based on water treatment equipment that is able to treat the required chemical and physical contaminants.

Subsurface investigation in the site indicated fill overlying soft, compressible, fine grained soils. The surface area is covered by nearly a 6-inch-thick concrete pavement. Groundwater was encountered at a depth of 6 feet below grade. Fill consisted of brown fine to coarse sand with gravel, brick, sand, glass, and cinders. Fill blow counts averaged 6 blows per foot (bpf). Native soils were encountered below fill and overlaid soft clay silts at approximately 30 feet below ground surface. Organic clays were encountered to a depth of around 95 feet and had blow counts averaging 0 to 2 bpf. The clays were identified as soft clays, specifically class 6, and the upper sands were classified as uncontrolled fill, in accordance with the NYC Building Code Classification system. Also CPT testing and borings were evaluated to determine impacts of the poor seismic site class of the site on the structural design.

Upon encountering such soft soil and the layer of uncontrolled fill, the recommendation for the foundation was to use piles to support the frame system utilized to elevate the equipment. The piles were evaluated for lateral and axial capacity and were designed to carry a load of approximately 43 kips of axial load. The proposed foundation to support the wall was driven, concrete filled and steel pipe piles designed based on NYC Building Code. Minimum tip elevation of the pile was -100 feet due to the thickness of the unsuitable soils. Figure 8 shows the type of frame system used to protect this equipment.

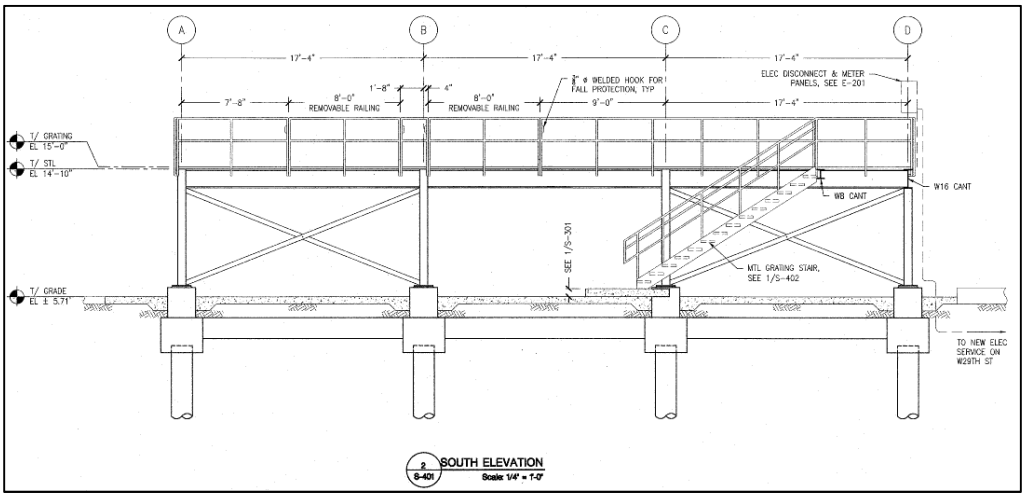


Fig. 8. Typical frame used.

5.3. LaGuardia Airport Pump House #6 and Electrical Substation– Elevating Structures – Pile Foundation

Several emergency generators and other equipment are determined too low to operate under extreme flood conditions. One example is the pump station and transformer at LaGuardia airport. Similarly numerous pump stations and generators around New York City require modification to meet the new design flood elevations. Examination of the FRIM No. 3604970094G map for the west end of the Airport

shows these facilities located within the AE Zone with base flood elevation (BFE) of 14 feet above NAVD datum. In addition, the location is specified as Limit of Moderate Wave Action (LiMWA), indicating wave heights are between 1.5 and 3 feet. Unlike the two examples mentioned above, this site was required to design not only for the flood inundation level but for resistance to active waves due to the open water adjacent the site. The design of any flood protection structure needs to take the resistance of waves into consideration.

In order to determine the most cost effective flood protection and foundation system for these facilities as well as adjacent buildings, various alternative schemes were evaluated with their associated risk levels. Considerations of bearing capacity, settlement and potential uplift were considered in the foundation designs. The following possibilities were considered in the design process for the subject flood mitigation:

a) Use of a localized wave attenuation structure confined within the vicinity of the subject facilities and their surroundings in order to limit the wave action and/or its propagation onto critical infrastructure. This entails the design of local flood gates for access to the buildings.
b) Implementation of flood-proofing measures for both buildings.
c) Elevation of vital equipment beyond the BFE with additional consideration for rise in sea level.
d) Use of a wave attenuation structure along the shoreline, which also can be part of a regional alternative to flood mitigation for the entire LGA facility.



Fig. 9. Aerial view of pump house and transformer locations.

The soil at this location is sand based fill at the surface, underlain by a thick layer of soft compressible bay sediment. LaGuardia's soil condition is known to be poor quality due to the more than 80 foot thick layer of compressible soil under the majority of the site. This results in the need for all structures at the site to be carried on piles.

In this case, the most practical solution for this small equipment was to build a frame to hold it at a higher elevation. When designing an elevated equipment frame for this site, the frame needs to be designed for an impact load of floating debris at the flood level. This often results in significant overturning moment on the frame. In this case the frame was design to be pile supported to carry the frame load and the overturning loads of impact. Unlike the Metro North site where the design team was able to carry the overturning moments through a large gravity based spread footing, the soft sediments here would have caused too much settlement under a mass footing.

After the potential options and the cost benefit of various solutions were evaluated, it was determined that the best course of action was to raise these facilities onto a steel frame system. The frame system was designed to be supported on steel piles with enough capacity to carry the axial and lateral loads created by the wave action and flooding debris, as can be viewed in Fig. 10.

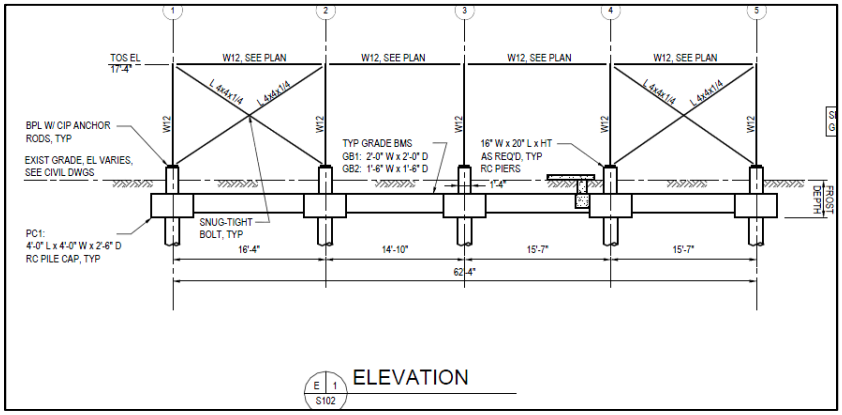


Fig. 10. Frame system designed.

5.4. Hammels Wye Electrical Substation – Flood Wall with Seepage Protection – Sheeting, Jet Grouting and Minipiles

Rail and Transit facilities are difficult to protect and often perimeter walls cannot protect them. In this case, the tracks were protected from scour during wave action by reinforcing the riprap levees surrounding the tracks and by adding debris fence to prevent debris from fouling the track (see Fig. 11 for more site details). But the tracks themselves were permitted to flood during storm events. A cross section of the track protection system is shown in Fig. 12. At this site, the tracks spilt around a critical electrical substation that powers Transit facilities. Unlike the track system, it was determined to protect this facility with a perimeter wall. The soil at the site was composed of loose sands that created the opportunity for excessive seepage under the proposed flood walls. The design team determined that sheet pile walls could be installed under the flood walls. However, there were several utilities crossing in these areas so a jet grout curtain was used to protect the perimeter from seepage. By using a combination of wash out protection and dry protection the design team was able to protect the critical elements of this facility.



Fig. 11. Aerial view of Hammels Wye transit facility.

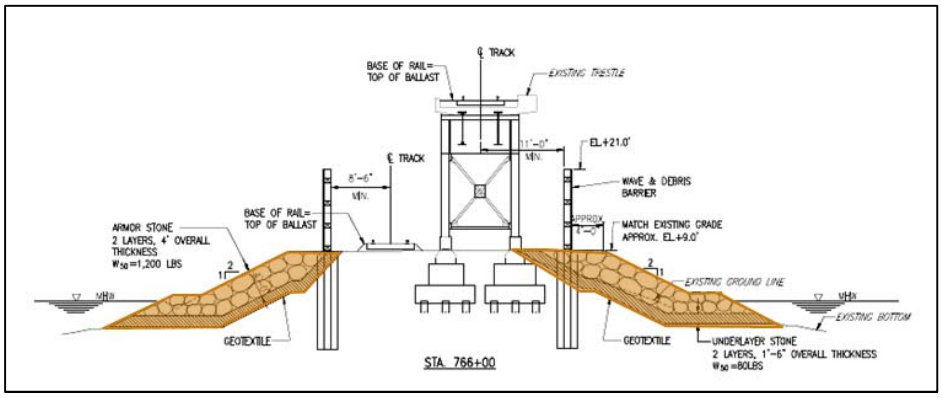


Fig. 12. Track scour protection.

5.5. Build it Back –Raising Residential Home in Far Rockaway

Resiliency efforts are different for residential buildings compared to infrastructures or substation located in the same neighborhood. For instance, Far Rockaway (in Queens) is a neighborhood with both residential houses and transit facilities/substations that were built next to the water. The soil condition in this area consists of fill layer with miscellaneous sand and silt followed by 10 foot of soft organic silty clay with roots and occasionally peat. This soft layer is underlain by deposits of medium to fine sand that is very permeable. As expected, ground water table is tidal and very close to the ground surface.

After Hurricane Sandy, some of these residential (one to two-story) houses experienced lots of damage. It was necessary to lift and raise the affected houses to stay above the DFE. Cribbing was used to lift the houses (see Figs. 13 and 14). Geotechnical issues encountered include providing stable subgrade under the cribbing and also utilize controlled dewatering scheme that prevents settlement of surrounded houses. In addition, helical piles were used as the foundation for the raised houses to provide higher resiliency. In this neighborhood, scour is one factor that has to be checked to ensure long-term stability of the deep foundations. Since the helical piles do not provide a robust lateral resistance to applied loads, steel casing was placed on top to provide more lateral resistance.

.



Fig. 13. Photo of residence being raised.

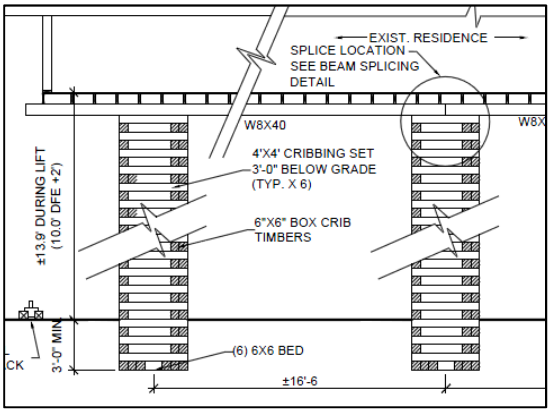


Fig. 14. Sketch of proposed cribbing support.

5.5. Bay Park Sewage Treatment Plant

This project included the construction improvements to the effluent pumping facility. The protection system of this facility involved protecting doors and windows locally with flood proofing. The building being protected was founded on a friction pile system bearing in natural sand soil. As a result, the design team needed to evaluate the existing piles and connections for tension capacity for buoyancy under flood conditions and it was determined the building could adequately resist the flood pressures.

6. SUMMARY AND CONCLUSIONS

Decisions to improve the flood resiliency of a facility involve many considerations. In an ideal world, site would be one hundred percent protected from future floods, however constraints such as cost, space, existing conditions often require the design team to determine which repairs are the most critical and have the best cost benefit ratio when determining proposed solutions.

7. REFERENCES

1. Hurricane Sandy's Rising Costs, New York Times, Nov 27, 2012
2. Hurricane Sandy Fast Facts, CNN. Com 7/13/2013
3. Plan NYC: A Stronger and More Resilient New York, New York City Office of Emergency Management, June 11, 2013

AXIAL CYCLIC DEGRADATION OF MARINE PILES: A STRAIN-BASED FATIGUE LIMIT

Aaron S. Bradshaw, PhD., P.E., University of Rhode Island, Kingston, RI, USA, abrads@uri.edu
Ryan M. Coulson, E.I.T., GZA GeoEnvironmental Inc., Norwood, MA, USA, ryan.coulson@gza.com

ABSTRACT

The offshore wind industry in the United States is slowly emerging with the recent construction of the first offshore wind farm located off the coast of Rhode Island. The turbines at the Block Island wind farm are supported by piled jacket structures, which historically have been used for much heavier oil and gas platforms. Offshore wind turbines have unique design requirements and the axial behavior of the supporting piles under cyclic loading is important to design. Cyclic degradation along the pile shaft can affect the capacity, deformation, and stiffness performance of the foundation and of the structure as a whole. This paper proposes a strain-based approach to estimate the fatigue (or endurance) limit of a cyclically loaded pile that may be applicable to long-term service loading. The method is applied to an existing load test dataset and the analysis results appear consistent with the observed pile response.

Keywords: cyclic degradation, driven pile, threshold shear strain, jacket structure, offshore wind

INTRODUCTION

The demand for renewable energy has been increasing in recent decades and wind power has seen a dramatic increase in popularity. In Europe, as of 2017 there were 4,149 grid-connected offshore wind turbines across 11 countries (windeurope.org), many of which are supported on monopile foundations. It wasn't until recently (2016) that the first offshore wind farm was constructed in the United States off the coast of Block Island, Rhode Island. The project included 5 piled jacket structures founded in terminal moraine deposits.

Future offshore wind development along the U.S. eastern seaboard could possibly utilize jacket structures in granular foundation soils. Loads from wave, wind, and turbine rotation induce cyclic loads on the foundation that have on the order of 10^8 loading cycles over the service life on the structure (Schneider and Senders 2010). Turbines located along the U.S. east coast have the added risk of hurricanes. As shown in Figure 1a, the lateral loads on a jacket structure are transferred primarily as axial compressive and possibly tensile loads on the supporting piles depending on the weight of the structure. The friction along the shaft of the pile can be prone to cyclic degradation, leading to reduced pile capacity and stiffness, and increased deformations.

An offshore wind turbine foundation must be designed for a variety of limit states including ultimate, serviceability, and fatigue limit states. For a jacket structure this would include an analysis of the ultimate axial pile capacity, axial stiffness, and axial deformations, all of which can be affected by cyclic loading both under extreme (i.e. storm) conditions as well as long-term service conditions. Axial pile stiffness is needed, for example, to estimate the natural frequencies of the structure as a whole and to assess dynamic and fatigue loads. The structure must be designed such that its natural frequency remains outside the loading frequencies of the waves and turbine blade passing frequencies to avoid resonance. Therefore, prediction of the axial response of the piles is important to the design of these structures.

© 2018 Deep Foundations Institute

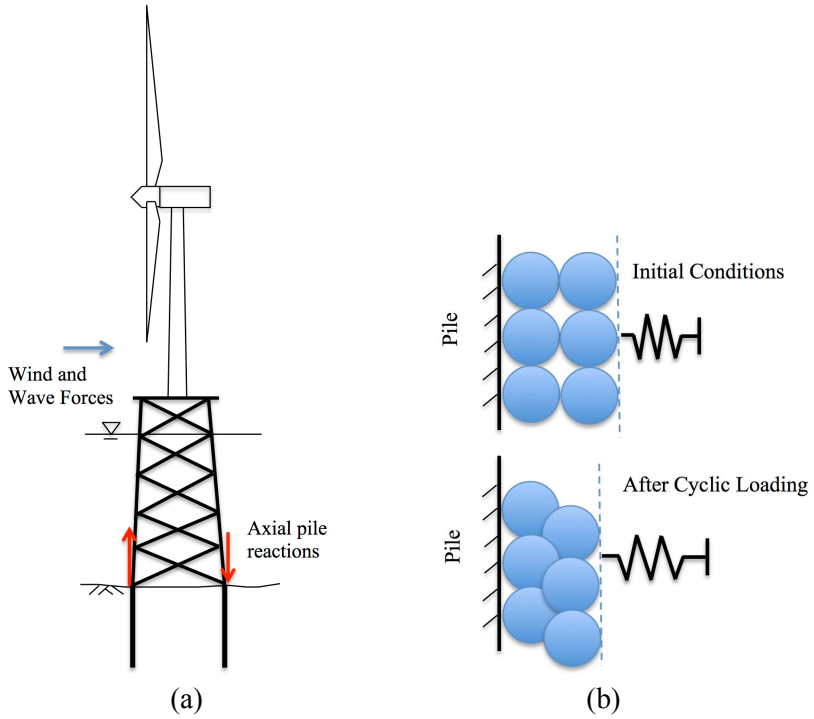


Figure 1- (a) Forces and axial pile reactions for a piled jacket structure, and (b) conceptual cyclic degradation mechanism near the soil-pile interface.

The mechanism of axial cyclic degradation of shaft resistance in sands is fairly well understood (e.g. DeJong et al. 2006, Tsuha et al. 2012). Conceptually, the mechanism is illustrated in Figure 1b. When a pile is axially loaded a shear band forms adjacent to the pile interface that has a thickness that is on the order of 5 to 10 times the D_{50} of the soil depending on the interface roughness. The particle size in the shear band will be affected if grain crushing occurs during pile driving. Cyclic axial loading, particularly with stress reversals, will induce cyclic shear stresses that can densify the soil within the shear band. Densification of the shear band, which is laterally constrained under constant normal stiffness conditions (represented by the spring in Figure 1b), results in a reduction in the lateral stress on the pile. If subsequent cyclic or static loads are then applied to the pile, the soil will likely dilate within the shear band, thereby restoring some of the lateral stress and friction on the pile (Lehane and White 2005). The decrease in the normal stress during cyclic loading is inversely proportional to the thickness of the shear band and the lateral stiffness of the soil confining the shear band. It is also recognized that the lateral stress will increase over time through creep mechanisms.

The current state-of-practice for the design of cyclically loaded offshore piles is based on the development of a cyclic stability diagram originally proposed by Poulos (1988). An example stability diagram is shown in Figure 3 which was developed using full scale load tests performed by Jardine and Standing (2000). The axes of the diagram include the mean cyclic load (Q_{mean}) normalized by the ultimate static capacity ($Q_{max\ static}$) and the single-amplitude cyclic load (Q_{cyc}) normalized by $Q_{max\ static}$. Based on the number of cycles to "failure" the diagram is broken up into three zones including "stable", "metastable", and "unstable". A stable pile may accumulate displacements slowly over hundreds of cycles; a metastable pile accumulates displacements moderately over tens to hundreds of cycles and failure developed within a range of 10^2 to 10^3 cycles; and an unstable pile develops rapid accumulation of displacements in under

100 cycles, resulting in pullout failure (Jardine and Standing 2012). Stability diagrams are unique to the pile and soil combination. They can be developed from full-scale load tests as was done in Figure 2. However, since a comprehensive load testing program may be impractical, stability diagrams may also be developed using a combination of numerical modeling and lab testing which accounts for degradation on a cycle-by-cycle basis (e.g., Randolph 2003). The time-dependent increase in the pile capacity/stiffness is also an important consideration.

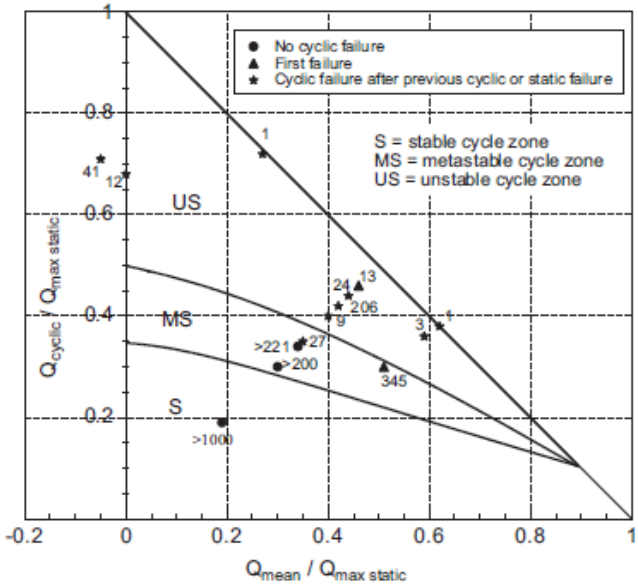


Figure 2 – Stability diagram from Jardine and Standing (2012) indicating the regions of stable (S), metastable (MS), and unstable (US) piles delineated by the number of cycles to failure.

This paper explores the concept of a fatigue limit (or endurance limit) that defines a cyclic load level below of which there is no cyclic degradation for an infinite number of loading cycles. This might be useful, for example, in the evaluation of long-term service loading conditions that would include very high numbers of cycles at relatively low amplitude loading. The mechanism that initiates the cyclic densification of the shear band as described above is similar to the mechanism that initiates residual pore pressure development during soil liquefaction. Dobry et al. (1982) discovered that there was a threshold shear strain, below which point a soil would not generate excess pore water pressures during undrained cyclic loading. This was the same threshold shear strain under which no permanent volumetric changes would occur during drained cyclic loading. This threshold shear strain concept was subsequently used as the basis for developing the strain-based method for evaluating liquefaction potential.

This paper uses the threshold shear strain concept as a basis for estimating an endurance limit for pile shaft resistance. First, a method is proposed to calculate the shear strain at the pile-soil interface and then the method is applied to an existing full-scale pile load test dataset published in Jardine and Standing (2000) and Rimoy et. al., (2013). This is the only full-scale load test data set known to exist on axially loaded piles in sand.

INTERFACE SHEAR STRAIN

In concept, if the strains within the shear band (i.e. at the interface) remain below the threshold shear strain, the pile should not degrade under cyclic loading. Therefore, the maximum cyclic shear strain in the

soil at the interface can be estimated from a static pile deformation analysis. There are a variety of numerical analyses that could be used to estimate shear strains in the soil. In this study, the shear strains in the soil were estimated by performing a 't-z' analysis, which is commonly used in engineering practice where the pile and surrounding soil are modeled as a system of springs.

The focus is on the small strain response under cyclic loading. Therefore, a novel approach is proposed below to develop site-specific "cyclic" t-z curves using an equivalent linear constitutive model commonly used in earthquake site response analyses. The approach involves estimating the small strain shear modulus (G_{max}) from the measured shear wave velocity and then reducing the modulus accordingly to account for non-linear soil behavior. The approach for developing the t-z curves in the study is based off that proposed by Randolph and Wroth (1978) for a linear elastic soil. The modified approach described below accounts for the non-linear behavior of the soil that exists even at low levels of strain.

At any specified depth, the shear stress in the soil can be calculated at any radial distance from the pile using the following equation:

$$\tau = \tau_0 \frac{r_0}{r} \quad [1]$$

τ=shear stress in the soil at a radius, r from the pile centerline, τ_o=shear stress at the pile-soil interface, and r_o=pile radius. Shear strain is related to shear stress by the following:

$$\gamma = \frac{\tau}{G} \quad [2]$$

where, γ=shear strain, τ=shear stress, and G=shear modulus. The nonlinear behavior of the soil is modeled through the following expression:

$$G = G_{max}\left(\frac{G}{G_{max}}\right) \quad [3]$$

where G=secant shear modulus, G_{max}=small strain shear modulus, and (G/G_{max})=normalized shear modulus that is a function of the level of shear strain. Combining the equations above results in an equation for the shear strain in the soil as a function of radial distance:

$$\gamma = \tau_0 \frac{r_0}{r} \frac{1}{G_{max}\left(\frac{G}{G_{max}}\right)} \quad [4]$$

The vertical displacement at the pile interface is then calculated for a specified shear stress by integrating Equation 4 radially from the pile radius to the magical radius (r_m) as defined in Randolph and Wroth (1978) where the shear stresses/strains become negligible. The integration is done numerically by breaking the soil into radial slices. Since the normalized shear modulus in Equation 4 depends on strain, which is also the dependent variable, the equation must be solved iteratively for each slice. The modulus reduction equations developed by Zhang (2005) were used in this study. Zhang experimented extensively with soils of different ages and plasticity index under a range of confining pressures in order to develop a database of G/G_{max} relations. The equations are given below:

$$\frac{G}{G_{max}} = \frac{1}{\left[1+\left(\frac{\gamma}{\gamma_r}\right)^{\alpha}\right]} \quad [5]$$

$$\gamma_r = \gamma_{r1}\left(\frac{\sigma_m'}{p_a}\right)^k \quad [6]$$

where σ_m'=initial mean effecting confining pressure, p_a=reference pressure (~100 kPa), γ=shear strain, γ_r =reference strain when G/G_{max}=0.5, γ_{r1}=reference strain at a mean effective confining pressure of p_a, α=age correction factor, and k = stress correction factor. Recommended values for γ_{r1}, α, and k are given in Zhang (2005) based on age and plasticity index.

The process described above is then repeated for different shear stresses to define the complete t-z curve. A maximum value of the interface shear stress should also be specified for the t-z curve using a static capacity model such as the 'Beta' method. The entire process is repeated at other depths and a family of t-z curves is developed along the length of the pile. A pile deformation analysis is then performed using any one of a number of available computer programs by inputting the developed t-z curves. To calculate the interface shear strains, a specified axial load is applied to the pile in the t-z model and the load distribution down the pile is calculated. The interface shear stress distribution is then calculated from the pile load distribution and the interface strain distribution is calculated in an iterative fashion using Equation 4 with $r=r_0$.

THRESHOLD SHEAR STRAIN

Laboratory data presented by Dobry et al. (1982) suggests that the threshold shear strain is independent of sand type, sample preparation method, and relative density. Theoretical work by Dobry et al. (1982) and Santamarina and Aloufi (1999) indicates that the threshold shear strain increases with effective confining pressure. A variety of laboratory studies have been conducted to estimate the threshold shear strain for different soil types. No studies were identified that have measured threshold shear strains under constant normal stiffness conditions, however, at strain levels below γ_t, the difference between constant normal stress and constant normal stiffness conditions are presumed to be negligible. Undrained cyclic triaxial tests performed by Dobry et. al. (1982) suggest that γ_t for saturated clean sand ranges from 0.012% to 0.028%. Others have performed tests on resonant column and drained cyclic simple shear tests on saturated clean sand and found similar values. An accepted range appears to be between 0.01% and 0.03% (Vucetic, 1994).

ANALYSIS OF LOAD TEST DATA

The approach described above was applied to existing static and cyclic load test data on 457 mm diameter pipe piles from a site in Dunkirk, France (Jardine and Standing 2000, Rimoy et. al., 2013). This included both static tests both tension and compression, as well as cyclic load tests in both one-way (tension only) and two-way (tension and compression). The piles were not instrumented down the length of the pile. The upper 2.5 m of pile section consisted of 20-mm thick ST 52 steel and the remaining portion consisted of 13.5-mm thick ST 44 steel. Pile lengths ranged from 18.85 m to 19.37 m. This paper follows the same nomenclature used by Jardine and Standing (2000) for pile labels and load test designations. Reaction piles are labelled R1 to R6. Load tests are labeled in the following code consistent with Rimoy et. at. (2013): M.YY.ZZN where M = testing campaign phase (out of 3), YY = pile name (R1-R6), ZZ = test

type (T, static tension; CY, axial cyclic), and N = test number in sequence from installation. See Rimoy et. al. (2013) and Jardine and Standing (2000) for a more detailed description of the load test program.

Seismic Cone Penetration Testing (CPT) was also performed as part of the Dunkirk study. Representative data were compiled from Jardine and Standing (2012) and Chow (1999) and plotted in Figure 4. As shown in the figure the test site consists mainly of layers of dense sand deposits separated by thinner layers of loose sand. A layer of organic material was encountered at a depth of 7.5m to 8.5m and the water table was 4.5 m below the ground surface.

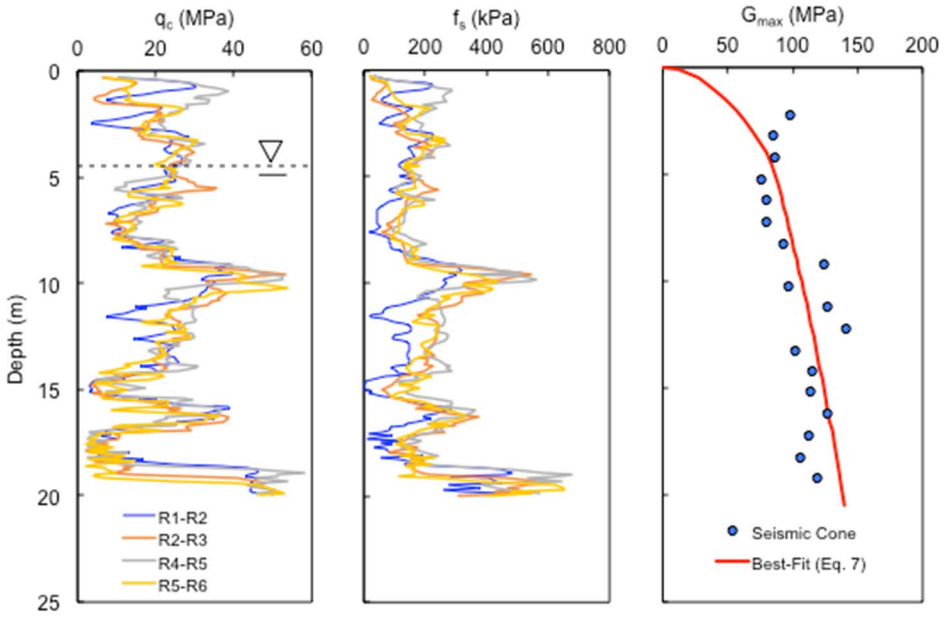


Figure 3 – Soil profile at the Dunkirk site. The data were compiled from Jardine and Standing (2000) and Chow (1996).

A single t-z model was developed in RSPile to represent all test piles, since the soil stratigraphy and pile length varied only slightly for each. The stratigraphy was broken up into 19 1-m thick layers and a t-z curve was constructed for each layer using the approach described above. According to Jardine and Standing (2000), Flandrian sand in the Dunkirk region was deposited less that 2 million years ago, which is considered a Quaternary deposit. According to Zhang (2005), the empirical factors for Quaternary sand with a plasticity index of 0 are $\gamma_{r1} = 0.075\%$, $\alpha = 0.83$, and $k = 0.316$. The following empirical model was fit to the seismic cone data as shown in Figure 3 and used to assign G_{max} values to each of the model layers:

$$G_{max} = A\left(\sigma_{v0}'\right)^{0.5} \quad [7]$$

where A=curve fitting constant, and σ_{v0}'=initial vertical effective stress. The maximum unit shaft resistance was calculated for each t-z curve using the "Beta" method in accordance with API (2000) assuming a lateral earth pressure coefficient (K) of 1 for a plugged pile and an interface friction angle of 27 degrees as reported in Jardine and Standing (2012).

As a first step the t-z model was used to simulate the static tension load tests. Figure 4 plots the model results along with the measured results for the seven static load tests that were performed. The modeled load-settlement curve fits the trend of the measured data very well particularly at low pile movements.

However, at larger pile head movements, the model slightly underestimates the observed pile movement. It is believed that this difference can be attributed to pile slippage at the soil-pile interface that can occur at low interface displacements, even before the maximum shear resistance is fully mobilized (DeJong and Westgate 2009). The t-z model described above assumes that slippage occurs only after the maximum unit shaft friction is reached.

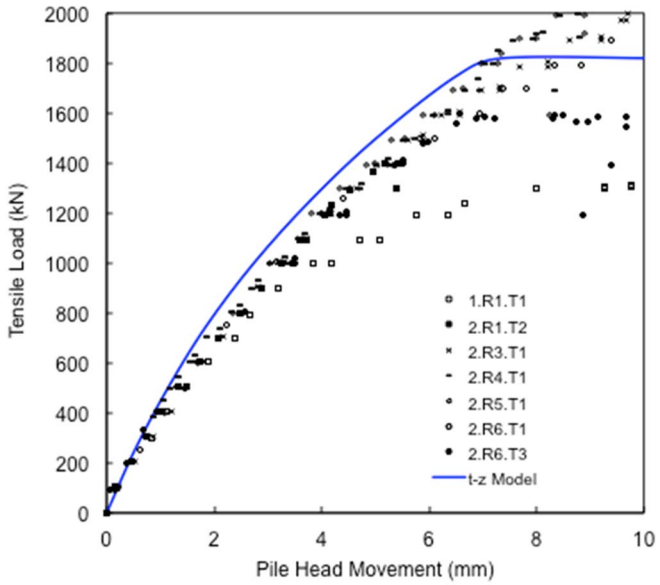


Figure 4 - Comparison between actual static load test data and the t-z model results.

The t-z model was then used to simulate the cyclic tension load tests. Since the static model does not update the soil properties on a cycle-by-cycle basis, it can be thought of as simulating the first cycle of loading. The test parameters including the amplitude of the cyclic load (Q_{cyc}), the mean cyclic load (Q_{mean}), and ultimate tensile static capacity (Q_T), and cycles to "failure" were compiled from Rimoy et al. (2013). Rimoy et al. (2013) also classified each of the tests as "stable", "metastable", or "unstable". Of the eleven tests only one of the tests was deemed "stable". For this pile, some stiffness degradation was observed, but the pile stabilized after about 500 cycles and the test was stopped after 1,000 cycles. Figure 5 plots that ratio of maximum cyclic load ($Q_{max}=Q_{mean}+Q_{cyc}$) to Q_T versus the number of cycles to failure. Three of the load tests did not reach failure and thus arrows indicate the possibility for higher numbers of cycles to failure. As shown in Figure 5, the general trend is typical of the cyclic resistance of soil where the cyclic load ratio decreases as the number of cycles to failure increases. As shown in the figure the piles were "metastable" or "unstable" when Q_{max}/Q_t was 0.6 to 1.0 and was "stable" at a value of 0.4.

Figure 6 plots the strain profiles calculated using the t-z model at load levels that represent the load levels that were applied in the cyclic load tests (i.e. Q_{max}/Q_t of 0.4 to 1.0). For reference the "typical" range of threshold shear strain of 0.01% to 0.03% is also shown in the figure. As shown earlier in Figure 5 when Q_{max}/Q_t was 0.6 to 1.0 the piles were observed to be "metastable" or "unstable". As shown in Figure 6, the profiles corresponding to Q_{max}/Q_t of 0.6 and 1.0, the shear strains were higher than the threshold shear strain at all depths. This means that cyclic degradation should start to occur at all depths down the pile starting with the first cycle of loading. The strain profile estimated for the "stable" pile represented by Q_{max}/Q_t =0.4 shows that the strains would not exceed the threshold shear strain over the bottom 1/3 of the pile. This suggests that only the soils in the upper 2/3 of the pile will begin to degrade in the first cycle. As degradation is initiated some of the load will be transferred to deeper portions of the pile and the

strains will be higher than shown by the static model. However, the results could explain why some degradation was observed even in the "stable" pile.

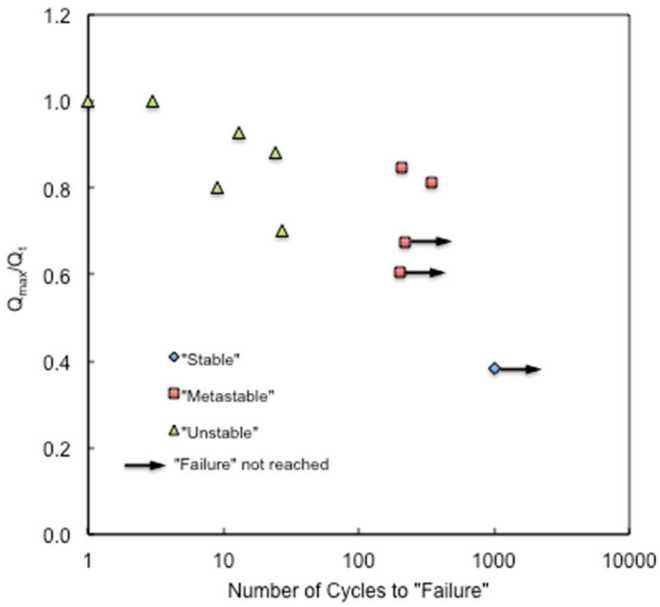


Figure 5 – Cyclic load test results presnted as a load ratio versus the number of cycles to failure.

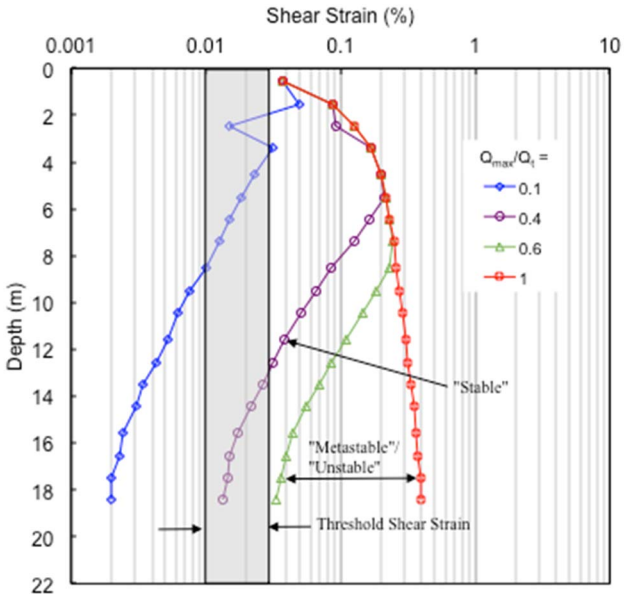


Figure 6 – Profiles of interface shear strain calculated with the t-z model.

The approach is used to show how a fatigue limit can be determined for the piles in this study. The maximum cyclic load level was incrementally reduced in the t-z model until the strain profile fell below or within the threshold level over the entire length of the pile. This occurred at approximately Q_{max}/Q_t = 0.1 as plotted in Figure 6. This would suggest that in the first cycle of loading the strains will not exceed

the threshold shear strains needed to induce permanent volume changes in the shear band and no degradation should occur with subsequent cycles. In other words, to avoid cyclic degradation entirely the maximum cyclic tensile load on the pile should be kept at or below 10% of the static tensile capacity. It is interesting to note that the strain-based approach could be easily applied to compressive loading by including the q-z curve at the toe of the pile, which is generally not expected to degrade during cyclic loading.

CONCLUSIONS

Cyclic degradation of shaft resistance in piles is an important consideration for the design of piled offshore wind jacket structures. Current methods typically employ a cyclic stability diagram, which can be developed from advanced numerical methods and laboratory testing. This paper explores the concept of a pile fatigue limit for cyclic axial loading using the threshold shear strain concept commonly associated with seismic liquefaction. A simple method was presented to estimate the interface shear strains using a static t-z analysis. Typical ranges of the threshold shear strain for sands were compiled. To test the viability of the approach, the analysis was applied to existing full-scale static and cyclic load test data from a site in Dunkirk, France. The developed t-z model was able to accurately capture the load-settlement response of the pile under static loading, particularly at small strains. For the cyclic load tests, in cases where the modeled strains were higher than the threshold shear strains, the piles were observed to be "metastable" or "unstable". The "stable" pile had calculated strains that were below the threshold values for approximately the bottom 1/3 of the pile thus suggesting some resistance to degradation. The model results were used to illustrate that in this case if the maximum cyclic tensile load is kept at or below 10% of the static tensile capacity of the pile, than no cyclic degradation should occur. The results are encouraging but further studies are needed to refine and validate the approach.

ACKNOWLEDGMENTS

The Authors would like to thank the anonymous reviewers for their comments. Also, thanks to Dr. James Schneider for his input and encouragement on an earlier draft of this paper.

REFERENCES

DeJong, J.T., and Westgate, Z.J., 2009. Role of Initial State, Material Properties, and Confinement Conditions on Local and Global Soil-Structure Interface Behavior. American Society of Civil Engineers, ASCE Journal of Geotechnical and Geoenvironmental Engineering, 2009.135:1646-1660.

DeJong, J.T., White, D.J., and Randolph, M.F., 2006. Microscale observation and modeling of soil-structure interface behavior using partical image velocimetry. Soil and Foundations, Vol. 46, pp. 15-28.

Dobry, R., R. S. Ladd, F. Y. Yokel, R. M. Chung, and Powell, D. (1982). "Prediction of pore water pressure buildup and liquefaction of sands during earthquake by the cyclic strain method," *NBS Building Science Series 138*, National Bureau of Standards, Gaithersburg, Maryland: 150

Jardine, R.J. and Standing, J.R., 2000. Pile Load Testing Performed for HSE Cyclic Loading Study at Dunkirk, France. Health and Safety Executive, London, UK, Offshore Technology Report OTO2000 008, Vol. 1-4.

Jardine R.J. and Standing J.R., 2012. Field axial cyclic loading experiments on piles driven sand. The Japanese Geotechnical Society, Soils and Foundations, pp. 723–736.

Lehane, B.M. and White, D.J. 2005. “Lateral Stress Changes and Shaft Friction for Model Displacement Piles in Sand.” Canadian Geotechnical Journal, 42, 1039-1052.

Poulos, H.G. (1988). Cyclic Stability Diagrams for Axially Loaded Piles. Journal of Geotechnical Engineering, 114(8), 877-895.

Randolph, M.F., and Wroth, P.C. (1978). “Analysis of deformation of vertically loaded piles.” Journal of the Geotechnical Engineering Division, 104(GT12), 1465-1487.

Randolph, M.F. (2003). RATZ Load Transfer Analysis of Axially Loaded Piles.

Rimoy, S.A., Jardine, R.J., and Standing, J.R., 2013. Displacement response to axial cycling of driven piles in sand. Institute of Civil Engineering Publishing, Vol. 166, Issue GE2, pp. 131-146.

Robertson, P.K., and Cabal, K.L., 2010. Guide to Cone Penetration Testing for Geotechnical Engineering. Gregg Drilling & Testing, Inc. 4th Edition.

Santamarina, J.C. and Aloufi, M. (1999). “Micro-scale interpretation of wave propagation in soils - fabric and fabric changes.” Proceeding, Pre-failure deformation characteristics of geomaterials, Torino '99, Balkema, Rotterdam.

Schneider J.A., and Senders, M., 2010. Foundation Design: A Comparison of Oil and Gas Platforms with Offshore Wind Turbines. Marine Technology Society Journal, Vol. 44, pp. 32-51.

Tsuha, C.H.C., Foray, P.Y., Jardine, R.J., Yang, Z.X., Silva., M., and Rimoy, S., 2012. Behavior of displacement piles in sand under cyclic axial loading. The Japanese Geotechnical Society, Soils and Foundations, pp. 393-410.

Vucetic, M., 1994. Cyclic Threshold Shear Strains in Soils. American Society of Civil Engineers, Journal of Geotechnical Engineering, Vol. 120, Issue 12, pp. 2208-2228.

Zhang, J., Andrus, R.D., and Juang, C.H., 2005. Normalized Shear Modulus and Material Damping Ratio Relationships. American Society of Civil Engineers, ASCE Journal of Geotechnical and Geoenvironmental Engineering, 2005, 131(4): 453-464.

BEHAVIOR OF BATTERED PILES UNDER LATERAL LOADS IN SANDY SOILS

Mohamed Ashour, Associate Professor of Civil Engineering, Dept. of Mechanical and Civil Engineering, Alabama A&M University, USA, E-mail: Mohamed.Ashour@aamu.edu

Jogeshwar P. Singh, JP Singh & Associates, Richmond, CA, USA, Email: jpsassoc@aol.com

Ahmed AlaaEldin, Teaching Assistant at Mansoura High Institute for Engineering and Technology, Egypt. E-mail: ah.a.eldin@gmail.com

ABSTRACT

The presented methodology allows the determination of the response of laterally loaded battered long piles in sandy soils based on the soil-pile interaction. The Strain Wedge (SW) model which was originally developed for laterally loaded vertical piles is modified to assess the behavior of laterally loaded battered piles with the consideration of soil and pile properties. The method predicts the pile-head response and associated p-y curves. The presented soil-pile model accounts for the variation of the direction and magnitude of the batter angles from the vertical position. Unlike current practice, the proposed technique also provides the p-y curves for battered piles in sandy soils based on soil and pile properties (i.e., sand relative density, friction angle, pile geometry, etc.). The proposed methodology has been validated through a number of comparisons with full/model-scale pile load tests.

Keywords: **battered pile, lateral load, p-y curve, sand.**

INTRODUCTION

The influence of pile battering on the lateral response of piles is rarely studied in the literature. Over the last decades and as suggested by Kubo (1962) and Zhang et al. (1999), a p-y multiplier is applied to predict the response of laterally loaded battered piles from an equivalent vertical one. Several researchers conducted model-scale piles load tests to understand the behavior of battered piles subjected to lateral load (Juvekar and Pise 2008; Meyerhof and Ranjan 1973; Meyerhof and Yalcin 1994). However, such tests were conducted on model piles with diameters less than 30 mm which may not have reflected actual soil-pile interaction. Battered piles are generally categorized as positive or negative battered piles according to the angle of pile installation as shown in Fig. 1. From the small-scaled and numerical models of battered piles, it was found that the lateral capacity of negative battered piles is larger than that of vertical ones. On the other hand, the positive battered piles have lower lateral capacity when compared to vertical piles (Fan-ren and Ji-Ming 2011; Juvekar and Pise 2008; Manoppo 2010; Reese et al. 2004; and Reese and Van Impe 2011).

The problem of laterally loaded vertical piles is solved as a Beam on an Elastic Foundation (BEF) through a set of p-y curves (i.e., non-linear springs) along the pile length. These p-y curves represent the soil properties and the pile width as suggested by Reese et al. (1974) and Meyer and Reese (1979) or account for soil properties and more pile properties (i.e., pile bending stiffness, pile-cross sectional shape and pile-head fixity) as addressed in the Strain Wedge (SW) method. The SW method was developed originally by Norris (1986) for a laterally loaded vertical flexible pile in uniform sandy soil and then upgraded for multi-layered soils by Ashour et al. (1998) and Ashour and Norris (2000). The procedure presented in this paper upgrades the SW method to account for pile battering. Unlike current practice (i.e., Kubo (1962) and Zhang et al. (1999)), the proposed

© 2018 Deep Foundations Institute

model determines the behavior of laterally loaded battered piles and associating p-y curves with the consideration of soil-pile interaction based on soil and pile properties. Kubo (1962) and Zhang et al. (1999) multipliers (Ω) are used to modify the values of the ultimate soil resistance (p_u) and the initial soil subgrade modulus (E_s) which contributes to predict the p-y curves of battered piles. But these modifiers don`t vary with the variation of soil type (i.e., relative density, D_r) and depth (Kubo 1962) or consider the variation in D_r but still constant with soil depth (Zhang et al. 1999). Ω is the ratio between ultimate soil resistance for battered and vertical piles ($\Omega = (p_u)_B / (p_u)_V$).

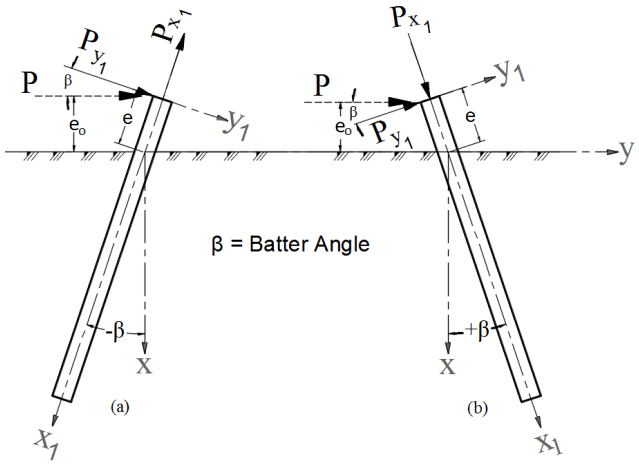


Fig. 1. Types of battered piles:(a) Negative battered pile (b) Positive battered pile

ANALYSIS PROCEDURE OF LATERALLY LOADED BATTERED PILE IN SANDY SOIL

The main concept of the SW model is that the traditional one-dimensional Beam on Elastic Foundation (BEF) pile response parameters can be characterized in terms of three-dimensional soil-pile interaction. Once the pile starts to move laterally, a 3D soil passive wedge starts to grow with the increase in the horizontal soil stress change ($\Delta\sigma_h$) and the associated side shear along pile sides (τ_s) (Figs. 2c and 3c). The mobilization in the geometry of the passive soil wedge and associated shear and deviatoric stresses (τ_s and $\Delta\sigma_h$) is governed by the concepts of the effective stress analysis and conventional triaxial load test (Figs. 2 and 3). Due to pile battering, the horizontal force (P) applied at the battered pile head is resolved to its components: a) lateral component [$P_{y1} = P\,cos(\beta)$] and b) axial component [$P_{y1} = P\,sin(\beta)$] (Fig. 1), where β is the pile battering angle.

The geometry of the mobilized passive wedge is governed by the mobilized fan angle (φ_m) and base angle (α_m) which both increase with increasing soil stress level, SL (=$\Delta\sigma_h/\Delta\sigma_{hf}$, where f is for the failing value) and its associated strain, ε, which change with the applied pile-head lateral load, P. The mobilized width of the face of the passive wedge ($\overline{BC}$) and α_m for a soil sublayer i are calculated as shown in Figs. 2 and 3 for negative and positive battered piles, respectively. The battered pile and surrounding soil are divided into a number of equal soil sublayers and pile segments with thickness (H_s) as shown in Figs. 2b and 3b for negative and positive battered piles, respectively. Each soil sub-layer (i) has a thickness H_s with an average vertical effective stress $(\overline{\sigma}_{vo})_i$, angle of internal friction (φ_i) and strain at 50% stress level $(\varepsilon_{50})_i$. Each pile segment of

length H_s has its own properties such as a cross-sectional shape and flexure stiffness (EI). As seen in Figs. 2c and 3c, the SW model satisfies the equilibrium among the forces acting on the mobilized passive wedge slice of soil (i.e., soil sublayer) and associated pile segment (Ashour et al. 1998). The lateral load at the pile-head is applied in an incremental fashion with increasing soil strain (ε_{y1}) in the y_1-direction of the passive soil wedge. For each load increment, the soil strain, ε_{y1}, is assumed to be constant along the depth of the wedge (h) and governs the resulting horizontal stress change ($\Delta\sigma_h$) (i.e., the deviatoric stress). The resulting SL value and associated $\Delta\sigma_h$ vary with depth under the same soil strain (ε_{y1}) as calculated from the soil constitutive model developed by Norris (1986) and shown in Fig. 4. The SL equation in Fig. 4 is an iterative formula which is a function of assumed developed soil strain ε and associated λ.

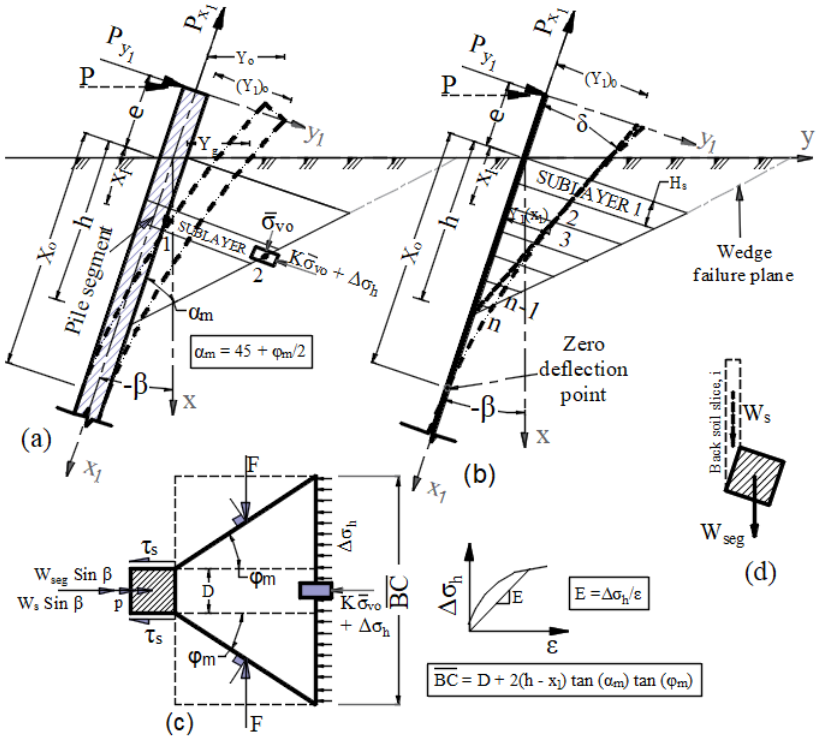


Fig. 2. Negative battered pile in uniform sand: (a) Characterization of the passive soil wedge (b) Multi-sublayers technique (c) Equilibrium of a soil sublayer at depth x_1 (d) Pile segment

Based on Mohr-Coulomb criteria, SL is expressed as:

$$SL_i = \frac{(\Delta\sigma_h)_i}{(\Delta\sigma_{hf})_i} = \frac{\tan^2\left(45+\frac{(\varphi_m)_i}{2}\right)-1}{\tan^2\left(45+\frac{\varphi_i}{2}\right)-1}, \text{ and } \quad (\Delta\sigma_{hf})_i = (\bar{\sigma}_{vo})_i\left[\tan^2\left(45+\frac{\varphi_i}{2}\right)-1\right] \qquad [1]$$

Where, $\Delta\sigma_{hf}$ is the value of the horizontal stress change at failure, and $(\bar{\sigma}_{vo})_i$ is the average vertical effective stress in sublayer i between points 1 and 2 (see Figs. 2a and 3a). The horizontal stress acting in the direction of the y_1-axis is assumed to be uniformly distributed at the face $\overline{BC}$ (i.e., the

width of the passive wedge) for each soil sublayer of the passive wedge. The initial horizontal stress in each soil sublayer is $\left[(\overline{\sigma}_3)_i = K(\overline{\sigma}_{vo})_i = (\overline{\sigma}_{vo})_i\right]$ assuming isotropic conditions of K = 1.

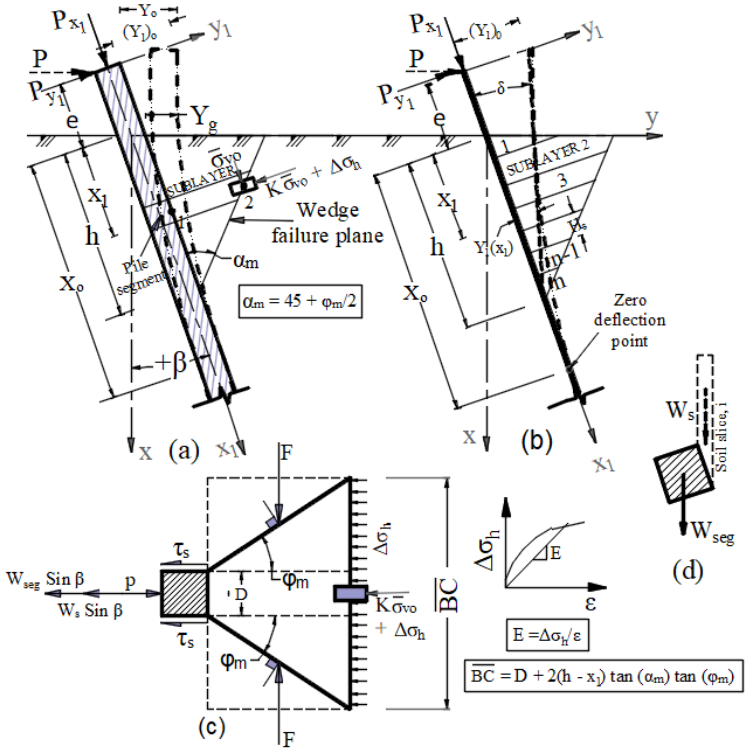


Fig. 3. Positive battered pile in uniform sand: (a) Characterization of the passive soil wedge (b) Multi-sublayers technique (c) Equilibrium of a soil sublayer at depth x_1 (d) Pile segment

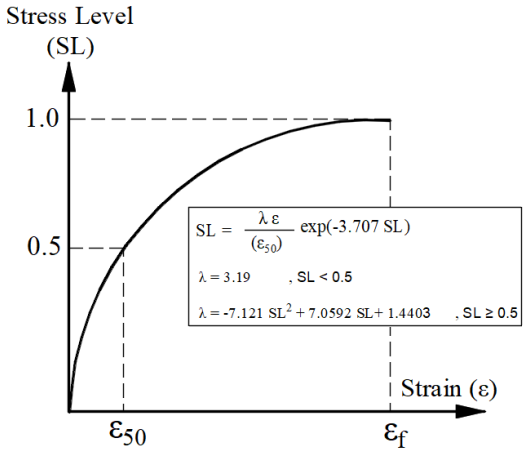


Fig. 4. Constitutive soil model employed in the SW model (after Ashour et al. 1998)

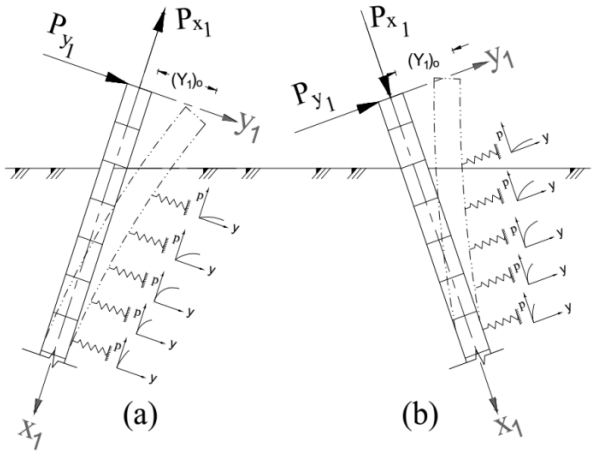


Fig. 5. Soil-pile model (a) Negative battered pile (b) Positive battered pile

At any level of lateral loading, refer to a certain depth (x_1) with an average vertical effective stress $\overline{\sigma}_{vo}$, the constitutive soil model (i.e., Fig. 4) is applied to assess the stress-strain relation as in the

triaxial test (i.e., the specimen at the face of the wedge, Figs. 2a and 3a). The stress level at a certain depth can be estimated using the strain at 50% of stress level (ε_{50}) (Fig. 4) which can be obtained from the triaxial test or the correlations suggested by Norris (1986) based on the soil void ratio and the soil coefficient of uniformity (C_c). The ever-changing soil Young`s modulus ($E = \Delta\sigma_h / \varepsilon$) varies with the value of $\Delta\sigma_h$ that acts at the face of the soil passive wedge (i.e., the deviatoric stress in the conventional triaxial test). The profile of soil-pile modulus of subgrade reaction (Es) (Fig. 5) is assessed at each step of lateral loading based on the pile properties, the value of soil Young`s modulus (E), and the mobilized geometry of the passive soil wedge. Using the E_s profile, the problem of BEF can be solved (Eq. 2) and the lateral deflection profile can be obtained along the pile length (y_1 versus depth x_1). The lateral deflection at the pile head obtained from BEF (Y_{BEF}) is compared to that calculated from the SW model analysis (as presented later) through an iteration process until reach an acceptable convergence. More details about the SW model analysis are provided by Ashour et al. (1996 and 1998) and Ashour and Norris (2000).

$$EI\frac{d^4y_1}{dx_1^4} + P_{x1}\frac{d^2y_1}{dx_1^2} + E_s(x_1)y_1 = 0 \qquad [2]$$

Where EI is the pile's flexural stiffness, $E_s(x_1)$ represents the soil-pile modulus of subgrade reaction at the depth in question and P_{x1} denotes the axial load on the pile segment.

SOIL-PILE INTERACTION (P-Y CURVES) FOR BATTERED PILES

The soil-pile reaction (p_i) for a sublayer i is evaluated based on soil sublayer/pile segment equilibrium given in Eq. 3 and presented in Figs. 2c and 3c for negative and positive battered piles, respectively.

$$p_i = \left[(\Delta\sigma_h)\,\overline{BC} - \left(W_{seg}\right)_i Sin\beta\right] S_1 + 2\,(\tau_s)_i\, D\, S_2, \qquad \text{(-ve Pile)} \qquad [3a]$$

$$p_i = \left[(\Delta\sigma_h)\,\overline{BC} + \left(W_s\right)_i Sin\,\beta + \left(W_{seg}\right)_i Sin\beta\right]\, S_1 + 2\,(\tau_s)_i\, D\, S_2, \quad \text{(+ve Pile)} \qquad [3b]$$

Where S_1 and S_2 represent pile cross-section shape factors of 0.75 and 0.5 for circular piles, and 1.0 each for square/rectangular piles (Briaud et al., 1984). The soil-pile side shear stress (τ_s) is given as

$$(\tau_s)_i = [(\overline{\sigma}_{vo})_s]_i \tan\left(\varphi_{sf}\right)_i \qquad \text{where, } \tan\left(\varphi_{sf}\right)_i = 2\tan(\varphi_m)_i \qquad [4]$$

$(\overline{\sigma}_{vo})_s$ is the effective stress at the soil-pile segment interface (point 1 in Figs. 2a and 3a for negative and positive battered piles, respectively) and τ_s is limited to an ultimate value ($\varphi_{sf} = \varphi$). The value of p_i is also limited to an ultimate value as

$$\left(p_{ult}\right)_i = (\Delta\sigma_{hf})_i \left(A_{ult}\right)_i D \qquad [5]$$

Where A_{ult} governs the maximum interaction between the pile cross section and surrounding soils when SL = 1 at depth (x_1). The lateral deflection for a soil sublayer i at a depth x_1 is assessed as

$$y_i = \frac{\varepsilon}{\psi}(h - (x_1)_i) \qquad [6]$$

Ψ is a function of the Poisson's ratio, mobilized friction angle (φ_m) and passive wedge base angle (α_m), and varies for sandy soils between 1.74 and 1.81 with an average value of 1.77 (Ashour et al. 1998). The profile of $(E_s)_i$ for each soil sublayer is assessed for each load increment ($(E_s)_i = p_i / y_i$). Once the E_s profile is obtained, the problem of BEF can be solved (Eq. 2) and the pile head lateral deflection can be obtained as $(Y_1)_{BEF}$ and the point of zero deflection $(X_o)_{BEF}$. Also, the lateral deflection at the pile head is calculated using the proposed method $\left((Y_1)_o = \sum_{i=1}^{n} H_s \frac{\varepsilon_i}{1.77}\right)$ for n of soil sublayers and the adjusted zero deflection depth (X_o = 1.44h). Values of $(Y_1)_{BEF}$, $(Y_1)_o$, $(X_o)_{BEF}$, and X_o are compared through an iteration scenario until an acceptable convergence obtained. Once the convergence occurs, the horizontal pile head deflection, Y_o, is equal to $Y_o = (Y_1)_o \cos(\beta)$.

VALIDATION

A Full-Scale Pile Load Test at Arkansas River

Alizadeh and Davisson (1970) performed a full-scale lateral load test on negatively battered steel H-section pile (β = -18.43˚) with a flexure stiffness EI of 71081kN-m^2 and a pile length (L) of 13.8m. the pile was a free-head driven pile in sandy soil with 18.06 kN/m^3 unit weight and 9.89 kN/m^3 submerged unit weight. The soil's angle of internal friction (φ) was 38° and the water table was 0.4m below the ground surface. The pile-head (i.e., the location of loading, e, Fig. 1) was 0.15m above the ground surface. Good agreements can be observed for the pile head response and the variation in maximum bending moment with the applied pile head load as shown in Fig. 6.

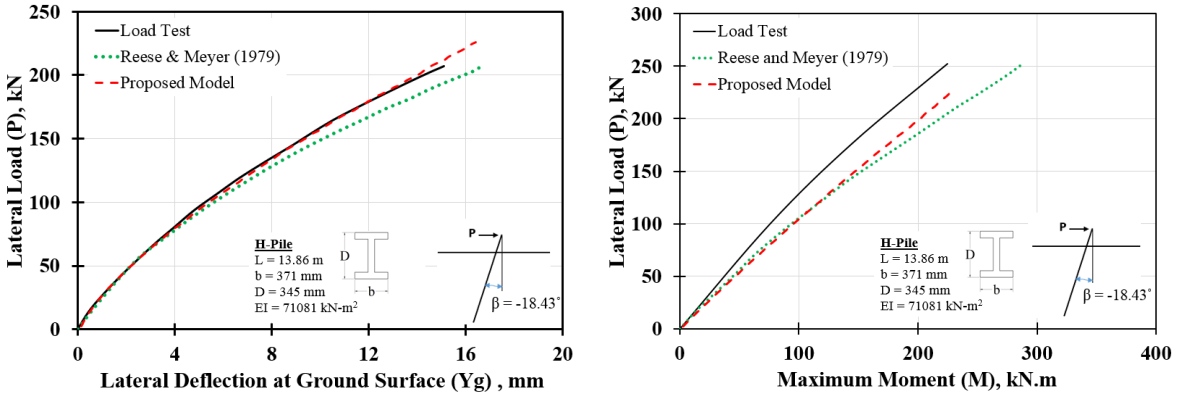


Fig. 6. Measured and predicted deflection and maximum bending moment of laterally loaded negative battered pile at the Arkansas River test

Full-Scale Tests at Oregon State University

Nimityongskul et al. (2012) carried out a series of full-scale lateral load tests on vertical and battered piles in 3m thick man-made compacted sand embankment with 43˚ internal friction angle and 19.9 kN/m3 unit weight underlained by a 3m of stiff clay which overlies a deep deposite of very dense sandy soil (γ' = 10.59 kN/m3 and φ = 48˚). A 9.15-m long and 0.324-m diameter steel pipe pile with 9.525mm wall thickness (t) and EI = 34481 kN-m^2 was used in these tests. Two piles with different installation angles (β = ±14) were studied. Figure 7 shows reasonable agreements between measured and calculated results for the lateral response of negative and positive battered piles, respectively.

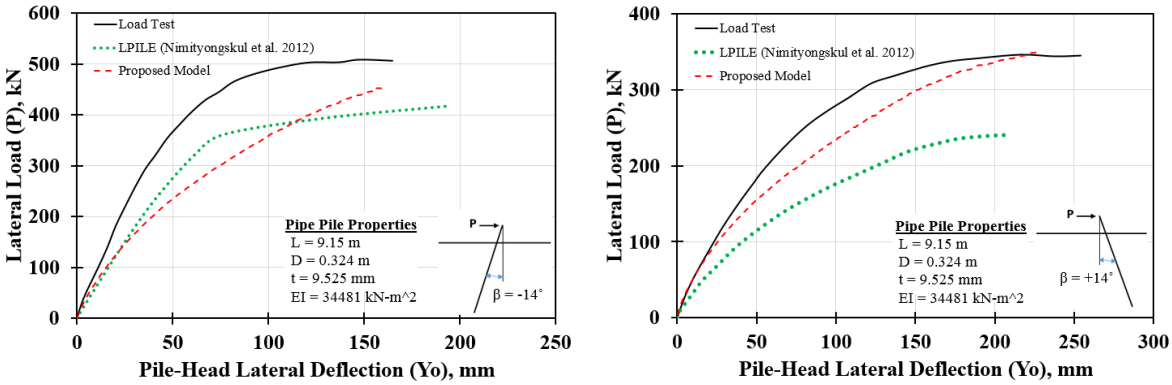


Fig. 7. Predicted and measured response of laterally loaded batterpiles at Oregon State University test

Centrifuge Pile Model Tests

Zhang et al. (1999) performed a number of centrifuge model tests in dry medium dense sand. The sandy soil had a relative density (D_r) of 36%, a dry unit weight of 14.50 kN/m^3 and an internal friction angle of 33.3^o. The model was tested at 45g. The scaled model used was a 0.43-m square pile 13.7m long and an EI of 206MN-m^2. The point of loading was 2.14m above the ground surface. There is a general good agreement between measured and calculated pile-head lateral load deflection response for both positive and negative battered piles as presented in Fig. 8.

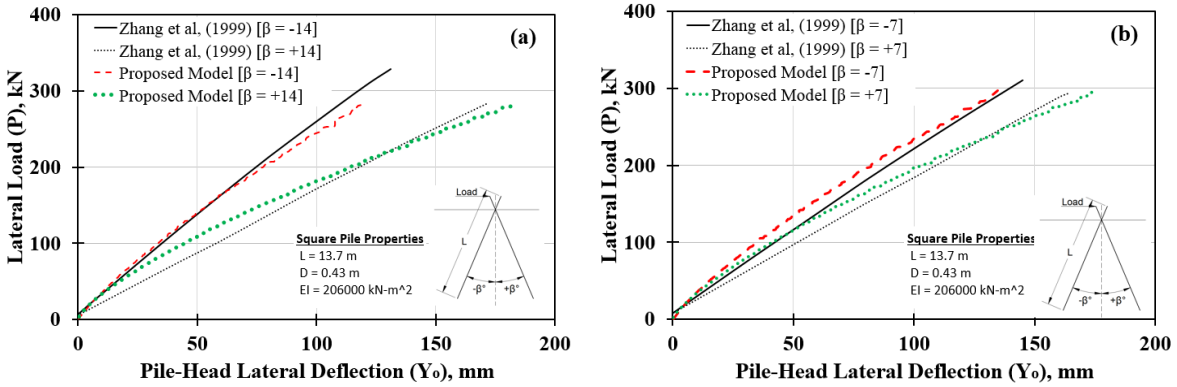


Fig. 8. Calculated and measured response of laterally loaded batter piles in centrifuge tests

RATIO OF ULTIMATE SOIL PILE REACTION (Ω)

As mentioned earlier, current practices predict the response of laterally loaded battered piles by modifying the set of non-linear p-y curves (i.e., obtained from field test or the method suggested by Reese et al. 1974) of an equivalent vertical pile (Kubo's 1962; Zhang et al. 1999).A comparison between the value of Ω (i.e., a multiplier) as obtained from the proposed model and the Unified Facilities Criteria (2004) using Kubo's (1962) procedure can be found in Fig. 9. Also, the influence of pile batter on the soil-pile reaction degrades with depth and becomes almost negligible beyond a certain depth (Fig. 10). Unlike current practices that employ a modification factor, the proposed

model can predict the p-y curves for battered piles using soil and pile properties and the batter angle (i.e., no multiplier). The soil properties employed in this study are summarized in Table 1.

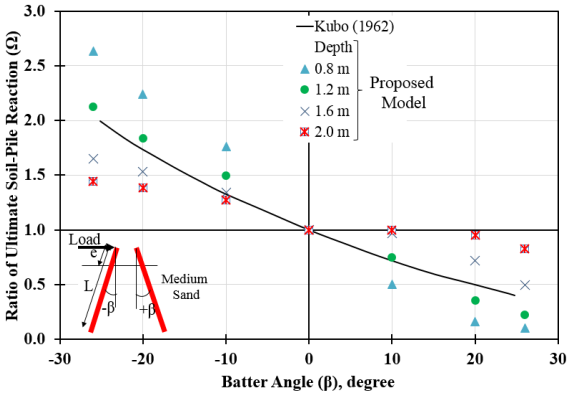


Fig. 9. Ratio of ultimate soil-pile reaction of battered to vertical piles in medium dense sand

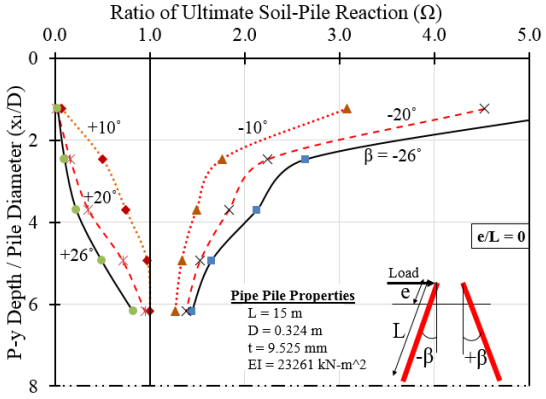


Fig. 10. Variation of ultimate soil-pile reaction ratio with depth in medium dense sand

Table 1. Sand Properties of the Presented Parametric Study

Sand State	Dr (%)	γ(kN/m^3)	φ (degree)	ε_{50}
Loose	30	17	30	0.0052
Medium	60	19	35	0.0037
Dense	80	21	40	0.0028

INFLUENCE OF PILE BATTER ANGLE (β) AND SOIL RELATIVE DENSITY (D_r)

Fig. 11 shows the influence of pile battering angle on the lateral response of battered piles embedded in Loose, medium dense and dense sandy soils (Table 1). The pile used in the study is a 20m long and 0.324m in diameter steel pipe pile with 9.525mm wall thickness (t) and EI = 34481 kN-m^2. Figure 11 exhibits the effect of positive and negative batter angles on the lateral response of the studied pile. The negative battered piles (β = -20) experienced a lateral response stiffer than that of vertical piles in a range from 30%, 40% to 60% with loose, medium dense, and dense sands, respectively (Fig. 11a). Also, the positive battered piles maintain lateral responses softer than those of a vertical pile by 55%, 50%, and 45% for loose, medium dense, and dense sands, respectively, as shown in Fig. 11b.

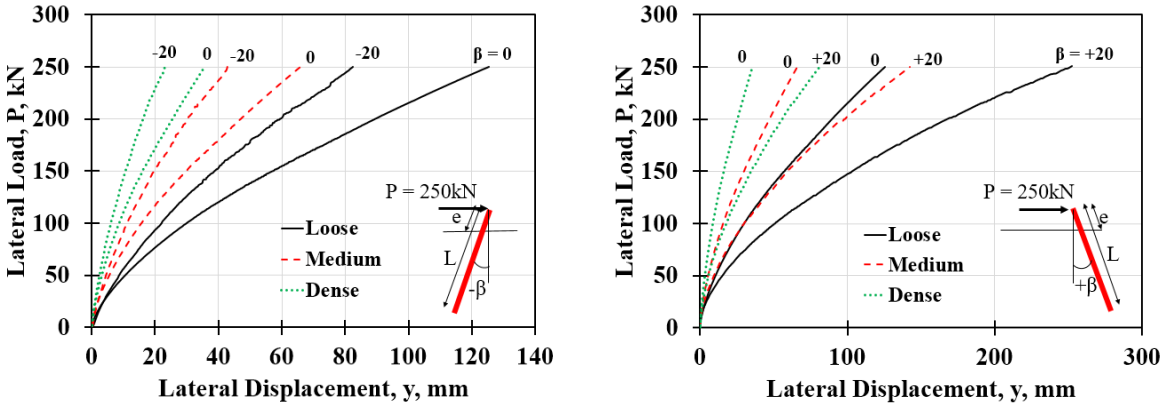


Fig. 11. Influence of soil's D_r on the lateral response of a pile with varying batter angles

CONCLUSIONS

The presented approach presented allows the prediction of the behavior of laterally loaded batter piles based on soil and pile properties. The lateral behavior of batterd piles and acompanying p-y curve are highly influenced by the magnitude and direction of the pile batter angle in addition to the soil properties (i.e., sand relative density). Compared to the vertical pile, the proposed model demonstrates the influence of pile battering on the shape of the p-y curve that deminishes with depth. Unlike current practice that models the battered piles based on a mutilpier used with the p-y curves for an equivelant vertical pile, the approach presented develops its own p-y curves for battered piles as a function of the pile installation angle and soil and pile properties. Moreover, the multiplier used with vertical pile's p-y curves is assumed to be contant with depth which is supposed to vary with depth and D_r. The multiplier deacreses with increasing D_r for negative battered piles and increases with increasing D_r for positive battered piles.

REFERENCES

Alizadeh, M., and Davisson, M. T. (1970). "Lateral load tests on piles-Arkansas River project." Journal of Soil Mechanics and Foundations Div. 96(5), PROC PAPER 7510, 1583 - 1604.

Ashour, M., Norris, G., and Pilling, P. (1998). "Lateral loading of a pile in layered soil using the Strain Wedge model." J. Geotech. and Geoenviron. Eng., 124(4), doi:10.1061/(ASCE)1090-0241(1998)124:4(303), 303-315.

Ashour, M., and Norris, G. (2000). "Modeling lateral soil-pile response based on soil-pile interaction." J. Geotech. and Geoenviron. Eng., doi:10.1061/(ASCE)1090-0241(2000)126:5(420),420-428.

Ashour, M., Pilling, P., Norris, G., and Perez, H. (1996). "Development of a strain wedge model program for pile group interference and pile cap contribution effects." Report – CCEER-96-4, FHWA, and CALTRANS, University of Nevada, Reno, 274pp.

Briaud, J. L., Smith, T., and Meyer, B. (1984). "Laterally loaded piles and the pressuremeter: comparison of existing methods. In laterally loaded deep foundations: Analysis and performance." ASTM International. West Conshohocken, Pa., 97-111.

Fan-ren, L., and Ji-ming, Y. (2011). "Study on proportional relationship of lateral capacity of batter pile by model experiments." Procedia Engineering, 8(16), pp. 8-13.

Juvekar, M. S., and Pise, P. J. (2008). "Behavior of rigid batter piles and pile groups subjected to horizontal load in sand." Indian Geotechnical Journal, 38(2), 221-242.

Kubo, K. (1962). "Lateral resistance of single free-head batter piles and single fixed-head vertical piles." Monthly Report of Transportation Technical Research Institute 12(2) (in Japanese).

Manoppo, F. J. (2010). "Behavior of the ultimate bearing capacity of single flexible batter pile under horizontal loads in homogeneous sand." Dinamika TEKNIK SIPIL 10(2), 116-119.

Meyerhof, G. G., and Ranjan, G. (1973). "The bearing capacity of rigid piles under inclined loads in sand. II: Batter piles." Canadian Geotechnical Journal, 10(1), 71-85.

Meyer, B. J., and Reese, L. C (1979). "Analysis of single piles under lateral loading." Report(No. FHWA-TX-79-38+ 244-1 Intrm Rpt.), TX: Center for Highway Research, Uni. of Texas, Austin.

Meyerhof, G. G., and Yalcin, A. S. (1994). "Behavior of flexible batter piles under inclined loads in layered soil." Canadian Geotechnical Journal,30(2), 247-256.

Nimityongskul, N., Barker, P., and Ashford, S. (2012). "Effects of Soil Slope on Lateral Capacity of Piles in Cohesive and Cohesionless Soils." Research Report of a Research Project Funded by Caltrans under Facilities Contract No. 59A0645, Oregon State University, Kiewit.

Norris, G. M., (1986). "Theoretically based BEF laterally loaded pile analysis." Proceeding in Paris, France. 3redInternational Conf. on Numerical Methods in Offshore Piling, Editions Technip.

Reese, L. C., Cox, W. R., and Koop, F. D. (1974). "Analysis of laterally loaded piles in sand." Offshore Technology in Civil Engineering Hall of Fame Papers from the Early Years, 95-105.

Reese, L.C., and Van Impe, W.F. (2011). Single Piles and Pile Groups under Lateral Loading, 2nd Edition. London: Taylor & Francis Group.

Reese, L. C., Wang, S. T., Isenhower, W. M., and Arrellaga, J. A. (2004). Computer program Lpile plus version 5.0 technical manual.Ensoft, Austin, TX.

UFC (Unified Facilities Criteria). (2004). Deep Foundations. TI 818-02 ed. Washington, DC 20314-1000: U.S. Army Corps of Engineers.

Zhang, L., McVay, M. C., and Lai, P. W. (1999). "Centrifuge modeling of laterally loaded single battered piles in sands." Canadian Geotechnical Journal,36(6), 1074-1084.

COMPARISON OF PILE FOUNDATIONS AND GROUND IMPROVEMENT FOR REDUCTION OF SEISMIC DISPLACEMENTS FOR A WASTEWATER TREATMENT PLANT

Ali Ghandeharioon, Klohn Crippen Berger Ltd, Vancouver, BC, Canada, +1 604 669 3800, aghandeharioon@klohn.com
Andrew Port, Klohn Crippen Berger Ltd, Vancouver, BC, Canada, aport@klohn.com

ABSTRACT

Nonlinear seismic deformation analyses using the finite difference program FLAC were performed for a wastewater treatment plant to estimate foundation displacement and performance of two proposed trickling filters during the 2475-year event design earthquake. The effective stress based constitutive model UBCSAND, which captures the cyclic behavior of both the "sand-like" and "clay-like" materials, was used to model the dynamic response of the soil strata. Dynamic analyses of the site indicated that in absence of ground improvement or deep foundations beneath the proposed trickling filters, those structures would undergo horizontal displacements in excess of 1 m and short-term differential settlement gradient of about 400 mm over 50 m as a result of seismic and post-seismic settlements. Three mitigation options were considered for limiting the seismic displacements and differential settlement gradients of the proposed trickling filters. These alternatives include vibro-replacement stone columns, vibro-replacement stone columns plus supplementary cutter soil mixing (CSM) configurations, and pile foundations. Various layouts for each mitigation option were considered including the lateral extent of the ground improvement, CSM walls and pile spacing. Seismic horizontal and vertical displacements of the proposed structures as well as post-earthquake consolidation settlements due to dissipation of excess pore water pressures in soil layers were assessed in all the analysis alternatives. The analyses indicate that all the alternatives considered have the potential to provide a comparable level of seismic and post-seismic performance. However, for similar performance levels, the ground improvement options need to extend well beyond the edges of the proposed structures, while the piles can be limited to just beneath the footprint of the structures.

Keywords: Seismic Deformation Analysis, FLAC, UBCSAND, Pile Foundation, Ground Improvement

INTRODUCTION

Annacis Island Wastewater Treatment Plant (AIWWTP) is owned and operated by Greater Vancouver Sewerage and Drainage District and services a population of approximately 1 million people in Vancouver, British Columbia. Wastewater is generated by residential, commercial, and industrial sectors and the treated effluent is discharged to Annieville Channel of Fraser River on the south side of Annacis Island. AIWWTP is located on a 51-hectare site and was commissioned in 1975 as a primary treatment plant, but has had two major expansions to meet the population growth needs, and to improve the treatment process efficiency through the provision of secondary treatment of the liquid stream. The current expansion includes construction of additional solids contact tanks and secondary clarifiers. Future expansions include the construction of proposed additional trickling filters. New expansion structures are required to be designed for post-seismic operation after the 2475-year event design earthquake.

Site response analysis and liquefaction assessments indicate that liquefaction would occur to significant depths (approximately 30 m) in the compact Fraser River sand deposits underlying the site. Dynamic analysis indicated that, in absence of ground improvement or deep foundations beneath the proposed trickling filters, these structures would undergo horizontal displacements in excess of 1 m towards the north, and short-term differential settlement gradient of about 400 mm over 50 m (1:125). Three mitigation alternatives were considered for limiting the displacements and differential settlement gradients of the

© 2018 Deep Foundations Institute

proposed trickling filters: (I) Vibro-replacement stone columns ground improvement, (II) Vibro-replacement stone columns plus supplementary cutter soil mixing (CSM), and (III) Pile foundations with no ground improvement. Different extents and configurations are modeled for the ground improvement options, and several pile spacings and connection details were considered for the pile foundation alternative.

SITE CHARACTERISTICS

The AIWWTP site consists of approximately 40 m of loose to compact, liquefiable Fraser River sand, overlying approximately 60 m of normally consolidated, compressible silts and clays over glacial till. The ground surface varies between El. 104.5 m and El. 106 m based on LIDAR survey. The groundwater level was taken to be El. 101.5 m for the analyses. Elevations in this paper are referenced to the AIWWTP datum, where El. 100 m is equal to Geodetic elevation 0 m. The effective stress based constitutive model UBCSAND, which captures the cyclic behavior of both the "sand-like" and "clay-like" materials, was used to model the seismic behavior of soils. During site investigation, thin-walled tube samples were collected from the silt and clay layer between 40 m and 100 m depth. Cyclic direct simple shear (DSS) testing was conducted on six samples. Following the DSS testing, the UBCSAND model was calibrated for each DSS test to provide a reasonable match between the pore pressure ratio R_u (i.e. the excess pore pressures generated divided by the initial effective stress) as well as the induced shear strains and number of cycles.

Recently completed ground improvement (GI) work in an adjacent area of the site consisted of densifying the sand layer in an area of approximately 43,000 square meters to a maximum depth of 34 m through the installation of 5,500 stone columns. A total of 138 cone penetration tests (CPTs) were conducted during densification trials and production work to confirm post-ground improvement CPT penetration resistance. The pre- and post-densification CPT results were used to provide properties for the native sand layer and ground improvement area, respectively. Figure 1 presents variations of CPT tip resistance, q_c, with elevation for pre- and post-densification treatment.

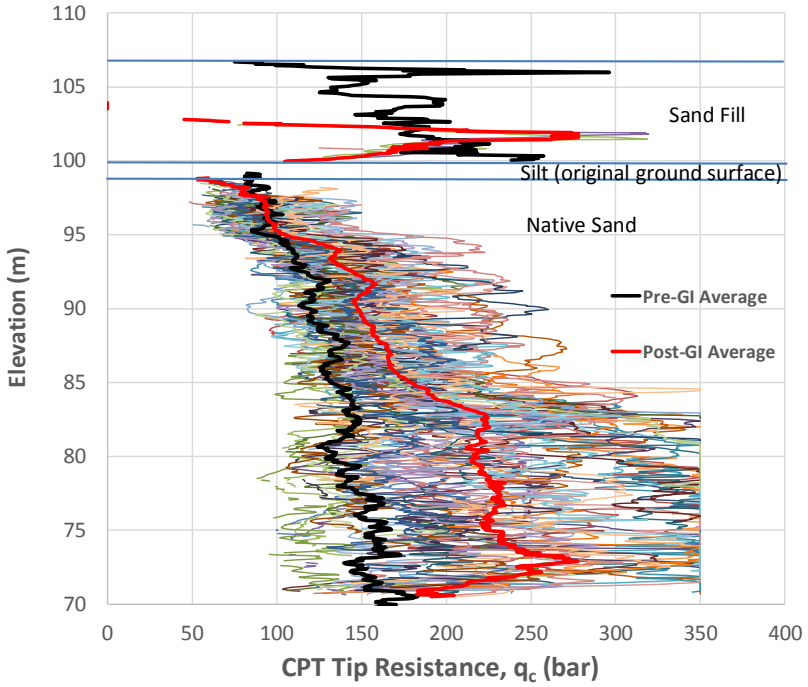


Fig. 1. Variations of cone penetration test (CPT) tip resistance with elevation at the site pre- and post-densification treatment

ANALYSES METHODOLOGY

Seismic deformation analyses were carried out using the finite difference program FLAC (Itasca, 2011) to evaluate the dynamic response of a north-south section through the proposed trickling filters, existing trickling filters, existing trickling filter pump station and primary sedimentation tanks. Figure 2 shows a plan view of Annacis Island Wastewater Treatment Plant, the proposed location for the proposed trickling filters and location of the section selected for the analyses. Stockpile 1 as shown in Fig. 2 will be removed for the construction of the proposed trickling filters, and therefore was not modeled in the analyses. The proposed trickling filters will be 52 m in diameter, and are confined by a storm water retention pond to the north and existing trickling filters to the south. The storm water retention pond has a maximum depth of 3.2 m and a side slope of 3H:1V. The minimum distances between the proposed trickling filters and the pond, and between the proposed and existing trickling filters are 33 m and 37 m, respectively. Figure 3 presents the site geology and FLAC model of the selected section. The existing trickling filters were constructed more than 20 years ago on a common raft without ground improvement. However, the primary sedimentation tanks were recently designed based on installing vibro-replacement stone columns. The analyses for the proposed trickling filters were performed in the groundwater mode with flow off during the static analyses, and flow on in the dynamic analyses, i.e. seismic analyses are not undrained.

The construction sequence was modeled in a simplified method in the analyses, where the excavation and construction of structures as well as ground improvement underneath structures were assumed to occur concurrently and were modeled from the start of the static analysis. Frictional interfaces were modeled between the base slab foundations of the structures and the soil below to allow relative displacements of the base slab and the soil.

An initial static analysis was carried out using an elastic perfectly-plastic constitutive model with Mohr-Coulomb failure criterion to establish in-situ stresses in the soil and ground improvement zone, where applicable, prior to the dynamic loading. The UBCSAND model was used to simulate the seismic behavior of both the soil and vibro-replacement ground improvement zone. Site structures were modeled using an elastic constitutive model.

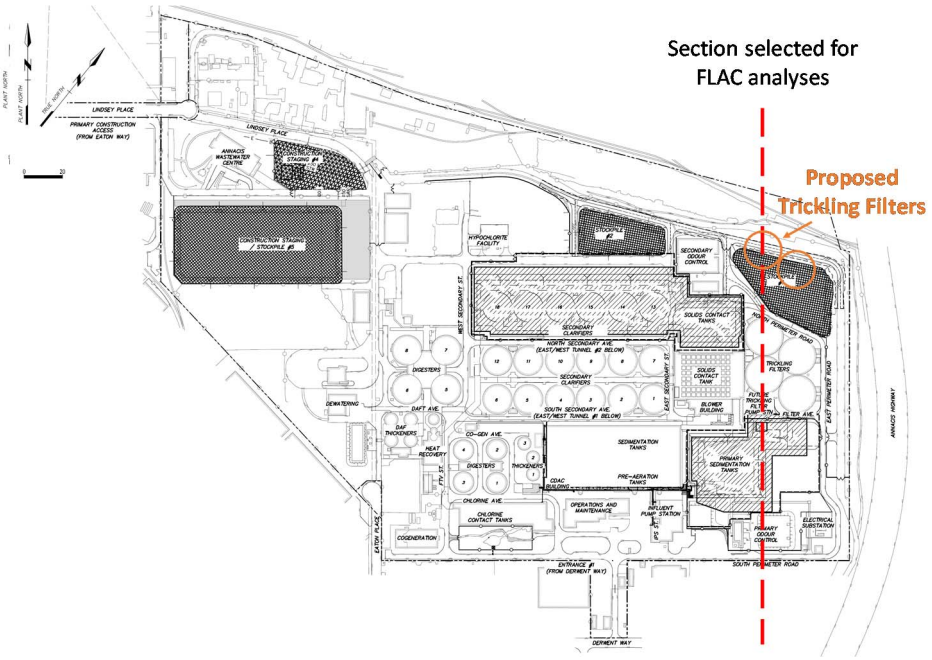


Fig. 2. Plan view of Annacis Island Wastewater Treatment Plant and the location of analysis section

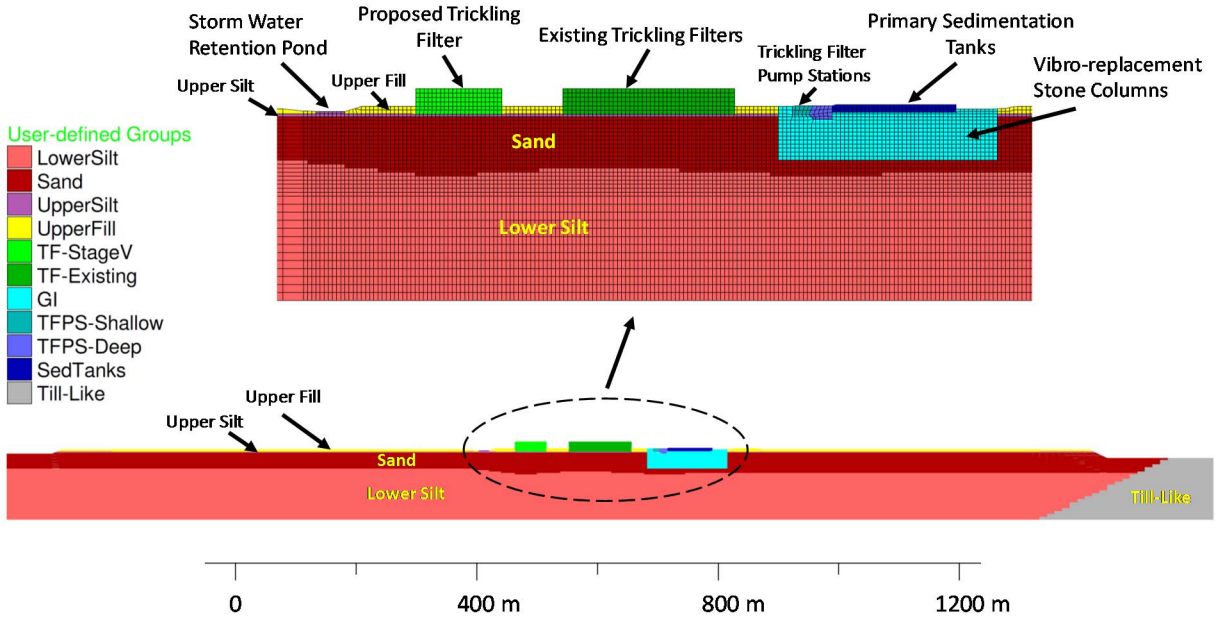


Fig. 3. Site geology and FLAC model of the analysis section

Eight design ground motion time histories were selected for the equivalent-linear site response analyses. The ground motion time histories consisted of three sets of 2475-year event earthquakes and one set of subduction ground motions. Each set of ground motions comprised of two orthogonal time history components (i.e. north-south and east-west components). The original time histories were obtained from the available ground motion databases and modified to match the National Building Code of Canada (National Research Council Canada, 2010) uniform hazard response spectra for Site Class C for the 2475-year motions. Similarly, for subduction earthquakes, the time histories were modified to match the firm ground spectral values from a deterministic seismic hazard model. Table 1 presents the design ground motions considered in the analyses.

While all eight design ground motions were considered for 1D site response analyses, only one time history was selected for the 2D FLAC analyses. The Landers east-west ground motion provides a close to average estimate of the Arias intensity, Newmark displacement and effective duration among the 2475-year event design earthquakes. Hence, the input motion representing the Landers east-west earthquake was applied as the velocity time history at the base and lateral boundaries of the model. The base was treated as rigid and taken to be at the top of the till layer at 115 m depth (El. -15 m). The lateral boundaries were modeled far away from the wastewater treatment plant so that the analyses response is not unduly influenced by the assumed lateral boundary condition.

Post-earthquake consolidation settlements due to dissipation of excess pore water pressures after the earthquake were estimated separately from the FLAC analyses using the following methods: (i) for sand materials, the approach suggested by Ishihara and Yoshimine (1992) was used, which translates the maximum shear strains developed in sands during the seismic loading to post-seismic volumetric strains, and (ii) for silt materials, the method developed by Sanin (2010) was used, which correlates the excess pressure ratio R_u at the end of shaking to the equivalent post-seismic volumetric strain.

Total settlements were divided into two categories, total short-term and total long-term settlements. The total short-term settlements were calculated by including post-seismic settlements induced in the top 55 m of soil stratum, which corresponds to settlements occurring due to dissipation of excess pore pressures in the sand and the upper portion of the lower silt layer. These settlements are likely to occur over days in

Table 1. Characteristics of the earthquake time histories considered in the analysis

Ground Motion	Category	Newmark Displacement (1) (mm)	Arias Intensity (2) (m/sec)	Effective Duration (3) (sec)
Loma Prieta – North South	2475-year	1980	2.40	15.48
Loma Prieta – East West	2475-year	2150	2.29	15.51
Landers – North South	2475-year	3250	3.14	30.66
Landers – East West	2475-year	3300	3.74	28.26
Chi Chi – North South	2475-year	3710	6.42	28.91
Chi Chi – East West	2475-year	3220	4.62	27.54
Average of 2475-year Motions	**2475-year**	**2930**	**3.77**	**24.39**
Mexico – North South	Subduction	750	0.69	26.68
Mexico – East West	Subduction	690	0.81	29.16
Average of Subduction Motions	**Subduction**	**720**	**0.75**	**27.92**

Notes:

(1) The Newmark displacements were calculated using the Newmark Java program published by USGS (open- file report 2003-5) using a yield acceleration of 0.01 g.
(2) Arial intensities were calculated by integrating the square of the acceleration time history and multiplying the result by $\pi/2g$.
(3) Effective durations were calculated as the time between 5% and 95% of Arias intensities.

the sand stratum to several weeks or months in the upper portion of the lower silt layer. The total long-term settlements were estimated by considering post-seismic settlements induced in the lower silt stratum below the top 55 m of soil due to dissipation of excess pore pressures in the lower silt deposit. These settlements are assumed to occur over a few years or many years due to the lower hydraulic conductivity of the silt and the large drainage distance for this deep layer.

Differential settlement gradients across structures were estimated by finding the difference between maximum and minimum vertical displacements, dividing by the width of the structure, and then converting to equivalent differential settlements over 50 m. Short-term differential settlement gradients were calculated by adding the absolute values of seismic and post-seismic differential settlement gradients. It is noted that the location of the maximum settlement gradient may not occur at the same location for the seismic and post-seismic cases. Nevertheless, this method is a simplified approach to calculate the differential settlement gradients.

SEISMIC ANALYSES AND DISCUSSIONS

Dynamic analyses were performed to evaluate the seismic response of the proposed trickling filters. The base case analysis represents the in-situ ground conditions at the location of the proposed trickling filters and in the vicinity of the storm water retention pond. Figure 4(a) shows the excess pore pressure ratio R_u for the base case analysis. As illustrated, the upper 8 m to 10 m of the sand layer under and in the proximity of the proposed trickling filter liquifies in the base case analysis. In the base case, the southern crest of the storm water retention pond, the proposed trickling filter and existing trickling filter undergo horizontal displacements in excess of 3 m, 1.1 m, and 0.3 m towards the storm water pond, respectively. The shear plane that started from the toe of the storm water retention pond extends to under the proposed trickling filter in the base case. Seismic and short-term differential settlement gradients were estimated to be 330 mm and 420 mm, respectively, over 50 m for the proposed trickling filter in the base case.

The first mitigation alternative considered for limiting the displacements and differential settlement gradients of the proposed trickling filters was vibro-replacement stone columns ground improvement. Various lateral extents of stone columns ranging from 0 m, 10 m, 15 m, 20 m and 25 m beyond the edge of

the raft foundation of the proposed trickling filters were considered for the analysis. Based on the post-densification CPT results of previous stone column ground improvement performed at this site, the zone of vibro-replacement was assumed to extend to a depth of 30 m below the ground surface, and to be a homogeneous mass of sand with an average energy normalized standard penetration test (SPT) resistance in clean sand of $(N_1)_{60\text{-}cs}$=20 after stone columns installation. The analysis results for a select scenario, where stone columns extend to 20 m beyond the edge of the proposed trickling filter are shown in Figure 4(b). It is shown that performing ground improvement eliminates the liquefaction in the upper part of the sand layer in the vibro-replacement region. The shear plane that started from the toe of the pond does not extend into the stone columns area. Constructing stone columns to 20 m beyond the edge of the raft foundation, reduces the horizontal displacements of the proposed structure to 130 mm to the north, and reverses the northward movement of the existing trickling filters to about 140 mm towards the south. Seismic and short-term differential settlement gradients are predicted to be 70 mm and 140 mm, respectively, over 50 m for the proposed trickling filter in this scenario.

The second mitigation option analyzed for reducing the displacements of proposed trickling filters was vibro-replacement stone columns plus supplementary cutter soil mixing (CSM) configurations. The CSM was taken to consist of 2 rows of 0.5 m-wide panels interconnected by perpendicular panels at 4 m c/c spacing to form soil cells of 2.5 m x 3.5 m by 30 m deep. The configurations considered for the CSM wall location included north of the proposed trickling filters along the south side of the storm water retention pond, or south of the proposed trickling filters, or in both locations. The CSM wall location along the storm water retention pond was selected to evaluate the potential benefit of the CSM to reduce structure displacements as a result of soil movement near the pond crest. The wall location between the proposed and existing trickling filters was selected because previous ground improvement work on site had shown the CSM wall could be highly effective in reducing stone column installation-induced settlement of adjacent structures.

The CSM wall was modeled as a homogenous region using an elastic perfectly-plastic constitutive model with a Mohr-Coulomb failure criterion. The representative properties of the homogenous region were estimated by considering the area replacement ratio of the CSM wall and ignoring any contribution from the soil between the CSM panels. The unconfined compressive strength (UCS) of the CSM wall was assumed to be 5 MPa, based on the tests carried out for a similar CSM wall installed during previous ground improvement at this site. Figure 5 shows a conceptual layout of the stone columns and supplementary CSM wall south of the proposed trickling filters for a combined ground improvement and CSM width of 20 m. In actuality, the corners of the ground improvement zone could likely be trimmed to better fit the available space. The analysis results for a select scenario, where the supplementary CSM is modeled only at the south of the proposed trickling filters, and the combined width of stone columns and CSM extend to 20 m beyond the edge of the proposed structure, are shown in Figure 4(c).

The analyses show that replacing a 3.5 m-wide section of stone columns with a homogenous region representing the CSM wall for a combined ground improvement width of 20 m resulted in essentially the same displacements and differential settlement gradients as the stone columns alone extending to 20 m beyond the edges of the structure. In other words, the supplementary CSM wall south of the proposed trickling filters, or north of the proposed trickling filters (along the crest of the pond) does not appear to provide any significant benefit over the stone columns alone in the FLAC model. However, installing a CSM wall along the north side of the existing trickling filters increases the separation distance between the edge of stone columns and the existing trickling filters by 3.5 m resulting in lower stone column installation-induced settlements of the existing structures. As well, similar CSM walls had been installed during previous ground improvement at the site, and were found to be very effective in reducing stone column installation-induced settlement of existing structures in the proximity of the stone column zone.

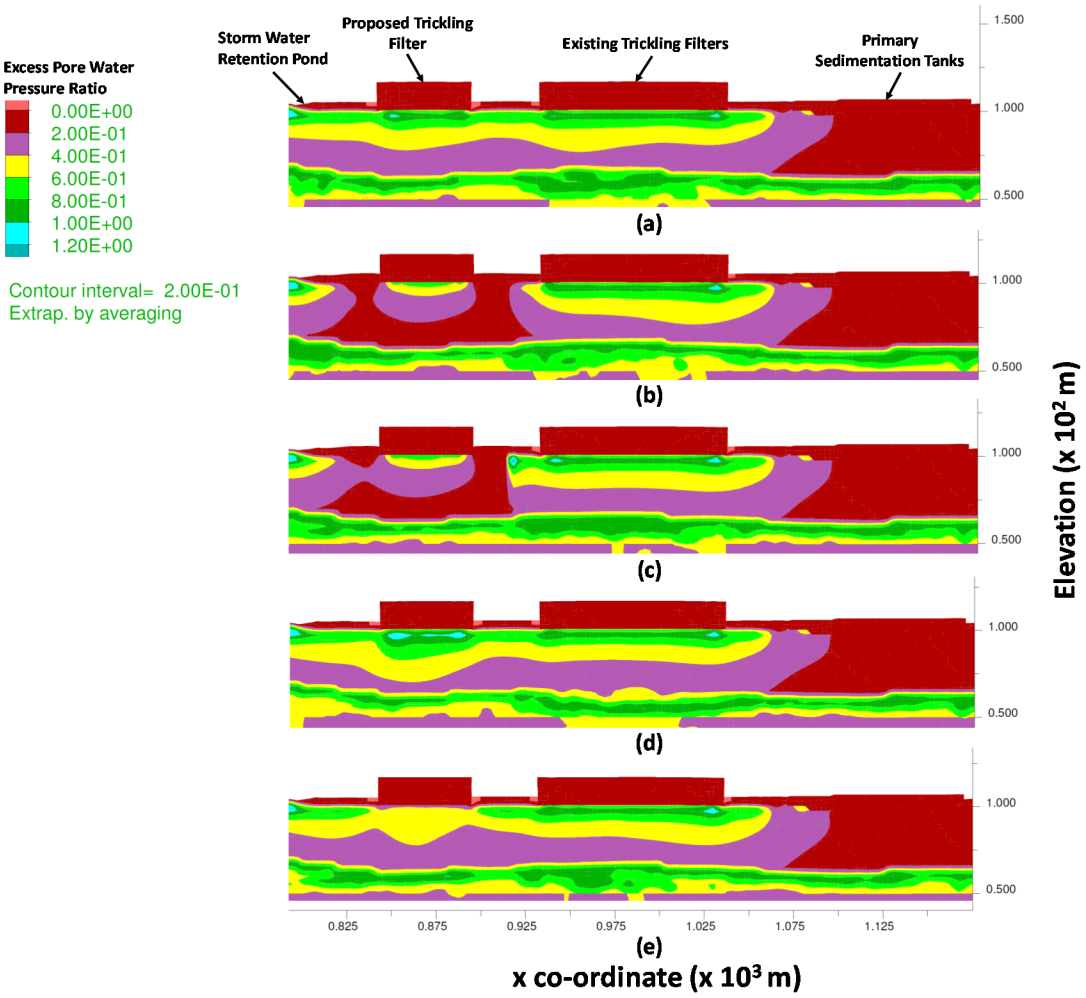


Fig. 4. Contours of the excess pore pressure ratio estimated at the end of earthquake for scenarios modeling the (a) base case, (b) stone columns under proposed trickling filters, (c) stone columns and CSM wall south of the proposed trickling filters, (d) piles under proposed trickling filters unconnected to the slab, and (e) piles under proposed trickling filters connected to the slab

The third mitigation option considered for reducing the displacements of proposed trickling filters was supporting the proposed structures on a piled raft foundation with 610 mm diameter, 12.5 mm-thick wall, open-ended, steel pipe piles driven to 50 m depth. Two scenarios were examined in the analysis, one with piles not connected to the raft foundation, but just functioning as soil reinforcement elements, and the second with piles structurally connected to the proposed trickling filter raft foundation. The analysis for a raft foundation with no ground improvement indicate that the raft foundation has adequate bearing resistance for the static and seismic load cases. The piles are only intended to reduce the seismic displacements to permit post-disaster immediate operation. Three different pile layouts with spacings of 3.0 m, 4.3 m and 5.8 m were examined. Stone columns or CSM walls were not included in combination with the steel piles.

The piles were modeled as structural elements connected to the soil mesh using normal and shear coupling springs. These coupling springs are nonlinear connectors that transfer forces and displacements between the pile elements and the grid at the pile element nodes. Figure 6 presents a schematic drawing of the pile element, coupling springs, and soil mesh in the FLAC model. The advantage of pile-spring model is that it allows relative movements between the pile and the adjacent soil and simulates the effect of the lateral displacement of soil around the piles as the pore pressure increases under seismic loading.

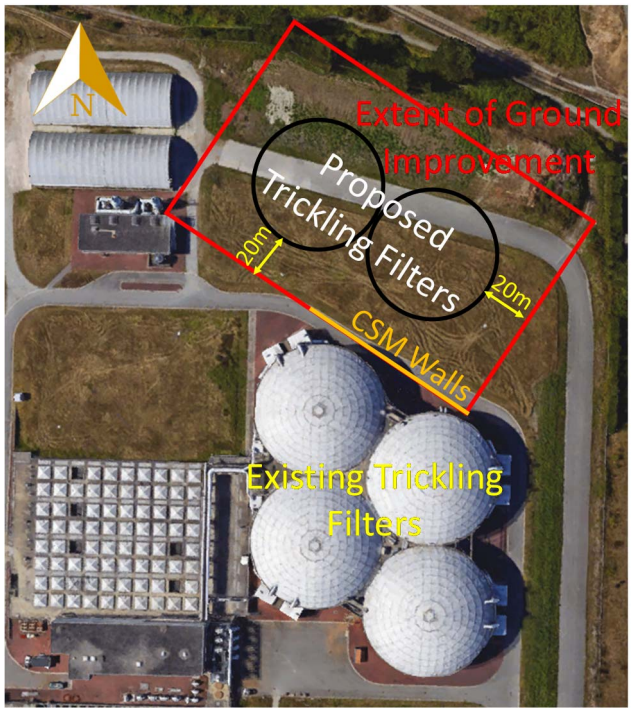


Fig. 5. Conceptual layout of vibro-replacement stone columns and supplementary CSM walls

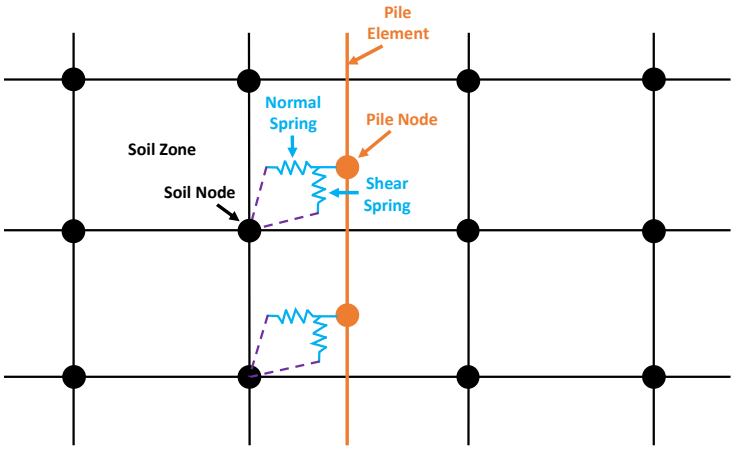


Fig. 6. Schematic drawing of the pile element, coupling springs, and soil mesh in the FLAC model

The stiffness and strength parameters of normal and shear coupling springs were proportional to the effective stress, and hence the excess pore pressure ratio R_u, in soils adjacent to the piles. For the static analyses, the normal and shear spring stiffness and strength were estimated based on the non-liquefied soil state. For the seismic analyses, the normal and shear spring stiffness and strength were progressively updated by calculating the instantaneous R_u in soils adjacent to the piles and then linearly interpolating for the spring stiffness and strength between spring parameters based on the non-liquefied soil state (R_u=0) and liquefied soil state (R_u=1).

For the scenario with piles not connected to the base slab, post-seismic settlements were conservatively estimated based on settlements of the ground surface under the slab. For the scenario with the piles connected to the raft foundation, the post-seismic settlement of the slab was assumed to be the same as the

settlement of the pile heads. In this scenario, the post-seismic settlement of piles was assumed to be the same as the settlement of the soil at the location of the neutral plane. Determining the location of the neutral plane is a complex analysis, particularly since the location of the neutral plane changes during and after the seismic event. Based on a previous analysis of pile-supported structures at this site, the neutral plane was assumed to occur at 50% of the pile length.

The analysis results for a pile spacing of 4.3 m are presented in Figure 4(d) for piles unconnected to the proposed trickling filter slab, and in Figure 4(e) for piles connected to the proposed structure slab. Table 2 presents the horizontal displacement, settlement and differential displacement gradient for the proposed and existing trickling filters under different analysis cases. As shown in Fig. 4(d), for the scenario with piles unconnected to the proposed trickling filter slab, the analyses indicate no change in pore pressure compared to the base case with no ground improvement. However, Fig. 4(e) shows that for the scenario with piles connected to the base slab, there is less excess pore pressure under the raft compared to the base case.

Horizontal displacements are between 230 mm (piles connected to slab) and 380 mm (piles unconnected to slab) depending on pile spacing. These displacements are comparable to the ground improvement case extending 10 m beyond the edges of the structure. Total long-term settlements vary from 480 mm to 710 mm depending on pile spacing and connection details, and are also larger than settlement for the ground improvement case extending 20 m beyond the edges of the proposed structure.

For the scenario with piles unconnected to the proposed trickling filter raft, differential settlement gradients improve slightly compared to the no ground improvement case. For the scenario with piles connected to the proposed trickling filter raft, differential settlement gradients were similar to the ground improvement

Table 2. Seismic and post-seismic displacements and differential settlement gradients for various analysis cases

Structure	Analysis Case	Horizontal Displacement (mm)	Settlement (mm)			Differential Settlement Gradient (mm over 50 m)	
			Seismic	Total Short-term	Total Long-term	Seismic	Total Short-term
Proposed Trickling Filters	Base Case – No GI under proposed trickling filters	-1120	120	410	620	330	420
	GI to 20 m beyond edges of proposed trickling filters	-130	110	280	490	70	140
	GI+CSM Wall south of proposed trickling filters	-120	120	300	510	70	120
	Piles 50 m long under proposed trickling filters, 4.3 m c/c, Unconnected to slab	-300	110	370	560	210	290
	Piles 50 m long under proposed trickling filters, 4.3 m c/c, Connected to slab	-250	110	300	520	40	140
Existing Trickling Filters	Base Case – No GI under proposed trickling filters	-300	80	400	610	160	240
	GI to 20 m beyond edges of proposed trickling filters	140	100	370	560	160	230
	GI+CSM Wall south of proposed trickling filters	150	70	380	580	160	220
	Piles 50 m long under proposed trickling filters, 4.3 m c/c, Unconnected to slab	-70	30	310	510	170	200
	Piles 50 m long under proposed trickling filters, 4.3 m c/c, Connected to slab	-10	80	380	570	190	240

Note: Negative horizontal displacement indicates movement towards the north.

case extending 20 m beyond the edges of the proposed structure and vary from 90 mm to 140 mm over 50 m depending the pile spacing. In the analyses with piles connected to the raft foundation, the total short-term and long-term settlement of the soil adjacent to the piles is approximately 100 mm to 120 mm more than the settlement of the piles. As the soil pulls away from the underside of the proposed trickling filter raft, the proposed structure could theoretically become supported by the piles alone. Hence, the raft foundation would need to be structurally robust to span between the piles.

The analyses indicate that all the alternatives considered have the potential to provide a comparable level of seismic and post-seismic performance. For the purpose of establishing conceptual-level budget for construction of the proposed trickling filters, both alternative II, i.e. vibro-replacement stone columns plus CSM walls, and alternative III, i.e. pile foundations unconnected to the proposed structure raft, were considered. These two mitigation alternatives are estimated to be of comparable cost and duration.

CONCLUSIONS

Finite difference seismic analysis of Annacis Island Wastewater Treatment Plant indicated that the proposed trickling filters would be subjected to large horizontal displacements and differential settlement gradients during earthquakes in absence of ground improvement or deep foundation due to the presence of liquefiable sand deposits and proximity to a storm water retention pond. The mitigation options considered for limiting the displacements and differential settlement gradients of the proposed trickling filters included: (I) Vibro-replacement stone columns ground improvement, (II) Vibro-replacement stone columns plus supplementary cutter soil mixing (CSM), and (III) Pile foundations with no ground improvement. Several extents and configurations were modeled for the ground improvement option, and various pile spacings and connection details were considered for the pile alternative. The conceptual design level FLAC analyses indicate that piles installed under the proposed trickling filters have the potential to provide a similar level of seismic and post-seismic performance as ground improvement extending 20 m beyond the edges of these proposed structures. However, since the piles do not need to extend beyond the edges of the proposed trickling filters, there is a benefit of much smaller footprint resulting in an increased separation distance between the piles and the existing structures, and hence, a potential reduction in the pile installation-induced settlement of other structures.

ACKNOWLEDGEMENTS

The writers sincerely appreciate Greater Vancouver Regional District (GVRD) for permission to publish this paper.

REFERENCES

Ishihara, K. and Yoshimine, M. (1992). “Evaluation of Settlements in Sand Deposits Following Liquefaction During Earthquakes”, Soils and Foundations, 32(1), p.173-188.

Itasca (2011). “FLAC - Fast Langrangian Analysis of Continua User’s Manuals.” Itasca Consulting Group Inc., Minneapolis, MN.

National Research Council Canada (2010). “National Building Code of Canada 2010”. National Research Council Canada, Ottawa, Ontario.

Sanin, M.V. (2010). “Cyclic Shear Loading Response of Fraser River Delta Silt”, Ph.D. Thesis, University of British Columbia, Vancouver, Canada.

DEVELOPMENT OF SITE-SPECIFIC ACCELERATION RESPONSE SPECTRA FOR A LIQUEFIABLE BRIDGE SITE

S. Ali Bastani, Ph.D., P.E., G.E., F. ASCE, GMU Geotechnical, Inc., 23241 Arroyo Vista, Rancho Santa Margarita, California, USA, Tel: 949.888.6513; abastani@gmugeo.com
Ashley Varni, M.Sc., E.I.T., GMU Geotechnical, Inc., 23241 Arroyo Vista, Rancho Santa Margarita, California, USA; avarni@gmugeo.com

ABSTRACT

Design acceleration response spectra (ARS) are directly correlated with dynamic forces and estimated dynamic bridge displacements, which make them a critical aspect of dynamic bridge design. Nonlinear site response analyses are performed for a 1,400-linear-foot bridge site with a S_C soil profile at the sides and a S_F soil profile in the middle to evaluate the soil profile effects on the bridge analyses.

One-dimensional seismic response analysis is commonly performed for site-specific response analysis. SHAKE or similar one-dimensional total-stress equivalent-linear approaches have been used since the 1970s. However, the equivalent linear method has deficiencies when the subsurface soils are susceptible to strain softening. Therefore, various assumptions are made when using the equivalent linear method by practitioners to estimate the S_F soil profile site response. With recent advancements in constitutive models, effective stress models have become more popular. Although the effective stress models are generally more complicated and require additional input parameters, they shed further light on the liquefaction mechanism and its effect on the surface ARS.

An equivalent-linear one-dimensional seismic response analysis and a non-linear effective-stress seismic response analysis, using DEEPSOIL, were performed to evaluate the ground surface ARS for a proposed bridge site in Orange County. The soil shear strengths were estimated based on cone penetration test results using empirical relationships. The shear modulus degradations (backbone curves) of soil layers were adjusted to match the estimated soil strength at failure. The ARS curves developed from each method were compared to determine the most suitable method for estimating a site-specific design ARS curve for a liquefiable site.

Considering that the bridge abutments and the outer bents are founded in bedrock, while the middle bents are founded in liquefiable soils, ARS curves were created for each subsurface condition. Taking into account limitations of the structural analysis software, recommendations were made to combine the multiple ARS curves into a single ARS curve for the structural bridge design.

Keywords: site response, liquefaction, nonlinear effective stress modeling

INTRODUCTION

Caltrans (2015) seismic bridge design is partially based on the bridge ductility. First, the displacement ductility capacities of the bents are estimated. Then, the displacement ductility demand is estimated based on the bridge period. The period of fundamental mode of vibration for each bent is estimated as follows, where "m" and "k" are the bent's associated mass and stiffness, respectively.

$$T = 2\pi \sqrt{\frac{m}{k}} \qquad [1]$$

© 2018 Deep Foundations Institute

Using the fundamental period of the bent, the corresponding spectral acceleration, "α", of the bent is estimated using the design spectrum, and the displacement demand is calculated from the following equation indicating that the design ARS have a direct effect on the magnitude of the displacement demand of the bridge.

$$\Delta_D = \frac{ma}{k} \quad [2]$$

The displacement demand ductility is calculated as the ratio of the displacement demand to the displacement capacity. Bridges passing over valleys generally have taller bents in the middle and shorter bents on the sides, resulting in higher fundamental periods in the middle and lower fundamental periods on the sides. However, Caltrans seismic design criteria mandates the fundamental periods of the bents be relatively the same (i.e., within a narrow fundamental period range), which forces the designer to increase the fundamental period of the side bents closer to the middle bents by deepening the bridge columns into the ground using isolation casing. Therefore, the 1st fundamental period of the bridges are generally moved towards the long periods.

Bridges with a longer period will be consequently affected by liquefaction of the subsurface soils which generally dampens the high frequency ground motions and amplifies the spectrum at longer periods. Therefore, an accurate evaluation of the liquefaction impact on the ARS is critical as it will have a significant impact on the bridge cost and its performance during the design earthquake.

PROJECT DESCRIPTION

A new bridge is proposed to span across a canyon in southern California as presented in Figure 1. The proposed bridge is 79 feet wide and 1,340 feet long measured along the bridge centerline. The bridge is an 8-span cast-in-place pre-stressed concrete box girder supported by two abutments and seven piers with each pier containing two columns. The bridge middle bents consist of 8-foot-diameter columns, which are bearing on 12-foot-diameter shafts.

In the vicinity of the proposed bridge crossing, the topography is characterized by a broad and gently sloping canyon bottom area that is up to about 1,000 feet wide. The canyon bottom is gently sloped with an approximate gradient of one degree towards southwest. The margins of the canyon are bounded by natural slopes that typically ascend flatter than 1.6H:1V (Horizontal:Vertical) up to elevated terraces. The steepest natural slopes are located at the southeastern abutment location. Slopes are generally flatter at the northwest abutment location, with a maximum gradient of 2.4H:1V.

The recent field investigations at the proposed site consisted of seven rotary wash borings, five Cone Penetration Tests (CPTs), three bucket auger borings, and one corehole. Surficial alluvium/older alluvium and lake deposits were observed during the recent subsurface exploration in the subject canyon up to 78 feet below the existing ground surface. The soils generally consist of loose to medium dense sand and silty sand interfingered with soft to firm silts and clays. Within the canyon, groundwater fluctuates with season and climate, and the static groundwater level generally exists at 0-10 feet below ground surface within the alluvial and lake deposits.

The site is located in the seismically active region of southern California. The San Joaquin Hills Blind Thrust fault, Newport-Inglewood (Offshore) fault, Elsinore fault, and South San Andreas fault zones are located about 11, 15, 25, and 77 miles from the site, respectively. The bridge spans over a potentially liquefiable creek bed with a high groundwater table. Bridge abutments and two of the side bents are underlain by nonliquefiable terrace and bedrock deposits.

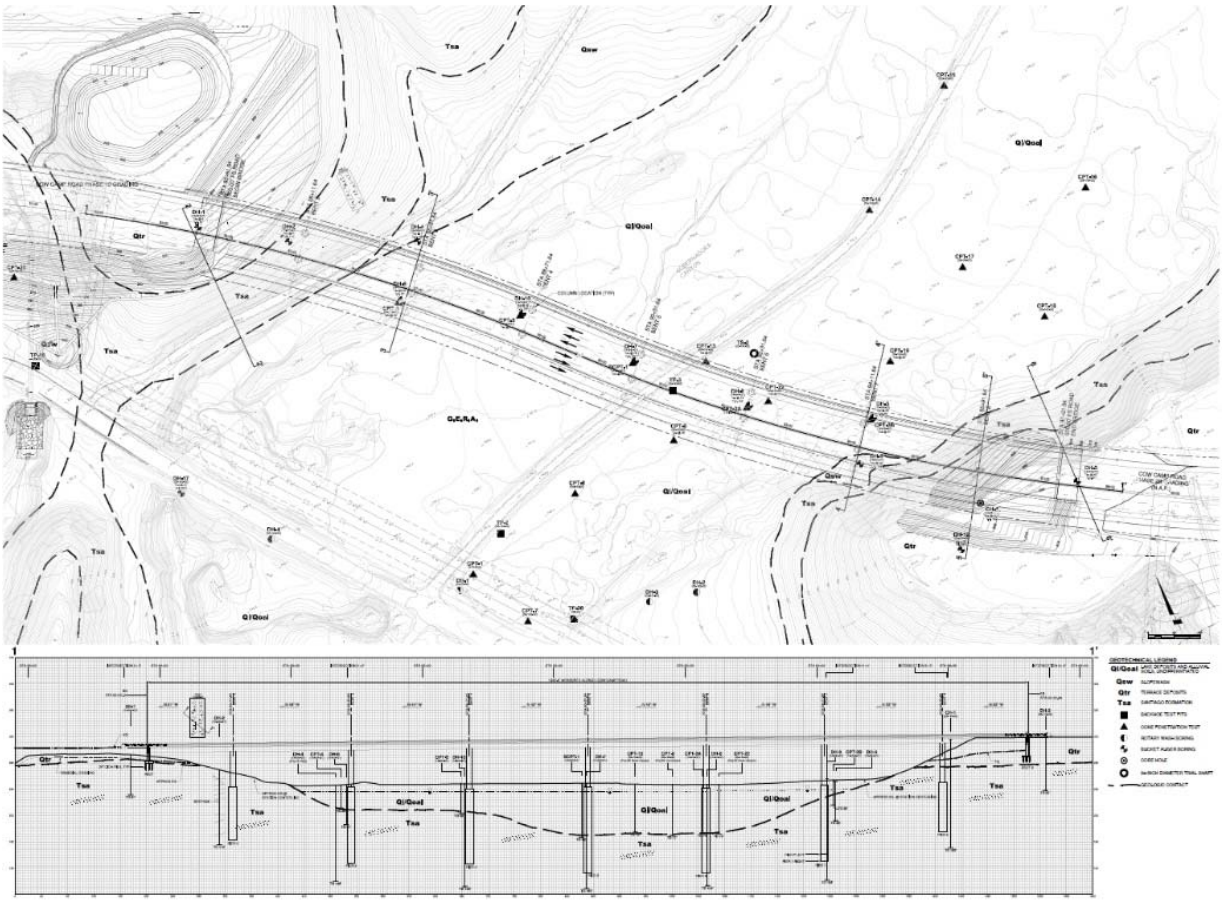


Fig. 1 - Proposed bridge profile.

LIQUEFACTION

Multiple liquefiable layers were identified using the Robertson (2009) method. Figure 2 presents the cyclic resistance ratio (CRR) profile and the cyclic stress ratio (CSR) for the design earthquake with an average return period (ARP) of 975-year at a seismic CPT at Bent 5 which was used as the representative profile for the deepest part of the alluvial deposits at the subject site. This figure also indicates that the liquefaction safety factor decreases by depth for layers with similar CRRs.

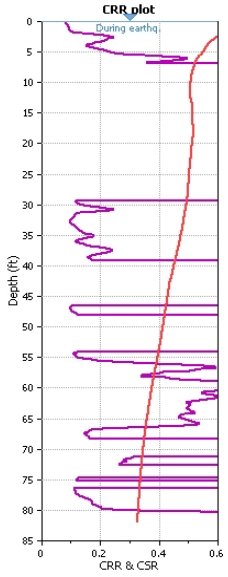


Fig. 2- CRR & CSR Profiles

SEISMIC HAZARD ANALYSIS

Three seismicity levels with ARP of 72-, 150-, and 975-year were considered in our evaluation. A bedrock average shear-wave velocity of 484 m/s was assumed for the reference rock and non-liquefied acceleration response spectra (ARS). The bedrock 975-ARP ARS was obtained from Caltrans ARS Online Version 2.3.06. The reference bedrock ARS for the other two return periods were estimated using OpenSHA Version 1.4.0 (Field et. al, 2003). In addition, ARS for a non-liquefied site using a V_{S30} of 229 m/s (measured at the seismic CPT with deep alluvial deposits) was also evaluated for the site using the same procedures. Figure 3 presents a comparison of bedrock and non-liquefied ARS based on the empirical relationships.

The ground motion hazard for three events were deaggregated using USGS Beta-Unified Hazard Tool. The deaggregration showed that earthquakes at a mean distance of about 31 to 38 kilometers and a mean magnitude of 6.7 dominated the hazard for 72- and 150-ARP events at the project site. The 975-ARP EQ is associated with activities at closer proximities with an approximate mean distance of 18 km and a mean magnitude of 6.6.

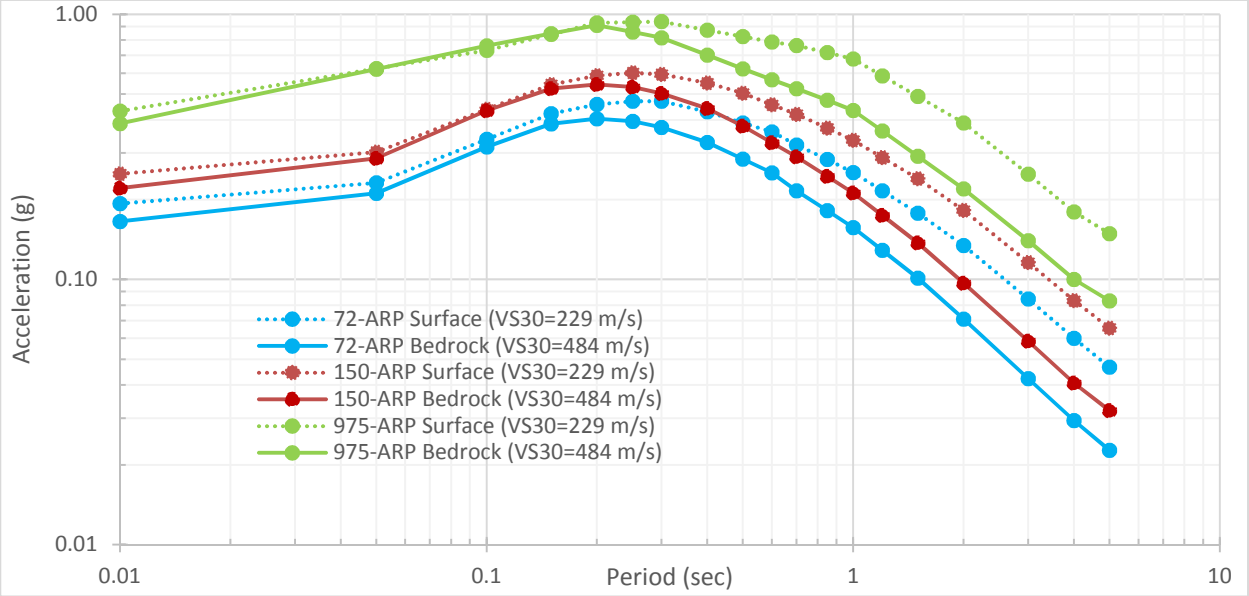


Fig. 3 – Bedrock and Non-Liquefied Surface ARS

GROUND MOTION SELECTION

Due to the close proximity of the San Joaquin Blind Thrust, Newport-Inglewood (strike slip), and Elsinore Fault Zones with different rupture mechanisms (reverser and strike slip), the criteria as presented in Table 1 was used to select seven ground motion recordings.

Table 1 – Ground Motion Search Parameters

Parameter	Range
Spectral Shape	To be consistent with the design Bedrock ARS
Magnitude	6 to 7
Distance	5 to 30 km & One Long Distance for San Andreas
V_{S30}	450 m/s to 550 m/s
Target ARS	Design 975-ARP ARS
Fault Type	Blind Thrust/Reverse & Strike Slip

For each selected horizontal ground-motion component, the response spectrum of the record was compared with the site design spectrum (target spectrum of 975-ARP). A distanced Darfield ground motion was selected as a potential distanced event that may affect the site with longer duration. Detailed information of the selected time histories and their associated seismological characteristics are summarized below in Table 2. Data was obtained from the PEER website Fault Normal (Rotated) ground motion to also capture the potential natural directivity effects.

A bridge period of 2.36 seconds was provided for this analysis by the Project Structural Engineer. A period range of 0.45 seconds to 3.75 seconds was utilized to yield the average ARS of the scaled ground motions to be approximately at or greater than the design bedrock ARS.

Table 2 – Selected Ground Motion Time Histories

Event	Station	Record Sequence Number	M_w	Mech.*	R_{rup} (km)	V_{S30} (m/s)	Unscaled PGA (g)
Iwate_ Japan	IWTH24	5656 (H1)	6.9	BT/R	5	486	0.53
Cape Mendocino	Centerville Beach Naval Facility	3746 (H2)	7.0	BT/R	18	459	0.48
Iwate_ Japan	Kurihara City	5818 (H1)	6.9	BT/R	13	512	0.43
Darfield_ New Zealand	OXZ	6948 (H2)	7.0	SS	31	482	0.15
Chi-Chi_ Taiwan-04	CHY080	2739 (H1)	6.2	SS	13	496	0.12
Imperial Valley-06	Cerro Prieto	164 (H2)	6.53	SS	15	472	0.16
Darfield_ New Zealand	WAKC	6980 (H1)	7.0	SS	73	484	0.13

* Mechanism: BT: Blind Trust, SS: Strike Slip, R: Reverse.

SITE RESPONSE ANALYSIS

One-dimensional effective stress finite element site response analyses were performed using DEEPSOIL Software Version V6.1.7.0 (Hashash, 2016) for the above three return periods (i.e. 72-, 150-, and 975-ARP). The scaled ground motions were applied as outcropping bedrock motions at the base of the one-dimensional model. Soil properties were estimated based on the measured shear wave velocities at the recent CPT soundings, the estimated shear strengths based on shear strength tests and CPT results, and an idealized subsurface stratification at the area of the central bridge bent with the deepest alluvium layer. The adopted idealized subsurface profile is presented in Figure 4.

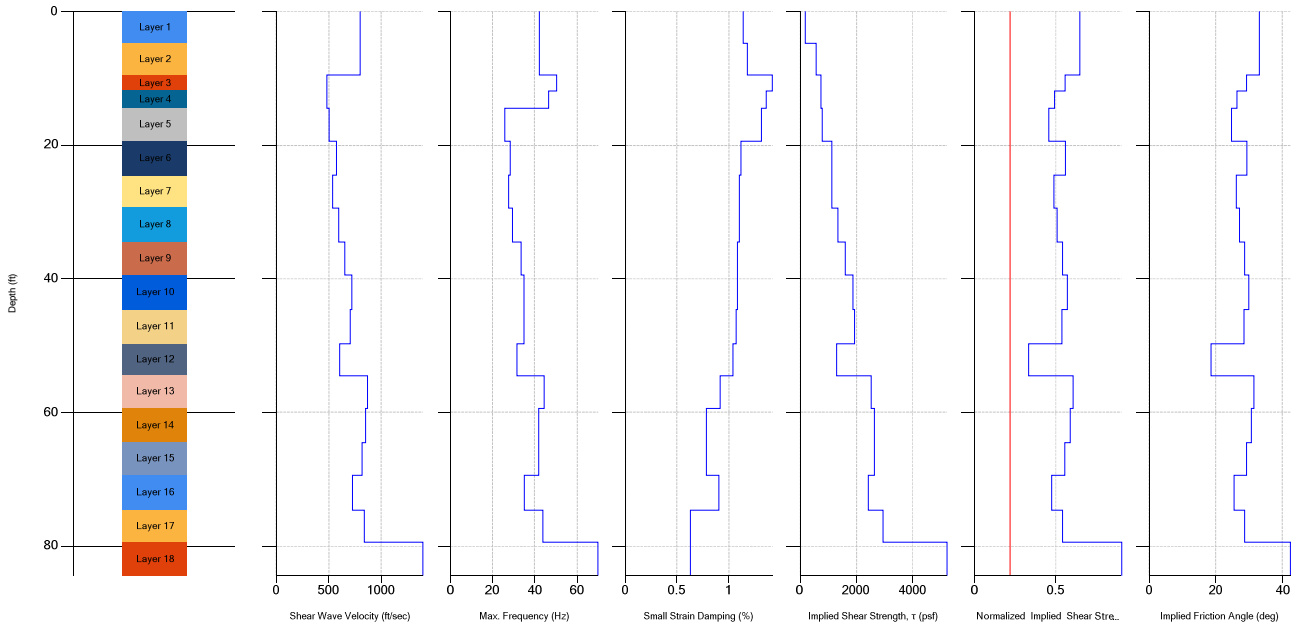


Fig. 4 – Adopted Idealized Profile

The site response analyses were performed using equivalent linear and nonlinear effective stress methods. Menq (2003) and Darendeli et al. (2001) shear modulus degradation and damping curves were utilized for granular and fine-grained soils, respectively, to capture the confining pressure effects on the backbone

curves. DEEPSOIL's General Quadratic/Hyperbolic Model was implemented to be able to adjust the shear strength of soil layers. The shear strength of the soil layers was adjusted to meet the expected layer shear strengths based on the laboratory tests and CPT results prior to liquefaction. Non-Masing Unload-Reload rule was also applied in the analyses to set forth the best effort to simultaneously fit the modulus degradation and damping curves.

The bedrock ground motions were amplified using both equivalent linear and nonlinear effective-stress methods for the low intensity 72- and 150-ARP ground motions. Softening of a deep clay layer (Layer 12) was observed during the slightly higher intensity shaking associated with the 150-ARP and the higher intensity 975-ARP ground motions. 975-ARP ground motions triggered liquefaction at a minimum of one shallow sandy layer (Layer 8 at a depth of 30-35 feet) at four of the seven ground motions, and two layers (Layers 8 and 16 at a depth of 70-75 feet) in the remaining three ground motion time histories, resulting in significant dampening of the surface ground motion ARS at short periods.

Figure 5 presents the ratio of the average of the nonlinear effective-stress surface ARS for the seven ground motions and the equivalent linear analyses. This figure indicates that the ARS generated by the nonlinear analyses were on average less than the equivalent linear ARS in short periods less than 1 second. The nonlinear ARS became greater than the equivalent linear ARS at long periods (>1-1.5 seconds) for low intensity shaking (72- & 150-ARP earthquakes) with a lower potential for inducing liquefaction. However, the ratio stayed flat with an increase of the ground motion period. The higher intensity shaking (975-ARP earthquake) had induced liquefaction in one or multiple layers and generally lowered the average nonlinear surface ARS relative to the average equivalent linear ARS with an exception of the long periods (>6 seconds). Stewart et al. (2008) and Kim et al., (2016) also showed that the nonlinear analysis results in lower spectral accelerations than the equivalent linear analysis for higher shaking levels, which was attributed to the larger high-strain damping by the nonlinear models.

The one-dimensional equivalent linear site response analysis is expected to provide a more conservative ARS than the one-dimensional nonlinear effective stress methods at the short periods; however, this conservatism is diminished at the long periods. Therefore, the nonlinear soil response and liquefaction effects should be considered for structures with long fundamental periods such as bridges and base-isolated buildings.

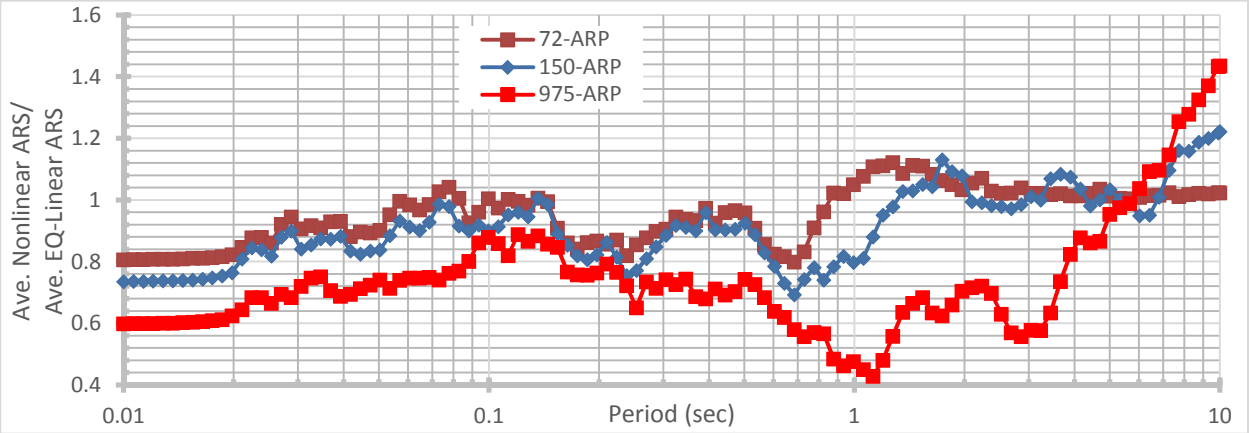


Fig. 5 – Ratio of Average Nonlinear ARS to Average EQ-linear ARS

Assuming that a structure with a short fundamental period of oscillation is located on relatively uniform and extended liquefiable soil deposits (i.e. wide zone of the deposits relative to the structure), and the structure is designed for the other liquefaction consequences (i.e., earthquake-induced settlement and lateral spreading), the nonlinear effect stress response analysis appears to result in a more economical ARS curve.

The liquefiable layer is considered to be infinitely extended in the one-dimensional models. Therefore, the ground motion dampening using these models could be exaggerated relative to the actual ground motions in the fields with localized liquefiable layers. Consequently, the extent of the liquefiable deposits need to be accurately assessed from the site geology, sedimentation history of the site, and via adequate field investigations.

Figure 6 presents the ARS for the individual ground motions for the equivalent linear and nonlinear analyses. In addition, the figure presents the Caltrans ARS for bedrock, nonliquefied soil site, the average of the estimated ARS, and the recommended enveloped ARS. As noted and shown on Figure 6, the equivalent linear analysis resulted in a significantly higher ARS at the midrange periods between 0.5 and 1.5 seconds. The average of the nonlinear effective-stress analyses was generally less than the Caltrans surface ARS; however, three out of the seven ground motions resulted in slightly higher ARS than the Caltrans soil site ARS at the periods ranging between 0.25 and 2.5 seconds.

The recommended ARS envelopes the Caltrans soil site and the nonlinear effective-stress ARS in order to utilize only one ARS curve for the structural analysis of the bridge while considering the bridge spanning over nonliquefiable terrace and bedrock deposits at the side bents and the variable depths of liquefiable deposits in the middle.

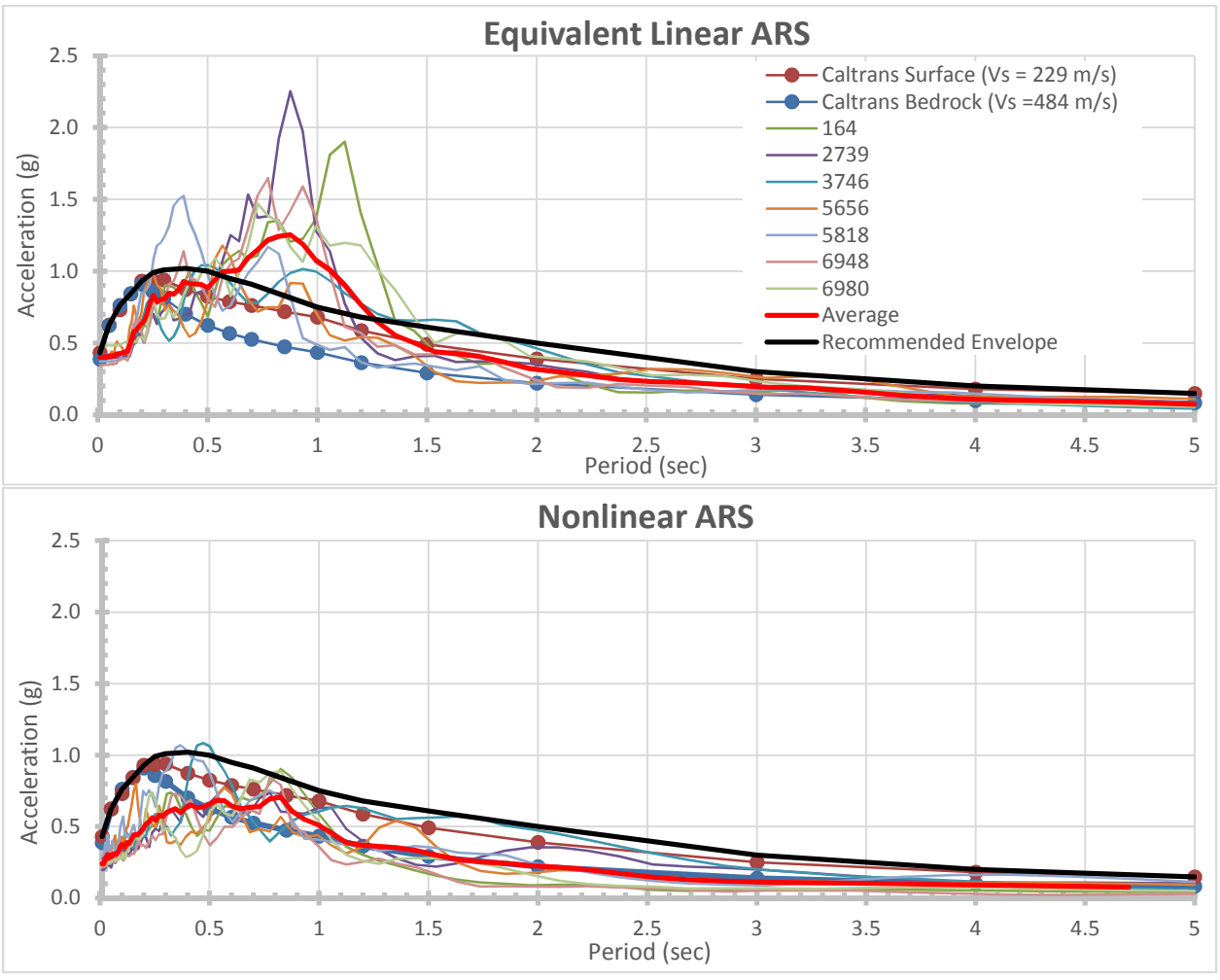


Fig. 6 – Equivalent and Nonlinear Effective-Stress 975-ARP Surface ARS

Therefore, the recommended ARS includes both the short period ground motions from the Caltrans soil site ARS for the abutments and bents that are not affected by the liquefiable soils in the canyon, and amplification of the long periods due to the liquefaction of the soft, deep deposits, avoiding potential overdesign and cost increases implied by the equivalent linear methodology.

CONCLUSIONS

A site response analysis was performed to evaluate the acceleration response spectra for a bridge spanning over non-liquefiable and liquefiable soil profiles. The subject bridge included a total of nine bents. The bridge abutments and the two side bents were founded on nonliquefiable dense terrace deposits and bedrock. The middle five bents of the bridge were founded on liquefiable deposits with variable depths ranging between 35 feet and 80 feet. A single surface ARS was requested for designing the subject bridge.

Nonlinear effective stress and equivalent linear site response analyses were compared for the subject site. In general, the equivalent linear analyses resulted in lower interlayer shear strains and globally amplified the ground motions resulting in a conservative ARS which will potentially incur additional cost. The authors recommend enveloping the results of the ARS from Caltrans and/or a site-specific seismic hazard analysis using empirical relationships and nonlinear effective stress analyses results to cover both nonliquefied and liquefiable soil profiles. The proposed method will eliminate the potential excessive amplifications induced by regular equivalent linear analysis and prevent unfounded assumptions for artificial shear modulus reduction to model liquefaction.

Site response analysis is still an evolving field of geotechnical engineering. Groholski et al. (2016) showed that variation of several parameters may result in underestimation or overestimation of the site response. Stewart (2016) discussed the site response uncertainty and its implications on seismic risk characterization. A limited number of ground motions are generally used for a site response analysis in practice. Therefore, results of nonlinear effective-stress analysis should be compared with the equivalent linear analysis and applicable regulatory code requirements in conjunction with engineering judgment in evaluating the final ARS recommendation.

REFERENCES

Darendeli, M.B. (2001), Development of New Family of Normalized Modulus Reduction and Material Damping Curves, Department of Civil, Architectural and Environmental Engineering, The University of Texas, Austin, Texas.

Field, E.H., T.H. Jordan, and C.A. Cornell (2003), OpenSHA: A Developing Community-Modeling Environment for Seismic Hazard Analysis, Seismological Research Letters, 74, no. 4, p. 406-419.

Groholski, DR, YMA Hashash, B Kim, M Musgrove, J Harmon, and JP Stewart (2016). "A simplified non-linear shear model to represent small-strain nonlinearity and soil strength in one-dimensional seismic site response analysis," J. Geotech. Geoenviron. Eng., 142(9), 04016042.

Hashash, Y.M.A. (2016), DEEPSOIL v6.1, Nonlinear and Equivalent Linear Seismic Site Response of One-Dimensional Soil Columns, Department of Civil and Environmental Engineering, University of Illinois at Urbana-Champaign, Dated June 22, 2016.

Kim, B, YMA Hashash, JP Stewart, EM Rathje, JA Harmon, MI Musgrove, KW Campbell, and WJ Silva (2016). "Relative differences between nonlinear and equivalent-linear 1D site response analyses," Earthquake Spectra, 32, 1845-1865.

Menq, Farn-Yuh (2003), Dynamic Properties of Sandy and Gravelly Soils, Department of Civil, Architectural and Environmental Engineering, The University of Texas, Austin, Texas. Metropolitan Water District, 2013, "Geotechnical Guidelines," Dated February 15, 2013.

Robertson, P. K., 2009, Interpretation of Cone Penetration Tests -a unified approach., Canadian Geotechnical Journal, Vol. 46, No. 11, pp 1337-1355

State of California Department of Transportation (Caltrans), 2015, Bridge Design Practice, Fourth Edition.

Stewart, J. P., Kwok, A. O.-L., Hashash, Y. M. A., Matasovic, N., Pyke, R., Wang, Z., and Yang, Z., 2008. Benchmarking of Nonlinear Geotechnical Ground Response Analysis Procedures, PEER Report 2008/04, Pacific Earthquake Engineering Research Center, University of California, Berkeley, 186 pp.

Stewart, JP (2016). "Joyner Lecture: Site response uncertainty and its implications for seismic risk characterization," EERI 2016 Annual Meeting, San Francisco, CA; SSA 2016 Annual Meeting, Reno, NV Seismological Research Letters, 87:2B, pp 516 (abstract). Video of presentation, from USGS Menlo Park, July 2016.

KINEMATIC RESPONSE CHARACTERISTICS OF A PILED RAFT FOUNDATION

Ramon Varghese, Indian Institute of Technology, Madras, Chennai, India, ramonvarghese@gmail.com

Boominathan A. Indian Institute of Technology, Madras, Chennai, India, boomi@iitm.ac.in

Subhadeep Banerjee, Indian Institute of Technology, Madras, Chennai, India, subhadeep@iitm.ac.in

ABSTRACT

Pile raft foundation system has been accepted as an economic foundation design for high rises and heavily loaded structures. Seismic response analysis of PR foundation systems involves complex pile-soil-pile interaction as well as raft-soil-pile interactions, for which simplified methods have limitations. Kinematic rocking of a pile group is known to be influenced significantly by the pile configuration. The presence of an embedded pile cap, or a raft, as in the case of a piled raft can further alter the dynamic characteristics of a pile group-soil system. In the present study, frequency dependent kinematic response factors are evaluated for piled raft foundation, using the substructuring approach based ACS SASSI program. Performance of the numerical analysis methodology is first evaluated with results from analytical and experimental studies reported in literature. The effect of pile layout on kinematic response is then studied for a piled raft in clay system based on a centrifuge shaking table test reported in literature. Kinematic response factors and horizontal impedances were determined for varying pile spacing ratios. The influence of raft has been found to increase kinematic translation by up to three times in the piled raft in clay system. Pile configuration is found to play a significant role in kinematic rocking of piled rafts. The presence of raft is observed to significantly reduce dynamic rotational stiffness coefficient in the dimensionless frequency range of 0.23 to 0.6, and increase damping coefficient after a dimensionless frequency of 0.4, for all pile configurations studied. The effect of an embedded raft is hence an important consideration while evaluating foundation input motion as well as impedances of piled raft foundations.

Keywords : piled raft, kinematic response, SASSI

INTRODUCTION

The Piled raft foundation (PR), is a composite foundation system that facilitates load sharing between pile and raft. It is an economic foundation option for high rises and heavily loaded structures. Soil structure interaction (SSI) in PR system involves raft-soil-pile, and pile-soil-pile interactions which needs to be considered in static or dynamic SSI analysis. The effect of pile can have substantial influence on foundation input motion, for seismic analysis (Di Laora et al. 2017). Piles are observed to depress a wide spectrum of the seismic excitation (Fan et al., 1991, Di Laora & de Sanctis, 2013). Although kinematic response of pile groups have been extensively studied in the past, the influence of the presence of raft on kinematic response characteristics of pile groups has not received much attention.

The effect of an embedded pile cap or raft on dynamic impedances of foundation was studied by researchers such as Liu and Ai (2017). Their findings suggest a prominent impact on vertical impedance of pile group with ground contacting cap, in the presence of soft layer below raft, at higher frequencies.

© 2018 Deep Foundations Institute

Emani and Maheshwari (2009) studied the problem of impedances of pile groups with ground contacting caps, and concluded that the effect of embedded pile cap may have a detrimental effect in comparison with free standing pile cap. From these studies, it is postulated that an embedded pile cap/raft can result in significant differences in dynamic stiffness and damping parameters, particularly at higher frequencies.

In the present study, kinematic response characteristics of a piled raft foundation system are studied by carrying out substructuring based three dimensional numerical analyses. The influence of pile layout, on kinematic translation and rotation, of a piled raft in clay, is investigated. The effect of an embedded raft on translational and rotational response is evaluated by analyzing piled rafts and pile groups with similar pile configuration.

KINEMATIC RESPONSE OF PILE FOUNDATIONS

It has been pointed out by past researchers (Mylonakis et al., 1997) that pile foundations filter out high frequency components while inducing a rotational component at the pile head. Foundation rotation induced by pile may lead to beneficial or detrimental responses, and hence cannot be ignored (Sextos et al., 2015). Both pile layout, and number of piles have been found to have an influence on kinematic rotation induced at the pile head. However, analyses reported in literature do not consider the influence of an embedded cap or raft, as in the case of piled raft foundation.

Kinematic response of pile foundation is a frequency dependent phenomenon. Frequency is commonly represented in a dimensionless form, a_o defined as in the following equation.

$$a_o = \frac{\omega d}{V_s} \quad [1]$$

where ω is frequency in rad/s, d is diameter and V_s is the shear wave velocity of the soil deposit.

Kinematic response at the pile head level can be portrayed in the form of kinematic response factors. The factor for translation (I_u) and rotation ($I_\emptyset$) are defined as in the following equations.

$$I_u = \frac{u_{PR}}{u_{ff}} \quad [2]$$

$$I_\emptyset = \frac{\emptyset_{PR}.d}{u_{ff}} \quad [3]$$

METHODOLOGY

Flexible Volume Sustructuring Method Using SASSI

The substructuring method involves partitioning a dynamic system into several subsystems. The global response is then obtained using the principle of superposition, essentially making the analysis linear. The flexible volume substructuring method (FVSM) in ACS SASSI program is adopted for SSI analysis in the present study (Lysmer et al. 1981, Ghiocel 2012). This method partitions the soil-foundation-structure system into three sub structures as shown in Fig. 1. Finite elements are used to model the foundation and near field soil, while a formulation based on the use of fundamental Green's functions, for layered media (Kausel, 1986), is utilized to model the free field soil. The FVSM method considers all nodes in the embedded part of foundation as interaction nodes. Complex impedances are calculated at each of the

interaction nodes, for each frequency of analysis. Nonlinear soil behavior is taken into account by considering strain dependent modulus and damping values for soil layers. For transfer function analyses discussed in the present study, the control point is defined at the ground level. The simplified equation of motion in frequency domain is presented in equation [4].

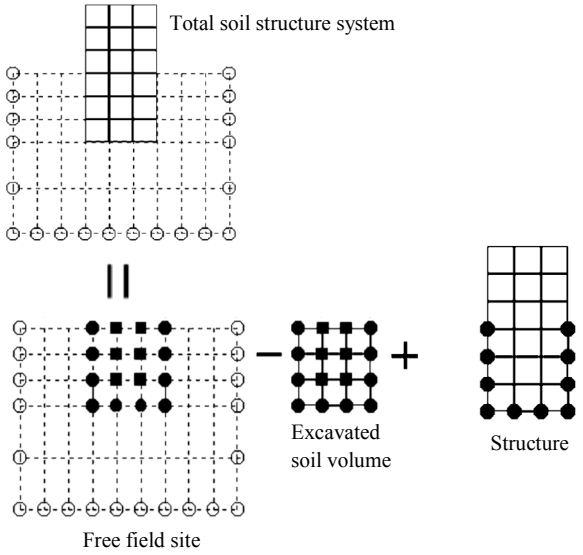


Fig 1. Implementation of the Flexible Volume Method (from Ostadan and Deng, 2010)

$$\begin{bmatrix} C_{ss} & C_{si} \\ C_{is} & (C_{ii} - C_{ff} + X_{ff}) \end{bmatrix} \begin{Bmatrix} u_s \\ u_f \end{Bmatrix} = \begin{Bmatrix} 0 \\ X_{ff} u_f{}' \end{Bmatrix} \quad [4]$$

In equation [4], C is the complex frequency dependent stiffness matrix and subscripts *s, i* and *f* refer to degrees of freedom for nodes at the superstructure, basement and excavated soil, respectively.

There are several options to model piles using finite elements. The technique that involves the use of a central beam element connected to peripheral nodes by means of rigid links is adopted in the present study. The volume occupied by pile in this method, would remain open apart for the framework of beam elements inside. Details of this modeling technique can be found in Jeremic et al. (2002) as well as Mayoral and Romo (2015). In order to capture pile-sol-pile as well as raft-soil-pile interactions, it becomes essential to explicitly model adjacent soil elements between piles. In the present study, soil elements are modelled using brick elements.

Performance Evaluation

The proposed methodology was used to evaluate kinematic response factors for a pile group reported by Fan et al. (1991). A 2x2 pile group model with spacing to diameter (*s/d*) ratio of 3, in homogeneous elastic soil layer is modeled. The case with *l/d* of 20 and E_p/E_s value of 1000 was considered. The soil between piles in the pile group was explicitly modeled using brick elements, to capture pile-soil-pile interaction. The pile cap was modeled using brick elements with no contact with soil elements at ground level. The kinematic response factors in translation and rotation, obtained at the pile cap level are presented in Fig. 2 (a) and (b). The simulation follows closely the analytical result reported in literature, apart from an under estimation of rotation beyond a dimensionless frequency range of 0.3.

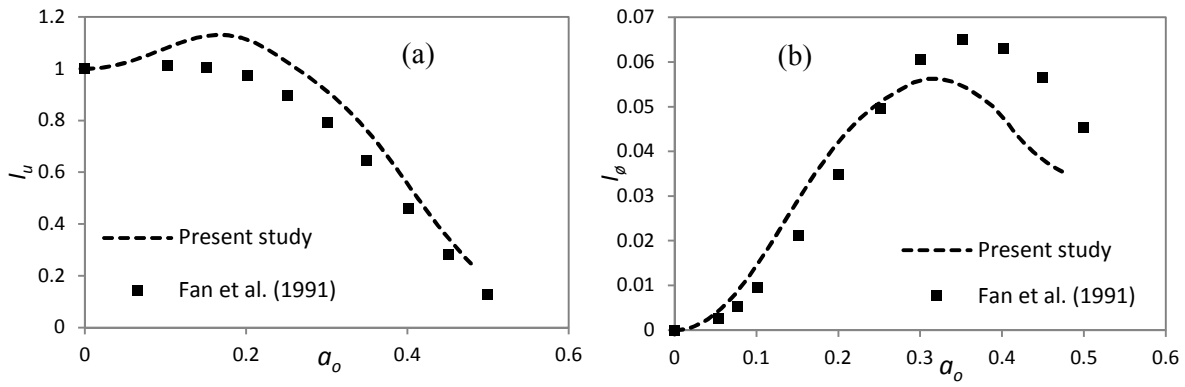


Fig 2. Kinematic response factor in (a) translation and (b) rotation for a 2x2 pile group

Another model was developed to simulate a centrifuge shaking table test with a piled raft foundation embedded in clay overlying sandy stratum, as reported in Banerjee et al. (2014). The prototype scale foundation model had four piles of 0.9m diameter and 13m length connected to a raft with dimensions 12.5m x 7.5m x 0.5m. An illustration of the PR clay system is presented in Fig. 3(a). Prototype flexural rigidity of the hollow steel with in-fill concrete piles was 94.5 GPa, and its unit weight was 25 KN/m3. A Vertical load of 605 tonnes, was applied on the top surface of the raft to simulate load from steel plates placed over the raft in the experiment. The soil layers consisted of clay layers with a shear wave velocity (V_s) of 45m/s at the top and 140 m/s towards the pile tip. The pile tip rested on a dense sandy stratum. The reader may refer to Banerjee (2009) for details of the input motion and test setup. Time history and Fourier spectra of the two input motion are presented in Fig 4. The iterative scheme to obtain strain dependent dynamic soil properties similar to that discussed in Schnabel (1972), is adopted using the inbuilt module in the ACS SASSI program.

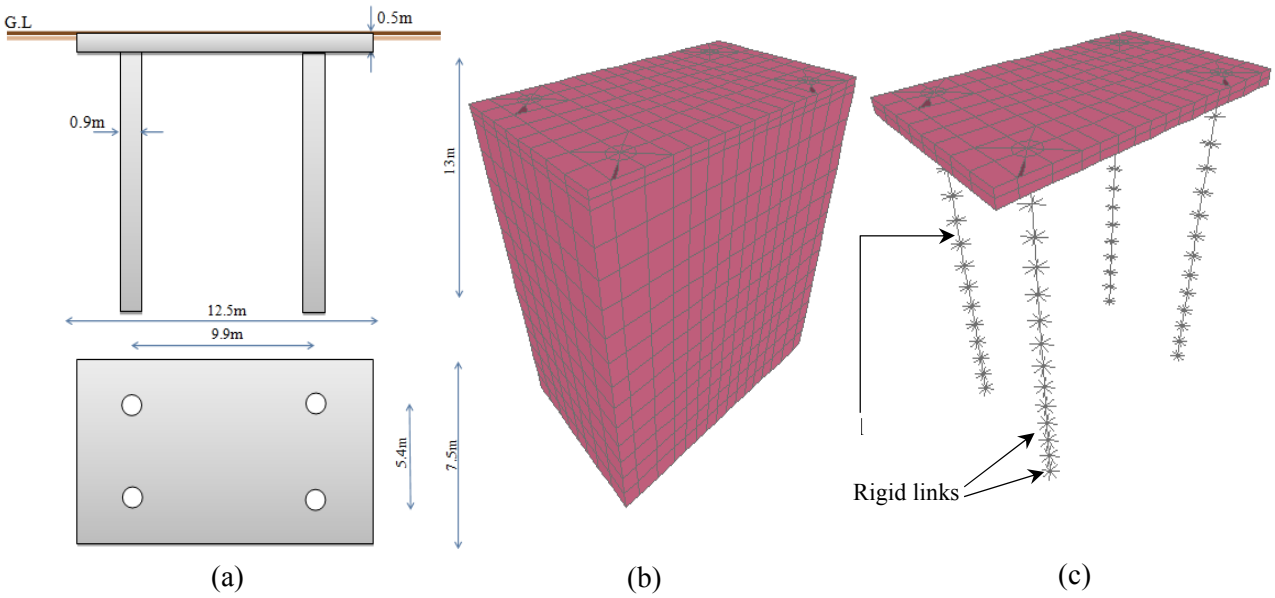


Fig 3. (a) Details of the piled raft foundation in clay (b) FE mesh of foundation with adjacent soil elements and (c) FE model of pile and raft

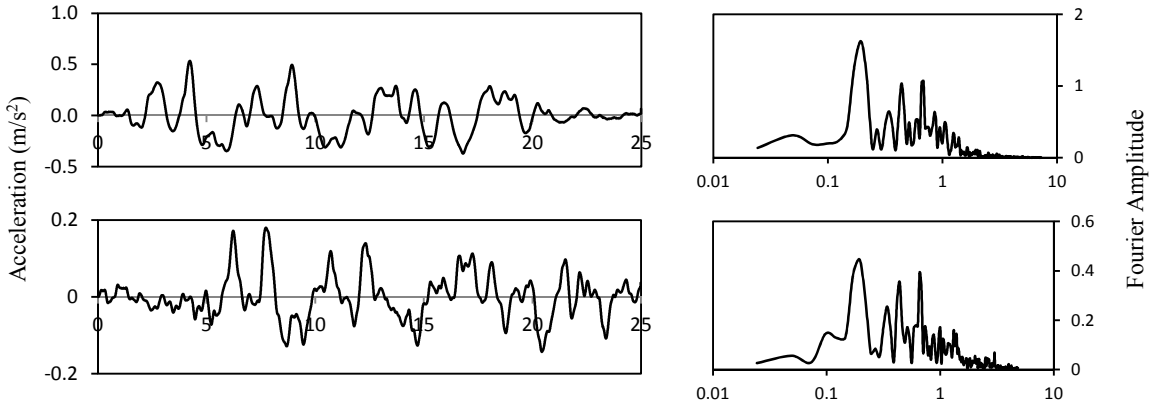


Fig 4. Time history and Fourier spectra of the first and second input motion

The raft was modeled using eight noded brick elements and piles were modeled using the central beam and rigid link technique as shown in Fig. 3(b) and (c). The beam elements of pile were 'inserted' into the raft, making contact with three nodes of the brick elements, and thus facilitating transfer of moments.

Response spectra obtained at the top of raft from the analysis, for the two input motions is presented along with that obtained from the experiment, in Fig. 5 (a) and (b). The simulation is found to reproduce predominant peaks observed in the experimental results. Peak spectral ordinate for the first input motion case, is underestimated by nearly 10% by the analysis. The presence of a couple of low period peaks is also observed in the simulated spectra. However this effect was also observed in nonlinear finite element simulations reported by Banerjee (2009).

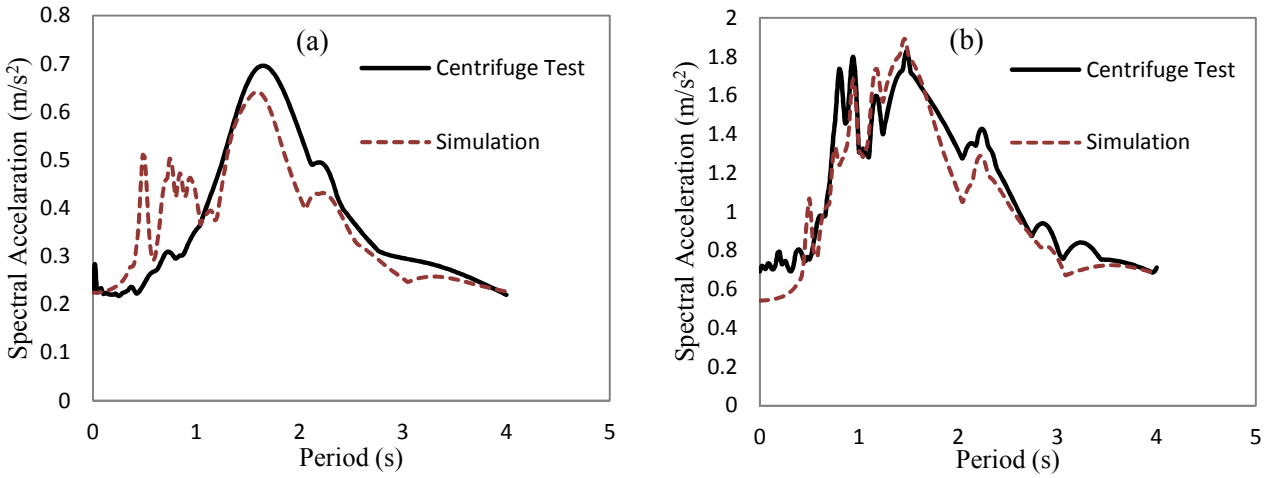


Fig. 5. Response spectra at the top of raft, for (a) first and (b) second input motions.

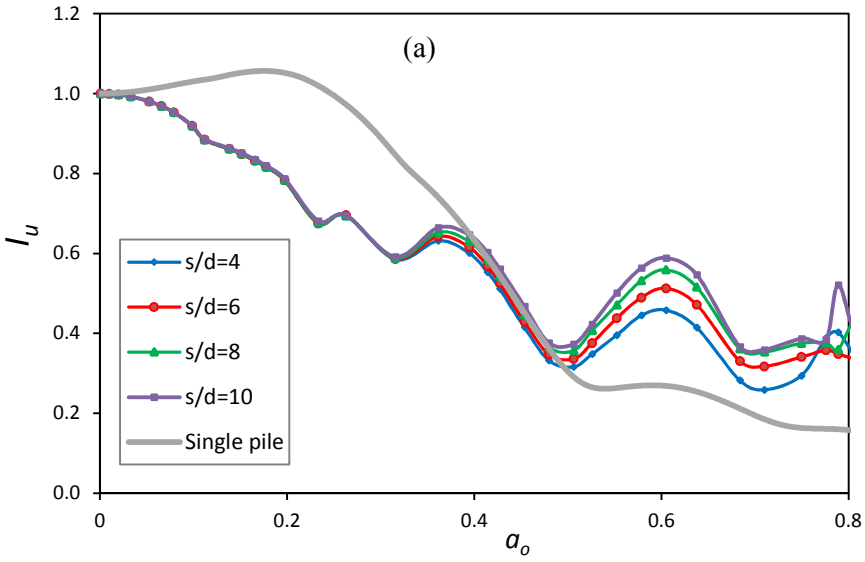
EFFECT OF PILE LAYOUT ON KINEMATIC RESPOPONSE

Pile configuration in a piled raft foundation is often decided upon considering column locations as well as the settlement profile of the raft, for the given superstructure loads. Pile configuration can be optimized to reduce differential settlements, especially in the case with piles as settlement reducers (Leung et al. 2010). The optimization criteria based on static loads, is aimed at maximizing stiffness or minimizing differential settlements. The area ratio of piled raft, defined as the ratio of gross area of pile group to the area of raft, is an important optimization parameter. To minimize differential settlements in many cases, piles can be provided closer to the center of raft i.e with reduced area ratio (Horikoshi and Randolph, 1998). However,

decreasing the area ratio can lead to undesirable rocking during seismic shaking due to decreased rocking resistance.

In the present study, the piled raft in clay system described in the previous section is employed to study the effect of pile layout on translational and rotational kinematic interaction factors (I_u and I_φ), at the raft level. Numerical models are developed with the same raft dimensions and soil properties as in the experiment, but with different pile configurations. The pile spacing was varied from spacing to diameter (*s/d*) ratio of 4 to 10, resulting in increasing area ratio of 0.3 to 0.66. The raft stiffness was increased to simulate rigid behavior by satisfying the relative stiffness criterion suggested by Simone (1966). A massless raft is considered in the kinematic response analyses carried out. Translational and rotational transfer functions were extracted at the center of the top surface of the raft.

The variation of I_u and I_φ with dimensionless frequency for different *s/d* ratio is presented in Fig 6 (a) and (b). The dimensionless frequency is calculated with a V_s value of 105m/s that corresponds to the average shear wave velocity across the length of pile. The translational response at the raft level is found to be unaffected by pile configuration, upto an a_o value of 0.3. It is observed that the peak value of the factor I_φ for *s/d* of 4 is two times the value for an *s/d* value of 10. Kinematic rotation is found to be significantly influenced by pile configuration, in agreement with the trend observed by Fan et al. (1991). Peak rotation is observed to double when pile spacing ratio increases from 4 to 10.



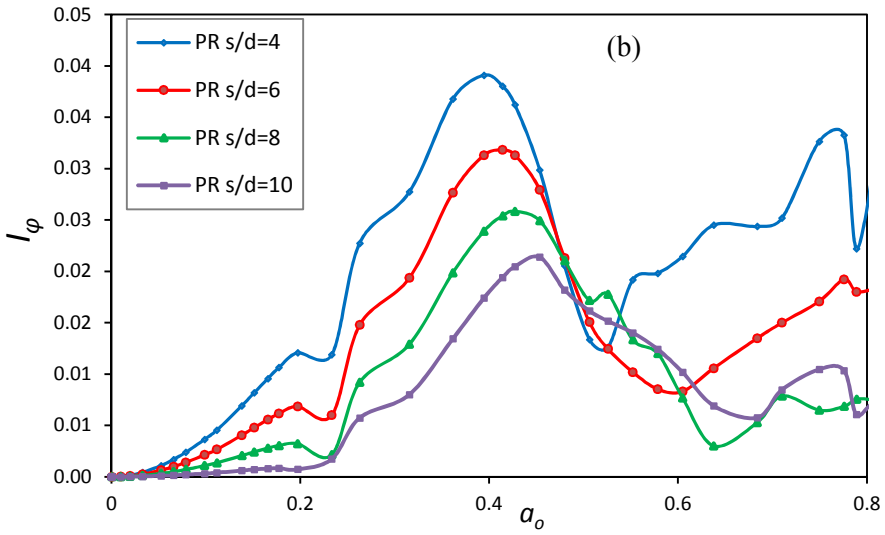


Fig. 6 Kinematic interaction factor in (a) translation and (b) rotation plotted against dimensionless frequency.

The effect of raft on the kinematic response of the corresponding pile group can be quantified by considering the ratio of amplitudes of motion of piled raft and pile group, ρ_{tr} and ρ_{rot} as defined in Eq. (5) and Eq. (6). These parameters form multipliers to obtain kinematic response factors of piled rafts from those of pile groups.

$$\rho_{tr} = \frac{u_{PR}}{u_{PG}} \qquad [5]$$

$$\rho_{rot} = \frac{\emptyset_{PR}}{\emptyset_{PG}} \qquad [6]$$

Three dimensional models were created for pile groups with the same pile configuration as in the piled rafts. For pile group models, the piles are connected to each other at their heads with rigid links to simulate fixed head condition and eliminating any embedment effect. Variation of kinematic response factor ratios ρ_{tr} and ρ_{rot} for different pile spacing is presented in Fig. 7 (a) and 7 (b) respectively.

It is interesting to note that the presence of a raft does not alter kinematic translation at the top of a pile group in the low frequency region, up to an a_o value of 0.3. The presence of raft is found to increase translational foundation motion, in the dimensionless frequency range of 0.4 to 0.65. As observed in Fig. 7 (b) irrespective of pile configuration, the presence of raft can be observed to reduce rotation up to an a_o value of 0.25. The greater the area ratio, the greater is the reduction in rotation at the low frequency range. However, the influence of raft becomes dependent on pile configuration beyond an a_o value of 0.25.

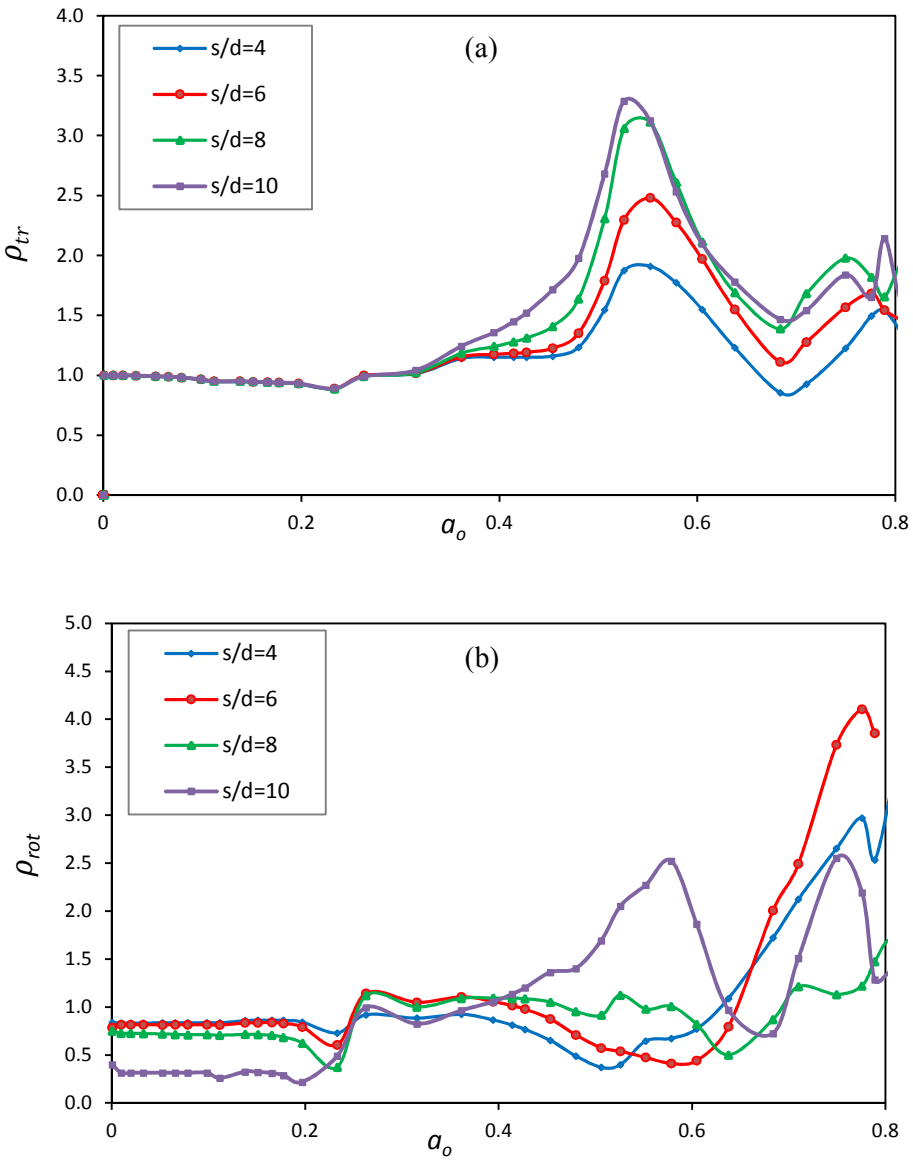


Fig. 7 Kinematic interaction factor ratio in (a) translation and (b) rotation

It is evident that the influence of raft on kinematic response is a function of frequency. Dynamic impedances of pile groups are also functions dependent on frequency. Studies by Liu and Ai (2017) have found that the presence of a soft layer below the raft has a significant impact on the impedance of pile group with ground contacting cap, at higher frequencies. To study the frequency dependent nature of the influence of raft, dynamic impedances are evaluated for the piled raft system considered in the present study. Complex impedances are evaluated from the ACS SASSI program by applying unit harmonic load at the raft level. Complex impedances $S_{ii}(\omega)$ are expressed as shown in equation 7.

$$S_{ii}(\omega) = K_{ii}(\omega) + i\omega C_{ii}(\omega) \quad [7]$$

where K and C are the stiffness and damping coefficients respectively, subscript ii represents the direction of excitation and displacement, and ω is the angular frequency of vibration. Impedances in horizontal

mode are obtained for the piled raft and pile group with varying pile spacing. The ratio of stiffness coefficients of piled raft (K_{PR}) and pile group (K_{PG}) is plotted against dimensionless frequency in Fig 8(a). Similarly the ratio of damping coefficients (C_{PR}/ C_{PG}) is presented in Fig. 8(b). The presence of raft is observed to significantly reduce dynamic stiffness coefficient in the dimensionless frequency range of 0.23 to 0.53, for all *s/d* ratios. The influence on damping coefficient is evident beyond an a_o value of 0.4. For the foundation soil system considered, the frequency range in which raft influences kinematic translation is found to be different from the range in which it influences horizontal impedances.

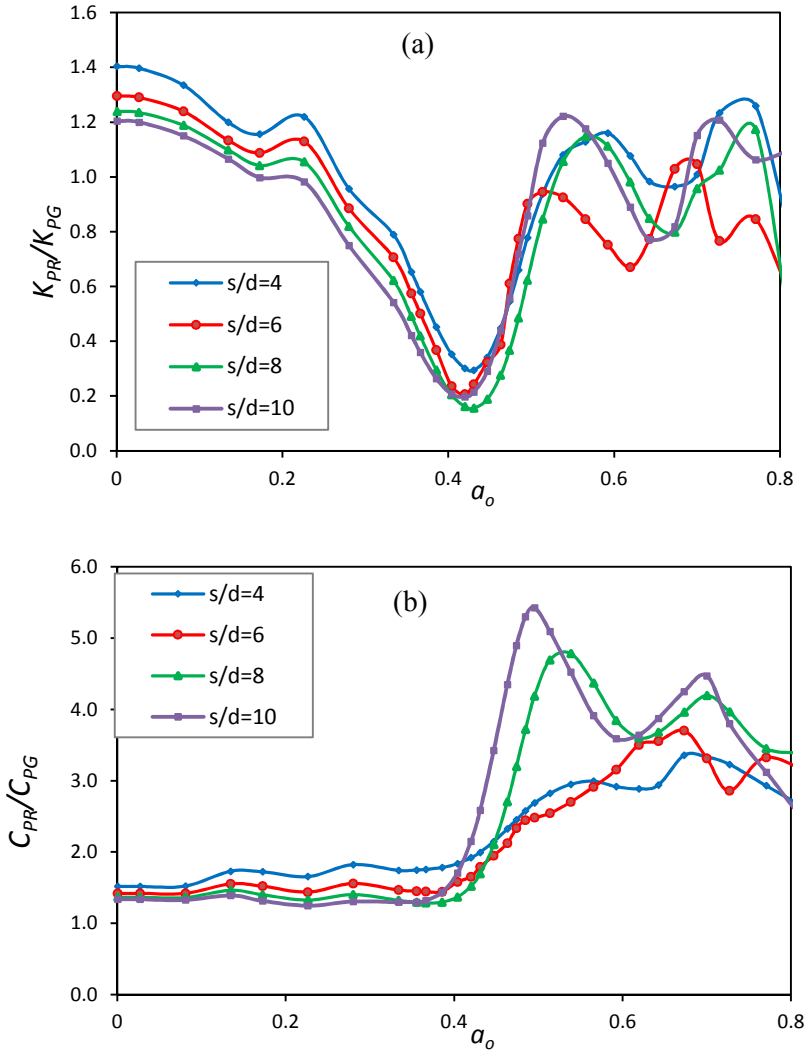


Fig. 8. Ratio of horizontal (a) stiffness and (b) damping coefficients for piled raft and pile group

CONCLUSION

Pile groups are known to induce rotations and filter out translational components of foundation input motion. In the present study, a substructuring based finite element formulation is used to investigate the effect of a raft on kinematic response characteristics, and rotational impedances of a piled raft foundation. The method of SSI analysis adopted, is first evaluated against results from analytical and experimental

studies reported in literature. Piled raft in clay systems with four different pile configurations, is then studied for kinematic responses to vertically propagating shear waves.

Kinematic rotation in the piled raft foundation was found to decrease with increasing pile spacing, similar to the behavior of pile groups. For a piled raft in clay system studied, the raft is found to increase translation in the dimensionless frequency range of 0.4 to 0.65. The presence of raft is observed to reduce rotation in all pile configurations up to an a_o value of 0.25, beyond which the response is influenced by the pile configuration. The presence of raft is observed to significantly reduce dynamic rotational stiffness coefficient in the dimensionless frequency range of 0.23 to 0.6, and increase damping coefficient after a dimensionless frequency of 0.4, for all *s/d* ratios.

The present study throws light on the alteration in kinematic response of pile groups, by the presence of an embedded raft. The influence of raft not only varies with frequency, but also on the configuration of piles. The influence of raft cannot thus be neglected in the evaluation of foundation input motion as well as impedances, for SSI analysis of structures supported by piled rafts.

REFERENCES

Banerjee, S. (2009). Centrifuge and numerical modelling of soft clay-pile-raft foundations subjected to seismic shaking. Doctoral Dissertation, National University of Singapore.

Banerjee, S., Goh, S. H., and Lee, F. H. (2014). Earthquake-induced bending moment in fixed-head piles in soft clay. Géotechnique, Thomas Telford, 64(6), 431–446.

Di Laora, R., & de Sanctis, L. (2013). Piles-induced filtering effect on the foundation input motion. Soil Dynamics and Earthquake Engineering, 46, 52-63.

Emani, P. K., and Maheshwari, B. K. (2009). Dynamic impedances of pile groups with embedded caps in homogeneous elastic soils using CIFECM. Soil Dynamics and Earthquake Engineering, 29(6), 963–973.

Fan, K., Gazetas, G., Kaynia, A., Kausel, E., and Ahmad, S. (1991). Kinematic Seismic Response of Single Piles and Pile Groups. Journal of Geotechnical Engineering, 117(12), 1860–1879.

Ghiocel, D. M. (2012). The SASSI Flexible Volume Substructuring Methodologies. *Ghiocel Predictive Technologies, Inc. Technical Note, GPT-001-430-2012, April*, *30*.

Horikoshi, K., & Randolph, M. F. (1998). A contribution to optimum design of piled rafts. Geotechnique, 48(3), 301-317.

Jeremić, B., Jie, G., Preisig, M., & Tafazzoli, N. (2009). Time domain simulation of soil–foundation–structure interaction in non-uniform soils. Earthquake Engineering & Structural Dynamics, 38(5), 699-718.

Leung, Y. F., Klar, A., & Soga, K. (2009). Theoretical study on pile length optimization of pile groups and piled rafts. Journal of geotechnical and geoenvironmental engineering, 136(2), 319-330.

Liu, C. L., and Ai, Z. Y. (2017). Vertical harmonic vibration of piled raft foundations in layered soils. International Journal for Numerical and Analytical Methods in Geomechanics, 41(17), 1711–1723.

Lysmer, J., Tabatabaie-Raissi, M., Tajirian, F., Vahdani, S., & Ostadan, F. (1981). *SASSI: A system for analysis of soil-structure interaction*.

Mayoral, J. M., & Romo, M. P. (2015). Seismic response of bridges with massive foundations. Soil Dynamics and Earthquake Engineering, 71, 88-99.

Mylonakis, G., Nikolaou, A., and Gazetas, G. (1997). Soil — pile — bridge seismic interaction : kinematic and inertial effects . part i : soft soil. Earthquake Engineering & Structural Dynamics, 26(October 1995), 337–359.

Ostadan, F., and Deng, N. (2012). *SASSI 2010 Version 1.0 User's Manual*.

Schnabel, P. B. (1972). SHAKE a computer program for earthquake response analysis of horizontally layered sites. EERC Report, Univ. of California, Berkeley.

Sextos, A. G., Mylonakis, G. E., & Mylona, E. K. V. (2015). Rotational excitation of bridges supported on pile groups in soft or liquefiable soil deposits. Computers & Structures, 155, 54-66.

LOAD TRANSFER CURVE OF PILES IN SANDS UNDER UPLIFT FORCES

Mohamed Ashour, Associate Professor of Civil Engineering, Dept. of Mechanical and Civil Engineering, Alabama A&M University, USA, Mohamed.Ashour@aamu.edu.

Jogeshwar P. Singh, JP Singh & Associates, Richmond, CA, USA, jpsassoc@aol.com

Aser I. Abbas, Project Engineer, EMC Co., aser.ibr@live.com.

ABSTRACT: The presented methodology predicts the pile head response (i.e. pile head load - displacement curve) and develops the load transfer (t-z) curve of piles in sandy soils under tension forces based on soil/pile properties and soil-pile interaction. The proposed approach improves the prediction of the t-z curve in sandy soils compared to current practice. The method employs a nonlinear soil constitutive model to calculate the mobilized shear stress/strain in soil at the soil-pile interface induced by pile upward displacement. The approach accounts for the influence of the pile slenderness ratio on the predicted t-z curve and is validated through comparisons with measured pile head response and t-z curves from full-scale pile load tests.

Keywords: Axial load, Pile, Sand, Tension, t-z Curve, Pile head stiffness

INTRODUCTION

Piles may be subjected to axial uplift forces due to either static loading or cyclic loading. The majority of methods are only concerned with the pile ultimate tensile capacity. However, the mobilized pile stiffness (i.e., pile-head load-displacement relationship) is essential to determine the interaction between the foundation and the superstructure and consequently the performance of the whole structure. Methods that assess the pile ultimate tensile capacity usually assume the failure surface at the soil-pile interface and estimate the local side shear resistance using a lateral earth pressure approach. The Naval Facilities Engineering Command (NAVFAC 1986) and the US Army Corps of Engineers (USACE 1991) employed Eq. 1 to assess the ultimate shear stress (τ) developed at the soil-pile interface.

$$\tau = k\bar{\sigma}_{vo} \tan\delta \quad [1]$$

Where $\bar{\sigma}_{vo}$ is the vertical effective stress, δ is the soil-pile interface friction angle and k is the coefficient of lateral earth pressure. Lower k values were suggested for tension loading compared to compression ones (NAVFAC 1986; USACE 1991).The Federal Highway Administration (FHWA) (O'Neill and Reese 1999) employed an updated earth pressure approach (β-method) to calculate the maximum value of shear stress for piles in sandy soils subjected to tension loading as given in Eq. 2.

$$\tau = \alpha\beta\bar{\sigma}_v \quad [2]$$

$$\beta = 1.5 - 0.245[D_m]^{0.5} \qquad 0.25 \le \beta \le 1.2 \quad [3]$$

For $N_{60}(uncorrected) \ge 15$ blows/0.3 m

$$\beta = [N/15]\{1.5 - 0.245[D_m]^{0.5}\} \qquad 0.25 \le \beta \le 1.2 \quad [4]$$

For N_{60} $(uncorrected)$ <15 blows/0.3 m

© 2018 Deep Foundations Institute

Where D_m is the depth below the ground surface in meters, β is calculated using Eqs. 3 and 4 and α is a reduction factor for tension loading adopted from a study made by De Nicola (1996) which typically ranges from 0.74 to 0.88.

The API (2014) suggested a β-method and 4 CPT based methods (ICP-05, UWA-05, Fugro-05, and NGI-05) to determine the pile shaft resistance in sandy soils. Gavin et al. (2011) reviewed the methods suggested by the API (2007), which remained unchanged in the API (2014), by comparing their predicted results with a comprehensive database of load tests. According to Gavin et al. (2011), the CPT methods provided improved and consistent results compared to the β-method which was found unreliable and biased to the pile slenderness and sand relative density. Gavin et al. (2011) reported that the ICP-05 and UWA-05 methods provided the most reliable predictions. The NGI-05 method was unconservative and exhibited large scatter and the Fugro-05 method was conservative and tended to provide better predictions for dense sand. Chattopadhyay and Pise (1986) proposed a method that predicts the ultimate tensile capacity for piles in sandy soils and assumed a curved failure surface that passes through the surrounding soil. In this method, the lateral extent of the failure surface is dependent on δ, the soil friction angle (ϕ), and the pile slenderness ratio (L/D).

In addition to pile load testing, other methods such as the finite element (numerical methods), the elasticity theory based methods, and the load transfer (i.e., t-z) methods are employed to evaluate the mobilized pile response under axial uplift forces in sandy soils. The reliability of the finite element based methods depend on the accuracy of input data and utilized soil/pile models. Methods that use the elasticity theory employ Mindlin's (1936) equation for a load within an elastic continuum and usually model the soil as a linear elastic material which is an oversimplification of the soil behavior. The load transfer (i.e., t-z) methods are widely used to assess the mobilized pile response due to their simplicity and ability to incorporate nonlinear soil behavior. The t-z methods have been criticized for modeling the soil as discrete springs (i.e. effect of soil mass continuity).

The FHWA (O'Neill and Reese 1999) and API (2014) suggest the use of empirical t-z curves where the maximum value of shear stress is mobilized at a displacement which is a percentage of the pile diameter. Furthermore, the FHWA procedure is designated for concrete bored piles and the API (2014) method is only applicable to steel driven piles. The t-z curves suggested by O'Neill and Reese (1999) were developed by O'Neill and Hassan (1994) based on an analysis of large database of compression load tests in cohesionless soils and is only valid for piles with diameters that range from 0.46-m to 1.53-m.

The current study presents a method that predicts the t-z curves of piles embedded in multi-layered sandy soil profiles subjected to axial uplift forces based on the soil-pile interaction. The methodology employs a soil nonlinear stress-strain relationship and accounts for the decrease in the mean effective stress resulting from tensile loading. Compared to other methods, the suggested technique has the ability to account for varying soil/pile properties in predicting the mobilized pile response.

METHODOLOGY

Pile resistance to tension loads is dependent on its own weight and the magnitude of shear transfer in skin friction, while no suction is developed at the pile base due to the high permeability of sandy soils. Therefore, the relationship between the local pile displacement and soil-pile shear transfer (i.e., t-z curve) constitutes the backbone of the mobilized pile response assessment procedure. In the proposed methodology the pile is discretized into segments. The pile segments are supported by nonlinear springs (i.e., t-z springs) to represent the soil resistance to the segments movements as shown in Fig.1.

Stress state in soil

It should be mentioned that the method of pile installation has a diverse range of influence on the pile side resistance and lateral earth pressure coefficient. Despite the complexity of pile installation effect, isotropic conditions are assumed (i.e., k=1 and $\bar{\sigma}_{3_0} = \bar{\sigma}_{v_0}$). Therefore, before pile loading the soil stress state is represented by a single point on the principal stresses axes on the Mohr-Columb failure plan. O'Neill and Rains (1991) observed that piles loaded in tension produce lower values of vertical effective stress and confining pressure than piles loaded in compression based on model tests on instrumented pipe piles in a pressure chamber. Accordingly, a reduced value of the vertical effective stress $(\bar{\sigma}_{v_0})_r$ is utilized as observed by O'Neill and Rains (1991) and suggested by De Nicola and Randolph (1993) to account for the effects of tensile loads on the pile shaft capacity as given in Eq.5. However, since the suggested technique aims to assess the mobilized pile response under axial uplift forces in multi-layered sandy soil profiles, η' is employed as a function of the mobilized shear modulus (G_{mob}) as given in Eq.6 and not the average shear modulus suggested by De Nicola and Randolph (1993).

$$(\bar{\sigma}_{v_0})_r = \bar{\sigma}_{v_0} * \left[1 - 0.2\, log_{10}\left(\frac{100}{L/D}\right)\right] * \left(1 - 8\eta' + 25\eta'^2\right) = \bar{\sigma}_{v_0} * \left[1 - 0.2\, log_{10}\left(\frac{100}{L/D}\right)\right] * \Omega \quad [5]$$

$$\eta' = \upsilon_p \tan\delta\, (L/D)\left(G_{mob}/E_p\right) \quad [6]$$

Where υ_p is the pile Poisson's ratio, δ is the soil-pile interface friction angle, L is the pile length, D is the pile diameter and E_p is the pile material Young's modulus.

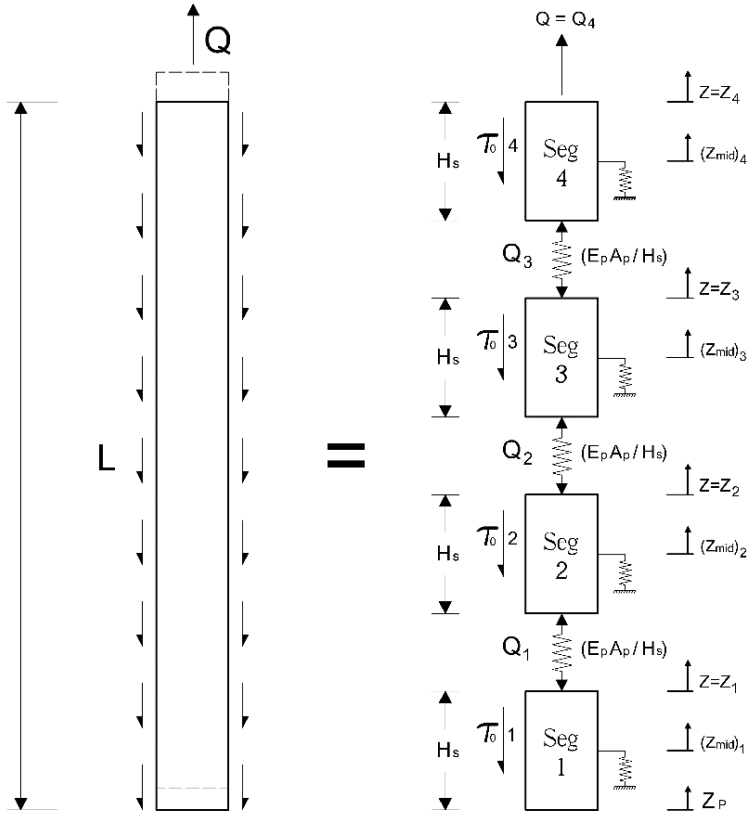


Fig. 1. Pile segments and soil-pile modeling under axial tensile force

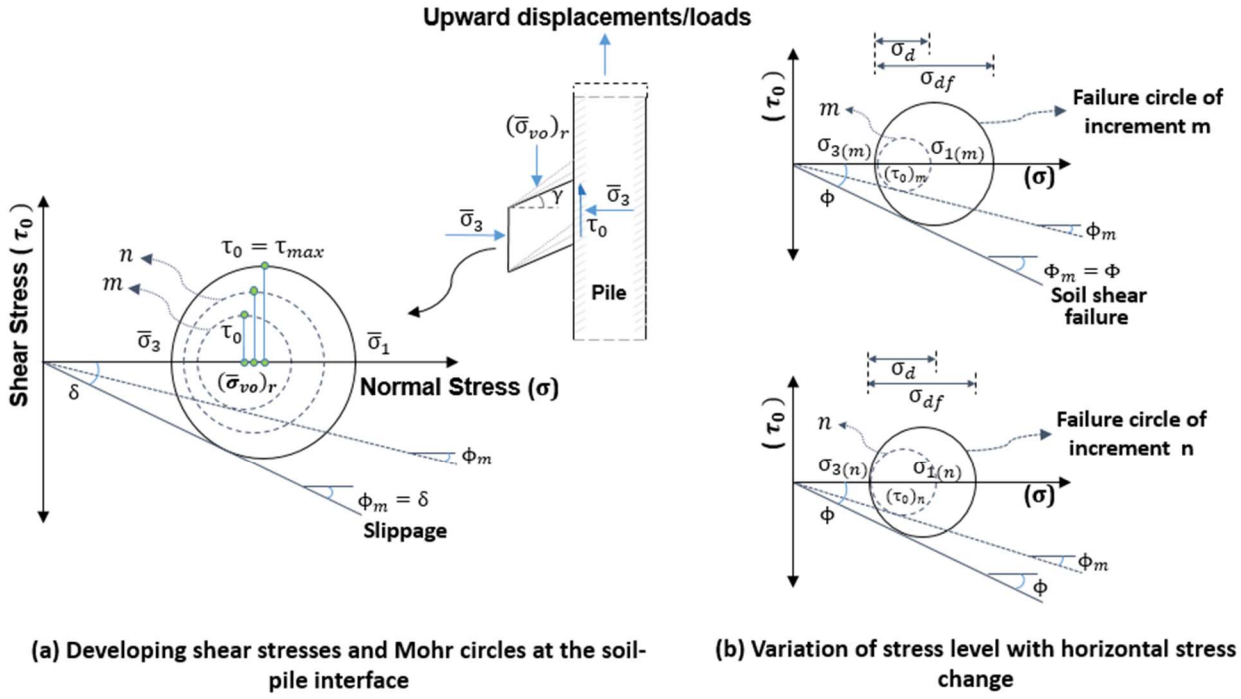
The adopted loading mechanism simulates the loading in the direct shear test. Each step of pile loading/movement develops a shear stress at the soil-pile interface which is represented by a Mohr circle with a radius τ_0, associating confining pressure $(\bar{\sigma}_{v_0})_r$ and principal stresses $\bar{\sigma}_1$ and $\bar{\sigma}_3$ on planes with rotation angles of 45 and -45 degrees from the sheared plane (i.e., plane of mobilized τ_0) as shown in Fig. 2a. Utilizing the concepts of the triaxial test at a given depth, $\bar{\sigma}_3$ and the deviatoric stress at failure (σ_{df}) associated to the current value of τ_0 can be calculated using Eqs. 7 and 8 respectively (Fig. 2b). Consequently, the stress level (SL) can be expressed as a function of the deviatoric stress (σ_d) and σ_{df} via Eq. 9. Also, the progress of shear stresses is accompanied by a decrease in G_{mob}, and an increase of $(\bar{\sigma}_{v_0})_r$ which is represented by a slight shift in the generated Mohr circles as shown in Fig.2a.

$$\bar{\sigma}_3 = (\bar{\sigma}_{v_0})_r - \tau_0 \quad [7]$$

$$\sigma_{df} = \bar{\sigma}_3 * \left[\left(\tan\left(45 + {}^{\Phi}/_{2}\right)\right)^2 - 1\right] \quad [8]$$

$$\text{SL} = \frac{\sigma_d}{\sigma_{df}} = \frac{2\tau}{\sigma_{df}} \quad [9]$$

Failure of the soil element adjacent to the pile shaft takes place when the mobilized friction angle (ϕ_m) reaches the sand friction angle (i.e. SL = 1 at $\phi_m = \phi$).However, slippage at the soil-pile interface might occur prior to soil shear failure depending on the pile surface roughness which is characterized by the soil-pile interface friction angle (δ).



(a) Developing shear stresses and Mohr circles at the soil-pile interface

(b) Variation of stress level with horizontal stress change

Fig. 2. Progress of shear stresses at the soil-pile interface

Pile displacements and corresponding soil strains

The soil around the pile is modeled as soil rings (i.e., sublayers) with thickness equal to pile segments H_s (Figs 1 and 3a). Pile upward movements cause deformations to the soil in the pile vicinity with a maximum value of vertical displacement at the soil-pile interface and then decreases with the radial

distance away from the pile shaft. Ropinsky and Morrison (1964) used radiography techniques to study the sand displacement patterns of instrumented model piles which is used by Ashour and Helal (2017) as a parabolic decreasing pattern of soil vertical displacement (Z_s) with radial distance (r) as given in Eq.10 (Figs 3b and 3c). Similar to the soil vertical displacement, the shear strain (γ) in soil maintains its maximum value at the soil-pile interface and then decreases radially from the pile shaft. γ in a soil slice at any distance from the pile shaft can be calculated using Eq. 11.

$$Z_s = Z_0 \left(\frac{r_0}{r}\right)^2 \quad [10]$$

$$\gamma_i = \frac{z_i - z_{i+1}}{r_{i+1} - r_i} = \frac{\Delta z_i}{\Delta r_i} \quad [11]$$

Where Z_0 is the soil vertical displacement at the soil-pile interface and r_0 is the pile radius.

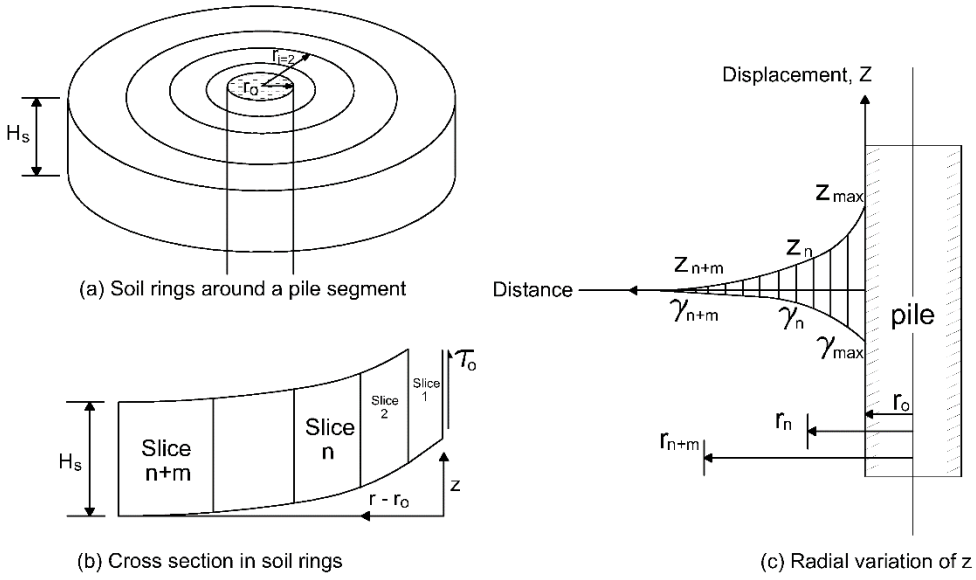


Fig. 3. Variation of shear displacement/strain in soil around the pile

Soil constitutive model (Stress-strain relationship)

The suggested approach employs the constitutive model presented by Ashour et al. (1998) for drained soils. The stress level (SL) and ε_{50} (soil normal strain at 50% SL) are utilized to develop the stress-strain curve up to failure as illustrated in Fig. 4. The soil Poisson's ratio (υ_s) is assumed to vary as a function of SL as suggested by Ashour and Helal (2017) and given in Eq. 12. Utilizing ε and υ_s, the Mohr circle of strains is employed to assess the shear strain (γ) via Eq. 13 and hence the value of G_{mob} using Eq. 14.

$$\upsilon_s = 0.1 + 0.4SL \quad [12]$$

$$\gamma = \varepsilon(1 + \upsilon_s) \quad [13]$$

$$G_{mob} = \frac{\tau}{\gamma} \quad [14]$$

The iterative process employed in the suggested technique to model the developing shear stresses/stains at the soil-pile interface to build the t-z curve up to failure is explained in detail as follows:

Assessment of the t-z curve and mobilized pile stiffness

The iterative process employed in the suggested technique to model the developing shear stresses/stains at the soil-pile interface to build the t-z curve up to failure is described in the flowchart presented in Fig. 5.

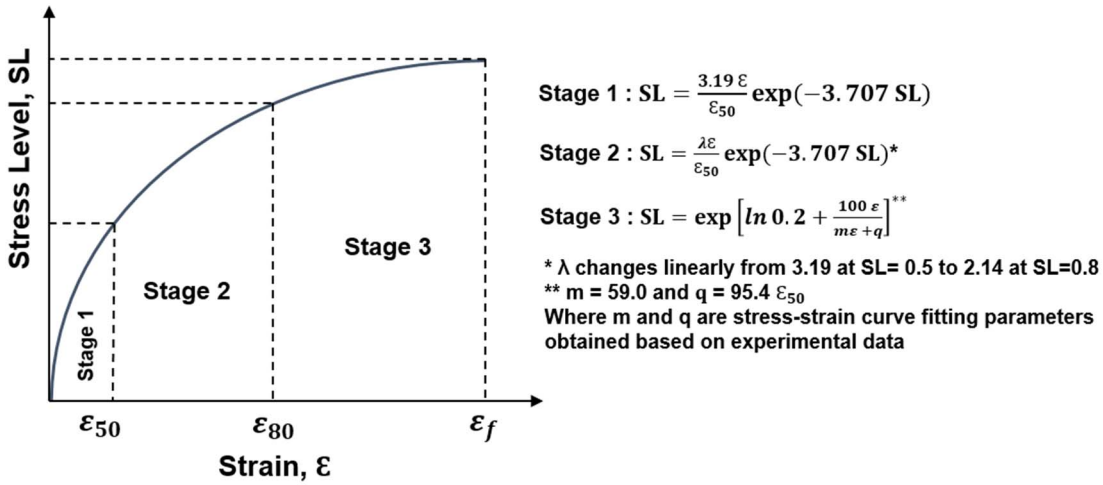


Fig. 4. Stress-strain soil model modified by Ashour et al. (1998) after Norris (1986)

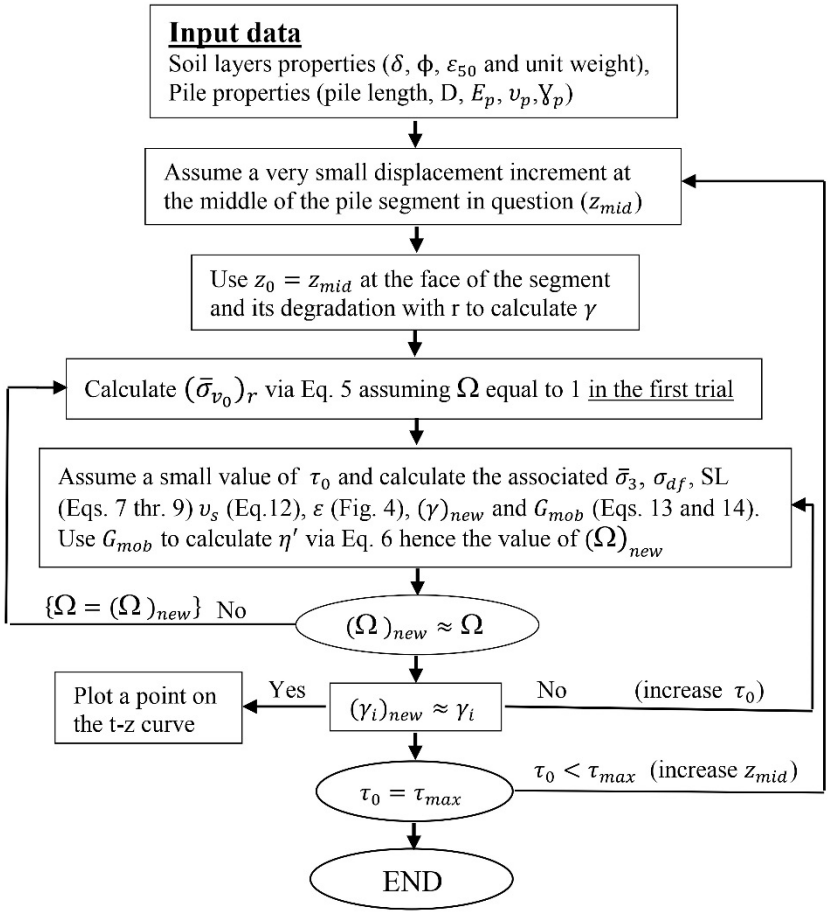


Fig. 5. A flowchart for the proposed model

A FORTRAN code is developed to predict the mobilized τ_0 versus pile displacements at any depth on the pile up to failure. Pile segments are modeled as linear springs to reflect the elastic extension of pile's material under tension loads. For each upward movement at the pile tip (i.e., displacement increment), the accumulation of the segment forces and vertical displacements at the pile top form a point on the pile-head load-displacement Q-Z curve. This procedure is repeated for larger values of pile tip displacements to build the whole Q-Z curve (i.e. pile-head stiffness-displacement k-Z curve) up to failure.

SOIL-PILE INTERACTION

In this section, the sensitivity of the proposed methodology to pile slenderness ratio (i.e., diameter and length) on the shape of the t-z curve in sands is illustrated. Medium dense Nevada sand properties is adopted in the current study (i.e., ϕ = 35 deg, γ = 19 kN/m^3, and ε_{50}= 0.0037). Figure 6a shows the t-z curves at a depth of 10-m for twenty-meter long piles with diameters of 0.5-m, 1.0-m and 1.5-m. The proposed approach provides a maximum value of the pile shear stress (i.e. τ_{max}) that varies with the pile diameter as a result of the pile slenderness ratio (L/D) effect. It can be also noticed that while the shear stress/strain zone of influence grows with the increase of the pile diameter (as given in Eqs. 10 and 11), the stress/strain at the soil-pile interface of small diameter piles develops faster compared to the larger diameter ones (Fig. 6a). Figure 6b shows the effect of the pile slenderness ratio (due to the increase of the pile length) on the t-z curve at a depth of 10-m for piles with the same diameter (1-m) and three different lengths (15-m, 20-m and 25-m). The presented approach provides a stiffer t-z curve at the same depth in response to increasing the pile length. As presented in Eqs. 5 and 6, the pile slenderness ratio affects the vertical effective and confining stress at the soil-pile interface of the pile under axial uplift force.

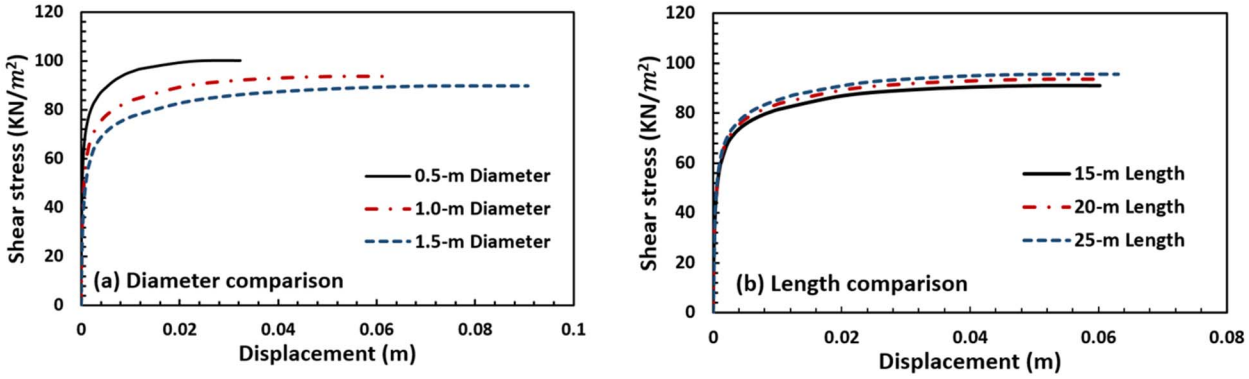


Fig. 6. Pile slenderness ratio effect (i.e., diameter and length) on the (t-z) curve at a depth of 10-m

COMPARISONS AND VALIDATION

The developed methodology is validated based on comparisons between predicted and field back-calculated t-z curves and mobilized pile-head response of instrumented piles subjected to axial tension forces in sandy soils. Further validation of the suggested technique can be also found in Ibrahim et al. (2017).

Old River, Louisiana full-scale field tests

Mansur and Kaufman (1958) performed four tension load tests on instrumented driven steel pipe piles. The piles tested in tension were piles number 2, 4, 5 and 6. These tests were part of a comprehensive pile testing program conducted for the Old River, Louisiana control project. Piles 5 and 6 were 17 inch (0.43-m) and 19 inch (0.48-m) in diameter and 45 feet (13.7-m) and 65 feet (19.8-m) in length respectively. Table 1 shows the soil properties reported by Mansur and Kaufman (1958) along with other properties interpreted for the use in the proposed model. Figure 7 shows the predicted and reported mobilized pile-

head load versus displacement curves for piles 5 and 6. At smaller pile-head displacements (Z), it can be noticed that the proposed model provides larger pile-head load compared to the measured one which is followed by better agreement as the pile-head displacement (Z) increases. For pile 6, Figs 8 (a and b) display the predicted and back calculated t-z curves at depths of 9.1-m and 19.05-m respectively. A reasonable agreement can be observed between the predicted and back-calculated t-z curves.

Table 1. Reported/interpreted input soil parameters used for tests (Old River, Louisiana test)

layer	Thickness (m)	γ_s(kN/m^3)	ϕ (deg)	C (kN/m^2)	ε_{50}
Silty sand	14.6 (48 ft)	11	28	10.8 (0.1 ton/ft^2)	0.02
Sand	15.2 (50 ft)	9	36	0	0.005

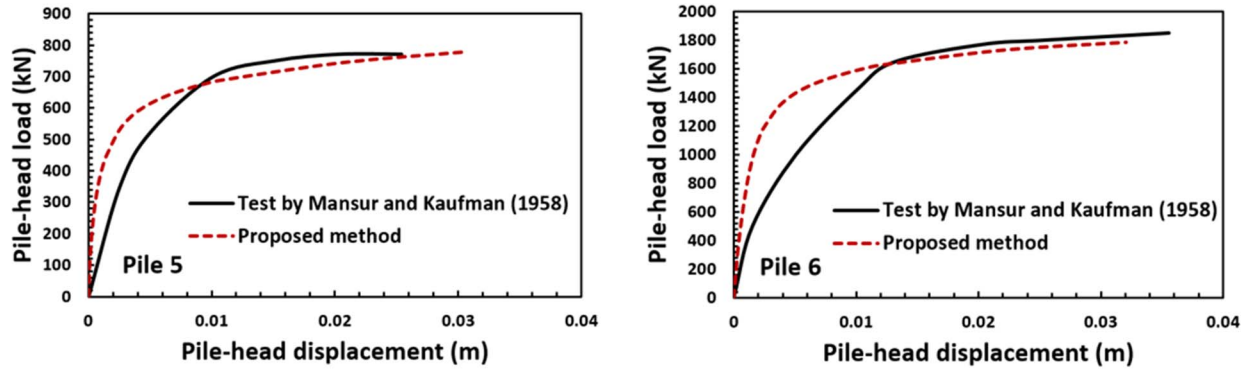


Fig. 7. Predicted and measured pile-head response of Louisiana tests

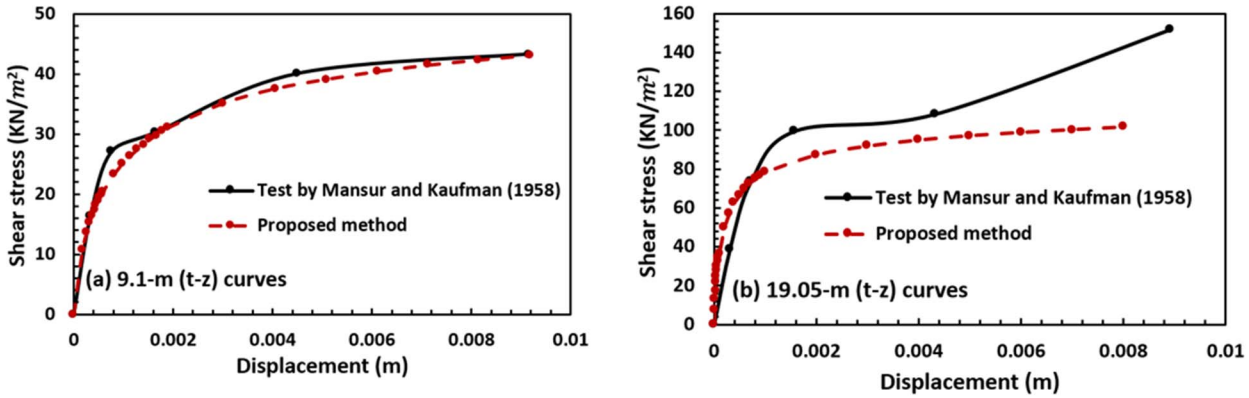


Fig. 8. Predicted vs. back calculated t-z curves at different depths for pile 6 (Louisiana tests)

Brazil tests (Southern central region)

Carvalhoand Albuquerque (2013) reported a study on three 10-m long instrumented bored piles with respective diameters of 0.35-m, 0.4-m, and 0.5-m to assess the performance of the three piles under uplift forces and to analyze the mechanism of load transfer between the piles and the subsoil. The top two soil layers were 62% and 61% sands respectively, and the remaining percentage was fines (silt and clay) (i.e. SM and SC) based on the USCS System. The water table was below the piles base. Table 2 presents the reported soil properties. Figure 9 shows the good agreement between predicted and measured pile-head load-displacement curves for the 0.35-m and 0.4-m diameter piles. A reasonable agreement can be noticed in Fig. 10 between predicted and back calculated t-z curves for the 0.35-m diameter pile.

Table 2. Reported/interpreted input soil parameters used for Brazil tests

Layer	Thickness (m)	γ_{moist}(kN/m^3)	ϕ (deg)	G_s	E	ε_{50}	δ (deg)
Silty sand	0 – 6	16.3	30	2.73	0.94	0.007	30
Clayey sand	6 – 12	18.9	23	2.76	0.71	0.005	23

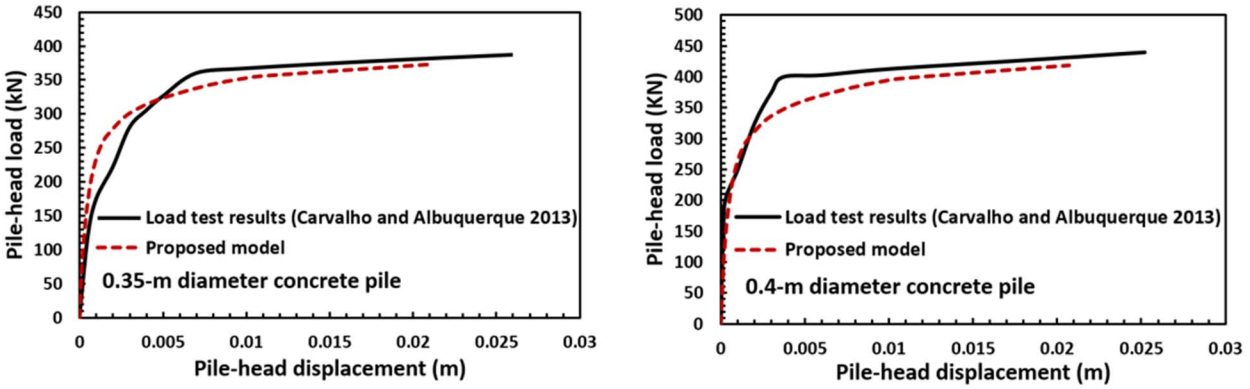


Fig. 9. Predicted and measured pile-head response of the Brazil tests

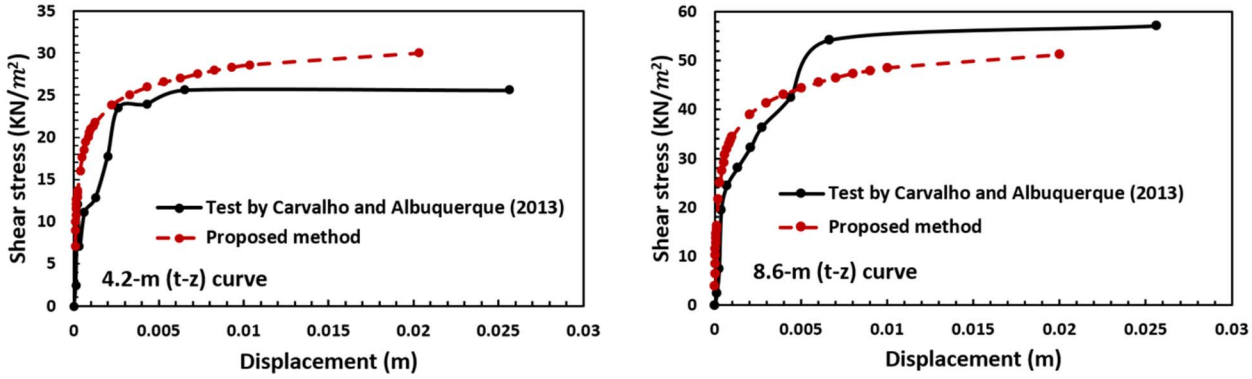


Fig. 10. t-z curves at different depth for the 0.35-m diameter bored concrete pile (Brazil test)

CONCLUSIONS

The proposed approach provides nonlinear t-z curves along a pile embedded in sandy soils and subjected to tension forces. The presented procedures clearly illustrate the construction of the t-z curves along the pile length with the employment of a nonlinear stress-strain curve for sandy soils. The variation of the shear stress/strain in the surrounding sandy soil at the soil-pile interface with the progress of pile tension force and pile displacement can be determined up to failure (i.e., excessive displacement/slippage). The consideration of the soil-pile interaction in the presented model allows the construction of a t-z curve that accounts for the variation of the sand relative density (i.e., sand's friction angle, ε_{50}, unit weight and overburden pressure) in addition to the pile dimensions. Unlike other methods, the current study also shows that the shear stress in the soil zone around the pile is influenced by the pile dimensions and develops faster along the piles of smaller diameters and larger slenderness ratio (i.e. a softer t-z curve by increasing the pile diameter). The presented comparisons with measured pile-head response and t-z curves highlight the capability of the proposed technique.

REFERENCES

API (American Petroleum Institute), 2014. Geotechnical and foundation design considerations. Addendum 1,ANSI/API recommended practice 2GEO, API Publishing Services, Washington, DC, USA.

API, 2007.Recommended practice for planning, designing and constructing fixed offshore platforms. API RP2A, Washington, DC, USA.

Ashour, M., Norris, G., and Pilling, P., 1998. Lateral loading of a pile in layered soil using the strain wedge model. J. Geotech. and Geoenviron. Eng., doi:10.1061/(ASCE)1090-0241(1998)124:4(303), 303-315.

Ashour, M., and Helal, A., 2017. Pre-and Post-Liquefaction Response of Axially Loaded Piles in Sands. International Journal of Geomechanics, doi:10.1061/(ASCE)GM.1943-5622.0000968

Carvalho D.D., and Albuquerque, R.D., 2013. Uplift behavior of bored piles in tropical unsaturated sandy soil. In: Proceedings of the 18th International Conference on Soil Mechanics and Geotechnical Engineering, 4, 2707-2710.

Chattopadhyay, B.C., and Pise, P.J., 1986. Uplift capacity of piles in sand. Journal of Geotechnical Engineer, doi:10.1061/(ASCE)0733-9410(1986)112:9(888).

De Nicola, A., and Randolph, M. F., 1993. Tensile and compressive shaft capacity of piles in sand. Journal of geotechnical engineering, doi:10.1061/(ASCE)0733-9410(1993)119:12(1952).

De Nicola, A., 1996.The performance of pipe piles in sand. Dissertation submitted for the degree of doctor of philosophy, Department of Civil Engineering, The University of Western Australia, Nedlands, Western Australia.

Gavin, K., Igoe, D., Doherty, P., 2011. Piles for offshore wind turbines: a state-of-the-art review. In: Proceedings of the Institution of Civil Engineers, Geotechnical engineering 164(GE4), 245-256.

Ibrahim, A., Ashour, M., and Altahrany, A., 2017. Pile response under axial tension forces in sand soils. Journal of Bridge engineering, doi:10.1061/(ASCE)BE.1943-5592.0001142.

Naval Facilities Engineering Command (NAVFAC), 1986. Foundations and earth structures. Design manual7.02, Naval Facilities Engineering Command, Alexandria, VA.

Norris, G.M. 1986. Theoretically based BEF laterally loaded pile analysis. Third Int. Conf. in numerical methods in offshore piling, Editions Technip. Paris, France.361-386.

Mansur, C.I., and Kaufman, R.I., 1958. Pile tests, Low-Sill structure, Old River, Louisiana. Journal of the Soil Mechanics and Foundations Division, (ASCE), 123 (1), 715-743.

Mindlin, R.D., 1936. Force at a Point in the Interior of a Semi-Infinite Soil. In Physics, vol. 7.

O'Neil, M. W., and Hassan, K. H., 1994. Drilled shafts: Effects of construction on performance and design criteria. In proceedings, International conference on deep foundations, FHWA, Orlando, FL, 1, 137 – 187.

O'Neil, M.W., and Reese L.C., 1999. Drilled Shafts: Construction procedures and design methods, FHWA-IF-99-025. U.S. Dept. of transportation, FHWA, Washington, DC.

O'Neil, M. and Raines, R., 1991. Load transfer for pipe piles in highly pressured dense sand. J. Geotech. Engrg., doi:10.1061/(ASCE)0733-9410(1991)117:8(1208), 1208-1226.

Robinsky, E. I., and Morrison, C. F., 1964. Sand displacement and compaction around model friction piles. Canadian Geotechnical Journal, 1(2), 81-93.

US Army Corps of Engineers (USACE), 1991.Engineering and design: Design of pile foundations. Engineer manual No.1110-2-2906, Washington, DC, USA.

NONLINEAR RESPONSE OF PILES WITH RIGID EMBEDMENT: LESSONS LEARNED FROM A REDUCED-SCALE EXPERIMENT

Camilla Favaretti, Ph.D[1], Anne Lemnitzer, Ph.D[2], Benjamin Turner, Ph.D., PE[3]

Pile foundations are extensively used in the construction of various types of superstructures, including tall buildings, bridges, freeways and offshore structures. A fully constrained tip embedment such as a rock-socket offers an attractive solution for achieving significant tip resistance and improving the load-carrying capability of the foundation element. In profiles with very soft surficial soil, rock-socketing often provides the only reliable source of axial and lateral resistance. In preparation of a large-scale testing program on rock-socketed piles at UC Irvine (UCI) geared towards studying the magnitude of shear amplification at the rock-soil boundary of pile foundations, a pre-test model-scale experiment was executed in the UCI Structural Laboratory. The objective of the model-scale experiment was to iterate and validate the test setup, study the influence of important boundary conditions, assess instrumentation techniques and sensor placement, and to gain preliminary insight into the small-scale specimen non-linearity. In addition, this model-scale study provides ample opportunity to compare lateral performance parameters with analytically predicted lateral load behavior using traditional soil resistance functions and limit state analyses and explore new techniques for the derivation of soil resistance functions.

The pile specimen had a pile diameter (D) of 10 inches and a total pile length of 125 inches. The pile was embedded in a 40 inch simulated rock socket overlain by 52 inch of medium dense sand (DR~50%). The pile extended 32 inches above the soil surface, where cyclic lateral loading was applied. The pile was installed in a laminar metal frame box with inside dimensions of 39 inches in width (W), 73 inches in length (L) and 86.1 inches in height (H) as shown in Figure 1. During testing, the box was restrained using a rigid bracing system consisting of concrete reaction blocks, wooden braces and steel girders.

The rock-socket concrete consisted of 4ksi strength concrete and is weaker than the concrete material of the pile (8ksi). This scenario represents the opposite case of the anticipated large scale specimens to be tested later and simulates a "strong pile" in weaker rock. Results enable an investigation whether the weaker "rock" will break out at the sand-rock interface and induce potential damage and failure evolution near the rock-socket boundary. The fill material consisted of locally acquired washed sand known as #16 Industrial Sand. The sand is poorly graded and classifies as *SP* per USCS. An extensive laboratory testing program revealed a coefficient of uniformity C_u of 1.78, a specific gravity G_s of 2.63, a maximum dry unit weight γ_d =120pcf at optimum water content, $w_{opt,}$ = 11%, and a minimum and maximum void ratio of 0.37 and 0.8,

[1] Geotechnical Engineer, Arup (New York), formerly Graduate Research Assistant, University of California Irvine, Department of Civil and Environmental Engineering, UC Irvine, Email: camilla.favaretti@arup.com
[2] Associate Professor, University of California Irvine, Department of Civil and Environmental Engineering, Email: alemnitz@uci.edu
[3] Project Engineer, Dan Brown and Associates, California. Email: bturner@dba.world

© 2018 Deep Foundations Institute

respectively. Direct shear testing using three representative confining pressures in the soil specimen yielded a friction angle $\phi = 44°$ and a cohesion c of 100 psf. The soil was dry pluviated into the box with a purpose-built, calibrated pluviation container with sieve attachments of size No. 6.



Figure 1a&b: Test setup of model scale pile in restrained soil box

Quasi-static, reverse cyclic lateral loading was applied to the pile head using a 150-kip capacity, 34-inch stroke actuator. The load protocol was guided by pre-test analytical load-deflection predictions using the commercially available software LPILE. The test pile was instrumented with internal and external strain gauges. Internal strain gauges were attached on two longitudinal opposite rebar at intervals of 6 inch. Four external strain gauges were attached in longitudinal and rosette configurations along the surface of the pile to capture bending and shear strains at the pile soil interface. Addition external sensors consisted primarily of string potentiometers and LVDTs to monitor the specimen deflection at the cantilever section (i.e., pile head) and to ensure that no horizontal movement along the laminar box occurs. A spray-painted grid with spacing of six-inch by six-inch was applied to the surface of the fill soil to monitor the extent of lateral surface deformation during loading.

The pile was subjected to cyclic lateral deformations up to a maximum displacement of 7.5 inch (0.75D). Specimen yielding was observed in push direction at 33mm (1.3in) horizontal displacement. The corresponding lateral load was 16kN (3.6kips). In the pull direction, yielding occurred at the same displacement level and a corresponding yield force of 17.34kN was measured. The ultimate load reached in the push direction was 18.7kN (4.2kips) at 190.5mm (7.5in) of pile head displacement. Post yielding, the pile produced continuous lateral deflection at no further increase of load (approx. 20.5kN). Soil densification near the pile circumference formed a settlement cone with depths of up to 12 cm near the pile perimeter, as shown in Figure 1b. Post-test excavation of the soil fill revealed large horizontal cracks around the pile at different elevations. Most substantial cracking developed on the east-west sides (bending direction) of the pile. Limited cracking with superficial concrete spalling occurred on the shear sides of the pile. The largest crack width (4in) indicated the region of plastic hinging, which was located at a vertical elevation of approximately 72cm (28in) above the top of the bedrock and approximately 61 cm (24 in) below the sand surface layer. This height corresponds to 2.6 pile diameters below ground surface. No cracking was observed at the pile-rock interface. This observation is important as the simulated rock was substantially weaker than the pile specimen and pile shear failure is presumed to occur in the rock socket region based on analysis methods commonly used in practice.

PERFORMANCE BASED SEISMIC RETROFIT DESIGN OF BROOKLYN BASIN WHARF

Sam Yao, Ph.D., P.E., Simpson Gumpertz & Heger, Oakland, CA USA
Ali Naeem, P.E., Simpson Gumpertz & Heger, Oakland, CA USA
Sara Barrett, P.E., Simpson Gumpertz & Heger, Oakland, CA USA

ABSTRACT

Brooklyn Basin Project is a multi-billion-dollar development of the former Port of Oakland 9th Avenue Terminal located along the Oakland Estuary of California. A centerpiece of the development is the 10-acre shoreline park which will be built on a 1,200 ft long by 225 ft wide historic wharf. The wharf was built in the 1930's on concrete and timber piles with a flat concrete slab. Prior to constructing the wharf, a rock dike was placed to protect the shoreline. The presence of the rock dike increased the hazards from lateral spreading of the underlying bay mud and non-ductile shear failure of piles driven through the dike. To open the park to the public, the wharf required a seismic retrofit in compliance with the California Building Code.

The paper presents the results and conclusions of the following topics:

- Structural condition assessment and repair strategies for the existing wharf deck, piles and jackets
- Application of the California Building Code (CBC Ch31F) for the performance-based seismic evaluation of existing piers and wharves
- Nonlinear pushover analysis of the wharf including the combination of inertial and kinematic effects
- Impact of rock dike on lateral spreading and kinematic effects and the significance of existing piles in stabilizing the lateral spreading of the rock dike
- Retrofit strategies for the wharf to meet the required seismic performance requirements per the California Building Code and reduce the demands on existing piles which were driven through the rock dike

Keywords: Performance-Based Seismic Design, Wharf, Seismic Retrofit, Pile Inspection, Repair and Strengthening, Lateral spreading, Kinematic and Inertial Seismic Loading.

INTRODUCTION

The 65-acre Brooklyn Basin Development project is located in Oakland, California. The project consists of 3,100 housing units, 200,000 sq. ft of retail and commercial space, along with various parks and public access improvements along the Oakland Estuary. A centerpiece of the development is the 10-acre Shoreline Park which will be built on a 1,200 ft long by 225 ft wide historic wharf. The wharf was built in the 1930's on concrete and timber piles with a flat concrete slab. As shown in Figure 1, the wharf deck and piles support the 9th Avenue Terminal Building.

The existing Terminal Building was used for storing materials and as a truck loading area. As part of the redevelopment, most of the existing building will be demolished to give way to a park space which will be a new addition to the shoreline park system. Figure 2 illustrates an overview of the complete development including the wharf and community center.

© 2018 Deep Foundations Institute

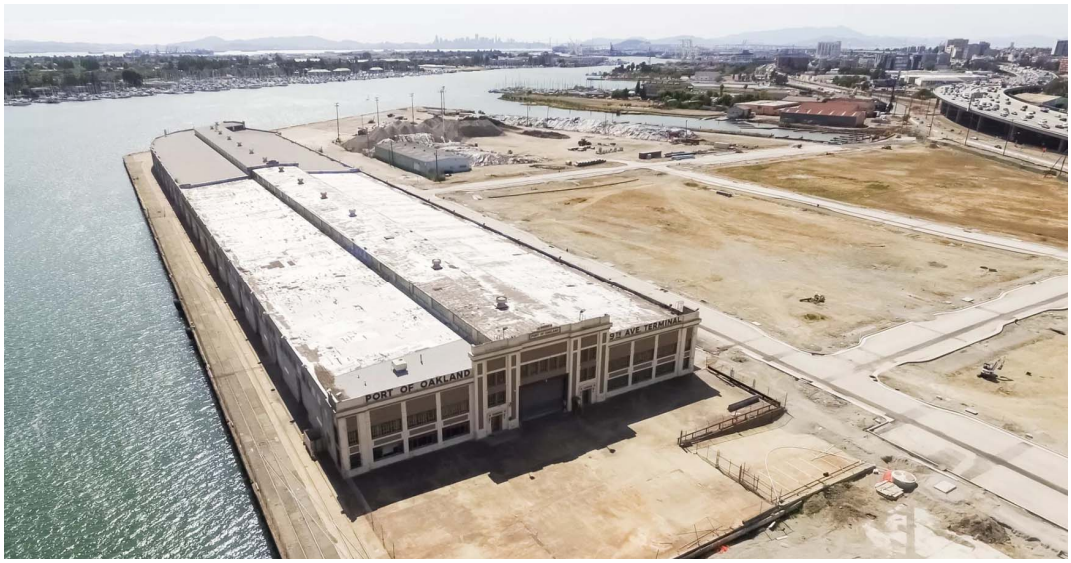


Fig. 1. Existing wharf and 9th Avenue Terminal Building



Fig 2. Future Development Including Public Park and Community Center on the wharf

PILE CONDITION ASSESSMENT

The wharf piles can be separated into two distinct support types. The wharf towards the land side is supported on 70-foot-long timber piles. The remaining wharf is supported on 18 in. square concrete piles with pile lengths varying between 60 to 100 ft. Figure 3 shows the reinforced pile jacket that encased both types of existing piles. This jacket was built with flared capitals at the deck and extended down below water. At the water side edge of the wharf is a 20-ft-wide timber apron, supported on creosote coated timber piles. These offshore timber piles showed severe deterioration and are slated for demolition. The tidal range at the project site is about 6.5-ft.

The concrete wharf deck thickness varies between 8.5 in. thick above the timber piles to 10 in. thick above the concrete piles. The terminal building is supported by concrete walls in the longitudinal direction and steel trusses in the transverse direction. The steel trusses frame into pilasters embedded in the concrete

walls. These pilasters and the interior truss columns are supported directly above double wharf piles and an extended pile cap.

Figure 4 shows a typical cross-section of the Wharf and the soil profile. The general stratigraphy of the project site consists of artificial fill, Young Bay Mud (YBM), Old Bay Mud (OBM) and Alluvial deposits. The soil profile and topography vary along the length of the wharf. A rock dike was constructed along the length of the project site to prevent slope failure during the wharf construction. After the rock dike was placed, the native soil was dredged to form a channel for the passage of large ships and the dredged YBM was placed inland of the rock dike. Timber piles were installed inland of the rock dike while concrete piles were installed through the rock dike and further offshore. The thickness of the YBM supporting the rock dike was an important consideration in assessing slope stability. The sliding wedge of the rock dike and underlying YBM would potentially impose significant kinematic loads on the piles.

To repurpose the wharf to a public park, the structure required a seismic retrofit in compliance with the California Building Code (CBC). Before conducting analysis, the existing conditions of the wharf and piles were studied by conducting a visual inspection and testing concrete cores. The wharf structure and terminal building are designed to achieve life safety performance levels for the design earthquake. Life safety is defined as the structural system experiencing some damage but can still support gravity loads, allow egress and does not result in loss of life or cause public hazard.

The pile assessment of the wharf was completed using ASCE Manual of Practice 130 "Waterfront Facilities Inspection and Assessment", which details rating criteria for varying degrees of damage. Pile inspections indicated that several piles were in deteriorated condition. Of the 2519 piles inspected, 279 piles were rated "Severe" and 187 piles were rated "Major".

The causes of the pile deterioration were determined to be a combination of seawater attack and corrosion of reinforcing steel. The most severe structural deterioration of the pile jackets occurs in the tidal and splash zone, where concrete spall and section loss of reinforcing steel bars were identified in many Severe-rated concrete piles. Some Severe-rated and Major-rated concrete piles and pile jackets exhibit various degree of concrete softening and microcracking in the tidal/splash zone and a few feet below the mean low water level. These deteriorations are mostly on concrete piles at the water edge of the wharf. The concrete jackets over timber piles near the landside are generally in fair to good conditions.

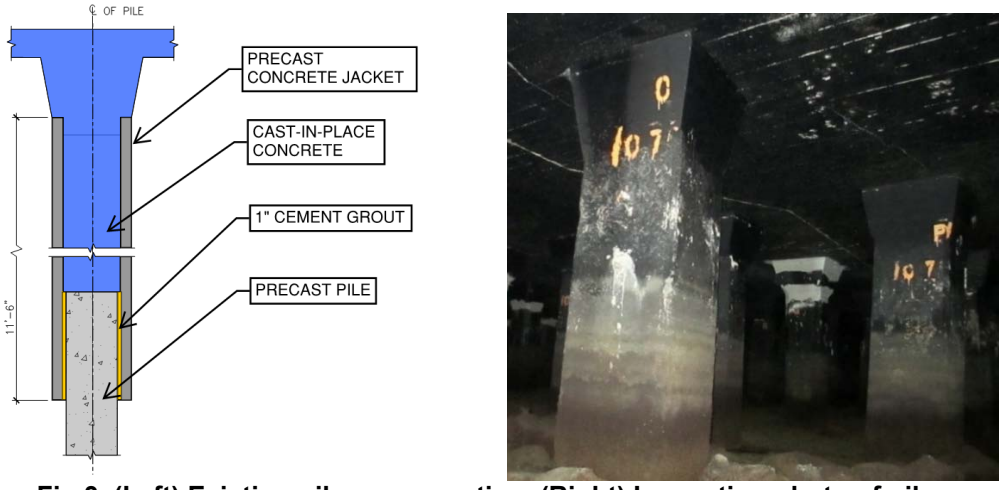


Fig 3. (Left) Existing pile cross-section, (Right) Inspection photo of piles

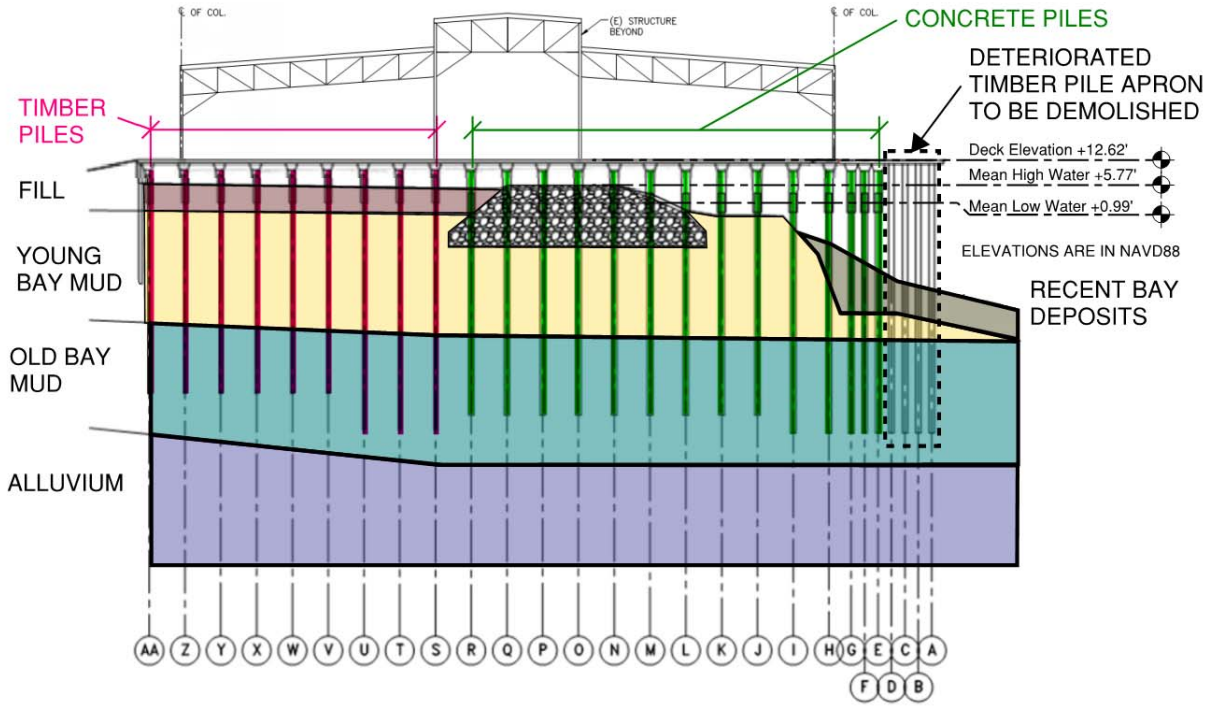
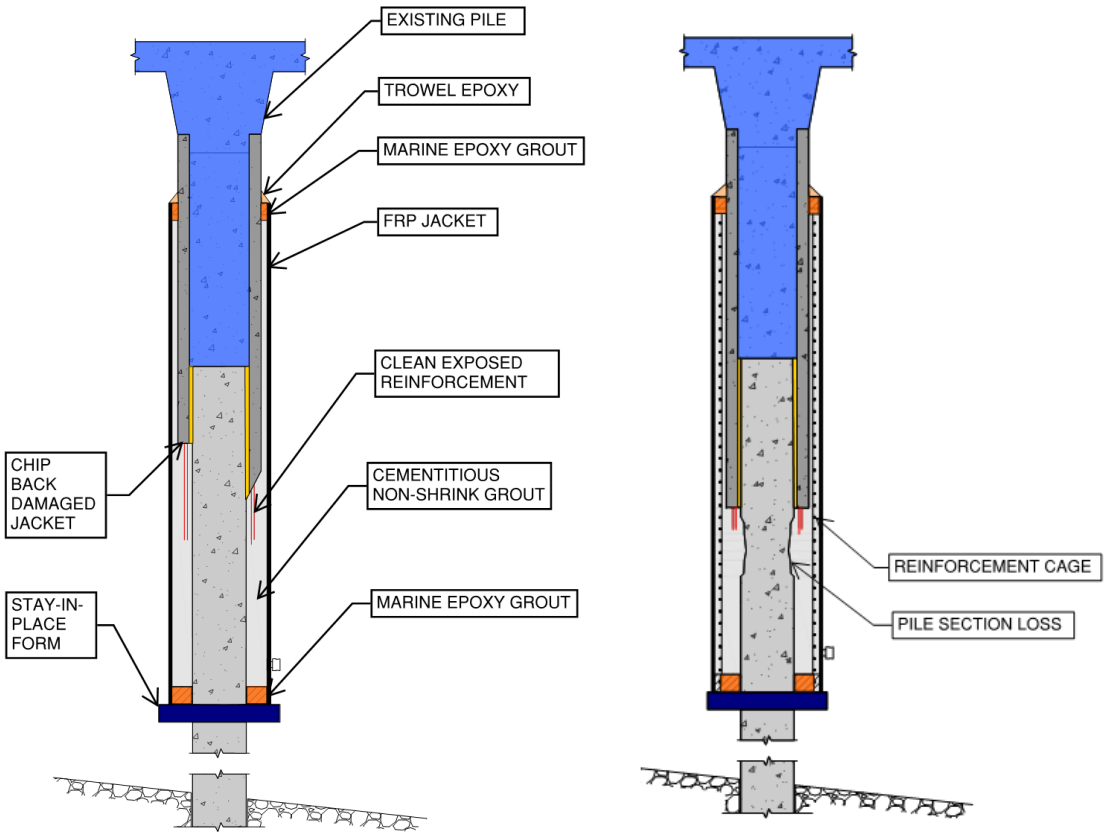


Fig. 4. Typical wharf and terminal cross-section and soil profile

PILE REPAIR PLAN

Pile repairs were only required in sections above the mudline since deterioration below the mudline was observed to be minimal. The repair plan focused on reducing the rate of pile deterioration in the tidal zone. Damaged pile jackets are encased in a fiber-reinforced plastic (FRP) jacket and filled with high-strength, non-shrink grout to replace the precast concrete jacket and provide protection for the pile in the tidal zone. Before the jackets are installed, existing jacket reinforcement is cleaned, and any softened concrete is chipped away. The encasement is designed to block further intrusion of seawater into the exposed pile and stop further softening of the concrete. The FRP jacket is more resistant than the existing precast jacket and does not deteriorate when in contact with seawater. It also reduces the corrosion rate of reinforcing steel by blocking oxygen permeation into the dry region of the pile above the tidal zone. For piles with section loss greater than 20%, a new reinforcing cage is incorporated into the FRP encasement (Figure 5). The reinforced strengthening option provides the desired protection in the tidal zone but also overcomes the lost section of the pile with the reinforced cage and high-strength grout encasement. The pile encasement method was selected for the following advantages:

1. It can be used for piles with various stages of damage, such as large section loss.
2. It fully restores and enhances structural strength of a damaged pile.
3. It stops ingress of seawater and chemical deterioration.
4. It reduces the corrosion rate of reinforcing steel by blocking oxygen permeation into the dry region of the pile above the tidal zone.
5. More durable than other repairs which significantly increases the pile service life.
6. No pollution to water in San Francisco Bay



(1) (2)

Fig. 5: (1) Pile FRP encasement repair detail, (2) Pile FRP strengthening repair detail

SEISMIC DESIGN CRITERIA

The project site lies in a high seismic area with several major faults within 30 miles including the Hayward and San Andreas faults. The probability of a moment magnitude of 6.7 or greater earthquake occurring on the San Andreas fault is 21-percent and that on the Hayward fault is 31-percent within 30 years (WGCEP, 2007). The site overlies a thick layer of soft clay Young Bay Mud (YBM). Therefore, seismic responses at this site can have significant amplification beyond the standard seismic spectra in CBC especially in the long periods. A site-specific ground motion hazard analysis was performed in accordance with ASCE 7-10. Nonlinear site response time history analysis was performed using software DEEPSOIL. As ASCE 7-10 dictates that the site-specific spectra cannot be less than 80 percent of the mapped MCE_R spectra, we enveloped the site-specific spectra and 80 percent of the mapped MCE_R. In order to perform displacement-based seismic analysis of the wharf structure, seismic design spectra at various levels of damping were derived using the methodology in FEMA 356. Figure 6 shows the seismic spectra for Design Basis Earthquake (DBE), which is about 2/3 of the MCE_R per CBC.

The wharf structure as a future public park is not essential to the post-event recovery, hence the structure is classified as Risk Category II. The wharf is required to achieve a level of seismic performance of life safety protection, i.e., the structure continues to support gravity load in the post-earthquake state, and seismic damage does not prevent egress from the wharf to the landside.

Prior to constructing the wharf, a rock dike was placed over the soft Young Bay Mud for the purpose of shoreline protection (see Figure 4). The presence of the rock dike increases the seismic risk of lateral

spreading and slope stability. Although there is no soil liquefaction risk at the site, the seismic analysis and retrofit design need to consider kinematic loads from lateral spreading due to the rock dike on soft clay as well as seismic inertia loads.

The seismic analysis and retrofit design are performed using a displacement−based design approach for Level 2 seismic performance in accordance with the "refined analyses" method in CBC Chapter 31F. Details are discussed in later part of the paper.

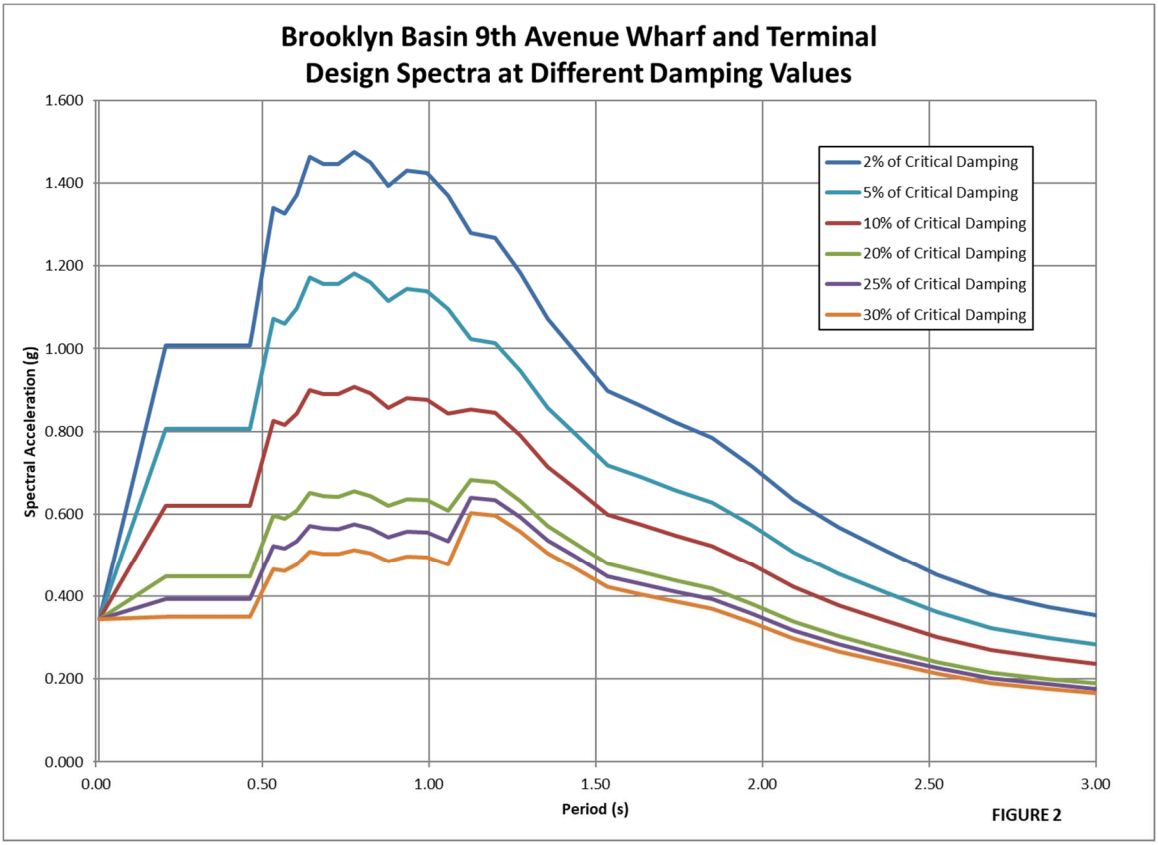


Fig. 6. Site specific spectra for wharf and terminal building at different damping values

SEISMIC RETROFIT DESIGN

Several retrofit measures were designed to meet the required CBC seismic criteria. The retrofits shown in Fig 7. are summarized in the following list:

- Drive landside 36 in. diameter steel pipe piles behind entire length of wharf. These stiff landside piles significantly enhance the seismic resistance of the structure against the inertia load and improve slope stability through pinning effects of the existing piles.
- Place reinforced concrete deck overlay over the entire wharf to strengthen the current deck and provide redundancy to the wharf structure
- In certain areas where the pinning effects of the existing piles alone cannot stabilize the slope, install closely spaced 36 in. diameter steel pipe piles to stabilize the slope.
- Demolish deteriorated timber apron and replace with new precast concrete piles and concrete deck tied to the existing wharf structure

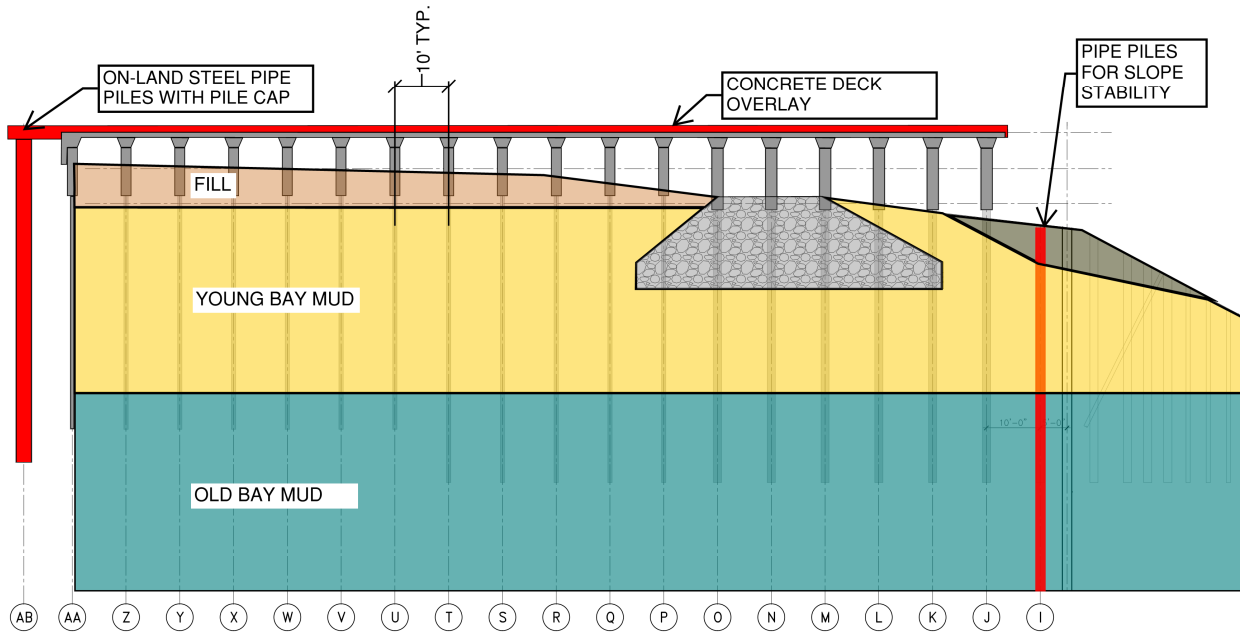


Fig. 7. (Top) Full elevation view, (Bottom) On-land pile detailed elevation

PUSHOVER ANALYSIS WITH INERTIAL AND KINEMATIC FORCES

The seismic evaluation of the wharf includes a nonlinear static pushover analysis using a three-dimensional finite element analysis in SAP2000 with the piles and P-Y soil springs. The displacement demand is calculated by using the so-call "refined analyses method" in CBC Chapter 31F which is consistent with the substitute structure approach in ASCE 61-14. This method directly incorporates the ductility, effective damping and design response spectra to provide displacement demands through an iterative process. The analysis procedure is illustrated in Figures 8a and Figure 8b.

The following seismic loading conditions are checked with the pushover analysis:

1. Seismic inertial loading due to ground shaking
2. Seismic kinematic loading due to ground deformations of the rock dike and underlying weak YBM
3. Combination of seismic inertial and kinematic loading in accordance with CBC (2013). The criteria in CBC (2013) specifies a combination of 100% kinematic load plus 25% inertial load. The seismic retrofit design was also checked for a combination of 100% kinematic plus 50% inertia loads, as recommended in Caltrans' "Guideline on Foundation Loading and Deformation Due to Liquefaction Induced Lateral Spreading" (2012).

The displacement capacity of the wharf was calculated by modeling pile hinges and tracking plastic deformations and rotations. Pile hinges were developed based on the pile cross section moment curvature responses at the expected axial loads. The displacement demand is then compared against performance points such as Immediate Occupancy and Life Safety which are defined within the hinge to monitor performance. The performance limit states are defined by code prescribed material strain limits to represent different damage criteria. In this case, the final design exhibited a displacement demand with pile material strains that do not exceed the Level 2, Live Safety limits in CBC Chapter 31F. The analysis was carried out with upper bound and lower bound soil parameters during inertial loading, and median or best-estimate soil parameters for kinematic loading. These were modeled in the finite element model through nonlinear

springs for each pile and soil type. Figure 9 shows the finite element model of the wharf including the community center and the weight of landscaping and live loads in the future public park.

Soil liquefaction is not a concern at the site. The kinematic load is induced by lateral spreading of the rock dike on the weak YBM. When slope failure occurs, we assumed that the majority of the soil shear strains occur within 5 feet of the sliding surface, and the rest of the sliding soil mass moves as a block. This assumption was generally confirmed by numerical analysis. The piles intersecting the failure wedge surface would impose pinning shear forces to the sliding block. Figure 10 illustrates the sliding wedge block, the assumed kinematic displacement, and the pinning forces of the piles. The kinematic loads and pile pinning forces were determined by iterations of (1) soil-structure interaction analyses using a finite element model with soil P-Y springs and (2) a pseudo-static slope stability analysis. In the finite element model, an assumed kinematic displacement was imposed on the P-Y springs along the piles and the pinning forces of the piles were calculated using the methodology in ASCE 61-14. Then, seismic slope stability analysis was performed including the calculated pinning forces. If the factor of safety against slope failure was less than 1, we adjusted the kinematic displacement and pseudo-static coefficient (k_h) and re-ran the finite element analysis to update the pinning forces. The new pinning forces were used to update the slope stability analysis. The iteration continues until the factor of safety against slope failure is above 1.0. The validate the calculations, the estimated kinematic displacements were compared with the calculated values from the methods in NCHRP 611 (2008), Bray and Travasarou (2007) and Martin and Qiu (1994).

Inertial and kinematic seismic load effects with a post-kinematic combination as shown in Figure 11. A nonlinear pushover model was utilized to apply 100% of the kinematic displacement. Then, an inertial pushover was then performed in both the offshore and landside directions. Shear demands in the pile and deck were increased by 25% to account for pile over-strength since flexural ductile failure of the pile was preferred over non-ductile shear failures. The design of the retrofit went through several iterations and was driven by reducing plastic strains and shear in the existing piles. The nonlinear pushover analysis indicates that the wharf structure can meet the Level 2 performance requirement in CBC at kinematic displacements up to 4 inches. At the east end and west end of the wharf, the weak YBM is thick and the estimated kinematic displacements are higher than 4 inches. At these locations, new 36" diameter steel pipe piles are installed to reinforce the seismic resistance against the slope failure and enforce the kinematic displacement to 4 inches or less. The additional pinning forces from the new retrofit piles were essential in achieving the target safety margin for the slope stability and the seismic Life Safety performance requirements in CBC.

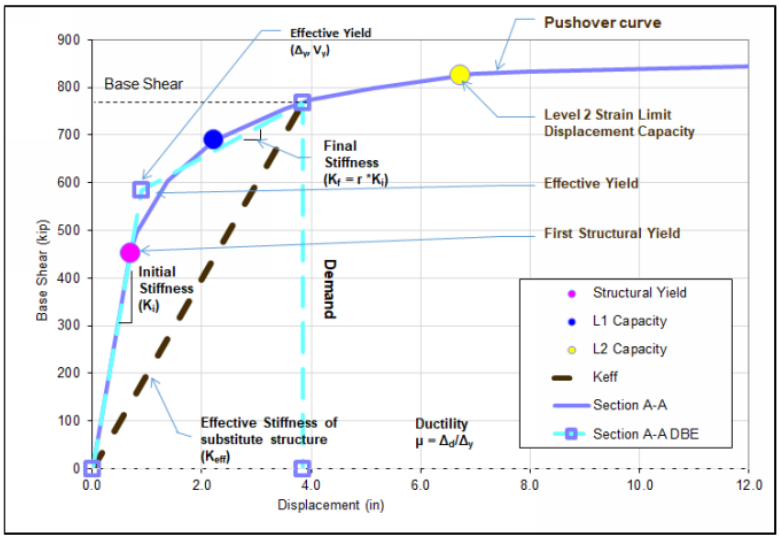


Fig. 8a. Refined analysis method for nonlinear pushover analysis approach in CBC

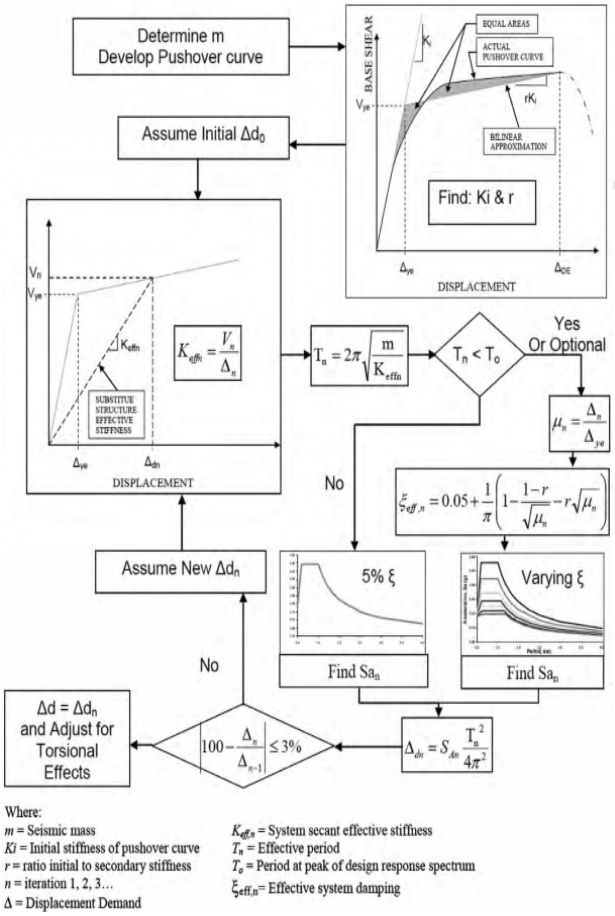


Fig. 8b. Performance based seismic nonlinear pushover analysis approach in CBC

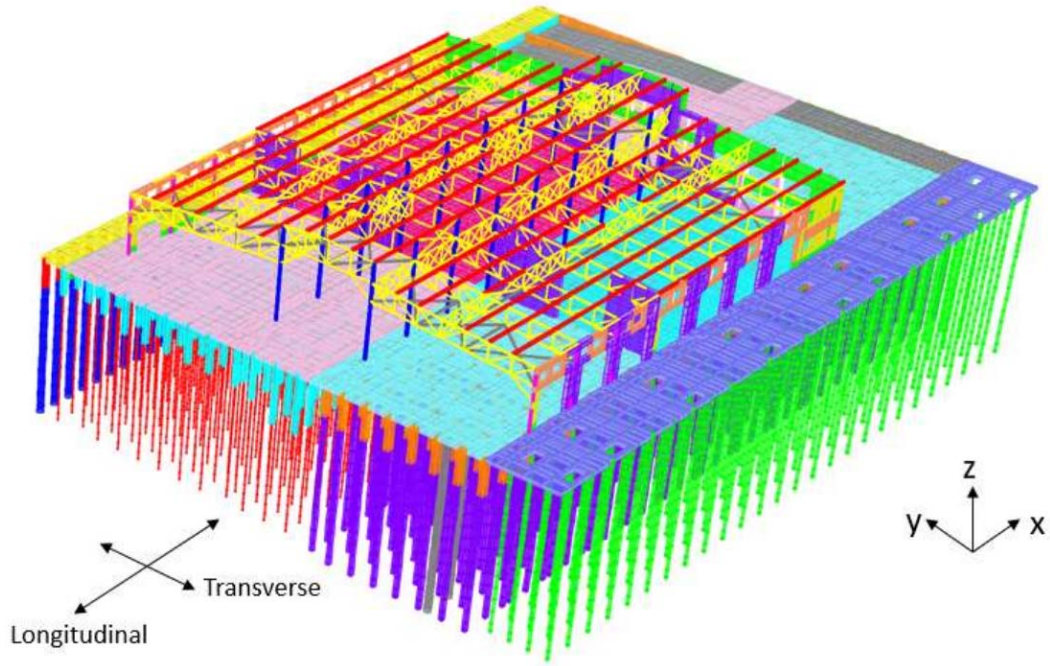


Fig 9. Three-dimensional partial SAP2000 model of retrofitted wharf with soil springs

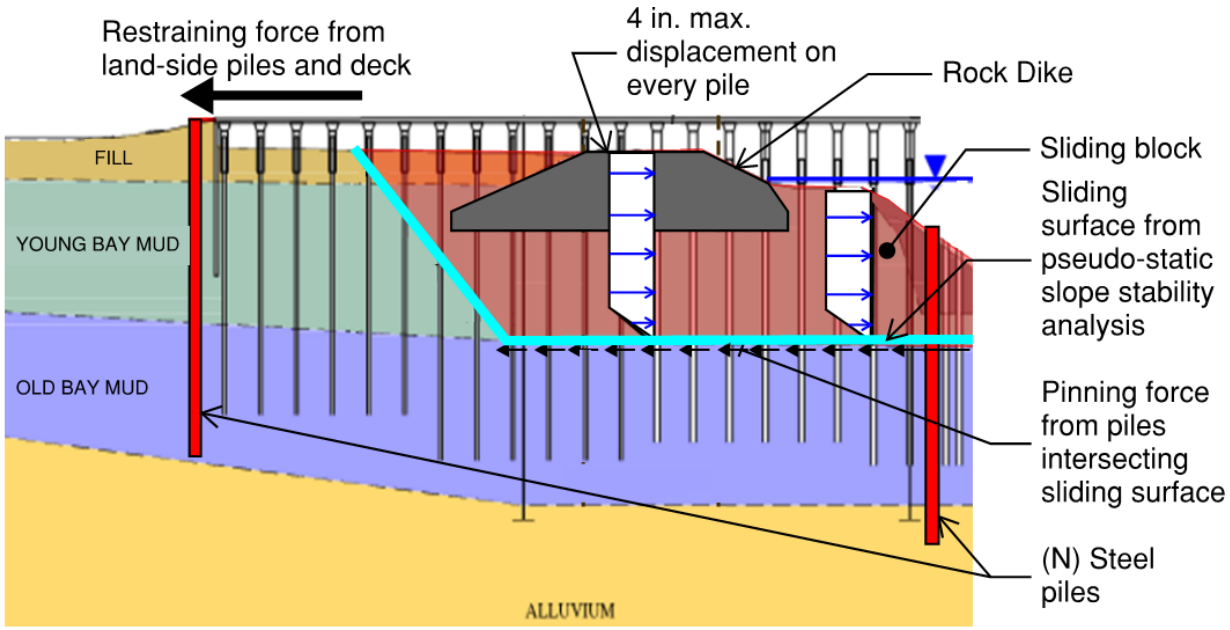


Fig 10. The potential slide failure wedge, assumed kinematic displacement, pile pinning forces, and new 36" diameter steel pipe piles

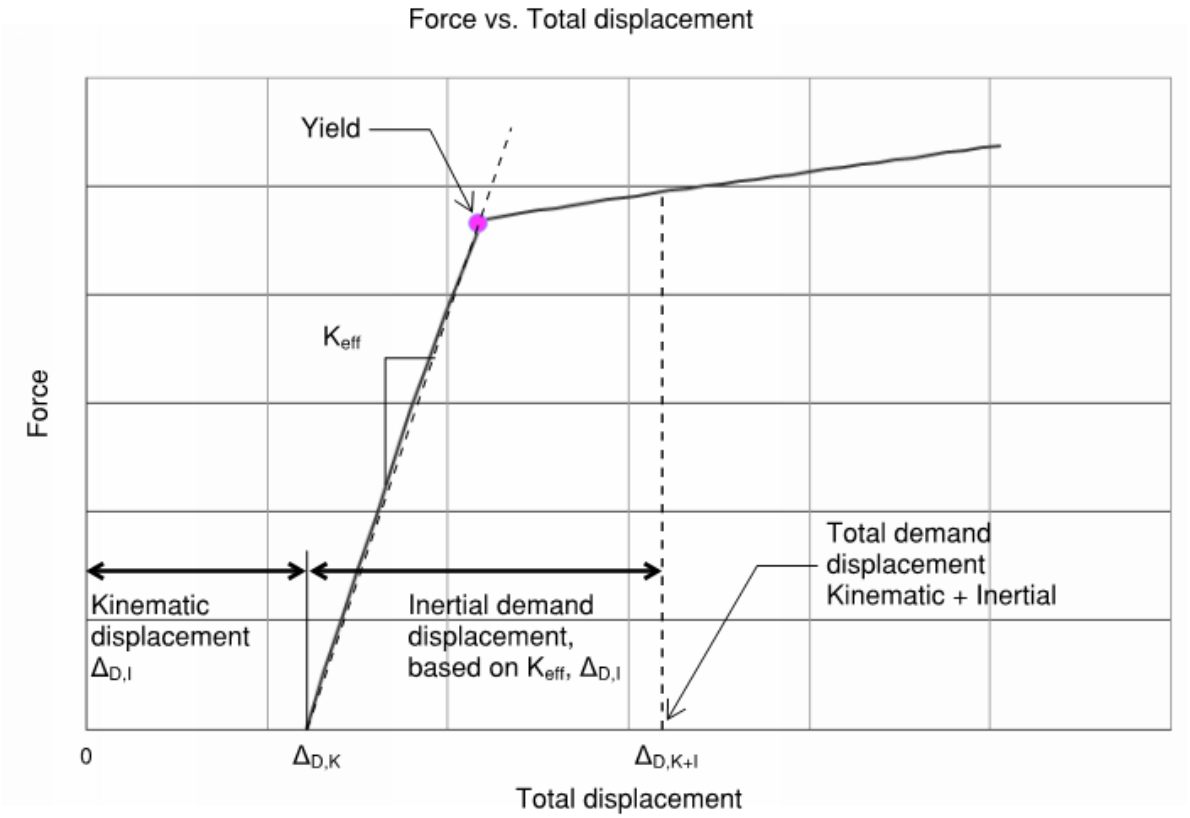


Fig 11. Combined kinematic and inertial pushover analysis

CONCLUSION

The seismic retrofit of the shoreline park at Brooklyn Basin in Oakland enables the repurpose of the industrial site to a public park. All 2519 existing piles were inspected and rated in accordance with ASCE Manual of Practice 130. The piles with significant damages are repaired using FRP encasement and strengthening with reinforcing cages and high strength grout. Performance based seismic design using nonlinear pushover analyses were performed in accordance with the refined method in CBC. New large diameter steel pipe piles were designed and installed to reduce the wharf's seismic displacement, reduce the plastic deformation and shear demands of the existing piles, stabilize the shoreline slope and minimize risk of lateral spreading. The seismic design and analyses demonstrates that retrofitted wharf structure and piles meet the seismic performance goals and requirements of the CBC.

ACKNOWLEDGEMENTS

Simpson Gumpertz & Heger is the structural engineer for the seismic retrofit project. ENGEO is the geotechnical engineer in this project.

REFERENCES

ASCE Manual of Practice 130 "Waterfront Facilities Inspection and Assessment", 2015

ASCE 7-10, Minimum Design Loads for Buildings and Other Structures, 2010

ASCE 61−14, Seismic Design of Piers and Wharves, 2014

Bray and Travasarou, Optimal Ground Motion Intensity Measures for Assessments of Seismic Slope Displacements, 2003 Pacific Conference on Earthquake Engineering, February 2003

California Building Code (CBC) Ch. 31F, 2013

Caltrans, Guideline on Foundation Loading and Deformation Due to Liquefaction Induced Lateral Spreading, 2012

ENGEO, Existing Geotechnical Conditions and Seismic Slope Stability, Brooklyn Basin Phase 1, Oakland, California. 2015

Federal Emergency Management Agency, FEMA-356 Prestandard and Commentary for the Seismic Rehabilitation of Buildings, 2000

Martin and Qui, Effects of Liquefaction on Vulnerability Assessments. NCEER Highway Project on Seismic Vulnerability of New and Existing Highway Construction, Year One Research Talks, Technical Research Papers, 1994

National Cooperative Highway Research Program, NCHRP Report 611, Seismic Analysis and Design of Retaining Walls, Buried Structures, Slopes and Embankments, 2008

Working Group on California Earthquake Probabilities (WGCEP), The Uniform California Earthquake Rupture Forecast (UCERF 2), 2007

SEISMIC HAZARDS EVALUATION AND LATERAL PILE DESIGN IN DIATOMACEOUS EARTH

Steffan, Matt, McMillen Jacobs Associates, Portland, Oregon, USA, 503-384-2913, steffan@mcmjac.com

Khosravifar, Arash, Portland State University, Civil and Environmental Engineering Department, Portland, Oregon, USA, 503-725-4280, karash@pdx.edu

ABSTRACT

An expansion of the City of Klamath Falls Wastewater Treatment plant required geotechnical seismic hazard evaluations and deep foundation design. The site is located on the shore of Lake Ewauna and is underlain by diatom rich lake deposits. Diatomaceous soils exhibit unique engineering properties that are not well understood. Cyclic Direct Simple Shear (CDSS) testing was performed on three undisturbed samples to evaluate cyclic and post-cyclic properties of the diatomaceous soils. Results from the CDSS testing indicated that the soils would not liquefy in the classical sense, though cyclic softening behavior was observed. The CDSS results were used to develop a Cyclic Resistance Ratio curve for the diatomaceous soil to compare with clean sand liquefaction curves. Seismic lateral pile capacities were developed using two approaches. One approach used conventional p-multipliers for liquefied soil and modified them to reflect expected excess pore pressure ratios. The other approach applied residual strength and fifty percent strain values from post-cyclic monotonic shear testing. A lateral spread hazard zone was identified along the Lake shoreline and reduced, seismic lateral pile capacities were recommended. The objective of this paper is to report the seismic design considerations for this project in a unique geologic and seismic setting.

KEYWORDS: diatoms, diatomaceous, cyclic shear testing, liquefaction, cyclic softening, lateral pile analysis

INTRODUCTION

The engineering properties of diatomaceous soils have rarely been studied and the cyclic behavior under seismic loading is generally unknown. Some of the critical geotechnical uncertainties of diatomaceous behavior include potential for large consolidation settlement, influence of irrecoverable strains due to diatom particle crushing, shear strength (peak and residual), and cyclic properties. This paper presents results of cyclic shear testing, seismic evaluations and seismic lateral pile design in diatomaceous soils performed for the expansion of a waste water treatment plant in the city of Klamath Falls, Oregon, site of the largest recorded earthquake in Oregon's history.

The expansion consisted of adding six new facilities at the existing Plant including influent pump station (IPS) and headworks, aeration basin, tertiary treatment, and other buildings. The IPS/headworks and aeration basin will be founded approximately 15 feet below ground. The other buildings will be founded at grade. The existing facilities are supported by timber piles that penetrate the surficial diatomaceous soils and terminate on a hard underlying deposit. Figure 1 shows the site plan and proposed additions.

The Project site is located immediately adjacent to Lake Ewauna whose shoreline slopes gently from the site to the west to a maximum lake depth of approximately 12 feet. Due to the active seismic setting and lake-side location, the potential vertical and lateral permanent ground deformations (PGD) associated with liquefaction settlement and lateral spreading, respectively, and earthquake induced strength loss were of primary interest. With the understanding that conventional empirical seismic correlations would not be

© 2018 Deep Foundations Institute

appropriate for these unique subsurface conditions, a major component of the geotechnical characterization was Cyclic Direct Simple Shear (CDSS) testing performed on undisturbed diatomaceous soil samples. The results of CDSS testing indicated "clay-like" cyclic behavior of the diatomaceous soils at this site and resulted in lower seismic design impacts than were calculated with conventional, simplified stress based estimates from penetration testing, as discussed subsequently.

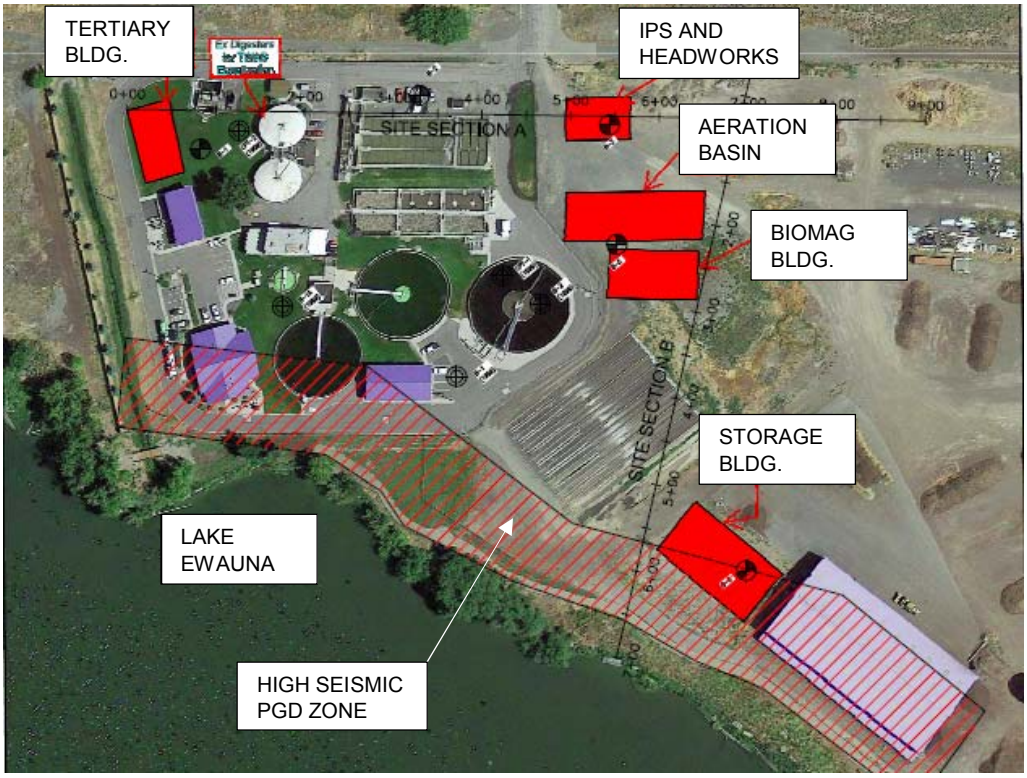


Fig. 1. Site Plan With New Facilities Indicated

GEOTECHNICAL CHARACTERIZATION

Diatomaceous soils are composed of the thin, hollow, siliceous skeletons of diatoms. Diatoms are a one cell aquatic plant which thrive in waters rich with dissolved silica. Such were the conditions during the Pliocene and Pleistocene in the great pluvial lake in the Klamath Basin which received ashfall from adjacent Cascade Mountain Range volcanic vents. Diatoms accumulated on the lake bottom with the volcanic ash and algae and formed thick deposits of diatom rich lacustrine deposits. The hollow diatoms create a soil structure with unusually low density and high water content, due to the hollow diatom structure.

The subsurface conditions consisted of approximately 30 to 35 feet of soft, recent deposits with diatomaceous silts, underlain by approximately 20 to 25 feet of layered stiff silts and medium dense silty sands, followed by stiff to hard, Pliocene aged lake deposits between approximately 50 and 60 feet below ground surface as indicated on Fig. 2. Groundwater levels were measured between 8 and 11 feet below ground surface. Consolidation testing indicated the recent deposits to be slightly over-consolidated with an estimated over-consolidation ratio of between approximately 2 to 3. The site was designated a Seismic Site Class E based on the shear wave measurements and soil index properties. Measured shear wave velocities from seismic cone penetrometer testing are shown on Fig. 3. Clean sand equivalent corrected blowcounts ($(N1)_{60cs}$) within the diatomaceous soils are shown on Fig. 4.

The foundation design included embedding auger-cast piles a minimum 10-feet into the underlying lake deposits. The geotechnical seismic hazard evaluations included the potential for settlement, strength loss and lateral spreading due to liquefaction in the upper diatomaceous rich recent deposits as well in some zones in the quaternary silt and sand.

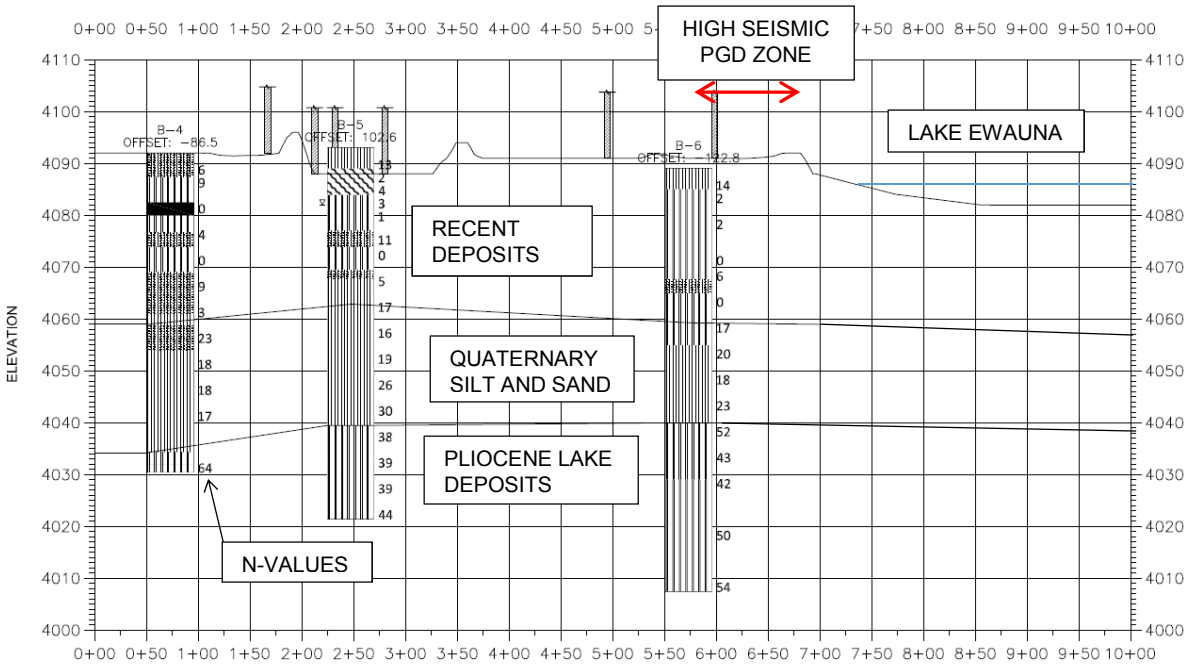


Fig. 2. Interpreted Geotechnical Profile

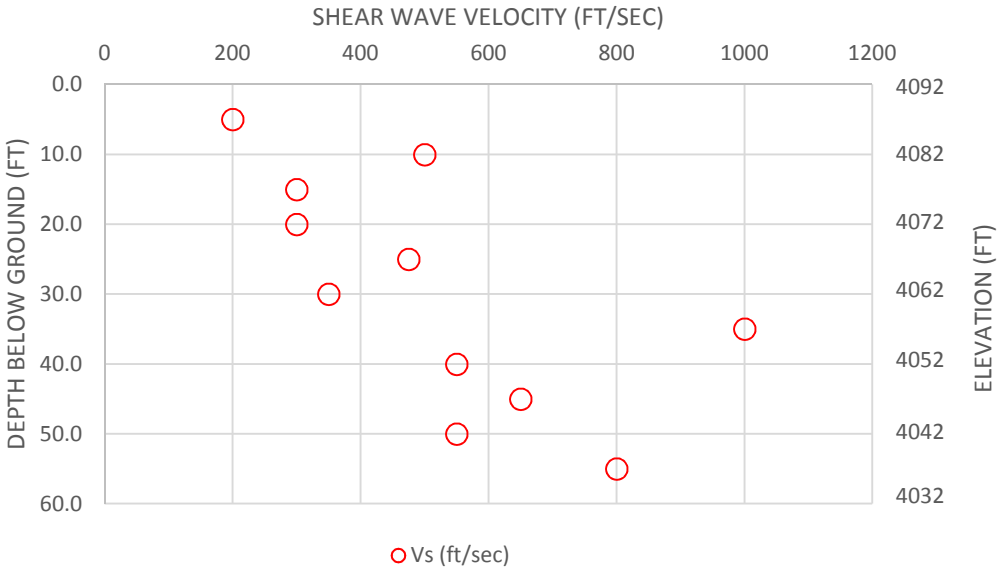


Fig. 3. Site Shear Wave Profile

Table 1 presents a summary of the soil index testing results from diatomaceous silt samples along with the liquefaction susceptibility results from Boulanger and Idriss (2005) and Bray and Sancio (2006). Informal microscopic photographs were taken of highly diatomaceous samples showing bowl and tube shaped diatoms (Figs. 5 and 6, respectively). The highly variable plasticity properties, mixed levels of liquefaction susceptibility, and range of corrected clean sand blowcounts warranted further inspection of the cyclic properties of the diatomaceous soils via the CDSS testing.

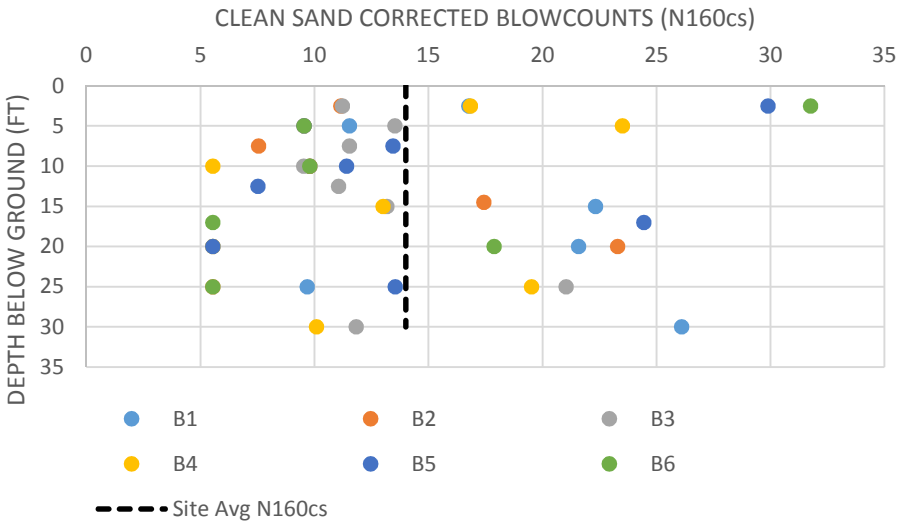


Fig. 4. Profile of Clean Sand Equivalent Corrected Blowcounts



Fig. 5. Photo of bowl shaped diatoms
(Photo courtesy of Benchmark Geolabs, LLC)



Fig. 6. Photo of tubular diatoms
(Photo courtesy of Benchmark Geolabs, LLC)

Table 1. Summary of Index Property Testing and Common Liquefaction Susceptibility Criteria

Boring	Sample Depth	Plastic Limit	Liquid Limit	Plasticity Index	Moisture Content	Boulanger and Idriss 2005	Bray and Sancio 2006
B-1	10	146	149	3	217	Sand Like	Susceptible
B-1	25	56	116	63	136	Clay Like	Not susceptible
B-2 (CDSS sample)	12.5	94	126	32	137*	Clay Like	Not susceptible
B-4	20	40	71	31	78	Clay Like	Not susceptible
B-5	15	174	165	NP	240**	Sand Like	Susceptible
B-5	20	40	75	35	97	Clay Like	Not Susceptible
B-6	10	92	136	44	169	Clay Like	Not susceptible
B-6	15	170	150	NP	251	Sand Like	Not susceptible

Table Notes:

* Dry density = 35 pounds per cubic foot

**Dry density = 22 pounds per cubic foot

1993 EARTHQUAKES AND DESIGN GROUND MOTIONS

The Klamath Falls earthquake sequence that occurred on September 20, 1993 resulted in two main shocks. These earthquakes registered Richter magnitudes 5.9 and 6.0 and are the largest recorded earthquakes in Oregon history. The epicenters were located approximately 16 miles (26 kilometers) west-north-west within the Mountain Lakes Wilderness (Wiley, 1993). The USGS Shake Maps from these events indicate Modified Mercalli intensity values between 5 and 6 at the Project site. This correlates to an estimate of peak ground acceleration of approximately 0.25g (Wald, 1999). The event resulted in extensive damage to unreinforced masonry buildings in Klamath Falls, and landslides throughout a 162 square mile area around the radius (rock falls and rock slides in road cuts and slumping failures in some road fills) (Wiley, 1993). However, the events did not appear to cause substantial liquefaction or lateral spreading. Most importantly for the Project was that the 1993 earthquakes did not result in observed PGD at the Plant. The lack of observed PGD from the 1993 events provided the opportunity to corroborate the results from CDSS testing with these observations.

To develop earthquake parameters for the CDSS testing and seismic evaluations, we assessed the ground motions from the 2014 USGS Unified Hazard Tool deaggregation (dynamic Version 4.1.1) for a 2,475 year return period and Site Class E, representing the Maximum Considered Earthquake geometric mean (MCE_G) ground motions. The deaggregation indicates a mean magnitude earthquake of 6.7 and a mean peak ground acceleration (PGA_M) of 0.61g which was used in our seismic lab testing and hazards evaluations, as discussed subsequently.

CYCLIC DIRECT SIMPLE SHEAR TESTING ON DIATOMACEOUS SOILS

The objectives of the CDSS testing was to gain an understanding of the cyclic behavior of the diatomaceous soils and to provide a rational basis to perform seismic hazard evaluations. Of particular interest was whether the material would exhibit "sand-like" or "clay-like" undrained cyclic behavior and to evaluate the degree of liquefaction or cyclic softening under the MCE_G loading. Post-cyclic monotonic shear testing was performed to provide basis for residual (i.e. post-earthquake) shear strength. Post-cyclic consolidation testing was performed on one sample to investigate potential for earthquake induced vertical settlement.

To develop the CDSS testing program, the estimated cyclic stress ratio (CSR) from the 1993 earthquakes and MCE_G ground motions were considered. The calculated values of CSR near the mid-point of the diatomaceous rich layer were 0.23 for the 1993 events, and 0.58 for the MCEG event. In order to develop a site specific curve of cyclic resistance ratio (CRR), CDSS testing was also performed at a CSR of 0.40 (which corresponds approximately to 975 year return interval ground motions).

CDSS testing was performed on 3 diatomaceous samples extruded from the thin walled ("Shelby tube") sampler advanced in boring B-2 from 12.5 to 14.5 feet below ground. The samples were consolidated to the estimated pre-consolidation pressure (90 kPa, 1,880 psf), unloaded to the estimated in-situ vertical effective stress (45 kPa, 940 psf), and then subjected to cyclic loading at the specified CSR level at 0.1 Hz (one load cycle per 10 seconds) until failure was achieved. In this study, failure was defined as the peak-to-peak (p-p) shear strain of 5 percent. Table 2 summarizes key information from the CDSS testing program.

Table 2. Summary of CDSS Results

Test	CSR	Corresponding Seismic Level	Cycles to 5% p-p Shear Strain	Excess Pore Pressure Ratio (r_u)	Strain at 50 Percent Undrained Shear Strength (ε_{50})	Post-cyclic Re-Consolidation Volumetric Strain (ε_v)
1	0.58	MCE_G (based on 2,475 Year Return Interval)	1	0.65	0.070	-
2	0.23	1993 Klamath Falls Earthquakes	>220	0.10	0.025	-
3	0.40	975 Year Return Interval	15	0.25	-	0.2% Vol strain*

Table Notes:

* Post-cyclic re-consolidation performed on this sample.

The CDSS test at the 1993 CSR level did not reach failure (5 percent p-p strain) which is consistent with the observation from that event. The MCEG test level failed the sample on the first loading cycle, resulting in excess pore pressure of approximately 65 percent. A representative stress-strain plot for CSR of 0.4 is shown on Fig. 7. The stress-strain plot is consistent with "clay-like" behavior, indicating that cyclic-softening rather than liquefaction would be appropriate for design. The CSR and number of cycles to reach failure from Table 1 were used to generate a site specific CRR curve, shown on Fig. 8. The relationship

between CSR and the number of cycles was approximated using a power relationship with the exponent (i.e. b-value) calculated as 0.17 which is within the expected range for clay-like behavior reported by Boulanger and Idriss (2014).

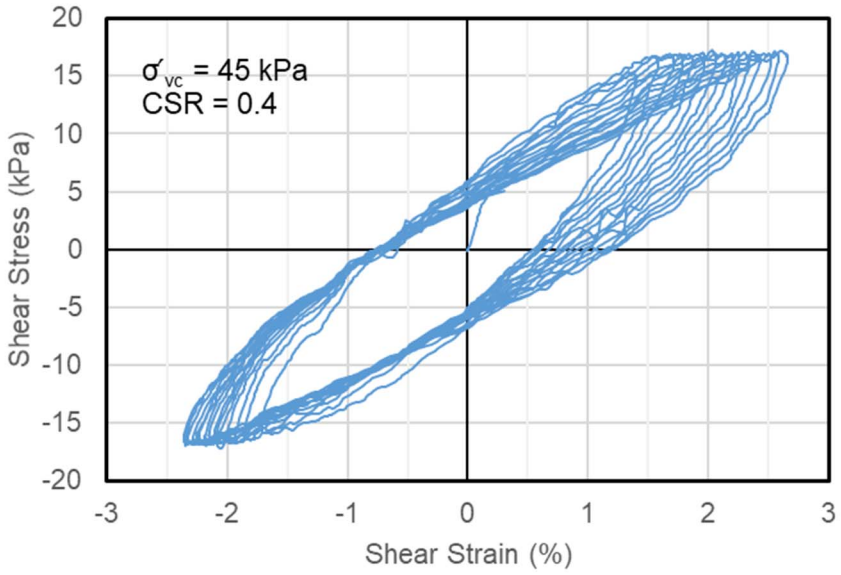


Fig. 7. CDSS Stress-Strain Plot from Test 3

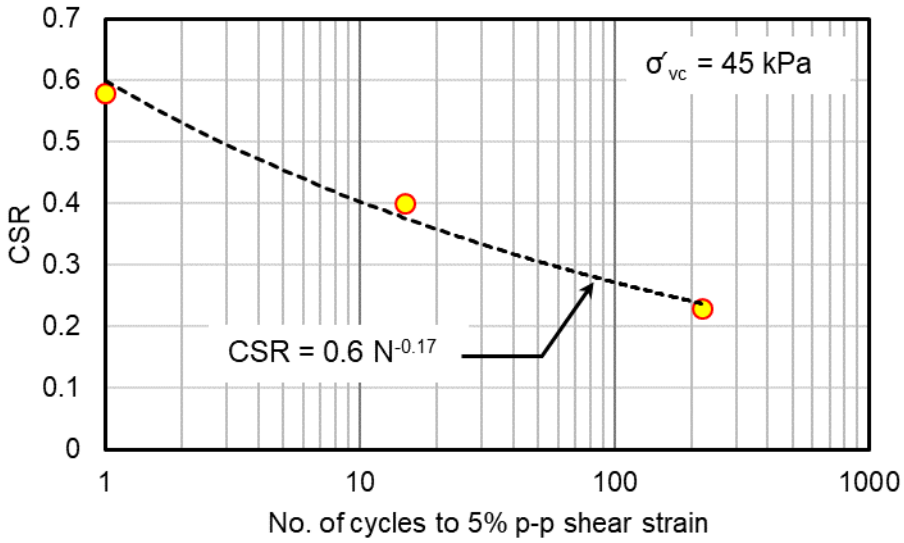


Fig. 8. CRR Curve Generated from CDSS Tests

SEISMIC HAZARDS EVALUATION

As indicated earlier, liquefaction susceptibility evaluations based on soil index properties were inconclusive. Liquefaction triggering was evaluated by performing simplified SPT-based method using results from in-situ penetration testing (Boulanger and Idriss, 2014), evaluating the results of the CDSS tests, and considering the observations from the 1993 earthquakes.

Liquefaction triggering based on the 1993 earthquake magnitude and PGA was first performed to compare calculated liquefaction settlements with the observations from the 1993 earthquakes. The site average calculated liquefaction settlement within the diatomaceous soils below the groundwater was 7 inches. To calibrate the SPT based triggering analysis with the observations from the 1993 earthquakes, clean sand equivalent corrected blowcounts ($(N1)_{60cs}$) were factored up until the resulting settlement was less than 1 inch. This required the $(N1)_{60cs}$ in the diatomaceous soils below groundwater to be factored up by an average value of 2.6.

The calculated MCE_G liquefaction factors of safety were generally less than 0.4 with a site average settlement of 9 inches. The factored values of clean sand blowcounts were then used to re-calculate the liquefaction factors of safety and settlement from the MCE_G. Using the factored values of $(N1)_{60cs}$, the calculated settlement from the MCE_G in the diatomaceous soils was reduced from 9 inches to 6 inches, as summarized in Table 3. A total liquefaction settlement of 6 inches within the diatomaceous layer below the groundwater corresponds to an average value of volumetric strain of approximately 2 percent. This value is consistent with published values of clay-like soils at the expected r_u of 65 percent (Beaty et al., 2014).

Table 3. Summary of Simplified Liquefaction Settlement Estimates

Seismic Event	Calculated Liquefaction Settlement* (inches) (Boulanger and Idriss 2014)	Calculated Liquefaction Settlement* Using Scaled $(N1)_{60cs}$ (inches)
1993 Klamath Falls Earthquakes	7	<1”
MCE_G	9	6

Table Notes:

* Site-wide average calculated value within the diatomaceous soil layer below the groundwater.

Results of the CDSS tests and SPT-based liquefaction triggering analyses indicated that applying correlations based on full liquefaction would tend to over-estimate the seismic hazard and that corrections to account for lower levels of r_u were appropriate for design.

Residual strength (i.e. post-earthquake strength) estimates for the diatomaceous soils were developed based on correlations to penetration testing (Boulanger and Idriss 2008; Kramer and Wang 2015; Weber 2015). These residual strength correlations are based on fully liquefied conditions with values of r_u generally above 90 percent. To account for the lower levels of r_u expected in the diatomaceous silts, the calculated residual strengths were scaled proportionately by the ratio of $100/r_u$. With the above described methodology, an average undrained residual shear strength of 300 psf was calculated for the diatomaceous silts below the groundwater and to approximate depths between 24 and 33 feet bgs.

The lateral spreading hazard was evaluated using the pseudo-static, semi-empirical procedure published by Bray and Travasarou (2007). Using this method, we calculated a yield acceleration of 0.37g that results in lateral spreading displacement estimate of 6 inches. To evaluate the potential extent of lateral spreading displacements of this magnitude, this yield acceleration was added to the slope stability model as a horizontal acceleration coefficient. The failure surfaces with factors of safety equal to or less than 1.0 represent zones where this level of lateral spreading may be encountered. Based on the lateral spreading evaluation, a zone within the approximate 100 feet from the edge of the bank was designated as a High Seismic PGD Zone where lateral spreading displacements on the order of 6 inches are estimated. It was recommended that critical site infrastructure be located outside of this zone in order to avoid significant increase in foundation costs to resist lateral spreading demands on the structures and foundations.

SEISMIC LATERAL PILE DESIGN

Due to the potential of lateral spreading impacts near the bank of the Lake, critical new facilities for the Plant expansion were moved outside the High Seismic PGD zone. Thus, additional lateral pile capacity to resist lateral spreading loads was not a design case. However, due to the expected levels of cyclic softening under the design earthquake, reductions in pile lateral capacity were evaluated. Lateral pile analyses of the proposed 24-inch-diameter auger-cast piles were performed using LPILE 2016 (Ensoft Inc.). The diatomaceous soils were modelled using the Matlock (1970) soft clay p-y curves. The soft clay p-y curves were modified to account for cyclic softening using two approaches, as described in CALTRANS (2012): the p-multiplier approach and the residual strength approach.

In the p-multiplier approach, a p-multiplier (m_p) for fully liquefied conditions is calculated, using Equation 1. To represent the clay-like behavior of the diatomaceous soils and expected lower levels of r_u, the calculated m_p was scaled proportionately by $100/r_u$. In the residual strength approach, an estimate of undrained residual shear strength was calculated (as described previously). The strain factor (ε_{50}) was based on the post-cyclic monotonic simple direct shear test at the MCE_G CSR (Test 1 from Table 2). These values were then used in the soft clay p-y model. Table 4 presents a summary of lateral pile design parameters used in these evaluations. A comparison of p-y curves at a depth of 20 feet bgs and 5 feet below the top of pile (for buried structures) is presented on Fig. 9. Table 5 presents a summary of the pile lateral capacity for a 0.5-inch pile head deflection based on fixed-head boundary conditions.

$$m_p=0.0031(N1)_{60cs} + 0.00034(N1)_{60cs}^2 \quad [1]$$

Table 4. Summary of Lateral Pile Design Parameters in Diatomaceous Layer

Average Effective Unit Weight (pcf)	Excess Pore Pressure, r_u (percent)	Static Condition		Seismic Condition: P-Multiplier Approach			Seismic Condition: Residual Strength Approach	
		Undrained Cohesion (psf)	Strain Factor (ε_{50})	Average $(N1)_{60cs}$	P-multiplier, m_p	Scaled m_p	Residual Strength (psf)	Strain Factor (ε_{50})
17	65	500	0.02	14	0.11	0.17	300	0.07

Table 5. Shear Force for ½ inch Pile Head Deflection on 24-inch Auger Cast Piles

Static Condition	Seismic Condition: P-Multiplier Approach	Seismic Condition: Residual Strength Approach
52.5 kips	28.8 kips	33.0 kips

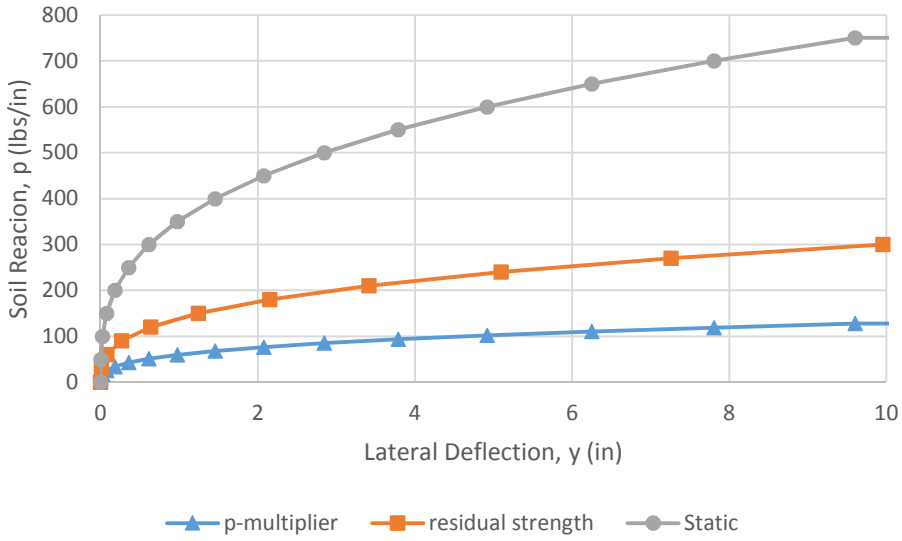


Fig. 9. P-y Curves at a depth of 20 Feet BGS, 5 feet below top of 24-inch diameter pile

As shown in Table 5 and Fig. 9, the p-multiplier approach provided the lower-bound estimate of seismic lateral pile response. Seismic lateral pile capacity using the p-multiplier and residual strength approaches were calculated to be approximately 55 and 63 percent of the static condition lateral capacity, respectively.

SUMMARY AND CONCLUSIONS

Diatomaceous soils have unique composition and structure and their basic engineering properties are not well understood. The unusually low density and high moisture content limits the applicability of many conventional geotechnical methods. The cyclic behavior of diatomaceous earth in Klamath Falls was investigated by using the CDSS test on undisturbed soil samples. The CDSS tests provided a rational basis for seismic design and indicated that the diatomaceous materials on site would exhibit cyclic degradation under the design earthquake loading. The material exhibited higher cyclic resistance than would be indicated with conventional, simplified procedures. Pile lateral capacity was evaluated by modifying conventional soft clay p-y curves with the results of the CDSS tests. The use of CDSS permitted economical foundation design by reducing uncertainty regarding cyclic behavior of diatomaceous soil and not over-stating the seismic hazards at the site.

REFERENCES

Beaty, M., Schlecter, S., Greenfield, M., Bock, J., Dickenson, S., Kempner, L, and Cook, K., 2014. Seismic Evaluation of Transmission Tower Foundations at River Crossings in the Portland-Columbia River Regrion. Proceedings of the 10th National Conference in Earthquake Engineering, Earthquake Engineering Research Institute, Anchorage, AK, 2014.

Bray, J.D. and Sancio, R.B., 2006. Assessment of the Liquefaction Susceptibility of Fine-Grained Soils. Journal of Geotechnical and Geoenvironmental Engineering, Vol. 132, No. 9, pp. 1165-1177.

Boulanger, R.W., and Idriss, I.M., 2005. Evaluating cyclic failure in silts and clays. Proceedings, Geotechnical Earthquake Engineering Satellite Conference on Performance Based Design in Earthquake Geotechnical Engineering: Concepts and Research. Prepared by TC4 Committee of ICSMGE, Japanese Geotechnical Society, Tokyo, pp. 78-86.

Boulanger, R.W., and Idriss, I.M., 2006. Liquefaction susceptibility criteria for silts and clays. Journal of Geotechnical and Geoenvironmental Engineering 132(11):1413–1426.

Boulanger, R.W., and Idriss, I.M., 2014. CPT and SPT Based Liquefaction Triggering Procedures, Report No. UCD/CGM-14/01, Center for Geotechnical Modeling, Department of Civil & Environmental Engineering, College of Engineering, University of California at Davis.

Bray, J.D., and T. Travasarou, 2007. Simplified procedure for estimating earthquake-induced deviatoric slope displacements. Journal of Geotechnical and Geoenvironmental Engineering 133(4):381–392.

CALTRANS. 2012. Guidelines on Foundation Loading and Deformation Due to Liquefaction Induced Lateral Spreading. Sacramento, California.

Enosft Inc., LPILE 2016 Computer Program, 2018.

Idriss, I.M., and Boulanger, R.W., 2008, Soil Liquefaction During Earthquakes, Earthquake Engineering Research Institute, Oakland, CA, 235 pp.

Kramer, S.L, and Wang, C., 2015. Empirical model for estimation of the residual strength of liquefied soil. Journal of Geotechnical and Geoenvironmental Engineering 141(9):04015038.

Matlock, H. 1970. Correlations for design of laterally loaded piles in soft clay. Proceedings of the II Annual Offshore Technology Conference, Houston, Texas, (OTC 1204): 577-594.

Petersen, M.D., Moschetti, M.P., Powers, P.M., Mueller, C.S., Haller, K.M., Frankel, A.D., Zeng, Yuehua, Rezaeian, Sanaz, Harmsen, S.C., Boyd, O.S., Field, Ned, Chen, Rui, Rukstales, K.S., Luco, Nico, Wheeler, R.L., Williams, R.A., and Olsen, A.H., (2014) "Documentation for the 2014 update of the United States national seismic hazard maps: U.S. Geological Survey Open-File Report 2014–1091", 243 p., https://dx.doi.org/10.3133/ofr20141091.

United States Geological Survey Shake Maps. Available at https://earthquake.usgs.gov/data/shakemap/; accessed 12 November 2018

Wald, D. J., Quitoriano, V., Heaton, T. H., and Kanamori, H., 1999. Relationships between Peak Ground Acceleration, Peak Ground Velocity, and Modified Mercalli Intensity in California. Earthquake Spectra, Volume 15, No. 3, August 1999,pp. 557-564

Weber, J.P. 2015. Engineering evaluation of post-liquefaction strength. Ph.D. diss., University of California, Berkeley. 158 pp.

Wiley, T.J., Sherrod, D.R., Keefer, D.K., Qamar, A., Schuster, R.L., Dewey, J.W., Mabey, M.A., Black, G.L., and Wells, R.E., 1993. Klamath Falls Earthquakes, September 20, 1993 – Including the Strongest Quake Ever Measured in Oregon, Oregon Geology, Volume 55, Number 6, November.

SPRING CONSTANTS OF BELLED CAISSONS FOR SEISMIC RETROFIT OF AN EXISTING CRITICAL STRUCTURE IN A SEISMICALLY ACTIVE AREA

Bidjan Ghahreman, Albus-Keefe & Associates, Inc., Anaheim, CA, USA, (714) 630-1626, bghahreman@albus-keefe.net

David E. Albus, Albus-Keefe & Associates, Inc., Anaheim, CA, USA (714) 630-1626, dalbus@albus-keefe.net

Ahmadreza Mortezaie, Albus, Albus-Keefe & Associates, Inc., Anaheim, CA, USA (714) 630-1626, rmortezaie@albus-keefe.net

ABSTRACT

The structural evaluation of seismic performance of an existing hospital in Long Beach, California, required spring constants of foundation elements. The structure included support by deep foundation elements comprised of belled (underreamed) caissons. The available relationships in the governing building code (ASCE41-13) to compute axial stiffness is not applicable due to the belled configuration of the caissons. The large diameter of the bells required consideration of the foundation medium to the axial stiffness; a detail not clearly described in ASCE 41-13. Furthermore, prescriptive equations in ASCE 41-13 used to estimate lateral stiffness only consider pile groups with the assumption that the only source of lateral stiffness is the axial reaction of individual piles. These assumptions were invalid for the project at hand where all caissons are configured as single foundation elements, not a pile group. In the present work, the approach taken to estimate seismic stiffness of single-belled caissons is described which accounts for the elastic behavior of the foundation medium below the bell base and lateral behavior of single-pile shafts. Results of the work provide a more satisfactory derivation of the spring constants consistent with current modeling methods.

Keywords: spring, constant, belled, caisson, seismic, retrofit, hospital, san pedro

INTRODUCTION

Seismic evaluation of an existing hospital in Long Beach, California, required geotechnical investigation followed by site-specific ground motion analysis. This evaluation was required by the Office of Statewide Health Planning and Development (OSHPD) in order to meet the requirements of the Structural Performance Category 4D (SPC-4D) published as a part of the 2016 California Building Code, CBC (Section 3412A). SPC-4D utilizes ASCE41-13, as modified by OSHPD, and involves two seismic performance objectives: BSE-1E (20% probability of exceedance in 50 years) and BSE-2E (5% probability of exceedance in 50 years). Spring constants and capacities of foundation elements were needed for evaluation of the structural performance of the building subjected to these two performance objectives.

Our review of the as-built foundation plans indicated that both shallow footings and caissons were used for support of the structure. The plans demonstrated that all caissons are belled (under-reamed) and are individual, i.e. not part of pile groups. In this paper, the subject site condition and foundation elements are described first. This is followed by details of assessing spring constants and vertical capacities for belled caissons. The new requirements of the 2016 CBC concerning the evaluation of critical facilities will likely entail evaluation of other structures with belled caissons due to the more extensive use of these foundations in the past. This paper proposes a method to address the conditions of individual belled caissons not explicitly considered in the current code provisions.

© 2018 Deep Foundations Institute

SITE AND FOUNDATIONS CONDITION

Local Geology

A site investigation was undertaken to characterize the underlying geologic and geotechnical conditions. The investigation included review of geologic publications, examination of historical aerial photographs, review of historical topographic maps, drilling of hollow-stem auger borings, and seismic cone penetration test (SCPT). The field investigation was performed in January 2016. A plan of the site and locations of site exploration are depicted on Fig. 1.

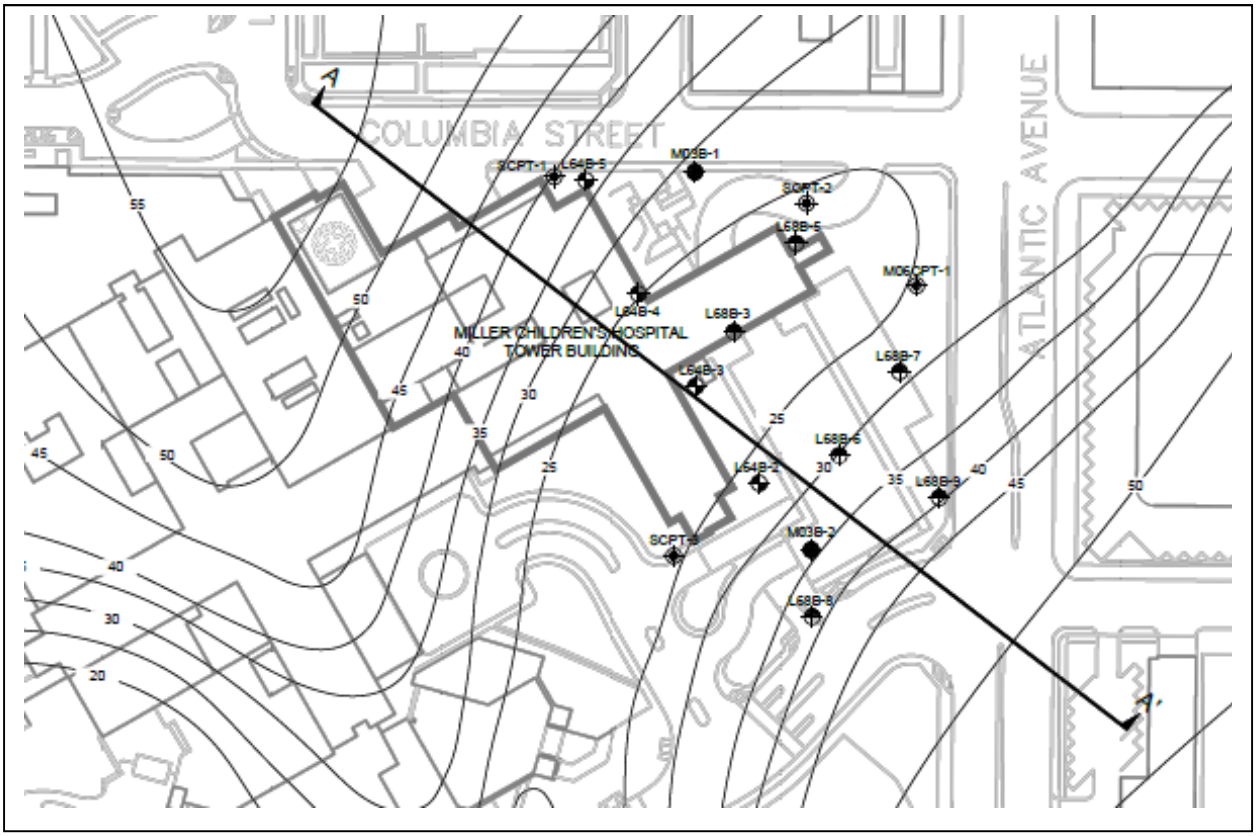


Figure 1-Site plan depicting locations of site exploration, historical topography, and location of cross section.

The site is within a seismically active area with the closest active fault, Newport Inglewood, located within approximately 0.4 kilometers (0.25 miles) of the site (CDMG 1986). Several other active faults are in proximity to the site and contribute to the potential ground motions.

Interpreted subsurface conditions for the site are depicted on the Geologic Cross Section, Fig. 2. The site is situated within a former drainage course that is currently filled with man-made fill soils (A_f in Fig. 2). Topography of the former drainage, and thereby the thickness of fill soils, was established using data gathered during subsurface investigation and review of old topographic maps (USGS 1925). Results of seismic cone penetration test (SCPT) soundings indicate the fills are mixtures of sands, silts, and clays that are dense or stiff. Based on current ground surface elevations, the thickness of fill varies from a few feet along the flanks of the former drainage course up to approximately 50 feet within the center of the former drainage course. A veneer of Holocene–age alluvial soils (Q_{al}) underlies the fill soils within the confines of the former drainage. The alluvial soils vary in thickness from nil to approximately 14 feet and are comprised primarily of stiff interbedded sandy silt, clayey silt and silty clay.

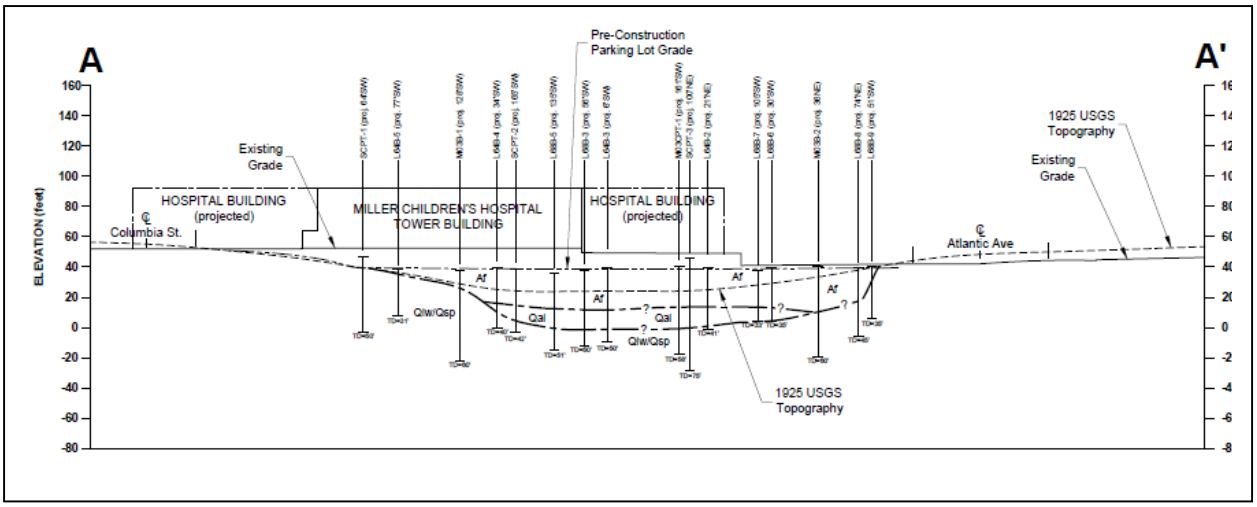


Figure 2-Geologic cross section depicting subsurface profile

The alluvial soils are underlain by a thick Pleistocene-age marine and non-marine bedrock unit assigned to the San Pedro Formation, Q_{sp} (Poland and Piper 1956). The San Pedro Formation is generally comprised of thick sequences of sandstone, silty sandstone, sandy siltstone, clayey siltstone and sandy claystone. These sediments are very dense in consistency. According to Poland and Piper (1956) these Pleistocene-age sediments extend to depths of 200 to 500 feet below the ground surface at the project site.

The interpreted shear wave velocity profiles obtained from SCPT and CPT soundings are presented on Fig. 3. The average shear-wave velocity within the upper 30 meters of the soil (V_{S30}) for the four soundings shown in this figure narrowly ranges between about 950 to 1,200 feet per second (ft/s) with an overall average of V_{S30}=1,076 ft/s despite the variable depth to San Pedro Formation across the explored area. This average shear wave velocity is very close to 1,200 ft/s that defines the limit between site classes C and D, as defined in Section 11.4.2 of ASCE 7-10. Accordingly, site class C/D was assigned to the project site and was used for seismic site hazard analysis for both BSE-2E and BSE-1E hazard levels.

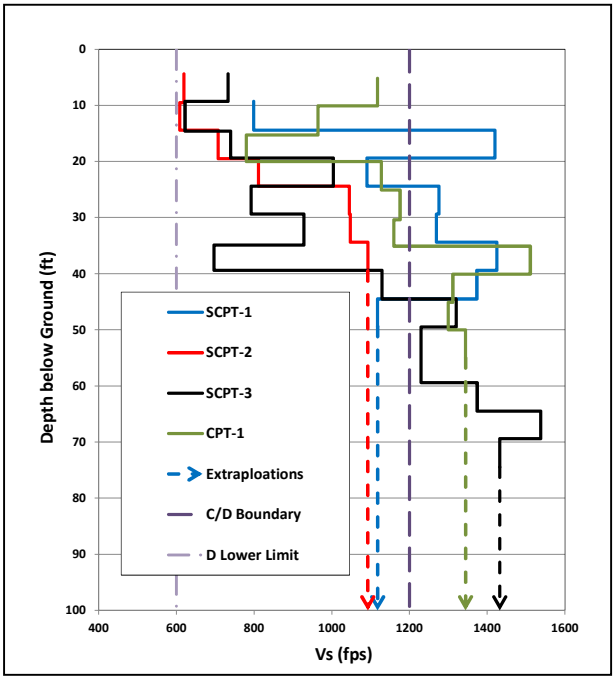


Figure 3-Plots of shear wave velocity profiles from seismic cone penetrometer soundings

Figure 3 suggests the San Pedro formation can be represented by an average shear wave velocity of 1,215 ft/s. This velocity is consistent with the average shear wave velocity reported for this formation in literature (Table 2.2 of PEER 2012/08).

Foundation Configurations

The subject building includes a basement with its floor located approximately 7 to 19 feet below the outside grade due to sloping conditions around the building. Review of the as-built foundation plans circa 1958 indicates that both shallow footings and caissons were used for the foundation. All foundation elements were founded on the San Pedro formation.

The focus of the present paper is on the behavior of the caissons. Figure 4 shows the typical configuration of caissons established from as-built plans of 1958. All of the caissons are belled (under-

reamed) at the base and have a straight shaft extending up from the bell section. The shafts are capped by pile caps 2 or 3 feet in thickness. Most of the caissons are tied in one direction to adjacent foundation elements (caissons or spread footings) by tie beams. Caissons generally have a center-to-center spacing of 30 feet, and as such, are considered to act as individual piles. Table 1 includes configurations of selected belled caissons in this project. For ease of reference in the remainder of this paper, each configuration in Table 1 is assigned a label, and will be used in the tables that follow. Using information provided in the foundation plans and results of site investigation, the parameters required in the relevant analyses were assigned as summarized in Table 2.

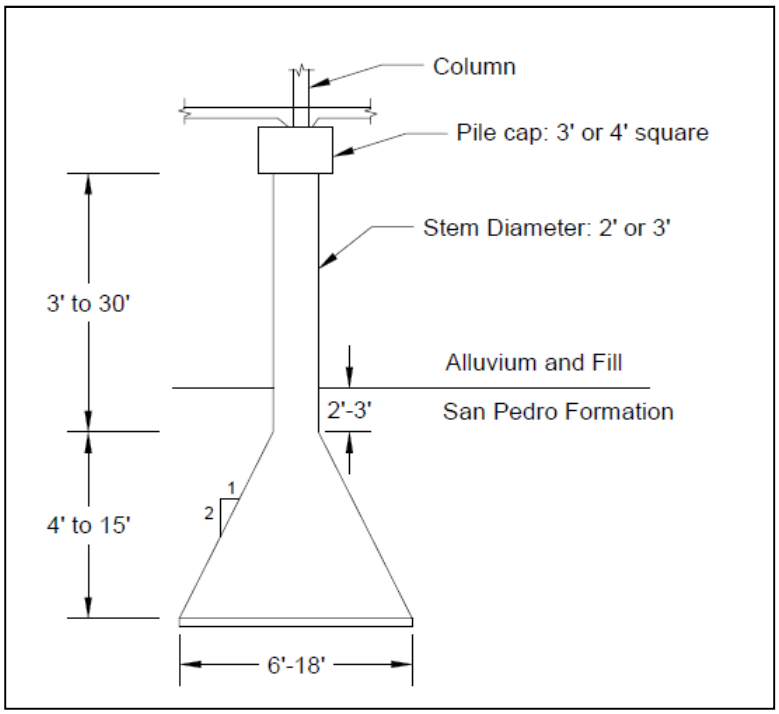


Figure 4-Typical configuration of caissons

AXIAL STIFFNESS

Per Section 8.4.4 of ASCE41-13, the spring constant of drilled shafts (or caissons) with a diameter greater than 24 inches should include both the structural spring constant and the foundation effect using a Winkler-type model. As indicated in Table 1, although some of the caissons have a shaft diameter of 24 inches, their interaction with the foundation medium (San Pedro formation) in the vertical direction is dominated by a greater bell diameter. As a result, all caissons in this investigation are treated as having diameters greater than 24 inches and as such, their interaction with the foundation medium was included using a Winkler-type model.

The vertical spring constant of a caisson, K_z, is estimated by considering the structural component of the pile represented by a spring constant, K_{sv}, and the foundation medium represented by a spring constant K_{gv}, as two springs in series. Thus:

$$K_z = \frac{1}{\frac{1}{K_{sv}} + \frac{1}{K_{gv}}} \qquad [1]$$

The vertical structural spring constant, $K_{sv,}$ was computed using the relationship for an elastic rod, as suggested by Equation 8-13 of ASCE41-13. For a rod with length L, cross sectional area A, and elastic modulus E, the stiffness (spring constant), K, is estimated as:

$$K = \frac{AE}{L} \qquad [2]$$

Table 1-Configuration of Selected Caissons

Label	Db (ft)	Dsh (in)	(EL)g (ft)	(EL)t (ft)	(EL)b (ft)	Lbell (ft)	tc (ft)	Ltotal (ft)
1	10.0	24	27.8	24.3	11.3	8.3	2.0	13.0
2	7.0	24	32.0	24.3	14.3	5.3	2.0	10.0
3	12.0	36	32.0	31.2	16.0	9.3	3.0	15.2
4	14.5	36	32.0	31.2	0.5	11.8	3.0	30.7
5	18.0	36	32.0	31.2	-1.0	15.3	3.0	32.2
6	12.0	36	32.0	31.2	1.0	9.3	3.0	30.2
7	10.5	36	32.0	31.2	2.0	7.8	3.0	29.2
8	7.0	24	32.0	31.2	5.0	5.3	2.0	26.2
9	8.5	24	32.0	31.2	3.0	6.8	2.0	28.2
10	6.5	24	32.0	31.2	7.0	4.8	2.0	24.2
11	9.5	24	32.0	31.2	7.0	7.8	2.0	24.2
12	13.0	36	32.0	31.2	-5.0	10.3	3.0	36.2
13	6.0	24	32.0	28.5	-5.0	4.3	2.0	33.5
14	11.0	36	32.0	28.5	-3.0	8.3	3.0	31.5
15	6.0	24	32.0	31.2	7.0	4.3	2.0	24.2
16	7.5	24	32.0	28.5	8.0	5.8	2.0	20.5
17	8.5	24	32.0	28.5	0.0	6.8	2.0	28.5
18	11.5	36	32.0	28.5	-3.0	8.8	3.0	31.5
19	12.0	36	32.0	28.8	-8.0	9.3	3.0	36.8
20	8.0	24	32.0	31.2	-7.0	6.3	2.0	38.2
21	10.0	24	32.0	31.2	-7.0	8.3	2.0	38.2
22	8.0	24	32.0	28.8	-3.0	6.3	2.0	31.8
23	7.0	24	32.0	31.2	-3.0	5.3	2.0	34.2

Label: Is assigned to each configuration for ease of reference in the rest of this paper.
Db: Diameter of the bell the base
Dsh: Diameter of the shaft
(EL)g: Elevation of the vicinity grade (in most cases, the elevation of the basement floor)
(EL)t: Elevation to of top of pile cap
(EL)b: Elevation of the bottom (base) of footing or elevation of base of caissons bell
Lbell: Length of bell (in vertical direction)
Ltotal: Total length of caisson
tc: Thickness of pile cap

Table 2-Summary of Properties of Foundation Elements and San Pedro Formation

Item	Value	Note
Caissons		
Compressive strength, fc	3,000 psi	
Elastic Modulus, E	449,570 ksf	Based on concrete strength fc = 3,000psi
Poisson's ratio	0.20	For concrete
San Pedro Formation		
Poisson's ratio	0.25	ASCE41-13, Section 8.4.2.2
Initial shear modulus, G_0	5,500 ksf	Based on design Vs (from SCPT)
BSE-1E: G	4,125 ksf	Using respective Sxs in ASCE41-13, Table 8-2 (for Average of Class C and D)
BSE-2E: G	3,080 ksf	
Total Unit Weight, γ	120 pcf	Based on lab testing
Friction Angle, φ	31.8 degrees	
Cohesion, C	475 psf	
Friction coefficient, μ	0.39	Based on 2/3 φ

Because caissons in this project are comprised of a bell section at the bottom, a stem (shaft) in the middle and a pile cap at the top, the cross-sectional area of a caisson (A) is not constant along the caisson length. As a result, each caisson was modeled as three springs in series representing the bell, shaft, and pile cap with axial spring constants K_b, K_{sh}, and K_c, respectively. The vertical structural spring constant of a caisson, K_{sv}, was thus computed as:

$$K_{sv} = \frac{1}{\frac{1}{K_b} + \frac{1}{K_{sh}} + \frac{1}{K_c}} \quad [3]$$

Each of the three constituting stiffnesses (K_b, K_{sh}, and K_c) was computed using Equation 2 with the pertinent values of L and A. For bells, the average cross-sectional area of the bell was used for "A". For pile caps, dimensions 4ft x 4ft x 3ft (i.e., 3-foot thick) were used for 3-foot-diameter shafts, and 3ft x 3ft x 2ft was used for 2-foot-diameter shafts.

ASCE41-13 is not specific on guidelines or procedures to estimate axial stiffness of the foundation (earth) material at the base of caissons (K_{gv} in Equation 1). Given the typically large area of the caisson bases, the relationships available for shallow footings were deemed applicable. For this, the base of a bell was represented by an equal-area square footing. The thickness of footing (t) was defined as the bell volume divided by its cross-sectional area at the base as a way of creating an equivalent rectilinear object. Footings with these equivalent dimensions were subjected to the flexural rigidity test outlined through Equations C8-2 and C8-3 of ASCE41-13. Using this relationship, all footings were categorized as "rigid" as would be expected given their large height to width aspect ratio. As a rigid element, the axial stiffness of the foundation material, $K_{gv,}$ can be computed using Equation 4-a (from Fig. 8-2 of ASCE41-13):

$$K_{gv} = \beta_z K_{z,sur} \quad [4\text{-a}]$$

where:

$$K_{z,sur} = \frac{GB}{1-\nu}\left[1.55\left(\frac{L}{B}\right)^{0.75}\right] + 0.8 \quad [4\text{-b}]$$

$$\beta_z = \left[1 + \frac{1}{21}\frac{D}{B}\left(2 + 2.6\frac{B}{L}\right)\right] \cdot \left[1 + 0.32\left(\frac{d(B+L)}{BL}\right)^{2/3}\right] \quad [4\text{-c}]$$

In the above equations, $K_{z,sur}$ is the vertical stiffness at ground surface in dimensions of force divided by length, β_z is the embedment correction factor, L and B are length and width of the footing (in this case, L=B for the equal-area square representing base of bell), D and d are depth to the bottom and top of the footing, respectively. Depth is measured from the prevailing grade, i.e., from basement floor in this case. The value ν is the Poisson's ratio of the foundation material (San Pedro formation). Per Section 8.4.2.2 of ASCE41-13, ν = 0.25 was used. G is shear modulus and is estimated using the initial shear modulus, G_0, as:

$$G = n \times G_0 \quad [5\text{-a}]$$

The effective shear modulus ratio, n, in Equation 5-a is a function of effective peak acceleration (Sxs/2.5) and is defined in Table 8-2 of ASCE41-13 as shown in Fig. 5.

The initial shear modulus, G_0 is estimated through Equation 5-b (Eq. 8-4; ASCE41-13):

$$G_0 = \gamma {V_{s0}}^2 / g \quad [5\text{-b}]$$

In the above, γ is unit weight and g is acceleration of gravity (32.17 ft/s^2). Using shear wave velocity V_{S0} = 1,215 ft/s for the San Pedro formation, discussed above, resulted in G_0 = 5,500 kilo pounds per square foot (ksf). The two seismic performances (BSE-1E and BSE-2E) included in this work resulted in two different values of S_{xs}, and thus two different values of effective shear modulus ratio (n) were required to be developed.

Table 8-2. Effective Shear Modulus Ratio (G/G_0)

	Effective Peak Acceleration, $S_{XS}/2.5$[a]			
Site Class	$S_{XS}/2.5 = 0$	$S_{XS}/2.5 = 0.1$	$S_{XS}/2.5 = 0.4$	$S_{XS}/2.5 = 0.8$
A	1.00	1.00	1.00	1.00
B	1.00	1.00	0.95	0.90
C	1.00	0.95	0.75	0.60
D	1.00	0.90	0.50	0.10
E	1.00	0.60	0.05	[b]
F	[b]	[b]	[b]	[b]

[a]Use straight-line interpolation for intermediate values of $S_{XS}/2.5$.
[b]Site-specific geotechnical investigation and dynamic site response analyses shall be performed.

Figure 5-Table of effective shear modulus ratio as presented in Table 8-2 of ASCE41-13

The resulting structural stiffness, K_{sv}, (Equation 3) and foundation stiffness, K_{gv}, (Equation 4) were used in Equation 1 to compute the caisson's axial (vertical) stiffness, K_z.

LATERAL AND ROCKING STIFFNESS

Relationships provided in GCR 12-917-21 (National Institute of Standard and Technology, NIST 2012) were used to estimate lateral stiffness, k_{xx}, of the caissons. Equation 6-a (Eq. 2-22a; GCR 12-917-21) shows the general relationship between dynamic stiffness (k_j^p) and static stiffness (K_j^p) through dynamic stiffness modifier, α_j^p:

$$k_j^p = K_j^p \times \alpha_j^p \qquad [6\text{-a}]$$

where:

$$K_j^p = \chi_j E_s d \qquad [6\text{-b}]$$

$$\chi_j = \left(w_{pj} + w_{sj} + w_{bj}\right) \mathrm{f}\left(E_p/E_s, L_p/d\right) \qquad [6\text{-c}]$$

$$\alpha_j^p = \mathrm{f}\left(E_p/E_z, \rho_p/\rho_z, w_{sj}, \nu, a_0^p\right) \qquad [6\text{-d}]$$

In the above, j represents the direction of interest for vibration. Because the symmetry of the caissons about their centerline, j represents any lateral direction. The variable d is the caisson diameter, E_s and E_p are the elastic moduli of the soil and the caisson, L_p is the caisson length, ρ_s and ρ_p are the mass densities of the soil and the caisson, and ν is the Poisson's ratio of the soil (ν = 0.25). The values of w_{pj}, w_{sj}, and w_{bj} are the weight factors, and represent the relative contribution of the caisson structural stiffness and caisson-soil interaction through lateral load transfer and through base resistance. These three weight factors always sum to unity ($w_{pj} + w_{sj} + w_{bj}$ =1.0), and unless they appear individually in equations for a particular mode of vibration, need not be estimated separately.

As indicated above, the dynamic stiffness modifier, α_j^p, is a function of the dimensionless frequency, a_0^p, defined through Equation 7 (Eq. 2-23 of GCR 12-917-21):

$$a_0^p = \frac{\omega d}{V_s} \quad [7]$$

The circular frequency ω = 2πf (where frequency, f=1/T) is estimated using the fundamental period of the structure (in this case T=1.54 seconds) and shear wave velocity in the soil along the caisson. The shaft diameter above the bell section was used to represent d. Finally, specific relationships for the two remaining parameters of Equations 6-c and 6-d, (i.e., χ_j and α_j^p for translation along x axis, where j = x) are given in Equations 8-a, 8-b, and 8-c, from Tables 2-4a and 2-4b of GCR 12-917-21:

$$\chi_x = \frac{1}{2}\pi^{1/4}\delta_x{}^{3/4}\left(\frac{E_p}{E_s}\right)^{1/4} \quad [8\text{-a}]$$

Where:

$$\delta_x = 2\left(\frac{E_p}{E_s}\right)^{-3/40} \quad [8\text{-b}]$$

$$\alpha_x^p = 1 - \frac{3\pi}{32\delta_x}\left(\frac{\rho_p/\rho_s}{1+\nu}\right)\left(a_0^p\right)^2 \quad [8\text{-c}]$$

The elastic modulus of soil, E_s, is related to the shear modulus of soil through Equation 9:

$$E_s = 2(1+\nu)G \quad [9]$$

G is related to the initial shear modulus, G_0, as discussed in relation to Equation 5-a, above. The shear wave velocity (Vs_0) of the materials the caisson were embedded in was computed as the weighted average of the measured shear wave velocities from SCPT, using thicknesses of the involved strata as the weighing factors.

Section 8.4.3 of ASCE41-13 provides a relationship for rocking stiffness, K_{xx} (rotational stiffness about a given horizontal axis). This relationship is specifically for pile groups where more than one pile is attached to a pile cap, and assumes that rocking stiffness is caused by the axial stiffness of individual piles in a pile group. However, all caissons involved in the present work are single piles where no pile cap covers more than one pile. As a result, rocking stiffness of caissons cannot be estimated using this equation. The rocking stiffness of individual caissons was estimated using a computer program such as LPILE, for lateral analysis of deep foundations. For this, the moment applied at the top of a caisson that would cause 1 inch of lateral movement was found iteratively. Rocking stiffness, $K_{xx,}$ was computed as the ratio between this moment (M_1) and the corresponding rotation (θ_1) of the caisson head (in radian) as indicated in Equation 10 below:

$$k_{xx} = \frac{M_1}{\theta_1} \quad [10]$$

Where :

M_1 = Applied moment at pile head to cause 1 inch lateral deflection
θ_1 = angle of rotation from vertical of pile head due to applied moment, M_1

CAPACITIES

For a majority of the caissons in this project, the ratio between depth of the caisson base and diameter of the base is smaller than 3, thus allowing the use of shallow foundations relations. For

most of the remaining caissons, this ratio is between 3 and 4, and only in a few cases the maximum is about 5.6. Because this ratio remains smaller than or close to 3, shallow footing relations are used to estimate the expected (ultimate) axial capacity for all caissons. The large diameter of the bells compared to shaft diameter and small ratio between total length and bell diameter suggest the contribution of side friction to axial capacity in compression is negligible, and thus was not included. The axial capacity is based on static parameters which per Appendix Section A.6.2 of ASCE41-13, may be increased by a factor of up to 2.0 in order to determine the "calculated" seismic capacity. In our analyses, a factor of 1.0 was conservatively used to establish the seismic capacity (i.e., calculated seismic capacity is equal to the calculated static capacity).

Expected axial capacities of caissons in uplift, P_{uu}, were estimated using Equations 3.35 and 3.36 proposed by Poulos and Davis (1980), with the upper limit of the uplift capacity (P_{uumax}) determined by Equation 3.37 of the same reference.

Lateral capacity of deep foundations (such as caissons) depend on the applied moment and shear. This fact can result in numerous possible capacities for the same caisson, particularly in a dynamic analysis. For this reason, lateral capacities for caissons were not evaluated. However, the lateral capacity of caissons is only needed to check that spring stiffnesses do not exceed the capacity. Once the structural analyses are performed, the resulting utilization of spring stiffnesses can be checked to confirm they do not approach reasonable capacity values. In the event utilization reaches values that may be near capacities, specific analyses can be performed on the lateral capacity of such cases.

Representing foundation material by linear elastic-plastic springs involves some uncertainty. The sources of some of this uncertainty are variability in soil profile and properties, mode of shear, effect of rate of shear and progressive failure, and inherent non-linear behavior of geotechnical material. To account for this uncertainty, an upper- and lower-bound approach to defining stiffness and capacity of the foundation elements is required to evaluate the sensitivity of the structural response to these parameters. Per ASCE41-13 (Section 8.4.2 and 8.4.3) the upper bound and the lower bound bearing and lateral capacities should be estimated through multiplying and dividing the calculated capacities and spring constants by $(1+C_v)$. C_v is the coefficient of variation defined as the ratio between standard deviation and mean (of the capacity) and should not be taken to be less than 0.5 for foundations controlled by sliding or bearing deformations. Per C8.4.2 (ASCE41-13) in the absence of detailed testing to determine C_v, variation by a factor of 2 (i.e., C_v=1) is recommended for investigation of soil variability and uncertainty.

SUMMARY OF RESULTS

For the caissons defined in Table 1, above, Table A-1 provided in Appendix A summarizes the resulting vertical stiffness Kz, ultimate axial capacity $(Q_{ult})_{comp}$, ultimate uplift capacity $(Q_{ult})_{up}$, lateral stiffness K_x, and rocking stiffness K_{xx}, for BSE-1E seismic criterion. The same results for BSE-2E seismic criterion are summarized in Table A-2 in Appendix A.

CONCLUDING REMARKS

The Office of Statewide Health Planning and Development (OSHPD) required seismic evaluation of an existing hospital in Long Beach, California in order to meet the requirements of the Structural Performance Category 4D (SPC-4D) published as a part of the 2016 CBC. SPC-4D utilizes ASCE41-13 as modified by OSHPD, and involves two seismic performance levels BSE-1E and BSE-2E, respectively corresponding to 20% and 5% probability of exceedance in 50 years.

One element of this evaluation is determination of spring constants and capacities of foundation elements. Review of the existing plans indicated that both shallow footings and belled caissons were used for the foundation. However, ASCE41-13 procedures to compute axial stiffness were not directly applicable to individual belled caissons present at the project. The large diameter of the bells required consideration of the foundation medium to the axial stiffness, a detail not described clearly in ASCE 41-13. Furthermore, ASCE41-13 procedures to estimate rocking (rotational) stiffness only consider pile groups and use the axial reaction of individual piles as the only source of lateral stiffness of a pile group. The provisions of ASCE41-13 were therefore considered inapplicable to this project where all caissons are configured as single foundation elements.

To overcome these hurdles, shallow footing relations were used to estimate axial spring constants and capacities of belled caissons. The lateral stiffness of single caissons was established by employing National Institute of Standard and Technology (NIST, 2012) relationships for piles, using the diameter of the stem to represent the caisson. Rocking (rotational) stiffness of individual caissons was estimated using computer a program for lateral analysis of deep foundations.

Depending on the type of structural dynamic analysis used for seismic evaluation of the structure, capacities may also be needed in addition to spring constants. Shallow footing relations were used to estimate the expected (ultimate) axial capacity for all caissons. Expected axial capacity of caissons in uplift was estimated using relationships in Poulos and Davis (1980). Lateral capacity of caissons depends on the applied moment and shear that were not known at the time of our evaluation. For this reason, lateral capacities for caissons were not evaluated. However, the lateral capacity of caissons is only needed to check that spring stiffnesses do not exceed the capacity and can be checked once structural analyses are completed and the applied shears and moments are known.

In order to account for uncertainty from various sources, an upper- and lower-bound approach to defining stiffness and capacity of the foundation elements is required to evaluate the sensitivity of the structural response to these parameters. Per ASCE41-13 in the absence of detailed testing, a factor of 2 is recommended to estimate the upper-bound and the lower-bound stiffnesses and capacities from the calculated values above.

REFERENCES

ASCE 7-10 (2010) Minimum Design Loads for Buildings and other Structure, Structural Engineering Institute (SEI) / American Society of Civil Engineers (ASCE).

ASCE 41-13 (2014) Seismic Evaluation and Retrofit of Existing Buildings, Structural Engineering Institute (SEI) / American Society of Civil Engineers (ASCE).

CBC (2016) California Building Code; California Code of Regulations, Title 24, Part 2, Volume 1 and 2, California Building standards Commission.

CDMG, 1986, State of California, Special Studies Zones, Long Beach Quadrangle Revised Official Map, effective July 1, 1986.

CDMG, 1998, revised 2006, Seismic Hazard Zone Report for the Long Beach 7.5-Minute Quadrangle, Los Angeles County, California, Seismic Hazard Zone Report 028, 1998 (revised January 13, 2006).

LPile (2018) Analysis and Design of Deep Foundations Under Lateral Loads, Ensoft, Inc.

National Institute of Standards and Technology (NIST), 2012, Soil-Structure Interaction for Building Structures, NIST GCR 12-97-21, NIST, US Department of Commerce.

PEER 2012/08 Report Guidelines for Estimation of Shear Wave Velocity Profiles, Pacific Earthquake Engineering Research (PEER) Center, December 2012.

Poland, J.F. and Piper, A.M., 1956, Ground-Water Geology of the Coastal Long Beach-Santa Ana Area, California, U.S.G.S. Water Supply Paper 1109.

Poulos, H. G. & Davis, E. H., 1980, Pile Foundation Analysis and Design, New York: Wiley.

United States Geological Survey (USGS), 1925, Topographic Map, 6-minute Clearwater Quadrangle.

APPENDIX A- Tables of Results

Table A-1-BSE-1E Seismic Criterion: Selected Caissons' Stiffness and Capacity

Label[(1)]	Kz (k/ft)	(Qult)comp (k)	(Qult)up (k)	Kx (k/ft)	Kxx (k.ft/rad)
1	130,974	7,619	941	42,462	31,875
2	102,662	3,787	696	40,769	17,568
3	174,191	10,984	1,118	64,360	102,941
4	116,259	25,906	4,040	50,981	113,000
5	133,696	42,205	5,589	54,266	115,842
6	103,250	17,257	3,178	48,189	120,098
7	97,861	12,765	2,594	46,694	122,549
8	52,090	5,114	1,394	28,589	34,247
9	53,079	8,044	1,940	29,610	35,461
10	53,889	4,148	1,131	28,440	32,258
11	65,602	9,069	1,719	31,540	31,250
12	92,094	23,327	4,673	47,246	139,000
13	40,192	4,775	1,739	26,837	35,971
14	94,715	15,813	3,537	46,526	122,549
15	52,161	3,521	1,038	27,916	32,258
16	66,182	5,403	1,237	30,758	3,125
17	52,556	8,674	2,291	29,553	35,461
18	97,131	17,334	3,714	47,116	122,549
19	86,850	21,020	4,892	46,050	138,889
20	38,704	8,960	2,949	27,829	35,329
21	41,764	14,153	3,840	29,154	35,971
22	46,110	8,216	2,502	28,585	35,461
23	41,234	6,253	2,098	27,527	35,971

(1) See Table 1 for configuration of the caissons with the same labels.

Table A-2-BSE-2E Seismic Criterion: Selected Caissons' Stiffness and Capacity

Label[(1)]	Kz (k/ft)	(Qult)comp (k)	(Qult)up (k)	Kx (k/ft)	Kxx (k.ft/rad)
1	107,888	7,619	941	33,525	31,875
2	82,974	3,787	696	32,188	17,568
3	140,286	10,984	1,118	50,813	102,941
4	104,346	25,906	4,040	40,251	113,000
5	120,348	42,205	5,589	42,844	115,842
6	92,520	17,257	3,178	38,046	120,098
7	87,254	12,765	2,594	36,866	122,549
8	48,026	5,114	1,394	22,572	34,247
9	49,399	8,044	1,940	23,377	35,461
10	49,220	4,148	1,131	22,454	32,258
11	60,096	9,069	1,719	24,901	31,250
12	84,380	23,327	4,673	37,302	139,000
13	37,841	4,775	1,739	21,188	35,971
14	85,275	15,813	3,537	36,733	122,549
15	47,589	3,521	1,038	22,040	32,258
16	59,359	5,403	1,237	24,284	3,125
17	48,962	8,674	2,291	23,333	35,461
18	87,478	17,334	3,714	37,199	122,549
19	79,680	21,020	4,892	36,357	138,889
20	36,921	8,960	2,949	21,971	35,329
21	39,913	14,153	3,840	23,018	35,971
22	43,367	8,216	2,502	22,568	35,461
23	38,958	6,253	2,098	21,733	35,971

(1) See Table 1 for configuration of the caissons with the same labels.

THE USE OF SEISMIC TRACE CHARACTERIZATION TO GUIDE THE ANALYSIS OF DST RESULTS TO OBTAIN MORE ACCURATE SOIL PARAMETERS

Erick Baziw
Baziw Consulting Engineers Ltd., Vancouver, Canada
Gerald Verbeek
Baziw Consulting Engineers Ltd., Vancouver, Canada

ABSTRACT:

Downhole Seismic Testing (DST) is a very popular applied seismology site characterizing tool within geotechnical engineering. A challenging aspect of DST is to characterize the acquired seismic data sets to determine the analysis method that will result in the most accurate interval velocity values. BCE has invested considerable resources into developing Seismic Trace Characterization (STC), which uses various independent parameters of the acquired data at a particular depth. Initial work in this area resulted in the selection of the linearity estimate from the polarization analysis, the cross correlation coefficient of the full waveforms at the particular depth and the preceding depth and a uniquely developed parameter referred to as the signal shape parameter for this characterization. Subsequent analysis in STC identified two other parameters: the Signal-Noise-Ratio (SNR) and the Peak Symmetry Differential (PSD). The paper briefly describes these parameters and then outlines how they can guide the data analysis to derive more accurate results, especially near surface, which is especially important to assess the liquefaction potential in areas prone to earthquakes, such as California. The process will be illustrated with actual data from another area prone to earthquakes, namely New Zealand.

1. INTRODUCTION

The near surface characterization of low strain in-situ shear wave velocities (V_S) has proven critical for liquefaction assessment. Liquefaction is a phenomenon in which dynamic loading of saturated soil results in the material properties to change suddenly from a solid state to a liquefied state. V_S is an important parameter for evaluating liquefaction potential due to fact that it is influenced by many of the variables that influence liquefaction (e.g., void ratio, soil density, confining stress, stress history, and geologic age (Andrus et al., 1997)). Aki and Richards (2002) also outline that the amplitude of ground motion should depend on the density and shear wave velocity of near surface soils and rocks according to the theory of wave propagation. Since the change in density with the increase in depth is relative minor compared to that of the shear wave velocity, the latter is a very useful parameter to represent site conditions (Stewart et al., 1997). Bray (2014) and his colleagues carried out an extensive geotechnical analysis of the catastrophic liquefaction that occurred in Christchurch, New Zealand in 2010 and 2011 and found that near surface rather than deep liquefaction resulted in extensive foundation damage.

Downhole Seismic Testing (DST) has proven to be a very powerful technique for measuring in-situ near surface V_S values (ASTM, 2017) and thus a valuable tool for liquefaction assessment. The main goal in DST is to obtain arrival times as the source wave travels through the soil profile of interest, and from these arrival times the velocities are then calculated by taking into account proper source wave raypaths (Baziw, 2002; Baziw and Verbeek, 2012 and 2016). In a DST configuration a seismic source is used to generate a seismic wave train at the

© 2018 Deep Foundations Institute

ground surface. One or more downhole seismic receivers are used to record the seismic wave train at predefined depth increments. The downhole receiver(s) may be positioned at selected test depths in a borehole or advanced as part of an instrumentation package as in the case of Seismic Cone Penetration Testing (SCPT). When triggered by the seismic source a data recording system records the response of the downhole receiver(s).

Near surface DST seismic data set can be particularly challenging to process compared to relatively deeper acquired traces as they are more effected by near surface measurement noise, "rod noise", near-field source waves, and reflections. Especially for those traces it is critical to have the ability to assess the quality of the DST seismic trace and to get guidance how to best analyze these traces.

BCE has invested considerable resources (Baziw and Verbeek, 2016a, 2016b, and 2017) into the characterization of acquired DST data sets and the guidance for data analysis that can be derived from this characterization. This paper summarizes that work and also describes proposed signal processing and post data analysis techniques for data sets with poor trace metrics.

2. THE STC PARAMETERS

Seismic Trace Chaacterization (STC) refers to quantifying the quality of the acquired DST seismic traces based upon independent seismic trace characteristics. This facilitates post data processing and provides a highly valuable quantification of the quality of the DST data set under analysis and subsequent interval velocity estimates. The analysis of numerous seismic data sets, many of which were recorded with triaxial seismic sensors, has resulted in a better understanding of how a seismic trace can be characterized. Typically, investigators have utilized the Cross-Correlation Coefficient (CCC), which gives an indication of the similarity between traces used in obtaining relative arrival times (Baziw, 1993), but this parameter has been proven to be an unreliable indicator due to the fact that measurement noise (random and systematic) can also be correlated and result in high CCC values. In order to overcome these limitations other parameters were added and over the years the number of parameters considered by the authors has increased to five. The five STC parameters are briefly outlined below due to length constraints on this paper, but the parameters are discussed in more detail in papers included in the References.

STC Trace Metric 1: Linearity (LIN) Estimates from the Polarization Analysis

Polarization Analysis (PA) refers to analyzing the source wave responses on multi-component seismic sensor packages (Kanasewich, 1981; Baziw and Verbeek, 2016b). A very important component of PA is obtaining linearity or rectilinearity estimates. Linearity values are obtained by diagonalizing the covariance matrix of the X(t), Y(t) and Z(t) recordings over the seismic event of interest and subsequently calculating the ratio of the principal axis of the diagonalized matrix. A measure of the rectilinearity is referred to as linearity and it is calculated as follows:

$$F(\lambda_1, \lambda_2) = 1 - \left(\lambda_2 / \lambda_1\right) \quad (1)$$

where λ_1 and λ_2 denote the largest eigenvalue and next largest eigenvalue of the diagonalized covariance matrix, respectively. The linearity approaches unity when the rectilinearity is high ($\lambda_1 \gg \lambda_2$) and approaches zero when the rectilinearity is low ($\lambda_1 \approx \lambda_2$). Since linearity values

nearing 1.0 identify seismic recordings that have highly correlated responses and strong directionality, the quality of the data set with a high linearity value can be considered good. Lower linearity values on the other hand indicate a lower quality trace (whether due to poor source generation, near-field waves, ambient noise that is not easily filtered out, source wave reflections, or differential probe coupling). Figure 1 illustrates an example X(t) and Y(t) source wave responses which have high linearity. In this case the peaks and troughs on the X(t) and Y(t) axis are aligned (Fig. 1(A)). This is also reflected in the hodogram (Fig. 1(B)) where the X(t) and Y(t) responses are plotted against one another and a least squares best fit straight line is applied. In Fig. 1(B) the plotted points have low deviation from the best fit least squares straight line.

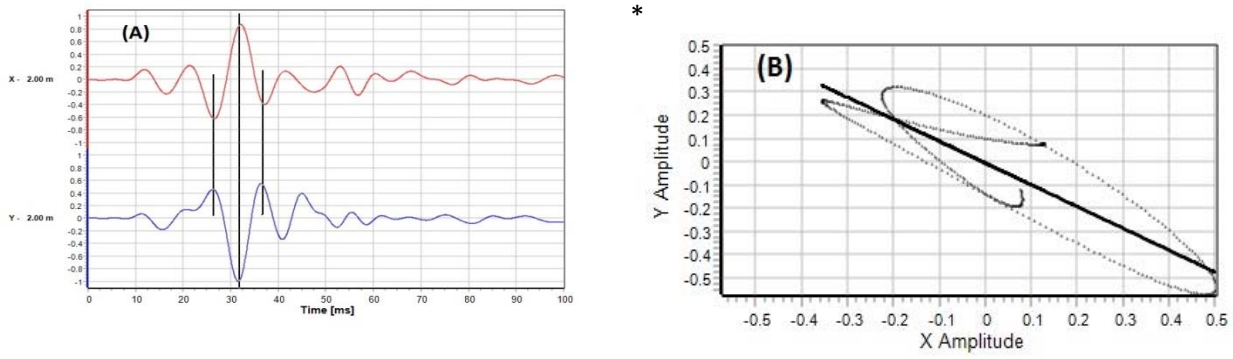


Figure 1: (A) DST X and Y axis seismic responses illustrating alignment of peaks and troughs. (B) Corresponding hodogram (light grey dots) and linear least squares best fit (dark black line) with a calculated linearity of 0.89

STC Trace Metric 2: Cross-Correlation Coefficient (CCC)

The cross-correlation between two time or distance offset seismograms is given as

$$\varphi_{xy}(\tau) = \sum_k X_k \, Y_{k+\tau} \tag{2}$$

Normalizing the cross-correlation of the zero mean seismic signals by their standard deviations gives the cross-correlation coefficient:

$$\rho_{xy}(\tau) = \sum_k X_k \, Y_{k+\tau} \Big/ \sqrt{\sum_k X_k^2} \sqrt{\sum_k Y_K^2} \tag{3}$$

The CCC between the two DST seismic traces gives an indication of the similarity between the two waves being correlated. CCC values approaching 1.0 indicate that the two waveforms are highly correlated. CCC values approaching 0 indicate very poor correlation (Baziw and Verbeek, 2016b).

STC Trace Metric 3: Signal Shape Parameter (SSP)

The SSP trace metric quantifies the deviation of the shape of the frequency spectrum from an ideal bell shape. Based upon frequency spectrum analysis of large sets of DST data it was determined that the shapes of high quality DST data sets had frequency spectrums closely resembling Gaussian bell-shape pdf curves (Baziw and Verbeek, 2016a), which can be described as follows:

$$p(f|\mu,\sigma^2) = \frac{1}{\sigma\sqrt{2\pi}} e^{-\frac{(f-\mu)^2}{2\sigma^2}} \tag{4}$$

where μ denotes the mean or expectation of the distribution and σ denotes the standard deviation with variance σ^2. Based on this observation a STC parameter was developed which quantified the deviation of the shape of the frequency spectrum of the seismic trace under analysis from a bell-shaped pdf curve.

*STC Trace Metric **4**: Peak Symmetry Differential (PSD)*

The PSD trace metric facilitates the identification of traces whose peak source wave responses have been significantly skewed due to measurement noise or source wave reflection interference. Figure 2 illustrates this phenomenon. In Fig. 2(A) we have an ideal source wave recording where no interference is present. In this case the time difference between the two zero crossings bounding the peak response (A1) are identical (Δt1 = Δt2). In Fig. 2(B) we have a source wave recording with interference, resulting in skewing or time shifting of the peak source wave response. The "peak symmetry" error assessment is also carried out on the adjacent peaks and/or troughs if the amplitude exceeds 70 % of that for the peak response. Obviously traces with a lower PSD value are of a lesser quality and require more attention during analysis.

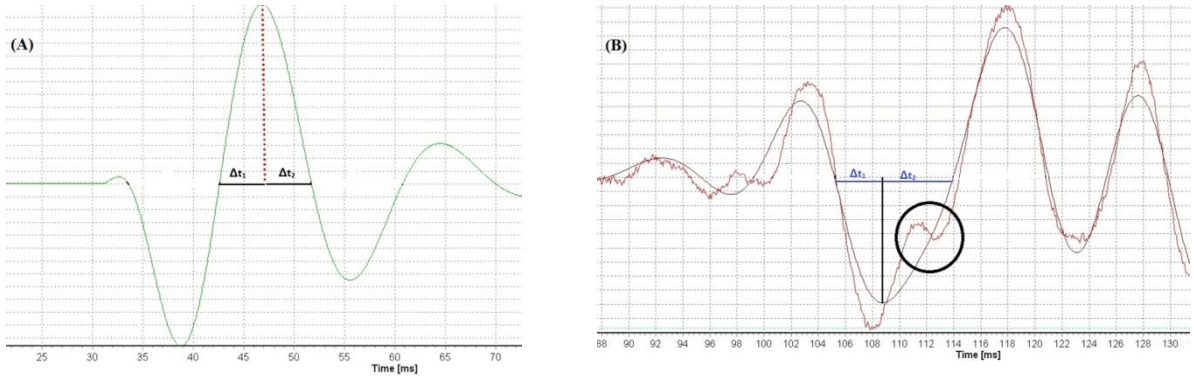


Figure 2. Source wave peak distortions due to measurement noise or source wave reflection interference. (A) Ideal source wave recording where no interference is present. (B) Source wave with interference resulting in skewing or time shifting of the peak source wave response. The black line is the unfiltered trace while the red line is the filtered trace where a low pass filter of 200 Hz was applied.

STC Trace Metric 5: Signal to Noise Ratio (SNR)

The SNR trace metric uses as input the as-recorded seismic trace and compares it with the filtered trace to quantify what portion of the spectral content of the recorded seismogram resides within the desired source frequency spectrum. While this parameter provides mainly insight in the quality of the data acquisition (such as gain settings, noise levels and testing environment) and does not really provide guidance for data analysis, it is nevertheless an important parameter. When during testing to establish SH interval velocities testing is performed from two sides, the SNR metric is very beneficial in selecting the outcome when there is a large spread between the two results.

It should be noted that it is possible for source wave distortions (such as near-field effects, reflections, refractions, and "dirty sources") to have spectral content which resides within the source wave frequency spectrum. Consequently the parameter value may imply a better quality trace than it really is.

3.0 RECOMMENDED DATA ANALYSIS and SIGNAL PROCESSING BASED on STC

All STC trace metrics vary from 0 to 1 where it is desired that they approach the optimal 1.0 value. Low LIN values are typically handled separately from SSP, CCC and PSD values. This is due to the fact that the LIN values directs the investigator on whether the full waveforms should be utilized for analysis or a preferential axis response, while the SSP, CCC and PSD trace metrics give indications of the quality of the seismic traces under analysis. Different seismic signal processing techniques are then applied based upon the SSP, CCC and PSD values.

3.1 Post Analysis and Signal Processing: Linearity Values

LIN estimates are derived from triaxial or biaxial seismic sensor configurations. For data analyses to obtain horizontally polarized shear wave (V_{SH}) velocity values the X- and Y-axis responses are of interest. LIN values for these responses approaching 1.0 are highly desirable and indicate that there is a preferred directionality of the source wave responses, and therefore the X- and Y-axis responses can be rotated on to the full wave form axis, which increases the signal-to-noise ratio. Generally, LIN values 0.8 or better indicate that the full waveforms can be utilized without any cause of concern, while lower values require corrective action as illustrated in the four test cases below.

3.1.1 Test Case LIN 1 – overall linearity values ≥ 0.8 with a few outliers due to poorly correlated source wave responses.

DST Data sets with these LIN values are typically of very good quality and the full wave forms can be used for data analysis. Generally, there are either dominant responses on the X axis and/or Y axis or highly correlated responses on the X and Y axis, but a few lower LIN values may need to be addressed. Figure 3 illustrates filtered (200Hz low pass) Vertical Seismic Profile (VSP). The filtered VSP illustrates X- and Y-axis responses with the dominant source wave responses on the Y axis. The corresponding LIN values are given in Table 1 and for most depths they exceed 0.8, in which case the full wave forms are utilized. However, lower LIN values occur at depths 1m, 2m and 9m.

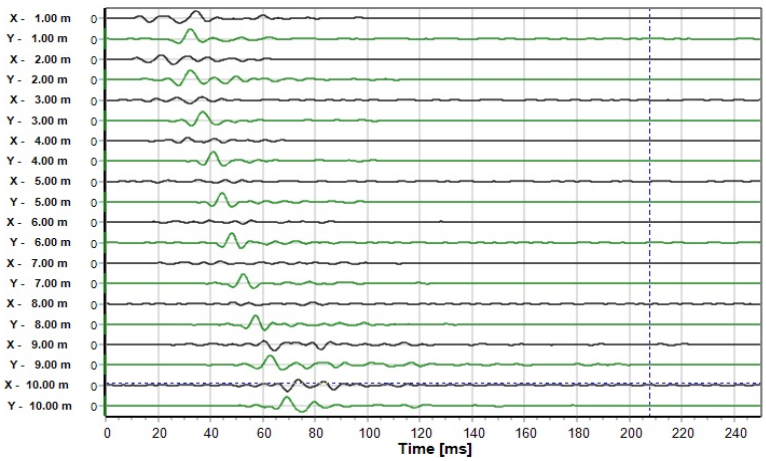


Figure 3. Filtered (200 Hz low pass) VSP [LIN 1]

Table 1. Linearity Values for [LIN 1]

Depth [m]	Linearity [0-1]
1	0.52
2	0.55
3	0.83
4	0.80
5	0.86
6	0.85
7	0.82
8	0.86
9	0.58
10	0.82

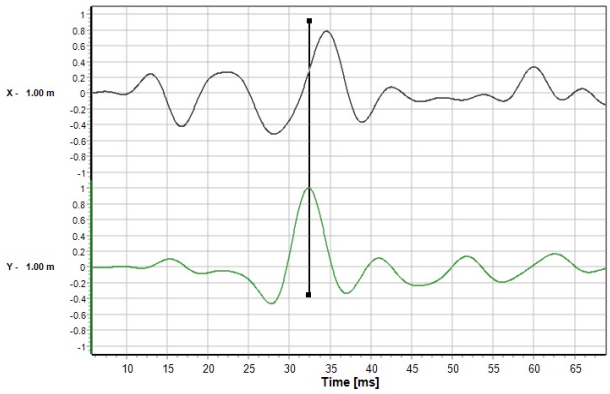


Figure 4. Filtered recorded traces at 1 m [LIN 1]

To overcome this the first step is to identify which axis shows the dominant response. If this is consistent with the full wave forms then the response on this axis can be used in the analysis. For example, the filtered VSP in Figure 3 clearly showed that the dominant responses reside on the Y axis. The filtered traces recorded at 1m are shown in Figure 4 and it is clear that the responses are not correlated (resulting in the low linearity value of 0.52 as shown in Table 1). It is also clear that there is a high quality Y-axis response recorded at this depth, which is in line with the dominant responses at the other depths. Therefore at 1 m the Y-axis response is utilized rather than the full wave form. This is also the case for the traces recorded at 2m and 9m which had associated low linearity values of 0.55 and 0.58, respectively.

3.1.2 Test Case LIN 2 – overall linearity values ≥ 0.8 with a few outliers due to low SNR

Data sets with these LIN values are typically of very good quality and the full wave forms can be used for post analysis. Generally, there are either dominant responses on the X axis and/or Y axis or highly correlated responses on the X and Y axis, but a few lower LIN values may need to be addressed. Figure 5 illustrates filtered (200Hz low pass) Vertical Seismic Profile (VSP) for test case LIN2. The filtered VSP in Figure 5 illustrates X and Y axis responses where there is no single axis that contains the dominant response at all depths. The corresponding and widely varying LIN values are given in Table 2.

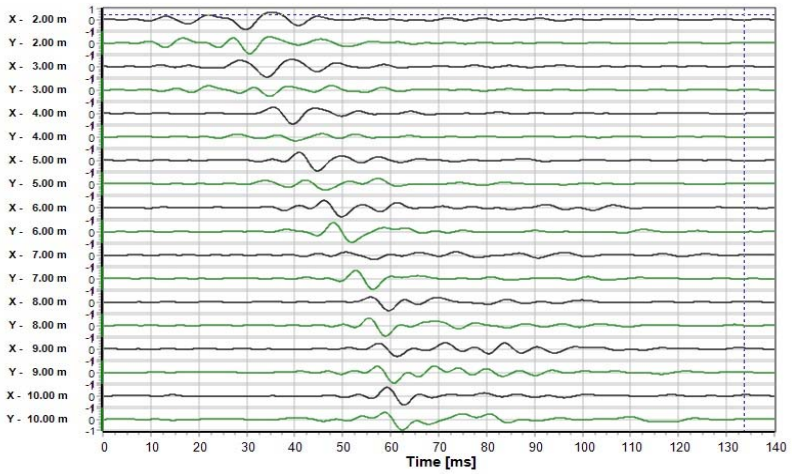


Figure 5. Filtered (200 Hz low pass) VSP [LIN 2]

Table 2. Linearity Values for [LIN2]

Depth [m]	Linearity [0-1]
2	0.58
3	0.70
4	0.84
5	0.62
6	0.30
7	0.80
8	0.81
9	0.48
10	0.81

Figure 6 illustrates the X- and Y-axis responses recorded at 10m, which demonstrates that the high linearity is due to correlated X and Y axis responses and not due to dominant responses on either the X or Y axis. This in turn means that the X and Y axis responses can be utilized in post analysis where poor linearity values occur due to noise responses and not poorly correlated source wave responses. Figure 7 illustrates the filtered X- and Y-axis responses at 2 m, where again the peaks and troughs of the source wave responses align, but the interference on the X axis (highlighted by the red circle) introduces such distortion on the X axis so that the LIN value is significantly reduced. For this case we can utilize the higher quality Y-axis response along with the full wave forms for other depths.

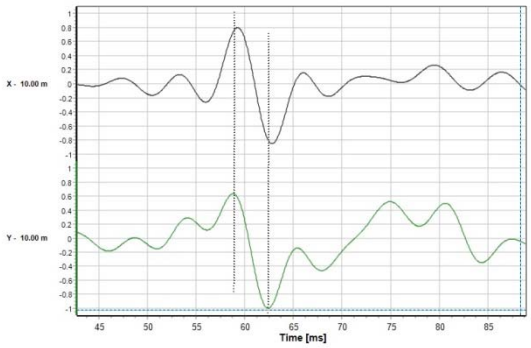


Figure 6. Recorded traces at 10 m [LIN 2]

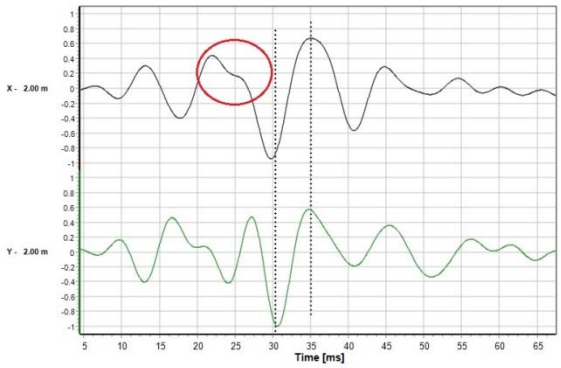


Figure 7. Recorded traces at 2 m [LIN 2]

3.1.3 Test Case LIN 3 – Overall low linearity values with poorly correlated X and Y axis responses, but with a dominant response at all depths on the same axis

For data sets with low LIN values we cannot utilize both X and Y axis responses in post analysis. The investigator must then select either the X or Y axis responses for data analysis and subsequently determine individual axis trace metrics values. Figure 8 illustrates filtered (200Hz low pass) Vertical Seismic Profile (VSP) for test case LIN3, where the Y-axis responses are clearly dominant and of higher quality. The corresponding LIN values are given in Table 3, suggesting very poorly correlated X- and Y-axis responses. In cases like this the investigator proceeds with the analysis using the higher quality responses, which in this case are obviously the Y axis responses.

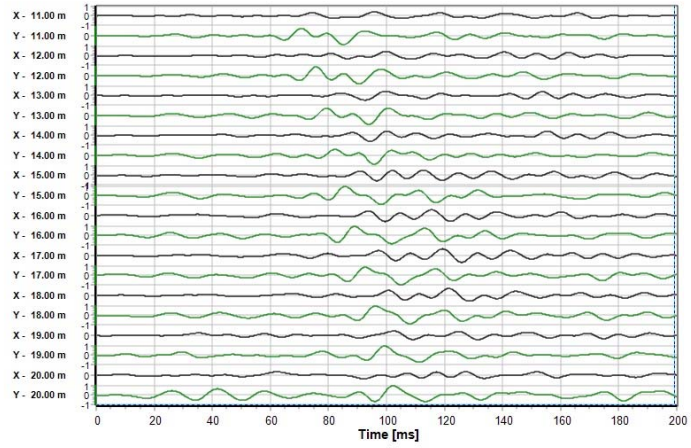


Figure 8. Filtered (200 Hz low pass) VSP [LIN 3]

Table 3. Linearity Values for [LIN3]

Depth [m]	Linearity [0-1]
11	0.76
12	0.80
13	0.72
14	0.69
15	0.65
16	0.61
17	0.57
18	0.67
19	0.75
20	0.67

3.1.4 Test Case LIN 4 – Overall low linearity values with poorly correlated X and Y axis responses and no dominant response on the same axis for all depths.

As mentioned before, for data sets with low LIN values the post-analysis cannot utilize X and Y axis responses randomly: the investigator must select either the X or the Y axis responses. But sometimes this is impossible and the X-axis responses have to be used for certain depth intervals and the Y-axis responses for others. In that case it is important that there is overlap when transitioning from X axis to Y axis responses and vice versa. For example, assume the investigator is going to use X axis responses for depths 1m to 6m and Y axis responses from 6m to 15m. In this case interval arrival times are obtained for traces between 1m and 6m utilizing the X-axis responses and a reference time for one of the depths between 1m to 6m. Next the Y axis responses for traces between 6m to 15m are utilized to obtain interval arrival times with the X axis arrival time for 6m as the reference time. The arrival time are then feed into an algorithm which takes into account raypath refraction when estimating interval velocities (Baziw, 2002; Baziw and Verbeek, 2012 and 2014).

3.2 Post Analysis and Signal Processing: CCC, SSP, and PSD Values

While the LIN value helps with the selection of the traces to be analyzed, the SSP, CCC and PSD trace metrics give indications of the quality of the seismic traces under analysis based upon the form and shape of the time series and corresponding spectral content. Several different combinations (high vs low) of SSP, PSD and CCC values can exist due to the fact that they address different characteristics of the acquired seismic trace. Based on the values of these parameters the most appropriate processing technique (batch signal decay, seismic feature decay and aggressive frequency filtering) is then selected as illustrated in the various test cases below, which assume threshold values for SSP, PSD and CCC of 0.6, 0.8 and 0.3, respectively.

3.2.1 Test Case SSP PSD CCC 1 – Good CCC and PSD values, but poor SSP values

Data sets with good CCC and PSD values but poor SSP values occur whenever there is source wave "ringing" as illustrated in the filtered (200 Hz low pass filter) VSP in Figure 9. Table 4 outlines the corresponding SSP, CCC, and PSD trace metric.

Table 4. SSP, CCC and PSD Values for [SSP PSD CCC 1]

Depth [m]	SSP [0-1]	CCC [0-1]	PSD [0-1]
20	0.547	0.9216	0.96
21	0.525	0.8266	0.48
22	0.379	0.8024	0.87
23	0.483	0.9151	0.65
24	0.556	0.9533	0.71
25	0.491	0.9671	0.79
26	0.51	0.9587	0.73
27	0.391	0.9379	0.96
28	0.428	0.9144	0.84
29	0.544	0.8841	0.61
30	0.363	0.8569	0.94

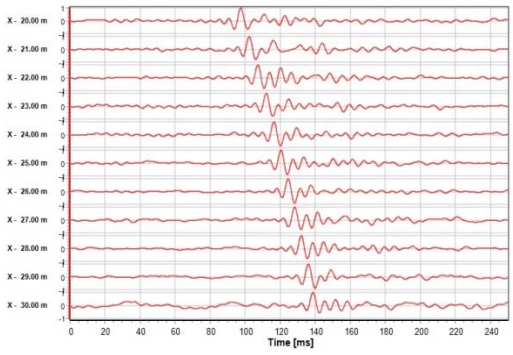


Figure 9. Filtered VSP [SSP PSD CCC 1]

Clearly only the SSP values are cause of concern and this is readily addressed through batch signal decay (BSD), which applies a time window around the peak responses moving forward and backward in time by two crossovers. The implementation of BSD on this data set is shown in Figure 10.

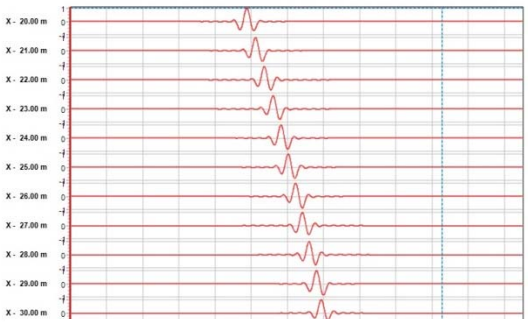


Figure 10. Filtered VSP after batch signal decay [SSP PSD CCC 1]

3.2.2 Test Case SSP PSD CCC 2 – Good CCC values, but poor PSD and SSP values

Data sets with very low PSD values generally are affected by extensive source peak skewing. This is illustrated in the filtered (200Hz low pass) VSP in Figure 11, while the trace metrics values of SSP, CCC and PSD are given in Table 5 with low PSD values between 10m and 13 m and also between 17 m and 20 m. The black circles outline in Fig. 11 outline the extensive peak

skewing. To address the low PSD values a consistent portion of the seismic source wave signature where there is minimal to no skewing is isolated throughout the profile (so-called Signal Feature Decay (SFD)). The seismic traces recorded between 12 m and 14 m shown in Fig. 12 clearly show that there is minimal first trough distortion, and therefore SDF is applied on this data set to isolate the first troughs. The results are illustrated in Figure 13.

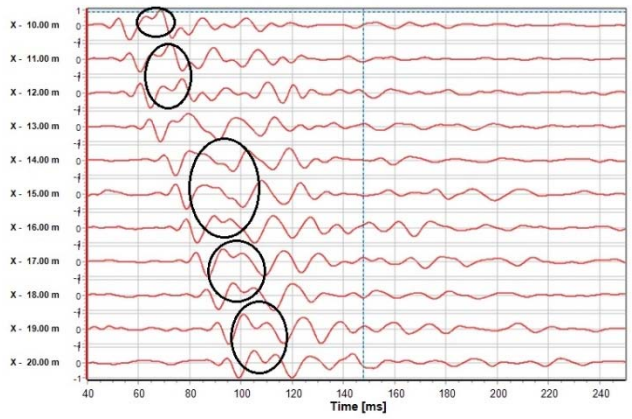


Figure 11. Filtered VSP with peak skewing areas highlighted [SSP PSD CCC 2]

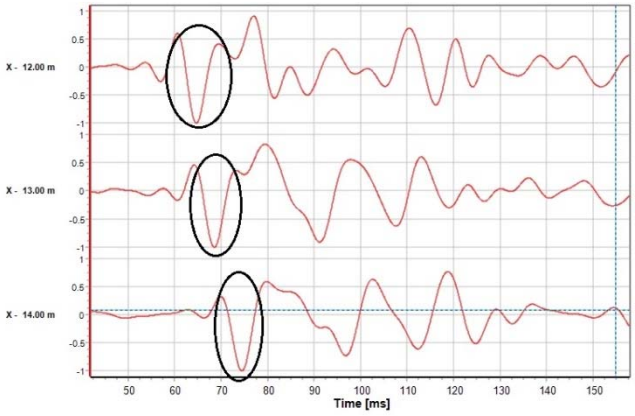


Figure 12. DST seismic traces between 12 m and 14 m [SSP PSD CCC 2] illustrating first trough responses.

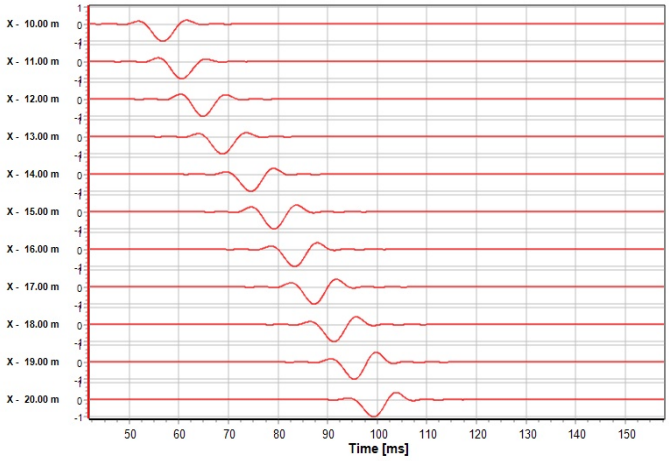


Figure 13. Filtered VSP after signal feature decay [SSP PSD CCC 2]

Table 5. SSP, CCC and PSD Values for [SSP PSD CCC 2]

Depth [m]	SSP [0-1]	CCC [0-1]	PSD [0-1]
10	0.49	0.9603	0.01
11	0.45	0.9239	0.01
12	0.39	0.9323	0.01
13	0.55	0.9144	0.01
14	0.47	0.8582	0.39
15	0.58	0.9283	0.96
16	0.53	0.9553	0.84
17	0.52	0.952	0.01
18	0.59	0.9884	0.01
19	0.56	0.9464	0.01
20	0.54	0.9814	0.01

3.2.3 Test Case SSP PSD CCC 3 – Good SSP and PSD values, but poor CCC values

If only the CCC values are low, SFD is again the suggested remedial action. In Fig. 14 a filtered (200Hz low pass) VSP is shown with the corresponding SSP, CCC and PSD trace metrics outlined in Table 6, which shows low CCC values between 3 m and 5 m with very good PSD values and SSP values very close to the desired 0.6 threshold except at a depth of 5 m. The dashed line in Fig. 14 clearly identifies the first trough responses in the entire VSP and Figure 15 then shows the VSP after isolating the first trough responses by SDF.

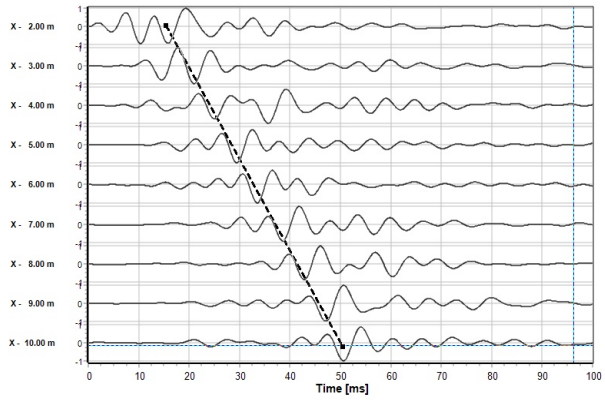


Figure 14. Filtered VSP with the first trough trend line [SSP PSD CCC 3].

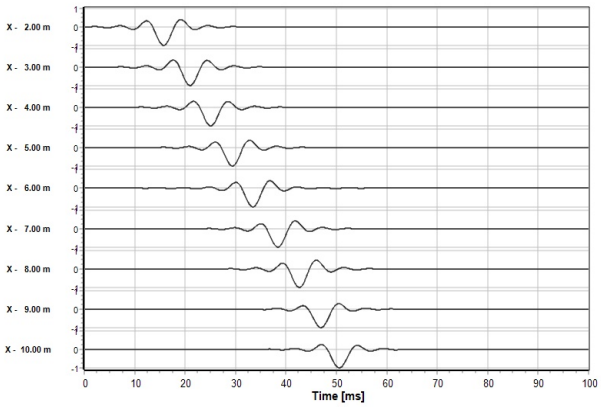


Figure 15. Filtered VSP after SDF applied [SSP PSD CCC 3]

Table 6. SSP, CCC and PSD Values for [SSP PSD CCC 3]

Depth [m]	SSP [0-1]	CCC [0-1]	PSD [0-1]
2	0.60	N/A	0.54
3	0.64	0.6497	0.69
4	0.59	0.5229	0.73
5	0.48	0.6394	0.75
6	0.46	0.8639	0.78
8	0.50	0.6862	0.85
9	0.59	0.8853	0.87
10	0.59	0.8558	0.83

Table 7. SSP, CCC and PSD Values for SSP PSD CCC 4

Depth [m]	SSP [0-1]	CCC [0-1]	PSD [0-1]
1	0.563	N/A	0.67
2	0.462	0.7526	0.07
3	0.45	0.6931	0.01
4	0.517	0.7264	0.37
5	0.75	0.833	0.99
6	0.6	0.9513	0.09

3.2.4 Test Case SSP PSD CCC 4 – Poor SSP, PSD and CCC values

In certain cases the entire VSP shows evidence of interference, resulting in poor SSP, PSD and CCC values. To address this type of data set an aggressive 120Hz low pass filter is applied so that the source wave interference is "smoothed". The "smoothed" responses then have SFD applied. This is illustrated on the filtered (200Hz low pass) VSP shown in Fig. 16, where there is evidence of significant source wave distortions throughout the source wave responses. Table 7 outlines the corresponding SSP, CCC and PSD trace metrics, while Figure 17 shows the data set after applying an aggressive 120Hz low pass filter and SDF on the "smoothed" second peak responses.

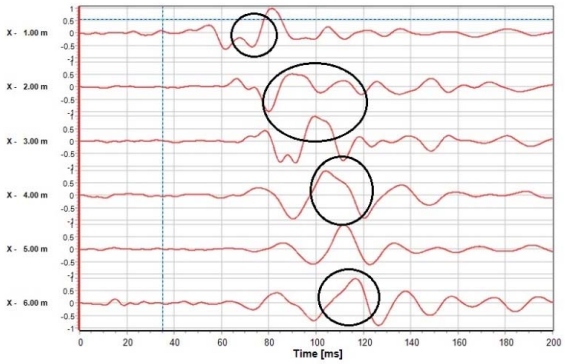


Figure 16. Filtered VSP with the evidence of interference at all depths [SSP PSD CCC 4]

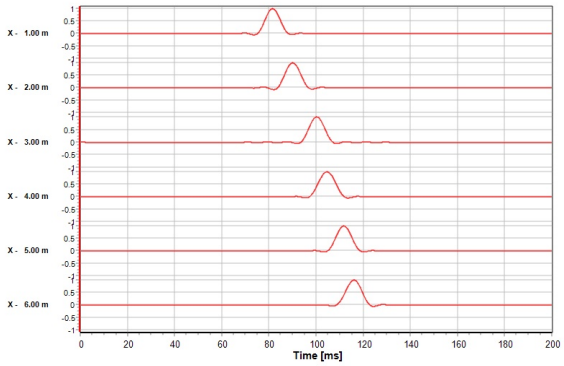


Figure 17. Aggressively filtered VSP after SDF [SSP PSD CCC 4]

3.3 Post Analysis and Signal Processing: SNR Values

When based on the LIN values the traces to be analyzed are selected, and based on the PSD, SSP and CCC values the most appropriate processing technique is determined, the SNR value can provide inside when there is a substantial difference between the outcome for the signals from the right side and the left side.

In Table 8 below the calculated interval velocities are shown for the right side and the left side, which reflect a larger spread (defined as ½ x (LS Velocity – RS)/Avg. Velocity) than desired (the objective is to have the spread within 10 %). Given the SNR values it can be concluded that the results for the right side are most likely more reliable, given the higher quality seismic traces at that side.

Table 8. RS and LS SNR and Interval Velocity Values

Depth [m]	SNR RS [0-1]	SNR LS [0-1]	RS Velocity [m/s]	RS Velocity [m/s]	Percent Difference (%)
2.000	0.95	0.74	N/A	N/A	
2.500	0.89	0.57	290	230	11.5
3.000	0.87	0.64	265	200	14

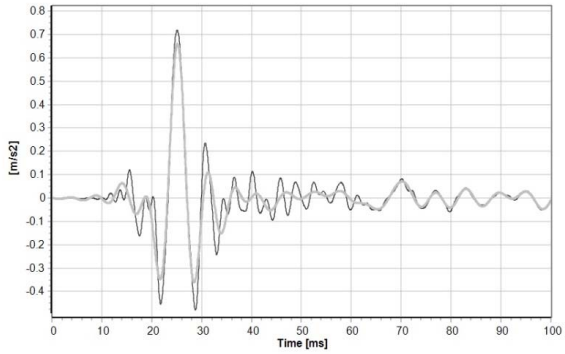


Figure 18. Unfiltered (black trace) superimposed upon filtered trace (light grey) for RS recorded at 2.5m.

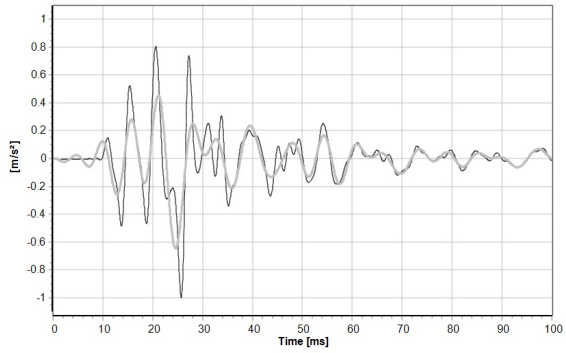


Figure 19. Unfiltered (black trace) superimposed upon filtered trace (light grey) for LS recorded at 2.5m.

CONCLUSIONS

Downhole seismic testing (DST) is a very popular applied seismology site characterizing tool within geotechnical engineering. One of the fundamental goals of DST is to quantify the shear wave interval velocities as this is an important parameter for evaluating the liquefaction potential due to fact that it is influenced by many of the variables that influence liquefaction. This paper has outlined BCE's newly Seismic Trace Characterization (STC), which is based on various independent seismic trace metrics of the acquired DST data at a particular depth. There are currently five independent trace metrics which are linearity (LIN), cross correlation coefficient (CCC), signal shape parameter (SSP), peak symmetry differential (PSD) and signal-to-noise ratio (SNR). LIN values nearing 1.0 identify seismic recordings which have highly correlated responses on the relevant axes and strong directionality. This will be the case for seismic traces recorded in TI medium with minimal measurement noise, clean source waves, and no signal

distortions (e.g., reflections). The CCC between the two DST seismic traces gives an indication of the similarity between the two waves being correlated. The SSP parameter quantifies the deviation of the source wave frequency spectrum from a desirable bell-shaped curve. High quality DST seismic traces are found to have characteristically bell-shaped curves similar to the probability density of a normal distribution. The PSD trace metric facilitates the identification of traces whose peak source wave responses have been significantly skewed due to measurement noise or source wave reflection interference. The peak responses of a seismic trace are critical when deriving arrival time estimates as they act as the predominant time markers. Finally, the SNR parameter quantifies the extent that the desired source wave frequency spectrum resides within the unfiltered recorded seismic trace. This paper has demonstrated with real data that the five STC parameters are highly beneficial in post signal processing where varying signal processing tools are applied based upon the derived STC values. In addition, the STC parameters quantify the quality of the recorded DST traces which provides for an assessment of the resulting derived interval velocities. It is the authors' intentions to have the application of STC parameters to post data analysis evolve based upon the data analysis of additional data sets..

REFERENCES

Aki, K. and Richards, P.G. 2002. Quantitative Seismology, 2nd edition, Sausalito, California: University Science Books.

Andrus, R.D., & Stokoe, K.H. (1997). "Liquefaction resistance based on shear wave velocity". National Center for Earthquake Engineering Research (NCEER) Workshop. Salt Lake, Utah, pp. 89-128.

ASTM (American Standards and Testing Methods). (2017). "D7400: Standard Test Methods for Downhole Seismic Testing." ASTM Vol. 4.09 Soil and Rock (II): D5877-latest.

Baziw, E. (2002), "Derivation of Seismic Cone Interval Velocities Utilizing Forward Modeling and the Downhill Simplex Method", Can. Geotech. J., 39(5), pp.1181-1192.

Baziw, E., and Verbeek, G. (2012). "Deriving Interval Velocities from Downhole Seismic Data", Geotechnical and Geophysical Site Characterization 4 – Mayne (eds), CRC Press, 1019–1024.

Baziw, E. and Verbeek, G. (2014). "Identifying Critical Layers using SCPT and Seismic Source Moveout." In the Proceedings of the 3rd International Symposium on Cone Penetration Testing, CPT'14, May 12-14, 2014 - Las Vegas, Nevada, 357-364.

Baziw, E., and Verbeek, G. (2016a), "Frequency spectrum "bell-curve" fitting as a component of SCPT interval velocity accuracy assessment", 5th International Conference on Geotechnical Site Characterization (ISC-5), Queensland – Australia, 5-9 Sept. Australian Geomechanics Society, 1431-1436.

Baziw, E. and Verbeek, G., (2016b)," Interval Velocity Classification Technique in Downhole Seismic Testing", http://www.bcengineers.com/images/BCE_IVC_2016.pdf.

Baziw, E. and Verbeek, G. (2017), "Quality Assessment of Seismic Data Sets and the Impact on Interval Velocity Estimates in DST", In Proceedings of the DFI 42nd Annual Conference on Deep Foundations, New Orleans - USA, October 24-27, 2017. Article #2821; publication #1037 (AM-2017).

Bray, J.D., Zupan, J.D., Cubrinovski, M. and Taylor, M., (2014), "CPT-based liquefaction assessments in Christchurch, New Zealand". Las Vegas, NV, USA: 3rd International Symposium on Cone Penetration Testing (CPT '14), 12-14 May 2014. 1-21. http://www.cpt14.com/cpt14-papers. (Conference Contributions - Papers in published proceedings).

Kanasewich, E.R., 1981, Time sequence analysis in geophysics. 3rd ed., The University of Alberta Press, Edmonton, AB. Chapter 19.

National Research Council, Commission on Engineering and Technical Systems (1985), Committee on Earthquake Engineering Liquefaction of soils during Earthquakes: Washington, D.C., National Academy Press.

Seed, H.B. (1979) "Soil liquefaction and cyclic mobility evaluation for level ground during earthquake", J. Geotech. Engr. Div., ASCE, 105, GT2, 201-225.

Seed, H.B., & Idriss, I.M. (1982) Ground motions and soil liquefaction during earthquakes: Earthquake Engineering Institute Monograph Series.